

ISMS 2016

3RD INTERNATIONAL
SYMPOSIUM ON MINE
SAFETY, SCIENCE AND
ENGINEERING

Operational and Environmental Mine Health and
Safety Practice and Innovation

Symposium Proceedings

<http://isms2016.proceedings.mcgill.ca>

August 13-19, 2016

McGill University, Montreal, CANADA

Editors: H.S. Mitri, S. Shnorhokian, M.K. Kumral, A. Sasmito, A. Sainoki



McGill



Operational and Environmental Mine Health and Safety Practice and Innovation

Published by McGill University (2016)

ISBN: ISBN 978-1-77247-005-5

EDITORS

HANI S. MITRI

SHAHE SHNORHOKIAN

MUSTAFA KUMRAL

AGUS SASMITO

ATSUSHI SAINOKI

Table of Contents

Preface	v
Organizing Committee	vi
International Advisory Committee and Editorial Board	vii
Part 1	
b-value as a criterion for the evaluation of rockburst hazard in coal mines <i>Grzegorz Mutke, Aleksandra Pierzyna, Adam Barański</i>	1
Quantitative evaluation of stope damage induced by seismic waves <i>Atsushi Sainoki, Hani S. Mitri</i>	6
Influence of weak planes on rockburst occurrence <i>Amin Manouchehrian, Ming Cai</i>	12
A model of rockburst including geological dynamic conditions and mining <i>Jun Han, Ting Ren, Tianwei Lan, Feng Zhu, Chen Cao, Hongwei Zhang, Guoshui Tang</i>	18
Rockburst experiences in Cheves Hydropower Project, Perú <i>Santiago Veyrat, Jose-Miguel Galera, Marcos Sancho, H. Andersson, W. Thoese, and, C. Rietschel</i>	24
Rockburst mitigation experiences on underground projects in the Cheves Hydropower project in the Peruvian Andes <i>Santiago Veyrat, Jose-Miguel Galera, Marcos Sancho</i>	38
Destress blasting on the border of safety pillars <i>Petr Konicek, Jiri Ptacek, Alejandro Mazaira</i>	45
Powered support selection for longwall workings in dynamic load conditions <i>Stanislaw Prusek, Sylwester Rajwa, Andrzej Walentek, Wojciech Masny</i>	54
Evolution of grouting methods for dynamic supports in broken ground <i>Francois Charette, Trond Skogseth</i>	60
Large scale panel destress blasting parametric study <i>Isaac Vennes, Hani Mitri</i>	65
Improving ground control safety in deep vein mines <i>Joseph Seymour, Donovan Benton, Michael Raffaldi, Jeffrey Johnson, Lewis Martin, Shawn Boltz, Jerald Richardson</i>	71
Numerical investigation of EDZ development around a deep polymetallic ore mine <i>Mountaka Souley, Marwan Al Heib, Vincent Renaud</i>	78
Estimating the probability of unsatisfactory performance associated with the instability of mine developments <i>Wael Abdellah, Hani Mitri</i>	84

Numerical modelling of time-dependent skin degradation of an isolated pillar <i>Atsushi Sainoki, Hani S. Mitri</i>	90
Quantitative analysis of haulage system instability in deep hard rock mines using numerical modeling <i>Shahé Shnorhokian, Bryce MacNeil, Hani Mitri</i>	96
Minimum strength required for resisting cyclic softening/failure of cemented paste backfill at early age <i>Tikou Belem, Mamert Mbonimpa</i>	102
Analysis of failure in a salt room and pillar mine <i>Farid Laouafa, Mehdi Ghoreychi</i>	108
Lessons in slope stability management from Kinross' Tasiast mine, Mauritania <i>Korhan Tasoren, Gillian Gardhouse, P.Eng., Dr. Jerry Ran, P.Eng.</i>	114
Effect of buttress on reduction of rock slope sliding along geological boundary <i>Ryota MORIYA, Daisuke FUKUDA, Jun-ichi KODAMA, Yoshiaki FUJII</i>	121
Validation of empirical rock mass classification systems for rock slopes <i>Hassan Basahel, Hani Mitri</i>	127
Application of InSAR for monitoring deformations at the Kiirunavaara Mine <i>Karola Mäkitaavola, Britt-Mari Stöckel, Jonny Sjöberg, Stephen Hobbs, Jonas Ekman, Michael Henschel, Anura Wickramanayake</i>	133
Modelling the impact of particle flow on rigid structures: experimental and numerical investigations <i>M.A. Meguid, Ge Gao, M.M. Abouelkair and M.Z. Abdelrahman</i>	140
A versatile model for the evaluation of subsidence hazards above underground extractions <i>Peter Cain, Ph.D., P.Eng., Dr. Ing. Karsten Zimmerman</i>	145
Slope stability analysis and prediction based on the limit equilibrium method of Luming Molybdenum Mine's West-I and North Region <i>HUANG Zhi-an, LIU Fang-zhe, WANG Hui, GAO Yu-kun</i>	154
Study on the similar materials simulation of the slope stability of the west- I zone in Luming Molybdenum Mine <i>Huang Zhian, YangFei, Wang Hui, Zhang Yinghua, GaoYukun</i>	159
Stability and access implications of open pit mining through old underground mine workings <i>John G. Henning</i>	165
Thermomechanical impact of Underground Coal Gasification exploitation <i>Laouafa Farid</i>	170
Escapeway Solutions <i>Allison Deadman, Steven Durkin, Vincent Lawrence</i>	176

Estimating stope vein footwall stability using various constitutive modelling techniques <i>Andrew Pyon, Atsushi Sainoki, Hani S. Mitri</i>	181
Redesigning the geometry of the Makala Coal Mine to improve safety and productivity <i>Jean-Pierre Tshibangu, Fanny Descamps</i>	187
Shear behaviour of regular and irregular rock joints under cyclic conditions <i>S. M. Mahdi Niktabar, K. Seshagiri Rao, Amit Kumar Shrivastava</i>	193
3D geological modelling method based on hybrid data model <i>Xue-xi Chen, De-fu Che</i>	199
Measurement and analysis of virgin-rock temperature in Huanren Metal Mine <i>CHANG De-qiang, LIU Jing-xian, MAO Ning, GE Shuang-you</i>	204
The tensile properties of GFRP bars at different loading rates <i>Wenxue Chen, Jun Wu, Yuzhao Jiao, Jiewen Zheng, Xue Li</i>	208
Part 2	
A definition and evaluation index system of aging mines <i>MA Hui, LIAN Huiqing, ZHU Hongjie</i>	214
Numerical simulation of thermodynamic performance in a honeycomb ceramic channel <i>Bo Lan, You-Rong Li</i>	219
Dust Dispersion Analysis Based on the Rosen-Rammler Distribution Function <i>Yao Haifei, Zhang Qun</i>	225
Fuzzy comprehensive evaluation of emergency capability of port coal storage base with G1 method <i>Siheng Sun, Guozhong Huang, LongzheJin, Yage Li, Xue Zhao</i>	231
Study on External Protective System of Waterproofing Refuge Chamber in Guilaizhuang Gold Mine <i>Shengnan Ou, Longzhe Jin, Song Li, Shu Wang, Yage Li, Zhiling Huang</i>	236
Hazard detection and comprehensive control technologies of the integrated resource coal mine goafs in China <i>Wen LI</i>	243
Multi-bed type oxidation reactor applied to the coal mine ventilation air methane <i>Weifeng Zou, Bo Lan, Jiandong Kang</i>	248
Water disaster investigation and control in coal mine of Southern China <i>LIANG Qing-hua</i>	254
The lifting and separating system for ground maneuvering rescue equipment <i>GAO Yukun, GONG Xuejiao, HUANG Zhian, ZHANG Yinghua</i>	258
Safety and stability of the maneuvering rescue platform <i>GAO Yu-kun, Ji Yu-Chen, HUANG Zhi-an, ZHANG Ying-hua</i>	264

The performance optimization experiment of a wet high-frequency vibrating grid <i>Zhang Yinghua, Liu Jia, Huang Zhian*, Gao Yukun</i>	268
Borehole docking system design for underground refuge chamber and ground maneuver rescue equipment <i>ZHANG Ying-hua, SONG Shou-yi, HUANG Zhi-an, GAO Yu-kun</i>	276
Use of the Analytic Hierarchy Process in safety control of rescue equipment <i>Zhang Yinghua, Sun Qian, Huang Zhian, Gao Yukun</i>	281
Research on new high-water solidified materials to reinforce coal and eliminate gas outburst <i>Yinghua Zhang, Peiling Zhou, Zhian Huang, Yukun Gao, Qiang Luo</i>	285
Key technologies for extinguishing large-area goaf fires in closely spaced shallow coal seams <i>Botao Qin, Quanlin Shi, Junzhe Yang, Hetang Wang, Lihui Zhang</i>	291
The assessment of emergency capability of coal mines based on AHP-fuzzy comprehensive method <i>Shu Jiao Tong, Zong Zhi Wu, Ru Jun Wang, Ying Quan Duo</i>	296
Study on local temperature controlling technology and equipment in heat disaster coal well <i>Haijun Wu, Haifei Yao, Changfu Xu, Haiyan Wang, Laizai Tan</i>	302
Effect of forming technology on oxygen supply performance of oxygen candles in refuge spaces <i>Liu Jian-guo, Jin Long-zhe, Gao Na, Wang Wei-xiang, Shen Jie</i>	308
Experimentation on a new type of mining emergency rescue relay cabin <i>Shen Jie, Gao Na, Jin Long-zhe, Fan Lin-yu, Wang Wei-xiang, Liu Jian-guo</i>	314
Chemical equipment failure probability correction model based on the Multi-layer Grey Evaluation Method <i>Yue Zhang, Wentao Yang, Yuanyue Zhu, Kai Zhang</i>	319
Mechanisms and applications of formatting unsafe behaviour motivation <i>Yuebing Zhang, Zhiliang Wang</i>	325
Examining safety and sustainability in longwall coal mining through case studies of disasters and reviewing global trends in environmental stewardship <i>Ben de Wit, Xinglong Zhao, Malcolm Scoble</i>	329
Research on Safety Incentive Model of Coal Miners and Strategy Analysis <i>Cao Qinggui, Xie Changzhen, Zhang Shouming, Zhang Sai, Liu Weihua</i>	335
A new Virtual Reality training system for underground coal mines <i>Hui Zhang, Xueqiu He, Baisheng Nie, Hani Mitri</i>	341

Study of roadside packing to go with gob-side entry retaining technology on crisp surrounding and blasting face in the Xinzhuang mine <i>Ya-ge LI, Wei-xiang WANG, Long-zhe JIN, Shu WANG, Jiang LU</i>	346
Optimization of bit nozzle parameters of reverse circulation sampling used in coal mines <i>Kang Jianning, Hu Qianting, Zhang Rui</i>	351
Electrical equipment certification in Canadian underground coal mines – problem solved? <i>Ronald (Ron) F. King, P.Eng., Peter Cain, Ph.D., P.Eng.</i>	358
Improving shovel safety using SAFEmine’s situational awareness technology <i>Marco de Werk, Todd Ruff</i>	364
An evaluation of Soma underground coal mine disaster with respect to risk acceptance and risk perception <i>H. Şebnem Düzgün, Evren D. Yaylacı</i>	368
From operational hazards to organizational weaknesses: changing the focus for improvement <i>Georges Loiselle, Dragan Komljenovic, Mustafa Kumral</i>	375
Risk management in the mining sector through complex systems <i>Maria S. Q. Domingues, Adelina L. F. Baptista, Miguel T. Diogo</i>	381
Application of Cognitive Task Analysis in mining operations <i>Serenay Demir, Elie Abou-Jaoude and Mustafa Kumral</i>	387
Avoiding workplace accidents: the importance of pre-job safety analyses <i>Colin Morrish</i>	393
Notification systems and risk management <i>Maria M. Antunes, Miguel T. Diogo, Joaquim Góis</i>	398
Full-scale fire experiments in an underground mine <i>Rickard Hansen</i>	403
Diesel exhaust exposures in an underground mine <i>Hugo Coulombe, Guillaume Lachapelle, Eve Neesham-Grenon, Stéphane Hallé, Maximilien Debia</i>	409
Liquid-solid coupling analysis of tailings dam under complex engineering conditions <i>Shuren Wang, Haiqing Zhang, Zhengsheng Zou, Xiliang Liu</i>	413
Numerical analysis of Westwood Mine tailings embankment stability during the restoration phase <i>Yaya Coulibaly, Tikou Belem, Li Zhen Cheng</i>	419
Application of an economy comparison model for mine cooling system technology <i>Miao Dejun, Chang Dehua, Tan Dongwei</i>	426

Behaviour of cable bolts in shear: experiment and mathematical modelling <i>Naj Aziz, Ali Mirza, Haleh Rasekh, Jan Nemcik, Xuwei Li</i>	432
Operating conditions of a mine fan under conditions of variable resistance <i>Zhang Yinghua, Chen Li, Huang Zhian, Gao Yukun</i>	442
Analysis of slag debris flow initiation based on laboratory tests of slag <i>Hongbiao Zeng, Hongming Yu</i>	447
Hydrogeological challenges and strategies at McArthur River Operation <i>Xiaoyou Yun, Baoyao Tang, Greg Murdock, Brian McGill, Brian Mattie</i>	453
Experimental Study on Bolt Pull-Out Property Coupled by Plate and Shotcrete <i>Xiliang LIU, Jiaqi GUO, Long Wan, Jianhua Wang</i>	459
Part 3	
Mathematical model for gas diffusion from non-homogeneous coal particles <i>Yanwei Liu, Mingju Liu, Hani S. Mitri</i>	465
Permeability prediction for coal reservoirs and reconstruction of a different scales pore-fractures network <i>Ni Xiaoming, Chen Wenxue, Li Zheyuan, Gao Xiang</i>	471
Quantitative risk assessment on large-scale oil depots of opencast coal mine <i>Ru Jun Wang, Shu Jiao Tong</i>	477
Development and realization of a coal and gas outburst simulation device <i>NIE Baisheng, HU Shoutao, LI Xiangchun, MENG Junqing, FAN Penghong</i>	482
The distribution and origin of hydrogen sulfide abnormal enrichment coal mines in China <i>Deng Qigen, Liu Mingju, Zhang Sai, Cui Xuefeng, Wen Jiejie</i>	487
Accumulation pattern of groundwater containing Hydrogen Sulfide in the southern Junggar basin in China <i>Deng Qigen, Liu Mingju, Cui Xuefeng, Wen Jiejie</i>	494
Application research on gas drainage technology at low permeability coal seam <i>Shengchu Huang, Li Zhang</i>	498
Influence of temperature on gas desorption-diffusion laws of coal particles <i>Linchao Dai</i>	503
Numerical simulation of gas migration tulle in mining-induced fractures field <i>Cao Jie, Li Minghui, Li Wenpu</i>	508
Methods of measuring the effective drainage radius of 3# coal seam in Huoerxinhe coal mine <i>Linchao Dai, Kai Wang, Jie Cao, Bo Wang</i>	514
Temperature Variation of Coal during the Gas Adsorption Process	520

<i>Tao Yang, Baisheng Nie, Xuexi Chen, Peng Chen</i>	
Statistical analysis of coal mine accidents in China from 2005-2013 <i>Xinsheng Hu, Zongzhi Wu, Rujun Wang, Yingquan Duo</i>	527
Analysis of coal crack and permeability characteristics slotted by water jet and the effect on gas outburst <i>Chunming Shen, Baiquan Lin, Lang Zhang, Dong Wang</i>	531
Numerical simulation on Gob gas migration law <i>He Ning, Xiang Cong</i>	536
Research on the negative pressure distribution law and its application for boreholes in coal seam bedding gas extraction <i>Linchao Dai, Kai Wang</i>	540
Mathematical simulation and experiment of CBM detection <i>LIANG Qing-hua</i>	547
Numerical modelling and rescaled range analysis on spontaneous combustion under surface methane drainage in a Chinese coal mine <i>Xincheng Hu, Shengqiang Yang, Wei Victor Liu, Jiawen Cai, Xiuhong Zhou</i>	552
The strength properties of fibre glass dowels used for ground control in coal mines <i>Naj Aziz, Wenxue Chen, Ali Mirzagherbanli, Jiao Yuzhao</i>	557
Numerical simulation for propagation characteristics of outburst shock wave and gas flow when outburst prevention facilities fail <i>Zhou Aitao, Wang Kai, Kong Yuyu, Liu Ang</i>	564
Influence of Fundamental Internal Parameters to Low-Temperature Critical Temperature in Coal Self-Ignition Process <i>WANG Hai-yan, YAO Hai-fei, ZHENG Zhong-ya, XU Chang-fu, ZHANG Qun, ZHU Hong-qing</i>	574
Experimental study of negative pressure gas drainage influences on coal moisture content <i>Shaojie Chen, Longzhe Jin, Xianglong Liu</i>	581
The laws of gas-solid coupling of coal-bed gas in deep high gassy coal seams <i>Zhou Aitao, Wang Kai, Shen shangkun</i>	585
Grey Correlation Model of influence factors analysis of ventilation time in single-way tunnel <i>Yang Cao, Hongguang Ji</i>	591
Numerical research on the airflow distribution in mine tunnels <i>Cui DING, Xueqiu HE, Baisheng NIE</i>	595
Application of a Ventilation Management Program for improved air quality <i>Euler De Souza</i>	600

Numerical Study of simultaneous methane and coal dust dispersion in a room and pillar mining face <i>Yueze Lu, Saad Akhtar, Agus P. Sasmito, Jundika C. Kurnia</i>	605
Reducing Heat Stress Exposure in Mines <i>Ryan Anderson, Euler De Souza</i>	611
Effect of hydrogen on explosion of methane-air mixture <i>YANG Chunli, LI Xiangchun, Xu Teng, Qu Wenzhong, Liu Yanli</i>	616
Drilling escape and rescue system in Wangjialing coal mine <i>Zhiling Huang, Longzhe Jin, Yuntong Ma, Hongmin Zhu</i>	622
Effects of immediate roof thickness on lower sub key strata movement in ends of large mining height panel <i>Chuang LIU, Huamin LI, Dongjie JIANG, Huigui LI, Junfa FENG</i>	628
Study on the performances of a protective door in coal permanent refuge havens <i>Gao Na, Jin Long-zhe, Fan Lin-yu, Shen Jie, Wang Wei-xiang, Liu Jian-guo</i>	634
Numerical modelling of the goaf: methodology and application <i>Samar S. Ahmed, Marwan ALHeib, Yann Gunzburger, Vincent Renaud, Jack-Pierre Piguet</i>	640
A coal enterprise scientific-technical progress evaluation system based on the Internet <i>Shanyang Wei, Longlong Yang, Zhongbei Li, Shiwei Ding</i>	647
Simulation of strata behaviour laws of a coal mine in Jungar Coalfield <i>Zhu Bin, Li Ge, Kou Weifeng, Li Haibin</i>	651
Goaf area exploration in Anjialing surface mine based on the C-ALS <i>WANG Jun, ZHOU You, ZHAO Ruhui</i>	658
Application of the strength reduction method in coal mine roof support design <i>Gabriel Esterhuizen, Ihsan Berk Tulu</i>	659
Numerical simulation of the migration laws of supports and surrounding rock for coal seams of large dip angle <i>Huang Zhian, Feng Caiyun, Wang Hui, Zhang Yinghua, Gao Yukun</i>	666
Theoretical analysis of support stability in large dip angle coal seam mined with fully-mechanized top coal caving <i>Zhang Yinghua, Ji Yucheng, Huang Zhian, Gao Yukun, Ji Yuchen</i>	672
Theoretical research on roof damage of the fully mechanized top-caving mining coal seam with deep dip angle <i>ZHANG Ying-hua, LUO Qiang, HUANG Zhi-an, GAO Yu-kun</i>	677
Characteristics of acoustic wave velocity variation in the process of deformation and failure of loading coal <i>LI Xiangchun, NIE Baisheng, YANG Chunli, CUI Zhe, MAO Yanjun</i>	681

Numerical Simulation Technique for Gateroad Stability Analysis under Fractured Ground Condition <i>Lishuai Jiang, Atsushi Sainoki, Hani S.Mitri, Nianjie Ma</i>	687
--	-----

Author Index	692
--------------	-----

ORGANIZING COMMITTEE

Xueqiu HE – International Chair

University of Science and Technology Beijing

Xiaolin YANG – International Chair

Henan Polytechnic University

Hani S. MITRI – General Chair

McGill University

Baisheng NIE – Technical Program Co-chair

China University of Mining and Technology Beijing

Mustafa KUMRAL – Technical Program Co-chair

McGill University

Agus SASMITO – Technical Program Stream Chair

McGill University

Longzhe JIN – Technical Program Committee

University of Science and Technology Beijing

Mingju LIU – Technical Program Committee

Henan Polytechnic University

Atsushi SAINOKI – Technical Program Stream Chair

McGill University

Shahe SHNORHOKIAN – ISMS Secretary

McGill University

Wenxue CHEN – ISMS Secretary

Henan Polytechnic University

Xiangchun LI – ISMS Secretary

China University of Mining and Technology Beijing

Na GAO – ISMS Secretary

University of Science and Technology Beijing

Monika SKONIECZNY – Tradeshow

McGill University

Isaac VENNES – Field Trips

McGill University

Andrew PYON – Workshop

McGill University

Hui ZHANG – Web site

China University of Mining and Technology Beijing

INTERNATIONAL ADVISORY COMMITTEE AND EDITORIAL BOARD

- Marwan AL-HEIB
- Victor ARAD
- Naj AZIZ
- Manoj BAGDE
- Ming CAI
- Euler DE SOUZA
- José-Miguel GALERA
- Yann GUNZBURGER
- John HENNING
- Guozhong HUANG
- Vlad KECOJEVIC
- Jun-ichi KODAMA
- Petr KONICEK
- Farid LAOUAFA
- Xiliang LIU
- Rudrajit MITRA
- Jan NEMCIK
- Vic PAKALNIS
- Jack-Pierre PIGUET
- Stanislaw PRUSEK
- Jerry RAN
- Mani Ram SAHARAN
- Malcolm SCOBLE
- Jean-Pierre TSHIBANGU
- Yongqiang YU
- Yinghua ZHANG

PREFACE

The mining industry faces significant challenges associated with the extraction of deeper ore deposits having increasingly more complex geotechnical and geological conditions. This inevitably led to much greater attention to personnel and equipment safety research and practice. In addition to this development, safety science itself has made remarkable progress in recent decades owing to leap advancements in engineering technologies, human physiology, data analysis and processing, as well as new business and organization structures. In this scope, mining, nuclear and aerospace industries allocate important resources and create initiatives to engage increasingly more safety science and research. In line with this, McGill University organized and hosted the 3rd International Symposium on Mine Safety Science and Engineering (ISMS 2016) in Montreal in collaboration with its partners, the University of Science and Technology Beijing, China University of Mining and Technology (Beijing), and Henan Polytechnic University. The symposium was held from August 13 to 19, 2106 with the theme “Operational and Environmental Mine Health and Safety Practice and Innovation”.

Essential objectives of ISMS 2016 were to discuss safety-related problems; to create awareness, synergy and recognition to mine safety; and, to ensure knowledge transfer and mobilization amongst industry practitioners, mining engineers and academics. The authors of the 119 papers in this volume of proceedings come from 12 countries – a testimony to the true international flavour of this symposium. The volume is organized in three main sections: (i) Hardrock (Seismicity and rock burst, blasting, support design, pillar and backfill stability, ground control, subsidence and slope stability); (ii) Technology (equipment, occupational health and safety, organizations and human factors); and (iii) Coal (gas and ventilation, ground control and coal mining techniques). All papers included in this set of proceedings have been peer-reviewed, edited and formatted to a uniform layout. The proceedings can be found online at

<http://isms2016.proceedings.mcgill.ca>

We would like to thank all the symposium sponsors for their generous support. We are indebted to members of the International Advisory Committee for their relentless efforts. Special thanks are due to the paper reviewers.

We sincerely hope that this volume of proceedings will be interest to mine safety practitioners, researchers and technology developers.

Editors

Hani S. Mitri

Shahe Shnorhokian

Mustafa Kumral

Agus Sasmito

Atsushi Sainoki

Part 1

Hardrock

***b*-value as a criterion for the evaluation of rockburst hazard in coal mines**Grzegorz Mutke ^a, Aleksandra Pierzyna ^b, Adam Barański ^c^a Department of Geology and Geophysics, Central Mining Institute, Katowice, Poland, 40-166^b Bobrek Mine, Polish Coal Company, Bytom, Poland^c Department of Mining Hazard, Polish Coal Company, Katowice, 40-039**ABSTRACT**

Every year, a few rockbursts with fatalities and several hundred meters of damaged excavations have occurred in the mines of the Upper Silesia Coal Basin (USCB) in Poland. This paper presents a method for assessing the levels of seismic and rockburst hazards, using continuous seismological observation in the Bobrek coal mine. This assessment is based on the study of the Gutenberg–Richter (G-R) relation for current and past mining in the coal field. According to many laboratory and field studies, the *b*-value may be an indicator of fluctuations in stress levels (Scholz, 1968; Gibowicz, 1974; 1979), and the consequent seismic hazard.

The novelty of the presented research is the development of a quantitative criterion based on *b*-value changes, calculated in moving time windows with a 1-day step, and the anomalies resulting from the comparisons of the temporal values of *b* with its average value for the past seismicity in the field of coal mining; $A_{G-R} = [(b_m - b)/b_m] \cdot 100\%$ (where b_m is the average value of *b* for the field of coal mining and *b* is the temporal value of coefficient *b*, calculated in time windows). This approach allows us to standardize the criterion to the current values of *b* in the investigated area (Table 1). In many measurement examples, high values of the temporal anomaly A_{G-R} and at the same time downwardly trending and low *b*-values before the occurrence of strong mining seismic events were documented in this paper and in studies by Pierzyna (2014). Particularly interesting results were obtained from mining and geological conditions that led to the formation of local zones of stress concentration (Dubínski, 1989), and increases in seismic activity and seismic hazard.

The *b*-value criterion is in agreement with the four basic levels of rockburst hazard used in Polish coal mines (Mutke et al., 2015).

KEYWORDS: Mining induced seismicity; *b*-value; seismic criterion

1. INTRODUCTION

The Gutenberg–Richter Law (G-R) is the most common model of a relation between the magnitude and number of seismic events (Gutenberg and Richter, 1954; Utsu, 1999). It is well documented in global earthquake seismology. Weak tremors are much more common than strong ones, and the frequency-magnitude relation takes on a logarithmic scale of the form $\log N(M) = a - b \cdot M$, where *N* is the number of seismic events with magnitude equal to or larger than magnitude *M*, *M* is the magnitude and *a* and *b* are coefficients related to seismicity.

The coefficient *b* in this law is used globally in statistical seismology to characterize and compare the levels of seismic activity in different areas of the earth's crust (Utsu, 1999; Shearer, 2009). This factor varies over time on regional or local scales (Gibowicz, 1974; 1979), and it reflects the change in the level of stress around the average value. Specifically, the *b*-value decreases prior to the occurrence of strong earthquakes (high state of stress) and increases after its occurrence (lower stress level after relaxation).

Relatively few uses of this factor to characterize the level of seismic and rockburst hazard in underground coal mines can be found in the literature (Lasocki, 1990; Holub, 1995; Fritschen, 2009; Mutke and Pierzyna, 2010; Pierzyna, 2014). The frequency-magnitude law works even down to magnitude -4.4 in deep mining (Kwiatek et al., 2011). Low *b*-values imply that strong mining seismic events prevailed in the studied set. In an assessment of rockburst hazard in Poland, strong mining tremors located close to the excavations and high stress level played fundamental roles (Mutke et al., 2015).

2. METHODOLOGY

In this work, a systematic analysis of the *b*-value and anomaly of the *b*-value, determined in time windows, was correlated with observed seismicity in time and with the geological and mining conditions.

To calculate the *b*-value in the G-R Law, applying the method of maximum likelihood has been proposed (Aki, 1965; Utsu, 1965; 1999; Marzocchi and Sandri, 2003):

$$b = (\log e) / (M_a - M_{\min})$$

where e is the base of natural logarithm, M_a is the sampling average of the magnitudes, and M_{\min} is the threshold of magnitude completeness.

The evaluation of its standard deviation in this study was based on the formula derived by Shi and Bolt (1982).

It should be emphasized that to calculate the b -value, the selection of a set of tremors is made in accordance with the principle of catalog completeness. It is identified on the basis of cumulative quantity histograms at magnitude intervals and also on the basis of the technical threshold of the seismological network capabilities in recording all seismic events.

The ongoing assessment of seismic hazard in LP No. 3/503 (backward analysis) was made by analyzing variations of the b -value, calculated in time windows with a moving 1-day step. A 20-day window was selected as optimal for the technological process (based on stationarity of the seismic process in mines (Lasocki, 1990), and the number of seismic events in a window of time (more than 30)). The useful quantitative category classifications for seismic and rockburst hazard levels provide an anomaly of the b -value, defined as follows:

$$A_{G-R} = [(b_m - b) / b_m] \cdot 100\%$$

where b is the temporal coefficient value, calculated in time windows, and b_m is the average value of b , determined for the entire catalog of seismic events previously recorded in the field panel of coal mining.

A high anomaly of the b -value should correlate with the preparation of the rock mass for the occurrence of strong mining related seismic events.

3. MONITORING SEISMICITY IN PANEL 3/503 AT THE BOBREK MINE

The field measurements and study of the b -value were performed in the Bobrek Mine, one of the deep coal mines in USCB, Poland. The database used for *back analysis* in the Bobrek Mine included seismic data as well as geological, mining, and technological data for 5 longwall panels (LP). Studies of the b -value were conducted for the seismicity during extraction of the 503 coal seam by LP No. 2 and No. 3, of the 509 coal seam by LP No. 91a and No. 92a, and of the 510 coal seam by LP No. 6 (Mutke and Pierzyna, 2010; Pierzyna, 2014). In this paper, we show a study of LP 3/503 in detail, mined from April 2009 to June 2010. Coal seam 503 was 3.0 m thick, the excavation face was approximately 350 m, and

the longwall panel was approximately 1000 m long, located 700 m below the ground surface. In total, 2996 seismic events were recorded with magnitudes ranging from $M_L = 0.1$ to $M_L = 3.8$ (M_L – local magnitude calculated using the empirical formula developed for Upper Silesia between seismic energy and magnitude calculated from the body wave: $\log E = 1.8 + 1.9 \cdot M_L$; (Dubiński and Wierzchowska, 1973)) The hypocenters of the strongest seismic events were located 300-800 m deeper than the level of the 503 coal seam (Marcak and Mutke, 2013).

Seismic monitoring in the “Bobrek-Centrum” mine was performed with a 64-channel underground seismic network (Seismological Observation System (SOS) designed by the Central Mining Institute in Katowice, Poland) consisting of 1 Hz velocity DLM2001 and DLM3D type probes. SEISGRAM and MULTILOK software were used to process and analyze the seismic data. Seismic stations were deployed underground as shown in Figure 1. The locations of the 2,996 seismic events are also shown in Figure 1.

A method for evaluating the completeness of seismic events during extraction of LP No. 3/503, due to technical reasons, involves an assumption that all seismic events will be triggered when the signal on the nearest five sensors exceeds the seismic noise level by two times. In the case of the LP No. 3/503 contour, the most distant of the five seismic sensors is located at a distance of 700 m. In such conditions, it is possible to obtain *catalog completeness* of mining tremors of local magnitude $M_L = 0.6$ and higher. For the whole area of the Bobrek Mine, the seismic *catalog completeness* begins from magnitude $M_L = 0.9$.

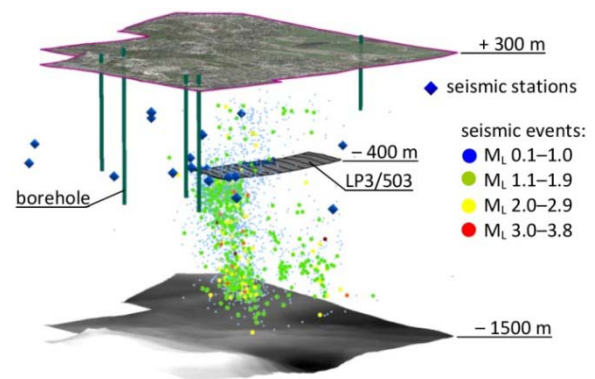


Figure 1: Bobrek Mine field site – deployment of seismic sensors around LP 3/503 (blue diamonds) and location of the mining tremors hypocenters (circles). Color of the circle indicates the size of the magnitude.

4. GUTENBERG-RICHTER RELATIONS FOR THE BOBREK MINE

4.1 The mean *b*-value for seismicity induced by mining in the Bobrek Mine in the years 1990-2013

The calculation of the frequency-magnitude relation at the Bobrek Mine was made for the seismic events of magnitude $M_L \geq 0.9$ recorded during the 1990-2013 years. The seismic catalog included 15700 seismic events.

The results of the GR distribution for the Bobrek Mine are illustrated in Figure 2. It is apparent that, for the higher magnitudes, i.e., in the range of 2-3.8, a slight downward deviation of the empirical values occurs from the theoretical straight line of the Gutenberg-Richter law. The average *b*-value amounted to $b_m=1.34$ for the 23-year period of mining and will be used as a reference for further calculation of rockburst hazard in the Bobrek Mine.

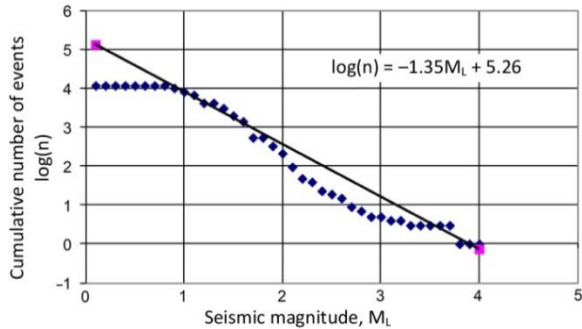


Figure 2: The cumulative distribution of seismic events above magnitude $M_L=0.9$ registered in the Bobrek Mine in the 1990-2013 years.

4.2 The changes in the *b*-value and anomaly of the *b*-value during the extraction of coal in panel No. 3/503

The mining in LP No. 3/503 induced very high seismicity with magnitudes higher than $M_L=3.5$. The coefficient of *b* for this seismicity reached a value of 0.99 and was 27% lower than the *b*-value obtained for mining in the whole area of the Bobrek Mine in the 1990-2013 years. This means that the mining in LP No. 3/503 took place under potentially higher seismic hazard than past mining in the Bobrek Mine. The main reasons for the high level of seismic hazard in LP No. 3/503 are due to mining in the axis of Bytom through the zone where there is high tectonic stress and in the local zones of stress concentration resulting from past mining conditions (remnants, edges).

The ongoing assessment of the seismic hazard level in LP No. 3/503 was made by analyzing fluctuations of the *b*-value calculated in 1-day time windows. The 1-day moving variations of the *b*-value

and 6 strongest tremors during the extraction of coal in LP No. 3/510 are plotted in Figure 3. The occurrence dates of these strong seismic events are indicated by arrows. The values of the *b* coefficient during the strongest seismic events ranged from 0.55 up to 0.9 and were much lower than the average value of $b_m=1.35$ calculated for seismicity in the Bobrek Mine.

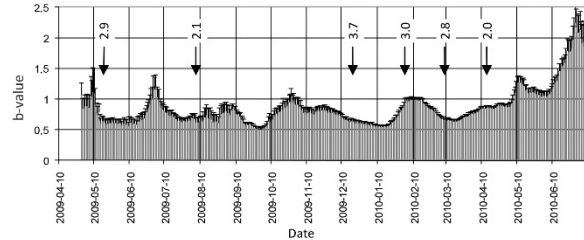


Figure 3: The changes in the *b*-value of the Gutenberg-Richter law, calculated in a time window of 20 days with a 1-day moving step in LP No. 3/503 during the period of April 2009 – June 2010. The darker lines represent the error bars calculated for every window's data using the equation derived by Shi and Bolt (1982). The strongest tremor of magnitude $M_L=3.7$ occurred on 16.12.2009 while the coefficient of *b* reached the lowest level.

They were also lower than the global average values of the *b* factor for seismicity, adopted in the literature as 1.0 for the world (Shearer, 2009). By referring these values to b_m , it can be found that the seismic anomaly ranged from 59% to 33%. The study of LP 3/503 clearly indicates that strong mining induced seismic events occurred when the observed *b*-value level was low and the anomaly of *b* was very high.

Particularly interesting results were obtained by Dubiński (1989) for representative mining and geological situations that led to the formation of local zones of stress concentration and, as a consequence, an increase in seismic activity and seismic hazard. In Figure 4, an example of mining conditions' influence on the distribution of the *b*-value is shown. The *b*-values were calculated in moving windows of time during the passage of LP No. 3/503 in the zone of impact of the 501 coal seam edge, located 27 meters higher. Lower values of *b* were obtained when the extracted face of LP No. 3/503 was on the unmined side of coal seam 501. During this time, the seismic activities increased significantly. The GR seismic anomaly reached a very high value, $A_{G-R} = 59\%$.

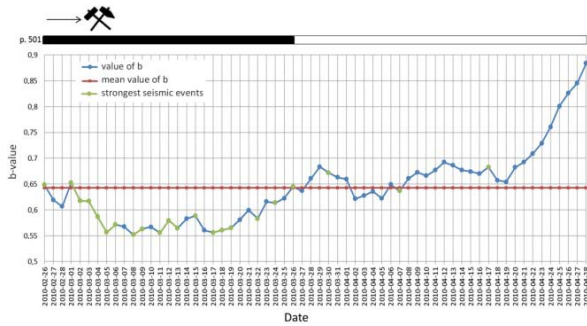


Figure 4: The distribution of the b -values obtained during the passage of the LP 3 coal face under the edge of the 501 coal seam.

5. CRITERION OF ROCKBURST HAZARD IN THE BOBREK MINE

The novelty of the results of the research presented lies in the development of quantitative criteria based on the analysis of the G-R distribution in a moving time window with a 1-day step, taking into account the anomalies of the b -value. This approach allows us to standardize criterial values to the temporal value of b calculated in time windows. In many examples described in the paper, high values of the anomaly of coefficient b and downwardly trending low b -values were documented before the occurrence of the strongest tremors. The b -value criterion corresponds to the four levels of rockburst hazard used in Polish mines (Table 1). In cases when the b -value criterion is used, it is easier to select and monitor the effectiveness of prevention activities. The primary prevention activities are based on the performance of blasting and rock fracturing ahead of the LP face line to induce stress relaxation in the area of mining. Another preventive action was the selection of appropriate support in the zones with high seismic hazards.

Table 1: b -value empirical criterion of rockburst hazard in the Bobrek coal mine.

Level of rockburst hazard	Anomaly of b -value, %	b -value condition
lack	$A_{G-R} < 0$	$b > b_m$
low	$25 > A_{G-R} \geq 0$	$b \leq b_m$
medium	$50 > A_{G-R} \geq 25$	$b < b_m$
high	$A_{G-R} \geq 50$	$b < b_m$

6. DISCUSSION

The results indicate the usefulness of b -value changes in moving time windows and the anomaly coefficient of b for evaluating the preparation of rock mass to induce strong seismic events in the Bobrek Mine.

As a result of the work described in this article, calculations were presented that led to the formulation of a local criterion for the ongoing assessment of seismic and rockburst hazards in the Bobrek Mine. This quantitative criterion, using the b -value and anomaly of b calculated in moving time windows, is novel in the field of the assessment of seismic and rockburst hazards in deep coal mines.

Documenting and analyzing the results of observations under the geological and mining conditions that cause stress concentration are especially important from the point of view of safe mining. This study presents the results of calculated distributions of b -values and anomaly of b for the following typical and frequently encountered mining situations and geological conditions:

- mining within the impact of coal seam edges,
- mining within the influence of remnants,
- mining within the influence of the fault,
- mining within the influence of tectonic stresses throughout.

Good results can be obtained when several indicators are used to assess the seismic hazard level (Mutke et al., 2015).

7. CONCLUSIONS

The use of the G-R law provides a reliable evaluation of potential areas of high seismicity in underground coal mining. The assessment is performed on the basis of estimating the b -value and its distribution for the current mining extent, using 1-day moving time windows.

Seismicity in mines primarily depends on the geological and mining conditions under which the operation is conducted. Studies have shown effective efforts to link changes of the b -value with various geological and mining conditions prone to stress concentration (e.g., edges of old exploitations, remnants, faults or other geological structures).

The novel result of this research lies in the development of a quantitative criterion of rockburst hazard assessment in the Bobrek Mine, elaborated on the basis of the b -value and on the anomaly of the b -value.

High anomalies of the b , the low value of b and a downward trend in b were documented before high seismic activity and the strongest seismic events. The b -value criterion was developed in accordance with the "complex criterion", which corresponds to the four levels of rockburst hazard assessment and is one of several seismological criteria used in Polish mines. The diverse mechanisms of seismic events in deep mining require the use of various seismic indicators.

The method presented in this paper can be used to assess seismic hazard in deep mines after

verification of the quantitative level of the b -value criterion. This should be done through analysis of former seismic data due to the variety of geological and mining conditions, i.e., *back analysis*. It should lead to improvement in the effectiveness of rockburst prevention and increases in the safety of the miners.

8. REFERENCES

- Aki K. (1965). Maximum likelihood estimate of b in the formula $\log N = a - bM$ and its confidence limits. *Bull. Earthquake Res. Inst. Tokyo Univ.*, 43, pp. 237-239.
- Dubiński J. (1989). Sejsmiczna metoda wyprzedzającej oceny zagrożenia wstrząsami górnictwymi w kopalniach węgla kamiennego. *Prace Naukowe GIG – seria dodatkowa. (The seismic profiling in seam method to mining tremors hazard assessment in coal mines. Scientific Work of GIG).* (in Polish)
- Dubiński J. and Wierzchowska Z. (1973). Metody obliczeń energii wstrząsów górotworu na Górnym Śląsku. *Prace GIG – komunikat 591. (Methods for calculation of seismic energy of mine tremors in Upper Silesia).* (in Polish).
- Fritschen R. (2009). Mining-induced seismicity in the Saarland, Germany. *Pure and Applied Geophysics* 167, pp 77-89. DOI 10.1007/s00024-009-0002-7.
- Gibowicz S. J. (1974). Frequency-magnitude, depth, and time relations for earthquakes in an island arc: North Island, New Zealand, *Tectonophysics* 23, p. 283.
- Gibowicz S. J. (1979). Space and time variations of the frequency-magnitude relation for mining tremors in the Szombierki Coal Mine in the Upper Silesia, Poland. *Acta Geophys. Pol.* 27, pp. 39-49.
- Holub K. (1995). Analysis of b -value in the frequency-energy distributions. *Publ. Inst. Geophys. Pol. Acad. Sc. M-19 (281)*, pp 153-162.
- Kwiatk G., Plenkers K., Nakatani M., Yabe Y., Dresen G. (2011). Frequency Magnitude characteristics down to magnitude -4.4 induced seismicity recorded at Mponeng Gold Mine, South Africa. *Bull. Seism. Soc. Am.*, Vol.100. No. 3, pp. 1165-1173.
- Lasocki S. (1990). Predykcja silnych wstrząsów górniczych. Prediction of strong mining tremors. *Zesz. Nauk. AGH. ser. Geofizyka Stosowana nr. 7. (1360)*, Kraków-AGH, 110 p.(in Polish)
- Marzocchi W., Sandri L. (2003). A review and new insights on the estimation of the b -value and its uncertainty. *Annals of Geophysics*, vol. 46, No 6, pp. 1271-1282.
- Mutke G. and Pierzyna A. (2010). Czasowe zmiany parametru „ b ” relacji Gutenberga-Richtera dla oceny zagrożenia sejsmicznego w ścianie 2 i 3 w pokładzie 503 w kopalni „Bobrek-Centrum”. *(Temporary changes the b -value of Gutenberg-Richter relationship to the assessment of seismic hazard in the longwall panels No. 2 and No. 3 in coal seam No. 503 in the mine "Bobrek-Centrum").* *Prace Naukowe GIG. Górnictwo i Środowisko. Kwartalnik Nr 4/3/2010*, pp. 298-309. (in Polish)
- Marcak H. and Mutke G. (2013). Seismic activation of tectonic stresses by mining. *Journal of Seismology*. Vol. 17/4, pp.1139-1148. DOI 10.1007/s10950-013-9382-3.
- Mutke G., Dubiński J., Lurka A. (2015). New criteria to assess seismic and rock burst hazard in coal mines. *Archive of Mining Sciences*, Vol.60, No.3., pp. 743-760. DOI: 10.1515/amsc-2015-0049. Electronic version: <ftp://mining.archives.pl>.
- Pierzyna A. (2014). Ocena stanu zagrożenia wstrząsami górnictwymi z wykorzystaniem relacji Gutenberga-Richtera (*Assessment of the State of Mining Tremors Hazard Using the Gutenberg-Richter Relationship*). PhD Thesis. (in Polish)
- Scholz C. (1968). The frequency-magnitude relation of microfracturing in rock and its relation to earthquakes. *Bull. Seism. Soc. Am.* 58, pp. 399-415.
- Shearer P.M. (2009) *Introduction to seismology*. Cambridge University Press. 396p. ISBN 978-0-521-70842-5.
- Shi Y. and Bolt B. A. (1982) The standard error of the magnitude-frequency b -value, *Bull. Seismol. Soc. Am.*, 72, pp. 1677– 1687.
- Stec K. (2007). Characteristic of seismic activity of the Upper Silesian Coal Basin in Poland. *Geophysical Journal International* ,168, pp. 757-768.
- Utsu T. (1965). A method for determining the value of b in formula $\log N = a - bM$, showing the magnitude-frequency relation for earthquakes. *Geophys. Bull. Hokkaido Univ.* 13.
- Utsu T. (1999). Representation and Analysis of the earthquake size distribution: a historical review and some new approaches. *Pure and Applied Geophysics*. No. 155, pp. 509-535.

Quantitative evaluation of stope damage induced by seismic waves

Atsushi Sainoki *, Hani S. Mitri

Department of Mining and Materials Engineering, McGill University, Montreal, Canada, H3A 0E8

ABSTRACT

In the present study, a methodology to evaluate damage around underground openings due to seismic waves arising from mining-induced fault-slip is proposed. First, expressions for an associated flow rule with a failure criterion developed for biaxial stress conditions are derived, which are newly implemented into FLAC3D code. With the code, stope extraction is simulated using a 3D mine-wide model encompassing a fault running parallel to a steeply dipping orebody. The failure criterion for biaxial stress conditions is applied to only the rockmass in the vicinity of stopes within the hanging wall. After extracting stopes in the orebody, mining-induced fault-slip is simulated in dynamic conditions, considering its trigger mechanism, i.e., stress drop caused by instantaneous shearing of fault surface asperities, using Barton's shear strength model. Damage to the rockmass caused by seismic waves is then evaluated with the increase in plastic strain. The proposed methodology takes into account the mechanism of mining-induced fault-slip, propagation of seismic waves, biaxial stress conditions on the surface of openings, and plastic strain as damage criterion.

KEYWORDS: stability of mine opening; mining-induced fault-slip; seismic waves; biaxial stress condition

1. INTRODUCTION

Stress redistribution caused by mining activities, such as stope extraction, can lead to the reactivation of pre-existing faults. As a result, fault-slip can occur, producing seismic waves. When the seismic waves hit underground openings, rockbursts could take place. Thus, in order to ensure a safe working environment and stable production, it is paramount to understand the mechanism of mining-induced fault-slip and elucidate the relation between the seismic waves and the damage to mine openings.

It is common that the numerical modelling of mining-induced fault-slip is conducted with the conventional Mohr-Coulomb failure criterion in static conditions (Hofmann and Scheepers, 2011). Importantly, the method does not replicate the actual mechanism of mining-induced fault-slip. In reality, the surface of faults in underground mines is undulating and has asperities that interlock with each other. Instantaneous stress drop caused by the shearing of such asperities, which is related to the occurrence of mining-induced fault-slip, cannot be accurately modelled with the conventional method. Furthermore, the numerical analysis in static conditions is incapable of producing seismic waves arising from fault-slip; hence it is impossible to evaluate damage to nearby mine openings inflicted by the seismic waves.

Recently, Sainoki and Mitri (2014a) have developed the methodology to simulate mining-induced fault-slip with Barton's shear strength model (Barton, 1973) in dynamic conditions, considering

the stress drop induced by asperity shear. The methodology is capable of modelling mining-induced fault-slip in a more robust way than the use of the Mohr-Coulomb failure criterion. Furthermore, as the analysis is performed in dynamic conditions, the propagation of seismic waves can be simulated. Although a number of studies have been undertaken about the effect of seismic waves on the stability of an underground opening, studies especially focused on the effect of seismic waves arising from mining-induced fault-slip have not been undertaken sufficiently. Recently, Wang and Cai (2015) examine the effect of seismic waves on an excavation while considering a point source of a fault-slip event, but the magnitude of fault-slip is an input parameter, that is, it fails to estimate damage induced by fault-slip that could take place under the ambient stress state.

Another important aspect to be considered is that a failure criterion around an opening where stress state is biaxial. It has been demonstrated that the consideration to the intermediate stress is required (Yun et al., 2010) in order to predict the failure of rock under biaxial stress conditions, where spalling resulting from extension fractures is expected (Diederichs, 2007). Due to the difficulty of considering or implementing failure criteria for such biaxial stress conditions, to the author's knowledge, such failure criteria have never been applied in the numerical modelling of underground openings.

In light of a literature review, the present study is focused on estimating the damage around an underground opening induced by seismic waves

*Corresponding author – email: atsushi.sainoki@mail.mcgill.ca

arising from mining-induced fault-slip whilst considering the failure of rockmass under biaxial stress conditions. The fault-slip is modelled in static and dynamic conditions whilst considering the asperity shear as its source mechanism, and damage induced by the seismic waves to a stope in a deep hard rock mine is evaluated whilst taking into account the failure under biaxial stress conditions.

2. METHODOLOGY

2.1 Constitutive model for fault

As discussed in the introduction, the effect of fault surface asperities is taken into consideration with the Barton's shear strength model (Barton 1973), which is expressed as follows:

$$\tau_{\max} = \sigma_n \tan \left[JRC \log_{10} \left(\frac{JCS}{\sigma_n} \right) + \phi_b \right] \quad (1)$$

where τ_{\max} and σ_n are the maximum shear strength and the normal stress acting on a fault; and JRC, JCS and ϕ are joint roughness coefficient, joint wall compressive strength, and friction angle, respectively. Comparison of Barton's shear strength model with the classical Mohr-Coulomb model is shown in Figure 1. As can be seen in the figure, the shear strength calculated from Barton's model is invariably greater than that from the Mohr-Coulomb model.

Barton's shear strength model is implemented into the ubiquitous joint model of FLAC3D (Itasca, 2009). The implementation procedure is based on the plastic flow rule, i.e., the increment of plastic strain is determined with the derivative of potential function with respect to its stress components and a scalar variable derived from the consistency condition. The detailed procedure of the implementation is provided in Sainoki and Mitri (2014a). In order to simulate fault-slip triggered by the shearing of fault surface asperities, JRC is instantaneously decreased during a dynamic analysis, which is described in more detail later.

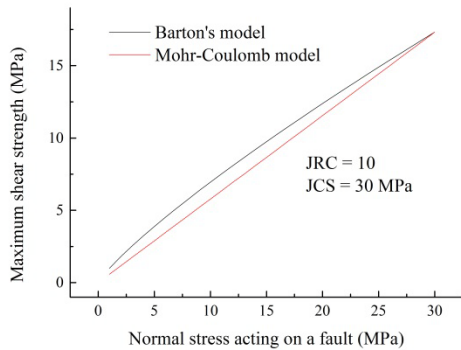


Figure 1: Barton's shear strength model.

2.2 Failure criterion under biaxial stress state and its implementation to FLAC3D

Yun et al. (2010) perform biaxial tests for several types of rock and establish a failure criterion under biaxial stress conditions, which are the stress conditions that take place on the surface of underground openings. The failure criterion is expressed as follows:

$$\frac{\sigma_1}{\sigma_c} = A + B \frac{\sigma_2}{\sigma_c} + C \left(\frac{\sigma_2}{\sigma_c} \right)^2 \quad (2)$$

where σ_1 , σ_2 and σ_c are the maximum compressive stress, intermediate stress and uniaxial compressive strength (UCS), respectively; and A , B , and C are material constants. In order to implement the equation as a yield criterion into FLAC3D, compression needs to be defined as a negative quantity and the equation is multiplied by UCS, consequently giving the following equation:

$$F = \sigma_1 + A\sigma_c - B\sigma_2 + C \frac{(\sigma_2)^2}{\sigma_c} \quad (3)$$

Note that compression has a negative quantity in Equation (3). Following the same procedure shown in Sainoki and Mitri (2014a), the scalar variable that determines plastic strain increments is expressed as follows:

$$\lambda = \frac{\{\partial F / \partial \boldsymbol{\sigma}\}^T [D] \{\Delta \boldsymbol{\epsilon}\}}{\{\partial F / \partial \boldsymbol{\sigma}\}^T [D] \{\partial g / \partial \boldsymbol{\sigma}\}} \quad (4)$$

where $[D]$ is an elastic matrix that relates strain with stress, and $\Delta \boldsymbol{\epsilon}$ is a strain increment vector. In the present study, an associated flow rule is assumed. The derivatives of the yield function with respect to each stress component are as follows:

$$\frac{\partial F}{\partial \sigma_1} = 1 \quad (5)$$

$$\frac{\partial F}{\partial \sigma_2} = -B + 2C \frac{\sigma_2}{\sigma_c} \quad (6)$$

$$\frac{\partial F}{\partial \sigma_3} = 0 \quad (7)$$

Then, the increments of plastic strain follow the plastic flow rule as follows:

$$\{\Delta \boldsymbol{\epsilon}^p\} = \lambda \left\{ \frac{\partial g}{\partial (\boldsymbol{\sigma})} \right\} \quad (8)$$

where $\Delta \boldsymbol{\epsilon}^p$ is a plastic strain increment vector, and g is plastic potential. As the plastic strain increments do not contribute to the stress increments, the stress correction to be made at each step during the iterative analysis of FLAC 3D is expressed as follows:

$$\{\Delta \boldsymbol{\sigma}\} = -\lambda [D] \left\{ \frac{\partial g}{\partial (\boldsymbol{\sigma})} \right\} \quad (9)$$

Figure 2 shows the failure criterion of granite under biaxial stress conditions derived from regression analysis (Yun et al. 2010). The material

constants, A , B , and C in Equation (3) are 0.998, 1.873, and -1.533, respectively. The present study uses the material constant of granite, although the rock type to which the failure criterion is applied is norite. Both norite and granite are hard rocks.

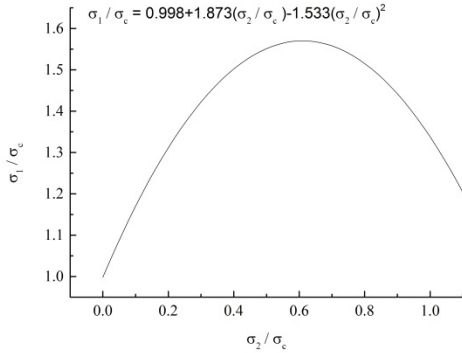


Figure 2: Failure criterion of granite under biaxial stress conditions.

2.3 Numerical model description

The present study focuses on an underground mine with a fault running parallel to a steeply dipping, tabular orebody. Such tabular orebodies are frequently encountered in hard rock mines in Canada and are extracted with sublevel stoping methods (Zhang and Mitri, 2008). Figure 3 depicts a numerical model encompassing such geological structures. As can be seen in the figure, the height, width, and length of the model are 300 m, 332 m, and 300 m, respectively. The dimensions are basically the same as that analyzed by Sainoki and Mitri (2014a), who determined that the effect of the external boundaries on the stress state around the orebody and the fault is negligible. The fault runs parallel to the orebody and steeply dips at 80° . Dense meshes are generated near the orebody and the fault in order to simulate stress re-distribution caused by mining activities as accurately as possible, while mesh density decreases towards the model outer boundaries. The total numbers of zones and grid points in the model are 215040 and 230643, respectively.

Stopes are modelled in the orebody and extracted according to the mining sequence as per sublevel stoping method with delayed backfill. Figure 4 shows stope dimensions and the mining sequence. It can be seen from the figure that each sublevel contains two stopes. In total, 18 stopes are designed. The mining sequence starts from the bottom and proceeds upwards. For each sublevel, the stopes on the hanging wall side are extracted first. As for dimensions of the stopes, the height is 30 m and the strike length is 200 m as shown in Figure 4(a) and (b), respectively. As a large amount of extraction of

orebody induces regional stress re-distribution that eventually triggers fault-slip, such long stope strike length is adopted rather than extracting numerous stopes on each level. Note that the stopes are backfilled immediately after the extraction.

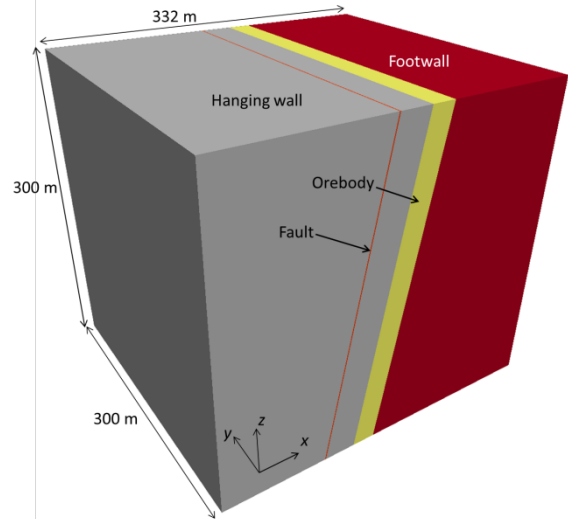


Figure 3: Isometric view of numerical model analyzed encompassing a fault running parallel to the orebody.

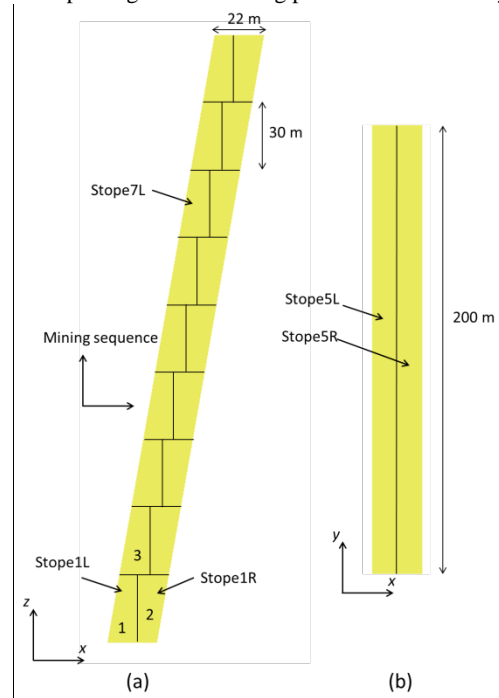


Figure 4: Stopes modelled within the orebody and mining sequence as per sublevel stoping method: (a) cross-section, (b) plan view at $z = 150$ m.

2.4 Analysis procedure

First, static analyses are performed, in which the stopes in the orebody are extracted and backfilled in accordance with the mining sequence after simulating in-situ stress state. The stope extraction is continued

until Stope7L, at which point the fault is adequately unclamped, consequently increasing potential for fault-slip sufficiently as shown in the study (Sainoki and Mitri, 2014b). Subsequently, based on the stress state after extracting stope7L, dynamic analysis is conducted. At the beginning of the dynamic analysis, the boundary condition is changed to viscous in order to prevent seismic waves arising from fault-slip from reflecting on the boundaries. At the same time, the stress state on the fault is examined, and then for the area where plastic shear movements are taking place along the fault, the JRC and friction angle of the fault are decreased, thereby inducing an instantaneous stress drop that drives fault-slip. The decrease in JRC represents shearing of fault surface asperities, while the reduction in friction angle denotes the transition from static to kinetic friction. At each step during the dynamic analysis, the stress state on the fault is checked and the change in the mechanical properties is performed if the conditions are satisfied. In this way, fault-slip is driven during the dynamic analysis.

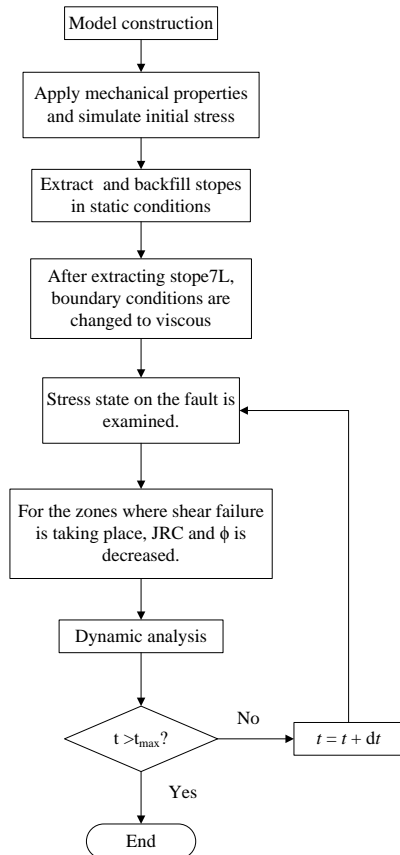


Figure 5: Analysis procedure for static and dynamic analyses.

2.5 Mechanical properties of rockmass and fault

Mechanical properties of the rockmasses are derived from the case study (Henning, 1998).

According to the study, rock types for the hanging wall, orebody, and footwall are rhyolite tuff, massive sulphide, and rhyolite, respectively, and the mechanical properties estimated from laboratory experiments are converted to those for rockmasses with the rockmass rating system proposed by (Bieniawski, 1989). Table 1 lists deformation modulus, E , cohesive strength, C , friction angle, ϕ , unit weight, γ , tensile strength, σ_T , and dilation angle, ψ . Note that the tensile strength is assumed to be one-tenth of the uniaxial compressive strength calculated from the cohesion and friction angle (Tesarik et al., 2003) and the dilation angle is assumed to be one-fourth of the friction angle (Hoek and Brown, 1997) except that for the backfill (Traina, 1983).

Table 1: Mechanical properties of rockmass and backfill.

	Hanging wall	Ore	Footwall	Backfill
E (GPa)	31	115	49	2.5
C (MPa)	2.6	11.5	4.3	0.1
ϕ (°)	38	48	39	35
γ (kN/m ³)	25.5	25.5	25.5	23.0
σ_T (MPa)	1.1	5.9	1.8	0.3
ψ ()	9.3	12.0	9.5	0.0

The mechanical properties of the fault that are applied to the ubiquitous joint model are listed in Table 2. The modulus of elasticity is set to one-tenth that of the hanging wall. According to Barton and Choubey (1977), basic friction angles of typical rocks range from 21° to 38°. The adopted value is an intermediate value of the range. Likewise, typically, JRC ranges from 0 to 20 (Barton, 1973), thus giving the intermediate value of 10. Regarding the dynamic friction angle, ϕ_d , the same value as that used by Sainoki and Mitri (2014a) is applied. It should be noted that the dynamic friction angle is applied to zones where the shear stress acting on the fault reaches the maximum shear strength during the dynamic analysis.

Table 2: Mechanical properties of a fault.

E (GPa)	ϕ (°)	JRC	ϕ_d (°)	γ (kN/m ³)
3.1	30	10	15	25.5

Regarding the material constants in Equation (2), the influence of geological conditions is taken into account with RMR (Bieniawski, 1989). Specifically, the equation proposed by Mirti (1994) is applied to B and C . As a result, the two parameters, B , and C , are decreased to 0.79, and -0.65, respectively. Regarding parameter A , it remains the same because UCS in the equation is directly decreased with the Hoek-Brown parameter s (Hoek and Brown, 1997).

3. RESULTS AND DISCUSSION

Figure 6 shows the particle velocity (PV) of grid points during the dynamic analysis in the sectional view at $y = 150$ m as well as the extent of fault-slip on the fault 0.4 s after the onset of the analysis. Note that the white-colored region in the figure is Stope7L. The propagation of seismic waves arising from the fault-slip can be clearly seen from the figure. Figure 6(a) shows PV after 0.01 s. It is found that extremely high PV exceeding 1 m/s takes place in the vicinity of the fault. As time goes by, regions with relatively high PV move away from the fault, indicating the propagation of seismic waves. After 0.04 s, ground motion occurs in extensive regions as a result of the wave propagation. At the same time, the maximum PV in the section decreases to 0.5 m/s due to wave attenuation. Note that the present study adopts the local damping system embedded in FLAC3D, assuming a local damping coefficient of 5 %.

Comparison of PV amongst the different stages suggests that the most intensive PV takes place near the stope after 0.02 s. Afterwards, the magnitude of PV near the stope continuously decreases due to the wave attenuation and propagation. Thus, the damage induced by the seismic waves is evaluated at the stage, i.e., 0.02 s after the onset of dynamic analysis.

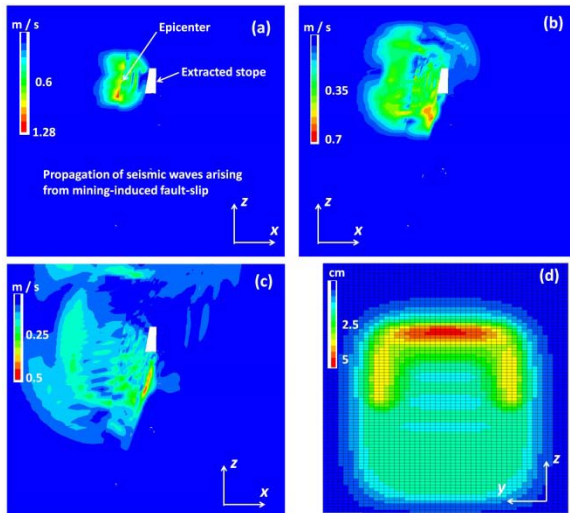


Figure 6: Particle velocity (PV) in the sectional view of the model at $y = 150$ m: (a) 0.01 s after the onset of the dynamic analysis, (b) 0.02 s, (c) 0.04 s, and (d) extent of fault-slip on the fault after 0.04 s.

In the present study, damage to the rockmasses is evaluated with the ratio of plastic strain to elastic strain as shown in Figure 7. The quantity or its variations are widely employed to evaluate damage. For instance, its inverse is used as the elastic damage model (Zhu et al., 2014).

Figure 8 shows damage induced solely by the seismic waves arising from fault-slip, i.e., damage due to the plastic strain induced by the extraction of stope is subtracted. It is interesting that damage does not increase uniformly in the region between the stope and the fault. For instance, a noticeable increase in damage can be observed within the following three locations: backfill under the stope, the hanging wall, and the upper part of the stope. Detailed discussion on the reason why the discrepancy in damage occurs is not made in the present study, but it is speculated that the concentration of damage is attributed to the state of stress before the fault-slip takes place and PV at the moment when the damage is computed. Hence, the distribution of damage might change at some degree if the damage is computed at different elapsed time. Note that emphasis should be placed on the developed methodology to evaluate damage induced by seismic waves quantitatively that considers the mechanism of mining-induced fault-slip.

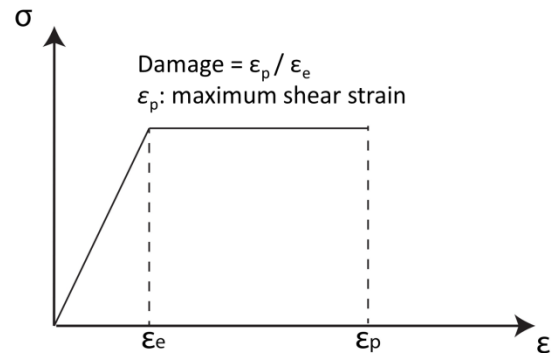


Figure 7: Schematic illustration to show damage calculation.

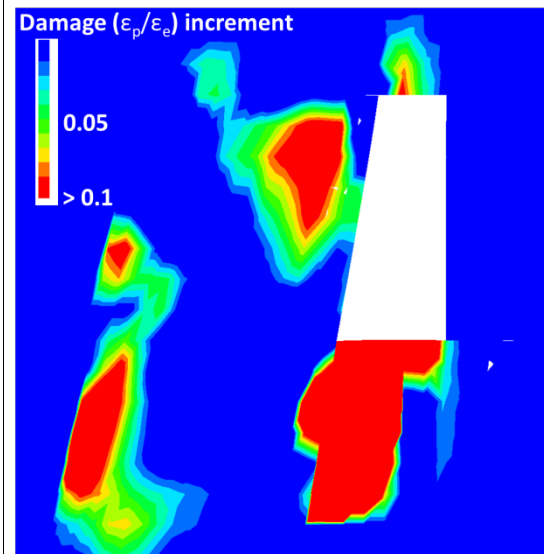


Figure 8: Damage induced by seismic waves.

4. CONCLUSIONS

The present study proposes a methodology to evaluate damage induced by seismic waves arising from fault-slip. In order to replicate the actual mechanism of mining-induced fault-slip, the effect of fault surface asperities is taken into account, whereby fault-slip is driven in dynamic conditions by an instantaneous stress drop due to the shearing of the asperities. The dynamic analysis enables the observation of the propagation of seismic waves, i.e., particle velocity, at given elapsed time after the onset of fault-slip. A methodology to evaluate damage induced by the seismic waves is proposed. It is then demonstrated that damage does not distribute uniformly around the stope. The proposed methodology helps to identify locations where noticeable damage takes place and to estimate the severity of the damage.

5. ACKNOWLEDGEMENT

This work is financially supported by a grant by the Natural Science and Engineering Research Council of Canada (NSERC) in partnership with Vale Ltd – Sudbury Operations, Canada, under the Collaborative Research and Development Program. The authors are grateful for their support.

6. REFERENCES

Barton, N. (1973). Review of a new shear-strength criterion for rock joints *Engineering Geology*, Volume 7, pp. 287-332

Barton, N., & Choubey, V. (1977). The shear strength of rock joints in theory and practice. *Rock Mechanics*, Volume 10, pp. 1-54

Bieniawski, Z. T. (1989). *Engineering rock mass classifications*. New York: Wiley.

Diederichs, M.S. (2007). The 2003 Canadian Geotechnical Colloquium: Mechanistic interpretation and practical application of damage and spalling prediction criteria for deep tunnelling. *Canadian Geotechnical Journal*, Volume 44, pp. 1082-1116.

Henning, J. (1998). *Ground control strategies at the bousquet 2 mine*. (Master), McGill University, Montreal, QC, Canada.

Hoek, E. (2007). *Practical rock engineering*.

Hoek, E., & Brown, E.T. (1997). Practical estimates of rock mass strength. *International Journal of Rock Mechanics and Mining Science*, Volume 34, No. 8, pp. 1165-1186.

Hofmann, G.F., & Scheepers, L.J. (2011). Simulating fault slip areas of mining induced seismic tremors using static boundary element numerical modelling. *Mining Technology*, Volume 120, No. 1, pp. 53-64.

Itasca. (2009). *FLAC3D - fast Lagrangian analysis of continua (Version 4.0)*. U.S.A.: Itasca Consulting Group Inc.

Mitri, H.S., Edrissi, R., & Henning, J. (1994). Finite element modelling of cable-bolted stopes in hardrock ground mines. Paper presented at the SME Annual Meeting, Albuquerque, New Mexico.

Sainoki, A., & Mitri, H.S. (2014a). Dynamic modelling of fault slip with Barton's shear strength model. *International Journal of Rock Mechanics and Mining Science*, Volume 67, pp. 155-163

Sainoki, A., & Mitri, H. (2014b). Evaluation of fault-slip potential due to shearing of fault asperities. *Canadian Geotechnical Journal*, Volume 52, No. 10, pp. 1417-1425.

Tesarik, D.R., Seymour, J.B., & Yanske, T.R. (2003). Post-failure behaviour of two mine pillars confined with backfill. *International Journal of Rock Mechanics and Mining Science*, Volume 40, No. 2, pp. 221.

Traina, L.A. (1983). *Experimental stress-strain behaviour of a low strength concrete under multiaxial states of stress*. Kirtland Air Force Base, NM: Air Force Weapons Laboratory.

Wang, X., & Cai, M. (2015). Influence of wavelength-to-excavation span ratio on ground motion around deep underground excavation. *Tunnelling and Underground Space Technology*, Volume 49, pp. 438-453.

Yun, X., Mitri, H.S., Yang, X., & Wang, Y. (2010). Experimental investigation into biaxial compressive strength of granite. *International Journal of Rock Mechanics and Mining Science*, Volume 47, pp. 334-341.

Zhang, Y., & Mitri, H. (2008). Elastoplastic stability analysis of mine haulage drift in the vicinity of mined stopes. *International Journal of Rock Mechanics and Mining Science*, Volume 45, pp. 574-593.

Zhu, W.C., Wei, C.H., Li, S., Wei, J., & Zhang, M.S. (2013). Numerical modeling on destress blasting in coal seam for enhancing gas drainage. *International Journal of Rock Mechanics and Mining Science*, Volume 59, pp. 179-190.

Influence of weak planes on rockburst occurrence

Amin Manouchehrian, Ming Cai *

Bharti School of Engineering, Laurentian University, Sudbury, Canada, P3E 2C6
MIRARCO, Laurentian University, 935 Ramsey Lake Road, Sudbury, Canada P3E 2C6
State Key Laboratory of Geomechanics and Geotechnical Engineering, Institute of Rock and Soil Mechanics, Chinese Academy of Sciences, Wuhan, 430071, China

ABSTRACT

Geological structures such as faults, joints, and dykes have been observed near excavation boundaries in many rockburst case histories. In this paper, the role of weak planes around tunnels in rockburst occurrence was studied. The Abaqus-Explicit code was used to simulate dynamic rock failure in deep tunnels. Firstly, the tool's usefulness for modelling geomaterials was improved by introducing material heterogeneity using Python scripting. The modelling results showed that heterogeneous models resulted in more realistic failure modes than homogeneous models. Secondly, rock failure near the excavation boundary of a tunnel without any adjacent geological structure was modelled and released kinetic energy from rock due to failure and velocity of failed elements at the tunnel wall were calculated. Then, a weak plane was added to the model. This resulted in more released kinetic energy and higher element velocity, indicating that rock failure became more violent in the models with weak planes. The modelling results confirm that the presence of geological structures in the vicinity of deep excavations is a necessary condition for the occurrence of rockburst. It can be used to explain localized rockburst occurrence in civil tunnels and mining drifts. The methodology for rockburst analysis presented in this paper can be useful for rockburst anticipation and control during mining and tunneling in highly stressed grounds.

KEYWORDS: Numerical simulation; excavation; heterogeneity; weak plane; rockburst

1. INTRODUCTION

Rockburst is an unstable and violent rock failure, and one of the most hazardous problems in deep mines and civil tunnels. Rockburst is associated with rapid ejection of broken rocks and is accompanied by a large amount of energy release (Hedley et al., 1992; Andrieux et al., 2013). The rockburst problem increases as mining activities progress to deeper grounds. Some efforts have been made to understand why rockburst happens, to anticipate where it will happen, and to predict how large a rockburst event will be. Having this knowledge would be valuable for rock support design.

Rockburst case histories reveal that rockburst damage locations are not uniform. In the other words, damage extent in a tunnel caused by a rockburst varies at different locations. The localized rockburst phenomenon originates from the complex mechanism that drives rockburst and the contribution of different factors on rockburst occurrence. Many factors that influence rockburst damage have been identified (Kaiser and Cai, 2012) but no one knows the exact conditions for the occurrence of a rockburst in a complex underground setting. Studies have documented the presence of geological structures such as faults, shears, and dykes in vicinity of rockburst locations (Hedley et al., 1992); however,

their role in rockburst occurrence and damage is not well understood.

Numerical models have been used to simulate unstable rock failure in laboratory tests (Kias and Ozbay 2013; Manouchehrian and Cai, 2016) and underground openings (Jiang et al., 2010; Gu and Ozbay 2015). A missing factor in the previous numerical works is the influence of geological structures on rockburst occurrence and damage. In this paper, the influence of weak planes (e.g. faults and shears) on rockburst occurrence and damage around underground openings is investigated using Finite Element Method (FEM).

2. ROCK FAILURE SIMULATION USING ABAQUS

Unstable rock failure is a dynamic phenomenon and should be treated as a nonlinear dynamic problem. Studies have shown that the explicit numerical method is more suitable than the implicit numerical method for solving nonlinear dynamic problems because the problem of convergence is eliminated. Abaqus is a FEM-based numerical tool which is equipped with implicit and explicit solvers, making it applicable for solving a large variety of physical and engineering problems (Dassault System, 2010). Manouchehrian and Cai (2016) simulated

uniaxial and poly-axial compression tests using the Abaqus-Explicit tool and demonstrated the suitability of the tool for simulating unstable or dynamic rock failure. In this study, this tool is used to simulate rockburst in deep tunnels.

Despite Abaqus's capability for simulating a large variety of engineering problems, its application in the geomechanical field is limited. A key characteristic of geomaterials is material heterogeneity, which cannot be readily modelled in Abaqus through GUI. Fortunately, Abaqus provides windows for adding and improving its capability using scripting and programming. Hence, for modelling rock-like materials, it is possible to introduce material heterogeneity into the models to produce more realistic results. In this section, a simulation of rock failure processes in compression using homogeneous material models is presented first, followed by an introduction of material heterogeneity into Abaqus models and a simulation of rock failure processes in compression using heterogeneous material models.

2.1 Homogeneous model

To study the failure mechanism using Abaqus, the laboratory tested mechanical properties of T_{2b} marble (Table 1) are used as the base case. T_{2b} marble is the host rock of the diversion tunnels at the Jinping II hydropower station in China (Zhang et al., 2012).

Unconfined and confined compression tests are simulated to investigate the failure mechanism of homogeneous rocks. An elasto-plastic Mohr-Coulomb strain-softening model with homogeneous material properties is used to model the strength behaviour of the T_{2b} marble. Table 2 presents the calibrated parameters for defining the strain-softening behaviour of the rock in the homogeneous model. A rectangular specimen with a height of 250 mm and a width of 100 mm is used for the simulation. In the unconfined compression test simulation, one end of the specimen is fixed in the maximum stress direction and the other direction is free (roller constraint) and a constant velocity of 0.03 m.s⁻¹ is applied directly to the other end to load the specimen. The same end boundary conditions are applied to the specimens in the confined compression test simulation and the confinements applied are 5, 10, 20, and 40 MPa. In the developed homogeneous model, a uniaxial compressive strength (UCS) of 113.6 MPa, a friction angle of 30°, and a cohesion of 32.9 MPa are calculated, which are similar to the reported laboratory test data (Table 1).

Figure 1b shows the failure pattern in the homogeneous models indicated by the maximum principal plastic strain. The figure shows that

confinement does not affect the failure pattern in the homogeneous model because all of them show distinct shear failure. Despite that the mechanical parameters of the T_{2b} marble are captured by the homogeneous model, it fails to capture the splitting failure under low confinement.

Table 1: Physical and mechanical properties of the T_{2b} marble (Zhang et al., 2014).

Parameter	Value
Density, ρ (kg.m ⁻³)	2780
Young's modulus, E (GPa)	55
Poisson's ratio, ν	0.27
Uniaxial compressive strength, UCS (MPa)	110.7*
Cohesion, c (MPa)	32.6
Friction angle, ϕ (°)	29

* UCS of the T_{2b} marble was reported between 100 and 160 MPa in (Zhang et al., 2014). This value was calculated according to $UCS = \frac{2c \cdot \cos\phi}{(1 - \sin\phi)}$ for the present study.

Table 2: Strain-softening parameters of the homogeneous model.

Cohesion		Tension cut-off	
Cohesion yield stress (MPa)	Shear plastic strain	Tension cut-off stress (MPa)	Tensile plastic strain
32.2	0	5.5	0
0.01	0.2	0.1	0.001

2.2 Heterogeneous model

In order to introduce heterogeneity into models, the material properties of each element are assigned randomly following normal distribution functions. The introduction of material heterogeneity cannot be conducted using the GUI and Python scripting is needed.

The developed Python script assigns randomly distributed material properties of E , c , and ϕ to the elements and the properties follow normal distribution functions. One example of execution of the developed technique to simulate a rectangular model with 4000 elements and 100 materials is presented in Figure 2 (each color represents one material). In this figure, μ and σ are the averages and the standard deviations of each parameter (E , c , and ϕ).

Heterogeneous model is used to simulate the mechanical properties of the T_{2b} marble (Table 1). A UCS of 113.5 MPa, a friction angle of 29.7° and a cohesion of 32.7 MPa are estimated for the heterogeneous model, which are similar to the laboratory test results.

Figure 1a shows photographs of the failed T_{2b} marble specimens in laboratory tests (Zhang et al., 2014) and Figure 1c presents snapshots of the plastic strain obtained by the numerical models. It is seen that in the heterogeneous model, the failure modes

change from splitting failure at zero confinement to shear failure at high confinements. The homogeneous material models cannot capture axial splitting at zero confinement but the heterogeneous material model successfully captures this failure mode. Hence, the developed heterogeneous material model in Abaqus enhances its capability for adding value to the tool in solving geotechnical engineering problems.

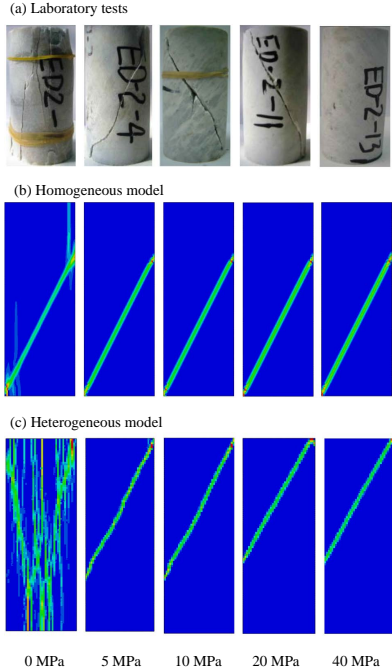


Figure 1: Failure patterns at different confinements from (a) laboratory tests (Zhang et al., 2014), (b) homogeneous model, and (c) heterogeneous model.

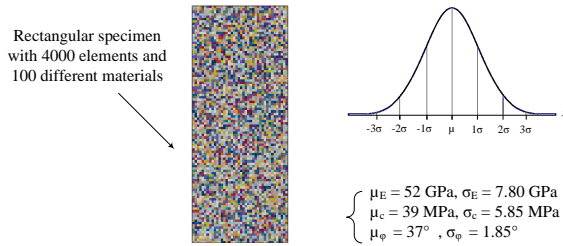


Figure 2: Generated heterogeneous material in Abaqus by Python scripting.

3. ROCKBURST SIMULATION

In this section, models are developed to study the influence of weak planes on rockburst occurrence and damage numerically. A circular tunnel with a radius (r) of 5 m is modelled. In the numerical models, the outer boundary width and height should be at least ten times of the tunnel diameter to exclude the effect of the outer boundary on stress redistribution around the tunnel. In this study, the models also include a fault with a varying length. Hence, the outer

boundary width and height are 15 times of the tunnel diameter to ensure that stress redistribution around the fault does not affect the modelling results. Figure 3 illustrates the model geometry.

Before any excavations, in situ stresses are applied to the outer boundaries and then the boundaries are fixed with roller constraints. Tunnel excavation is then simulated. The horizontal (σ_x) and vertical (σ_z) in situ stresses are assumed to be 30 and 60 MPa, respectively. Gradual excavation of the tunnel is simulated by stress reduction at the tunnel boundary in ten steps.

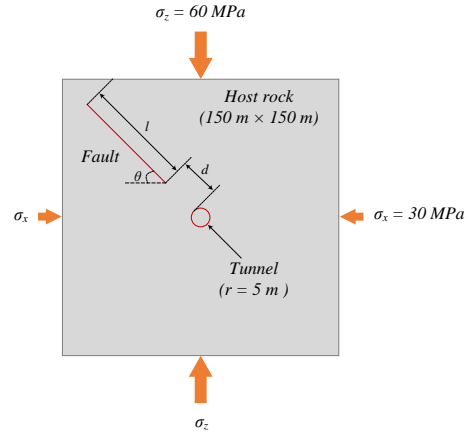


Figure 3: Model geometry and boundary conditions.

An elasto-plastic Mohr-Coulomb strain-softening model with heterogeneous material properties is used to model a rock mass with its physical and mechanical properties presented in Table 3. In the developed heterogeneous model, the mean values of E , c , and ϕ are 21 GPa, 22 MPa, and 31° , respectively and coefficients of variation (COV) of them are 5%. The adjusted parameters for defining the strain-softening behaviour of the rock mass are presented in Table 4.

Table 3: Physical and mechanical properties of the rock mass.

Parameter	Value
Density, ρ ($\text{kg}\cdot\text{m}^{-3}$)	2500
Young's modulus, E (GPa)	20
Poisson's ratio, ν	0.2
Uniaxial compressive strength, UCS (MPa)	69.3
Cohesion, c (MPa)	20
Friction angle, ϕ ($^\circ$)	30

Table 4: Parameters with COV = 5% for defining the post-peak behaviour of the rock mass.

Cohesion		Tension cut-off	
Cohesion yield stress (MPa)	Shear plastic strain	Tension cut-off stress (MPa)	Tensile plastic strain
22.0	0	3.0	0
0.01	0.2	0.1	0.005

Firstly, a tunnel without any adjacent geological structure is modelled. Shear and tensile failures around the tunnel, indicated by the maximum principal plastic strains, are illustrated in Figure 4. The figure shows a symmetric failure around the tunnel, with shear failure zones located at 3 and 9 o'clock because the maximum in situ principal stress direction is vertical.

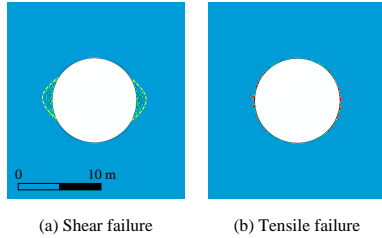


Figure 4. Failure zones around the tunnel without any nearby geological structures.

Figure 5a shows the velocity of elements around the tunnel at the beginning of Step 10 (at the time of failure). The figure shows a maximum velocity of 1.78 m.s^{-1} in one node at the tunnel surface. The minimum velocity of the failed elements is 0.14 m.s^{-1} . In this study, the velocity of all failed elements around the tunnel during the running time is tracked and then an average velocity (V_{max}) is calculated. The maximum of the average velocity (\bar{V}_{max}) during the running time is picked to interpret the results. In this case, the average of maximum velocity of the failed elements around the tunnel (\bar{V}_{max}) is 0.58 m.s^{-1} . When failure is stable, the ejection velocity of the failed rocks is low (Milev et al., 2002). The maximum kinetic energy per unit volume (KE_{max}) from the failed rocks, which can be used as an indicator of rock failure intensity, is 0.65 kJ.m^{-3} . In this case, failure can be considered as stable; if it were in the field, the failure would be in the form of spalling, spitting, or shallow slabbing.

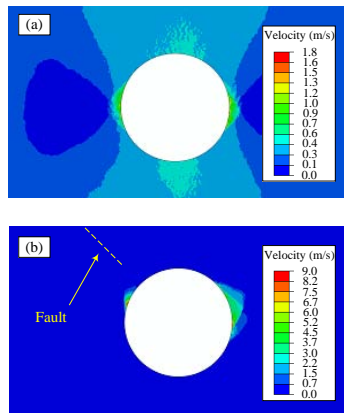


Figure 5: Velocity of the elements in the models (a) without and (b) with a nearby fault.

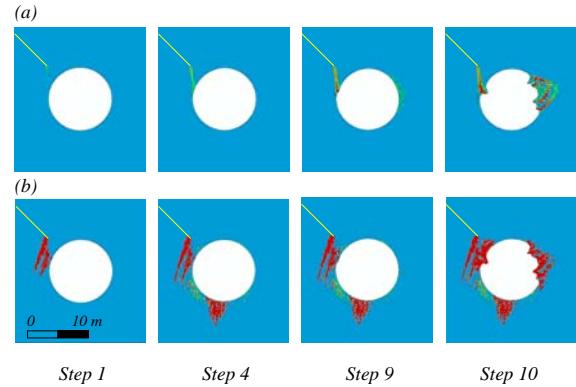


Figure 6: Failure development around the tunnel with a nearby fault: (a) shear failure, (b) tensile failure ($l = 80 \text{ m}$, $d = 2.5 \text{ m}$, and $\theta = 45^\circ$).

Next, a fault with a dip of $\theta = 45^\circ$, a length of $l = 80 \text{ m}$ and at a position of $d = 2.5 \text{ m}$ from the tunnel wall is added to the model (see Figure 3). A Coulomb model with a friction coefficient of 0.4 and zero cohesion is used to model the fault.

Development of failure around the tunnel at Steps 1, 4, 9, and 10 is shown in Figure 6. The figure shows initiation of tensile and shear fractures at the tip of the fault at Step 1 excavation. Then, the shear fractures propagate toward the tunnel face (Step 4) and rocks between the fault and the tunnel are ruptured. Meanwhile, tensile fractures are initiated at the bottom of the tunnel. Figure 7 shows the relative movement of the fault at four different points along the fault (the fault tip and three other points at a distance of 1 m from each other). A relative slip of about 25 mm occurs at point p-1 after the excavation is completed. The slip rate is the highest at Step 9. Slip of the fault due to excavation causes compression at positions of 1 to 4 o'clock (Step 9).

At Step 10, the failed rocks on the right tunnel wall would blow out violently with a $\bar{V}_{max} = 3.4 \text{ m.s}^{-1}$ (Figure 5b) and a failure pit with a depth of 3 m would be created. The maximum unit kinetic energy

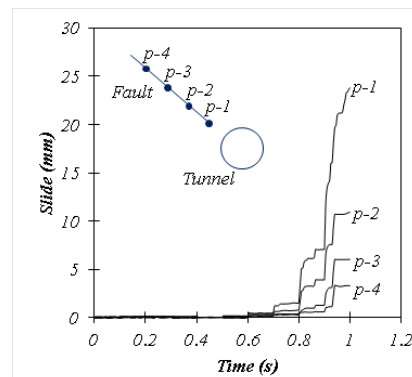


Figure 7: Relative movement of the fault during the running time.

is 6.97 kJ.m^{-3} .

Tunneling near a fault with different fault lengths is simulated to understand the influence of the fault length (l) on rockburst damage. The length of the fault (l) is varied at $l = 0, 20, 40, 60,$ and 80 m , resulting in l/r ratios of $0, 4, 8, 12,$ and 16 , respectively. The same modelling procedure described above is used.

The influence of l on \bar{V}_{max} and KE_{max} is presented in Figure 8. The figure indicates that an increase in the fault length results in increases of both \bar{V}_{max} and KE_{max} . According to Figure 8, when $l = 0$ (i.e. there is no fault), the V_{max} is low (0.58 m.s^{-1}) and the rock failure can be considered as stable. \bar{V}_{max} and KE_{max} increase rapidly as the l/r ratio increases. For example, for $l/r = 16$, $\bar{V}_{max} = 3.4 \text{ m.s}^{-1}$ and $KE_{max} = 6.97 \text{ kJ.m}^{-3}$, which indicates that the rock failure is more violent than the models with shorter fault length. In such a case it can be expected that a rockburst is likely to occur. The failure zones around the tunnel for various l/r ratios are presented in Figure 9, with tensile and shear failure zones shown separately. It is seen that as the l/r ratio increases, the failure zone becomes large.

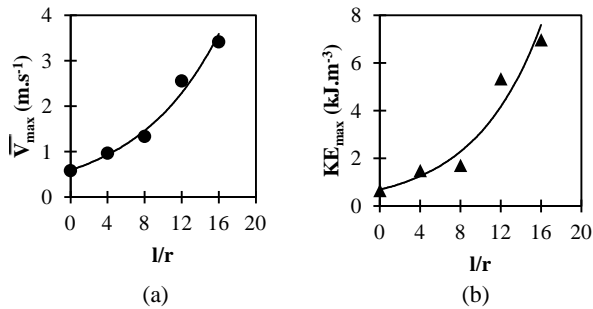


Figure 8: Influence of fault length on (a) \bar{V}_{max} and (b) KE_{max} .

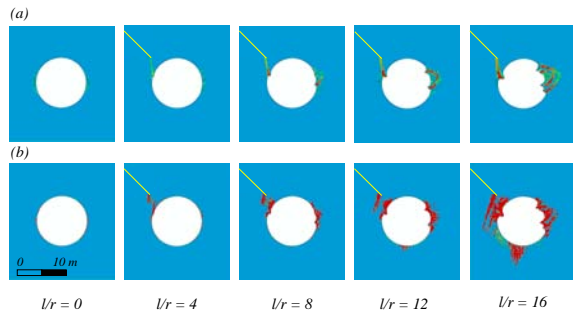


Figure 9: Failure zones around the tunnel in models with different fault lengths: (a) shear failure, (b) tensile failure.

Figure 10 shows the total displacement distribution around the tunnel at the end of Step 9

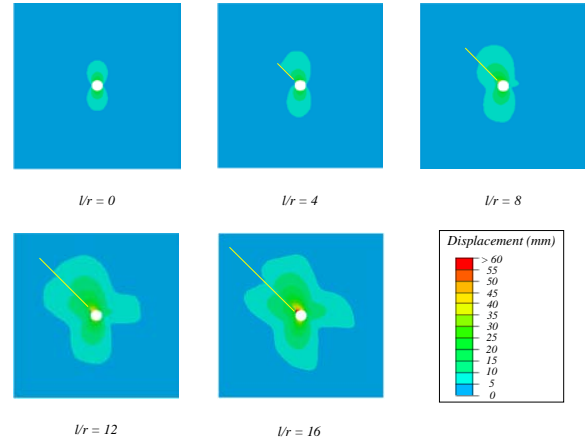


Figure 10: Displacement around the tunnel in models with different fault lengths.

excavation (before the sidewall fails). The figure shows that when the fault is longer, a larger volume of hanging wall rock can move toward the tunnel and push the rocks near the tunnel wall boundary, particularly the rocks on the right wall side. Hence, more strain energy release is possible if there is a sudden rock failure. This explains why the unit maximum kinetic energy is high for large l/r ratios. Furthermore, the displacement field also indicates that the mine system stiffness is low when the l/r ratio is high because the rocks surrounding the failed rocks can have more deformation.

The concept of mine system stiffness has been used by some researchers to explain rockburst in underground mines (Aglawe, 1999; Wiles, 2002). Although it is difficult to calculate mine system stiffness quantitatively in a tunnel setting, an analogy to Loading System Stiffness (LSS) in laboratory testing can be made. Laboratory test results show that the modes of failure (stable and unstable) depend on the relative stiffness of the rock and the loading system (Wawersik and Fairhurst, 1970). A soft loading system is capable of storing more strain energy than a stiff loading system. Thus when a rock specimen fails, the failure is stable under a stiff loading system and unstable under a soft loading system. Despite the difference in the loading in the field and in laboratory, it can be seen that an increase of l decreases the mine system stiffness and as a result, unstable rock failure can happen around the tunnel. This can be clearly seen from the results presented in Figure 8 to Figure 10.

Reduced mine system stiffness can be considered as a main effect of weak planes near openings in deep underground mines, which can potentially lead to rockburst. According to the simulation results, it is seen that the size of a weak plane is an important factor that influences rockburst damage.

4. CONCLUSION

In this paper, the Abaqus-Explicit code was used to study the role of weak planes in rockburst occurrence and damage. Firstly, Abaqus's usefulness for modelling geomaterials was improved by introducing material heterogeneity using Python scripting. The modelling results showed that heterogeneous models resulted in more realistic failure modes than homogeneous models. Secondly, rock failure near the excavation boundary of a tunnel without any adjacent geological structure was modelled and the released kinetic energy due to rock failure and velocities of elements at the tunnel boundaries were calculated. When a weak plane was added to the model, it resulted in more released kinetic energy and higher element velocity, indicating that rock failure became more violent in the model with the weak plane. The modelling results indicated that the failure became more violent when the weak plane length was longer.

It was shown that weak planes around a tunnel may change the loading system stiffness of the failed rocks and induce rockburst because when there is a weak plane near an underground opening, a large volume of rock is able to move. The approach presented in this study can capture dynamic response of a rock mass. In particular, the ability to estimate ejection velocity and released kinetic energy provides a new approach for dynamic rock support design.

5. ACKNOWLEDGEMENT

Financial supports from the Natural Sciences and Engineering Research Council (NSERC) of Canada, Vale, LKAB, CEMI, MIRARCO, and the Open Research Fund of the State Key Laboratory of Geomechanics and Geotechnical Engineering, Institute of Rock and Soil Mechanics, Chinese Academy of Sciences (Grant NO. Z015001) for this work are gratefully acknowledged.

6. REFERENCES

Aglawe, J. (1999) Unstable and Violent Failure around Underground Openings in Highly Stressed Ground. Queen's University.

Andrieux, P., Blake, W., Hedley, D. G. F., Nordlund, E., Phipps, D., Simser, B., and Swan, G. 2013. Rockburst Case Histories: 1985, 1990, 2001 & 2013, Sudbury, Ont: CAMIRO Mining Division for the Deep Mining Research Consortium; 2013.

Dassault System, (2010). ABAQUS 6.10 Users' manual. Providence, RI, USA: HKS Inc.

Gu, R., and Ozbay, U. (2015) Numerical investigation of unstable rock failure in underground mining condition. *Computers and Geotechnics*, Volume 63, pp. 171-182.

Hedley, D. G. F., Mineral, C. C. f., Technology, E., Association, O. M., and Laboratories, M. R. (1992) Rockburst Handbook for Ontario Hardrock Mines: Energy, Mines and Resources Canada, Canada Center for Mineral and Energy Technology.

Jiang, Q., Feng, X.T., Xiang, T. B., and Su, G.-S. (2010) Rockburst characteristics and numerical simulation based on a new energy index: a case study of a tunnel at 2,500 m depth. *Bulletin of engineering geology and the environment*, Volume 69, No. 3, pp. 381-388.

Kaiser, P. K., and Cai, M. (2012) Design of rock support system under rockburst condition. *Journal of Rock Mechanics and Geotechnical Engineering*, Volume 4, No. 3, pp. 215-227.

Kias, E., and Ozbay, U. (2013) Modeling Unstable Failure of Coal Pillars in Underground Mining Using the Discrete Element Method. Paper presented at the 47th Rock Mechanics/Geomechanics Symposium. Paper ID: ARMA 13-174.

Manouchehrian, A., and Cai, M. (2016) Simulation of unstable rock failure under unloading conditions. *Canadian Geotechnical Journal*, Volume 53, No. 1, pp. 22-34.

Milev, A., Spottiswoode, S., Noble, B., Linzer, L., Van Zyl, M., Daehnke, A., and Acheampong, E. (2002) The meaningful use of peak particle velocities at excavation surfaces for the optimisation of the rockburst criteria for tunnels and stopes. SIMRAC Final Project Report GAP, 709.

Wawersik, W. R., & Fairhurst, C. (1970) A study of brittle rock fracture in laboratory compression experiments. *International Journal of Rock Mechanics and Mining Sciences & Geomechanics Abstracts*. Volume 7, No. 5, pp. 561-575.

Wiles, T. (2002) Loading system stiffness-a parameter to evaluate rockburst potential. Paper presented at the First International Seminar on Deep and High Stress Mining, Australian Centre for Geomechanics, Perth, Australia.

Zhang, C., Feng, X. T., Zhou, H., Qiu, S., and Wu, W. (2012) Case histories of four extremely intense rockbursts in deep tunnels. *Rock mechanics and rock engineering*, Volume 45, No. 3, pp. 275-288.

Zhang, C., Feng, X. T., Zhou, H., Qiu, S., and Yang, Y. (2014) Rock mass damage induced by rockbursts occurring on tunnel floors: a case study of two tunnels at the Jinping II Hydropower Station. *Environmental Earth Sciences*, Volume 71, No. 1, pp. 441-450.

A model of rockburst including geological dynamic conditions and mining

Jun Han^{a,b,*}, Ting Ren^{a,b}, Tianwei Lan^{a,c}, Feng Zhu^a, Chen Cao^b, Hongwei Zhang^a, Guoshui Tang^a

^a College of Mining, Liaoning Technical University, Fuxin, China, 123000

^b School of Civil, Mining and Environmental Engineering, University of Wollongong, Wollongong, Australia, 2522

^c Center of Geodynamics of the Earth's Interior of Moscow State Mining University, Moscow, Russia, 119991

ABSTRACT

Rockburst poses a serious threat to mining safety and can occur under certain combinations of geological and mining conditions. A model of fault-slip burst based on the energy distribution in the rock mass was developed to investigate the mechanics of rockburst and to determine guidelines for safe excavation and operation of underground coal mines. In this model, the energy of the fault involved in the rockburst is assumed to be spherical. The rockburst energy is a combination of the energy from the spherical fault-slip rock mass and the elastic energy from the rock mass ahead of the roadway excavation. We derive the threshold energy for rockburst occurrence from the critical energy condition based on the balance of dissipated and released energy. This method can be applied to estimate the safe distance that tunnel excavation can advance towards the geological structure before rockburst occurs.

KEYWORDS: rockburst; energy; mechanics; geological structure; spheroid

1. INTRODUCTION

Rockburst is a sudden and violent failure of a large volume of overstressed rock, resulting in the instantaneous release of large amounts of accumulated energy (Mine Safety and Health Administration, 1984). Rockburst often leads to rock failure and collapse. It can cause damage to mines, injuries to mine workers, and disruption to mining activity. Several factors are known to affect rockburst: the depth of mining, properties of the rock mass (lithology, elastic modulus, strength, and quality), thickness of the mined deposit, the geological structure of the mine area, and geotechnical characteristics of the rock mass. Additionally, some mining factors can influence the occurrence of rockburst: the mine design, mining method, roof control method, pattern of deposit excavation, concentration of mining operations, and the spatial limits of the mining operations (Dou and He, 2001; Hudyma, 2004; Zhang et al., 2009; Butra, 2010).

The occurrence of rockburst, a sudden rock failure characterized by the breaking up and expulsion of rock from its surroundings, implies that a large amount of energy was released. Cook (1966) defined rockburst as an energy phenomenon and developed the energy release rate (ERR) method. Hoek and Brown (1980) provided graphic illustrations of explosive brittle fracturing in deep hard-rock mines. The only feature common to most rockbursts is that the rock failure is sudden and the strain energy is released from a volume of stressed rock (Ortlepp 1983). Salamon (1983) investigated the

energy changes that occur during mining activities and showed that part of this energy is stored in the rock mass surrounding the excavation. Generally, the instability occurs if the elastic energy released in the deformation process is greater than the fracture energy. He also pointed out three sources for this energy release: a) the strain energy stored in the surrounding rock mass, b) the change in the potential energy of the rock mass, and c) the slippage along the rock wall contact. Petukhov and Linkov (1983) associated the instability of rock mass with rockburst or coal bump and noted that if the potential energy accumulated in the high-stress zone is high enough to destroy the rock near the mine's working area, a rockburst will occur. Mitri et al. (1999) used the energy storage rate (ESR) as a measure of the underground conditions rather than as an indicator of seismicity. Beck (2002) proposed a quantitative assessment and interpretation of rockburst in a hard rock mine using the "factor of safety". Zhao et al. (2003) proposed the minimum energy principle of rock dynamic failure. Xie et al. (2009) established a strength-loss criterion associated with the intensity of energy dissipation and a failure criterion associated with the strain energy release.

Rockbursts occur under certain combinations of geologic and mining conditions. The connection between rockburst and the geology of the mining area was made following the first reported rockburst, which occurred on the 2500 level of the Sunshine Mine in April 1939 (Whyatt, 2002). Brown (1984) indicated that rockbursts induced by mining are

associated with unstable equilibrium states that may involve: a) slips on pre-existing discontinuities; b) fracturing of rock mass. This leads to the definition of two broad classifications of rockbursts: (1) Type I rockburst, resulting from fault slip events; (2) Type II rockburst, resulting from the failure of the rock mass itself, including strain burst and pillar burst. A degree of rockburst hazard is inevitably associated with the stress near the mine working area and the distance between the mine wall and the maximum stress zone (Petukhov and Linkov, 1983). Recognition of the geologic features that contribute to rockburst events is an important part of strategic planning aiming to minimize these hazards. Many rockburst events are associated with geological factors such as faults, folds, irruptive rock, and tectonic stress. (Batugina and Petukhov, 1990; Driad-Lebeau et al., 2005; Wang et al., 2012; Drzewiecki, 2013). The authors used the term ‘geological dynamic condition’ to describe this state (Han et al., 2013; 2014). Experience in the Coeur d’Alene district in Idaho, USA indicates that certain rock types and various kinds of discontinuities increase the risk of rockburst. Whyatt (2002) showed that ultimate stress state is created by the action of the pre-mining and mining induced stresses. The *in-situ* stress, as well as the rockburst hazards, varied with the geological features in the Coeur d’Alene district (Whyatt 2000).

In China as of 2012, there are 142 coal mines which have had rockbursts. As mining operations become deeper, the frequency and intensity of rockbursts has been increasing accordingly. The prediction and prevention of rockburst is very important for mining safety and continuous operation. Many rockbursts are affected by the geological structure around the mine area and by the mining operation. The current study investigates the energy of the rock mass in mines and the processes of energy release and equilibrium, in order to gain a better understanding of the occurrence of rockburst in various geological and mining conditions.

2. ENERGY OF ROCK MASS

The conservation of energy in rock during its deformation and failure is a dynamic process that represents energy conversion and the equilibrium of the mechanical energy produced by external loads, thermal energy, and the internal energy of the rock according to the non-equilibrium thermodynamic theory. Initially, the rock is in a stable equilibrium state (Figure 1, Position a). After external loading, the rock begins to deform. The mechanical energy produced by the external load and thermal energy is continuously converted into internal energy of the rock. Therefore, the internal rock energy increases and the rock gradually departs from the initial stable

state. For a certain load, a dynamic equilibrium exists among the work of the external load, the thermal energy, and the internal energy; thus, the rock is in a steady state. When the external load become too large, the steady state of the rock moves to the nonlinear non-equilibrium region, away from the equilibrium zone; hence, the rock mass becomes unstable. At the critical state (Figure 1, Position b), the rock state changes abruptly to another state (Figure 1, Position c) with relatively low internal energy, leading to the collapse of the rock. The high stress level destabilizes the rock; whether the rock fails is determined by the internal energy dissipation and the nonlinear dynamic mechanism (Peng, 2011).

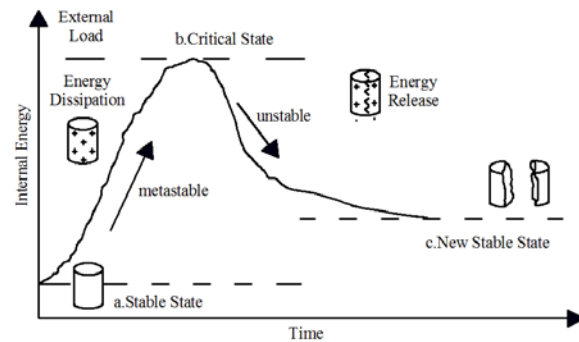


Figure 1: Thermodynamic change during rock deformation and failure (Peng, 2011).

According a rock volume element produce deformation under loading, the total input energy produced by external load is U , as shown in Figure 2 $U=U_i^d+U_i^e$ (1) where U_i^d is the dissipated energy and U_i^e is the releasable elastic strain energy.

The releasable elastic strain energy U_i^e can be described as

$$U_i^e = \frac{1}{2E} [\sigma_1^2 + \sigma_2^2 + \sigma_3^2 - 2\mu (\sigma_1\sigma_2 + \sigma_2\sigma_3 + \sigma_1\sigma_3)] \quad (2)$$

where E is the elastic modulus; μ is the unloading Poisson's ratio; and σ_1 , σ_2 and σ_3 are the major principal stress, intermediate principal stress, and minor principal stress, respectively.

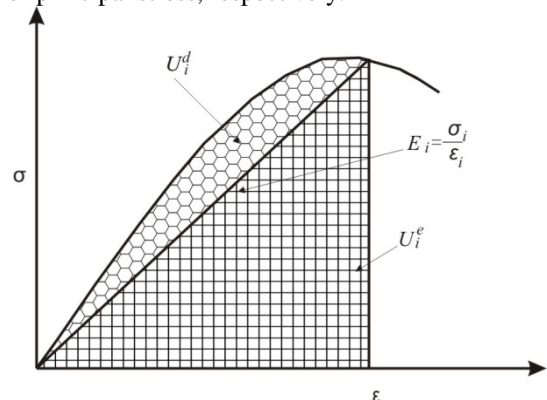


Figure 2: Relationship between dissipated energy and releasable strain energy of rock volume element (Xie et.al 2005).

3. ROCKBURST OCCURRENCE AT MINING AND GEOLOGICAL STRUCTURE

We constructed a model of a fault-slip rockburst that includes the mining conditions and geological dynamic conditions. The model simulates a fault ahead of the roadway excavation work. The area influenced by the fault is a sphere with a radius R . As the roadway is excavated, a plastic and an elastic zone are produced ahead of it. The distance between the sphere boundary and the working end of the roadway excavation is L . L_p and L_e are the lengths of the plastic zone and elastic zone that develop ahead of the excavation, respectively. H is the height of the roadway and L_o is the length of the undisturbed zone - original zone. The stress in the plastic and elastic zones is lower than in the original zone (Figure 3.a).

The rock mass attains energy from the deformation of the rock mass at the *in-situ* stress field; it depends on the volume of the rock mass and the *in-situ* stress. We assume that the energy source of the geological structure involved in the rockburst is contained within the sphere. The elastic energy of the sphere U_G is

$$U_G = \frac{2\pi}{3E} [k_1^2 + k_2^2 + k_3^2 - 2\mu(k_1k_2 + k_1k_3 + k_2k_3)] \rho^2 g^2 H^2 R^3 \quad (3)$$

where ρ is the density of the overburden; g is the gravitational acceleration; H is the depth; E is the elastic modulus of the rock; k_1 , k_2 , and k_3 are the ratios of σ_1/σ_h , σ_2/σ_h , and σ_3/σ_h , respectively, where $\sigma_h = \gamma g H$ is the pressure of the overlying strata.

As the roadway is excavated, the fracturing of the coal and rock extends forward, the head of the excavation becomes closer to the sphere of influence, and the volume of the elastic zone gradually decreases (Figure 3.b). When the elastic zone is too small to resist the superimposed stress, rock failure will occur and a large amount of energy will be released (Figure 4). The sphere will also release much energy. This leads to the occurrence of a rockburst. The energy released from the sphere after failure is:

$$\Delta U = U_G - U_Z \quad (4)$$

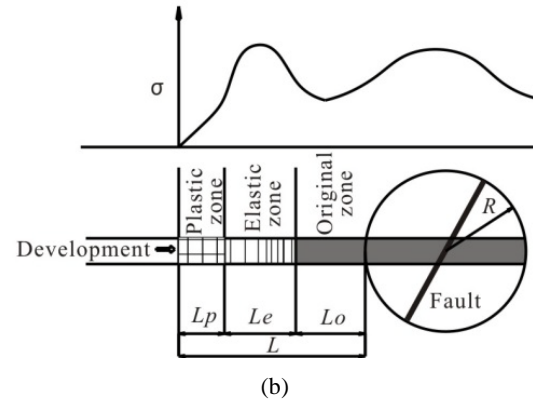
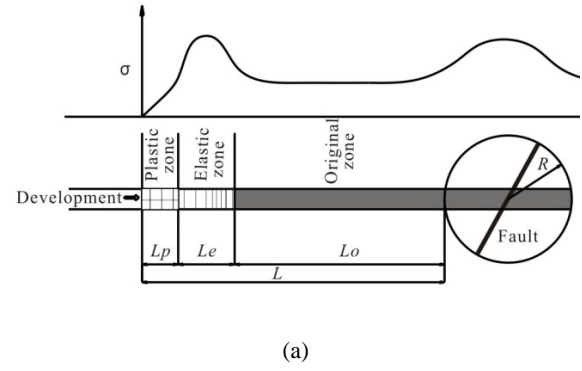


Figure 3: A model of mining and geological dynamic condition.

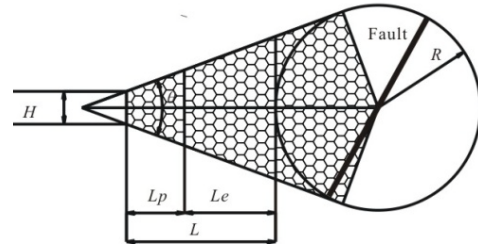


Figure 4: The energy calculation diagram of rockburst.

where U_Z is the gravitational energy. According to the principle of minimum energy of the failed rock, the minimum energy of the failed elastic zone is

$$U_{sd} = \frac{\sigma_c^2 V}{2E} \quad (5)$$

where V is calculated as follows

$$V = \frac{1}{3} \cos^2 \frac{\theta}{2} \sin \frac{\theta}{2} \pi R^3 + \frac{1}{3} \frac{\cos^4 \frac{\theta}{2}}{\sin \frac{\theta}{2}} \pi R^3 - \frac{1}{3} \pi \frac{\sin^2 \frac{\theta}{2}}{\cos^2 \frac{\theta}{2}} \left(\frac{2}{\sin \frac{\theta}{2}} R - R - l_e \right)^3 \quad (6)$$

$$\cos \frac{\theta}{2} = \frac{2hR \pm 2\sqrt{h^2 R^2 + (2R+l)l} [4(l+R)^2 + h^2]}{4(l+R)^2 + h^2} \quad (7)$$

$$\sin \frac{\theta}{2} = \sqrt{1 - \cos^2 \frac{\theta}{2}} \quad (8)$$

The parameters in equations (6), (7), and (8) are

shown in Figure 4.

The elastic energy of this zone is

$$U_{SE} = \frac{1}{2E} \int (\sigma_1^2 + \sigma_2^2 + \sigma_3^2 - 2\mu(\sigma_1\sigma_2 + \sigma_1\sigma_3 + \sigma_2\sigma_3)) dV \quad (9)$$

The energy released in the rockburst U_C can be expressed as

$$U_C = \Delta U + U_{SD} - U_{SD} \quad (10)$$

where ΔU is the energy released from the sphere, U_{SE} is energy of the elastic zone, and U_{SD} is the energy released from the elastic zone during rock failure.

The minimum energy required for the rockburst to occur is expressed as

$$U_{min} = \frac{1}{2} \rho v_0^2 \quad (11)$$

where v_0 is the velocity of the ejected rock during the rockburst event, and $v_0 \geq 10$ m/s (Ortlepp and Stacey, 1994; McGarr, 1997).

If $U_C \geq U_{min}$, then rockburst will occur. Thus, $U_C = U_{min}$ is the critical condition for rockburst occurrence.

This method can be applied to calculate the length of the elastic zone l_e and then determine the distance of rockburst treatment.

4. CASE STUDY OF THE LAOHUTAI COAL MINE

4.1 Background

The Laohutai coal mine is located in the central Fushun coal field, Fushun city, Liaoning Province. To the east lies the Longfeng coal mine and to the west is the Shengli coal mine. The length of the coal seam strike from east to west is 5 km and the width along the dip in the north-south direction is 2 km (Figure 5).

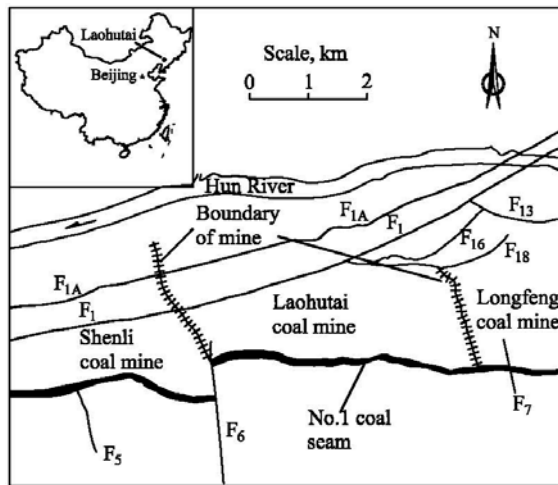


Figure 5: Location and regional geology of Laohutai coal mine.

The overlying rocks include argillite, shale, and oil shale. The thickness of the main coal seam, coal seam No.1, varies from 0.6 to 110.5 m, with an average thickness of 58 m. The main geological structure of the Laohutai coal mine is a syncline trending NEE. The wings of the syncline are asymmetric; the south wing extends smoothly while the north wing inclines abruptly, and is even inverted. There are 14 large faults, including F_1 , F_7 , F_{26} , and F_{18} . The largest one is F_1 which has a drop of more than 1000 m. The deepest buried depth of the coal seam is more than 1000 m.

The Laohutai coal mine is one of the largest state-owned coal mines in China and has been operating for more than 100 years. The mining method is fully mechanized top coal caving and the annual production is about 3 million tons. The Laohutai mine has been associated with various operational challenges such as gas outburst, rockburst, spontaneous combustion, and water inrush and is considered one of the most hazardous mines in China. Rockburst events occurred in 1975 and reached a peak in 2001 (Figure 6). The maximum magnitude of rockburst at the Laohutai mine was $M_L 3.7$. Figure 6 shows the mine rockbursts and associated seismicity during 1993–2014.

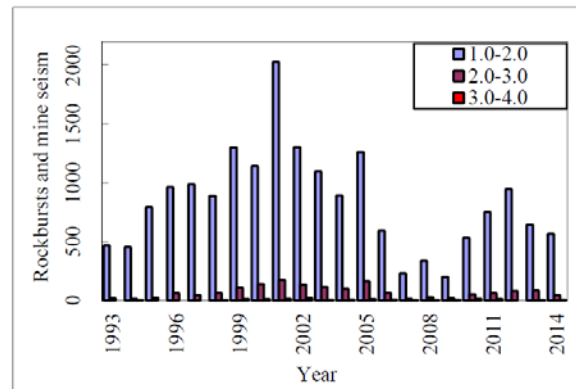


Figure 6: Rockburst and mine seismicity during 1993–2014.

4.2 Rockburst of Longwall 73005

Longwall 73005 (LW73005) is located in the central part of the Laohutai coal mine at a depth of 749–802 m. Figure 7 shows the layout of LW73005. There are eight faults in LW73005: F_3 , F_7 , F_{26} , F_{32} , F_{36} , F_{37} , F_{38} , and F_{39} .

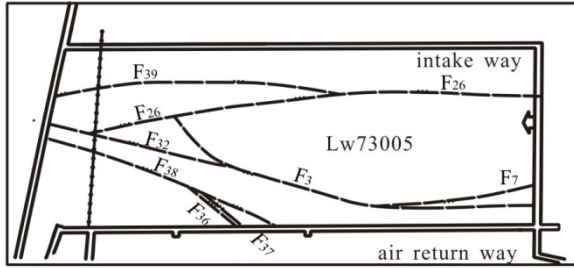


Figure 7: Layout and geological structures of LW73005.

Fault F_{36} was encountered during the excavation of the air return roadway. We use our model to estimate the special range of the energy released by drilling or/and blasting near the fault. According to *in-situ* stress measurements of the Laohutai coal mine, the ratios k_1 , k_2 , and k_3 in Eq. (3) are 2.0, 1.0, and 0.7. The energy of the sphere can then be described as

$$U_G = \frac{2\pi}{3E} (5.49 - 8.2\mu) \rho^2 g^2 H^2 R^3 \quad (12)$$

When the rockburst occurs, the energy released from the sphere is

$$\Delta U = \frac{2\pi(10.2\mu^2 - 12.69\mu + 4.49)\gamma^2 H^2 R^3}{3E(1-\mu)} \quad (13)$$

The result is shown in Table 1. The bigger the ΔU of sphere, the bigger the l_e , and the longer the distance of treatment. Based on the calculation, the safe distance of treatment is 36 m. Thus, when the development of roadway reaches a distance of 36 m from F_{36} , drilling and/or blasting should be carried out to release energy and prevent a fault-slip burst.

Table 1: Parameters of spheroid and distance of treatment.

No.	Work face	H (m)	h (m)	R (m)	l_p (m)	ΔU (MJ)	l_s (m)
1	LW73005	778	3.6	6.3	2	91	36

5. CONCLUSIONS

According to the theory of energy exchange and equilibrium in rock mass we constructed a model of fault-slip burst in a mining environment. The geological structure is included and assumed as a sphere during the rockburst occurrence. The rockburst energy is a combination of the energy of the sphere and the energy of the elastic zone that develops ahead of the tunnel excavation. Part of the energy is dissipated in the elastic zone. When that energy rises above the critical rock failure energy, rockburst will occur. This method can be applied to estimate the safe distance and the rockburst treatment that should be taken when performing roadway excavation towards a geological structure, before rockburst occurs.

6. ACKNOWLEDGEMENT

The work presented in this paper was financially jointly supported from the General Project of the National Natural Science Foundation of China (Grant No. 51104085, 51274117), the Natural Science Foundation of Liaoning (Grant No. 201204407) and Program for Liaoning Excellent Talents in University (Grant No. LJQ2013035).

The authors are especially grateful to Dr. Hai Rong for fruitful discussions and advice. Thanks are also due to Mr. Bob Kininmonth for improving the English of this paper.

7. REFERENCES

- Batugina, I.M. and Petukhov, I.M. (1990) Geodynamic zoning of mineral deposits for planning and exploitation of mines. A A Balkema Publishers, Netherlands, 1990, pp. 34-35.
- Beck, D.A. and Brady, B.H.G. (2002) Evaluation and application of controlling parameters for seismic events in hard-rock mines. International Journal of Rock Mechanics and Mining Sciences. DOI: 10.1016/S1365-1609(02)00061-8.
- Butra, J. and Kudelko, J. (2010) Rockburst hazard evaluation and prevention methods in Polish copper mines. Cuprum, volume 4, No. 61, pp. 5-20.
- Cook, N.G.W., Hoek, E., Pretorius, J.P.G., Ortlepp, W.D. and Salamon, M.D.G. (1966) Rock mechanics applied to the study of rockbursts. The Journal of the South African Institute of Mining and Metallurgy. Volume 66, pp. 435-528.
- Dou, L.M. and He, X.Q. (2001) Theory and technology of rock burst prevention. China University of Mining and Technology Press, Xuzhou, 124p.
- Driad-Lebeau, L., Lahaie, F., Heib, A.M., Josien, J. P., Bigarre, P. and Noirel, J.F. (2005) Seismic and geotechnical investigations following a rockburst in a complex French mining district. DOI: 10.1016/j.coal.2005.03.017.
- Drzewiecki, J. (2013) A model of rock mass fracturing ahead of the longwall face as a consequence of intensity of exploitation. DOI: 10.13168/AGG.2013.0013.
- Han, J., Liang, B., Zhang, H.W., Zhu Z.J., Rong, H. and Liang H.P. (2013) Tectonic stress environment of coal and rock dynamic hazard in Kailuan mining area. Journal of China Coal Society, Volume 38, No. 6, pp. 1154-1160.
- Han, J., Zhang, H.W., Lan, T.W. and Li, S. (2014) Geodynamic environment of rockburst in western Beijing coalfield. Journal of China Coal Society. DOI: 10.13225/j.cnki.jccs.2013.1426.
- Hoek, E. and Brown E.T. (1980) Underground excavations in rock. Institution of Mining and Metallurgy, London, 527p.

Hudyma, M.R. (2004) Mining-Induced Seismicity in Underground, Mechanised, Hardrock Mines –Results of a World Wide Survey. Australian Centre for Geomechanics Research Report, 66 p.

McGarr, A. A Mechanism for High Wall-rock Velocities in Rockbursts. *Pure and Applied Geophysics*, Volume 150, No. 3-4, pp. 381.

Mine Safety and Health Administration. (1984) Hearing on Proposed Standards for Ground Control Metal/Nonmetal Mines, Spokane, WA, June 19.

Mitri, H. S., Tang, B. and Simon, R. (1999) FE modelling of mining-induced energy release and storage rates. *The Journal of The South African Institute of Mining and Metallurgy*, Volume 99, No. 2, pp. 103–110.

Ortlepp, W.D. and Stacey, T.R. (1994) Rockburst mechanisms in tunnels and shafts. *Tunnelling and Underground Space Technology*, Volume 9, No. 1, pp. 59–65.

Peng, Y.D., Ju, Y., Xie, H. and Li, L.Y. (2011) Energy conversion and damage evolution of rocks under cyclic loading conditions. In: Kwasniewski, Li and Takahashi (eds.). *True Triaxial Testing of Rocks*, CRC Press/ Balkema, Leiden, pp. 331-342.

Petukhov, I.M. and Linkov, A.M. (1979) The theory of post-failure deformations and the problem of stability in rock mechanics. *International Journal of Rock Mechanics and Mining Science & Geomechanics Abstract*, Volume 16, No. 2, pp. 57-76.

Petukhov, I.M. and Linkov, A.M. (1983) *Mechanics of rock bursts and outbursts*. Nauka, Moscow, 32-33p.

Salamon, M.D.G. Energy considerations in rock mechanics: fundamental results. *Journal of the South African Institute of Mining and Metallurgy*, Volume 84, pp. 233–246.

Wang, C.W., Jiang F.X. and Liu, J.H. (2012) Analysis on control action of geologic structure on rock burst and typical cases. DOI: 10.13225/j.cnki.jccs.2012.s2.030.

Xie, H.P., Li, L.Y., Peng, R.D. and Ju, Y. (2009) Energy analysis and criteria for structural failure of rocks. *Journal of Rock Mechanics and Geotechnical Engineering*, Volume 1, No. 1, pp. 11–20.

Xie, H.P., Ju, Y. and Li, L.Y. (2005) Criteria for strength and structural failure of rocks based on energy dissipation and energy release principles. *Chinese Journal of Rock Mechanics and Engineering*, Volume 24, No. 17, pp. 3003–3010.

Zhao, Y.S., Feng, Z.C. and Wan, Z.J. (2003) Least energy principle of dynamical failure of rock mass. *Chinese Journal of Rock Mechanics and Engineering*, Volume 22, No. 11, pp. 1781–1783.

Rockburst experiences in Cheves Hydropower Project, Perú

Santiago Veyrat ^a, Jose-Miguel Galera ^{b,*}, Marcos Sancho ^c, H. Andersson ^d, W. Thoese ^e, and, C. Rietschel ^f

^a Subterra Ingeniería SL, Madrid, Spain, 28015

^b Subterra Ingeniería Ltda., Santiago, Chile, 7750181

^c Subterra Perú SAC, Lima, Perú, 18

^d Constructora Cheves, SAC (joint venture Hochtief Solutions AG, SalfaCorp SA and ICCGSA), Lima, Perú

^e Constructora Cheves, SAC (joint venture Hochtief Solutions AG, SalfaCorp SA and ICCGSA), Lima, Perú

^f Constructora Cheves, SAC (joint venture Hochtief Solutions AG, SalfaCorp SA and ICCGSA), Lima, Perú

ABSTRACT

Cheves Hydropower Project is located in Peru and consists in approximately 20 km of tunnels and two caverns. Most of the Headrace tunnel has been excavated in igneous and metamorphic rocks with high overburden. A high number of stress release events took place during the excavation of the tunnels and caverns. The intensity of these events varies from acoustic emission to a violent rockburst. The paper describes the methodology developed to mitigate the rockburst hazard.

1. INTRODUCTION

Cheves hydropower project is located on Huaura River and Checras River, under the Andean Mountains of Peru, North of Lima (see Figure 1).



Figure 1: Cheves Hydropower Project location.

Cheves Project was developed by Empresa de Generación Eléctrica Cheves S.A, a company of the Statkraft Group. The construction was executed by Constructora Cheves, SAC (joint venture Hochtief Solutions AG, SalfaCorp SA and ICCGSA).

In reference to the design of the project, Empresa de Generación Eléctrica Cheves engaged Norconsult with responsibility for the design of the permanent works including the layout, overall stability, and permanent support of the underground works.

Meanwhile Subterra Ingeniería developed the initial support design to Constructora Cheves SAC according to the scope including in the contract signed between the Owner and the Contractor. Constructora Cheves and Subterra Ingeniería didn't have responsibility for the final layout and the long term stability of the works.

This paper and all the above comments are referring only to the scope of work carried out by Constructora Cheves and Subterra Ingeniería.

The project is composed of three small dams and the underground works that dominate the infrastructure, representing approximately 20 km of tunnels:

- Transfer tunnel, between the Huaura Intake and the Checras reservoir presents a length of 2,580 m.
- Headrace tunnel is 9,693 m long (22.6 m² and 30.1 m²), with an upper section at a grade of 2 % and a lower section inclined 14 %. An intermediate adit with a length of 700 m, and a surge tunnel were built at the junction of the lower and upper tunnels, with approximately 700 m long, also inclined 14 %. The end of the Headrace tunnel splits into two short penstock tubes, taking the flow to the generating units in the

powerhouse cavern (60 m long by 32 m high and 15.5 m wide). The transformer cavern (27.5 m long by 14 m high and 11.2 m wide) is immediately adjacent, connected both caverns through an access tunnel. A tunnel access as well as several tunnels completes the Power House complex.

- Tailrace tunnel is 3,312 m long (24.9 m² cross section) tailrace tunnel discharge the water downstream the project.

Kaiser and Cai (2013) define a rockburst as damage to an excavation that occurs in a sudden and violent manner and is associated with a mining-induced seismic event. This general term 'rockburst' is independent of the cause of damage and thus is used for strain, pillar, and fault slip bursts.

During the construction of the Cheves Project more than 850 stress release events were recorded. The most important part of these events took place in the Headrace Tunnel, and a large number of them were recorded around the Powerhouse complex.

Initially, the stress events turned out in the area under the influence of the Powerhouse, especially when the excavation of the cavern began. In December of 2011 and during January 2012 several stress relief events were reported and described as banging or cracking sounds. On January 2012 a minor rockburst with projections of rocks and shotcrete occurred at the access tunnel about 15 m behind the face.

During the followings months, evidence of stress releases continued with events of low intensity, mainly loud relief, slight crumbling, crackling and banging sounds. These events were mainly reported in the by-pass tunnels around the powerhouse. Consequently, these areas were reinforced.

However, on the 21st of March 2012 a strong stress event occurred in the Powerhouse area affecting various tunnel sections. The main stress discharges were reported as two short delayed bursts in the tunnel access and by-pass tunnels. A follow up investigation at the same day in the afternoon revealed that after the main bursts further cracking and minor bursting occurred in the powerhouse cavern.

The areas around the powerhouse were reinforced as a consequence of these events. The excavation of the Powerhouse continued, whereas the works in some tunnels were stopped.

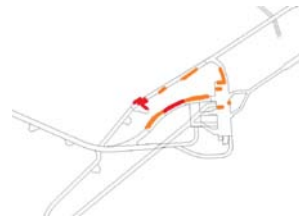


Figure 2: Areas affected by the stress event occurred on 21/03/2012 and a picture of the effects in the by-pass tunnel.

Once the excavation of the Headrace tunnel started from the Powerhouse complex towards the Checra dam, stress events were reported continuously during the excavation, mainly as banging or cracking sounds (acoustic emissions). Finally, a rockburst from the face took place at the tunnel face on July 2012. A complete methodology was developed to mitigate the rockburst hazard during the excavation of the tunnels after this event.



Figure 3: Rockburst at the tunnel face in the Headrace tunnel.

2. GEOLOGICAL AND GEOTECHNICAL FRAME

Cheves Hydropower Project is located in the Huaura basin in the Andes. The Geology is complex with sedimentary, volcanic, igneous, and metamorphic formations along the project. According with its position in the Andes, the area is under active tectonic and seismicity is moderate in the project area.

The Headrace tunnel and the Powerhouse complex have been excavated in relatively hard rock. The geology in the area of the caverns proved to be structurally complex given the presence of major tonalites intrusions with associated sub-horizontal shear joints. Careful consideration was given to aspects such as in situ stresses and rock mass strength. Figure 4 shows the geological section of the Headrace tunnel.

Figure 4: Headrace tunnel geological profile.

2.1 Lithologies and Basic geomechanical data

In this section a geotechnical characterization of the different rocky formations that were found in the downstream part of the Headrace Tunnel are described.

- Churin Bajo Stock. Consist in intrusive rocks with tonalite / quartz-monzonite composition. In general, they show a high strength, low to moderately weathered in the surface, showing thin coats of iron oxides in fractures, which are persistent. The contact with Casma Group andesites produces silicification processes resulting in hornfels, which present highly brittle behaviour and severe fracturation.
- Casma Group. This group corresponds to stratified sequences of volcanic rocks with interbedded sedimentary rocks. Volcanic rocks consist mainly in andesites which appear severely brecciated with a porphyritic texture. In general, they show a

high strength, except when intercalations of sedimentary rocks are detected. Sedimentary rocks consist in sandstones, white quartzites, brown to grey shales and layers of limestone with isolated intercalations of marls.

- Chimu Formation. It is composed by quartzite banks with interbedded with thin quartzose sandstone strata, bituminous shale and occasional coal lenses. In general, quartzites banks show very high strength but brittle behaviour with many fractures showing thin coats of iron oxides. Shales and quartzose sandstones appear highly fractured, with low strength and stiffness and also ductile behaviour.
- Hornfels. The contact with Casma Group andesites produces silicification processes resulting in hornfels, which present highly brittle behaviour and severe fracturation.

The representative values for these formations at intact rock level are shown in Table 1 below:

Table 1: Intact rock properties.

LITHOTYPE	LITHOLOGY	OVERBURDEN (m)	RQD (%)	ρ_{ap} (t/m ³)	σ_{ci} (MPa)		Modulus Ratio	E_i (MPa)	ν	mi
					RANGE	VALUE				
Churin Bajo Stock (KsTi-qzmo)	Tonalites	580-700	40-60	2.62	100-150	110	400	44,000	0.24	25
		700-780	70-90			125		50,000		
	Tonalites (Fault zone)	1100-1200	30-50	2.62	80-120	90	400	36,000	0.24	25
Churin Bajo Stock (KsTi-hf)	Hornfels	525-700	30-50	2.62	80-120	90	550	49,500	0.24	19
Casma Group (Ki-ca)	Andesites (Fault Zone)	135-200	30-50	2.62	100-150	80	400	32,000	0.24	25
		250-350	40-60			110		44,000		
		175-525	60-80			130		52,000		
Chimu Formation (Ki-ch)	Quartzites with shales and sandstones interbedded (Fault Zone)	500-525	10-30	2.62	30-80	40	375	15,000	0.24	20
		25-200	10-30			40		15,000		
		200-450	30-50			70		26,250		
		450-600	10-30			40		15,000		

The contact with Casma Group andesites produces silicification processes resulting in hornfels, which present highly brittle behaviour and severe fracturation.

2.2 Structure

The Headrace tunnel presents a complex geological structure as it is excavated in sedimentary deposits (coal seam included), volcanic rocks, igneous rocks and metamorphic rocks.

The initial part of the tunnel excavated in the Chimu formation is strongly folded and affected by fault systems. The contact between volcanic materials and sedimentary deposits is also defined by fault systems. An igneous intrusion (Churin Bajo Stock) is in contact with the volcanic deposits (Casma Group).

2.3 Overburden and natural stress field

Initially, the natural stress field assumed was derived from regional information as well as from the tectonic frame. It was considered an unfavourable scenario with the vertical stress according to the overburden (lithostatic load) and the following ratio

between horizontal and vertical stresses: $K_H=1.5$ (with a strike of N-60°-E) and $K_h=1.0$.

This stress frame is a key matter for design purposes, thus three different stress measurements were developed, the first using overcoring techniques and the last two using hydro fracturing stress measurements.

The measurements using overcoring provided magnitudes of the maximum principal stress σ_1 ranging between 18.6 to 59.8 MPa. According to the mean value the resulting relation between horizontal and vertical stresses would be around 1.2 and an orientation quite similar to the one obtained by geological estimations (N-45°-E), but the scatter of the results was relatively high.

For this reason, two different on site measurements using hydro-fracturing were established. The obtained magnitudes were similar in both cases, with relatively low values of horizontal stresses. Consequently, the natural stress field was defined as follows:

- σ_v between 21.7 and 22.1 MPa
- σ_h between 12.8 and 13.7 MPa ($K_h=0.62$)
- σ_H between 20.3 and 21.3 MPa ($K_H=0.96$)

The orientation of the maximum horizontal stress was N-95°-E.

3. ROCKBURST HAZARD MITIGATION METHODOLOGY

Rockburst and stress releases took place mainly in the Headrace tunnel and the powerhouse complex. Headrace tunnel was excavated in sedimentary deposits (coal and sandstones), andesite, volcanic breccias, granodiorites, and hornfels. Most part of the events took place in areas excavated in igneous and metamorphic rocks.

A specific stress risk assessment was done in addition to the geological assessment at the tunnel face during the tunnel excavation, in order to collect all the information coming from the tunnel. Three stages were defined to manage the risk of rockburst

or stress releases. These measures can be classified in prediction, prevention and protection.

3.1 Prediction

It was considered that rockburst and/or stress releases are highly unpredictable. Basically, the unique method for rock burst prediction that is considered as partially efficient is to implement a microseismic monitoring net. These systems have been developed in deep mines and require long record periods with some years for calibration to perform reliable predictions. It must also be considered that a mine usually has a well-developed layout of roadways and excavation allowing the installation of seismic nets. For these reasons the application of this technique to Cheves was considered unreal.

The proposal for prediction is the systematization of all the stress events, registering them in a systematic and precise way from simple noises, fissures progression on the shotcrete, minor projections and spalling or popping. Consequently, it is proposed to increase the efficiency of the high stress events records to ensure that all of them are duly registered:

- Stresses events at the face: noises, rock cracks, minor projections, spalling or presence of platy rock chips.
- Stresses events behind the face: fissures and cracks at the shotcrete, spalling at the walls.
- Statements from key personnel in the vicinity.

According to Kaiser and Cai (2012) there are many factors that have an influence on rockburst damage and the severity of the damage. Table 2 summarizes the main factors and groups them into four categories, i.e. seismic event, geology, geotechnical, and mining. Factors in the first two groups (seismic event and geology) determine the intensity of dynamic load at the damage locations, and the factors in the last two groups (geotechnical and mining) determine site response due to seismic impulses.

Table 2: Main factors influencing rockburst damage (modified from Kaiser and Cai, 2012)

Seismic event	Geology	Geotechnical	Mining
Event magnitude Seismic energy release Distance to seismic source	In situ stress Rock Type Beddings Geological structures (dykes, faults, and shears)	Rock Strength Joint fabric Rock brittleness	Mining induced static and dynamic stresses Excavation span Extraction ratio Mine stiffness Excavation sequence (stress-path), blasting Installed rock support system Backfill Production rate

A sheet record was defined to collect all valuable information after every stress event:

- Production: Date/Time; Blast time; Phase of production cycle;

- Geometry: chainage, section, area affected, overburden.
- Geology: lithology, structural geology

- Stress classification: stress effect and consequences.

A stress release classification was developed for the project based on previous experiences from the main contractor in the Gothard Tunnel. This classification was divided in four categories according to the characteristics and effects of stress releases.

Table 3: Stress Release Classification developed for Cheves Hydropower Project.

Stress Class	Description
0	Loud Relief, slight crumbling: crackling, banging, crumbling in surrounding rock mass
1	Stress-induced spalling without rock fall: rock surface cracks suddenly, creating scales up to 5cm, appearance of dust clouds
2	Stress-induced loosening or rock fall at lateral rock surface or face in unsupported area: rock breaks rough and very loud. Rock support system might be slightly damaged (Fissures in shotcrete).
3	Heavy Bangs with explosive rock fall: pieces or slabs of rock are thrown suddenly with loud bangs in radial direction from lateral rock surface (in supported and unsupported areas). The rock support system is damaged (Cracks in shotcrete, torn-off anchors, bent ring beams).

3.2 Prevention

The prevention of these types of stress phenomena is rather complicated but some techniques can be implemented. The three following measures were recommended:

- Preconditioning blasting ahead of the face
- Change of the shape of the face to a concave geometry
- Reduction of the round length

In relation to the use of preconditioning blasting ahead of the tunnel face, these blasts can minimize the effects of future possible rockbursts at the face (face burst), reducing the stress magnitudes at and ahead the face. This technique consists basically in the execution of blast drill holes ahead of the face at specific depths and locations using high velocity detonation explosives and full confinement of it. As a result, the rock mass quality beyond the face is decreased artificially, “distressing” the rock mass in the vicinity of tunnel to be excavated, and allowing the release of tension that otherwise could result in a rock burst.

The design of the preconditioning blast is based on the following criteria:

- Not generate an intense fracture the rock but yes “distressing” the rock mass, in order to not difficult following blast and support at face
- Focus the decompressing effect within the perimeters of the tunnel section by

generating fractures in the rock that allow to adjust the stress.

The preconditioning blast was executed by 3 holes of 51 mm and 4 m long, loaded on the last 2 meters with bulk Slurrex explosive. These holes were proposed to be drilled on a vertical alignment with the tunnel axis, in between production holes.

Analysing the energy distribution, we can predict that energy from production holes interacts with preconditioning holes. These combinations of energies are expected to create a tunnel free face with a set of cracks concentrated vertically. After a first test shot it must be evaluated how those perform. Proper performance implies both a continuous set of vertical cracks interconnected and a good enough rock mass to be drilled around pre-conditioning holes.

Because cracks induced on fully confined holes are due to tension created by a shock wave, it is not intended to use the gas energy of the explosive for either crack extension or rock displacement. For this reason, explosive charges can be unconfined. Expect however a flyrock potential increase that can damage equipment or infrastructure if not properly protected.

Figure 5 below shows the energy distribution at -2.2 m (top left), -3 m (top centre) and -4 m (top right) with a 3-hole configuration at 51 mm with Slurrex.

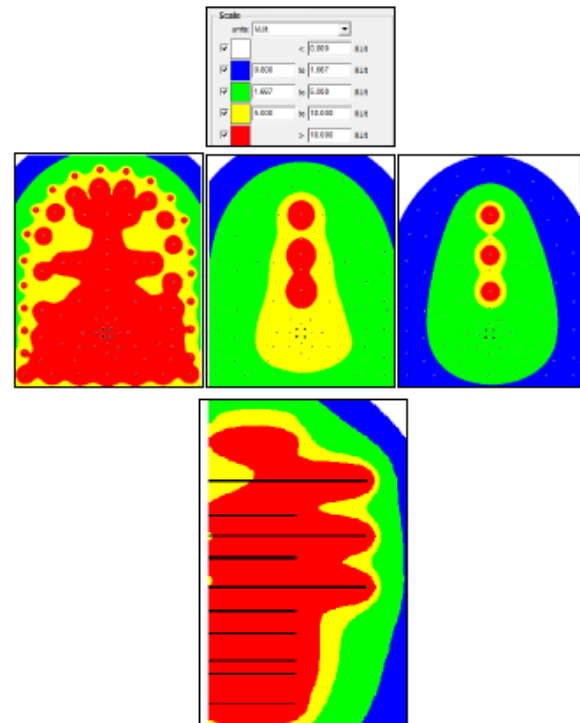


Figure 5: Energy distribution of preconditioning blast with a 3-hole configuration at 51 mm with Slurrex.

A second measure recommended was to change the face excavation shape from planar to a concave

geometry as planar planes always accumulate higher stresses than curved planes. In relation with this same effect it was also suggested to the Owner the possibility of changing the shape of the tunnel section to a Horse-shoe or even more, with curved walls with high potential risk of rockburst. Nevertheless, this measure was not finally implemented.

Finally, the reduction of the round length was considered a less effective measure with a minor effect in the release of stresses and consequently in the rockburst occurrence, but it has a notable effect on shortening the construction cycle and therefore decreasing the exposure of the personnel at the face.

3.3 Protection

Two different types of measures were proposed in order to protect the tunnel workers at the face:

- To reduce the vulnerability and exposure of the personnel.

It was recommended to reduce the vulnerability and the exposure of the tunnel workers at the tunnel face as risks factors. For this reason, basic measures were adopted, as to carry out scaling using mechanical facilities and protective cages for workers and machinery.

- To install a temporary support at the face.

Two different support elements were basically used: shotcrete and/or rock bolts (swellex). In both cases the purpose was to avoid rock fragment ejections from the face.

According to previous experiences in Gothard Tunnel, it was recommended that a layer between 5.0 and 10.0 cm of shotcrete with steel fibres, as well as a

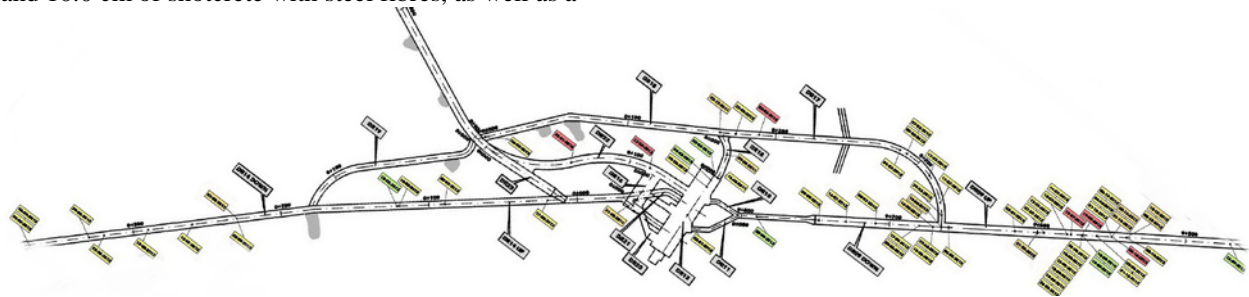


Figure 7: Distribution of stress events around the Powerhouse.

An analysis of the stress events over time shows an erratic distribution of events. There were several months in which the stress events had more influence over the project. Figure 8 shows the distribution of the stress events and the number of events in each tunnel over time.

The data demonstrates that Headrace tunnel has been the most affected by stress events, and the

variable number of swellex bolts be installed at the face. These bolts were always longer than the advance round length.

4. ROCKBURSTS RECORD AT THE HEADRACE TUNNEL

As mentioned before, 859 stress events were reported between Aug. 2012 and Jul. 2014, 48% of which were recorded as banging noises without rock ejections or support damages, 41% of the events were classified as Stress Class 2 and 3 with rock support damages, and only 16% of the events involved violent rock ejections or/and support. Figure 6 shows the distribution of the events according to intensity.

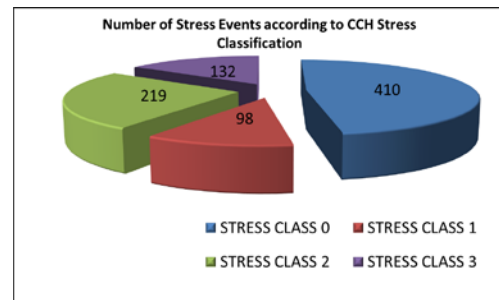


Figure 6: Stress Events intensity distribution according to CCH classification.

About 90% of the events were recorded in the Headrace tunnel. The rest of the events were recorded in the tunnels surrounding the Powerhouse.

influence of these events has three clear steps. From Jan. 2012 to Dec. 2012 it is possible to define an increasing tendency, a quiet period during Jan. 2013, and an increasing tendency from Feb. to Apr. 2013.

The chart also shows that the stress events continued after the tunnels completion, when the support was removed in some tunnels to execute the required concrete plugs.

CHEVÉ'S HYDROPOWER PROJECT - STRESS EVENTS SUMMARY																											
Date	Preload	08/2012	09/2012	10/2012	11/2012	12/2012	01/2013	02/2013	03/2013	04/2013	05/2013	06/2013	07/2013	08/2013	09/2013	10/2013	11/2013	12/2013	01/2014	02/2014	03/2014	04/2014	05/2014	06/2014	07/2014	Total	
DR02	0	0	0	0	0	0	0	0	0	0	0	0	0	0	0	0	0	0	0	0	0	0	0	0	0	0	0
DR04	0	0	0	0	0	0	0	0	0	0	0	0	0	0	0	0	0	0	0	0	0	0	0	0	0	0	0
DR05	0	0	0	0	0	0	0	0	0	0	0	0	0	0	0	0	0	0	0	0	0	0	0	0	0	0	0
DR07	0	1	1	0	0	0	0	0	0	0	0	0	0	0	0	0	0	0	0	0	0	0	0	0	0	0	2
DR08	0	3	6	2	10	8	4	2	5	10	2	1	3	3	7	4	5	0	0	0	0	0	0	0	0	0	85
DR09 US	11	1	21	08	45	105	3	39	111	120	13	25	12	18	10	10	36	29	3	9	0	0	0	0	0	0	685
DR10 US	7	0	8	0	0	0	0	0	0	0	0	0	0	0	0	0	0	0	0	0	0	0	0	0	0	0	24
DR10	0	0	0	1	0	0	0	0	0	0	0	0	0	0	0	0	0	0	0	0	0	0	0	0	0	0	1
DR11	0	0	0	1	0	1	0	0	0	0	0	0	0	0	0	0	0	0	0	0	0	0	0	0	0	0	2
RD11	0	0	0	0	1	0	0	0	0	0	0	0	0	0	0	0	0	0	0	0	0	0	0	0	0	0	1
DR06	0	0	0	0	0	0	0	0	0	0	0	0	0	0	0	0	0	0	0	0	0	0	0	0	0	0	0
DR13	4	0	0	1	0	0	0	0	0	0	1	0	0	0	0	0	0	0	0	0	0	0	0	0	0	0	6
DR14 US	5	0	0	0	0	0	0	0	0	0	0	0	0	0	0	0	0	0	0	0	0	0	0	0	0	0	5
DR14 US	3	4	2	0	3	1	1	1	0	0	0	0	0	0	0	0	0	0	0	0	0	0	0	0	0	0	21
DR15	0	0	0	0	0	0	0	0	0	0	0	0	0	0	0	0	0	0	0	0	0	0	0	0	0	0	0
DR16	0	0	1	0	0	0	0	0	0	0	0	0	0	0	0	0	0	0	0	0	0	0	0	0	0	0	1
DR17	9	0	0	0	0	0	0	0	0	0	0	0	0	0	0	0	0	0	0	0	0	0	0	0	0	0	9
DR18	3	0	0	0	0	0	0	0	0	0	0	0	0	0	0	0	0	0	0	0	0	0	0	0	0	0	3
DR19	0	0	0	0	0	0	0	0	0	0	0	0	0	0	0	0	0	0	0	0	0	0	0	0	0	0	1
DR22	1	0	0	0	0	0	0	0	0	0	0	0	0	0	0	0	0	0	0	0	0	0	0	0	0	0	1
DR23	1	0	0	0	0	0	0	0	0	0	0	0	0	0	0	0	0	0	0	0	0	0	0	0	0	0	1
Total	44	23	37	79	63	113	14	42	117	136	16	26	15	21	17	14	41	35	9	8	0	3	9	0	0	859	
STRESS CLASS	Preload	08/2012	09/2012	10/2012	11/2012	12/2012	01/2013	02/2013	03/2013	04/2013	05/2013	06/2013	07/2013	08/2013	09/2013	10/2013	11/2013	12/2013	01/2014	02/2014	03/2014	04/2014	05/2014	06/2014	07/2014	Total	
STRESS CLASS 0	25	21	20	51	21	43	8	8	45	62	5	17	7	7	8	12	11	11	4	0	0	0	0	0	0	0	412
STRESS CLASS 1	3	1	3	1	7	3	2	13	13	23	0	1	0	0	0	0	0	0	25	0	0	0	0	0	0	0	36
STRESS CLASS 2	0	1	0	16	20	20	2	17	34	16	11	7	8	11	9	1	29	2	0	0	0	0	0	0	0	0	210
STRESS CLASS 3	7	7	1	1	9	43	4	4	23	29	9	1	0	0	0	2	4	0	0	0	0	0	0	0	0	0	182
Total	44	23	37	79	63	113	14	42	117	136	16	26	15	21	17	14	41	35	9	8	0	3	9	0	0	859	

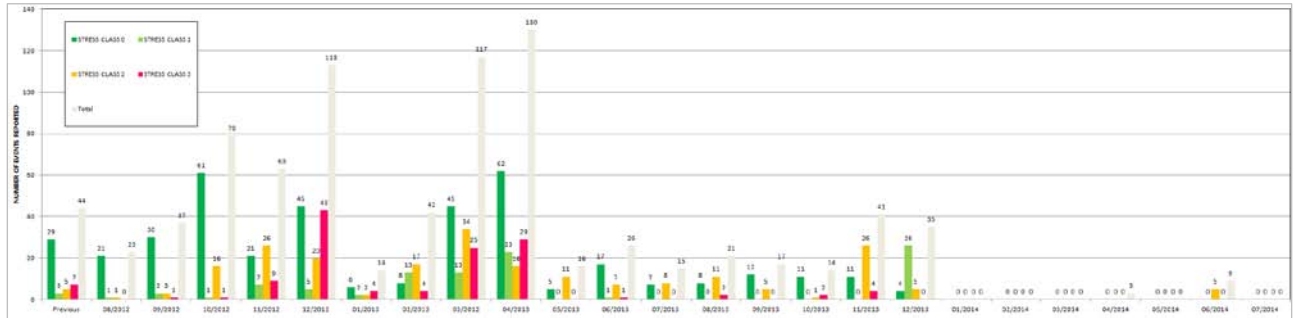


Figure 8: Stress Events distribution according to CCH classification and tunnels.

5. PARAMETRICAL ANALYSIS OF THE STRESS EVENTS

A detailed record of all stress events was carried out and statistical analysis was implemented to understand the rockburst phenomena in the project. The analysis confirmed that the overburden in the tunnels was related with the following factors:

- Overburden
- Lithology
- Jointing and other structures
- Rock mass quality
- Time after blasting

- Round length
- The follow describes the particular analysis for Headrace tunnel.

5.2 Overburden

Headrace tunnel was designed with a positive slope of 14%. The overburden considered in the vertical tunnel axe shows an increasing tendency. The overburden is close to 850 m at the powerhouse area and rises to approximately 1.450 m. Figure 9 shows the topographical longitudinal section with the overburden.

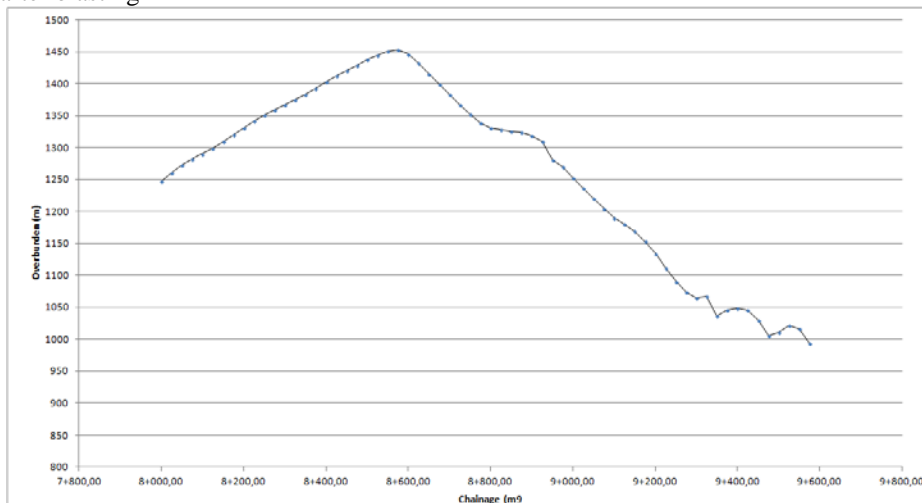


Figure 9: Headrace tunnel overburden.

It will be shown later that minor changes in the overburden due to the presence of irregular topography will have a significant influence on the stress release.

The next figure shows the relationship between stress events and depth. It would be expected that

there would be more events deeper in the excavation, however, it was observed that major events occurred between 1000 and 1150 m in the Headrace tunnel and about 800 m around the Powerhouse.

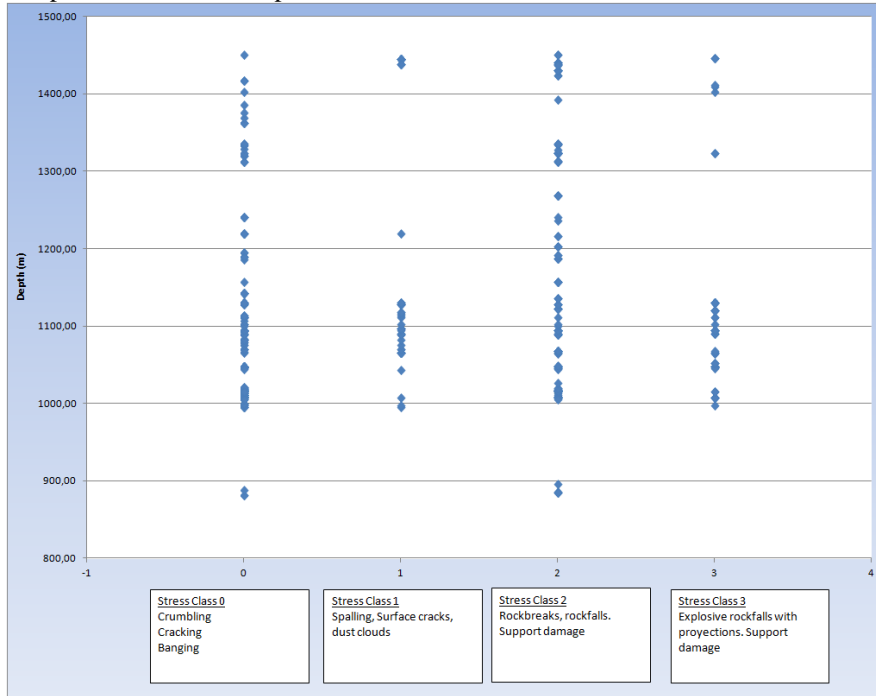


Figure 10: Stress Events vs. Depth.

5.3 Lithology

Headrace tunnel has been excavated in different lithology: hornfels, quartzmonzonite, subvolcanic breccias, and granodiorite. The influence of the stress events on each lithology has been different along the excavation period. The geological conditions after each event were recorded, considering the lithology and the rock mass quality.

A statistical analysis of the results clearly shows that lithology with higher brittle behaviour had suffered a higher number of stress events. It has also been checked that not only areas with good rock conditions are affected by overstress, but also zones where rock mass quality in terms of RMR values are considered fair ground. Figure 11 shows the distribution of stress events in relation to lithology.

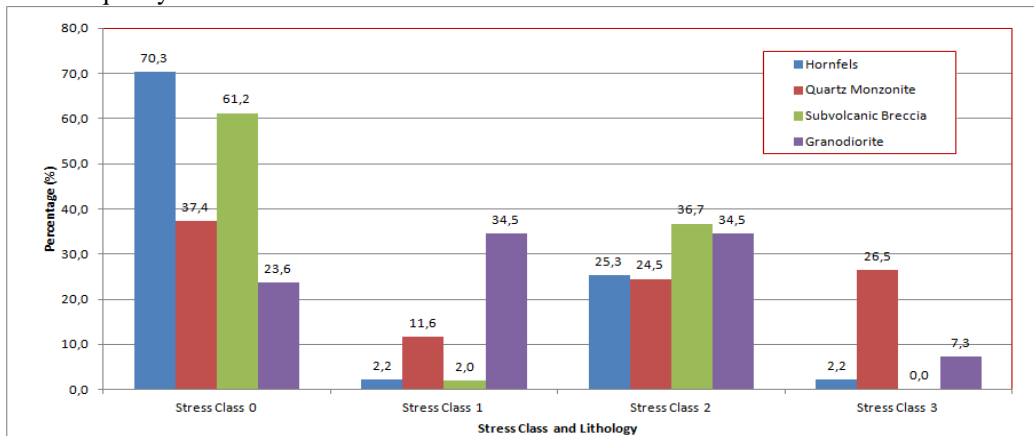


Figure 11: Stress Events vs. Lithology.

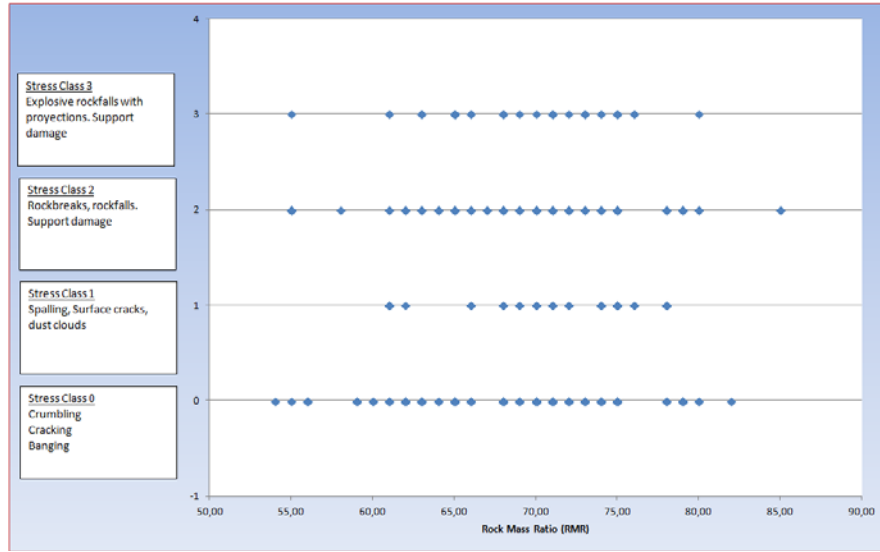


Figure 12: Stress Events vs. RMR.

5.4 Geological Structure

The presence of the same joint set family was detected in most of the stress events. An analysis of the stronger events and information from core drillings executed at the tunnel face confirmed that rockbursts are highly controlled by the geological

structures. Only eleven (11) events represent the 60% of the events described in Headrace tunnel and sum the 79% of the Stress Class 3 events reported. The joint system at the areas where this rockburst took place was analyzed, as shown in Table 4.

Table 4: Structural data mapped after rockburst events.

CH		Lithology	JOINTS					
			J1		J2		J3	
Start	End		DIP	DIP DIR.	DIP	DIP DIR.	DIP	DIP DIR.
9+557,50	9+555,50	Metamorphic Rock-Hornfels	10	320	75	220	80	190
9+555,50	9+553,00	Metamorphic Rock-Hornfels	11	308	49	347	74	140
9+553,00	9+550,20	Metamorphic Rock-Hornfels	18	300	50	155	45	280
9+490,70	9+487,80	Subvolcanic breccia contact with Hornfels	45	295	60	5		
9+487,80	9+485,50	Metamorphic Rock-Hornfels	75	5	60	305		
9+408,30	9+405,50	Metamorphic Rock + Qz-Monzonite	65	100	15	300		
9+405,50	9+403,30	Metamorphic Rock + Qz-Monzonite	72	115	35	240		
9+403,30	9+400,70	Metamorphic Rock + Qz-Monzonite	35	328	55	154	5	140
9+297,90	9+295,10	Metamorphic Rock + Qz-Monzonite	70	140	20	290	45	200
9+295,10	9+292,50	Metamorphic Rock + Qz-Monzonite	83	148	11	109	50	320
9+246,40	9+244,20	Metamorphic Rock + Qz-Monzonite	35	280	55	165	80	55
9+226,10	9+223,80	Metamorphic Rock + Qz-Monzonite	20	260	85	320		
9+208,70	9+205,90	Metamorphic Rock + Qz-Monzonite	25	220	70	250	43	330
9+203,60	9+201,20	Metamorphic Rock + Qz-Monzonite	44	285	84	140		

Figure 13 shows the stereographic analysis of these joints system. As it can be observed the presence of two joint sets with two parallel systems each one were deduced.

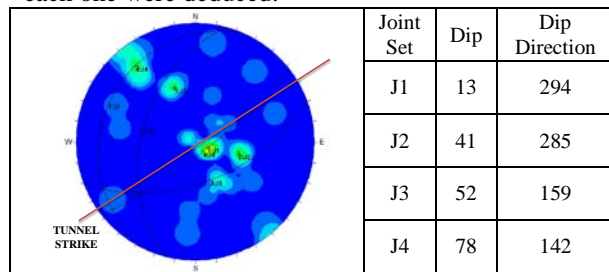


Figure 13: Stereographic analysis.

According to this analysis, the presence of sub-horizontal joints dipping to the left wall, and sub-vertical joints dipping to the right wall of the tunnel have to be considered as a sign of possible stress release.

It was also detected that when shear zones associated to the joints system were encountered at the face, the stress events usually turned out. This fact was also detected in the core drillings carried out at the tunnel face. This is clear in the photos shown in Figure 14.



Figure 14: Tunnel face at rockburst events in Headrace tunnel.

5.5 Rock mass quality

The rock has been described according the Rock Mass Rating. In all cases the RMR represents a good quality rock mass. Figure 15 shows the relation between the stress events and the RMR value.

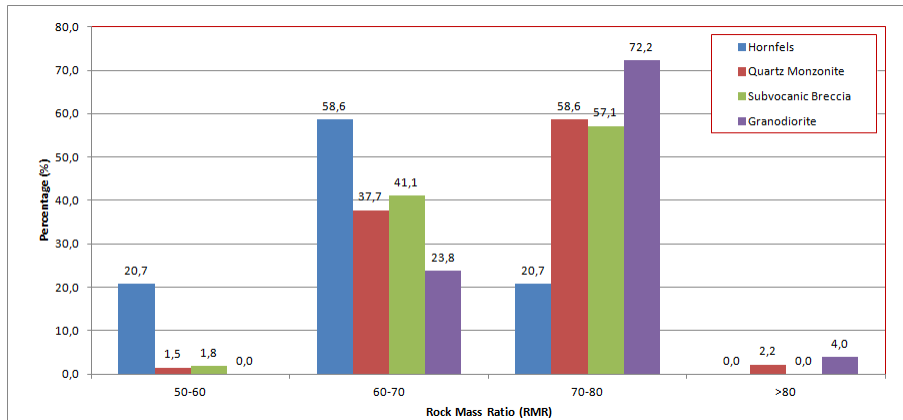


Figure 15: Rock Mass rating (RMR) vs. Lithology.

5.6 Time after Blasting

A detailed analysis of the time in which the event took place after blasting was carried out for the stress events that took place in the Headrace tunnel. In a

first analysis the relationship between the stress class of the event and the time in which it took place was analysed. Figure 16 shows this analysis.

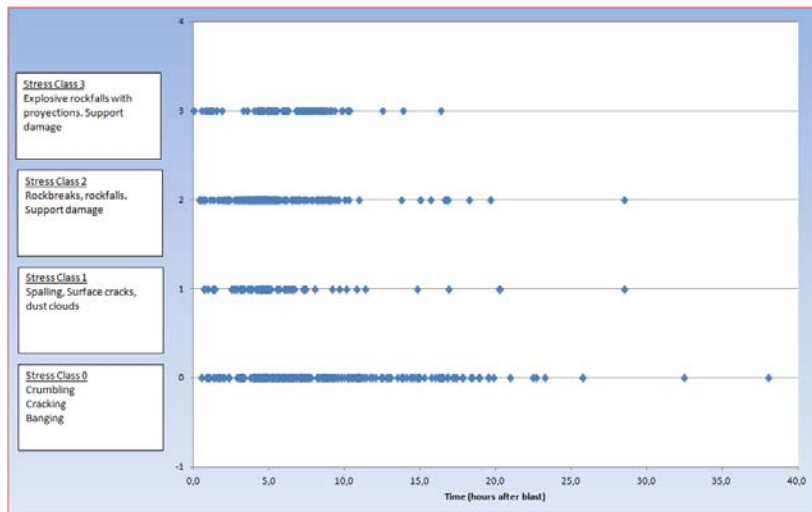


Figure 16: Stress class vs. Time Event.

The chart shows that the violent events occurred in range of 10 hours after blast; meanwhile it is possible to detect lighter stress releases in a wide range of more than 24 hours.

A statistical analysis of these events were carried out in order to analyse the possibility of implementing a re-entry strategy as it is usual in other

projects or in mining activities. Figure 17 shows the distribution of the stress events in relation with time after blasting.

Both analyses show that the time event occurrence after blast presents a broad range that makes difficult to define a re-entry strategy.

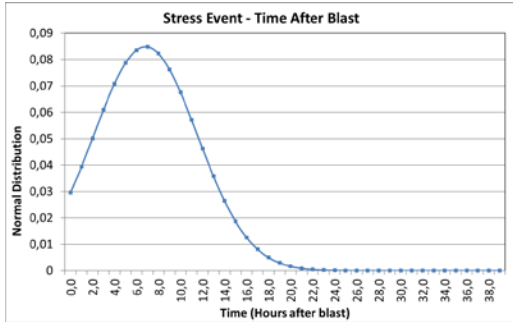


Figure 17: Normal distribution of the Stress Event time after blast. (Theoretical curve).

5.7 Round Length

A rounds length analysis was carried out during the excavation of Headrace tunnel in cases with stress releases as a first step. Figure 18 presents the normal distribution of round length in those cases in which a stress releases occurred.

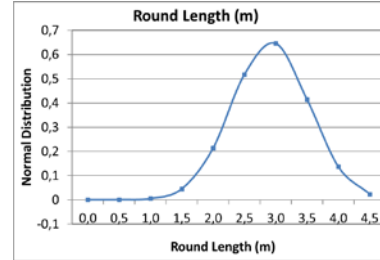


Figure 18: Normal distribution of the round length in rounds with stress event. (Theoretical curve).

According to the results, rounds in which stress releases turned out are between 2.5 and 3.5 m long. In Figure 19 the number of stress releases per round is presented. This chart shows clearly that the major part of the events occurred with rounds longer than 2.5 m. However, the tendency is not so clear.

The distribution of events according to stress classes established by CCH and in relation with the round length has been analyzed. The Figures 20(a)-(d) represent these analyses. The charts clearly show that stress releases are more likely in longer rounds, from 2.5 to 3.5 m.

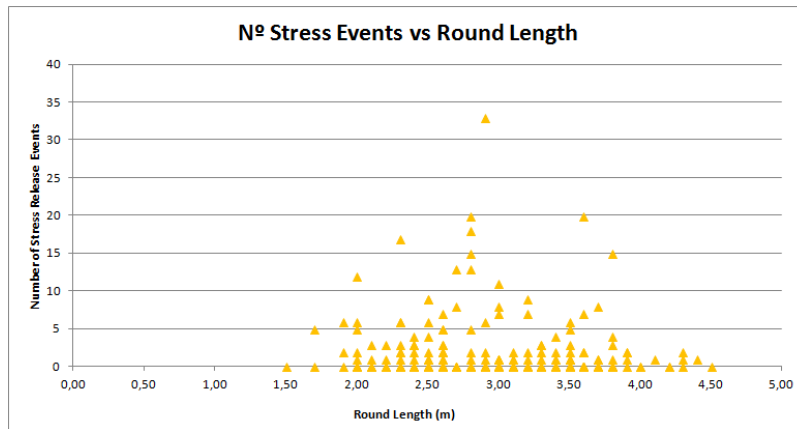


Figure 19: Number of stress events vs. round length.

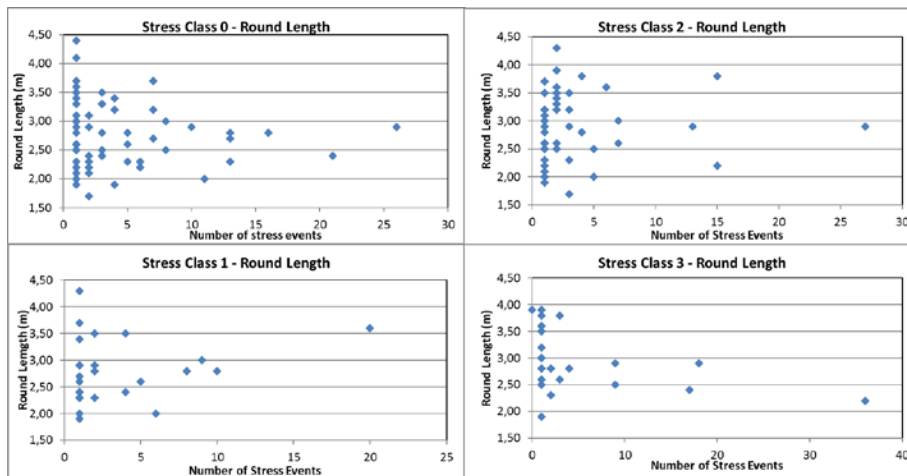


Figure 20(a)-20(d): Number of stress events per each stress class vs. round length.

5.8 Global analysis

A final analysis considering all the previous described parameters was done in order to define the weight of each factor and in order to define alarm signs that permit to anticipate risk areas.

The overall analysis for the Headrace tunnel is shown in Figure 21. The stress events recorded at each chainage have been represented in this chart, according to the stress event classification developed, in conjunction with the rock mass rating (RMR), the overburden, the round length, and the lithology.

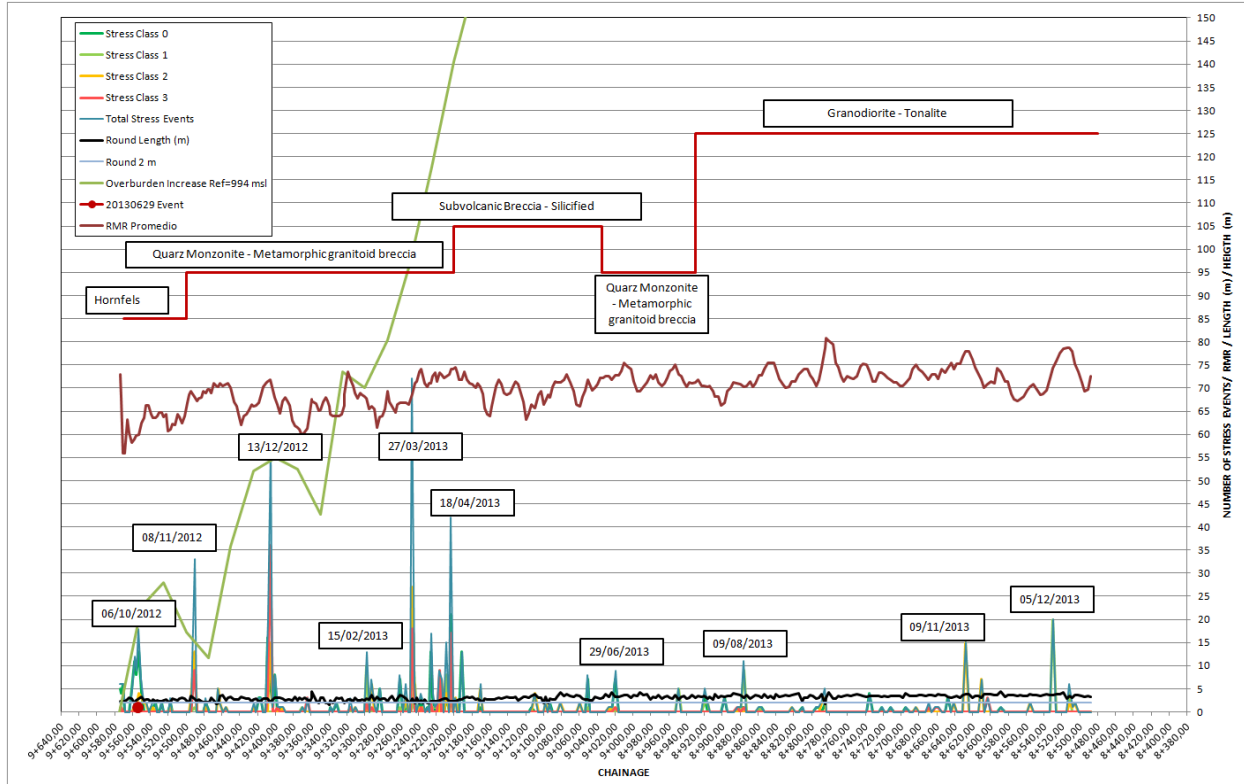


Figure 21: Stress factors comparison.

Based in the results, it is clear that the main factor was the lithology, as most of the events and intense events were recorded in quartzmonzonite, meanwhile other lithologies such as volcanic breccias presented less rockburst prone conditions. In Quartzmonzonite, rockburst and/or stress release occurred systematically. Meanwhile in subvolcanic breccias “quiet periods” were recorded for a stretch of approximately 60 m. In massive intrusive rock (granodiorite) some periods without stress released evidences were detected, however it is not clear the reason for this lack of stress activity.

6. ROCKBURST PRONE CONDITIONS SUPPORT

Several support measures were implemented to mitigate the rockburst prone conditions during the excavation of the tunnels in the Cheves project, both at the face and behind the face. The support design included the following items:

- Reduce the round length

- Destress the rock in advance with pre-conditioning blasting
- Pre-stabilise the face with swellex bolts, longer than the round length
- Double shotcrete layer and welded wire mesh to support the advanced section in combination with rockbolts

During the excavation of the Headrace tunnel and due to the intensity/severity of the stress events several changes were introduced in the support with successful results.

- Continuous monitoring of stress releases
- Increased the bolt pattern in some areas
- Fully grouted bolts (with a sleeve to protect the beginning of the bolts) were implemented in fault/shear areas with a huge improvement in the rock support
- The use of a high tensile chain link mesh fixed to the section with split set bolts and mechanically installed
- Modifications in the shotcrete thickness were also implemented with good results

- Additional swellex (3 m long) were instructed to provide a pre-stabilization of the section with good results
- Different rounds length according to the reported stress behaviour

However, the design support has been working out on the limit of its capacity as it has been affected several times by huge stress events with dramatic consequences. The designed system consisted of two layers of shotcrete and welded wire mesh has been affected several times in such way that it was required a complete repair works in order to provide enough safety environments to continue with the advance of the tunnel.

The damages on the rock support have varied from fissures on the shotcrete to collapse/projection of concrete slabs, going through the welded wire mesh.

7. CONCLUSIONS

Rockburst has been extensively described in deep mining, but nowadays there are several civil projects that require the construction of deep tunnels.

Table 5: Stress classification proposed.

Stress Class	Denomination			Description
0	Stress relief			Loud Relief, slight crumbling: crackling, banging, crumbling in surrounding rock mass
1	Spalling			Stress-induced spalling without rock fall: rock surface cracks suddenly, creating scales up to 5cm, appearance of dust clouds
2	Intense Spalling			Stress-induced loosening or rock fall at lateral rock surface or face in unsupported area: rock breaks rough and very loud. Rock support system might be slightly damaged (Fissures in shotcrete).
3	3.I	Minor Rockburst	Damage severity > 0.25 m	Heavy Bangs with explosive rock fall: pieces or slabs of rock are thrown suddenly with loud bangs in radial direction from lateral rock surface (in supported and unsupported areas). The rock support system is damaged (Cracks in shotcrete, torn-off anchors, bent ring beams).
	3.II	Moderate Rockburst	Damage severity > 0.75 m	
	3.III	Major Rockburst	Damage severity > 1.50 m	

Support measures to mitigate the rockburst conditions have to be continuously adapted to the stress and ground conditions. However, it has been proven that welded wire mesh provides safe conditions to avoid rock and shotcrete slabs ejections.

8. ACKNOWLEDGEMENTS

The authors would like to express their gratitude to SN Power, specifically Paul Lazenby and Kjell Ingemarsson, for granting permission to publish this work.

9. REFERENCES

Aydan, Ö., Genis, M., Akagi, T., Kawamoto, T. 2001. Assessment of Susceptibility of Rock Bursting in Tunnelling in Hard Rocks. *Modern Tunneling*

Under these circumstances it is necessary to consider an overstress analysis of the projects in the design stage.

It is important to establish an adequate classification of the stress release events that take place during the excavation of the tunnels, and record all relevant information in order to carry out a continuous analysis of the project.

The stress classification developed for the Cheves project has provided good results to avoid misunderstanding of what is a stress release and what can be considered a rockburst. However, it needs to be improved and for this reason it has been considered to subdivide the stress class 3 in three categories considering the intensity of the damage. Moreover, the damage severity classification established by Kaiser et al. (1996) has been considered.

It is important to differentiate between stress releases, that not caused damaged (only cracking and banging sounds), and rockburst where a damage to the excavation and/or support took place.

Science and Technology, Adachi et al (eds), 2001 Swets & Zeitlinger.

Barton, N. 2002. Some new Q-value correlations to assist in site characterization and tunnel design. *Int. J. Rock Mech. & Min. Sci.* Vol. 39/2:185-216.

Bieniawski, Z. T. 1976. Rock Mass Classification in Rock Engineering. *Proceedings, Symposium on Exploration for Rock Engineering, Johannesburg*, pp. 97-106.

Bieniawski, Z. T. 1989. *Engineering Rock Mass Classifications*. New York: Wiley.

Brox, D. 2013. Evaluation of overstressing of deep hard rock tunnels. *World Tunnel Congress 2013 Geneva Underground – the way to the future!* G. Anagnostou & H. Ehrbar (eds).

Cai M. and Champaigne D. 2009. *The Art of Rock Support in Burst-Prone Ground. RaSiM7: Controlling Seismic Hazard and Sustainable Development of Deep Mines.*

Cai M. 2011. Rock Mass Characterization and Rock Property Variability Considerations for Tunnel and Cavern Design. *Rock Mech Rock Eng* (2011) 44:379–399.

Castro, S.O., Soler, J. P., Andrade C.F and Delucchi H.A. Rock Mass Stress Release in the Alfafal Main Water Tunnel: Evidence and Remedial Actions.

Diederichs, M.S., J.L. Carvalho and T.G. Carter, 2007. A modified approach for prediction of strength and post yield behaviour for high GSI rock masses in strong, brittle ground, 1st Canada-U.S. Rock Mech. Symp., 249-257.

Hoek, E. Brown, E. 1980. Underground Excavations in Rock. Institution of Mining and Metallurgy.

Hoek, E., P.K. Kaiser and W.F. Bawden, 1995. Rock Support for Underground Excavations in Hard Rock. A.A. Balkema, Rotterdam, 215 p.

Hoek, E. & Diederichs, M. S. 2006. Empirical Estimation of Rock Mass Modulus. *Int. J. Rock*

Internal documents. 2012-2014. Cheves Hydropower Project. Constructora Cheves, SAC (joint venture Hochtief Solutions AG, SalvaCorp SA and ICCGSA), Lima, Peru. Not published.

Internal documents. 2012-2014. Cheves Hydropower Project. Contract Documents. Basic Design Report. SNPpower and Norconsult, Lima, Peru. Not published

Mech. Min. Sci., 43, pp. 203-215.

Kaiser, P.K., Diederichs, M.S., Martin, C.D., Sharp, J. and Steiner, W. (2000) Underground Works in Hard Rock Tunnelling and Mining, in Proceedings International Conference on Geotechnical and Geological Engineering (GeoEng2000), 19–24 November 2000, Melbourne, Australia, pp. 841–926.

Kaiser, Peter K. 2006. Rock Mechanics Considerations for Construction of Deep Tunnels in Brittle Rock. Asian Rock Mechanics Symposium, Singapore.

Kaiser, P. K. 2011. How highly stressed brittle rock failure impacts tunnel design

Kaiser, P. K., S. Maloney, P. Vasak and G. Wang, 2009. Seismic excavation hazard evaluation in underground construction. 7th RaSiM6, Dalian, China, 1-26.

Kaiser, P. K. and Cai M. 2012. Design of rock support system under rockburst condition. *Journal of Rock Mechanics and Geotechnical Engineering*. 2012, 4 (3): 215–227

Kaiser, P. K. and Cai M. 2013. Critical review of design principles for rock support in burst-prone ground – time to rethink! *Ground Support 2013* — Y. Potvin and B. Brady (eds).

Lee, S.M., Park, B.S., Lee, S.W. 2004. Analysis of rockburst that have occurred in a water way tunnel

in Korea. Paper 3B 24 — SINOROCK2004 Symposium *Int. J. Rock Mech. Min. Sci.* Vol. 41, No. 3.

Malek, F.; Suorineni, F. T., Vasak, P. Strategies for Rockburst Management at Vale Inco Creighton Mine.

Martin, C.D., P.K. Kaiser and D.R. McCreath, 1999. Hoek-Brown parameters for predicting the depth of brittle failure around tunnels. *Canadian Geotechnical Journal*, 36(1):136-151.

Norwegian Geotechnical Institute, NGI (2013). Using the Q-system (handbook). Rockmass classification and support design.

Palmstrøm A. 1995. Characterizing Rock Burst and Squeezing by the Rock Mass Index. Design and Construction of underground Structures, New Delhi, 23 - 25 February 1995

Palmstrøm A. 1996. Characterizing Rock Masses by the RMI for Use in Practical Rock Engineering. *Tunnelling and Underground Space Technology*, Vol. 11, No. 3, pp. 287-303.

Rocscience Inc. 1997, Examine3D Version 4.0 - 3D Engineering Analysis for Underground Excavations. www.rocscience.com, Toronto, Ontario, Canada

Rocscience Inc. 2002, RocLab Version 1.0 - Rock Mass Strength Analysis using the Generalized Hoek-Brown failure criterion. www.rocscience.com. Toronto, Ontario, Canada.

Rocscience Inc. 1999, Dips Version 5.0 - Graphical and Statistical Analysis of Orientation Data. www.rocscience.com, Toronto, Ontario, Canada.

Stillborg, E.B. and Hamrin, H. 1990. Solving the rock burst problem with Swellex. *Tunnels Tunnelling*, p.67, 5pp., (in English), Mar. 1990.

Tooper, A.Z., Kabongo, K.K., Stewart, R.D. and Daehnke, 2002. A. The mechanism, optimization and effects of preconditioning. *The Journal of The South African Institute of Mining and Metallurgy*

Rockburst mitigation experiences on underground projects in the Cheves Hydropower project in the Peruvian Andes

Santiago Veyrat ^a, Jose-Miguel Galera ^{b,*}, Marcos Sancho ^c

^a Subterra Ingeniería SL, Madrid, Spain, 28015

^b Subterra Ingeniería Ltda., Santiago, Chile, 7750181

^c Subterra Perú SAC, Lima, Perú, 18

ABSTRACT

The main problems related with the design and construction of tunnels and caverns under high overburden are analyzed in this paper. As an example, the recent experiences during the construction of the Cheves Hydropower project in the Peruvian Central Andes are described. During its construction, 850 rockburst events were recorded, enabling designers to collect data and make some correlations that may be useful for future projects.

KEYWORDS: tunnel, cavern, depth, rock support, rockburst.

1. INTRODUCTION

Cheves Hydropower plant is located in the central highlands of Peru, close to Lima, in the basins of the Huaura and Checras rivers. The project was developed by the “Empresa de Generación Eléctrica Cheves SA”, a company of the Norwegian group Statkraft. The construction, with a \$400 million budget for the civil works, is currently in operation. The company responsible for construction is a consortium (Constructora Cheves) formed by Hochtief Solutions AG (Germany), SalfaCorp (Chile) and ICCGSA (Peru). In relation to the project design, Norconsult, as Owner Engineering, was the consultant company in charge of the permanent works design, including the layout, the long-term stability and the final support of the underground works. Subterra, acting as the Contractor Engineering, was in charge of the initial support of the underground works, as well as of the geotechnical engineering during the construction. This article therefore only describes the work developed by both the Contractor and Subterra.

The project includes the construction of two concrete dams upstream from the headrace tunnel (Huaura and Checras dams), interconnected through a transfer tunnel of 2.58 m long. The second dam leads the water to the headrace tunnel of about 10 km long. The project also considered a third dam downstream from the powerhouse (Picunche dam), whose function is regulation and irrigation.

To summarize, the Cheves Hydropower project's components are described as follows:

- Huaura dam (concrete dam of 13 m high),
- Transfer tunnel (hydraulic channel that leads the water from Huaura dam to Checras dam, with a length of 2.580 and a cross section of 16 m²),
- Checras dam (concrete dam of 25 m high),
- Headrace tunnel (9.693 m long and cross sections between 22 and 30 m², where the first stretch has an inclination of 0.9% and the last one 14%),
- Surge tunnel of 700 m long and 14% and one adit tunnel with similar dimensions but no slope,
- Powerhouse cavern (60 m long, 32 m high and 15.50 m width) and Transformer cavern (27.5 m long, 14 m high and 11.20 m width),
- Access tunnel to the powerhouse and drifts (1.700 m in total),
- Tailrace tunnel (3.312 m long and 25 m²) and
- Picunche dam (earth dam of 15 m high).

Therefore, the total length of the tunnels, considering the access tunnel and all the drifts is about 20 km.

Figure 1 shows a longitudinal section of the project showing all the already described components of the hydropower project.

As it can be observed, there is a section in the Headrace tunnel, linked to the steepest stretch where the overburden is systematically above 1.000 m, being the maximum around 1.500 m. Basically, the dynamic or stresses related events took place in that tunnel section as well as in the cavern complex at the Powerhouse area.

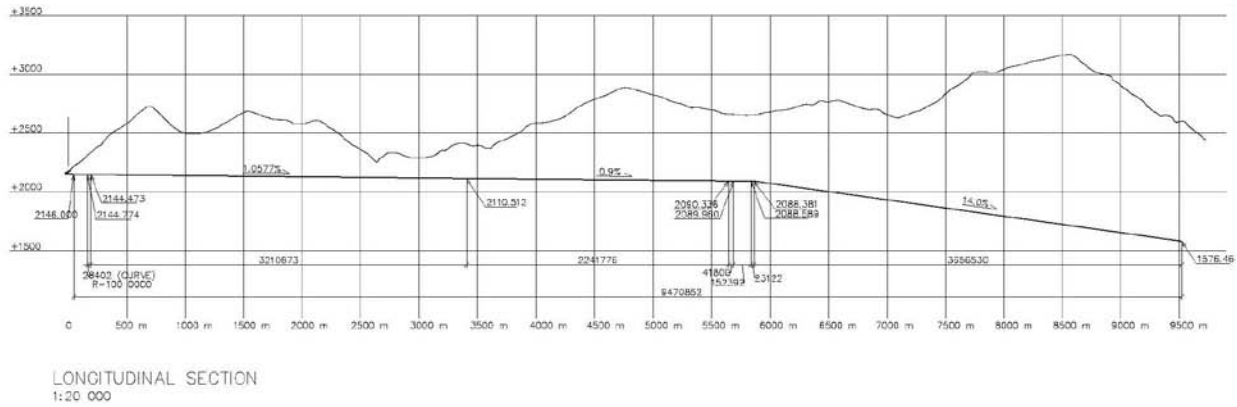


Figure 1: Longitudinal section of Cheves Hydropower project.

2. GEOLOGY

Cheves Hydropower project is located in the Huaura River Basin, within the Central Andean Range. This region is close to the Nazca plate, and therefore affected by active tectonics and high seismicity.

The geology of the area is complex, with volcano-sedimentary, volcanic rocks; plutonic and related contact metamorphic groups.

Figure 2 shows a longitudinal section of the project showing all the described geological groups.

The headrace tunnel and powerhouse area, in which the dynamic events were recorded, have been excavated in hard rock: granites and hornfels.

In the case of the caverns, both are located in a structurally complex area due to the presence of intrusions of tonalite associated with subhorizontal shear joints and metamorphic rocks.

The properties of the geological groups are as follows:

- Chimu Formation: formed by quartzite banks interbedded with layers of quartz sandstone, shale, and occasionally coal layers. Quartzite has a high strength and a brittle response, with multiple fractures filled with iron oxide.
- Volcano-sedimentary rocks: belonging to the Chimu formation, are formed by blocks embedded in a green matrix, with a moderate-high level of fractures and weathering.
- Casma Group: andesite with a porphyry texture.
- Stock Churin Bajo: formed by intrusive rocks as tonalite, granodiorite and quartz-monzonite. These rocks have high strength, and low to moderate weathering, with iron oxides fillings in the fractures.

Hornfels: metamorphic rocks resulting from the contact between the andesite and the intrusive rock. They are very silicified and brittle. The representative values for these formations at intact rock level are shown in Table 1.

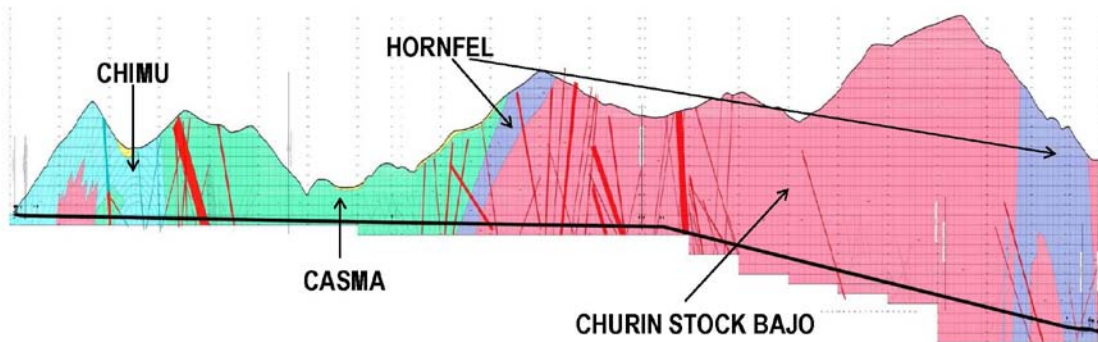


Figure 2: Geological longitudinal section of the project

Table 1: Intact rock properties.

LITHOTYPE	LITHOLOGY	ρ_{ap} (t/m ³)	σ_{ci} (MPa)		E_i (MPa)	ν	mi
			RANGE	VALUE			
Churin Bajo Stock (KsTi-qzmo)	Tonalites	2.62	100-150	110	44,000	0.24	25
				125	50,000		
	Tonalites (Fault zone)	2.62	80-120	90	36,000	0.24	25
Churin Bajo Stock (KsTi-hf)	Hornfels	2.62	80-120	90	49,500	0.24	19
Casma Group (Ki-ca)	Andesites (Fault Zone)	2.62	70-120	80	32,000	0.24	25
			100-150	110	44,000		
	Andesites		120-200	130	52,000		
Chimu Formation (Ki-ch)	Quartzites with shales and sandstones interbedded (Fault Zone)	2.62	30-80	40	15,000	0.24	20
			30-80	40	15,000		
	60-120		70	26,250			
	30-80		40	15,000			

As it was explained before, rockburst events were related to the two latest groups, high strength and stiff lithology.

3. ROCKBURST AND OTHER STRESS RELATED EVENTS

Rockburst was first recorded in the deep mines of South Africa, but is now becoming more important in the Civil Engineering sector due to the construction of deep tunnels. Rockburst is defined as a violent and sudden failure of the rock mass, clearly linked to excavations in competent rock with significant overburden, as well as in the presence of structures and dykes. As long as the overburden goes up, the connection between the natural stress and the strength and/or stiffness of the rock mass increases, and therefore the likelihood of rockburst increases as well.

Figures 3 and 4 show an example of two rockbursts that happened in Cheves project, the first one behind the excavation face, near the Powerhouse cavern, and the second one at the excavation face during the construction of the Headrace tunnel.



Figure 3: Rockburst in a drift near the Powerhouse Complex.

The impact of this phenomenon can be summarized in the following points: accidents in the tunnel that may affect the workforce, costs linked to the production stoppage, damage in the facilities and extra charges due to the repair works in the tunnel and replacement of equipment and machinery.



Figure 4: Rockburst at the face excavation in the headrace tunnel.

3.1. Description of the recorded stress events

Rockburst events in Cheves project took place in the tunnels excavation with overburdens above 900 m, mainly in two geological formations, the intrusive and the metamorphic rock.

These events boost themselves in the presence of brittle rock and geological structures, happening either at the face excavation or behind the face in the reinforced sections. Most of the events occurred after the blasting in the unsupported area, provoking events ranging from sounds and cracks to violent rock ejections. In some cases the events happened behind the excavation, up to 500 m, damaging the installed rock support. Other dynamic events were

induced by the simultaneous excavation of multiple drifts, principally in the powerhouse area.

All the recorded events were assessed and a classification was performed in order to establish the magnitude of the event and take actions directed to define suitable rock support and to ensure safety (Figure 5).

Stress Class	Description
0	Crackling and bangs in the surrounding rock mass.
1	Stress-induced spalling without rock fall: rock surface cracks suddenly, creating scales up to 5cm, dust clouds.
2	Stress-induced loosening or rock falls at lateral rock surface or face in the unsupported areas. Rock support system may be slightly damaged.
3	Heavy bangs and violent rock falls. Rock blocks and slabs are violently ejected. The rock support system is damaged.

Figure 5: Rockburst at the face excavation in the headrace tunnel.

3.2 Variables involved in Cheves Hydropower project

There are many aspects involved in the rockburst phenomenon. Kaiser and Cai (2012) summarized all of the related causes, namely: seismic events, geology (in situ stress, lithology, beddings, dykes, faults, etc.), geotechnical features (rock strength, joint fabric, rock brittleness, etc.), and mining (static and dynamic stress induced by mining, excavation span, extraction ratio, excavation sequence, rock support, etc.).

Records and analysis of all the rockbursts that happened during the construction of Cheves Hydropower project enabled the designers to determine the most significant variables involved in the phenomenon and establish control and mitigation procedures as well as designing special rock supports to ensure safe excavation.

It must be emphasized that about 850 rockbursts were recorded during the construction.

The main variables are summarized as follows:

- Overburden:** rockbursts started to happen above 850 m of overburden, where the natural stress is particularly high at about 23 MPa.
- Horizontal in situ stress:** the knowledge of the natural in situ stress field is essential for the numerical design of the excavations. For this reason, overcoring and hydro-fracturing tests were performed in the vicinity of the powerhouse, obtaining the following

principal stresses: $\sigma_1 = 21.7 - 22.1$ MPa, $\sigma_2 = 20.3 - 21.3$ MPa, $\sigma_3 = 12.8 - 13.7$ MPa. The stress ratios K_0 vary from 0.62 to 0.96, showing a relatively low value. The in situ stress measured presents an orientation similar to the one obtained by geological estimations (N-45°-E).

- Lithology:** the most severe rockbursts turned up in the most brittle rock, linked to the Hornfel group. There were also rockbursts, but less severe, in the intrusive rocks (granodiorite and quartz-monzonite), but in these cases always with overburdens above 1.000 m. For this reason, the relation between rockburst and geomechanical rock mass quality has been analyzed.
- Joint sets and related structures:** there were very unfavorable joint systems during the tunnel excavation, like subhorizontal joints and subvertical and subparallel to the axis tunnel. In particular, the more severe rockbursts were recorded in relation with low dip structures.
- Induced stresses:** the excavation of multiple faces at the same time, as well as the existence of close excavations played a key role in the probability of rockburst events. This issue had a significant impact on the powerhouse area due to the great number of close drifts, as can be observed in Figure 6, in which the rockburst events are highlighted in orange (medium intensity) and red (high intensity).
- Seismicity and active tectonics:** Cheves hydropower project is located in a highly seismic area, where a correlation between natural seismicity and rockbursts was clearly observed.



Figure 6: Rockbursts record in the Powerhouse area.

4. ROCKBURST ANALYSIS

The assessment of 850 rockbursts in Cheves hydropower project enabled the designers to collect some results and conclusions that may be useful for other projects. The following charts provide the most relevant results obtained after analyzing the data.

Figure 7 compares the rockburst intensity and the overburden. It is noticeable that 75% of the events took place between 1,000 to 1,150 m of overburden. In this stretch the average was more than 1.0 events per linear meter of tunnel, and events between 1,100 and 1,150 m of overburden took place at a ratio of 3.5 events per linear meter of tunnel.

This distribution is strongly conditioned by others factors, in particular by the lithology.

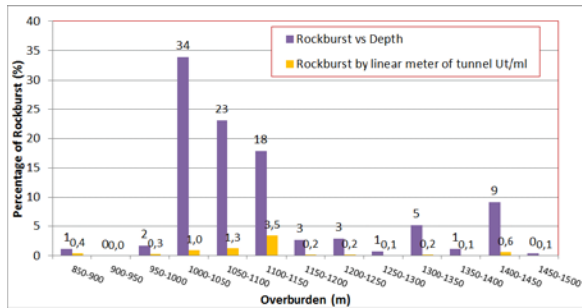


Figure 7: Overburden vs. rockburst and event by meter.

The rock mass rating (RMR) and the rockburst intensity are analyzed in Figure 8. Most of the severe events (stress class 3) belong to rock class II and I, i.e. when the RMR is higher than 61.

Another interesting analysis is the relation between the rockburst intensity and the time after blasting (Figure 9). It must be highlighted that the most severe events are located in the first ten hours after the blasting was carried out.

Finally, the relation between the blasting length and the number of events is analyzed in Figure 10. It's worth mentioning an increase in the number of rockbursts in parallel to the increase of the blasting length. It can be observed that there is no clear relation between rockburst occurrence and the blasting length.

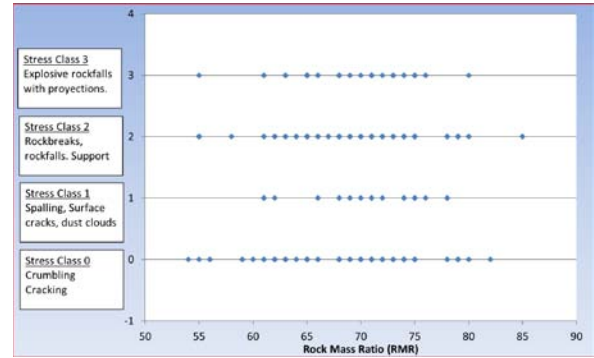


Figure 8: Rockburst intensity vs. RMR index.

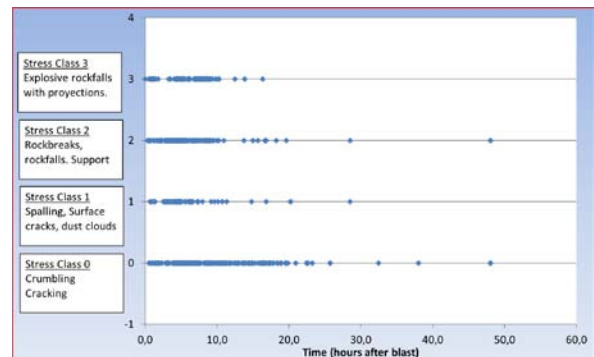


Figure 9: Rockburst intensity vs. time after blasting.

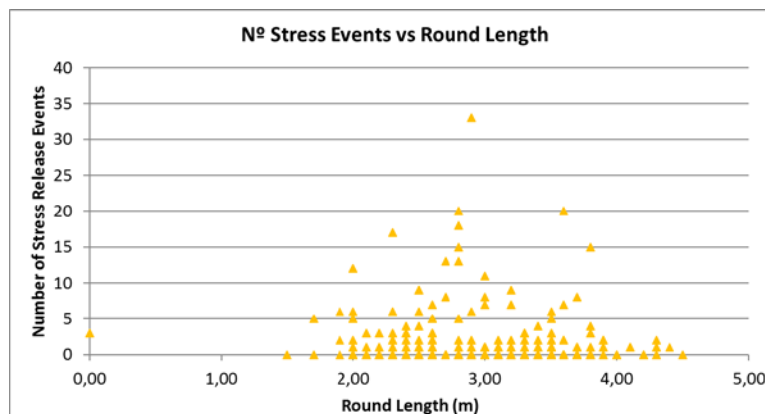


Figure 10: Blasting length vs. number of events.

5. ROCK SUPPORT AND MITIGATION PROCEDURES

Worldwide research on controlling the rockburst phenomenon provides guidelines to minimize the

consequences and mainly guarantee the safety of the workforce inside the tunnel.

Rock supports will inevitably be damaged after a rockburst event, requiring repair works and reinforcements, but a proper design must provide a flexible support that is enough to resist the dynamic loads set by the rockburst, and therefore comply with the following aims: reinforce, retain (rock mass bulking) and hold, avoiding violent rock projections. Figure 11 shows this concept.

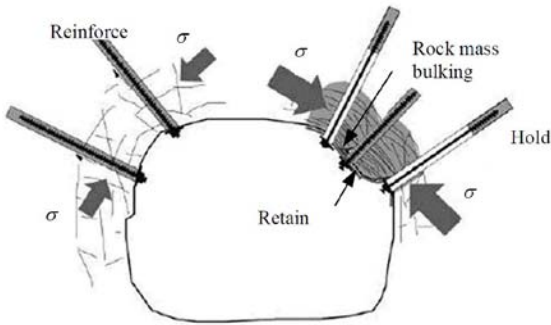


Figure 11: Requirements for an adequate support for dynamic events (Kaiser and Cai, 2012).

In the particular case of Cheves Hydropower project, the rock support was specifically designed to cope with rockburst events and high stress levels, consisting of long grouted rock bolts and double layer of fibre reinforced shotcrete with a welded wire mesh embedded in the shotcrete, which provided the required ductility against the dynamic loads.

The rock support was made of a high performance shotcrete with an UCS between 40 and 50 MPa and 6-7 kg/m³ of plastic fibers or alternatively 40 kg/m³ of steel fibers, obtaining more than 1.400 J in the panel test, according to the EFNARC requirements. Figure 12 shows this concept of a double-layered support.

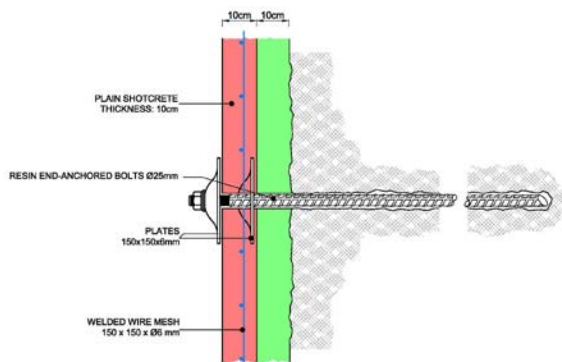


Figure 12: Rocksupport designed for high stress levels.

Additional protection measures were also considered during the excavation in rockburst prone conditions:

- a) Mechanical scaling and reinforced machinery in order to protect the workforce at the tunnel face.
- b) Apply a “sacrificial” layer of fibre reinforced shotcrete at the face and install temporary swellex rockbolts also at the face, with the aim of avoiding rock ejections from the face.
- c) Install temporary swellex rockbolts in the cross section just after shotcreting the first layer, in order to stabilize the section and ensure the safety of the workforce during the process of finishing the installation of the remaining rock support.

The following procedures were also implemented as prevention measures against the rockbursts:

- a) Preconditioning blasting ahead the excavation face, performed before the regular blasting, with the aim of reducing the rock mass quality by creating new cracks (Figure 13).

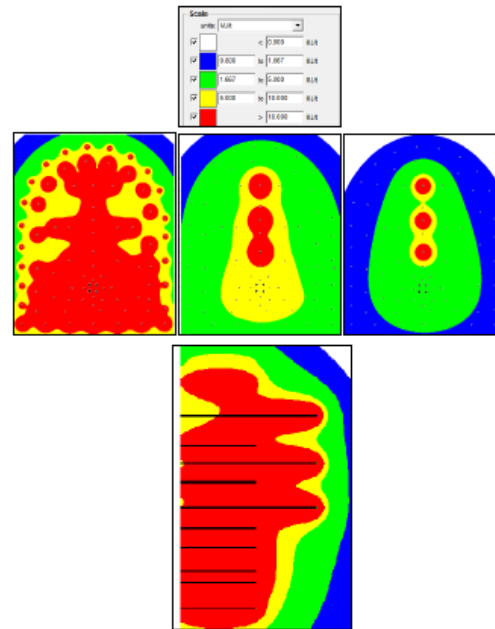


Figure 13: Energy distribution in a preconditioning blasting with 3 holes of 51 mm diameter charged with Slurrex.

- b) Change the shape of the section to a concave geometry, as straight sidewalls always accumulate higher stress than a curved geometry.
- c) Reduction of the blasting length. As it was mentioned before, a reduction of the blasting length may help to decrease the likelihood of severe dynamic events. It will also shorten the construction cycle and the time

that the workforce is exposed under an unsupported section.

The following figure shows a scheme of the temporary rock support installed at the face and the preconditioning blasting layout:

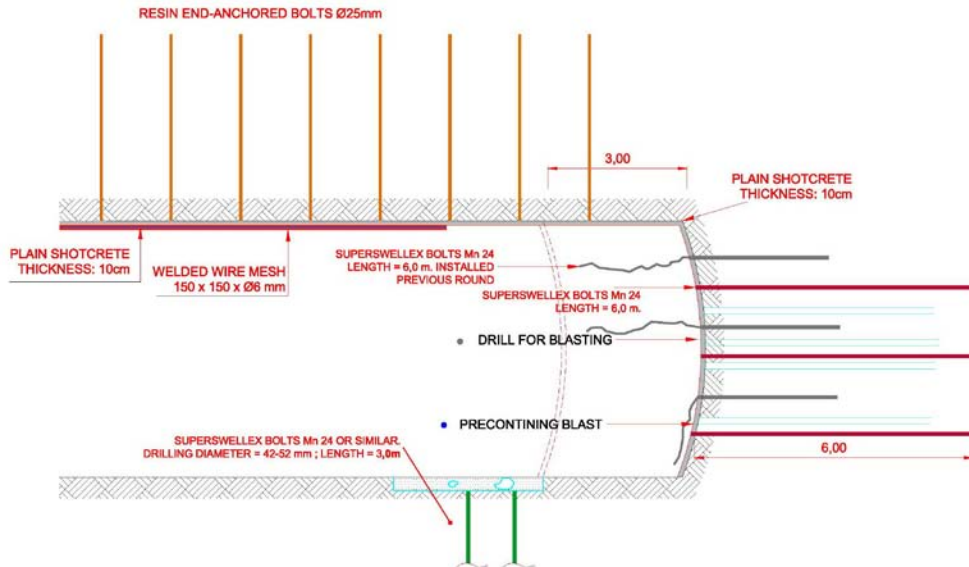


Figure 14: Combination of protection and prevention measures at the excavation face in rockburst prone conditions.

6. CONCLUSIONS

Rockburst has been extensively described in deep mining, but nowadays there are several civil projects that require the construction of deep tunnels. Under these circumstances it is necessary to consider an overstress analysis of the projects in the design stage.

Specific support measures shall be implemented in the tunnel design in order to mitigate the adverse effects of the rockburst and stress releases, especially to provide a safe environment for workers.

Each project shall be analyzed, however the experiences from Cheves Project specifically can be used for extrapolation.

The support measures described in this paper were effective during the construction period. The support consisted of an integrated system (1) reinforced the rock mass to strengthen it, (2) retained broken rock to prevent fractured block failure, and (3) held fractured blocks and securely tied back the retaining element(s) to stable ground.

7. ACKNOWLEDGEMENT

The authors want to express their gratitude, to Hochtief Solutions AG: Hans Andersson, Wolfgang Thoese, Carsten Rietschel and Carlos Leal. And also to Statkraft: Paul Lazenby.

8. REFERENCES

- Kaiser, P. and Cai, M. (2012). Design of rock support system under rockburst condition. *Journal of Rock Mechanics and Geotechnical Engineering*.
- Stacey, T., Rojas, E. (2013). A potential method of containing rockburst damage and enhancing safety using a sacrificial layer. *The Journal of the Southern African Institute of Mining and Metallurgy*.

Destress blasting on the border of safety pillars

Petr Konicek^a, Jiri Ptacek^{a*} and Alejandro Mazaira^a

^a Department of Geomechanics and Mining Research, Institute of Geonics AS CR v.v.i., (Institute of Clean Technologies), Ostrava, Czech Republic 71000

ABSTRACT

Destress blasting used at the border of safety pillars represents a special kind of destress blasting. The main goal of this type of destress blasting is to separate relatively more deformed mining areas from a non-mined safety pillar area such as a shaft pillar or cross-cut pillar, in order to reduce the impact of high stress concentration in areas within the safety pillar. Destress blasting is carried out in rigid, competent rocks adjacent to hardcoal seams 5 m to 6 m thick at depths ranging from 700 m to 1000 m below the surface. Total explosive charge of up to 3450 kg is fired simultaneously in three to seven fan-pattern and line-pattern boreholes drilled from the maingate and the tailgate, when the longwall face approaches to within round 100 m of the safety pillar border. Use of this type of destress blasting from hardcoal longwall mining in the Czech part of the Upper Silesian Coal Basin is described here. Natural and mining conditions are described together with the design parameters of destress blasting, registered seismic activity during longwall mining, and evaluation of the stress relief effect calculated from the monitored seismological data. The present study argues for using this kind of destress blasting as a proactive rockburst prevention method during mining of thick hardcoal seams. Destress blasting can decrease high stress levels and consequently minimize rockburst hazards on the border regions of the safety pillars.

KEYWORDS: Coal mining, rockburst, destress blasting

1. INTRODUCTION

Rockburst is one of the most hazardous problems encountered during underground excavations. This phenomenon always involves a violent energy release with large rock deformation and rock ejection that can cause severe damage to openings, equipment, and mine facilities, potentially also causing fatalities (Linkov 1996; Kaiser and Cai 2012). Rockburst is an inherent problem found in overstressed rocks. The stress redistribution caused by excavations induces high stress concentrations around the openings, especially when the excavation is surrounded by thick layers of hard, competent rocks which are capable of storing high amounts of strain energy. At great depth, the mining-induced stress interacts with the high in situ stress of the rock mass causing unfavourable stress concentrations that can trigger explosive rockbursts.

Destress blasting is a very important proactive measure to reduce rockburst risk in areas which are highly prone to violent rock failure in many mining regions. Destress blasting has been used for almost a century mainly in ore mining, but it also presents a very important destress method in the hardcoal mining industry. It is nowadays used as a standard destress technique in high rockburst risk areas in longwall mining in the sedimentary deposits of the Upper Silesian Coal Basin (UCSB).

Destress blasting performed at the borders of mining safety pillars is a special type of destress

blasting and is referred to as the ‘cutting destress blasting’ method. This method aims to decrease the stress concentrations within the safety pillar area, and to protect the pillar from deforming due to mining activity.



Figure 1: Location of the Upper Silesian Coal Basin.

This paper presents the results of three case studies of cutting destress blasting application at the mining of coal seam No. 504 of the Lazy Colliery, in the Czech part of the UCSB (Figure 1). The methodology of each case is described, as well as the blasting efficiency, which is assessed by the calculated seismic effect.

2. DESTRESS MODEL

Safety pillars are non-mined zones where the rock mass is kept relatively intact in order to protect

*Corresponding author – email ptacek@ugn.cas.cz

important openings, transportation, and ventilation for areas acting as shafts and main roadways.

Safety pillars usually experience significant stress concentrations due to the stress migration from the surrounding mined out areas (Dvorsky and Konicek, 2005).

Cutting destress blasting is a special destress blasting performed at the borders of the safety pillars. This kind of destress blasting has the main goal of creating a physical separation between the deformed mining areas and the non-deformed safety pillar area in order to decrease the impact of additional stress induced inside the safety pillar area. In this way the high stress concentrations can be reduced in specific rock mass regions on the boundary of mined out areas, and lower the risk of rockburst in intact areas in the rock mass. This separation is achieved by cutting the rock mass to create an artificial discontinuity plane that isolates the safety pillar area and protects it from deforming (Dvorsky and Konicek, 2005). In this way, more uniform load and stress distribution occurs in rock mass.

A cutting destress blasting is typically performed by firing a number of blastholes, all located in the same plane. These blastholes can be drilled either

using a lineal layout (i.e. parallel to each other with fixed spacing between them) or using a fan layout (i.e. all of them drilled from the same location but at different angles) (Figure 2). Blasting parameters, such as blasthole length, orientation, and the explosive charge, vary depending on the specific conditions of each area. Groups of blastholes are generally fired in different stages and no firing time delay between blastholes is used at each stage. Using no delay favours the formation of a single breaking plane between the blastholes, instead of the formation of large fractures in all directions around the blastholes.

The cutting destress blasting projects studied in this paper were carried out at the ending part of five panels of the coal seam No. 504. Blasting works of cases No. 1 and No. 2 (panels 140 914 and 140 704, respectively) were performed to protect the shaft safety pillar located at the center of the colliery. Blasting works of case No. 3 (panels 140 302, 140 304, and 140 306) were performed to 'cut out' the safety pillar of SW cross-cuts area

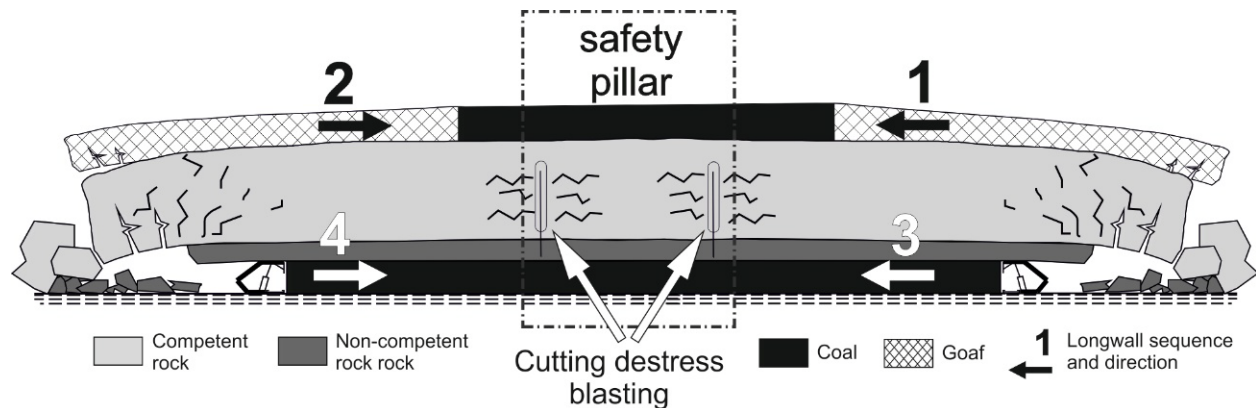


Figure 2: Profile of the cutting destress blasting layout.

3. SITE CONDITIONS

3.1. Geology

The coal seam No 504 is up to 6 m thick and is located up to 800 m below the surface in the lower part of the Sedlove Members (Figure 3). This formation is a sequence of sedimentary rocks that is mainly formed by thick layers of competent sandstones, conglomerates and sandy siltstones. The uniaxial compressive strengths of these sandstones and the conglomerates range between 70 MPa and 120 MPa (Konicek et al., 2013).

Layers of non-competent rocks such as mudstone and siltstone also occur, although they are much thinner and are generally adjacent to coal beds. Coal seams No. 512 and No. 530 have a thickness up to 8 m and are located between 50 m and 80 m above the seam No. 504, depending on the location and about 800 m below surface. The coal of this area has a laboratory compressive strength average of 15 MPa (Konicek et al., 2013).

The Lazy Colliery is highly affected by brittle as well as ductile deformations. The main brittle tectonic elements in this area are large extensional faults with orientation N-S and E-W and amplitudes of tens of meters, and ductile asymmetric anticlinal

structure with N-S direction of fold axis. Main structures establish the limits of different mining blocks in the colliery. Tectonic elements can act as significant stress relief zones, but they also create unregular stress fields in rock mass.

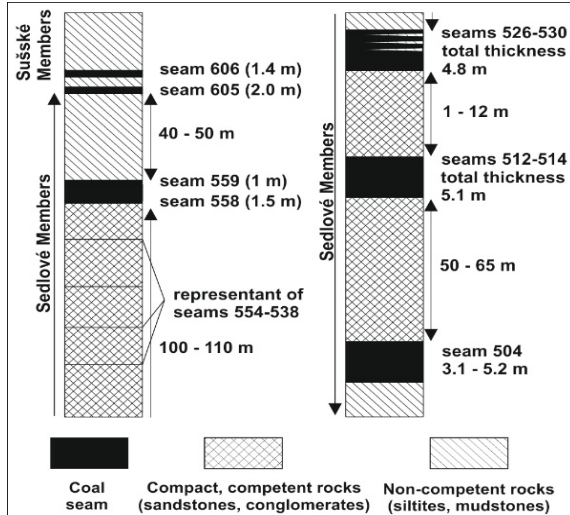


Figure 3: Simplified lithological section of the Sedlove Members in the Lazy Colliery.

3.2. Geomechanics

Mined out panels from upper coal seams No. 512 and 530 and from adjacent areas must be taken into account for the geomechanical analysis of the studied areas. Stress migrates from mined and deformed areas into intact zones of the rock mass that have not been exploited yet. This additional stress in intact rocks produces dangerous stress concentrations that can trigger rockburst during the excavation of new longwalls or galleries. Safety pillars are highly prone to suffer high stress concentrations because of their low deformation level. For that reason, mining works approaching safety pillar borders may significantly increase the risk of rock failure and consequently the rockburst.

Since the energy produced by rock failure rises with the increase of rock strength and brittleness, the occurrence of thick, competent rock strata with high UCS overlaying the seam No. 504 permits the appearance of high stress concentrations that can induce intense rockbursts. Rockburst produced in panels close to safety pillars can seriously worsen the safety and stability not only in the working area, but due to another additional stress, also into the safety pillar itself.

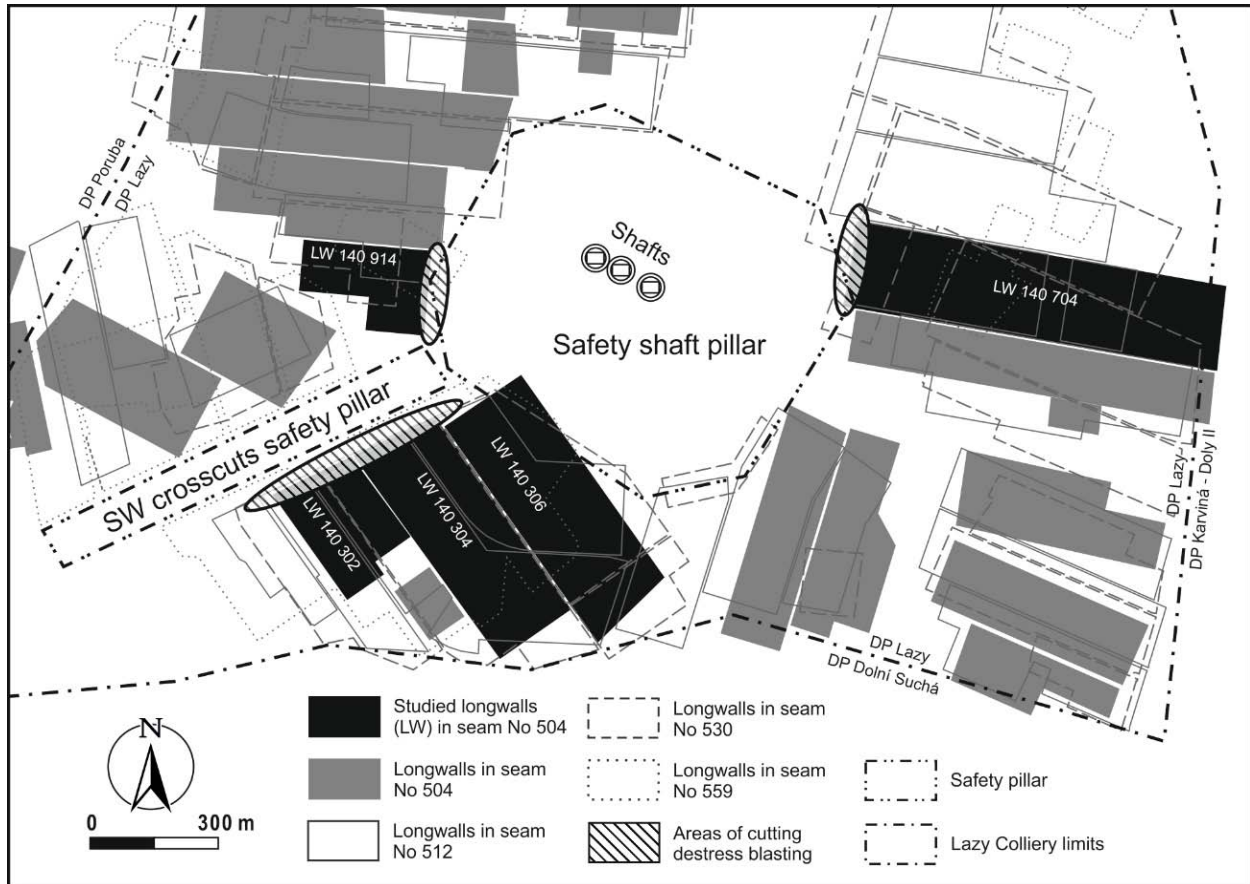


Figure 4: Location of the safety shaft pillar, the SW crosscuts safety pillar and the performed cutting destress blasting.

3.3. Mining

Coal seams of the Lazy Colliery are mined using the longwall caving method. Typical panel sizes are several hundred meters long. The position and orientation of extracted panels in different coal seams are generally not superimposed, due to uneven geological properties and coal pillars left in them (lesser seam thickness, faults etc.) In some cases, coal pillars are left to protect certain zones, such as in the safety pillar areas (Konicek et al., 2013) (Figure 4).

4. CASE NO 1 – LAZY COLLIERY LONGWALL 140 914

Destress blasting works were performed at the longwall 140 914 before and during its excavation. These works included the special cutting destress blasting, which was carried out at the border of the central safety shaft pillar.

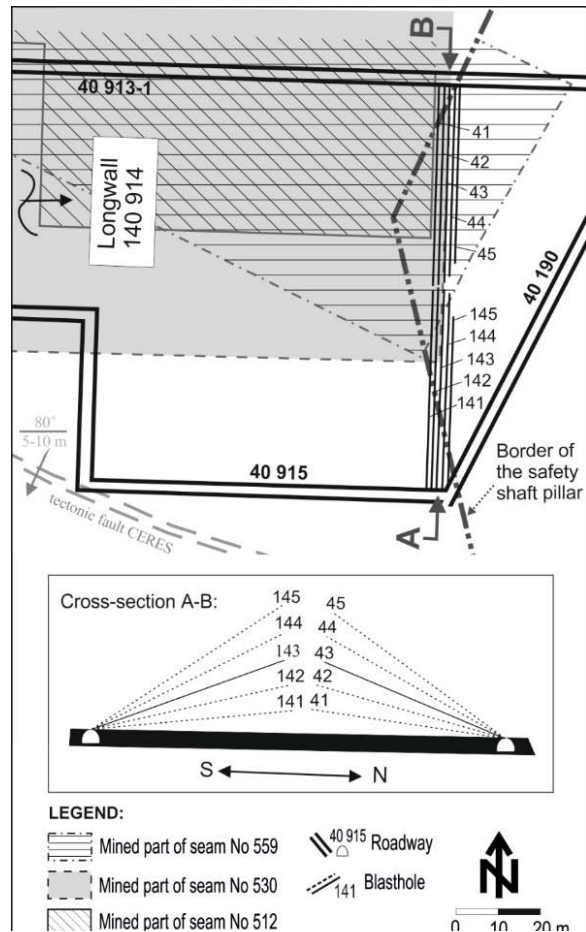


Figure 5: Scheme of the cutting destress blasting carried out in the longwall 140 914 at the border of the safety pillar.

In order to create a physical boundary between the safety pillar and the longwall area, two groups of five blastholes (a total of 10 blastholes) were drilled from the north and south gate-roads into the longwall's overburden. All blastholes were drilled in exactly the same vertical plane, forming two symmetric blasthole fans (Figure 5). The lengths of the blastholes ranged from 93 m to 100 m and their inclination angles varied from 4° to 35° (upwards). They all were drilled with a diameter of 93 mm.

Each group of blastholes was fired separately in two stages, i.e. blastholes No. 41–45 in stage No. 12 and No. 141–145 in stage No. 13 (the stages were numbered for the entire panel mining). Explosives in holes of each stage were fired without a time delay. The explosive charge of each blasthole varied from 595 kg to 780 kg, according to its length and position. The total charge fired in each stage (No. 12 and No. 13) was 3450 kg. The average percentage of the loaded lengths of these blastholes was 74%. All holes were pneumatically charged with gelatine type explosive Perunit 28E and sand was used for the stemming. Blasting parameters are summarized in Table 1.

These two blasting stages were fired when the longwall face was located about 158 m and 152 m from them, respectively. This distance was considered enough to prevent undesirable rock deformations in the safety pillar before it was isolated by the cutting destress blasting.

A continuous seismic monitoring was carried out during mining of the longwall No. 140 914 using local and regional seismic networks and geophones installed in the gate-roads of the panel. The results of seismic monitoring showed that the seismic activity had noticeably grown in the regions loaded by additional stress concentration at the edges of the mined parts of the upper coal seams. The seismic events induced during the longwall mining were mainly located in its overburden, in the area outside from the vertical projection of the upper mined panels of seams Nos. 512 and 530, where the additional stress was concentrated.

From the seismic monitoring it is also clear that the seismic activity rose with the increase of the rate of longwall face advance, the rate of mined coal volume and implementation of destress blasting.

The efficiency of the cutting destress blasting was evaluated by the seismic effect (SE), which is calculated by the equation

$$SE = \frac{E_{OKC}}{K_{OKC}Q}$$

where E_{OKC} is the seismic energy calculated from seismic monitoring in the Ostrava-Karvina Coalfield (OKC), K_{OKC} is a combined coefficient characterized

by natural and mining conditions in OKC (i.e. $K_{OKC} = 2.1$), and Q is the explosive charge (Konicek et al 2013).

In this case, the calculated SE in both blasting stages was 33.1 and 54.2 respectively. This means that the energy released by each blasting was 33.1 and 54.2 times larger than the energy from the explosive. The excess of energy measured in both stages corresponds to the release of the strain energy accumulated in the rock mass.

Hence, it can be stated that the cutting destress blasting carried out in this case had a very high destress effect. The calculated SE can be also evaluated by a qualitative classification according to the criteria shown in Table 2 (Konicek et al 2013). Thus, the efficiency of these cutting destress blasting was 'excellent'. It is seen from the high SE values that the stress concentration at the border of the safety shaft pillar was significantly high and it could have induced rockburst phenomena if the destress blasting had not been applied.

Table 1: Destress rock blasting parameters conducted in longwall 140 914.

Stage	Blasthole number (-)	Explosive charge (kg)	Released seismic energy (J)	SE (-)	SE evaluation (-)
12	41-45	3450	2.40E+05	33.1	Excellent
13	141-145	3450	3.80E+05	54.2	Excellent

Table 2: Classification for evaluation of the seismic effect (Konicek et al 2013).

Seismic effect	Evaluation of seismic effect (SE)
$SE < 1.7$	Insignificant
$1.7 \leq SE < 3$	Good
$3 \leq SE < 6$	Very good
$6 \leq SE < 12$	Extremely good
$SE \geq 12$	Excellent

5. CASE NO. 2 – LAZY COLLIERY LONGWALL 140 704

The area of the longwall 140 704 was significantly influenced by additional stress induced from mined panels in the upper coal seams Nos. 512 and 530, and from mined panels from the same seam located next to it, to the south and to the east. The occurrence of competent rock strata overlaying the seam No. 504 led to critical stress concentrations that induced two intense rockbursts that occurred soon after the start of mining in this longwall. The virgin stress state (vertical components varied between 12 MPa and 21MPa) and induced stress have been determined there. Induced stresses reached up to five multiples of the original stress state (Ptacek et al., 2015). Due to the high rockburst risk of this area, rock failure prevention measures were implemented as soon as the mining of this panel started, including destress blasting. Destress blasting carried out in the longwall 140 704 were very similar than those presented in the case No. 1. In this case, the longwall

also finished at the border of the safety shaft pillar and, in consequence, special destress blasting had to be applied to isolate and protect the safety pillar area from the mining activity.

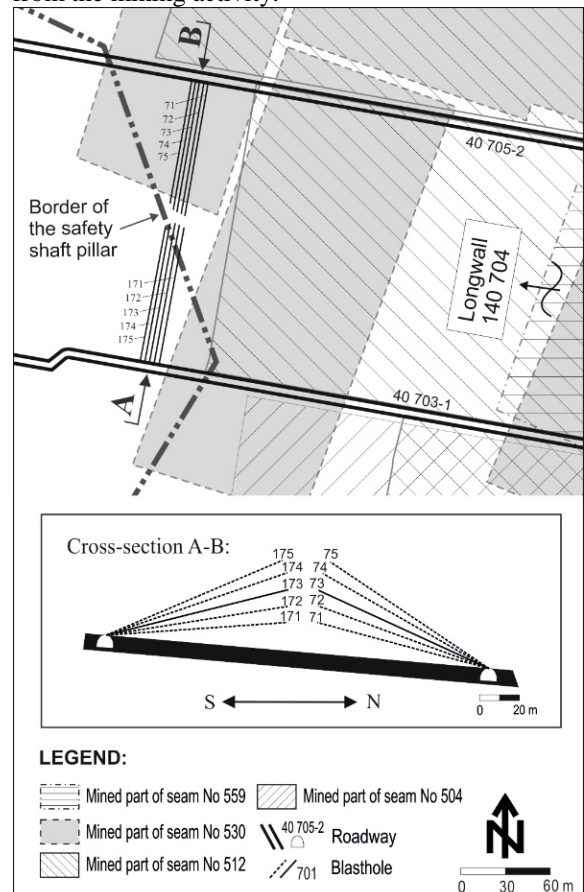


Figure 6: Scheme of the cutting destress blasting carried out in the longwall 140 704 at the border of the safety shaft pillar.

Again, two groups of five blastholes (a total number of 10 blastholes) were drilled upwards into the overburden strata; one group from the northeastern gate-road (blastholes Nos. 71–75) and the other from the southwestern gate-road (blastholes Nos. 171–175). Each group was drilled with a fan layout and all blastholes from both groups were located in the same vertical plane (Figure 6). The 95 mm diameter blastholes were drilled with inclination angles between 4° and 34°. The length of the blastholes ranged from 93 m to 100 m. All blastholes were fired in two stages (i.e. one group per stage), and the explosive in both stages were fired without time delay.

The explosive charge of each blasthole varied depending on its length and position, ranging from 415 kg to 700 kg. The total amount of explosive fired in each stage was 2900 kg in first stage and 2975 kg in second stage. The average percentage of the gelatine loaded lengths of these blastholes was 68%. All blastholes were charged pneumatically with a

gelatine type of explosive and sand was used for the stemming. Blasting parameters are summarized in Table 3. Both stages were fired when the longwall face was located about 168 m and 132 m from the holes, respectively. This distance was considered enough to prevent undesirable rock deformations in the safety pillar before it was isolated by the cutting destress blasting.

Local and regional seismic networks were used to register the seismicity induced by destress blasting. The calculated SE (see in previous section) of these cutting destress blasting was 24.6 for the first stage and 44.8 for the second stage. According to the evaluation criteria shown in Table 2, destress efficiency of these blasting works was considered 'excellent'. These results show a very high stress release at the border of the safety shaft pillar, which suggests that an important improvement of the safety conditions in both the longwall and the safety pillar area was achieved by using destress blasting (Ptacek et al. 2015).

Table 3: Destress rock blasting parameters conducted in longwall 140 704.

Stage	Blasthole number (-)	Explosive charge (kg)	Released seismic energy (J)	SE (-)	SE evaluation (-)
19	71-75	2900	1.50E+05	24.6	Excellent
20	171-175	2975	2.80E+05	44.8	Excellent

6. CASE NO 3 – LAZY COLLIERY LONGWALLS 140 302, 140 304 AND 140 306

A safety pillar had been left in the third mining block of the Lazy Colliery in order to protect the galleries of the SW cross-cuts (SWC). This intact rock area starts from the coal seam No 606+605 at the depth 240 m below surface and continues downwards vertically to the level of the coal seam No. 504 (at up to 670 m below the surface). The safety pillar area is about 900 m long and 200 m wide and has NNE-SSW direction. Mining activity around the SWC safety pillar in the seam No. 504 could produce undesirable rock deformations in the protected area. Moreover, additional stress from adjacent mined panels in seam No. 504 and from mined panels in upper seams Nos. 512 and 530 could also produce dangerous stress concentration in the intact rock of the safety pillar, what might induce intense rockbursts.

For that reason, a large cutting destress blasting was performed to protect the safety SWC pillar from rock deformation and dangerous rock failure. Destress blasting works were designed to isolate the intact rock mass of the SWC safety pillar from the goaf over longwalls 140 302, 140 304 and 140 306,

which were located next to the south-eastern border of the safety pillar in the seam No 504 (Fig. 7).

A total of 52 blastholes were drilled within the rock mass between the coal seams Nos. 504 and 512 from three different roadways. The length of the blastholes ranged from 25 m to 80 m and all of them were drilled with a diameter of 93 mm. Blastholes 501–528 were drilled in a linear layout along the roadways 40 380 and 40 390 (both located in the seam No. 504), with inclination angle of 41° (upwards) and with 7 m of spacing between them (Fig. 7). Blastholes 529–533 were drilled in a fan layout from the end of the roadway 40 390 (located 50 m above seam No. 504) with inclination angles ranging from 4° to 35° from horizontal (upwards). Blastholes 1–14 were drilled in a fan layout from roadway 30 309-4 (located in the seam No. 504) with inclination angles ranging from -58° (downwards) to 29° (upwards). Blastholes 15–19 were drilled in a fan layout from the roadway 40 315 with inclination angles ranging from 8° to 31° (upwards). All blastholes were drilled exactly in the same vertical plane. Blasting parameters are summarized in Table 4.

The blasting was performed in 13 different stages. The number of blastholes fired in each stage varied from 3 to 7. Depending on the blasthole length

and its position, the lengths of the charges varied between 18 m to 60 m and the stemming lengths from 7 m up to 20 m. The amount of explosive fired in each stage ranged between 1130 kg and 2760 kg.

All charges in each stage were fired simultaneously (no delay). The blastholes were charged pneumatically with plastic explosive Perunit 20 and sand was used for the stemming.

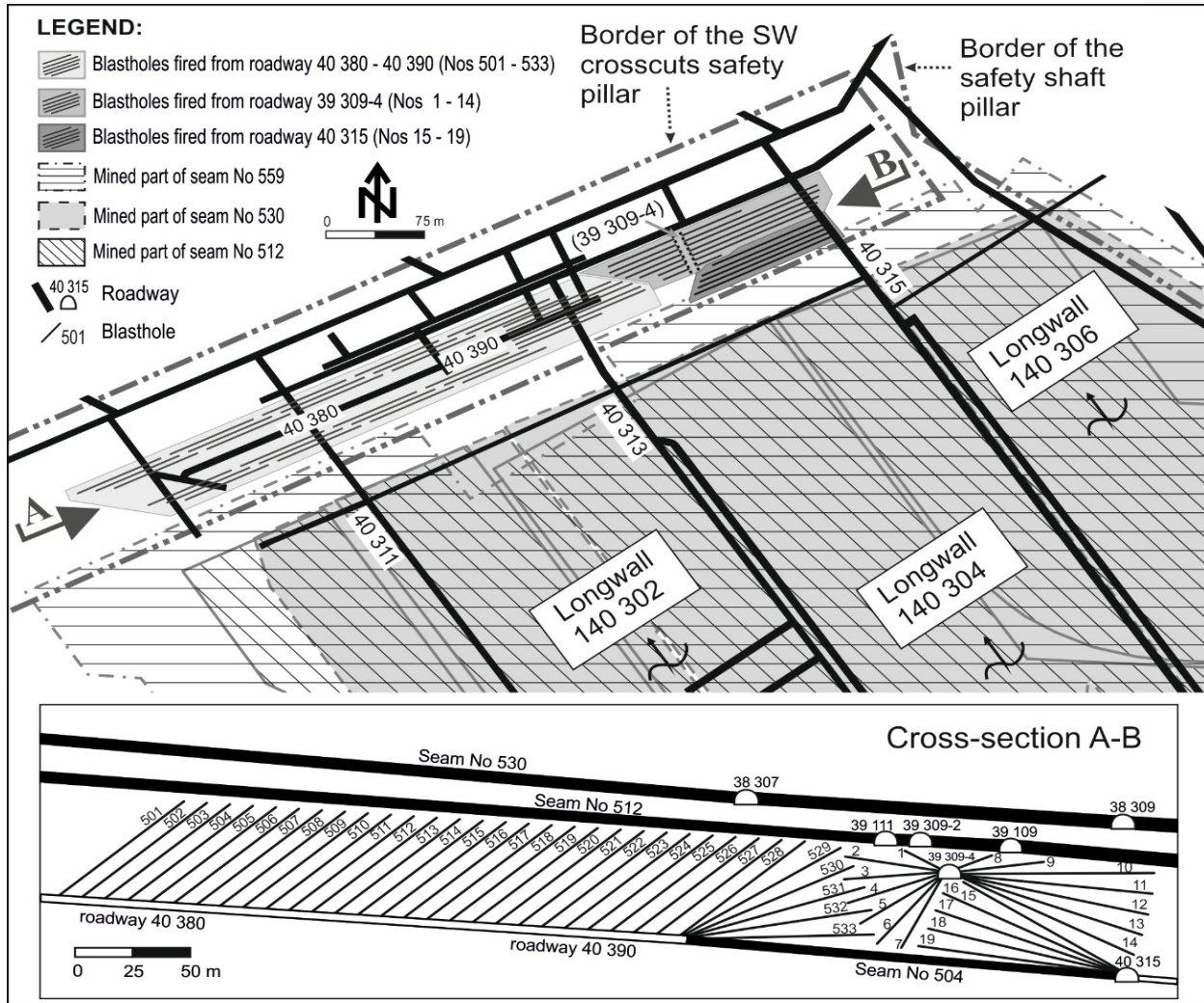


Figure 7: Scheme of the cutting destress blasting carried out in the longwalls 140 302, 140 304 and 140 306 at the border of the SW cross-cuts safety pillar.

Stages Nos. 1–5 were fired before the coal extraction in adjacent longwalls 140 302, 140 304 and 140 306 had started. Stages Nos. 6–12 were fired at a distance of 350 m to 240 m from advancing longwall face 140 302. Stage No. 13 was fired at a distance of 430 m from advancing longwall face 140 304 (longwall 140 302 was already finished). According to registered seismicity in the area, the SE of each blasting stage has been calculated (see previous section). The blasting works at the border of the SWC safety pillar presented different destress efficiency levels. Thus, stages Nos. 7 and 8 were

‘extremely good’ (SE was 6.3 and 7.4), stages Nos. 1–6 and 10–13 were ‘very good’ (SE values ranged from 3.2 to 5.9) and stage No. 9 was ‘good’ (SE was 2.8). These results show an important destress efficiency at the border of the SWC safety pillar, although it was lower than in the two cases presented above. No rockbursts occurred during further advancing of the mining works in the longwalls 140 302, 140 304, and 140 306 after the cutting destress blasting was performed. This fact can be considered as a sign of improvement of the stress conditions in the area surrounding the SWC safety pillar.

Table 4: Destress rock blasting parameters conducted in longwalls 140 302, 140 304 and 140 306.

Stage	Blasthole number (-)	Explosive charge (kg)	Released seismic energy (J)	SE (-)	SE evaluation (-)
1	501-504	1560	1,70E+04	5.2	Very good
2	516-519	1656	1,50E+04	4.3	Very good
3	505-508	1656	1,50E+04	4.3	Very good
4	520-523	1656	1,20E+04	3.5	Very good
5	512-515	1688	2,10E+04	5.9	Very good
6	509-511	1130	1,30E+04	5.5	Very good
7	524-527	1728	2,30E+04	6.3	Extremely good
8	1-7	1488	2,30E+04	7.4	Extremely good
9	12-14	1275	7,60E+03	2.8	Good
10	8-11	1296	1,50E+04	5.5	Very good
11	528-530	1344	1,10E+04	3.9	Very good
12	531-533	1506	1,00E+04	3.2	Very good
13	15-19	2760	2,00E+04	3.5	Very good

7. CONCLUSION

Over the years, different safety pillars have been established in the Lazy Colliery in order to protect important mining infrastructures. Although mining activity is not carried out in these protected areas, coal extraction in adjacent panels can induce undesirable rock deformation and dangerous stress concentration within the safety pillars. Proactive destress measures have been used to avoid these problems when the faces of the longwalls in the seam No. 504 were approaching the central safety shaft pillar, or the safety pillar of the SW cross-cuts. The implementation of cutting destress blasting at the border of these safety pillars has allowed to cut out the rock mass to create an artificial boundary between the safety pillar areas and the longwall areas. This separation has reduced the stress concentrations encountered in the intact rocks of the safety pillar limits. Seismic monitoring showed that for all cases, blasting induced beneficial stress release. The calculated seismic effect of all blasting stages was

evaluated as good, very good, extremely good and excellent. After the cutting destress blasting were performed in the selected areas, coal extraction in the mentioned longwalls finished satisfactorily without any occurrence of rockbursts or other incidents in neither the longwall areas, nor the safety pillar areas. Therefore, the main aims of the cutting destress blasting were achieved.

8. ACKNOWLEDGEMENT

This article was written in connection with project ICT - Sustainability program. Identification code: LO1406. Project is supported by the National Program for Sustainability I (2013-2020) financed by the state budget of the Czech Republic.

9. REFERENCES

Dvorsky, P., Konicek, P., 2005. Systems of rock blasting as a rock burst measure in the Czech part of Upper Silesian Coal Basin, In Proceedings of the Sixth International Symposium on Rockburst and

Seismicity in Mines, pp 493–496, (The Australian Centre of Geomechanics: Perth).

Kaiser, P and Cai, M, 2012. Design of rock support system under rockburst condition, *Journal of Rock Mechanics and Geotechnical Engineering*, 4(3):215–227.

Konicek, P, Soucek, K, Stas, L and Singh, R, 2013. Long-hole destress blasting for rockburst control during deep underground coal mining, *International Journal of Rock Mechanics and Mining Sciences*, 61:141–153.

Konicek, P., Ptacek, J, Stas, L, Kukutsch, R, Waclawik, P and Mazaira, A, 2014. Impact of destress blasting on stress field development ahead of a hardcoal longwall face, *Rock Engineering and Rock Mechanics: Structures in and on Rock Masses - Proceedings of EUROCK 2014* (ed: Alejano, Perucho, Olalla and Jiménez), pp 585–590 (Taylor and Francis: London).

Linkov, AM, 1996. Rockbursts and the instability of rock masses, *International Journal of Rock Mechanics and Mining Sciences & Geomechanics Abstracts*, 33(7):727–732.

Ptacek, J., Konicek P., Stas L., Waclawik P. & Kukutsch R., 2015. The rotation of principal axes and changes of stress due to mine induced stresses. *Canadian Geotechnical Journal*, 2015, 52(10), 1440-1447.

Powered support selection for longwall workings in dynamic load conditions

Stanisław Prusek^a, Sylwester Rajwa^b, Andrzej Walentek^b and Wojciech Masny^{b*}

^a General Director of Central Mining Institute, Plac Gwarkow 1, Katowice, Poland.

^b Department of Extraction Technologies and Mining Support, Central Mining Institute, Plac Gwarkow 1, Katowice, Poland.

ABSTRACT

Currently in Poland hard coal is mined in two Coal Basins namely Upper Silesian and Lublin. In Poland, there were 30 underground hard coal mines that produced 72.5 million tons of coal in 2014. For underground hard coal (steam coal and coking coal) seam extraction, the longwall method is used and retreat longwalls with natural roof caving in the gob are the most common. Currently it is estimated that about half of the hard coal output in Poland originates from seams located in areas of rock burst hazard. In this paper, the most important data concerning the geological and mining conditions in Polish hard coal collieries are presented with particular emphasis on tremors, rock bursts, and fatalities. Moreover, the article shows information about seismic events which occurred between 2003 and 2012 in underground mines belonging to one of the coal companies in Poland. In addition, negative consequences of those dynamic phenomena in the longwall workings are described. In order to avoid damage of powered supports in geomining conditions where dynamic phenomena occur, different types of protective means are applied. In the paper the methodology of assessing the powered support yield ability is described.

1. INTRODUCTION

In Poland the production of hard coal (i.e. steam coal and coking coal) is conducted in increasingly harder geological and mining conditions, resulting from the still growing depth of mining operations and numerous former exploitations in the mined longwall panels in the form of edges and/or residues. These factors generally increase the level of natural hazard in Polish mines. A very important one is rock burst hazard associated with the occurrence of rock mass tremors. The hazard directly affects both personnel safety and the continuity of coal production.

Rock mass tremors induced by mining operations may result in rock bursts or decompressions. According to Polish regulations (Ordinance of the Minister of Internal Affairs and Administration of 2002) a rock burst is defined as a dynamic phenomenon caused by a rock mass tremor which results in destroying or damaging a working, or its fragment, leading to the complete or partial loss of its functionality or making it dangerous to use. While decompression is defined as a dynamic phenomenon caused by a rock mass tremor which causes damage to a mine working (or its fragment), it does not result in loss of functionality nor renders it unsafe for personnel.

Hard coal mining operations, in areas where dynamic phenomena occur, requires considering both static and dynamic load while designing support both for headings and longwalls, as, when a tremor occurs, there is an increase in the value of load exerted on a support, and the main task of a properly designed support ought to be maintaining the stability of a

mine working and providing the proper level of safety for personnel.

This article presents basic information concerning the hard coal mining industry in Poland, with special attention to data on rock mass tremors. Then, the most common forms of damage to a longwall powered support resulting from dynamic phenomena are characterised. There is also information on a method applied in Polish mining industry to secure a powered support against effects of additional load resulting from rock mass tremors.

2. GENERAL CHARACTERISTICS OF HARD COAL MINING IN POLAND

Hard coal deposits in Poland are mined in two coal basins, namely Lublin Coal Basin (LZW) and Upper Silesian Coal Basin (GZW). Lublin Coal Basin is located in the south-eastern part of Poland, near the border with Ukraine. At the moment one coal mine - LW Bogdanka, operates there. The Upper Silesian Coal Basin is located in the south of Poland near an urban agglomeration, with Katowice in its centre. Mining operations in the Upper Silesian Coal Basin have been conducted for over 200 years.

In 2014, there were 30 underground hard coal mines operating in Poland, which produced 72.5 million tons of coal. The basic hard coal mining system is the longwall system with single gateroads. In 2014, there were 118 operating longwalls (Cybulski and Malich 2015). The average depth of mining operations was slightly over 700 m. In all the mines coal is produced in multiple seams which often

results in an increase in rock burst hazard due to influences of former exploitation like edges or residues of previously mined seams. There are also other hazards in Polish mines: seismic, caving, gas, dust, water, climate, radiation and fire.

In the conditions of the Polish mining industry in longwalls with roof cave-in, two-legged shield supports with a lemniscate system are most common. In the type of support, two-stage legs, more seldom one-stage ones with mechanical or hydraulic extenders, are applied. The inside diameter of the legs is usually between 200 and 250 mm. Recently, there has been a tendency to increase the inside diameter of the leg casings to 300 mm and more, which results in the necessity to increase the section pitch to 1.75 m. An increase in setting load and yield load of a section is tightly associated with deteriorating mining conditions and its aim is to provide good conditions for supporting the roof in a longwall. The most numerous group of powered supports are the ones of minimum height ranging between 0.8 and 1.2 m, and maximum between 3.1 and 3.6 m. Supports of higher operation height range (up to 5.0 m), are rarely used (Rajwa et al. 2009).

Between 2003 and 2014 hard coal mining operations in the Upper Silesian Coal Basin resulted in approximately 14,000 tremors of seismic energy $E \geq 10^5$ (local magnitude, $M_L \geq 1.7$) and 32 rock bursts which caused material and personnel losses. In recent years, 19 tremors have had energy $E \geq 10^8$ J, and two had $E \geq 10^9$ J (Stec 2015).

Table 1 presents coal production in Poland between 2003 and 2014, including production in seams threatened by rock bursts, and the number of

rock bursts, accidents, and length of damaged workings in running meters (Patyńska 2015).

Data presented in Table 1 show that in 2003–2014 hard coal production decreased from slightly over 100.0 million tons to 72.5 million tons. In the analysed period, between 39% and over 50% of coal was produced in seams with rock burst hazard. As a consequence of the rock bursts a total of 520 metres of mine workings was destroyed, and approximately 3,600 metres of mine workings was damaged.

3. MOST COMMON TYPES OF DAMAGE TO POWERED SUPPORT CAUSED BY ROCK BURSTS AND DECOMPRESSION

Within the framework of the project acronymed I²Mine titled “Innovative Technologies and Concepts for the Intelligent Deep Mine of the Future”, realized by the Central Mining Institute, consequences of rock bursts and decompressions which occurred in 2003–2012 in all the coal mines of Kompania Węglowa S.A (KWSA), the biggest producer of hard coal in the European Union, were analysed. In the period, in KWSA’s coal mines there were 18 rock bursts and 14 decompression events. It was observed that 76% of the rock bursts and decompression events occurred during mining operations in longwall panels, 24% of them occurred while driving roadways. Consequences of rock bursts and decompression, which coincided with longwall operations, were mainly apparent in gateroads (49% of cases). Moreover, in 31% of cases the damage was observed in longwalls themselves and in 20% in other adjacent mine workings.

Table 1: Total coal production, including production in seams threatened by rock bursts, accident rate, number of rock bursts, number of accidents, and length of workings damaged by rock bursts in 2003–2014 - (Patyńska 2015).

Year	Total production		Production in seams threatened by rock bursts		Accident rate (accidents/production)	Number of rock bursts	Accidents related to rock bursts		Consequences in workings	
	million tons		% of total				fatal	other (serious and light)	destroyed and collapsed (m)	damaged (m)
2003	100.40	41.8	40.9	0.18	4	2	16	110	145	
2004	96.99	39.2	39.4	0.11	3	0	11	0	358	
2005	99.50	41.0 ¹⁾	41.2 ¹⁾	0.13	3	1	12	0	270	
2006	94.50	42.15	44.6	0.25	4	4	20	0	> 510	
2007	87.40	44.6 ¹⁾	49.43 ¹⁾	0.11	3	0	10	0	530	
2008	83.60	41.9 ²⁾	50.12	0.31	5	0	26	0	710	
2009	77.50	34.3 ³⁾	43.8	0.06	1	0	5	0	101	
2010	76.10	35.8 ⁴⁾	47.04	0.18	2	2	12	30	87	
2011	75.50	34.2 ⁵⁾	45.36	0.08	4	1	6	0	168	
2012	79.20	37.60	47.47	0.04	1	1	2	170 ¹⁾	210 ¹⁾	
2013	76.47	36.90	48.25	0.07	1	0	5	50	113	
2014	72.50	36.00	49.66	0.00	1	0	0	160	390	

¹⁾ - approximated data

Table 2 shows numerical values of the most important parameters characterising dynamic phenomena. Load coefficient n_{tz} , presented in Table 2 is calculated with the following empirical dependence presented by Biliński (2005).

Table 2: Basic parameters of rock bursts and decompression occurring in Kompania Węglowa S.A.'s mines, 2003-2012 (Prusek, Masny 2015)

Parameter	Phenomenon			
	Rock burst		Decompression	
	min	max	min	max
Seismic energy of tremor, (J)	7.0E+05	2.0E+08	4.0E+04	8.0E+07
Peak particle velocity PPV , (m/s)	0.064	0.598	0.014*	0.353
Depth of mine working, (m)	630	1,085	545	1,130
Distance between tremor hypocentre and tremor effects, (m)	24	567	37	572
Vertical distance between tremor effects and tremor-prone layer (m)	3	245	10	460
coefficient n_{tz}	1.10	1.51	1.05	1.53

* PPV is estimated due to low accuracy to locate tremor hypocenter

Data presented in Table 2 show that workings and their support were damaged at seismic energy of tremor of 4.0E+04 J and relatively low load coefficient $n_{tz}=1.05$. A probable cause of such a situation in such cases was significantly high static load exerted on a support prior to a tremor, just before the dynamic phenomenon.

The calculated values of peak particle velocity PPV , being an empirical criterion of assessing stability of workings subjected to the influence of mine tremors, or the analysed 18 rock bursts and 14 decompression events were contained between 0.014 m/s and 0.598 m/s. The values are confirmed by Mutke's (2008) research. He determined that in the conditions of Polish hard coal mines workings lose stability when PPV is between 0.050 and 1.000 m/s.

The conducted analyses of dynamic phenomena in KWSA's mines enabled determination of the most common forms of damage to workings and support in longwalls, see Figure 1.

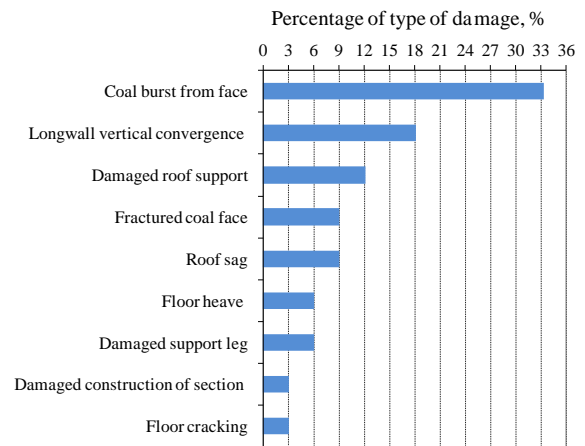


Figure 1. Types of damage to longwalls and shield support caused by dynamic phenomena, % (Prusek and Masny 2015).

Following the data presented in Figure 1, we can conclude that in longwalls, due to the dynamic influence of the rockmass, coal bursts from the sidewall into the working – 33% were most common (Figure 2a). In over 18% of longwalls there were roof sags (Figure 2b).

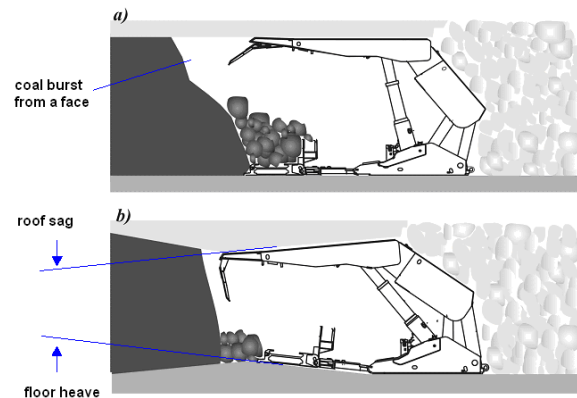


Figure 2. Characteristic forms of damage to longwall caused by rock bursts or decompressions (Prusek and Masny 2015).

Coal bursts from sidewall into a working (Figure 2a) result from the fact that the coal face, usually of the lowest strength parameters, is the largest surface of a longwall which is not secured with a shield support. Only in two of the analysed rock bursts and decompression events was a coal burst additionally accompanied by roof sag in the tip to face distance. Another characteristic form of damage observed in longwalls, associated with dynamic phenomena, is convergence, as it is presented in Figure 2b. More often it is caused by a floor heave than by a roof sag (Prusek and Masny 2015).

Referring to the most common types of damage to powered supports in a longwall, it can be concluded that they affect mainly: legs, valve batteries, spherical head connections between the legs and canopy/base, and lemniscate bars. Hydraulic legs are most often torn or their rod is broken, as shown in Figures 3a and 3b.

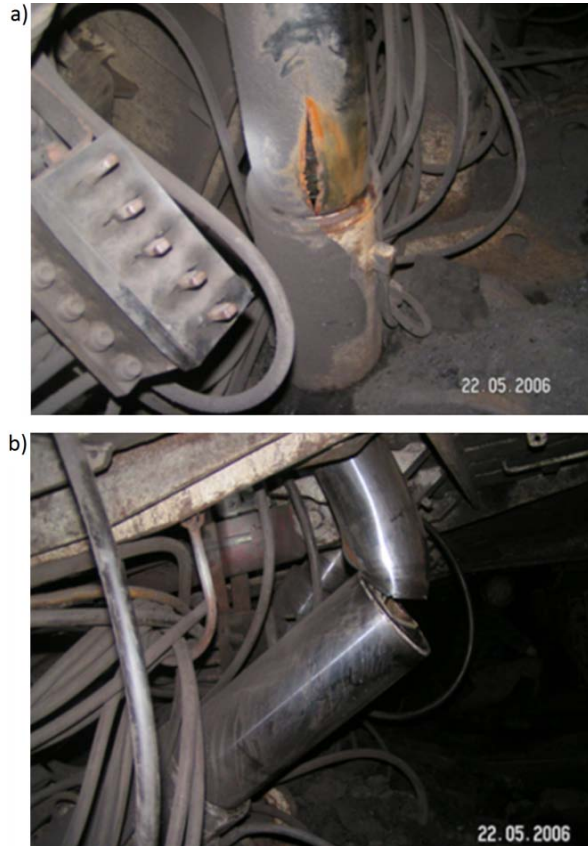


Figure 3. Damage to hydraulic legs of powered roof support caused by dynamic phenomena; a) - torn, b) - broken (Prusek and Masny 2015).

4. PROTECTING POWERED SUPPORT FROM CONSEQUENCES OF ROCK BURSTS

A lot of actions have been taken to limit consequences of damage to powered support or of stability loss in mine workings. It means preventing rock bursts with periodic destressing in zones where they concentrate or inducing rock mass tremors. The most often applied methods are: watering a seam, destressing drilling, loosening blasting, torpedo blasting, directed hydrofracturing of rocks, directed blasting fracturing, and destressing a seam through mining adjacent seams (Brauner 1994; Junker et al. 2006). Moreover, there are also various types of underground tests (Li et al. 2014; Turek et al. 2015) and laboratory tests (Player et al. 2008) aimed at

assessing the influence of increased load induced by seismic phenomena on the support and stability of mine workings.

According to Polish legislation (Ordinance of the Minister of Economy of 2002) a powered roof support which is to work in longwalls driven in areas of rock mass tremors has to be flexible to absorb dynamic load. That is why, for many years, the Central Mining Institute has been conducting research into assessing the flexibility of powered roof supports (Prusek et al. 2005; Rajwa et al. 2009; Stoiński 2015; Stoiński et al. 2015). By “support flexibility”, according to GIG’s methodology, we mean the property of a powered roof support which enables it to absorb dynamic load safely, without exceeding values of its safety factor coefficient. The Central Mining Institute’s method assumes that hydraulic legs and flow rate of the hydraulic system are the key elements making a given support flexible. The calculated minimal height of liquid column in the under piston space of a hydraulic leg (PT) and the determined flow rate of the system (together with a yielding valve) allows determination of the operation height range of a powered support, at which it is considered to be flexible under dynamic load (coefficient n_{tz}). In the calculations the value of maximum load on a leg and its nominal load are compared, in accordance with the following condition:

$$F_{max} < k \cdot F_N \quad (1)$$

where:

F_{max} – value of maximum expected load on leg, considering rock mass tremor energy, N

F_N - leg nominal load, N.

k – safety factor coefficient for hydraulic leg determined in laboratory (usually 1.5 or 2.0).

The value of maximum forecast load of a leg F_{max} is determined analytically with the course of load versus time $f(t)$, based on a model of one degree of freedom, and the equation (Stoiński et al. 2015):

$$f(t) = \frac{1}{\cos \alpha} \{ F_w + F_d [1 + k_d e^{-\delta t} - \sin(\omega t - \varphi)] \} \quad (2)$$

where:

F_w – leg setting load, N,

F_d – dynamic force of load, $F_d = n_{tz} \cdot F_r - F_w$, N,

F_r – yield load, N,

n_{tz} – load coefficient,

k_d – computational coefficient,

ω – angular velocity, rad/s⁻¹,

φ – shift angle of the force with respect to input function, rad,

α – yaw angle of the leg from the normal to the support base, rad,

δ – equivalent damping resulting from hydraulic valves and rock displacement resistance, s^{-1} ,
 t – time, s.

Flexibility of a section is also associated with flow rate of the hydraulic system, applied to limit pressure in the under piston space of a leg. It is important the configured hydraulic system securing the under piston space of a hydraulic leg does not limit flow Q_u in selected yielding valves. The hydraulic system ought to have both optimised liquid streams geometry, and determined characteristics of flow of given elements in the whole system. Flow of liquid in the leg hydraulic system can be assessed in laboratory tests (Stoiński 2015) or by using numerical modelling based on ANSYS CFX software (Fig. 4) (Doległo et al. 2009). Figure 4 presents a sample result assessing flow of liquid in the hydraulic system securing the space under piston.

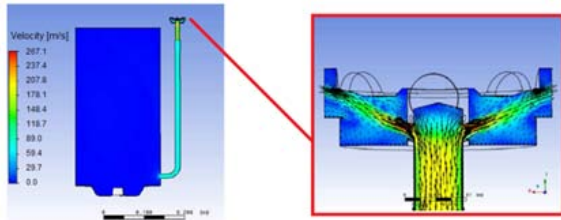


Figure 4. Assessment of flow of liquid in leg hydraulic system performed with ANSYS CFX software (Doległo et al. 2009).

The factors which in practice are most often considered while assessing flexibility of the support are: value of load coefficient n_{tz} , flow rate of the yielding valve of a hydraulic leg Q and ratio of setting load and yield load n_0 . An example of the assessment of powered support flexibility at heights between 1.8 and 3.4 m, applied in conditions where rock mass tremors occur are presented in Figure 5.

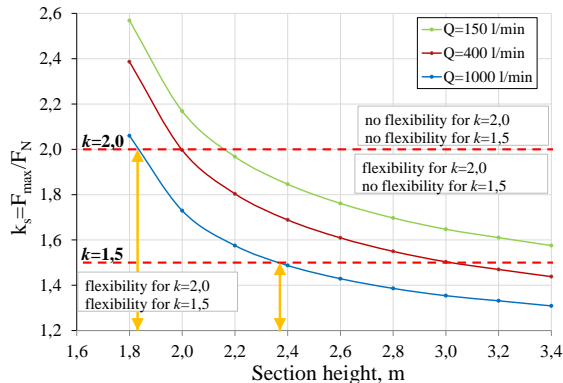


Figure 5. Change in leg overload coefficient k_s depending on operation height of shield and flow rate of yielding valve Q (assumptions: coefficient $n_0=0.66$; values of load coefficient $n_{tz}=1.2$) (Prusek 2015).

Proper selection of flow rate of yielding valves Q has a significant influence on support shield flexibility. In Figure 5 it can be observed that an increase in flow rate of the yielding valve results in an increase in the range of height of the support at which it is flexible for the calculated (determined) dynamic load. For the yielding valve of flow rate $Q=1000$ l/min, the analysed shield support, with the legs tested in laboratory conditions at safety factor coefficient $k=2.0$, meets the flexibility condition in the height range of 1.85–3.30 m, while for coefficient $k=1.5$, it does in the height range of 2.35–3.30 m.

5. SUMMARY

Statistical data presented in the article and analyses concerning the consequences of observed rock bursts and decompression events prove that they are phenomena posing a threat to personnel safety, and have a significant influence on the continuity of production. Recent years' practice showed that by applying a proper set of rules and safety measures it is possible to limit the above-mentioned threats significantly. According to the GIG's method, to improve flexibility of a powered roof support, presented in the article, it is believed that sufficiently strong construction of the leg is significant. The construction ought to ensure its further operating when pressure in its under piston space increases to the double value of nominal pressure (safety factor coefficient $k=2.0$). Then, the flow of the liquid stream is optimized and a yielding valve of flow rate resulting from the forecast dynamic load is selected. Moreover, it is favourable, from the point of view of the ability to absorb greater dynamic load by a powered roof support, to apply possibly the highest values of setting load (value of coefficient n_0 increases). It is also possible to try to lower values of yield load. However, such a decision ought to be preceded with other analyses concerning proper co-operation between the powered roof support and the rock mass to stabilise the roof of a longwall.

6. ACKNOWLEDGEMENTS

Article presents a brief part of work carried out by the Central Mining Institute within the frame of research under the project: I²M Innovative Technologies and Concepts for the Intelligent Deep Mine of the Future. The project was implemented under The Seventh Framework Programme of the European Union.

7. REFERENCES

Biliński A. (2005): Metoda doboru obudowy ścianowych wyrobisk wybierkowych i chodnikowych do warunków pola eksploatacyjnego (Method of

selecting support for conditions in mining panel). CMG Komag, Gliwice.

Brauner, G. (1994): Rockbursts in coal mines and their prevention. Balkema, Rotterdam, str. 144.

Cybulski K., Malich B. (2015): Zagrożenie pyłowe.: Raport roczny o stanie podstawowych zagrożeń naturalnych i technicznych w górnictwie węgla kamiennego 2014 (Dust hazard: Yearly report on basic natural and technical hazards in hard coal mining in 2014). Praca zbiorowa pod kierunkiem J. Kabiesza. pp. 41-60.

Doległo L., Gil J., Stoiński K. (2009): Analityczna ocena wydajności objętościowej układu hydraulicznego stojaka zmechanizowanej obudowy ścianowej (Analytical assessment of volumetric efficiency of hydraulic system of a powered roof support leg). *Maszyny Górnicze* 4/2009 pp 9-18

Junker M. et al. (2006): Gebirgsbeherrschung von Flözstrecken. Verlag Glückauf, Essen.

Li L., P. Hagan P., Saydam S. (2014): A review of ground support systems performance subjected to dynamic loading. Conference Paper, DOI: 10.1201/b16955-183 Conference: EUROCK 2014, At Vigo, Spain, Volume: Rock Mechanics and Rock Engineering: structures on and in rock masses.

Mutke G. (2008): Stability of the underground mine workings in the near-field zone of seismic events. In : 21st World Mining Congress 2008 – New Challenges and Vision for Mining. Underground Mine Environment. 7-12 September 2008 – Poland – Cracow. University of Science & Technology (AGH), pp. 89-97.

Patyńska R. (2015): Zagrożenie tąpnięciami.: Raport roczny o stanie podstawowych zagrożeń naturalnych i technicznych w górnictwie węgla kamiennego 2014 (Rock burst hazard: Yearly report on basic natural and technical hazards in hard coal mining in 2014). Praca zbiorowa pod kierunkiem J. Kabiesza. pp. 96-107.

Player, J. R., E. Villaescusa, and A. G. Thompson. 2008. "An examination of dynamic test facilities." In 2008 Australian Mining Technology Conference, Sep 16, 2008, Twin Waters Queensland: The Australasian Institute of Mining and Metallurgy.

Prusek S. (2015): Stateczność wyrobiska ścianowego podczas eksploatacji pokładów węgla kamiennego z zawalem skał stropowych (Stability of longwall during hard coal mining operations with roof caving). Książka w druku.

Prusek S., Masny W. (2015): Analysis of damage to underground workings and their support caused by dynamic phenomena. *Journal of Mining Science*, Vol. 51, No. 1, pp. 63–72.

Prusek S., Rajwa S., Stoiński K. (2005): Kriterien zur Abschätzung des Risikos von

Strebschaden. *Glückauf-Forschungshefte* 2005, no 3, pp. 92-95

Rajwa S., Masny W., Prusek S. (2009): Powered Support in Conditions of Rock Mass Tremor Occurrence in the Polish Mining Industry. *Aachen International Mining Symposia, 5th International Symposium – High Performance Mining*, RWTH Aachen, pp. 359-373.

Rozporządzenie Ministra Gospodarki z dnia 28 czerwca 2002 r. Dz. U. Nr 139 poz. 1169 z późniejszymi zmianami, w sprawie bezpieczeństwa i higieny pracy, prowadzenia ruchu oraz specjalistycznego zabezpieczenia przeciwpożarowego w podziemnych zakładach górniczych (Ordinance of the Minister of Economy of 28 June 2002 on occupational health and safety, management of operation and specialist fire protection in mining facilities extracting mineral resources).

Rozporządzenie Ministra Spraw Wewnętrznych i Administracji z dnia 14 czerwca 2002 r. Dz. U. Nr 94, poz. 841 z późniejszymi zmianami, w sprawie zagrożeń naturalnych w zakładach górniczych (Ordinance of the Minister of Internal Affairs and Administration of 14 June 2002 on natural risks in mining plants)

Stec K. (2015): Zagrożenie sejsmiczne. W: Raport roczny o stanie podstawowych zagrożeń naturalnych i technicznych w górnictwie węgla kamiennego 2014. Praca zbiorowa pod kierunkiem J. Kabiesza. Główny Instytut Górnictwa (Seismic hazard: Yearly report on basic natural and technical hazards in hard coal mining in 2014), Katowice, pp. 82-95.

Stoiński K. (2015): Doświadczenia i obserwacje własne z wpływu oceny „upodatkowania” zmechanizowanych obudów ścianowych na ich optymalizację konstrukcji (Experience and own observations of influence of assessing “flexibility” of shield supports on optimising their construction). IX Międzynarodowa Konferencja Techniki Urabiania organizowana w ramach III Polskiego Kongresu Górniczego Kraków-Krynica.

Stoiński K., Prusek S., Rajwa S. (2015): Dobór przepływów w układzie zabezpieczającym stojak zmechanizowanej obudowy ścianowej – opis przypadku (Flow selection in the system securing a shield support leg. Case study). XXIII. Międzynarodowa konferencja naukowo-techniczna TEMAG 2015. Ustroń, 21-23.10.2015 r.

Turek M., Prusek S., Masny W. (2015): Obudowa podporowo-kotwowa w kopalniach węgla kamiennego (Steel arch support with roof bolts hard coal mines). Monografia, wydaw. GIG.

Evolution of grouting methods for dynamic supports in broken ground

Francois Charette ^a, Trond Skogseth ^b

^a Rock Reinforcement Division, Normet Canada, Lively, Canada, P3Y 0B3

^b Rock Reinforcement Division, Normet International, Surnadal, Norway, 6650

ABSTRACT

Rockbursts are seismic events of deep or high stress mines that often lead to damages to the ground support system. Even when the rock at the contour of the excavation is broken, rockbursts can occur behind this softened zone and further damage the support system. In these broken conditions, the ductility of the ground support system is still critical, but the installation of grouted tendons is rendered tedious or very inefficient by the problems associated with inserting cartridges of resin inside the boreholes. The same practical issues with resin cartridges arise while bolting in squeezing ground conditions or in damaged pillars.

This study aims to investigate alternative methods of grouting dynamic rockbolts by methods other than the polyester resin cartridges traditionally used by the mining industry. In particular, the use of injected resin grout for reinforcement is analysed in the field. The static anchorage capacities of the injected resin is evaluated using D-Bolts and Self-Drilling Bolts (SDB) by the mean of pull out tests, and compared with the performance of similar bolts anchored with resin cartridges in hard rock conditions, and grouted with cementitious grout. Drop tests evaluation of the resin were postponed due to scheduling difficulties.

The study also includes a field evaluation of the installation method, sequence and bolting speed, for typical length tendons. The implications of the installation with injected grout on the resulting capacity and estimated safety performance are discussed.

1. BACKGROUND

Rockbursts are seismic events of deep or high stress mines that often lead to damages to the ground support system. Even when the rock at the contour of the excavation is broken, rockburst can occur behind this softened zone and still damage the support system. In these broken conditions, the ductility of the ground support system is still critical, but the installation of grouted tendons is rendered tedious or very inefficient by the problems associated with inserting cartridges of resin inside the boreholes (Pritchard and McClellan, 2011; Simser and Pritchard, 2012).

Field studies performed by Normet have established that the typical time to install a fully grouted 2.4 metre long rock bolt with resin cartridges in very broken ground can vary between 5 and 25 minutes. Beside the very low productivity of such an operation, there is always the possibility that the anchorage may not be continuous along the bar, and that the bolt performance can be negatively affected by a poor anchorage capacity and risks of corrosion. Because safety factors rely on an adequate encapsulation of the rock bolt, uncertainty on the grout continuity is a major parameter that will affect the safety of the ground support.

Ground failures and rock ejection due to incomplete encapsulation of the rockbolt are rarely published outside of a mining organization, but have been observed (Figure 1). As mines operate deeper than ever before, the rockmass is increasingly under stress and broken, and at risk of experiencing severe energy release events. While the immediate contour of excavations rapidly deteriorates, leading to a crown of broken ground, the intact rock is still at risk for strain bursts. Moreover, fault slip bursts can occur at proximity of broken ground and lead to potentially serious damages to infrastructure and personnel injuries.

Cost considerations have often relegated pumpable resins to very specific applications, but improvements in formulations and manufacturing have led to basic volumetric cost similar to polyester resin cost.



Figure 1: Bolt and rock ejected during a rockburst due to poor encapsulation of the rockbolt in resin.

The reconditioning of damaged excavations and pillars is also an operation that is almost always performed in broken ground conditions. Open fractures hinder the insertion of resin cartridges, and increase the time and costs related to the rehabilitation of excavations. Increases of up to 30% of the resin costs due to resin loss or cartridges deterioration have been observed in the field. As well, the uncertainty of full encapsulation creates a potential hazard that cannot be evaluated by pull testing or field observation, and situations like the one described at Figure 1 can occur.

Very often, the use of friction bolts is the only available solution to allow adequate anchorage of the ground support system (Yao et al, 2014); albeit not a permanent solution, it provides consistent, although limited, tendon capacity in difficult ground conditions. The use of injected resin was documented by Pritchard and McClellan (2011).

2. DIFFERENT ALTERNATIVES

As part of Normet's development projects, a polyurethane resin grout specially formulated for

rockbolting was developed to be used in underground mines and tunnels. After laboratory installations and exploratory testing were successful, the resin was then to be tested in underground mine conditions. It was necessary to evaluate the environmental and mechanical performance parameters in order to assess the potential of the resin as an alternative to polyester resin cartridges and cementitious grout.

The resin formulation leads to a highly thixotropic behaviour that prevents the resin from flowing out of vertical upholes after injection is completed. The resin becomes thick in a matter of seconds and in most case will not flow readily through fissures less than 25 mm wide. In case of larger fissures, the resin will flow out but migration will be halted by the thickening process and resin loss will be minimized and the borehole completely filled. Once the movement of the resin slows down, the setting process begins. It should be noted that in those open fissures cases, polyester resin in cartridge will also flow out of the holes due to centrifugal force created by the spinning of the rockbolt inside the hole, and it is not possible to know what is grouted and what is not.

A first test using a mechanized bolting rig was performed in an underground testing facility in Finland (Figure 2). The operation was a success and the bolts were pulled up to a load of 170 kN (yield load of the D-Bolt 20 mm). The process was then reviewed to be used in North American mining operations, and the testing continued in Canada and USA.



Figure 2: Drilling and injection of pumpable resin using a fully mechanized bolting rig.

The approach of resin injection in Canada was first evaluated under a reconditioning framework, with less time pressure on the operation than regular development bolting. A slower set resin was used and the holes were drilled previous to the injection and bolts installation, allowing us to measure full exposure to the chemicals and to perform bolt tensioning shortly after installation. The site chosen

for this first field testing was the Norcat test mine, located in Onaping, Ontario. The measurement of the exposure levels was performed by Workplace Safety North, a Division of the Government of Ontario Ministry of Labor.

The resin injection application was then expanded to the usage in extreme ground conditions, where Self-Drilling Bolts (SDB) are nearly the only efficient way to install tendons. The underground mine site was located in Carlin, Nevada.

3. FIELD TESTING

3.1 D-Bolts Application

The first field evaluation included the injection of resin and the installation of D-Bolts, a high strength yieldable tendon (Figure 3). The D-Bolt is used extensively in Ontario and in Sweden, as a highly energy resistant ground support. The objectives of the tests were to evaluate if the rockbolts could be installed and tensioned within a reasonable amount of time, and if the loading capacity was only realistic for reconditioning or if it allowed a normal bolting sequence to take place. For this small scale test, a small air operated pump was used, and 22 kg containers of the resin materials brought on site (Figure 4).



a) D-Bolt and plate



b) Self-Drilling bolt and accessories

Figure 3: Normet bolts: a) D-Bolt rockbolt (top) used as dynamic support in underground mines, and b) Self-Drilling Bolts (SDB) used in extremely broken ground conditions.



Figure 4: Pump and resin containers used during the test grouting of the D-Bolts.

The test with D-Bolts was performed with manual drilling equipment, i.e. stoper and jackleg drills. For the sake of simplicity, the holes were pre-drilled, which allowed to focus on the specifics of installation and air quality monitoring. A total of 18 bolts were installed on the site, 6 at a lower wall level and 12 in the back, from a scissor truck (Figure 5). The bolts in the wall were used to get comfortable with the operation and the air monitoring instruments and procedures. Then for every hole in the back, resin was injected and a rock bolt was inserted immediately. The operation took approximately 10 minutes for the 12 bolts. Then, all the rockbolts were immediately tightened to approximately 150 lbs-ft; tensioning delay from installation varied from 10 minutes to approximately 5 minutes. From Van Ryswyk (1983), Tadolini (1991) and Barry et al. (1956), such tensioning torque values could lead to a load in the order of 6000 to 10000 lbs or 3 to 5 tons.



Figure 5: Scissor truck used to install rockbolts in the back of the excavation.

Unfortunately, it was not possible to pull the bolts immediately after the installation. Pull testing of some of the bolts (2 in the wall and one in the back) was performed after 24 hours and the results are presented in Figure 6. For comparison, a typical laboratory pull test result is also presented on that graph and it confirms the excellent anchorage of the bolt in the resin.

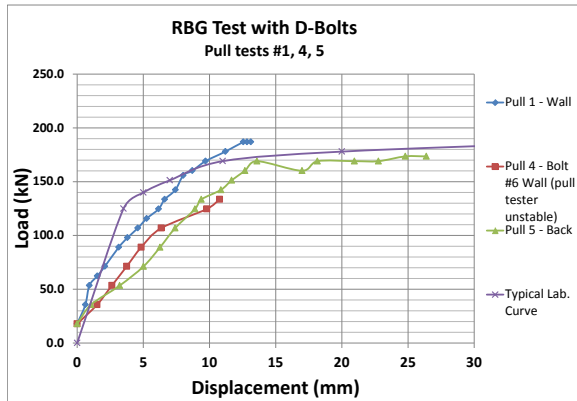


Figure 6: Pull out results of D-Bolts anchored with RBG grout.

3.2 Self-Drilling Bolts Applications

The second trial was performed in very broken and weak ground. Self-drilling bolts, referred here as SDBs or often referred as Self-Drilling Anchors or SDAs (Figure 3) were installed with a mechanized bolting rig (Figure 7) and grouted using the RBG resin grout, and pull tested after 2 hours, 3 hours, and 24 hours. Another set of two (2) bolts were grouted using regular cementitious grout. Results are presented in Figure 8. The bars are hollow threaded bars on which a one-time use drill bits can be fitted.

The pull out curves showed that the resin grout allows at least 12 tons of pull out after 2 hours, and also stiffens rapidly (3 hours pull out exhibit a much steeper loading curve than 2 hours pull out curve). For this trial, the short term pull out were conducted up to 12 tons only, to make sure the grout was not damaged for future pull tests. Also, stiffness of the resin after 3 hours compares well with cement after 24 hours.

The 24 hours pull out results showed also that the bolts can be loaded to a very high level, and the test on Bolt #4 and Bolt #9 were halted only due to issues with the pull testing equipment.

3.3 Environmental Assessment

The measurement of the potentially hazardous isocyanates was performed by a consultant hygienist from Workplace Safety North. The Iso-Check

method was used on 2 operators as well as upwind and downwind locations, and the measurements were conducted during the injection in the wall, and in the back of the excavation. Results of sampling lead to an exposure level that was extremely low, for all people participating to the sampling process.



Figure 7: Mechanized bolting rig used to install the Self-Drilling rock bolts.

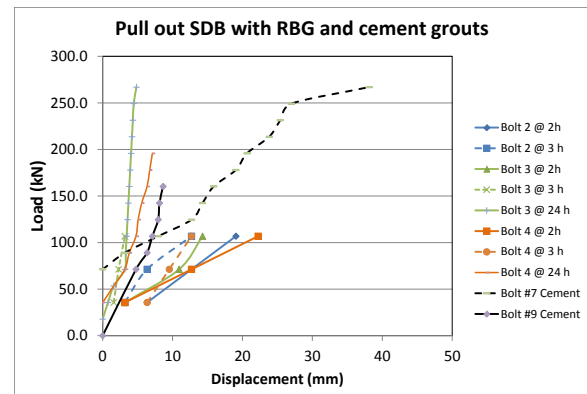


Figure 8: Pull out results of SDBs anchored with RBG grout.

4. PERFORMANCE EVALUATION

During the field tests, basic operational data was recorded. Drilling time, installation time including bolt handling, grouting, and tensioning was recorded. Average values are listed in Table 1, and an estimate of the bolting rate was also calculated from the field data. For the case of the cemented self-drilling bolt, the tensioning was performed during the next shift or day, so the performance of the next shift was affected by the tensioning time. Using a faster setting resin allows for a higher productivity but necessitates more experienced operators and well maintained equipment. The calculations are based on a

conservative 360 minutes of effective bolting operation during the shift.

Table 1: Probable performance calculations based on field measurements.

Operation	DBolt/Rockbolt		SD Bolts		
	Slow resin (min.)	Fast resin (min.)	Slow resin (min.)	Fast resin (min.)	Cement grout (minutes)
Drilling	2	2	2	2	2
Grouting	3	3	3	3	3
Tensioning	5	2	5	2	3+24h
Total:	10	7	10	7	8+24h
Bolts/shift	36	51	36	51	(36+25)/2 =30

Note 1: basis of 360 minutes effective work per shift

Note 2: cement grout effective time is 360 minutes minus 36 bolts from previous shift x 3 minutes tensioning per bolt = 252 minutes

5. CONCLUSIONS

The field testing of the RBG resin was successful in showing the potential of using injection resin to replace resin cartridges or cement injection in ground support operations in broken rock masses that makes cartridges injection in boreholes difficult.

The first advantage of the method is to provide a better and safer anchorage for the rockbolt. Because of the thickness of the injected resin, the bolt is fully encapsulated in the borehole, also filled of resin. Contrary to the rotation of the rebar or D-Bolt necessary to mix resin cartridges, the insertion and rotation do not push away the grout in the open fractures in the borehole. The uncertainty of proper encapsulation is eliminated or reduced to a minimum.

The anchorage capacity of the resin is also equivalent to the polyester resin used in cartridges, with a similar stiffness after a few hours. The anchorage capacity is also as good as when using cementitious grout.

Cost wise, the pumpable resin is not really more expensive than resin in cartridge when one considers the resin loss, broken cartridges and handling time associated with cartridges in broken ground. Although it would be seen as using more material than resin in cartridge, it is because the hole is filled and the bolt fully encapsulated. Some resin loss in fissures will not negatively alter the performance of the bolt, and will likely reinforce the rock mass. So in that sense, the injected product is cost competitive with polyester resin cartridges and offers a high performance alternative in broken ground conditions that reduces tremendously the risk of anchorage failure due to poor encapsulation.

6. ACKNOWLEDGEMENT

The authors want to acknowledge the personnel of the Norcat Test Mine for their contribution in

making this initial trial a success. As well, the authors want to thanks Newmont Mines personnel for their expertise, support and discussions. Also, the contributions of Martin Robbins of Normet International and Jason Chevrier of WSN for their expertise, support and enlightening comments before and during the tests was deeply appreciated.

7. REFERENCES

- Barry, A.J., Panek, L.A., McCormick, J.A., 1956. Use of torque wrench to determine load in roof bolts. Part 3, Expansion type 5/8 inch. R.I. 5228, 8p.
- Pritchard, C.J., McClellan, R.S. (2011). Injectable resin, A highly adaptable ground support anchoring system. In Proc. CIM Conference and Exhibition, Montreal, Canada.
- Simser, B., Pritchard, C.J. (2012), Innovative ground control at Xstrata's Nickel Rim South mine, Sudbury, Ontario. In Proc. Workplace Safety North Ground Control Conference, Sudbury, Canada, April.
- Van Ryswyk, R. (1983). Mechanical rockbolt performance evaluated from pull tests. In: Proceedings of the International Symposium on Rock Bolting, Abisko, August 28-September 2, Stephansson, O., editor. Balkema.; pp. 473-476.
- Yao, M., Forsythe, A., Punkkinen, A. (2014). Examples of ground support practices in challenging ground conditions at Vale's operations in Sudbury. In Proc. Workplace Safety North Ground Control Conference, Sudbury.

Large scale panel destress blasting parametric study

Isaac Vennes*, Hani Mitri

Department of Mining and Materials Engineering, McGill University, Montreal, Canada, H3A 0E8

ABSTRACT

The purpose of this parametric study is to quantify the effect of panel destressing on a steeply dipping remnant ore pillar. A large-scale destress blast program is simulated in the hanging wall of the ore pillar using the finite difference program FLAC3D. The simplified model consists of a 10MT ore pillar divided into 20 stopes on two levels. Two panels are destressed in the hanging wall to cover 8 stopes, followed by the mining of 4 stopes in the stress shadow in a retreat sequence. The varied parameters are the rock fragmentation factor (α) and stress reduction factor (β) of the destress panel. The effect of panel destressing is evaluated based on the volume of ore at risk in the stress shadow as well as the sudden stress change in the stope caused by the destress blast. Overall, a successful blast with a realistic stress reduction factor and rock fragmentation factor reduces the major principal stress in the nearest stopes by 10 MPa to 25 MPa. This yields a reduction of ore at risk volume ranging from 8% to 50% in the stress shadow as the first 4 stopes are mined.

1. INTRODUCTION

Rockbursts occur when the rock has been loaded beyond its failure point, manifesting as a sudden and violent failure of rock. Contributing factors to the occurrence of rockbursts are high stress, stiff strata, rapid mining rate, and large excavation area among others.

Destress blasting is a rockburst control technique which employs explosives to fracture the rock, reducing its stiffness and releasing stored elastic strain energy. To reduce the risk of rockbursts, destress blasting can be directly applied to the rock to be extracted such as for drift development and crown pillar destressing for overhand cut and fill. Another strategy is panel destressing, where relatively large volumes of rock (greater than 10 Kt) are destressed in the hanging wall of the orebody, such that the ore to be bulk mined lies in the stress shadow of the destress panel. In this case, panel destress blasting aims to reduce the risk of rockbursts by reducing the magnitude of the major principal stress in the ore to be mined. This strategy has been applied Star Morning Mine (Karwoski and McLaughlin 1975), in Brunswick mine (Andrieux 2005; Andrieux, et al. 2000) and Fraser mine (Andrieux 2005). The two latter applications were deemed successful based on recorded stress changes, seismicity, and measured displacements. At Fraser Mine, a sudden decrease of 1.5 MPa in the direction major principle stress was recorded in the stress shadow 25 meters away from panel. In Brunswick mine, a sudden 4 MPa stress drop in the direction of the major principal stress was measured 20 meters away from panel.

In both case studies, the magnitude of the sudden and long term stress decrease in the stress shadow

appears to be a small proportion of the mining induced major principal stress. To evaluate the effectiveness of the panel destress blasting strategy, the effect of this stress decrease on the burst proneness of the ore in the pillar needs to be examined. In this paper, a parametric study is conducted with a linear elastic numerical model. The purpose is to quantify effect of destress blasting in terms of stress reduction and ore at risk in the panel stress shadow by varying the rock fragmentation factor (α) and the stress reduction factor (β).

2. DESTRESS BLASTING MECHANISMS

Destress blasting is understood to reduce the stress borne in rock by inducing fracturation, demonstrated to be along pre-existing fracture planes (Lightfoot et al., 1996). This induced fracturation is thought to have multiple effects that reduce burst proneness. Firstly, the induced fracturation reduces the stiffness of the rock (Blake, 1972) as well as the load bearing ability. Secondly, as the blast induced cracks propagate, the stored elastic strain energy is dissipated as seismic energy (Tang and Mitri, 2001), resulting in an instantaneous reduction of stresses in the rock. Finally, destress blasting mobilizes the rock mass along pre-existing fractures, equivalent to plastic strain. As rockbursts are normally associated to brittle elastic rock failure, a destressed zone will yield gradually rather than fail suddenly as a rockburst (Saharan, 2004). However, when examining the effectiveness of panel destressing with a linear elastic model, the modification of the failure mechanism in the panel will not affect the burst potential of the destressed ore. Therefore, only the

*Isaac Vennes – email : isaac.vennes@mail.mcgill.ca

former two effects need to be considered in this study.

3. DESTRESS BLASTING MODEL

3.1 Modelling Technique

Multiple techniques have been developed to simulate destress blasting, starting with the rock fragmentation factor α (Blake, 1972), which reduces the Young's modulus of the rock targeted by the destress blast. Tang (2000) expanded on Blake's fragmentation factor by adding the stress reduction factor to take into account the strain energy that is instantaneously released by the blast as seismic energy. Tang deems the inclusion of β necessary in light of case studies where α is unrealistically low; a realistic range for α is 0.4 – 0.6, combined with $\beta > 0.4$. Finally, Saharan (2005) proposed that α and β should vary anisotropically, since blast induced fractures tend to propagate in the direction of the major principal stress.

In this study, the technique described by Tang (2000) is applied to the destress panels. Six combinations of α and β are tested, assumed to lie along the line $\alpha + \beta = 1$. The most optimistic combination with highest rock fragmentation and stress reduction tested is $\alpha = 0$ and $\beta = 1$, equivalent to the panel material being extracted. The combination with lowest stress reduction and rock fragmentation tested is $\alpha = 0.8$ and $\beta = 0.2$. A base case model with no destress blast is also run ($\alpha = 1$, $\beta = 0$). The parameters α and β are assumed isotropic.

To simulate a destress panel, the modulus of elasticity is reduced in the panel by the factor α which ranges from 0 to 1:

$$E_{destress} = E\alpha \quad [1]$$

In addition, the residual stress tensor in the targeted zones is applied following the equation:

$$\{\sigma_D\} = (1 - \beta) \cdot \{\sigma\} \quad [2]$$

where β ranges from 0 to 1, and where

$$\{\sigma\}^T = (\sigma_{xx}, \sigma_{yy}, \sigma_{zz}, \sigma_{xy}, \sigma_{yz}, \sigma_{xz}) \quad [3]$$

The balanced stress state in the panel prior to destressing is replaced with the residual stress state $\{\sigma_D\}$ defined by equation [3]. This removes a proportion of the strain energy in the panel equal to the factor β , causing an imbalance between the model boundary work and strain energy in model. A new equilibrium reached after solving model where the

final stress tensor in the panel lies between the initial stress tensor and the residual stress tensor.

3.2 Panel Geometry

The total mass targeted by a destress blast can be estimated based on the drill hole diameter (Andrieux, 2005). Assuming 2 rows of blastholes, the targeted mass M_e can be estimated as:

$$M_e = 2 * (16 * d) * H * L * \rho_r \quad [4]$$

where d is the blasthole diameter, H the height of the panel, L the strike length of the panel, and ρ_r the density of the rock. The explosive energy applied in reported destress blasting case studies ranges from 10 cal/kg to 500 cal/kg (Andrieux, 2005). Since most applications of destress blasting aim to directly precondition the rock to be extracted, the applied explosive energy is low and the drill hole diameter small: 43 mm to 54 mm for Creighton Mine (O'Donnell, 1992; Oliver et al., 1987), 45 mm for Campbell Mine (Makuch et al., 1987), and 35 mm to 63.5 mm for Macassa Mine (Hanson et al., 1987).

However, panel destressing case studies all lie on the high end of this range (200-500 cal/kg) with large blasthole diameters ranging from 115 mm for Star Morning mine (Karwoski and McLaughlin, 1975) and Fraser Mine (Andrieux, 2005) to 165 mm for Brunswick Mine (Andrieux et al., 2000). Based on equation 4, the targeted panel thickness based on the reported blasthole diameters ranges from 3.7 m to 5.3 m. In this study, a 3 m panel thickness is assumed, equivalent to two rows of 3.5" (89 mm) blastholes.

4. EVALUATION OF STRAINBURST POTENTIAL

The first step of the study is to confirm need for destress blasting. For a linear elastic numerical model, the available criteria are either based on energy or stress state. Multiple methods based on energy calculations have been proposed such as the Energy Release Rate (ERR) (Cook, 1967), and the Burst Potential Index (BPI) (Mitri et al., 1999). However, a limitation of ERR is that rock mass critical strain energy is not factored in. The ERR is therefore not a suitable criterion for this study, as it does not evaluate the need for destressing, only its effect. On the other hand, the BPI defined by Mitri is for uni-axial conditions and therefore only applicable to stope and drift faces and not to bulk of pillar.

Finally, the brittle shear ratio (BSR) was developed based on a study by Martin and Kaiser (1999), where rock was found to undergo brittle shear as the ratio between the deviatoric stress and the uni-axial compressive strength exceeded 0.4. The BSR proposed by Castro et al. (1997), is expressed as:

$$BSR = \frac{\sigma_1 - \sigma_3}{UCS_{intact}} [5]$$

The risk of strainbursts was deemed significant when the ratio exceeds 0.7. Therefore, ore zones with a BSR exceeding 0.7 are termed ‘at risk’. With an initial pillar BSR due to mining induced stresses at 0.2, there is no immediate need to destress. However, after the extraction of first 4 stopes, 11.4% of the remaining ore is at risk, equivalent to 36000 tonnes.

5. MODEL CONSTRUCTION

5.1 Model Geometry

Pillar and panel zones are built manually with finite difference numerical modelling software FLAC3D. Host rock zones and ore zones that are not in pillar generated with Kubrix (Itasca, 2016). The pillar hanging wall and footwall are vertical. The pillar consists of 20 stopes on 2 levels, with 10 stopes per level. On each level, there are 5 stopes along the orebody strike, 2 along the thickness. The stope dimensions are 12 m x 15 m x 30 m (strike x thickness x height). The panel dimensions are 15 m x 3 m x 60 m (strike x thickness x height).

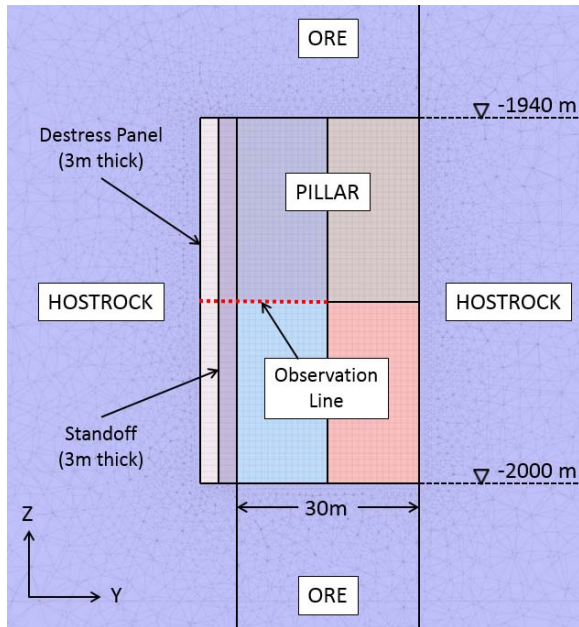


Figure 1: Model elevation view along orebody thickness. Strike of the orebody and pillar is 60 m in the x-direction.

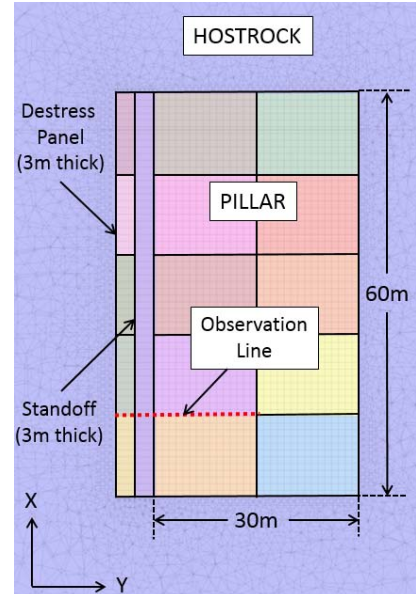


Figure 2: Model plan section view of the ore pillar.

The model boundary is set 160 meters away from the pillar, such that the pillar extraction causes a stress change smaller than 1% at the boundary. For the mesh sensitivity analysis, the zone size in the pillar is kept constant at 1 m x 1 m x 1 m, while the boundary surface mesh is varied from 8 m x 8 m to 15 m x 15 m. Monotonic convergence of maximum displacement is obtained at 10 m x 10 m boundary mesh (see Figure 1). This yields an optimal model with 1500000 elements. The panel zones are 0.25 meters along the panel thickness, 1 m along the panel strike, and 1 m along the panel height.

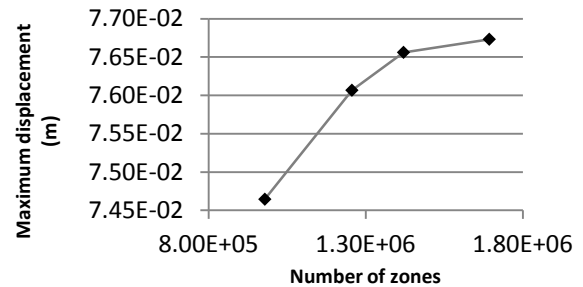


Figure 3: Model mesh sensitivity analysis.

5.2 Model Material Properties

Table 1: Material properties.

	Young's Modulus (GPa)	Poisson's Ratio	Unit Weight (MN/m ³)	Intact UCS (MPa)
Ore	27.6	0.28	0.037	140
Host Rock	37.8	0.24	0.029	150
Backfill	2.0	0.30	0.024	N/A

The numerical model is linear elastic. The elastic material properties are shown in Table 1, along with the intact UCS. The properties are provided by a case study mine.

5.3 Model Loading

The model external x-face constrained in the x direction, the model external y-face constrained in y direction. Bottom face constrained in z-direction. The top boundary free, with applied overburden stress.

$$\sigma_3 \text{ (MPa)} = \sigma_{zz} = 0.029 * \text{depth (m)} \text{ [6]}$$

The far field x and y stress are initialized in all zones following equations [7] and [8], adjusting for the effect of Poisson's ratio due to model weight. The initial stresses are oriented such that the major principal stress is perpendicular to the orebody and panel strike.

$$\sigma_1 \text{ (MPa)} = \sigma_{yy} = 10.825 + 0.032 * \text{depth (m)} \text{ [7]}$$

$$\sigma_2 \text{ (MPa)} = \sigma_{xx} = 8.687 + 0.024 * \text{depth (m)} \text{ [8]}$$

5.4 Mining Sequence

To set up the ore pillar, the orebody is mined bottom up in 10 stages, with vertical lifts ranging from 30 to 40 meters. The ore above the pillar is mined first. After each lift, the void is backfilled. Each stope is mined in six 5 meter lifts. The pillar is mined in retreat from hanging wall to footwall, west to east, bottom to top. For the parametric study, 2 panels are destressed simultaneously and the first 4 stopes of the described sequence are mined in the stress shadow.

6. RESULTS

The effect of panel destressing is quantified in terms of the stress drop over the strike of the hanging stopes and in terms of ore at risk (BSR>0.7) in the stress shadow of the panel. To begin, the major principal stress in the pillar is 80 MPa following extraction of upper and lower orebody. The variation of major principal stress in the stress shadow for varying destress blasting input parameters is shown in Figure 3. The stress drop in proportion to the initial stress in the stope is shown in Figure 4.

For a high rock fragmentation and stress reduction effect ($\alpha=0.1, \beta=0.9$), an immediate stress drop of 10 MPa to 25 MPa is obtained in the hanging wall stope (10% to 30% stress change). Immediately after the destress blast, the volume of ore at risk in the stress shadow is reduced by 10%. After extracting 4 stopes in the stress shadow, the destress blast reduces the volume of ore at risk by 50% as shown in Figure 5. On the other hand, for a low rock

fragmentation and stress reduction effect ($\alpha=0.8, \beta=0.2$), the obtained stress reduction is below 3 MPa (4% stress change). The destress blast yields an immediate 2% reduction of ore at risk. After 4 stopes, the destress blast reduces ore at risk by 5%.

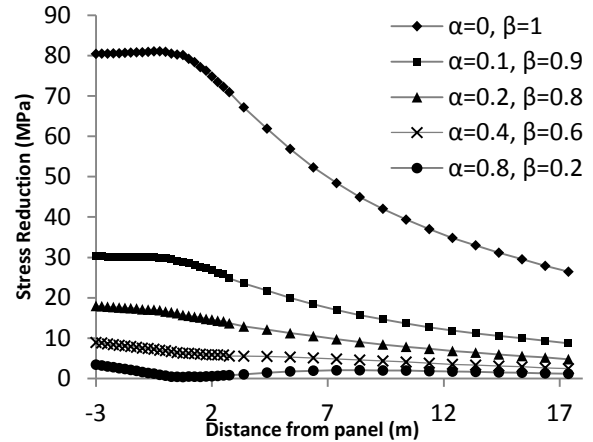


Figure 4: σ_{yy} drop due to destress blast along observation line shown in Figures 1 and 2.

In both cases, the destressing effect is not detectable immediately after the destress blast with the ore at risk criterion. Since the bulk of the pillar BSR is well below 0.7, the destress blasting stress reduction in shadow does not necessarily translate to reduction of ore at risk. Comparison with the destress blasting case studies of Brunswick mine and Fraser Mine, where a 4 MPa drop at 20 meters and a 1.5 MPa drop 25 meters were measured in the direction of the major principal stress immediately after the destress blast, suggests that $0.2 < \alpha < 0.4$ and $0.6 < \beta < 0.8$. Applying these destress blasting parameters to the parametric study model yields a reduction of ore at risk ranging from 8% to 50% in the stress shadow during the extraction of the first 4 stopes.

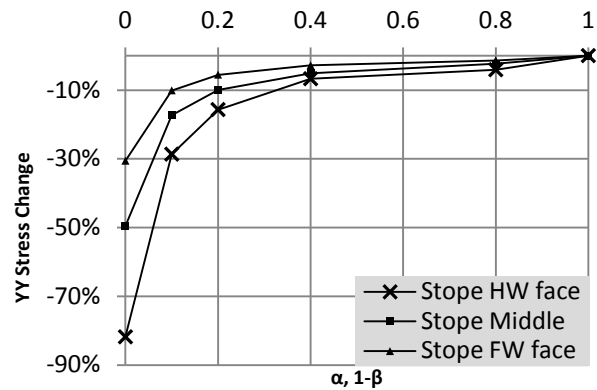


Figure 5: σ_{yy} change in HW stope. Observation points are along the observation line shown in Figures 1 and 2.

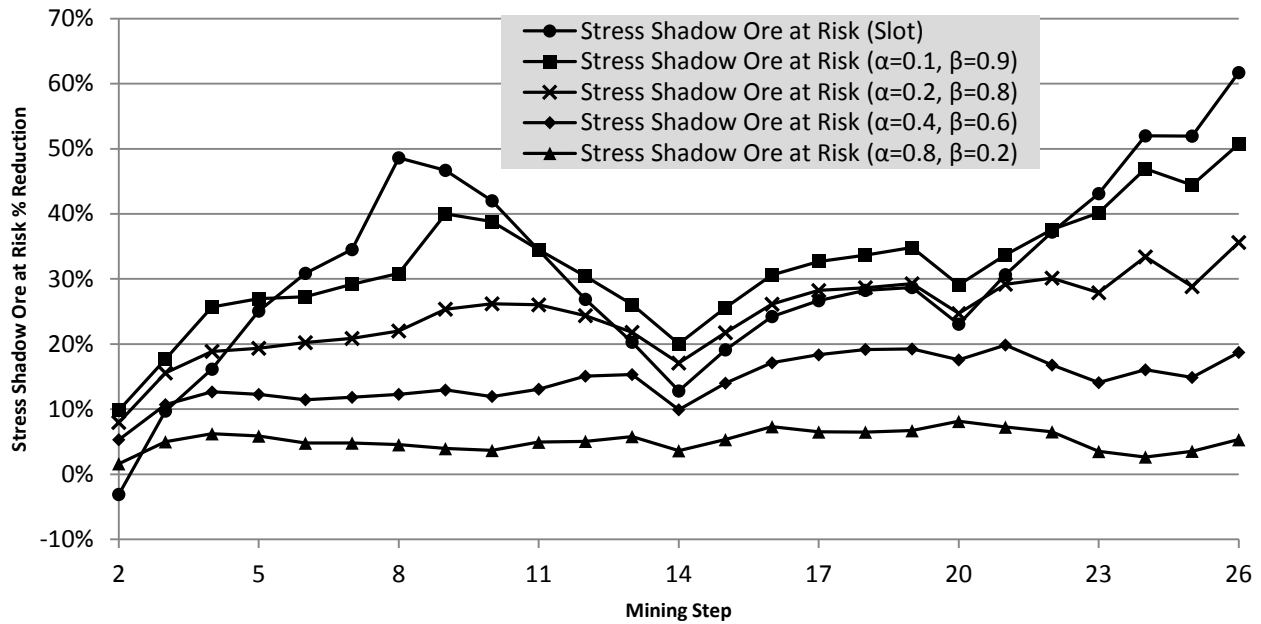


Figure 6: Ore at risk reduction in stress shadow with respect to scenario with no destress blast. Shown are the destress blast (step 2), extraction of stope 1 (steps 3-8), extraction of stope 2 (9-14), extraction of stope 3 (15-20), extraction of stope 4 (21-26).

7. CONCLUSIONS

In this study, panel destress blasting is shown to reduce the volume of ore at risk in a highly stressed ore pillar by 8% to 50% in the stress shadow, given an obtained rock fragmentation factor between below 0.4 and a stress reduction factor above 0.6. These values are realistic when compared to the observed immediate stress changes at Brunswick Mine and Fraser Mine following a panel destress blast, where 200-500 kcal/kg of explosive energy was applied. Panel destressing can therefore be an effective tool to reduce risk to operations when bulk mining the ore pillar.

However, it is assumed in the parametric study that the pre-mining major principal stress is normal to the destress panel. Also, the destressed modulus of elasticity and stress release are assumed to be isotropic. These results therefore reflect a best case scenario for a panel destressing program.

8. REFERENCES

Andrieux P (2005) Application of rock engineering systems to large-scale confined destress blasts in underground pillars. Laval University
 Andrieux P, Brummer R, Liu Q, Mortazavi A, Simser B (2000) Large-Scale Panel Destress Blast at Brunswick Mine. In: 23rd Study Dession on Blasting Techniques, vol. SEEQ, Quebec
 Blake W (1972) Rock-burst mechanics. Quarterly of the Colorado School of Mines 67(1):1-64

Castro LAM, Grabinsky MW, McCreath DR (1997) Damage initiation through extension fracturing in a moderately jointed brittle shear rock mass. International Journal of Rock Mechanics and Mining Sciences (34):110-113

Cook NGW (1967) Design of underground excavations. In: 8th US Rock Mechanics Symposium, Minnesota, pp 167-193

Hanson D, Quesnel W, Hong R (1987) Destressing a Rockburst Prone Crown Pillar: Macassa Mine. In: CANMET

Itasca (2016), Kubrix [Computer Software]; retrieved from www.itascacg.com/software/kubrix

Karwoski WJ, McLaughlin WC (1975) Rock preconditioning to prevent rockbursts - report on a field demonstration. In, vol. United States Department of the Interior, Bureau of Mines

Lightfoot N, Kullman DH, Toper AZ, Stewart RD, Gronder M, Rensburg ALJv, Longmore PJ (1996) Preconditioning to Reduce the Incidence of Face Bursts of Highly Stressed Faces. In, vol. CSIR: MININGTEK

Makuch A, Neumann M, Hedley DGF, Blake W (1987) Destress Blasting at Campbell Red Lake Mine. In: Canada/Ontario/industry Rockburst Research Project, CANMET, Elliot Lake Laboratory

Martin CD, Kaiser PK (1999) Predicting the depth of stress induced failure around underground excavations in brittle rocks. In: 49th Canadian Geotechnical Conference, St-John's, pp 105-114

Mitri HS, Tang B, Simon R (1999) FE modelling of mining-induced energy release and storage rates.

The Journal of the South African Institute of Mining and Metallurgy:103-110

O'Donnell JDP (1992) The use of destress blasting at Inco's Creighton Mine. In: MASSMIN 92, vol. SAIMM, Johannesburg, pp 71-74

Oliver P, Wiles T, MacDonald P, O'Donnell D (1987) Rockburst control measures at Inco's Creighton Mine. In: 6th Conference on Ground Control in Mining, West Virginia

Saharan MR (2004) Dynamic Modelling of Rock Fracturing by Destress Blasting. McGill University

Tang B (2000) Rockburst Control using Destress Blasting. McGill University

Tang B, Mitri HS (2001) Numerical modelling of rock preconditioning by destress blasting. Ground Improvement 5:1-11

Improving ground control safety in deep vein mines

Joseph Seymour*, Donovan Benton, Michael Raffaldi, Jeffrey Johnson, Lewis Martin, Shawn Boltz, Jerald Richardson

Spokane Mining Research Division, National Institute for Occupational Safety and Health, Spokane, WA, USA, 99207

ABSTRACT

Researchers with the National Institute for Occupational Safety and Health (NIOSH) in Spokane, WA, USA are conducting research in cooperation with the Hecla Mining Company at the Lucky Friday Mine in northern Idaho to improve ground control safety in deep vein mines. Because Hecla is mining at depths of more than a mile beneath the surface, the geology and ground stresses create unique requirements for mining and ground support. Special measures are being implemented by Hecla to limit the intensity of mining-induced seismic events and to avoid compromising the static and dynamic capacity of their ground support systems. NIOSH researchers are collaborating in these efforts by monitoring and assessing the fault slip mechanisms that initiate these seismic events and by quantifying the performance characteristics of the ground support systems.

KEYWORDS: rockburst; seismicity; dynamic ground support

1. INTRODUCTION

NIOSH researchers in Spokane, WA are conducting research in cooperation with the Hecla Mining Company at the Lucky Friday Mine in northern Idaho to develop improved methods for ground control safety in deep vein mines. Hecla is currently using underhand cut-and-fill mining methods to mine Ag-Pb-Zn ore from narrow, steeply dipping veins in the Gold Hunter deposit at a depth of over 7000 feet. Mining-induced stress increases near a large sill pillar in the mine's main production vein have created challenges for mining in these rockburst-prone ground conditions (Figure 1). As the sill pillar is being mined, its vertical extent decreases, which concentrates and progressively increases the stresses acting in the remaining portion of the pillar, thus increasing the potential for strain bursts. As mining progresses, local stresses are also being reoriented along the strike direction of problematic faults that intersect the sill pillar and dip 50° to 60° to the north. This compounds the rockburst issue by increasing the potential for fault-slip seismicity.

To reduce mining-induced seismic activity, the local stress field is being altered to reduce the magnitude of the stresses in the sill pillar and more favorably reorient the stresses acting along the faults. A nearby, sub-parallel, less-economic vein is being mined and backfilled to create a stress shadow that diverts the high horizontal stresses away from the mining horizon in the sill pillar and redistributes these stresses to more stiff, intact rock beyond the periphery of the mined shadow slot. The stress shadow also reduces the potential for fault-slip seismic events by

reorienting and reducing the stresses that act along the orientation of these problematic faults.

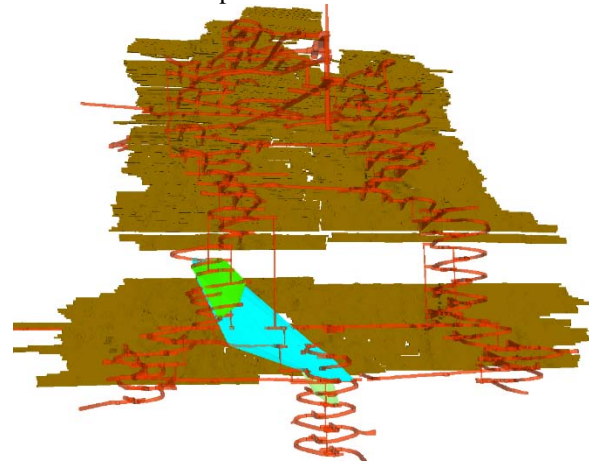


Figure 1: Schematic of development entries (red), backfilled stopes (brown), and faults (blue and green) in the Gold Hunter extension of the Lucky Friday Mine.

Current research activities include the use of seismic monitoring, photogrammetry, geotechnical instrumentation, 3D visualization, material property testing, ground support testing, and numeric modeling. This paper briefly discusses these research tasks and presents some of the technical innovations that have been developed.

2. SEISMIC EVENT MONITORING

NIOSH researchers are monitoring mining-induced seismic events at the Lucky Friday Mine using three seismic monitoring systems: Hecla's in-mine microseismic system, regional surface seismic stations,

*Corresponding author – email: zia8@cdc.gov

and a third monitoring system called the Intermountain Seismic Network (IMSN). The IMSN was developed and installed by NIOSH researchers to determine the source mechanisms of large mining-induced events (i.e., >1.5 magnitude). This system is currently comprised of eight close-in stations and one far-field station; however, it is being expanded to include additional far-field surface stations, as well as sensors installed underground at the mine. The far-field stations will be positioned distant enough from the anticipated seismic sources so that P and S wave arrivals will have sufficient separation to allow more detailed assessment of source mechanisms.

As shown in Figure 2, each IMSN surface station has a standard configuration consisting of an antenna/solar mast structure for the photovoltaic system, a vault for the battery/power distribution system, and another vault for telemetry/seismic equipment. The station's field-hardened, modular design not only protects the sensitive seismic equipment and electronics but also provides flexibility for installing different seismometers. Having a common configuration for each station simplifies the installation procedures, reduces troubleshooting time, and decreases the need for spare components. Personnel installing and maintaining the stations are able to quickly locate equipment, components, and power disconnects. The close-in stations are strong-motion stations with force-balanced triaxial accelerometers and seismometers, whereas the far-field stations use broadband triaxial seismometers. Seismic data is transmitted by radios or wireless cellular modems depending on site telemetry requirements.

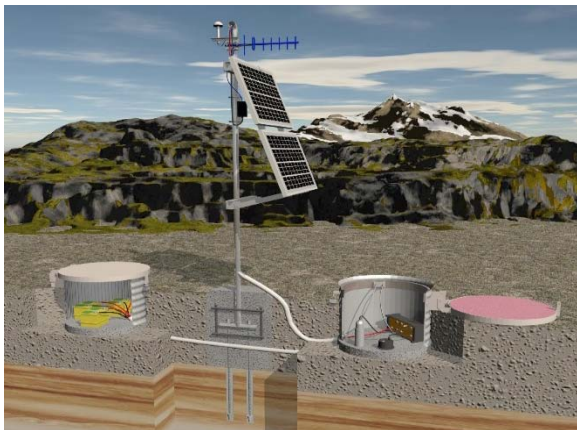


Figure 2: Typical configuration of an IMSN surface station for monitoring mining-induced seismic events.

Both the IMSN network and Hecla's microseismic monitoring system provide real-time waveforms of a seismic event that are in turn used to determine its location and magnitude. Because Hecla's

in-mine sensors are located much closer to the active workings than the IMSN surface stations, their in-mine network can detect much smaller mining-induced seismic events. Furthermore, because their microseismic sensors are installed on different levels within the mine, their underground network also provides a much more accurate depth or elevation component for the location of an event. Focal mechanisms or moment tensors are calculated to determine the source of the event (e.g., slip on an existing fault or mining-induced rock mass fracturing). It is essential to identify the mechanism that caused the event in order to gain a better understanding of the ground conditions and also to develop appropriate methods for mitigating the effects of future events. The seismic moment, a measure of the energy released from an event, is also being determined and will be compared with numerical modeling results to gain additional insight.

3. PHOTOGRAMMETRY

Photogrammetry is a valuable tool for monitoring complex geometric changes on irregular surfaces. NIOSH researchers are using this technology in the laboratory to monitor large-scale tests with shotcrete support systems (see Section 7) and also at the Lucky Friday Mine to monitor bulk movement in underground entries and shear displacements along exposed fault planes. An explanation of the NIOSH photogrammetry system and further details concerning the software, hardware, methodology, field applications, and results are provided by Benton et al. (2014; 2015; 2016).

Quarterly photogrammetric surveys of exposed faults at the Lucky Friday Mine were initiated in January 2013 and are currently ongoing. The surveys are conducted at nine locations on seven different sublevels where two faults intersect the 54 ramp near the Gold Hunter orebody. As explained in Section 5, three-dimensional point cloud reconstructions of these sites are also used for mine visualization purposes. Using photogrammetric data from these sites, cross sections of the faults are compared over time to visualize and measure the geometric changes that have occurred. These cross sections may be developed at any location and at any orientation, thereby providing a comprehensive analysis of the movement at each site.

Photogrammetric measurement techniques are also being used to aid in the interpretation of displacement measurements from crackmeters that were installed by Hecla engineers to monitor fault movement. As shown in Figure 3, the vibrating-wire crackmeter measures displacement between two anchor points and thus, provides only a unidimensional measurement of the fault's movement (i.e., a

displacement measurement along a single orientation). In contrast, the point cloud measurements obtained from photogrammetry provide a more complete three-dimensional characterization of the fault's movement and thus, help identify and quantify bulk ground movement, such as rib dilation, as opposed to actual movement along the fault. Using photogrammetry, a three-dimensional displacement vector can be calculated for an individual point or an entire vector field can be determined for a surface.



Figure 3: Crackmeter installed across an exposed fault in the wall of a ramp entry at the Lucky Friday Mine.

4. GEOTECHNICAL INSTRUMENTATION

Besides the crackmeters mentioned above, NIOSH researchers have also installed two sets of biaxial stressmeters (BSM's) to monitor stress changes in the host rock—five BSM's near the 5550-14 stope to measure stress changes during mining of the stress shadow stope and five BSM's near the 5550-11 stope to measure stress changes during production mining in the 30 vein. As noted by Seymour et al. (1999), the BSM is a rugged and reliable vibrating-wire instrument that is grouted in a drill hole to measure the magnitude and direction of the secondary principal stress changes in a plane perpendicular to the longitudinal axis of the instrument. Most of the stressmeters were installed in vertical drill holes to monitor changes in horizontal stress at vertical horizons near the sill pillar. Data from these instruments is being analyzed in conjunction with seismic monitoring data to determine the effect of mining advance and seismic events on stress distribution.



Figure 4: Single-acting closure meter and two earth pressure cells installed in the 5550-11W stope prior to backfilling.

Prior to backfilling, closure meters and earth pressure cells have been installed in the 5550-11 stope and the 6350-15 stope to monitor hanging wall-to-footwall closure and horizontal stress changes within the backfill as underhand cut-and-fill mining advances (Figure 4). Because of their robust design, the NIOSH closure meters have been able to provide stope closure measurements for over a year through more than five successive mining cuts beneath the location of the instruments (Figure 5). The geotechnical instruments are being monitored by underground data acquisition systems that are in turn connected to a computer server located on the surface, where the data is stored and displayed on a real-time basis.

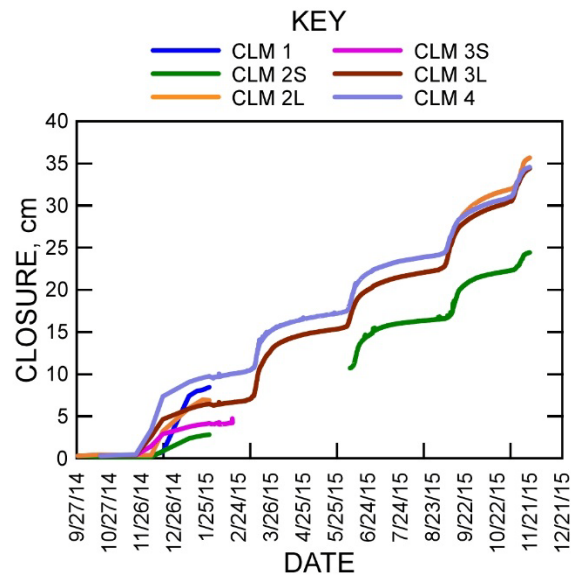


Figure 5: Horizontal closure measurements for the backfilled 5550-11 stope.

5. 3D VISUALIZATION

Complex spatial relationships between mining, seismicity, and problematic faults are being tracked by NIOSH researchers using a 3D visualization tool that was developed using the Unity® game engine (Unity

Technologies, 2015). As illustrated in Figure 6, this software tool integrates collected data and images by spatial location and time and thus helps the user interpret and analyze the complex interactions of diverse spatial and temporal data via a single, concise, interactive display (Orr et al., 2015). The 3D visualization contains a model of the mine workings, pertinent geologic structure, and quarterly photogrammetric surveys. Each of these components, as well as areas of active mining, can be stepped through time to observe changes. The visualization tool has two user modes. One mode allows the user to navigate around the rock mass and view stored data such as seismic events and instrument measurements. Another mode allows users to enter the mine workings and view data associated with specific workings, such as photogrammetric reconstructions (Figure 7). Future data may also include measured fault movements and the locations and characteristics of ground fall incidents.

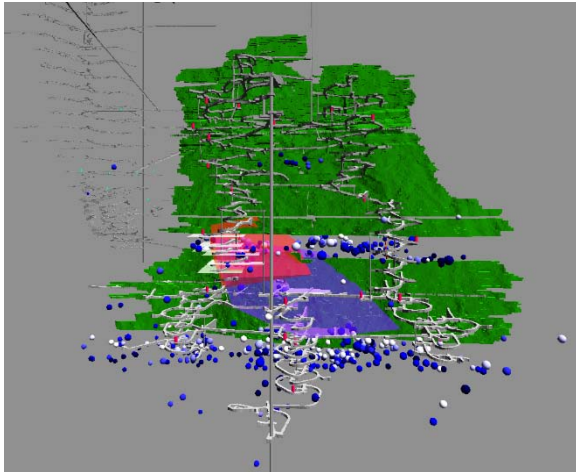


Figure 6: Unity visualization of Gold Hunter underground workings with problematic faults denoted in red and purple and seismic events represented by colored spheres.



Figure 7: Unity visualization showing a photogrammetry reconstruction of a ramp entry on the 5750 sublevel.

6. MATERIAL PROPERTIES TESTING

Drill core recovered from the BSM holes was logged and tested to characterize rock properties, improve the interpretation of stressmeter readings, and also provide inputs for numeric modeling. Standard tests were performed with representative samples from four different rock types, including unconfined compressive strength (UCS) tests, indirect tensile strength tests, and triaxial compressive strength tests. Because the Gold Hunter host rock is comprised of thinly bedded argillites, testing was performed both parallel and perpendicular to the bedding to determine anisotropic properties. Depending on rock type and bedding orientation, average UCS values ranged from 97 to 122 MPa, while average tensile strengths ranged from 4 to 11 MPa. Elastic properties were determined from UCS tests with strain-gauged samples. Young's modulus ranged from 41 to 90 GPa, and Poisson's ratio varied from 0.11 to 0.27. Triaxial compression tests were also conducted to determine Mohr-Coulomb strength properties (cohesion and friction angle).

Similar tests were performed to measure the strength and elastic properties of cemented paste backfill samples recovered from the mine (Johnson et al., 2015). These tests indicated that the tensile strength of the paste backfill ranged from about $\frac{1}{9}$ to $\frac{1}{12}$ of its compressive strength. Furthermore, UCS tests with strain-gauged samples provided a Young's modulus ranging from 2.28 to 3.59 GPa and a Poisson's ratio of 0.17 (Figure 8). Elastic properties for cemented paste backfill are difficult to measure and therefore, not widely reported in the literature.



Figure 8: Paste backfill sample equipped with strain gauges.

7. GROUND SUPPORT TESTING

The ability of ground support to withstand loading from a large seismic event depends in large part on its ability to maintain its support capacity while yielding and undergoing significant deformation. In deep mines, energy-absorbing rockbolts are often used in conjunction with surface support such as mesh and shotcrete to retain rockburst-prone ground. To quantify and evaluate the support strength and energy capacity

of ground support systems utilizing shotcrete, NIOSH researchers designed and constructed a High-Energy High-Displacement (HEHD) test machine for conducting large-scale tests with reinforced shotcrete panels (Figure 9).



Figure 9: High-Energy High-Displacement test machine for conducting large-scale tests with reinforced shotcrete panels.

During a test, a large shotcrete panel is restrained by four rockbolts embedded in the concrete columns and then loaded from beneath by a spherical loading head attached to a hydraulic ram. The force and displacement applied by the ram (136 metric tons and 27 cm, respectively) are recorded during the test using an advanced data acquisition system. A more detailed explanation of the HEHD test machine is provided by Martin et al. (2015). Measuring the load-displacement characteristics of a full-scale shotcrete panel while it is restrained by rockbolts provides a more representative indication of the actual ground support provided by this material in an underground mine. As shown in Figure 10, the type of reinforcement embedded within the shotcrete has a major effect on the support capacity and behavior of the panel. As the force on the shotcrete panel increases, the shotcrete deforms and cracks, allowing the tensile loads in the panel to be redistributed to the more ductile fibers or mesh.

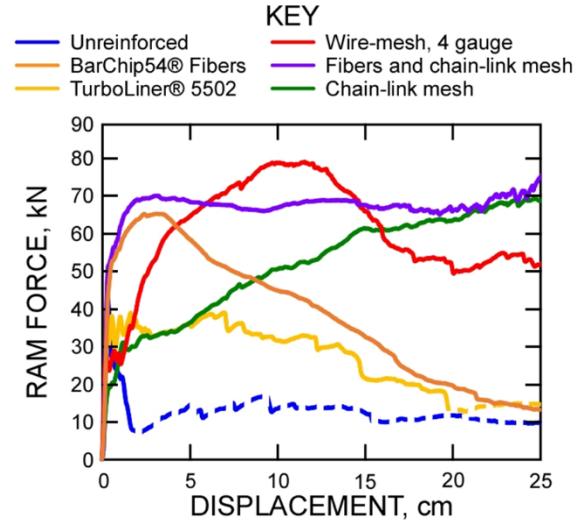


Figure 10: Force versus displacement graph for shotcrete panels with different types of reinforcement.

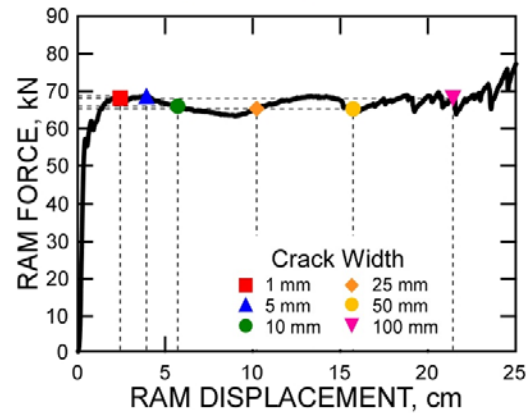


Figure 11: Force, displacement, and crack width opening for a shotcrete panel reinforced with chain-link mesh and 54-mm-long macro synthetic fibers at a 6.5-kg/m³ dosage.

Photogrammetry is used during the HEHD tests to measure the volumetric deformation of the panel and the opening width of cracks that are developed within the shotcrete. The force and energy applied to the panel are referenced to these photogrammetric measurements as shown in Figure 11. Using this information, the panel tests results are then compared with field observations in underground mines to estimate the remaining support capacity of the applied shotcrete based on photogrammetric volume calculations or visual observation of crack widths (Raffaldi et al., 2016a).

8. NUMERICAL MODELING

Map3D™ (<http://www.map3d.com>), a boundary element software program, is being used to evaluate mining-induced stress changes and fault stability in

response to sill pillar mining (Figure 12). As expected, stresses in the sill pillar increase as the vertical extent of the pillar decreases. As mining advances, these stress increases result in an increased potential for strain bursts in the pillar accompanied by a relaxation of the normal forces acting on the faults, which in turn lead to an increased potential for fault-slip seismicity. In the model, horizontal closure of the backfill stopes is roughly calibrated to actual in-mine measurements.

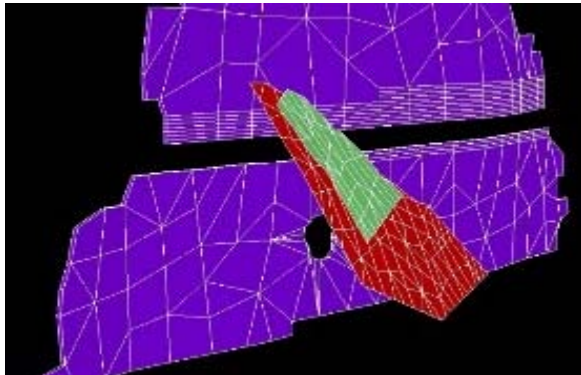


Figure 12: Map3D model geometry showing backfilled stopes (purple), faults (green and red), and remaining sill pillar and host rock (black).

The finite difference code, FLAC3D™ (<http://www.itascag.com/software/flac3d>), is being used to model the Gold Hunter sill pillar. Host rock and backfill properties are based on the in situ measurements and laboratory testing described earlier in this paper. FLAC3D™ allows for a detailed extraction sequence to be simulated in which the orebody is sequentially mined and backfilled. The model has been used to back-calculate the rockmass deformation modulus and cohesive strength in the vicinity of the Gold Hunter sill pillar.

The discrete element code, UDEC™ (<http://www.itascag.com/software/udec>), is being used to perform fully dynamic simulations of rock fracture and ejection caused by seismic loading. A synthetic rock mass was modeled consisting of a series of discrete blocks that can fracture and shear or fully detach from the model in response to loading (Raffaldi and Loken, 2016b). This has been incorporated into a model of a typical mine drift and is being used to investigate energy transfer between the ejected rock and the reinforcement and surface support components of the ground support system (Raffaldi and Loken, 2016c).

9. CONCLUSIONS

Research is being conducted by NIOSH in collaboration with the Hecla Mining Company at the Lucky Friday Mine to develop improved technologies for ground control safety in deep vein mines. To gain a

better understanding of mining-induced seismic events and fault-slip seismicity, a network of surface seismic stations near the mine site are being monitored on a real-time basis along with geotechnical instruments installed underground in the host rock, backfill, and at fault locations. To provide further insight, photogrammetry surveys are periodically being conducted to monitor bulk movement in underground entries and to measure shear displacement along exposed faults. Much of this information is being incorporated in 3D visualization software to help synthesize and interpret the data in terms of the mine's infrastructure, production stopes, and geology. Laboratory tests are being performed to measure the material properties of the mine's host rock, shotcrete, and cemented paste backfill. Large-scale tests are being conducted to determine the ground support characteristics of reinforced shotcrete systems. Finally, several different types of numeric models are being used gain a better understanding of the geomechanical behavior of the host rock and backfill, particularly in regard to seismic loading. Advances in these research areas will hopefully lead to improved ground support and mine design practices for deep underground mines.

10. ACKNOWLEDGEMENTS

The authors thank Mark Board, Bob Golden, and Eric Zahl from the Hecla Mining Company for their technical input and professional assistance with this research. We also gratefully acknowledge the other NIOSH researchers in Spokane who have contributed to this project, most notably Steve Iverson, Doug Tesarik, Bob Hammond, Derrick Chambers, Pete Swanson, Curtis Clark, Heather Lawson, Mike Stepan, Habte Abraham, Seth Finley, and Mark Powers.

Mention of any company or product does not constitute endorsement by the National Institute for Occupational Safety and Health. The findings and conclusions in this report are those of the author(s) and do not necessarily represent the official position of NIOSH.

11. REFERENCES

- Benton DJ, Iverson SR, Martin LA, Johnson JC, Raffaldi MJ (2016). Volumetric measurement of rock movement using photogrammetry. *Intl Journal of Mining Science and Technology*, Vol 26, Issue 1, Jan 2016, pp.123-130.
- Benton D, Boltz M, Raffaldi M, Iverson S (2015). Using photogrammetry to monitor underground mining environments. *ARMA e-Newsletter: Imaging and Remote Sensing in Rock Mechanics*, Spring 2015, Issue 15, pp. 11-16.
- Benton D, Iverson S, Johnson J, Martin L (2014). Photogrammetric monitoring of rock mass

behavior in deep vein mining. In Proc 33rd Intl Conf on Ground Control in Mining, Morgantown, WV, July 29-31, 2014, pp. 221-227.

Johnson JC, Seymour JB, Martin LA, Stepan M, Arkoosh A, Emery T. (2015). Strength and elastic properties of paste backfill at the Lucky Friday Mine, Mullan, Idaho. In Proc 49th U.S. Rock Mechanics / Geomechanics Symp, June 28 - July 1, 2015, San Francisco, CA, ARMA 15-776, 12 pp.

Martin L, Clark C, Johnson J, Stepan M (2015). A new high force and displacement shotcrete test. SME Annual Meeting, Feb 15-18, 2015, Denver, CO: Preprint 15-090, 8 pp.

Orr TJ, MacDonald BD, Iverson SR, Hammond WR (2015). Development of a generic mine visualization tool using Unity. In Proc 37th Intl Symp on the Application of Computers and Operations Research in the Mineral Industry, Fairbanks, AK, May 23-27, 2015, F-2015-055, 7 pp.

Raffaldi MJ, Loken MC (2016b). Rock mass modeling approach for simulating wave propagation, rock fracture, and rock ejection. In Proc 50th U.S. Rock Mechanics / Geomechanics Symp, June 26-29, 2016, Houston, TX, ARMA 16-0393, 12 pp.

Raffaldi MJ, Loken MC (2016c). Framework for simulating fracture, ejection, and restraint of rock around a mine drift subjected to seismic loading. In Proc 50th U.S. Rock Mechanics / Geomechanics Symp, June 26-29, 2016, Houston, TX, ARMA 16-0394, 16 pp.

Raffaldi M, Benton D, Martin L, Johnson J, Stepan S (2016a). Assessing the mechanical behavior of large-scale shotcrete panels. SME Annual Meeting, Feb 15-18, 2016, Phoenix, AZ, Preprint 16-036, 13 pp.

Seymour JB, Tesarik DR, McKibbin RW, Jones FM (1999). Monitoring mining-induced stress changes with the biaxial stressmeter. In Proc 5th Intl Symp on Field Measurements in Geomechanics, FMGM99, Dec. 1-3, 1999, Singapore, pp. 55-60.

Unity Technologies (2015). Unity Manual. <http://docs.unity3d.com/Manual/index.html>.

Numerical investigation of EDZ development around a deep polymetallic ore mine

Mountaka Souley ^{a*}, Marwan Al Heib ^a, Vincent Renaud ^a

^a INERIS, c/o Ecole des Mines de Nancy, Campus ARTEM, CS 14234, Nancy, France, F-54042

ABSTRACT

This paper deals with the development of a non-linear constitutive model of rock mass and its verification to predict a damaged zone. Simulations of triaxial compressions provide a verification of the implementation with a good agreement between predictions and theoretical values of peak and residual strengths as well as the transition between brittle failure and ductile response. The applicability of the model to predict potential failure around stopes of a deep polymetallic ore mine is checked. The present study highlights the interest to consider more realistic rheology of hard rock masses compared with the elastic perfectly plastic models of underground deep mines.

KEYWORDS: Brittle-ductile behaviour; constitutive model; verification; Garpenberg mine; numerical modelling

1. INTRODUCTION

Damage by microcracking is the main dissipation process associated with inelastic behaviour and failure in most brittle materials such as rocks, concrete and ceramic composites. Under high *in situ* and induced stresses and high anisotropic stress ratios, an excavation damaged zone (EDZ) may be formed around underground openings excavated into brittle rocks. The failure mechanism in this damaged zone is the initiation, growth and coalescence of cracks and fractures and is directly related to the constitutive behaviour of rock mass. Experimental studies on brittle rocks have shown that there are many different mechanisms by which cracks can be initiated and grown under compressive stresses (Steif, 1984; Horii and Nemat-Nasser, 1986.). The involved mechanisms include sliding along pre-existing cracks and grain boundaries, pore crushing, elastic mismatch between mineral grains and dislocation movement, etc. Indeed, irreversible deformations and failure of rocks subjected to stresses occur through progressive damage as micro-cracks initiate and grow at small scale and coalesce to form large-scale fractures and faults. Over the past decade, several constitutive models have been developed providing a more realistic description of damage for brittle rocks in relation to experimental observations (Zhu et al. 2009).

In the framework of the European program I₂Mine (<http://www.i2mine.eu/>), INERIS has developed an innovative tool (stress monitoring tool) aimed to better understand the behaviour of the rock mass resulting from the mining process of Garpenberg deep mine (superposed rooms and pillars and vertical stopes between depths 1100 and 1300 m,

Figure 1) in Sweden. Several seismic sensors and strain gauges were installed in a deep area of the mine (approximately at 1150 m deep) to monitor the evolution of induced stresses during the exploitation and the related induced seismic activities.

The objective of this paper is to study the mechanical behaviour of the main galleries and the pillars by incorporating the stages of the underground work through advancing numerical modelling. At first approach, we are limited to 2D models that take into account the initial state of stress (anisotropic) and the mine operations.

More precisely, the purpose of this paper is to present: (a) a numerical implementation of an elastoplastic model obeying to the Hoek–Brown criterion and taking into account the brittle/ductile transition between the brittle failure and the ductile behaviour depending on the mean stress as generally observed on most rock samples: that is to say, the initiation and growth of cracks for brittle rocks are modeled by a softening behaviour in the post-peak in the framework of plasticity theory, (b) the corresponding verification based on simulation of triaxial compression tests. Finally, the numerical modelling provides the localization of EDZ and the potential instability area in the vicinity of stopes located around the pilot area of the mine works at the Garpenberg mine (New Boliden company).

2. PROPOSED RHEOLOGICAL MODEL AND NUMERICAL IMPLEMENTATION

The mechanical behaviour of geomaterials is widely varied and depends mainly on the confining stress (or mean stress) and the loading paths. At low stress confining levels, rocks break by the creation of

*Corresponding author – email: Mountaka.Souley@ineris.fr

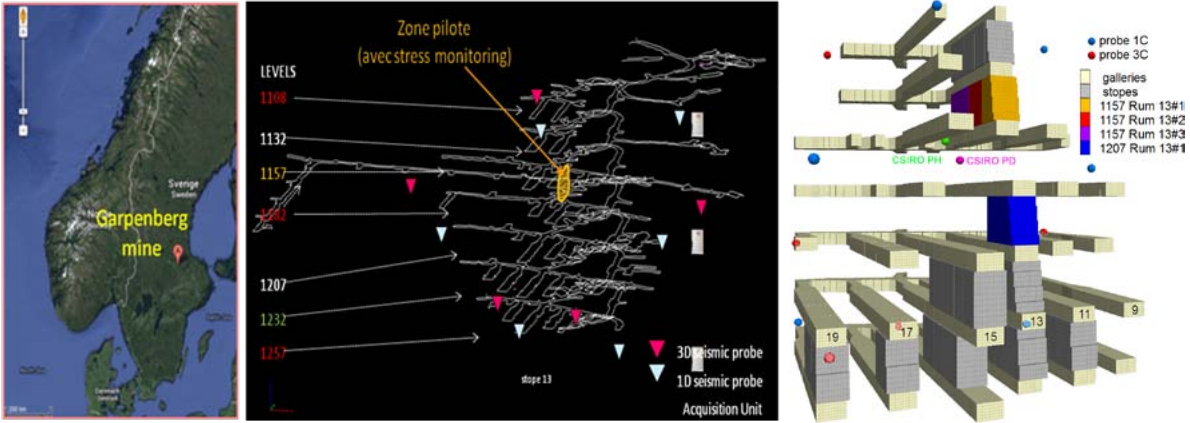


Figure 1: Experimental set-up (stress and microseismic measurements) in the Swedish mine Garpenberg: (a-left) the mine location; (b-centre) operating plan and location of the pilot area; (c-right) 3D mesh of galleries and stopes.

one or more shear planes or bands accompanied by a strain-softening behaviour characterized by microcracks dilatancy and grains rotation at the microscopic scale. Under high mean stresses, rocks undergo a hardening behaviour which is microscopically associated with volumetric strains. More precisely, for most geomaterials subjected to triaxial compressions under low to moderate confining pressures, it is generally observed the following typical characteristics of stress-strain curves: (a) a linear isotropic and elastic behaviour after a short non-linear phase corresponding to the closure of the initial pores and the progressive contact walls of the original micropores and microcracks (b) a strain-hardening in the pre-peak region corresponding to the initiation and the growth of microcracks modeled generally by the plasticity theory or the damage mechanics through the concept of effective stress and the hypothesis of strain equivalence (c) a strain-softening after reaching the peak strength (failure) associated with a progressive loss in material cohesion and then a decrease in strength (d) a phase where the rock strength remains practically constant. Relative to the elasto-brittle materials where the initial microcracks closure and the growth of microcracks in the pre-peak domain can be neglected in a first approximation (as it is the typical case of hard rock masses studied herein at the Garpenberg mine), the present study considers an isotropic elastic linear behaviour before the peak.

The Hoek-Brown criterion widely used in the field of rock mechanics and rock engineering, whose limitations were documented by detailed discussions of the simplifying assumptions (Hoek and Brown, 1980), was generalized in terms of the three stress invariants in this study. One of the most important limitations is the non-dependency of the criterion on the intermediate principal stress, σ_2 . Subsequent experimental studies have since suggested that the

intermediate principal stress has a substantial influence on the rock strength (e.g. Haimson, 2006). This has led to the development of several 3D versions of the Hoek-Brown failure criterion (Priest, 2005; Zhang, 2008).

It is well known that the three principal stresses σ_1 , σ_2 and σ_3 can alternatively be expressed in terms of mean stress (p), generalized deviatoric stress (q) and Lode's angle (θ) and vice versa, which allows to express the classical Hoek-Brown criterion in 3D-stresses space (p , q , θ). After some manipulations, the generalized yield function is proposed on the basis of Souley et al. (2011):

$$F_s = \frac{4 \cos^2 \theta}{3} \frac{q^2}{\sigma_c} - m \left(\frac{\cos \theta}{\sqrt{3}} - \frac{\sin \theta}{3} \right) q + m p - s \sigma_c \quad (1)$$

where σ_c is the uniaxial compressive strength of the intact rock, m , s represents the rheological behaviour parameters whose significance and quantification differ from the dimensionless empirical parameters of Hoek-Brown reflecting the strength of the intact rock, the natural fractured rock mass and therefore consideration of a possible scale effect and fracturing at the large scale. The parameter m quantifies the frictional strength and s (measuring the induced cracks) is related to the rock cohesion.

Let (m_p, s_p) and (m_r, s_r) be respectively the values of parameters (m , s) at the peak and the beginning residual phase. Assuming a transition between brittle and ductile behaviour, equation (1) makes it possible to express a relationship between the peak and residual strength parameters:

$$m_r = m_p + (s_p - s_r) \frac{\sigma_c}{\sigma_3^{b-a}} \quad (2)$$

In the absence of experimental data on the residual strength, almost null value of s_r can be considered as a good approximation in relation to

sliding along the macroscopic failure planes or shear bands. For softening phase, the same yield function (equation 1) is used by introducing the softening internal variable (ζ). In accordance with the yield function used, (a) the generalized plastic strain is chosen to represent the internal variable, (b) m linearly varies with ζ between the peak and the beginning of residual phase ($0 < \zeta \leq \zeta_r$, representing the shear plastic strain) whereas s varies non linearly (c) m and s remain constant in the residual domain:

$$d\xi = \sqrt{\frac{2}{3}} d\mathbf{e}^p : d\mathbf{e}^p \quad m = m_p + (m_r - m_p) \frac{\xi}{\xi_r} \quad (3)$$

$$s = s_p + (s_r - s_p) \left(2 - \frac{\xi}{\xi_r} \right) \frac{\xi}{\xi_r} \quad (4)$$

where $d\mathbf{e}^p$ is the increment of deviatoric plastic strain tensor in post-peak or residual regions.

Assuming for this type of rock materials that the plastic dilatancy occurs only near the peak strength and cannot exceed a threshold rate (β_m) for a certain value of deformation and by adapting a non associated flow rule (generally accepted for rock materials), we propose the following plastic potential (G_s) which allows to express the constitutive relationship between the increments of stresses ($d\mathbf{\sigma}$) and total strains as follows ($d\mathbf{\underline{\epsilon}}$):

$$G_s = q - \beta_m (1 - e^{-b_1 \xi}) p \quad (5)$$

$$d\mathbf{\underline{\sigma}} = \left[\underline{\underline{C}} - \frac{\left(\underline{\underline{C}} : \frac{\partial F_s}{\partial \underline{\underline{\sigma}}} \right) \otimes \left(\underline{\underline{C}} : \frac{\partial F_s}{\partial \underline{\underline{\sigma}}} \right)}{\frac{\partial F_s}{\partial \underline{\underline{\sigma}}} : \underline{\underline{C}} : \frac{\partial G_s}{\partial \underline{\underline{\sigma}}} - \frac{\partial F_s}{\partial \xi} \frac{\partial G_s}{\partial q}} \right] d\mathbf{\underline{\epsilon}} \quad (6)$$

In addition to the two elastic constants: Young modulus and Poisson ratio (E , ν), the needed parameters for the proposed model are: m_p , m_r , σ_3^{b-d} , s_p , s_r , σ_c , ξ_r , β_m and b_1 . All of these parameters can be identifiable from triaxial compression tests (3 minimum) carried out from low confining pressure (or without) to high confining pressure (characterizing σ_3^{b-d}). Finally the proposed model was implemented in the three-dimensional explicit finite-difference code, *FLAC^{3D}*, where a perfect elastoplastic model with the Hoek-Brown criterion in the (σ_1 , σ_3) plane already exists in the commercial version.

The most input data used in this paper are from laboratory tests, field studies, reports and papers. More precisely, the Young's modulus (E), Poisson's ratio (ν) and the unconfined compressive strength (σ_c) have been obtained from the point and biaxial load tests or uniaxial compression loading carried out

on samples (complex ores containing zinc, lead, silver, copper and gold) taken from the measuring holes at -883 m and -967 m levels (Edelbro, 2008; van Koppen, 2008). These parameters and the empirical constants m_p and s_p , and dilatancy at failure were confirmed by many numerical studies aimed to the calibration of the mechanical characteristics, the determination of the in situ stresses (at -880 m level and from one access gallery at -1155 m level, respectively carried out by Boliden and INERIS) and the understanding of the failure mechanism (for instance spalling, shear failure, slabbing, buckling or other types of compressive failure) as well as the back-evaluation of fallout extent observed in the field.

It is known that it is often very difficult to get the full stress-strain curves of the post-peak behaviour particularly for hard rock masses exhibiting brittle behaviour. As first approach, we retained the values of additional parameters (s_r , σ_3^{b-d} , ξ_r , β_m and b_1) summarized in Table 1: a sensitivity analysis on these parameters will be conducted in parallel to the interpretation of the in situ stress measurements at 1155 m coming in the future and whose deformation measurement systems have already been installed from an access gallery at -1155 m level (Figure 1c).

Table 1: Numerical values of input model parameters.

Parameter	Value	Parameter	Value
E (MPa)	80000	s_r (-)	$10^{-5} s_p$
ν	0.2	σ_3^{b-d} (MPa)	$\sigma_c \sqrt{s} \approx 63$
m_p (-)	10	ξ_r (-)	0.0025
s_p (-)	0.112	β_m (-)	$\tan(15^\circ)$
σ_c (MPa)	188	b_1 (-)	750

3. NUMERICAL IMPLEMENTATION AND MODEL VERIFICATIONS

In order to verify the implemented model, seven triaxial compression tests with confining pressures ranged from 0.01 to 75 MPa have been simulated. The input parameters used for this exercise are summarized in Table 1.

Figure 2 presents the deviatoric stress versus axial and lateral strains curves for different confining pressure (σ_3). We note that the post-peak behaviour is confining pressure dependent: the transition stress between brittle failure and ductile behaviour is clearly marked and the numerical transition stress, σ_3^{b-d} , occurs for a confining pressure of 63 MPa in accordance with the input numerical value.

Figure 3 shows a comparison in terms of the peak and residual strengths between the predictions and theoretical expression in equation (1) (with $\theta = 30^\circ$ for triaxial compression loading path). The match is very good as may be seen in this figure, where numerical and analytical solutions coincide.

The relative error for peak and residual strengths is less than 0.3 % and 0.7 % respectively for peak and residual strengths. This validates the numerical implementation of the proposed elastoplastic model in $FLAC^{3D}$.

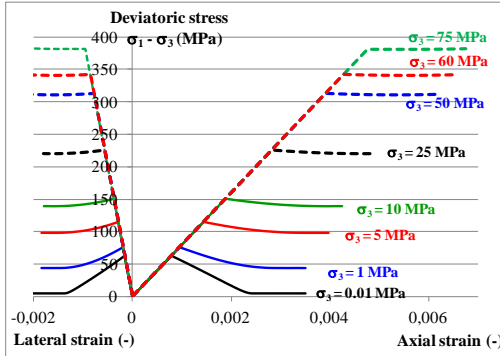


Figure 2: Numerical results of triaxial compression tests.

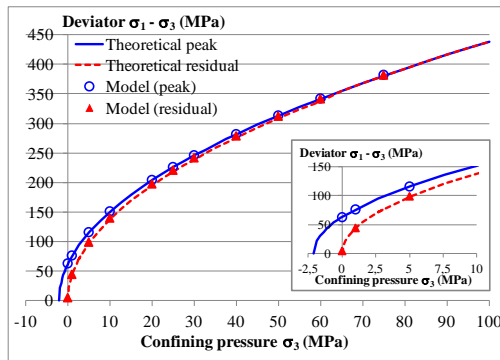


Figure 3: Peak and residual strengths: numerical and analytical solutions.

4. APPLICATION TO GARPENBERG MINE

The aim of this section is to provide a verification of the implementation for non-triaxial stress paths and to show numerically the ability of the model to evaluate the extent of potential damaged zones in relation to the excavation of one or more stopes.

In the Garpenberg mine, polymetallic ore is extracted which contains zinc, silver, lead, copper and gold. The ore has fold axis and the depth is 500-1300 m below the surface. During the mining operations of the upper level (-883 m and -967 m levels), several field studies and numerical modellings were performed with the aim to calibrate certain mechanical characteristics, back-determine the initial and induced *in situ* stresses and to understand the potential failure mechanisms. The results of these observations and measurements were also used as input data for the preliminary 3D modelling of the initial stress field prevailing at the lower level around 1155 m deep before the future excavation of stopes and for which stress

measurements are available using CSIRO cells (Figure 4).

To retrieve the initial stress state (at 1155 m), a 3D numerical model has been carried out with several assumptions. A specific methodology for verifying the correlation of measured stresses (where locations are illustrated in Figure 4) with computed stresses (after mining operations of the upper level) is developed: it consists of creating a stress data bank with the numerical model according to the range of measured stress tensors. Because the dependence between initial and induced stresses is strongly non-linear, it is very difficult to find what is the initial stress tensor that produces the correct measured stresses after the excavation of many galleries and stopes and after a partial backfilling of the stopes (chambers). Nevertheless, it was possible to estimate the initial stress tensor corresponding to level -1155 m. The horizontal and vertical directions are principal with the following principal values 47.5 MPa (x-horizontal direction), 55 MPa (y-horizontal direction) and 20.5 MPa (vertically). This stress state was used to uniformly load the numerical 2D-model shown in Figure 4.

As illustrated in Figure 1c, to model the mine geometry in 2D as first stage, we can consider a double symmetry in the vertical and horizontal directions. The geometrical model for 2D-modelling with $FLAC^{3D}$ assuming plane strain conditions is shown in Figure 4. Null normal displacements are imposed at the boundary limits (symmetry). The access galleries are 10 m wide and 6 m high. Finally, typical primary stope sizes are: 80 m long (along Y-direction), 10 m wide, and 19 m high.

The modelling sequences were performed as follows: (a) model without excavations was consolidated under the previous initial *in situ* stresses, using roller boundaries to the model sides respectively parallel to x- and z-axis for seeking symmetry (step 0); (b) four galleries are simultaneously excavated, numerical model is stepped until equilibrium (step 1) and (c) stopes 1 and 2 are simultaneously deleted and the numerical model is stepped until equilibrium.

The plastic zones corresponding to the galleries excavation (phase 1) (or failed with behaviour in residual or transition between peak and residual) are limited to the galleries skin. This is consistent with the observed fallouts (whose extension is around 0.05 m) or predicted by numerical analysis conducted at -880 m level. This is also consistent with the strength of the rock masses ($\sigma_c/\sqrt{s} \approx 63$ MPa) and the magnitude of induced stresses. In considering for example the case of the gallery sides and assuming the linear elasticity behaviour and neglecting variations of axial stress, the expected orthoradial, radial, and axial

stresses are globally 16, 0, and 50 MPa. This confirms the failure at the walls. Moreover, away from the wall, the presence of a non null radial stress significantly increases the rock mass strength by the term $(m_p \sigma_r \sigma_c)$, which explains the limited character of failed area around the galleries.

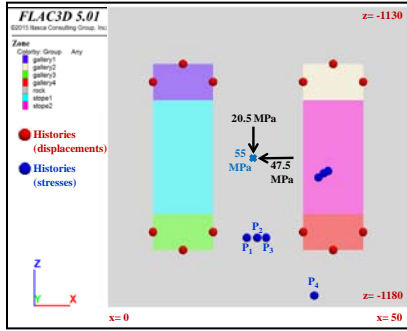


Figure 4: Geometrical model with position of history points.

After excavating the two stopes in a 2D model, the extent of plastic zones is concentrated in the pillar (Figure 5), in the compressive region where the maximum deviatoric stress is located (at the heart of pillars between stopes along the symmetry axis). Figure 5a shows the distribution of plastic zones in the pillars (and therefore strain localization). In fact, the most compressive stresses are located at the singularity levels (corners of galleries), but as the mean stress also increases in magnitude, it is the same for the failure strength. Excavation of stopes results in complete release of the horizontal stress, causing predominantly tensile stresses over the whole width and substantially all the height of pillars. Therefore, the failures can be initiated at the center of pillars and propagate along an inclined plane at first and then sub-vertically following the localization of the plastic zones. As a consequence of stress projections on the current yield envelop, we observed decreases in the vertical and axial stresses. This is well illustrated in Figure 6, which shows the distribution of horizontal and vertical stresses at the end of step 2.

For comparison purpose and in order to capture the contribution of the proposed rheological model (#1), another simulation is performed with a basic perfectly plastic model with Hoek-Brown's criterion (model #2). In this case, the plastic zones are also developed in the heart of the pillars but in a very limited area compared to the results of the model #1 (previously presented) without plastic strain localization (Figure 5b). Specifically, the examination of the principal stresses $(\sigma_1, \sigma_2, \sigma_3)$ at the pillar center delimited by the two stopes for the two models 1 and 2 provides the following stress

values: (-20.5, -17.5, 0.75 MPa) and (-48, -35.5, 0.85 MPa) respectively for #1 and #2 (compressive stresses < 0). Finally, Figure 6b clearly shows a significant increase in vertical stress (σ_{zz}) near the changes of orientations of failure plane locations, indicating some eventual seats of potential risks of instability.

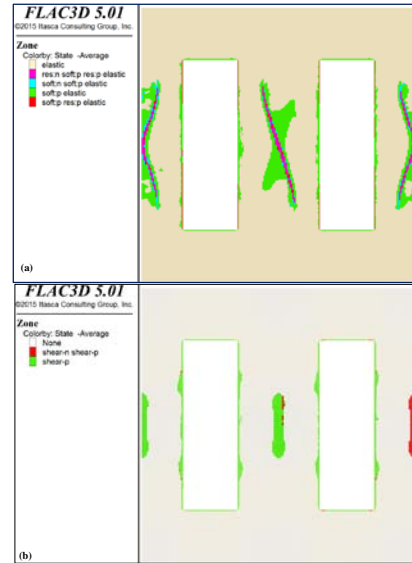


Figure 5: Extent of plastic zones around the stopes: (a) model #1 (b) model #2.

The quantitative comparison between the two models was conducted on the stress values at the end of step 2 (points 1 to 4 illustrated in Figure 4) and reported in Table 1 in terms of stress ratios with respect to the initial stress state before the excavations of galleries and stopes.

One can note that in both cases, the four points are outside the plastic domain induced by galleries and stopes. The points $P_1, P_2,$ and P_3 are located in the pillar between the two lower galleries and point P_4 is located at the floor of a stope. Table 2 reveals a slight difference between the models on the relaxation at $P_1, P_2,$ and P_3 and compression at P_4 of the horizontal stresses (along x and perpendicular to the model cross section). Conversely, over-stresses develop in the vertical direction at $P_1, P_2,$ and P_3 positions with more magnitude (15 to 35%) for #1 compared to #2, resulting from the failure occurred a little earlier in the pillar of stopes, and then a new stresses redistribution.

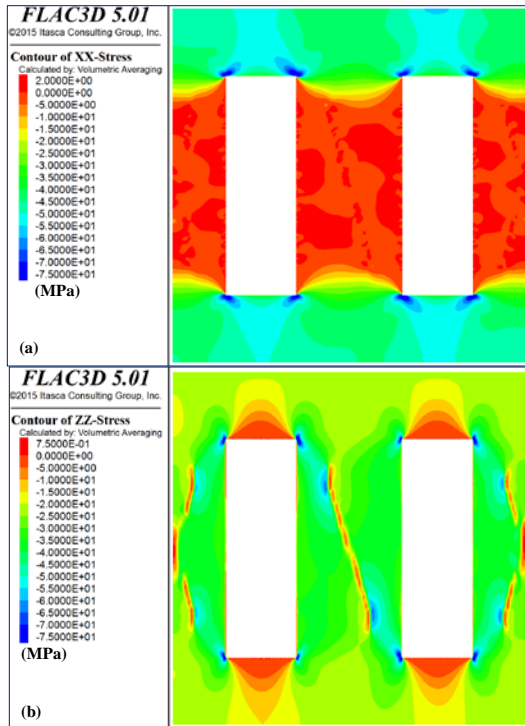


Figure 6: Horizontal (top) and vertical (down) stresses: model #1.

Table 2: Ratio of horizontal (σ_{xx}), vertical (σ_{zz}) and axial (σ_{yy}) stresses.

Model	$\sigma_{xx}^* P_1$	$\sigma_{zz}^* P_1$	$\sigma_{yy}^* P_1$
#1	0.38	1.45	0.93
#2	0.41	1.59	0.94
Model	$\sigma_{xx}^* P_2$	$\sigma_{zz}^* P_2$	$\sigma_{yy}^* P_2$
#1	0.39	1.31	0.92
#2	0.42	1.57	0.94
Model	$\sigma_{xx}^* P_3$	$\sigma_{zz}^* P_3$	$\sigma_{yy}^* P_3$
#1	0.41	1.22	0.91
#2	0.41	1.58	0.94
Model	$\sigma_{xx}^* P_4$	$\sigma_{zz}^* P_4$	$\sigma_{yy}^* P_4$
#1	1.04	0.96	1
#2	1.05	0.87	1

5. CONCLUSION

This paper presents the development of a constitutive model for brittle hard rock masses, its numerical implementation in the three-dimensional code *FLAC^{3D}*, as well as its verification. Simulation of triaxial compression tests at different levels of confining pressure provides a verification of the implemented model. The resulting curves display three regions (elastic, softening in post-peak, and residual phase) as well as a transition between brittle failure and ductile behaviour as generally observed on hard and brittle rocks. The ability of the proposed model to predict the potential failure regions (damaged zones) around deep underground excavations in hard rocks is successfully tested. In

particular, the importance of considering the post-peak behaviour to predict strains and failure zones localization, and consequently the advantage over the approaches without strain softening is shown.

It is often difficult to characterize the post-peak behaviour parameters from laboratory tests on such hard rocks in relation to the brittle nature of their behaviour. These parameters can be viewed as calibration parameters, which can be back-determined on the base of the in situ observations. The prospect of this work after a full 3D modelling back-analysis would complete this numerical development by implementing the energy balance in view of assessing the proneness to rockbursts or strain bursts.

6. REFERENCES

- Edelbro C. (2008). Strength, fallouts and numerical modeling of hard rock masses. Doctoral thesis 2008:56, Lulea University of Technology, 80p.
- Haimson B. (2006). True triaxial stresses and the brittle fracture of rock. *Pure Applied Geophysics*. Volume 163(5–6), pp. 1101–1130.
- Hoek E. and Brown ET. (1980). Underground excavations in rock. The Institution of Mining and Metallurgy, London.
- Horii H. and Nemat-Nasser S. (1986). Brittle failure in compression: splitting, faulting and brittle-ductile transition. *Philos. Trans. R. Soc. (London)*, Series A, Vol. 319, pp. 337-374.
- Priest S.D. (2005). Determination of shear strength and three-dimensional yield strength for the Hoek–Brown criterion. *Rock Mechanics and Rock Engineering*. Vol. 38(4), pp. 299–327.
- Souley M., Armand G., Su K. and Ghoreychi M., (2011). Modelling of the viscoplastic behaviour including damage for deep argillaceous rocks, *Physics and Chemistry of the Earth*, 36, pp. 1949–1959.
- Steif P.S. (1984). Crack extension under compressive loading. *Engineering Fracture Mechanics*. Volume 20(3), pp. 463-473.
- van Koppen M.J.G. (2008). Estimation of the Risk for Mine Induced Seismicity in Large Scale Mining in the Garpenberg Mine. Master of Science, Delft University of Technology, Netherlands.
- Zhang L. (2008). A generalized three-dimensional Hoek–Brown strength criterion. *Rock Mechanics and Rock Engineering*. Vol.41(6), pp. 893–915.
- Zhu Q.Z., Kondo D. and Shao J.F. (2009). Homogenization-based analysis of anisotropic damage in brittle materials with unilateral effect and interactions between microcracks. *Int J of Num and Anal Methods in Geomech*. Vol. 33, pp. 749–72.

Estimating the probability of unsatisfactory performance associated with the instability of mine developments

Wael Abdellah^a, Hani Mitri^b

^{a,*} Department of Mining and Metallurgical Engineering, Assiut University, Assiut, Egypt, 71516

^b Department of Mining and Materials Engineering, McGill University, Montreal, Canada H3A0E8

ABSTRACT

Mine developments are the main access to extract tabular ore deposits in deep underground mines. Therefore, their stability is considered the principal priority during the mine production plan. The success of ore extraction mainly depends on the stability and serviceability of mine developments. Mine development instability is expensive and is a risk to personnel and equipment and in turn, it raises operational costs (e.g. repair costs, slashing, rehabilitation costs, costs of adding secondary support, miners wages and delay of production) (Ellefmo, and Eidsvik, 2009; Abdellah et al. 2014a; 2014b; 2014c). This paper aims to develop a hybrid approach in which deterministic numerical modelling is integrated with probabilistic methods to estimate the probability of unsatisfactory performance (e.g. rating and ranking) associated with the instability of mine developments with respect to mining sequences adopting Rosenblueth's Point-Estimate Method (RPEM). A three-dimensional, elastoplastic, finite difference model (FLAC3D) is created (Itasca, 2009). The results are presented and categorized with respect to the probability of instability and the mining stage.

KEYWORDS: Mine developments; numerical modelling; Rosenblueth's Point-Estimate Method (RPEM); probability of unsatisfactory performance

1. INTRODUCTION

Many Canadian metal mines adopt a sublevel stope mining method with delayed backfill, as shown in Figure 1. In this method, ore is mined out into stopes (blocks), which are drilled and blasted. The blasted ore from each stope is mucked out with loaders and transported from a draw point to a nearby ore pass or dumping point. Mine developments (e.g., haulage drifts, cross-cuts and their intersections) are the only access where loaders and/or trucks travel through on multiple levels. Therefore, their serviceability must remain active for a few years (e.g., production plan of the mine) (Wei et al., 2012; Zhang and Mitri, 2008). The following five parameters should be considered in the design process: safety, serviceability (e.g., quality of technical solution), economics (e.g., cost), environment, and rockmass properties. For example rockmass properties alone are complex and are associated with uncertainty in deep underground mines. These five factors should be maintained and combined together in the decision-making process.

Consequently, wrong decision may lead to unwanted risks. In order to facilitate decision-making, probabilistic analysis should be adopted (Einstein, 1996; Sturk et al., 1996; Abdellah et al.,

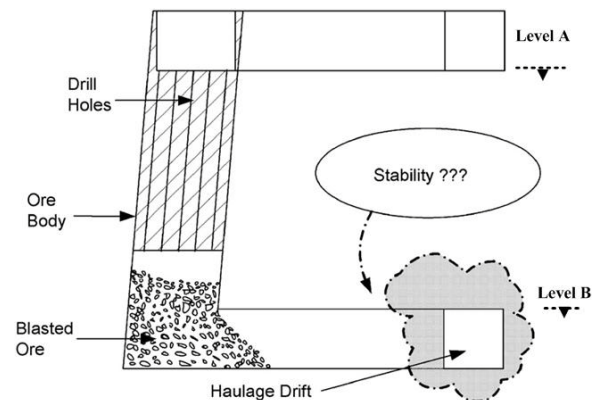


Figure 1: Section view shows sublevel stope mining method

2014c). The stability performance of mine developments could be evaluated by adopting analytical, empirical, and numerical modelling techniques. The analytical methods such as those provided by Kirsch (1898), Bray (1977), Bray and Lorig (1988), and Ladanyi (1974) cannot provide adequate solutions for complex mining problems. Empirical methods such as the stability graph method, have become widely used in Canadian underground mines. These methods are based on the past experiences and rockmass classification systems.

They employ certain geomechanical characteristics of the rockmass to provide guidelines on stability performance and to determine the rock support requirements. However, these methods cannot take all the important influence factors into account. Therefore, numerical methods have become widely accepted in mine design and feasibility studies.

Numerical methods have the potential not only to solve complex mining problems, but also to help engineers and researchers better understand and assess failure mechanisms, estimate geotechnical risks, and design rock reinforcement systems more effectively. Numerical analyses can be performed deterministically or probabilistically. In a deterministic analysis, the average values of the rockmass properties are used as input parameters, and a unique model result is obtained. However, no information can be obtained about the likelihood of failure due to the inherent variability of model input parameters. Thus, probabilistic methods are employed to carry out stochastic analyses to overcome this shortcoming. The uncertainty associated with the estimation of rockmass properties has a significant impact on the design of underground excavations. Thus, a reliable estimate of the strength and deformation characteristics of rockmass is required for the stability analysis. Therefore, probabilistic analysis is adopted in this investigation using Rosenblueth's point-estimate method (RPEM).

2. FAILURE EVALUATION CRITERION

In order to assess the stability of the mine development intersection, a performance criterion must first be selected. This may be one of numerous conditions such as maximum permissible floor heave ratio or roof sag ratio, or allowable stress concentration factor (normally associated with linear elastic analyses), or a yielding condition such as Mohr-Coulomb or Hoek-Brown (Zhang and Mitri, 2008; Abdellah et al., 2012). The choice of a performance criterion is dependent on the application and field observations. In this current study, a yield-based criterion has been selected in which Mohr-Coulomb is used as the failure condition. The strength-to-stress ratio is a readily available parameter in FLAC3D (ITASCA, 2009) and a form of a safety factor. For mining applications, it is recognized that the factor of safety of permanent mine openings such as mine shaft and mine infrastructure should be higher than that used for mine developments, which are required to be opened and functional for the life of a mine (production) plan. Therefore, in this study, a strength-to-stress ratio of 1.4 was deemed an appropriate safety factor, given the fact that the required service life of the developments in the study area is only a few years.

Also, the unsatisfactory performance is determined when the extent of the strength-to-stress ratio contours, corresponding to Mohr-Coulomb strength-to-stress ratio <1.40 exceeds the anchorage limit of the rockbolt from the excavation surface. For a 2.40 m bolt, the minimum support limit from excavation surface is 2.10 m. Thus, the stability of mine development intersection becomes unsatisfactory if the following two conditions are met together:

- Mohr-Coulomb strength-to-stress ratio based yielding <1.40 .
- Extent of the strength-to-stress ratio contours >2.10 m.

3. CASE STUDY

To examine the stability of mine development intersections, a plan view of the 1540 level is shown in Figure 2. The study zone is divided into the following three zones; hanging wall (HW), orebody, and footwall (FW). Haulage drifts, mine developments and their cross-cuts are driven into the footwall rockmass. The stope dimensions are $12 \times 15 \times 30$ m (L \times W \times H). The stopes are extracted and then tight filled with a mixture of pastefill and waste rock.

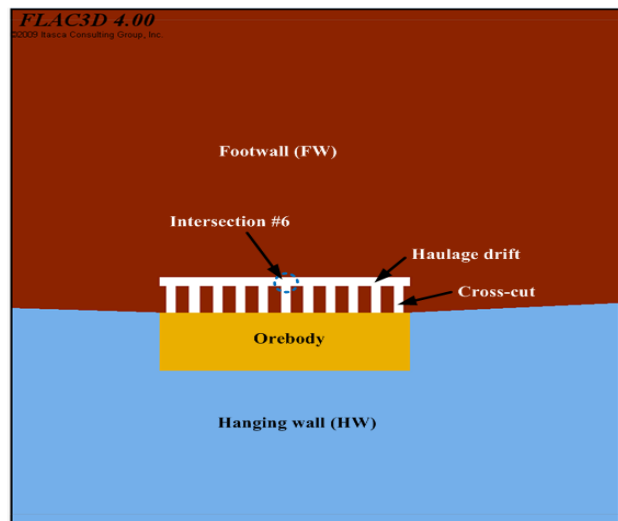


Figure 2: Level plan shows the mine development intersection#6 under the study.

The orebody has a strike length of approximately 220 m. To maintain better ground conditions, the stoping sequence from one level to another and along the ore strike should follow a pyramid shape as shown in Figure 3. Such sequence helps mitigate stress concentration and facilitate secondary stope mining thus increasing safety and mining recovery rate. The stability analysis is conducted for the orebody, whereby a planned sequence of 72 stopes

over six production levels (1600, 1570, 1540, 1510, 1480 and 1450) is simulated in the form of 18 mine-and-fill numerical model steps. While doing so, the strength-to-stress ratio is monitored on level 1540 at the intersection of the haulage drift with the cross cut #6 location.

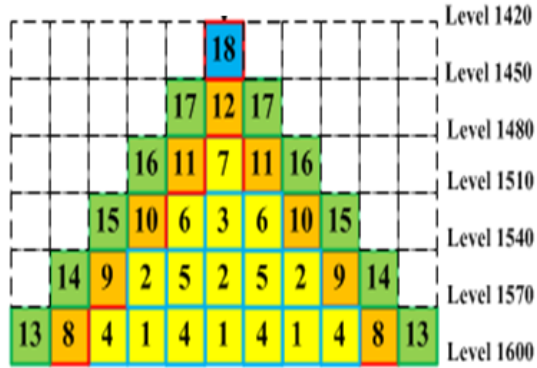


Figure 3: Pyramidal shape stopping sequence along the orebody strike.

4. NUMERICAL ANALYSIS

Rockmass properties are significant geotechnical design input parameters. These parameters are never known precisely. There are always uncertainties associated with them. Some of these uncertainties are due to lack of knowledge or limited collected data and some are intrinsic. Furthermore, some may arise from errors in testing (e.g. estimating strength of intact rocks, mapping the joint spacing, assessing the joint surface condition), and random data collection. All these uncertainties are attributed to the inherent nature of the rockmass characterization (Glaser and Doolin, 2000). Therefore, it is important to address the effect of these parameters on the design using probabilistic methods of analysis. Well assessment of uncertainty in rockmass characterization can assist to better understand how the decision of rock support design systems is affected by it.

In this investigation, the focus is the uncertainty arising from the rockmass properties (e.g. rockmass of footwall) and their effect on the stability of mine development intersections (e.g. which are driven in the footwall). Probabilistic methods provide a rational and efficient means of characterizing the inherent uncertainty that is common in geotechnical engineering. Because of the inherent uncertainty associated with parameters such as the rockmass properties around the openings, there is also uncertainty as to when and where additional rock support is required. Thus, predicting the probability of unsatisfactory performance using probabilistic analysis approaches together with the developed

numerical modelling (deterministic techniques) becomes necessary.

4.1 Deterministic analysis

Deterministic analysis is performed to investigate the effect of mining sequence on the stability of the intersection #6 on level 1540. The physical and geomechanical properties of rockmasses used in the deterministic analysis are listed in Table 1 (Abdellah et al., 2013).

Table 1: Physical and geomechanical properties of rockmass properties used in the model (Abdellah et al., 2013).

Rock	Rockmass properties						
	C MPa	ϕ ($^{\circ}$)	σ_t MPa	E GPa	ν	γ Kg/m ³	Ψ ($^{\circ}$)
HW	5.1	52	0.53	45.5	0.24	2780	13.0
ORE	4.3	46.7	0.56	43.8	0.30	4530	11.68
FW	5.7	54.9	0.51	65.0	0.23	3170	13.73
BF	1	30	0.01	0.01	0.30	2000	7.50

The deterministic results show that the values of strength-to-stress ratio deteriorates as mining progresses in the roof, wall, pillar corner left, and pillar corner right. However, the two conditions of failure evaluation criterion are met in the roof after mining step 6 until the end of mining activity (e.g., from step 6 to step 18), whilst the conditions are not met in the wall of the intersection #6 during the whole mining steps. The two evaluation conditions are achieved in the pillar corner left after mining step 9 and in the pillar corner right after mining step 10. The complete deterministic analysis results of strength-to-stress ratio with respect to all 18 mining steps modelled are plotted in Figure 4. As can be seen, the wall the strength-to-stress ratio is well above the threshold of 1.4 thus suggesting satisfactory performance (e.g., the depth of the boundary limit is zero along all mining steps). For the roof at the intersection #6, the strength-to-stress ratio drops below the 1.4 limit after mining step 6. For the pillar corner left and pillar corner right, the ratio drops after mining steps 9 and 10, respectively.

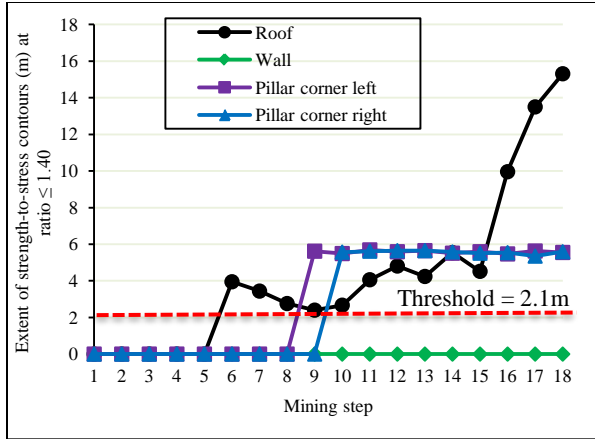


Figure 4: Extent of strength-to-stress contours at ratio of ≤ 1.4 at various mining step (deterministic analysis).

In light of these results, it can be said that secondary support may be recommended after mining step 6 in the roof (i.e. after 30 stopes have been extracted). For pillar corner left and pillar corner right, the secondary support may be recommended after mining step 9 (i.e., after 40 stopes have been extracted) and step 10 (i.e., after 44 stopes have been extracted), respectively. While these results are useful, the effect of the inherent uncertainty in rockmass properties is still unknown; hence the probabilistic analysis is necessary. This is presented in the following section.

4.2 Probabilistic analysis

Due to the heterogeneity of the rockmass, data from underground excavations are limited. Therefore, a great deal of uncertainty is inherent in the design of underground excavations. In order to develop a reliable design approach, one must use methods that incorporate the statistical variation of the numerical model input parameters representing the rockmass properties, i.e. mean, variance and standard deviation, as well as the design of rock failure criteria (Kwangho et al., 2005). Probabilistic material properties of the footwall are assigned (see Table 2). The means and standard deviations of these values are picked from the assumed normal distribution.

The sensitivity analysis can be carried out by varying a single parameter (random variable) at each run based on a specified coefficient of variation (COV) and monitoring the effect of this variation on the applied performance criterion. The variable at each run has one value of $(\mu - \sigma)$, or $(\mu + \sigma)$ while keeping all other parameters constant (no change in their average values). Sensitivity analysis gives a good understanding of the effect of certain parameters on the overall model behaviour. However, no distribution is obtained for the output parameters (random variables).

Based on the parametric study (sensitivity analyses) that has been conducted by Musunuri (Musunuri et al., 2009), the most influential model input parameters on the stability of mine haulage drift are Young Modulus (E), cohesion (C), and angle of internal friction (ϕ).

Table 2: Stochastic properties of footwall rockmass.

Rockmass property	Mean, μ	Standard deviation, σ	Coefficient of variance, δ
Cohesion (MPa)	5.70	1.14	0.20
Friction angle, ($^\circ$)	54.90	10.98	0.20
Young's Modulus, (GPa)	65.0	13.0	0.20

4.2.1 Probabilistic results

The stochastic material properties of the footwall are assigned as listed in Table 2 above. The mean and standard deviations of these values are selected from a normal distribution. The Rosenblueth's (Rosenblueth, 1975) point-estimate method (RPEM) of 2^n (i.e., where n is number of stochastic input parameters) is adopted in this investigation for the above three input variables. The stochastic analysis results are plotted in Figure 5 for an average of 8 simulations (i.e., $2^3 = 8$).

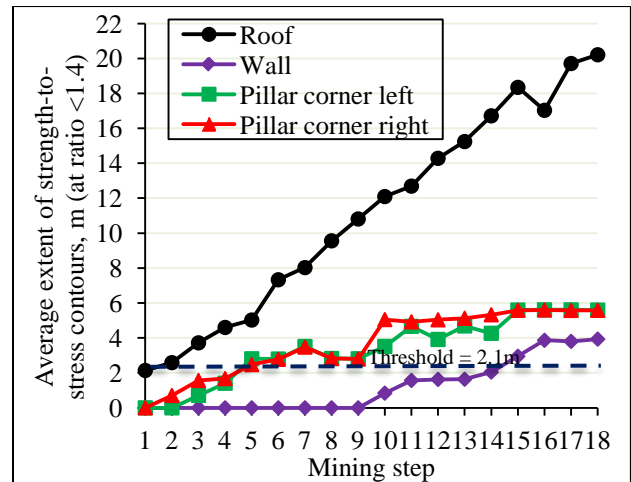


Figure 5: Average extent of strength-to-stress contours at ratio of ≤ 1.4 at various mining steps (stochastic analysis).

As depicted in Figure 5, the stochastic analysis agrees with the deterministic analysis in terms of showing that the strength-to-stress ratio deteriorates as mining progresses. In the roof of intersection #6 at 1540 level, the strength-to-stress ratio falls below threshold (i.e., ratio < 1.4 and length > 2.1 m) after mining step 1, versus step 6 with deterministic analysis. In the wall, the ratio does not fall below the

threshold in the deterministic analysis, whereas with stochastic analysis, it falls below threshold after mining step 15. For the pillar corner left, the performance criterion becomes unsatisfactory after mining step 5 with stochastic analysis where it deteriorates after mining step 9 with deterministic analysis. For pillar corner right, the failure also occurs after mining step 5 with stochastic analysis whereas its instability occurs after mining step 10 with deterministic analysis.

Comparing these two methods of analysis, stochastic results call earlier for secondary supports than with deterministic analysis (i.e., roof calls for secondary support after mining step 1 comparing with the deterministic analysis (after mining step 6)). Wall in deterministic analysis seems to be more stable and no support is required during the whole mining step comparing with probabilistic analysis (i.e., support may be required after mining step 15). Pillar corner left and right require support after mining step 5 with probabilistic analysis, compared with mining steps 9 and 10 with deterministic analysis. Thus, stochastic results appear to be more conservative than the deterministic analysis. The reason behind this is that the stochastic method takes into account the inherent uncertainty associated with input variables (i.e., rockmass properties). The deterministic analysis only uses the average values of rockmass properties as input parameters and gives only a single value as an output. However, the probability of unsatisfactory performance should be estimated to decide when and where secondary support is needed.

4.3 Probability of unsatisfactory performance

The probability of unsatisfactory performance is estimated for the roof, wall, pillar corner left and pillar corner right of intersection #6 at 1540 level, with respect to mining step. The suggested rating and ranking of likelihood of failure are given in Table 3. Standard normal distribution tables (Z-tables) are used to estimate the probability of failure, P_f . The P_f is obtained by subtracting the shaded area $\left(\text{shaded area, } Z^* = \left(\frac{\text{Threshold (X)} - \text{average value}(\mu)}{\text{standard deviation} (\sigma)} \right) \right)$; under the probability density function (PDF) curve from the unity which represents the total area ($P_f = 1 - Z^*$). The results for the probability of unsatisfactory performance are plotted and categorized in Figure 6. As can be seen, the probability of unsatisfactory performance at the roof of the intersection #6 is certain after mining step 4 (i.e., $P_f > 85\%$). Thus, the need for secondary support is necessary at this early stage (i.e., before

step 4). On the other hand, the wall calls for secondary support at latest stages (i.e., after mining step 16) as the probability of unsatisfactory performance becomes likely (i.e., $60 < P_f < 85\%$). The pillar corner right and left call for secondary support at middle stages (i.e., after steps 10 and 11, respectively) as the probability of instability becomes certain (i.e., $P_f > 85\%$).

Table 3: Suggested rating and ranking of probability of unsatisfactory performance (Abdellah et al., 2012).

Rating	Ranking	Probability of Unsatisfactory Performance, P_f	
1	Rare	< 5%	May occur in exceptional circumstances
2	Unlikely	5%-20%	Could occur at some time
3	Possible	20%-60%	Might occur at some time
4	Likely	60%-85%	Will probably occur in most circumstances
5	Certain	>85%	Expected to occur in most circumstances

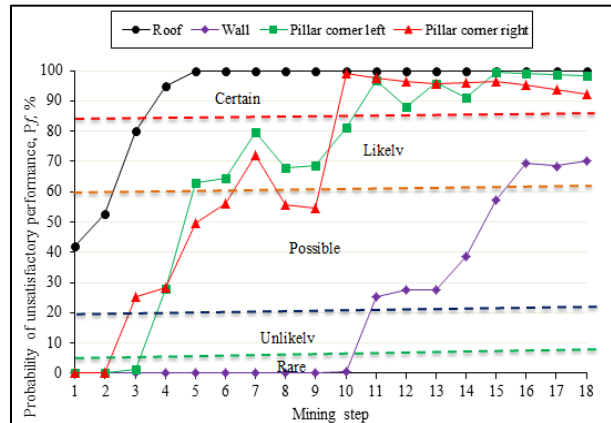


Figure 6: Probability of unsatisfactory performance at roof, wall, and pillar corner left and right of intersection #6 at level 1540 at various mining step.

5. CONCLUSION

Mine developments, such as haulage drifts, cross-cuts and their intersections, play a vital role in providing access to ore extraction areas for mine production. The stability of mine developments is thus of crucial importance during the life of a mine plan. This paper examines the stability of mine development access intersection #6 with respect to planned mining sequence. A 3D elastoplastic finite difference model is created using FLAC3D and employed in conjunction with the probabilistic method of analysis (RPEM) of 2ⁿ, for a development intersection situated 1.5 km below the ground surface. The stability or performance of the

intersection is evaluated in terms of the strength-to-stress ratio. The stability performance of mine intersection is evaluated on the basis of the primary rock support length comprising 2.4 m resin grouted rebars in the roof and wall. The stability performance of the intersection is considered unsatisfactory if the strength-to-stress contours correspond to ratio <1.4 and extends beyond the anchorage limit of the rockbolt (i.e., >2.1 m).

The results are presented and categorized with respect to probability, instability, and mining stage. The probability of unsatisfactory performance, P_f , of the intersection #6 is certain ($P_f > 85\%$) in the roof after mining step 4, and is likely (i.e., $60 < P_f < 85\%$) in the wall after mining step 16 (i.e., at the end of the mining step). The pillar corners right and left call for secondary support at the mid of mining step (i.e., steps 10 and 11, respectively) as the probability of instability is certain (i.e., $P_f > 85\%$). Therefore, these results shed light on the requirement for the installation of enhanced support at the intersection during the planned mining step.

6. REFERENCES

- Abdellah, W., Raju, D., Mitri, H. S., and Thibodeau, D. (2014a). "Stability of underground mine development intersections during the life of a mine plan". *International Journal of Rock Mechanics & Mining Sciences (IJRMMS)*: 72 (2014) 173–181.
- Abdellah, W., Mitri, H. S., Thibodeau, D. and Moreau-Verlaan, L., (2014b). "Risk indexing tool for mine planning", *Journal of the Southern African Institute of Mining and Metallurgy (SAIMM)*. Volume 114, June 2014. Pp. 1-9.
- Abdellah, W., Mitri, H. S., Thibodeau, D. and Moreau-Verlaan, L., (2014c). "Geotechnical Risk Assessment of Mine Development Intersections with respect to Mining Sequence". *Journal of Geotechnical and Geological Engineering (JGGE)*. June 2014. Volume 32, Issue 3, pp. 657-671.
- Abdellah, W., Mitri, H. S., Thibodeau, D. and Moreau-Verlaan, L., (2013). "Stability of Mine Development Intersections – A Probabilistic Analysis Approach". *Canadian Geotechnical Journal (CGJ)*, 2014, Vol. 51, No. 2. Pp. 184-195. Doi: 10.1139/cgj-2013-0123
- Bray, B. (1977). "An analysis of rock behaviour in an experimental stoping block at the Mount Isa Mine. Geomech Abstr." *Int. J Rock Mech Min Sci* 14: 59-66.
- Bray, B. and L. Lorig (1988). "Analysis of rock reinforcement using finite difference methods." *Comp Geotech* 5(2): 123-149.
- Ellefmo, S. L., and Eidsvik, Jo. Local and Spatial Joint Frequency Uncertainty and Its Application to Rock Mass Characterisation. *Rock Mechanics Rock Engineering* 42 (2009), 667-88.
- Glaser, S. D., and Doolin, D. M., New directions in rock mechanics - report on a forum sponsored by the American Rock Mechanics Association. *International Journal of Rock Mechanics and Mining Sciences* 37 (2000) 683-698.
- ITASCA, Fast Lagrangian Analysis of Continua in 3 Dimensions (FLAC3D), User's Manual Ver. 4.0, Itasca Consulting Group Inc., Minneapolis, Minnesota 55401 USA, 2009.
- Kirsch, G. (1898). "Die theorie der elastizität und die bedürfnisse der festigkeitslehre" *Veit Ver Deut Ing* 42: 797-807.
- Ladanyi, B. (1974). Use of the long-term strength concept in the determination of ground pressure on tunnel linings. *Advances in rock mechanics, proceedings of the third congress, International Society of Rock Mechanics, Denver: National Academy of Sciences.*
- Musunuri, A., W. Wei, et al. (2009). Assessment of drift stability using probability of failure. . In *Proc Eighteenth International Symposium on Mine Planning and Equipment Selection*. A. Mehrotra, F. K. and H. G. eds. Singhal, R.K. Banff, AB: 987-996.
- Rosenblueth, E. (1975). "Point estimates for probability moments" *Proc. Nat. Acad. Sci.* Vol. 72, No. 10: 3812-3814.
- Wei, W., Mitri, H. S. & Kelly, C. May 5-9, 2012. 'Evaluating Immediate Mining Induced Ground Movement the Performance of the Primary Support System.' Paper presented at In *Proceedings of 21st Canadian Rock Mechanics Symposium, RockEng12*.
- Zhang, Y. & Mitri, H. S. 2008. 'Elastoplastic stability analysis of mine haulage drift in the vicinity of mined stopes.' *International Journal of RockMechanics and Mining Sciences (IJRMMS)*, 45, 574-93.

Numerical modelling of time-dependent skin degradation of an isolated pillar

Atsushi Sainoki *, Hani S. Mitri

Department of Mining and Materials Engineering, McGill University, Montreal, Canada, H3S1R7

ABSTRACT

This study focuses on the instability mechanism of an isolated pillar, caused by time-dependent skin degradation and strength heterogeneity. The time-dependent skin degradation is simulated with a non-linear rheological model capable of simulating tertiary creep. The inherent strength heterogeneity is realized with Weibull's distribution. The results obtained from the analysis show that pillar degradation is limited to the regions near the surface or the skin until two months after ore extraction, but afterwards degradation starts to extend deeper into the pillar, eventually leaving a highly stressed pillar core due to stress transfer from the failed rock regions. Rockburst potential indices show that the risk increases exponentially at the core as time goes by. It is then demonstrated that the progressive skin degradation cannot be simulated with the conventional strain-softening model assuming brittle failure. The parametric study with respect to the degree of heterogeneity reveals that heterogeneity is key to the occurrence of progressive skin degradation. Although the average UCS in the model with a high degree of heterogeneity is almost the same as that in the model with a low degree of heterogeneity, degradation of the rockmass extends deep into the pillar only when the pillar material is highly heterogeneous.

KEYWORDS: pillar stability; underground mine; skin degradation; rheological model; time-dependent failure

1. INTRODUCTION

A pillar is a rockmass that remains to increase the stability of underground openings. The stability of isolated pillars is crucial because the failure of pillars can lead to fatal accidents and might cause the collapse of rockmass in an extensive area (Cording et al., 2015). Furthermore, pillars can be the cause for rockburst in the case of deep hard rock mines because of the high strain energy stored within the pillar and characteristics of rockmass exhibiting extremely brittle behaviour. Hence, the stability of isolated pillars needs to be evaluated and assessed in an appropriate manner.

A number of studies have been undertaken to estimate the stability of pillars (Martin et al., 2000). In addition, various empirical equations have been proposed for the estimation of a factor of safety (FOS) (Potvin et al., 1989; Sjöberg, 1992; Van der Merwe, 2003). Notwithstanding the significant efforts, pillars with a high FOS occasionally fail and collapse, which would be attributed to unknown uncertainties.

As such uncertainties, the strength heterogeneity of rockmass and time-dependent degradation of a pillar skin would be considered. Indeed, the degradation of a pillar skin, which is represented by spalling, scaling, or strength decay, has been studied by many researchers (Cording et al., 2015; Napier et al., 2012). The schematic illustration of spalling that takes place in a deep hard rock mine is delineated in Figure 1. As can be seen in the figure, due to the

spalling, the side wall of the pillar is loosened and loses load-bearing capacity, consequently inducing additional loads to the core of the pillar. When the region undergoing strength degradation is sufficiently large, FOS of the pillar can decrease to a critical value due to the increase in stress acting in the pillar and the decrease in the cross section of an intact region. In previous studies, the typical simulation technique to simulate the degradation of a pillar side wall is to employ an exponential function to estimate the time-dependent strength decay of rockmass or to decrease rockmass strength in a loosened region under low confining stress near a pillar surface. Importantly, both of the simulation techniques are based on field observations or unverified assumptions

The present study focuses on the time-dependent skin degradation of an isolated pillar due to the occurrence of creep behaviour that eventually leads to the critical failure of rockmass whilst considering the strength heterogeneity with Weibull's distribution (Weibull, 1951). The mechanism and process of stress transfer from loosened near-surface regions to the intact area of the pillar are investigated with the non-linear rheological constitutive model with input parameters derived from laboratory experiments. The comparison of the rheological model with the classical Mohr-Coulomb model taking into account brittle failure (strain-softening) is made in order to emphasize the importance of considering the time-dependent degradation of a pillar skin.

*Atsushi Sainoki – email : atsushi.sainoki@mail.mcgill.ca

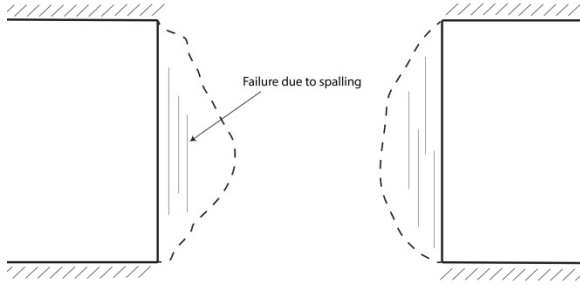


Figure 1: Schematic illustration of skin degradation of an isolated pillar due to spalling.

2. METHODOLOGY

2.1 Constitutive model

As indicated by Scholz (1968), the creep behaviour of rockmass is essentially the progressive development of microcracks, which pertains to the degradation of rockmass. Thus, the present study employs a creep model. To date, a number of constitutive models have been proposed and employed to simulate the creep behaviour of rockmass (Barla et al., 2012). Importantly, few of the models are capable of simulating tertiary creep that causes rockmass to fail. In order to take tertiary creep into consideration, the present study employs the non-linear rheological model proposed by Okubo et al. (2006). The advantage of the constitutive model over the other models considering tertiary creep (Barla et al. 2012) is that the analytical solution of creep lifetime, i.e., time to final rupture, is provided (Okubo et al., 2006).

The non-linear rheological model is expressed as follows:

$$\frac{d\lambda^*}{dt} = \frac{1}{t_0} \left(\frac{m}{n+1} \right)^{n-m+1} (\lambda^*)^m (\sigma^*)^n \quad (1)$$

where λ^* is compliance normalized by its initial value, λ_0 ; σ^* is called severity; n and m represent the degree of time dependency and ductility of rock, respectively; t is time; t_0 is time that it takes for the axial stress applied to a rock specimen to reach its peak axial value during an unconfined compression test. In the present study, t_0 is determined whilst assuming a uniaxial test with a typical axial strain rate. The constants, n and m , for granite are taken from the database (Okubo et al., 2006). The constant, n , is derived from uniaxial compressive strengths obtained from unconfined compression tests under different axial strain rates, while the constant, m , is estimated from the shape of a post-peak behaviour curve (Okubo et al., 2006).

The severity, σ^* , is given using deviatoric stress as follows:

$$\sigma^* = \frac{\sigma_1 - \sigma_3}{\sigma_{\max} - \sigma_3} \quad (2)$$

where σ_1 and σ_3 are the maximum and minimum principal stresses, respectively; σ_{\max} is the maximum stress calculated from a failure criterion. Note that compression is a positive quantity in the equations. The severity for tensile failure is calculated as follows:

$$\sigma^* = \frac{|\sigma_3|}{\sigma_t} \quad (3)$$

where σ_t is the tensile strength of rock. The larger one of the severities determined by Equations (2) and (3) is adopted as σ^* and substituted into Equation (1). As Poisson's ratio, ν , is expected to increase with the progression of rock degradation, Okubo et al. (1993) use the following equation to relate ν with λ^* :

$$\nu = 0.5 - \frac{0.5 - \nu_0}{\lambda^*} \quad (4)$$

where ν_0 is an initial Poisson's ratio. The modulus of elasticity is calculated with λ^* as follows:

$$E = \frac{E_0}{\lambda^*} \quad (5)$$

where E_0 is an initial value of modulus of elasticity. Regarding the failure criterion to calculate the severity, the classical Mohr-Coulomb failure criterion is employed because of its simplicity. As this study does not aim at calibrating analysis conditions and mechanical properties of rock based on actual field measurements, the use of the Mohr-Coulomb failure criterion is deemed sufficient. In addition to that, it is noteworthy that although Equations (1) to (5) indicate that compliance might increase even under initial stress conditions before mining activity starts, it has been confirmed that the increase in compliance is extremely small even when several hundred million years passed if there is no mining activity.

2.2 Generalized simulation procedure

When the non-linear rheological model is employed, an iterative analysis is carried out, of which the generalized procedure is shown in Figure 2. As can be seen in the figure, after the numerical model construction, in-situ stresses are applied if necessary. This means that when the time dependent behaviour of in-situ rockmass in an underground mine is examined, in-situ stress conditions need to be simulated. On the other hand, when the time-dependent behaviour of a rock specimen during a laboratory test is simulated, there is no need to apply such in-situ conditions to the model. As the present study applies the rheological model to two different numerical models representing a room-and-pillar mine and an unconfined compression test under a constant strain rate, the difference in the initial boundary conditions between the two numerical models is described for clarification. At the third step,

the conditions that cause creep behaviour are applied. In the case of room-and-pillar mining, the condition is ore extraction and the generation of an isolated pillar, while in the case of laboratory test, axial strain that increases with time, is applied to the top boundary of the rock specimen. Subsequently, a static analysis is carried out and if the elapsed time, t , has not yet reached the pre-determined t_{max} , the maximum and minimum stresses are computed for each zone. Then, the mechanical properties are updated according to Equations (1) to (5).

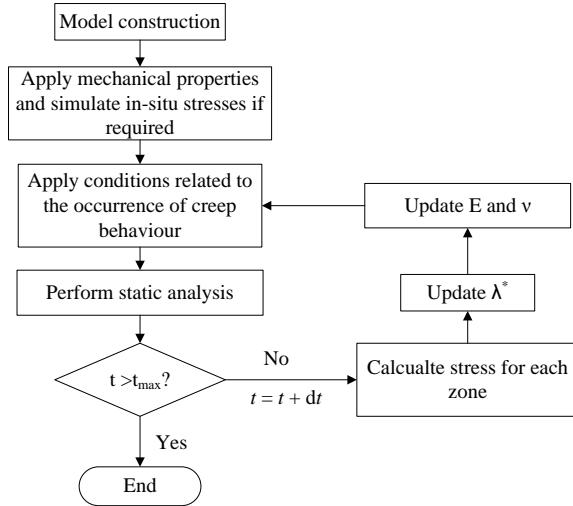


Figure 2: Procedure of iterative analysis.

2.3 Numerical model description

Figure 3 shows a 3D numerical model analyzed in the present study, which is constructed with FLAC3D (Itasca, 2009). The symmetry of the pillar is taken into account, that is, the pillar in the figure represents one-fourth of the actual pillar with the width of 10 m. The green-coloured region is extracted during analysis, and the dimension is determined so that the FOS of the pillar falls between 1.0 and 1.4. The FOS is evaluated with empirical equations (Potvin et al., 1989; Sjöberg, 1992). The stability of pillars with FOS in the range is uncertain (Martin, 2000) and assumed to be affected by a number of factors such as the time-dependent degradation. Thus, it is worth examining.

Pre-mining stress state is based on the equations proposed by Diederichs (1999). The mining depth is assumed to be 1500 m. The stresses computed from the equations are applied to each zone in the model. Note that the maximum horizontal stress is applied in the x-direction. Fixed boundary conditions are employed, that is, the displacements on the model outer boundaries are fixed in the direction perpendicular to the boundaries.

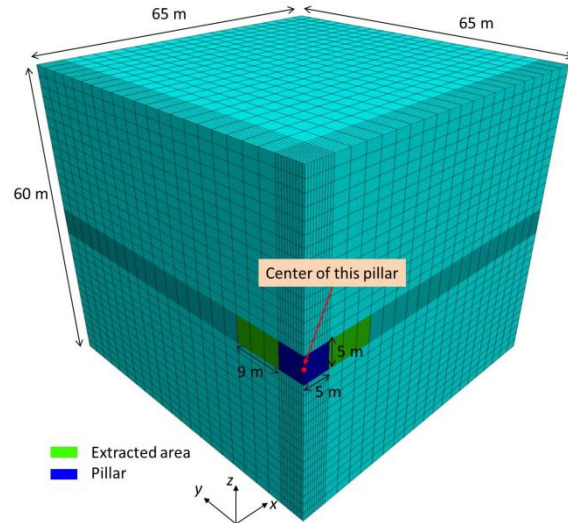


Figure 3: Numerical model analyzed.

2.4 Mechanical properties

Granite is assumed as the main type of rockmass composing the pillar. In order to convert mechanical properties obtained from laboratory experiments to those for the rockmass, RMR = 92 is assumed, which is the upper limit of rockmass encountered in the Canadian Shield (Martin, 2000). Herein, RMR is the rockmass rating system proposed by Bieniawski (1989). The mechanical properties of intact granite are derived from the study (Yun, 2008). Using the RMR, the deformation modulus, E , in Table 1 is obtained with the equation (Mitri et al., 1994). The uniaxial compressive strength is calculated with the Hoek-Brown failure criterion while substituting $\sigma_3 = 0$. The tensile strength is assumed to be one-tenth of the uniaxial compressive strength (Tesarik et al, 2003). For the constants in Equation (1), $n = 51$ and $m = 51$ are derived for granite (Okubo et al., 2006).

Table 1: Mechanical properties of granite for rockmass.

E (GPa)	ν	σ_c (MPa)	C (MPa)	ϕ (°)	σ_T (MPa)	Density (kg/m ³)
59	0.26	116	14.8	63	11.6	2600

2.5 Strength heterogeneity of rockmass

The inherent strength heterogeneity of rockmass is taken into account with the Weibull's distribution, which is expressed as:

$$f(u) = \frac{\alpha}{u_0} \left(\frac{u}{u_0}\right)^{\alpha-1} \exp\left[-\left(\frac{u}{u_0}\right)^\alpha\right] \quad (6)$$

where u and u_0 are a mechanical property and a scale parameter related to the average value of the mechanical property, respectively; α represents the degree of heterogeneity. In a base model, $\alpha = 5$ is

taken. Figure 4 shows the heterogeneity of UCS for the case.

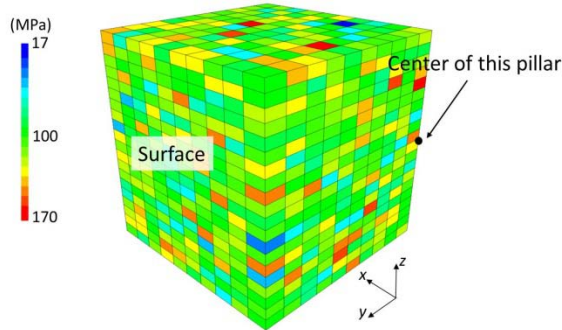


Figure 4: Heterogeneity of UCS simulated with the Weibull's distribution ($\alpha = 5$).

2.5 Determination of upper limit of λ^*

Although the rheological model assumes that λ^* increases infinitely, its upper limit needs to be determined to ensure computational stability. To do so, a uniaxial test is simulated with a cylindrical model under a constant strain rate. When the upper limit is low, the strain softening during post-peak behaviour is not sufficiently simulated. During the simulation, displacements are applied to the top boundary at the third step in Figure 2. Analyses are performed while changing the upper limit from 50 to 1000. It is then found that when the upper limit is 1000, brittle behaviour is adequately replicated. It should be noted, however, that when the brittle failure takes place, λ^* does not reach 1000 in all the zones because failure takes place locally. Thus, it is not appropriate to apply the upper limit to the pillar model, directly. In light of the result, the average value of λ^* in the cylindrical model at the failure is computed. The computed average is near 285. Thus, after rounding up, the upper limit is set to 300 for the pillar model.

3. RESULTS

3.1 Time-dependent skin degradation

Figure 5 shows change in the maximum compressive stress within the pillar with time. It is found from the figure that the pillar surface can carry stress immediately after the extraction. The low stress regions are limited to the zones with particularly low initial strength. There is no noticeable change in the stress state until 33 days after the extraction. However, when 72 days have passed, low stress regions extend to almost entire the surface, indicating that the rockmass near the surface lost load-bearing capacity due to the time-dependent degradation. After 187 days, the degradation of rockmass extends deeper into the pillar, and the pillar core carries extremely high stresses due to the stress transfer from

the failed regions. This indicates that the pillar becomes extremely burst-prone.

In order to investigate the burst proneness of the pillar, brittle shear ratio (BSR) proposed by Castro et al. (2012) and burst prone index (BPI) proposed by Mitri (1999) are computed at the center of the pillar. As can be seen from Figure 6, both of the indices do not show a noticeable increase until 72 days, whereas, after that, the indices increase exponentially, indicating that the failure propagation becomes uncontrolled. Eventually, after 226 days have passed, BPI and BSR increase to 222% and 1.33, respectively. As expected, both the values indicate extremely high possibility of a rockburst taking place.

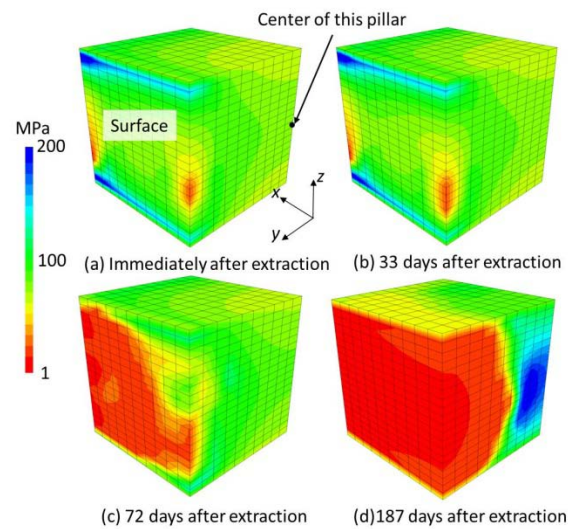


Figure 5: Maximum compressive stress in the pillar.

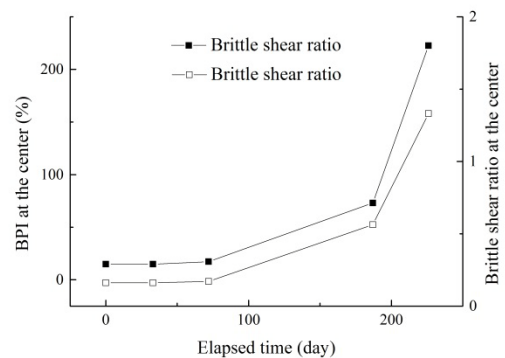


Figure 6: Burst proneness at the center of the pillar.

3.2 Comparison with strain-softening model

In order to make the difference between the non-linear rheological model and the conventional strain-softening model clearer, the comparison between the models is made. The strain-softening model employs the conventional Mohr-Coulomb criterion with the

consideration to strain-softening behaviour, that is, when failure takes place, the cohesion is decreased to zero. A static analysis is conducted with the same model as shown in Figure 4.

Figure 7 shows the maximum compressive stress obtained from the analysis. Remarkably, there is a clear difference in the stress state within the pillar between the models. When the strain-softening model is employed, the region with low stresses occurs only near the surface. The considerably high stresses at the pillar core shown in Figure 5(d) are not found in Figure 7, implying that the use of the conventional model might underestimate the possibility of failure when there is the heterogeneity of strength. Conversely, when the rockmass is completely homogeneous, there will be no large difference between the two models.

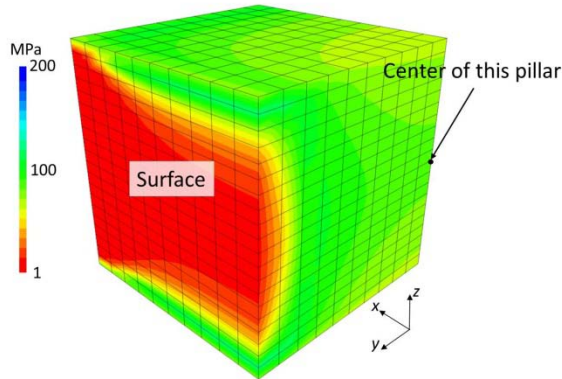


Figure 7: Maximum compressive stress obtained from strain-softening model.

3.3 Effect of degree of strength heterogeneity

In addition to the model shown in Figure 4, another model is constructed with $\alpha = 6$ in Equation (6). The model is shown in Figure 8. The larger α , the more homogeneous the model becomes. Except for the parameter, the same procedure is taken. Interestingly, the analysis reveals that the progressive skin degradation does not occur even after 7 years when $\alpha = 6$. It should be noted that, in terms of an average UCS in the pillar, there is no large difference between the two models. Indeed, the average UCS is 107 MPa and 108 MPa for the models with $\alpha = 5$ and 6, respectively. It is thus unlikely that the occurrence of the intensive degradation of rockmass shown in Figure 5 is determined by the slight difference in the average UCS.

In light of the results and with respect to each zone in the pillar, the minimum UCS in adjacent zones is investigated. Figure 8 shows the results. For instance, when $\alpha = 5$, the number of zones that have adjacent zones with UCS between 30 MPa and 50 MPa is approximately 240. The figure obviously displays the difference between the two models.

When α is low, the possibility that zones with low UCS are present in the vicinity of each zone is clearly higher. From the figure, it can be deduced that the intensive skin degradation shown in Figure 5(d) occurs due to the chain effect of failure through zones with low UCS, i.e., stress transferred from a failed zone causes failure in adjacent zones, which eventually escalates into the chain effect. Zones with extremely low UCS exist even when $\alpha = 6$. However, in order for the failure to propagate to adjacent zones, zones with low UCS must exist in the vicinity of the failed zone. When $\alpha = 5$, it is assumed that the conditions are satisfied, so that the failure becomes uncontrolled after sufficient time has elapsed. Importantly, the chain effect cannot be adequately simulated with the strain-softening model as shown in Figure 7 because the non-linear rheological model simulates strength degradation with tertiary creep even if the maximum stress is less than the maximum strength.

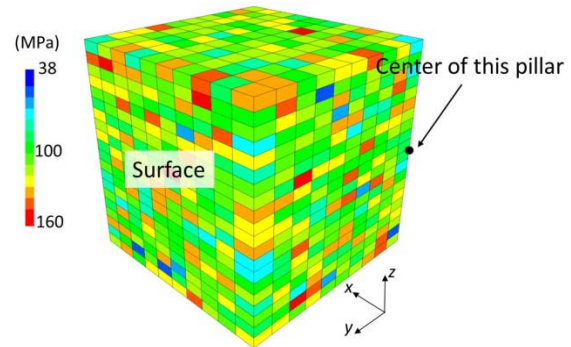


Figure 8: Heterogeneity of UCS simulated with the Weibull's distribution ($\alpha = 6$).

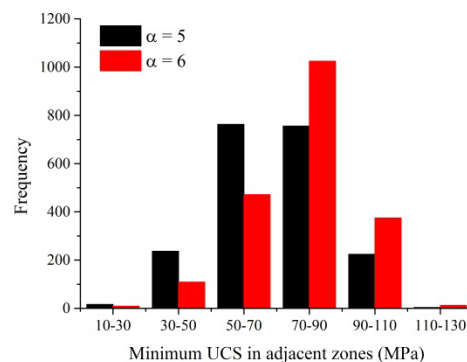


Figure 9: Relation between minimum UCS of adjacent zones and the total number of zones with the adjacent zones within the pillar.

4. CONCLUSIONS

The time-dependent skin degradation of an isolated pillar in a deep hard rock mine is simulated with a non-linear rheological model whilst taking into

account the inherent strength heterogeneity of the rockmass. Analysis results show that the skin degradation extends deep into the pillar when sufficient time has elapsed, resulting in a highly stressed pillar core due to the stress transfer from the failed region. Rockburst potential indices calculated at the core show extremely high risk for rockburst. The analysis conducted with the conventional strain-softening model demonstrates that the propagation of skin degradation into the inside of the pillar cannot be replicated with the strain-softening model, emphasizing the importance of the time-dependent skin degradation. The propagation of failure into the inside of the pillar is not simulated in the model with lesser strength heterogeneity, although an average UCS within the pillar is almost the same for the two models. It is then deduced that the presence of adjacent zones with low UCS is a key to the progressive skin failure because it gives rise to the chain effect of failure with stress transfer from the failed zone to the adjacent zones.

5. ACKNOWLEDGEMENT

This work is financially supported by a grant by the Natural Science and Engineering Research Council of Canada (NSERC) in partnership with Vale Ltd – Sudbury Operations, Canada, under the Collaborative Research and Development Program. The authors are grateful for their support.

6. REFERENCES

Barla, G., Debernardi, D., & Sterpi, D. (2012). Time-dependent modeling of tunnels in squeezing conditions. *International Journal of Geomechanics*, Volume 12(6), pp. 697-710

Bieniawski, Z. T. (1989). *Engineering rock mass classifications*. Wiley, New York

Castro, L.A.M., Bewick, R.P., & Carter, T.G. (2012). An overview of numerical modelling applied to deep mining. *Innovative Numerical Modelling in Geomechanics*, pp. 393-414.

Cording, E.J., Hashash, Y.M.A., & Oh, J. (2015). Analysis of pillar stability of mined gas storage caverns in shale formations. *Engineering Geology*, Volume 184, pp. 71-80

Diederichs, M.S. (1999). *Instability of hard rockmass: the role of tensile damage and relaxation* (PhD), University of Waterloo, Waterloo, Canada.

Itasca. (2009). *FLAC3D - fast Lagrangian analysis of continua* (Version 4.0). U.S.A.: Itasca Consulting Group Inc. .

Martin, C.C., & Maybee, W.G. (2000). The strength of hard-rock pillars. *International Journal of Rock Mechanics and Mining Science*, 37, 1239-1246.

Mitri, H.S., Edrissi, R., & Henning, J. (1994). Finite element modelling of cable-bolted stopes in hardrock ground mines. Paper presented at the SME Annual Meeting, Albuquerque, New Mexico.

Mitri, H.S., Tang, B., & Simon, R. (1999). FE modelling of mining-induced energy release and storage rates. *Journal South African Institute of Mining and Metallurgy*, 99(2), 103-110.

Napier, J.A.L., & Malan, D.F. (2012). Simulation of time-dependent crush pillar behaviour in tabular platinum mines. *The Journal of The South African Institute of Mining and Metallurgy*, 112, 711-719.

Okubo, S., & Fukui, K. (2006). An analytical investigation of a variable-compliance-type constitutive equation. *Rock Mech. Rock Eng.*, 39(3), 233-253.

Okubo, S., & Jin, F. (1993). Simulation of rock behaviour around circular roadway by non-linear rheological model. *Journal of the Mining and Materials Processing Institution of Japan*, 109, 209-214.

Potvin, Y., Hudyma, M.R., & Miller, H.D.S. (1989). Design guidelines for open stope support. Paper presented at the Bull Can Min Metall.

Scholz, C.H. (1968). Mechanism of creep in brittle rock. *Journal of Geophysical Research*, 73(10), 3295-3302.

Sjöberg, J. (1992). Failure modes and pillar behaviour in the Zinkgruvan mine. Paper presented at the 33rd U.S. Rock Mechanics Symposium, Sante Fe. Rotterdam.

Tesarik, D.R., Seymour, J.B., & Yanske, T.R. (2003). Post-failure behaviour of two mine pillars confined with backfill. *International Journal of Rock Mechanics and Mining Science*, 40(2), 221.

Van der Merwe, J.N. (2003). New pillar strength formula for South African Coal. *The Journal of The South African Institute of Mining and Metallurgy*, 103(5), 281-292.

Weibull, W.A. (1951). Statistical distribution function of wide applicability. *Journal of applied mechanics*, 18, 293-297.

Yun, Xiaoyou. (2008). *Geomechanical behaviour of biaxially loaded rock*. (PhD), McGill University, Montreal, Canada.

Quantitative analysis of haulage system instability in deep hard rock mines using numerical modelling

Shahé Shnorhokian ^{a,*}, Bryce MacNeil ^a, Hani Mitri ^a

^a Department of Mining and Materials Engineering, McGill University, Montreal (QC), Canada, H3A 0E8

ABSTRACT

Haulage drifts and related infrastructure are crucial to the success of underground mining operations. In the sublevel stoping mining method, they are developed well before any extraction commences in a given section of the orebody. One of the more complex design parameters is the relative distance of a haulage drift from the orebody as it runs parallel to its strike. Opposing considerations from operational and ground control teams need to be balanced, with the former preferring a shorter distance for increased productivity and the latter requesting a further distance for safety and stability. Numerical codes are one of the analytical tools used frequently in making these decisions by providing mining-induced stress and displacement magnitudes using a properly calibrated model. In this study, a simplified model is constructed of a typical tabular orebody within the geological settings of the Canadian Shield, striking East-West and dipping steeply to the south. Three other formations with the same strike and dip are added to the model, along with two intrusive dykes at variable distances from the orebody and the drift. The rockmass properties for all formations are obtained from a previous work on a case study mine in the Canadian Shield, and the model is calibrated based on in-situ stress measurements there. Two stope sequences comprising two simultaneous mining fronts are implemented and analyzed for the orebody; a diminishing pillar one that moves from both east and west to the middle, and a center-out option that moves from its center to the sides. In both cases, 24 mine-and-backfill stages – comprising 6 stopes each – are needed to completely extract the orebody. A quantitative assessment of instability around the drifts, crosscuts, and stopes is conducted at each stage for a level at a depth of 1490 m. Two instability parameters – the brittle shear ratio (BSR) and a low compressive-tensile stress state – are combined with volumetric analysis to obtain the quantity of potentially unstable rockmass. The relative proximity of the drift and stopes to the dykes is evaluated and observed to have an impact on the results. A combined numerical-volumetric approach is found to provide a useful tool for comparing different sequences and obtaining information on the type, location, volume, and timing of rockmass instability.

KEYWORDS: drift instability; modelling; stope sequence; brittle shear ratio; low compressive-tensile stress

1. INTRODUCTION

Haulage drifts, crosscuts, and the intersections they form constitute a vital component of operations in underground hard rock mines. They are especially crucial for certain mining methods such as sublevel open stoping where considerable resources need to be allocated at the onset of operations to develop them (Hamrin, 1998; Bullock, 2011). Hence, it is crucial that they remain stable for an extended period of time while mining is conducted in a certain area. The distance of the haulage drift from the stopes requires an informed and experienced decision able to satisfy two opposing requirements. On one hand, it needs to be as close to the orebody as possible to optimize ore haulage activities. On the other hand, it needs to be far enough from the stopes so as not to be influenced by stress redistributions resulting from ore extraction. The literature is rich with studies that have examined drift stability using a number of techniques such as instrumentation and monitoring (Kendorski, 1993;

Kaiser et al., 2001; Diederichs et al., 2004), and numerical approaches (Martin et al., 1999; Zhang and Mitri, 2008; Cai and Kaiser, 2014). Empirical methods used for drift stability and support design constitute the basis of several rockmass classification schemes (Bieniawski, 1989; Grimstad and Barton, 1993; Hoek et al., 2002). Kaiser et al. (2000) provide an extensive summary of the different approaches available for drift stability analysis. One of the fundamental concerns in deep hard rock mines is the occurrence of rockbursts that pose safety concerns to personnel and cause severe damage to the network of drifts and crosscuts. A number of recommendations on different mitigation and support measures have been presented over the years (Gay et al., 1995; Kaiser et al., 1996; Cai, 2013).

Numerical modelling provides a useful analytical tool for determining design parameters such as the optimum distance of the drift from the stopes while satisfying the criteria mentioned above. In addition to

*Corresponding author – email : shaheshnorhokian@mail.mcgill.ca

calculating induced stresses and displacements, it can compare the merits of several stope sequences based on the location and relative timing of any potential instability. Starting with the geometry and rockmass properties of the formations, an instability criterion can be combined with simple volumetric analysis for a quantitative assessment of stope extraction options.

In this study, a conceptual model is constructed with the finite difference code FLAC^{3D} (Itasca, 2006) to represent a typical underground hard rock metal mine in the Canadian Shield. A combination of volumetric analysis and two instability indicators – the brittle shear ratio (BSR) and a low compressive-tensile stress state – are used to quantitatively assess potential ground control issues in drifts, crosscuts, and intersections for a level at a depth of 1490 m.

2. MODEL SETUP

The model is constructed in FLAC^{3D} to replicate typical geological conditions in the Canadian Shield, comprising several formations with east-west strikes and dips of approximately 80° to the south. A central greenstone formation hosts the orebody and typical igneous intrusions in the area are represented by two dykes trending WNW-ESE and running sub-parallel to the orebody. Based on its geometry and strike, the north dyke is at a further distance from the haulage drift in the western part of the mine. Inversely, the south dyke is closer to the orebody in the western part and moves away from it in the east. The variable proximity of the dykes to the drifts and orebody is used to examine their impact on mining-induced stresses and associated potential instability.

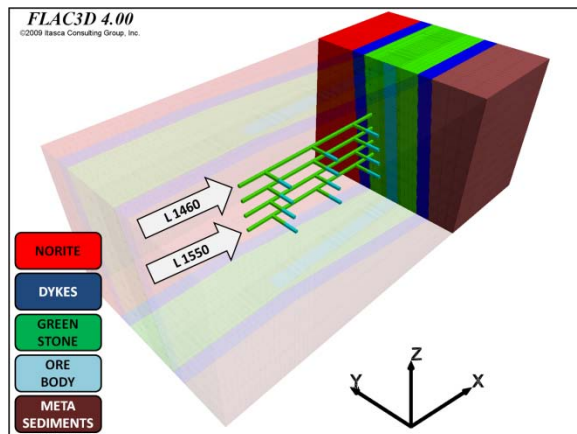


Figure 1: 3D view of numerical model with geological formations and drift-crosscut system on active levels.

The orebody is tabular in shape, and extends 360 m in the E-W direction with a thickness of 30 m in the N-S direction. Four active levels – L 1550, L 1520, L 1490, and L 1460 – are set up at depths between 1430 m to 1550 m (120 m in height), along

with extensions in all three axis directions to have the model boundaries far from any openings created by mining activities. Each level includes 32 stopes with individual L × W × H dimensions of 20 × 15 × 30 m for a volume of 9000 m³ per stope.

The final model dimensions are 840 m (E-W), 390 m (N-S), and 300 m in depth. A total of 862000 zones are generated with the mesh density increasing in the areas of study. Figure 1 presents the general layout of the mine and the geological formations.

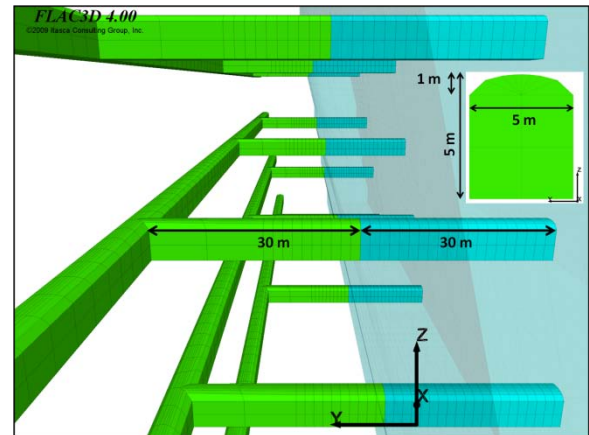


Figure 2: Close-up view of drift-crosscut system on L 1490.

Haulage drifts are constructed in the footwall of each of the four active levels at a constant distance of 30 m from – and parallel to – the orebody. From the drift, three perpendicular crosscuts 60 m in length are extended to the orebody, with the initial 30 m within the greenstone footwall and the remaining segment cutting into the stopes. These are 120 m apart along the strike and similar to the drifts, they measure 5 × 5 m in cross-section with an arch of 1 m at the center of the roof. A drift-crosscut intersection is presented in Figure 2 along with a typical cross-sectional view.

The input rockmass properties for the model are based on previous publications by the authors for a case study mine in the Canadian Shield (Shnorhokian et al 2015). They are presented in Table 1 for all the formations in this study.

Table 1: Input rockmass properties for numerical model.

Geological formation	Density (kg/m ³)	Bulk K (GPa)	Shear G (GPa)	UCS (MPa)
Norite	2919	31.1	22.3	190
Dyke	3001	46.3	29.1	224
Greenstone	2989	27.9	21.8	277
Ore	4531	125.6	18.5	91
Metasediments	2768	11.0	7.9	146
Backfill	2000	0.2	0.1	2

Pre-mining stresses in the model are generated using boundary tractions, a method first developed by

McKinnon (2001) for a homogeneous rockmass, which was expanded subsequently for heterogeneous cases (Shnorhokian et al., 2014). Model calibration is conducted by comparing magnitudes of pre-mining stresses in the north dyke and norite formations with readings at comparable depth in the Canadian Shield.

3. STOPE SEQUENCE ALTERNATIVES

After pre-mining stress calibration is conducted, haulage drift-crosscut networks on all active levels are excavated simultaneously. Two stope sequences are then implemented between L 1550 and L 1430, comprising two simultaneous mining fronts. In the first one, operations commence from the eastern and western sides of the orebody and move towards the center and this is called the diminishing pillar option. In the second sequence, ore extraction starts from the middle and moves towards the sides and this is called the center-out approach. In both sequences, 6 stopes are extracted and backfilled per stage for a total of 24 stages to mine the orebody on all the active levels.

4. INSTABILITY CRITERIA

In order to examine potential instability around the drifts and crosscuts, two criteria are used from the literature related to failure mechanisms and mining-induced seismicity generation (McCreary et al., 1993; Trifu and Shumila, 2002). The brittle shear ratio (BSR) was developed by several authors (Castro et al., 1997; Martin et al., 1999) as an indicator for potential strainbursts. It compares the differential stress ($\sigma_1 - \sigma_3$) around an opening to the unconfined compressive strength (UCS) of intact rock. A ratio above 0.7 is indicative of major strainburst and damage potential (Castro et al., 2012). A second criterion used is the low compressive-tensile stress state (Diederichs and Kaiser, 1999; Diederichs, 2003), and values below 0.5 MPa are considered to represent rockmass failure for this study. The analysis focuses on a single active level – from L 1490 to L 1460 – for a quantitative comparison of the instability criteria for all 24 stages.

5. RESULTS AND DISCUSSIONS

5.1 Brittle shear ratio (BSR)

Table 2 presents the volume of rockmass above BSR 0.7 for the central formations between L 1490 and L 1460 in the diminishing pillar and center-out sequences. It also provides the volume of mined-and-backfilled stopes between these levels at Stages 4, 8, 12, 16, and 20, with all the ore having been extracted at Stage 24.

From the results, it can be observed that only the orebody exhibits BSR values above the 0.7 threshold.

Figure 3 presents the locations of potentially unstable rockmass at Stage 8 in the diminishing pillar option, and they are seen to coincide with the two advancing mining fronts. While its rockmass properties indicate that the orebody is stiff, its relatively low UCS value also contributes to elevated BSR readings. Similarly, regions of unstable rockmass are confined to mining fronts in the center-out sequence, advancing from the center to the sides.

Table 2a: Diminishing pillar: volume (m³) > BSR 0.7.

Geology	Drift	Stage 4	Stage 8	Stage 12	Stage 16	Stage 20
GS	0	0	0	0	0	0
Dyke	0	0	0	0	0	0
Ore	0	1875	11305	10397	18206	20323

Table 2b: Center-out: volume (m³) > BSR 0.7.

Geology	Drift	Stage 4	Stage 8	Stage 12	Stage 16	Stage 20
GS	0	0	0	0	0	0
Dyke	0	0	0	0	0	0
Ore	0	2268	13988	15634	21608	15259

Table 2c: Volume of total ore mined at each stage ('000 m³).

Geology	Stage 4	Stage 8	Stage 12	Stage 16	Stage 20	Stage 24
Ore	324	270	216	162	54	0
Backfill	0	54	108	162	270	324
Total	324	324	324	324	324	324

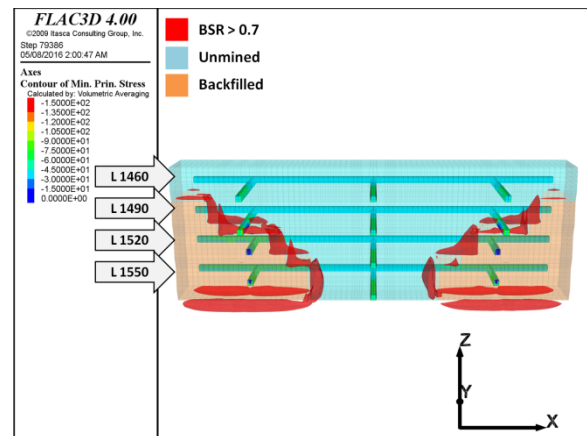


Figure 3: Stage 8 – diminishing pillar: BSR > 0.7.

While volumes of rockmass above a BSR of 0.7 indicate zones of potential mining-induced seismicity for the mining operation, the only development segments adjacent to them are those crosscuts that extend into the stopes. As the mining fronts advance, the eastern and western crosscuts on L 1490 are engulfed with potentially unstable rockmass at Stage 8 in the diminishing pillar sequence and at Stage 12 in the center-out one as shown in Figure 4.

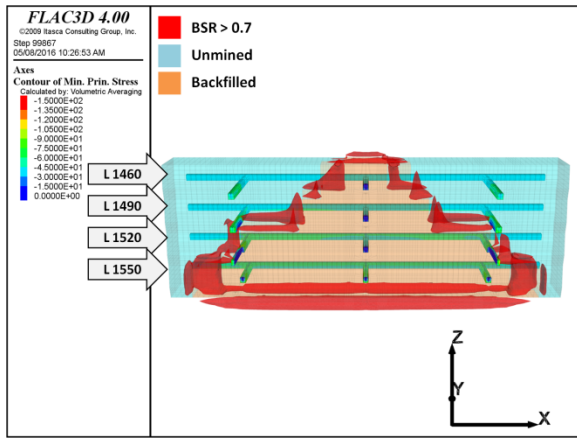


Figure 4: Stage 12 – center-out: BSR > 0.7.

When mining is confined to L 1550 and L 1520 in the initial stages, a relatively small volume of BSR instability ($\sim 1875 \text{ m}^3$) is detected on the study level between L 1490 and L 1460 in the diminishing pillar sequence. This value increases to almost 11300 m^3 at Stage 8 as the mining front reaches L 1490 and remains within the same range at Stage 12 ($\sim 10400 \text{ m}^3$). In the center-out option, larger volumes of unstable rockmass with elevated BSR conditions persist at all times except towards the end at Stage 20. In both mining sequences, regions of instability always coincide with the locations of the mining fronts. Hence, the center-out option exhibits more unstable rockmass at the onset of mining when the fronts are close to each other in the middle of the orebody, and registers a significant drop at Stage 20 when they have moved to its sides. In a reverse trend, the diminishing pillar sequence shows a slightly lower volume of unstable rockmass at the onset when the mining fronts are at the sides, and the volume of instability increases to a maximum at Stage 20 when the mining fronts form a pillar of minimum width in the center.

The expected effect of unstable rockmass with elevated BSR values is an increase in mining-induced seismicity. There is a general potential for rockbursts in the crosscuts at all times but a more specific risk of potential failure appears once the zone of influence of unstable rockmass reaches the excavation (Figures 3 and 4).

5.2 Low compressive and tensile stress

Table 3 presents the volumes of potentially unstable rockmass under low compressive and tensile stress conditions. When compared to the previous one, the extent is observed to be more widespread. The volumes of unstable rockmass in the orebody are comparable to the ones with the BSR criterion, and fluctuate with mining operations until Stage 24. The

difference is that the volumes with a potential low compression or tensile stress instability mechanism extend to the greenstone unit that forms the footwall and immediate hanging wall on either side of the orebody. Hence, they are no longer restricted to the mining fronts only as can be observed in Figure 5. In addition, the unstable rockmass volumes within the greenstone formation continuously rise with each mining stage until the end.

Table 3a: Diminishing pillar: volume (m^3) of $\sigma_3 < 0.5 \text{ MPa}$.

Geology	Stage 4	Stage 8	Stage 12	Stage 16	Stage 20	Stage 24
GS	0	3987	13614	19493	32484	16629
Dyke	0	0	0	0	0	0
Ore	1369	13127	6299	11055	11020	0

Table 3b: Center-out: volume (m^3) of $\sigma_3 < 0.5 \text{ MPa}$.

Geology	Stage 4	Stage 8	Stage 12	Stage 16	Stage 20	Stage 24
GS	0	5349	14738	17289	23099	16551
Dyke	0	0	0	0	0	0
Ore	2392	11254	5716	12262	9919	0

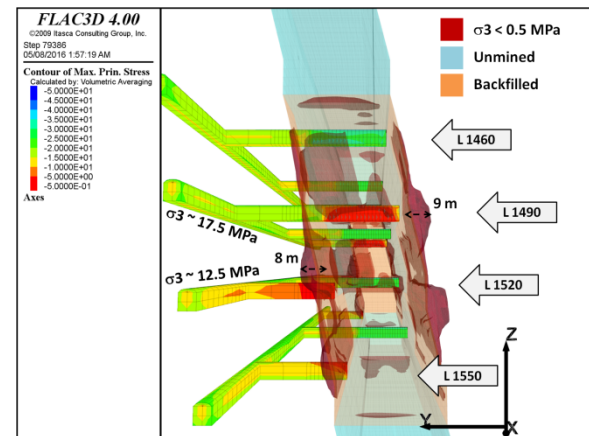


Figure 5: Stage 8 – diminishing pillar: $\sigma_3 < 0.5 \text{ MPa}$.

In the hanging wall, these regions constitute potential volumes of unplanned dilution that could move into the stope once it is mined out. In the footwall, unplanned dilution is still a possibility at the top of the study level near L 1460. However, sections near the bottom that are close to crosscuts represent potential instability and fall-of-ground, especially in the roofs. It is not only the temporary section of a crosscut within a given stope that is at potential risk, as was the case with the BSR criterion. Rather, the remaining section within the greenstone footwall is also affected by the volume of unstable rockmass. The western crosscut on L 1490 is shown in Figure 6 with an outline of rockmass under low compressive and tensile stress above it. Important quantitative parameters such as the volume of potential failure, its

location in the roof of the crosscut, and distance from the orebody can be calculated easily based on this analysis, as shown in Figure 5 and 6. Similarly, the extent of potential unplanned dilution that may affect the hanging wall on the level below is seen in the same figures.

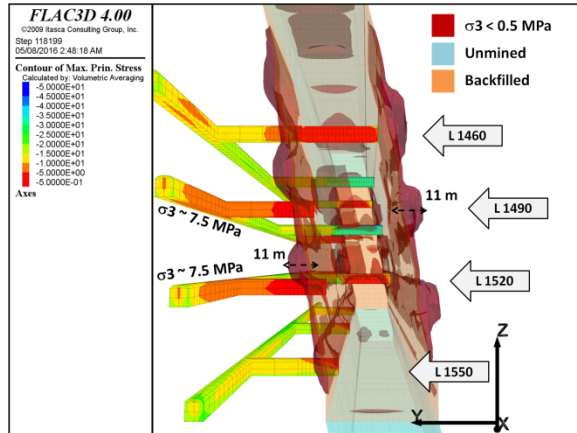


Figure 6: Stage 16 – diminishing pillar: $\sigma_3 < 0.5$ MPa.

One of the advantages of a quantitative analysis is that volumes of unstable rockmass in different locations can be assessed regarding their impact on mining operations. The volume in the greenstone unit can be subdivided into its footwall and hanging wall components with the latter representing between 43 and 48% of the total unstable rockmass during all mining stages in the diminishing pillar sequence (Table 4a). Thus, it quantifies the unplanned ore dilution that can potentially be expected from the hanging wall. It follows that between 52 and 57% of the unstable rockmass is located in the footwall, and these volumes can act as sources of potential dilution and crosscut instability.

Table 4a: Diminishing pillar: volume (m^3) of $\sigma_3 < 0.5$ MPa.

Geology	Stage 4	Stage 8	Stage 12	Stage 16	Stage 20	Stage 24
GS	0	3987	13614	19493	32484	16629
HW	0	1906	5908	8797	14092	5514
FW	0	2081	7706	10696	18392	11114

Table 4b: Center-out: volume (m^3) of $\sigma_3 < 0.5$ MPa.

Geology	Stage 4	Stage 8	Stage 12	Stage 16	Stage 20	Stage 24
GS	0	5349	14738	17289	23099	16551
HW	0	2393	5625	7323	7921	6864
FW	0	2957	9114	9965	15178	9687

Table 4b presents the same data for the center-out sequence and a simple comparison between the two indicates important trends. In terms of hanging wall instability, the volumes are consistently smaller

in the center-out option from Stage 12 onward but higher at Stage 8. The footwall side shows smaller volumes for this sequence from Stage 16 onward but higher numbers before. This phenomenon has a valid explanation related to the location of mining fronts. In the diminishing pillar approach, mining proceeds from the sides to the center and instability increases in volume as the pillar develops there. In the center-out option, operations commence from the center and the largest volumes of instability can be observed at the beginning (Stages 8 and 12) when both mining fronts are in close proximity in the center.

Another trend observed is the relative volumes of unstable rockmass in the greenstone formation once mining operations end. While the total numbers are comparable, the diminishing pillar option ends with a much more voluminous instability in the footwall (67%) than in the hanging wall (33%). Although the footwall has a higher volume of unstable rockmass in the center-out option as well at 59%, compared to the 41% in the hanging wall, the distribution is a more balanced one.

6. CONCLUSIONS

A conceptual model is constructed in FLAC^{3D} for a typical tabular, steeply dipping orebody in the Canadian Shield that uses the sublevel open stope method. A series of drifts and crosscuts are replicated on four active levels and two stope sequences with two simultaneous mining fronts are implemented. In the first case, ore extraction moves from the sides to the center while the reverse takes place in the second one. The brittle shear ratio and low compressive-tensile stress state are used as instability criteria, and are coupled with volumetric analysis for quantitative comparisons. It is observed that in both sequences, the potential BSR instability zones are restricted to the orebody and mining fronts. However, zones under low compressive and tensile stress conditions can be found in the greenstone footwall and hanging wall, in addition to the stopes, and pose a risk to crosscuts. Their relative distribution between the footwall and hanging wall is observed to be a more balanced one in the center-out option than in the diminishing pillar sequence.

7. REFERENCES

- Bieniawski, Z.T. (1989). Engineering rock mass classifications: a complete manual for engineers and geologists in mining, civil, and petroleum engineering. Wiley-Interscience, New York, 272 p.
- Bullock, R.L. (2011). Comparison of underground mining methods. In: SME Mining Engineering Handbook, Darling P. (ed.), SME, pp. 385-403.

- Cai, M. (2013). Principles of rock support in burst-prone ground. *Tunnelling and Underground Space Technology*, Volume 36, pp. 46-56.
- Cai, M. and Kaiser, P.K. (2014). In-situ rock spalling strength near excavation boundaries. *Rock Mechanics and Rock Engineering*, Volume 47, pp. 659-675.
- Castro, L.A.M., Grabinsky, M.W., McCreath, D.R. (1997). Damage initiation through extension fracturing in a moderately jointed brittle shear rock mass. *International Journal of Rock Mechanics and Mining Sciences*, Volume 34, No. 3-4, pp.110e.1-110.e13.
- Castro L.A.M., Bewick R.P., and Carter T.G. (2012). An overview of numerical modelling applied to deep mining. In: *Innovative numerical modelling in geomechanics*, Azevedo R. (ed.), CRC Press – Taylor & Francis Group, pp. 393-414.
- Diederichs, M.S. (2003). Rock fracture and collapse under low confinement conditions. *Rock Mechanics and Rock Engineering*, Volume 36, No. 5, pp. 339-381.
- Diederichs, M.S. and Kaiser, P.K. (1999). Tensile strength and abutment relaxation as failure control mechanisms in underground excavations. *International Journal of Rock Mechanics and Mining Sciences*, Volume 36, pp. 69-96.
- Diederichs, M.S., Kaiser, P.K., and Eberhardt, E. (2004). Damage initiation and propagation in hard rock during tunneling and the influence of near-face stress rotation. *International Journal of Rock Mechanics and Mining Sciences*, Volume 41, pp. 785-812.
- Gay, N.C., Jager, A.J., Ryder, J.A., and Spottiswoode, S.M. (1995). Rock-engineering strategies to meet the safety and production needs of the South African mining industry in the 21st century. *Journal of the South African Institute of Mining and Metallurgy*, Volume 95, No. 3, pp. 115-136.
- Grimstad, E. and Barton, N. (1993). Updating the Q-System for NMT. In: *Proceedings of the International Symposium on Sprayed Concrete – Modern Use of Wet Mix Sprayed Concrete for Underground Support*, Kompen, Opsahl, and Berg (eds.), Norwegian Concrete Association, pp. 46-66.
- Hamrin, H. (1998). Choosing an underground mining method. In: *Techniques in Underground Mining*, Gertsch, R.E. and Bullock, R.I.(eds.), SME, pp. 45-85.
- Hoek, E., Caranza-Torres, C.T., Corcum, B. (2002). Hoek-Brown failure criterion – 2002 edition. In: *Proceedings of the North American Rock Mechanics Society (NARMS-TAC 2002)*, Bawden, H.R.W., Curran, J., and Telsenicki, M. (eds), pp. 267-273.
- Itasca (2006). Itasca Software Products – FLAC^{3D}. Itasca Consulting Group Inc., Minneapolis.
- Kaiser, P.K., Tannant, D.D., and McCreath, D.R. (1996). Drift support in burst-prone ground. *CIM Bulletin*, Volume 89, No. 998, pp. 131-138.
- Kaiser, P.K., Diederichs, M.S., Martin, D., Sharpe, J. and Steiner, W. (2000). Underground works in hard rock tunnelling and mining. In: *GeoEng2000*, Technomic Publishing Company, pp. 841-926.
- Kaiser, P.K., Yazici, S., and Maloney, S. (2001). Mining-induced stress change and consequences of stress path on excavation stability – a case study. *International Journal of Rock Mechanics and Mining Sciences*, Volume 38, No. 2, pp. 167-180.
- Kendorski, F.S. (1993). Some modes of deformation and failure of lined tunnels. *International Journal of Rock Mechanics and Mining Sciences Abstracts*, Volume 30, No. 7, pp.1497-1501.
- Martin, C.D., Kaiser, P.K., and McCreath, D.R. (1999). Hoek-Brown parameters for predicting the depth of brittle failure around tunnels. *Canadian Geotechnical Journal*, Volume 36, No. 1, pp. 136-151.
- McCreary, R.G., Grant, D., and Falamagne, V. (1993). Source mechanisms, three-dimensional boundary-element modelling, and underground observations at Ansil Mine. In: *Proceedings of the 3rd International Symposium on Rockburst and Seismicity in Mines*, Young, R.P. (ed.), pp. 227-232.
- McKinnon, S.D. (2001). Analysis of stress measurements using a numerical model methodology. *International Journal of Rock Mechanics and Mining Sciences*, Volume 38, pp. 699-709.
- Shnorhokian, S., Mitri, H.S., and Thibodeau, D. (2014). A methodology for calibrating numerical models with a heterogeneous rockmass. *International Journal of Rock Mechanics and Mining Sciences*, Volume 70, pp. 353-367.
- Shnorhokian, S., Mitri, H.S., and Moreau-Verlaan, L. (2015). Stability assessment of slope sequence scenarios in a diminishing ore pillar. *International Journal of Rock Mechanics and Mining Science*, Volume 74, pp. 103-118.
- Trifu, C.I. and Shumila, V. (2002). Reliability of seismic moment tensor inversions for induced microseismicity at Kidd Mine, Ontario. *Pure and Applied Geophysics*, Vol. 159, pp. 145-164.
- Zhang, Y. and Mitri, H.S. (2008). Elastoplastic stability analysis of mine haulage drift in the vicinity of mined stopes. *International Journal of Rock Mechanics and Mining Science*, Volume 45, pp. 574-593.

Minimum strength required for resisting cyclic softening/failure of cemented paste backfill at early age

Tikou Belem*, Mamert Mbonimpa

Research Institute in Mining and Environment (RIME), Université du Québec en Abitibi-Témiscamingue (UQAT), Rouyn-Noranda, Canada, J9X 5E4

ABSTRACT

This paper attempts to assess empirically the liquefaction susceptibility of cemented paste backfill (CPB) at early age (≤ 7 days). Early age CPB can be categorized as a “clay-like” material because their plasticity index, $PI \geq 5$ ($PI = Liquid\ Limit, LL - Plastic\ Limit, PL$). For clay-like material such as CPB, the liquefaction susceptibility can be characterized by the “cyclic softening” or “cyclic failure” which is assessed using an empirical method developed for clays and clay-like materials. This analysis allowed the determination of the minimum undrained shear strength required to resist cyclic softening (failure) of cemented paste backfills which is directly related to the unconfined compressive strength (UCS).

KEYWORDS: Mine tailings; cemented paste backfill, Binder; undrained shear strength; cyclic softening

1. INTRODUCTION

The mining industry generates significant socio-economic benefits, but also generates huge amounts of solid wastes such as mill tailings and waste rock. These solid wastes can generate environmental pollution due to their inadequate containment. Due to more stringent environmental regulations, cemented paste backfill (CPB) allow to return a large part of mill tailings (up to 50%) for underground open stopes filling, hence improving ground support and ore recovery (Potvin et al., 2005; Belem and Benzaazoua, 2008). CPB is a mixture of mill tailings with a binding agent and mixing water. The purpose of binder addition is to generate typical unconfined compressive strength (UCS) ranging from 500 kPa up to 4.5 MPa, depending on the type of backfill (slurry backfill, cemented rockfill, or cemented paste backfill).

CPB cost generally accounts for between 10% and 20% of the total operating cost of a mine from which hydraulic binder represents up to 75-80% of that cost (Grice, 1998). That is why mining companies seek to reduce the binder cost by reducing the amount of binder in the CPB mixtures. One of the promising options to reduce backfilling operation costs is a partial replacement of typical cement (i.e., general use Portland cement) by industrial by-products and or other supplementary cementitious materials (Belem and Benzaazoua, 2008). Unfortunately, a reduction in the amount of binder could lead to a substantial decrease in the mechanical properties of CPB, particularly at early age (from 0 to

7 days of curing). Such a reduction in the mechanical properties of CPB may trigger cyclic softening/failure at early age due to several sources (consecutive sequences of blasting, rock burst, seismic events, ground vibration, etc.). In common usage, liquefaction refers to the loss of strength in saturated, cohesionless material due to the build-up of pore water pressures during dynamic loading (Sladen et al., 1985).

The cyclic actions of an earthquake or blast detonation have the effect of increasing the potential for paste backfill softening, causing compression, which reduces the volume of voids by increasing pore water pressure as well. This implies a loss or a significant reduction of undrained shear strength due to pore pressure in the backfill, which means shear strain under constant volume. This is essentially due to rapid shaking, too short because the dissipation of pore pressure accumulated in the fluid may have started (Seed and Idriss, 1971).

The main objective of this paper is to assess empirically the cyclic softening (liquefaction susceptibility) of cemented paste backfill at early age (curing time ≤ 7 days) by providing preliminary results. The liquefaction susceptibility will be assessed through the “cyclic softening or failure” analysis (for clay-like materials such as CPB) based on empirical method. The specific aim is to verify experimentally whether the cost of binder can be reduced by lowering the CPB binder content while keeping sufficient undrained shear strength to resist cyclic softening. Hence, the empirical method should allow determining the minimum undrained shear

*Corresponding author – email : Tikou.Belem@UQAT.ca

strength related to the unconfined compressive strength (UCS) for resisting cyclic softening (or failure) of CPB.

2. SIMPLIFIED PROCEDURE FOR CYCLIC SOFTENING ASSESSMENT

2.1 Susceptibility to dynamic loading

For cohesive materials such as CPB, the cyclic action of an earthquake or blast detonation is deeply influenced by the number of cycles N of the earthquake, the relative density D_r (density index) and the grain size of the material. The response of soil to seismic loading varies with soil type and state (void ratio, effective confining stress, stress history, etc.). Seed et al. (2003) and Boulanger and Idriss (2005) distinguished between “sand-like” and “clay-like” behaviour. According to Seed et al. (2003), sand-like soils are susceptible to cyclic liquefaction when their behavior is characterized by Plasticity Index ($PI = LL - PL$) < 12 and Liquid Limit (LL) < 37 and natural water content (w_n) $> 0.8(LL)$. Clay-like soils are generally not susceptible to cyclic liquefaction when their behaviour is characterized by $PI > 12$ but they can experience “cyclic softening”. These criteria are generally conservative. Boulanger and Idriss (2005) suggested that sand-like behaviour is limited to $PI < 7$, while clay-like behavior can be expected for fine-grained soils that have $PI \geq 7$, although a slightly lower transition point for soils with a CL-ML classification (perhaps $PI \geq 5$ or 6) would be equally consistent with the available data. Based on this soil classification, CPBs can be categorized as clay-like materials. Also, it was observed in the literature that the plasticity index, PI of uncemented mine tailings from hard rock varies between 1 and 10.

2.2 Empirical assessment of cyclic softening

Most of the existing work on cyclic liquefaction has been primarily for earthquakes. Seed et al. (2003) developed a comprehensive methodology to estimate the potential for cyclic liquefaction due to earthquake loading, originally developed by Seed and Idriss (1971). The evaluation procedure used worldwide is termed the “simplified procedure” (U.S. National Center for Earthquake Engineering Research, NCEER, 1998) as described by Youd (2001), which uses generally conservative assumptions. The simplified approach to evaluate the triggering of seismic liquefaction involves comparing the Cyclic Stress Ratio (CSR_M) caused by the design earthquake of magnitude M_w with the Cyclic Resistance Ratio (CRR_M) of the soil pertaining to an earthquake of magnitude $M_w = 7.5$. A factor of safety against

liquefaction FS_{Liq} is defined as the ratio of $CRR_{M=7.5}$ to CSR_M :

$$FS_{Liq} = \frac{CRR_{M=7.5}}{CSR_{M=7.5}} = \frac{CRR_{\sigma=1, \alpha=0} K_\sigma K_\alpha}{CSR_M} MSF \quad (1)$$

where $CRR_{M=7.5}$ = cyclic resistance ratio pertaining to a magnitude 7.5 earthquake = $CRR_{\sigma=1, \alpha=0} = CRR$ for level ground conditions and an effective overburden stress (σ'_{v0}) of one atmosphere (≈ 100 kPa); K_σ = correction factor for the effects of σ'_{v0} on CRR ; K_α = correction factor for the effects of static initial shear stress on CRR ; α = static horizontal shear stress ratio ($\alpha = \tau_s/\sigma'_{v0}$); τ_s = static horizontal shear stress (kPa); MSF = Magnitude Scaling Factor (also called magnitude-correlated duration weighting DWF_M) for adjusting the induced CSR during earthquake of magnitude M_w to an equivalent CSR for an earthquake magnitude, $M_w = 7.5$. If $\alpha = 0$, i.e. $\tau_s = 0$ (no sloping), then $K_\alpha = 1$.

The recommended MSF by the NCEER Workshop in 1998 (Youd, 2001) is given as follows:

$$MSF = \frac{174}{M^{2.56}} \quad \text{Eq.(2)}$$

where M_w = moment magnitude of the earthquake. More recently, Idriss and Boulanger (2006) proposed an updated version given as follows:

$$MSF = 6.9 \exp\left(\frac{-M}{4}\right) - 0.058 \leq 1.8 \quad (3)$$

A simplified method to estimate CSR_M was also developed by Seed and Idriss (1971) based on the maximum (or peak) ground horizontal acceleration (PGA or a_{max}) at the site. The cyclic stress ratio proposed by Seed and Idriss (1971) is given as follows:

$$CSR_M = 0.65 \left(\frac{a_{max}}{g} \right) \left(\frac{\sigma_{v0}}{\sigma'_{v0}} \right) r_d \quad (4)$$

where a_{max} (= PGA) is in g ($1g = 9.81 \text{ m/s}^2$); σ_{v0} = total vertical stress (kPa) and σ'_{v0} = effective vertical stress (kPa) at depth z (m). The parameter r_d in Eq. 4 is a stress reduction coefficient that accounts for the flexibility of the soil column. Youd (2001) proposed the following relations suggested by the NCEER (1998):

$$\begin{cases} r_d = 1.174 - 0.0267z & 9.15\text{m} < z \leq 23\text{m} \\ r_d = 0.744 - 0.008z & 23.0\text{m} < z \leq 30\text{m} \end{cases} \quad (5)$$

For depth $z > 34$ m, Idriss (1999) also proposed the following relationship:

$$r_d = 0.12 \cdot \exp(0.22 \cdot M) \quad (6)$$

Because of the cohesive nature of clay-like materials, they tend to develop smaller pore pressures under undrained cyclic loading than sand-like materials. Therefore, clay-like materials do not reach zero effective stress with resulting large deformations under cyclic loading (not susceptible to cyclic liquefaction). However, when the cyclic stress ratio (CSR) is large relative to the undrained shear strength ratio (S_u/σ'_{vc} ; where S_u = undrained shear strength, σ'_{vc} = effective vertical confining stress) of clay-like materials, cyclic strain or softening can develop. However, post-earthquake volumetric strains tend to be small. Boulanger and Idriss (2005) used the term "cyclic failure" (instead of liquefaction) to describe this build-up of strain under cyclic loading in clay-like soils. Boulanger and Idriss (2004) showed that the CRR for cyclic failure in clay-like materials is controlled by the undrained shear strength ratio. These authors recommended the following relation for $CRR_{M=7.5}$ (for a moment magnitude 7.5 earthquake) of clay-like soils:

$$CRR_{M=7.5} = 0.80 \left(\frac{S_u}{\sigma'_{vc}} \right) K \quad (7a)$$

and

$$K_\alpha = 1.344 - \frac{0.344}{\left(1 - \frac{\tau_s}{S_u} \right)^{0.638}} \quad (7b)$$

where K_α was previously defined in Eq. (1); (τ_s/S_u) = ratio of static initial shear stress and undrained shear strength. Boulanger and Idriss (2004) also suggested that there is no need for overburden correction factor K_σ which is taken implicitly into account in the undrained shear strength ratio.

3. PROCEDURE FOR CYCLIC FAILURE ASSESSMENT OF CPB

Knowing that $S_u = UCS/2$ for saturated CPB sample and that the most common parameter in backfill engineering is UCS, equation 7 along with equations 1 – 6 can be combined in the following forms, for a given total vertical stress σ_{v0} ($= \gamma_{wet}z$) at a given depth:

$$FS_{Failure} = \left(\frac{0.8 \cdot UCS}{2} \right) \left(\frac{g}{a_{max}} \right) \frac{K_\alpha \cdot MSF}{(0.65 \cdot \sigma_{v0} \cdot r_d)}$$

$$= 0.6154 \left(\frac{g}{a_{max}} \right) \left(\frac{UCS \cdot K_\alpha}{\sigma_{v0} \cdot r_d} \right) MSF \quad (8)$$

where UCS = Unconfined Compressive Strength (kPa) of CPB; σ_{v0} = initial total vertical stress (kPa) at a given depth z (m); K_α = correction factor for static shear stress (always = 1 for vertical stopes but should be around 0.8-0.9 for sub-vertical stopes); a_{max} , r_d and MSF are previously defined.

Vibration amplitude in the CPB is weaker than that in the rock. The magnitude of vibration (or peak particle velocity PPV) recorded in CPB was in the range 25 – 65 mm/s (0.025 – 0.065 m/s). Signal frequencies are about 20 – 120 Hz (Liu, 2004). The PPV can be converted to peak ground horizontal acceleration (PGA or a_{max}) for sine waves using the following relation (e.g., Dowding, 1985):

$$a_{max} (g) = \frac{2\pi \cdot PPV (m \cdot s^{-1}) \cdot f (Hz)}{9.81 (m \cdot s^{-2})} \quad (9)$$

where PPV = peak particle velocity ($m \cdot s^{-1}$); f = frequency or number of oscillations per second (Hz); 9.81 m/s^2 correspond to 1g.

The calculated a_{max} corresponding to blasts ranged from 0.3g to 5.0g compared to a minimum a_{max} value of 0.1g necessary to trigger cyclic liquefaction of soils. These values may seem too high, but it is for a very short period of time (0.07 – 0.13 sec). For comparison, the range of frequency band for strong motion (usually causing structural damage during strong ground shaking of about 5 – 30 seconds) is ~0.05 Hz to ~10 Hz (Berkley Seismological Laboratory).

A blast vibration can be compared to a strong motion (1 – 10 Hz) through the calculation of kinetic energy E_k released [$E_k = Mass_{CPB} \cdot PPV^2 / (2 \cdot a_{max})$]. The calculated E_k is in the range $10^{-3} \cdot Mass_{CPB} - 4 \cdot 10^{-4} \cdot Mass_{CPB}$ for the observed magnitude of blast vibration PPV in the range of 25 – 65 mm/s (20 – 120 Hz). This corresponds to a range of equivalent moment magnitude M_w of 4.4 – 6.1 earthquakes with a maximum duration of 0.13 sec. The corresponding a_{max} will be in the range 0.009g to 0.08g. When considering that a real earthquake of magnitude 6 can last about 8 seconds compared to 0.13 seconds for the blast, a simple rule of three gives an equivalent actual energy released by the blast that should be (1/8)*(1.3/10) lower (approximately 62 times smaller than an actual earthquake).

From equation (8), the UCS values can be directly used, for the first time, to assess the cyclic failure (or softening) of CPB materials. Furthermore, equation (8) can be rearranged to provide the minimum compressive strength (UCS_{min}) required for resisting against cyclic failure or softening of CPBs due to strong motion. The minimum compressive strength ratio (UCS_{min}/σ_{v0}) is given as follows:

$$\frac{UCS_{min}}{\sigma_{v0}} = 1.625 \left(\frac{a_{max}}{g} \right) \left(\frac{r_d}{K_\alpha \cdot MSF} \right) FS_{min} \quad (10)$$

where FS_{min} = minimum factor or safety against cyclic failure of CPB (≥ 1.0); $\sigma_{v0} = \gamma_{wet} * z$ (total unit weight of CPB (kN/m^3) x depth of concern in a backfilled stope (m)).

If $FS_{min} = 1.0$, the Cyclic Resistance Ratio ($CRR_{M=7.5}$) is equal to the Cyclic Stress Ratio generated by a magnitude M_w earthquake (CSR_M/MSF). It is believed that this condition is not conservative enough to resist to cyclic failure triggering. Based on slope stability analysis principles, it may be recommended that the minimum factor of safety against cyclic failure should be $FS_{min} = 1.1$. Putting this value along with $K_\alpha = 1.0$ into equation (10) yields:

$$\frac{UCS_{min}}{\sigma_{v0}} = 1.7875 \left(\frac{a_{max}}{g} \frac{r_d}{MSF} \right) \quad (11)$$

Equation (11) shows that the minimum compressive strength ratio (UCS_{min}/σ_{v0}) depends on the stress reduction coefficient r_d (see equation 5) that accounts for the flexibility of the CPB Mass.

It should be noted that UCS_{min} or UCS_{min}/σ_{v0} can be represented as a function of backfilled standalone stope depth z (or the total or overburden stress σ_{v0}), the maximum or peak ground horizontal acceleration (a_{max} or PGA) or Magnitude M_w earthquake.

4. SAMPLE APPLICATION

4.1 Cemented paste backfill mixtures preparation

The backfill specimens were prepared using tailings sampled from Brunswick's mine (BM). The CPB batch of mixtures were prepared by adding progressively the appropriate mass of tailings, binder and mixing water to a Hobart mixer and mixed for about 10 minutes. The binder type used was the high sulphate resistant Portland cement HS. Four different CPB mix recipes were considered with five binder contents (= mass of binder/mass of CPB): 1, 1.5, 1.75 and 2% (corresponding to binder ratio $B_{w\%} =$ mass of binder/mass of dry tailings = 1.22, 1.84, 2.15 and

2.47 wt%, respectively). For all the mixtures the average solid mass concentration $C_{w\%}$ was about 83% which correspond to standard slump height ranging between 140 and 165 mm (5½ and 6½ inches). The CPB mixtures were poured into 76 mm diameter and 152 mm height capped plastic molds (3 in x 6 in) and left to cure in a humidity chamber at ambient temperature (25°C) and > 90% relative humidity. The strength development is assessed for undrained noted UD (non-perforated molds) and drained noted FD (perforated molds). The curing times were 3, 7, 28 and 56 days.

4.2 Unconfined compression tests

The cyclic failure potential will be assessed on saturated CPB specimens at early age (≤ 7 days) curing times, through the unconfined compression tests in order to determine the UCS values which corresponds two time the undrained shear strength ($UCS = 2 * S_u$), assuming Tresca criterion. The compression tests were performed using a MTS 10/GL universal hydraulic press of 50 kN loading capacity (compression rate of 1 mm/min).

5. RESULTS

5.1 UCS and S_u data

Figure 1 shows the relationship between binder content and UCS values. It can be observed that water drainage induces an increase in UCS due to self-weight consolidation. This figure can be used mainly to determine how the cement content can be reduced while maintaining the same strength performance of the CPB.

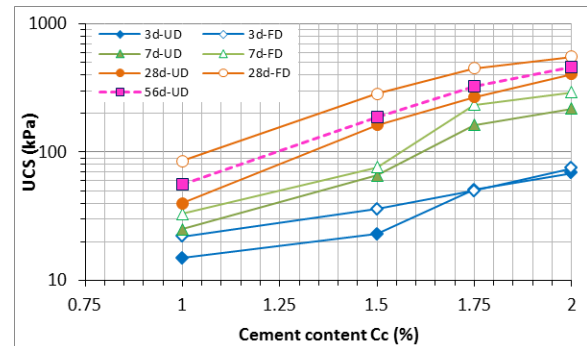


Figure 1: Relationship between binder content and UCS for drained and undrained CPB specimens

Table 1 contains the UCS data from Figure 1 and the corresponding calculated undrained shear strength S_u . The undrained strength S_u can be obtained directly from the UU triaxial test, direct simple shear (DSS) test, direct shear test (fast shear rate) or uniaxial compression test (saturated specimens). The simplest way is to calculate S_u from the UCS data (S_u

= UCS/2) assuming or ensuring that the CPB specimens are saturated (Belem and Benzaouza, 2008 showed that when the CPB specimens are unsaturated, $S_u \neq UCS/2$).

Table 1: UCS and corresponding undrained shear strength S_u values of the Brunswick’s Mine CPB

Binder (%)	Curing (day)	UCS (kPa)	$S_u = UCS/2$ (kPa)	Relative consistency
1	3	15	7.5	Very soft
1	7	25	12.5	Soft
1.5	3	23	11.5	Very soft
1.5	7	66	33	Medium
1.75	3	51	25.5	Medium
1.75	7	162	81	Stiff
2	3	69	34.5	Medium
2	7	218	109	Very stiff

5.2 Cyclic failure potential of CPB

For this evaluation, 30 m slope height is considered. As the CPB is assumed fully saturated, the water table level is supposed to be on top of any slope (depth $z = 0$ m). It is assumed that the minimum pore water pressure before any shaking is the hydrostatic pressure ($u_0 = \gamma_w * z = 9.81z$ kPa). Table 2 presents the total ($\sigma_{v0} = \gamma_{wet} * z$) and effective ($\sigma'_{v0} = [\gamma_{wet} - \gamma_w]z$) stresses calculated at backfilled stope depths of 15, 20 and 30 m (with tailings specific gravity of 4.03 and $C_{w\%} = 83\%$, the calculated $\gamma_{wet} = 26$ kN/m³).

Table 2: Total and effective vertical stresses

Depth z (m)	σ_{v0} (kPa)	u_0 (kPa)	σ'_{v0} (kPa)
15	390	147	243
20	520	196	324
30	780	294	486

Table 3 presents the results of calculated factor of safety against cyclic failure $FS_{Failure}$ with $a_{max} = 0.074g$ (earthquake moment magnitude $M_w = 6$), $MSF = 1.482$, $r_d = 0.458$, and $K_\alpha = 1$ (no sloping of the backfill mass).

Table 3: Calculated factor of safety against cyclic failure or deformation for BM’s CPB

binder (%)	Curing (day)	$S_u = UCS/2$ (kPa)	CSR (M=6)	CRR (M=7.5)	$FS_{Failure}$ (M=6)
1	3	7.5	0.024	0.0124	0.52
1	7	12.5	0.024	0.0206	0.86
1.5	3	11.5	0.024	0.0189	0.79
1.5	7	33	0.024	0.0544	2.28
1.75	3	25.5	0.024	0.0420	1.76
1.75	7	81	0.024	0.1334	5.59
2	3	34.5	0.024	0.0568	2.38
2	7	109	0.024	0.1795	7.52

If $FS_{Failure} > 1.0$, the CPB will not fail cyclically; if $FS_{Failure} \leq 1$, the CPB is likely to undergo cyclic failure. From Table 3 it is clear that the CPB prepared with only 1% of binder ($B_{w\%} = 1.22\%$) will probably undergo cyclic failure or large softening ($FS_{Failure} < 1.0$). The same observation is made for CPB with 1.5% of binder ($B_{w\%} = 1.84\%$) cured after 3 days only. Nevertheless, after 7 days of curing this CPB develops sufficient undrained shear strength to resist cyclic failure. Therefore, Table 3 suggests that the recommendable minimum binder proportion for the CPB to resist cyclic failure is 1.75% ($B_{w\%} = 2.15\%$). The binder proportion can however be lowered to 1.5% ($B_{w\%} = 1.84\%$) if the minimum allowed curing time is 7 days, but this is not safe.

Figure 2 shows the relationship between UCS_{min}/σ_{v0} required to resist cyclic failure as a function of backfilled stope depth z and for FS_{min} of 1.0 (critical case) and 1.1. These curves can be considered as “cyclic softening or failure curves” and are compared to the actual UCS data of the prepared cemented paste backfill. The shape of these curves is dictated by the stress reduction factor r_d .

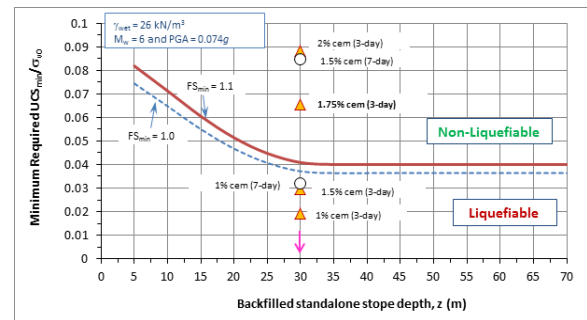


Figure 2: Relationship between UCS_{min}/σ_{v0} required for resisting cyclic failure as a function of stope depth z

6. DISCUSSION

The minimum compressive strength UCS_{min} required for resisting against cyclic failure of CPB specimens in this study at the bottom of 30 m height stope ($\sigma_{v0} = 780$ kPa) is 32 kPa only, for a moment magnitude $M_w = 6$ earthquake ($a_{max} = 0.074g$). The Japanese Port and Harbour Research Institute (1996) have observed similar low values for cemented sands. Their test results showed that when UCS was in the range 49 – 98 kPa, the cemented sand could not undergo liquefaction. Based on shaking table tests ($a_{max} = 0.25g$), they also found that by adding 1% (by dry mass of sand) of cement and after 7 days of curing the cemented sand (with an average UCS of 29 kPa) didn’t liquefied. It was concluded that the percent of cement addition required for treatment to produce a material that will not undergo liquefaction differs according to the soil type. It should be noted

that there are very few studies on the evaluation of liquefaction potential of cemented paste backfill (Blight, 1990; Belem et al., 2013). Blight (1990) suggests that, even very severe lateral accelerations (up to 10g!), will induce only moderate shear stresses (about 100 kPa) in the backfill contained in a narrow, tabular stope. Since then, it is customary to assume that a CPB having a UCS of about 100 kPa will never undergo liquefaction.

7. CONCLUSION

This paper presents the evaluation of the possibility to lower CPB binder content used for stope filling without causing liquefaction (or “cyclic failure”). The cyclic failure or softening (equivalent to liquefaction for clay-like materials such as CPB) was assessed based on empirical method proposed by leading world experts on liquefaction, namely Boulanger and Idriss (2005). This method is based on comparing the Cyclic Resistance Ratio of a soil subjected to shaking by an earthquake of $M_w = 7.5$ ($CRR_{M=7.5}$) to the Cyclic Stress Ratio imposed to the soil by a shaking due to an earthquake of M_w (CSR_M). A Magnitude Scaling Factor (MSF) is used for the calculation of the Factor of Safety against the cyclic failure $FS_{Failure}$ which must be higher than 1.0 to resist cyclic failure or softening. Sample application of this method shows that CPBs prepared with 1% of cement (at 3 and 7 days of curing) and 1.5% of cement at 3 days of curing will undergo cyclic failure or softening for an earthquake of magnitude $M_w = 6$ ($a_{max} = 0.074g$).

Based on the Boulanger and Idriss (2005) empirical model, a procedure using the UCS values is proposed for the assessment of cyclic failure of CPB in general. For the first time it is possible to connect the cyclic failure (softening) potential with the minimum required strength value (UCS_{min}) and the height of the backfilled stope. However, further study is needed for validating and refining the proposed method by performing cyclic direct simple shear (DSS) testing or direct shear test at fast shear rate on different CPB mixture recipes at early ages.

8. ACKNOWLEDGEMENT

This research was financially supported by NSERC discovery grant. The authors would like to acknowledge their helpful support.

9. REFERENCES

Belem T., Effenguet H., Mbonimpa M. (2013). Estimation of required minimum binder content by assessing the liquefaction potential of early age cemented mine backfill. Proc. of 66th Canadian Geotechnical Conference, Montreal, Quebec, Canada, September 29 - October 3, 2013, 8p.

Belem, T. and Benzaazoua, M. (2008). Underground mine paste backfill technology: applications and design methods. Geotechnical and Geological Engineering. Vol. 26(2): 147-174.

Blight, G.E. (1990). The effect of dynamic loading on underground fill in South African gold mines. Victor de Mello tribute volume. Editorial Edgar Bluicher, Sao Paulo, Brasil, pp. 37-44.

Boulanger, R. W., and Idriss, I. M. (2005). New criteria for distinguishing between silts and clays that are susceptible to liquefaction versus cyclic failure. Proc., Technologies to Enhance Dam Safety and the Environment, 25th Annual United States Society on Dams Conf., USSD, Denver, 357-366.

Grice T. (1998). Underground mining with backfill. Proceedings of the 2nd Annual Summit on Mine Tailings Disposal Systems, 1998, Brisbane, 14 p.

Idriss I.M. (1999). An update to the Seed-Idriss simplified procedure for evaluating liquefaction potential, Proc., TRB Workshop on New Approaches to Liquefaction, January, Publication No. FHWA-RD-99-165, Federal Highway Administration.

Idriss, I.M., and Boulanger, R.W. (2006). Semi-empirical procedures for evaluating liquefaction potential during earthquakes. Soil Dynamics and Earthquake Engineering, 26: 115-130.

Liu, K. (2004). Blast vibration monitoring and Blast damage evaluation. 1st Noranda/Falconbridge Blasting Workshop, September 27-28, 2004. 12 p.

Potvin, Y., Thomas, E., and Fourie, A.B. (eds) (2004). Handbook on mine fill, Australian Centre for Geomechanics, Perth, Australia, ISBN 0-9756756-2-1.

Seed, H. B., and Idriss, I. M. (1971). Simplified procedure for evaluation soil liquefaction potential. Journal of the Soil Mechanics and Foundations Division, ASCE, 97(SM9): 1249-1273.

Seed R. B., Cetin K. O., Moss R. E. S., Kammerer A. M., Wu J., Pestana J. M., Riemer M. F., Sancio R.B., Bray J.D., Kayen R. E., and Faris A. (2003). Recent advances in soil liquefaction engineering: A unified and consistent framework. Keynote presentation, 26th Annual ASCE Los Angeles Geotechnical Spring Seminar, Long Beach, Calif.

Sladen, J. A., D'Hollander, R. D., and Krahn, J. (1985). The liquefaction of sands, a collapse surface approach. Canadian Geotechnical Journal, 22(4), 564-578.

Youd, T.L. (2001). Liquefaction resistance of soils: summary report from the 1996 NCEER and 1998 NCEER/NSF Workshops on evaluation of liquefaction resistance of soils. Journal of Geotechnical and Geoenvironmental Engineering, 127(4): 297 - 313.

Analysis of failure in a salt room and pillar mine

Farid Laouafa, Mehdi Ghoreychi

Institut National de l'Environnement Industriel et des Risques- INERIS, F-60550 Verneuil-en-Halate, France

ABSTRACT

Failure mechanisms have been investigated in a salt mine (Alsace Potash mines, Esat of France) excavated by the room and pillar method, a part of which is under study for chemical waste storage. This part is located at a depth of about 550 meters. Some singular failure modes appear in the roof mine. These modes are perpendicular to the axis of the gallery and are created by tensile stresses. Such a failure mode is rarely observed in classical mines (coal, construction stones, etc.). 3D modelling of the site has been required for accurate description of the physical mechanisms. The results show that the failures and more generally the roof behaviour are controlled by the deformation of the pillars inducing tensile forces in the roof. The results also show that the creep or the viscoplastic behaviour of the salt is a key element that explains the existence of such failure and their evolution over time. A parametric analysis of the properties of overburden, geometrical pillar features slenderness, confirm the conclusion. Namely, time-dependent deformation of large salt pillars generates their lateral extension and induces roof deformation and failure in tension. The numerical results are in full agreement with in-situ observations.

KEYWORDS: Salt mine; modelling; failure; creep

1. INTRODUCTION

Part of the salt mine belonging to Alsace Potassium Mines (MDPA) excavated by the room-and-pillar method has been used as a storage area for industrial waste (Figure 1).



Figure 1: Example of waste storage.

Storage began in 1999, in a specifically designed area (rooms and pillars) with a configuration comprising galleries 2.8 to 3 m high and 5.5 m wide, with pillars 20 m wide per side. Convergence measurements were taken at regular intervals and observations were also recorded regarding the mechanical behaviour of the structures. The storage project was stopped in 2002 and several options are being considered regarding the future of the site.

Cracks in the mine roof and bed separations were observed. In particular, transverse cracks relative to the axis of a gallery appeared in 2015 in addition to longitudinal cracks of the roof and bed separations. In

order to determine the mechanical strength of the mine, INERIS was asked by the MDPa to identify the origin and consequences of these cracks.

The present study focuses in particular on the network of cracks due to mechanical failure (caused by the stress levels) observed in the roof and facings of some galleries running perpendicular to their axis. These more or less open cracks intersect a longitudinal fracture. The aim of this article is to analyse the mechanisms that led to this mode of failure in the roof.

Numerical modelling shows that the origin of the “transverse” cracks perpendicular to the axis of the galleries is linked to the creep of the salt pillars. In other words, the mechanism of deformation of the roof in the immediate vicinity is controlled mainly by that of the pillars. As these pillars are extremely massive (20 m wide), during their vertical and transverse deformation (continuous deformations related to salt creep), they pull down the roof in the immediate vicinity.

Although fracturing phenomenon along the axis galleries is often encountered in underground mines and quarries (coal, building stone...), transverse cracking is much more rare. Indeed it is strongly related to the intrinsic nature of salt, which deforms as there are stress deviators within it. It is on this mechanism that the paper will focus.

2. DESCRIPTION OF THE SITE

The site examined by this study covers an area of about 4 hectares, 700 m x 600 m. It is located at a depth of approximately 550 m and exploited by the classical abandoned room and pillar method. The pillars are 20 m x 20 m square. The chambers are 5.5 m wide and 2.8 m high (Figures 2 and 3). The worked proportion (ratio of excavated surface to total surface) is 38%. Storage is accessible through aisles called double tracks, 4m wide, separated by 3m-wide pillars.



Figure 2: Section through Storage Area and location of cracks (blue) (MDPA, 2015) (Key: Bloc – Block).

Figure 3 is a zoomed-in image showing the design of the access tracks.

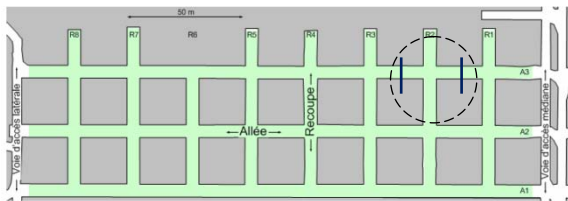


Figure 3: Zoomed-in image of pillars, aisles and intersections and location of cracks (blue) (MDPA, 2015).

Key : Voie d'accès latérale - Side access route; Voie d'accès médiane - Middle access route; allées - aisles; recoupe - intersection; R1, R2... - I1, I2...

The site is located in the Alsace Potassium Mines which have been exploited throughout the last century. The formerly exploited level is about twenty meters above the level of storage. A very large pillar called *stot* was left for the overlying exploitation.

This is an unworked part, and includes two Potash layers worked by the method of making long

cuts before caving in the roof (by removing the support structure).

Thus, significant subsidence of a maximum of 5.5 m was measured at the surface. The storage area is more or less affected by mechanical disturbances, induced caving, and *stot*.

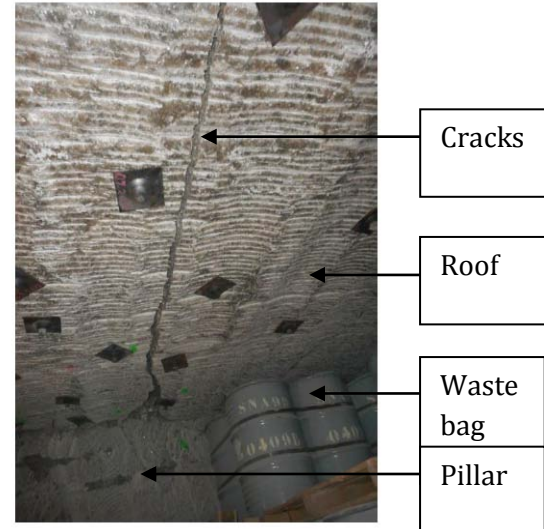


Figure 4: View of a transverse crack in the roof (MDPA 2015).

A visual inspection of the site revealed the existence of Mode 1 open cracks (Figure 4). One of the vertical cracks runs longitudinally in the direction of the track, practically in the middle of it (classic “flexion” mechanisms) resulting in horizontal traction.

It is however intersected by cracks perpendicular (transversal) to the track (Figure 4). These cracks are mainly at mid-width of the (20 m wide) pillars. It was observed that the transverse cracks are more or less open. They cross the roof and facings of the track.



Figure 5: Example of separation of roof (source, MDP A 2015).

As for bed separation (Figure 5), this affects the bed of rock salt in the roof immediately above the

tracks at the marly-anhydrite insoluble interlayers that are frequent at MDPA site.

In order to analyse the mechanical response of this structure, we must correctly define the intrinsic characteristics of its constituent material, namely salt, which will be the subject of the next section.

3. MECHANICAL BEHAVIOUR OF SALT

The main aspects of the rheological behaviour of rock salt are generally the same, whatever the variety. They can be summarised as follows:

- 1- a more or less marked aptitude for creep.
- 2- the absence of any viscoplasticity.
- 3- the rates of deferred deformations increase, in a non-linear manner, with deviatoric stress.
- 4- the rate of creep also increases exponentially with temperature. This dependency is expressed by the Arrhenius Law.
- 5- salt creep is accelerated after a crack occurs (resulting in so-called called “tertiary” creep observed in the laboratory, which results in the sample being ruined).
- 6- salt creep is accelerated in the presence of humidity and brine.
- 7- Above a certain level of stress, salt will crack. Unlike creep, the damage threshold of salt depends both on the mean stress and the deviator (like most rocks).
- 8- the damage thresholds (microcracking) and macroscopic breaking (maximum resistance) thresholds of salt fall in the presence of brine.

In light of these main traits of the thermomechanical behaviour of rock salt, two main rheological models have been proposed for the viscoplastic behaviour (creep) of this material: i) The Lemaitre model. According to this model, salt creep slows down over time and its development is expressed by a time power law, ii) the Norton (also called Norton-Hoff) model, widely used for salt throughout the world. This model considers that beyond a short transient phase, creep reaches a stationary state (linear evolution). We would also point out that the Norton and Lemaitre models are designed for the viscoplastic behaviour of rock salt and are not aimed at modelling the damage and rupture of this material. We used in this study the Norton model, on the basis of our findings on the results obtained during a previous study (Laouafa, 2010) focussing on the *in situ* convergence measurements (Figure 6).

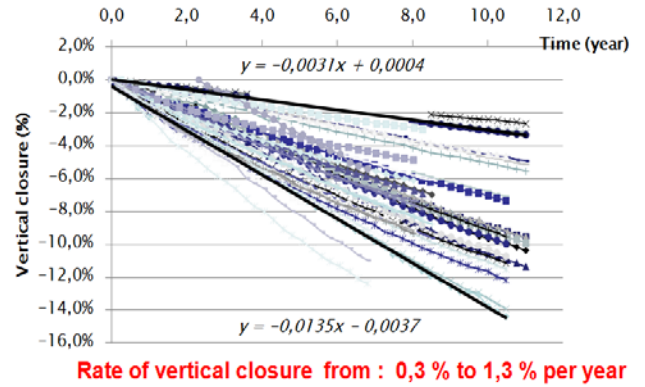


Figure 6: Rate of vertical closure, at different points of the mine (MDPA 2015).

Figure 6 clearly shows the linearity of convergence as a function of time, hence the use of the Norton model described below. For this model, the rate of viscoplastic strain $\underline{\underline{\dot{\epsilon}}}^{vp}$ is expressed as follows (in tensor form):

$$\underline{\underline{\dot{\epsilon}}}^{vp} = A \exp(-B/T) (Q/Q_0)^n \frac{\partial Q}{\partial \underline{\underline{\sigma}}} \quad (1)$$

Q is the von Mises effective stress (MPa) and A , B , n : model parameters; $Q_0 = 1$ MPa

Table 1: Creep model used by INERIS, adjusted against *in situ* measurements (Laouafa, 2010).

Elastic Parameters		Viscoplastic Parameters (Norton model)		
E (MPa)	ν (-)	A (j^{-1})	B(K)	n (-)
25000	0.25	0.022	4700	4.0

4. NUMERICAL MODELLING

4.1 Numerical Model and Assumptions

Although the storage area has no particular symmetry (Figure 3), a quasi-periodic “unit cell” can be seen, consisting spatially of pillars, aisles and intersections.

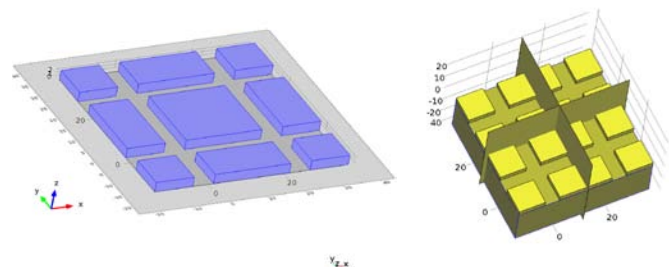


Figure 7: Plan and 3D view of the pillars, galleries and planes of symmetry.

In order to optimise the calculations without reducing their accuracy, a unit cell (Figures 7 and 8) composed of a 20 m x 20 m pillar 2.80 m high, aisles and intersections 5.5 m wide and the roof of the storage area positioned at -550 m (depth) was used.

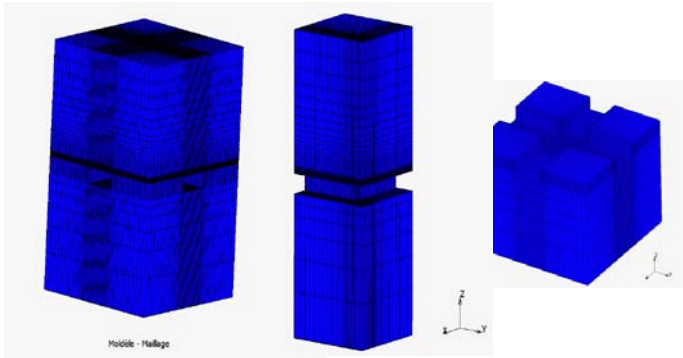


Figure 8: 3D view of pillar, galleries and unit cell and zoom-in view of the galleries.
Key: Modèle... - Mesh Model

The idealized geological medium is composed entirely of salt (Table 1), without taking into account the few marly seams in the roof. The dimensions of the model, the state of initial stress and the set boundary conditions are described below.

The dimensions of the model (Figure 8) are as follows:

- Width 25.5 m
- Length 25.5 m
- Height 42.80 m (wall 20 m and roof 20 m and pillar 2.80 m)

The boundary conditions are as follows:

- Plane of symmetry for the four vertical sides
- Plane of symmetry at the base of the model
- Pressure of 11.45 MPa (weight of the overburden).

The initial conditions are as follows:

- Range of initial lithostatic and isotropic stresses (hypothesis supported for evaporites):

$$\sigma_{xx}(z) = \sigma_{yy}(z) = \sigma_{zz}(z) = \gamma \times z \quad (2)$$

In regards to the chronology and time span of the study, aisles and intersections were simulated numerically in about ten days. It does not follow the real chronology but allowed the stabilization of the evolving problem over time. The period of time considered since the voids were created is from 10 to 15 years.

4.2 Numerical results

This sub-section is dedicated to numerical results. We will focus only on the tensile stresses generated in the gallery roof, the main subject of this paper. Figure 9 shows the spatial extent of the zones under horizontal traction (S_{yy} , stress component) (blue) affecting the roof and pillars after 10 years of creep. Note that S_{yy} (orthogonal to the gallery axis) tractions develop on facets perpendicular to the axis of the gallery. Note also that the edge of the pillars and part of the roof is also affected by tractions.

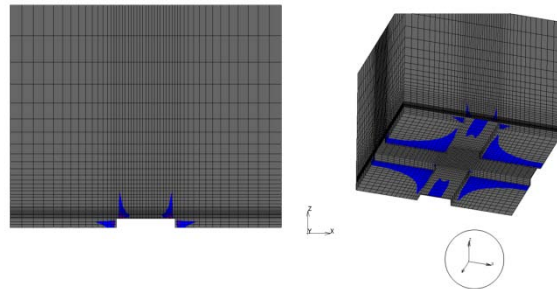


Figure 9: Positive horizontal S_{yy} Stress (traction): Side view (left) and bottom view of the roof 10 years after excavation (obtained using the reference model).

Figure 10 shows (wireframe view) the 3D spatial distribution of the zones subjected to S_{yy} traction .

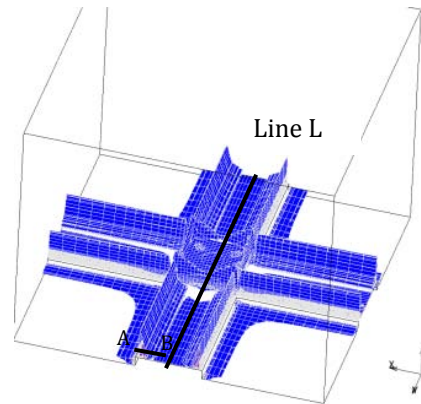


Figure 10: 3D view of the zones affected only by traction in direction y ($S_{yy} > 0$) in the roof and pillar after 15 years (obtained using the reference model). The aisle, intersection, roof and pillars are shown.

From a more quantitative viewpoint, the paper is interested in what follows the time evolution of these tractions induced by creep of the pillars. For this Line L (parallel to the gallery axis), in direction y , located at mid-span of the roof, and segment AB,

located along the edge of the model (Figure 11) (perpendicular to the gallery) is considered.

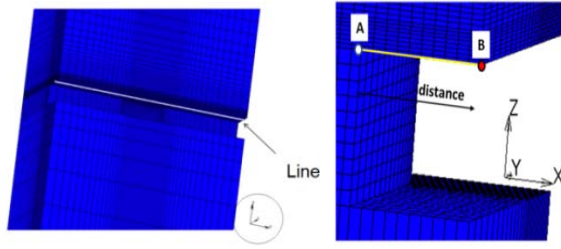


Figure 11: Definition of Line L under analysis passing through the roof of the storage area and parallel to the y-axis and Transverse segment AB (perpendicular to the axis of an aisle), located on the roof at mid-width of the pillar.

Figure 12 shows the distribution of horizontal stress S_{yy} along Line L at two moments: 5 and 10 years. Initially (all structures in virgin state), S_{yy} equals around -13 MPa (negative due to compression).

The redistribution of the stresses due to the works (here modelled with no phasing and virtually instantaneous) at $t=0$ changes continually over time. Note, for example, that 5 years after the works, S_{yy} stress is still under compression but gradually comes under traction domain.

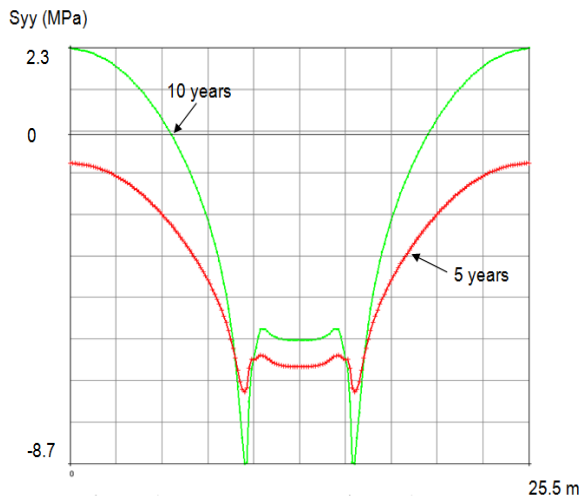


Figure 12: Distribution of horizontal stress S_{yy} along line L at 5 and 10 years (computed using the reference model).

The horizontal-axis represents the distance in m and the vertical-axis the stress in MPa. The sign convention is that of continuum mechanics (stress positive in traction and negative in compression).

This result is confirmed in Figures 13 and 14, which focus solely on the time evolution of the

horizontal stress S_{yy} at point B and for different configurations (hard or soft roof, slenderness, or excess-load roof).

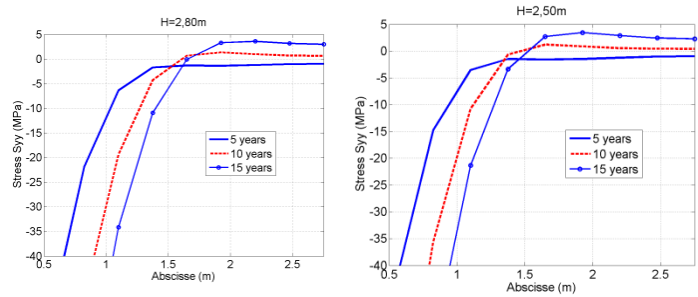


Figure 13: Distribution of S_{yy} stress along segment AB (Figure 10) after 5, 10 and 15 years. For two pillar heights (H).

Key: - Abscisse - distance-axis

A reduction in S_{yy} stress was observed, passing gradually from compression to traction and reach failure state within 10 and 15 years. This corresponds exactly to the period when the cracks appeared in the roof.

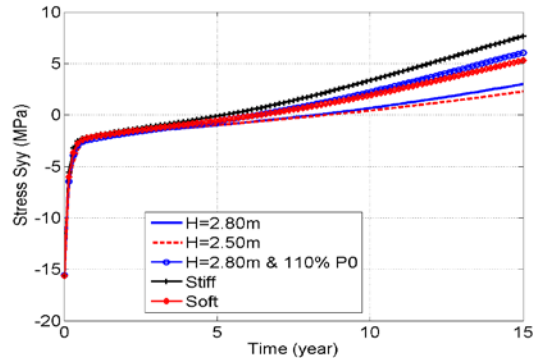


Figure 14: Temporal evolution of horizontal S_{yy} stress at point B, as a function of time, since excavations began and for the different configurations.

These results show that the creep of the salt pillars is the main factor responsible for these significant variations in stress in the immediate roof area of gallery. The combined effect of this mode of failure and cracking occurred in two perpendicular directions (longitudinal and related roof separation) threatens the security of the site.

5. CONCLUSION

The 3D models (finite elements) clearly show that the creep of the salt mine is the primary cause of the cracking observed in situ. In particular, the transverse cracking affecting the galleries is caused by the gradual horizontal expansion of the pillars whose height continuously decreases (and leads to the expansion of the pillar, salt creep occurring with no variation in volume) due to the effect of salt creep. This expansion of the pillars forces the roof to stretch, which causes horizontal tensile stresses increasing over time. These stresses, on exceeding the salt's tensile strength (very low, 1 to 2 MPa maximum, in the short term and practically negligible in the long term) give rise to transverse cracks, which manifest themselves sooner or later in the pillars of all of the tracks.

6. ACKNOWLEDGEMENT

The authors wish to warmly thank the MDPA (Mines de Potasse d'Alasce) for their support and their active contribution to the work which allowed carry out the study.

7. REFERENCES

- Cristescu N., Hunsche U. 1991. A constitutive equation for salt, 7th Int. Cong. Rock Mech., Aachen, Sept. 16-20, Balkema
- Cristescu N., Hunsche U. (1998). Time effects in Rock Mechanics, Wiley.
- Ghoreychi M. (1990). Conséquences du comportement thermomécanique du sel pour la conception et la sûreté d'un enfouissement de déchets radioactifs. Stockage en Souterrain, Presses des Ponts et Chaussées, 229-243.
- Laouafa, F. (2010). Etude géomécanique du stockage de StocaMine. Rapport INERIS-DRS10-108130-14273A.
- Laouafa, F. (2010). Analyse critique des études géomécaniques du stockage de StocaMine, Rapport d'étude INERIS-DRS-10-108130-04240A, 2 avril.
- Mogenier, C. (2015). Rapport d'étude géophysique -Wittelsheim Bloc 21 / Allée 3 – 00029074. SOLDATA Geophysic.
- Roman, J. (2015). Stockage de déchets StocaMine. Note de synthèse suite à la « visite d'inspection du 6 novembre 2014 ». MDPA.

Lessons in slope stability management from Kinross' Tasiast mine, Mauritania

Korhan Tasoren ^{a, *}, Gillian Gardhouse, P.Eng. ^b, Dr. Jerry Ran, P.Eng. ^c

^a Senior Geotechnical Engineer, Kinross Tasiast Mauritanie Limited SA, Nouakchott, Mauritania, BP 5051

^b Senior Geotechnical Engineer, Kinross Gold Corporation, Toronto, Canada, ON M5J 2V5

^c Geotechnical Services Director, Kinross Gold Corporation, Toronto, Canada, ON M5J 2V5

ABSTRACT

The continued monitoring and optimization of a mining operation are essential extensions of a feasibility study. While the ultimate goal is to mine to the planned design in a safe and economic fashion, such efforts are challenged on a daily basis by changing ground conditions. Success in a dynamic mining environment requires a strong understanding of historical instabilities and wall control blasting, along with well-defined near wall excavation and clean-up procedures, and an advanced slope monitoring system. This paper presents several cases describing different modes of slope failure experienced at Kinross' Tasiast mine site, and the operational and design measures implemented to manage and monitor these instabilities. Routine data collection practices and blasting designs that have been introduced to minimize wall damage and steepen slope angles are also discussed.

1. INTRODUCTION

The Tasiast mine (Tasiast) is an open pit gold mining operation that is owned and operated by Kinross Gold Corporation. The mine is located in northwestern Mauritania, approximately 300 km north of the capital city of Nouakchott (Figure 1).

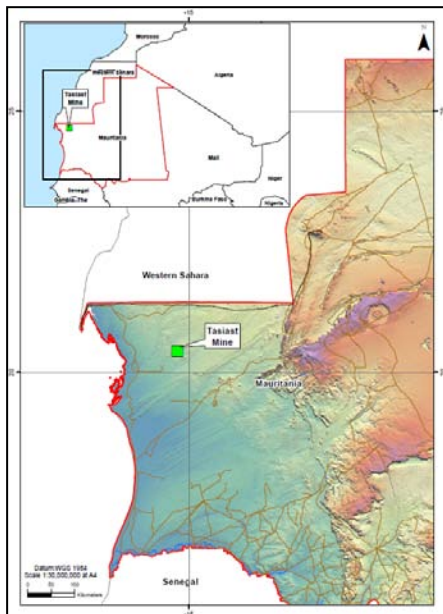


Figure 1: Location of the Tasiast mine site.

Today there are two active mining zones at Tasiast: the Piment Zone and the West Branch Zone

(Figure 2). The Piment Zone hosts eight small, narrow pits. The largest of these pits is known as Piment Central and is 0.9 km long and 0.5 km wide, with a depth of 0.2 km. Mining commenced at Piment in 2007 and commercial production was reached in 2008. To the south of the Piment zone is the West Branch Zone. The West Branch pit is the largest of the four pits located in this area. In 2009, the mineralized Greenschist Zone was discovered at West Branch, prompting additional exploration and study to support an expanded project. A feasibility study was subsequently completed in 2014. The final pit shell in the current design measures 1.8 km long by 1.4 km wide and is approximately 0.5 km deep. The pit is now in the first phase of operation.

Since extraction began in 2007, a number of minor slope failures have occurred at Tasiast. Back analyses were performed in some cases, and slope designs and implementation procedures were optimized to minimize blasting damage and monitor slope movements.

This paper presents typical slope failure modes observed at Tasiast, results of the corresponding back analyses, and lessons learned in slope stability management.

2. MINE GEOLOGY

At Tasiast, gold mineralization at the regional scale occurs in two parallel trends: the Piment Zone, with a strike length of 4.5 km, and the Greenschist Zone, with a strike length of approximately 1.5 km.

Both zones are characterized by oxidized and transition materials to a depth of 50 m to 100 m, which are then underlain by fresh rock. The dominant and controlling structure of the eight to ten sets of identified geological discontinuities and features is the foliation, which dips toward the hanging wall of the deposits (east).

Groundwater flow occurs in the oxidized zone and into the transition zone. Following the start-up of mining, local scale flow shifted the hydraulic gradient toward and into the pits. Below the transition zone, there is virtually no groundwater movement due to the low hydraulic conductivity of the fresh bedrock. There is no regional-scale groundwater flow in the Tasiast area (SWS, 2014).

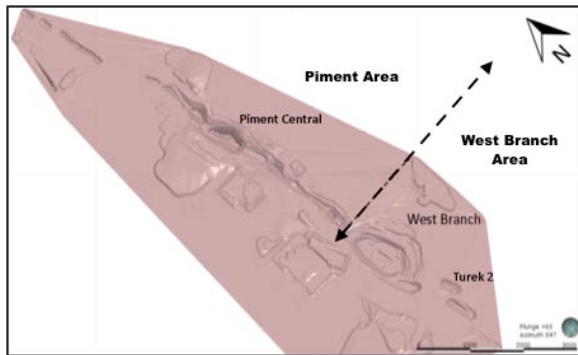


Figure 2: Mining area layout showing studied pits.

3. GEOTECHNICAL DATA AND PIT DESIGN

The latest geotechnical study and pit design for West Branch were completed in 2014. In addition to previous geotechnical investigation programs, the 2013 drilling campaign consisted of eight dual purpose geotechnical and hydrogeological holes totaling 4,609 m. Oriented core logging, field and laboratory testing, borehole televiewer surveying, and pit mapping methods were also used to collect geotechnical data. Golder Associates, the consulting firm behind the 2014 geotechnical investigation, selected Cai's Geological Strength Index (GSI) for rock mass classification purposes.

The West Branch pit is divided into four geotechnical domains based on geological, structural and rockmass similarities, as well as wall orientation due to the nature of the foliated/bedded host rock (Figure 3). Each domain is sub-divided into oxide, transition, and fresh categories based on the intensity of weathering. Two different rockmass qualities have been identified within the transition zone and subsequently categorized as the upper and lower transition zones for geotechnical slope design purposes.

Slope stability analyses completed for West Branch were based on the developed geological, structural, rockmass quality, and hydrogeological models. Two numerical modeling methods (Limit Equilibrium and Finite Element) were used to establish slope angles and obtain the corresponding Factor of Safety values for the slopes. Recommended slope design parameters are shown in Table 1.

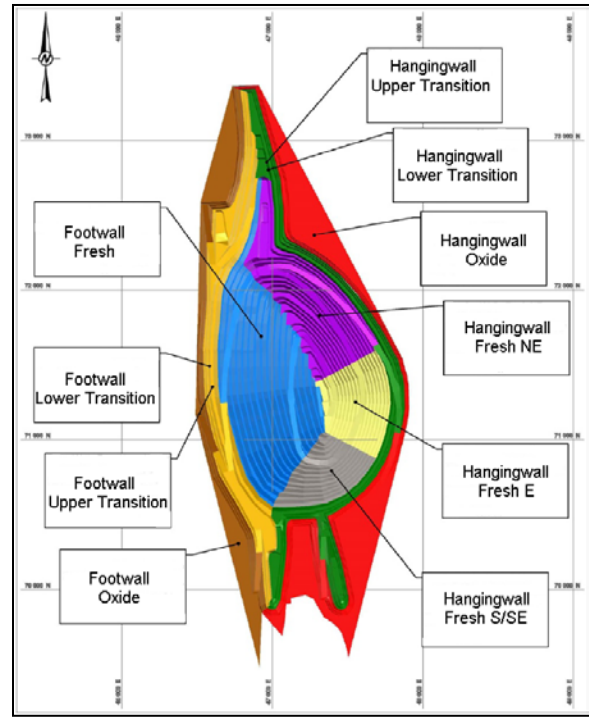


Figure 3: West Branch open pit geotechnical sectors. Modified from Golder (2014).

Table 1: West Branch slope design recommendations.

Sector	Depth (m)	Bench Face Angle (°)	Bench Height (m)	Berm Width (m)
HW oxide	0-30	60	10	6.5
HW transition	30-100	65	10/20	6.5/8.5
HW fresh	>100	75	30	10.5
FW oxide	0-30	45	10	6.5
FW transition	30-100	45	10/20	6.5/8.5
FW fresh	>100	45	30	10.5

4. HISTORICAL SLOPE FAILURES AND DESIGN IMPLEMENTATIONS

Pit slope stability is an important aspect of providing a safe and productive working environment at a mine site. Slope failures have historically occurred in the upper zones of operating pits at Tasiast. Circular, planar, wedge, and toppling failure modes have been observed and are generally

attributed to the weak rockmass and excessive blasting damage. Although none of these failures were large in scale, the insights gained can be used to make operational and design improvements.

4.1 Piment Central Pit Rockfall Incident

A loose rock fell 50 m from a bench crest to the pit floor on the hanging wall side of the Piment Central Pit during a night shift. The slope monitoring radar was able to detect the movement, which was caused by crest damage, but was unable to send an alarm to the site geotechnical team because the movement was sudden rather than progressive (Figure 4). The radar data indicated that the loose rock had a mean displacement of 1.10 mm and a velocity of 2.5 mm/h (Figure 5).

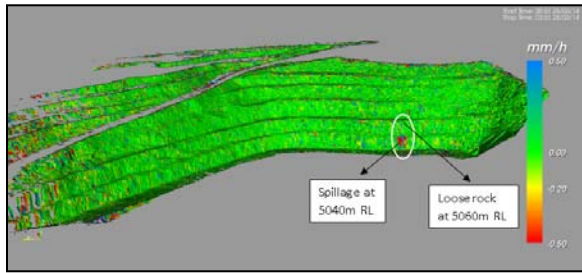


Figure 4: Slope monitoring system screen shot of the movement area during the event.

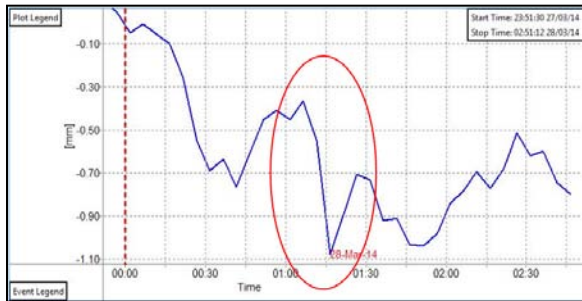


Figure 5: Displacement graph of the event.

RocFall software (Rocscience) was used to back analyze the rockfall event and calculate the displacement. The weight of the rock mass was estimated to be 200 kg. A face profile was created using AdamTech photogrammetry software. The actual distance from the toe at the pit bottom to the final resting location of the spilled rock was measured at 10.75 m in the field and calculated at 10.015 m by the RocFall model, demonstrating that the model is an adequate representation of the event (Figure 6).

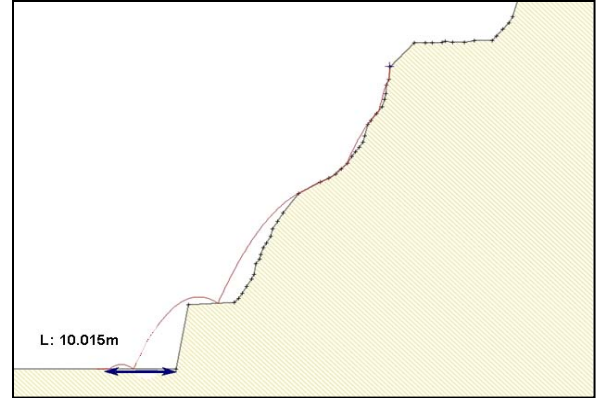


Figure 6: Back analysis of the rockfall incident using RocFall software.

The root cause of the failure was the presence of loose rocks on the broken crest due to blasting damage, excessive sub-drilling, and poor face clean-up practices. The geological characteristics of the region adjacent to the blast and further up the slope dictate the potential for blast-induced damage (Read & Stacey, 2008). The hazard area was identified, a high windrow was built along the ramp 10 m away from the toe, and a 15 m standoff distance procedure was put in place for the rest of the pit to prevent similar incidents. A 20 m vertical mid-bench presplit blasting design was applied to the pit hanging wall to reduce production blast damage to the face, since a proper trim blast could not be implemented in such a narrow and small scale mining environment. Significant improvements have been observed in the condition of the face and in pit design compliance since implementing the pre-split design (Figure 7).

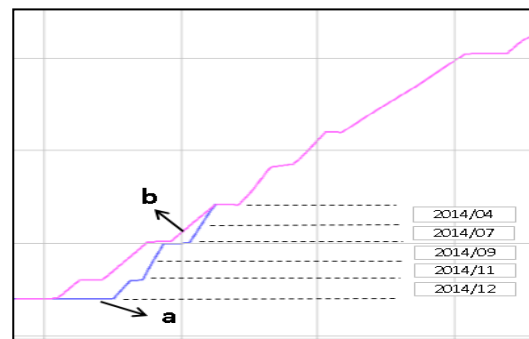


Figure 7: a) Actual pit wall design after implementing pre-splitting procedures; b) Predicted pit wall without wall control blasting.

4.2 Planar Failure at West Branch Footwall

The West Branch footwall design bench face angle (BFA) was limited to 45° to avoid undercutting the foliation, which dips at 42° to 46°. The foliation

strikes 350° and has an average spacing of 2.5 m. Previous blast designs used in the early stage of the project did not consider these design limitations, which led to excessive damage in the oxide and transition zones on the footwall. This was exacerbated by the use of standard full depth vertical blast holes near the wall.

Several small, bench scale planar failures were experienced as a result of damaged or narrow catch berms, and broken toes. The typical failure dimension was limited to 20 m long by 2 m wide by 30 m high due to the condition of the rockmass and the intersection of joint sets.

To prevent blast damage, a modified trim blast design was applied to the area near the footwall (Figure 8). Two stepped holes were introduced to break the rock along the foliation surface and achieve the pit design. This approach resulted in smooth face conditions along the foliation plane and improved pit design compliance on the footwall.

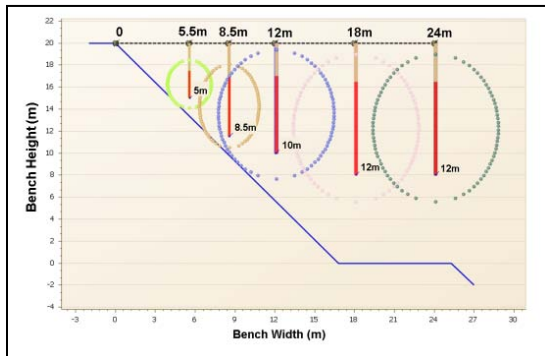


Figure 8: An example of a modified footwall trim blast design.

4.3 Turek 2 Pit Rockmass Failure

The Turek 2 pit is one of the oxide satellite pits that will eventually become part of the West Branch pit as mining progresses. The Turek 2 pit has 10 m high benches with 6.5 m wide catch berms and a 65° BFA. It is 45 m deep. Approximately 400 tons of material fell several benches to the bottom of the pit, resulting in a failure area 25 m long, 3 m deep and 25 m high. A 75° foliation angle was measured on the pit face where the failure occurred.

Back break was observed on the catch berm parallel to the strike of the foliation after production blasting. No consideration for wall control had been included in the blast design, such that a high energy charge was used in soft rock, causing damage to the final wall. Rainfall flow marks were found on the top of the pit in the failure area during the incident investigation. Over-digging was observed on the face, resulting in a very narrow catch bench berm. Together these factors contributed to the failure.

SLIDE v5.0 software (Rocscience) was used to back analyze the failure. Inputs included a high resolution photogrammetry face profile (Figure 9), steep transient water table profile behind the face, and density, cohesion, and friction angle values. Different combinations of the input parameters shown in Table 2 were analyzed to simulate conditions similar to those of the failure. The SLIDE v.5.0 results are shown in Figure 10. All of the condition combinations suggest a Factor of Safety (FOS) of 1.0 (Table 3).

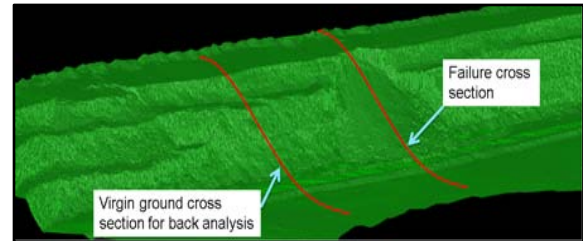


Figure 9: Photogrammetric surface of the failure area.

Table 2: Back analysis results using different combinations of conditions.

Unit Weight (kN/m ³)	Friction angle (degree)	Cohesion (kPa) Wet	Cohesion (kPa) Half Dry	Cohesion (kPa) Dry	FOS
23	30	31	25	19	1.0
23	32	27	20	14	1.0
23	34	24	15	9	1.0
23	36	20	11	3	1.0
23	37	17	8	0	1.0

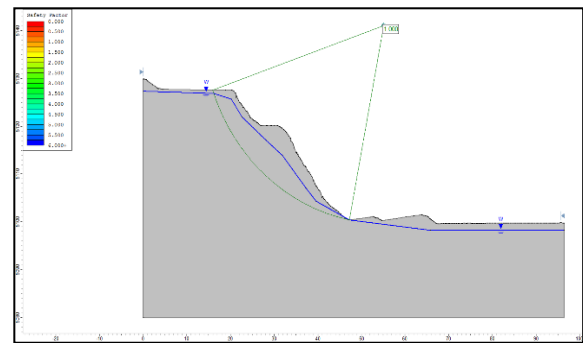


Figure 10: SLIDE v5.0 section of the hanging wall.

The pit design was reviewed and modified after the failure. A 15 m wide catch berm was left on the hanging wall, and a radar system was set-up to detect any further movement. A similar type of movement was observed by the slope monitoring system on the northern side of the failure (Figure 11). Blasted

material was left as a buttress to prevent excessive movement along the face. Only a toe charge was applied to the first row of the production blast to further reduce vibrations and related damage.

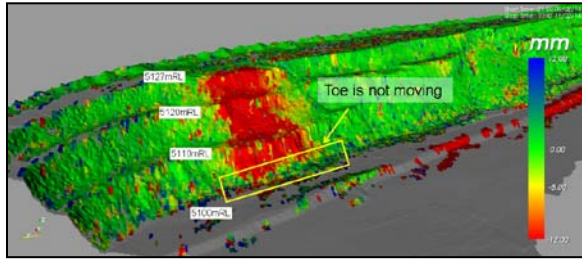


Figure 11: Movement at the northern side of the failure.

The following rockmass characteristics were determined as a result of the back analysis: the cohesion is 19 kPa, the friction angle is 30° and the unit weight is 25 kN/m³ for similar types of material. The effect of weathering in the oxide zone was greater in the hanging wall of the Turek 2 pit than in the West Branch area. Based on this, the Turek 2 pit geometry was modified to 10 m high benches with 7 m wide catch berms and a 55° bench face angle.

4.4 Summary of Failures

Table 3 summarizes the different failures, actions and outcomes discussed in this section.

Table 3: Summary of the failures and the actions taken in response.

Pit	Area	Summary
Piment Central	Problem & Cause	Rockfall due to broken crest resulting from excessive sub-drilling and poor face clean-up practices
	Analysis	Review of monitoring data Back analysis to calculate displacement
	Solution	Implemented mid-bench pre-splitting Built windrow appropriate distance away Implemented standoff distance procedure
	Result	Improved face condition Increased compliance to design
West Branch	Problem & Cause	Planar failure due to in-compliance with pit design dimensions
	Analysis	Blasting design review Pit design review
	Solution	Two stepped blast hole design applied
	Result	Smooth face conditions along the foliation plane Improved pit design compliance

Turek 2	Problem & Cause	Rockmass failure due to excessive blasting damage and rainfall infiltration
	Analysis	Field investigation Photogrammetry survey Back analysis Review of monitoring data
	Solution	Revised pit design based on the back analysis results Enlarged catch berm Modified blasting design
	Result	Planned pit production completed without safety issues or ore loss

5. ONGOING DATA COLLECTION AND MONITORING

Ongoing geotechnical data collection at Tasiast consists of face mapping, application of photogrammetry techniques for measuring structures (Figure 12) and bench configurations, pore pressure measurements from twelve vibrating wire piezometers around West Branch, and wet blast hole and grade control hole mapping, where available, to support pit inspection and operation.

Recently, data from face mapping and structural measurements were used to update the structural and geotechnical models. The geotechnical model was subsequently used in a fragmentation study to better understand the effects of energy distribution across major and minor joint sets. This is significant because blasting loosens existing structures to liberate rock blocks and create new fractures within the intact material (Kanchibotla et al., 1999). Rockmass elasticity parameters and the intensity of structures (in-situ block size) are known to have significant influence on the efficiency of blasting at Tasiast. As a result of the study, fragmentation was improved in the ore zone, and the cost of drilling and blasting was reduced while maintaining the quality of fragmentation in the two main rock types.

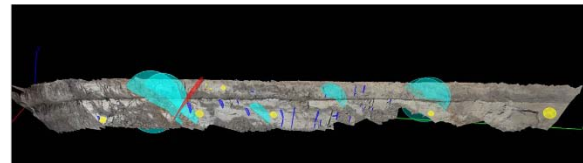


Figure 12: Structural measurements obtained along the West Branch footwall using photogrammetry.

The control and management of water is a fundamental component of most successful large open pit mining operations (Beale & Read, 2013). Pore pressure data obtained from vibrating wire piezometer holes and mapping of wet blasting or grade control holes assist groundwater studies and

provide guidelines for pit dewatering activities on a daily basis (Figures 13 and 14).

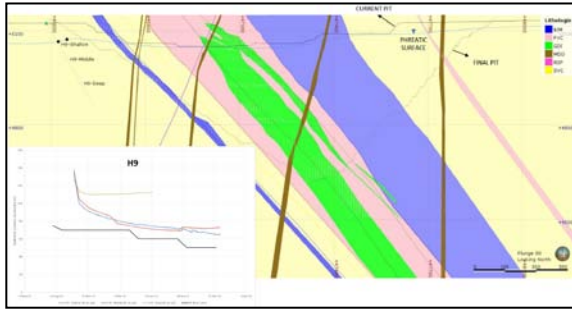


Figure 13: Cross section of vibrating wire piezometer hole.

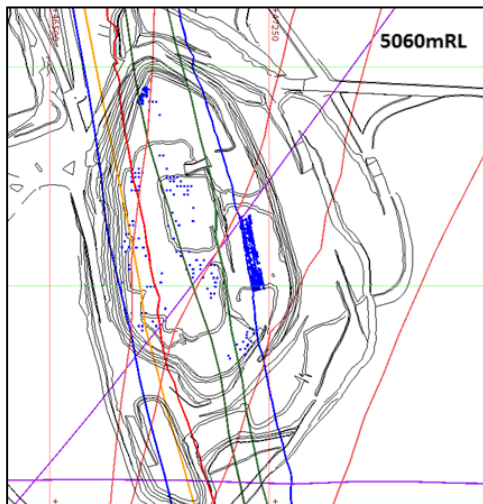


Figure 14: Plan view of West Branch major structure and wet drill hole mapping correlation.

The Tasiast mine currently has two synthetic aperture slope monitoring radar systems. These systems have been used for tactical and strategic monitoring in different pits since 2013 (Figure 15). Parameters for alarm set-up include area (m^2), velocity (mm/hour), and time interval (hour or day). These parameters must be low enough to provide an early warning when a slope is starting to move, but also high enough to prevent false alarms. The system collects continuous data in three minute scan intervals and backs up historical files to an external storage unit for further analysis. Interpreted data are transmitted to the Guardian slope monitoring software in the office to be filtered based on site thresholds. Any type of movement above the set thresholds triggers the alarm, prompting the software to send email and SMS alerts to relevant personnel. The site slope movement action plan is summarized in Figure 16.



Figure 15: IBIS-FMT slope monitoring radar in action.

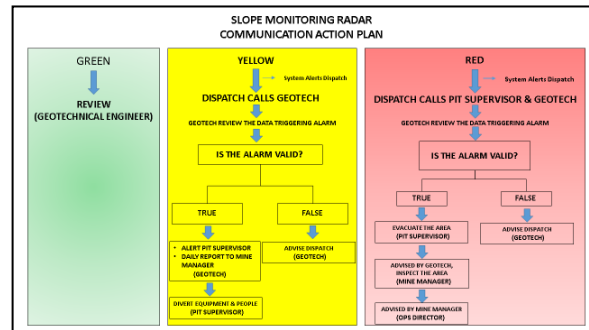


Figure 16: Summary of the slope movement action plan.

6. CONCLUSIONS

Bench excavation at the Tasiast mine site is controlled through a variety of measures, including the use of appropriate equipment, standard operating procedures, and marked lines or pegs, in order to minimize face damage and crest loss. When there are localized failures, wider catch benches and safety berms are commonly used to protect personnel and equipment. Areas of concern related to slope movement or restricted operating space are monitored by one of two ground-based synthetic aperture radar units. These units provide real time measurements and send out alert messages based on preset threshold values.

Exposed benches are routinely mapped for geological and geotechnical features using manual and photogrammetric techniques. The collected data, together with the existing database, feed the mine's geotechnical model and permit both predictive analyses and back analyses of slope stability.

Blasting against pit walls in particular has significant impact on slope stability and achievement of the design configuration, as well as implications for safety, productivity and mining costs. Various blasting designs have been applied to both footwall and hanging wall slopes. In general, hanging wall slopes are protected from excessive damage by pre-shearing prior to trim shots or modified production blasts, while trim shots and modified production blasts with two stepped stab holes are used when

blasting against footwall slopes. These modifications to the blast design support a safe and economic mining operation.

7. ACKNOWLEDGEMENT

The authors would like to thank Rahadian Widiadi and Moulay Ahmed Hamoudy for their support, and Kinross Gold Corporation for permission to share these lessons by publishing this paper.

8. REFERENCES

Beale, G. and Read, J. (2013) Guidelines for Evaluating Water in Pit Slope Stability. 49 p.

Cai, M., Kaiser, P. K., Uno, H., Tasaka, Y., & Minami, M. (2004). Estimation of rock mass deformation modulus and strength of jointed hard rock masses using the GSI system. *International Journal of Rock Mechanics and Mining Sciences*, 41: 3-19.

Golder Associates. (2014). Tasiast West Branch Open Pit Slope Design Recommendations – Revision 1, Technical Memorandum. Buckinghamshire: Golder Associates UK Ltd.

Kanchibotla, S. S., Valery, W. and Morrell, S. (1999). Modelling fines in blast fragmentation and its impact on crushing and grinding. In *Explo'99: A Conference on Rock Breaking*, Kalgoorlie, WA, November 7-11, AusIMM, Vol. 99, pp. 137-144.

Read, J. and Stacey, P. (2008) Guidelines for Open Pit Slope Design. 275 p.

Schlumberger Water Services. (2014). Hydrogeological characterization of the West Branch Pit, Tasiast, Mauritania. Shrewsbury: Schlumberger Water Services.

Effect of buttress on reduction of rock slope sliding along geological boundary

Ryota MORIYA*, Daisuke FUKUDA, Jun-ichi KODAMA, Yoshiaki FUJII

Faculty of Engineering, Hokkaido University, Sapporo, Hokkaido, Japan, 060-0808

ABSTRACT

In open-cut limestone mines in Japan, huge rock slopes with a geological boundary between limestone and bedrock have been formed by mining activities. In addition, latent sliding plane near the toe of the slopes may be formed through the development of damaged zones with an increase in size of the rock slope. It has been reported that inelastic time-dependent sliding deformation of rock slopes along both the geological boundary and the latent sliding plane can occur. In this case, one of the countermeasures to suppress sliding deformation is an application of rock buttress to the slope surface where the sliding is taking place. However, the effect of rock buttress on reduction of the rock slope sliding has not yet been clarified. In this paper, the effect of rock buttress on reduction of the rock slope sliding is discussed based on a 2-dimensional finite element analysis using a non-linear visco-elastic model. The results indicate that (i) the degree of deterioration of sliding plane at the time of the application of rock buttress significantly affects the expected life of rock slope, (ii) there is an optimum height for rock buttress,, (iii) larger Young's modulus of rock buttress results in a longer expected life of rock slope, and (iv) the balance of increase and decrease of normal and shear stresses on the sliding plane by buttress is important and the obtained results can be changed by the difference of friction angle and the geometry of the sliding plane.

1. INTRODUCTION

In open-cut limestone mines in Japan, huge rock slopes have been formed by mining activities (Obara et al., 2000). In Japan, limestone deposit is often found on inclined bedrock and a part of the limestone deposit is left on the bedrock, such as schalstein to prevent the bedrock from weathering (Nakamura et al., 2003). Thus, the rock slopes include a geological boundary between limestone and bedrock. In addition, with increases in size of the rock slope, the stress state near the toe of slope can be severe and a damaged zone can develop. Therefore, it is necessary to pay attention to the deformation behaviour at the geological boundary and the toe of slope for the estimation of slope stability. Moreover, it is important to consider effective countermeasures in case dangerous signs such as sliding deformation at these parts are observed. One of the countermeasures to suppress the sliding deformation is application of rock buttress to the slope surface where the sliding is taking place. However, the effect of rock buttress on reduction of the sliding has not yet been clarified.

In this paper, the effect of rock buttress on reduction of inelastic time-dependent rock slope sliding, for example, how the height and stiffness of rock buttress affects slope deformation is discussed based on self-developed 2-dimensional (2-D) finite element code using a non-linear visco-elastic model.

2. MODELLING SLIDING DEFORMATION OF ROCK SLOPE

The aforementioned inelastic time-dependent sliding deformation of rock slope was modelled first to investigate the effect of rock buttress on the reduction of the sliding. Figure 1 shows the 2-D model of rock slope with geological boundary (blue line) and latent sliding plane (red line). Hereafter the term "sliding plane" is used to indicate both geological boundary and latent sliding plane. It was assumed that the rock slope was already formed by partially excavating the left side of a mountain. The height and angle of slope were set at 270 m and 45°, respectively. The geological boundary was set parallel to the slope surface and latent sliding plane from the slope surface, with an angle of 18° from the horizon, and intersected with geological boundary near the toe of slope. The intact rock mass was represented by 6-node and 8-node solid elements and assumed to be isotropic linear elastic body, while the

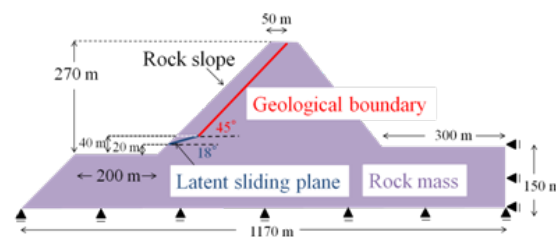


Figure 1: Schematic of 2-D FE model.

sliding deformations along the sliding plane were represented by 6-node joint elements (Pande et al., 1979) and assumed to be a non-linear visco-elastic body. The nodal displacements perpendicular to the right and bottom boundaries of the model were fixed at zero. All the analyses were conducted under plane strain conditions.

By applying downward gravitational force to the entire model, linear elastic analysis was conducted and the initial stress state of both the solid and joint elements was simulated. This state was regarded as time $t = 0$ for the non-linear viscous sliding deformation analysis along the joint elements, i.e. sliding plane. This viscous sliding deformation was expressed by decreasing shear stiffness, $K_s(t)$, of joint elements with time. For the way in which $K_s(t)$ decreased, we extended the constitutive equation of variable compliance type proposed by Okubo (1992) as follows:

$$\frac{d\lambda^*(t)}{dt} = \frac{1}{t_0} \left(\frac{m}{n+1} \right)^{\frac{m}{n-m+1}} (\lambda^*(t))^m (\sigma^*(t))^n \dots\dots\dots(1)$$

where $\lambda^*(t) (= K_s(0)/K_s(t))$ is normalized compliance and monotonically increasing function with time; t_0 is a time constant; m and n are degree of ductility and time-dependency of rock, respectively (Okubo, 1992); $\sigma^*(t)$ is severity representing how close the present stress state of a joint element is to a failure envelope expressed by Mohr-Coulomb failure criterion. To make the following discussion simpler, it was assumed that rock mass was homogeneous and only $K_s(t)$ changes with time while other physical properties are constants, as shown in Table 1. The upper limit of $\lambda^*(t)$, λ^*_{lim} , was set at 10000 and joint elements whose $\lambda^*(t)$ reached λ^*_{lim} were regarded as completely fractured.

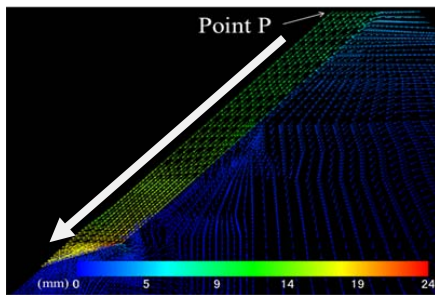


Figure 2: Distribution of viscous displacement around the rock slope at $t = 1$ year (case A).

It is also important to consider the degree of deterioration of the sliding plane at the stage of construction of buttress. In this study, the following two cases were considered:

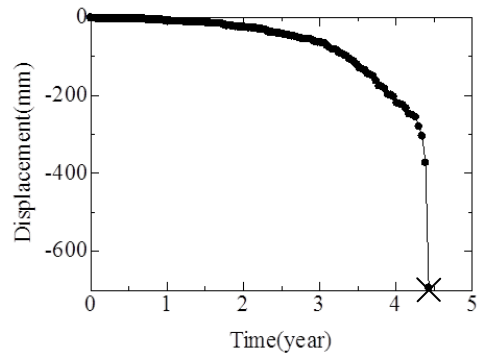
- Case A: $\lambda^*(0)$ of the entire sliding plane was set at 1.1 and $\lambda^*(t)$ increased according to equation (1).
- Case B: $\lambda^*(0)$ of the geological boundary and latent sliding plane were set at λ^*_{lim} and 1.1,

respectively, and $\lambda^*(t)$ of only latent sliding plane increased according to equation (1).

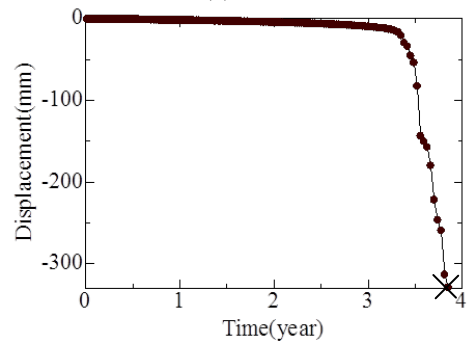
Table 1: Physical properties used in the analysis.

Solid element (Rock mass)	Values	Joint element (Sliding plane)	Values
Young's modulus, E	1.0 GPa	Initial Shear stress, K_{s0}	3.4 MPa
Poisson's ratio, ν	0.25	Normal stress, K_n	1.0 MPa
Unit weight, γ	27.0 kN/m ³	Cohesion, c	0.7 MPa
		Friction angle, ϕ	50°

To demonstrate that the inelastic time-dependent sliding deformation of rock slopes can be successfully simulated by the proposed approach, an example of the analytical results for case A is shown in Figure 2. This figure shows the distribution of viscous displacement around the rock slope between $t = 0$ and 1 year. It was found that rock mass above the entire sliding plane showed obliquely downward sliding relative to the sliding plane. Case B was also found to show the same tendency.



(a) Case A



(b) Case B

Figures 3 : Temporal change of horizontal viscous displacement at point P in Figure 2. Time at "x" represents t_{life} .

Figures 3(a) and (b) show the results of the temporal change of horizontal viscous displacement at the top of the mountain (point P in Figure 2) for

cases A and B. It is clear that both cases first showed a gradual increase of displacement followed by a sudden increase. In cases A and B, the entire sliding plane was regarded as collapsed when λ^* of all joint elements reached λ^*_{lim} in about 4.5 years and 3.8 years, respectively.

From the above results, because the non-linear time-dependent sliding deformation of rock slopes along the sliding plane was successfully expressed, it is possible to discuss whether the application of rock buttress can extend the time when λ^* of all joint elements reaches λ^*_{lim} , i.e. expected life of rock slope, t_{life} , by suppressing the sliding deformation along the sliding plane.

3. EFFECT OF ROCK BUTTRESS ON REDUCTION OF ROCK SLOPE SLIDING

3.1 Effect of height of rock buttress

In order to investigate the effect of rock buttress on t_{life} , the model shown in Figure 4 was analyzed in which various heights of buttress, $h_{but} = 30\text{ m} - 130\text{ m}$, with the fixed width were considered. The rock buttress was expressed by 6-node and 8-node linear elastic solid elements with Young's modulus E_{but} , Poisson's ratio ν_{but} and unit weight γ_{but} . In the following analyses, solid elements corresponding to the rock buttress were deactivated until $t = 50\text{ s}$, and then activated at $t = 50\text{ s}$. The aforementioned two cases of degree of deterioration of the sliding plane, cases A and B, were analyzed.

Figure 5 compares temporal changes of horizontal viscous displacement at the top of the slope at point P in Figure 2 with/without rock buttress for cases A and B. The physical properties of buttress were fixed at $E_{but} = 0.01\text{ GPa}$, $\nu_{but} = 0.25$ and $\gamma_{but} = 2.7\text{ kN/m}^3$. Both cases A and B show that t_{life} with buttress is more or less long than that without buttress in the range of h_{but} investigated in this study. Especially, t_{life} in cases A and B became the longest when h_{but} was 90 m and 110 m, respectively. Table 2 shows t_{life} with rock

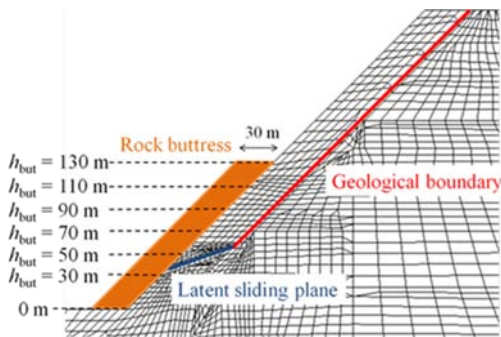


Figure 4: Various heights of buttress, h_{but} , analyzed in this paper.

buttress of various heights normalized by that without rock buttress. From the results of Figure 5 and Table 2, it is suggested that the degree of deterioration of sliding plane at the time of the application of rock buttress significantly affects t_{life} and that optimum h_{but} should exist depending on the degree of deterioration of the sliding plane. In other words, the ability of rock buttress to extend t_{life} will be compromised once h_{but} exceeds the optimum value.

Table 2: t_{life} with rock buttress of various h_{but} normalized by t_{life} without rock buttress.

h_{but}	30 m	50 m	70 m	90 m	110 m	130 m
Case A	1.1	1.2	1.6	1.7	1.3	1.1
Case B	1.0	1.2	2.0	6.4	6.6	4.2

Figures 6 and 7 show the stress state on sliding

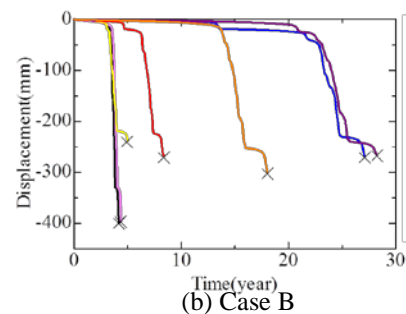
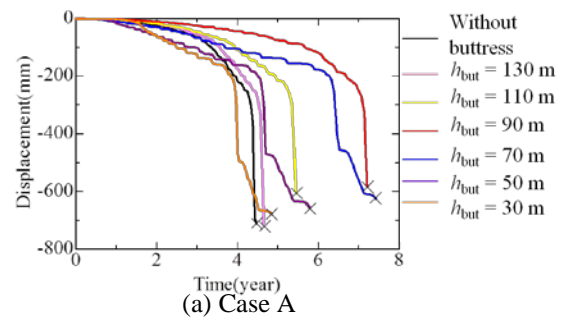


Figure 5: Temporal changes of horizontal viscous displacement at the top of the slope (Point P in Figure 2) with/without rock buttress. Time at "x" represents t_{life} .

plane just before and after the application of rock buttress in case where h_{but} was 90 m and 110 m, which showed the longest t_{life} in cases A and B, respectively (See Table 2). In these figures, black and red lines represent the stress state of joint elements

before and after the application of rock buttress, respectively. Horizontal axes in these figures represent the position on sliding plane in which latent sliding plane is in from 0 m (slope surface near the toe) to 63 m (the intersection of latent sliding plane and geological boundary) and is in from 63 m to 353 m (top of slope); Compressive normal stress, σ_n , and shear stress, τ , causing normal fault are expressed by negative values; absolute value of severity, $|\sigma^*|$, closer to 1 indicates that the stress state is closer to failure envelope.

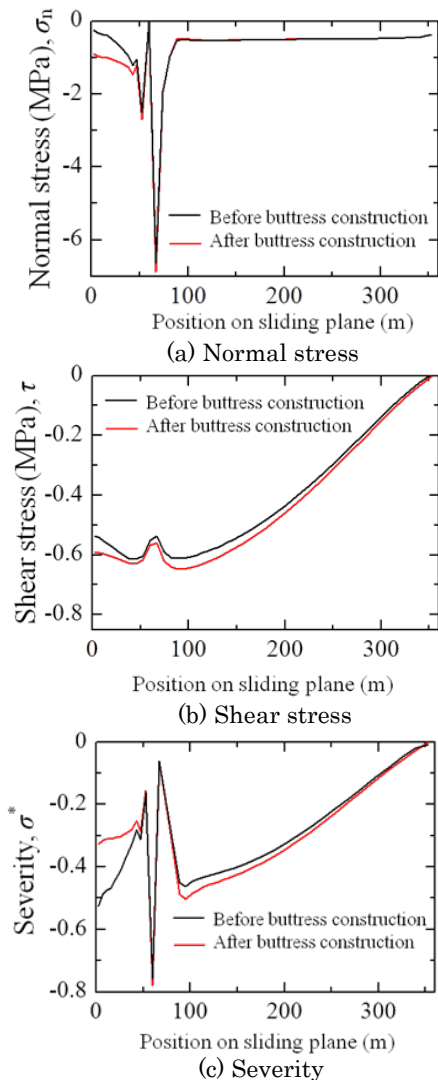


Figure 6: Change of stress states on sliding plane before and after applying buttress (Case A).

These results show that the application of rock buttress mainly affects the zone of latent sliding plane. Especially, when σ_n pressing the latent sliding plane increased, the result was a decreasing effect of $|\sigma^*|$ in both cases A and B. τ promoting sliding deformation along the entire sliding plane in case A and latent sliding plane in case B increased, resulting in the increasing effect of $|\sigma^*|$. For h_{but} investigated in this study, the increasing effect of $|\sigma^*|$ due to increase of τ along the entire sliding plane was smaller than the decreasing effect of $|\sigma^*|$ due to an increase of σ_n of latent sliding plane. Thus, the application of rock buttress results in extending t_{life} . However, it is also suggested that the application of rock buttress with much larger height than those investigated in this paper should enhance τ promoting sliding deformation along the entire sliding plane and t_{life} could be shorter than t_{life} without the rock buttress. The process of sliding plane failure was found to progress from the toe of slope to the top of the slope.

3.2 Effect of Young's modulus of rock buttress

The effect of Young's modulus of rock buttress, E_{but} , on reduction of rock slope sliding was also investigated. Three cases, $E_{but} = 0.01$ GPa, 0.1 GPa and 1 GPa, were analyzed only for $h_{but} = 90$ m and 110 m in cases A and B, respectively. It is worth mentioning that the effect of Poisson's ratio, ν_{but} , was also investigated in the preliminary analysis, however, the effect of the change of ν_{but} was negligible therefore this paper only discusses the effect of E_{but} .

Figure 8 shows temporal changes of horizontal viscous displacement at the top of the slope (Point P in Figure 2) for each E_{but} in cases A ($h_{but} = 90$ m) and B ($h_{but} = 110$ m). Table 4 shows t_{life} with rock buttress for each E_{but} , normalized by t_{life} without rock buttress. These results clearly show that the larger E_{but} resulted in longer t_{life} . In particular, the condition of $E_{but} = 1.0$ GPa resulted in about 18-times longer t_{life} than t_{life} without rock buttress and the smallest viscous horizontal displacement.

Figures 9 and 10 compare the stress state on sliding plane just after the application of rock buttress for each E_{but} in cases A and B. The meaning of vertical and horizontal axes of these figures is the same as those of Figures 6 and 7. Because a relatively clear difference of the tendency between each E_{but} was found only near the slope surface on the latent sliding plane, these figures only show the results for the latent sliding plane near the slope surface. Regardless of cases A and B, larger E_{but} resulted in smaller σ_n and smaller τ . In case A, although only the results at latent sliding plane near the slope surface are shown in the figure, larger E_{but} reduced τ promoting sliding deformation for the entire sliding plane, which significantly decreased $|\sigma^*|$. On the other hand, change of E_{but} locally affected σ_n (as in Figure 9(a)) and caused little difference for the remaining sliding plane, resulting in a local increase of $|\sigma^*|$ only near the slope surface. $|\sigma^*|$ for entire sliding plane

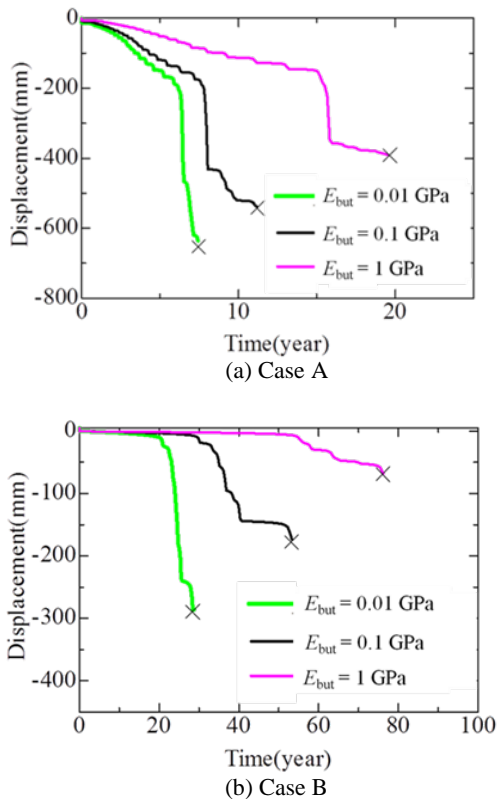


Figure 8: Effect of E_{but} on temporal changes of horizontal viscous displacement at the top of the slope (Point P in Figure 2). Time at “x” represents t_{life} .

Table 4: Expected life of rock slope with buttress normalized by that without buttress for various E_{but} in Cases A ($h_{but} = 90$ m) and B ($h_{but} = 110$ m).

E_{but}	0.01	0.1	1.0
Case A ($h_{but}=90$ m)	1.7	2.5	4.4
Case B ($h_{but}=110$ m)	6.6	12.5	17.9

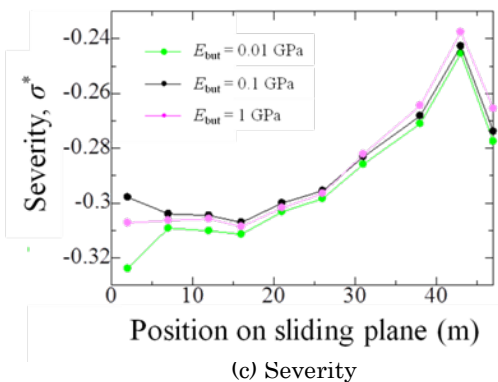
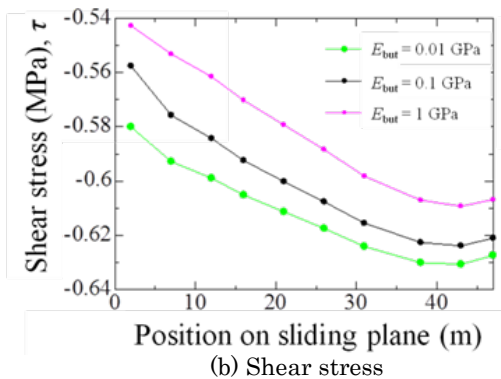
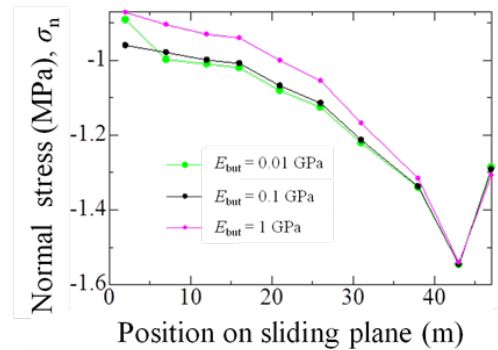


Figure 9: Comparison of stress state on sliding plane after applying buttress with different E_{but} (Case A).

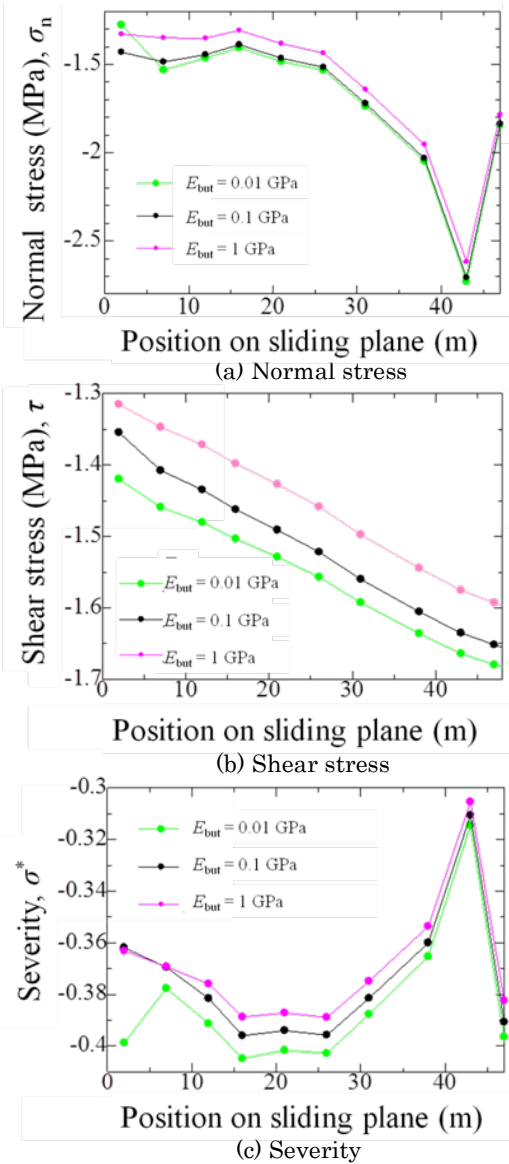


Figure 10: Comparison of stress state on sliding plane after applying buttress with different E_{but} (Case B).

decreased and t_{life} extended. A similar explanation can be made for the results of case B.

From the above discussion, in the case of fixed h_{but} , it is preferable to apply stiffer rock buttress using such cement in order to effectively extend t_{life} .

4. CONCLUSIONS

In this study, non-linear time-dependent sliding deformation of rock slope along the sliding plane was analyzed by 2-D FEM, and the effect of rock buttress on reduction of the rock slope sliding was discussed.

The obtained knowledge is summarized below:

- The deterioration of sliding plane at the time when rock buttress was applied significantly affected the expected life of rock slope.
- The optimum height of rock buttress was found to exist.
- Stiffer rock buttress with larger Young's modulus resulted in the longer expected life of the rock slope.
- The balance of increase and decrease of normal and shear stresses on sliding plane by buttress is important, and the obtained results can be changed by the difference of friction angle and the geometry of the sliding plane.

5. REFERENCES

- Nakamura, N., Tsukayama, Y., Hirata, A. and Kaneko, K., (2003), Displacement Measurement of Rock Slope with Cover Rock and its Interpretation, J. MMIJ, Vol. 119, pp. 547-552 (in Japanese with English abstract)
- Obara, Y., Nakamura, N., Kang, S. S. and Kaneko, K. (2000), Measurement of local stress and estimation of regional stress associated with stability assessment of an open-pit rock slope, Int. J. Rock. Mech. Min. Sci., 37, pp. 1211-1221
- Okubo, S. (1992), Analytical Consideration of Constitutive Equation of Variable Compliance Type, J. MMIJ, Vol. 108, pp. 601-606 (in Japanese with English abstract)
- Pande, G. N. and Sharma, K. G. (1979), On joint/interface elements and associated problems of numerical ill-conditioning Int. J. Numer. Anal. Meth. Geomech, Vol. 3, pp. 293-300

Validation of empirical rock mass classification systems for rock slopes

Hassan Basahel*, Hani Mitri

Department of Mining and Material Engineering, McGill University, Montreal, Canada, H3A 0E8.

ABSTRACT

Many classification systems have been proposed in the literature to identify the state of stability of rock slopes. Most of these classification systems involve factors relevant to the general condition of the rock mass, for example, intact rock strength (UCS), geometry and condition of discontinuities, and groundwater condition. Such factors represent the basic part of most of the classification systems, which refer to the well-known Bieniawski's Rock Mass Rating or RMR system. However, these factors were initially developed for underground excavations. Therefore, these classification systems have been subjected to many criticisms and were questioned for their suitability for rock slopes.

In this paper, some of the common classification systems for rock slopes are used to identify their suitability for rock cuts. Twenty two sites of rock cuts in mountainous roads affected by heavy rainfall in the southwestern part of Saudi Arabia have been selected as case studies, and four empirical methods are examined for these case studies. The selected methods are Slope Mass Rating or SMR (Romana, 1985), continuous SMR (Tomás, 2007), Chinese SMR (Chen, 1995), and a graphical SMR (Romana, 2012). The stability conditions for each site have been determined by each of these methods and a comparison between the results is made for the case of plane failure mode. It is shown that some of the empirical methods are not applicable such as Chinese SMR (for slopes less than 80 m high), and the graphical SMR method when the slope angle is more than 80°.

KEYWORDS: Empirical methods; SMR; graphical SMR; continuous SMR

1. INTRODUCTION

Rock slope failure is one of the most common problems in roads, highways, and railways constructed in mountainous and rugged areas. This has the potential to cause road infrastructure and property damage, injuries, and even fatalities.

Different techniques have been proposed to address rock slope instability. One of these methods is rock mass classification systems (empirical methods) representing an important tool to assess the engineering behaviour of the rock mass. Empirical relations between rock mass properties and the behaviour of the rock mass in relation to a particular engineering application are combined to give a method of designing the rock structure. Over the last few decades the rock mass classification systems have been commonly used to assess the stability of rock slopes and identify those of high risk of instability (Pantelidis, 2009).

Rock mass classification procedures (empirical methods) were initially developed for underground excavations as a means to evaluate discontinuous rock mass. The classification systems were developed primarily empirically by establishing the parameters of importance, giving each parameter a numerical value and a weighting factor. This led, via empirical formulae, to final rating for a rock mass. The final rating is related to the stability of the underground

excavation used for the development of the classification system (Hack et al., 2003).

In this paper, rock mass classification systems are discussed in terms of their suitability and validity for the analysis of rock slope stability. Some of these systems are addressed in this study. These are: Slope Mass Rating or SMR (Romana, 1985), Chinese Slope Mass Rating (Chen, 1995), Continuous Slope Mass Rating (Tomás, 2007), Graphical Slope Mass Rating (Tomás, 2012).

Twenty two sites have been selected in the southern-west of Saudi Arabia (Figure 1), in order to examine these four classification systems for their suitability and applicability to rock slope stability assessment. These empirical methods are discussed in the following section.

2. CLASSIFICATION SYSTEMS FOR ROCK SLOPE ASSESSMENT

A number of classification systems have been adopted for assessing the rock mass and the stability conditions of rock slopes. These classification systems are described below. The Rock Mass Rating (RMR) system developed by Bieniawski (1973-1989) is considered the basis of all empirical systems. RMR system was first developed to analyze the rock mass condition in tunnels; it was later modified to analyze slopes and foundations. The RMR value is computed

*Corresponding author – hassan.basahel@mail.mcgill.ca

by adding ratings values of five parameters according to Bieniawski (1989). These are: 1) Strength of intact rock, 2) Rock quality designation (RQD), 3) Spacing of discontinuities, 4) Condition of discontinuities, and 5) Water inflow through discontinuities. These five parameters represent the basic RMR. Bieniawski added a parameter in 1979 to the basic RMR system as an adjustment for discontinuity orientation (Aksoy, 2008). The adjustment parameter for discontinuity orientation was derived for tunnels and dam foundations but not for slopes. Bieniawski (1989) recommended the use of Slope Mass Rating (Romana, 1985), for determining the value of the discontinuity orientation. The RMR system gives a value which ranges between 0 and 100.

2.1 Slope Mass Rating (SMR)

Slope Mass Rating system was proposed by Romana in 1985 as a tool for the preliminary assessment of slope stability. SMR system provides a number of simple rules about the instability modes and required support measures. SMR classification is based on the Rock Mass Rating by Bieniawski (1979). Two kinds of structural failure modes are considered in this classification. These are planar and toppling failures.

The SMR value is obtained from the basic RMR score (ignoring the discontinuity orientation factor from RMR) by subtracting a factorial adjustment factors depending on the joint-slope relationship and adding a factor depending on the method of excavation as expressed in the following equation:

$$SMR = RMR_{basic} + (F_1 \times F_2 \times F_3) + F_4 \quad (1)$$

In the above, RMR is the basic score of the rock mass rating. F1 is an adjustment factor, which depends on parallelism between joints and slope face strike. It ranges from 1 when near parallel, to 0.15 when angle between strikes is 30 degree (Table 1). F2 is an adjustment factor that refers to joint dip angle in the planar mode of failure. It varies from 1 for joints dipping more than 45° to 0.15 for joints dipping less than 20°. F3 is an adjustment factor that reflects the relationship between the slope face and joint dip. F3 ranges from 0 when the angle is more than 10 degree "Very favorable", to -60 when the angle is less than -10 degree "Very Unfavorable". F4 is an adjustment factor that depends on the method of excavation. The values are selected empirically as follows:

1) Natural slope "more stable" F4=+15, 2) Pre-splitting F4=+10, 3) Smooth blasting F4= +8, 4) Normal blasting F4=0. 5. Deficient blasting "damage stability" F4= -8.

The SMR classification was modified by Anbalagan et al. (1992), where the wedge failure was added to the system. Both planar and wedge failures

are considered as different cases in the modified SMR, but in this paper this modified SMR will not be discussed and only the plane failure will be addressed.

2.2 Chinese Slope Mass Rating (CSMR)

The Chinese slope mass rating (CSMR) was proposed by Chen in 1995, where two coefficients were added to the Romana's system (SMR). These two coefficients are the slope height factor (ζ), and the discontinuity factor (λ), as shown in the following equation.

$$CSMR = (\zeta \times RMR_{basic}) + [\lambda \times F_1 \times F_2 \times F_3 + F_4] \quad (2)$$

ζ can be defined from the following relationship

$$\zeta = 0.57 + 0.43 \times \frac{80}{H} \quad (3)$$

H is the slope height in meter

λ is based on the discontinuity type as follows:

$\lambda=1$ for faults, long weak seams filled with clay

= 0.8 to 0.9 for bedding planes, large scale joints with gauge, and

= 0.7 for joints, tightly interlocked bedding planes.

Regarding the slope height the Chinese slope mass rating is applicable for slope height more than 80m and any slope equal to 80m or below the equation will be used without the factor of slope height.

2.3 Continuous Slope Mass Rating (CoSMR)

This system uses a continuous function for SMR adjustment factors. It was proposed by Tomás et al. (2007). In this system continuous functions for F1, F2, and F3 correction parameters have been developed.

The proposed F1, F2, and F3 continuous functions that best fit discrete values of Romana's system are expressed as:

$$F_1 = \frac{16}{25} - \frac{3}{500} \arctan\left(\frac{1}{10}(|A| - 17)\right) \quad (4)$$

$$|A| = |\alpha_j - \alpha_s| \text{ for planar failure}$$

$$= |\alpha_j - \alpha_s - 180| \text{ for toppling failure}$$

$$= |\alpha_i - \alpha_s| \text{ for wedge failure}$$

Where α_j , α_s and α_i are the joint dip direction, slope dip direction, and the trend of the line of intersection of two planes.

$$F_2 = \frac{9}{16} + \frac{1}{195} \arctan\left(\frac{17}{100}B - 5\right) \quad (5)$$

Where B is the dip angle of the joint for planar and toppling failure modes (β_j), and the plunge of the line of intersection of two planes for wedge failure mode (β_i).

B is arctangent function expressed in degree.

$$F_3 = -30 + \frac{1}{3} \arctan C \quad (6)$$

The relationship (6) is used for slopes with planar and wedge failures.

$$F_3 = -13 - \frac{1}{7} \arctan(C - 120) \dots (7)$$

The relationship (7) is used for slopes with toppling failure.

Where C is the absolute difference in angle between the joint dip and slope dip in case of planar failure mode $|\beta_j - \beta_s|$, and between the plunge of the line of intersection of two planes and the dip of the slope $|\beta_i - \beta_s|$ for the wedge failure mode, and the sum of the two dip angles of the joint and slope for the mode of toppling failure $|\beta_j + \beta_s|$.

2.4 Graphical Slope Mass Rating (GSMR)

A graphical method was proposed by Tomás et al. (2012), where he designed new Stereo plots based on the planar, wedge, and toppling failures to determine the rating values of the slope mass rating correction factors. The two correction factors for joint direction and dip; F1 and F2, respectively, are grouped in one term (ψ). The projection of great circles for main joint sets, as well as the slope face are laid on these proposed stereo plots in accordance with the type of failure. Subsequently, the rating values of F1, F2, and F3 are determined for each kind of failure. Then the equation of the SMR is as follows:

$$SMR = RMR_{basic} + (\psi \times F_3) + F_4 \dots (8)$$

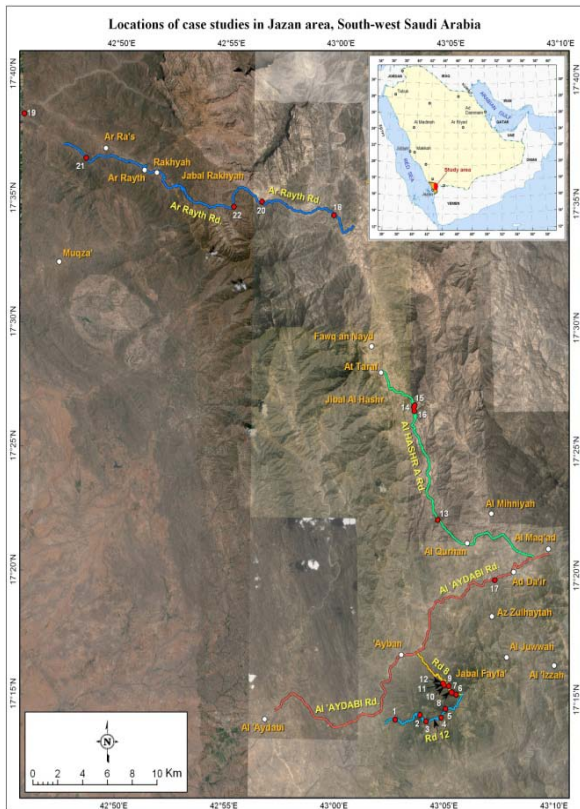


Figure 1: Locations of case studies in Saudi Arabia.

3. LOCATION OF THE STUDY AREA

The study area is located in Jazan region in the south-western part of Saudi Arabia (Figure 1). It is located between Lat. 16° and 18° N, and long between 42° and 44° E.

Twenty-two sites of rock cuts along the mountainous roads in the study area have been selected. These case studies were chosen on the basis of slopes with structurally controlled failure (Figure 2), slopes with stress-controlled failure (Figure 3), and stable slopes. A field trip has been done to identify these sites and collect necessary geological and geotechnical data from each site.

These sites are distributed as follows: Five sites along road 12, seven sites on road 8, four sites on Al Hasher road and five sites along Al Raith road and 1 site on Al 'Aydabi road (Figure 1).



Figure 2: Site #1 along road 12 represents an example of structurally controlled failure.



Figure 3: Site # 21 on Al-Raith road exposed to failure due to stress controlled factor (completely weathered).

4. DISCUSSION OF RESULTS

The results of the RMR-system indicate that the rock cuts sites (1, 2, 3, 4, 5, 6, 10, 14, 16, 17, and 18) have RMR values between 41 and 57 and are classified as fair. While, four locations (7, 11, 12, 13) have RMR values between 63 and 79 and are

classified as good. One site which is 18 gave poor rock quality with RMR value of 37.

The RMR system was not applied in some sites such as 8, 9, 15, 20 and 21 because the degree of weathering is high (completely weathered), so the discontinuities are not well-defined and their properties could not be assigned. Also, the failure behaviour of these locations is most likely to be non-structurally controlled; discontinuities do not contribute to the occurrence of the failure, thus, the slope's instability could be affected by water and/or seismic forces (stress controlled failure).

The four rock mass classification systems are applied for only the structurally controlled sites. In this paper, planar failure mode has only been addressed for all these classification systems analyses. SMR (Romana, 1985) results for rock cuts indicate that all scores are below 50 and categorized from partially stable to unstable in conservative case (no limit range between the strike direction of slope face and joints). While, the SMR values will be decreased until less than 15 when the strikes difference between the slope face and the joint be around ± 20 , and the rock cuts will be categorized completely unstable (Table 1).

The Chinese SMR system is applied to the case studies without slope height factor as the heights of all sites are less than 50 m, and only the discontinuity factor (λ) has remained in the Chinese SMR equation. However, the results of this method show a significant increase in the SMR values than in Romana's system (Table 1). The reason for this increase is likely due to the low values of the discontinuity factor for most rock cuts with average value of 0.7. This means tight joints (high cohesion), which leads to increased SMR values and thus an increase in the degree of the stability condition.

The results of the continuous SMR (Table 1) indicated that the range of SMR values are between 29 to 46, and it can be observed that the results of this method are in a reasonable range, where there are no abnormal values as found in the discrete SMR by Romana, where some values are below 10 as in sites 1, 4, 10.1 and 22. Therefore, the continuous functions for the corrections F1, F2 and F3 gave some kind of reality to SMR scores.

The graphical SMR method results (Table 1) indicate that there are no differences between this system and Romana's system results. The reason for these similarities in the results probably due to the concept used in the graphical system was the same of the original SMR (Romana, 1985), which is the discrete rating for the correction factors of F1, F2, and F3, but the difference was in the method of application by using the stereo plots to determine these correction factors.

There are some difficulties in application of the graphical method especially in adjustment factor (F3), when the slope face angle is equal to or more than 80° , which makes the application of graphical method impossible, such as in sites 6, 7.2, and 10.2.

5. CONCLUSION

Four empirical methods, SMR (Romana, 1985), Chinese SMR (Chen, 1995), Continuous SMR (Tomas, 2007) and Graphical SMR (Tomas, 2012) are applied to twenty-two sites of rock cuts located in a rugged area along mountainous roads in the southwestern part of Kingdom of Saudi Arabia.

The main purpose of this study is to validate these classification methods, and compare their results for assessment the stability conditions of the rock cuts.

All these methods take into account condition of the rock mass presented by RMR system, and the relationship between the dip and the direction of slope face and joints which presented by the correction factors of F1, F2, and F3, as well as the effect of the method of excavation (F4).

The results of discrete SMR (Romana, 1985) give varying scores for SMR and not in tight range where in some locations the values are underestimated.

Chinese SMR adds two factors to the original SMR formula, slope height factor and discontinuity factor, but in this study the factor for slope height has been eliminated, as the slope height for all case studies is below 80m. Although, the discontinuity factor has enhanced the SMR values, but the factor of slope height makes this method not applicable in a correct manner in rock cuts below 80m, as the height will be ineffective.

The continuous SMR system results showed no large difference among the scores unlike the discrete SMR by Romana because new continuous functions have been proposed in this method for adjustment factors F1, F2, F3 calculations rather than the discrete function in Romana's system.

The graphical SMR system has also been used in this analysis, and it has been observed that the results of this method have almost the same results of Romana's system as both of them using the discrete method to determine the correction factors of the relation between the slope face and the joints.

In conclusion, the continuous SMR that is proposed by Tomas (2007) is closest to the reality from the other methods. Also if the continuous RMR (Sen and Sadagah, 2002) used rather than the discrete RMR (Bieniawski, 1989), this may lead to enhance

Table 1: Results of the four empirical methods in case of plane failure mode for structural failure sites.

Site No.	Slope face	Joint	SMR ₍₁₉₈₅₎	CSMR ₍₁₉₉₅₎	CoSMR ₍₂₀₀₇₎	GSMR ₍₂₀₁₂₎	Field observations
1	60/040	51/040	7	22	46	7	MW, slope height 18m
2	69/014	46/341	31	34	29	31	MW, slope height 19m
3	77/055	40/095	35	38	32	35	MW, slope height 15m
4	60/269	55/283	9	12	33	9	MW, slope height 8m
5	78/020	No (P)	-	-	-	-	MW, slope height 19m
6	80/026	No (P)	-	-	-	N/A	MW, slope height 11m
7	1	70/190	62/195	13	26	45	SW, slope height 18m
		58/244	47	50	46		
	2	80/010	70/050	48	51	45	N/A
8	Soil-rock slope (completely weathered)						Slope height 13m

Table 1: Continued.

Site No.	Slope face	Joint	SMR ₍₁₉₈₅₎	CSMR ₍₁₉₉₅₎	CoSMR ₍₂₀₀₇₎	GSMR ₍₂₀₁₂₎	Field observations	
9	Soil-rock slope (completely weathered)						Slope height 13m	
10	1	70/285	40/275	4	4	36	MW, slope height 30m	
		40/275	38	4	36	N/A		
	2	88/285	77/239	38	38	36	N/A	
11	76/320	No (P)	-	-	-	-	MW, slope height 10m	
12	70/250	No (P)	-	-	-	-	MW, slope height 8m	
13	1	67/030	66/015	20	30	45	MW, slope height 18m	
			34/080	47	50	45		48
	2	74/023	66/015	12	25	46		12
			34/080	48	51	44		48
14	66/095	44/059	38	41	22	38	MW, slope height 22m	
15	Soil-rock slope (completely weathered)						Slope height 26m	
16	70/130	40/074	36	38	33	36	MW, slope height 33m	
17	76/154	44/102	44	47	41	44	MW, slope height 23m	
		64/186	43	46	42	43		
18	1	65/070	No (P)	-	-	-	HW, slope height 15m	
	2	66/057	No (P)	-	-	-		
	3	74/008	70/008	41	44	38		41
19	74/190	55/209	3	16	34	3	HW, slope height 36m	
		60/225	36	39	34	36		
20	Soil-rock slope (completely weathered)						Slope height 11m	
21	Soil-rock slope (completely weathered)						Slope height 28m	
22	65/140	50/154	8	20	39	8	MW, slope height 29m	

(P) Planar failure. (SW) Slightly weathered. (MW) Moderately weathered. (HW) Highly weathered.

the SMR values and unique scores for SMR will be assigned to the rock cuts (Tomás et al. 2007).

These empirical methods are suitable only with structurally controlled slopes, and for non-structurally controlled slopes (highly weathered slopes) will be difficult to apply as the structures features are not well-defined, and the stress control factors will be unknown (i.e. water pressure and seismic force).

6. ACKNOWLEDGMENT

The authors are very grateful to Saudi Geological Survey for their technical support by provided the field data and all technical information and unlimited support throughout the progress of this work.

7. REFERENCES

- Anbalagan, R., Sharma, S., Raghuvanshi, T.K.. (1992). Rock mass stability evaluation using modified SMR approach. In: Jha, P.C. (Ed.), Rock Mechanics Proceedings of the Sixth National Symposium on Rock Mechanics, pp. 258–268.
- Aksoy, C. (2008). Review of Rock Mass Rating Classification: Historical Developments and Applications and Restrictions. Journal of Mining Science, Vol. 44, No. 1.
- Bieniawski ZT. (1979). The Geomechanical Classification in Rock Engineering Applications, Proceedings of 4th International Congress on Rock Mechanics, International Society for Rock Mechanics, Salzburg, Vol. 2, pp. 41-48.
- Bieniawski ZT. (1989). Engineering rock mass classifications. New York: Wiley, 251pp.

Chen, Z. (1995). Recent developments in slope stability analysis. In: Fujii, T. (Ed.), Keynote Lecture: Proc. 8th Int. Cong. Rock Mech, vol. 3, pp. 1041–1048.

Hack R, Price D, Rengers N. (2003). A new approach to rock slope stability-a probability classification (SSPC). Bull Eng Geol Environ 62:167-84.

Pantelidis, L. (2009). Rock slope stability assessment through rock mass classification systems. Int J Rock Mech Min Sci 46(2):315–325.

Romana, M. (1985). New adjustment ratings for application of Bieniawski classification to slopes. In Proc. Int. Symp. On the Role of Rock Mech., pp 49-53. Zacatecas.

Tomás, R., Delgado, J., Serón, J.B. (2007). Modification of slope mass rating (SMR) by continuous functions. International Journal of Rock Mechanics and Mining Sciences 44,1062–1069.

Tomás,R., Cuenca,M., Cano,J., Gárc -Barbra. A. (2012). A graphical Approach for Slope Mass Rating (SMR). Engineering Geology, vol.124.67-76.

Application of InSAR for monitoring deformations at the Kiirunavaara Mine

Karola Mäkitaavola ^a, Britt-Mari Stöckel ^a, Jonny Sjöberg ^{b,*}, Stephen Hobbs ^c, Jonas Ekman ^d, Michael Henschel ^e, Anura Wickramanayake ^f

^a Luossavaara Kiirunavaara Aktiebolag, LKAB, Kiruna, Sweden, SE-981 86

^b Itasca Consultants AB, Luleå, Sweden, SE-977 75

^c Cranfield Space Research Centre, Cranfield University, Cranfield, United Kingdom, MK43 0AL

^d Department of Computer Science, Electrical and Space Engineering, Luleå University of Technology, Sweden, SE-971 87

^e MDA Geospatial Services, Ottawa, Canada, K2E 8B2

^f Self-employed

ABSTRACT

An integral part of sublevel cave underground mining is the associated caving of the surrounding host rock. This causes mining-induced ground surface deformations on both the hangingwall and footwall side of the orebody. The municipality of Kiruna, in northern Sweden, is located in close proximity to the LKAB Kiirunavaara mine and is thus unavoidably affected by the mining activities. To be able to plan for an urban transformation, as the effects of mining approach the city infrastructure, it is necessary to monitor the ground deformations on a regular basis. Historically, GPS-monitoring has been used, with an extensive network of measurement hubs in place. New techniques for monitoring ground deformations are, however, constantly evaluated. As part of this process, LKAB has conducted a five-year research and development project on deformation measurements using radar satellites and the InSAR technology. The project has included a monitoring component and a research- and technology transfer component. The overall findings of the monitoring program, and the associated research and development work are presented. Particular emphasis is put on achieved accuracy and the implications for the ability to reliably monitor the progressing deformations toward the municipality and existing infrastructure. Lessons learnt from the conducted work are presented, followed by recommendations on future use of InSAR for this type of application.

KEYWORDS: Sublevel caving; mining-induced deformations; DInSAR; CTM; CR

1. INTRODUCTION

1.1 Background

It is an undisputable fact that sublevel cave mining results in ground deformations, in particular on the hangingwall side of the orebody, but to some extent also on the footwall side. The deformations are categorized into continuous deformations, not causing fracturing and/or damage, and discontinuous deformations, in which fracturing and caving develops (Figure 1). In the long-term perspective, it is not possible to have any residential buildings or infrastructure within the fracture zone and cave zone.

The Kiirunavaara mine, in northern Sweden, is an iron ore mine owned and operated by the Luossavaara-Kiirunavaara Aktiebolag (LKAB) mining company. The mine is currently exclusively mined underground using large-scale sublevel caving. Annual production amounts to 28 million metric tons of crude ore.

The municipality of Kiruna is located in close proximity to the mine and thus subject to a process of "urban transformation", as the effects of mining

approach the city infrastructure. Monitoring of ground deformations on a regular basis is necessary to be able to plan for this urban transformation accordingly.

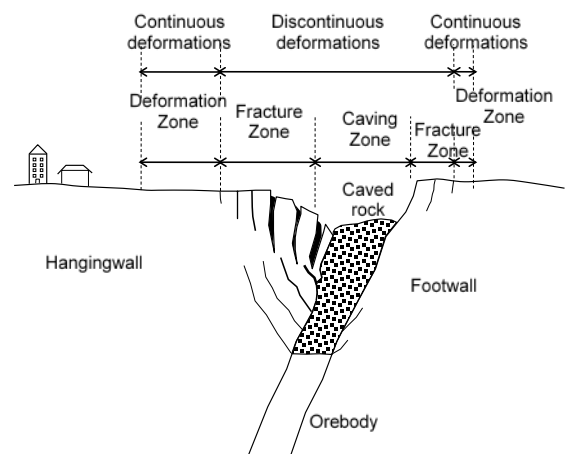


Figure 1: Mine-induced fracturing and deformations on the hangingwall and footwall in sublevel cave mining (schematic, not to scale).

GPS-monitoring is used in Kiruna for this purpose, with a measurement network presently (fall of 2015) comprising 372 hubs. Readings are taken four times per year. The allowable mining-induced ground deformations in Kiruna are regulated through a ruling in the Environmental Court in Sweden. The "environmental criterion" states that the ground outside the mining industrial area cannot be affected by more 0.3 % strain (horizontally) and 0.2 % tilt (vertically), illustrated schematically in Figure 2.

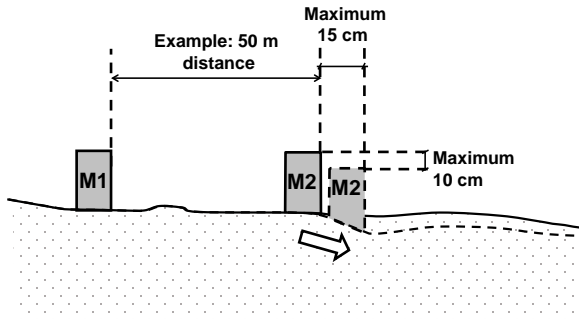


Figure 2: The environmental criterion for allowable mining-induced ground deformations, illustrated for a hub-to-hub distance of 50 m.

Results from the GPS measurements are generally satisfactory and used for establishing the limits of the environmental criterion per the above. However, the work load associated with these measurements is fairly extensive. Moreover, GPS measurements require installations of measurement hubs, with additional hubs required as the area of mining-induced ground deformation increases as a result of mining at larger depths. New and alternative techniques for ground deformation monitoring are thus constantly being evaluated to fulfill the needs of LKAB.

1.2 Work Description

In 2009, LKAB initiated a five-year research and development project on deformation measurements using radar satellite techniques, so-called InSAR technology. The aim of the project was to investigate the application of InSAR for measuring mining-induced ground deformations, to possibly reach the same, or better, measurement precision as in GPS measurements. The project objectives were to:

- Assess the use InSAR technology for LKAB's purposes — as a replacement and/or complement to current GPS measurements.
- Further develop the InSAR technology for winter conditions in high latitudes, aiming at improving precision.

- Conduct a technology transfer to LKAB with the goal of LKAB being able to produce results (deformation maps) in-house from satellite data.

The project was divided into two major components: (i) monitoring, and (ii) research and technology transfer, as shown in Figure 3. The monitoring work was carried out by MDA Geospatial Services, using data from the RADARSAT-2 satellite. MDA also provided technology transfer from MDA to LKAB. The supplementary research work involved Cranfield University and Luleå University of Technology as research partners. The work was conducted in the form of a doctoral thesis project. In addition, supplementary graduate student projects were carried out at both universities.

The overall research objective was to seek to improve the precision in InSAR-measurements for the conditions at the Kiruna site, i.e., at high latitudes and with snow cover during a large portion of the year. The research work was monitored through a reference- and steering group with representatives from both universities and from LKAB.

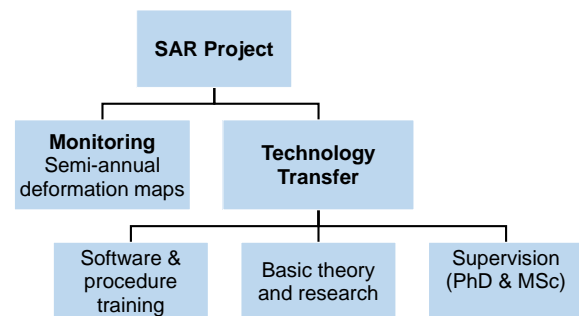


Figure 3: Components of the LKAB InSAR project.

2. MONITORING PROGRAM AND RESEARCH RESULTS

2.1 Historical Analysis

Initially, a historic analysis of InSAR data collected over the time period of 1992 to 2009, was conducted. The data analyzed was from the ERS and ENVISAT satellites, collected from three separate tracks in 74 images. The study was aimed at quantifying the historical ground deformation in the vicinity of the Kiruna mine operations.

A total of 30 deformation maps were created. The recorded deformation pattern was generally as expected, and with the best results obtained for the waste rock dump areas, which provided high coherence between image pairs. The large gaps in the time series of data, and the (relatively) low number of usable image pairs precluded an analysis of so-called

"hard targets", or CTM (Coherent Target Monitoring) from these satellites. The work showed, however, that CTM analysis using RADARSAT-2 using a continuous time series during the remainder of the project would likely be successful. The existing infrastructure in the town of Kiruna and the industrial area would provide excellent sources of persistent scatterers year round. Thus, data from 2008 and 2009 from RADARSAT-2 were included in the first deliverable from the monitoring program.

2.2 Monitoring Program

Monitoring of ground deformations was conducted during the period of 2009 to 2014, by MDA Geospatial Services, Inc. Data was obtained from the RADARSAT-2 satellite, with a return period of 24 days. The monitoring program involved using differential InSAR (DInSAR), coherent target monitoring (CTM), persistent InSAR technique (PSInSAR), and supplementary Corner Reflectors (CR) in areas where there were little or no natural or artificial backscatters. A total of 60 corner reflectors (two at each installation point) were initially installed in the Kiruna area, with 6 more reflectors added later, see Figure 4.

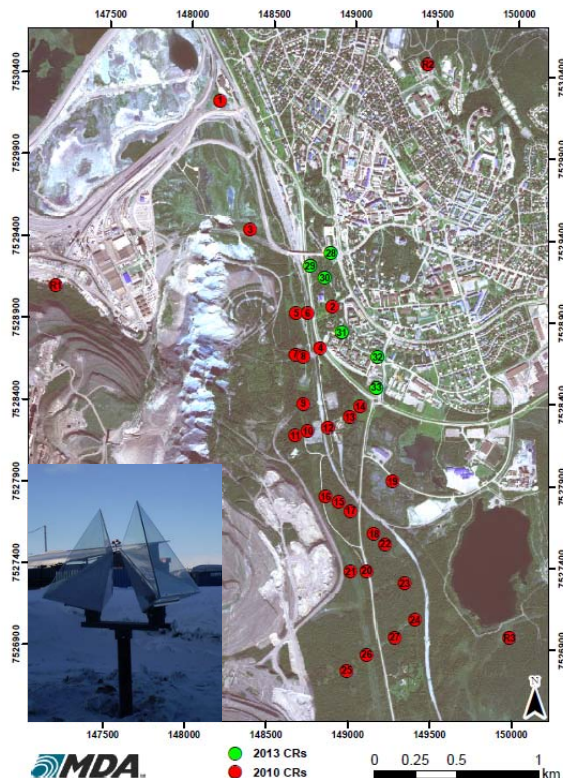


Figure 4: Corner reflectors (CR; see inset) installed in the Kiruna area.

Satellite data is collected for different beam modes, with different incident and aspect angles. Early on, it was found that accuracy in the north-south direction was not satisfactory, primarily due to the polar orbit of (all) satellites (traveling in a nearly north/south orientation). Thus, "line-of-sight", measurements and decompositions into east-west and vertical deformations were more reliable. The final beam combination used for the larger part of the project was U6D, U25A, and U70D.

2.3 Accuracy Assessment

By comparing two independent 3D decompositions, uncertainties in the east/west, vertical, and north/south deformation motion of CRs were found to be 2 mm, 14 mm, and 91 mm, respectively. For the CTM targets, these uncertainties were found to increase slightly to 4 mm, 17 mm, and 113 mm. Uncertainties are minimized for directions with a close to orthogonal basis but the north/south deformation measurement remain poorly constrained.

By considering a 2D decomposition for motion in the east/west (horizontal) and vertical directions, the precision could be further improved, see also Henschel et al. (2015). For a preferred set of 2D decompositions (among a large number tested), the uncertainty in the CR measurements was found to be approximately 2 mm in both the east/west and vertical directions. For the CTM, these uncertainties increase slightly to 4 mm and 3 mm in the east/west and vertical directions respectively.

Thus, by using dual beam coverage, the horizontal east-west and vertical deformation is captured with good precision. The method was applied to all data for the Kiruna site, with previously collected data re-analyzed in the final deliverable.

2.4 Monitoring Data

The data were compiled, analyzed and interpreted, and results then delivered to LKAB every six months, covering the time period from November 2009 to October 2014. The deliverables included: (i) RADARSAT-2 imagery for each beam mode used, (ii) conventional deformation maps, and (iii) time series profiles of individual point targets (including both CR and CTM). Continuous improvements were made for the deliverables during the project.

The CTM results were based on 250,000 points (between the individual beams), and the data was then subsampled to 25 x 25 m cells before the beam combinations were performed. The collocation of available points in each beam resulted in a total of 23,850 points for the motion estimation.

The delivered deformation maps were used to assess overall trends in the data. Moreover, time series plots were created for selected CTM points that

were deemed of particular interest for LKAB, and thus subject to more detailed interpretation.

2.5 Comparison with GPS Data

An example of a time series plot for CR targets is shown in Figure 5. Ground deformations from GPS measurements are plotted for comparison, also for the E-W deformation. The GPS data are accumulated deformations from a starting date as close as possible to the start data of the InSAR measurements. The precision in the GPS measurements has been estimated to 7 mm in the horizontal direction (through a repeatability test).

These examples indicate that both the trends and magnitudes of ground deformation are similar for the InSAR and GPS measurements, which lend some reliability to the InSAR data. Additional work should, nevertheless, be undertaken to confirm these findings for other areas and other CRs.

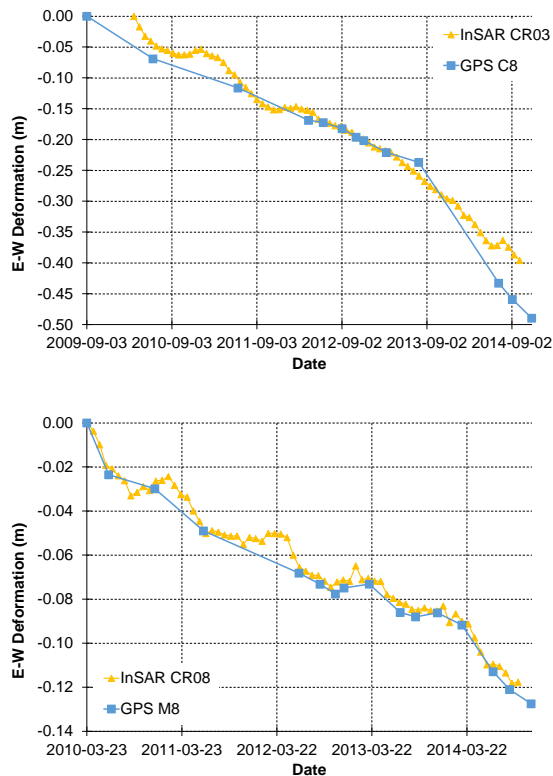


Figure 5: Cumulative deformation measurement for CR03 and CR08, compared with GPS data from nearby points C8 and M8, in the east-west direction.

A different methodology was used by Wickramanayake et al. (2015), in which the GPS-data were first re-calculated to line-of-sight direction to enable more accurate comparison. All calculations were done for the U6D beam model. In addition to using sequential interferograms (interferograms that have the shortest temporal baseline) to extract the CR

deformation measurements, the so-called "small baseline subset" (SBS) technique was also used. With this technique, different subsets of interferograms are linked together to extract the complete deformation time series. Two sets of SBS techniques were employed — one in which all interferograms were used, and one in which only interferograms with a high average coherence (threshold set at 0.25) were utilized, essentially meaning that several winter image pairs were discarded.

An example of the results is shown in Figure 6. The difference between GPS and InSAR CR data is large for two of the applied analysis techniques, whereas a relatively good agreement is found when the InSAR data was extracted using only high average coherence interferograms (CR-InSAR-SBAS-COR). The mean error compared to the GPS measurements is 1.1 mm with 10.7 mm standard deviation, and the correlation coefficient is 0.88.

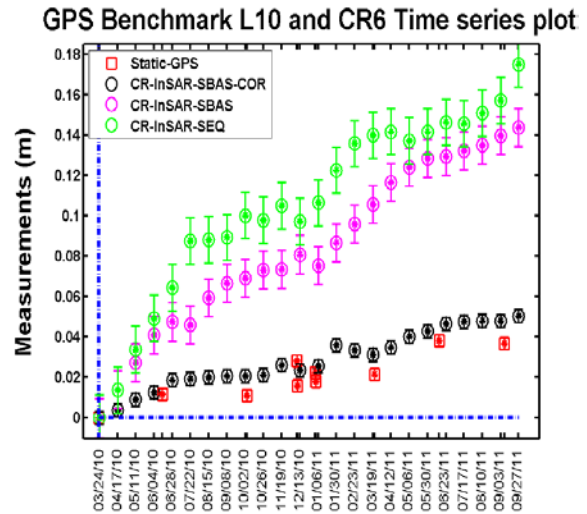


Figure 6: Time series plots of double difference CRInSAR measurements (CR6) and double difference Static-GPS measurements (L10) for different InSAR analysis techniques.

The large difference between the CR-InSAR-SBAS-COR and CR-InSAR-SBAS in Figure 6 may be because the InSAR winter measurements (due to snow) appear to have larger phase errors than the summer measurements. This additional phase can be reduced by using only those interferograms with higher average spatial coherence values and the SBAS techniques, as described above. There is, however, the risk of losing entire sets of interferograms related to a particular (winter) image when interferograms with low coherence are removed. It should also be pointed out that errors resulting from the ground snow layer and from the

snow layer on top of the corner reflector shield have not been separated. The next step would be to quantify the error contribution from each component.

2.6 Strain Calculations

An important potential application of the InSAR measurements is the ability to assess the location of where the environmental criterion (cf. Section 1.1) is satisfied. The same methodology as used for GPS measurements was applied to the InSAR data, using CR measurements. An example of the calculated strains is shown in Figure 7, together with the corresponding location of the strain limit calculated from GPS measurements.

The agreement between InSAR-derived strains and GPS-derived strains is reasonably good, with the InSAR data generally slightly larger strains. It appears likely that InSAR data can be used for assessing the "environmental criterion". However, more work is required to come up with a robust method for strain calculation, possibly also requiring additional CRs and/or including CTM targets to increase coverage.

2.7 Seasonal Coherence Variation

In the work by Wickramanayake et al. (2016), the degree of spatial coherence was studied to identify the seasonal variation in interferograms. A total of 561 differential interferograms were used, and arranged in three different ways for the analysis, with the first including common master

interferograms (with the summer master image), the second including the sequential interferograms that have the shortest temporal baseline, and the third accounting for all possible combinations of the interferograms (full network of interferograms).

As expected, seasonal variation in spatial coherence due to the ground snow layer in winter was found. Only less than 50% of the available RADARSAT-2 images were suitable for DInSAR deformation measurements. However, there was significant summer-to-summer coherence for some regions even over the course of a few years. The master image should thus be a summer image to achieve high coherence. Even with a longer temporal baseline, the summer-to-summer interferograms for the barren and flat waste rock areas provide almost the same coherence. Forest areas, on the other hand, lose coherence with an increase in the temporal baseline and do not regain it seasonally. A next step would be to study the seasonal variation in coherence in natural or man-made targets/persistent scatterers.

2.8 Technology Transfer

The purpose of the technology transfer was to build up knowledge and know-how within LKAB regarding InSAR-technology. MDA provided LKAB with high-level training for a larger group and more targeted training to a smaller group, including software and hardware tools to be able produce deformation maps independently.

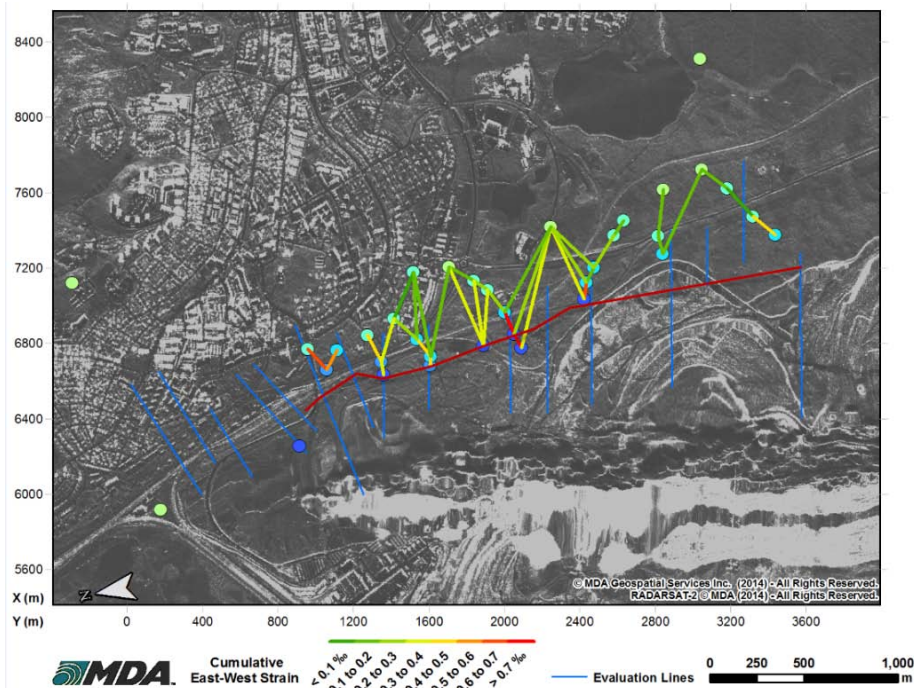


Figure 7: Spatial distribution of CR strain measurements in the east-west direction for the period of March 2010 to April 2014, with green representing low strain and red representing high strain. The environmental criterion limit determined from GPS measurements, corresponding to 0.3 % strain, is shown with a red line.

An "in-house" technology transfer was also accomplished, through regular meetings and training sessions on InSAR processing with LKAB staff. During the course of the project, it became clear that the goal of producing deformation maps independently by LKAB was probably too ambitious. However, the technology transfer ensured that LKAB staff acquired a deeper understanding on InSAR technology, and thus can critically assess results and assumptions made in the analysis.

3. DISCUSSION AND CONCLUSIONS

InSAR-technology allows measurements over large areas, with fewer measurement hubs (CRs) compared to GPS measurements. DInSAR measurements providing deformation maps worked well for identifying trends and patterns in ground deformations. The technique is, however, dependent on achieving high coherence between image pairs, which has proven challenging at the Kiruna site.

Measurements on Corner Reflectors (CR) and "hard targets" (CTM) provided high-precision data for specific points. The CTM measurements are particularly appealing since they do not require installation of reflectors, and were found to work very well in urban environments. A potential problem is the ambiguous phase unwrapping that can arise in cases where deformations between successive satellite passes are large. The project work has shown that by including a large number of measurement points in the analysis, it is possible to reduce the effects of this potential error source, although it cannot be completely eliminated. However, in areas where infrastructure is, or is planned to be removed, due to mining effects, CTM coverage is poor and must likely be supplemented with CR installations.

While the east-west and vertical deformation components can be satisfactorily analyzed, resolving deformations in the north-south direction with an acceptable accuracy was not possible. The improved accuracy obtained through a dual beam acquisition is promising for future work, implying that higher precision can be obtained with fewer beam modes, for east-west and vertical deformations.

Comparison between GPS and InSAR data are important since this provides a tool to "ground truth" the InSAR data at this site. This constitutes an important next stage to further the application of InSAR for the specific tasks of interest for LKAB, particularly for determining the limits to the environmental criterion for allowable deformations.

Coherence effects and whether e.g., certain winter images should be discarded or not from the analysis also warrant further work. A robust methodology must be in place for the data analysis, without risking the loss of important information.

4. RECOMMENDATIONS

The requirements on the possible future use of InSAR in Kiruna should be further defined, including what monitoring and interpretation techniques that are most applicable for these conditions. More work on comparing CR/CTM InSAR data with GPS measurement data should be conducted, to further "ground truth" the InSAR data. The long series of GPS data at Kiruna provide excellent opportunities to "calibrate" InSAR results and minimize e.g., phase and unwrapping errors. This step is also important to determine what methodology should be used for InSAR processing and to what extent images with low coherence can be discarded.

Additional Corner Reflectors should be installed in areas with poor CTM coverage and poor backscatter. These are relatively inexpensive and would supplement the DInSAR and CTM data. The location of CRs should be based on the results from GPS-measurements, and a geomechanical perspective, to increase understanding of the mining-induced ground deformations. Additional CRs would also help in better delineating the location of the environmental criterion strain limit from InSAR data.

5. ACKNOWLEDGEMENTS

The work presented in this paper has been fully funded by LKAB. The authors would like to thank LKAB for permission to publish this paper. We would also like to thank Jimmy Töyrä and Carlos Quinteiro of LKAB for paper review; Wendy Branson (project leader) and Brad Lehrbass of MDA Geospatial Services for excellent cooperation; Stefan Buehler and Tore Lindgren of Luleå University of Technology for academic supervision; Dr. Priya Fernando of EADS Astrium for project support; and Bo Fjällborg and Anders Berg of LKAB.

6. REFERENCES

Henschel, M., Dudley, J., Lehrbass, B., Sato, S. and Stöckel, B-M. (2015). Monitoring slope movements from space with Robust Accuracy Assessment. In Proc. Slope Stability 2015, Cape Town, October 12-14, The Southern African Institute of Mining and Metallurgy, pp. 151-160.

Wickramanayake, A.A.B, Mahapatra, P., Buehler, S.A., Ekman, J., Hobbs, S. and Mendrok, J. (2015). Comparison between Static-GPS and corner reflector InSAR (CR-InSAR) measurements at a high latitude site. Submitted for publication.

Wickramanayake, A.A.B, Henschel, M.D., Hobbs, S., Buehler, S.A., Ekman, J. and Lehrbass, B. (2016). Seasonal variation of coherence in SAR interferograms in Kiruna, Northern Sweden. *International Journal of Remote Sensing*, 37:2, pp. 370-387, DOI: 10.1080/01431161.2014.915435.

Modelling the impact of particle flow on rigid structures: experimental and numerical investigations

M.A. Meguid^a, Ge Gao^b, M.M. Abouelkair^c and M.Z. Abdelrahman^c

^a Associate Professor, Civil Engineering and Applied Mechanics, McGill University, Montreal, Canada, H3A 0C3

^b Graduate student, Civil Engineering and Applied Mechanics, McGill University, Montreal, Canada, H3A 0C3

^c Undergraduate Research Trainee, Civil Engineering and Applied Mechanics, McGill University, Montreal, Canada, H3A 0C3

ABSTRACT

Gravity-driven debris flow of granular particles down an inclined slope is a problem of growing concern in mountainous regions and poses a significant risk to people, roads, and other infrastructure. Different aspects of the problem have been previously investigated using physical modelling and numerical analysis. However, three dimensional pressure distribution on a barrier wall resulting from debris flow over a rough slope is scarce in the literature. In this study, a series of experiments are conducted to track the movement of granular particles down a slope and measure the impact pressure imposed by the flowing particles on a nearby vertical wall. The particles are released from a container located at the top of the slope and the velocity profiles are recorded using marked pebbles and a high-speed camera. The effect of the debris volume, slope angle, and distance to the wall on the velocity profiles and impact forces are investigated. Validated using the experimental results, discrete element simulations are performed using PFC^{3D} to evaluate the effect of particle sizes on the flow characteristics and final impact pressure on the structure. Analysis showed that impact energy is highly affected by the slope inclination, particle velocity, and runout distance.

1. INTRODUCTION

The numerical modelling of granular mass movement under the influence of gravity (e.g. debris flows, avalanches, etc.) has received significant research attention over the past decade. Various methods have been used to investigate the flow-like mass runout behaviour including finite element analysis (Crosta et al., 2002; 2003) and discontinuous deformation analysis (DDA) (Wu, 2010; 2011). The DDA method represents debris flow using sliding blocks and therefore, this method may not be suitable to model the rapid movement of loose particles.

Discrete element method (DEM) was first proposed by Cundall and Strack (1979) and because the method naturally takes discontinuity into account, it has been successfully used to simulate debris flow problems (Li et al., 2012; Liu and Koyi, 2013; Zhao et al., 2015). However, very few studies focused on the three-dimensional analysis of gravel movement over a rough inclined surface considering the dynamic impact of the moving particles on nearby structures. McDowell et al. (2011) and Li et al. (2012) studied the dynamic behaviour of flowing particles using different sizes of four-ball clumps validated using velocity profiles measured in the laboratory. Lo et al. (2010) decomposed fluctuating particle flow velocity filed on rough inclines into best-fit and fluctuating components using three-

dimensional DEM. These studies provided some insight into the effect of surface roughness on the dynamic behaviour of flowing particles, however, the impact of particle flow on nearby protective structures is yet to be fully understood.

In this study, an experimental investigation is conducted to understand the mechanics of debris flow over rough inclines in a controlled laboratory environment. High-speed camera and tactile pressure sensors are used to track particle movement and measure the impact force on a barrier wall, respectively. Discrete element analysis is also performed using walls and spheres to model the laboratory experiment for three different slope angles. Preliminary results are presented and conclusions are made regarding the recorded velocity profile for each slope inclination and the associated displacements as well as stress distribution resulting from the impact of particles on the vertical wall.

2. EXPERIMENTAL PROGRAM

The experiments were performed using river pebbles with an average particle diameter of 5 cm, as shown in Figure 1.



Figure 1: The river pebbles used in the experiments.

The surface of the slope and the horizontal runout section are designed and built using smooth aluminum plates, lined with perforated sheets to create a bumpy (rough) surface. A stiff rubber sheet of 2 mm in thickness is used to simulate the rough surface. The sheet is punched with round holes 5 cm in diameter arranged in a hexagonal pattern at 8 cm center spacing (See Figure 2).

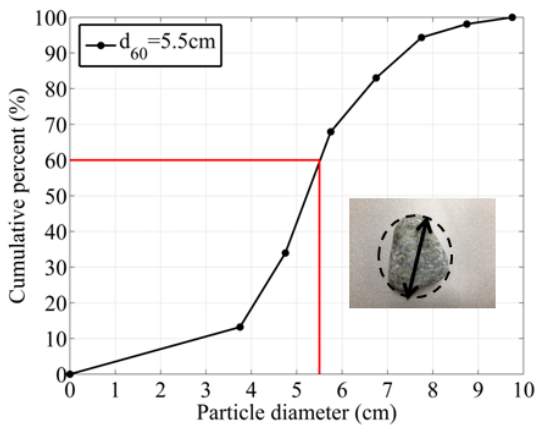


Figure 2: Particle size distribution.

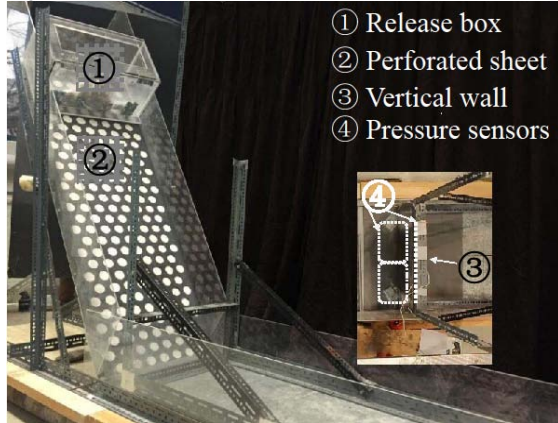


Figure 3: Experimental setup.

2.1 Test Setup

The slope, 1.82 m long and 0.62 m wide has the 0.03 m high Perspex sides so that all activity within it is visible. The slope inclination can be adjusted to cover a range of angles between 0 and 90° to the horizontal. The setup is equipped with a Perspex release box with a hinged door at the top of the slope. During the test, the river pebbles are released through the hinged door and allowed to travel freely down the slope and runout onto a flat base. A high-speed camera (Canon T3i) that can take 30 frames per second at a maximum resolution of 1280 x 720 pixels was used to track the position of the marked pebble.

Two tactile sensing pads with pressure capacity of 20 psi were fixed at the particle landing location and similar pads were fixed directly on the vertical wall. These pads were connected to a data acquisition system to monitor the impact forces on the ground (horizontal plane) and on the wall (vertical plane) as a result particle movement. The layout of these sensors can be seen in Figure 3.

3. DEM SIMULATION

The Discrete element method is known to consider the interaction among distinct particles at their contact points. It is generally a dynamic process that reaches static equilibrium when the internal and external forces are balanced (Tran et al., 2014). The numerical simulations are performed in this study using the discrete element program, PFC^{3D}. A detailed description of the code can be found in the relevant manual (ICG, 2014).

The numerical simulations are carried out as depicted in Figure 4. A discrete element sample that consists of 53 spherical particles is generated to follow the particle size distribution of the material used in the experiment, as shown in Figure 2. Spherical particles are used in this preliminary analysis to reduce computational cost and at the same time capture the mechanical response associated with particle flow. The micromechanical parameters used in the analysis are listed in the Table 1.

The sloped section is simulated using bonded particles arranged in a hexagonal pattern with an average particle diameter of 5.5 cm (see Figure 2). This procedure captures to a reasonable extent the characteristics of the perforated sheet used in the experiment, and reproduces a bumpy surface that allows for the rolling resistance to be automatically considered.

Once the generated particles have reached an equilibrium state in the release box, particle flow is initiated by removing the wall facets of the release box allowing the particles to freely flow down the slope.

A total of 12 particle flow simulations are performed in this study using various slope inclination angles (30°, 45° and 60°) and wall location with respect to the toe of the slope (0 cm, 25 cm, 40 cm, and 60 cm).

The particle friction coefficient was determined using the repose angle test. It is worth noting that friction coefficients that range from 0.37 to 0.5 were used by other authors (e.g. The reference paper written by the McDowell et al., 2011 & Lo et al., 2010).

Table 1: Particle properties used in DEM tests.

Property	Unit	Value
Contact model		Linear (no-tension)
Density	kg/m ³	2620
Effective Modulus	(Pa)	20E8
Stiffness ratio		1.5
Friction coefficient		0.45
Viscous damping ratio		
Normal		0.5
Shear		0.5
Number of particles		53

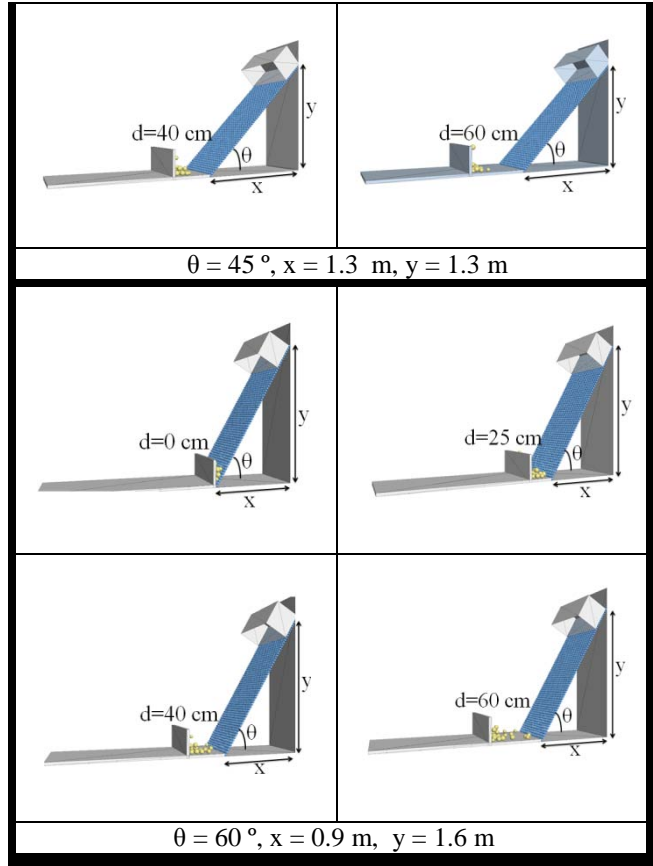
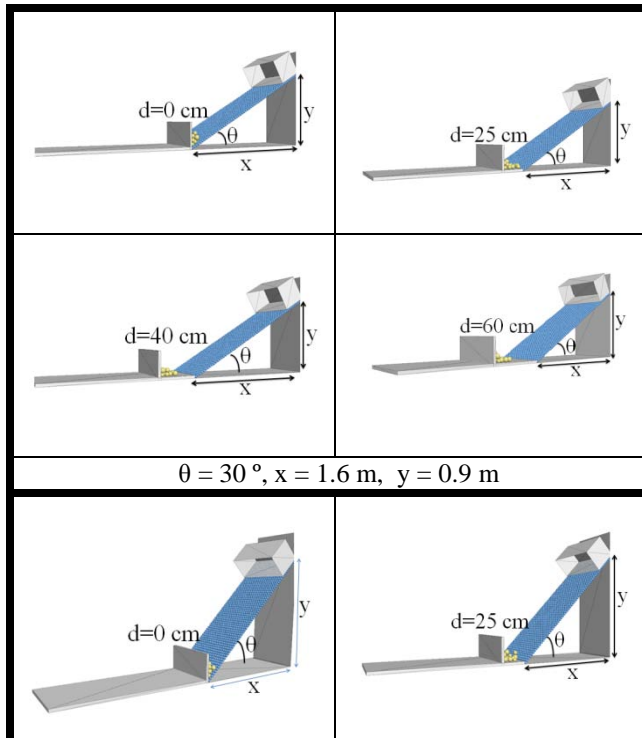


Figure 4: DEM setups of particle flow for different inclination angles and separation distance from the wall.

4. RESULTS

4.1 Particle mobility

The recorded and calculated results for the three investigated slope inclination angles (30°, 45° and 60°) are summarized in this section.

Displacement profiles with time are shown in Figure 5. Results reveal that for a given elapsed time from the beginning of the test, particle displacement increased with the increase in slope inclination. For example, when the elapsed time reached 0.6 sec. particles had moved 0.7 m, 1.2 m, and 1.5 m for slope angles 30°, 45°, and 60°, respectively. In all investigated cases, the rate of change in displacement was found to increase up to a maximum maintained value. The flowing particles started to slow down as they approach the toe of the slope. Calculated displacements are generally found to be in good agreement with the measured values for different inclination angles.

The velocity profiles obtained from the experiments and the DEM simulations are presented in Figure 6. Results show that, the maximum measured velocity increased from 3 m/s to 6 m/s when the slope angle increased from 30° to 60°. The

time required to reach the maximum velocity decreased from about 0.7 seconds to 0.3 seconds when the slope angle increased from 30° to 60°. It was also found that the maximum calculated velocity is slightly smaller compared with the measured one, particularly for a slope angle of 60°. On the other hand, particle acceleration (defined by the slope of the velocity-time relationship) calculated using DE analysis is slightly higher compared with the values measured in the experiments. In addition, a significant deceleration response was calculated (see Figure 6) after the maximum velocity was reached. The difference in acceleration responses between the calculated and measured values can be attributed to the simplified spherical shaped particles used in the analysis.

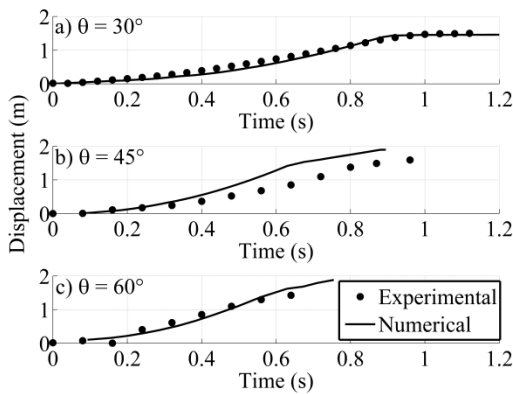


Figure 5: Displacement profiles for different inclination angles with the wall located at the toe of the slope.

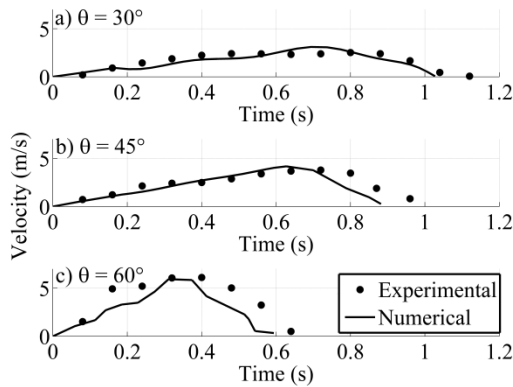


Figure 6: Velocity profiles for different inclination angles with wall located at the toe of the slope.

4.2 Impact pressure onto the vertical wall

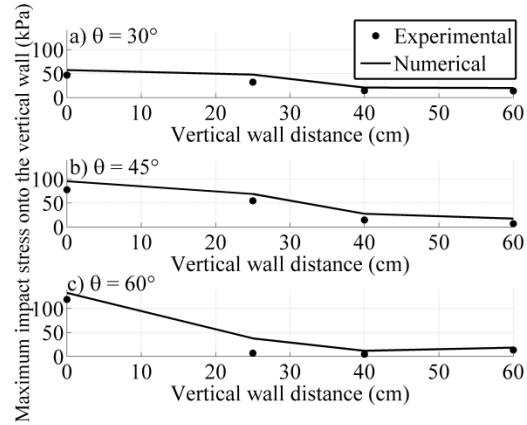


Figure 7: Impact stress onto the vertical wall considering the different conditions.

Figure 7 shows the relationship between the maximum impact stress measured on the vertical wall and the inclination angle of the slope. It can be seen that the location of the vertical wall has a significant impact on the impact pressure. The largest impact pressure was reached at an inclination of 60° and was found to be approximately 35% higher than that measured for 30° and 45° slope angles. Figure 6 also shows that, at wall distances of 25 cm and 40 cm, higher impact pressure was recorded for slope angle of 45° as compared to those measured at angles of 60°. It is also evident from the results that with the increase in vertical wall distance from the toe of the slope, the impact pressure for inclination angle of 60°, significantly dropped to a very small value. This can be attributed to the fast dissipation of energy in the moving particles for such a steep slope.

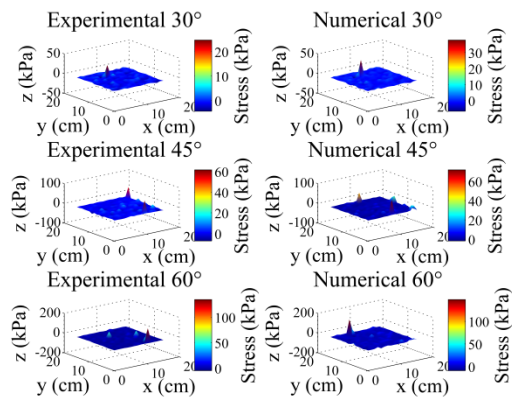


Figure 8: Contour of impact pressure on the vertical wall considering different inclination angles.

Figure 8 illustrates contours of the impact pressure on the vertical wall when placed right at the toe of the slope. It is apparent that the distribution of

impact pressure on the vertical wall was irregular as observed in the experiments and as confirmed using the numerical simulations. It has been found that for the investigated slope inclination angles, the calculated pressure was consistently larger than that measured in the experiments. Additional numerical simulations are needed to investigate the role of particle shape on particle movement pattern and the impact forces on the barrier wall.

5. DISCUSSION

The above results suggest that a simplified DEM simulation using spherical shaped particles was able to capture some of the important features of particle flow on different inclined slopes. Reasonable agreement was found between the measured and calculated particle velocities as well as the impact pressure on a vertical wall located near toe of the slope. The numerical simulation provided slightly higher impact pressure in most of the investigated cases as compared to those measured in the experiments with a difference of about 10%.

The maximum velocity calculated from the DEM analysis was found to be slightly higher than the measured value. It was also found that observed pebble movement during the experiments is sensitive to the particle geometry. Further analyses will be needed to explore the role of particle geometry on the micro-scale response and the sensitivity of the solution to the contact model used in the DEM simulations.

6. SUMMARY AND CONCLUSIONS

Laboratory experiments were conducted to investigate particle flow on a rough incline for three different slope angles. Particle velocity and displacement patterns are measured and the results are used to validate a discrete element model. Impact pressure induced by the flowing particles on a vertical wall located at some distance from the toe is also measured. The suitability of discrete element methods to realistically simulate the observed behaviour is evaluated. Despite the complexity of particle flow behaviour observed in each test, DEM was able to reasonably produce a response that is consistent with that found in the experiments. The model was to some extent able to capture the interaction between particles and the perforated sheet as well as the vertical wall where particle flow is dominated by coupled sliding and rolling movement.

7. ACKNOWLEDGEMENT

This research is supported by the Natural Sciences and Engineering Research Council of Canada (NSERC) under Grant No. 311971-11.

8. REFERENCES

- Crosta, G., Imposimato, S., and Roddeman, D. (2002). Numerical modelling of large landslide stability and runout, EGS 27th General Assembly, Geophysical Research Abstracts, European Geophysical Society, 4, EGS02-A-0224.
- Crosta, G., Imposimato, S., and Roddeman, D. (2003). Numerical modelling of large landslides stability and runout. *Natural hazards and earth system sciences* 3, pp. 523-538.
- Cundall, P. A. & Strack, O. D.L. (1979). A discrete numerical model for granular assemblies. *Géotechnique* 29, No.1, pp. 47-65.
- Giani, G. P., Giacomini, A., Migliazza, M., and Segalini, A. (2004) Experimental and theoretical studies to improve rock fall analysis and protection work design. *Rock Mech. Rock Engng.* 37(5), pp. 369-389.
- ICG (Itasca Consulting Group, Inc.) (2014) PFC3D, v5.0 Minneapolis, MN:ICG.
- Jiang, J.C., Kazuyoshi, Y., and Takuo, Y. (2008). Identification of DEM parameters for Rockfall Simulation Analysis. *Chinese Journal of Rock Mechanics and Engineering.* 12, pp. 2418-13
- Li, H., McDowell, G.R., and Lowndes, I.S. (2012). A laboratory investigation and discrete element modelling of rock flow in a chute. *Powder Technology* 229, pp.199-205
- Liu, Z.N. and Koyi, H.A. (2013). Kinematics and internal deformation of granular slopes: insights from discrete element modelling. *Landslides* 10, pp.129-160.
- Lo, C.Y., Bolton, M.D., and Cheng, Y.P. (2010). "Velocity fields of granular flows down a rough incline: a DEM investigation." *Granular Matter*, 12, 477 – 482.
- McDowell, G.R., Li, H. and Lowndes, I. S. (2011). The importance of particle shape in discrete element modelling of particle flow in a chute. *Géotechnique Letters* 1, pp. 59-64.
- Tran, V.D.H., Meguid, M.A., Chouinard, L.E. (2014). Discrete element and experimental investigations of the earth pressure distribution on cylindrical shafts. *Int J. Geomech.*, 10.1061/(ACSE) GM.1943-5622.0000277. pp. 80-91.
- Wu, H.J. and Chen, C.H. (2011). Application of DDA to simulate characteristics of Tsaoiling landslide. *Computers and Geotechnics* 38, pp. 741-750.
- Wu, H.J. (2010). Seismic landslide simulations in discontinuous deformation analysis. *Computers and Geotechnics* 37, pp. 594-601.
- Zhao, T., Utili, S., and Crosta, G. (2015). Rockslides and impulse wave modelling in the Vajont Reservoir by DEM-CFD analyses. *Rock Mech. Rock Engng:* 1–20. doi:10.1007/s00603-015-0731-0.

A versatile model for the evaluation of subsidence hazards above underground extractions

Peter Cain, Ph.D., P.Eng. ^{a*}, Dr. Ing. Karsten Zimmerman ^b

^a Director of Engineering, DMT Geosciences Ltd., Calgary, Alberta, Canada, T2R 0E4

^b Head, Expert Body for Ground Movement, DMT GmbH & Co. KG, Essen, Germany

ABSTRACT

All underground extraction – oil, gas, water and minerals – results in subsidence of the surface to some degree. Subsidence can cause damage to infrastructure – roads, powerlines, gas and oil pipelines, buildings – and to the natural surface, with the development of cracking, potholes, changes in hydrogeology and destabilization of slopes. Pre-extraction estimates of the amount of subsidence and the hazards it might produce are difficult to determine with accuracy, and the most frequent approach is to model the surface movements in response to extraction using empirically based models.

There are a number of large underground coal mine projects on the drawing board in British Columbia and Alberta despite the current prolonged episode of reduced coal prices. Fortunately, almost all of these projects target metallurgical coal, for which windmills, hydro and nuclear “clean” power sources provide no substitute and in fact, on which they depend for their construction. Each of these projects will have to demonstrate satisfactory mitigation of hazards arising from potential subsidence before they will be allowed to proceed.

DMT Geosciences Ltd of Calgary, AB has recently worked with an underground mine proponent to model subsidence over an entire mine layout, in native coordinates and for multiple seam extraction, using a proprietary influence function model. Currently calibrated using a best estimate of western coal subsidence characteristics, the model itself will undergo additional calibration as monitoring data above the actual mine is obtained.

The model itself is fairly easy to use, quick to run and provides results in an easily managed format for graphical display. As well as mining subsidence, it has in the past been shown to predict surface movements due to oil and water extraction at depth. For the current project, the results obtained in the initial subsidence prediction phase have allowed areas of potentially hazardous or damaging surface movements to be determined.

KEYWORDS: subsidence; modelling; surface safety; environmental management

1. INTRODUCTION

North East British Columbia has a long history of large scale open pit coal mining targeting metallurgical coal for overseas markets. As in most coalfields, the easy coal has gone, but there remains substantial resources of good quality coal accessible by underground methods. The Wapiti Project, owned by Canadian Dehua, reported a resource in excess of 1 billion tonnes, and Glencore is proceeding with the Sukunka Project which has underground resources to be mined after an initial open pit.

All of these are major projects in an established mining area, but they will attract considerably more environmental scrutiny than they might have done in the past. The environmental issues associated with surface mines – waste rock disposal, selenium leaching, dust and habitat destruction – are well known to the local regulators. Underground mines, however, are largely a mystery to them.

Although underground mining has a number of environmental advantages, mitigating many of the

disadvantages of surface mines, a significant concern is the effect of subsidence and the hazards it might present on the surface. This concern has become apparent during the environmental assessment process for another major underground coal mining project in NE BC.

This paper describes methods used to estimate the surface subsidence, their shortcomings and advantages, and to present some of the results that demonstrate how the output can be used to identify potential areas of surface hazard after undermining.

2. PROPOSED MURRAY RIVER PROJECT

The Murray River Project in the Peace River Coalfield of British Columbia is joint venture between three Chinese companies, operated by HD Mining International Ltd of Vancouver, BC. Figure 1 shows the locations of the coalfields of British Columbia. Figure 2 shows the principal property owners within the Peace River Coalfield.

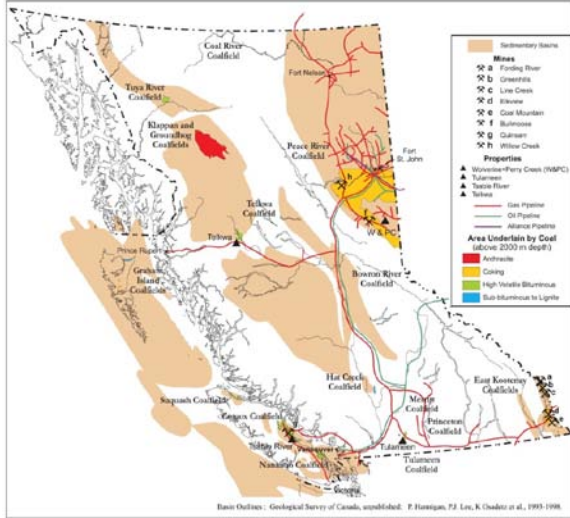


Figure 1: Coalfields of British Columbia.

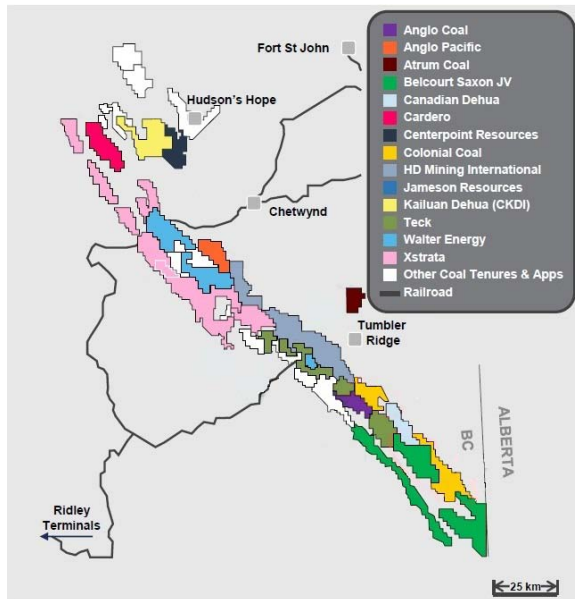


Figure 2: Principal Property Holders in the Peace River Coal Field.

The Murray River Project property lies centrally in the Peace River Coalfield between the historic open pit properties of Quintette and Bullmoose. Anglo American and Walker Energy have also operated open pit mines in the immediate area, now mothballed due to low prices.

The coal is found in the Gates Formation of the Upper Cretaceous period and sits at depths of between 500 m and 1300 m (Figure 3).

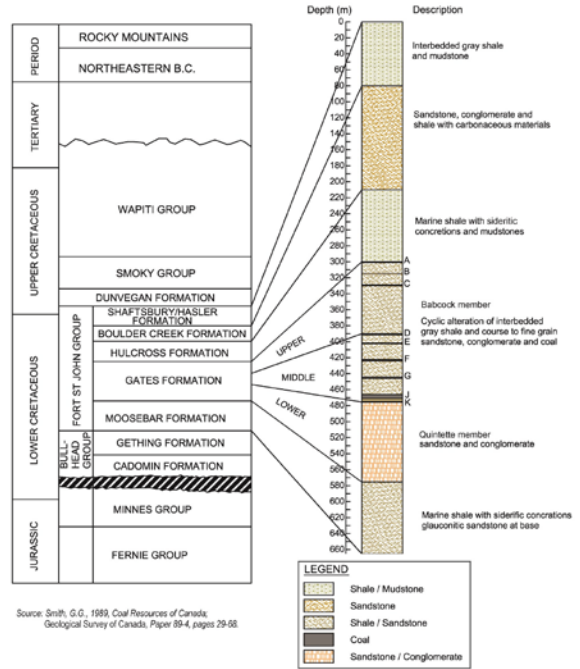


Figure 3: Typical Strata Column at the Murray River Property.

The proposed underground mine extends about 10 km along strike (NNW-SSE) and about 5 km to the dip. There are five target seams, identified as D through J from the top down (Table 1), with a total extraction of about 25 m, all of it from superimposed longwalls, many of them using the longwall top coal caving method. The proposed layout is shown in Figure 4.

Table 1: Target Coal Seams.

	Thickness	Lithology
	70-80 m	Mudstone, siltstone and coal. The lower part of the group is a thick layer siltstone. Contains A, B and C seams, none of which are mineable.
	> 55 m	Sandy mudstone, mudstone and coal, including three minable coal seams: D; 0.4 – 5.71 m, 2.12 m avg. E; 0.05 – 6.52 m, 2.32 m avg. F; 0.67 – 7.51 m, 3.46 m avg.

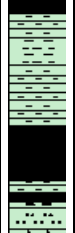
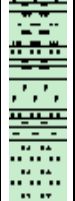
	>40 m	Mudstone, sandy mudstone and coal, including two workable seams: G/I; 0.4 – 3.52 m, 1.6 m avg. J; 2.6 – 9.2 m, 6.19 m avg.
	100 m	The lithology consists of thick-layer sandstone, included with thin-layer mudstone. Mainly medium sandstone, followed by gritstone, included with mudstone.



Figure 4: Layout of the Proposed Mine Panels showing planned and current infrastructure.

The mine extends beneath boreal forest as well as oil and gas exploration and production infrastructure – pipelines, well-heads and compressor stations. The terrain itself is a valued environmental component, as it is home to a number of species including caribou and some valued fish species. Disturbance to rivers and streams including the potential for slope instability in some of the deeply incised valleys, is a major concern.

Almost the entire oil and gas industry infrastructure is protected in the mine plan by pillars left in the coal underground. However, service roads and power lines criss-cross the area and the effects of subsidence must be assessed

3. SUBSIDENCE ASSESSMENT

The project proponents were asked to provide an assessment of the effects of subsidence on surface features which included some deeply incised river valleys, and specifically on valued environmental components. Regulators were concerned that large amounts of subsidence could occur as a result of multiple superimposed panels with extracted thicknesses of up to 25 m and that subsidence might

result in stream reversals, wetland destruction and slope instability in sensitive areas.

The initial subsidence estimates were made by consultants with experience of subsidence estimation in western North America. The estimates were made using a proprietary influence function model. Because there was no local data to use to calibrate the model, subsidence parameters known to provide reasonably accurate estimates of subsidence under similar conditions in the western United States were used.

The subsidence estimation model used required the translation of the panel coordinates into a Cartesian coordinate system with the panels parallel to either the x- or y-axis and the size of the model limited subsidence estimation to a single mining district, although all five seam extractions were modelled. The simplification of the panel layouts resulted in the elimination of the pillars between the panels.

Although there was no concern over the resulting estimates, the model used for the initial assessment was limited to 3,000 data points which results in either long distances between estimation points or the segmentation of the mine plan. It was thus not able to provide coverage of the entire mine area without segmenting the mine layout and converting coordinates, and analysis of linear features was thus made very difficult.

On reviewing the initial set of results, the regulators asked for a mine-wide subsidence estimate as well as subsidence estimates along the courses of the major streams. The additional information required from the environmental reviewers dictated a change in approach to the subsidence modelling. The modelling software originally selected would require too much time and post processing and another option was sought.

4. SPS 4D SOFTWARE

DMT's SPS 4D subsidence prediction software based on the stochastic prediction model of Sroka (1978). The software is designed to predict multi-panel and multi-seam subsidence influences both on objects at surface and on objects within the rock mass. The software is especially suited for calculating subsidence effects of inclined seams and inclined overburden strata with respect to unsymmetrical rock mass behaviour. In addition to predicting subsidence by longwall coal mining, the software has been successfully used to estimate subsidence caused by oil, gas and water production.

4.1 Theory

The process of subsidence starts with the extraction of material (oil, gas, water or coal and

other minerals) from underground. The shape of the occurring subsidence trough depends on various, often hardly known parameters. For a model description of mining effects a relation between cause (material extraction) and effect (ground movements) is necessary. This relation can be set up by a transformation function describing the rock mass behaviour (Figure 5a).

The main influences in the case of longwall coal mining are the thickness of the mined seam, the depth of the mining works, the inclination of the seam and the dimensions and shape of the panel. Also important is a time factor, describing the delay in time between the extracted coal volume and the occurrence of the corresponding subsidence trough. However in this study only final subsidence values were sought, so the time factor model was not implemented.

For calculating the subsidence of a longwall operation with the computer program the mined area can be divided into small mining elements (Figure 5b).

The subsidence potential of one mining element is calculated within the program by using the Gaussian distribution as influence function. Using super-positioning of all mining elements, the software is able to calculate the final subsidence trough induced by mining of the whole longwall (Figure 5c). Consequentially it is also possible to estimate subsidence in every stage of face advance.

Final surface subsidence induced by mining a single mining element can be calculated using equation 1.

$$s(x, y, z) = \frac{k}{\pi} \frac{aV}{R^2} \cdot \exp\left(-k \frac{d^2}{R^2}\right) \quad (1)$$

where: $k = -\ln(0,01)$, the fixed parameterization value of Ruhrkohle method

a = mining factor ($a \in [0,1]$), volume of subsidence trough divided by extracted volume

V = volume of mining element depending on element area and mining height

R = radius of influence, $H \cdot \cot\gamma$

H = mining depth

γ = angle of influence

$d = \sqrt{(x - x_A)^2 + (y - y_A)^2}$ distance between mining element (x_A, y_A) and calculation point (x, y)

The parameter k is necessary because the Gaussian function used to determine vertical subsidence is asymptotic. The value of k forces a vertical subsidence value of zero at the edge of the subsidence trough although it reduces the estimate of subsidence very slightly at the maximum subsidence point.

The volume and location of every mining element is known and depends on the specific layout and dimension of the longwall panel. The only parameters that depend on the mining site specific geology characters are the mining factor and angle of influence. These parameters have to be determined from *in-situ* observations or estimated based on similar locations. In this case, the initial modelling used parameters selected by consultants with experience in similar conditions, and these values were used in the SPS 4D computations.

The derivation of equation 1 yields the tilt in x- and y-direction of the calculation point.

$$T_x(x, y, z) = \frac{\partial}{\partial x} S(x, y, z) \quad (2)$$

$$T_y(x, y, z) = \frac{\partial}{\partial y} S(x, y, z) \quad (3)$$

When calculating horizontal displacement it is assumed that horizontal displacement is proportional to tilt. In this way it is possible to calculate ground deformations. Equations 4 to 6 show the calculation of horizontal displacement in x- and y-direction and for a point at surface.

$$U_x = -B \cdot T_x(x, y, z) \quad (4)$$

$$U_y = -B \cdot T_y(x, y, z) \quad (5)$$

$$\text{with: } B = \frac{R}{\sqrt{2k}} \quad (6)$$

Field measurements of subsidence in North America and elsewhere show that maximum tilt does not occur directly above the edge of the panel but is instead located in a distance d towards the mined panel (the so-called edge effect). The edge effect is integrated in the model by applying a specific roof convergence model which is parameterized by value d – the edge effect distance.

For full details of the model theory and development, refer to Zimmermann (2011).

4.2 Implementation

In significant contrast to the modelling software originally selected, SPS 4D applies a finite element based processing approach, which enables non-rectangular panel processing directly using the native coordinate system. This makes a comprehensive prediction for a multi-panel and multi-seam mine layout, presented in this article, very easy. For example, the initial software deployed could only process 3,000 points of data, so the larger the area being modeled, the lower the resolution of the output data. SPS 4D allowed up to 100,000 data points, in native coordinates, and has recently been expanded to 400,000 points. If a data point spacing of $1/20^{\text{th}}$ of the depth is followed (NCB, 1975), this would allow single pass subsidence estimation of a 1,000 m deep

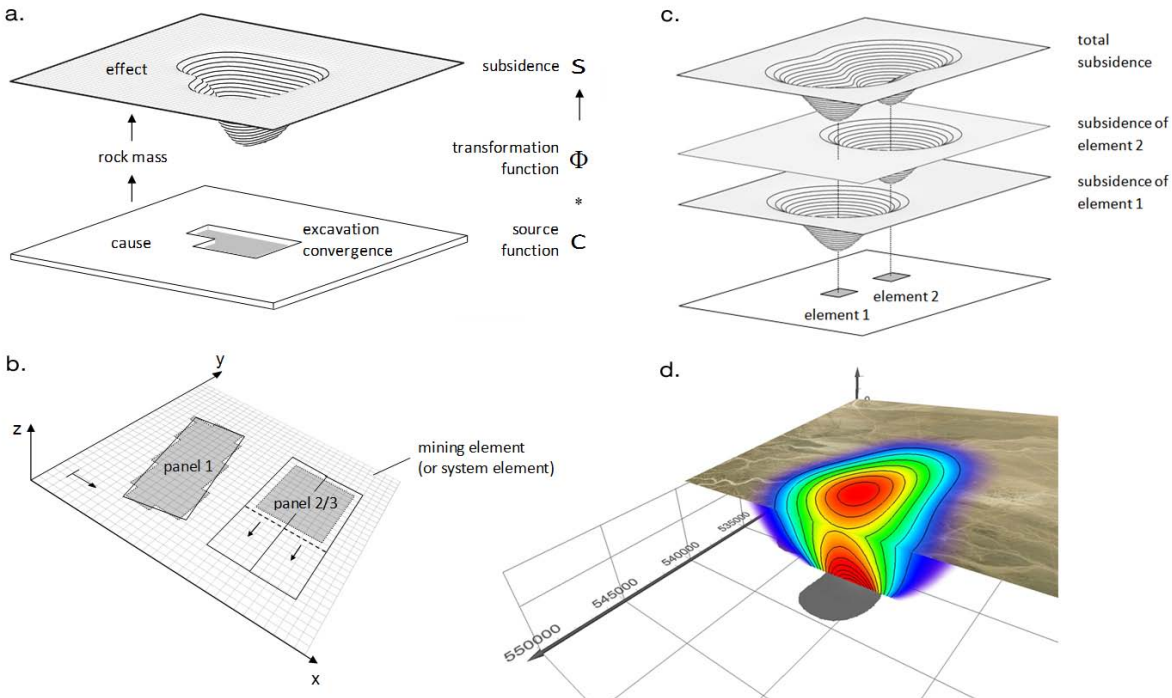


Figure 5: Illustration of the subsidence modelling principals and method (after Sroka et al, 1988 and Zimmermann, 2011).

coal mine over an area of about 900 km². This is large enough for most practical purposes.

SPS 4D is implemented in conjunction with a proprietary data manipulation package, Surfer™. Using a front-end and back end processing package already on the market greatly simplified implementation. Surfer™ is relatively inexpensive, easy to learn and widely used, making it an ideal partner in this process.

Outline coordinates of 84 individual longwall panels in 5 seams at depths ranging from 500 to 1400 m were entered in BC Provincial grid coordinates. Panel outlines, depths and seam thicknesses are entered as individual text files. The seam model can be displayed before processing begins (Figure 6).

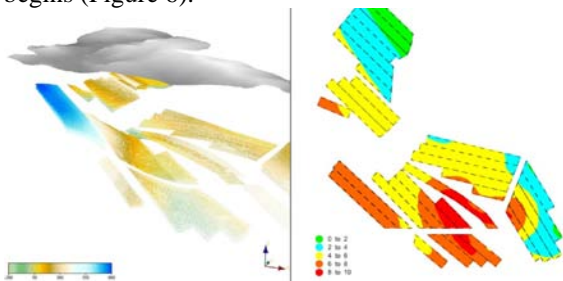


Figure 6: Illustration of model parameters; Left – 3D plot of surface and mine panels with depth referring to zero level [m], Right – Plan plot of seam thickness [m].

4.3 Calibration

Subsidence models are “calibrated” to produce estimates which match, as closely as possible, the subsidence experience of the area by adjusting three major model parameters: the influence angle, the subsidence or mining factor and the edge effect distance. The most accurate estimates from subsidence models are obtained when there is sufficient data from actual subsidence profiles to estimate the values of these parameters. Even then, parameters are chosen which err on the conservative side and model estimates tend to overpredict.

When no site specific *in-situ* data is available, data from sites with similar structure, rock properties and conditions are used to determine initial parameter values for initial subsidence estimates while the required data is collected and aggregated into the model to improve the accuracy of estimates.

There is no observed data for the Murray River coalfield. The original subsidence estimates used model parameters were based on past experience and knowledge of subsidence in the western part of the USA (the closest similar mining conditions for which subsidence measurements were available). This is a common approach to subsidence estimation in new mining areas.

The initial model parameters were reviewed by DMT and compared to the very limited subsidence data available in western Canada. The high percentage of “hard rock” in the overburden was also

considered. The parameters used in the initial model were ultimately accepted as applicable for implementation in SPS 4D.

There was thus no argument with the assumptions used in the initial model, but it was important to be able to show the environmental review panel that the change in model mid-process was irrelevant. A comparison of the two models using the same parameters was performed.

Figures 7 and 8 show the subsidence profile results of the two models after one, two and four panels extracted. The only significant difference between the models is the appearance of reduced subsidence over pillars in the SPS 4D results. The SPS 4D model could accurately resolve pillars between panels, whereas the initial model could not, so they were omitted.

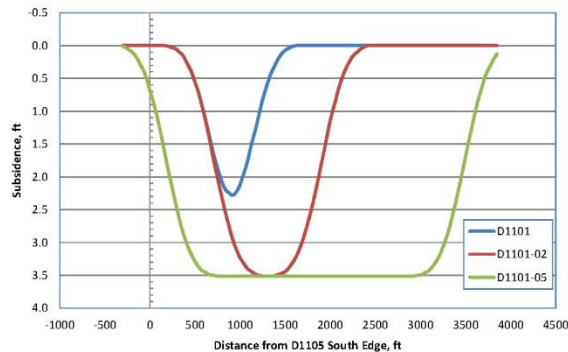


Figure 7: Subsidence Profile from the First Model.

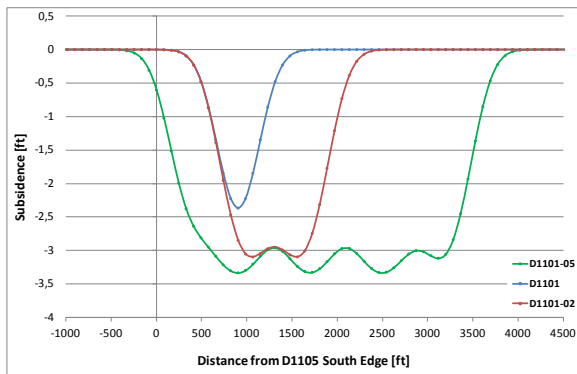


Figure 8: SPS 4D Subsidence Profiles.

The similarity of the results, and the additional resolution of the DMT model, convinced the reviewers to accept the new model.

Although neither of the models has had the benefit of observed subsidence data with which to calibrate it, every effort has been made to use representative subsidence parameters which will give a conservative estimate of the subsidence effects.

Both the project proponent and the regulators understand that the results obtained are *estimates*,

even though they have been designed to err on the conservative side. Both the project proponent and the regulators understand the importance of gathering accurate subsidence measurements to refine the model and allow accurate site specific calibration for future assessments.

5. MODELLING

The first stage of the model was to obtain a digital elevation model (DEM) of the topography above the mining area. The DEM was constrained to a distance of 900 m beyond the mining limits to reduce the number of data points for which subsidence was to be predicted. Even so, the Lidar data was too dense to allow timely modelling, so a subset of the elevations at 15 m northings and eastings was produced. This resulted in slightly less than 200,000 data points. The end of mine life subsidence was subsequently calculated for each of these points.

The spacing of the points, 15 m, was a compromise between the accepted “bay length” over which strains associated with subsidence are conventionally calculated and the data density required to properly describe changes in topography.

The “bay length” (distance between measurement points) is usually recommended as 0.05 times the depth (NCB, 1975). Any less, and calculations become too time consuming; any more, and the strain estimates are affected. The range of depths of working at Murray River is 500 m to 900 m, resulting in bay lengths of 25 m to 45 m respectively.

Terrain changes are quite substantial over short distances over much of the mine area, and DMT felt that a 25 m DEM would not be effective, hence the 15 m discretization chosen.

Once the surface DEM had been prepared as a simple x,y,z data file, the mine layout was digitized in AutoCAD and the coordinates of each of the 84 panels were prepared as another simple data file. At this point, the data files could have been prepared with elevations and seam thicknesses for each corner point, and the software would have interpolated these values across each panel at 10 m intervals. This interpolation interval is user selectable, but 10 m seems to produce adequate results.

Instead of interpolating between panel corners, AutoCAD 3D-polyline files of base of seam elevation and seam thickness were prepared as simple x,y,z strings. The software accepts these files and interpolates both depth and thickness more accurately than if corner points alone were used. By way of example the base of seam elevations for the lowermost J seam derived for each panel and

contoured using the integrated “Surfer package, are shown in Figure 9.

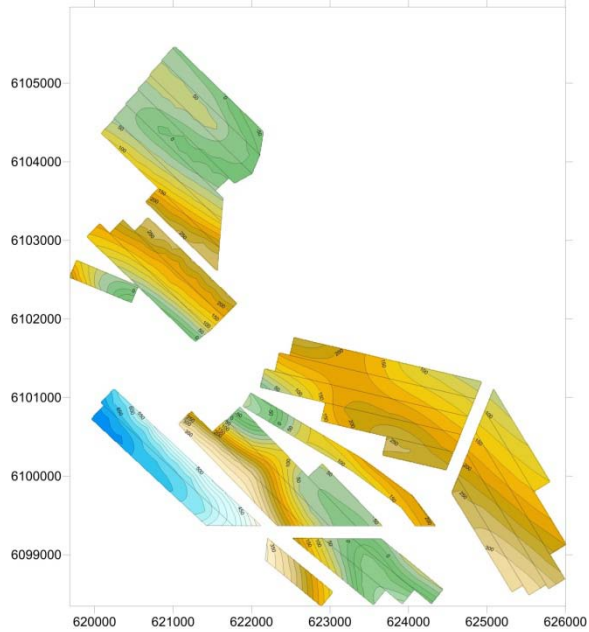


Figure 9: Contoured Seam Elevations from Data.

The effect of subsidence on a fish-bearing creek in the area was of particular interest. To assess potential hazards, elevations along the creek bed were interpolated from the GIS system at roughly 5 m intervals, resulting in about 14,000 points.

Once the data sets were completed, the model was allowed to run. Total subsidence after completion of mining was determined for each of the DEM surface points and for each of the M20 Creek bed data points. Despite the capacity of the model, the surface DEM exceed the number of points that it could handle, and the mine layout model was completed in two sections, although the model has subsequently been modified to allow up to 400,000 points to be modelled

6. RESULTS

Figure 10 shows the surface elevations contoured from the DEM subset. The dark line is the creek of interest. Towards the east end of the creek it runs through a deeply incised valley and the stability of the slopes was in question.

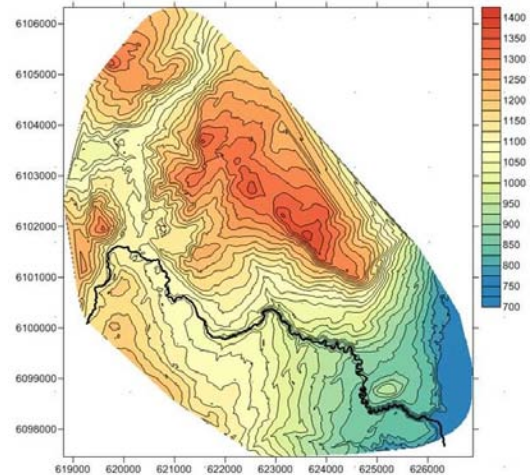


Figure 10: Contoured Surface Elevations and the Major Creek.

Figure 11 shows the contoured total subsidence, which reaches close to 10 m under shallow, multiple thick seam workings. This area was identified as having potential for hazardous crack or surface fracture development. Fortunately it is largely wilderness and the risk to people and infrastructure was assessed as low.

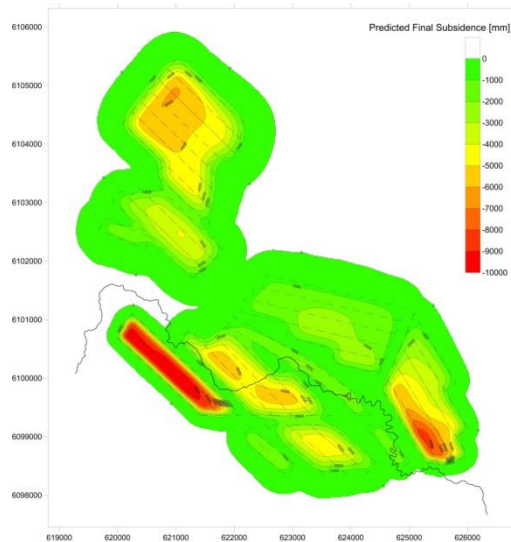


Figure 11: Contoured Total Subsidence.

Figure 12, showing areas of concentrated tensile and compressive strain, matches the areas of major subsidence as expected.

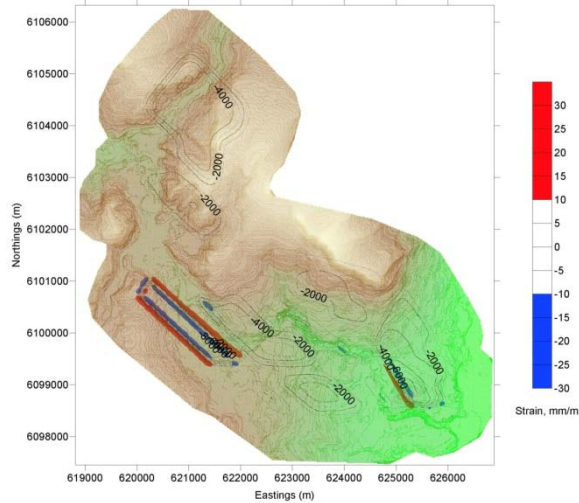


Figure 12: Contoured Strain.

Figure 13 shows a unique feature of the SPS 4D model, its ability to estimate subsidence along non-linear features in significant detail. The stream trace is represented by 14,000 points which, and the results indicate the areas of greatest potential surface hazard. This allows the project proponent to plan mitigation for habitat loss based on a realistic assessment of the physical requirements. Figure 14 shows the stream bed profile from which possible flow reversals or changes to stream bed morphology can be determined. Steepening will result in increased

erosion and possible destruction of spawning beds. Flattening will result in deposition and silting up potential.

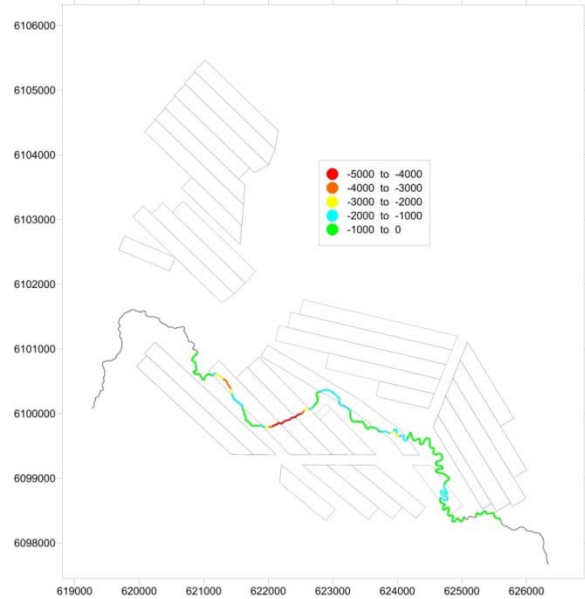


Figure 13: Subsidence along the Stream Bed.

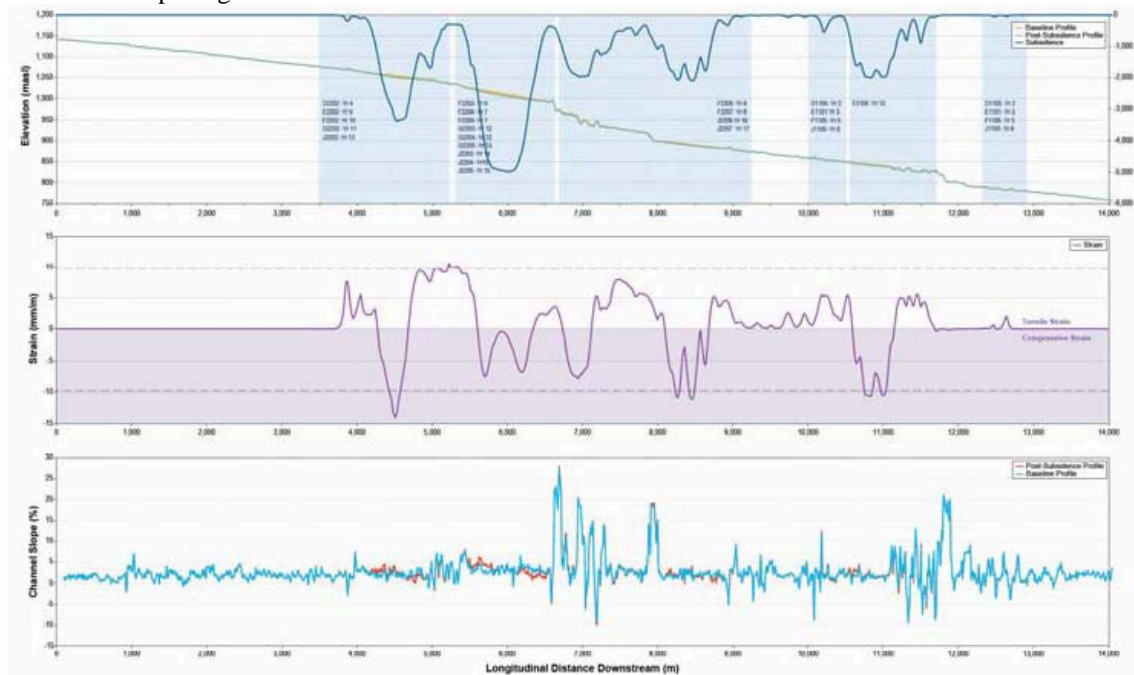


Figure 14: Subsidence along the Stream Bed Illustrated as a Stream Bed Profile.

7. CONCLUSIONS

The modelling work demonstrated firstly that the SPS 4D model could produce results in North America similar to North American models. In areas where large amounts of subsidence data exists this isn't a problem – models can be calibrated to local conditions. However, in a new mining field with no existing data it is important to be able to have a degree of confidence that the results are meaningful.

Secondly, the formulation of the model and the use of a proprietary front and back end made data input and visualization and more importantly, results visualization, very easy. The identification of zones of significant subsidence and the potential for surface hazards, and the effects of subsidence on stream courses and wetlands was made significantly easier using the proprietary visualization software.

The presentation of the results, albeit with a number of caveats regarding the nature of the estimates and the need for extensive subsidence monitoring and observation to verify the results and confirm the mitigation strategies, was successful.

Subsidence estimation is a tricky field. Model results are only estimates, approximations of the actual result. The only sure way to increase the reliability of the model outputs and hence the assessment of the hazards, is to calibrate the model with as much field data as possible. The proponent in this case has committed to a multi-year Lidar and surface survey monitoring program to ensure that the subsidence estimates become increasingly more accurate and hence the potential hazards are more accurately identified for mitigation.

8. ACKNOWLEDGEMENTS

The authors would like to acknowledge the support of HD Mining International Ltd., of Vancouver, BC, for whom this work was undertaken and who have supported the presentation of the results at this conference.

The views expressed are those of the authors alone and may not represent the views of HD Mining International or their employers.

9. REFERENCES

NCB (1975) "Subsidence Engineers Handbook" National Coal Board Production Department, London, UK, 1975

Shadbolt, C. (1987) "A Study of the Effects of Geology on Mining Subsidence in the East Pennine Coalfield" PhD Thesis, University of Nottingham, March, 1987.

Sroka, A. (1978) "Teoria S. Knothego w ujęciu czasoprzestrzennym", *Geodezja* 24, S. 73-85, Kraków, 1978 (in Polish language)

Sroka, A. et al. (1988) "Vorausberechnung von Gebirgsbewegungen bei geneigten flözartigen

Lagerstätten unter Berücksichtigung anisotroper Gebirgseigenschaften, des Durchbaugrades und des zeitlichen Konvergenz- und Verzögerungsverhaltens des Gebirges; Abschlussbericht des Forschungsvorhabens" Ha 526/15-1 am Institut für Markscheidewesen; Technische Universität Clausthal (Deutschland), 1988 (in German language)

Tandanand, S, and Powell, LR. (1984) "Influence of Lithology on Longwall Mining Subsidence" *Mining Engineering*, December pp 1666-1670.

Zimmermann, K and Fritschen, R. (2007) "Study about the dynamic influences of longwall mining in the US on surface objects" Proceedings of the 26th International Conference on Ground Control in Mining, Morgantown, WV., 2007

Zimmermann, K. (2011) "Prediction and Analysis of Dynamic Ground Movements induced by Near-Surface Coal Mining in the USA" PhD Thesis, University of Freiberg, 2011 (in German language)

Slope stability analysis and prediction based on the limit equilibrium method of Luming Molybdenum Mine's West-I and North Region

HUANG Zhi-an, LIU Fang-zhe, WANG Hui*, GAO Yu-kun

State Key Laboratory of High-Efficient Mining and Safety of Metal Mines (University of Science and Technology Beijing), Ministry of Education, Beijing, China, 100083

ABSTRACT

Slope stability is directly related to the safety of mine production, which is one of the key factors influencing the mining production benefit. The present study used China Railway Resources Group Co., LTD Luming Molybdenum Mine's west-I and north area as the main research background and established a numerical simulation model for the selected profile according to the slope engineering geological conditions and mining design of Luming Molybdenum Mine. The profiles included three profiles from the West-I region and three profiles from the North region. The safety factor was calculated and analyzed by the limit equilibrium method and Geo-Slope software. Slope stability was evaluated. An optimization design was carried out on the sections not meeting the requirements, and afterwards the safety factor met the requirements, with the slope being generally stable.

KEYWORDS: surface mining; slope stability; limit equilibrium method; Geo-Slope

1. INTRODUCTION

The proportion of coal mining at home and abroad has increased in the last century. In recent years, with the continuous development and utilization of resources, there has been an overall trend towards deep sunken open pit mining. The deep mining process has led to increases in slope height and mining depth, resulting in poor slope stability and safety. In addition, for large open-pit mines, the optimization of slope angle is one of the important means to make full use of resources, and could reduce production costs and increase mining benefit. According to Sun (1988), with the increase of the slope angle, billions or trillions could be saved in stripping rock costs. Therefore, in the process of deep mining in open-pit mines, there is a prominent contradiction between ensuring the slope safety and improving the economic benefit.

Luming Molybdenum Mine is an open-pit mine that was designed with steep slope mining and relief for the stripping process, with the stripping direction going from the plate to the footwall of the ore body. Luming Molybdenum Mine is a typical high and steep slope strip mine, therefore it is of great significance to China to ensure safe and efficient production to meet demands for molybdenum resources.

Based on the above requirements, the early field engineering geological investigation and field data gained by the rock physics mechanics test are analyzed, and the impact exerted on the slope stability by the geological conditions of Luming

Molybdenum Mine West-I area and North area are studied using the limit equilibrium analysis method, slope stability analysis, and the numerical simulation software Geo-Slope. Finally, optimization measures are put forward.

2. LIMIT EQUILIBRIUM ANALYSIS THEORY

The limit equilibrium method design procedures are an important and most commonly used method for the analysis of slope stability. Broadly speaking, the method also belongs to a kind of numerical analysis method, but due to its generality and practicability, it is often listed as a separate class of methods. The limit equilibrium method is comprised of cutting the soil along a slip surface within the scope of the sliding trend into a bar or oblique, establishing the equilibrium equation of all the sliding soil based on the analysis of the stress of the blocks, and on this basis, determining the safety factor of slope stability (Li, 2010). These methods assume that soil rigid sliding or rotating occurred along a potential slip surface, and sliding soil mass is the ideal rigid-plastic body (Zhou, 2004). The method does not consider the soil stress-strain relationship. It assumes that the safety factor of the degree of shear strength mobilization and the shear strength of the various points along the sliding surface are the same, and assumes its safety factor expression with the deformation characteristics of the landslide area in addition to the landslides regional geological conditions and stress conditions. The differences

*Corresponding author – email : wanghuiustb@live.cn.

between the Fellenius, the Bishop, and the Janbu are only the assumptions for interslice force or sliding surface interaction force to eliminate the static indeterminateness and the method of deriving the safety factor. Limit equilibrium methods are widely used in engineering due to their advantages such as the easy model and the convenient and easy to understand formula.

An early limit equilibrium method was presented in 1916 by Peterson, and followed by many scholars such as Fellenius, Taylor, Bishop, Janbu, Morgenstern and Price, Spencer, Sarma (Sarma, 1979; Chen and Morgenstern, 1983) who were devoted to improving the method. At present, the rigid-body limit equilibrium method has been developed from two-dimensional to three-dimensional. The greatest benefit of this solution is the constitutive relation expression in engineering, and thus it has a clear physical concept, giving it the advantage of a simple and rigorous solution. There are several methods to calculate slope stability based on the principle of limit equilibrium method. The present study mainly uses the Swedish article points method, Janbu method, Bishop method, Spencer method, Sarma method, and Morgenstern - Price method

3. THE GEO-SLOPE SOFTWARE

3.1 GEO-Slope software introduction

The SLOPE/W module of Geo-Slope software was used for the calculations. SLOPE/W has become the most widely used software in geotechnical engineering professional slope analysis. It includes a variety of methods (Morgenstern-Price, GLE, Spencer, Bishop, Ordinary, Janbu, Sarma, Corps of Engineering, and Lowe-Karafiath) to analyze geotechnical engineering problems, such as shape change of the slip plane, condition of pore water pressure, soil properties, and different loading ways. Finite element method can be combined with the theory of limit equilibrium to calculate and analyze the slope stability. It can also use the parameters to analyze the stability. SLOPE/W software can analyze almost all of the SLOPE problems in geological structures, such as civil engineering and mining engineering

3.2 Selection of study section

Preliminary was completed concerning the Luming Molybdenum Mine engineering geological conditions, rock mass structure characteristics, the physical and mechanical properties and quality of the rock, and the rock mass mechanics parameters. This laid the foundation for the simulation. For the sake of convenience, the field engineering geological zoning, and the early stages of the rock mass quality

evaluation results, three sections of West-land three sections of North were chosen to evaluate the slope stability. The optimization of design was carried out for the instability profiles.

According to the actual situation of the field, the principles of the selection profile are as follows:

(1) Close to or through the drill as far as possible, to ensure the accuracy of the research.

(2) Set the section vertical to the slope strike in order to simplify the problem about analyzing the slope stability to plane strain problem, and reduce the calculation error.

(3) Ensure the selected profile through the F3 and F4 fault, in order to research how the faults affect the slope stability of the region.

(4) Make the profile through the fracture zones as far as possible, in order to study how the fracture zones affect the slope stability.

Based on the above principle, six representative profiles were ultimately chosen to research the slope stability of the West-1 and the North area. The locations are shown in Figure 1, labeled clockwise as sections 1-1, 2-2, 3-3, 4-4, 5-5, and 6-6.

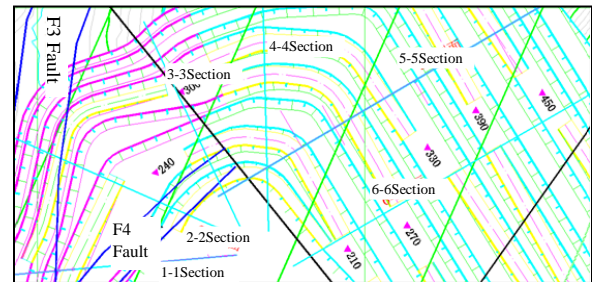


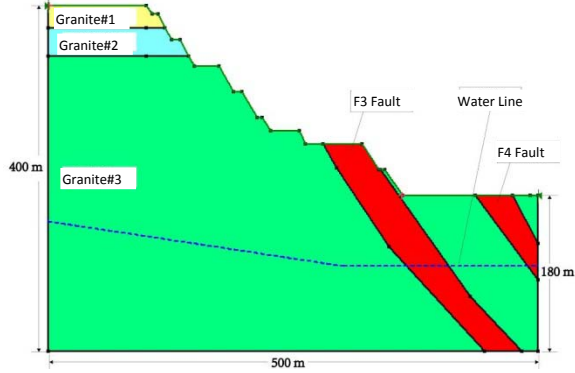
Figure 1: The research section of the west-1 district and the north district.

3.3 Establishment of the calculation model

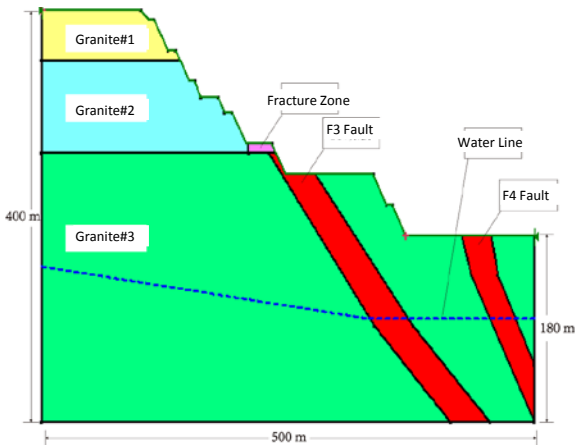
According to the above theory combined with Luming Molybdenum Mine's actual situation and the engineering geological zoning information, sections 1-1, 2-2, 3-3 of West-land sections 4-4, 5-5, 6-6 of North were selected as the research areas. The slope stability was analyzed by adopting the method of limit equilibrium theory. According to the geological conditions and actual mining situation, deformation of rock mass in the vertical and profile direction is negligible. Therefore by using the plane strain model assumption, the deformation of the vertical and the calculating section direction is assumed to be zero.

The calculation model is shown in Figure 2. The length of the 1-1 and 2-2 sections model is 500 m and the height is 400 m. The 3-3 section model length is 500 m and the height is 420. Sections 2-2 and 3-3

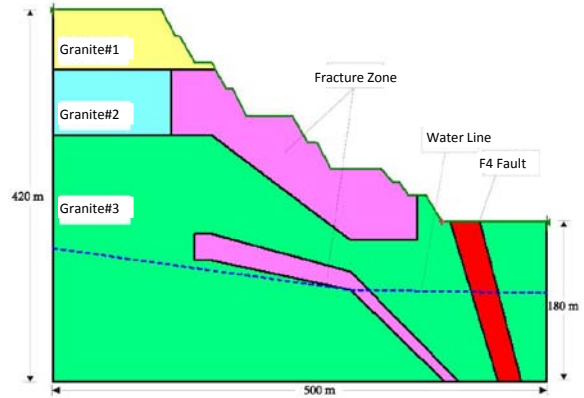
have fracture zones. Sections 1-1 and 2-2 pass through the F3 and F4 faults, the 3-3 section passes through the F4 fault, which should be considered to have an effect on the slope stability during calculations. The 4-4 section model of North length is 500 m along the horizontal axis and the height is 420 m. The 5-5 section model length is 800 m and the height is 540 m. The 6-6 section model length is 700 m and the height is 550. For the 4-4 section, there is a big range of fracture zone, which should be considered when calculating the impact on the slope stability.



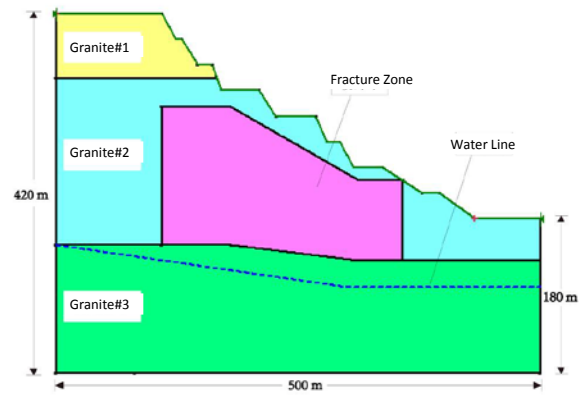
(a): West-I 1-1 section calculation model



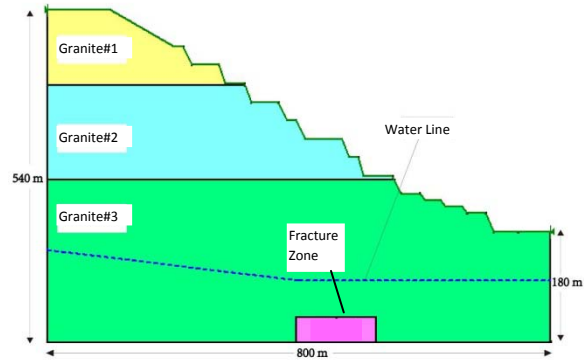
(b): West-I 2-2 section calculation model



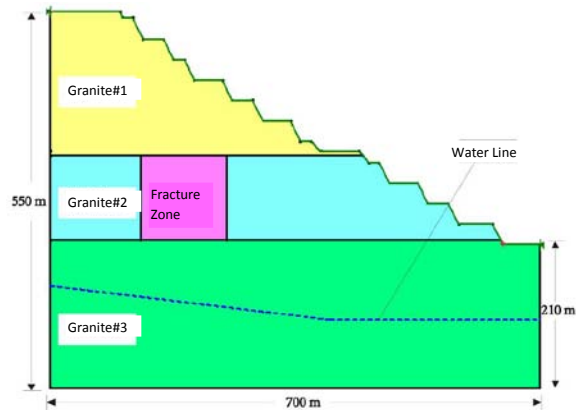
(c): West-I 3-3 section calculation model



(d): North 4-4 section calculation model



(e): North 5-5 section calculation model



(f): North 6-6 section calculation model
Figure 2: West - I area and North area of Luming Molybdenum Mine calculation model.

4. NUMERICAL SIMULATION AND ANALYZING OPTIMIZATION RESULTS

4.1 Simulation optimization analysis of West-I

(1) Simulation analysis of West-I

The safety factor with different calculation methods is as shown in Tables 1 and 2. In the 1-1, 2-2, 3-3 profile of West-I, the minimum safety factors are $F_s=1.213$, $F_s=1.202$ and $F_s=1.086$, respectively. According to the Bishop method, the safety factor is less than 1.3, so the slope is not stable.

(2) Optimization analysis of the West-I slope

According to the calculation results for the 1-1 profile, slope overall stability is poor. The reduction of the slope angle between the 180m-210m platform should be considered. The slope angle should be optimized from 59° to 57° . The result is as shown in Table 1.

According to the calculation results for the 2-2 profile, the slope angle should be optimized between the 270m-300m platform, from 64° to 60° . The result is as shown in Table 1.

According to the calculation results for the 3-3 profile, the slope angle between 300m~330m platform should be reduced from 64° to 60° . The safety factor did not meet the requirement that $F_s > 1.3$, the slope angle should be optimized between the 330m~360m platform, and reduced from 65° to 63° . The result is as shown in Table 2.

Table 1: Safety factor summary of 1-1, 2-2 profile.

	1-1 profile 59°	1-1 profile 57°	2-2 profile 64°	2-2 profile 60°
Swedish slice method	1.247	1.316	1.217	1.333

Bishop method	1.365	1.389	1.345	1.408
Janbu method	1.213	1.278	1.202	1.317
M-P method	1.288	1.344	1.289	1.380

Table 2: Safety factor summary of 3-3 profile.

	3-3 profile 64°	3-3 profile 60°	3-3 profile 63°
Swedish slice method	1.129	1.253	1.326
Bishop method	1.143	1.299	1.367
Janbu method	1.097	1.274	1.332
M-P method	1.086	1.238	1.305

The slope angle of 300 m~330 m platform to 60° , and slowing the slope angle of 330m~360 m platform to 63°

4.2 simulation optimization analysis of 4-4 profile of North

(1) Simulation analysis of 4-4 profile of North

The safety factor of 4-4 profile was $F_s=1.168$, so the slope angle should be optimized.

(2) Optimization analysis of the 4-4 profile

According to the calculation model of 4-4 profile, the slope angle between the 240m~270m platform should be optimized from 65° to 61° . The safety factor is as shown in Table 3.

Table 3: Safety factor summary of 4-4 profile.

	4-4 profile 65°	4-4 profile 61°
Swedish slice method	1.197	1.313
Bishop method	1.291	1.346
Janbu method	1.168	1.302
M-P method	1.276	1.378

(3) Simulation analysis of 5-5, 6-6 profile of North

According to the calculation results of 5-5 and 6-6 profile, the minimum safety factors are $F_s=1.306$ and $F_s=1.303$, respectively, which meets the requirements of the slope design specification. The safety factors are as shown in Table 4.

Table 4: Safety factor summary of 5-5, 6-6 profile.

	5-5 profile	6-6 profile
Swedish slice method	1.351	1.311
Bishop method	1.368	1.397
Janbu method	1.306	1.303
M-P method	1.359	1.352

5. CONCLUSIONS

(1) Six typical profiles of West-1 and North zones were selected and studied. The principles of the selection profile are as follows: close to or through the drill as far as possible; set the profile vertical to the slope strike; ensure the selected profile through the F3 and F4 fault; make the profile as far as possible through the fracture zones.

(2) Before optimization, the safety factors of the 1-1, 2-2, 3-3 profile of West-1 and 4-4 profile of North were $F_s=1.213$, $F_s=1.202$, $F_s=1.086$, and $F_s=1.168$, respectively, so the slope is not stable. The minimum safety factors of 5-5 and 6-6 profiles were 1.306 and 1.303, respectively, meeting the requirements of the slope design specification.

(3) After optimization, the minimum safety factors of the 1-1, 2-2, 3-3, 4-4 profiles were $F_s=1.307$, $F_s=1.317$, $F_s=1.305$, and $F_s=1.302$, respectively, meeting the requirements of the slope design specification. The possibility of slope instability is very small within the stable state.

According to the above analysis results, the optimization of the slope angle of the final slope has a certain effect. If the condition is permitted, the field should strengthen the construction management and monitoring in the process of mining, and take measures to control those sensitive areas using gentle slope mining and avoiding the placement of heavy objects on the top of the slope in order to reduce accidents and ensure safe production.

6. ACKNOWLEDGEMENT

It is with great pleasure that we acknowledge the generous financial support of National Natural Science Foundation of China (project number: 51474017) and Natural Science Foundation of Xinjiang Uygur Autonomous Region of China (2014211B013).

7. REFERENCES

- CHEN, Z. Y., MOGENSTERN, N. R.. (1983). Extensions of the generalized method of slices of stability analysis. Canadian Geotechnical Journal. Volume 20, No. 1, pp. 104-119
- Li, S. P.. (2010). Overview on application of slope stability analysis method. Yangtze River. Volume 41, No. 20, pp. 12-15, 31
- Sun, G. Z.. (1988). Rock texture mechanics. Science Publishing Company, 381p.
- Sarma, S. K.. (1979). Stability analysis of embankments and slope. Journal of Geotechnical Engineering. Volume 105, pp. 1511-1524
- Zhou, Y.. (2004). The most dangerous sliding surface search in the slope stability analysis. Dalian University of Technology, 65p.

Study on the similar materials simulation of the slope stability of the west-I zone in Luming Molybdenum Mine

Huang Zhian, YangFei, Wang Hui*, Zhang Yinghua, GaoYukun

State Key Laboratory of High-Efficient Mining and Safety of Metal Mines (University of Science and Technology Beijing), Ministry of Education, Beijing 100083, China

ABSTRACT

Based on a study of the geological data and rock mechanics parameters of the Luming Molybdenum Mine and according to the slope stability in the excavation process of the weak structure of the mining area, the similar material simulation test was developed. Using the proportion of geometric similarity constant 300, the laboratory model was set up for a 3-3 profile, and arranged with displacement monitoring points and stress monitoring points. Then the excavation process of the actual slope was simulated with this model and finally conclusions were made after collecting relevant data, as follows: in the process of open-pit slope excavation, the bench slope was affected by a weak structural plane and excavation disturbance. The bench slope was destroyed due to deformation failure, especially in the cross area of the weak structure plane and fault and the area of the bench slope located in weak structural plane.

KEYWORDS: slope; stability; similar material; experimental simulation

1. INTRODUCTION

Research on stability for slope engineering has always been one of the core problems in the field of mining engineering, and the main content of slope engineering research relates to the mechanisms of deformation and failure. Under the comprehensive effect of various internal and external factors, stability is characterized by certainty and randomness, making it difficult to adopt the mathematical analytical method to solve the problem of stability for slope engineering (Yang, T.H. et al., 2011). Directly using an experimental study of the actual structure size is also impossible and has great limitations. With the principles of similarity theory, using the similar physical model for slope stability research has been one of the effective ways to solve the problem of slope engineering, and the development of slope engineering research also shows that it is an effective method.

Based on the experiment method of the similar material simulation, this study simulates the Luming Molybdenum west-I area slope engineering deformation and failure process, and studies the deformation and failure rules. The test of similar material mixture is conducted to get all kinds of material proportion, then a similar material simulation experiment is conducted to simulate the excavation sequence, and finally the stress and displacement data are collected for stability analysis (Yin, Z.G. et al., 2011; Zhang, H. et al., 2011).

Combined with the numerical simulation results, the purpose of this study is to find the 3-3 section of Luming Molybdenum on the west-I slope potential damage area through a similar material simulation, and to provide technical support for the safety production.

2. THE BASIC PRINCIPLE OF SIMILAR EXPERIMENTS

The theoretical basis of similar material simulation experiment are three laws, according to the theory of similarity, and they are mainly geometric similarity, kinetic similarity, and dynamical similarity which are to satisfy the single value geometric conditions, physical conditions and time conditions, boundary conditions, and initial conditions (Wu, W., 2011). The similarity criteria are as follows:

(1) Geometric similarity

$$\frac{L_m}{L_p} = C_l \quad (1)$$

In the formula: M represents the similar model, P represents the engineering prototype, C is similarity ratio, the same below.

(2) Time similarity

$$C_t = \sqrt{C_l} \quad (2)$$

(3) Bulk density similarity

*Corresponding author – email :wanghuiustb@live.cn.

$$\frac{\gamma_m}{\gamma_p} = C_\gamma \quad (3)$$

(4) Stress similarity (elastic modulus, strength, etc):

$$\frac{\sigma_m}{\sigma_p} = C_\sigma = C_\gamma \cdot C_l \quad (4)$$

$$(C_E = C_\gamma \cdot C_l, C_R = C_\gamma \cdot C_l)$$

3. MODEL SELECTION AND THE SELECTION OF SIMILAR MATERIAL

3.1 Selection of similar model

This study is based on the investigation of geological data and mechanical parameters of rock mechanics parameters in the early period of a mining area, and the area of potential safety hazard is mainly in the fault area of F4 and F3. In order to confirm with numerical simulation research, the profile of the selected analog simulation is 3-3 section (as shown in Figure 1). Rock mechanics parameters are shown in Table 1.

Table 1: Rock and soil physical and mechanical parameter table of west- I area slope engineering of Luming Molybdenum.

Lithology	Density	Elasticity modulus	Poisson's ratio	Shear elasticity	Internal friction angle	Cohesive force	Compressive strength	Depth
	103kg/m ³	GPa		GPa	°	MPa	MPa	m
Granite 1	2.526	4.82	0.28	1.88	29	0.12	0.061	0-93
Granite 2	2.592	5.34	0.23	2.17	33	0.21	0.457	93-147
Granite 3	2.614	6.52	0.2	2.72	37	0.25	0.512	147-
Crushed zone	2.173	1.44	0.33	0.54	19.01	0.075	0	

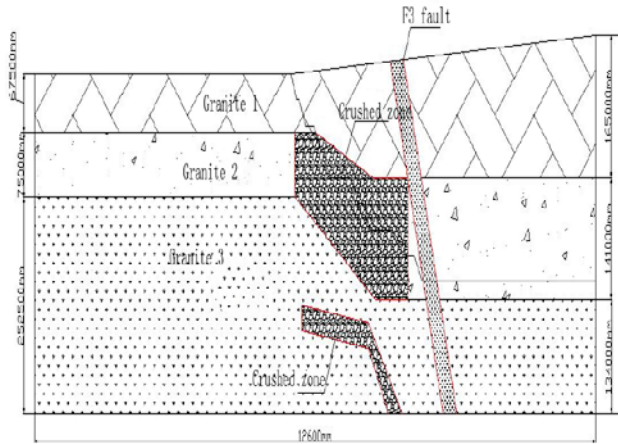


Figure 1: 3-3 Profile geological map.

2.2 Determine similar conditions

(1) The geometric similarity constant

Length similarity constant: $\alpha_L = L_H / L_M$, L_H -the thickness of prototype, L_M -the thickness of model. In the choice of geometric similarity constant $\alpha_L = 300$ (empirical value), due to the fact that the prototype height is 440 m and the horizontal width is 1260 m, the simulation size, height, and thickness should be 4200 m, 1467 m, 250 m, respectively.

The planestrain conditions are used in the experiment, and the thickness of each layer in the similar model are respectively:

$$L_{M1} = L_{H1} / \alpha_L = 50 \text{ m} / 300 = 167 \text{ mm};$$

In the same way, the thickness of L_{M2} , L_{M3} , L_{M4} are 300 mm, 297 mm, 870 mm.

(2) The time similarity constant

$$a_t = \sqrt{a_L} = (300)^{1/2} = 17.32$$

(3) The bulk density similarity constant

$\alpha_\gamma = \gamma_H / \gamma_M$, γ_H -prototype unit weight, γ_M -model bulk density. γ_M -generally is 13.7-17.68 kN/m³, after considering comprehensively the option is 16.5 kN/m³.

With the granite 1 unit weight as the prototype unit weight, the unit weight similar constant is calculated as follows:

$$\alpha_\gamma = \gamma_H / \gamma_M = \frac{2.526 \times 9.8}{16.5} = 1.5$$

(4) The intensity of similar constant

$\alpha_C = C_H / C_M$, C_H -the intensity of the prototype, C_M -the model intensity. The intensity similarity constant is equal to the density of similar strength.

(5) Stress similarity constant

$$\alpha_\sigma = \frac{\sigma_H}{\sigma_M} = \frac{\gamma_H H_H}{\gamma_M H_M} = \alpha_L \frac{\gamma_H}{\gamma_M} \quad (5)$$

So, $\alpha_\sigma = \alpha_L \cdot \gamma_H / \gamma_M \approx 450$

Type: σ_H —the original rock stress or strength; the unit is kN/m³, same below.

σ_M —the stress or strength of model; σ_p — prototype average density

2.3 The selection of similar material, strength calculation and material ratio

River sand was chosen as the raw material, where the density is 1.35-1.45 g/cm³, lime and gypsum as cement, and the density is 2.60-2.75 g/cm³ and 0.936 g/cm³.

The model strength is calculated, according to the similarity calculation formula:

$$\sigma_M = \sigma_p / \alpha_L \alpha_\gamma \quad (6)$$

Type: σ_M - simulation strength of the rock (ore) in the model, unit for MPa; σ_p - actual strength of the rock(ore) in the prototype, unit for MPa.

α_L 、 α_γ represent the geometric similarity ratio and bulk density, respectively. Therefore, the simulated strength of the corresponding rock is: the

compressive strength and bulk density of the first layer of granite model, which are:

$$\sigma_M = 19.37 \times \frac{1}{300 \times 1.5} = 0.043(MPa) ;$$

$$\gamma_{M1} = \frac{\gamma_H}{\alpha_\gamma} = \frac{2.526}{1.5} = 1.68 \text{ kN/m}^3 ;$$

In the same way, as for the second and third layer of the granite and the fracture zone model, the compressive strength of σ_{M2} , σ_{M3} , σ_{M4} are 0.102 MPa, 0.114 MPa, 1.78×10^{-4} MPa and the bulk density for γ_{M2} , γ_{M3} , γ_{M4} are 1.728 kN/m³, 1.74 kN/m³, 1.45 kN/m³.

Based on the literature (Duan, H.G. et al., 2011), the dosage of aggregate, cement, gypsum and water are all factors that affect the strength of the specimens. After many matching tests, a ratio that satisfies the requirement is selected (as shown in Table 2).

Table 2: The matching parameter table of rock mass similar material experiment for Luming north slope engineering.

Position	Lithology	Simulation of compressive Strength(MPa)	Simulated bulk density(kN/m ³)	The ratio of no.	Proportion material
1	Granite1	0.043	1.68	12:01:00	Sand, Lime, Gypsum
2	Granite2	0.102	1.728	873	Sand, Lime, Gypsum
3	Granite3	0.114	1.74	955	Sand, Lime, Gypsum
4	Crushed zone/ Fault	1.78×10^{-4}	1.45	-	Mica, Sand Mixture

4. THE FABRICATION OF SIMILAR MODEL AND ARRANGEMENT OF MEASURING POINTS

4.1 The fabrication of similar model

The building process of the similar model (Figure 2) of this project is as follows:

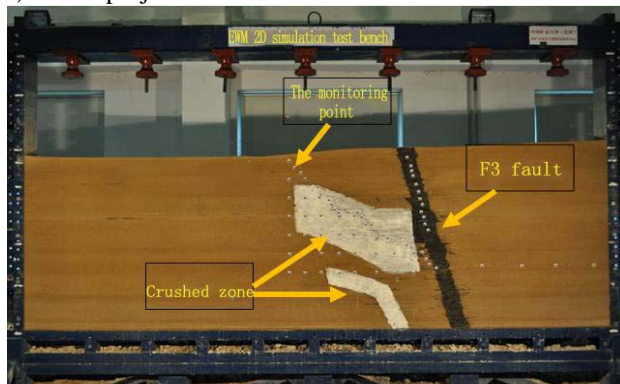


Figure 2: The similar mode of the west 3-3 profile for Luming Molybdenum.

Firstly set up the subject building of the model and compound the material, then smoothly place the

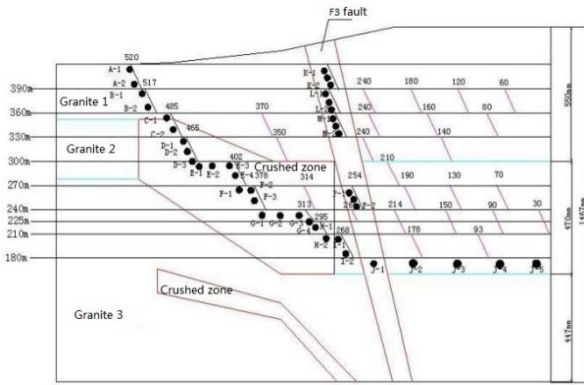
material on the model. After the similar material is a little dry, remove the template and arrange the monitoring points.

4.2 Arrangement of the stress monitoring points

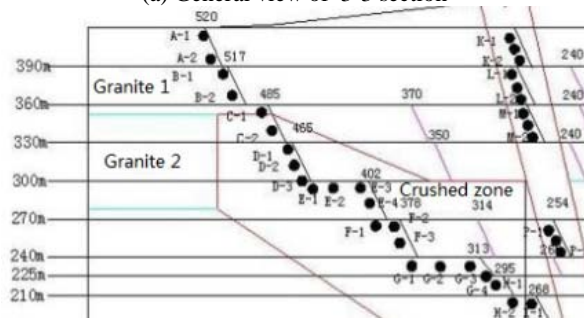
The strain gauges are arranged near the slope and crushed zone, in fault, at a total of 48, and the position of the specific placement is shown in Figure 3. As for the experiment limit, we mainly research the vertical strain. Pressure measurement applies to the testing system of the static strain, and the system includes a data collection box, a microcomputer and the supporting software.

4.3 The arrangement of the displacement monitoring points

In order to observe the slope surface and the regulation of the movement and deformations of overlying strata for the working face, the observation points of displacement are set up on the surface of the slope, the earth's surface, and different positions of overburden layers for the molybdenum mine, respectively. The arrangement of designed points for a 3-3 profile similar model is shown in Figure 3.



(a) General view of 3-3 section

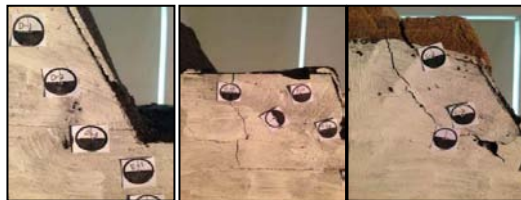


(b) Partial enlarged detail of 3-3 section

Figure 3: The arrangement of strain gauges, displacement monitoring points for 3-3 section similar model.

5. THE EXPERIMENT RESULTS OF SIMILAR SIMULATION ANALYSIS

The experiment results of 3-3 section stress change and displacement change were researched and analyzed, and eventually the section stability conditions were determined.



(a) Damage phenomenon of 360 m level

(b) Damage phenomenon of 330 m level

(c) Damage phenomenon of 300 m level

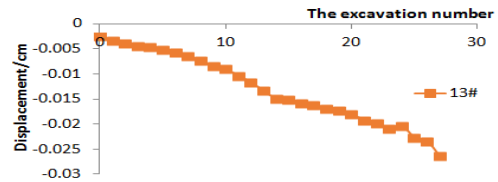
Figure 4: Deformation and damage of slope during excavation of 3-3 profile in the west area.

The analysis of Figure 4 shows that during the excavation of western 3-3 profile, 360 m, 330 m, 300 m represent elevation, and the macro deformation and failure of the slope are mainly embodied in the 360 m level, 330 m level and 300 m level. With the continuous excavation of the adjacent level, the original micro cracks penetrate mutually and expand

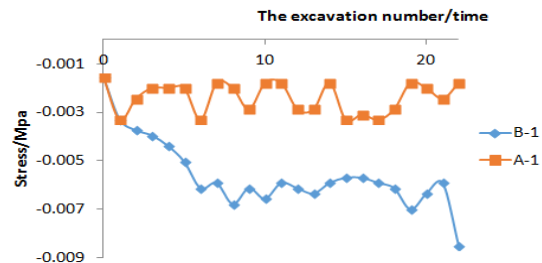
continuously, resulting in obvious macro deformation and reduction.

5.1 Simulating analysis of stress variation about 3-3 section

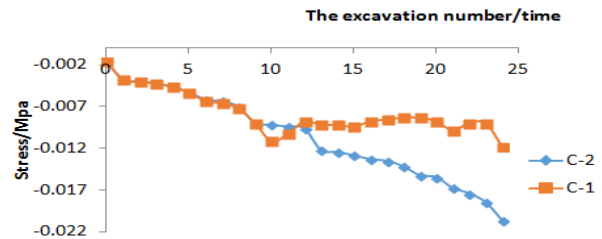
The excavation is divided into 8 levels and the monitoring data of each excavation is acquired. Figure 5 is the stress monitoring data after each step of excavation.



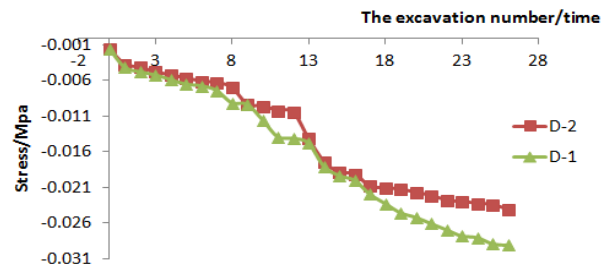
(a) 210 m level excavation stress change curve



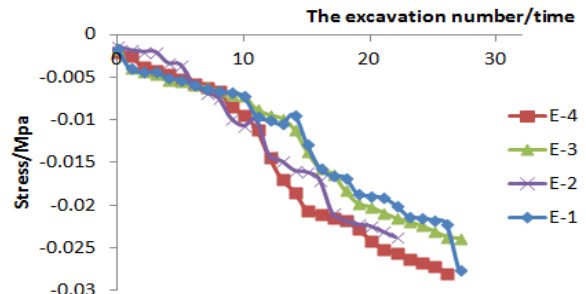
(b) 390 m and 360 m level excavation stress change curve



(c) 330 m level excavation stress change curve



(d) 300 m level excavation stress change curve



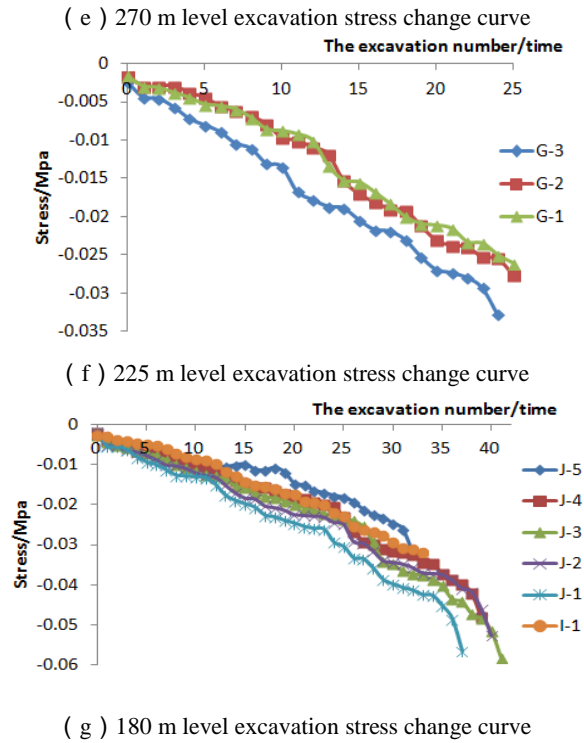


Figure 5: The stress change curve of 3-3 profile during excavation in west area.

We can find from Figure 5 that:

(1) With the continuous excavation process, stress values from the 390 m-180 m level excavation had a rising stage, but overall the rise kept to a gentle degree.

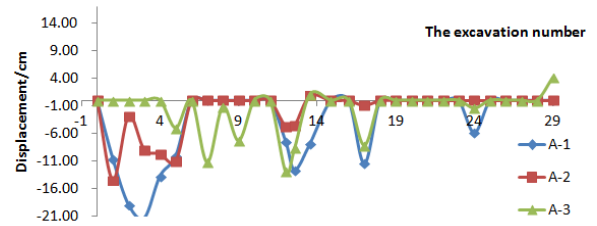
(2) When excavation approached a certain level, its stress appeared to increase. After the exploiting was completed, stress reduced and pressure relieved quickly. Figure 5 shows that as for the NO.A-1 points (390 m level) and NO.B-1 points (360 m level), the two stress variation curves were parallel but the difference was relatively larger than other slopes, indicating that the stability of the 360 m level was poorer than other side slopes.

On the same level, stress change curves of two different monitoring points have large differences, indicating that the stability of the level is poor. The differences of the stress variation curve in the 330 m level and 300 m levels indicates that the stability was poorer than some other side slopes. There were some differences in stress curves in the 270 m, 225 m, 180 m levels nearby, indicating that there was a small possibility of slope instability during excavation. The 5# strain monitoring gauge at the 180 m level slope was laid in fault, and the rate of the stress changes was large, indicating there was the existence of instability phenomenon due to the fault through 180 m level slope.

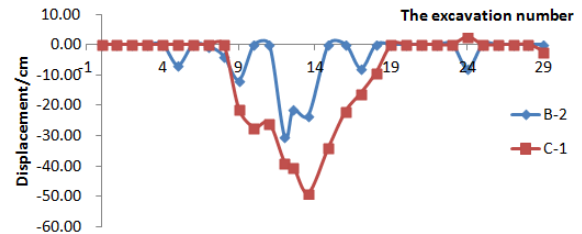
In conclusion, 3-3 profile was not stable, the reason being that the slope was in the crushed zone, which resulted in instability phenomenon due to the variation of stresses.

5.2 The analog simulation displacement change rule of 3-3 profile

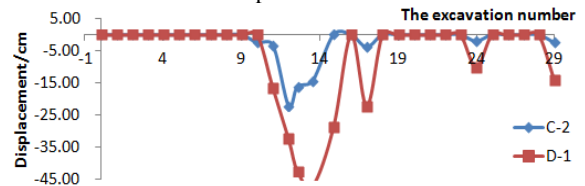
According to research data (Liu, L.P. et al.; 2000 Zeng, Y.W., 2005), in the slope stability analysis process, big displacement deformation of the slope occurs mainly in poor structural surfaces and bench slope areas. The similar simulation study focused on the 30 monitoring data analysis in the area near the bench slope and the monitoring results are shown in Figure 6.



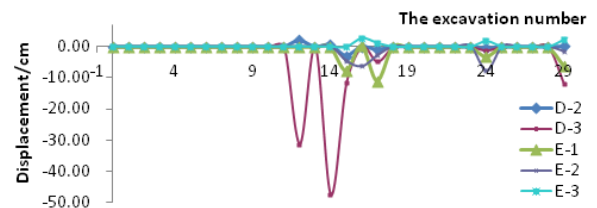
(a) The change curve of the 390 m level excavation displacement



(b) The change curve of the 360 m level excavation displacement



(c) The change curve of the 330 m level excavation displacement



(d) The change curve of the 300 m level excavation displacement

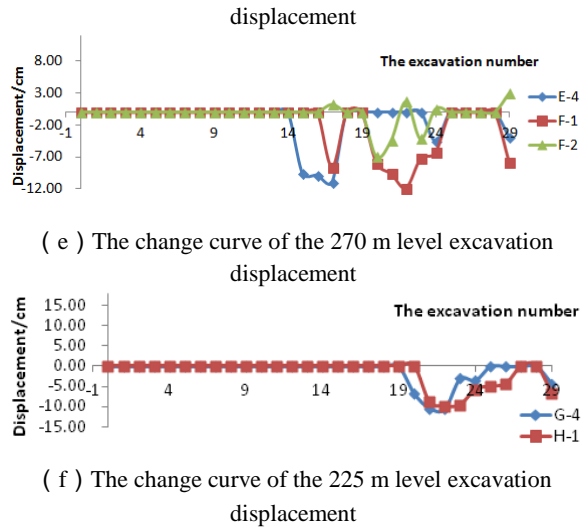


Figure 6: 3-3 section displacement monitoring deformation.

As Figure 6 shows about the similar deformation and displacement monitoring figure of slope excavation, displacement has a certain change in the 29 times simulation of excavation process about the open pit slope. The negative displacement represents sink and positive displacement represents bounce. In Figure 6, from the displacement monitoring and deformation trend of excavation in the 180 m-390 m levels, we can find that the overall deformation of the slope is mainly in the sinking trend, with bounced as the secondary trend. The displacement of deformation ranges from a few centimeters to more than 20 centimeters. What we can analyze from the displacement deformation monitoring diagram and the picture of damaging during the excavating is that the fracture phenomena mainly appears in zone 360 m, zone 330 m, zone 300 m, and zone 270 m, which have F3 fault or are crossed by crushed zones. There is much more obvious fracture growing phenomena especially in the 300 m-360 m levels.

6. CONCLUSIONS

Based on the similar material simulation experiment, theoretical analysis of west-larea Luming Molybdenum 3-3 section of the slope stability was analyzed, and the following conclusions were drawn:

In 3-3 section 360 m level, 330 m, 330 m level, the 180 m level stability are poorer, and instability may exist. The 3-3 section on 360 m level is the most likely to experience instability. To sum up, because the slopes are located in the fracture zone and the stress change leads to instability, the 3-3 profile is obviously not stable.

7. ACKNOWLEDGEMENT

It is with great pleasure that we acknowledge the generous financial support of National Natural Science

Foundation of China (project number: 51474017) and Natural Science Foundation of Xinjiang Uygur Autonomous Region of China (2014211B013).

8. REFERENCES

- Duan, H.G., Jiang, Z.Q., Zhu, S.Y., et al.(2011). Centrifuge model tests on rock brusting induced by great depth highly stressed roof strata of weak structural plane. *Journal of Central South University*, Volume 31, NO. 9, pp: 2774-2782.
- Liu, L.P., Jiang, D.Y., Zheng, S.C., et al. (2000). The recent progress of the slope stability analysis methods. *Journal of Chongqing University(Natural Science Edition)*, Volume 15, NO.3, pp: 115-118.
- Wu, W. (2011). The slope instability analysis of the causes and prevention and management. *Mining Technology*, Volume 12, NO. 5, pp: 44-46 .
- Yang, T. H., Zhang, F. C., Yu, Q.L., et al. (2011). Research situation of open-pit mining high and steep slope stability and its developing trend. *Rock and Soil Mechanics*, Volume 32, NO.5, pp: 1437-1451, 1472.
- Yin, Z.G, Li, X.F, Wei, Z.A, et al. (2011). Similar simulation study of deformation and failure. *Chinese Journal of Rock Mechanics and Engineering*, Volume 14, NO. 1, pp: 2913-2923.
- Zeng, Y.W. (2005). Slope Stability Analysis By Combining Fem With Limit Equilibrium Method. *Chinese Journal of Rock Mechanics and Engineering*, Volume 7, NO. 2, pp: 5355-5359 .
- Zhang, H., Liu, Q.S., Liao, X.G. (2011). Control and Support of Open - pit Slope. *Mining Research and Development*, Volume7, NO. 4, pp: 34-36, 40.

Stability and access implications of open pit mining through old underground mine workings

John G. Henning*

Goldcorp Inc., Vancouver, BC, Canada

ABSTRACT

Increasingly, mining operations are looking at developing large open pits down through old, abandoned underground workings in order to extract remnant ore left within pillar zones. Maintaining pit wall stability while mining through major scale underground stope zones presents both a risk and challenge that can have significant impact on overall pit economics and viability. Potential operational problems associated with the interactions between the stopes and the pit walls may occur, necessitating pit wall redesign, ground support installation and operational rescheduling. In addition, anticipated interactions of the pit shell with underground mine workings must be closely evaluated to maintain a safe working environment. Using illustrative examples, this paper discusses how operational hazards and risks to pit wall stability can be assessed and mitigated.

KEYWORDS: Open Pit mine; highwall stability; underground workings; stope interaction; hazard awareness

1. INTRODUCTION

Maintaining pit wall stability while mining through major scale underground workings presents both a risk and challenge that can have significant impact on overall pit economics and viability. Potential operational problems associated with the interactions between the stopes and the pit walls, such as shown in Figures 1 and 2, may occur. These interactions may require pit wall redesign, ground support installation and operational rescheduling.

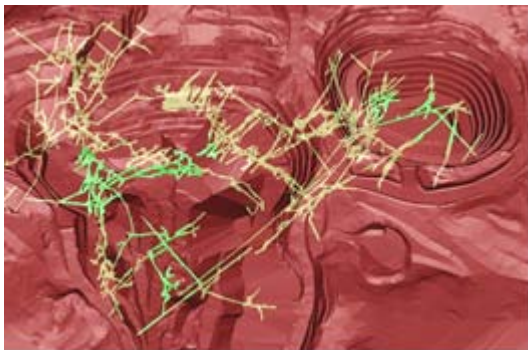


Figure 1: Example of underground workings within designed open pit mine (Kliche et al., 2000).

2. CASE EXAMPLE, DOME OPEN PIT

The Porcupine Gold Mining Camp, located near Timmins, Ontario, Canada, has been in continuous production since 1910. Over that period, approximately 65 million ounces of gold have been produced by more than 50 Underground mining operations. In recent times, Open Pit mining has been

performed to exploit mineralization left by some of these underground mines. While each surface mine has unique design attributes, the practices initially established at the Dome Mine, were essential in permitting safe open pit mining practices.

The Dome Mine began underground production in 1910. Over the years, more than 900 underground stopes have been mined and hundreds of kilometers of drifts, sublevels and raises developed. Underground mining methods included shrinkage, cut and fill and longhole. Longhole stope tonnage may be in excess of 1.0 M tons with vertical heights of 300 m, widths of 60 m and lengths of 180 m. Not all stopes were backfilled upon completion.



Figure 2: Example of a Shrinkage stope daylighting into pit floor.

Open pit operations began in 1988 to supplement underground production. When completed in 2006, the bottom of the Dome pit had reached a depth of

* Corresponding author – email : john.henning@goldcorp.com

335m. The pit was mined with 9 m bench heights, with 11m-wide catch benches established at 27m intervals. Inter-ramp wall angles vary with lithology, ranging from 39° to 54° with average of 49°. Bench face angles were typically between 65° and 75°.

In 2002 the pit began to intersect voids in its final wall, and re-designs of the pit and alternate planning had to be undertaken. The intersection of underground stopes/voids with the Dome Pit's ultimate pit high wall resulted in stability issues that had safety, design, scheduling, operational, and economic impacts.

Much of the planning and design of the pit was driven by the interaction of large voids with the pit wall, as illustrated in Figure 3. The success of the Dome pit depended on the ability to design around the underground voids, profitably maximize ore recovery and maintain production, Miller (2003).

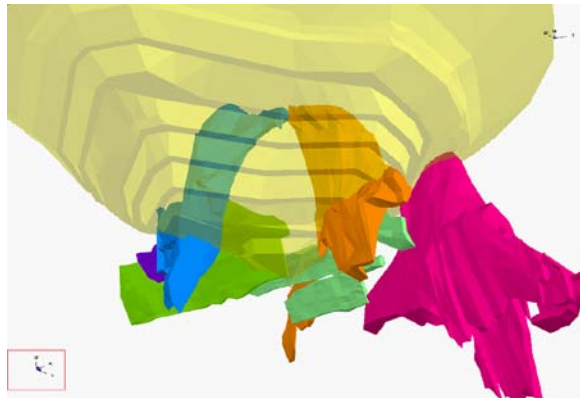


Figure 3: Interaction with mined underground stopes and the Dome pit (yellow colour).

3. INTERACTION WITH MINE WORKINGS

The interaction of the Dome pit with previously mined underground stopes presented a challenge to stability design in the walls, and pit floor. An examples of stope exposure in the pit wall is provided in Figure 4.

Stopes were assessed on a case-by-case basis. Special attention was directed towards stopes which may impact the pit ramp or catch bench due to location or size, stopes with unknown fill conditions, and stopes with unstable wall conditions. In addition, since some mine workings adjacent to the pit dated back more than 75 years, the exact location, geometry and condition of individual stopes and associated development is not always known.



Figure 4: Pit wall undercut by stope.

3.1 Void Definition

Potential voids are identified and defined using a variety of sources. A geometric model based on the open pit and underground mine plans, created with sophisticated design software, provides a 3-dimensional view of interactions between the pit excavation and mine workings.

Other data sources available for void definition include:

- Historical sections of underground voids
- Stope files and records of backfilling
- Underground visual confirmation of voids
- Confirmation of voids via diamond drilling
- Probe drilling from pit floor and measurement of rock, fill and void
- 3D survey via borehole scanner of intercepted voids

Based on the results of void definition, engineering planners design probe holes to verify underground voids. On the basis of proximity to voids, the pit floor is subdivided into non-restricted, cautionary and restricted lanyard areas to ensure safety of personnel.

3.2 Geotechnical design

Geotechnical information is used for the design the pit geometry and for ground support design to achieve acceptable factors of safety, quantify failure mechanisms and assess risk. Available geotechnical data includes:

- 3-dimensional lithological model for the pit
- Bench scale mapping for structure and rock mass quality
- Major feature recognition and mapping (fault, slips and joints)
- Underground level and stope mapping and history
- Rock and backfill characteristics and strength parameters

Problematic stopes were identified and their stability assessed using a range of techniques, including:

- Conventional kinematic analyses to examine potential for wedge, planar and toppling failure of the designed final wall in the vicinity of the identified stope,
- Detailed analyses of potential 3-dimensional wedge block geometry and necessary wedge support capacity, and
- Numerical analysis (2-dimensional and 3-dimensional) to evaluate overall stability interaction issues and to quantify geotechnical assumptions.

Examples of stability modelling at the Dome pit are described in Carter et al. (2009), Henning (2009), and in Palmer et al. (2003).

4. STABILITY DESIGN TACTICS

Ground support or pit geometry re-design are used to establish stable walls conditions when in close proximity to mine workings or when regions of low quality ground are encountered.

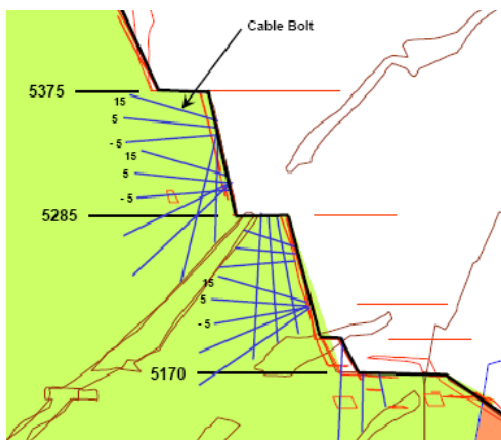


Figure 5: Example of Cable bolt support pattern around underground mine workings (Carter et al, 2009).

4.1 Ground support

Ground support is installed to locally stabilize the rockmass around mine workings or in sectors of low quality ground. Ground support measures used include:

- Cable bolting. Bulbed cables, up to 36m long are installed into the pit wall or floor. Support patterns, such as that shown in Figure 5, are designed on a case-by-case basis. Up to four 25 tonne cables are installed per hole. On occasion, the cables may also be plated, as illustrated in Figure 6.
- Rock bolting, strapping and/or screening is used to provide surface confinement in poor

quality rock. Screening is draped over the wall or installed as catch fences (see Figure 7) to control the descent of small loose rock in sensitive areas or where catch bench spacing has been modified.

- Backfill exposures are stabilized by replacement of the existing fine grain fill (sand or tailings) with a covering of waste rock, allowing a steeper angle of repose. In sensitive areas, fiber reinforced shotcrete has been used to reduce unraveling risk.
- Voids are backfilled in advance of pit mining. Depending on proximity to the ultimate pit wall, unconsolidated and consolidated backfill are used. On occasion, some voids may be filled with concrete.
- Typically a minimum one-to-one pillar is maintained above voids, otherwise sill pillars are blasted down. In the case of large stopes, drop raises may be used to fill the voids with broken waste muck prior to blasting down the sill.



Figure 6: Cable bolt reinforcement above void in pit wall.



Figure 7: Catch fence installation along bench.

4.2 Pit wall geometry redesign

Pit wall geometry is redesigned to minimize impact of voids on pit wall stability. An example of pit re-design around a stope is shown in Figure 8. Design measures used include:

- Increase or decrease bench face angles and berm widths
- Alter ramp width or grade
- Change location of ramp

4.3 Wall control blasting

Preshear blasting is routinely performed along the final pit walls in order to create a smooth, stable face. The goal of the blasting is to create a crack in the rock along the line of the pit wall, but to not fragment or displace the rock.

In areas adjacent to voids, a single row of 114mm diameter preshear holes are drilled at an angle of 80°. Spacing between holes (usually 1.2 m) may be reduced in low quality rock. Elsewhere, 165 mm preshear holes were drilled at 1.8 m spacing.

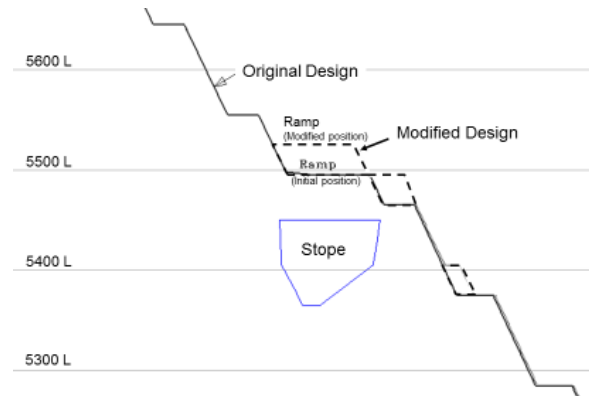


Figure 8: Pit wall re-design to increase pillar dimension around a stope.

5. HAZARD AWARENESS

In addition to hazards associated with pit wall stability, a major concern associated with working around underground workings is that areas of subsidence, or “sinkholes”, may occur unexpectedly. Most of the existing mine openings have been modeled in 3-D. However, there is always the possibility of the presence of unknown openings, or that some openings have failed / caved to a larger than anticipated dimension.

Subsidence can be defined as “the sudden collapse of material into a void beneath it”. Subsidence occurrences can be triggered by the thaw of frozen ground (spring time), heavy rains, and by nearby pit blast vibrations.

5.1 Identification of Hazard Areas

Areas where subsidence may be anticipated, where near-surface voids are known to exist, and mined areas connecting to surface are all considered to be Hazard Areas. In the Pit, these areas are identified by:

- Physical barriers (Temporary fencing, Berms, etc.)

- Delineator cones and pickets. The type and severity of potential hazard can be indicate by colour coding or delineator size. See example, Figure 9.

Safety procedures at the mine dictate what areas can be accessed, and what precautions are required.

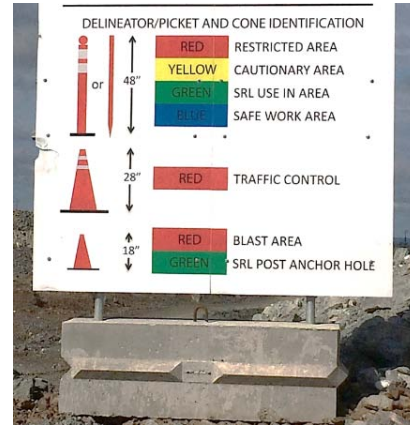


Figure 9: Example of visual hazard identification.

6. MONITORING

The objective of the instrumentation is to provide warning of the onset of movement in stope sidewalls, crown pillars, filled stope openings and final pit walls. Of particular importance to the monitoring program are zones of potential instability encompassing many stopes. Due to the absence of reinforcement in many of these zones, it is imperative that deterioration of stope sidewall stability or fill subsidence be identified promptly.

Monitoring is used to provide an early warning of ground movement to ensure safety of workers. The instrumentation program at Dome Mine consists of several different types of monitors to provide an early detection system, including:

Visual inspections

Visual inspections are performed on an on-going basis to identify evidence of instability, as indicated by crack formation, unraveling, falls of ground, loss of fill, damaged ground support, unexpected breakthrough into void, or subsidence. Unusual occurrences are reported for further review.

Multi Point Borehole Extensometers

Multi-Point Borehole Extensometer (MPBX) instruments are used on occasion as a quantitative early detection system for progressive ground failure in the vicinity of mine workings. Each MPBX consists of six nodes grouted in place and attached to the instrument head by a thin flexible rod. These instruments directly measure displacement of the nodes relative to the head.

Sloughmeters

Sloughmeters are installed into filled stopes to monitor for potential subsidence. These instruments are used as a qualitative early detection system for progressive ground failure. Consisting of ten nodes grouted in place, each node forms a loop for current flow. Should a node be lost (or sloughed), this will be indicated by no current flowing through the loop.

Monitoring of survey prisms

Survey prisms are mounted onto the surface of the pit wall at locations of anticipated instability, such as on potentially unstable wedge intersections. At locations adjacent to the intersection of the pit wall with large backfilled voids, prisms may be installed systematically on a dense (15 m x 15 m) pattern to permit close monitoring of a specific region.

The prisms are monitored several times per day by an automated Robotic Total Station (RTS) survey system, used in conjunction with Geodetic Monitoring software.

Radar

Slope Stability Radar can be used to remotely monitor pit highwall stability. Advanced analysis tools allow for long term trending and hazard identification. Alarms warn of accelerated slope movement prior to wall failure

Underground Mine Voids. Proc. 3rd International Symposia on Rock Slope Stability, 9 – 11 Nov 2009, Santiago, Chile. 13 pg.

Henning, J.G., 2009. Selective highwall mining at the Dome Open Pit mine. 3rd Canada-US Rock Mechanics Symposium (RockEng 09), Toronto, May 2009. 8pg.

Kliche, C., Hladysz, Z., and Franzen, V., 2000. A slope stability analysis for the Trojan Pit expansion at the Wharf Resources Mine, Black Hills, SD. In proc. SME Annual Meeting, 28 Feb – 1 Mar 2000, Salt Lake City, Utah. 18pg.

Miller, P. 2003. Dome Pit Highwall Stability in areas intersected by underground stopes. 3rd Biennial Placer Dome Mining Engineering Conference, October 2003, Kalgoorlie, Western Australia.

Palmer, P.G., Dimock, T., and Cameron, A.R., 2003. Stability analysis of the 653 stope impacting the Dome Mine Open Pit. CIM Mine Operators Conference, Saskatoon, SK, Oct 2003.

7. CONCLUSION

Design and stability of Open Pits developed through historic underground workings are influenced by ‘typical’ factors, such as rock mass condition, and by ‘atypical’ factors – in the form of underground mine workings.

To anticipate and mitigate risks, voids intersecting the pit wall and floor are identified, defined, and assessed. Strict hazard awareness protocols are required. Pit designs are adjusted around anticipated and intercepted workings.

Highwall stability is monitored by an ongoing program of visual inspections for changing conditions, coupled with regular tracking of potential displacements both at the pit surface (survey prisms and radar) and within the wall (extensometers).

8. ACKNOWLEDGEMENTS

The support of Goldcorp Inc. and of Porcupine Gold Mines, for permission to publish is gratefully acknowledged.

9. REFERENCES

Carter, T.G, Rougier, M., Palmer, P., Miller, P.M, and Henning, J.G., 2009. Wall Stability Implications of Large Open Pit Mining through

Thermomechanical impact of Underground Coal Gasification exploitation

Laouafa Farid

Institut National de l'Environnement Industriel et des Risques- INERIS, F-60550 Verneuil-en-Halate, France

ABSTRACT

Underground mining by coal combustion (Underground Coal Gasification - UCG) raises questions regarding the mechanical behavior of the site and the stability of the overburdened rock layers. By studying the underground reactor, its inlet and outlet, the key roles played by mechanical damage and thermo-mechanical phenomena were confirmed. Deformation or collapse above the cavity may cause a collapse in the overlying layers or a subsidence at the surface level. These phenomena highly depend on the thermo-poro-mechanical behaviour of the surrounding rock (host rocks). The numerical results presented in this paper were derived from models based on different assumptions describing a raw geological background. Both 3D and 2D nonlinear finite element modelling was conducted based on two different approaches. Based on the analysis of the numerical results, we were able to highlight the main factors influencing the behaviour and mechanical stability of the overburden, and consequently the UCG process evolution.

KEYWORDS: Underground; coal; combustion; mining; thermomechanic; modelling

1. INTRODUCTION

Underground Coal Gasification (UCG) is a process in which coal is burnt in situ without an explicit extraction of the matter (Bell 2011; Bhutto et al. 2013; Shafirovich et al. 2009). The efficiency of the process depends on the combustion properties of coal rock and other thermodynamic features of the physical phenomenon (temperature, pressure, mass transport related variable) (Williams 1985; Speight 2013).

In terms of cavity shape and its time evolution, the UCG resembles the longwall mining method (Peng et al. 1982, 1984, 2007; Shabanimashcool, 2012).

The UCG process involves high temperatures of around 1000°C, which will affect the host rock, changing its mechanical properties. Based on different tests and research of mudstone specimens from coal seams, Luo et al. (2011) shows that high temperatures cause thermal expansion of mudstone, and that the expansion increases with temperature, producing expansive stress in the surrounding rock of underground gasifiers. Brittle cracks are the main type of deformation. The temperature dependency of rock behavior has been the subject of intense research (Bauer 1983; Deng'gina et al. 1994; Dwivedia et al. 2008; Fjaer et al. 1992; Ide et al. 2010; Somerton 1992; Wolf 2006).

The UCG process may also have other environmental impacts in terms of pollution of groundwater and surface subsidence. The groundwater may be affected by gas or others chemical species transported through the rock porous matrix, and the initial or induced cracks and micro-cracks. At the ground surface, soil subsidence is expected. The extent of subsidence is dependent on the location of

the coal seam, its thickness, and the mechanical properties of the overburden.

The purpose of our article is related to the thermo-mechanical effects induced by the UCG process.

In this framework we performed finite element analyses of a case study coal site that could be exploited by this method. The numerical results presented in this paper were derived from models based on different assumptions describing a raw geological background. Both 3D and 2D nonlinear finite element modelling was conducted based on two approaches. The first one assumed the rock media as a perfect thermo-elastoplastic continuum. In the second one, and in order to simulate explicitly large space scale crack propagation, a method based on finite element deactivation was developed, which is built on a finite element mesh refinement and uses two failure criteria.

On the basis of the analysis of the numerical results, we were able to highlight two main factors that influence the behavior and mechanical stability of overburden, and consequently the sustainability of the UCG process.

2. UCG PROCESS

In the case of UCG, the shape of the cavity (first factor) and its evolution with time can be strongly modified by the thermo-mechanical behaviour of the host rocks. The second factor is the presence of a heat source whose location and intensity evolve with time. The thermal properties of rocks depend strongly on their mineralogical composition, porosity (ϕ), saturation, etc (Fjaer et al. 1992). Table 1 below gives values of porosity (ϕ), thermal conductivity (λ) and specific heat capacity (ρ)

c_p), where ρ is the material density. Somerton (1992) has shown that for different rock materials, the thermal properties are not constant but temperature dependent.

Table 1: Thermal properties of some materials (Jaeger et al. 2007).

Rock Type	ϕ	α ($1/^\circ\text{K}$)	λ ($\text{W}/\text{m}^\circ\text{K}$)	ρc_p ($\text{J}/\text{m}^3^\circ\text{K}$)
Berea sandstone (dry)	0.162	1.5×10^{-6}	2.34	1.76×10^6
Boom clay (wet)	0.450	3.3×10^{-6}	1.70	2.82×10^6
Granodiorite	—	4.7×10^{-5}	2.70	1.90×10^6
Halite Salt (wet)	0.001	4.0×10^{-5}	6.62	1.89×10^6
Water	—	6.6×10^{-5}	0.60	4.17×10^6
Kerosene	—	3.2×10^{-4}	0.13	1.67×10^6

In Figure 1, we describe the Underground Coal Gasification (UCG) process. The injection of air is performed by a vertical well, while syngas (synthetic gas) resulting from coal combustion is extracted by the other well. The coal seams are made to react underground with insufficient oxygen for complete combustion to create syngas. Air is usually used as an oxidant. The oxygen and water within the coal seam react with the coal to produce syngas, which is withdrawn through a production well.

Figure 1 depicts the so called CRIP (Controlled, Retractable Injection Point) method, in which the injection point is gradually withdrawn as coal is consumed. This specific UCG industrial process uses two parallel wells also called Knife-edge CRIP. In this case the distance between the two wells axes is taken to be 20 m. The thickness of the coal seam is equal to 17.3 m. It is assumed that the total width of the burning front is equal to 30 m.

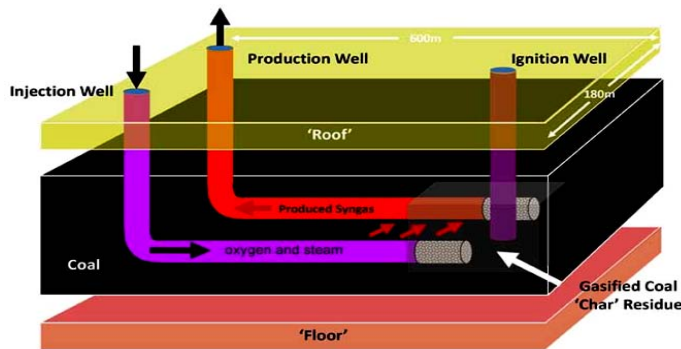


Figure 1: Schematic illustration of the adopted UCG industrial process with two wells.

The temperature at the combustion front is about 1000°C (after Total, a French multinational integrated oil and gas company). The burning front is assumed to be a straight plane at 1000°C and its normal velocity is about

$0.3\text{ mm}/\text{min}$ (after Total Company). The temperature within the cavity can reach several hundred degrees Celsius.

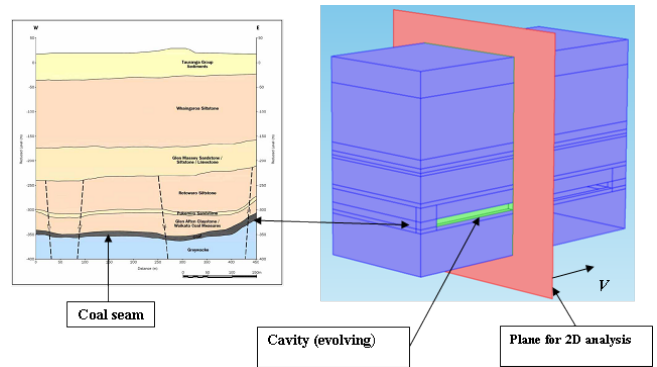


Figure 2: Stratigraphy and location of coal seam (on the left) and 3D numerical model (on the right). A 2D plane passing through the middle of exploitation used in plane strain numerical analyses. V stand for the burning front velocity.

In the case of a cavity (or gallery) having a geometric configuration such as that shown above, the deformation mechanism is mainly plane strain (plane perpendicular to the axis of the cavity). The plane strain analyses are based on a cavity width of 30 m. These dimensions assume that combustion extends 5 m transversely from two casings installed 20 m away from each other.

The reader can refer to Fjaer et al. (1992) for the mechanical and thermal properties of some of the rocks. Among all these properties that have been identified, some representative averaged values were extracted. The properties used in these models are as follows): Thermal conductivity: $2\text{ W}/\text{m}/\text{K}$, Heat capacity: $800\text{ J}/\text{kg}/\text{K}$, density: $2500\text{ kg}/\text{m}^3$.

The Young's Modulus of the coal is taken as 2.5 GPa and Poisson's ratio as 0.3 . The Young's modulus of overburden is assumed to vary from 5 GPa to 25 GPa and the Poisson's ratio is equal to 0.3 . Several computations have been performed by varying these parameters within realistic value ranges, and they do not change our conclusions based on our modeling work. Low values for the Young's Modulus are assigned to the layers close to the surface in order to consider them as dead load. The thermal expansion coefficient of rocks is equal to $10^{-5}\text{ }^\circ\text{C}^{-1}$.

3. 2D AND 3D THERMOMECHANICAL MODELLING

The objective is to analyze the spatial extent of plasticity (damage) in the vicinity of the cavity. The model size is deliberately reduced to the dimensions defined in Figure 3. Although the model has a vertical plane of symmetry (through the axis of the cavity), the calculations were carried out on the whole 2D model to analyze a component of the robustness of the numerical

model (maintaining the symmetry of the mechanical response).

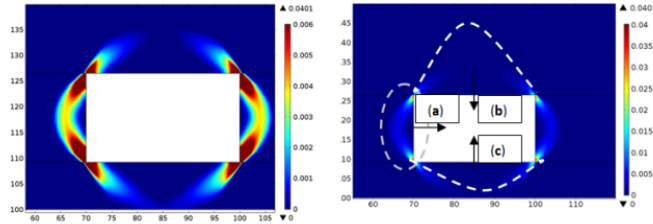


Figure 3: Spatial distribution of the effective plastic strain (in the left) and schematic of potential movements (failure, rockfalls, collapse,...) on the right.

Let us recall that the definition of the effective plastic strain is as follows:

$$\varepsilon_{eq}^p = \int_0^t \dot{\varepsilon}_{eq}^p dt \quad \text{with} \quad \dot{\varepsilon}_{eq}^p = \sqrt{\frac{2}{3} \dot{\varepsilon}_{ij}^p \dot{\varepsilon}_{ij}^p}$$

We observe that plasticity affects a part of the cover and the coal wall. However, the extension is limited but the coal layer is also affected.

We can assume that the hypotheses of material continuity and classical thermo-elastoplastic framework are too conservative. In other words, if the analysis was performed in the framework of fracture mechanics, linear or nonlinear (Broek 1986), we would certainly have found a lower overall stability rather than local rockfall from the roof and major collapse in coal (Figure 3, right). Likewise, it is reasonable to assume that overburden massive coal generally consists of calcareous clay layers, sometimes sandy, is layered, heterogeneous, and marked by discontinuities at different scales. The overall strength properties are quite low. Therefore, the choice of pair of values (cohesion, friction angle) representative of the whole overburden is critical for the prediction of the extent of the damaged area. We can a priori assume that the uniaxial compression strength of the overburden seldom exceeds 3 to 5 MPa overall. This leads to an extension of the damage larger than calculated above. These failure types can affect the combustion process as the combustion front may break and, due to the failures at the edge of the cavity, change the kinetics, the size, and shape of the combustion front, and therefore the shape of the cavity. They can also affect the direction of the cavity evolution. It is observed that the greatest displacement naturally lies in the cavity roof. The effect on the surface (subsidence) will be presented in the section dedicated to 3D models. If it is not explicitly specified, the criterion for the *adaptive mesh refinement* is based upon the value of the equivalent plastic strain.

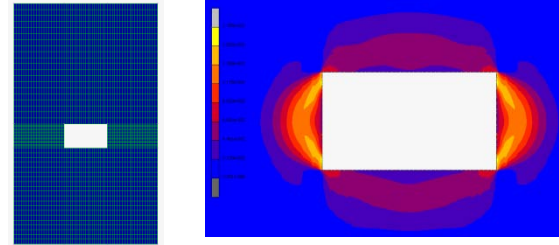


Figure 4: 2D finite elements mesh (left) and effective plastic strain (right) (L=30 m).

The model on which we performed our analysis is illustrated by its finite element mesh in Figure 4. The width of the cavity is 30 m. This approach required the use of another finite element code that allows adaptive mesh refinement and the possibility of deactivating a number of elements (MARCTM finite elements code, MSC Software, 2014). Figure 4 shows also spatial distribution of plasticity and Figure 5 presents the mesh density when using finite element refinement and deactivation in order to simulate crack propagation.

It was observed that the extension of the plasticity zone for a cavity of 30 m width is limited in space but still significant.

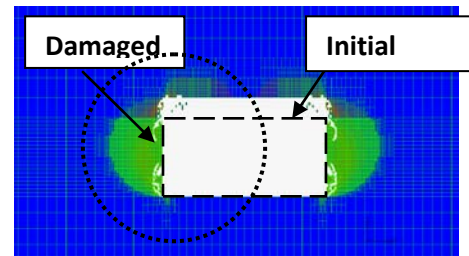


Figure 5: Example of result with adaptive mesh refinement and element deactivation (L = 30 m). The effective plastic deformation range from 0 to 0.17.

The results in Figure 4 are obtained through a classical approach and the elastoplastic continuum medium (i.e., overburden and coal) is assumed to be continuous and remains so regardless of the degree of "damage". Figures 5, 6, and 7 show the same computation, but using a deactivation (roughly simulating fracturing) of finite elements based on adaptive mesh refinement. We observe that with the most intense element concentration (small elements and therefore finer mesh), the damage zone becomes more detailed. Note also that the computation highlight the "failure" in the walls of the cavity and the collapse of part of the roof of the cavity.

On the basis of the spatial distribution of the mesh, it is easy to foresee the shape and damaged areas. The extent of mesh refinement is limited only by the power of the computer. The refinement is an *h-refinement* (based on subdivision of the finite element), which is different than *p-refinement* (based on the degree of the finite element).

The effect of the fineness of the mesh is shown in Figures 6 and 7.

The rock properties (reduction of cohesion and friction angle by 40%) were decreased and the cavity was widened to 30 m. The initial mesh was regular and relatively coarse (in size).

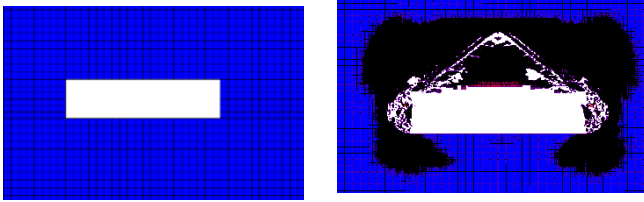


Figure 6: Initial mesh (left) and after dynamic computation, using adaptive mesh refinement and finite element deactivation (right). (Cavity width=30 m).

Figure 6 shows the distribution of fracturing in the overburden, in the coal walls, and the mesh density in the plasticity zones. Figure 7 (right) shows a focus of quality of mesh refinement required in order to carry out the calculation. The "triangular" shape of the collapse area in the roof and high degradation of coal wall are to be noted. This failure mode, described here in a very simplified way, is commonly observed in situ in the case of underground mines or quarries. The figures represent results at an instantaneous state (observation at a given time t) because the elements are allowed to move in the dynamic analysis. The inertial terms induced by gravity and the fractures play an important role and this analysis therefore differs fundamentally from the quasi-static approach. The cavity extends laterally until the coal zone is sufficiently undamaged (by failure). The combustion process which is already a chaotic phenomenon would be difficult to formalize in such condition. The combination of burning and fracturing/block falling should influence the rate of combustion in the cavity.

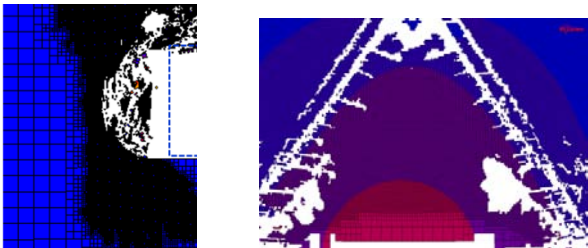


Figure 7: Focus of the coal wall and roof meshes (several thousand elements).

The modelling results depicted in Figures 6 and 7 present the main failure mechanisms as described by Whittles et al. (2007). The coal wall, the roof, and part of the floor are damaged by the cavity creation. This numerical computation using adaptive mesh refinement and element deactivation seems relevant for this study as they contain much information performed even on an idealized geometry such as failure and damage of the roof

and wall being important outcomes. It should be noted that such mechanisms are those generally observed during underground mining. In the case of UCG, these failures can disrupt the function of the reactor, alter the path of the combustion front, and so on.

4. SUBSIDENCE AND ROOF DEFORMATION

The 3D computations are performed on the geometric model shown in Figure 8. The cavity and its spatio-temporal evolution are not explicitly created. More precisely, the initial cavity, a purely geometrical shape, has the dimensions of the final "cavity". However, it applies to the boundaries of the cavity pressure and temperature whose laws of spatial and temporal evolution describe the expansion of the cavity.

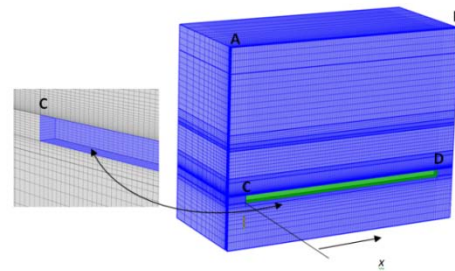


Figure 8: 3D mesh and location of the coal seam.

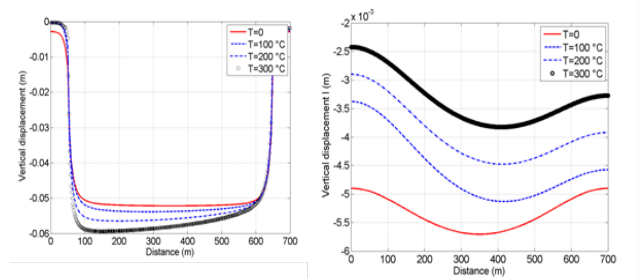


Figure 9: Vertical displacement of the roof of the cavity (segment CD) when it is created (left) and surface subsidence (segment AB) when the whole cavity is created (right) for 4 temperatures fields inside the cavity.

The first remark concerns the vertical displacement of the roof of the cavity. Asymmetry (with respect to the reference solution $T=0$) occurs. Note in the modelling the "front" of combustion moves from left to right. The higher the temperature, the greater the intensity of movement (left increases), and the asymmetry is more pronounced. This is explained by the fact that by conduction and due to the intensity of the temperature difference, the part to the left is longer subjected to a high temperature. Consequently the extension of the temperature will be greater in the rock matrix. There is also a shift to the right for the maximum subsidence. The surface subsidence is induced not only by the excavation of the cavity, but also by thermal effects. That the subsidence is negative

indicates that the contribution of the rock mass thermal expansion in the uprising is lower than the displacement induced by stress modification due to underground excavation. The following 3D results are given as an illustration and show the burning front evolution. Elastoplastic models with adaptive refinement and 3D finite element deactivation were performed in order to assess the consequences of a possible "fracturing".

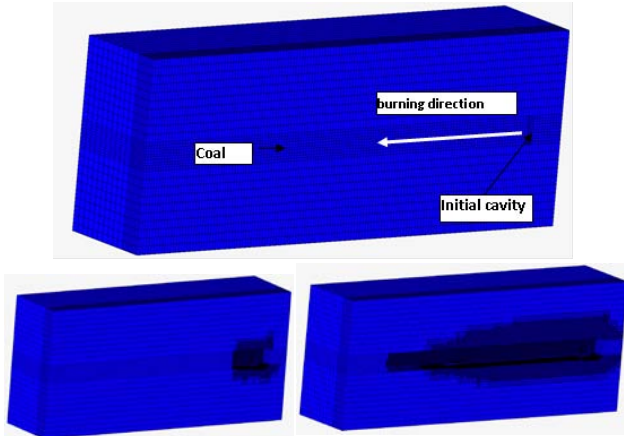


Figure 10: Example of induced "fracturing" during time and the space evolution of the cavity.

5. STRATIFIED ROOF

In this short subsection we analyze briefly the behavior of a stratified roof composed of marl and sandstone (Figure 11). The elliptical cavity is located in the coal layer. The remaining rock is sandstones.

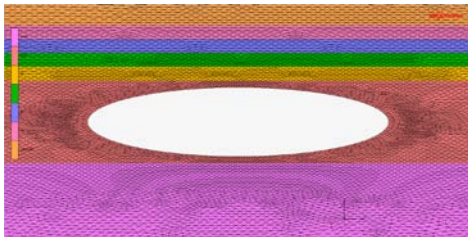


Figure 11: Mesh of the elliptical burning cavity and stratified roof.

After a given extend of the burning cavity (assumed elliptical in this sub-section), we applied a given temperature to its boundary (200 °C). After a given time we obtained the following displacement field as illustrated in Figure 12.

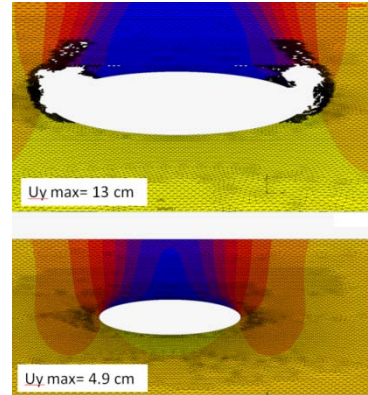


Figure 12: Vertical displacements field using two methods: Pseudo fracturing (top) and continuum model (bottom).

One can observe that the intensity of the vertical displacement and the final shape is strongly dependent on the assumption of a perfect continuum. The effect of the presence of layers with different mechanical parameters is show in Figure 13.

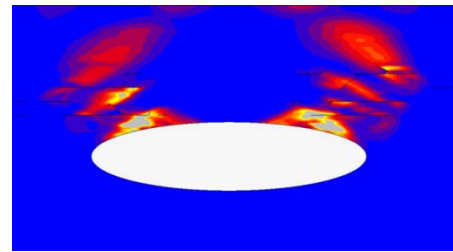


Figure 13: Effective plastic strain distribution with crack propagation.

The spatial distribution of the effective plastic strain is totally different when we take into account a layered roof. In this configuration that exhibits a stratified roof we highlight the transient effect of temperature. Indeed, thermal effects are more important when the medium is stratified and thus heterogeneous. The differential thermal and/or mechanical properties induce incremental strains and shear at interfaces layers. The case presented here is an academic and theoretical case. In real environments, we encounter heterogeneities at the porous matrix level, where it is well known and demonstrated that they induce an increase of the Von Mises stress. In addition, the results for a stratified medium show that solving such problems by using continuous media assumptions is far too conservative.

6. CONCLUSIONS

Geomechanical evaluations of the rock mass properties remain very important processes during Underground Coal Gasification. An accurate stability analysis of the consequence of UCG requires a global characterization of the rock constituting the overburden. All of the different factors contribute to instability of the

host rock during and after the gasification process. Unlike the stresses induced by void creation and their redistribution (as encountered in conventional mining), UCG introduced additional thermal stresses in the vicinity of the reactor. Thermal expansion may induce buckling or elastoplastic instability due to the increase of compressive stresses. The problem, which can be defined as transient bifurcation, is quite complex. The shape of the cavity and its evolution in time remain an important parameter which influences the stability of the host rock. Nevertheless, the evolution of the cavity in space and time has some random character due to the non-control of the parameters driving the combustion process and also due to the effects of host rock behavior. Caution must be taken when using a specific technique for UCG simulation.

7. ACKNOWLEDGEMENT

The work performed in this paper is supported by the EU project COGAR, Grant Agreement RFCR-CT-2013-00002.

8. REFERENCES

- Bell D.A., Towler B.F., Fan M. (2011). Coal Gasification And Its Applications. Elsevier
- Bhutto A.W., Bazmi A.A., Zahedi G. (2013). Underground Coal Gasification: From fundamentals to applications. Progress in Energy and Combustion Science 39, pp. 189-214
- Broek D. (1986). Elementary Engineering Fracture Mechanics, 4th ed., Kluwer, Dordrecht
- Den'gina N.I., Kazak V.N., Pristash (1994). Changes in rocks at high temperatures. Geotechnological methods. Plenum Publishing Corporation, pp. 472-777.
- Dwivedia R.D., Goela R. K., Prasada V.V.R., Sinhab (2008). Thermo-mechanical properties of Indian and other granites. International Journal of Rock Mechanics & Mining Sciences. 45, pp. 303-315
- Fjaer E, Holt R M, Horsrud P, Raaen A M , Risnes R (1992) Petroleum related rock mechanics. Elsevier
- Ide T.S., Pollard D, Orr F M (2010) Fissure formation and subsurface subsidence in a coalbed fire. International Journal of Rock Mechanics and Mining Sciences. Vol.7: 81-93
- Jaeger J.C., Cook N.G.W., Zimmerman R.W. (2007). Fundamentals of Rock Mechanics. Fourth Edition. Blackwell
- Luo J., Wang L. (2011). High-Temperature Mechanical Properties of Mudstone in the Process of Underground Coal Gasification. Rock Mech Rock Eng 44:749-754
- Marc Software (2014). Marc user manual.
- Peng S.S., Chiang H. S. (1982) Roof Stability in longwall coal face. in Stability in Underground Mining, Brawner C O ed. American Institut of mining, Metallurgical and petroleum Engineers, Inc.
- Peng S.S., Chiang H.S. (1984) Longwall Mining. Wiley
- Peng S.S., Zhang J. (2007). Engineering Geology for Underground Rocks. Springer-Verlag, Berlin Heidelberg.
- Shafirovich E., Varma A. (2009). Underground Coal Gasification: A Brief Review of Current Status. Ind. Eng. Chem. Res. 4 : 7865-7875
- Somerton W. H. (1992). Thermal properties and temperature-related behavior of rock/fluid systems. Elsevier.
- Speight J.G. (2013). The Chemistry and Technology of Coal. Third Edition. CRC Press
- Williams F. A. (1985). Combustion Theory The Fundamental Theory of Chemically Reacting Flow Systems Second Edition. Princeton University
- Wolf K. H. A. A.(2006). The Interaction between Coal Fires and Their Roof Rocks. Phd thesis, Delft University of Technology

Escapeway Solutions

Allison Deadman^a, Steven Durkin^b, Vincent Lawrence^c

^a General Manager, Safescape, Bendigo, Australia, 3551, allison@safescape.com

^b Managing Director, Safescape, Forrestfield, Australia, 6058. steve@safescape.com

^c Mining Engineer, MMG Golden Grove, vincent.lawrence@mmg.com

ABSTRACT

The requirement for secondary egress from underground workings has long been regulated in Australia. Escapeway systems have evolved from simple airleg rising ladders and timber ladders to steel galvanized ladders and more recently fully enclosed polyethylene ladders.

The polyethylene ladder - Safescape Laddertube - was introduced to the underground mining industry in 2010. It is a cylindrical, enclosed, modular plastic ladder designed for use in underground escapeways and access ways. The design of Safescape Laddertube has many advantages, one of those being that it is enclosed therefore minimizing the risk to climbers of exposure to fretting rock. In 'standard' installations there have occasionally been changes in the ground conditions which have resulted in significant fretting or rock burst causing deformation in the Laddertube. In addition there is on occasion a requirement to position an escapeway in ground that has highly stressed or squeezing ground conditions, presenting mines with potential for failure of ground resulting in serious damage to these escapeways.

As a result, Safescape have developed a number of proactive solutions that can be used at the time of installation which will eliminate or minimize the effects of ground that is not 'competent'. These solutions address the need for ground support and eliminate the need for the traditional methods of ground support in a rise such as bolt and mesh, which also means we no longer need to put people in unsupported ground to complete this high risk work.

Despite being a recent development in escapeway systems, Laddertube is effectively being used in a variety of applications, meeting the specific needs of underground mines worldwide.

KEYWORDS: Perlite; Laddertube; Ground support; Polyliner; Raiseliner

1. DEVELOPMENT OF LADDERTUBE ESCAPEWAY LADDER

Legislation exists in all developed mining countries covering the requirement for producing mines to ensure miners working underground have access to an alternative exit from working areas. The primary reason for this is for insurance against a significant ground collapse in the main travelway, which would otherwise result in the entrapment of personnel for an extended period.

In many mines with sub-horizontal orebodies or mines with excessive ventilation requirements such as uranium mines, secondary egress is taken care of by mining multiple primary accesses, multiple shafts or declines accessible from all working areas. Where sub-vertical mines exist with limited strike extent, the most common methods of providing secondary egress include ladderways, raise climbers and headframes with rope hoists.

Ladderways have historically been the preferred choice where the length is limited. Compared to the alternatives, ladderways are more popular because they are simple, self-escape systems and do not

require support from personnel on the surface. They are relatively cheap to install and maintain and they are reliable provided that they are maintained in good condition.

Up until recently the most common ladderways found in Australian mines consisted of timber stiles with 20 mm black steel rungs or a simple steel design (Figure 1a). Steel modular caged ladders (Figure 1b) offered additional support to the user in terms of mesh cages and inclusion of rest platforms. One of the problems with these systems is that over time when exposed to ground water they tend to deteriorate. In 2010 Laddertube (Figure 1c) fully enclosed polyethylene ladders were developed as an alternative to conventional steel and timber ladders.

This style of ladderway has proven very popular due to the speed and safety of its installation as well as the fact that it does not corrode when exposed to the highly saline and acidic ground water often found in Australian mines.



(a) Simple steel design (b) Steel cage (c) Laddertube
Figure 1: The evolution of escapeway ladders.

2. PASSIVE GROUND SUPPORT – A NEW APPROACH

To date Safescope have installed as well as trained site personnel in the installation of laddertube in 9 countries, all of which have a variety of ground conditions. The methodology and solution for dealing with the ground conditions are each dealt with individually to ensure the best possible outcome.

The two main methods of ground support used where the rise is not already supported are Perlite fill and Polyliner support.

2.1 Perlite

Perlite is used as a loose filled surface support medium. It does not add strength to the excavation, but merely stops any scats that become loose from moving. This system is ideally suited to rock that is subject to fretting over time or unravelling due to stress shadow changes. If the issue is low strength rock with a high stress field there are better options including the use of thick poly liners with concrete fill in the annulus.

2.2 A case study – Xanthos Escapeway

Golden Grove Mine site is located in the Mid-West region of Western Australia and has two copper, lead and zinc producing underground mines. It is owned by MMG Pty Ltd. and has been in production since 1990. The mining method used in both underground mines is a combination of vertical crater retreat (VCR) mining and sub-level stope mining. On average, the underground operations extract between 1.2-1.7 mtpa of both copper and zinc/lead based ore. The present mine life of six years is expected to be extended based on the current exploration program.

Gossan Hill, one of the two underground mines at Golden Grove has been in operation since 1998. Over this period a ladder way system has been developed as a second means of egress. Currently this ladder way system extends from the lowest levels of the mine to the surface, a total of 1100m vertical. To begin with the mine developed air-leg raises between levels which were furnished with narrow wooden ladders with steel rungs. As handheld mining became

less prevalent there was a shift to raisebore holes, which were furnished with steel caged ladders. Steel caged ladders had been installed in Gossan Hill since 2000 up until 2010. During 2010, as a business development program, Safescope Laddertube was considered as a possible substitute for the steel caged ladders. Cost, time and safety were all taken into consideration when comparing the two.

Based on the comparison it was decided that Safescope would be trialed, with the first ladder way being delivered to site in December 2010 and installed in January 2011. Despite some challenges when installing this initial Laddertube, it was decided to continue using the Safescope product and since that time 11 separate Laddertube escapeways totaling 570m have been installed at Golden Grove.

Like most underground mines, Gossan Hill is ever extending in a downward direction. The challenge associated with this depth is the increased stresses acting on mine openings. One of the inherent advantages of using Laddertube was that the ladder could be installed in a smaller, more stable raisebore hole which would not require any form of ground support. The second round of Laddertube installed at Gossan Hill was in the lowest reaches of the mine in close proximity to impending stoping activities. Even with this smaller more stable raisebore hole, problems were still encountered during the installation phase of the Laddertube. The raise bore hole was fretting, causing scat sized material to dislodge and fall from the walls of the raisebore hole. This was the first time Laddertube had been exposed to such severe ground conditions.

Recommendations were made by Safescope to fill between the outside of the Laddertube and raisebore hole to limit the amount of rock material that could continue to dislodge. The decision was made to continue with the install. Some months after the ladderway had been installed, the Laddertube experienced minor deformation. This was due to small scat sized material falling and accumulating between the raisebore and the outside of the Laddertube. Stopping in the area had already commenced and an acceptable material to fill the void had not been decided upon. This particular escapeway was never filled and shortly after stoping was completed in the area the ladderway was decommissioned as a result of substantial deformation.

The next round of Laddertube installed at Gossan Hill was in the upper region of the mine which had more favourable ground conditions. This allowed time to develop a means to fill the void which would reduce the chance of the Laddertube deforming in other high stressed regions of the mine. Over a six-month period numerous types of material were

trialed, ranging from washed aggregate to aerated concrete. The final product which was decided upon was a light weight, free flowing material called Perlite. The material was relatively cheap and easy to deliver and install.

While Safescape had had success with concrete and cemented sandfill in the past, the downfall of this method is that Laddertube can only handle a static hydraulic head pressure of 2 m of water. This means that concrete can only be poured in 1 m lifts, which makes for a slow and repetitive process to fill longer escapeways.

The Xanthos ore body is a high grade region of ore located between 1000 m to 1600 m below the surface. Mining of this ore body was set to commence late 2013. Prior to any stoping activities the installation of a 200 m long ladderway extending from a neighbouring decline was required. A 1.5 m diameter raisebore hole had been developed between the Ethel and Xanthos declines in 2011. For a 12 month period this hole was used to supply secondary ventilation from the Ethel decline in order to top up the low ventilation flows experienced in the Xanthos area. This system was then later decommissioned when the Xanthos primary ventilation (Figure 2) upgrade was completed. Plans were then set in place to refurbish the 200m long raisebore hole in order to create a secondary means of egress for this region of the mine.

Two options were presented to management at the time. The first option was to go with the conventional steel ladder with a mesh protective cage. This option also required the raise to have ground support consisting of steel mesh and bolts. The second option was to continue using the Laddertube product with the additional protection of filling the void with Perlite. The cost comparisons between the two options were similar with the Safescape option representing a 10% saving compared to steel and the time frame available meant that the longer duration of the steel installation was not critical.

As a result, both cost and time were considered minor benefits of the Safescape option. The next consideration was whether the raise could be used to house additional services such as a rising main dewatering pipe. The steel caged ladders had this as an advantage over the Laddertube product as while it could be installed outside of the Laddertube, it would not be accessible for repairs in the future. This requirement was later discarded and this factor was made redundant and accordingly the final and deciding factor was safety. When comparing the safety of the two options the Laddertube product has a clear advantage over the steel cage ladderway, specifically as management considered the process of bolting and meshing the 200m long raise as high risk.

Therefore Laddertube was decided upon as the preferred option.

Perlite is the generic name for naturally occurring siliceous volcanic rock. Perlite ore is crushed and screened to various size ranges and then exposed to a rapid heating process taking it up to 850°C at which point the water inside the material vaporizes and causes the softened rock to expand. Tiny glass like bubbles are produced which account for the lightweight and exceptional physical properties of expanded perlite. The resultant lightweight product is a white granular material that handles and pours easily. It provides a quick, inexpensive and permanent method for filling vertical spaces.

Perlite has been the subject of numerous health studies conducted by scientific and governmental research organizations. Significantly, no test result or information indicates that Perlite poses any health risk. Indeed, the uniform result of all health studies points to the conclusion that Perlite and perlite products are safe for consumer use. As with all workplace dusts, Perlite can function as a nuisance dust, so exposure limits are set at those levels. For some workers, exposure can result in temporary physical irritation, discomfort, impaired visibility and enhancement of accident potential. This nuisance dust was encountered during the filling process at Golden Grove and while the irritation caused could be easily resolved by using dust masks or respirators, the installers took the extra step to build a water spray mist to help reduce the dust generated.

2.3 Project performance at Xanthos Escapeway

Installation of the Xanthos escapeway began in the first half of 2013. Due to the additional complexity of installing a 200 m ladder it was decided to use Safescape technicians to complete the entire install as opposed to MMG personnel who had previously been trained in the installation methodology. The technicians arrived on site and completed a three day induction before any work was undertaken. Setting up the site to commence the install required a full day. The time to install the entire 200 m was an additional two days. It then took another days work to anchor and fit out the inside of the Laddertube with rest platforms and a static line fall arrest system. The entire install of the Laddertube itself was completed in less than five days.

The placement of Perlite was undertaken by MMG personnel. This required 230 cubic metres of Perlite to fill the annulus between the raisebore and the Laddertube. The first 100 m section and middle 46m section were undertaken without any issues but during the placement of the bottom 46 m section rock material was dislodged from the walls of the raisebore hole. This caused damaged to the

Laddertube which required remedial work to be undertaken by MMG personnel.

A jumbo was used to chip out the shotcrete seal and bleed the slabs of rock that had fallen and squeezed the Laddertube. Once this rock was removed, the Laddertube was pushed back to its original shape and the seal was replaced before completing the perlite fill process.

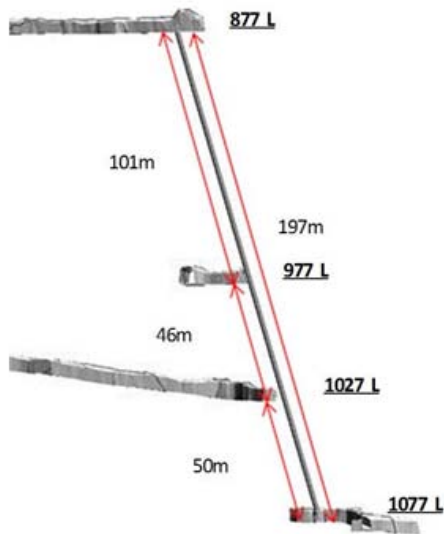


Figure 2: Xanthos primary ventilation network.

While Perlite fill provides mines with a passive ground support solution, in some instances the ground conditions require a more robust solution.

2.4 Polyliner ground support

Highly stressed or squeezing ground conditions or rock bursts, present mines with potential for failure of ground support and can result in serious damage to escapeways. In the mining context, a practical definition for squeezing ground conditions is when the total displacement of an excavation or more specifically, the drive closure reaches at least tens of centimetres within the life expectancy of a supported drive. In general, mine drives are designed to be in operation up to two years (ACG, 2015).

Installing conventional mesh and bolted ground support in escapeway rises is both costly and dangerous, while steel cans installed is a costly and time-consuming process. An alternative to placing individuals in unsupported ground to install ground support which would be quicker and more cost effective than existing solutions was the desired outcome.

Faced with a number of sites which had conditions that were resulting in ground failure and subsequent damage to their escapeway ladders,

Safescape made the decision to investigate further a system used in a client's mine in Idaho, USA. This system involves the installation of a thick poly liner followed by a fill around of concrete in a single pass with the escapeway ladder then installed inside the liner (Figure 3).

The liner used by Australian clients is a product produced by Enviropipes. The Enviropipe is dual wall HDPE (PE100) or Polypropylene pipe that are corrugated on the exterior and are smooth on the interior. The standard dimensions are 1050 mm ID, 1216 mm OD, and weigh approx. 215 kg per 3 m length. A larger dimension is available for sites that required them. The modules are high performance and very durable. The pipes do not rust, corrode, crack, shatter or degrade.

The liners are installed by lowering it down the raise and adding pieces, much the same as installation of the Laddertube (Figure 4). Concrete is used to secure the liner in place and support the wall rock. The bottom of the raise is sealed and an initial pour is made to a height of 1m. The concrete is then allowed to cure before pouring the rest in increments. In an installation with a void space of 0.5 m the maximum concrete lift heights allowable to avoid overstressing the pipe are as follows:

- 1050 mm SN8 Enviroculvert – maximum 2.4 m concrete lift
- 1200 mm SN8 Enviroculvert – maximum 2.6 m concrete lift

A safety factor of 1.5 has been used in determining the allowable fill heights. The following assumptions have been used in the design calculations;

- i. The maximum differential concrete height around the pipes perimeter is to be no more than 200 mm
- ii. The allowable lift heights shall be measured parallel to the pipeline
- iii. The concrete is assumed to have a density of 2400 kg per cubic metre
- iv. Due to the variable nature of the initial set times of concrete and dependency on admixtures, the initial set time from the time of concrete pour should be requested from the supplier
- v. Consecutive concrete pours shall then occur at a minimum of 60 minutes after initial set of the previous pour.

increases efficiency and safety hand in hand. Safescape's polyethylene escapeway ladders are proving a versatile and welcome addition to underground mines in Australia and abroad.

4. ACKNOWLEDGEMENT

MMG site management
Safescape Administration and Operations personnel
Hecla Lucky Friday Mine

5. REFERENCES

Australian Centre of Geometrics 2015, Australia, accessed on 24th May 2016, http://www.acg.uwa.edu.au/research/squeezing_task_force)



Figure 3: Installation using Polyliner.

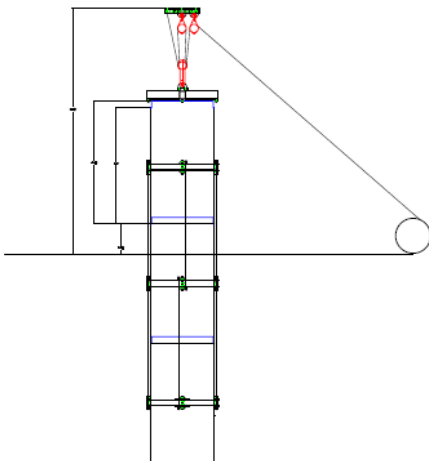


Figure 4: Installation setup for Polyliner.

The installation of polyliners has been successful in providing sites with a cost effective, time efficient solution and importantly, a safe installation process to sites.

3. CONCLUSION

The Australian mining industry is known for leading the world in terms of productivity and safety in underground mining. These escapeway projects are examples of mine operators discarding the status quo and finding a new way to work that both

Estimating stope vein footwall stability using various constitutive modelling techniques

Andrew Pyon, Atsushi Sainoki, Hani S. Mitri

Department of Mining and Materials Engineering, McGill University, Montreal, Canada, H3A 0E8

ABSTRACT

Operating in weak narrow vein mines presents many issues in terms of ore productivity. Maintaining stable mining excavations and limiting unplanned overbreak are some of the main concerns in narrow vein mining. The use of numerical modelling has become a popular method because it is capable of examining stress patterns and identifying rockmass failure. This paper will focus on creating a 3-dimensional constitutive numerical model for narrow vein mines that incorporate weak rockmass properties. The selected Case Study Mine is an underground narrow vein mine joining a weak material known as talc-chlorite-schist. The construction of this model will be associated with the unplanned ore dilution determined by surveyed profiles from the mine site.

KEYWORDS: Numerical modelling; ore dilution; rock mechanics; underground mining; footwall stability; failure criterion

1. INTRODUCTION

The selected Case Study Mine, located 50 km west of Val d'Or, Quebec, Canada, was chosen for this study as it held a weak rockmass known as talc chlorite schist that presented important stability issues in the stopes. Over the course of its operations, the existence of schist material represented 70% of ore dilution from planned stopes and over 1 metre of wall displacements from drifts due to squeezing ground. Such difficulties are not to be overlooked and are worth investigating.

2. ORE DILUTION IN NARROW VEIN MINING

Ore dilution is defined as the unsolicited waste rock caused by overbreak of stopes. A poor control of dilution will induce the extraction of excess waste materials, which will present more handling of the rock as well as unnecessary additional costs. Rock overbreak comes from several causes such as the quality of geology, ore continuity, planarity of the walls and dip of the orebody (McCarthy, 1993).

There are a number of approaches to establish overbreak benchmarks in stopes. The most common ones are related to the relaxation of stope surfaces. Relaxation typically occurs when tensile stresses are created through opening of existing joints or the creation of new cracks formed by induced stresses (Potvin, 1988). It is therefore projected that once the rockmass exhibits mining-induced tensile stresses, unplanned dilution occurs. This is stated as $\sigma_3 \leq 0$, i.e. when σ_3 is tensile. Other dilution criteria related to relaxation are: 1) $-\sigma_3 \leq \sigma_t$, i.e. when σ_3 is tensile and is lower than the tensile strength, and 2) when the

rockmass yields (Zniber, et. al., 2009). However, dilution can take many other forms of failure such as spalling, bending, wedge failure, crushing, etc. A combination of these failure modes is also possible leading to complex dilution occurrences. During the process of applying various numerical constitutive models, failure conditions will be examined to get a better grasp of rock behaviour.

3. CASE STUDY MODEL

The Case Study Mine is located within the Cadillac-Larder Lake Fault Zone. This zone contains the Archean-age Piché Volcanic rock in which many of the gold-mineralized structures are inside the hinges of the folds. There are 2 central groups of rockmasses where mining will be detained. One is the Piché group containing mafic to ultra-mafic talc-chlorite schist combined with intrusive volcanic rocks such as basalt. This group is known to be highly anisotropic in which the rockmass is extremely foliated.

The second group is called the Cadillac group comprised mostly of fine grained sedimentary Greywacke. The orebody is situated between these two rockmasses with widths varying between 3 to 8 metres and 85° dip.



Figure 1: Foliated schistose rockmass in footwall buckling towards the drift (Case Study Mine).

4. METHODOLOGY

4.1 NUMERICAL MODELLING SOFTWARE: FLAC3D

To perform an in depth dilution analysis in a 3-dimensional medium, FLAC3D (Fast Lagrangian Analysis of Continua) was selected. This software is a 3-D finite-difference program that uses well defined numerical formulations between geotechnical materials (Itasca, 2012). Geometric models are arranged by polyhedral elements in which failure laws are given based on elastic or plastic behaviours. The main advantage of using this tool is its ability to accurately represent the effect of plasticity in a 3-D medium. This is most suitable for ductile materials similar to the case of the Piché group at the Case Study Mine.

4.2 MODEL SETUP

Since the rockmass structures are fairly continuous at steep dips, it is best to construct the model into layers. 4 sections have been assigned to distinguish the main alterations within the heterogeneous nature of the rockmass. These are *Volcanic Zone*, *Orebody Zone*, *Weak Schist Zone* and *Sediment Zone*. Each of these layers consists of different rock compositions based on geological mapping of the Case Study Mine. The extents of these zones are defined when there are prominent changes in the arrangements of the rock. The model is designed as a brick and each boundary is widened to at least 5 times the size of one stope allowing calibration for far field stresses. Smaller meshes were applied in the area of interest and were gradually enlarged towards the boundaries. Meshes were adjusted until displacements and stresses converged to a stable state. The final model contains 1,234,800 elements.

The stope of interest for this study is at a depth of 1040 metres from ground level. A Cavity Monitoring System (CMS) was used to survey the overbreak approximately one week after blasting. Figure 2a shows a section view of the mined stope profile. As can be seen, significant footwall dilution and little hangingwall dilution took place. This is mainly because of the strong volcanic hangingwall basalt rock. Cablebolts were installed in the drift sidewalls. It is worth noting that other influences such as stope undercut, blasting and drilling were not accounted for in this model. The model contains sill drifts in between openings. Stopes are located midpoint of the *Orebody Zone* in which it dips at an angle of 85° south. Figure 2b shows the final isotropic view of the model along with its dimensions.

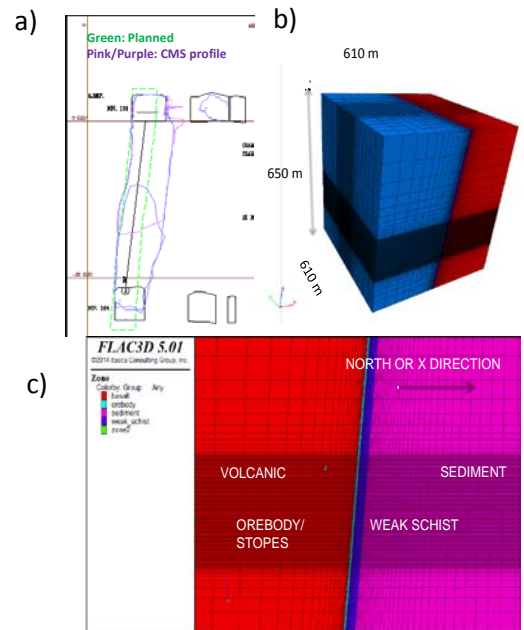


Figure 2: Case Study Mine Model a) Surveyed profile of the stope b) Perspective view c) Side view against the x-axis.

4.3 ROCKMASS CLASSIFICATION OF CASE STUDY MINE

Based on laboratory tests and field observations, rockmass parameters have been compiled into a database. Uniaxial compressive strength tests (UCS) were performed on intact core samples to acquire UCS values, the intact Young's Modulus of Elasticity (E_i), poisson's ratio (ν) and intact Hoek & Brown fit parameter (m_i). The Damage Factor (D) was also obtained from underground field observations.

Rock samples were classified as Sedimentary Wacke rocks, Intrusive Volcanic rocks and Schistose

rocks. Once compiled into a database, Hoek & Brown parameters are calculated to translate into equivalent rockmass values (Hoek & Brown, 2002). These were further converted into Mohr-Coulomb parameters with a best-fit linear relationship between major and minor principal stresses. Doing so, attaining equivalent equations for the angle of friction (ϕ'), cohesive strength (c') and tensile strength (σ_t') for each rockmass are made possible.

FLAC3D also requires using elastic constants such as Bulk Modulus (K) and Shear Modulus (G) to specify volumetric change and shear resistance of rocks. These are found by incorporating the Young's Modulus of Elasticity for the rockmass (E_{rm}) and Poisson's ratio (ν):

$$K = \frac{E_{rm}}{3(1-2\nu)} \quad (1)$$

$$G = \frac{E_{rm}}{2(1+\nu)} \quad (2)$$

The dilation angle (ψ), a function of volumetric change, is measured as $\psi = \frac{\phi'}{4}$.

The final rockmass properties are given in Table 1.

4.4 IN-SITU STRESSES

In order to reach a more realistic approach, stresses were applied on the boundaries of the numerical model. Doing so, an uneven distribution of internal stresses will travel through the different layers of rock. Stresses will be re-adjusted depending on the properties of each material before moving on to the next (R.P. Bewick, 2009). The applied stresses were adapted to stress tensor results that were previously measured (Arjang, 1996). The bottom boundary is fixed with rollers and vertical stress (σ_v) was applied on top with the following equation:

$$\sigma_v = \gamma H \quad (3)$$

Where γ is the average unit weight of the rockmass in MN/m³ and H is the depth of the mine. Additionally, stresses were applied on the x and y axes until the tensor values were achieved. The tensor is at a depth of 900 metres below surface with $\sigma_{\text{maximum}}=51.8$ MPa, $\sigma_{\text{intermediate}}=35.8$ MPa and $\sigma_{\text{minimum}}=19.0$ MPa. This was assumed to be positioned at coordinates $x=300$, $y=305$ and $z=350$ in the *Sedimentary Zone* of the model. It was also ensured that this tensor was within 300 metres of model boundaries to account for far field stresses. The final stresses that were applied on the boundaries were determined to be $\sigma_{xx}=50$ MPa, $\sigma_{yy}=21$ MPa and $\sigma_{zz}=18$ MPa.

5. NUMERICAL STRESS RESULTS

Before moving on, it was necessary to examine the stress fields before selecting a representative constitutive model. FLAC3D's *Ubiquitous Joint Model* was selected for the weak material since it accounts for plasticity and anisotropic behaviour of the rockmass. All other rock zones will be evaluated as isotropic elastic models due to its brittleness.

When excavating the first primary stope, lower stresses (-2 to 25 MPa) are observed in the *Weak Schist Zone* while high stresses (20 to 50MPa) are in the host rocks. Note that in FLAC3D, negative numbers refer to compressive stresses and positive numbers refer to tensile stresses. The major (σ_1) and intermediate (σ_2) principal stresses have relatively similar values in the schistose zone (0 to 25 MPa). As for the minor principal stresses (σ_3), few pockets of negative stresses are observed on the footwall face. This shows the presence of relaxation occurring in the abutment's surface.

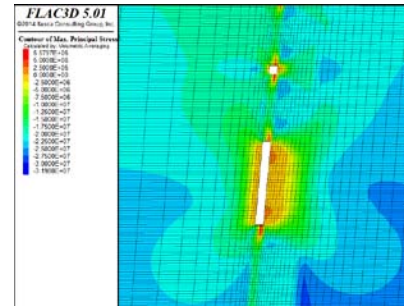


Figure 3: Post-mining section view of minimum principal stresses (σ_3).

The directions of these stresses were also perceived by looking at the σ_{xx} , σ_{yy} and σ_{zz} contours of the model. The stress contours in the y-axis (σ_{yy}) of the model displays the highest values which depicts the maximum principal stresses. The stresses in vertical direction (σ_{zz}) correlate with the intermediate principal stresses. The stress contours in the x-axis (σ_{xx}) shows the lowest, hence, minimum principal stresses.

Table 1: Selected rockmass parameters for numerical modelling study.

	HW Basalt	Orebody	FW Weak Schist	Sediment Wacke
Young's Modulus (E_{rm}) GPa	18.9	7.29	2.17	23.3
Bulk Modulus (K_{rm}) GPa	9.27	3.8	1.13	1.14
Shear Modulus (G_{rm}) GPa	8.15	3.09	0.92	10
Cohesion (c) MPa	4.9	2.7	2.2	4.3
Friction Angle (ϕ)°	44.2	31.5	27	42.7
Dilation (ψ)°	11	7.88	6.8	10.68
Tensile Strength (σ_t)	-0.3	-0.05	-0.05	-0.2
Poisson's Ratio (ν)	0.16	0.18	0.18	0.16

From these observations, the highest stresses occur in the y and z directions, both parallel to the footwall abutment. This suggests that a spalling or a slabbing type failure might arise.

6. DILUTION FAILURE MODES AT CASE STUDY MINE

6.1 RELAXATION (TENSILE) FAILURE

As previously mentioned, relaxation of rock occurs when the expansion of joints loosens the rock and falls off due to gravity pull. In this model, the failure criterion is expressed as $\sigma_3 < 0$. FLAC3D's *Elastic Transversally Isotropic (Anisotropic)* model was chosen for the *Weak Schist Zone*. A Young's modulus ratio of 1 to 7 was chosen in direction perpendicular to the planes of weakness. Figure 4 shows the areas of relaxation (in red) and the CMS profile of the first excavated primary stope (in white). A fine layer of tensile failure is observed in the footwall which is underestimating CMS results. This method is thus not recommended to analyze ore dilution in weak rock properties. Although tension is clearly shown in field observation, the rock's ductile behaviour renders the no-tension model ineffective.

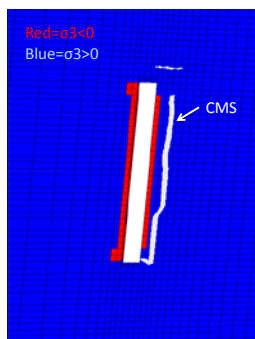


Figure 4: No-tension ($\sigma_3 < 0$) analysis in elastic transversally isotropic (anisotropic) model.

6.2 BIAXIAL FAILURE

Biaxial failure occurs when poly-axial loading near rock surface causes an accumulation of mining-induced planar stresses (Yun et. al., 2010). This in turn can cause a wide variety of failures such as spalling, slabbing, buckling and crushing. An *Elastic Transversally Isotropic (Anisotropic)* constitutive model was selected in order to account for high stresses and disregarding the effect of material's peak strength. σ_1 and σ_2 results show that the tensor values in the *Weak Schist Zone* range from 0 to 90 MPa. These values were then plotted in order to see if a failure pattern exist. Figure 5 illustrates a σ_1/σ_c versus σ_2/σ_c plot where σ_c represents the UCS of intact rock. Tensors were grouped by their σ_3 values and divided by σ_c for normalization purposes.

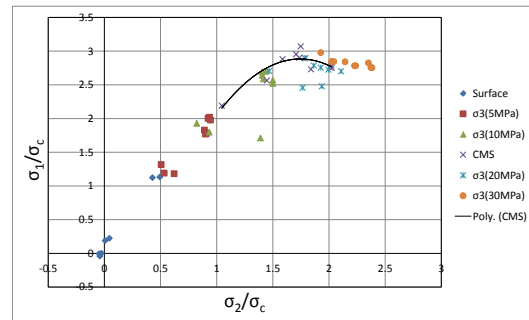


Figure 5: σ_1/σ_c vs σ_2/σ_c tensors along footwall width.

An increase in biaxial stresses was observed as it went deeper into the footwall. With an increase in σ_2 , σ_1 rises until it reached equilibrium of 90 MPa. A best fit polynomial was then conducted for tensors along the CMS overbreak profile which showed that σ_3 ranges from 10 MPa to 30 MPa. Given that the ranges of biaxial stresses along the overbreak outline are $2.19 < \sigma_1/\sigma_c < 3.07$ and $1.04 < \sigma_2/\sigma_c < 2.02$, it can be made possible to evaluate dilution profiles in

foliated talc-chlorite-schist as a result of biaxial loading. However, further models are needed to validate these results.

6.3 SHEAR AND TENSILE YIELDING

Shear or tensile yielding was analyzed by conducting a *Ubiquitous Joint Model*. This constitutive model takes into consideration planes of weakness on a perfectly elasto-plastic Mohr-Coulomb model. Failure criteria are designated by its Mohr-Coulomb envelopes as well as the weak-plane of failure. Additional joint properties were employed which were dramatically reduced from the rockmass properties (0.5 MPa for joint cohesion and 12° for joint friction angle). This was done to reflect the utmost critical joint conditions. Figure 6 shows the yielding states on the model before excavation.

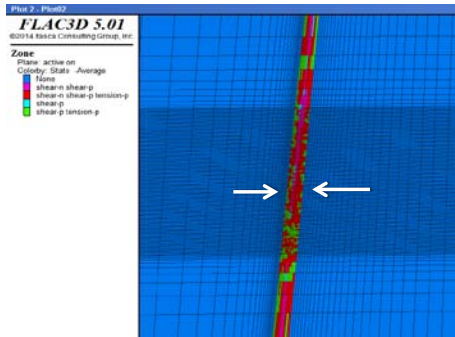


Figure 6: Yielded states of Case Study Mine model before excavation with directions of applied loads.

The weak material undergoes shear and tensile yielding in its entirety as indicated by the green, red, purple, cyan and pink colors (the “-n” in the legend signifies failure now and “-p” signifies failure in past iterations). This is primarily due to the effect of having weak material constrained within stronger materials. The arrangement of rocks will cause high loads on the weaker material, which results in yielding. Evaluating shear or tensile yield in response to dilation is therefore not desirable since yielding has occurred prior to excavations.

6.4 EFFECTIVE PLASTIC STRAIN FAILURE

The *Effective Strain* is defined as the amount of body rotation and distortion due to deviatoric principal strains. Uneven amounts of strains in the principal directions can cause the material to change its shape and volume. This behaviour can ultimately obstruct the rockmass and result in dilation. The *Equivalent Total Strain* (ϵ_e) is calculated according to the following equation (Xia and Wang, 2001):

$$\epsilon_e = \sqrt{\frac{2}{9} [(\epsilon_x - \epsilon_y)^2 + (\epsilon_y - \epsilon_z)^2 + (\epsilon_z - \epsilon_x)^2] + \frac{1}{3} (\gamma_{xy}^2 + \gamma_{yz}^2 + \gamma_{zx}^2)} \quad (4)$$

Where:

ϵ_x , ϵ_y and ϵ_z = total principal strain in the x, y and z-axis, respectively.

γ_{xy} , γ_{yz} and γ_{zx} = total shear strain in xy plane, yz plane and zx plane respectively.

For this analysis, the *Ubiquitous Joint model* was selected to account for the plasticity of the rockmass and planes of failure. Given that the material behaves as a perfectly-elasto plastic model, it is essential to determine at what strain amount will be affected by dilation. Since failure occurs when there is permanent or irreversible strain in the material, it is required to measure the amount of strain from the point of yield stress to the point of dilation as shown in Figure 7, which is also known as the *Equivalent Plastic Strain* or E.P.S.

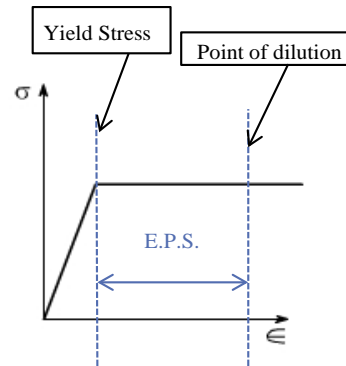


Figure 7: Illustration of perfectly elasto-plastic curve and applied E.P.S.

The *Effective Plastic Strain* generated amounted to 15% to achieve the CMS overbreak profile as shown in Figure 8.

Although the use of *Effective Plastic Strain* gives fair results in identifying ore dilation, more studies are needed for validation; especially since the geological and mining conditions fluctuate at varying depths.

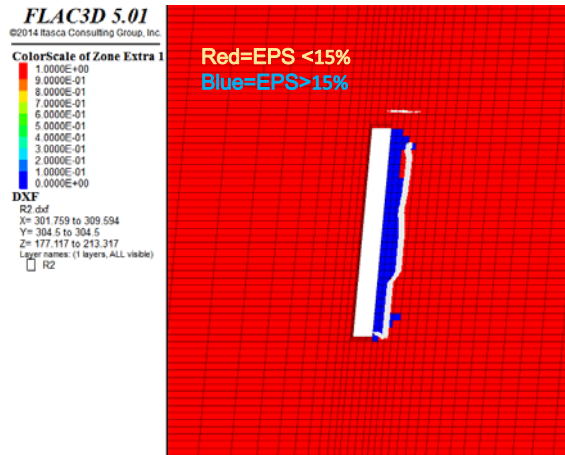


Figure 8: Comparison of CMS profile with 15% Effective Plastic Strain (midpoint).

7. CONCLUSIONS

The no-tension model proves to be ineffective due to the minimal tensile in the footwall. However, failure under biaxial loading condition is noticeable due to the stresses applied on the stope footwall face. This needs to be validated with other stope models for future studies. From the *Ubiquitous Joint Model*, the shear and tensile yields cannot be implemented since yielding states occur at pre-mining stages. This event is primarily caused from the application of high loads of the stronger rockmasses into the *Weak Schist Zone*. Finally, the *Effective Plastic Strain* has been examined. The actual (measured) overbreak of the stope corresponds to 15% *Effective Plastic Strain*. Although these results are encouraging, further studies are needed to validate this method.

8. ACKNOWLEDGEMENT

This research paper was made possible through the help and support from the members of the McGill Mine Design Lab team.

9. REFERENCES

- Arjang, B., (1996). In situ ground stresses in the Abitibi Mining District. CIM Bulletin, 89, no. 996, p.65-71.
- Bewick, R.P., Valley, B. and Runnalls, S. (2009). Global Approach to Managing Deep Mining Hazards, Proceedings of the 3rd CANUS Rock Mechanics Symposium, Toronto, May 2009, Paper 3994
- Brewis, T. (1995). Narrow Vein Mining 1 – Steep Veins. Mining Magazine. Vol.173, No.3, pp.116-130
- Henning, J. and H.S. Mitri (2007). Numerical modeling of ore dilution in blasthole stoping.

International Journal of Rock Mechanics and Mining Sciences. Res. 44: 5, pp. 692-703

Hoek, E., C.T. Carranza-Torres and B. Corkum. (2002). Hoek-Brown failure criterion - 2002 edition. In Proceedings of the Fifth North American Rock Mechanics Symposium and 17th Tunneling Association of Canada Conference, Toronto, 7-10 July 2002, pp. 267-273

ITASCA (2012). FLAC3D - Fast Lagrangian Analysis of Continua. 5.0 ed. U.S.A.: Itasca Consulting Group Inc.

McCarthy, P. (1993). Economics of Narrow Vein Mining, Narrow Vein Mining Seminar, The Australasian Institute of Mining and Metallurgy, pp.89-97

Miller, F., Potvin, Y. and Jacob, D. (1992). Laser measurement for open stope dilution. CIM Bulletin 1992, pp.85:96-102

Potvin, Y., (1988). Empirical open stope design in Canada. PhD. Thesis, University of British Columbia, Vancouver

Xia, K. and Wang, J. (2001). Shear, Principal, and Equivalent Strains in Equal-Channel Angular Deformation, Metallurgical and Materials Transactions A, Volume 32A, pp.2639-2647

Yun et. al., (2010). Experimental Investigation into Biaxial Compressive Strength of Granite. International Journal of Rock Mechanics & Mining Sciences. 47. pp.334-341

Zniber, E. M., et. al. (2009). Effect of stope undercutting on its wall overbreak. Proceedings 43rd US Rock Mechanics Symposium, held in Asheville, NC June 28th – July 1, Paper No. ARMA 09-200

Redesigning the geometry of the Makala Coal Mine to improve safety and productivity

Jean-Pierre Tshibangu*, Fanny Descamps

Department of Mining Engineering, University of Mons (UMONS), Mons, Belgium, 7000

ABSTRACT

Makala is a room-and-pillar coal mine situated in the Katanga Province (DR Congo), close to the city of Kalemie (eastern part of the country). It exploits the so-named Lukuga Coal Basin, which is composed of four coal seams numbered 1 to 4. The economically mineable are 1 (about 2m thickness) and 2 (1 to 1.5m thickness). This coal basin shows some similarities with south-African deposits (Cahen 1961, in Carte Géologique du Zaïre). From the West the deposit plunges towards the East with an average dip of 8°. Mining operations using room-and-pillar method started in 1914 on the northwestern part of the deposit, following the outcrops of coal seams. Currently only seam 1 is being mined out and the workings are being developed southwards to avoid the higher overburden towards the East. Despite the increasing thickness of the overburden, the geometry of the method does not vary, and consists of rooms 4m wide and pillars of 8x6m, leading to a recovery of about 60%. The main gallery lays from North to South for more than a kilometer. Panels situated on the western part of the main gallery are composed with stable pillars, while on the eastern part one can observe some typical problems like pillar fracturing, ground heave and roof falls. In this last case we noticed that the roof of seam 1 is of poor mechanical quality.

In order to understand the geomechanical problems, we first built a 3D geometrical model, updating the mine layout and incorporating both geological and topographical data. This modelling has been achieved using the GEOVIA-GEMS software. The approach helped in assessing as accurately as possible the overburden to be taken into account when calculating the weight to be supported by pillars. From the defined geometry, we used the modified tributary area method (Brady and Brown 1999) to redesign the pillars accordingly. 2D numerical modelling has been used as well to assess the stability of the roof and dimension timber support used in the mine.

KEYWORDS: room-and-pillar mining, mine design, tributary area

1. INTRODUCTION

Makala is a room-and-pillar coal mine situated in the Katanga Province (DRC), close to the city of Kalemie. This coal basin was discovered in 1911 and mining started in 1914 on the northwestern part of the deposit, following the outcrops of coal seams. Currently, only seam 1 is being mined out and the workings are being developed southwards to avoid the higher overburden towards the East.

Despite the increasing thickness of the overburden, the geometry of the method does not vary: it consists in 4m wide rooms and 8x6m pillars, leading to a recovery of about 60%. Whereas panels situated on the western part of the main gallery are composed of stable pillars, typical problems are encountered on the eastern part: pillar fracturing, ground heave, and roof falls. In addition, the roof of seam 1 is of poor mechanical quality.

This study intends to understand the geomechanical problems and propose a new design for the pillars accounting for the increasing depth of the orebody. Meanwhile, a 2D numerical simulation

is conducted to assess the stability of the roof and dimension of the timber support used in the mine.

2. GEOLOGICAL CONTEXT

The Katanga coalfields (Luena, Lukuga...) are similar to southern African ones (Cahen 1961, in Carte Géologique du Zaïre). The coal deposits were formed during Permian and Carboniferous ages and resulted in lenticular coal seams with a high ash content and highly volatile matter content. Different explorative works have been undergone in the area (1930, 1953 to 1954, early 2000...) but the most complete geological description is the one from Jamotte (1931) which is based on 15 core drillings (total length 1800 m), trenches and outcrops observation. Table 1 gives a typical succession of geological formations as observed in drillholes S1 and S4.

The Makala mine is located in the Lukuga Basin (Figure 1). The orebody has been affected by faults during the formation of the Tanganyika graben.

*Corresponding author – email : jean-pierre.tshibangu@umons.ac.be

Table 1: Geological formations in the seam 1 neighborhood.

Geological formation	Thickness S1 (m)	Thickness S4 (m)
H3: feldspathic sandstone	4	3.72
Seam 2 with a footwall of psammitic sandstone	0.9	1.15
H2: zone Psammites, sandy sometimes	1.8	3.33
H1: coarse sandstone, feldspathic, conglomerate sometimes	4.13	7.3
Seam 1 with a footwall in grey argillaceous shale	2.4	1.81
Psammites and black shales with coal	2.85	2.29

The mined area is situated to the East of the Hôpital Fault and to the South of the Lukuga River, where the thickest outcrops of seam 1 have been found in the Nikuha Valley. The orebody strikes in a N-S or NE-SW direction, with an 8° dip to the E-SE. Figure 2 gives a typical cross-section of the orebody showing the increase of the overburden towards the East.

According to the available data (Woitrin and Delvaux), if we consider the panel defined by the 200m barrier pillar separating the mined area from the Lukuga River, the Hôpital Fault to the West, the Kaniki Fault to the South-West and the Kandeke Fault to the East, the coal in seam 1 may represent 7 642 250 mineable tons. This assessment is based on a 2 m thickness of the seam 1 and a recovery of about 60% by the room-and-pillar mining. Mining seams 2 and 3 could also represent another 7 642 250 tons. For the whole basin, Cailteux (2006) assesses the coal reserves to more than 75 million tons, meaning that this area has interesting potential.

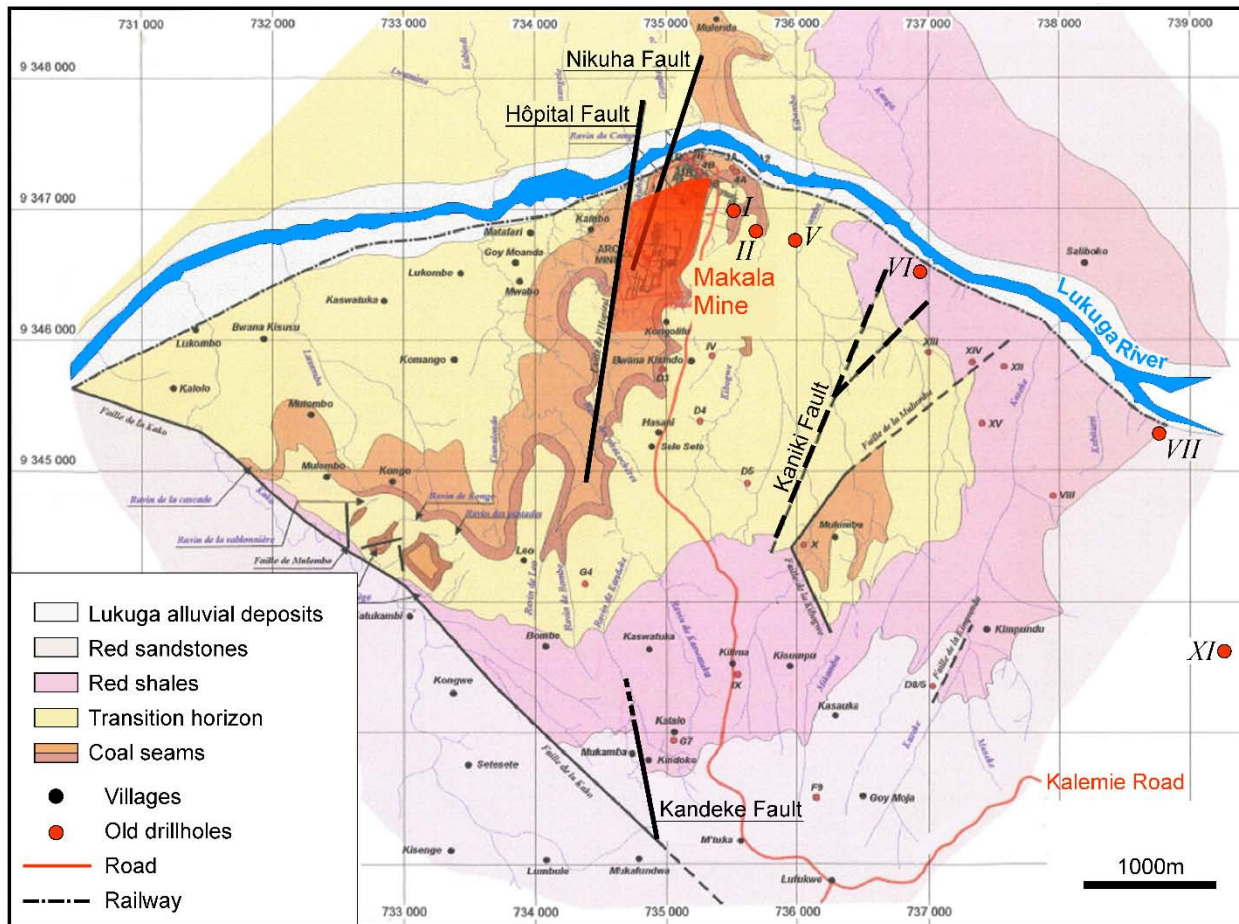


Figure 1: Geological map of the Lukuga coalfield (modified from EGMF, after Jamotte 1931).

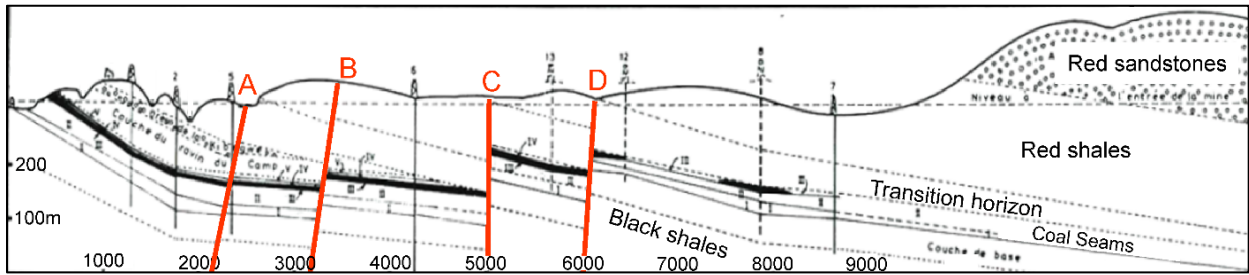


Figure 2: Typical cross-section of the orebody through drillholes I, II, V, VI, VII, XI (Jamotte 1931). A, Mikamba Fault. B, Kaniki Fault. C, Fault. D, Mulumba Fault.

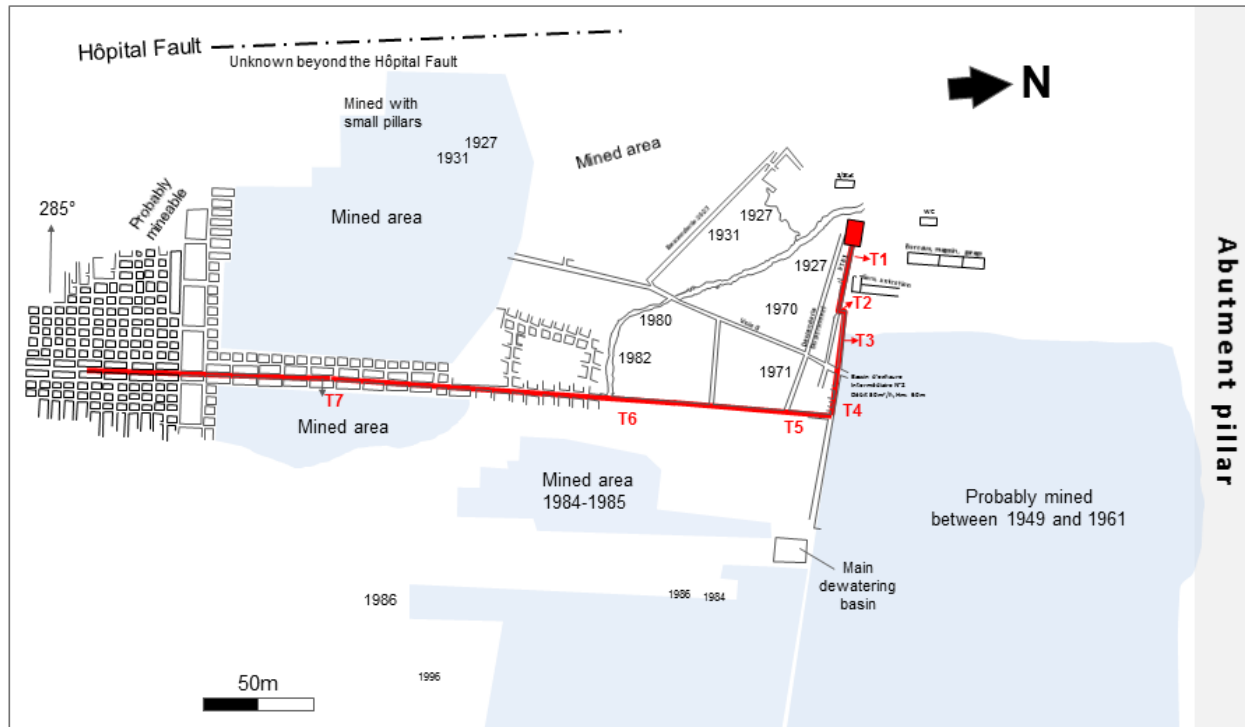


Figure 3: Mining map at Makala. In red, the main access from surface to the face.

3. MINING METHOD

Generally, only the seam 1 is mined even if in some areas the seam 2 has been also mined. Since 1914, the deposit has been mined by a room-and-pillar method with abandoned pillars. The mining operations started on the northern part and evolved towards the South. An abutment pillar with a width of 200 m has been left to the North to prevent water income from the Lukuga River (Figure 3). The main access is an inclined shaft that follows the seam and oriented according to the dipping. It crossed the Nikuha Fault and, due to the slip of this fault (8 m), the seam 2 has partly been mined in this area before the shaft joins again seam 1.

The inclined shaft is used for coal extraction to surface by means of a conveyor belt. It joins a directional gallery (or main gallery) with a N-S direction. This gallery is surrounded by a row of large pillars (20 x 6 m) for stability purposes. The longest part of the conveyor belt is installed in this directional gallery (more than a kilometer). A parallel way situated westerly with respect to the directional gallery is dedicated to workers.

When developing the layout, panels are created every 100 m along the directional gallery, leaving a row of barrier pillars (40 x 20 m) between panels. When the main gallery is mined out for a panel, 4 m-wide raises and declines are mined on dip before cross-cutting the long pillars. Residual pillars in the

panel have dimensions of about 8 x 6 m, giving a theoretical recovery of about 60%.

4. NEW DESIGN FOR THE MAKALA MINE

4.1 Rock mass qualification and mechanical properties of the rocks

The roof is made of an argillaceous material, with very bad mechanical behavior. In some places, mainly at crossings, roof falls are observed, leading to 50 cm to 1 m depth holes in the roof. A new pilot-gallery to be enlarged for a decline has been dug in 2011 to access the southern part of current mining operations. It is intended to improve ventilation. During the authors' visit on site, bad quality rocks were observed along its side walls.

A more detailed evaluation of the quality of the rock mass has been performed, using the Rock Mass Rating (RMR, Bieniawski 1973, 1984) and the Geological Strength Index (GSI, after Hoek and Brown 1998). Following the rock description along the new decline, the RMR is estimated between 20 and 40, corresponding to a poor quality rock mass. The GSI parameters are considered as "blocky/disturbed" and "poor" to "very poor", leading to GSI values of 25-30 for the coal seam 1 and the hanging wall.

In terms of mechanical properties, no experimental data were available for the coal, the hanging and the foot wall. The properties were assessed using bibliographic data (Vutukuri and Lama 1974, Hoek and Brown 1998) and by considering the low RMR value. The pillar strength is estimated to 5 MPa.

4.2 3D geometrical model of the overburden

A geological model needed to be built and coupled to the topography and the geometry of the workings in order to assess the thickness of the overburden. 13 drillholes described by Jamotte (1931) and a recent topography were used for this purpose. Mining data included an Autocad file delivered by EGMF for older workings, an up-to-date paper mine map (1/1000) and a recent file with survey data dealing with the access ways. We built the model using the GEOVIA-GEMS software.

The seam 1 is known to cross some faults but their position is not precisely documented. Therefore, the seam has been modelled as a monocline and its extension is limited to the surroundings of the mined area.

Based on available data, the geometry of the mining works has been modeled. Several vertical cross sections (W-E) have been plotted through the 3D geometrical model. Figure 4 shows the vertical cross-section 800N on which one can observe the

dipping of seam 1 from left to right, the waving topography, and the description of a core drillhole.

In order to assess the overburden, Figure 5 gives the minimum (bottom) and maximum (top) elevations measured on each vertical section. The deepest works are found in the 800N cross-section but in this case an assumption was made on the topography due to missing data.

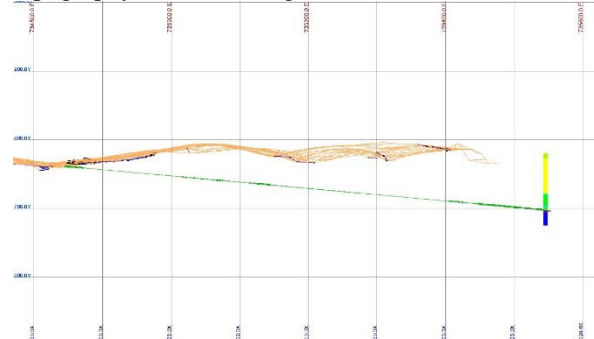


Figure 4: The 800N vertical cross-section showing the trace of seam 1, surface topography, and a description of a borehole.

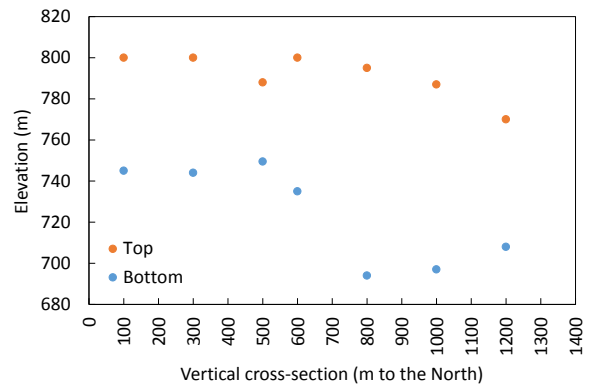


Figure 5: Measured elevations (top and bottom) in the vertical cross-sections from the 3D model.

4.3 New pillar design based on modified the tributary area method

The tributary area method (Brady and Brown 1999) is widely used in room-and-pillar mining design. The approach is accepted when the panel width is larger than the depth of the mined area. In the Makala mine case, this method can be considered as valid since the depth is about 50-60 m for 100 m panels.

The method for pillar design is rather simple but, due to the quality of the available data, it seems sufficient in comparison to more sophisticated methods like numerical simulations. The pillar strength is given as:

$$R_p = R_0 h^\alpha w^\beta \quad (1)$$

with R_p , the pillar strength, R_0 , the rock strength, h , the pillar height, w , the pillar width. Parameters α and β

are assessed to -0.8 and 0.5 respectively, following values from the literature (Brady and Brown 1999). In the Makala mine, we obtain a pillar strength of 6.36 MPa.

The safety factor is defined as the ratio between the pillar strength to the mean vertical stress. Considering a mining depth of 60m and a specific gravity of 25 kN/m³, the vertical stress before mining is 1.5 MPa. The ratio between the surface of the area supported by the pillar and the section of the pillar is 2.5 and the stress on the top of pillars is 3.75 MPa. The safety factor equals 1.7.

The assessment of safety factors is based on empiricism. Salamon (Brady and Brown 1999) studied the performance of South-African coal mines pillars. From his analysis, one can see that intact pillars generally correspond to safety factors between 1.3 and 1.9. A reasonable approach for the Makala mine would be to suggest a safety factor of 1.6.

Due to the dipping of the seam, the pillar dimensions should change with the depth. In particular, the pillar size could be reduced in shallower panels resulting in an increased recovery. However, for deeper areas, the pillar size should increase and additional support may be necessary.

We computed the variation of the safety factor with the pillar width for various mining depths (Figure 6). The abacus indicates that for a depth of 90m, with the current assumptions, a 1.6 safety factor cannot be reached even with 10 m wide pillars.

Based on the abacus, the pillar width is computed for a given depth in order to reach a safety factor of at least 1.6. The recovery ranges from 85% at a depth of 10 m to 52% for a depth of 70 m.

4.4 2D numerical simulation for assessing the stability of the roof and timber support

This approach is intended to better understand the mechanical behavior of the roof and adjacent pillar, and then assess the loading on support.

We assume a plane strain geometry (long continuous pillars) for a typical case occurring at 60m depth, and for two sets of mechanical properties corresponding to rock mass of either medium or poor quality. Computations were performed using the FLAC2D software.

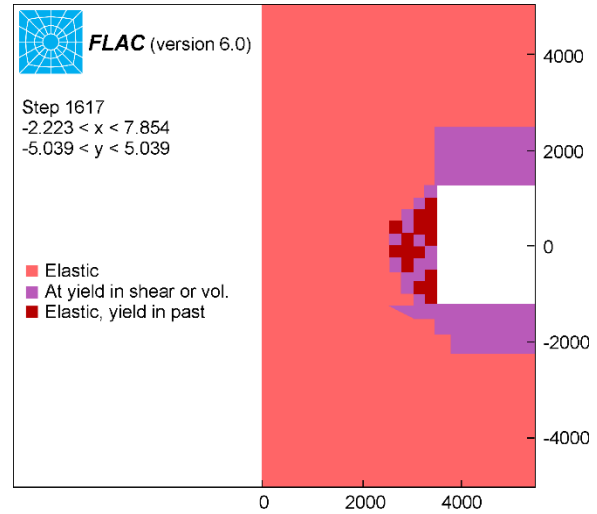


Figure 7: Yielding around a pillar in the case of a poor quality rock mass.

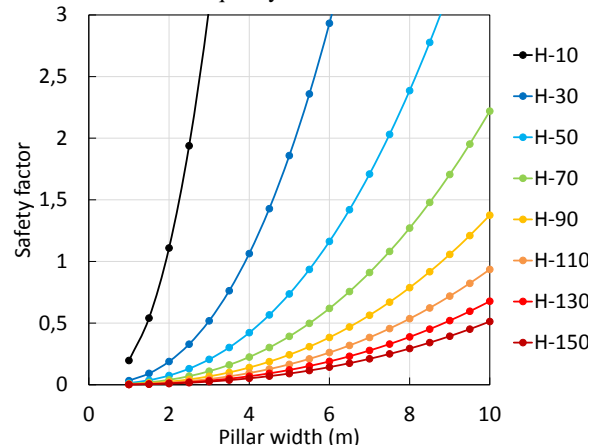


Figure 6: Safety factor as a function of pillar width for various mining depths.

Figure 7 corresponds to a case of poor quality rock mass when no support is installed. It shows a typical result gathered in terms of failure and plasticity and one can observe that both side walls, roof and ground are severely affected. In this case some support is to be envisaged, for instance by using roof bolts, or reduce the size of the rooms as suggested in section 4.3.

Depending on the technology and the distance at which the support is placed with respect to the current face, the extension of the damaged (or failed) zone can be limited. Different techniques can be envisaged: roof bolts, shotcrete, steel arches, etc. but the region of Makala is difficult to access for usual supplies. For roadways (4 m width), we then recommended mainly the use of either timber support or steel sets because the components can be accessed locally. For timber, we assessed the diameter of 15 to 17 cm, while for steel sets a H19 type was

recommended. The normal spacing is 1 m from a set to the next but this can be reduced when geological conditions are very poor. A shotcrete can also be used for long duration roadways and galleries.

5. CONCLUSIONS

The Makala mine in DR Congo has been mined since the early 20th century using a room-and-pillar method. Despite an 8° dipping deposit, the dimensions of pillars and rooms do not change with the depth of operations, involving a low recovery at low depth and potential stability problems at higher depth. Geological studies have emphasized the remaining resources in the coalfield and a new design of the mine was necessary to improve recovery and ensure stability of future works.

During a visit undergone in 2011, the authors observed typical stability problems consisting in roof fall and ground heave for most of stopes situated on the eastern part of the main gallery. In order to understand the mechanical behavior of pillars, a 3D model was built including geological data gathered from drillholes, an updated general layout of the workings (mine map), and the surface topography. Analyzing the built model allowed an assessment of the variation of thickness of the overburden above the developed mine.

In a second step, the modified tributary area method is applied in order to assess the safety factor and also propose, for a given safety factor that we chose to be about 1.6, pillar dimensions depending on the mining depth.

Finally, a numerical simulation using the finite difference method is undergone in order to assess the stability of the working based on different sets of mechanical properties of the rock mass. To enforce safety, some recommendations have been made for support, especially for roadways and main galleries.

6. ACKNOWLEDGEMENT

The authors acknowledge HeidelbergCement for funding this research.

7. REFERENCES

- Bieniawski, Z.T. (1973). Engineering classification of jointed rock masses. *Trans S. Afr. Inst. Civ. Engrs* 15, pp. 335-344.
- Bieniawski, Z. (1984) *Rock mechanics design in mining and tunneling*. Balkema, Rotterdam.
- Brady, B.H.G., Brown, E.T. (1999) *Rock Mechanics for underground mining*. Chapman & Hall, Kluwer Academic Publishers – London.
- Cailteux, J. (2006) *Le charbon de Makala, synthèse géologique et de son exploitation*. Rapport interne EGME/DRD numéro RT031.

Hoek, E., Brown, E. (1998) Practical estimates of rock mass strength. *International Journal of Rock Mechanics and Mining Sciences*, 34 (8), pp. 1165-1186. Elsevier.

Jamotte, A. (1931) *Contribution à l'Etude Géologique du Bassin Charbonnier de la Lukuga ; Comité Spécial du Katanga, Annales du Service des Mines*.

République du Zaïre, Département des mines – Direction de la Géologie, 1974. *Notice Explicative de la carte géologique du Zaïre au 1/2 000 000*.

Vutukuri, V. S., Lama, R. D., Saluja, S. S. (1974) *Handbook on mechanical properties of rocks: testing techniques and results, Volume 1*, Trans Tech Publications.

Woitrin, M., Delvaux, B. (1984) *Charbonnages du Tanganyika, informations générales ; internal report*.

Shear behaviour of regular and irregular rock joints under cyclic conditions

S. M. Mahdi Niktabar^{a,*}, K. Seshagiri Rao^a, Amit Kumar Shrivastava^b

^a Department of Civil Engineering, Indian Institute of Technology Delhi, New Delhi, India, 110016

^b Department of Civil Engineering, Delhi Technology University, New Delhi, India , 110042

ABSTRACT

Rock masses often have sets of joints or fractures and almost all failures are due to the presence of these discontinuities. Natural joints have irregular surfaces, and the correct evaluation of shear strength and deformation of these irregular joints is very important for the analysis and engineering design of rock structures. These joints are often subjected to dynamic loads because of earthquake and blasting during mining and rock cutting. Hence, it is important to correctly evaluate the shear behaviour of regular and irregular rock joints under dynamic conditions. In the present study, synthetic rock joints are prepared with plaster of Paris and regular joints are replicated by keeping regular asperities with asperity angles 15° - 15° and 30° - 30° . Irregular rock joints are prepared by keeping the asperity angles 15° - 30° and 15° - 45° . The sample size and amplitude of roughness are kept constant for both regular and irregular joints, at $298 \times 298 \times 125$ mm and 5 mm respectively. Shear tests have been performed on these joints with a large scale direct shear testing machine by keeping the frequency and amplitude of shear loads constant under cyclic load conditions and varying the normal stress. The shear strength of rock joints increases with increase in the asperity angle and normal load during the first cycle of shearing. With the increase in the number of shear cycles, the shear strength reduces for all the asperity angles, but the rate of reduction is greater in the case of high asperity angles. Test results indicate that the shear strength of irregular joints is higher than regular joints at different cycles of shearing at low normal stresses. The mechanism of the shearing for regular and irregular joints is different under the cyclic conditions at low normal stresses. Shearing and degradation of joint asperities on regular joints between loading and unloading are the same, but for irregular joints they are different at low normal stresses. Shear strength and joint degradation are more significant on the slope of asperity with higher angles on the irregular joint, until two angles of asperities become equal during the cycle of shearing and it starts to behave like a regular joint.

KEYWORDS: Cyclic shear behaviour; shear strength; regular joint; irregular joint; joint dilation

1. INTRODUCTION

Shear stress and deformation behaviour of rock joints play an important role for design and analysis of underground structures, foundation, slope stability and risk assessment of underground disposal. Many researchers in the field of rock mechanics and rock engineering have presented the shear behaviour of jointed rock, based on peak stress-strain along the joint under unidirectional or monotonic (static) shear loads. However, joints are subjected to dynamic loads due to earthquake, blasting, and vibration, which can be simulated as shear along the joint under cyclic loads. In this condition, load direction is reversed on the shearing plane repeatedly. In the present work, a physical model is prepared in order to examine the shear behaviour of a natural jointed rock mass. In the past shear behaviour of regular joints under cyclic conditions was studied by many researchers (Huang et al., 1993; Hutson & Dowding, 1990; Homand et al., 2001; Jafari et al., 2003; Indraratna et al., 2012; Mirzaghobanali et al., 2013; Niktabar et al., 2015). However, joints in the rock mass are irregular and have different roughness. In the present study regular

and irregular joints with asperity angles 15° - 15° and 30° - 30° and 15° - 30° and 15° - 45° are prepared accordingly. Joints with irregular asperities are more representative and closer to natural joints. Each cycle is divided into four stages as described by Lee et al. (2001), such as forward advance (FA), forward return (FR), backward advance (BA), and backward return (BR); for better understanding, the four stages are illustrated in Figure 1. The FA movement at first shear cycle is similar to static or monotonic shear loads.

To study the effect of irregular asperities on the shear behaviour of rock joints under cyclic conditions, a series of tests were performed on regular and irregular jointed samples.

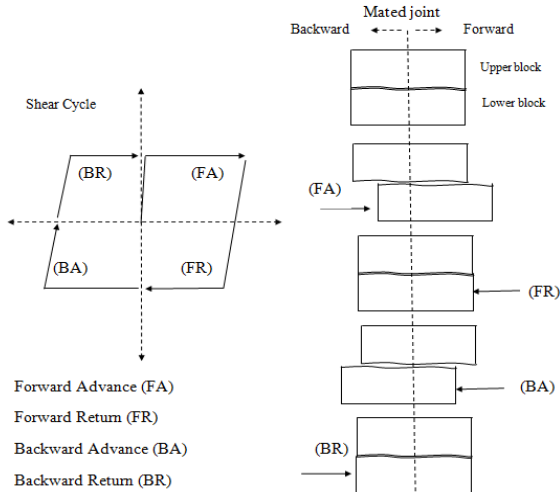


Figure 1: Load direction and joint movement under shear cyclic condition.

2. SAMPLE PREPARATION

Similar sample preparation methodology is adopted for preparing both regular and irregular joints, except for the use of different asperity plates to create different asperity angles. A model material is found in such a way that it can easily be handled and reproducibility of the sample can be ensured. To achieve this, different brands of plaster of Paris and dental plasters at different moisture content and curing period in isolation or combinations were assessed. Finally, plaster of Paris (POP) was selected because of its universal availability and its ability to mould into any shape when mixed with water to produce the desired joints, as well as its long term strength being independent of time once the chemical hydration is completed. The prescribed percentage of water was decided so as to achieve proper workability of the paste and required strength to simulate the soft rock. Different water POP ratios were tried in order to obtain desired strength and workability. The ratio which was finally selected was 0.60. Size of samples and amplitude of asperities are $298 \times 298 \times 125$ mm and 5 mm respectively for all of the joints based on moulds and asperity plates. The asperity plates of different angles like 15° - 15° and 30° - 30° and 15° - 30° and 15° - 45° were designed and fabricated to produce desired asperities in the sample. The POP with 60% of the moisture was mixed in the mixing tank for 2 minutes and then the material was poured in the casting mould which was placed on the vibrating table as presented in Figure 2. Vibrations were given to the sample for a period of 1 minute to remove any entrapped air. The sample was demoulded from the mould after 45 minutes and kept for air curing for 14 days before testing. Pre-test regular and irregular joints are shown in Figures 3

and 4, respectively. The uniaxial compressive strength of model material at 0.60 water cement (POP) ratio and after 14 days of air curing was 6 MPa.

3. LARGE-SCALE DIRECT SHEAR APPARATUES

A servo controlled large-scale direct shear system designed by Shrivastava and Rao (2012) was modified to be able to carry out tests under cyclic shear conditions. This system is illustrated in Figure 5, which consists of three main units, namely the 1)

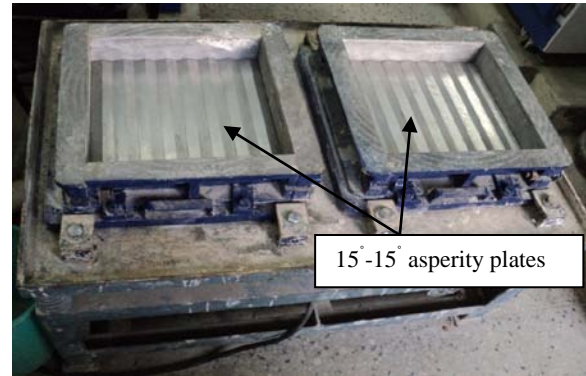


Figure 2: Set up for sample preparation.

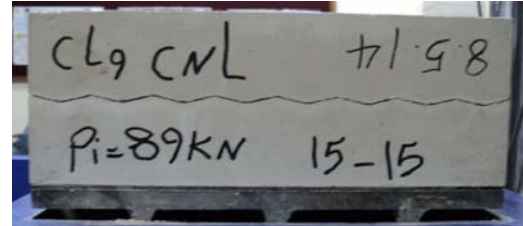


Figure 3: Regular joint (15° - 15° asperity angle).

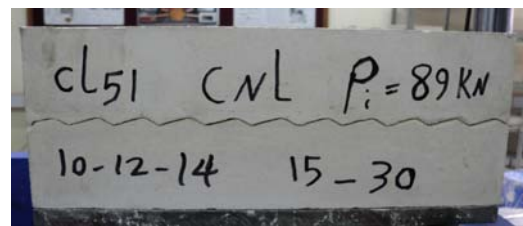


Figure 4: Irregular joint (15° - 30° asperity angles).

loading unit, 2) data acquisition with controlling unit and, 3) hydraulic power pack. Maximum capacity of the normal and horizontal load cell was 500 KN and 1000 KN, respectively. The size of each shear box was $300 \text{ mm} \times 300 \text{ mm} \times 448 \text{ mm}$. This system can work under both static and cyclic condition.

4. EXPERIMENTATION

The cyclic shear tests were conducted on regular and irregular joints under different normal stresses. Normal stresses are 0.1 MPa and 1 MPa as low and high, respectively. The frequency and amplitude of shear loads are set to constant values of 0.01 HZ and ± 8 mm, respectively for all cyclic shear tests. Each type of specimen is tested on thirty shear cycles under constant normal load conditions. The orientation of samples with irregular joints is important when loaded because of the different asperity angles. Experimental results are plotted, first and last shear cycles are shown in black and red colors in the graphs and from 2-29 shear cycles are presented in blue color for clarity.



Figure 5: Large scale direct shear testing machine.

4.1 Low normal stress ($P=0.1$ MPa)

Shear stress versus horizontal displacement on the joints with asperity angles (a) $15^\circ-15^\circ$, (b) $30^\circ-30^\circ$, (c) $15^\circ-30^\circ$ and (d) $15^\circ-45^\circ$ at $P=0.1$ MPa are presented in Figure 6. Figure 6 (a) indicates that no significant change is observed on the peak shear stress from first to last (30) shear cycles on the joint with $15^\circ-15^\circ$ asperity angle, whereas it decreases with increasing number of shear cycles for $30^\circ-30^\circ$ asperity angle, as shown in Figure 6 (b). The peak shear stress at initial cycles for the joint with $30^\circ-30^\circ$ asperity angle is more than for the $15^\circ-15^\circ$ asperity angle, but it decreases for $30^\circ-30^\circ$ asperity angle and the peak shear stress is less than for the $15^\circ-15^\circ$ asperity angle after several shear cycles, i.e. peak shear stress on joint with $30^\circ-30^\circ$ asperity angle is less than $15^\circ-15^\circ$ asperity angle at 30 shear cycles. Normal displacement versus horizontal displacement on the joints with asperity angles (a) $15^\circ-15^\circ$, (b) $30^\circ-30^\circ$, (c) $15^\circ-30^\circ$ and (d) $15^\circ-45^\circ$ at $P=0.1$ MPa is presented in Figure 7. The dilation angle for $15^\circ-15^\circ$ asperity angle is constant during 30 shear cycles as shown in Figure 7(a), but it decreases by increasing the number of shear cycles for $30^\circ-30^\circ$ asperity angle

and dilation on the joint after several shear cycles is converted to compression (positive normal displacement) as indicated in Figure 7 (b). Mechanism of the shear is changed from sliding on the low asperity angle ($15^\circ-15^\circ$) to shearing on the joint with the high asperity angle ($30^\circ-30^\circ$) at the same normal stress under cyclic shear loads.

Irregular joint shear behaviour is significantly different from that of the regular joint. Shear strength of the irregular joint as indicated in Figure 6(c) is more than that of the regular joint as presented in Figure 6(b) on the same slope of asperities at different cycles of shearing. With increasing irregularities (the difference of angles between two slopes of asperities is increased) or the joint with $15^\circ-45^\circ$ asperity angle, the peak shear stress is increased. However, it rapidly decreases with increasing number of shear cycles, as shown in Figure 6(d). No significant change is observed on peak shear stress on the lower slope of asperities or backward movements. Figures 7(c) and (d) reflect that dilation and dilation angle is more on the higher slope of asperities and decreases gradually until it is equal with the lower slope of asperities. However, dilation and dilation angle of the regular joints both are constant or decrease gradually and equally on forward and backward movements from first to last shear cycles, as indicated in Figures 7(a) and (b). Irregular joints have a tendency to convert to regular joints at low normal stress under cyclic shear loads. Degradation of irregular joints is more predominant on the slopes at higher angles rather than at lower angles on the asperities.

4.2 High normal stress ($P=1$ MPa)

Shear stress versus horizontal displacement on the joints with asperity angles (a) $15^\circ-15^\circ$, (b) $30^\circ-30^\circ$, (c) $15^\circ-30^\circ$ and (d) $15^\circ-45^\circ$ at $P=1$ MPa is presented in Figure 8. Normal displacement versus horizontal displacement of the same joints at $P=1$ MPa is indicated in Figure 9. The peak shear stress increases with the increasing normal stress for all types of joints. In addition, the peak shear stress increases with the increasing asperity angle and irregularity of the joint at first shear cycle (in forward advance). After two or three shear cycles, all types of joints reach relatively the same shear stress level and behaviour of the joints changes from non planar to planar, due to the complete shearing of asperities of the joint at high normal stress. This joint behaviour or transition from nonplanar to planar becomes more obvious as the normal stress on the joint under cyclic loads increases. With increasing normal stress, compression is created on the joints. Small dilation is observed on regular joints only at first cycle at high normal stress, as presented in Figures 9(a) and (b).

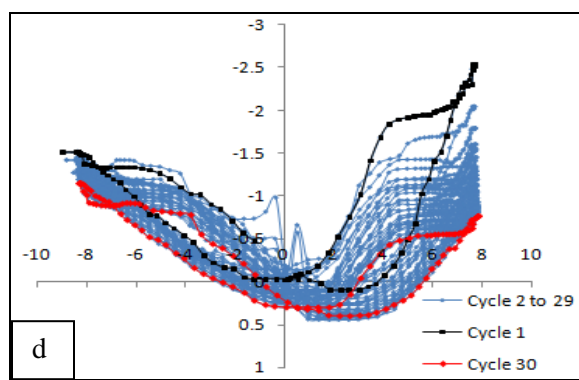
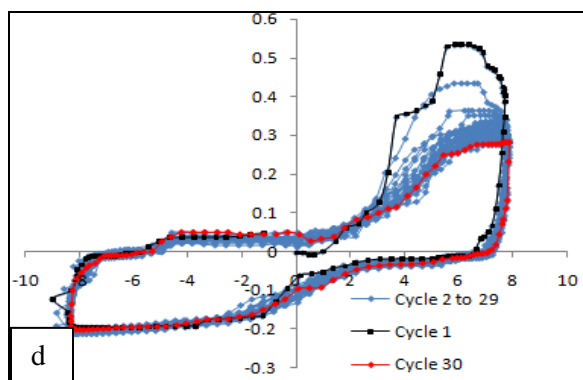
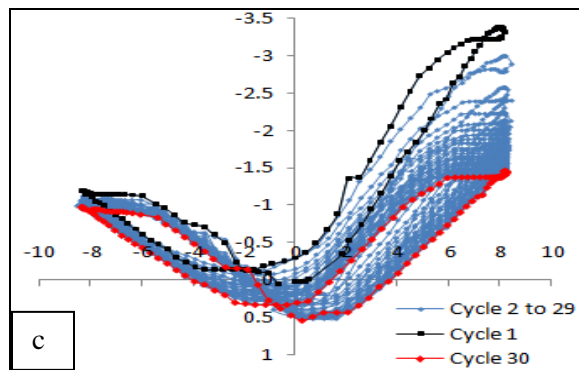
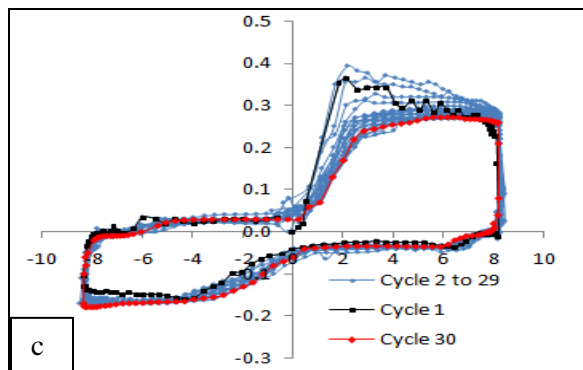
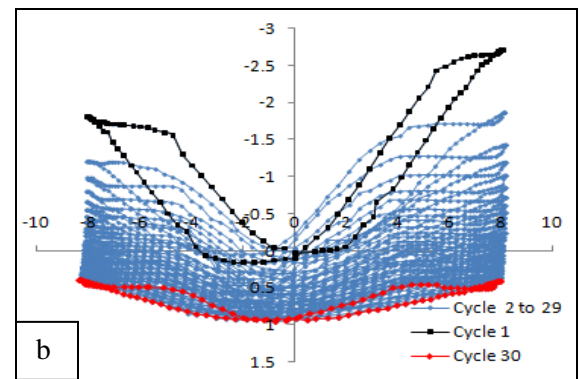
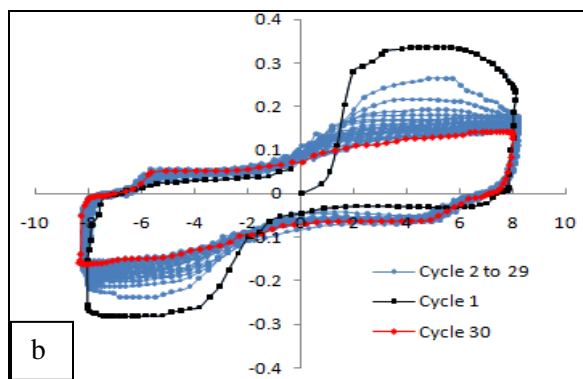
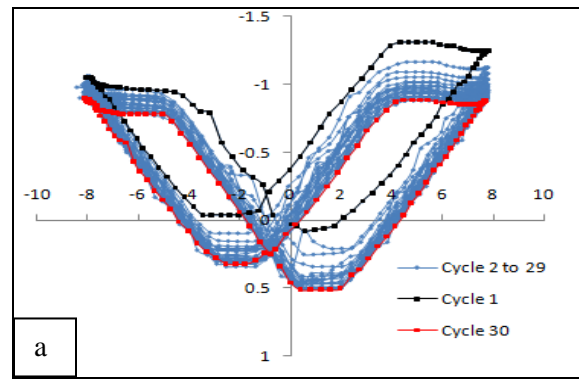
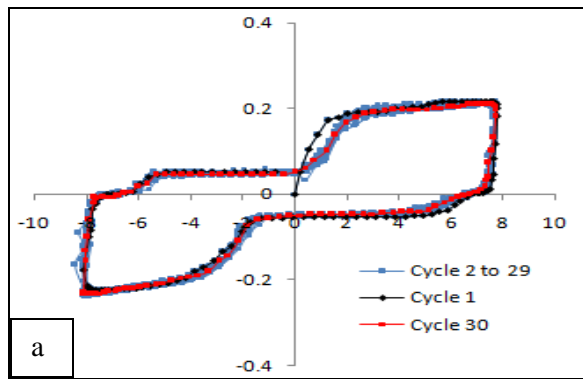


Figure 6 : Shear stress versus horizontal displacement on the joints with asperity angles, (a) 15°-15°, (b) 30°-30° (c) 15°-30° and (d) 15°-45° at P=0.1 MPa.

Figure 7: Normal displacement versus horizontal displacement on the joints with asperity angles, (a) 15°-15°, (b) 30°-30°, (c) 15°-30° and (d) 15°-45° at P=0.1 MPa.

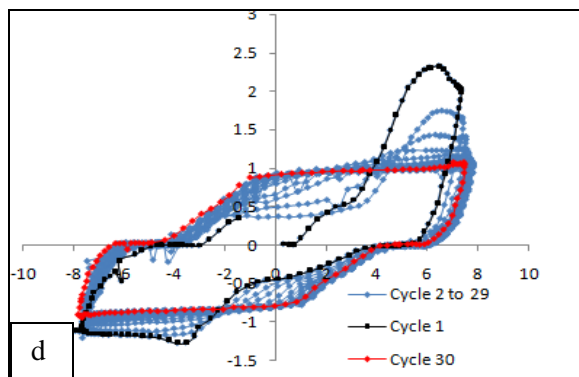
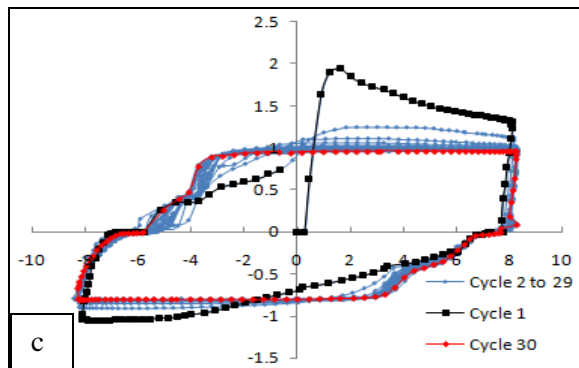
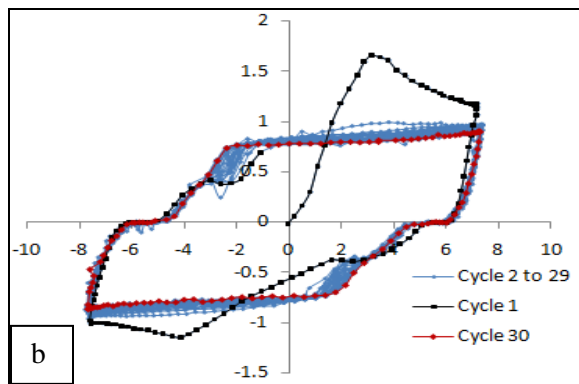
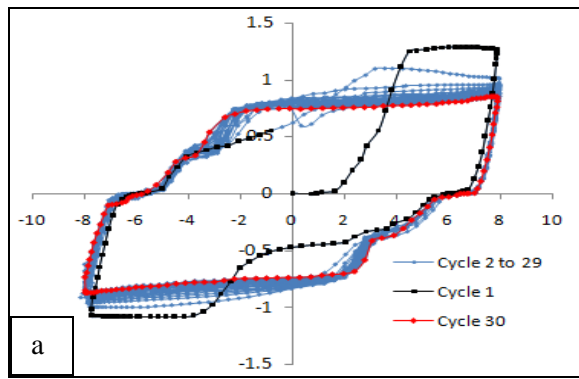


Figure 8 : Shear stress versus horizontal displacement on the joints with asperity angles, (a) 15°-15°, (b) 30°-30°, (c) 15°-30° and (d) 15°-45° at P=1 MPa.

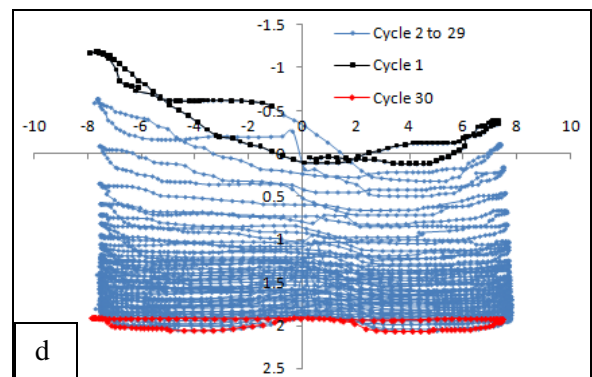
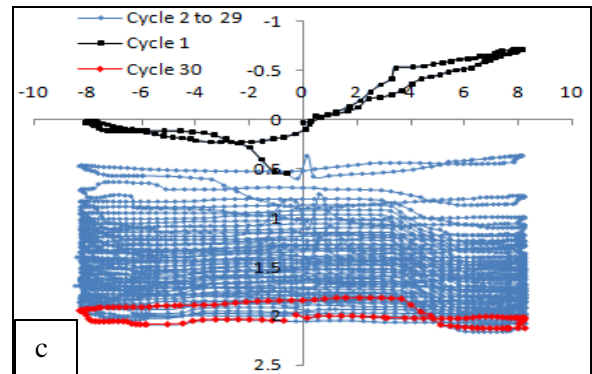
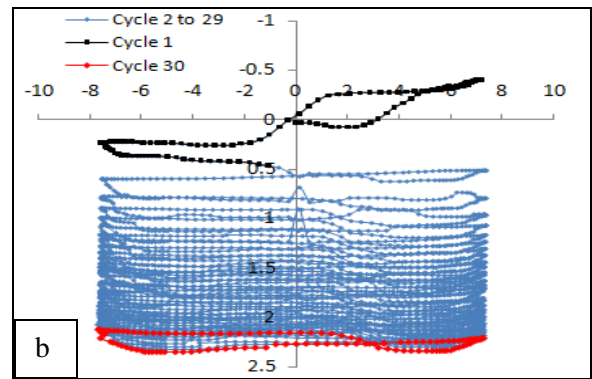
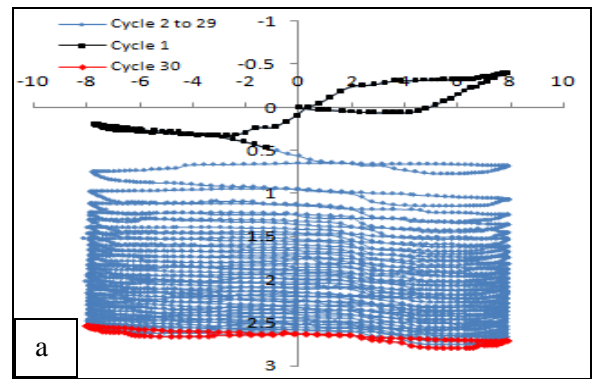


Figure 9 : Normal displacement versus horizontal displacement on the joints with asperity angles, (a) 15°-15°, (b) 30°-30°, (c) 15°-30° and (d) 15°-45° at P=1 MPa.

In the case of irregular joints, dilation and dilation angles start to increase in the backward movement with increasing irregularities as shown in Figure 9 (d). Dilation and dilation angles on the slope of asperities with lower angles increases in backward movement with respect to the other joints, and it is either due to increase in slope angle because of deformation on another part of slope in first movement, or some debris getting deposited on this slope due to first shearing and joint degradation on the slope of asperity with higher angle. Horizontal displacement corresponding to peak shear stress decreases with increase in asperity angle, whereas it increases with the increasing irregularity of the joint.

5. CONCLUSION

The test results indicate that the shear strength of rock joints increases with increase in asperity angles and normal loads at first cycle of shearing. With the increase in the number of shear cycles, the shear strength reduces for all the asperity angles (except a joint with a low asperity angle at low normal stress). However, the rate of reduction is greater in the case of asperities with higher angles. Natural rock joints are irregular, but most prior studies have been conducted on regular joints. In the present study, cyclic shear tests were performed on both regular and irregular joints for comparison. Shear strength of irregular joints was found to be higher than that of regular joints at different cycles of shearing at low normal stress. The analysis of design of structure on rocks by using the above test results makes the design safer and more economical. The mechanism of shearing for regular and irregular joints is different under cyclic conditions. Shear strength and degradation of asperities on the regular joints between loading and unloading are the same at low normal stress, whereas for irregular joints they are different. Shear strength and joint degradation are more on the slope of asperity with higher angles on the irregular joints, until two angles of asperities become equal under shear cycles at low normal stress when it starts behaving like the regular joints.

6. ACKNOWLEDGEMENT

The authors wish to thank for the financial support of this research from Indian Institute of Technology Delhi. We are thankful to Mr. Jattinder Singh, Managing Director, of Hydraulic Engineering and Instruments Company, New Delhi, for extending help during the modification of shear testing machine.

7. REFERENCES

Huang X, Haimson BC, Plesha ME & Qiu X. (1993). An investigation of the mechanics of rock

joints. *International Journal of Rock Mechanics and Mining Sciences*. Volume 30, No. 3, pp. 257–269.

Hutson, R. W., & Dowding, C. H. (1990). Joint asperity degradation during cyclic shear. *International Journal of Rock Mechanics and Mining Sciences*. Volume 27, No. 2, pp. 109-119.

Indraratna, B., Mirzaghorbanali, A, Oliviera ,D, A, F. Premadasa, w (2012). Shear behaviour of rock joints under cyclic loading. Proceedings of the 11 th, Australia - New Zealand conference on Geomechanics : Ground Engineering in a Changing World, In G. A. Narsilio, A. Arulrajah & J. Kodikara (eds.), pp. 1256-1261.

Jafari, M. K., Amini Hosseini, K., Pellet, F., Boulon, M., & Buzzi, O. (2003). Evaluation of shear strength of rock joints subjected to cyclic loading. *Journal of Soil Dynamics and Earthquake Engineering*. Volume 23, No. 7, pp. 619-630.

Lee, H. S., Park, Y. J., Cho, T. F., & You, K. H. (2001). Influence of asperity degradation on the mechanical behavior of rough rock joints under cyclic shear loading. *International Journal of Rock Mechanics and Mining Sciences* Volume 38, No. 7, pp. 967-980.

Mirzaghorbanali, A Nemcik, j. & Aziz, N. (2013). Effects of Shear Rate on Cyclic Loading Shear Behaviour of Rock Joints Under Constant Normal Stiffness Conditions. *International Journal of Rock Mechanics and rock engineering*. Volume 47, No. 5, pp. 1931-1938.

Niktabar. S. M. M. Rao, K.S, & Shrivastava, A.K . (2015) Shear Behaviour of rock joints under cyclic condition. Special Publication, *Journal of Engineering Geology*, October 2015. pp. 277-286.

Shrivastava, A. K, & Rao, K .S. (2013), Development large scale direct shear testing machine for unfilled and infilled rock joint under constant normal stiffness condition, *American Society for Testing and Materials*, Volume 36, No. 5, pp. 1-11.

3D geological modelling method based on hybrid data model

Xue-xi Chen ^{a,*}, De-fu Che ^b

^a Department of Safety, North China Institute of Science and Technology, Beijing, China, 101601

^b Center for RS/GPS/GIS and Digital Mine, Northeastern University, Shenyang, Liaoning, China, 110004

ABSTRACT

Based on a comprehensive analysis of research findings using a 3D geological model made by predecessors, a new method using a hybrid data model is proposed to construct 3D geological models. This method takes borehole as its main modelling data source. The modelling process is comprised of the following steps: 1) generate the triangle irregular network (TIN) adhering to the Delaunay's law of ground surface according to borehole's collar data, 2) down the borehole extend each triangle of TIN into generalized tri-prism (GTP) with knowledge inference rule, 3) convert GTP model into tetrahedral network (TEN) model or boundary representation (B-reps) model according to a certain conversion algorithm. This mixed modelling method integrates the advantages of TIN, GTP, TEN and B-reps model. The model is not convenient for updating data dynamically, but makes it easy to construct 3D geological models, carry out visualization and spatial analysis, and extend the applicable scope of 3D geological models. Based on the constructed 3D geological model in Central Business District (CBD), Beijing, some engineering applications including arbitrary cutting, virtual excavation design, virtual wandering, and others are demonstrated. The flexibility and practicality of this modelling method is tested.

KEYWORDS: borehole data; 3D geological modelling; hybrid data model; knowledge inference rule; engineering application

1. INTRODUCTION

In recent years there has been an increased demand for simulating 3D geological information in mine, geology, environment, and geotechnical engineering. This has promoted research on 3D geological modelling and its application (Cao and Wang, 2004). Many scholars have put forward their respective 3D geological models, such as triangle irregular network (TIN) model (Lemon and Jones, 2003), boundary representation (B-reps) model (Wang, 2003; Cheng et al., 2004), tetrahedral network (TEN) model (Chen, 1995), tri-prism (TP) model (Gong et al. 2004; Zhang and Bai, 2001; Rui et al., 2004), and generalized tri-prism (GTP) model (Wu, 2004). Although TIN modelling is mainly used to describe the interface of geological bodies and is convenient to show and update data, it cannot describe the internal properties of geological mass. B-reps model records all the spatial data that constitutes a geological entity by complete vector structure and makes it easy to carry out spatial query and topology analysis, but it is inconvenient for describing a geological entity accurately with a curved surface. TEN modelling has advantages in quick geometry shows and transformation and visualization for complex geological entities. However, it produces a great deal of redundant data when describing stratified geological bodies due to the complex construction algorithm. TP models and

GTP models are easy to build and give consideration to both interface and internal properties. However, section visualization is more complicated, with a great number of deformation triangular prisms produced in the process of repeated free cutting.

Thus, a new method using a hybrid data model to construct 3D geological models is proposed to solve the problems discussed above. The first step is to generate ground surface TIN according to Delaunay's law based on borehole's collar data and to establish basic topology relationship among boreholes. The second step is to extend TIN triangle into GTP down the borehole with certain rules, to build the overall described model of the geological body. The third step is to convert GTP into TEN or B-reps via a corresponding conversion algorithm for visualization operation and spatial analysis. This mixed modelling method integrates the corresponding advantages of each model, such as convenient data updates for TIN, simple construction algorithm for GTP, convenient visualization operation for TEN, and spatial query for B-reps, making up for the defects of each single model.

2. 3D GEOLOGICAL MODEL BASED ON HYBRID DATA MODEL

*Corresponding author – email: xuexichen1210@163.com

2.1 3D Geological Model

The 3D geological model based on hybrid data model was designed for practical application, as is shown in Figure 1. This model includes such models as TIN, GTP, TEN, and B-reps and abstract geometry elements such as node, edge, arc, triangle, super-face, GTP, tetrahedron, and super-body. The component elements of B-reps such as node, arc, super-face, and super-body are called boundary geometry elements. These kinds of elements are mainly used to express topology relationships between geological entities. Node, edge, triangle, GTP, and tetrahedron are called volume geometry elements. Unlike boundary geometry elements, they are mainly used to express geometry topology structure change in the interior of geological entities. This model also defines constraints between geometry modelling elements that not only are the theoretical basis for spatial analysis, 3D visualization, and 3D query in 3D models, but also a guarantee of unity, correctness, and uniqueness for 3D geometry object reconstruction.

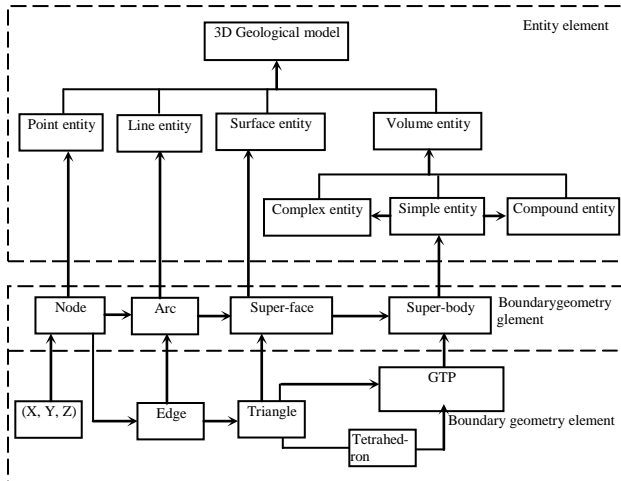


Figure 1: 3D geological model based on hybrid data model.

Geological entity is usually divided into the following: like point entity, line entity, surface entity, and volume entity. For volume entity, it can be divided further into three types: simple entity, complex entity, and compound entity. Complex entity is the combination of simple entities that belong to the same type while compound entity is the gathering of simple entities affiliated to different types. Both complex entity and compound entity are defined by simple entity. Simple entity is defined by surface entity. Surface entity is defined by line entity. Line entity is defined by point entity. Obviously, this entity description method has a clear hierarchy and is convenient for organizational management.

2.2 Data Structure

According to object-oriented theory and methods, entity elements and geometry elements in Figure 1 can be designed to various object classes and be built to corresponding topology structures combined with a practical application. Their own member variables are thought of as data structure. In this paper only the main data structures of node, triangle, and GTP which have a close connection with modelling inference and algorithm efficiency are discussed.

Data structure of point:

```
class CBoreholePoint: public CObject //point class
{
    long PointID; // ID mark of point
    char AttributeID; //attribute mark
    double x, y, z; // x, y, z coordinate of point
    int StratumNO; //number of stratum
    CString BoreholeNO; //number of borehole
    CBoreholePoint*PrevPoint,*NextPoint;//previou
-s point and next point in point chain
    .....}

```

Data structure of triangle:

```
class CTriangle: public CObject //triangle class
{
    long TriangleID; //ID mark of triangle
    CTriEdge *Edge1, *Edge2, *Edge3; //three
edges of triangle
    CGtriprism *UpGtriprism, *DownGtriprism; //
GTP of triangle up and down
    CTriangle*PrevTriangle,*NextTriangle;//previou
-s triangle and next triangle in triangle chain
    .....}

```

Data structure of the GTP:

```
Class CGtriprism: public CObject // GTP class
{
    long GtriprismID; // ID mark of GTP
    CTriangle *UpTriangle, *DownTriangle; //
triangle at top and bottom of GTP
    long TENDivNO; //code of sectioning the GTP
into tetrahedron
    .....}

```

According to point data structure shown above, AttributeID is used to mark special points, such as the fault point. StratumNO is the code of stratum where the point is located. Its order increases progressively from ground surface to the lower. Attribute code of point is the lower adjacent stratum code. PrePoint and NextPoint are the previous point and the next point, respectively, on a point double linked list. On the one hand, point double linked lists are convenient for the retrieval of logical points of boreholes for extension. On the other hand, previous point and next point can be linked together when drawing under OpenGL driver, automatically solving deviation problems in a real situation. Therefore this double linked list helps improve modelling efficiency.

In data structure of triangle, PreTriangle and NextTriangle are the previous triangle and the next triangle on a triangle double linked list. Triangles whose three vertexes are subject to the same borehole number constitute of triangle double linked list. This double linked list efficiency can be improved when triangles extend into GTP along the borehole. In the data structure of GTP, TENDivNO is the section code. Based on this, it will section the GTP into tetrahedron by linking diagonals of quadrilateral at the side of GTP one by one.

3. 3D GEOLOGICAL MODELLING METHOD BASED ON HYBRID DATA MODEL

3.1 The Formation of Ground Surface TIN

The formation of ground surface TIN is the basis for mixed model construction. The process of regarding borehole's collar coordinates as data points and generating TIN according to Delaunay's law and establishing a basic topology relationship between boreholes is named the formation of ground surface TIN. The incremental insertion is one of the construction algorithms to generate Delaunay triangulation. The algorithm is suitable for ground surface modelling based on borehole data because of its simple principles. The basic steps are as follows (Wu et al., 1999). Firstly, define an initial polygon that contains all borehole data points. Secondly, construct an initial triangulation in the defined initial polygon, and then conduct iteration until all data are processed. The iteration should be as follows, to insert a P data point and to find the T triangle that contains P in the triangulation, then link P and the three vertexes of T to form a new triangle. Third, optimize triangulation using the Local Optimization Procedure (LOP) to meet Delaunay's law.

For fault ruptures above the ground, the constraint relationship between discrete points will be enhanced due to fault when constructing Delaunay triangulation at the orifice. It can be solved by viewing the fault line as a constraint and adopting an algorithm named constrained Delaunay triangulation. These kinds of algorithms mainly include constrain graph methods, divide-conquer algorithms, triangulation growth methods, encryption algorithms, and two-step methods. The diagonal exchanging algorithm that forcibly inserts constrained boundary is simpler, easier to realize, and is more practical than the other two-step methods (Li and Tan, 1999).

3.2 3D Geological Model Construction Method Based on the GTP

After the generation of TIN, the triangle can be extended down the borehole to form GTP. The main steps to form GTP are as follows.

1) Choose a triangle from TIN and set it to be the triangle of the first GTP.

2) As shown in Figure 2, a new triangle can be formed by extending three vertexes of previous triangles down the three boreholes according to stratum ID.

The stratum is formed in a sequence and always of different distribution map, which reflects ordinal relationship of abnormal stratum pinching out during geological formations. Besides, stratum can be broken and be constrained by the fault. Therefore, it is necessary to reflect this geologic structure rule when triangle extending down. In order to ensure correctness and uniqueness when reasoning the relationship mentioned above. The reasoning rules are as follows.

As shown in Figure 2(a), if none of three vertexes of the current extending triangle are the fault point, the next point of the corresponding borehole will be vertexes of a new triangle with the same code. As shown in Figure 2(b), once the code is different, vertex whose number is less than other's will be extended into a new triangle vertex along the corresponding borehole. Vertex whose number is bigger will be unchanged.

If the current extending triangle has one or two fault point(s) among the three vertexes, whether the attribute of next point of the rest of vertexes is the same as the attribute of fault point should be checked. If attribute is the same, fault point cannot be extended down regardless of number size until all the rest of the vertex extend down into the same attribute. Figure 2(c) shows that triangle 111 is extended down into triangle 221. The black circle dot represents fault point while the black triangle represents fault surface. Otherwise all vertexes can extend down based on number size. As is shown in Figure 2(c), triangle 222 extends down to form triangle 333.

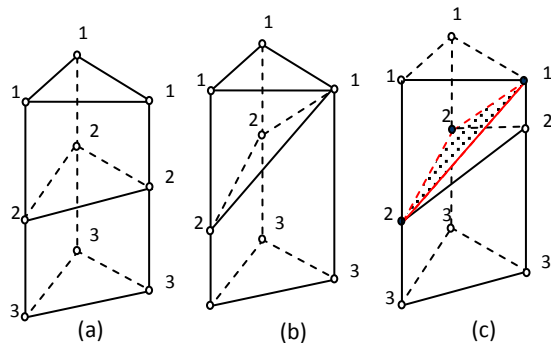


Figure 2: Down expanding rule of triangle.

In such situation as all current vertexes of the extending triangle are fault points, the way the triangle extends down to form a new triangle according to number size can be the same as the situation without any fault points. In Figure 2(c), triangle 221 is extended down to form triangle 222.

3) Construct GTP according to corresponding relationship between previous triangle and the next triangle on the triangle double linked list and borehole point list, then record reflected information and regard the next triangle as with the previous triangle.

4) Repeat step 2) and 3) until all vertexes of the previous triangle lie in the bottom of the borehole.

5) Repeat steps 1) to 4) until all TIN is traversed.

If there are new data about the borehole, only the local ground surface TIN should be modified and be extended down to generate new GTP. This method is convenient for dynamic modification. It can also automatically reason complex geological structures such as fault and pinch-out. This method has a simple construction algorithm.

3.3 Tetrahedron Generation and Boundary Conversion of GTP

After construction of the whole 3D geological model, it is necessary to transform the GTP model into a tetrahedron model or the B-reps model for visualization and engineering application analysis. The former is realized by the method named the smallest vertex identifier (Chen et al., 2004). Firstly, number each vertex of GTP uniformly for identification. This must meet the two following conditions. 1) The identification number is invariable and unique. 2) The identification numbers can be compared with each other. Secondly, the vertexes that have the smallest identification number are selected by comparing the identification numbers of four vertexes in each quadrangle at side of GTP, and then they are linked to the corresponding vertexes in the opposite face in order to finish tetrahedron division. To ensure that the geological body is described completely by GTP and to save memory space, it is not directly sectioned into a tetrahedron. Instead it will add tetrahedron division code to its data structure. Connection code of diagonal of the side face constitutes these codes in order, and each GTP element includes three mark bits, each of which has a corresponding connection way about the diagonal. Thus, tetrahedron division is finished by searching the identification number of GTP. This method has a certainty and is easy to program. What's more, it does not need to store data of adjacent GTP elements for local operation. Only in this way, can a global unit be sectioned and compatible.

Boundary conversion is done through special data structure of GTP. According to topology relationship between GTPs, not only adjacent volume elements are easy to be found, but also boundary volume elements whose bottom triangle or side quadrangle is located in the boundary can be searched. For a boundary triangle, it will be added to a triangle-linked list expressed by an entity boundary. Boundary quadrangles should be sectioned into triangles by the smallest vertex identifier before being added to the linked list. The following are the procedures for boundary conversion. Firstly, initialize the triangle-linked list expressed by entity boundary to dynamically store s boundary triangle. Secondly, extract a GTP from the GTP linked list and search information as to adjacent volume elements according to the stored topology relationship among adjacent volume elements. If the top triangles or the bottom triangles are not the adjacent volume elements or the adjacent volume elements are of a different attribute, it will be added to the linked list. Side quadrangles in the same situation should be sectioned into two triangles by the smallest vertex identifier before being added to the linked list. Lastly, the second step should be repeated until the GTP linked list is fully processed.

Entity boundary expression not only contributes to analysis on spatial topology relationships between geological entities, but also simplifies visualization operations for those geological entities whose internal information is not needed.

4. ENGINEERING APPLICATION CASE

Based on modelling methods mentioned above, the 3D geological modelling system GeoMo^{3D} was developed by using VC++6.0 and the 3D graphic drawing tool OpenGL. An engineering application experiment was carried out and combined with actual geological exploration data from the Beijing Central Business District. The studies area contained a total of 46 primitive boreholes. The stratum is divided into 10 layers, as is shown in Figure 3(a). Because a 3D geological model based on a hybrid data model can unify all surfaces of volume elements to be boundary triangles and can transform all volume elements into tetrahedrons, it is easier to perform normal analyses such as a random section plane or layer display. Above all, it is possible to conduct special visualization operations, such as virtual excavation and spatial query. Figure 3(b) is a fence diagram that is found by repeatedly sectioning the tetrahedron model. It clearly shows every internal detail of the geological model, which helps to learn the geological structure. As shown in Figure 3(c), by designing a virtual tunnel in the tetrahedron model and intersecting, we can observe the distribution situation

of exposed geological structures after excavation. Figure 3(d) shows that we can study the spatial relationships between tunnel and stratum using the B-reps model. It can provide reference information for excavation design and influence analysis.

5. CONCLUSIONS

3D geological models can guide geological analysis in relevant application domains. This has practical value for project planning, excavation design, environmental impact analysis, and disaster prevention and reduction. Based on a comprehensive analysis of previous research findings related to 3D geological models, a new hybrid data model was proposed to construct a 3D geological model. It is not only convenient to dynamically update data, but also makes it easy to construct 3D geological models and to carry out visualization and spatial analysis. It automatically reasons complex geological structures such as faults and pinch-out, extending the applicable scope of 3D geological models. The successful development and application of the 3D geological modelling system GeoMo^{3D} demonstrates that this new modelling method has flexibility and practicability. There is further work to be done in order to better serve relevant application fields of geological engineering. For example, to improve the functions such as virtual design of geological bodies, attribute query and spatial analysis and inference are necessary.

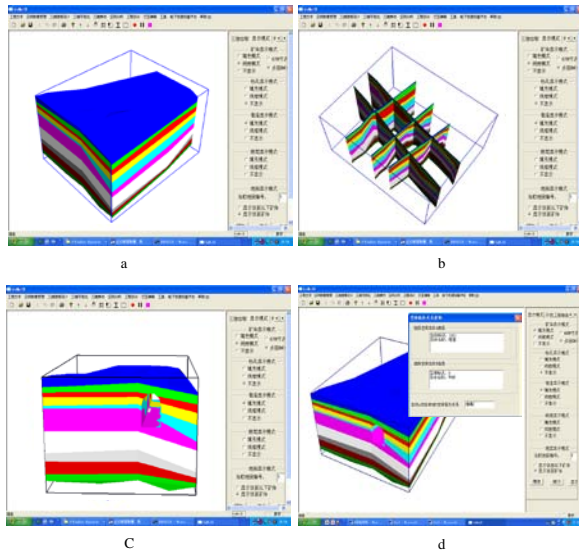


Figure 3: Application case of 3D geological modelling.

6. REFERENCES

Cao D Y, Wang Z G. (2004). Direct 3D-interaction in 3D geological model visualization. *Journal of China University of Mining and Technology*. Volume 33, No. 4, pp. 384-387

Cheng P G, Liu S H, Wang W, et al. (2004). Study and application of a new 3D geological model construction method. *Journal of Jilin University(Earth Science Edition)*. Volume 34, No. 2, pp. 309-313

Chen X Y. (1995). A workstation for three-dimensional spatial data research. In: *The Fourth International Symposium of LIESMARS*, Wuhan, pp. 42-51

Chen X. X, Wu L. X, Shi W. Z, et al. (2004). Diagonal generation by Smallest Vertex Identifier in GTP model. *Geography and Geo-Information Science*. Volume 20, No. 3, pp. 17-21

Gong J Y, Cheng P G, Wang Y D. (2004). Three-dimensional modeling and application in geological exploration engineering. *Computers and Geosciences*. Volume 30, No. 4, pp. 391-404.

Lemon A M, Jones N L. (2003). Building solid models from boreholes and user-defined cross-section. *Computers and Geosciences*. Volume 29, No. 3, pp. 547-555

Li L X, Tan J R. (1999). Multiple diagonal exchanging algorithm for inserting constrained boundary in constrained Delaunay triangulation. *Chinese Journal of Computers*. Volume 2, No. 10, pp. 1115-1118

Rui X P, Yang Y G, Xi Y T. (2004). Study on visualization of 3D stratum based on triangular prism. *Journal of China University of Mining & Technology*. Volume 33, No. 5, pp. 584-588

Wang C X. (2003). Study on geological modeling in 3D strata visualization. *Chinese Journal of Rock Mechanics and Engineering*. Volume 22, No. 10, pp. 1722-1726

Wu L X. (2004). Topological relations embodied in a generalized tri-prism(GTP) model for a 3D geoscience modeling system. *Computers and Geosciences*. Volume 30, No. 4, pp. 405-418

Wu X B, Wang S X, Xiao C S. (1999). A new study of Delaunay triangulation creation. *Acta Geodaetica et Cartographica Sinica*. Volume 28, No. 1, pp. 28-35

Zhang Y, Bai S W. (2001). An approach of 3D stratum modeling based on tri-prism volume elements. *Journal of Image and Graphics*. Volume 6, No. 3, pp. 285-290

Measurement and analysis of virgin-rock temperature in Huanren Metal Mine

CHANG De-qiang^{a, b, *}, LIU Jing-xian^{a, b}, MAO Ning^{a, b}, GE Shuang-you^a

^a Institute of Safety Engineering, School of Resource & Civil Engineering, Northeastern University, Shenyang, China, 110004

^b Key Laboratory of Ministry of Education on Safe Mining of Deep Metal Mines, Northeastern University, Shenyang, China, 110004

ABSTRACT

With the increase of mining depth, the heat-harm in high temperature deep mines has become increasingly prominent and become a new obstacle for the development of mining in China. Two pitheads from Huanren Metal Mine, a nearly one-thousand-meter-depth mine, were taken as the study objects of this paper. The deep-hole temperature measuring method was adopted to determine the rock temperature. The original rock temperature was analyzed theoretically, and the ventilation cooling depth, the geothermal gradient, and the distribution model of the rock temperature were calculated and verified. The temperature of the deep rock was predicted and some pertinent suggestions to control the thermal hazard were put forward. The results show that the ventilation cooling depth of this mine is 20 m, and the geothermal gradient of the two pitheads is 2.3°C/100 m and 3.6°C/100 m. The model of the airflow temperature agrees well with the measured values. The research in this paper can provide theoretical and technical support for heat-harm prevention and control in Huanren Metal Mine and other similar mines.

KEYWORDS: metal mine; virgin-rock temperature; measurement; geothermal gradient

1. INTRODUCTION

In present day China, about 35 to 40 percent of the mines have entered the deep mining stage and the mining depths of nearly one hundred metal mines are more than 1000 meters. It can be predicted that in the next few decades more and more underground mines will move into deep mining (Dong et al., 2009; Gu and Li, 2003). With the increasing mining depth, the heat-harm has become increasingly prominent, which seriously affects the health of workers, greatly reduces labor productivity, and increases the accident rate. The high temperature in deep mines has become a new obstacle for the development of mining in China. As the most direct and important underground heat source, heat from the wall rock takes about 48% of the total heat transferred into underground air (Donoghue et al., 2000; Hartman et al., 2012). Therefore, the measurement and analysis of the virgin-rock temperature provides very important basic data for temperature-humidity air conditioning.

This study aimed to investigate the virgin-rock temperature and the temperature distribution in the rock and determine the geothermal gradient and the heat flow transferred from the rock to the air flow in Huanren Metal Mine. As a nearly one-thousand-meter-depth mine, two pitheads in Huanren Metal Mine were taken as the study objects. The deep-hole temperature measuring method was adopted to

determine the rock temperature. The original rock temperature was analyzed theoretically. The ventilation cooling depth, the geothermal gradient, and the distribution model of the rock temperature were calculated and verified. The temperature of the deep rock was predicted. The research in this paper can provide theoretical and technical support for heat-harm prevention and control of Huanren Metal Mine and other similar mines.

2. MEASUREMENT

2.1 Measurement instrument

Virgin-rock temperature can be calculated based on the data obtained from borehole temperature (Vost, 1976). In this paper, the temperature was tested in a deep borehole with armored type k thermocouple. The compensating wire for the thermocouple was 25 meter long and sealed and protected by a Teflon tube. The temperature was displayed by a digital thermometer which was designed for type k thermocouple. The measuring range was from -50.0°C to 1300°C, the resolution was 0.1°C, and the precision was 0.1% ±0.4°C.

Fifteen thermocouples were used in the measurement; these thermocouples were all calibrated before the test to ensure the accuracy of the data.

2.2 Measurement scheme

(1) Measurement of ventilation cooling depth

The temperature of the virgin-rock at the certain depth in a small range is the same when the properties of the rock are homogeneous. In the mine, if the distance between the surrounding rock and the wall of the laneway is longer than the ventilation depth, the temperature of the rock will be a constant, which is the virgin-rock temperature at this level. In the test, three horizontal boreholes in typical rock whose depths were not less than 25 meters were selected as the sampling holes. The thermocouples were put deeply at the bottom of the sampling holes and the openings of the hole were sealed with mud. In the next 24 hours, the temperature in the holes was allowed to stabilize, and then the temperature and the distance between the sample point and the laneway wall were recorded. Next, the thermocouple was pulled out several meters and the test was repeated until the entire thermocouple was pulled out. The ventilation cooling depth is the distance between the sample point and the laneway wall from which the rock temperature does not increase and the highest temperature is exactly the virgin-rock temperature at this level.

(2) Measurement of geothermal gradient

The geothermal gradient is an important indicator to rate the heat-harm in the mine and the essential data to predict the heat-harm and guide the temperature lowering. The geothermal gradient can be calculated with the data obtained by measuring the virgin-rock temperature of different levels. In this paper, the borehole for the rock temperature sampling was ready-made. The measurement was carried out according to the following steps:

(a) Choose seven different levels in which the boreholes meet the test request can be found. The distribution of the levels should be uniform from the top to the bottom as far as possible. The borehole should be horizontal, dry, and without flowing water in it. The depth of the hole should not be less than 25 meters. The bottom of the borehole should keep far away (>25 meters) from the structures which may affect the rock temperature, such as the shaft, goaf, chamber, and so on.

(b) Insert the thermocouple into the borehole until the depth is not less than the ventilation cooling depth measured previously. Seal the opening with mud.

(c) Record the temperature after 24 hours.

(3) Position of the sample point

According to the test request, the in-site condition was analyzed and the measure point was

decided. Some boreholes in the level of -500 m, -530 m, -560 m, -600 m, -630 m, -660 m, -690 m in the Songlan Pithead and -420 m, -480 m, -540 m, -630 m, -720 m, -760 m, -840 m in the Xiangyang Pithead were selected.

3. DATE ANALYSIS

3.1 Determine the ventilation cooling depth

As the typical rocks in the two pitheads were the same, this measurement was only carried out in the Songlan Pithead. The data from three boreholes were collected at the level of -600 m. Rock temperatures at various distances to the wall in the borehole are shown in Figure 1.

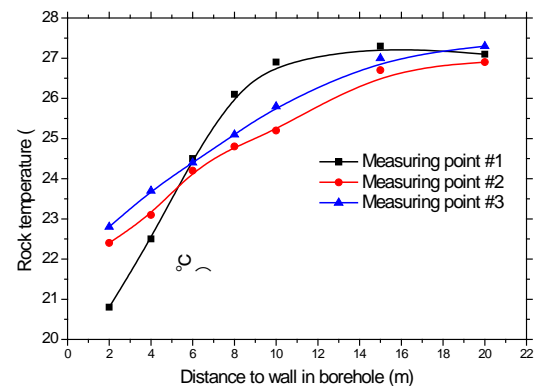


Figure 1: Rock temperature vs. Distance to wall in borehole.

Due to the different velocities and temperature of the air flow around the sample point, there were obvious differences in the initial point and the change process of the rock temperature between the three sample points. The rock temperatures all gradually increased with the distance between the temperature sample point and the wall of the laneway, then stabilized and were not affected by the outside air flow when the distance was more than 15 meters. When the distance reached 20 meters, the rock temperature of the three points became the same and no more change occurred with increased distance, that is to say, the ventilation cooling depth in the mine was 20 meters, and the temperature at this depth was the virgin-rock temperature.

3.2 Calculate the geothermal gradient

After in-site measurement, the virgin-rock temperature at different levels in the Songlan Pithead and Xiangyang Pithead were obtained, as shown in Tables 1 and 2.

Table 1: Virgin-rock temperature at different levels in Songlan Pithead.

Level of sample points	-500m	-530m	-560m	-600m	-630m	-660m	-690m
Relative depth to 1st sample point (m)	0	30	60	100	130	160	190
Equivalent height (1/100m)	0	0.3	0.6	1	1.3	1.6	1.9
Virgin rock temperature (°C)	21.4	22.3	23.7	24.9	26.1	27.3	28.0

Table 2: Virgin-rock temperature at different levels in Xiangyang Pithead.

Level of sample points	-420m	-480m	-540m	-630m	-720m	-760m	-840m
Relative depth to 1st sample point (m)	0	60	120	210	300	340	420
Equivalent height (1/100m)	0	0.6	1.2	2.1	3	3.4	4.2
Virgin rock temperature (°C)	19.3	20.2	21.6	23.5	25.8	26.7	28.7

The geothermal gradient was derived by the fitting method. The levels of the sample points were transferred to equivalent height by Equation 1 while the temperatures remained unchanged. Then the data of height and temperature was fitted with a line, where the geothermal gradient is the slope of the line.

$$h' = \frac{h_{max} - h}{100} \quad (1)$$

Where h_{max} is the maximum of all the levels, m; h is the original levels of the sample points, m; h' is the equivalent height, 100 m⁻¹. According to the results of the geothermal gradient fitting shown in Figures 2 and 3, the geothermal gradient of Songlan Pithead was 3.6°C/100 m while that of Xiangyang Pithead was 2.3°C/100 m. Compared with the average geothermal gradient of the earth crust, which is 2.5°C/100 m, the geothermal gradient in the Xiangyang Pithead is normal while that in the Songlan Pithead is larger and should be paid more attention to for the possible heat harm when the mining depth is further increased.

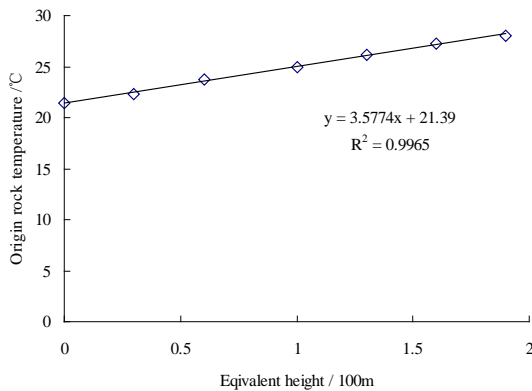


Figure 2: Geothermal gradient fitting of Songlan Pithead.

3.3 Distribution model of the virgin-rock temperature

The virgin-rock temperature at certain depths can be calculated by Equation 2.

$$t_n = t_a + \frac{(H - H_a) \times G}{100} \quad (2)$$

Where t_n is the virgin temperature of the rock which is H meters below the earth surface, °C; t_a is the rock temperature of the zone of constant temperature, °C; H is the depth of the rock from the earth surface, m; H_a is the depth of the zone of constant temperature, m; G is the geothermal gradient, °C/100 m.

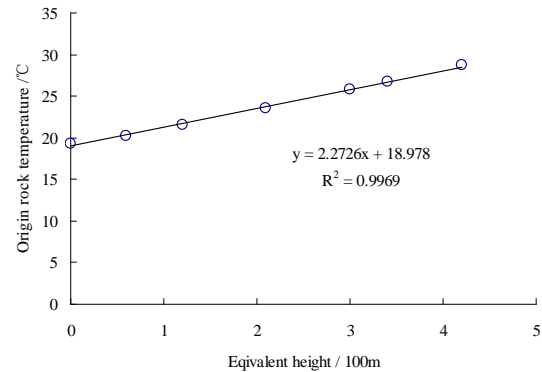


Figure 3: Geothermal gradient fitting of Xiangyang Pithead.

According to the information from the mining company, the depth of the zone of constant temperature in Huanren Mine is 30 meter, t_a is 4.4°C for the Songlan Pithead and 9.9°C for the Xiangyang Pithead. The distribution models of the virgin-rock temperature for the Songlan Pithead and Xiangyang Pithead are Equations 3 and 4, respectively.

$$t_{n,s} = 4.4 + \frac{(H - 30) \times 3.6}{100} \quad (3)$$

$$t_{n,x} = 9.9 + \frac{(H - 30) \times 2.3}{100} \quad (4)$$

Based on these two equations, the temperature of the deep rock can be predicted. Take Songlan Pithead as example, the virgin-rock temperature will increase to 30°C when the mining depth reaches -741 m. If the mining depth reaches -936 m, the virgin-rock

temperature will be 37°C which will be a severe problem.

3.4 Air flow temperature

Based on the assumption that the inlet air temperature in the laneway is constant and the heat transfer in the rock is stable, according to the heat exchange between air and rock, the air temperature can be calculated by Equation 5 (Ventilation Research Laboratory, 1976).

$$t_l = \frac{(S-1)t_n + t_0}{S} \quad (5)$$

Where t_0 is the inlet air temperature in the laneway, °C; t_l is the temperature of the air which is L meters far away from the inlet, °C; S is calculated as:

$$S = 10^{\frac{L \cdot K \cdot P}{2600Q}} \quad (6)$$

Where L is the distance from the inlet, m; P is the circumference of the laneway, m; Q is the air quantity, $\text{m}^3 \text{s}^{-1}$, K is calculated as:

$$K = \frac{8.7\lambda}{1.33 + \frac{\lambda}{v^{0.8}}} \quad (7)$$

Where λ is the heat transfer coefficient, $\text{W/m}^2 \text{°C}^{-1}$; v is the average velocity of the air flow, m/s.

In order to verify the applicability of the model, the data from -600 m level in the Songlan Pithead were put into the model, the value of the parameters were listed in the Table 3.

Table 3: value of the parameters from Songlan Pithead

Parameters	$t_0 / \text{°C}$	$v / \text{m/s}$	$t_n / \text{°C}$	P / m	L / m	$\lambda / \text{W/m}^2 \text{°C}$
Value	12.8	1	26.9	10	95	2.975

Based on the model, the temperature at the sample point is 20.6°C while the measured temperature is 20.3°C, the error is 1.48%. The model agreed well with the measured data and can be used to predict and control the heat-harm in the mine.

4. CONCLUSION

In this paper, Songlan Pithead and Xiangyang Pithead, two of pitheads of Huanren Metal Mine, were studied. The virgin-rock temperature was measured, the obtained data was analyzed theoretically, the ventilation cooling depth, the geothermal gradient and the distribution model of the rock temperature were calculated and verified, and the temperature of the deep rock was predicted. The results showed that the ventilation cooling depth in the Huanren Metal Mine is 20 meters. The geothermal gradient in Songlan Pithead is 3.6°C/100 m while that in Xiangyang is 2.3°C/100 m. The Songlan Pithead should be paid more attention to due to the possible heat harm when the mining depth is further increased. The model to calculate the airflow temperature is in agreement with the measured data, which showed its good applicability in this mine. This model can give strong support to predict and control the heat harm in the mine. The heat harm in the Huanren Metal Mine has already appeared preliminarily and is not serious at this time, but it should be closely monitored. With the increasing mining depth, the heat harm will become more and more severe. At the early stage, it can be improved by optimizing the ventilation network. After that,

more effective cooling measures should be taken into consideration.

5. ACKNOWLEDGEMENT

This work was supported by the National Natural Science Foundation of China (51404064), the Fundamental Research Funds for the Central Universities (N130401002).

6. REFERENCES

- Dong, L.-j., Li, X.-b. and Li, P.-p. (2009). Crucial Understanding and Decision-Making Technology for Deep Mining, *Nonferrous Metals*, Volume 61, pp. 116-120.
- Donoghue, A. M., Sinclair, M. J. and Bates, G. P. (2000). Heat Exhaustion in a Deep Underground Metalliferous Mine, *Occup. Environ. Med.*, Volume 57, pp. 165-174.
- Gu, D.-s. and Li, X.-b. (2003). Science Problems and Research State of Deep Mining in Metal and Nonferrous Mines, *Mining Research and Development*, Volume 23, pp. 1-5.
- Hartman, H. L., Mutmansky, J. M., Ramani, R. V. and Wang, Y. (2012). *Mine Ventilation and Air Conditioning*. John Wiley & Sons, pp.120.
- Vost, K. (1976). Rapid Changes of Air Temperature in Underground Airways, *J. S. Afr. Inst. Min. Metall.*, Volume 77, pp.262-268.
- Ventilation Research Laboratory (1976). Prevent Hoisting Shaft from Freezing through Preheating Air by Geothermal Energy, *J. Northeast. Univ.*, Volume 3, pp. 36-46.

The tensile properties of GFRP bars at different loading rates

Wenxue Chen^{a, b, *}, Jun Wu^a, Yuzhao Jiao^c, Jiewen Zheng^a and Xue Li^d

^a School of Civil Engineering, Henan Polytechnic University, Jiaozuo, China, 454000

^b Opening Project of Key Laboratory of Deep Mine Construction, Henan Polytechnic University, Jiaozuo, China, 454000

^c Shandong Safety Industrial Co., Ltd., Tai'an, Shandong, China, 271000

^d School of Resource and Safety Engineering, China University of Mining and Technology, Beijing, China, 100083

ABSTRACT

In order to study the effect of loading rates on the tensile property indexes of GFRP (Glass Fiber Reinforced Polymer) bars, the tensile property experiments were conducted at four different loading rates by utilizing the electro-hydraulic servo universal testing machine. The results show that: with increases in loading rate, the ultimate tensile strength and the ultimate tensile strain increase, while the elastic modulus almost remains constant with the average value 28.5 GPa; the failure mode of specimens belongs to splitting failure and the stress-strain curves show a linear relationship. Based on the results and analyses, a loading rate of 2 mm/min is recommended when conducting experiments to determine the tensile property indexes of GFRP bars.

KEYWORDS: GFRP bar; tensile property; loading rate; stress-strain curve; elastic modulus

1. INTRODUCTION

GFRP bar (Glass Fiber Reinforced Polymer bar) is a composite made up of a resin matrix and continuously twistless glass fiber reinforcement through the pultrusion process. Compared to rebar, it boasts advantages such as being light-weight, high strength, chemical corrosion resistant (Micelli et al., 2004; Kim et al., 2008), fatigue resistant (Uomoto and Nishimura, 1995), anti-electromagnetic and inflaming retardant, thus becoming an ideal alternative which is gradually applied in civil (and mining) engineering fields (Liu and Zhou, 2014.). Rebar is a plastic material while GFRP bar is a brittle material; therefore the structure design concepts of the two are different. In order to ensure the safety of the structure design, it is essential to deeply study the mechanical properties of GFRP bar. However, in terms of tensile loading rate, there are some differences among experiment specifications and researchers when conducting the tensile experiment to determine the tensile property indexes of GFRP bar.

“ACI 440.1R-03” (ACI Committee 440, 2003a) provides that the tensile loading rate should be controlled at 100-500 MPa/min and “ACI 440.3R-04” (ACI Committee 440, 2004b) provides that the specimen should be damaged in 1-10 min, no matter what load control or displacement control is adopted. “GB/T1447-2005” (GAQSIQ of the PRC and Standardization Management Committee of the PRC, 2005a) and “GB/T 13096-2008” (GAQSIQ of the PRC and Standardization Management Committee of the PRC, 2008b) also provide that the tensile loading

rate should be controlled at 5 mm/min when determining the ultimate tensile strength and 2mm/min when determining the elastic modulus as well as the ultimate tensile strain. Moreover, there are several specifications that not give a specific loading rate when conducting the tensile experiment, such as “MT/T 1061-2008” (State Administration of Work Safety, 2008) and “JG/T 351-2012” (MHURC of the PRC, 2008).

It is the fact that the loading rates adopted by the researchers are also not the same when they carried out in tensile experiments. For example, Brahim Benmokrane (Benmokrane et al., 2000) adopted a loading rate of 250 MPa/min when he researched the tensile properties of AFRP and CFRP bars. Young Jun You (You et al., 2007) adopted the loading rate according to the specification “ASTM-D-3916” (ASTM, 2002) when he conducted the tensile experiments of FRP bars. There was no specific loading rate given by S. Kocaoz (Kocaoza et al., 2005) when he studied the tensile properties of GFRP bars. Besides the researchers mentioned above, there have also been a wide range of researchers from China completing tensile experiments of GFRP bars, and the loading rates they chose also varied widely. $5 \times 10^{-5} \text{ s}^{-1}$ were used by Jikai Zhou (Zhou et al., 2008) 4kN/time by Jing Chen (Chen et al., 2012), 2 mm/min by Xinyue Zhang (Zhang et al., 2005). Particularly, Guowei Li (Li et al., 2012) adopted a group of loading rates which were 2, 4, 6, 10, 15 mm/min to research their effect on the tensile property indexes of GFRP bars.

In this paper, in order to study the effect of

*Corresponding author – email : wen1xue2@126.com

loading rates on the tensile property indexes of GFRP bars, four different loading rates were adopted, which were 2, 10, 20, 50 mm/min respectively.

2. EXPERIMENTAL PROGRAM

2.1 Experimental materials

The whole thread GFRP bars adopted in this paper are produced by Shandong Safety Industrial Co., Ltd., which have right-handed thread. The pitch of this GFRP bar is 10 mm, and the inner diameters as well as the outer diameter are 18 mm and 20 mm, respectively. The matrix material is unsaturated resin and the reinforcement is the ECR24-2400D-601 type glass fiber produced by Shandong Glass Fiber Composite Co., Ltd. The specifications of seamless steel pipe are: 38 mm in outer diameter, 6.5 mm in thickness, and 50 mm in length; the efficient silent broken agent is produced by Beijing Yuyi special cement plant and the recommended water cement ratio is 28%-35%; the type of strain gauge is BX120-5AA and the value of sensitivity coefficient K is 2.08.

2.2 Specimens preparation

Due to the low transverse strength of GFRP bar, if the clamping is directly carried out at the ends, it will be quickly crushed before the tensile failure occurs. In order to avoid this defect, both ends of GFRP bar are protected by the seamless steel pipes, and are bonded by the efficient silent broken agent, thus relying on the huge expansion pressure to provide axial shear stress.

ACI 440.1R-03 (ACI Committee 440, 2003a) and ACI 440.3R-04 (ACI Committee 440, 2004b) recommend that the effective tensile length should be no less than 40 times as long as the nominal diameter of the GFRP bar and should be no less than 100 mm. JG/T 351-2012 (MHURC of the PRC, 2008) also provides that the effective tensile length should be 400-600 mm. Due to the limitation of the maximum tensile space of WAW-600B type electro hydraulic servo universal testing machine used in this experiment, the specifications of specimens are made as follows: the full length is 600 mm, and the anchorage length at both ends is 200 mm, thus the rest effective tensile length is 200 mm. The schematic sketch of the specimen is shown in Figure 1.

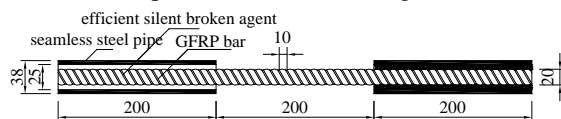


Figure 1: The schematic sketch of the specimen.

2.3 Experimental instruments

The instruments used in this experiment include

WAW-600B type electro hydraulic servo universal testing machine and XL2118C type stress-strain comprehensive parameter testing instrument, as shown in Figure 2.



Figure 2: WAW-600B type electro hydraulic servo universal testing machine and XL2118C type stress-strain comprehensive parameter testing instrument.

2.4 Experimental methods

The tensile experiments are conducted by utilizing WAW-600B type electro hydraulic servo universal testing machine with the displacement control method adopted and the loading rate were 2, 10, 20, 50 mm/min respectively. The tensile strain were recorded by XL2118C type stress-strain comprehensive parameter testing instrument with the quarter-bridge connection method used, and the strain gauge was attached to the middle area of the specimen.

3. EXPERIMENTAL RESULTS AND ANALYSES

The experimental results of tensile properties of GFRP bars at different loading rates are listed in Table 1.

3.1 The load-displacement curves and the stress-strain curves

The load-displacement curves and the stress-strain curves are shown in Figures 3 and 4, respectively. During the experiment, the strain gauges were destroyed due to the deformation of the specimen. As a result, the strain value in the second half of the tensile experiment process was not recorded.

As shown in Figure 3, there are platforms about 2 mm in the initial stage because there are minimal gaps between the clamps and the slots. If pre-loading is applied, then these platforms can be eliminated. It can be seen from Figure 4 that the stress-strain curves are consistent with the load-displacement curves in terms of the trends, which display a linear relationship.

3.2 Failure mechanism

During the experiments, there is no occurrence of anchorage failure, which indicates that this anchorage method is effective and reliable. The tensile failure

mode belongs to splitting failure. To be precise, the fiber split is evenly distributed throughout the entire scale of effective tensile length and it looks like a

lantern as the fibers are scattered after splitting. The splitting failure mode is shown in Figure 5.

Table 1: The experimental results of tensile properties of GFRP bars at different loading rates.

Specimen No.	Loading rate V(mm/min)	Ultimate load F_u (kN)		Ultimate strength σ_u (MPa)		Elastic modulus E(GPa)		Ultimate tensile strain ϵ_u (%)	
MGSL20-200F-1	2	150.88		480.5		31.0		1.55	
MGSL20-200F-2		157.06	154.18	500.2	491.0	27.6	29.5	1.81	1.67
MGSL20-200F-3		154.60		492.4		30.0		1.64	
MGSL20-200F-4	10	166.80		531.2		26.2		2.03	
MGSL20-200F-5		168.04	164.88	525.2	525.1	26.0	27.4	2.06	1.93
MGSL20-200F-6		159.80		509.0		29.9		1.70	
MGSL20-200F-7	20	160.54		511.3		25.7		1.99	
MGSL20-200F-8		170.92	165.30	544.3	526.4	27.8	27.8	1.96	1.90
MGSL20-200F-9		164.45		523.7		30.1		1.74	
MGSL20-200F-10	50	165.28		526.4		31.9		1.65	
MGSL20-200F-11		169.08	167.54	538.5	533.6	27.3	29.3	1.97	1.83
MGSL20-200F-12		168.26		535.9		28.8		1.86	

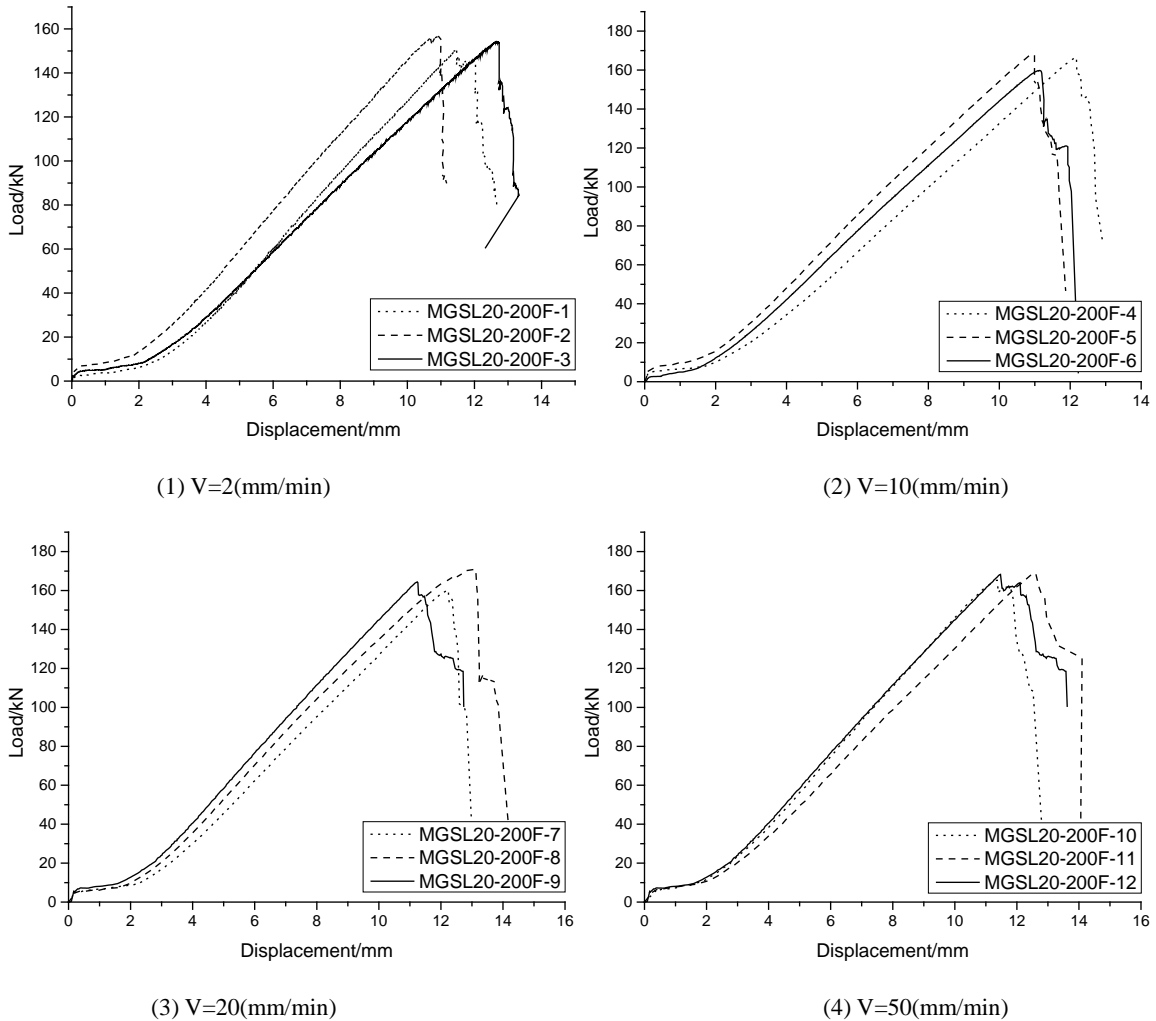


Figure 3: The load-displacement curves.

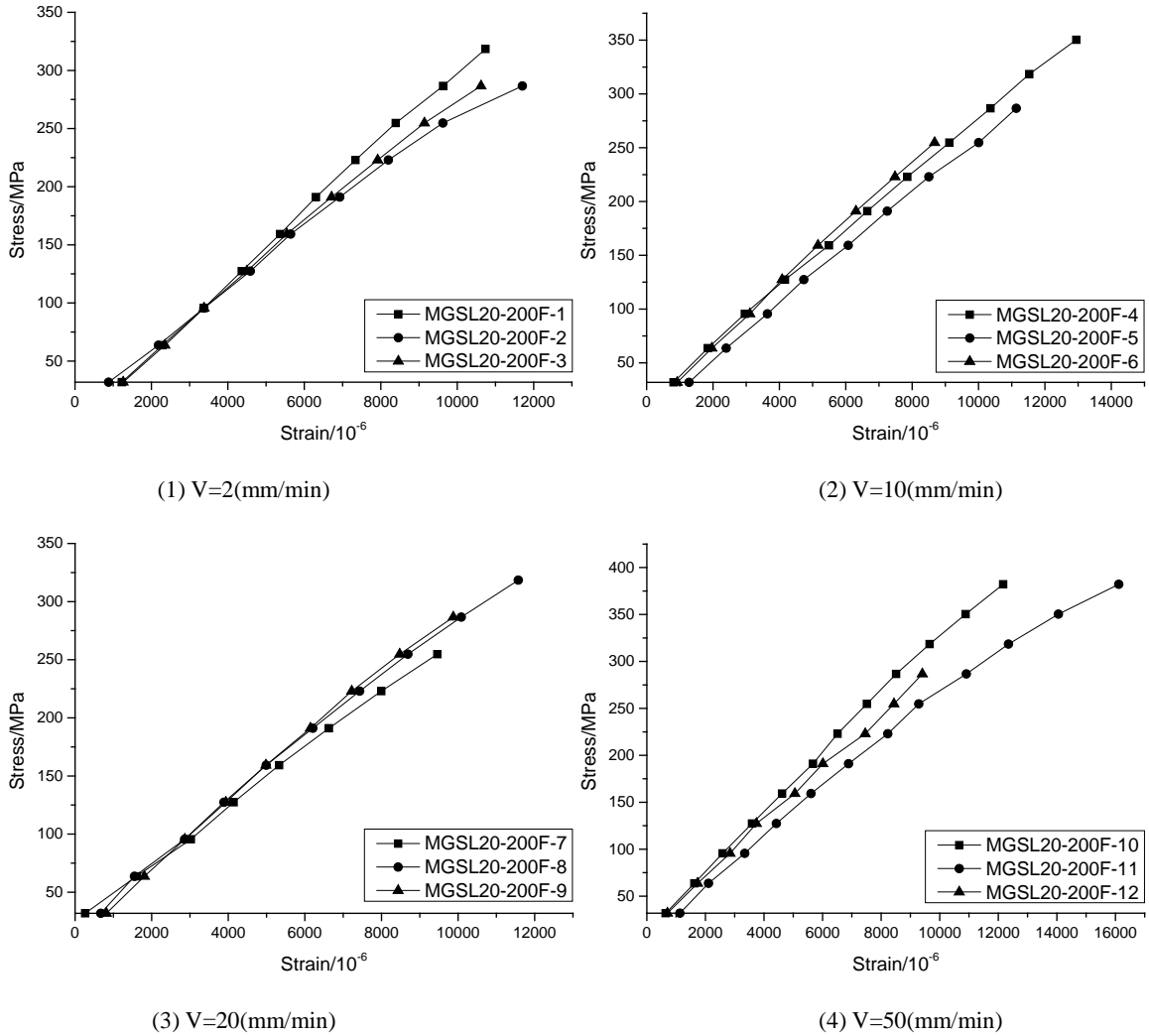


Figure 4: The stress-strain curves.



Figure 5: The splitting failure mode.

In the process of experiments, when the load is increased to about 45% of the ultimate load, the resin

and the fibers begin to split, accompanied by a clear and crisp sound. With the increase of the load, the splitting sound is continuous, and white cracks can be clearly seen on the splitting spot at the same time. When it nearer to the failure load, the splitting sound becomes louder and more concentrated, and the fibers are split from the outside layer to the inside layer. Finally, the specimen is damaged, accompanied with an abruptly loud sound.

Based on the analyses of experimental phenomena mentioned above, the tensile failure mechanism of GFRP bars can be interpreted as follows: in the loading process, the external fibers firstly bear the stress, and then the resin matrix transfers them to the internal fibers. Therefore, it is not uniformly and equivalently distributed on the cross section, but an inversely trapezoidal distribution that the stress gradually decreases from the circumference to the center. That is to say, with the increase of the stress, the external

fibers firstly reach the ultimate stress and fracture with the stress redistribution at the same time. As the stress continues to increase, the fibers fracture gradually from the external layer to the internal layer, and eventually the specimen is damaged. The failure mode belongs to brittle failure.

3.3 Ultimate strength

The ultimate strength of GFRP bars at different loading rates is shown in Table 1 and Figure 6.

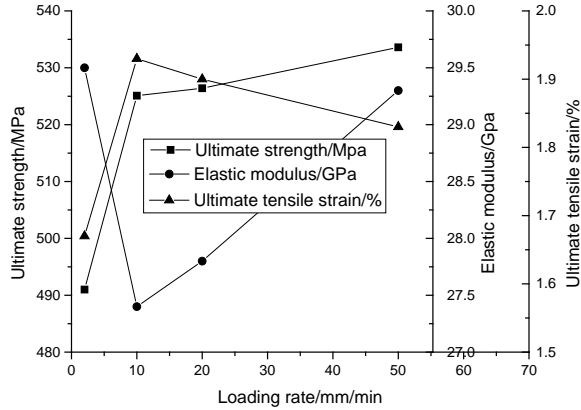


Figure 6: The trend graph of property indexes of GFRP bars.

As can be seen from Table 1, the ultimate strengths are 491, 525.1, 526.4, and 533.6 MPa when the loading rates are 2, 10, 20, 50 mm/min, respectively. Compared to loading rate of 2 mm, the ultimate strength at loading rates of 10, 20, and 50 mm/min increases by 6.9%, 7.2%, and 8.7%, respectively. When comparing the latter loading rate with the former one, the corresponding ultimate strength is increased by 6.9%, 0.3%, and 1.4%, respectively.

According to Figure 6, it is particularly noticeable that the ultimate strength sees a dramatically increasing trend between the loading rates of 2mm/min and 10 mm/min, and afterwards it grows upwards steadily. This is because the stress on the cross section of GFRP bar is an inversely trapezoidal distribution, which leads to the fact that the external fibers reach the ultimate stress and fracture before the internal fibers. When the loading rate is lower, there is enough time for the external fibers to reach the ultimate stress and fracture, which precedes the external fibers. Consequently, they are not fractured in the meanwhile so that the ultimate strength is lower. However, when the loading rate is higher, there is not enough time for the external fibers to precede the internal fibers, and they almost reach the ultimate stress and fracture at the same time, thus the ultimate strength is higher.

It is clear that the ultimate strength increases significantly when the loading rate of 2 mm/min changes into 10 mm/min and the increase is relatively

higher when the loading rate exceed 10 mm/min. Taking the above factors into consideration of engineering safety, a loading rate of 2 mm/min is recommended when conducting experiments to determine the tensile ultimate strength of GFRP bars.

3.4 Elastic modulus

Due to the instability of the strain values recorded by the instrument in the latter loading stage, the strain values in the former loading stage, which are relatively stable, are used to calculate the elastic modulus. The calculation formula is shown as follows:

$$E = \frac{F_1 - F_2}{(\varepsilon_1 - \varepsilon_2)A}$$

Where E is the elastic modulus of specimen, and the unit is GPa; A is the cross-sectional area of specimen, and the unit is mm^2 ; F_1, ε_1 are the load which is 20 kN and its corresponding strain, and the units are kN and dimensionless; F_2, ε_2 are the load which is 50 kN and its corresponding strain, and the units are kN and dimensionless.

As can be seen from Table 1 and Figure 6, all of the elastic moduli of the specimens range between 25.7 GPa and 31.9 GPa, and the average value is 28.5 GPa. When the loading rates are 2, 10, 20, and 50 mm/min, the average values of the elastic moduli are 29.5, 27.4, 27.8, and 29.3 GPa, respectively, and change by 3.5%, -3.9%, -2.5%, and 2.8%, respectively compared to the average value of 28.5 GPa. As the changes are small and there is no obvious regularity, it is believed that the loading rates have little effect on the elastic modulus.

3.5 Ultimate tensile strain

The calculation formula of the ultimate tensile strain is as follows:

$$\varepsilon_u = \frac{F_u}{EA}$$

Where ε_u is the ultimate tensile strain, and the unit is dimensionless. F_u is the ultimate load, and the unit is kN.

As can be seen from Table 1, when the loading rates are 2, 10, 20, and 50 mm/min, the average values of the ultimate tensile strain are 1.67%, 1.93%, 1.90%, and 1.83%, respectively. Compared to a loading rate of 2 mm, the ultimate tensile strain at loading rates of 10, 20, and 50 mm/min increases by 15.7%, 13.7%, and 9.6%, respectively. Comparing the latter loading rate with the former one, the corresponding ultimate tensile strain increases by 15.7%, -1.7%, and -3.6%, respectively.

Theoretically, as the elastic modulus is an intrinsic property of GFRP bar, the trend of the ultimate tensile strain should resemble the trend of the ultimate

strength with the increases in loading rate in Figure 6. In reality, this is not the case and they see an opposite trend after the loading rate of 10 mm/min. This non-conformity can be interpreted by the discreteness of the elastic moduli, which are obtained through calculation.

4. CONCLUSIONS

Based on the above experimental results and analyses, it can be concluded that:

With loading rate increases, the ultimate tensile strength and the ultimate tensile strain increase, while the elastic modulus remains almost constant with the average value at 28.5 GPa;

The failure mode of specimens belongs to splitting failure, and the fibers gradually fracture from the external layer to the internal layer.

The stress-strain curves show a linear relationship, which belongs to the scope of elastic deformation.

A loading rate of 2 mm/min or less is recommended when conducting experiments to determine the tensile property indexes of GFRP bars.

The anchorage method adopted in this paper is effective and reliable, but utilizing the strain gauges to record the strain values should be improved, and an extensometer is recommended.

5. REFERENCES

ACI Committee 440. (2003a). ACI 440.1R-03. Guide for the Design and Construction of Concrete Reinforced with FRP Bars. American Concrete Institute, Farmington Hills

ACI Committee 440. (2004b). ACI 440.3R-04. Guide Test Methods for Fiber-Reinforced Polymers (FRPs) for Reinforcing Or Strengthening Concrete Structures. American Concrete Institute, Farmington Hills

American Society Testing and Materials. (2002). ASTM D 3916. Standard test method for tensile properties of pultruded glass-fiber-reinforced plastic rods

Benmokrane, B., Zhang, B., Chennouf. A. (2000). Tensile properties and pullout behavior of AFRP and CFRP rods for grouted anchor applications. *Construction and Building Materials*, No. 14, pp. 157-170

Chen, J., Huang, J., Chen. Q. (2012). Test research on tensile mechanical properties of GFRP rebar. *Building science*. Volume 28, No. 7, pp. 43-46

General Administration of Quality Supervision, Inspection and Quarantine of the People's Republic of China, Standardization Management Committee of the People's Republic of China. (2005a). GB/T 1447-2005. Fiber-reinforced plastics composites-Determination of tensile properties. Standards Press of China, Beijing

General Administration of Quality Supervision, Inspection and Quarantine of the People's Republic of China, Standardization Management Committee of the People's Republic of China. (2008b). GB/T 13096-2008. Test method for mechanical properties of pultruded glass fiber reinforced plastic rods. Standards Press of China, Beijing

Kim, H.Y., Park, Y.H., You, Y.J., Moon, C.K. (2015). Short-term durability test for GFRP rods under various environmental conditions. *Composite Structures*, No. 83, pp. 37-47

Kocaoza, S. Samaranayake, V. A., Nanni, A. (2005). Tensile characterization of glass FRP bars. *Composites*, No. 36, pp. 127-134

Li, G., Ge, G., Ni, C., Dai, J., Mu, C. (2012). Effect of loading rate on tensile properties of full-scale specimen of large-diameter glass fiber reinforced polymer(GFRP) bar. *Rock mechanics and engineering*, Volume 31, No. 7, pp. 1469-1477

Liu D., Zhou J. (2014). Discussion on the application of fiber reinforced plastics bars in Civil Engineering. *Engineering Technology*. DOI:10.13751/j.cnki.kjyqy.2014.07.195

Micelli, F., Nanni, A., Chen, S. (2004). Durability of FRP rods for concrete structures. *Construction and Building Materials*, No. 18, pp. 491-503

Ministry of Housing and Urban-Rural Construction of the People's Republic of China. (2012). JG/T 351-2012. Fiber reinforced composite bars. Standards Press of China, Beijing

State Administration of Work Safety. (2008). MT/T 1061-2008. Fiber-glass reinforced plastics bar of bolt and accessories. The Coal Industry Press, Beijing

Uomoto T., Nishimura T. (1995). Static and fatigue strength of FRP rods for concrete reinforcement. In: *Non-Metallic (FRP) Reinforcement for Concrete Structures - Proceedings of the Second International RILEM Symposium*, L. Taerwe. (eds.), CRC Press, pp. 100-107

You, Y.J., Park, Y.H., Kim, H.Y., Park, J.S. (2007). Hybrid effect on tensile properties of FRP rods with various material compositions. *Composite Structures*, No. 80, pp. 117-122

Zhang, X., Ou, J., Wang, B., He, Z. (2005). Comparison experimental study on mechanical property of different GFRP bars. *Fiber Reinforced Plastics/Composites*, No. 2, pp. 9-25

Zhou, J., Du, Q., Chen, L., Ma, X. (2008). Experimental study on size effect in tensile mechanical properties of GFRP rebar. *Journal of Hohai University*, Volume 36, No. 2, pp. 242-246

Part 2

Technology

A definition and evaluation index system of aging mines

MA Hu i^a, LIAN Huiqing^a, ZHU Hongjie^b

^a Safety Engineering College, North China Institute of Science and Technology, City, Beijing, China ,101601

^b China Shenhua International Engineering Co., Ltd, Beijing, China,100007

ABSTRACT

Because of the limited storage of coal resources, coal production progresses from growth to decline until eventual mine closure. At present, aging mines have no clear name, conception, defined definition, and complete system. Based on the analysis of the mine life cycle and the problems associated with mine development and conceptions in the past, this paper aims to construct an evaluating index system of decrepit mines and define the index of weight layer by application of the analytic hierarchy process (AHP), so as to provide a basis for development planning of mine enterprises, and law-making for resource-based cities and countries.

KEYWORDS: aging mines; define; evaluation index system

1. THE LIFE CYCLE OF A MINE

Due to the fact that mineral resources are finite and non-renewable, mining enterprises trend from birth to death and prosperity to decline, just like organisms. The whole process of mine production and the service cycle must go from exploration, building a well, putting into production, stable industry, aging, and finally being shut down. This is called the life cycle of a mine.

According to "The economic structure transformation of resources city", the statistics from August 2003 by the national development and reform commission, there are altogether 118 resource-based cities in China, including 63 coal cities, 12 non-ferrous metal cities, 8 ferrous metallurgy cities, 9 oil cities, and 5 other cities. These account for about 18% of the number of cities around the country and a total population of 154 million people. China has determined 69 resource-exhausted cities (counties and districts). As of the middle of the 20th century, two-thirds of state-owned mines have entered the aging stage and 440 mines will be closed. 50 resource cities are experiencing resource failure in a total of 390 mines. 3 million workers have been laid-off and 10 million families' lives have been affected.

The definition of aging mines and determination of an evaluation index system is very important due to the complexity of the work of aging mines closed underground material recycling equipment, the shunt placement of mine workers, and the processing and handling of history of creditor's rights debt.

The definition and evaluation index system of aging mines is basic research which includes evaluation theory, research methods, index systems, and a classification scheme. At present, aging mines

are short of a scientific definition, complete statistical analysis conclusions and comprehensive research. This has adverse effects on the development of large coal mining enterprises and the decisions of government developing. At the microscopic level the definition and evaluation index system of aging mines can make sure the limited storage characteristics of coal resources are considered in advance. The index can choose the important point and analyze the enterprise development strategy and change into the developing period from the senescence phase, avoid influence on layoffs, cut down the number of persons employed and upper and lower relation in coal mining enterprises. At the macroscopic scale, the index system of aging mines can help to more easily determine the weight index for local government rewards for mining enterprises in provinces. Based on the above reasons, it also provides theoretical support and practical suggestions for macroscopic development strategy, medium-long term plan policies and regulations for local government.

2. DEFINITION OF AGING MINES

The definition of aging mines is a complex problem. Previous scholars have studied resource depletion, but face closed mine appellation is different. Common appellations are old mining, aging depleted mines, resource crisis mines, old mines, middle-late mines and crisis mines, and so on. The definition of aging mines also has different points of view, as follows.

(1) Some people like Lu Guxian believe that resources crisis mines are due to a shortage for mineral resources in the mining areas, the drying up of the recoverable reserves, or due to the change of

market conditions of the commodity price fluctuations, changes in supply and demand so that the economical development and utilization of its reserves of mineral resources are difficult to continue. This leads to the decline of mine production, significant excess production capacity, and deterioration of operating conditions. Therefore in the present or the future there is a certain period of time where it is difficult to maintain normal production and business operation and facing closure or bankruptcy of mining enterprises.

(2) Jia Yanjie thinks that aging mines mainly have the following signs: consumption of mining reserves more than two-thirds of the mine recoverable reserves; the residual service life of mine is less than 10; the number of tons of coal reaches to 3 people which 1 time more than the period of development and stability; the tons of coal to investment is 80 yuan, more than 60% higher than the stable stage; the mine production has begun to decline and the Nissan's level has dropped for stability and design ability.

(3) Li Qing and Li Kerong point out the quantitative standard of the coal enterprises in different stages of the life cycle. We can judge it from the mining coefficient of fixed number of years and the mining ability structure coefficient. The so called mining coefficient of fixed number of years is judged mainly from the main business continued ability in the future of coal mining, total reserves, and the perspective of overall production capacity in the future.

(4) On the basis of investigation and research, the original state coal industry bureau made the standard for coal mine resource depletion, and high ash and sulfur turn around. It believes that one of the following two conditions must be met in order to be considered an aging or resource depleted mine. Based on the 1991 No. 211 document on May 13 of the original coal, the mine can adopt reserves to reduce, without augmenting resources at depths and peripheries, with remaining recoverable reserves of around 20% for the original design. According to the actual recoverable reserves, mine design capability must consider the reserve coefficient calculation of residual service life of coal mine of no more than 5 per mine.

(5) In the study of coal aging scrap best point, some people like Huang Shude analyzed the different well types, at different fixed number of years of the production and development trend of production under conditions of mine production and operation and put forward the mine into the aging point judgment index system.

(6) On the basis of the name of mine and its basic concepts, Lu Gang unified the designation of

aging mines, defined the concept of aging mines, and pointed out that the aging of mines is to point to recoverable resources drying up, basic coal production capacity experiencing a sharp drop in production, and difficulty maintaining normal production and operation of the mine.

In conclusion, many scholars concentrated on the remaining recoverable reserves, residual length of service, production capacity, tons of coal cost, etc. These scholars did not consider enterprise economic benefits (especially not the income of coal industry to GDP), the degree of deep and peripheral resources available, recycling feasible extent of loss of resources, resources recycling feasible degree, national policies, and regulations compliance and safety. Based on this analysis, the current study puts forward the idea that the aging mine is one that experiences a production plateau, economic downturn, the remaining resources occurrence condition deteriorates, cannot meet the normal mining economic and technological conditions, tons of coal cost, production capacity and the status of the mine is not in conformity with the provisions of the state.

3. CONSTRUCTION EVALUATION INDEX SYSTEM OF AGING MINES

3.1 Evaluation Index System of Aging Mines

According the characteristics of aging mines and the principle of index system construction and introduction the meaning of evaluation index should be settled. The principles of the index system include the objectivity, system, comparability, feasibility, and dynamic.

Table 1: Evaluation index system of aging mines.

Object hierarchy	Rule hierarchy	Indicator layer
Mine grew into senescence phase	Mine economic efficiency(A)	Sales profit ratio(A1)
		Asset-liability ratio(A2)
		Non-Coal Industry income ratio (A3)
	living condition of mineral resources (quality and quantity) (B)	The residual service life for mine (B1)
		Reserve-production ratio decrease rate (B2)
		The utilization degree of deep department and outer resources (B3)
	Economy technology condition (C)	The economic and reasonable mining depth (C1)
		Feasibility of resources loss recycled (C2)
		Feasibility of resource reutilization(C3)

	the ton coal synthesizes cost (D)	The per ton coal employees (D1)
		The per ton coal funds input (D2)
productivity and safe condition(E)		Whether match national laws and regulations (E1)
		Megaton coal mortality (E2)
		Safety investment cost rate (E3)
The social responsibilities performance condition (F)		The social contribution rate (F1)
		Capita income of employee(F2)
		The total tax (F3)

3.2 The assurance of weight of index evaluation index

The layer analytical (AHP) was put forward in the 20th century by a teacher, T.L. Saaty at the American Pittsburgh University. It is a kind of system analysis method that combines fixed amount and quality together and imitates the person's decision thinking process. It is used to solve complicated systems with many factors, especially hard fixed amounts of the analytical method of social systems. AHP belongs to the index sign comparison method, and it can judge with the consistency examination to check whether the related index sign importance has a logic mistake. It gets rid of artificial understanding of limits from a person to a great extent, so it can be extensively applied in each professional field. This text applied layer analytical method assurance the decrepitude mineral well all levels index sign weight of index. The layer analyzes the foundation theory of methods.

(1) Aiming at rule hierarchy weight of index with the AHP method, calculating results are shown in Table 2.

Table 2: Weight of rule hierarchy index.

T	A	B	C	D	E	F	weight of index
A	1	2	3	4	5	6	0.373
B	1/2	1	2	3	4	5	0.252
C	1/3	1/2	1	2	3	4	0.160
D	1/4	1/3	1/2	1	2	3	0.101
E	1/5	1/4	1/3	1/2	1	2	0.064
F	1/6	1/5	1/4	1/3	1/2	1	0.043

Calculating processes are as following:

Firstly, number out each element's product in a judgment matrix, it accumulates: M 1=720; M 2=60; M 3=4;M 4=0.25; M 5=0.0167; M 6=0.00139;

Secondly, computes Mi of 6 \bar{W}_i ; $\bar{W}_1 = 2.934$; $\bar{W}_2 = 1.979$; $\bar{W}_3 = 1.260$; $\bar{W}_4 = 0.794$; $\bar{W}_5 = 0.505$;

$$\bar{W}_6 = 0.334$$

Thirdly, carry on unitary processing or regular processing to $P = (\bar{W}_1, \bar{W}_2, \bar{W}_3, \bar{W}_4, \bar{W}_5, \bar{W}_6)$; that is

$$W_i = \frac{W_i}{\sum_{i=1}^6 W_i}$$

$$W_1=0.373 \quad W_2=0.2518 \quad W_3=0.160 \quad W_4=0.1014 \quad W_5=0.0642 \quad W_6=0.0425$$

Fourth, the above characteristic vector is the power begged while it still needs to carry on consistency examination towards the judging matrix:

① Compute the biggest characteristic value of

$$\lambda_{\max} = \sum_{i=1}^6 (PW)_i / nW_i = 1/n \sum_{i=1}^6 (PW)_i / W_i$$

②The consistency examines;

$$C_R = C_I / R_I ; \quad C_I = (\lambda_{\max} - n) / (n - 1)$$

if n=6 , $R_I = 1.24$, $\lambda_{\max} = 6.12$, $C_R = 0.0199 < 0.1$,the consistency examination passes.

(2) Compute an index sign layer index sign power with reason respectively heavy, as Tables 3-8 show.

1) According to Mine economic efficiency (A1), asset-liability ratio (A2), the non-Coal Industry income ratio (A3) influence toward mine economic efficiency degree is different, calculating the power of each index sign heavy, as Table 3 shows.

Table 3: Weight of mine economic efficiency index.

A	A1	A2	A3	weight of index
A1	1	2	3	0.540
A2	1/2	1	2	0.297
A3	1/3	1/2	1	0.163

2) According to the residual service life for mine (B1), tReserve-production ratio decrease rate (B2), the utilization degree of deep department and outer resources (B3) to measure the degree of different by mineral well resources endow to a condition, compute index weight of index..

Table 4: Weight of resources reserves index.

B	B1	B2	B3	weight of index
B1	1	1/2	2	0.297
B2	2	1	3	0.540
B3	1/2	1/3	1	0.163

3) The economic and reasonable mining depth (C1), study on the feasibility of resources loss recycled (C2), study on the feasibility of resource reutilization (C3), measurement for mineral well economic technique conditional of the important degree is different, to draw out each index sign

weight of index, as shown in Table 5.

Table 5: Weight of economic technique condition index.

C	C1	C2	C3	weight of index
C1	1	2	3	0.540
C2	1/2	1	2	0.297
C3	1/3	1/2	1	0.163

4) The per ton coal funds input (D2) and the per ton coal employees (D1) to the ton coal cost is different which gets the conclusion of an each index sign of weight of index.

Table 6: Weight of ton coal comprehensive cost index.

D	D1	D2	weight of index
D1	1	3	0.75
D2	1/3	1	0.25

5) Whether match national laws and regulations (E1), Megaton coal mortality (E2), safety investment cost rate (E3), these three factor's influence on the productivity and safety condition is different. Compare the matrix and weight of index as Table 7 shows.

Table 7: Weight of productivities and safe condition index.

E	E1	E2	E3	weight of index
E1	1	2	3	0.540
E2	1/2	1	2	0.297
E3	1/3	1/2	1	0.163

6) The social contribution rate (F1) and capita income of employee (F2), total tax amount (F3) three second class index signs towards measuring the importance that the Corporate Social Responsibility implements condition is different to get the comparing matrix and weight of index, as in Table 8.

Table 8: Weight of social responsibilities implement condition index.

F	F1	F2	F3	weight of index
F1	1	1/2	2	0.297
F2	2	1	3	0.540
F3	1/2	1/3	1	0.163

According to the above analysis calculation, we can get a decrepitude mineral well evaluation index sign weight of index, as Table 9 shows.

Table 9: Decreptitude mineral well evaluation index system.

Name of Standard layer index	Weight of index	Index sign layer inde name	Weight of index
Mine economic efficiency (A)	0.373	Sales profit ratio (A1)	0.540
		Asset-liability ratio(A2)	0.297
		Non-Coal Industry income ratio(A3)	0.163
living condition of mineral resources (B)	0.252	The residual service life for mine (B1)	0.297
		Reserve-production ratio decrease rate (B2)	0.540
		The utilization degree of deep department and outer resources(B3)	0.163
Economy technology condition (C)	0.160	The economic and reasonable mining depth (C1)	0.540
		Study on the Feasibility of resources loss recycled (C2)	0.297
		Study on the Feasibility of resource reutilization (C3)	0.163
the ton coal synthesizes cost (D)	0.101	The per ton coal employees (D1)	0.75
		The per ton coal funds input (D2)	0.25
productivity and safe condition (E)	0.064	Whether match national laws and regulations (E1)	0.540
		Megaton coal mortality (E2)	0.297
		Safety investment cost rate (E3)	0.163
The social responsibilities performance condition (F)	0.043	The social contribution rate (F1)	0.297
		Capita income of employee (F2)	0.540
		The total tax (F3)	0.163

Making use of the layer of this text introduction analysis method to draw out the power of each evaluation of index sign can provide a theoretical foundation to see whether the mineral well gets into a decrepitude period, from the decrepitude mineral well evaluated index sign of system index sign analysis, mine economic efficiency A, living condition of mineral resources B, and economic technique condition C takes the most space. Sales profit ratio

A1, reserve-production ratio decrease rate B2, and the economic and reasonable mining depth C1, again occupy an important position in this layer. The index signs of national laws and regulations E1 and capita income of employee F2 should also be considered.

4. CONCLUSION

The main conclusions from the analysis of the conception of the decrepitude mineral well and the decrepitude mineral well definition index system are as follows:

On the foundation of the analytical mineral well life cycle and the decrepitude mineral well conception, we analyzed the existing concepts of shortage and put forward a new decrepitude mineral well conception, namely that a decrepitude mineral well occurs after the mineral well's steady production period, the surplus resources endows with a claim check piece depravation because the economic efficiency falls, the economic technique condition can not satisfy the mine, the ton coal cost significantly increases, and the productivity and safe condition do not satisfy the nation's rules.

(2)Owing to the foundational research on the resource potential of the decrepitude mineral wells and the definition of the decrepitude degree, evaluation theory, research on method, index sign system and classification project, the decrepitude mineral well lacks a scientific definition, integrity statistics, analysis and comprehensive study, and a decrepitude mineral well evaluation index system.

Following the principles of objectivity, system and comparison, possibility and dynamic state were used to set up a decrepitude mineral well evaluation index sign system. Mineral mountain economic efficiency's standard layer index sign is 7, and the sell profit margin index sign layer is 17.

The layer analysis method was applied to assure all levels index sign power in decrepitude mineral well evaluation. This provides a basis for making development programming of mineral mountain enterprises from both the micro view and the macro view for resource cities and nation's farsighted development and law establishment.

5. ACKNOWLEDGEMENT

I'd like to express my sincere thanks to all people helped me, especially Mrs LIAN Huiqing, Mr ZHU Hongjie, Miss Dong Lili and Miss Pei Ying, always support and encourage me in the process of paper writing.

The paper is supported by The central university basic scientific research business expenses (3142014021).

6. REFERENCES

- GUO Yuhong. Characteristics of input and output and economic evaluation method of aging mine [J].Coal Economic Research.1990(11):39-41
- HUANG Shude, GAO Yongju, ZHENG Guanghua. Research of best point of scrap in aging coal mine [J]. Journal of Henan Polytechnic University(Natural Science). 1993, 34 (5): 28- 29
- LU Gang, CHENG Wei , HAN Keqi. Simulation study on the life cycle identification of the aged coal mine and mine[J]. Journal of Henan Polytechnic University (Natural Science Edition) .2009,28 (5) :659~694
- LU Gang.Research on Residual Coal Workability Evaluation and Remining Technology of Aged Coal mine[D] China University of Mining and Technology,2010
- MA Hui, LIAN Huiqing, ZHU Hongjie. SWOT analysis of aging mines' low carbon development[J]. The 2nd International Symposium on Mine Safety Science and Engineering. 2013,259-261
- REN Yixin, HAN Gang, DING Ru, WANG Ning. Construction of circular economy mode of old coal mine. Mining and Metallurgical Engineering, 2008,28 (4) :108~113
- WANG Chun, WANG Baicheng. Research and practice of old coal mine mining technology[J]. Coal Technology,2006,25(2):48~50
- WEI Guangxing. Summary and remarks of enterprise life cycle theory [J].Productivity Research. 2005,(6):52-53

Numerical simulation of thermodynamic performance in a honeycomb ceramic channel

Bo Lan ^{a,b,*}, You-Rong Li ^a

^a Key Laboratory of Low-Grade Energy Utilization Technologies and Systems of Ministry of Education, College of Power Engineering, Chongqing University, Chongqing, China, 400044

^b China Coal Technology Engineering Group Chongqing Research Institute, Chongqing, China, 400037

ABSTRACT

In order to understand the thermodynamic performance in a honeycomb ceramic channel, a 3D numerical simulation was carried out using FLUENT. The effects of mass flow rate, solid heat capacity, and reversal time on temperature efficiency were investigated. Results show that with the increasing mass flow rate, the temperature efficiency decreases linearly and the pressure drop increases linearly in each half-cycle. For computed cases the effect of solid heat capacity on the temperature efficiency is negligible. With the increasing reversal time, the temperature efficiency decreases slowly in the bed heated period, and is not influenced in the bed cooled period.

KEYWORDS: numerical simulation; honeycomb ceramic channel; thermodynamic performance; temperature efficiency

1. INTRODUCTION

Methane (CH₄) is a greenhouse gas (GHG) that is 21 times more potent than carbon dioxide (CO₂) in terms of trapping heat in the atmosphere over a timeframe of 100 years (Gosiewski et al., 2008). Ventilation air methane (VAM) emitted from underground coal mines constitutes a major part of greenhouse gas emissions from coal mining and is a wasted resource. The utilization methods of VAM have been studied extensively in recent years (Su et al., 2005; Su et al., 2006; Yin et al., 2010; Karacan et al., 2011; Baris, 2013; Krzysztof et al., 2014; Martinez et al., 2014; Zhang et al., 2014).

The utilization methods can be divide into ancillary use and principle use (Su et al., 2005). For the ancillary use, VAM is used to substitute ambient air in combustion processes, including gas turbines, internal combustion engines, and coal-fired power stations. For the principle use, the methane in VAM is used as a primary energy source.

Nowadays, only the thermal flow-reversal reactor (TFRR) and catalytic flow-reversal reactor (CFRR) are seriously taken into account for industrial usage. The only difference between these two devices is with respect to the use of catalyst. Honeycomb ceramic is the most important component of TFRR and CFRR. However, the thermodynamic characteristics of honeycomb ceramic channel have not been clearly studied.

The aim of this study is to investigate the temperature migration rule in honeycomb ceramic beds, and examine the effects of mass flow rate, solid

heat capacity, and reversal time on temperature efficiency.

2. PHYSICAL AND MATHEMATICAL MODEL

2.1 Physical model

There are millions of honeycomb ceramic channels in a regenerative oxidation bed. The flow and thermal performance of each honeycomb ceramic channel is similar to the others.

The geometry of a single honeycomb ceramic channel and the coordinate system is shown in Figure 1. The channel size is 3 mm × 3 mm and the wall thickness is 0.7 mm. The length is 300 mm.

One heat exchange cycle is comprised of two flow reversals, so each flow reversal is a half-cycle. During the first half-cycle, hot gas enters from the right and leaves through the left. The bed is heated and the fluid is cooled down. This half-cycle is called the bed heated period. After a time interval the flow direction is reversed. Cold VAM enters from the left and leaves through the right. The bed is cooled down and the VAM is heated. This half-cycle is called the bed cooled period.

* Corresponding author – email: lbmky@163.com

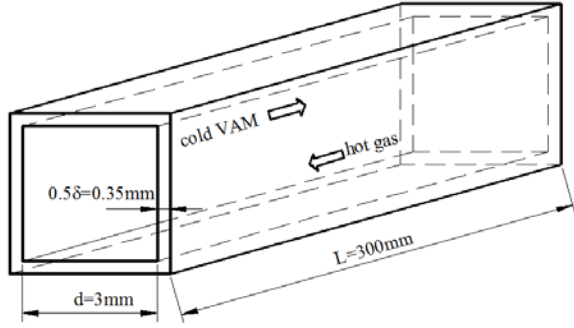


Figure 1: Physical model.

2.2 Governing equations

The honeycomb ceramic channel has a three-dimensional unsteady flow. There are three different heat transfer processes: heat conduction process inside the fluid, heat convection between the solid and fluid, and heat conduction inside the solid.

The following assumptions are introduced in the present model: (1) radiative heat transfer is neglected because air, oxygen, and nitrogen are not able to emit and absorb radiation energy; (2) the heat dissipation on the outer wall of the channel is neglected; (3) the air physical parameters are applied for VAM and hot fluid; (4) methane oxidation generally occurs in the combustion chamber, rather than in the honeycomb ceramic channel, and this paper focuses on the heat transfer law in the honeycomb ceramic channel, ignoring the effect of methane oxidation.

With the above assumptions, the governing equations of flow and heat transfer could be expressed as follows:

Continuity equation

$$\frac{\partial \rho}{\partial t} + \nabla \cdot (\rho U) = 0 \quad (1)$$

where ρ , t , U are the fluid density, time, velocity, respectively.

Momentum equation

$$\frac{\partial (\rho U)}{\partial t} + U \cdot \nabla (\rho U) = -\nabla p + \mu \nabla^2 U + S \quad (2)$$

where p , μ , S are pressure, the fluid dynamic viscosity, source term, respectively.

Fluid energy equation

$$\frac{\partial (\rho T)}{\partial t} + \nabla \cdot (\rho U T) = \nabla \cdot \left(\frac{\lambda}{c_p} \nabla T \right) + \Phi \quad (3)$$

where T , λ , c_p , Φ are temperature, the fluid conductivity, the fluid specific heat, dissipative function, respectively.

State equation

$$p = \rho R_g T \quad (4)$$

where R_g is the gas constant.

Solid energy equation

$$\frac{\partial (\rho_s T)}{\partial t} = \nabla \cdot \left(\frac{\lambda_s}{c_{ps}} \nabla T \right) \quad (5)$$

where ρ_s , λ_s , c_{ps} are the solid density, conductivity, specific heat, respectively.

2.3 Physical parameters of fluid and solid

The physical parameters of fluid are listed in Table 1.

Table 1 :The physical parameters of fluid.

Items	Unit	Value			
		273 K	473 K	773 K	1173 K
ρ	kg/m ³	1.293	0.746	0.456	0.301
C_p	J/(kg·K)	1005	1026	1093	1172
λ	10 ⁻² W/(m·K)	2.44	3.93	5.74	7.63
μ	10 ⁻⁶ kg/(m·K)	16.7	26	36.2	46.7

The physical parameters of solid are defined as follows:

$$\rho_s = 2500 \quad \text{kg/m}^3 \quad (6)$$

$$\lambda_s = 0.000666T + 1.305 \quad \text{W/(m·K)} \quad (7)$$

$$C_{ps} = 0.23T + C_{ps0} \quad \text{J/(kg·K)} \quad (8)$$

where C_{ps0} is a parameter determined by the solid material.

2.4 Boundary conditions

A symmetrical boundary condition is applied for the outer walls of the honeycomb ceramic ($x=0\text{mm}$, $x=3.7\text{mm}$, $y=0\text{mm}$, $y=3.7\text{mm}$), and adiabatic boundary condition for the front and back wall ($z=0\text{mm}$, $z=300\text{mm}$). A coupled boundary condition is used for the inner walls of the honeycomb ceramic channel.

Mass-flow-inlet boundary condition is applied for the inlet, and pressure-outlet boundary condition for the outlet. The inlet temperatures of hot and cold fluid are constant and equal to 1173 K and 293 K, respectively.

2.5 Numerical methods

The model is solved by FLUNET. The governing equations are discretized by the finite difference method. The central difference approximation is applied for the diffusion terms and the second order of upwind scheme is used for the convection terms.

The SIMPLEC algorithm is applied to couple the pressure and velocity variables.

In order to check the validation of this model, a simulation is carried out under the same conditions with the case carried out by (Zhang et al., 2010). In the case, The channel size is 3 mm × 3 mm, the wall thickness is 1 mm, and the length is 100 mm. The obtained pressure drop is 15.7 Pa with inlet velocity of 2 m/s, which is comparable with the result of 15 Pa carried out by Zhang (2010).

Table 2: The seven cases (A-G) computed in this work.

Items	Unit	A	B	C	D	E	F	G
C_{ps0}	J/kg·K	907	907	907	750	1050	907	907
Q_m	kg/s	1×10^{-5}	1.5×10^{-5}	2×10^{-5}	1×10^{-5}	1×10^{-5}	1×10^{-5}	1×10^{-5}
t_r	s	30	30	30	30	30	15	45

3.1 Thermodynamic performance in the honeycomb ceramic channel

In the bed heated period the hot fluid temperature (T_h) is higher than the solid temperature (T_s), and heat transfers from the hot fluid to the solid. As time goes by, the solid temperature increases gradually. The solid temperature profile along the flow direction moves upward, as shown in Figure 2. It leads to a reduction of the temperature difference between the fluid and solid. The heat storage capacity of the solid reduces and the fluid outlet temperature increases. As a result, the fluid temperature distribution moves upward over time. The temperature change rates of the hot fluid and solid are -1.83 K/s and 2.14 K/s, respectively.

In the bed cooled period the rules are reversed. Due to the lower cold fluid temperature (T_c), heat transfers from the solid to the fluid. The temperature distribution of the cold fluid and solid along the flow direction moves down over time, as shown in Figure 3. The temperature change rates of the cold fluid and solid are 1.77 K/s and -2.12 K/s, respectively.

Logarithmic mean temperature differences between the fluid and solid decrease over time in each half-cycle, as shown in Figure 4. Meanwhile the heat flux on the inner walls of the channel decreases linearly, and the heat transfer capability deteriorates, as shown in Figure 5.

3.2 Effect of mass flow rate

In order to evaluate the heat exchange performance of the honeycomb ceramic channel, the temperature efficiency is defined as follows:

The temperature efficiency in bed heated period

3. RESULTS AND DISCUSSION

A 3D numerical simulation is carried out to investigate the thermodynamic performance by varying mass flow rate, solid heat capacity, and reversal time. In this work seven cases are computed, as shown in Table 2. The mass flow rate and reversal time are represented as Q_m and t_r , respectively.

$$\varepsilon_h = \frac{T_{h,i} - \bar{T}_{h,o}}{T_{h,i} - T_{c,i}} \quad (9)$$

where $T_{h,i}$ and $\bar{T}_{h,o}$ are the inlet and average outlet temperatures of the hot fluid, respectively, and $T_{c,i}$ is the inlet temperature of the cold fluid.

The temperature efficiency in bed cooled period

$$\varepsilon_c = \frac{\bar{T}_{c,o} - T_{c,i}}{T_{h,i} - T_{c,i}} \quad (10)$$

where $\bar{T}_{c,o}$ is the average outlet temperature of the cold fluid.

Figure 6 shows the effect of mass flow rate on the temperature efficiency. In the bed heated period, the temperature efficiency decreases linearly with the increase in mass flow rate. The reason is that more heat is intaken by a higher mass flow rate, and the solid cannot fully absorb the increasing heat, and more heat is carried out by the hot fluid. In the bed cooled period, the temperature efficiency also decreases with the increasing mass flow rate.

Figure 7 shows that the pressure drops are increasing with the increase in mass flow rate in each half-cycle. With the same mass flow rate, the pressure drop in the bed heated period is higher than that in the bed cooled period.

The above results indicate that reducing mass flow rate is positive for improving temperature efficiency and reducing pressure drop.

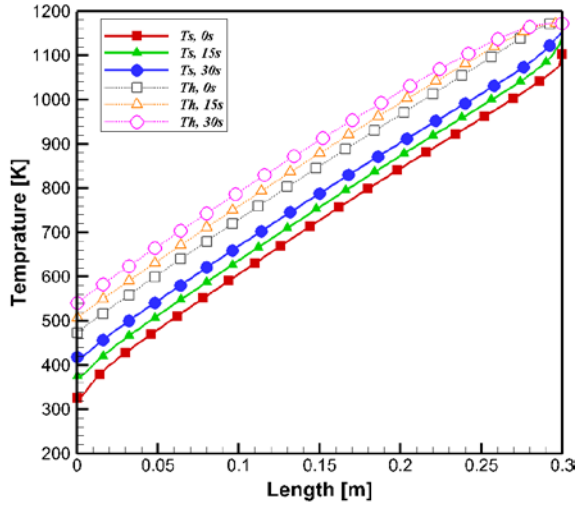


Figure 2: Temperature distributions of the hot fluid and solid along flow direction in bed heated period for case A.

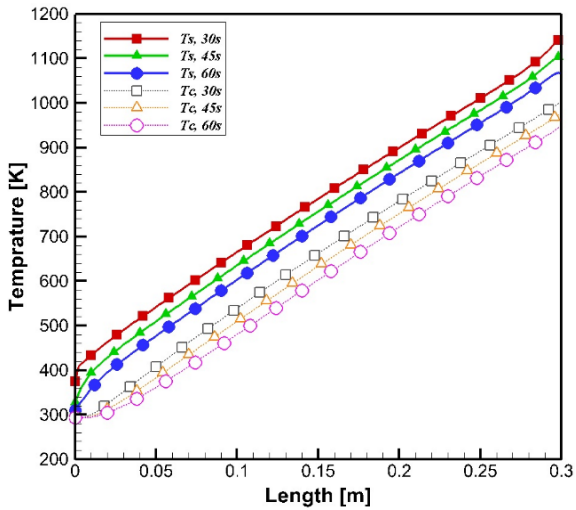


Figure 3: Temperature distributions of the cold fluid and solid along flow direction in bed cooled period for case A.

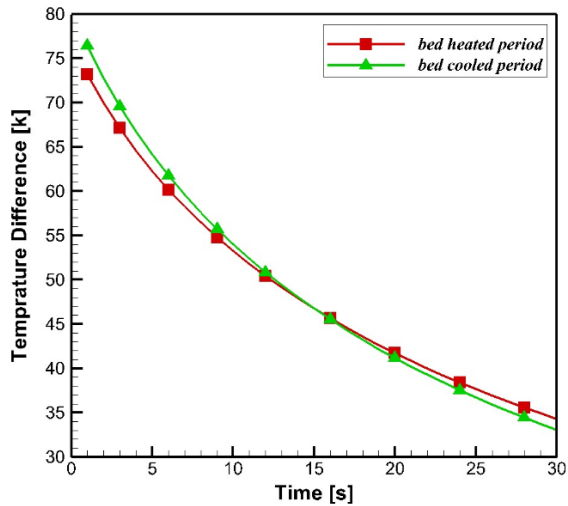


Figure 4 :Variation of logarithmic mean temperature difference between the fluid and solid in one heat exchange cycle for case A

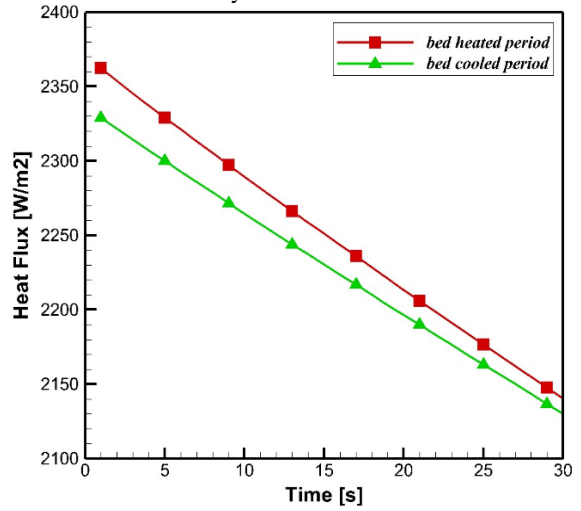


Figure 5: Variation of heat flux in one heat exchange cycle for case A.

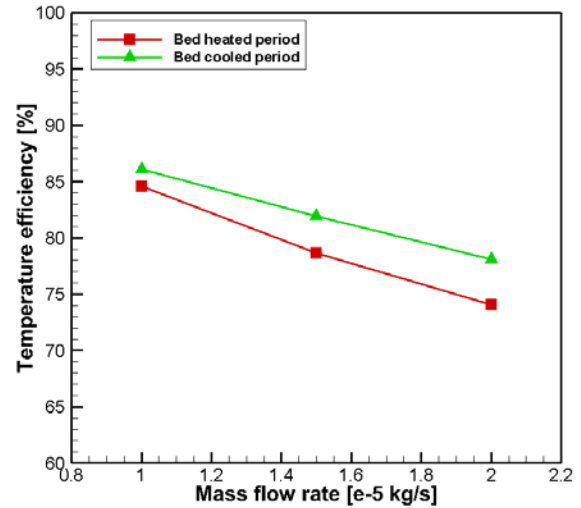


Figure 6: Effect of mass flow rate on the temperature efficiency.

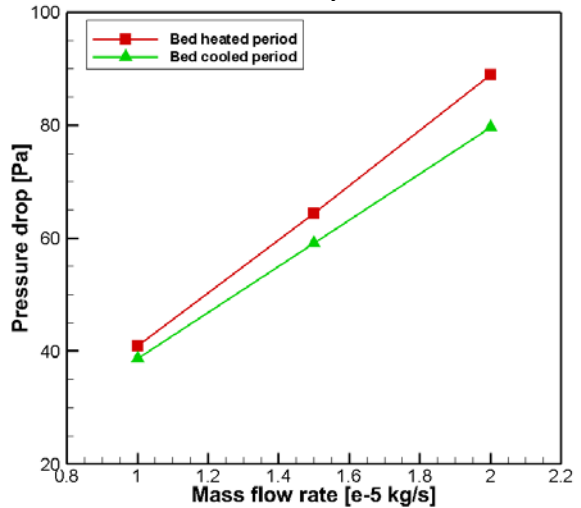


Figure 7: Effect of mass flow rate on pressure drop.

3.3 Effect of solid heat capacity

Figure 8 shows that the larger the specific heat is, the more significant the variation of outlet temperature in each half-cycle. However the variation of average outlet temperatures is small for both hot and cold fluid in three computed cases.

As shown in Figure 9, in the bed heated period the temperature efficiency is almost not influenced by heat capacity, and in the bed cooled period the temperature efficiency increases slowly with the increasing heat capacity.

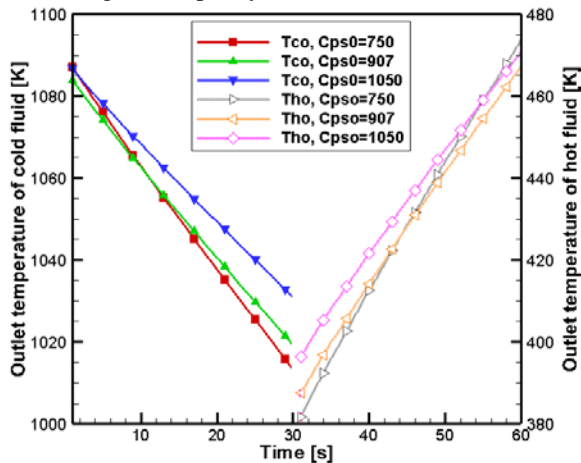


Figure 8: Outlet temperatures of hot and cold fluid in one heat exchange cycle ($T_{h,o}$: hot fluid, $T_{c,o}$: cold fluid).

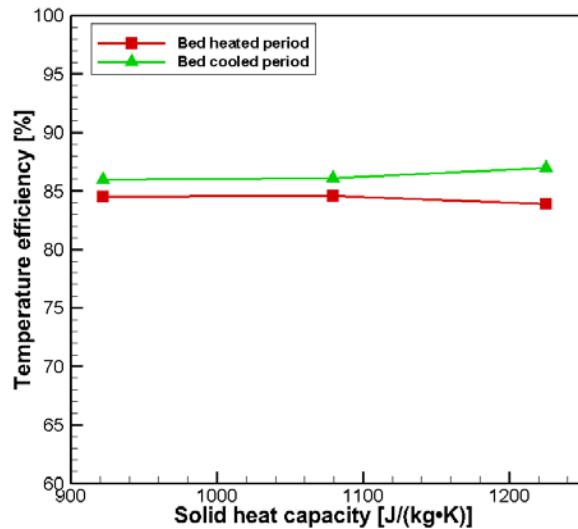


Figure 9: Effect of solid heat capacity on the temperature efficiency.

3.4 Effect of reversal time

Figure 10 shows the effect of reversal time on the temperature efficiency. In the bed heated period, the temperature efficiency decreases slowly with the increasing reversal time. In the bed cooled period, the

temperature efficiency is almost not influenced by reversal time.

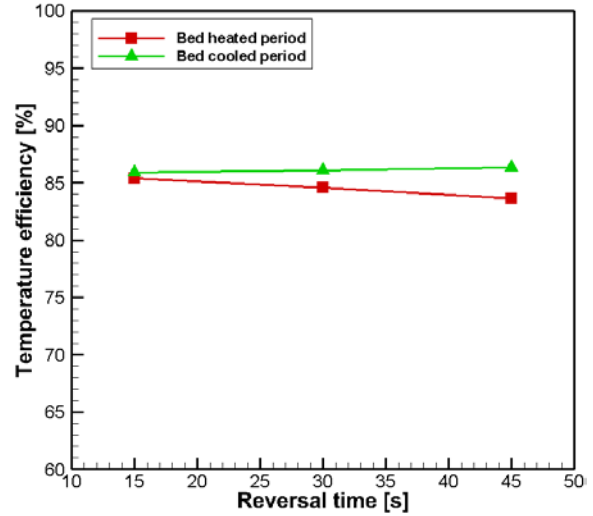


Figure 10: Effect of the reversal time on the temperature efficiency

4. CONCLUSION

A 3D numerical simulation was performed to investigate the thermodynamic performance in honeycomb ceramic channel. The following conclusions were made:

1) In the bed heated period the temperature change rates of the hot fluid and solid are -1.83 K/s and 2.14 K/s, respectively. In the bed cooled period the change rates of the cold fluid and solid are 1.77 K/s and -2.12 K/s, respectively. Logarithmic mean temperature differences between the fluid and solid decreased over time in each half-cycle, and the heat flux on the inner walls of the channel decreased linearly.

2) With the increasing mass flow rate, the temperature efficiency decreased linearly, and the pressure drop increased linearly in each half-cycle.

3) For computed cases the effect of solid heat capacity on the temperature efficiency is ignorable.

4) With the increasing reversal time, the temperature efficiency decreased slowly in the bed heated period, and was almost not influenced in the bed cooled period.

5. ACKNOWLEDGEMENT

This work is supported by National Science and Technology Major Project (Project Number 2011ZX05041-005).

6. REFERENCES

Baris K. (2013). Assessing ventilation air methane (VAM) mitigation and utilization opportunities: A case study at Kozlu Mine, Turkey.

Energy for Sustainable Development, Volume 17, pp. 13-23.

Gosiewski K., Matros Y.S., Warmuzinski K., Jaschik M., and Tanczyk M. (2008). Homogeneous vs. catalytic combustion of lean methane—air mixtures in reverse-flow reactors *Chemical Engineering Science*, Volume 63, pp. 5010-5019.

Gosiewski, K., and Pawlaczyk, A. (2014). Catalytic or thermal reversed flow combustion of coal mine ventilation air methane: What is better choice and when. *Chemical Engineering Journal*, Volume 238, pp. 78-85.

Martinez D.M., Cluff D.L., and Jiang X. (2014). Numerical investigation of the burning characteristics of ventilation air methane in a combustion based mitigation system. *Fuel*, Volume 133, pp. 182-193.

Karacan C.O., Ruiz F.A., Cote M., and Phipps S. (2011). Coal mine methane: A review of capture and utilization practices with benefits to mining safety and to greenhouse gas reduction. *International Journal of Coal Geology*, Volume 88, pp. 121-156.

Karakurt I., Aydin G., and Aydiner K. (2011). Mine ventilation air methane as a sustainable energy source. *Renewable and Sustainable Energy Reviews*, Volume 15, pp. 1042-1049.

Su, S., Beath, A., Guo, H., and Mallett, C. (2005). An assessment of mine methane mitigation and utilization technologies. *Progress in Energy and Combustion Science*, Volume 31, pp. 123-170.

Su S., and Agnew J. (2006). Catalytic combustion of coal mine ventilation air methane. *Fuel*, Volume 85, pp. 1201-1210.

Yin J., Su S., Yu X.X., and Weng Y.W. (2010). Thermodynamic characteristics of a low concentration methane catalytic combustion gas turbine. *Applied Energy*, Volume 87, pp. 2102-2108.

Zhang Y.X., Doroodchi E., and Moghtaderi B. (2014). Utilization of ventilation air methane as an oxidizing agent in chemical looping combustion. *Energy Conversion and Management*, Volume 85, pp. 839-847.

Zhang Z.X., Liu Y.Q., Gao Z.Q., and Liu R.X. (2010). Simulation study of flow and heat transfer in ceramic regenerator. *ICE&Powerplant*, Volume 116, pp. 18-22.

Dust Dispersion Analysis Based on the Rosen-Rammler Distribution Function

Yao Haifei ^{a,b}, Zhang Qun ^{a,b}

^a Safety Branch, China Coal Research Institute Company Limited, Beijing, China, 100013

^b National Key Lab of Coal Resource High Efficient Mining and Clean Utilization, Beijing, China, 100013

ABSTRACT

According to the principle of deriving mine dust distribution from the Rosen-Rammler distribution function, dust particle size distribution data at four places on the 4339 working face in Wangzhuang Coal Mine were regression-analyzed so as to get the dust particle size distribution law. The results show that in the area of 5 m away from the working face in the intake airway, the percentages of mine dust of less than 5 μm , 5 to 10 μm and larger than 10 μm in particle size are 14.8%, 32.5% and 52.7%, respectively, with a concentrated distribution of 5 to 20 μm . The size of mine dust concentrates in the range of 5 to 10 μm for the transfer point, in the range of 5 to 10 μm for the 50# support of the working face, and in the range of 5 to 20 μm for the area of 20 m away from the working face in the outlet lane. Some corresponding dust-proof suggestions were finally put forward on the basis of the characteristic of mine dust distribution in different places.

KEY WORDS: mining; mine dust; dispersion; distribution functions; regression analysis

1. INTRODUCTION

As one of the most important properties of dust, dispersion is defined as the ratio of various sizes of dust in the whole composition, which has important relationship with miner's silicosis (Jin, 1993). The particle size distribution law of dust has closed relationship with the labor environment, the implementation of dust-suppression measure and the choice of dust-suppression equipment (Shi et al., 2007).

All the dust particle size distribution measured by various methods and instruments are needed to explore the accurate distribution law using a suitable mathematical method (Isabelle et al., 2005). The common distribution laws are as follows: normal distribution, logarithmic normal distribution and Rosen-Rammler distribution (Wang, 1991).

The mineral and rock that can generate dust during mine production are brittle materials. The dust formed by brittle materials demonstrates the skewed distribution law which has higher bias coefficient (Wang and Hu, 1994). The logarithmic normal distribution can be used to fit the skewed distribution, but it can't fit accurately because of the bias coefficients of different dust particle size distribution can't be no difference (Bhaskar, 1988). It is reported that the Rosen-Rammler distribution function as a kind of empirical formulas which has closed relationships with specific dust particle size distribution, can be used to express skewed dust particle distribution (Ou, 2006; Zhen et al., 2005). The reasonable dust-suppression measures can be proposed by the evaluation of workplace

environment and dust effects according to the Rosen-Rammler distribution.

2. THE DERIVATION MECHANISM OF THE FORMULA

The expression of Rosen-Rammler distribution function as follows (Dai, 2000),

$$R = 100e^{-\beta \cdot x^n} \quad (1)$$

R—The cumulative distribution of quality, indicate the ration of greater than the accumulative total value of one kind of dust in all kinds of dust, that is the residual rate on the sieve (or named cumulative distribution on the sieve), %;

x—The dust particle size, μm ;

β , n—The coefficients related with dust particle size.

The relationship between R and dust particle size is nonlinearity according to the Rosen-Rammler distribution function. The nonlinear relation can be transformed to linear relation by the transformation method.

The detailed process as follows:

$$R = 100e^{-\beta \cdot x^n} \implies \frac{100}{R} = e^{\beta \cdot x^n} \implies \ln\left(\frac{100}{R}\right) = \beta \cdot x^n$$

Natural logarithm:

$$\ln\left[\ln\left(\frac{100}{R}\right)\right] = \ln\beta + n \ln x,$$

(2)

Imagine $\ln x_i = x'_i$, $\ln \left[\ln \left(\frac{100}{R} \right) \right] = y'_i$, $\ln \beta = a$, $n = b$, formulation (2) can be exchanged to: $y'_i = a + bx'_i$.

Actually, the regression value can be named estimated value (expressed by $\bar{y}_i = a + bx'_i$) because of the deviation between regression value and actual value. Then this issue can be calculated by linear regression methods.

The common standard to evaluate the regression line is the least squares theory. The existed experimental point: $(x'_i, y'_i) (i=1,2,3,\dots,n)$, the minimum regression line of quadratic sum $\sum_{i=1}^n (y'_i - \bar{y}_i)^2 = \sum_{i=1}^n (y'_i - a - bx'_i)^2$ is the best.

The minimum of regression line of quadratic sum is existed according to the quadrature methods in calculus. a, b are:

$$b = \frac{Lx'y'}{Lx'x'}; a = \bar{y}' - b\bar{x}'$$

(3)

In the equation:

$$\bar{x}' = \frac{\sum_{i=1}^n x'_i}{n}; \bar{y}' = \frac{\sum_{i=1}^n y'_i}{n}$$

$$Lx'x' = \sum_{i=1}^n (x'_i - \bar{x}')^2 = \sum_{i=1}^n x_i^2 - \frac{1}{n} \left(\sum_{i=1}^n x'_i \right)^2;$$

$$Lx'y' = \sum_{i=1}^n (x'_i - \bar{x}') (y'_i - \bar{y}') = \sum_{i=1}^n x'_i y'_i - \frac{1}{n} \sum_{i=1}^n x'_i \sum_{i=1}^n y'_i$$

The detailed regression calculated procession:

(1) Calculated the number of various dust particle sizes according to the analysis result of dust sample using microscope.

(2) Calculated the weight of various dust particle size. The volume of dust is calculated according to the volume calculated method of sphere because of homogeneous of dust.

(3) Calculated the ratio of the weight of various dust particle size in the total weight.

$$P_{wi} = \frac{n_i d_i^3}{\sum_{i=1}^n n_i d_i^3} \times 100\% \quad (4)$$

3. THE EXAMPLE ANALYSIS

3.1 The Introduction of Working Face

3# coal seam as the continental lake type coal mined in the 4339 working face in Wangzhuang Coal Mine is in lower-middle part of geological stratification located in Shanxi group of Permian System. The thickness of stable coal seam is about 7.06~7.30m, average 7.18m, the angle of coal seam is about 0° ~15°, average 7.5°. The outside of working face is westward uniclinal structure, the angle of inclination is relative larger (can achieve to 15° partly).

The dust of coal is explosive. The length of flame is 30mm, spontaneous combustion has not happened. The pressure and temperature of ground is normal. The temperature is 16~18°C. The tangent line of working face is 185.5m which has the direction of north-south; the length of excavation: wind road is 730m, shipping road is 710m. Working face is inclined longwall, retreating comprehensive mechanized top-coal, backward type comprehensive mechanized top-coal drawing a low mining overall height all caving mining method. The ventilation of working face is E type.

3.2 The Statistical Parameters of Dust Dispersion in Working Face

The parameters of dust particle size dispersion in 4339 working face were listed in Table 1~4. The test places are 5m away from the working face in intake airway, transfer point, the 50# support of the working face and 20m away from the working face in outlet lane.

Table 1: Statistical parameter of dust particle size distribution 5m away from the working face in intake airway

Particle size (μm)	<2	2~5	5~10	>10	Σ
Particle Number (n)	204	17	7	1	229
Number particle size dispersion n/Σn	89.08%	7.43%	3.06%	0.43%	100.00%
Represent particle sized (μm)	1	3.5	7.5	15	
The equivalent amount of weight nd ³	204	729	2953	3375	7261
Number particle size dispersion nd ³ /Σnd ³	2.81%	10.04%	40.67%	46.48%	100.00%
Quality of the cumulative Σnd ³	204	933	3886	7261	7261
Quality of the cumulative dispersion R	100.00%	97.19%	87.15%	46.48%	

Table 2: Statistical parameter of dust particle size distribution in transfer point

Particle size (μm)	<2	2~5	5~10	>10	Σ
Particle Number (n)	190	49	18	2	259
Number particle size dispersion n/Σn	73.36%	18.92%	6.95%	0.77%	100.00%
Represent particle sized (μm)	1	3.5	7.5	15	
The equivalent amount of weight nd ³	190	2101	7594	6750	16635

Number particle size dispersion $nd^3/\sum nd^3$	1.14%	12.63%	45.65%	40.58%	100.00%
Quality of the cumulative $\sum nd^3$	190	2291	9885	16635	16635
Quality of the cumulative dispersion R	100.00%	98.86%	86.23%	40.58%	

Table 3: Statistical parameter of dust particle size distribution in 50# support of the working face

Particle size (μm)	<2	2~5	5~10	>10	\sum
Particle Number (n)	222	106	22	1	351
Number particle size dispersion $n/\sum n$	63.25%	30.20%	6.27%	0.28%	100.00%
Represent particle sized (μm)	1	3.5	7.5	15	
The equivalent amount of weight nd^3	222	4545	9281	3375	17423
Number particle size dispersion $nd^3/\sum nd^3$	1.27%	26.08%	53.27%	19.37%	100.00%
Quality of the cumulative $\sum nd^3$	222	4767	14048	17423	17423
Quality of the cumulative dispersion R	100.00%	98.73%	72.65%	19.38%	

Table 4: Statistical parameter of dust particle size distribution 20m away from the working face in outlet lane

Particle size (μm)	<2	2~5	5~10	>10	\sum
Particle Number(n)	230	65	22	4	321
Number particle size dispersion $n/\sum n$	71.65%	20.25%	6.85%	1.25%	100.0%
Represent particle sized (μm)	1	3.5	7.5	15	
The equivalent amount of weight nd^3	230	2787	9281	13500	25798
Number particle size dispersion $nd^3/\sum nd^3$	0.89%	10.80%	35.98%	52.33%	100.0%
Quality of the cumulative $\sum nd^3$	230	3017	12298	25798	25798
Quality of the cumulative dispersion R	100.00%	99.11%	88.31%	52.33%	

3.3 The Regression Calculation of Dust Dispersion Degree in Working Face

by the cumulative distribution of quality were listed in Table 5~8.

The representative particle sizes d (listed in Table 1~4) and regression calculated data obtained

Table 5: Regression dust particle size 5m away from the working face in intake airway

Particle size X(μm)	y'_i $(\ln \cdot \ln \frac{100}{R})$	x'_i $(\ln x)$	$(y'_i)^2$ $(\ln \cdot \ln \frac{100}{R})^2$	$(x'_i)^2$ $(\ln x)^2$	$x'_i \cdot y'_i$ $(\ln \cdot \ln \frac{100}{R}) \cdot \ln x$
2	-3.5578	0.6931	12.6577	0.4804	-2.4659
5	-1.9838	1.6094	3.9356	2.5902	-3.1928
10	-0.2664	2.3026	0.0710	5.3020	-0.6134
\sum	-5.8080	4.6051	16.6643	8.3726	-6.2721

Table 6: Regression dust particle size in transfer point

Particle size X(μm)	y'_i $(\ln \cdot \ln \frac{100}{R})$	x'_i $(\ln x)$	$(y'_i)^2$ $(\ln \cdot \ln \frac{100}{R})^2$	$(x'_i)^2$ $(\ln x)^2$	$x'_i \cdot y'_i$ $(\ln \cdot \ln \frac{100}{R}) \cdot \ln x$
2	-4.4684	0.6931	19.9667	0.4804	-3.0971
5	-1.9095	1.6094	3.6463	2.5902	-3.0732
10	-0.1033	2.3026	0.0107	5.3020	-0.2378
\sum	-6.4812	4.6051	23.6236	8.3726	-6.4080

Table 7: Regression dust particle size in 50# support of the working face

Particle size X(μm)	y'_i $(\ln \cdot \ln \frac{100}{R})$	x'_i $(\ln x)$	$(y'_i)^2$ $(\ln \cdot \ln \frac{100}{R})^2$	$(x'_i)^2$ $(\ln x)^2$	$x'_i \cdot y'_i$ $(\ln \cdot \ln \frac{100}{R}) \cdot \ln x$
2	-4.3598	0.6931	19.0076	0.4804	-3.0218
5	-1.1409	1.6094	1.3018	2.5902	-1.8362
10	0.4953	2.3026	0.2453	5.3020	1.1404
\sum	-5.0055	4.6051	20.5546	8.3726	-3.7176

Table 8: Regression dust particle size 20m away from the working face in outlet lane

Particle size X(μm)	y'_i $(\ln \cdot \ln \frac{100}{R})$	x'_i $(\ln x)$	$(y'_i)^2$ $(\ln \cdot \ln \frac{100}{R})^2$	$(x'_i)^2$ $(\ln x)^2$	$x'_i \cdot y'_i$ $(\ln \cdot \ln \frac{100}{R} \cdot \ln x)$
2	-4.7172	0.6931	22.2523	0.4804	-3.2695
5	-2.0849	1.6094	4.3469	2.5902	-3.3555
10	-0.4345	2.3026	0.1888	5.3020	-1.0004
Σ	-7.2366	4.6051	26.7880	8.3726	-7.6254

3.4 The Deduction of Distribution Function of Dust Dispersion Degree in Working Face

Take the place of 5m away from the working face in intake airway for example. According to the datum in Table 1, the follows can be achieved:

$$Lx'y' = \sum_{i=1}^n x'_i y'_i - \frac{1}{n} \left(\sum_{i=1}^n x'_i \right) \left(\sum_{i=1}^n y'_i \right)$$

$$= -6.2721 - (4.6051) \times (-5.8080) / 3$$

$$= 2.6434$$

$$Lx'x' = \sum_{i=1}^n x'^2_i - \frac{1}{n} \left(\sum_{i=1}^n x'_i \right)^2$$

$$= 8.3726 - (4.6051)^2 / 3$$

$$= 1.3036$$

$$b = Lx'y' / Lx'x' = 2.6434 / 1.3036 = 2.0277$$

$$a = \bar{y}' - b\bar{x}' = \frac{1}{n} \sum_{i=1}^n y'_i - b \cdot \frac{1}{n} \sum_{i=1}^n x'_i$$

$$= \frac{-5.8080}{3} - 2.0277 \times \frac{4.6051}{3} = -5.0486$$

$$n = b = 2.0277, \quad a = \ln \beta = -5.0486,$$

$$\beta = e^{-5.0486} = 0.0064$$

The dust particles distribution function in the place of 5m away from the working face in intake airway in Wangzhuang Coal Mine:

$$R = 100e^{-0.0064x^{2.0}}$$

(5)

When R=50%, the dust and particles size is median diameter expressed by x_{50} , then $\ln\left(\frac{100}{R}\right) = \beta x^n$,

$$\ln\left(\frac{100}{R}\right) = \beta x^n, \quad \text{that is} \quad \ln 2 = \beta x^n_{50}, \quad \text{so}$$

$$x_{50} = \sqrt[n]{\frac{\ln 2}{\beta}} = \sqrt[2]{\frac{\ln 2}{0.0064}} = 10.407 \mu m.$$

Table 9: Quality cumulative distribution of dust distribution 5m away from the working face in intake airway

X(μ)	0	1	2	3	4	5	6	7	8	9	10	20	30	40	50
R(%)	100	99.4	97.5	94.4	90.3	85.2	79.4	73.1	66.4	59.5	52.7	7.7	0.3	3.6E-03	1.1E-05

The dust particles distribution function in the place of transfer point in Wangzhuang Coal Mine is $R = 100e^{-0.0018x^{2.72}}$ and Table 10 can be listed.

It can be observed from Table 10 that the percentage of the particle size lower than 5μm is 13.4%, 5~10μm is 47.75%, larger than 10μm is 38.9%. And the

The deduction method is the similar to the above. The dust particles distribution function of transfer point, 50# support of the working face and 20m away from the working face in outlet lane can be obtained as follows:

$$R = 100e^{-0.0018x^{2.72}} \dots x_{50} = 8.92 \mu m \quad (6)$$

$$R = 100e^{-0.0018x^{3.04}} \dots x_{50} = 7.09 \mu m \quad (7)$$

$$R = 100e^{-0.0015x^{2.67}} \dots x_{50} = 9.95 \mu m \quad (8)$$

The dust particles size dispersion law can be obtained by Rosen-Rammler distribution function and the method is similar to the above.

3.5 The Analysis of the Quality Cumulative Distribution of Dust Dispersion Degree in Working Face

The dust particles distribution function in the place of 5m away from the working face in intake airway in Wangzhuang Coal Mine is $R = 100e^{-0.0064x^{2.0}}$ and Table 9 can be listed.

Table 9 showed the value of dust dispersion degree in some range of particle size. The percentage of the particle size lower than 5μm is 14.8%, 5~10μm is 32.5%, larger than 10μm is 52.7%, larger than 30μm is 0.3% in the place of 5m away from the working face in intake airway. It is indicated that the dust particle size is within 5~20μm. It is reported that the dust size lower than 5μm is the most harmful to human and is the key element leading to miner's silicosis (Liu, et al., 2007). The air in intake airway is fresh, so the big particle size entrained dust is the reentrainment of dust after blow excitation deposition, which is less harmful to human.

particle size larger than 20μm is 0.2%. It is indicated that the dust particle size is mainly in 5~10μm, and there are few big size particles. As one of the most important dust generated places, automatic sprinkling water spray can be used to restrain the dust in transfer point.

Table 10: Quality cumulative distribution of dust distribution in transfer point

X(μ)	0	1	2	3	4	5	6	7	8	9	10	20	30	40	50
R(%)	100	99.8	98.8	96.5	92.5	86.6	79.0	69.9	59.8	49.2	38.9	0.2	7.2E-07	1.5E-16	2.1E-31

The dust particles distribution function in the place of 50# support of the working face in Wangzhuang Coal Mine is $R = 100e^{-0.0018x^{3.04}}$ and Table 11 can be listed.

It can be observed from Table 11 that the percentage of the particle size lower than 5 μ m is 21.3%, 5~10 μ m is 64.8%, larger than 10 μ m is 13.9%. And there are few particles whose size is larger than 20 μ m. It is indicated that the dust particle size is mainly in 5~10 μ m and the concentration of respirable dust is higher. So this place is the key prevention area of this working face.

It can be concluded that the method of coal seam water injection, coal winning machine interior and exterior spray and air curtain dust technology play good effects in this working face. However, the better effect can be achieved by other elements such as the properties of coal, the condition of coal layer and the choice of the parameter of cutting mechanism (the type, size, amount, acutance and setting direction of picks). For the situation that the dust has spread, the flow field of airflow should be tested and the nozzle and wet dust collector should be rightly set to prevent the dust spreading to sidewalk area.

Table 11: Quality cumulative distribution of dust distribution in 50# support of the working face

X(μ m)	0	1	2	3	4	5	6	7	8	9	10	20	30	40	50
R(%)	100	99.8	98.5	95.0	88.5	78.7	65.9	51.3	36.7	23.9	13.9	8.9E-06	6.6E-23	1.0E-56	5.4E-113

The dust particles distribution function in the place of 20m away from the working face in outlet lane in Wangzhuang Coal Mine is $R = 100e^{-0.0015x^{2.67}}$ and Table 12 can be listed.

It can be observed from Table 12 that the percentage of the particle size lower than 5 μ m is 10.4%, 5-10 μ m is 40%, larger than 10 μ m is 49.6%. And the particle size larger than 20 μ m is 1.2%. It is

indicated that the dust particle size is mainly in 5-20 μ m.

Dust removal by ventilation and water wet are the main dust prevention measures in intake airway. The two measures have good effect in first settling but it cannot last as the increasing of dust. The dust will be risen again by the wind and the concentration of dust in intake airway will be increased again. Spray binder can prevent dust, dust will be wetted and cannot fly again (Qi et al., 2007).

Table 12: Quality cumulative distribution of dust distribution 20m away from the working face in outlet lane

X(μ m)	0	1	2	3	4	5	6	7	8	9	10	20	30	40	50
R(%)	100	99.9	99.0	97.2	94.1	89.6	83.6	76.3	67.9	58.9	49.6	1.2	1.9E-04	4.6E-11	4.0E-21

4. CONCLUSION

In this work, the properties, range of application, deduction mechanism and regression method of the Rosen-Rammler distribution function were discussed. The usage and analysis method of this function was explained by the example of 4339 working face. According to the related advices and evaluations obtained by the regression law on the effect of dust prevention measures, we can get the conclusions as follows:

(1) The Rosen-Rammler distribution function as a kind of empirical formulas can explain skewed dust particle distribution. The data processed by the Rosen-Rammler distribution function can describe the dust particle distribution law.

(2) The percentage of the particle size lower than 5 μ m is 14.8%, 5~10 μ m is 32.5%, larger than

10 μ m is 52.7%, larger than 30 μ m is 0.3% in the place of 5m away from the working face in intake airway. It is indicated that the dust particle size is in 5~20 μ m.

(3) The dust particle size is mainly in 5~10 μ m, and there are few big size particles in the place of transfer point. Transfer point can restrain the dust by automatic sprinkling water spray.

(4) It is indicated that the dust particle size is mainly in 5~10 μ m and the concentration of respirable dust is high in the place of 50# support working face. It can be concluded that the method of coal seam water injection, coal winning machine interior and exterior spray and air curtain dust technology play good effects in this working face. However, the better effect can be achieved by other elements such as the properties of coal, the condition of coal layer and the choice of the parameter of cutting mechanism (the type, size, amount, acutance and setting direction of

picks). For the situation that the dust has spread, the flow field of airflow should be tested and the nozzle and wet dust collector should be rightly set to prevent the dust spreading to sidewalk area.

(5) It is indicated that the dust particle size is mainly in 5~20 μ m in the distance of 20m away from the working face in outlet lane. Spray binder can prevent dust, dust will be wetted and cannot fly again.

5. ACKNOWLEDGEMENT

The authors gratefully acknowledge foundation by International Cooperation in Science and Technology Special Project (2015DFR70900).

6. REFERENCES

Bhaskar, R. (1988). Experimental studies of dust dispersion in mine airways. *Mining Engineering*, No. 3, pp. 191-195.

Dai, L.Y. (2000). Research on the Rosin-Rammler particle size distribution function. *Industrial Safety and Dustproof*. Volume 16, No.3, pp. 15-17.

Isabelle, D., Jean-Luc, H., and Bernard, B. (2000). Taking-off modal of particles with a wide size distribution. *Chemical Engineering and Processing*. Volume 44, pp. 160-162.

Jin, L.Z. (1993). *Coal Mine Dust Control*. Beijing, Coal Industry Press, 318p.

Liu, Y., Jiang, Z.A., Cai, W., Zhou, F.Z., Guo, D., and Liu, B.D. (2007). Numerical simulation of the dust movement rule in fully-mechanized coal faces. *Journal of University of Science and Technology Beijing*. Volume 29, No.4, pp. 351-353.

Ou, S.N. (2006). Researches and experimentation of the synthetical dust-prevention technology in Weijiadi Coal Mine. Beijing, Civil & Environment Engineering School, University of science and technology Beijing.

Qi, H.G., Jin, L.Z., and Fu, Q.G. (2006). Research and Application of efficient fire suppression and dustproof material. Beijing, Coal Industry Press, 163p.

Shi, C.H., Ou, S.N., and Jin, L.Z. (2007). A study and analysis on the law of motion of the coal dust. *Journal of University of Science and Technology Beijing*. Volume 29, No.2, pp. 1-5.

Wang, B., and Hu, S.X. (1994). Study on the law of mine dust distribution in Tie jing shan. *China mining*. Volume 1, No.3, pp. 71-72.

Wang, C.B. (1991). Measurement results and analysis of dust dispersion. *Safety in coal mines*. No.5, pp. 26-27.

Zhen, G.B., Kang, T.H., Cai, Z.Y., and Yin, Z.H. (2006). Applied the Rosin-Rammler Distribution Function to Study on the Law of Coal Dust Particle-Size Distribution. *Journal of Taiyuan*

University of Technology. Volume 37, No.3, pp. 317-319.

Fuzzy comprehensive evaluation of emergency capability of port coal storage base with G1 method

Siheng Sun^{a, b}, Guozhong Huang^{a, *}, Longzhe Jin^{a, b}, Yage Li^{a, b}, Xue Zhao^{a, b}

^a Department of Safety Science and Engineering, University of Science and Technology Beijing, Beijing, China, 100083

^b Mine Emergency Technology Research Center, Beijing, China, 100083

ABSTRACT

Port coal storage base has strategic significance in China's energy; once an accident occurs, the level of emergency capacity is very important. Therefore, in this paper, the fuzzy comprehensive evaluation method based on the G1 method is proposed for emergency capability assessment. Firstly, the Delphi method is used to establish the index system of emergency capability assessment. To determine the index weight, the G1 method, a kind of method where it is needless to test its consistence, is adopted to calculate the weight of each index. The fuzzy comprehensive evaluation model for the emergency capability assessment is then made. Finally, the feasibility and effectiveness of the method are illustrated using an example. Results show that the method provides a new perspective and tool for emergency capability assessment.

KEYWORDS: emergency capability assessment; index weight; G1 method; fuzzy comprehensive evaluation

1. INTRODUCTION

Port coal storage bases are not only an important base for energy storage, but also an important channel for the "coal transportation from west to east and north to south". Once an accident occurs, it will have a significant impact on the state power supply. Although most of the port enterprises have prepared an emergency plan, there are still many problems such as imperfect plans, imperfect emergency equipment, and the lack of social rescue linkage mechanisms. Therefore, it is necessary to comprehensively evaluate emergency abilities and strengthen the construction of emergency capacities for the weak link, in order to improve the disposal capacity of port accidents and reduce accident losses.

2. THE INDEX SYSTEM OF EMERGENCY CAPABILITY ASSESSMENT

Emergency capability assessment of port coal storage bases involves is very complicated. This system needs to be integrated with the relevant factors affecting the emergency response capability according to the level of the factors and the relationship between the factors.

The Delphi survey method is adopted to select the evaluation index, according to the feedback from the expert and emergency capability evaluation plan of port coal storage bases (Tian and Yang, 2008). The index system contains nine primary indexes, marked U1, U2, ..., U9: monitoring and early warning, emergency support, emergency organization, training and drills, launched the emergency response,

command and coordination, emergency disposal, recovery and rehabilitation, and survey summary.

30 representative grade two indexes are selected on the basis of studying the features and contents of primary indexes, marked as U11, U23, U73, etc. The index system is shown in Table 1.

Table 1: Index system of emergency capability assessment.

Assessment object	Primary Index	Grade Two Index
Emergency Capability Assessment of Port Coal Storage Base	monitor and warn	risk identification and analysis
		safety monitoring
		safety check
		accident warning
	emergency support	emergency response team
		emergency supplies
		emergency equipment
		emergency fund
	emergency organization	emergency plan
		emergency regulations
		emergency organization
	training and drills	personnel training
		emergency drills
	emergency launch	alarm and notification
		emergency personnel response

		field emergency disposal
	command and coordination	emergency command decision
		coordination organization
		emergency resources deployment
	emergency disposal	emergency team level
		medical aid ability
		logistic support
		alert evacuation
	recovery and rehabilitation	technical support
		in-place cleaning
		recovery disposal
	survey summary	rehabilitation disposal
		accident investigation
		accident summary
		revise the emergency plan

3. DETERMINE THE INDEX WEIGHT WITH G1 METHOD

The AHP method (Saaty, 1980) has been widely applied to calculate the weight of each index at present. When this method meets many factors or big problems (Liu et al., 2006), it is difficult for the judgment matrix to meet the requirement of consistence and hard to further divide into groups. In this paper, the G1 method (Guo, 2002), a kind of method where it is needless to test its consistence, is adopted to calculate the index weight of each factor in evaluating the emergency capability of port coal storage bases.

3.1 Determine the order relation

Definition: If the evaluation index X_i is more important (or not less) than X_j relative to a certain evaluation criterion (or goal), denoted as $X_i > X_j$.

Definition: If the evaluation index of X_1, X_2, \dots, X_m , compared with an evaluation criteria (or target) has the following relationship type, the order relation is determined according to the ">".

$$X_i > X_j > \dots > X_k \quad i, j, \dots, k = 1, 2, \dots, m$$

Establish the order relations for the evaluation index set $\{X_1, X_2, \dots, X_m\}$ according to the following steps:

1) Select the most important or least important indicator from the index set containing m indexes, marked X_i .

2) Select the most important or least important indicator from the rest of the index set containing $(m-1)$ indexes, marked X_j .

.....

Select the most important or least important indicator from the rest of the index set containing $(m-(k-1))$ indexes, marked X_n .

.....

Mark the rest index as X_k .

Thus, the sequence of order can be determined. The next step is to determine the level of importance between adjacent indicators.

3.2 Determine the level of importance between adjacent indicators

Experts use r_k to express the degree of importance of the adjacent index between X_{k-1} and X_k .

$$r_k = \omega_{k-1} / \omega_k \quad k = m, m-1, \dots, 3, 2$$

The level of importance between adjacent indicators can be calculated according to the order relation.

For the value of r_k , refer to Table 2.

Table 2: The level of importance between indicators

r_k	Instruction
1.0	Index X_{k-1} and index X_k are equally important
1.1	The ratio of the index X_{k-1} and index X_k between equally important and slightly important
1.2	Index X_{k-1} is more slightly important than index X_k
1.3	The ratio of the index X_{k-1} and index X_k between slightly important and obviously important
1.4	Index X_{k-1} is more obviously important than index X_k
1.5	The ratio of the index X_{k-1} and index X_k between obviously important and strongly important
1.6	Index X_{k-1} is more strongly important than index X_k
1.7	The ratio of the index X_{k-1} and index X_k between strongly important and extremely important
1.8	Index X_{k-1} is more extremely important than index X_k

3.3 Calculate the index weight

$$\omega_{k-1} \geq \omega_k \quad k = m, m-1, \dots, 3, 2$$

$$\omega_m = (1 + \sum_{k=2}^m \prod_{i=k}^m r_i)^{-1} \quad (1)$$

$$\omega_{k-1} = r_k \omega_k \quad k = m, m-1, \dots, 3, 2 \quad (2)$$

ω_k represents the weight of the NO. k index.

The G1 method is especially suitable for when there are many factors and a large scale.

4. FUZZY COMPREHENSIVE EVALUATION

The fuzzy comprehensive evaluation method (Tong, 2010) is a kind of comprehensive evaluation method for complex systems with multiple levels and multiple factors, based on fuzzy mathematics and applying the principles of fuzzy relation synthesis to quantify the unclear boundary factors. Because the assessment is concerned with many factors, the multi-level fuzzy evaluation method is used in this paper. Based on fuzzy mathematics theory (Xu Ge-ning, 2010), the fuzzy comprehensive evaluation of the emergency capacity of the coal storage base is carried out.

4.1 Evaluation factors

According to the index system of emergency capability assessment, determine the evaluation factors.

set: $U = \{U_1, U_2, \dots, U_9\}$, $U_1 = \{U_{11}, U_{12}, U_{13}, U_{14}\}$, $U_2 = \{U_{21}, U_{22}, U_{23}, U_{24}\}$, $U_3 = \{U_{31}, U_{32}, U_{33}\}$, $U_4 = \{U_{41}, U_{42}\}$, $U_5 = \{U_{51}, U_{52}, U_{53}\}$, $U_6 = \{U_{61}, U_{62}, U_{63}\}$, $U_7 = \{U_{71}, U_{72}, U_{73}, U_{74}, U_{75}\}$, $U_8 = \{U_{81}, U_{82}, U_{83}\}$, $U_9 = \{U_{91}, U_{92}, U_{93}\}$

4.2 Comment sets

Comment set is a set of evaluation results of the evaluation object. According to the fuzzy characteristic of emergency response capability evaluation index, 5 grades of reviews (i.e., excellent, good, general, poor and very poor) were used as the evaluation sets to evaluate emergency capability assessment of port coal storage bases, marked $V = \{v_1, v_2, v_3, v_4, v_5\}$. In order to more directly reflect the evaluation results, the 5-comment sets were assigned a value from 0-100, as shown in Table 3.

Table 3: The values of comment sets.

value	100-80	80-60	60-40	40-20	20-0
Comment sets	excellent	good	general	poor	Very poor

4.3 Degree of membership

Because it is difficult to quantify the impact of emergency response capabilities, the fuzzy statistical method is used to determine the degree of membership. The expert graded the indicators according to the given set of V, and then registered the statistics of the frequency of each target. The membership degree of

index u_{ij} is a ratio between the frequency and the total number of experts.

$$r_{ijl} = n_{ijl} / N$$

By determining the membership degree, the fuzzy evaluation matrix is obtained.

$$R_i = \begin{bmatrix} r_{i11} & \cdots & r_{i15} \\ \vdots & \ddots & \vdots \\ r_{im1} & \cdots & r_{im5} \end{bmatrix}$$

4.4 The assessment of Primary Index

According to the weight matrix ω_i and evaluation matrix R_i , carry on the grade two index and primary index evaluation calculation.

$$R = B_i = \omega_i R_i = \begin{bmatrix} \omega_1 R_1 \\ \omega_2 R_2 \\ \omega_3 R_3 \\ \cdots \cdots \\ \omega_9 R_9 \end{bmatrix}$$

4.5 Fuzzy comprehensive assessment

After each evaluation index of the index layer is evaluated, the evaluation matrix C is obtained by fuzzy comprehensive evaluation of the criteria layer index U_i .

$$C = WR = [c_1, c_2, c_3, c_4, c_5]$$

The comprehensive evaluation matrix C is characterized by the form of membership degree, but the result is not very intuitive. Select the median value of the value of the critical value of the evaluation grade, $D = (90, 70, 50, 30, 10)$, as the rank weighted vector of the evaluation set:

$$E = CD^T$$

According to E value, determine the level of emergency response capability level.

5. DETERMINE THE EMERGENCY CAPABILITY LEVEL

By analyzing one of the port coal storage base in Hebei province, the emergency capability was evaluated.

5.1 Calculate the index weight with G1 method

Use the G1 method to calculate the weight of each layer index, taking U1—U9, 9 primary indexes as the criteria layer indexes as an example. First, rank the importance of each index of the criterion layer. The sequence relationship identified by the expert is

U7>U2>U1>U6>U5>U4>U8>U3>U9, recorded as $x_1 > x_2 > x_3 > x_4 > x_5 > x_6 > x_7 > x_8 > x_9$.

Experts give the importance ratio r_k of adjacent indicators x_k and x_{k-1} according to Table 2. The ratios are $\frac{\omega_1}{\omega_2} = r_2 = 1.2$, $\frac{\omega_2}{\omega_3} = r_3 = 1.3$, $\frac{\omega_3}{\omega_4} = r_4 = 1.2$, $\frac{\omega_4}{\omega_5} = r_5 = 1.1$, $\frac{\omega_5}{\omega_6} = r_6 = 1.3$, $\frac{\omega_6}{\omega_7} = r_7 = 1.4$, $\frac{\omega_7}{\omega_8} = r_8 = 1.3$, $\frac{\omega_8}{\omega_9} = r_9 = 1.1$. According to formulas (2) and (3), calculate the ω_i in order and get the criterion layer index weight vector:
 $w = (0.416, 0.1841, 0.0454, 0.0825, 0.1073, 0.118, 0.2209, 0.059, 0.0412)$

Similarly, weight the grade two indexes. The results are as shown in Table 4.

Table 4: The index weight values of the index system.

Primary Index	weight	Grade Two Index	weight
monitor and warn	0.1416	risk identification and analysis	0.1696
		safety monitoring	0.285
		safety check	0.3419
		accident warning	0.2035
emergency support	0.1841	emergency response team	0.1534
		emergency supplies	0.2761
		emergency equipment	0.184
		emergency fund	0.3865
emergency organization	0.0454	emergency plan	0.3431
		emergency regulations	0.2451
		emergency organization	0.4118
training and drills	0.0825	personnel training	0.5455
		emergency drills	0.4545
emergency launch	0.1073	alarm and notification	0.3125
		emergency personnel response	0.3125
		field emergency disposal	0.375
command and coordination	0.118	emergency command decision	0.4588
		coordination organization	0.2353
		emergency resources deployment	0.3059
emergency disposal	0.2209	emergency team level	0.3296
		medical aid ability	0.169

		logistic support	0.2197
		alert evacuation	0.128
		technical support	0.1537
recovery and rehabilitation	0.059	in-place cleaning	0.3093
		recovery disposal	0.433
		rehabilitation disposal	0.2577
survey summary	0.0412	accident investigation	0.2841
		accident summary	0.3409
		revise the emergency plan	0.375

5.2 Determine the degree of membership

Choose the expert judgment method to calculate the index membership degree. Taking a13 as an example, select ten experts to judge. If 2 experts think it's excellent, 4 good, 3 general, 1 poor, the degree of membership is (0.2,0.4,0.3,0.1,0).

After statistical analysis, the results are as shown in Table 5.

Table 5: The evaluation index membership degree.

	V1	V2	V3	V4	V5
U11	0.2	0.4	0.3	0.1	0
U12	0.3	0.4	0.2	0.1	0
U13	0.4	0.4	0.2	0	0
U14	0.2	0.4	0.4	0	0
U21	0	0.1	0.3	0.4	0.2
U22	0.1	0.2	0.3	0.4	0
U23	0	0.1	0.3	0.4	0.2
U24	0.1	0.2	0.4	0.3	0
U31	0.1	0.3	0.4	0.1	0.1
U32	0.1	0.2	0.5	0.1	0
U33	0.1	0.3	0.5	0.1	0
U41	0	0.2	0.4	0.3	0.1
U42	0.1	0.2	0.5	0.1	0.1
U51	0.1	0.3	0.4	0.1	0.1
U52	0.1	0.2	0.4	0.2	0.1
U53	0.2	0.2	0.5	0.1	0
U61	0.1	0.3	0.4	0.2	0
U62	0.1	0.2	0.4	0.2	0.1
U63	0	0.1	0.4	0.3	0.2
U71	0	0.1	0.3	0.4	0.2
U72	0	0.1	0.3	0.5	0.1
U73	0	0	0.4	0.4	0.2
U74	0.1	0.2	0.4	0.2	0.1
U75	0.1	0.2	0.3	0.3	0.1
U81	0.1	0.3	0.4	0.2	0
U82	0.1	0.2	0.5	0.1	0.1

U83	0.1	0.3	0.4	0.2	0
U91	0.2	0.4	0.4	0	0
U92	0.2	0.4	0.3	0.1	0
U93	0.1	0.3	0.4	0.2	0

According to the results of Table 5, the fuzzy relation evaluation matrix R_i is constructed. Taking U1 as an example, the corresponding evaluation matrix is:

$$R_1 = \begin{bmatrix} 0.2 & 0.4 & 0.3 & 0.1 & 0 \\ 0.3 & 0.4 & 0.2 & 0.1 & 0 \\ 0.4 & 0.4 & 0.2 & 0 & 0 \\ 0.2 & 0.4 & 0.4 & 0 & 0 \end{bmatrix}$$

5.3 The assessment of Primary Index

To evaluate the primary index U1:

$$B_1 = \omega_1 R_1 = (0.2969, 0.4, 0.2577, 0.454, 0)$$

In the same way, the results of other primary index evaluation can be obtained.

$$R = \begin{bmatrix} R_1 \\ R_2 \\ R_3 \\ R_4 \\ R_5 \\ R_6 \\ R_7 \\ R_8 \\ R_9 \end{bmatrix} = \begin{bmatrix} 0.2969 & 0.4 & 0.2577 & 0.0454 & 0 \\ 0.0663 & 0.1663 & 0.3387 & 0.3614 & 0.0675 \\ 0.1 & 0.2755 & 0.4412 & 0.1490 & 0.0343 \\ 0.0455 & 0.2 & 0.4455 & 0.2091 & 0.1 \\ 0.1375 & 0.2313 & 0.4375 & 0.1313 & 0.0625 \\ 0.0694 & 0.2153 & 0.4 & 0.2306 & 0.0847 \\ 0.0282 & 0.1062 & 0.3348 & 0.37598 & 0.1549 \\ 0.1 & 0.2567 & 0.4433 & 0.1567 & 0.0433 \\ 0.1625 & 0.3625 & 0.3659 & 0.1091 & 0 \end{bmatrix}$$

5.4 Fuzzy comprehensive assessment

Using fuzzy comprehensive evaluation to determine the risk level:

$$C = WR = [0.1043 \quad 0.22 \quad 0.3649 \quad 0.2351 \quad 0.0757]$$

$$E = CD^T = 50.84$$

Therefore, the comprehensive evaluation of emergency capability of the coal storage base in Hebei province is 50.84, between 60 and 40. The level is general and needs to strengthen.

6. CONCLUSION

The Delphi method is used to establish the index system of emergency capability assessment. Using the G1 method can reduce the amount of calculation and easily find the index weight.

The fuzzy comprehensive evaluation model is established according to the fuzzy feature of the index. The feasibility and effectiveness of the method were illustrated by an example.

This paper provides a new perspective and tool for emergency capability assessment. However, emergency capability assessment is complex and imperfect, and therefore still requires further study.

7. ACKNOWLEDGEMENT

First and foremost, I would like to show my deepest gratitude to my supervisor, Professor Jin Longzhe and Huang Guozhong. They are respectable, responsible and resourceful scholars, who have provided me with valuable guidance in every stage of the writing of this thesis. When establishing the index system, calculating the numerous index weight, they put forward the valuable comments for the selection of the index and calculation method. I shall also extend my thanks to my scientific research team for their kindness and help. Finally I wish for grand success of ISMS 2016.

8. REFERENCES

- GUO Ya-jun. (2002). Comprehensive Evaluation Theory and Method, Beijing: Science Press, 167 p.
- LIU Jian, ZHENG Shuang-zhong and DENG Yun-feng. (2006) Weight Determination of Indexes in Evaluation of Emergency Response Ability Based on G1. China Safety Science Journal. Volume 16 NO.1, pp. 30-33.
- Saaty.T.L.(1980) The Analytic Hierarchy Process, Mcgraw-Hill (Tx), New York. TIAN Yi-lin and YANG Qing. (2008) Study of the Evaluation Index System Model of the Emergency Capability on Emergency, Journal of Basic Science and Engineering, Volume 4 NO.2, pp. 200-207.
- TONG Rui-peng. (2010). The Application of Common Safety Evaluation Method, Beijing: China Labor and Social Security Publishing House, pp. 200-205.
- XU Ge-ning, JIANG Fan. (2010). Safety Assessment on the Crane based on FAHP, Journal of Safety and Environment. Volume 10 NO.2, pp. 196-200.

Study on External Protective System of Waterproofing Refuge Chamber in Guilaizhuang Gold Mine

Shengnan Ou^a, Longzhe Jin^{a, b, *}, Song Li^c, Shu Wang^{a, b}, Yage Li^a, Zhiling Huang^a

^a School of Civil and Environment Engineering, University of Science and Technology Beijing, Beijing, China 100083

^b Mine Emergency Technology Research Center, University of Science and Technology Beijing, Beijing, China 100083

^c Shandong Gold Guilaizhuang Mining Co. Ltd., Shandong, China 273300

ABSTRACT

Refuge chamber, which have a positive impacts on facilitating escape for miners trapped underground by a fire, explosion, or rock collapse, need further perfection and research with respect to waterproofing function at present in China in case of mine floods. A waterproofing refuge chamber, designed for the survival of 50 miners for at least 96 hours, along with its waterproofing, airtight, and other essential requirements has been proposed in Guilaizhuang gold mine in Shandong province. Focusing on the external protective system of the water-proof refuge chamber, critical items (including the water-proof door, bulkhead, and lining) are systematically presented in this paper. Specifics like exhausting and draining under water, were also take into consideration in the research. Accordingly, a waterproofing evacuation unit, emergency evacuation unit, and emergency drainage unit were designed. Tests and simulation results indicated that the refuge chamber had good positive pressure maintenance, air-tight property, and water-proof performance.

KEYWORDS: water-proof protective refuge chamber; external protective system; protective performance; field test; simulation analysis

1. INTRODUCTION

Refuge chamber, constructed by concrete and flame retardant inflatable material, equipped with sufficient breathable air, adequate foods and water, reasonable carbon dioxide scrubbing and temperature control (MSHA, 2008), have a positive impact on facilitating escape for miners trapped underground by a fire, explosion, or rock collapse (Saleh, 2011). Current researches in the field has mainly discussed the protective characteristics in cases of gas outburst, fire, and explosion emergencies in underground mines (Gao, 2013; Meyr Jr, 2013). As investigated, a significant amount of non-coal mines, especially those located in north, south, and south-west of China, are under complex hydrological-geological condition. In addition, most mines are continuously digging into deeper mining, where the risk of water burst increases as the depth of the tunnel increases (Xing, 2010). Thus, current emergency refuge technology needs further perfection and research with respect to the water-proof function to improve its applicability and safety.

In this paper, a water-proof refuge chamber was proposed in Guilaizhuang gold mine in Shandong province according to the practical situation in the underground mine. It was designed for the survival of 50 miners for at least 96 hours. This paper focuses

on its external protective system. Compared with current refuge chamber in China, the water-proof function and both anti-hydrodynamic pressure and anti-penetrability performance were taken into consideration in this case. Critical items (water-proof door, bulkhead, and lining were included), as well as some specifics items (like exhausting and drainage in flood scenario) were systematically studied and presented in the paper. Then, site tests and simulation through ABAQUS software were carried out to verify the protective performance.

2. ESSENTIAL REQUIREMENTS

Based on an overall consideration of geological conditions, major hazard and accident underground, production status and mining plan, as well as current escape and rescue plan, the refuge chamber was set adjacent to the main roadway at the absolute altitude of -150 m, and 200 m away from the eastern mining boundary. Essential requirements were as follows:

(1) Capacity & Size

When in water inrush or other emergency case, miners should preferentially escape from the harmful environment to above ground; refuge chamber are for those miners trapped underground (Brake, 1999). According to statistical data of underground workers, up to 46 miners can be counted as protective objects.

Thus, the refuge chamber was designed for the survival of 50 miners for at least 96 hours, with a reserve factor of 1.2.

According to relevant regulations (State Administration of Work Safety, 2011), refuge chamber should contain two entrances, a living zone area of no less than 60 m², and a transition zone should be more than 3 m². Considering the width of devices and operability, dimensions of the living zone profile are 4500 mm × 3500 mm (net width × net height), with an available area of 81 m², while the transition zone area is 2700 mm × 2700 mm, and 27 m² respectively.

(2) Waterproofing

Guilaizhuang gold mine, once a open pit surface mine, has been transferred to underground mining. The nearest entrance is at the elevation of -30 m. According to the geologic investigation report, this mine is under medium-complicated hydrologic condition. Uncertain quantity of karst caves, existing at an elevation of approximately -30m and recharged by atmospheric precipitation, were the main sources of inflows into the mines. Table 1 tabulates mine inflow rate of each main roadway.

Table 1: Mine inflow rate of each main roadway.

Elevation of roadway (m)	Aquifer thickness (m)	Drawdown (m)	Inflow rate (m ³ /d)
-50	42.77	180.13	9100
-100	52.77	230.13	12353
-150	56.07	280.13	14553

The vertical distance from the aquifer and nearest entrance to the refuge chamber is 120 m. Assuming an inundated case with reserve factor of 1.2, the refuge chamber is expected to resist 1.5 MPa hydrodynamic load. As there is electrical equipment, food, water and other components stored inside, the water-proofing protection grade of the refuge chamber should be at level two (no water penetration is acceptable, damp area should be less than 2% tolerable), according to Chinese National Standard GB 50108-2001 (MOHURD, 2008).

(3) Other requirements

Other requirements include: airtight, high temperature and fire resistant; functions of gas monitoring, warning alarm, telecommunication and signaling transmission; adequate power, energy, food, water and first aid tools; proper components for basic survival needs. (State Administration of Work Safety, 2011).

3. WATERPROOF CONSTRUCTION & AUXILIARY FACILITIES

3.1 Door & Bulkhead

Over-sized or over-weight doors may increase operation difficulty and even cause failure to open or close the door for the miners injured in the accident. Thus, a thin-shell water-proof door (ML type, Wuhan Mingqing Environmental Protection Engineering Technology Co., Ltd) with dimension of 1500mm *W* × 1800mm *H* was applied in this case. The doorframe, an I-shaped composite frame structure, and door leaf, stiffened thin-shell structure with square rubber strip mounted around, were wedged by a cuneiform slide block mechanism to achieve the expected sealing requirement. As tested underground, the average time to fully open then close the door with two miners was in the range of approximately 4 to 6 minutes. During the incident, trapped sediment with the water flow would lead to leakage through the gap between the doorframe and leaf. Thus, to reduce the likelihood of such sediment retention, the floor of the refuge chamber was designed to be 500 mm higher than the outer roadway floor, and a 200 mm high threshold was set.

Water-tight bulkhead, expecting to withstand 1.5 MPa water pressure, was designed as a wedge-shaped reinforced concrete structure, with a thickness of 1000 mm (determined by calculation on the basis of shear strength theory and compressive strength theory). Available experiences have suggested that seepage in poured concrete structures often occurred at cracks or pipe penetrations. Thus to maintain integrity of the wall, the embedded through-pipes, which were installed in-situ during the casting of the concrete, were all designed as U-shape, passing through under the wall. All the through-pipes were sealed carefully with expanding water bar and sealant. Rigid water-proofing casing was adopted for exhaust, compressed-air-supplying, water-supplying, drainage, and reserved pipes; while flexible water-proof casing was adopted for those power cable through-pipes. The distances from the pipe to wall angle and between adjacent through-pipes were designed under the requirements of technical code for waterproofing of underground works (MOHURD, 2008).

3.2 Supporting structure

The cross-section of the refuge chamber was a classic three-centered arch, and the composite shell lining, which consisted of a supporting layer and water-proofing layer, was applied. The supporting layer was designed to take ground load or other load, while the waterproofing layer was mainly for water-proofing and air-tight purpose.

(1) Supporting layer

Based on engineering analogies, the main parameters for the supporting layer were listed as follows: anchor, made of deformed steel bar with one

direction of screw thread rotating leftward and without longitudinal bar ($\Phi 20 \text{ mm} \times 2400 \text{ mm}$), was installed according to the distribution of $800 \text{ mm} \times 800 \text{ mm}$ (row \times column); primary sprayed concrete lining was constructed with 50 mm thick concrete (intensive grade of C25); secondary sprayed lining was of 100 mm thickness, with reinforcement of steel bars ($\Phi 10 \text{ mm}$) at a grid of $150 \text{ mm} \times 150 \text{ mm}$; third poured concrete lining was constructed by C30 concrete, with a thickness of 100 mm.

(2) Waterproofing layer

The waterproofing lining was constructed of water-tight concrete (strength grade: C40; impermeability grade: P8) and steel mesh ($\Phi 10 \text{ mm}$), with the main reinforcement of $300 \text{ mm} \times 300 \text{ mm}$ grid, and connecting reinforcement of $600 \text{ mm} \times 600 \text{ mm}$ grid. The thickness of lining was 350 mm (calculated by thick wall cylinder theory).

Self waterproofing components (wall and waterproofing layer) are the main part to resist potential harmful substance from outside, their actual performance can be influenced by several factors (Qi, 2007):

- Anthropropic aspects like improper design or maintenance, construction quality dissatisfaction, etc.;
- Environmental aspects like high temperature fume, harmful gases, mineral water, impulsion pressure, and drilling-and-blasting operations nearby, etc.;
- Inherent defects of concrete, which would gradually grow with time and cause structural performance deterioration.

Among the mentioned factors, anthropic implications can be controlled by reasonable designation and management. However, being involved in complex disaster surrounding, concrete performance, especially permeability, may decrease afterwards, and further causing structural damage. Both watertightness and airtightness would be affected. This will be fully studied in the future.

3.3 Auxiliary facilities

(1) Water-proof evacuation unit

Overpressure relief valve, of which the outlet installed at a height of 0.5 m above the floor of the refuge chamber, was used for regulating pressure inside the refuge chamber. It is possible that water outside could flow inside through the valve in the event of water inrush. Thus, a particular designed evacuation unit, composed of a controlling component (consisted of hydrostatic release unit, guide sleeve, piston, cylinder barrel, etc.), brake valve (installed out of the refuge chamber), and pressure release valve (installed inside the refuge chamber), was mounted at the outlet of the

overpressure relief valve. In a normal state, the brake valve remains open so that the overpressure relief valve can work regularly to keep a safe air pressure inside the refuge chamber. When the outer water pressure rises to 5 kPa (critical pressure of the hydrostatic release unit), the outer brake valve would close automatically by controlling component to prevent the water inflow and keep refugees safe. In this case, to avoid over-pressure inside the refuge chamber, compressed air lines or borehole should be cut off; and habitable circumstances will be sustained by a compressed oxygen/air cylinder or chemical oxygen generator, with the assistance of air scrubbing and conditioning methods.

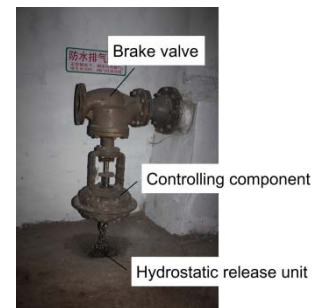


Figure 1: Water-proof evacuation unit.

(2) Emergency evacuation unit

The refuge chamber may be completely isolated from the external environment once the evacuation unit described in Section 3.1 closed down in water inrush emergency. Based on our previous study, within a totally sealed space (internal volume of 24.5 m^3) with 10 subjects living in it, the barometer readings varied from -400 Pa to 1200 Pa in the duration of nearly 9 hours, and it was predicted that the maximum pressure would be up to 8718 Pa in 96 hours (Li et al., 2015). In addition, if air supplied by compressed air lines running throughout the mine was not cut off in time due to wrong operation or other reasons after the evacuation unit closed, the pressure inside the refuge chamber would rapidly rise to a hazardous level. Thus for the sake of safety, an emergency evacuation unit with capacity of $100 \text{ m}^3/\text{h}$ was installed in the refuge chamber. The outlet of the evacuation line was placed in the -110 m level roadway, and proper protection measures were taken.

(3) Emergency drainage unit

Wastewater in the refuge chamber can be drained via floor drains when the water level in the main roadway is lower than 600 mm. Otherwise, an emergency drainage unit with the capacity of $20 \text{ m}^3/\text{h}$ and discharge head of 50 m would be used.

4. TESTS & SIMULATION ON PROTECTIVE PERFORMANCE

4.1 Hydrostatic test of water-proof door

The hydrostatic test of the water-proof door was carried out in Structure Mechanics Laboratory of China Ship Scientific Research Center in Jiangsu Province. The door was mounted in a flat position as required (SAC, 1991); then pressurize hydrostatic pressure to 2.0 MPa by a pressure gradient of 0.5 MPa, and maintain for 30 minutes. A total number of 20 measuring points were monitored in the experiment. Figure 2 shows the distribution and the strain changing curve of five representative points. No deformation or leakage was observed on the door frame after the experiment. The door showed a perfect water-resistant performance.

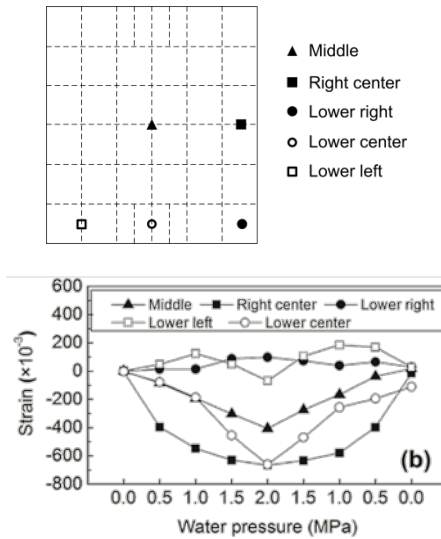


Figure 2: Hydrostatic test of water-proof door: (a) five typical measuring points distribution; and (b) strain curve at each point.

4.2 Positive pressure maintenance test

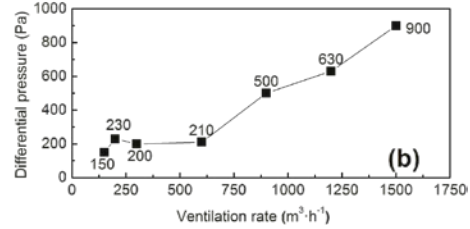


Figure 3: Positive pressure maintenance: (a) experimental site; and (b) change curve of differential pressure between inside and outside of refuge chamber.

In the experiment, all the openings were sealed and the door was closed, but to keep the evacuation unit operating at a normal state, and regulate the ventilation airflow rate at 150, 200, 300, 600, 900, 1200, and 1500 m^3/h respectively. It can be seen that, the differential pressure in and out of the refuge chamber, as shown in Figure 3, increased with ventilation rate. The maximum differential pressure was up to 900 Pa, but not harmful to health. The results indicated that the refuge chamber is able to maintain and regulate inner pressure as required.

4.3 Air impermeability performance test

The refuge chamber was kept in a completely confined state during the test. All doors and openings are closed as well as the evacuation unit. Pressurize the inner space with compressed air until the differential pressure rises above 1000 Pa. The changing curve of differential pressure afterwards was shown in Figure 4. It can be seen that the pressure decreased rapidly from nearly 1300 Pa to below 250 Pa in the first 200 seconds, then stabilized at around 50 Pa in 10 minutes. The airtight requirement is fulfilled.

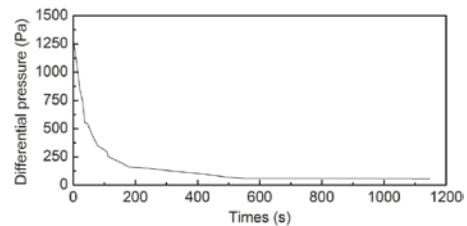


Figure 4: Air permeability performance.

4.4 Test & Simulation on water-proof lining

(1) Property of waterproofing concrete sample

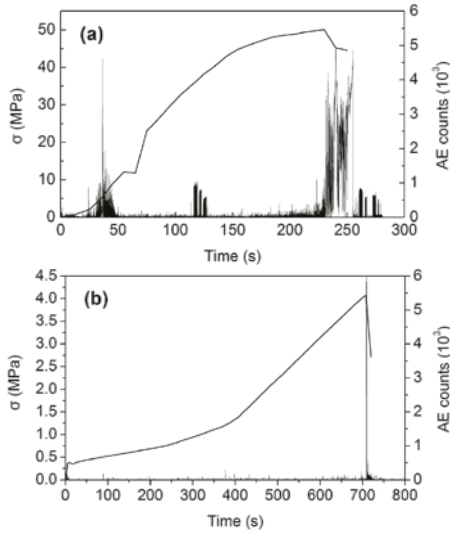


Figure 5: Experimental results of water-proof concrete sample: (a) uniaxial compressive behaviour; and (b) splitting tensile behaviour.

The uniaxial compressive behaviour, splitting-tensile behaviour, and anti-penetrability performance of concrete sample were tested according to Chinese National Standards (MOHURD, 2002; MOHURD, 2009). Acoustic emission (AE) was adopted to reveal the damage evolution of each sample. The following experimental equipment was used: WEP-600 hydraulic universal tester (Changchun Chaoyang Test Instrument Co., Ltd), DH3821 static strain testing analyzer (Jiangsu Donghua Testing Technology Co., Ltd; resolution: $1\mu\epsilon$; system indication error: $\leq 0.2\% \pm 3\mu\epsilon$); SZ120 resistance wire strain gauge (Xingtai Kehua Resistance Strain Gauge Plant; sensitivity: $2.06 \pm 0.1\%$); PCI-2 6 channel AE system (Physical Acoustics Co., Ltd); BY-HS16B concrete impermeability instrument (China Academy of Building Research; nominal pressure: 1.6 MPa; pressure maintenance error: ± 0.05 MPa). All the tested samples were kept in standard conditions for 28 days.

The tested concrete samples presented an average ultimate compressive strength of 50.27 MPa, splitting tensile strength of 4.24 MPa, and impermeability coefficient of 1.53×10^{-11} m/s. Figure 5 shows the stress and AE counts changing curve of one of the samples under centric axial compression and splitting tension states respectively. With the increasing magnitude of stress, especially near the critical point, internal cracks formed and propagated, leading to final damage. Due to significantly lower tensile strength, stresses produced by loads, temperature changes, shrinkage, settlement, etc. would induce active or dormant cracks on the concrete structure. Thus, in the following simulation analysis, a concrete damage plasticity model was employed to identify the possible crack information zones within the waterproof lining.

(2) Simulation on water-proof lining

A two-dimensional model of waterproof lining for calculating its seepage and stress fields in water inrush emergency was established by ABAQUS software. The finite element mesh extended to $40 \text{ m} \times 40 \text{ m}$, seven times the excavation size. The tunnelling process, consisting of excavation and support installation steps (six steps in total), was simulated in the analysis by adding and removing corresponding elements. After the step-by-step tunnelling process, a pore pressure of 1.3 MPa was loaded on the boundary of the top surface, 1.7 MPa at the bottom, while at the vertical boundary the pore pressure linearly increased with depth. Mohr-Coulomb plasticity model, elastic-plastic model, and concrete damaged plasticity models were adopted in the calculation to identify the behaviour of corresponding material. As concrete is strong in compression but weak in tension, only the tension damage behaviour was considered in the simulation. Tensile damage was specified as a function of cracking displacement, calculated on the basis of the stress-strain curve obtained in Section 3.4.1 and relevant references (Jankowiak, 2005; Guo, 1997). Model details are shown in Table 2.

Table 2: Parameter setting of calculation model.

No.	Part	Material model	Element	Material properties
1	Surrounding rock	Classic Mohr-Coulomb plasticity model	CPE4RP	Young's modulus: 10.0GPa; poisson's ratio: 0.26; cohesion: 2.0MPa; internal friction angle: 35° ; dilation angle: 0° ; and void ratio: 0.639.
2	Anchor	Elastic-plastic model	T2D2	Density: 7800kg/m^3 ; Young's modulus: 214GPa; poisson's ratio: 0.27; and sectional area per anchor: $3.14 \times 10^{-4} \text{m}^2$.
3	Rebar	Elastic-plastic model	T2D2	Density: 7800kg/m^3 ; young's modulus: 190GPa; poisson's ratio: 0.3; and sectional area per rebar: $7.85 \times 10^{-5} \text{m}^2$.
4	Concrete	Concrete plasticity damage model	CPE4RP	Poisson's ratio: 0.2; dilation angle: 30° ; Flow potential angle: 0.1; biaxial and uniaxial tensile ultimate strength ratio: 1.16; constant stress ratio: 0.667; viscous coefficient: 0.0005; compression recovery: default; stress and strain data of C25 concrete: research results taken from Guo (Guo, 1997); parameters of C40 concrete (young's modulus, stress, strain, permeability)

MOHURD. (2008). GB 50108-2008 Technical code for waterproofing of underground work. Beijing: China planning press.

MOHURD. (2009). GB/T 50082-2009 The Test Method of Long-term and Durability on Ordinary Concrete. Beijing: China Architecture and Building Press.

MSHA. (2008). Health Administration, US Department of Labor. 30 CFR Parts 7 and 75 Refuge Alternatives for Underground Coal Mines; Final Rule.

Qi, F. (2007). Study on waterproof test and anti-crack technique of fiber concrete structure in subway station. Shanghai Jiao Tong University.

SAC. (1991). MT258-1991 ML-type thin shell waterproof gate. Beijing: China Standards Press.

State Administration of Work Safety. AQ 2033-2011 Regulations for construction of emergency refuge system in metal and nonmetal underground mine. Beijing: China Standards Press.

Saleh, J. H., and Cummings, A. M. (2011). Safety in the mining industry and the unfinished legacy of mining accidents: Safety levers and defense-in-depth for addressing mining hazards. *Safety science*, Volume 49, No.6, pp. 764-777.

Xing, D. M., Ye, Y. C., and Zhao, W. W. (2010). Statistical Analysis and Safety Management Countermeasure of Mine Water Inrush Accident in China. *Metal Mine*, No. 6, pp.178-181.

Hazard detection and comprehensive control technologies of the integrated resource coal mine goafs in China

Wen LI

Mine Safety Technology Branch of China Coal Research Institute, Beijing, China, 100013
State Key Laboratory of Coal Mining and Clean Utilization(China Coal Research Institute), Beijing, China, 100013
Beijing Mine Safety Engineering Technology Research Center, Beijing, China, 100013

ABSTRACT

Goaf disaster has become a major problem for the integrated resource coal mines in China. Based on an analysis of goaf disaster types and characteristics, hazard detection and comprehensive control technologies are systematically put forward. The control technologies include goaf hazard detection technologies which combine ground survey with undermine detection; the goaf risk classification and assessment technologies combined with risk degree classification, qualitative with quantitative evaluation; the goaf disaster monitoring technologies which combine local and regional monitoring with joint monitoring undermine and on the surface; the goaf comprehensive control technologies which combined open stripe grouting with roof caving on the surface or undermine; and the goaf safety guarantee technologies which combine matching funds and policy support with administrative supervision. The results show that goaf disasters are divided into four types according to the disaster forms in integrated resource coal mines. The four types are comprised of the abandoned old goafs or permeable pit shafts, goaf fires including coal combustion and gas explosions, the poisonous and harmful gas in goaf emissions, and the abnormal geological disasters. The goafs have the characteristics of unknown distribution, different kinds of disaster types, concealment, and unpredictability. The control principles were summarized and put forward in the form of an advance summary of ground survey, an undermine detection follow up, hazard assessment and evaluation, in-place monitoring and supervising, comprehensive control for disaster reduction, and a guarantee of safety measures.

KEYWORDS: integrated resource coal mines; goafs; ground survey; undermine detection; monitoring; disaster prevention and control; safety guarantee.

1. INTRODUCTION

Since September 2005, China has been carrying out the integration of coal mines. The number of coal mines has been reduced from 25,000 in the year 2005 to 11,000 in the year 2014.

The integrated resource coal mines have experienced a series of hazards and accidents, such as water, fire, or roof hazards caused by unknown goafs due to the original local small coal mines often having a lack of basic data. The problem of goaf hazards has become a major trouble facing the integrated resource coal mines in China.

Aimed at coal mine goaf hazards, much research has been carried out on the instability mechanism of goaf pillars and roofs (Liu et al., 2014; Wang et al., 2008; Zhang et al., 2008), geophysical detection technology (Li et al., 2011b; Liu et al., 2012), and comprehensive prevention and control technologies (Li, 2011a; Li et al., 2014; Li W and Li J, 2015; Zhang et al., 2013) in coal mine goafs. However, there is a lack of systematic analysis concerning the goaf types, characteristics, detection, and control technologies. Based on the analysis of goaf hazard

types and characteristics, hazard detection and comprehensive control technologies are systematically put forward. The available technologies include the goaf hazard detection technologies which combine ground surveys with undermine detection; the goaf risk classification and assessment technologies combined with qualitative and quantitative risk degree classification evaluation; the goaf hazard monitoring technologies which combine local and regional monitoring with joint monitoring undermine and on the surface; the control technologies which combine open stripe grouting with roof caving on the surface or undermine; and the goaf safety guarantee technologies which combine matching funds and policy support with administrative supervision. The present study aims to construct a system and framework for the hazard detection and comprehensive control technologies of the integrated resource coal mine goafs in China.

2. MAIN TYPES OF INTEGRATED RESOURCE COAL MINE GOAF HAZARDS IN CHINA

According to the statistics of State Administration of Coal Mine Safety in China, since the year 2000, there have been 103 accidents of coal mines goaf hazards in integrated resource coal mines. Based on the complex geological conditions, the goaf hazards were divided into four types according to the hazard forms. These four types are comprised of the abandoned old goafs or permeable pit shafts, goaf fires including coal combustion and gas explosions, the poisonous and harmful gas in goaf emissions, and the abnormal geological disasters, including goaf collapse, ground subsidence, and mine earthquakes induced by sudden large-scale goaf collapse.

Statistics show that the total number of abandoned old goaf or permeable pit shaft accidents is the largest, accounting for 61% of all accidents. Roof limestone water is responsible for 44.4% of abandoned old goaf water disasters. Roof aquifer waters, including roof sandstone water and roof limestone water are the main waters filling the goafs.

3. CHARACTERISTICS OF INTEGRATED RESOURCE COAL MINE GOAF HAZARDS IN CHINA

There are four characteristics of integrate resource coal mine goaf hazards in China.

Firstly, the distribution of abandoned old goafs is unknown due to disorderly exploitation and lost historical mining data. The goafs have become a major security risk.

Secondly, the goafs have different kinds of hazard types. The occurrence of accidents in coal mine goafs is the result of the combined action of mining, geology, and management. In addition, the goaf hazards may be triggered by other hazard types, such as water or fire hazards.

Thirdly, the goafs are concealed and accidents happen suddenly. Generally speaking, unless the surface collapses or cracks, there is underground dynamic mine pressure, abnormal gas concentration, or water inrush, the goaf hazards are often difficult to find. Once they occur, they are difficult to control.

Fourthly, goaf hazards are unpredictable. Because of the different geological and mining conditions, the occurrence of goaf accidents are not regular, and are difficult to predict. In recent years, some coal mine groups and research institutes have carried out related research, but the prediction of goaf hazards is still in the exploration stage.

4. DETECTION TECHNOLOGIES OF INTEGRATED RESOURCE COAL MINES GOAFS HAZARD

The analysis of 103 cases of coal mine goaf accidents showed that most of the accidents were induced by unknown abandoned old goafs. The detection technologies were limited and proper safety management was not in place.

In recent years, cities in Midwest China such as Ordos City, Yulin City, Linfen City, and Jincheng City have carried out coal mine goaf detection work within the scope of whole cities, and have achieved remarkable results. These practical experiences provide reference for the integrated resource coal mine goaf prevention and control.

4.1 Ground survey

Most of the integrated resource coal mine goafs cannot be reached. Ground surveys are the most suitable method to adapt underground advanced geological detection or drilling methods in lanes near abandoned goafs. Ground survey includes field reconnaissance and surveying, geophysical ground detection, and ground drilling. The work process involves data collection and analysis, exchanging with coal mine technical personnel, field reconnaissance and surveys (including remote sensing geological surveys), range determination, geological detection methods and scheme design, data acquisition, data processing and interpretation, drilling verification and data reinterpretation, report preparation, return visits to the results, revising reports, and the final report submission.

The main methods for goaf geophysical ground detection are the shallow seismic method, the high density resistivity method, the controlled source audio frequency magnetotelluric method, and the Eh4 magnetotelluric method.

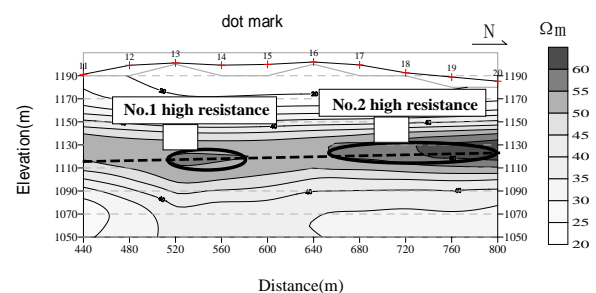


Figure 1: The typical apparent resistivity comprehensive profile including goafs.

The typical apparent resistivity comprehensive profile including goafs is shown in Figure 1. The darker color indicates higher resistivity. Between the distances of 510m to 590m and 650m to 800m, there are two higher apparent resistivity regions from

which the presence of old abandoned goafs were deduced. They were verified by drilling boreholes.

4.2 Undermine detection

For integrated resource coal mines, especially those that are threatened by water inrush hazards, it is recommended to adapt the principles of 'forecasting in advance, detection before tunneling or mining'. Undermine detection includes undermine drilling detection, geophysical detection, and geochemical detection. Undermine drilling detection is the conventional method, while geochemical detection is often used to detect water quality or source when water inrush hazards may happen. Undermine geophysical detection involves advanced detection in tunnels, inner working face detection, as well as roof and floor detection.

Advanced detection in tunnels is mainly used in the detection of abandoned goafs and their water distribution, fault, collapse columns, or other abnormal structures in front of tunnel. Conventional geophysical detection methods are the mine transient electromagnetic method, the mine DC resistivity method, the mine seismic method including the Rayleigh wave method, and the reflected wave method.

The typical apparent resistivity comprehensive profile of advanced detection in tunnels is shown in Figure 2. The blue color indicates lower resistivity. In front of the left tunnel about 60m from the tunnel face there exists a lower resistivity region, from which water bearing goafs were deduced. The water in the lower resistivity region was later drained.

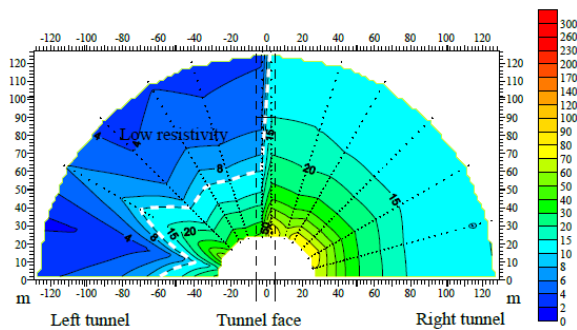


Figure 2: The typical apparent resistivity comprehensive profile of advanced detection in tunnel.

Inner working face detection is mainly used in the detection of fault, collapse columns, or other water bearing structures in the working face. The conventional geophysical detection methods are the mine DC electric perspective methods (including audio frequency electric perspective method and resistivity CT method), the radio wave perspective or

CT methods, the mine reflected wave method, and the mine channel wave seismic method.

Roof and floor detection is mainly used in the detection of aquifers, impermeable layers, water conducting passages, limestone karst and its development, faults in the roof and floor, and fracture development zones. The conventional geophysical detection methods are the mine transient electromagnetic method, the electrical sounding and electrical section methods, the high-density resistivity method, and the mine reflected wave method or transmission wave method.

5. COMPREHENSIVE PREVENTION AND CONTROL TECHNOLOGIES FOR INTEGRATED RESOURCE COAL MINE GOAF HAZARDS

Based on extensive practice, the principles for the comprehensive prevention and control of integrated resource coal mine goaf hazards were summarized and put forward, including ground surveys in advance, undermine detection follow up, hazard assessment and evaluation, in-place monitoring and supervising, comprehensive control for hazard reduction, and guarantees of safety measures.

5.1 Goaf hazard assessment and evaluation

With changes in the ecological environment of coal mines, mining conditions, mining methods, and intensity, goaf hazards have become a dynamic process. It is important to carry out risk grading classification and assessment, qualitative evaluation, and quantitative evaluation of goaf hazards.

The qualitative evaluation of goaf hazards mainly includes the Safety Checklist Analysis Method, the Accident Tree Analysis Method, the Event Tree Analysis Method, and the Preliminary Hazard Analysis Method. The quantitative evaluation of goaf hazards mainly includes the Fuzzy Comprehensive Evaluation Method, the Analytic Hierarchy Process Method, and the Index Classification Method. The Index Classification Method is often used to determine the impact of various mining and geological factors and establish a risk classification index.

For example, There are 20 influence factors for old abandoned goafs in Shendong mining area. They are mining height, dip angle of coal seam, buried depth of goafs, fault distribution near goafs, uniaxial compressive strength of overlying rock and coal pillars, principal stress differences between maximum and minimum, the direction of ground stress, the accumulation of water in goafs, spontaneous combustion in goafs, goaf area, the ratio

between coal pillar width and height, the ratio between mined and remained, the conditions of roof control, ground subsidence conditions, the goaf seal conditions, the surrounding coal seam mining conditions, whether the goafs instability events happened or not, the distribution of surface buildings above goafs, and the remain time of goafs.

The Index Classification Method is used to comprehensively assess the risk of old abandoned goafs in Shendong mining area. The Index W is listed in formula as follows,

$$W = \frac{\sum_{i=1}^n G_i}{\sum_{i=1}^n G_{i_{max}}} \quad (1)$$

In formula (1), $G_{i_{max}}$ represents the maximum rating value of number i influence factor, G_i represents the actual rating value of number i influence factor, and n represents the number of influence factors.

Five risk grading classification was divided as Grade I risk (especially significant risk, $W \geq 0.85$), Grade II risk (significant risk, $0.75 \leq W < 0.85$), Grade III risk (greater risk, $0.65 \leq W < 0.75$), Grade IV risk (general risk, $0.50 \leq W < 0.65$), Grade V risk (less risk or no risk, $W < 0.50$). 154 old abandoned goafs were assessed using the Index Classification Evaluation System in Shendong Mining area. The results are shown in Table 1.

Table 1: The risk assessment results of old abandoned goafs in Shendong mining area.

Coal mine name	Goafs num.	Grade				
		I	II	III	IV	V
DALIUTA	39	0	0	1	38	0
SHANGWA	7	0	1	3	3	0
HALAGOU	8	0	0	5	3	0
WULANMULUN	12	0	0	0	12	0
BULIANTA	10	0	0	0	10	0
SHIGETAI	7	0	0	1	6	0
LIUTA	9	0	0	5	4	0
CUNCAOTA1	2	0	0	0	2	0
CUNCAOTA2	8	0	1	0	6	1
YUJIALIANG	48	0	0	3	45	0
BAODE	4	0	0	1	3	0
Total	154	0	2	19	132	1

5.2 Monitoring and supervisory technologies of goafs

The monitoring and supervisory systems of goafs are far from established in normal coal mines, besides lots of monitoring equipment being installed within some advanced coal corporations in China. The

monitoring currently involves the displacement monitoring of overlying strata destruction, the surface subsidence monitoring, and the monitoring of coal pillar stability. The goaf monitoring systems may borrow the experiences of seismic network layout for rock burst monitoring, develop micro-seismic monitoring technology, automatic monitoring technology of internal displacement of rock mass, and temperature on-line monitoring technology.

A set of monitoring systems was developed in the Shendong mining area involving micro-seismic monitoring, working face pressure monitoring, borehole stress monitoring, rock mass internal displacement monitoring, ground borehole television watching, and surface displacement monitoring, which all provided basic research for dynamic pressure control when mining under room and pillar goafs. In addition, borehole seismic technology was introduced for overburden failure monitoring of goafs in Yitai Coal Group.

The comprehensive monitoring system of goafs is shown in Figure 3.

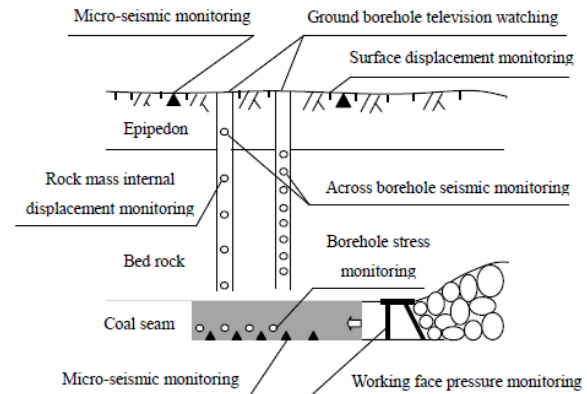


Figure 3: The comprehensive monitoring system of goafs.

5.3 Comprehensive control technologies of goafs

For abandoned old goafs or permeable pit shafts, goaf fires including coal combustion and gas explosion, and poisonous and harmful gases in goaf emissions, ground surveys and undermine detection should be carried out. The design of water drainage, ventilation, and fire control should then be put forward. Finally, special measures should be made according to the goaf hazard types and degree.

For the abnormal geological hazards including goaf collapse, ground subsidence, mine earthquakes induced by sudden large-scale goaf collapse, the open stripe is adopted where there are no important buildings on the surface of the goaf and the buried depth is less than 100m. In addition, the grouting method is often adopted where there exists important buildings, and the roof caving method is adopted

where the goaf recovery rate is more than 40% and the coal beneath the goaf needs to be mined.

5.4 safety measures for guarantee of goafs

The safety technologies mainly involve matching funds, policy support, and administrative supervision.

First of all, the matching of funds by the government or coal groups should be implemented. Secondly, goaf detection, prevention and control should be supported by the state, provincial, and industrial policy. Thirdly, administrative supervision by the government and the coal industry is an important link in preventing goaf hazards. In addition, technical measures are another fundamental guarantee of safety.

6. CONCLUSIONS

China faces a long and hard process in the prevention and control of integrated resource coal mine goaf hazards, because goafs have the characteristics of unknown distribution, different kinds of hazard types, concealment, and unpredictability. The following control principles should be implemented: ground surveys in advance, undermine detection as a follow up, hazard assessment and evaluation in time, monitoring and supervising in place, comprehensive control for hazard reduction, and guaranteed safety measures.

7. ACKNOWLEDGEMENT

The study was supported by National Natural Science Foundation of China (51304117), Science Development Foundation of China Coal Technology & Engineering Group Corp (2014QN013), Innovation Foundation of China Coal Research Institute (2014JC07).

8. REFERENCES

- Li C.Q and Yao X. (2004). The theoretical study and application of a new technique for the treatment of mined-out area. *Gold*. Volume 25, No. 3, pp. 22-25.
- Li W. (2011). Risk Assessment of Room Method Goafs Instability. *China Safety Science Journal*. Volume 21, No. 3, pp. 95-100.
- Li W, Mu Y, Zhang J.Y and Xu Y.J. (2011). Optimization of surface detection technology and method of mine goafs. *Coal Science and Technology*. Volume 39, No. 1, pp. 102-106.
- Li W, Zhang B and Bi Z.W. (2014). Isolation roof caving control and monitoring technology of room and pillar method goafs. 2014 ISRM European Rock Mechanics Symposium (EUROCK 2014), Rock Engineering and Rock Mechanics: Structures in and on Rock Masses, London: Taylor and Francis Group. pp. 931-936.

Li W and Li J. (2015). Coaf disaster characteristics of resource integration coal mines and their control countermeasures. *Safety in Coal Mines*. Volume 46, No. 7, pp. 179-181,185.

Liu C.Y, Yang J.X, Yu B, etc. (2014). Destabilization regularity of hard thick roof group under the multi gob. *Journal of China Coal Society*. Volume 39, No. 3, pp. 395-403.

Liu R.T, Li W and Ma H.S. (2012). Field investigation and surface detection techniques of abandoned coal mine goafs. *Cai(ed.) Rock Mechanics: Achievements and Ambitions*. Taylor & Francis Group. pp. 27-30.

Wang J.A, Shang X.C, Liu H, etc. (2008). Study on fracture mechanism and catastrophic collapse of strong roof strata above the mined area. *Journal of China Coal Society*. Volume 33, No. 8, pp. 850-855.

Zhang J.Y. (2008). The laws of overlying strata influenced by newly increased load on the surface above worked-out area. *Journal of China Coal*. Volume 33, No. 2, pp. 166-170.

Zhang J.Y, Wang H.F, Zhang B, etc. (2013). Exploration of mining goaf and comprehensive control technology of safety hidden dangers. *Coal Science and Technology*. Volume 41, No. 10, pp. 76-80.

Multi-bed type oxidation reactor applied to the coal mine ventilation air methane

Weifeng Zou^{a,b,*}, Bo Lan^{a,b}, Jiandong Kang^{a,b}

^a Key Laboratory of Low-grade Energy Utilization Technologies & Systems of Ministry of Education, College of Power Engineering, Chongqing University, Chongqing, China, 400044

^b Chongqing Research Institute Co.,Ltd. of China Coal Technology & Engineering Group, Chongqing, China, 400037

ABSTRACT

The utilization of coal mine ventilation air methane plays an important role in saving energy, reducing pollution, improving the safety in coal mine production, and adjusting the energy structure. The thermal flow-reversal reactor is one of the main technologies of ventilation air methane utilization which is at a critical stage of industrial application. The thermal flow-reversal reactor of MEGTEC company and those designed by some Chinese scholars generally use a two-bed type. The gas that is detained in the oxidation chamber and reversal valves will not enter the combustion chamber, but through the chimney directly into the atmosphere when switching the flow direction, the average oxidation rate of the reactor will be reduced due to the residual gas.

In order to solve the problems including low oxidation rate of methane, pressure build-up of the main fan, and high failure rate of valves in existing two-bed type oxidation reactor of coal mine ventilation air methane, an innovative structure with multi-bed type oxidation reactor has been designed. The paper analyzes the unique advantages of the multi-bed type oxidation reactor by elaborating on the working principles of three-bed and five-bed type device. In the design of the oxidation device for industrial demonstration projects, the device whose processing capacity is 100,000 m³/h adopts the five-bed type structure from the aspects of methane oxidation rate, waste heat utilization effect, cost, etc. The thermodynamic calculation process of regenerative chambers as the core unit of the oxidation device is described in this paper.

The technology has an industrial demonstration project whose reactor uses a five-bed type design located in Chongqing Songzao Datong No.1 mine. This project can produce 64800 t of superheated steam and reduce emissions of CO₂ equivalent to 107000 t annually, and therefore has excellent energy-saving and emission reduction benefits.

KEYWORDS: multi-bed type; coal mine ventilation air methane; thermal flow-reversal oxidation; industrial application

1. INTRODUCTION

Coal bed methane is a kind of clean and efficient energy which is one of the rising unconventional natural gases in recent years. The ventilation air methane (VAM) accounts for about 60% of total methane emissions from coal mines, and its utilization plays an important role in saving energy, reducing pollution, improving the safety in coal mine production, and adjusting the energy structure (Gosiewski et al., 2009). However, the development of the utilization technology is restricted by factors such as low concentration, large air volume and instability of ventilation air methane. The thermal flow-reversal reactor (TFRR) is one of the main technologies of VAM utilization which is at a critical stage of industrial application. The small thermal oxidation device has a processing capacity of 1000 m³/h and was designed by Zheng. It uses a two-bed horizontal type (Zheng et al., 2009). The methane

oxidation rate is slightly higher than 95% of this device. The thermal oxidation device with a maximum processing capacity of 1000 m³/h was designed by Lv. It also uses a two-bed horizontal type (Lv et al., 2011). The device should be operated steadily when the flow is in the range of 400-800 m³/h and the concentration of methane is in the range of 0.5%-0.8%. The thermal oxidation device has a maximum processing capacity of 500 m³/h and was designed by Wang. It uses a two-bed vertical type and some experimental studies are carried out based on this device (Wang et al., 2012). The MEGTEC Company whose oxidation device uses a two-bed vertical type also is the most representative of this technology abroad. It has been found that the current oxidation device of VAM on the regenerative chamber structure is generally a two-bed type. However, the gas that was detained in the oxidation chamber and reversal valves will not enter the

* Corresponding author – email: zwf_cqmky@163.com

combustion chamber but goes through the chimney into the atmosphere directly when switching the flow direction, so the average oxidation rate of the reactor will be reduced due to the residual gas (Kang et al., 2015). To solve this problem, this paper puts forward the design idea of the multi-bed type for the structure of thermal flow-reversal reactors.

2. THE NECESSITY OF DEVELOPING THE MULTI-BED REGENERATIVE OXIDATION REACTOR

2.1 Working principle of two-bed type regenerative oxidation reactor

For a two-bed type oxidation reactor, there are two combustion chambers, one as the inlet and the other as the outlet of mixed gas. After the reactor is heat-actuated, the VAM flows at ambient temperature from the low temperature side (e.g., chamber 1) into the regenerative chamber, then is heated, oxidized and released as thermal energy. The released energy during methane oxidation is recovered by ceramic as the gas moves to the outlet side of the chamber. This process is often referred to as the upper half cycle of the circulating operation. At this time, chamber 1 is in the thermal release stage and chamber 2 is in the thermal storage stage. The direction of VAM flow should be switched and the reversed process carried out, and the system should be auto-thermal operational with continuous transformation between two chambers at high temperature and low temperature.

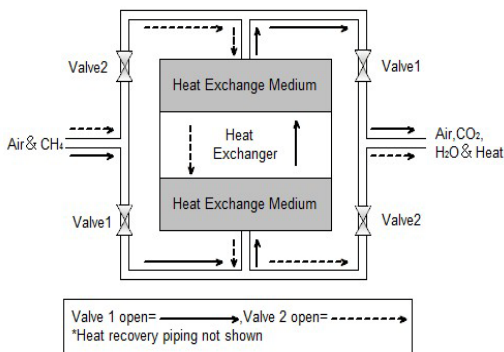


Figure 1: Schematic of two-bed type TFRR.

2.2 Disadvantages of two-bed type TFRR

Chongqing Research Institute of China Coal Technology & Engineering Group independently developed a small test device of TFRR with a processing capacity of 1000 m³/h during the 11th Five-Year Plan period of China, named Low Concentration Coal Bed Methane Utilization Technology and Equipment which belongs to the

National Science and Technology Major Project. A lot of studies have been carried out based on the utilization system of coal mine ventilation air methane. The experimental system is shown in Figure 2.



Figure 2: Diagram of two-bed type TFRR experimental system.

The two-bed type thermal flow-reversal reactor has some inevitable disadvantages due to structure, as follows.

- There will be a large fluctuation of the gas flow rate from the total intake to zero when switching the flow direction, so that the main fan will be suppressed and its life will be affected.
- The flue gas flow rate of the waste heat boiler will periodically fluctuate, which may affect the quality of the superheated steam in the use of waste heat.
- The large size of valves results in a large force being required for action and failure rate will be high.
- The gas distribution in the regenerative chamber and the combustion chamber is not uniform and it is not conducive to the oxidation of methane in VAM because of the large cross section of the regenerative chamber.
- The gas who was detained in the oxidation chamber and reversal valves will not enter the combustion chamber but go through the chimney into the atmosphere directly when switching the flow direction, so the average oxidation rate of reactor can only reach 95% due to the residual gas.

3. WORKING PRINCIPLE OF MULTI-BED TYPE TFRR

The core idea of multi-bed regenerative oxidation reactors is to add some regenerative chambers for oxidizing the methane in VAM, and also to add a regenerative chamber whose main function is sweeping. For a three-bed type oxidation reactor, as shown in Figure 3, there are three regenerative chambers, one as the inlet, one as the outlet of mixed gas, and another as the inlet of sweeping gas. For a five-bed type oxidation reactor,

as shown in Figure 4, there are five regenerative chambers, two as the inlet, two as the outlet of mixed gas, and another as the inlet of sweeping gas. The data in Table 1 uses the five-bed type oxidation reactor as an example. A complete working cycle consists of five cycles, where each regenerative chamber periodically switches between the three stages of thermal storage, sweeping, and thermal release.

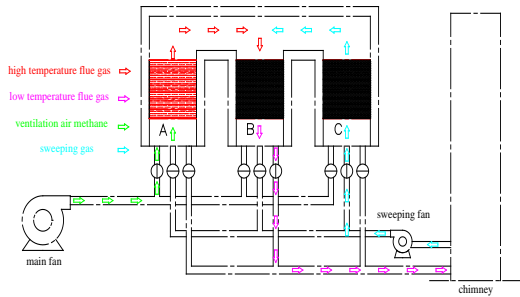


Figure 3: Structure schematic diagram of three-bed type TFRR.

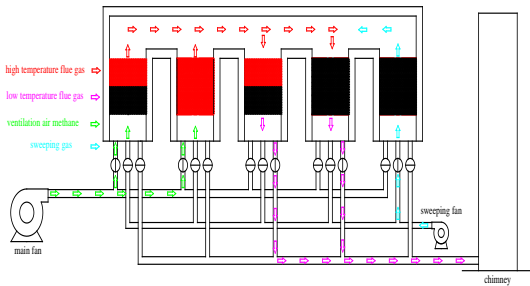


Figure 4: Structure schematic diagram of five-bed type TFRR.

Table 1: Work process of five-bed type TFRR.

No.	Bed 1	Bed 2	Bed 3	Bed 4	Bed 5
Cycle 1	a	a	b	b	c
Cycle 2	c	a	a	b	b
Cycle 3	b	c	a	a	b
Cycle 4	b	b	c	a	a
Cycle 5	a	b	b	c	a

Note: a. thermal storage, b. thermal release, c. sweeping

The present study also considered the situation of increasing the number of bed on the basis of the five-bed type oxidation reactor. The numerical simulation and theoretical calculation of the seven-bed and nine-bed type oxidation reactor were carried out. It was found that there would need to be a large number of valves due to the increase of the oxidation beds. The control of oxidation reactors is very complex and not conducive to its stable operation. In addition, the cost will increase and the economical profits will be

reduced. Therefore, the so-called multi-bed type of TFRR in industrial applications usually refers to the three-bed or five-bed type devices.

4. ADVANTAGES OF MULTI-BED TYPE TFRR

Compared with the two-bed type oxidation reactor, the multi-bed type oxidation reactor has the following advantages:

a. There are more than two chambers in the multi-bed type oxidation reactor and one of them is designed to sweep the detained gas. The methane in VAM is not oxidized and distributed between the reversal valves and regenerative chamber to the combustion chamber in the traditional structure of the oxidation reactor when the flow direction is switched, so it avoids discharging into the atmosphere directly.

b. The cross-sectional area of the oxidation chamber should be decreased, and its gas distribution is more uniform due to the smaller processing capacity of a single chamber of the multi-bed type oxidation reactor. This avoids the non-uniform distribution of gas in traditional oxidation reactors which should oxidize the larger flow rate of mixed gas.

c. The working state should be changed from intake to sweep in only one chamber of the inlet chambers, and the rest of the inlet chambers remain unchanged when switching the flow direction. The gas flow rate is less, and the effect of waste heat utilization is better.

5. INDUSTRIAL APPLICATION OF MULTI-BED TYPE TFRR

5.1 Selection of industrial device

An industrial demonstration project will be established in the 12th Five-Year Major Project (Direct use technology of low concentration coal bed methane) as a continuation of the research tasks of 11th Five-Year Major Project of China. Based on the summary of the application, the industrial device whose processing capacity is 100000 m³/h will be intended to adopt a multi-bed type structure design.

The results obtained by calculating and analyzing the parameters of two-bed, three-bed, and five-bed type structures according to the design and calculation method of the regenerative heat exchanger are shown in Table 2. The industrial device whose processing capacity is 100000 m³/h adopted the five-bed type structure from the aspects of methane oxidation rate, waste heat utilization effect, cost, etc.

Table 2: Comparison of different structure types.

	two-bed type	Three-bed type	Five-bed type
Single cross-sectional area of regenerative chamber (m ²)	4×5.5=22	4×5.5=22	4×2.95=11.8
Single volume of regenerative chamber (m ³)	46	46	23
Total volume of regenerative chamber (m ³)	92	138	115
Volume of heat preservation material (m ³)	107	145	177
Device size(m³)	14.4×4.7×8	18.6×4.7×8	18.45×4.7×8
Reversing valves	DN1300	DN1300	DN1000
Number of reversing valves	4	6	10
Number of sweeping valves	0	3	5
Cost of regenerative chamber (RMB, Million Yuan)	110.4	165.6	138
Cost of valves (RMB, Million Yuan)	60	99	95
Cost of heat preservation material (RMB, Million Yuan)	53.5	72.5	88.5
Total cost (RMB, Million Yuan)	223.9	337.1	321.5
oxidation rate of methane	95%	98%	98%

5.2 Design of industrial device

The thermal flow-reversal reactor of coal mine ventilation air methane is a precise and complex system. The whole device is composed of the regenerative chambers, combustion chambers, some valves, and so on. As the core part of the device, the regenerative chamber is the cornerstone in the course of whole device design. The heat exchange area, the volume, and the size of the regenerative chamber are calculated according to the design method of the regenerative heat exchanger. The thermodynamic calculation process is as follows:

- a. The heat (Q) required for VAM in a cycle of flow reversal

$$Q = V_f (c_f' t_f'' - c_f' t_f') \tau_h \quad (1)$$

Where: V_f is the flow rate of VAM that be heated, m³/s.

c_f', c_f'' are the inlet and outlet specific heat of VAM, J/(kg·K).

t_f', t_f'' are the inlet and outlet temperature of VAM, °C

τ_h is the duration of VAM for heating, s.

- b. The flue gas outlet temperature(t_y'') of regenerative chamber

$$t_y'' = \frac{1}{c_y''} \left(c_y' t_y' - \frac{Q}{V_y \tau_y \eta} \right) \quad (2)$$

Where: V_y is the flow rate of flue gas, m³/s.

c_y', c_y'' are the inlet and outlet specific heat of flue gas, J/(kg·K);

t_y' is the inlet temperature of flue gas, °C

τ_y is the duration of flue gas for cooling, s.

η is the heat efficiency of regenerative chamber, $\eta = 0.9 \sim 0.95$.

- c. The logarithmic mean temperature difference (Δt)

$$\Delta t = \frac{\Delta t_{\max} - \Delta t_{\min}}{\ln \Delta t_{\max} / \Delta t_{\min}} \quad (3)$$

Where: $\Delta t_{\max} = t_y' - t_f''$, $\Delta t_{\min} = t_y'' - t_f'$.

- d. The convection heat transfer coefficient (α)

$$\alpha = 7.5 \phi \frac{W^{0.5}}{de^{0.33}} \quad (4)$$

Where: $\phi = 0.184T^{0.25}$, the temperature correction factor, T is temperature, K.

de is the equivalent diameter of honeycomb ceramic, m.

W is the velocity of flow at the minimum cross section, m/s.

- e. The integrated heat exchange coefficient (K)

$$K = \frac{\left[\frac{1}{\alpha_y \tau_y} + \frac{1}{\alpha_f \tau_f} + \frac{S}{6\lambda} (1/\tau_y + 1/\tau_f) \right]^{-1}}{(\tau_y + \tau_f)} \quad (5)$$

Where: S is the thickness of honeycomb ceramic, m.

α_f, α_y are the convection heat transfer coefficient of VAM-side and flue gas-side, W/(m²·K).

λ is the thermal conductivity of honeycomb ceramic, W/(m·K).

- f. The heat exchange area of a regenerative chamber (A)

$$A = \frac{Q}{K \Delta t \eta (\tau_y + \tau_f)} \quad (6)$$

- g. The volume of a regenerative chamber (V)

$$V = \frac{A}{a_v} \quad (7)$$

Where: a_v is the specific surface area of honeycomb ceramic, m^2/m^3 .

h. The horizontal cross-sectional area of a regenerative chamber (F)

$$F = \frac{V_f}{W_f \sigma} \quad (8)$$

Where: W_f is the velocity of VAM, m/s.

i. The height of regenerative chamber (H)

$$H = \frac{V}{F} \quad (9)$$

According to the calculation formulas above, the basic parameters of the industrial device (processing capacity of VAM is 100000 m^3/h) are given and the FORTRAN software are used for thermodynamic calculations. The related parameters and calculation results are shown in Table 3.

Table 3: Parameters and thermodynamic calculation results.

No.	Items	Units	Numerical values
1	VAM Processing capacity of single oxidation bed	m^3/h	50000
2	Inlet temperature of VAM	$^{\circ}C$	20
3	Outlet temperature of VAM	$^{\circ}C$	787
4	Flow rate of flue gas	m^3/h	50000
5	Inlet temperature of flue gas	$^{\circ}C$	900
6	Outlet temperature of flue gas	$^{\circ}C$	60
7	Heat loss coefficient	%	5.0
8	Logarithmic mean temperature difference	$^{\circ}C$	70
9	Duration of the cycle of flow reversal	min	3
10	Volume of honeycomb ceramic	m^3	23.35
11	Circulation cross-sectional area	m^2	11.12
12	Height of honeycomb ceramic	m	2.1
13	Total volume of honeycomb ceramic	m^3	116.75
14	Size of regenerative chambers	$m \times m \times m$	18.45m \times 4.7m \times 2.6m
15	Velocity of VAM	m/s	1.86

In this point, it is necessary to point out that the parameters obtained such as the height of the honeycomb ceramic and the circulation cross-sectional area are based on the determined parameters and structure of the honeycomb ceramic. In this paper, the selection of honeycomb ceramic and its layout principles are omitted, see Figure 5.

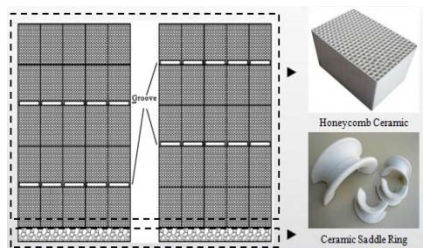
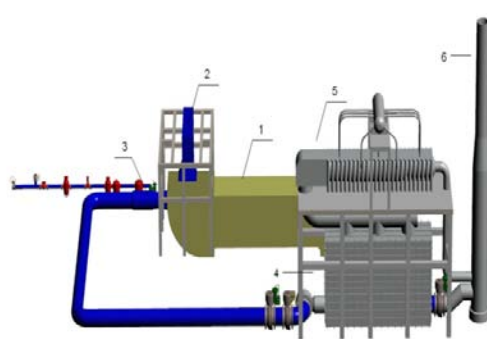


Figure 5: Schematic diagram of ceramic's layout.

5.3 Industrial demonstration project

The industrialization of this utilization technology is promoted through the establishment of the industrial demonstration project of the VAM. Some industrial tests were carried out about the industrial demonstration system in which the reactor uses a five-bed type design in Chongqing Songzao Datong No.1 mine, to investigate the effect of collecting cover, test the methane oxidation rate of

the reactor, test the technology of steam produced by waste heat, and to improve and perfect the industrial device according to the test results.



1. Diffusing tower. 2. VAM collecting cover. 3. Mixer. 4. TFRR. 5. Waste heat boiler. 6. Chimney.
Figure 6: Schematic diagram of industrial demonstration system for VAM utilization.

The whole system is composed of the VAM collecting and mixing system, regenerative oxidation reactor, the waste heat utilization system, and the monitoring system, as shown in Figure 6. The ventilation air methane is exhausted from the ventilating shaft and sent into the pipeline after collection by the collecting cover, then brought into

the oxidation reactor by induced-draft fan. The methane in VAM is heated and oxidized and the oxidation products such as CO_2 and H_2O (water vapor) are discharged into the atmosphere. The burner in the combustion chamber will burn diesel oil to preheat the regenerative ceramic for starting the reactor. In the test of waste heat utilization the drainage gas is mixed with VAM in order to make the volume fraction of methane reach 1%, and take part of the high temperature flue gas to the boiler, to produce superheated steam.



Figure 7: Scene diagram of industrial demonstration project.

The construction of the demonstration project was completed in October 2015 at which point the system was debugged. It is estimated that when it is put into operation, it will produce 64800 t of superheated steam and reduce emissions of CO_2 equivalent to 107000 t annually, and therefore has excellent energy-saving and emission reduction benefits.

6. CONCLUSIONS

a. Through the introduction of working principles of the traditional two-bed type oxidation reactor, it is found that this type of reactor has some disadvantages including low oxidation rate of methane, pressure build-up of the main fan, and the high failure rate of valves.

b. In view of the design idea for a multi-bed type oxidation reactor, their unique advantages are pointed out by comparing with the two-bed type oxidation reactor.

c. By calculating and analyzing the parameters of two-bed, three-bed, and five-bed type structures, the industrial oxidation reactor whose processing capacity is $100000 \text{ m}^3/\text{h}$ adopted the five-bed type structure design, and according to the design and calculation method of the regenerative heat exchanger, the thermodynamic calculation process and results of regenerative chamber were introduced.

d. When the demonstration project located in Chongqing Songzao Datong No.1 mine is put into operation, it will produce 64800 t of superheated steam and reduce emissions of CO_2 equivalent to

107000 t annually, and therefore has excellent energy-saving and emission reduction benefits.

7. ACKNOWLEDGEMENT

This study was financially supported by National Science and Technology Major Project of China (2011ZX05041-005).

8. References

Deng, H.X., Xiao, Q. and Xiao, Y.H. (2014). Design method of thermal flow-reversal reactor for ventilation air methane based on regenerative heat exchange model. *Journal of China Coal Society*, Volume 39, No. 7, pp. 1302–1308.

Feng, T., Wang, P.F. and Hao, X.L. (2012). Experimental study on thermal flow-reversal oxidation of coal mine ventilation air low concentration methane. *China Safety Science Journal*, Volume 22, No. 10, pp. 88–93.

Gosiewski, K. and Warmuzinski, K. (2007). Effect of the mode of heat withdrawal on the asymmetry of temperature profiles in reverse-flow reactors. *Catalytic combustion of methane as a test case. Chemical Engineering Science*, Volume 62, pp. 2679–2689.

Gosiewski, K., Pawlaczyk, A. and Warmuzinski, K. (2009). A study on thermal combustion of lean methane-air mixtures: simplified reaction mechanism and kinetic equations. *Chemical Engineering Journal*, Volume 154, pp. 9–16.

Kang, J.D., Lan, B. and Zou, W.F. (2015). Design and application on five-bed type thermal accumulation oxidized device of mine ventilation air methane. *Coal Science and Technology*, Volume 43, No. 2, pp. 136–139.

Lv, Y., Jiang, F. and Xiao, Y.H. (2011). Experimental study of coal mine ventilation methane oxidization. *Journal of China Coal Society*, Volume 36, No. 6, pp. 973–977.

Wang, P.F. (2012). Study on theory and experiment of thermal flow-reversal oxidation of coal mine ventilation air methane. Central South University, Hunan, China.

Xiao, Q., Deng, H.X. and Lv, Y. (2012). Lean methane-air premixed-gas heating process research. *Journal of Mining & Safety Engineering*, Volume 29, No. 2, pp. 295–300.

Zheng, B., Liu, Y.Q. and Liu, R.X. (2009). Oxidation of coal mine ventilation methane of thermal flow-reversal reactor. *Journal of China Coal Society*, Volume 34, No. 11, pp. 1475–1478.

Zhou, X. (2009). Experiment study of coal mine ventilation air methane oxidation. Institute of Engineering Thermophysics Chinese Academy of Science, Beijing, China.

Water disaster investigation and control in coal mine of Southern China

LIANG Qing-hua

China Coal Technology Engineering Group Chongqing Research Institute, Chongqing, China, 400039

ABSTRACT: The number of coal mines in Southern China was the possession of more than 60% of the total coal. This area was a large undulating terrain, and the terrain was so complex that the exploration was very difficult. The water damage had a great effect on southern mines. They were mainly threatened by the karst water and the goaf water. This thesis was studied through mining geophysics and its methods, which were able to fit the characteristics of karst regions. Using those methods, we could detect and determine the location, size, distribution, and water-filled situation of geological anomalies that was closely related to mineral water disasters. Based on the characteristics of the mine on geology, water damage, mine drainage, this thesis studied the prevention and control measures for coal mine features in southern China to carry out scientific governing for mine water damage.

The number of coal mines in Southern China takes up more than 60% of the total coal. This area is large undulating terrain, and landform was complex, so it was very difficult to explore^[1]. There were greater affected by water damage. They were mainly threatened by limestone karst water and the goaf water. Due to faults or karst pipeline conducts water body, this made a great deal of mine water inflow and high drainage costs, and also often caused water inrush accidents^[2]. It was a great threat to mine safety production. Meanwhile, long time of the small coal mining caused a large number of the formation of shallow goafs^[3]. The area of water accumulation was not clear, which brought great secure risk to the later period of mine^[4,5]. Therefore, the study of exploratory methods to water disasters and governing ways had an important reference significance in China Southern mine.

1. THE SOUTHERN CHINA MINE WATER DISASTER CHARACTERISTICS

There was a large topography of Southern region and a complex landform in China. Southern mine karst water disaster and goaf water disaster had certain regularity^[6].

1) Karst water inrush was the main pipe flow, and it was fast and violent. So the disaster was very strong. In the process of roadway development, it would encounter a variety of karst water, which mainly for cave, collapse column, underground rivers and other pipeline flow.

2) Relationship between the distribution and structure of the cave was close. Caves were often interlinked with underground rivers, the surface of rivers, and even other aquifers. Distribution between

caves was also closely related to the structure of stratigraphy.

3) Goaf water scope was unclear, and the goaf water inrush was generally rapid. Due to more mountains in the south of China, mine production capacity was small. Because of a shortage of funds, most of mines were not equipped with the necessary geophysical and geochemical exploration means, the power of prevention and control water was relatively weak.

2. THE MINING EXPLORATION METHODS AND EQUIPMENT IN SOUTHERN CHINA

For example, in the mining area of Zunyi, mine water disaster exploration, based on caves, underground rivers and goafs, was the main target of probe. According to various geophysical methods and applicable results of hydro geological exploration in the Southern mine, we chose three karst hydro-geology geophysical methods that were ground transient electromagnetic method (TEM), underground geological radar (GPR) and mining transient electromagnetic method (TEM). Our exploration approaches were mainly hydro-geological investigation, ground geophysical, underground geophysical prospecting and drilling.



Figure 1: Southern Coal geophysical and complex terrain construction site

1) Mine hydro-geological investigation: Through the mine hydro-geological investigation in many regions, we mainly found the relationship of the mine among water source, channel, fill, diameter and discharge. Southern mining, which mainly water-filled channel had faults, karst pipeline, goafs, closed poor drilling.

2) Ground geophysical exploration: To enhance the signal of noise ratio and resolution of data collection as the core guiding ideology, taking into account the ground conditions of the Southern mine complex, we mainly chose the V8 multifunctional electrical meter, high-current transient electromagnetic instrument and super high density electric method.

3) Combined with large fixed source of TEM and Large current of TEM, we observed that under the condition of geological and topographical, the large fixed source of TEM had the advantages of high efficiency, high exploration depth, and could penetrate the high resistivity shielding layer. With this method, we could obtain good geological results in guiding water structure and water bearing zone detection.

In the case of poor conditions of terrain, large current of TEM could reduce the power supply coil and the receiving coil in this area. It made the efficiency multiplied in this field. We had achieved good detective results with these two detection methods.

For two examples of Changqing Mine and Lushuidong Mine in Southern China (Figure 2 and Figure 3), the figure fully reflected the region's stratigraphic changes, but also reflected the goaf water situation.

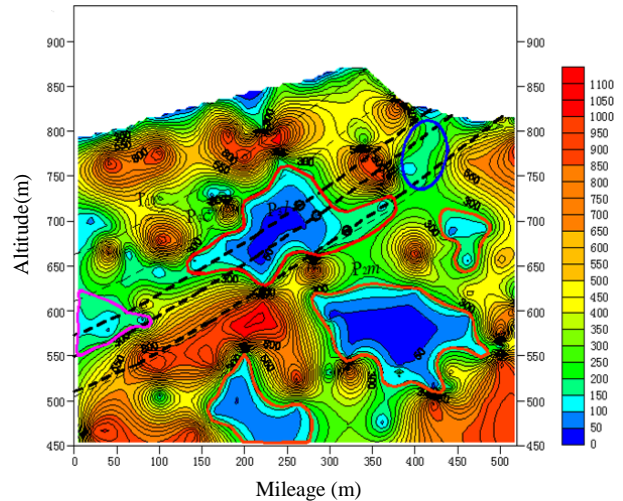


Figure 2: Changqing Mine apparent resistivity contour sectional view

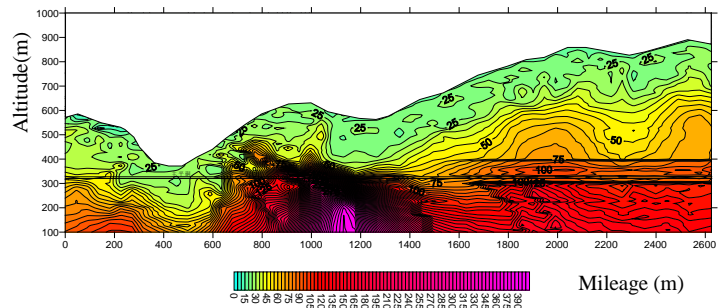


Figure 3: Lushuidong Mine apparent resistivity contour sectional view

4) A good exploration, combined with underground geophysical exploration and geochemical exploration: A variety of geophysical and geochemical exploration was a useful means to complement. Mine of GPR could carry out closely effective detection (30-50m) in front of the tunnel face, mine of TEM could be effectively detected on the water body for remote detection (80-100m), and mine in geochemical exploration was mainly water contented recognition for the goaf.

Considering that there exist 20m blind areas in mine TEM, We need to avoid blind areas in mine detection. After a lot of practice, we adopt the mine TEM tracking detection used as shown in Figure 4. The detection distance is 100m, and the driving distance is 80m; the next cycle reaches 80m to detect. In accordance with such 80m cycle detection, we can avoid blind area. By analyzing TEM response

characteristics of typical water flowing abnormal body, apparent resistivity contour is low resistance in a large scope when goaf or large collapse column is in the water filling conditions, and the continuity of low resistivity anomaly is better.

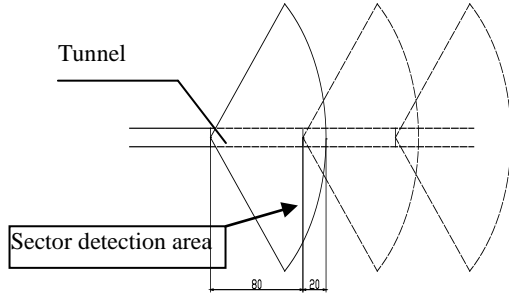


Figure 4: The track layout of sector detection the driving face

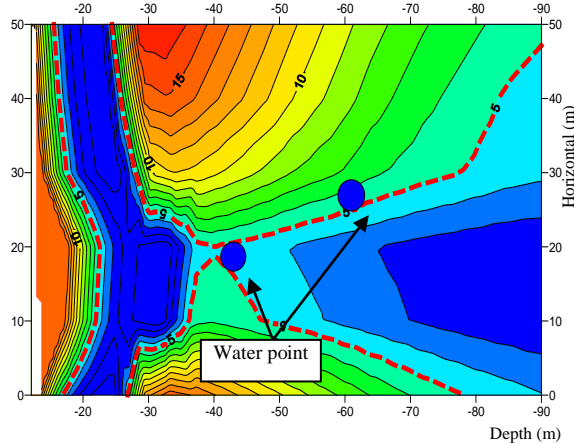


Figure 5: The contour map of apparent resistivity for tunnel detection

On the contrary, there is no blind area of the radar, which can detect continuously. Radar echo reflection method is mainly used for analysis.

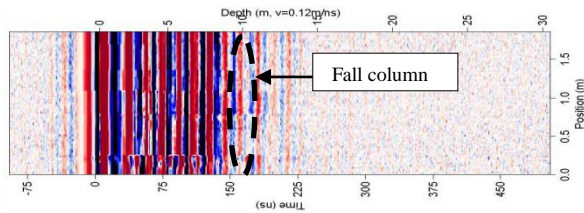


Figure 6: The radar detection results map of 3# coal concentrated track tunnel in coal mine mining area (10.9m fall column boundary)

3. THE COAL MINE WATER DISASTER'S CONTROL METHODS IN SOUTHERN CHINA

The principle of control mine water disaster was "Prevention, plugging, discharge, drainage and cut" in China. According to Southern mining

characteristics of geology, water disaster, mine drainage, combined grouting sealing and interception, we should carry out scientific control of mine water disaster.

1) Karst water drainage

Drainage was the best way to karst water governing. According to the hydro-geological conditions of mine, main methods were used in hydrophobic drilling, hydrophobic tunnel and other projects to carry out drainage.

2) Plugging on water gushing point

When tunnel crossed over the water inrush that threaten collapsed column in karst fracture zone, we should take advance pre-grouting method and ensure mine safety.

3) Drainage for thin coal seam of goaf water

Goaf water range and pressure in hydrocephalus should be clear before drainage. If we weren't sure, we could take geophysical method to identify the scope and the amounts of goaf water. At the same time, we still need to perform the mining policy while probing, to prevent local or other low-lying water.

4) Tests for water disaster treatment effect

For safe's sake, we had examined the effect of treatment on mine water disaster. The main test methods were geophysical exploration and drilling. Geophysical methods of water-rich region, drainage or grouting treatments were used to solve it.

4. EXPERIENCES AND CONCLUSIONS

1) The main method of exploration of the South mine area was transient electromagnetic method (TEM). In the case of flat terrain, TEM with large fixed loop was generally used to detect, and in the case of steep terrain, TEM with large current was generally used to detect. Coal mine detection by TEM and Ground Penetrating Radar (GPR), was combined with drilling, which could solve the water detection.

2) The commonly used method of water disaster governance was adit water gravity in South China coal mine. In the aspect of karst water prevention, drainage was the best way to control. Slip-casting was also a better way for controlling karst water. The control effect of mine water disaster must be inspected. After inspection and safety, the production of work could be carried out.

5. REFERENCES

DONG Shu-ning, et al. (2008). Practical technology and equipment for mine water prevention and control, Coal Science and Technology, Volume 36, No. 3, pp. 8-11.

LIU Zhi-xin. (2008). Study on the distribution and application of mine transient electromagnetic field. China University of Mining and Technology, Xuzhou, pp.35-40.

LIANG Qing-hua, WU Yan-qing, SONG Jin. (2010). Study on the qualitative analysis and application of radio wave tunnel perspective. Journal of Chongqing University(Natural Science Edition), Volume 33, No. 11, pp. 113-118.

YANG Si-Tong, CHENG Jiu-Long. (2012). The method of small structure prediction ahead with Rayleigh channel wave in coal roadway and seismic wave field numerical simulation. Chinese Journal Geophysics, Volume 55, No. 2, pp. 655-662.

LIU Sheng-dong, LIU Jing, YUE Jian-hua. (2014). Development status and key problems of Chinese mining geophysical technology, Journal of China Coal Society, Volume 39, No. 1, pp.19-25.

Wang Dong-wei, et al. (2011). Application of mine transient electromagnetic method to advanced detecting of roadway head. Chinese Journal of Engineering Geophysics, Volume 8, No. 4, pp. 403~407.

WANG Shuang-mei. (2006). Summary of research methods on height of transmissive fracture belt [J]. Jiangsu Geology, Volume 30, No.1, pp. 64~66.

The lifting and separating system for ground maneuvering rescue equipment

GAO Yukun, GONG Xuejiao, HUANG Zhian*, ZHANG Yinghua

State Key Laboratory of High-Efficient Mining and Safety of Metal Mines (University of Science and Technology Beijing), Ministry of Education, Beijing, China, 100083

ABSTRACT

At present, the research of our country specific emergency system of ground maneuvering rescue equipment has not been carried out. The field of special mine rescue equipment lacks specific lifting and separating facilities. To solve the above problems, this study innovatively designed a Lifting and separating system that matches with the ground maneuvering rescue equipment. The design of the Lifting and separating system mainly includes the following four aspects: the Lifting control room, Lift arm material section, size of telescopic boom, and the Selection of hydraulic cylinder for telescopic boom. This study uses ANSYS for the research and analysis. In the process of mine rescue, this system can enhance the economy and flexibility of hedge facilities and improve the technology of mine safety emergency rescue in China. The system also has important economic value and social significance for enterprises.

KEYWORDS: lifting and separating system; mine rescue; ANSYS simulation

1. INTRODUCTION

At present, the field of mine special rescue equipment (Liu, 2010) still lacks specific lifting and separating facilities. Large and middle rescue equipment is mostly used in external miniature truck cranes or gantry cranes (Schlick, 1975), which is influenced by the site space and manoeuvrability.

The platform for the Lifting and separating system was designed to solve the above problems. The system design is based on the platform control unit, which has the advantages of being built-in, lightweight, having a simple structure, and convenient operation.

The main purpose of the system is for use in mine rescue. The system has the effect of seismic noise reduction and integrated management and control (Zhang, K.J., 2012), and therefore the built-in platform, independent control room, and the

equipment unit can be assembled and separated quickly. This is conducive to the rapid expansion of the rescue platform and rescue construction (Xu and Du, 2009).

2. COMPOSITION OF LIFTING AND SEPARATING SYSTEM

The Lifting and separating system mainly includes four parts (Liu, 1999): hydraulic pump station, boom, control unit, and auxiliary facilities. The hydraulic pump station is in the right side of the rescue vehicle control area and the telescopic boom and crane and other major components with the anchor buckle are on the platform of two high strength steel truss. The structure is stable and reliable. The structure is shown in Figures 1 and 2.

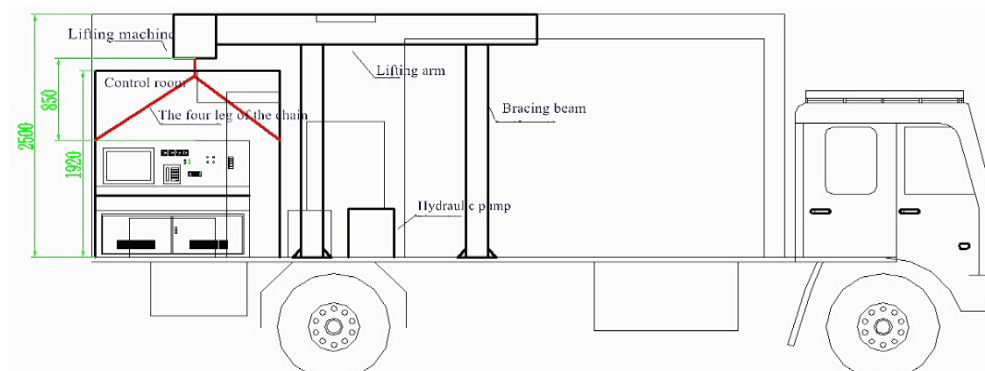


Figure 1: Arrangement of lifting and separating system.



Figure 2: Assembly and assembly drawings for lifting and separating system.

3. DESIGN OF LIFTING AND SEPARATING SYSTEM

The design of the lifting separation system (Cun and Sun, 2010) mainly includes two parts, namely the lifting and hoisting systems.

3.1 Study on the design of the control room

The system of hanging arm lifting the control room (Lin, 2012) is located on the tail of the platform, weighing about 1 tonne and the load distribution is uniform. The console, locker, air conditioning, and machine weight are arranged around the room, increasing the torque balance.

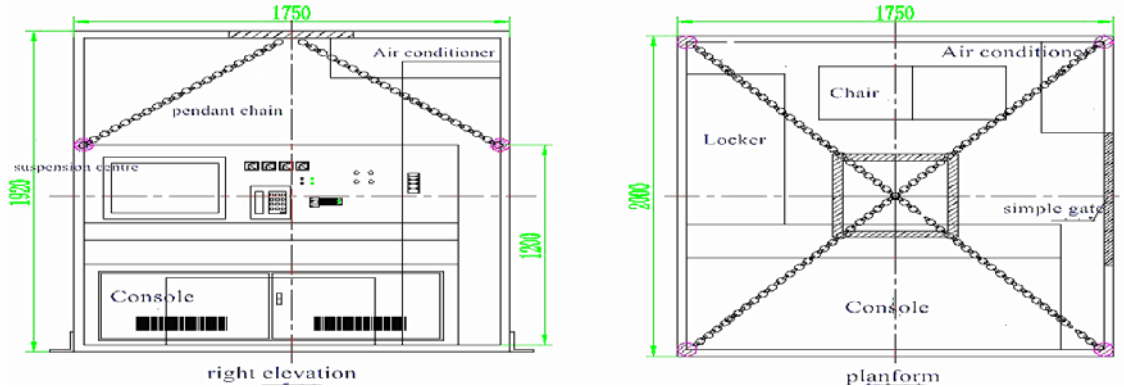


Figure 3: Design of control room layout.

In order to test the scientific nature and rationality of the design of the control room and to ensure the safety of the experiment (Liu, 2005), a 2 min driving test is carried out. For the test to achieve the desired effect the load control room layout should be reasonable and the design requirements of hoisting should be met.

3.2 Determination of material section of boom

(1) Selection of telescopic boom material

At present, the material of the lifting arm is made up of various types of alloy steel and low carbon steel. Heavy lifting appliances mainly use high strength low carbon alloy steel, and the medium and

Device specific parameters are as shown in Table 1 and equipment layout is as shown in Figure 3.

Table 1: Size, weight of the control room equipment.

Part	Dimensions (length * width * height)mm	Weight kg
box body	inside (1670*1920*1850)	500
	outside (1750*2000*1920)	
Operating table	750*1500*1200	125
Air conditioner (Inside)	680*190*240	7
Air conditioner (Outside)	620*200*440	24
File cabinet	900*390*1700	25
Chair	800*320*500	10
Fire Extinguisher		16
Others		
Total		707
Remarks	Design of lifting the maximum load of 1000kg	

small cranes adopt 16Mn. Considering the cost and the design of the lifting weight is not large, the crane material design uses 16Mn.

(2) Section of the telescopic boom

The main body of the main arm uses 16Mn material. Overall the choice of materials and structure of the design considers safety and the economic applications of the principle (Huang and Ou, 2011). It is optimal to reduce the weight of the boom and to achieve the overall optimization of the suspension arm and the whole system performance (Chen, 2012).

3.3 Determination of dimensions of telescopic boom

(1) The design of the main and sub arm's length

The design of the main boom length is determined by the basic arm length and the extended length.

$$l_{\max} = l_0 - (k-1)a + (k-1)l = l_0 + (k-1)l \quad (1)$$

In the optimization design platforms, according to engineering experience, lap length should be extended to the length of 1/4 to 1/5 for the second section crane arm, and $l' = (0.2 \sim 0.25) l_i$ for the second section hanging arm.

The second section telescopic boom is fully recovered from the main arm, and there is a long distance C, which mainly is the main arm of the hydraulic cylinder stretching mechanism and the fastening device. This space is often within the range of 0.25-0.44 m. Therefore, the main pair of two arm structure lengths has the following relations:

$$l_i^0 = l_{i+1}^0 + c - a \quad (2)$$

The two section telescopic boom, lap length of the second section telescopic boom, and jib is equal to 1/5 of the extended length. The main vice hanging arm joint length and the length of the structure are:

$$l_2' = 0.2l; \quad l_2^0 = 1.2l \quad (3)$$

$$l_1^0 = 1.2l + (k-1)(c-a) \quad (4)$$

(2) Check the length of the main and auxiliary arm

Through the above calculation, we can know that the length of the main arm is satisfied with the length of 4-31, and the length of the second sections can meet the design requirements and engineering use.

$$l_0 = l_1^0 + a(k-1) \geq 1.2l + (k-1)c = 1.2(l+a) + (k-1)c \quad (5)$$

According to the above calculations and verification, the vice arm of the section and the length of the relevant surplus: $l_1^0 = 3.1(m); l_2^0 = 1.6(m); a_2 = 0.3(m)$

In summary, the boom sections design size and cross section are determined as shown in Figure 4.

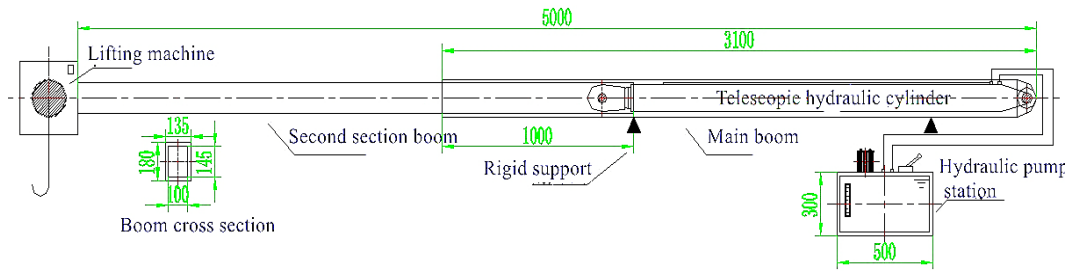


Figure 4: Boom size chart.

3.4 Calculation and selection of hydraulic cylinder for telescopic boom

(1) The inner diameter of the cylinder of hydraulic cylinder

Set the maximum load of the arm $Q=1.5 T$ for the telescopic cylinder to bear the maximum pressure:

$$F_{\max} = 1.9Q = 2.85T \quad (6)$$

Combined with the practical requirements, the hydraulic cylinder of the allowable working pressure is 5 MPa, $D=60.03$ mm, combined with the inner diameter of hydraulic cylinder, $D=63$ mm.

(2) Hydraulic cylinder piston rod diameter calculation

a. Design

Combined with the movement speed of the piston rod, $\varphi = 1.33$. $d=31.38$ mm. Combined with the series of piston rod diameter, $d=32$ mm.

b. Hydraulic cylinder strength test

The platform lift arm is 16Mn, so σ_b is 345 MPa;

n is the safety factor and considering the security, the n is 5 after testing the strength of the hydraulic cylinder to meet the design requirements.

c. Hydraulic cylinder stability test

It can be determined when the piston rod size is $d=50$ mm, the arm is safe and reliable, and meets the strength and stability calculations.

(3) Calculation of the hydraulic cylinder wall thickness and diameter

The platform telescopic hydraulic cylinder wall thickness and diameter to meet the strength requirements under load. $D_1=67$ mm.

To sum up, we can draw telescopic hydraulic cylinder structure parameters of hydraulic cylinder diameter: 63 mm. Hydraulic cylinder diameter: 67 mm; piston rod diameter: 50 mm.

4. THE FINITE ELEMENT ANALYSIS OF TELESCOPIC ARM BASED ON ANSYS

4.1 Finite element model of telescopic boom

(1) Entity model

The first section is 180*135 mm, the wall thickness is 17.5 mm, the length is 3100 mm; the second section is 145*100 mm, the wall thickness is 10 mm, the length is 2900 mm, the assembly depth is 1000 mm; the material is structural steel, the elastic modulus is 200 GPa, the Poisson's ratio is 0.3.

The geometric model is shown in Figure 5.

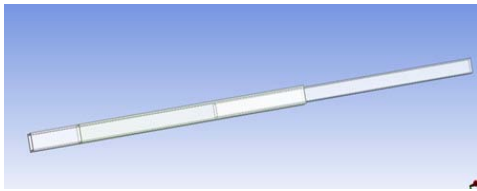


Figure 5: Geometric model of telescopic boom.

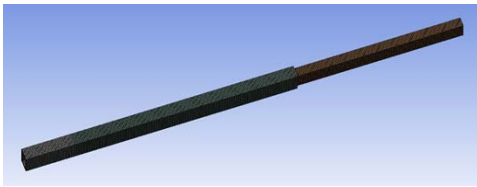


Figure 6: Grid division of telescopic boom.

(2) Unit selection and grid division

The platform lift arm model was built to select the unit. Shell element shell63 and solid45 were selected for the simulation of solid element to choose the unit body belonging to 8 node 6 unit, hanging arm model scale: node number 3201, unit number 41821. Grid divisions are as shown in Figure 6.

(3) Model of the contact of the boom

Because of the telescopic arm, between the main and auxiliary boom depends mainly on the chute and the plate of a lubricated contact force transfer. Therefore, we must deal with the model of the contact of the boom.

(4) Arm loading and constraint handling

The load of the telescopic boom mainly includes: the control room load, steel wire rope, and the supporting force of pull arm. Under the premise of considering the surplus coefficient, the control room load is 1t, as shown in Figure 7. The C is applied to the 9800N surface.

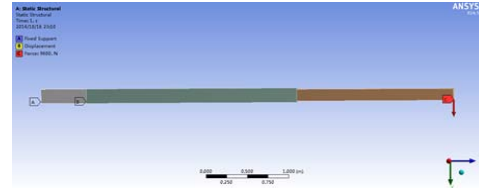


Figure 7: Constraint and load chart of the telescopic arm.

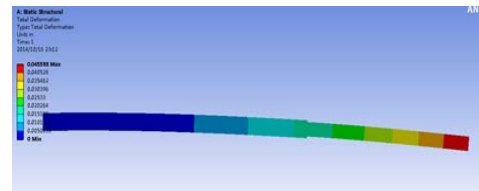


Figure 8: working plan of the telescopic boom

4.2 Analysis of finite element calculation results of telescopic boom

In order to verify the security and reliability of the telescopic boom, the second section of the boom is completely out of the operating conditions for simulation verification.

(1) The overall structure

As shown in Figure 8, the maximum deflection of the structure is 45.6 mm. The maximum stress of the structure is 167.4 MPa, far less than the allowable stress of the material ($[\sigma] = 345 \text{ MPa}$), which appears in the first section of the arm frame and the second arm frame. These results are shown in Figures 9 and 10.

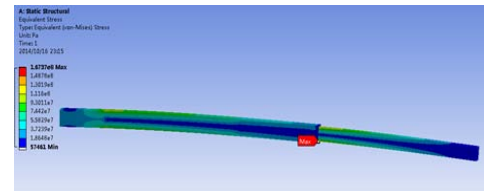


Figure 9: The overall structure of telescopic boom.

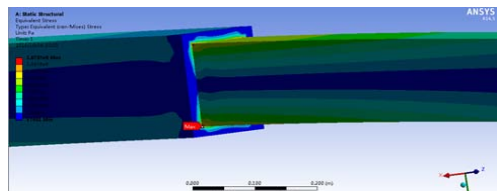


Figure 10: The maximum stress concentration point of the structure of telescopic boom.

(2) The second cantilever crane;

Through Figure 2, we can know that in the 11 section of the arm, the stress concentration is mainly distributed in the junction with the first arm, the

intersection of the arm, and the maximum stress concentration is consistent with the overall simulation results.

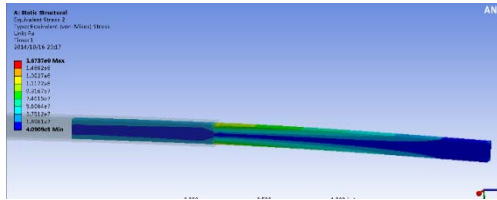


Figure 11: Stress chart of the second cantilever crane.

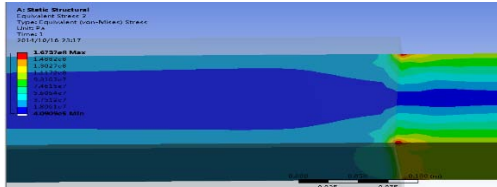


Figure 12: Maximum stress concentration point of the second cantilever crane.

(3) The first cantilever crane

The maximum deflection of the first cantilever crane is 16.8 mm, as shown in Figure 13, less than the overall structure maximum deflection of 45.6mm. The supporting role of the main arm of the hydraulic cylinder is minimal, which in turn verifies the rationality of the hydraulic cylinder structure.

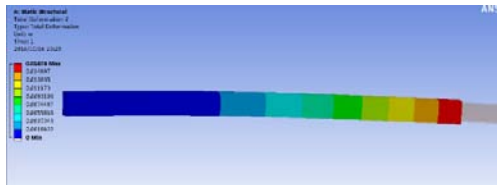


Figure 13: Working plan of the first cantilever crane.

5. CONCLUSIONS

1) According to the uniformity of load distribution, the control room of the crane hoisting system has been designed and is comprised of the console, locker, air conditioning, and outside machines, increasing the torque balance. The lifting point is arranged in the control indoor four beam column side with a special four legged chain sling connected. The field test achieved the desired effect, showing that the load control room layout is reasonable and satisfies the design requirements of hoisting.

2) The design uses rectangular cross sections. The main arm of the main body uses 16Mn as material, and for the four corners of the weld and

other stress concentrations, alloy steel is used. This not only optimizes the weight of the boom but also achieves the overall optimization of the performance of the split system of the arm and the whole hoisting system.

3) The telescopic boom is composed of two parts, the main arm and the outer part. The length of the main, sub arm's length, design size, and cross section were determined.

4) Based on the ANSYS finite element simulation, we know that when the two rectangular arms are made of 16Mn material, the section size meets the designing demand, and the maximum rated starting weight is 1 tonne and the extension length is 1.9 m, the strength and stiffness of the arm conforms to the safety requirements. The whole telescopic boom is safe and reliable.

6. ACKNOWLEDGEMENT

It is with great pleasure that we acknowledge the generous financial support of National Natural Science Foundation of China (project number: 51474017) and Natural Science Foundation of Xinjiang Uygur Autonomous Region of China (2014211B013).

7. REFERENCES

- Chen, T.T. (2012). A visual management and monitoring tool for cross-organization emergency response workflows. *Information Technology Journal*. Volume 11, pp. 1341-1356.
- Cun, T.T.Y and SUN, L. (2010). Development history of 20t hydraulic excavator for Hitachi construction machine. *Engineering machinery and maintenance*. Volume 8, pp. 88-92.
- Huang, Y.J. and Ou, J.C. (2011). Status and development trend of sudden disaster emergency rescue equipment. *China Hospital*. Volume 15, pp. 52-53.
- Lin, J. (2012). Mine rescue "Noah's Ark" -- Jiang Lu Electromechanical group Co. Ltd of mine rescue vehicle function. *Hunan security and disaster prevention*. Volume 1, pp. 36.
- Liu, Q.H. (2010). Analysis and Prospect of technical status of rescue and rescue vehicle. *China Emergency Rescue*. Volume 5, pp. 16-17.
- Liu, Q.D. (1999). Study on sliding type loader. *Engineering Machinery*. Volume 10, pp. 32-34.
- Liu, Y. (2005). The first China mine rescue car made in Xiamen. *Xiamen Daily*. Volume 11, pp. 17.

Schlick, D. (1975). Mine emergency operations of the mining enforcement and safety administration. United States Department of the Interior Mining Enforcement and Safety Administration Informational Report. Volume 11, pp. 34-35.

Xu, K.S. and Du, P.D. (2009). System to Guarantee Emergence Response Equipment emergency rescue equipment. Forestry Labour Safety. Volume 2, pp. 11-16.

Zhang, K.J. (2012). Importance of scientific management for mine rescue equipment. Reform and opening. Volume 2, pp. 89.

Safety and stability of the maneuvering rescue platform

GAO Yu-kun, Ji Yu-Chen, HUANG Zhi-an*, ZHANG Ying-hua

State Key Laboratory of High-Efficient Mining and Safety of Metal Mines (University of Science and Technology Beijing), Ministry of Education, Beijing 100083, China

ABSTRACT

With the continuous developments in the field of mining rescue, mechanical rescue equipment has been growing more complex and automatic, which leads to higher requirement for the safety, stability, and carrying ability of platform foundations. In response to these requirements, the present study designed an overall layout of the maneuvering rescue platform equipment. Upon consideration of the load arrangement rationality of the rescue platform, the humanity and convenience of the on-board equipment function, and the safety of the electric device, the overall layout of the vehicle was divided into two units: the device unit and the control unit. After completing the overall layout design, the security and stability of the platform was verified and analyzed. The results proved that the design of the maneuvering rescue platform met the requirements for the stability and safety of the mine rescue mission. The platform can be quickly deployed over a long distance with suitable mobility and carrying capacity.

KEYWORDS: maneuvering rescue platform; stability; modifications

Once a water permeating accident or other mine gas outburst accident occurs, emergency rescue platforms should arrive in the rescue site and establish temporary rescue command posts in the shortest possible time (Huang and Ou, 2011). The village, field, and hillsides on the way to mine rescues can be difficult to maneuver (Zhang, 2012; Yu, 2000), therefore, the security and stability of rescue platforms is very important.

1. THE OVERALL LAYOUT OF THE MANEUVERING RESCUE PLATFORM

The nature of the maneuvering rescue platform and other specialty vehicle design modifications is basically the same. The main difference is that the ultimate goal of the maneuvering rescue platform design is to reach the rescue site and accomplish the rescue mission. The roads to the rescue site are mostly rugged and complicated to maneuver. Therefore, the vehicles need to be more reliable and stable.

When maneuvering rescue platforms, the characteristics of the on-board equipment need to be considered, including device functions, volume, mass, and many other factors. Maneuvering rescue platforms integrate the air supply system, power supply system, the flow of food supply systems, monitoring, and control communications systems. Once the destruction of the underground system has occurred, the maneuvering rescue platform can provide power, communications, and food for the refuge chamber through the orifice docking device.

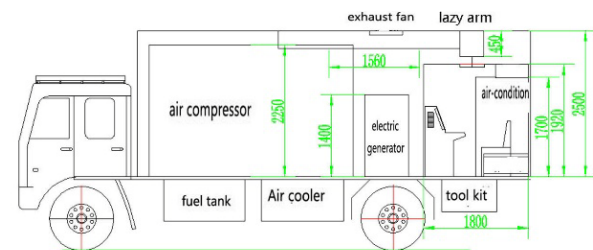


Figure 1: Layout left view of the maneuvering rescue platforms.

The overall layout of the vehicle is divided into two units: the device unit and the control unit. As shown, the device unit is made up of the air compressor, water tanks, generators, transformers, pump station, and most of the power and rescue equipment. The functions of the control unit are controlling communications, electricity transmission, monitoring, and other functions.

2. THE DISTRIBUTION OF LOAD AND THE CENTER OF MASS

In maneuvering rescue platform design, what needs to be considered is the quality of different vehicle equipment, features, and rational layout location equipment. This is necessary to facilitate the operator's quick and accurate control. Intrinsic safety design needs to be performed according to equipment function and reasonable partition. By calculating the distance between the gravity center of the main harness and the front axle of the platform, the relative space position of the vehicle equipment should be reasonably arranged. In order to fully ensure platform

security, it is necessary to improve the system's practicality and aesthetics (Liu, 1994; Cui, 1986). The calculation is as follows:

1) Establish a Cartesian coordinate system. The origin of coordinates is in the vehicle axle. The extension of the two vehicle axle is the Y-axis and the roof plumb line is the Z axis. Coordinate positive direction is chosen, as shown in Fig.2.

2) The major equipment parameter list is shown in Table 1, including mass and the centroid location, with the relative distance of the axes and the like.

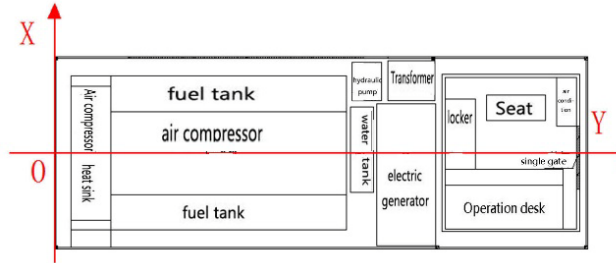


Figure 2: Maneuvering rescue platform x-y coordinate system schematic.

Table 1: Maneuvering rescue platform centroid position of major equipment and the quality of their list.

NO.	moment	Parts Names	Weight G/Kg	Centroid Y-axis distance/mm
1	F ₁	air compressor	4500	1950
2	F ₂	electric generator	540	4465
3	F ₃	transformer	460	4525
...
n-2	F _{n-2}	lazy arm	310	5297
n-1	F _{n-1}	control board	125	5735
n	F _n	water tank	600	3903
	F _{sum}	Sum	8750	2460.98
NO.	moment	Parts Names	Centroid height Z/mm	Centroid X-axis distance /mm
1	F ₁	air compressor	1875	0
2	F ₂	electric generator	1480	-465
3	F ₃	transformer	950	886
...
n-2	F _{n-2}	lazy arm	3032	0
n-1	F _{n-1}	control board	1260	-697
n	F _n	water tank	1680	105
	F _{sum}	Sum	1608.49	5.48

3) From Table 1, the total equipment weight is G=8750kg. Fukuda Ollin CTX5200 vehicle chassis parameters are used to allow a maximum carrying

capacity of G_{max}=1T>G, which is within the allowable load range, and not overweight.

$$F_{rear} = \frac{\sum_{i=1}^n F_i Y_i}{L} = \frac{32371456}{5200} = 6225.28\text{kg} \quad (2-)$$

$$1) F_{front} = F - F_{rear} = 8750 - 6225.28 = 2524.72\text{kg}$$

$$(2-2) F_{left} = \frac{F \times (\frac{B}{2} + X)}{B} = \frac{7966715}{1810} = 4401.50\text{kg}$$

$$(2-3) F_{right} = F - F_{left} = 8750 - 4401.5 = 4348.5\text{kg}$$

$$(2-4)$$

According to the above calculation:

Platform chassis front axle maximum load F_{front axle}=3250 kg>F_{front} = 2524.72 kg, rear axle maximum axle load F_{rear axle} = 6750 kg>F_{rear} = 6225.28 kg. The overall design of the platform weight does not exceed the original parameters of the permissible range of the vehicle, and it was in line with the safety requirements. On the other hand, after the platform modifications, load was close to full capacity. It is important to note the use of usual safe driving tactics, and to avoid the use of emergency brakes. While in the latter part of the platform design, what needs to be further considered is the streamlining harness, use of lightweight materials, optimized chassis, and other measures to increase the flexibility of the platform.

3. LONGITUDINAL STABILITY

In order to ensure the platform with security and stability, longitudinal stability studies of the modified platform were performed.

The rescue platform utilized the Fukuda standard commercial chassis without any modifications, so there were no parking brake problems. The only major considerations for longitudinal stability of the platform analysis are the longitudinal tipping and longitudinal slippage (Zhang, 1997; Shuichi, 1981), as shown in Figure 3.

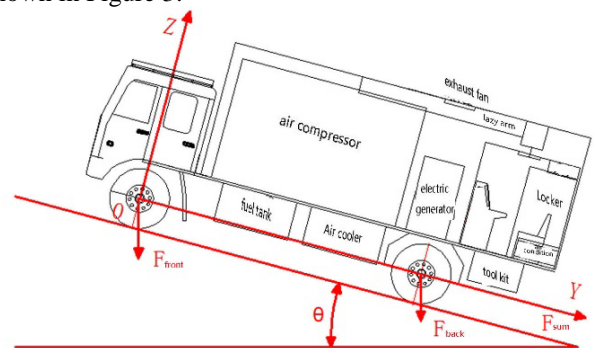


Figure 3: Maneuvering rescue platforms longitudinal stability diagram.

Verification is calculated as follows:

Platform maximum sideslip angle is calculated

as:

$$\theta_{\text{slip}} = \arctan \frac{Y \times \phi}{L - Z \times \phi} = \arctan \frac{2460.981 \times 0.5}{5200 - 1608.49 \times 0.5} = 15.64^\circ \quad (3-1)$$

When climbing, the maximum slope angle is calculated as:

$$\theta_{\text{downhill}} = \arctan \frac{L - Y}{Z} = \arctan \frac{5200 - 2460.98}{1608.49} = 59.53^\circ \quad (3-2)$$

When downhill, the maximum slope angle is calculated as:

$$\theta_{\text{climbing}} = \arctan \frac{Y}{Z} = \arctan \frac{2460.98}{1608.49} = 56.83^\circ \quad (3-3)$$

Calculation of the above formula shows that $\theta_{\text{slip}} < \theta_{\text{climbing}}$, $\theta_{\text{slip}} < \theta_{\text{downhill}}$, $\theta_{\text{slip}} < \theta_{\text{turn}}$, suggesting that when vehicle instability occurs, sliding phenomenon occurs. However, overturn will not occur, which ensures the platform's longitudinal stability and security. In addition, the results show that θ_{climbing} and θ_{downhill} are about four times the θ_{slip} , which shows that the overall vehicle longitudinal conversion is quite reliable. Once sliding occurs, the driver of the maneuvering rescue platform would have enough time to correct for the slide. This ensures the safe emergency disposal.

4. LATERAL STABILITY

The lateral stability of the platform directly affects how the vehicle travels in horizontal centrifugal force. Horizontal centrifugal force is related to the stability of the vehicle state and must be determined in the reliability test and verified as an important platform indicator for road safety. Research on lateral stability mainly includes two aspects: cornering stability and cross slope stability.

4.1 Cornering stability

Analysis shows that the platform has a tendency to tilt outwards when subjected to centrifugal force around a corner.

The centrifugal force on the platform is inversely proportional to the turning radius, but is proportional to the speed.

If the platform corner has a minimum radius of $R_{\text{min}}=6.25$ m (chassis factory parameters). then

cornering limit speed when the platform slides is calculated as:

$$V_{\text{slip}} = \sqrt{g \times \phi \times R_{\text{min}}} = \sqrt{9.8 \times 0.5 \times 6.25} = 5.53 \text{m/s} \quad (4-1)$$

Cornering limit speed when platform rollover occurs is calculated as:

$$V_{\text{turn}} = \sqrt{\frac{R_{\text{min}} \times b \times g}{2Z}} = \sqrt{\frac{6.25 \times 9.8 \times 1930}{2 \times 1608.49}} = 6.06 \text{m/s} \quad (4-2)$$

In the formula, car gage $b=1930$ mm (chassis factory parameters).

It can be seen from the above calculation process, $V_{\text{turn}} > V_{\text{slip}}$, that platform lateral stability is reliable when cornering. Also, the surplus quantity of the V_{turn} and V_{slip} is relatively low, indicating that although safety of the platform is not a problem, there is room for improvement in stability. Vehicle rollover under conditions of the limit cannot be ruled out, because of the high speed or too-small turning radius. The best way to improve stability is to reduce the overall centroid height Z of the platform to achieve $V_{\text{turn}} \gg V_{\text{slip}}$ over the state, which is also an important aspect of late platform optimizing.

4.2 Cross slope stability

Cross slope stability, with respect to the platform, is measured by:

$$\frac{b}{2 \times Z} > \phi \quad (4-3)$$

$$\frac{b}{2 \times Z} = \frac{1930}{2 \times 1608.49} = 0.60 \quad (4-4)$$

According to the results, $0.60 > \phi = 0.50$, therefore, the design with the cross slope is safe. However, in order to better ensure the safety of the platform, the platform should be loaded with a reasonable arrangement: for example, compact integrated devices should be chosen and the equipment should be put in a lower position. The purpose of reducing centroid height by the above means is to increase the driving safety of the platform.

4.3 Wind resistance

Platform modified equipment for the purpose of cooling and elimination of flue gas is placed in the roof of the vehicle platoon, which indirectly increases the wind age area of the vehicle with increases of platform height.

The Bernoulli equation shows:

$$w_p = \frac{v^2}{1600} \quad (4-5)$$

Consider that the work conditions of the platform are no more than 5 wind strength, and therefore take 5 wind speed ($v = 10.7 \text{ m/s}$) for the authentication parameter in formula 4-6:

$$w_p = \frac{10.7^2}{1600} = 0.0072 \text{ kN/m}^2 \quad (4-6)$$

The roof platform exhaust fan height is about 0.25 m, and the wind area is about 0.45 m^2 , so the exhaust fan wind torque:

$$F = w_p \times 0.25 \times 0.45 = 81 \text{ kg} \cdot \text{m} \quad (4-7)$$

The overturning moment platform can afford:

$$F_{platform} = F \times Z = 8750 \times 1.61 = 14087.5 \text{ kg} \cdot \text{m} \quad (4-8)$$

From the above calculation, $G = F = 8750 \text{ kg}$, $Z = 1.61 \text{ m}$, $F \ll F_{platform}$. This shows that the drag generated by the wind on the exhaust fan for emergency rescue platforms is negligible. The platform has wind resistance and the ability to resist overturning.

5. CONCLUSIONS

A platform was modified to ensure the uniformity and reasonable load distribution as much as possible. The platform had good stability when loaded, with uphill and downhill angles being within the maximum angle limit.

Platform rollover would not occur when loaded and cornering within the maximum allowed angle. The platform would be permitted within the maximum load under conditions of full and full fittings.

The cooling fan on the roof caused an increase in the wind area due to the increased height, however the wind resistance was reduced. The platform has wind resistance and the ability to resist overturning.

6. ACKNOWLEDGEMENT

It is with great pleasure that we acknowledge the generous financial support of the Hebei central energy Fengfeng Group, the National Natural Science Foundation of China (project number: 51474017) and Natural Science Foundation of Xinjiang Uygur Autonomous Region of China (2014211B013).

7. REFERENCES

Cui J. (1986). Special purpose vehicle design. Shaanxi science and technology press. 115 p.
Huang Y J, Ou J C. (2011). Status and development trend of sudden disaster emergency rescue equipment. Chinese Hospitals, Volume 15, No. 12, pp. 52-53.

Liu Z Y, He X G. (1994). Special purpose vehicle structure. Wuhan University of technology press. 175 p.

Shuichi Iida. (1981). Commonly used indicator of physics. Science press. 236 p.

Yu Z S. (2000). Automobile theory. China Machine Press. 15 p.

Zhang H X. (1997). Automobile design. China Machine Press. 89 p.

Zhang K J. (2012). The significance of mine rescue equipment scientific management. Reform & Openning, No. 2, pp.89.

The performance optimization experiment of a wet high-frequency vibrating grid

Zhang Yinghua, Liu Jia, Huang Zhian*, Gao Yukun

State Key Laboratory of High-Efficient Mining and Safety of Metal Mines (University of Science and Technology Beijing), Ministry of Education, Beijing, China, 100083

ABSTRACT

Dust preventing is of great significant in mine safety production. The wet high-frequency vibrating grid is one of the most efficient dedusting systems. Therefore, optimizing the dedusting parameters of wet high-frequency vibrating grids is meaningful in controlling dust. Two of the most important parts of wet high-frequency vibrating grids are the spray dedusting system and the vibrating grid filtration system. This study optimized these two systems respectively to obtain the influence of various factors on the two systems by using the method of orthogonal experiment and then chose the two factors which have the greatest impact on comprehensive optimization. The results can be used in mine dedusting practice to reduce the incidence of pneumoconiosis and improve work efficiency.

KEYWORDS: Vibrating wire grid; dust removal mechanism; orthogonal experiment; performance optimization

1. INTRODUCTION

Underground dust is wide spread and lasts for a long time, therefore, dust suppression by spraying has always been the main measure to control mine dust. A variety of forms are in practice, such as wind-water spraying, magnetized water dust suppression, pre-charged water spray dust suppression, high-pressure spraying, etc. (Liu et al., 2011; Wang, 2010; Dong, 2014). Traditional dedusting methods can be divided into dry dedusting and wet dedusting. Mine dust is always damp, therefore the bag filter and electrostatic precipitator can't be used normally. Wet dust collectors used in mines mainly include the venturi scrubber, cyclone dust collector, foam dust catcher, impact dust collector, self-swash dust catcher, and dust removal fan. These dust collectors have simple structures, convenient maintenance, and reliable operation (Song, 2010; Chen, 2013; Li et al., 2011). However, as the underground conditions are complex and changeable, some new equipment and technology has not been generalized effectively (Shi, 2005).

The wet high-frequency vibrating grid is one of the most efficient dedusting systems. Optimizing the dedusting parameters of the wet high-frequency vibrating grid is meaningful in controlling dust. This study first did deep research on the dedusting mechanism of the wet high-frequency vibrating grid and then optimized the vibrating grid system and the spray system of the grid by an orthogonal experiment. Afterwards the wet high-frequency vibrating grid system was synthetically optimized.

2. DEDUSTING MECHANISM OF WET HIGH-FREQUENCY VIBRATING GRID

The wet high-frequency vibrating grid includes spray dedusting and vibration fiber grid dedusting. When the dust-laden air flows through the sprayer, some dust is crashed, intercepted, condensed, and settled. Spray dedusting mainly uses inertial impaction, interception, and Brownian diffusion and other short-range dust catching mechanisms. Vibrating grid dedusting is uses sonic vibration. By the acoustics principle, the particles in the sound field will vibrate under the effect of sound waves. The small particles have high vibration velocity and large particles have low vibration velocity, which make different sizes of particles agglomeration power forward, so that the larger particles will get closer to the small particles and collide, combine into larger particles, making it easier to be trapped. Supplemented by spraying dedusting, this method can achieve high efficiency of reducing the respirable dust concentration. The acoustic agglomeration effect of the vibrating grid is also related to its amplitude, where the greater the amplitude, the higher the collection efficiency. The amplitude is related to the wind speed flow where the higher the wind speed, the greater the amplitude of the vibrating grid, the sound condensation effect is more significant, and the dedusting effect is better. However, at, extremely high wind speeds, damage will be caused to the vibrating grid.

3. OPTIMIZATION EXPERIMENT RESEARCH ON WET HIGH-FREQUENCY VIBRATING GRID DEDUSTING PARAMETERS

3.1 Experimental procedure and principle

1) Measure the dust mass flow through before and after the wet high-frequency vibrating grid

Put the filter membrane into the culture dish with tweezers moistened with alcohol, and weigh them in the one over ten-thousand analytical balance after drying them in the drying oven, record the initial data. Start the two dust samplers before and after the grid to obtain the filters with dust before and after dedusting. Place the filters into the culture dish originally used to weigh and record the data. Subtract the initial mass from the total mass of dust filters and culture dish to obtain the dust mass before and after dedusting. Refer to the following formulas:

$$M_{\text{before}} = M_1 - M_0 \quad (1)$$

$$M_{\text{after}} = M_2 - M_0 \quad (2)$$

M_{before} is the dust mass before dedusting. M_1 is the total mass of filters and culture dish before dedusting. M_0 is the initial mass of filters and culture dish. M_{after} is the dust mass after dedusting. M_2 is the total mass of filters and culture dish after dedusting.

2) Determination of dedusting efficiency

Side-sampling is applied in this experiment. Place two dust samplers before and after the grid in the simulating roadway. Start two dust samplers at the same time, set the flow rate to 20 L/min and the sampling time to two minutes. Take out the membrane filter according to the above method to weigh the filter and calculate the dedusting efficiency according to the following formula:

$$\eta = \frac{1000 \cdot (M_{\text{后}} - M_{\text{前}})}{L \cdot t} \quad (3)$$

η is the dust concentration of sample point, mg/m^3 ; M_{before} is the dust mass before dedusting, mg ; M_{after} is the dust mass after dedusting, mg ; L is the sampling flow rate, L/min ; t is the sampling time, min .

3) Determination and calculation of dedusting resistance

The experiment indicates the dedusting resistance with pressure loss, and set the airflow of inlet pipe and outlet pipe to be equal, then the average total pressure difference between the airflow of inlet and outlet pipe can be obtained by the average static pressure difference. The two sections of the static pressure difference can be measured with a pitot tube and compensation micro-manometer and calculated as:

$$\Delta P = P_1 - P_2 \quad (4)$$

ΔP is the pressure loss, Pa; P_1 is the pressure at the inlet section, Pa; P_2 is the pressure at the outlet section, Pa.

3.2 Design and production of wet high frequency vibrating grid dedusting experiment system

1) Production of vibrating grid board

Set the iron grid board frame internal and external size as $35 \text{ cm} \times 35 \text{ cm}$, $27 \text{ cm} \times 27 \text{ cm}$ according to the simulation roadway size. Wrapped the Nylon lines equally spaced around the two sides of the vibrating grid frame and make the fibers remain extremely tight. The produced vibrating grid is shown in Figure 1:



Figure 1: Vibrating grid.

2) Spray system connection

The nozzle parameters of the spray system are as follows: the diameter is 1.5 mm, rated pressure is 4 Mpa, diffusion angle is 70° , and the measuring device used a LZS – 15 flow meter.

The devices were connected by 25 mm high pressure rubber hose, and the metal ring pipe connectors were used to connect the connection parts. The spray system connection order is shown in figure 2.

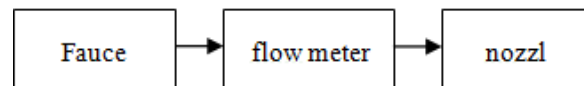


Figure 2: Spray system connection order.

3) Assembly of dust generation system

Dust generation system is made up of a fan and dust injection parts. In order to simulate the wind speed in the actual roadway (3-5 m/s), choosing the BPT12-13 pipeline ventilation fan as the generation

device, its air volume $Q = 150 \text{ m}^3/\text{h}$, and wind speed is about 4.2 m/s .

The experimental design is shown in Figure 3:

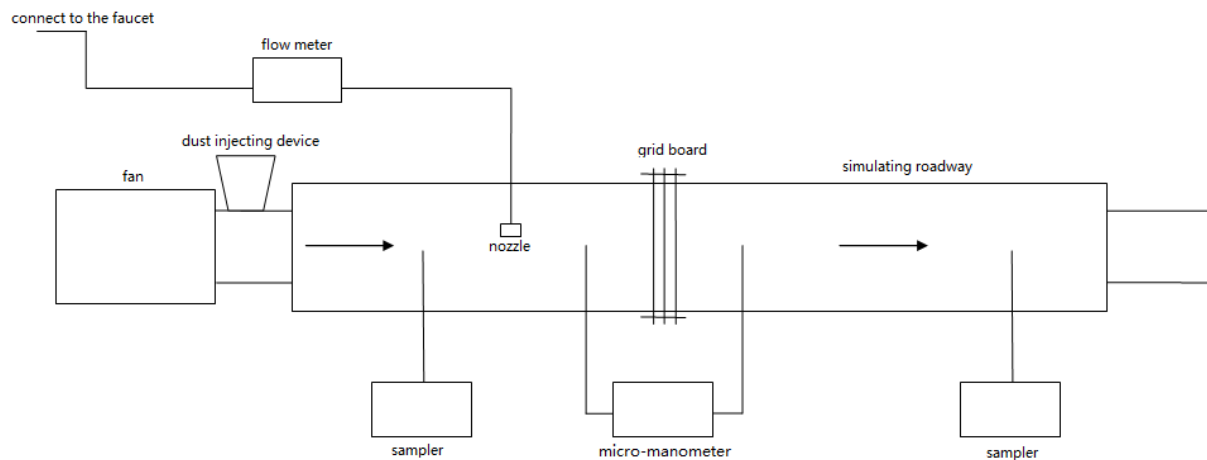


Figure 3: Experimental device design.

3.3 Vibrating grid dedusting orthogonal experiment

To obtain the most efficient parameter combination of the fiber grid dedusting system, select the collection efficiency as assessment indicator. Maintaining water quantity as 1.33 L/min , spray

distance as 15 cm , carrying on the orthogonal experiment under this condition, the experimental results are shown in Table 1. Analyze the variance on the above data, the results are shown in Table 2.

Table 1: Vibrating grid dedusting orthogonal experimental results.

Line	1	2	3	Experimental Condition	Experimental Result
Factor	Grid Board number	Fiber Diameter	Parallel Number		
1	1	1	1	A1B1C1	89.1
2	1	2	2	A1B2C2	92.5
3	1	3	3	A1B3C3	94.6
4	2	1	2	A2B1C2	92.3
5	2	2	3	A2B2C3	94.4
6	2	3	1	A2B3C1	96.8
7	3	1	3	A3B1C3	95.9
8	3	2	1	A3B2C1	98.0
9	3	3	2	A3B3C2	99.2
Mean Value 1	92.067	92.433	94.900		
Mean Value 2	94.500	94.967	95.33		
Mean Value 3	98.367	97.533	94.967		
Range	6.300	5.100	0.700		

Table 2: Vibrating grid dedusting efficiency variance analysis

Factor	Square of Deviance	Degree of Freedom	F Ratio	F Critical-value	Significance
Grid Board Number	60.562	2	1441.952	19.000	*
Fiber Diameter	29.016	2	928.952	19.000	*
Parallel Number	0.736	2	17.524	19.000	
Error	0.04	2			

Draw pictures on grid board number, fiber diameter, and parallel number. The abscissa is the

actual level and ordinate is the average dedusting efficiency, as shown in Figure 4.

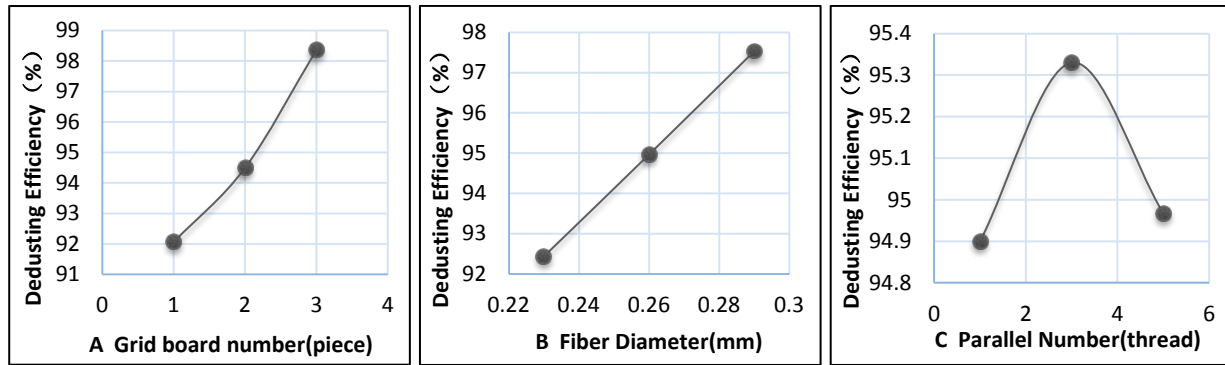


Figure 4 : Factors affecting dedusting efficiency analysis of orthogonal experiment.

The significant analysis shows that the factors affecting the dedusting effect order are as follows: grid board number, fiber diameter, and parallel number. Therefore, select grid board number and fiber diameter as two factors for the integrated optimization orthogonal experiment factors.

The optimal level is the highest total level of the three factors' optimal level. It can be obtained from Table 1 that the optimal combination is when the grid board number is 3, the fiber diameter is 0.29 mm, the parallel number is 2 (A3B3C2), and the dedusting efficiency is 81.2%.

3.4 Spray dedusting orthogonal experiment

To obtain the most efficient parameter combination of the spray dedusting system, select the collection efficiency as the assessment indicator. Maintain the grid board number as 2, fiber diameter as 0.26 mm, and carry on the orthogonal experiment under these conditions. The experimental results are shown in Table 3. Analyze the variance of the data. The results are shown in Table 4.

Table 3: Spray dedusting orthogonal experimental results.

Line	1	2	3	Experimental Condition	Experimental Result
Factor	Spray Water Volume	Spray Distance	Nozzle Angle		
1	1	1	1	A1B1C1	90.0
2	1	2	2	A1B2C2	93.1
3	1	3	3	A1B3C3	91.9
4	2	1	2	A2B1C2	93.2
5	2	2	3	A2B2C3	95.4
6	2	3	1	A2B3C1	93.0
7	3	1	3	A3B1C3	97.9
8	3	2	1	A3B2C1	99.7
9	3	3	2	A3B3C2	98.3
Mean Value 1	91.667	93.700	94.233		
Mean Value 2	93.867	96.067	94.867		
Mean Value 3	98.633	94.400	95.067		
Range	6.966	2.367	0.834		

Table 4: Spray dedusting efficiency variance analysis.

Factor	Square of Deviance	Degree of Freedom	F Ratio	F Critical-value	Significance
Spray Water Volume	76.096	2	352.296	19.000	*
Spray Distance	8.869	2	41.060	19.000	*
Nozzle Angle	1.136	2	5.259	19.000	
Error	0.22	2			

Draw graphs of the spray water volume, spray distance, and nozzle angle. The abscissa is the actual

level and ordinate is the average dedusting efficiency, as shown in Figure 5.

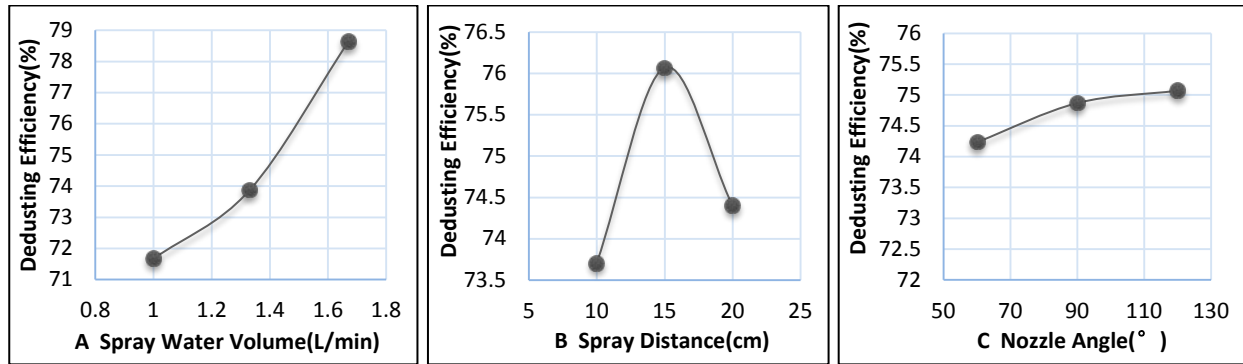


Figure 5: Factors affecting dedusting efficiency analysis of orthogonal experiment.

The significant analysis shows that the factors affecting the dedusting effect order is as following: spray water volume, spray distance, and nozzle angle. Therefore, select spray water volume and spray distance as two factors for the integrated optimization orthogonal experiment factors.

The optimal level is the highest total level of the three factors' optimal level. It can be obtained from Table 3 that the optimal combination is that the spray water volume as 1.67 L/min, the spray distance as 15 cm, the nozzle angle as 60° (A3B2C1), and the dedusting efficiency is 79.7%.

3.5 Wet high frequency vibrating grid dedusting-parameter optimization experiment

According to the two orthogonal experiments above, choose four factors for comprehensive optimization experiments, namely, grid board number, fiber diameter, spray water volume, and spray distance. Select dedusting efficiency and dedusting resistance as evaluation indicators.

1) Dedusting efficiency orthogonal experimental result analysis

The dedusting efficiency orthogonal experimental results are shown in Table 5. Analyze the variance of the data. The results are shown in Table 6.

Table 5: Dedusting efficiency orthogonal experimental result.

Line	1	2	3	4	Experimental Condition	Experimental Result
Factor	Fiber Diameter	Spray Water Volume	Grid Board Number	Spray Distance		
1	1	1	1	1	A1B1C1D1	88.8
2	1	2	2	2	A1B2C2D2	93.9
3	1	3	3	3	A1B3C3D3	98
4	2	1	2	3	A2B1C2D3	92.1
5	2	2	3	1	A2B2C3D1	95.5
6	2	3	1	2	A2B3C1D2	95.2
7	3	1	3	2	A3B1C3D2	93.3
8	3	2	1	3	A3B2C1D3	93.1
9	3	3	2	1	A3B3C2D1	97.3

Mean Value1	93.567	91.400	92.367	93.867		
Mean Value2	94.267	94.167	94.433	94.133		
Mean Value3	94.567	96.833	95.600	94.400		
range	1.000	5.433	3.233	0.533		

Table 6: Dedusting efficiency variance analysis.

Factor	Square of Deviance	Degree of Freedom	F Ratio	F Critical-value	Significance
Fiber Diameter	1.580	2	3.700	19.000	
Spray Water Volume	44.287	2	103.717	19.000	*
Grid Board Number	16.087	2	37.674	19.000	*
Spray Distance	0.427	2	1.000	19.000	
Error	0.43	2			

Draw graphs of fiber diameter, spray water volume, grid board number, and spray distance. The

abscissa is the actual level and ordinate is the average dedusting efficiency, as shown in Figure 6.

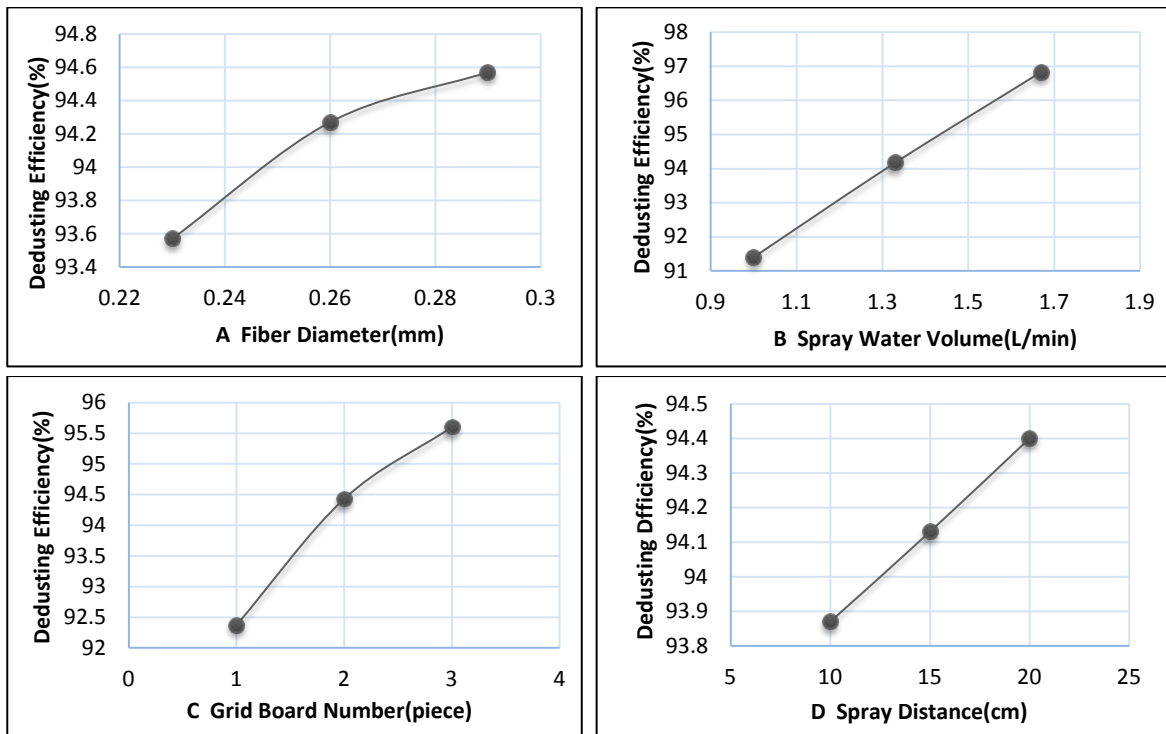


Figure 6: Factors affecting dedusting efficiency analysis of orthogonal experiment.

The significant analysis shows that the factors affecting the dedusting effect order are as follows: spray water volume, grid board number, fiber diameter, and spray distance.

The dedusting resistance orthogonal experimental results are shown in Table 7. Analyze the variance of the data. The results are shown in Table 8.

2) Dedusting resistance orthogonal experimental result analysis

Table 7: Dedusting resistance orthogonal experimental results.

Line	1	2	3	4		
Factor	Fiber Diameter	Spray Water Volume	Grid Board Number	Spray Distance	Experimental Condition	Experimental Result
1	1	1	1	1	A1B1C1D1	33.15
2	1	2	2	2	A1B2C2D2	60.37
3	1	3	3	3	A1B3C3D3	83.83
4	2	1	2	3	A2B1C2D3	56.63
5	2	2	3	1	A2B2C3D1	81.66
6	2	3	1	2	A2B3C1D2	48.02
7	3	1	3	2	A3B1C3D2	79.81
8	3	2	1	3	A3B2C1D3	44.87
9	3	3	2	1	A3B3C2D1	69.26
Mean Value1	59.117	56.530	42.013	61.357		
Mean Value2	62.103	62.300	62.087	62.733		
Mean Value3	64.647	67.037	81.767	61.777		
Range	5.530	10.507	39.754	1.376		

Table 8: Dedusting resistance variance analysis.

Factor	Square of Deviance	Degree of Freedom	F Ratio	F Critical-value	Significance
Fiber Diameter	45.970	2	15.390	19.000	
Spray Water Volume	166.119	2	55.614	19.000	*
Grid Board Number	2370.569	2	793.629	19.000	*
Spray Distance	2.978	2	1.000	19.000	
Error	2.99	2			

Draw graphs of fiber diameter, spray water volume, grid board number, and spray distance. The

abscissa is the actual level and ordinate is the average dedusting resistance, as shown in Figure 7.

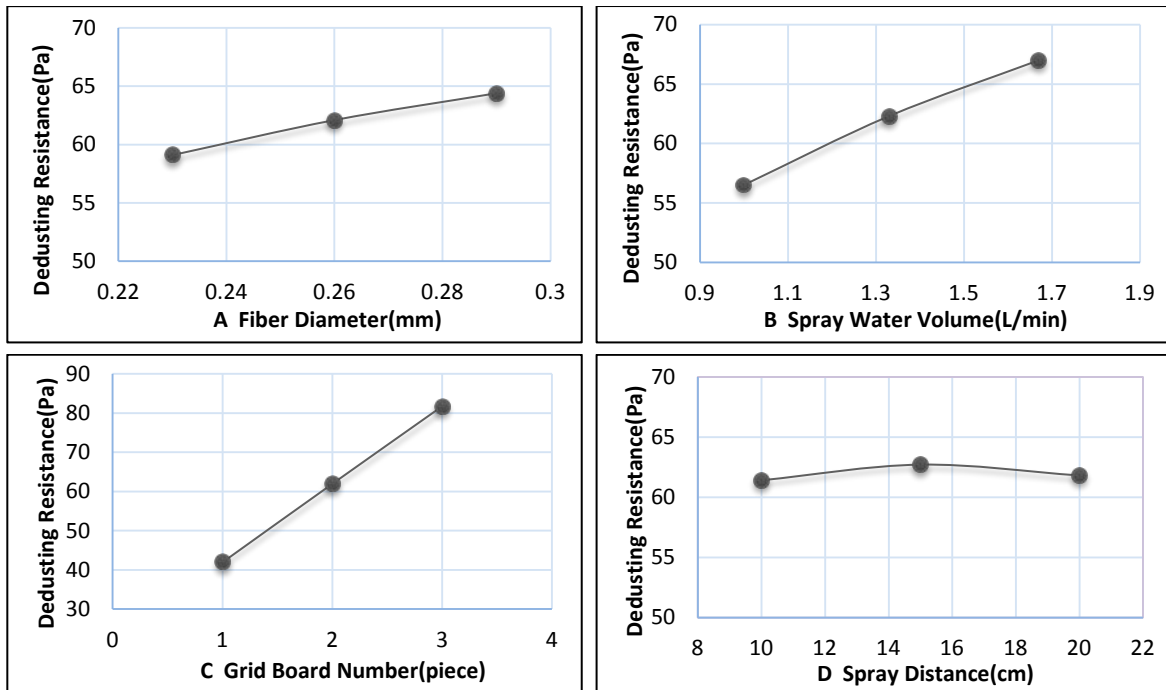


Figure 7: Factors affecting dedusting resistance analysis of the orthogonal experiment.

The significant analysis shows that the factors affecting the dedusting effect order are as follows: grid board number, spray water volume, fiber diameter, and spray distance.

3) Determine the optimal level combination

The optimal level is the highest total level of the four factors' optimal level. It can be obtained from Tables 5 and 7 that the optimal combination is when the fiber diameter is 0.23 mm, spray water volume is 1.67 L/min, grid board number is 3 and spray distance is 20 cm (A1B3C3D3), the dedusting efficiency is 78.0%, and the dedusting resistance is 83.83 Pa.

It can be seen from Figures 6 and 7 that the combination of A3B3C2D1 might be called the best combination. Its dedusting efficiency is 77.3% and dedusting resistance is 69.26 Pa. Compared with combination A1B3C3D3, combination A3B3C2D1 has lower dedusting efficiency, but its dedusting resistance is also smaller, thus it can be obtained that the wet high frequency vibrating grid dedusting optimal combination of parameters is that the vibrating grid fiber diameter is 0.29 mm, the spray water volume is 1.67 L/min, the grid board number is 2, and the spray distance is 10 cm, namely A3B3C2D1.

4. CONCLUSION

In the orthogonal experiment of the vibrating grid, the influence factors on the dedusting effect are ranked as follows: grid board number, fiber diameter, and parallel number. Therefore, we select grid board number and fiber diameter as the integrated optimization orthogonal experiment factors. Firstly, grid board should be used more in the system in consideration with dedusting resistance, economic costs and other factors. Secondly, fine fiber diameter is supposed to be avoided according to the material and costs.

In the orthogonal experiment of spray dedusting, the influence factors on the dedusting effect are ranked as follows: spraying rate, the distance of spray, and the angle of nozzle. We select the first two factors as the integrated optimization orthogonal experiment factors. Firstly, spraying rate is supposed to be increased in consideration of dedusting resistance and costs. Secondly, at a distance of 15 cm between the spray and grid board the performance is best. In practice, the actual distance can be magnified.

We obtain four factors used by a comprehensive optimization experiment through previous experiments. Their dust removal effect rankings are as follows: grid board number, fiber diameter, spraying rate, and the distance of spray. By analyzing the combination of parameters, we conclude that the

optimal combination of wet high-frequency vibrating grid parameter values are: 0.29 mm (vibrating wire grid fiber diameter), 1.67 L/min (spraying rate), 2 (grid board number), and 10 cm (distance of spray).

5. ACKNOWLEDGEMENT

It is with great pleasure that we acknowledge the generous financial support of National Natural Science Foundation of China (project number: 51474017) and Natural Science Foundation of Xinjiang Uygur Autonomous Region of China (2014211B013).

6. REFERENCES

- Chen, Y.H. (2013), Experiment on charged fog dedusting technology. *Modern Mining*, Volume 8, pp. 105-106.
- Dong, W.Y. (2014), China coal mine dust control technology status and prospects. *Science and Technology Information*, Volume 4, pp. 225-227.
- Liu, Y.B., Bai, Y.H. and Hou, J.G. (2011). Talking about the development of fully mechanized sublevel caving and the existing problems and countermeasures. *Coal Mine Safety*, Volume 06, pp. 160-162.
- Li, Y.C., Zhang, Y.H. and Xiong, S.S. (2011), Study on dedusting technology with high-pressure atomizing and vibrating fiber grid. *Nonferrous Metals (Mining Section)*, Volume 1, pp. 58-61.
- Song, J.G. (2010), High pressurized external spraying dust control technology of fully mechanized coal mining face and applied research. *Coal Engineering*, Volume 10, pp. 43-45.
- Shi, X.X. (2005), Current development and dust control technology research of fully mechanized coal faces. *Journal of Safety Science and Technology*, Volume 1, No. 1, pp. 41-43.
- Wang, H.Q. (2010), Coal mine dust and removal technology and optimization of existing. *Yunnan Vocational Institute of Energy Technology*, Volume 24, pp. 26-28.

Borehole docking system design for underground refuge chamber and ground maneuver rescue equipment

ZHANG Ying-hua, SONG Shou-yi, HUANG Zhi-an*, GAO Yu-kun

State Key Laboratory of High-Efficient Mining and Safety of Metal Mines (University of Science and Technology Beijing), Ministry of Education, Beijing 100083, China

ABSTRACT

In order to target the problems of poor and low efficiency that arise during the borehole docking process of ground equipment and refuge chamber in emergency refuge system, this study presents a borehole docking system designed for ground maneuver rescue equipment. The system includes three parts: the hole docking device and orifice docking device and docking fixation device. The bottom hole docking device is inside the refuge chamber which is designed for three lines: the food transmission pipe, air pressure pipe, and power and signal transmission line. The orifice docking device is mainly for fast docking of ground equipment and emergency rescue vehicles, and the external protection sealing device is designed to protect orifice docking device from harsh outdoor environments. The docking fixation device is the connecting fastening core of the borehole docking device and is responsible for safeguarding system functions such as air pressure, power transmission, and food supply. Field test results show that the system runs well after the docking of emergency rescue vehicle and refuge chamber. Air pressure, water supply, and power transmission run smoothly. The operation of monitoring, control, and personnel positioning systems is normal. The borehole docking system met the needs of the refuge chamber. It enhanced the flexibility and economy of the mine refuge facility.

KEYWORDS: emergency refuge system; refuge chamber; borehole docking system

1. INTRODUCTION

The establishment of an emergency refuge system is an effective guarantee of mine safe production. As the main part of the coal mine safety facilities, the borehole type refuge chamber has the advantage of having high security and no limit to refuge time (Sun, H., 2014). At present, the ground supporting facilities of borehole type permanent refuge chambers are mostly the control rooms. A large number of necessities and rescue equipment are stored in the ground control room, which has led to the high cost of its construction and maintenance. This limits the application of the borehole type refuge chamber (Han et al., 2011; Wang et al., 2011). Therefore, the development of ground maneuver rescue equipment which is suited for underground emergency rescue systems came into being. The ground maneuver rescue equipment matched with borehole type refuge chambers can provide ground emergency rescue for the underground refuge chamber (Ni and Yao, 2014). The current designs of borehole docking systems for ground maneuver rescue equipment are not perfect, therefore, it is necessary to design a new borehole docking system.

On the basis of the original borehole of the refuge chamber, the present study describes the design of a new kind of borehole docking system for the ground maneuver rescue equipment. The system

mainly includes three parts, including the bottom hole docking device, orifice docking device, and docking fixation device.

2. BOTTOM HOLE DOCKING DEVICE

The bottom hole docking device is placed inside the underground refuge chamber and connected with the upper orifice docking device. The upper and lower parts are connected with quick connectors; they can be used to convey wind, water, power, and signal. These transmission functions and physical interfaces are independent of each other (Hu, J., 2010).

2.1 *Underground connection mode*

The connection modes of the high-pressured air hose, power cable, monitoring and control line, shielded transmission line and food (water) transmission pipeline in the refuge chamber are shown in Figure 1.

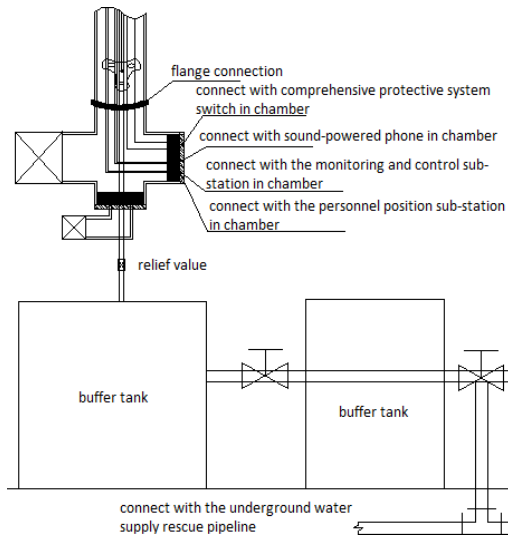


Figure 1: Diagram of underground connection mode.

2.2 Docking device configuration

The structure of the bottom hole docking device is designed to fully take into account the principles of safety and reliability. Bottom hole docking is divided into three lines. At the bottom there is liquid food (water) transmission line interfaces. Both sides are for interfaces of a high-pressured air hose and a power cable. Their internal connections are shown in Figure 2.

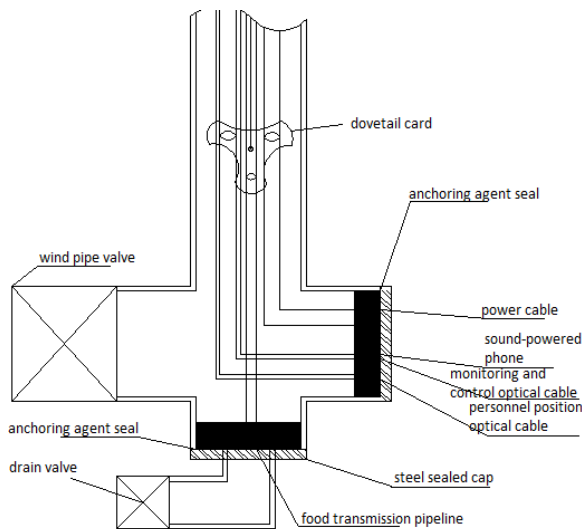


Figure 2: Design of docking device interface connection.

Transmission connections of power supply, communication signal, monitoring, and control signals are achieved using aviation plug fast connections. One end of the cables connected with the pipes is associated with underground docking device interfaces, and the other end is connected with

the rescue platform fast interface panel. The power cable uses a dedicated transmission fast interface. The esophageal flow path uses the threaded hose quick connector and the high-pressured air hose uses a flange bolt connection. The concrete connection mode of these pipelines is shown in Figure 3.

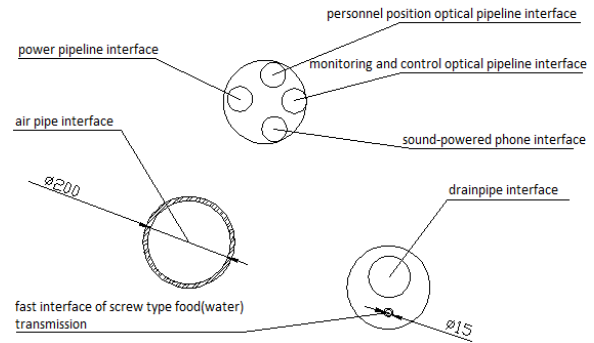


Figure 3: Pipeline interfaces schematic diagram.

3. THE ORIFICE DOCKING DEVICE

The orifice docking device is mainly for fast docking between ground equipment and emergency rescue vehicles. It shortens the connection time because it can help build temporary command places quickly. The location of the orifice docking device should be carefully considered. According to the position of the underground refuge chamber and ground environment, it should be placed in a flat, open area. The design of protection and auxiliary equipment should also be reasonable, easy to open, waterproof and fireproof, with security explosion-proof characteristics.

3.1 External protection sealing devices

External obturator is the establishment of an external protective cover to protect the orifice docking device. It should be waterproof, fireproof, and explosion-proof. At the same time it should have a protective effect on various orifice pipe interfaces and quick connectors. The docking device should be intact when the device is used to dock and it should achieve the best possible effect (Zhou et al., 2013). The design is shown in Figure 4.

In order for the external protection obturator to better fulfill its function, it is constructed of high strength isolating walls as a framework for external protective equipment. It is made up of the four following parts:

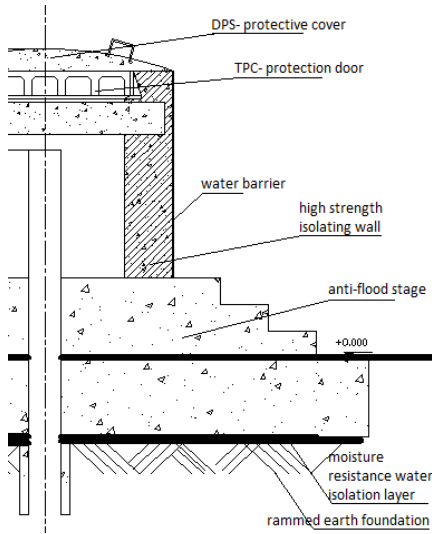


Figure 4: Design of external protection sealing devices.

1) The foundation

External protective devices are generally located in flat areas, where there is small gravel and prime soil compaction. The foundation is excavated to make it solid and reliable, backfilled with the original soil, and then the ground water is treated with high-grade cement.

2) Anti-flood stage

Moisture generated by rainwater can impact all types of electronic devices and internal pipe joints of protection devices. Therefore, they should be built with an anti-flood stage of more than 1m higher than the flood level at the high strength isolating wall. Meanwhile, in order to facilitate the job of rescue workers, treads and drainage ditches need to be established beside the anti-flood stage.

3) High strength isolating wall

A high strength isolating wall is constructed with masonry and concrete made of high index cement. Orifice size is determined according to the specific conditions of each mine. The thickness of the wall is generally around 0.3 m, with a height of no less than 1.2 m. After the masonry wall is built to waterproof the wall outside, waterproof coating can be brushed in the wall, or the pasted tarpaulins approach can be used.

4) Protection door

The TPC-protective door needs to be airtight. One side of the door should lock, as rescue personnel need to unlock the door. Due the inaccessibility to non-staffs, after opening the TPC-protective door, staff can perform regular maintenance.

5) Protective cover

Because of harsh protection conditions outside, setting the TPC-protective cover over the DPS- protection door can be more effective to protect it

from corrosion and other damage due to rain and sunlight all year around. After finishing the TPC-protective cover, a circular bottom arch is poured on the high strength of the wall. The arch radius is consistent with the radius of the high strength wall.

3.2 System docking device

The analog bottom hole docking device and orifice system device can be divided into three parts: the liquid food (water) pipeline interface, high-pressured air hose interface, and the power signal line interface. Except for the intermediate part of the orifice that sets aside space for the connection, the space is connected with the closed holder (Jin et al., 2012; Wang, 2013). The design is as shown in Figure 5.

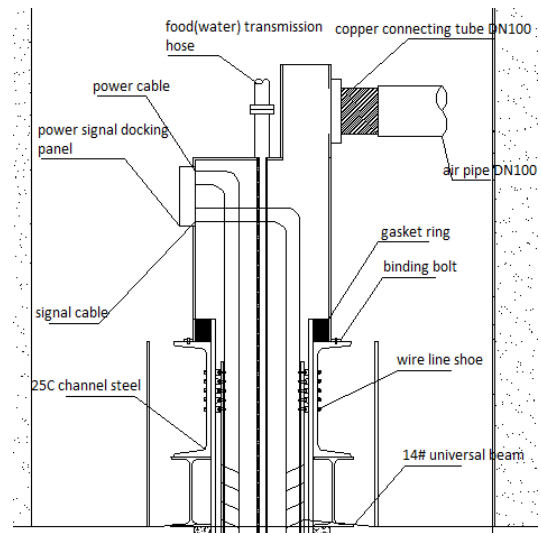


Figure 5: Design of docking system device.

1) Water pipe docking

(1) Liquid food transmission pipeline

One end of the liquid food delivery pipeline is connected with the orifice docking system by screw-type quick connector; the other end is connected with the maneuver rescue platform using D-type quick connectors.

(2) Chamber water-rescue system switching device

When the underground water system is damaged or the water pressure gauge displays abnormally in the refuge chamber, and the water quality is significantly turbid, the water rescue valve can be turned on, taking advantage of the rescue platform to help deliver water.

2) Air pressure and oxygen supply pipeline docking

(1) Gas transmission pipeline

After the mine disaster, the gas transmission pipeline (the main source of chamber's oxygen) is capable of transporting a steady stream of fresh air to

the chamber in order to prolong the survival time of the trapped personnel. To ensure the interface works effectively and to extend the service life of the interface, when not in use the interface must be sealed with a Jacob locking plug to prevent foreign matter entering the system to pollute the water.

(2) Oxygen self-help system switching device in chamber

When the return air system is damaged or the draft indicator shows that the air may be mixed with poisonous gases, and air transportation is significantly decreased, the air pressure supply value can be turned on, taking advantage of the rescue platform to provide enough air to the chamber.

3) Power system docking

(1) Power signal cable

The power signal cable that connects the rescue platform with the refuge chamber has the Mining Products Safety Approval and Certification. It has good insulating performance, stable transmission, the external protective layer is waterproof, anti-wet, and has protective ability.

Taking into account the scene of the rescue complex, the length of the pipeline should be appropriate, multiplied by the number of not less than 1 of the rich coefficient, in order to prepare for use.

(2) Power system switching device in chamber

Normally the power of the underground refuge chamber is connected to underground circuits through comprehensive security lines. After the mine disaster, underground substations may be damaged and the power ring network may not supply power normally. The independent power supply line of the maneuvering rescue platform will be turned on to supply power. For operation, one must open the power system switching device. The power generation unit on the rescue platform will provide power in the chamber.

4) Monitoring and control, personnel positioning, communication docking device

The device integrates all the interfaces used for monitoring and control, personnel location, and telephone communication. Generally it is divided into two parts: the power docking interface and signal docking interface.

(1) Power docking interface

The power interface is provided with a fast interface of three-phase four wire system. It can provide 660 V, 380 V, 220 V, 127 V stable AC power supply, and provide power for the maneuver rescue platform and refuge chamber.

(2) Signal docking interface

The signal interface includes three kinds of interfaces: monitoring and control, personnel location, and telephone communication. Their functions are the establishment of the communication

between the maneuver rescue platform and the underground refuge chamber, the real-time monitoring of the indoor personnel, the change of the environment parameters. They also provide detailed information for the field rescue.

4. DOCKING FIXATION AND OTHER ANCILLARY DEVICES AND FIELD TEST

4.1 Docking fixation device

The docking fixation device is the connecting fastening core of the borehole docking device. The device controls the oxygen pressure to the chamber, power transmission, liquid supply, monitoring and personnel positioning, telephone communication function. The device is mainly composed of H steel, high strength bolts, dovetail card, wire rope, and other components. The specific layout is shown in Figure 6.

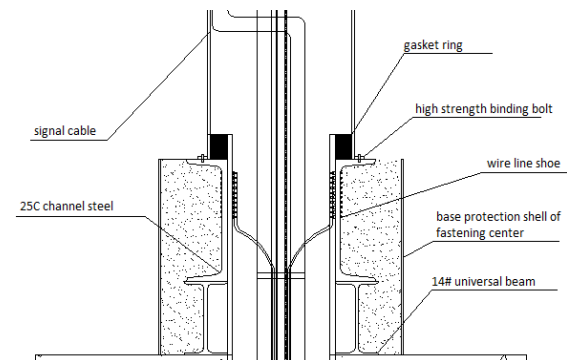


Figure 6: Internal connection diagram of the system.

4.2 borehole docking accessory device

The accessory device of the protection of the borehole is mainly made of two kinds of surface protective coating and outdoor rescue equipment.

1) Surface protective coating

In addition to the external orifice brush waterproof coating, it can also be brushed with anti-corrosion, rust-proof, non-toxic, anti-aging lipids ester paint. The paint safety level is adequate to satisfy the regulation of *Standard for Hygienic Safety Evaluation of Equipment and Protective Materials in Drinking Water* which is issued by the Ministry of Health P. R. China. It can prevent coating due to prolonged exposure, weathering, and erosion as a result of potential harmful ingredients from the orifice pipe into the refuge chamber.

2) Outdoor rescue equipment

(1) Military tents

The standard hexagonal military tent is chosen in outdoor rescue equipment. It is made of steel pipe

frame. Its structure is simple and reliable and is quick and easy to disassemble. The tent is wind resistant and the waterproof performance is good, with a large interior space. It has a compact structure and a collection of special canvas bags. It can be placed on the platform side of the toolbox, for instant access and long-distance transport.

(2) Explosion proof lamp

The case is made of a special aluminum alloy material. It can withstand strong impact, lighting protection class up to IP66. The lamp has a turning angle of 360°, tilt angle of 135°, and any position can be illuminated via hand-held lamp. It has an optional tripod, lifting in the 1.2 m to 3 m height range. The lamp can be adjusted in height by an optional handle, to meet the needs of various rescue work site lighting.

4.3 Field test

After connecting the emergency rescue vehicle with orifice docking device, rescuers can clearly observe real-time data of refuge chamber monitoring and control, personnel positioning and other facilities. At the same time, through the phone or via video communication, the rescuers can quickly and conveniently communicate with the underground experimenters. After turning on the control mechanism, the pressure of the air, the water, and the power supply run smoothly, meeting the design requirement of the refuge chamber.

5. CONCLUSIONS

The borehole docking system to connect ground maneuvering rescue equipment with underground refuge chambers consists of three parts: the bottom hole docking device, orifice docking device, and docking fixation device. The system is mainly connected to the ground and underground for air, food (water), power, monitoring and control, personnel positioning, communication and other functions.

All components of the system have been tested strictly in the field. The system can satisfy the needs of rapid orifice docking after underground emergency situations. The system has a low cost, high mobility, good compatibility, and is safe, reliable, and easy to maintain. It improves the convenience and economy of permanent refuge chamber.

The underground docking device and orifice docking device developed for ground maneuvering rescue vehicles can connect ground supply system and underground rescue system in a short time, improving the rescue efficiency.

6. ACKNOWLEDGEMENT

It is with great pleasure that we acknowledge the generous financial support of National Natural

Science Foundation of China (project number: 51474017) and Natural Science Foundation of Xinjiang Uygur Autonomous Region of China (2014211B013).

7. REFERENCES

- GAO, N., JIN, L., WANG, L. and YOU, F. (2011). Research and application of oxygen supply system in Changcun Coal Mine refuge haven. *Journal of China Coal Society*. Volume 5, pp. 149-153
- HU, J. (2010). Permanent and temporary fixed shelters construction in mining area. *SHANXI Coal*. Volume 30, No. 7, pp. 71-72,82
- JIN, L., ZHAO, Y., GAO, N. and WANG, L. (2012). Research and design of permanent refuge chamber in GUANGXI Dachang copper mine. *Mining Technology*. Volume 12, No. 5, pp. 40-42
- Ni H, Yao Y. (2014) Construction method and development tendency of mine refuge chamber. *Coal Engineering*, Volume 46, No. 1, pp. 12-13,17
- Sun H. (2014) Research and design on ground drilling type refuge chamber. *China High Tech Enterprises*, No. 19, pp. 26-28
- WANG, R. (2013). Design and application analysis of large diameter rescue hole refuge chamber. *Zhongzhou Coal*. No. 4, pp. 87-89
- WANG, T., ZHAO, Y., JIANG, Y. and SONG, Y. (2011). Design and application of underground refuge cave in mine. *Coal Mining Technology*. Volume 16, No. 4, pp. 33-36
- ZHOU, J., JIANG, S., PEI, W. and ZHANG, Z. (2013). Ground boreholes system design for permanent refuge chamber in Xishahe Mine. *Safety in Coal Mines*. Volume 44, No. 1, pp. 97-99

Use of the Analytic Hierarchy Process in safety control of rescue equipment

Zhang Yinghua, Sun Qian, Huang Zhian*, Gao Yukun

State Key Laboratory of High-Efficient Mining and Safety of Metal Mines (University of Science and Technology Beijing), Ministry of Education, Beijing, China, 100083

ABSTRACT

Ground maneuver rescue equipment is complex, therefore, systematic analysis and risk assessment of the rescue equipment needs to be carried out. This evaluation method provides positive guidance and reference for the management and maintenance of the equipment system.

At present, many countries adopt the risk matrix method to assist in decision-making about the safety control of important systems. There is a relationship between the possibility and importance of the factors that influence the development of the transaction. The risk matrix method can be used to find this relationship and to stratify the data. It also has a good effect on systems in which objective judgment is weak. The present study refers to the mature evaluation system in the field of abroad car production, combines the actual rescue situation of Fengfeng District in Jizhong Energy Group, and aims to establish a subjective evaluation system with special characteristics for underground emergency refuge systems. This evaluation system uses the method of scoring combing weight combined with the analytic hierarchy process. It provides a scientific basis and effective reference for daily use and maintenance of the entire system.

KEYWORDS: analytic hierarchy process; ground maneuver rescue equipment system

1. INTRODUCTION

Ground maneuver rescue equipment which supports the emergency refuge system is complex. During routine maintenance and rescue drills, it requires not only that the relative rules must be executed in installation and operation, but also that the unit of high weights in the system are controlled (Gao and Mu, 2000).

At present, many developed countries use the risk-matrix method for decision-making on major affairs and safety control of important systems. When processing systems with large amounts of data, this method does not have high reliability and accuracy. When using the risk-matrix method, the consistency of the risk matrix should be tested (Sun and Liu, 1999). If it cannot pass the test, it should be checked and adjusted until it has passed the test. On one hand, this method is time-consuming and laborious; on the other hand, the consistency of the evaluation matrix is low, due to differences in experience and understanding of evaluation personnel (Hartman, 2002).

To solve these problems, this study refers to the mature evaluation system of the field of abroad car production, combines the actual rescue situation of Fengfeng District in Jizhong Energy Group, and attempts to establish a subjective evaluation system with consideration for the special characteristics of underground emergency refuge systems. This evaluation system uses the method of scoring

combing weight combined with the analytic hierarchy process. Through the evaluation of personnel subjective scores on the factors that influence the criterion layer, the weight of the safety control index and the total score are concluded (Zhang, 2000). Lastly, the validity and necessity of AHP application will be proven through the computer consistency test and adjustment. This evaluation system assesses the safety status of maneuver rescue equipment systems objectively, and identifies risks and vulnerabilities. It can reduce the difference of consistency between the evaluation matrixes and thought of judges, propose the orientation of the safety control, and provide a scientific basis and effective reference for daily use and maintenance of the entire system. This method can evaluate the protection focus of maneuver rescue equipment systems effectively, and have a positive effect on safety management of the entire system.

2. ANALYTIC HIERARCHY PROCESS

The analytic hierarchy process divides all kinds of factors which affect the decision-making objectives into target layer, criterion layer, and scheme layer. Through the interaction between the levels, the weight of each factor to the target level can be determined qualitatively and quantitatively, in order to help the decision makers to make the appropriate decision (Chen and Crolla, 1996).

*Corresponding author – email : huang_za@qq.com

First, the AHP lists the factors that affect the target, and sets them into different levels according to the logic of the relationship between them. Second, it builds a hierarchical model according to the degree of membership between different levels. Then it determines the ranking from the bottom layer combing the subjective judgment and the mathematical method of the evaluation personnel. Finally, according to the calculated weight factor, it determines the impact of the target level and can assist decision makers to judge the planning (Jing et al., 2006).

After the establishment of the matrix, it should be judged by a consistency test to determine whether it is reasonable or not. If it passes the verification, the evaluation system meets the requirements. If it did not pass the verification, the judgment factor should be checked and adjusted, so that it can be in accordance with the logical relationship of the mathematical judgment. After the consistency test of

the criteria layer, the consistency between the levels of the hierarchical model is tested (Guo et al., 2008a).

3. ESTABLISHMENT OF FUZZY EVALUATION INDEX SYSTEM FOR RESCUE EQUIPMENT SYSTEMS

3.1 Hierarchical structure model

The influence factors on the safety and stability of the ground maneuver rescue equipment system are many, so it is necessary to take comprehensive consideration, combine the evaluation of individual performance index, and make a reasonable summary before establishing the AHP hierarchy model (Guo et al., 2008b). Referring to the mature evaluation system in the field of abroad car production (Xu et al., 2009), and combining the actual rescue situation of Fengfeng District in Jizhong Energy Group, a hierarchical structure model was established, as shown in Figure 1.

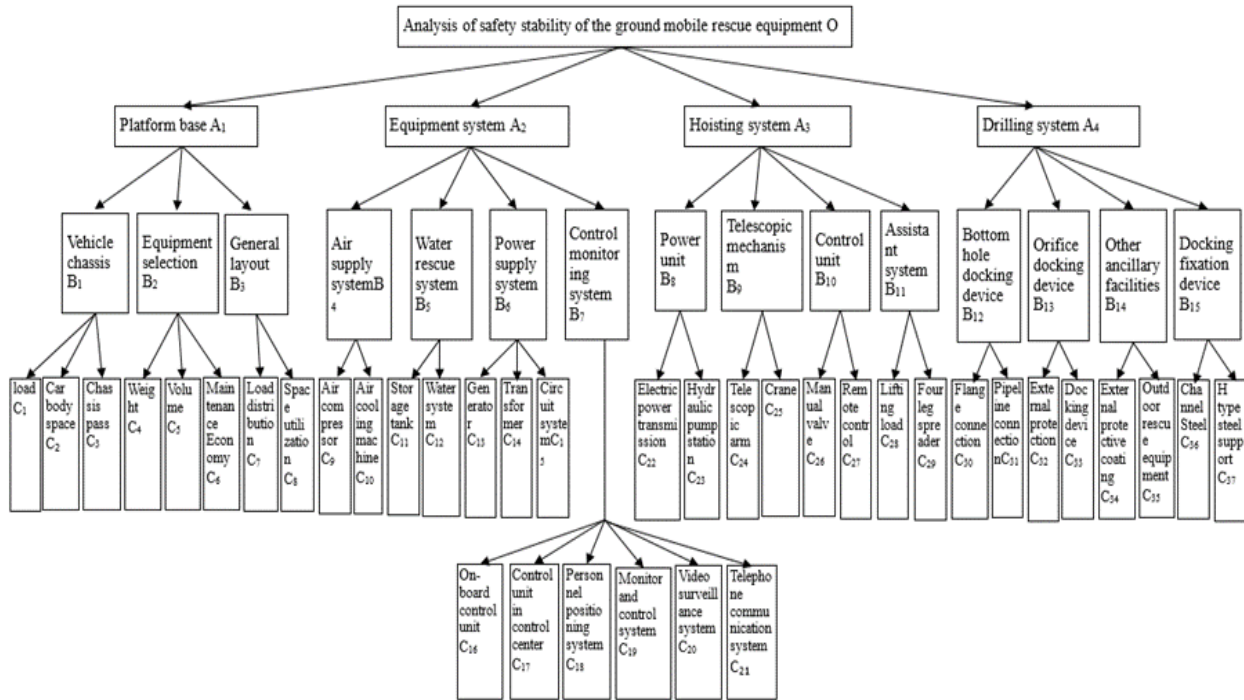


Figure 1: Hierarchical structure model of the ground maneuver rescue equipment system.

3.2 Scoring the scheme layer

Referring to the mature evaluation system of Society of Automotive Engineers, and combining the actual rescue situation (Fan et al., 2004), the scheme layer is scored by percentile system. With 5 points as a file, the higher the score, the more important it is. Specific scoring is as follows: C₁=70, C₂=75, C₃=75,

C₄=80, C₅=85, C₆=75, C₇=85, C₈=80, C₉=80, C₁₀=80, C₁₁=75, C₁₂=80, C₁₃=90, C₁₄=85, C₁₅=80, C₁₆=85, C₁₇=85, C₁₈=85, C₁₉=85, C₂₀=85, C₂₁=90, C₂₂=80, C₂₃=80, C₂₄=85, C₂₅=80, C₂₆=75, C₂₇=80, C₂₈=80, C₂₉=80, C₃₀=75, C₃₁=80, C₃₂=70, C₃₃=80, C₃₄=70, C₃₅=70, C₃₆=80, C₃₇=80.

3.3 Establishing judgment matrix

According to the above data, five evaluation personnel establish the pairwise comparison matrix, the comparison matrix values are as follows.

Safety stability:

$A_1/A_2=1/4$, $A_1/A_3=1/3$, $A_1/A_4=2$, $A_2/A_3=1$,
 $A_2/A_4=3$, $A_3/A_4=3$;

Platform base:

$B_2/B_3=1/2$, $B_2/B_1=1/2$, $B_3/B_1=2$;

Equipment system:

$B_5/B_6=1/4$, $B_5/B_4=1/3$, $B_5/B_7=2$, $B_6/B_4=1$,
 $B_6/B_7=3$, $B_4/B_7=3$;

Hoisting system:

$B_{10}/B_{11}=3$, $B_{10}/B_9=1/2$, $B_{10}/B_8=1/2$, $B_{11}/B_9=1/3$,
 $B_{11}/B_8=1/3$, $B_9/B_8=3$;

Drilling system:

$B_{13}/B_{12}=2$, $B_{13}/B_{15}=3$, $B_{13}/B_{14}=4$, $B_{12}/B_{15}=3$,
 $B_{12}/B_{14}=2$, $B_{15}/B_{14}=2$;

Vehicle chassis: $C_1/C_2=1/2$, $C_2/C_3=3$;

Equipment selection:

$C_4/C_6=2$, $C_4/C_5=1$, $C_6/C_5=1/2$;

Air supply system: $C_9/C_{10}=3$;

Water rescue system: $C_{11}/C_{12}=1/2$;

Power supply system:

$C_{14}/C_{13}=1$, $C_{14}/C_{15}=1/2$, $C_{13}/C_{15}=1/2$;

Control monitoring system:

$C_{19}/C_{18}=1$, $C_{19}/C_{20}=1/2$, $C_{19}/C_{17}=2$, $C_{19}/C_{16}=2$,
 $C_{19}/C_{21}=1/2$, $C_{18}/C_{20}=1/2$, $C_{18}/C_{17}=1/2$, $C_{18}/C_{16}=1/2$,
 $C_{18}/C_{21}=1/2$, $C_{20}/C_{17}=1$, $C_{20}/C_{16}=1/2$, $C_{20}/C_{21}=1/3$,
 $C_{17}/C_{16}=1/2$, $C_{17}/C_{21}=1/2$, $C_{16}/C_{21}=1/2$;

Power unit: $C_{22}/C_{23}=1$;

Telescopic mechanism: $C_{25}/C_{24}=1/3$;

Control unit: $C_{27}/C_{26}=1$;

Assistant system: $C_{29}/C_{28}=2$;

Bottom hole docking device:

$C_{31}/C_{30}=2$;

Orifice docking device: $C_{32}/C_{33}=1/2$;

Other ancillary facilities: $C_{34}/C_{35}=2$;

Docking fixation device: $C_{37}/C_{36}=2$.

4. SYSTEM APPLICATION BASED ON THE ANALYTIC HIERARCHY PROCESS

First, the hierarchical structure is drawn as shown in Figure 1.

Secondly, the judgment matrix of all levels should be assigned with values, and the consistency should be tested to ensure that the calculated value of the judgment matrix is less than 0.1. The consistency of the combination weight vector is also tested to ensure the level of comparative judgment.. When the judgment matrix is not consistent, it is reasonable to carry out inspection and make adjustments.

Software can sort the weight of the scheme layer and other layers quickly and facilitate the follow-up studies. The weight value of each factor is as follows:

$C_1=0.0101$, $C_2=0.0232$, $C_3=0.0088$, $C_4=0.0106$,
 $C_5=0.0106$, $C_6=0.0053$, $C_7=0.0501$, $C_8=0.0167$,
 $C_9=0.0549$, $C_{10}=0.0198$, $C_{11}=0.0169$, $C_{12}=0.0337$,
 $C_{13}=0.0111$, $C_{14}=0.0111$, $C_{15}=0.0223$, $C_{16}=0.0387$,
 $C_{17}=0.0274$, $C_{18}=0.0217$, $C_{19}=0.0345$, $C_{20}=0.0322$,
 $C_{21}=0.0657$, $C_{22}=0.0473$, $C_{23}=0.0473$, $C_{24}=0.1228$,
 $C_{25}=0.0409$, $C_{26}=0.0370$, $C_{27}=0.0370$, $C_{28}=0.0116$,
 $C_{29}=0.0232$, $C_{30}=0.0096$, $C_{31}=0.0192$, $C_{32}=0.0161$,
 $C_{33}=0.0322$, $C_{34}=0.0073$, $C_{35}=0.0036$, $C_{36}=0.0100$,
 $C_{37}=0.0050$.

5. ANALYZING RESULTS OF THE ANALYTIC HIERARCHY PROCESS

5.1 Analyzing the scheme layer

By comparing the above results, it can be found that the weight value has the following rules:

$C_{24}>C_{21}>C_9>C_7>C_{22}>C_{23}>C_{25}>C_{16}>C_{26}>C_{27}>C_{19}$
 $>C_{12}>C_{20}>C_{33}>C_{17}>C_2>C_{29}>C_{15}>C_{18}>C_{10}>C_{31}>C_{11}>C_8$
 $>C_{32}>C_{28}>C_{13}>C_{14}>C_4>C_5>C_1>C_{36}>C_{30}>C_3>C_{34}$.

It can be concluded that the telescopic arm, telephone communication system, air compressor, load distribution, and power transmission have more influence on security and stability of the system. Therefore, they should be a main focus of the design, use, and maintenance process. When analyzing the factors with higher weights, it can be found that these factors will directly affect the security and stability of the whole system.

5.2 Analyzing the criterion layer

The score of each criterion layer can be calculated by combining with the index weight coefficient of the target layer and the subjective evaluation of each criterion. For example, factors of the criterion layer related to platform base A_1 are load C_1 , car body space C_2 , chassis pass C_3 , weight C_4 , volume C_5 , maintenance economy C_6 , load distribution C_7 , space utilization C_8 . The weight coefficient of each index is 0.0101, 0.0232, 0.0088, 0.0106, 0.0106, 0.0053, 0.0501, 0.0167. Then the score of platform based A_1 is: $0.0101 \times 70 + 0.0232 \times 75 + 0.0088 \times 75 + 0.0106 \times 80 + 0.0106 \times 85 + 0.0053 \times 75 + 0.0501 \times 85 + 0.0167 \times 80 = 10.848$.

In the same way, the total score of other indicators can be calculated, as shown in Table 1.

Table 1: The score of criterion layer.

criterion layer	score
Platform base A_1	10.848
Equipment system A_2	33.072
Hoisting system A_3	29.797
Drilling system A_4	7.922

From Table 1, it can be seen that the equipment system A2 and the hoisting system A3 are more important for the safety and stability of the whole system. The influence factors are two times more than the influence of the platform base A1 and drilling system A4.

The score of equipment system A2 is slightly higher than the score of hoisting system A3. It is necessary to strengthen the daily safety management and control of the equipment system and hoisting system. Although the score of platform base A1 and drilling system A4 is not high, the key factors affecting the system also need to strengthen their safety management and control.

6. CONCLUSIONS

At present, there is no specific evaluation system for ground maneuver rescue equipment. Referring to the mature evaluation system of the field of abroad car production combined with the actual rescue situation of Fengfeng District in Jizhong Energy Group, this study established a subjective evaluation system with consideration for the special characteristics of underground emergency refuge systems.

In order to minimize the subjective uncertainty, this evaluation used the method of scoring combing weight combined with analytic hierarchy process. Through the evaluation of personnel subjective score on the factors that influence the criterion layer, the weight of the safety control index and the total score were found.

The validity and necessity of AHP application will be proven through a consistency test of computer and adjustment. This evaluation system objectively assesses the safety status of maneuver rescue equipment systems and identifies risks and vulnerabilities. It can reduce inconsistencies between the evaluation matrixes and thought of judges.

Through comprehensive consideration of the results of the evaluation test results and the weight coefficient of the ground mobile rescue equipment system, this study proposes the orientation of the safety control, and provides a scientific basis and effective reference for daily use and maintenance of the entire system.

7. ACKNOWLEDGEMENT

It is with great pleasure that we acknowledge the generous financial support of National Natural Science Foundation of China (project number: 51474017) and Natural Science Foundation of Xinjiang Uygur Autonomous Region of China (2014211B013).

8. REFERENCES

- Chen, D.C. and Crolla D A.A. (1996) Comprehensive study of subjective and objective vehicle handling behavior. *Vehicle System Dynamics*. Volume 25, No. 1, pp. 66-68.
- Fan, X.Y., Qiao, J.P. and Chen, Y.B. (2004) Application of analytic hierarchy process in assessment of typical landslide danger degree. *Journal of Natural Disasters*. Volume 13, No. 1, pp. 72-76.
- Gao, Y. and Mu, D.Y. (2000) AHP method in assessment of airline safety. *China Safety Science Journal*. Volume 10, No. 3, pp. 38-41.
- Guo, J.Y., Zhang, Z.B. and Sun, Q.Y. (2008) Study and applications of analytic hierarchy process. *China Safety Science Journal*. Volume 18, No. 5, pp. 147-153.
- Guo, J.Y., Zhang, Z.B., Sun, Q.Y. (2008) Applications of AHP method in safety science. *Journal of Safety Science and Technology*. Volume 4, No. 15, pp. 69-73.
- Hartman D. (2002) Application of the analytic hierarchy process to select characterization and risk-based decision-making and management methods for hazardous waste sites. *Environmental Engineering and Policy*. Volume 3, No. 1-2, pp. 1-7.
- Jing, Q.Z., Jiang, X.H., Yang, J.S. and Zhou, Y.F. (2006) Study on index system of capability of production safety in coal mine based on AHP. *China Safety Science Journal*. Volume 16, No. 9, pp. 74-79.
- Sun, R.S. and Liu, H.H. (1999) Assessment theory and practice for airline safety. *China Safety Science Journal*. Volume 9, No. 3, pp. 69-74.
- Xu, Y., Zhou, Y., Sun, X. and Yu, Y. (2009) Synthesized assessment method for coal mine safety based on fuzzy analytic hierarchy process. *China Safety Science Journal*. Volume 19, No. 5, pp. 147-152.
- Zhang, J.J. (2000) Fuzzy analytical hierarchy process. *Fuzzy System and Mathematics*. Volume 14, No. 2, pp. 80-88.

Research on new high-water solidified materials to reinforce coal and eliminate gas outburst

Yinghua Zhang, Peiling Zhou, Zhian Huang*, Yukun Gao, Qiang Luo

State Key Laboratory of High-Efficient Mining and Safety of Metal Mines(University of Science and Technology Beijing), Ministry of Education, Beijing, China, 100083

ABSTRACT

As coal and gas outburst is one of the main mine disasters, it is very important to prevent and eliminate the coal and gas outburst. Grouting setting liquid into coal can strengthen the coal seam, increase rigidity coefficient (f), and reduce expansion energy of gas. According to the related experimental procedures of cement paste, experiments on the performance of complex materials that high-water material added with different admixtures were carried out. Results showed that: as the increase of water-cement ratio (W/C), the mobility and setting time were all increased, but compressive strength and rupture strength were declined, furthermore, high-water material showed early strength, which can reach 80% of 14 days compressive strength when it is 7 days. As a rapid setting and early strength cement, Na_2SiO_3 had the best effects on shortening setting time, when dosage was 3% , the initial setting time and the final setting time were 13min and 21min shorter than blank samples, while the compressive strength increased more than 2 times. As retarder, the initial setting time can extend to 83min when compounding with tartaric acid of dosage of 0.4%. Through the orthogonal experiment the best additive ratio was determined, which was W/C=2, tartaric acid with dosage of 0.2%, Na_2SiO_3 with dosage of 3%, bentonite with dosage of 12%. Reinforcement simulation experiment showed that, grouting radius of new setting liquid was 250mm when grouting pressure was 60KPa, 7d rupture strength and compressive strength were 5.2MPa and 6.4MPa, and were 37% and 88% higher than ordinary high water material, which was effective for reinforcing coal and eliminating gas outburst.

Key words: gas outburst; setting liquid; reinforce coal; high-water solidified materials; rapid setting and early strength cement, retarder

1. INTRODUCTION

Gas outburst is one of the natural disasters that threaten the safety of coal mine (Qin, B.T. et al., 2013). Forming coal sample simulation results showed that, the stress and gas pressure was the power of gas outburst, and the strength of coal was the resistance, thus, gas outburst can be prevented by reinforcing the strength of coal(Yong, Q.L. et al., 2005; Zhu, J.K., 2011; Fu, J.H. et al., 2009).

Reinforcing coal and eliminating gas outburst is that grouting setting liquid into coal, which can infiltrate into the space of the coal and reinforce the coal (Gao, G.F., 2006). The study of grouting setting liquid by domestic and foreign scholars showed that setting liquid has effective effects on prevention of gas outbursts, the lower of its permeability and the greater of its consolidation strength, the better of its effects (Anon et al., 2006; Huang, Z.A. et al., 2010). High water material is a new type of special cement mixed material, whose water cement ratio can be as high as 3:1, and have the characteristics of good liquidity, good permeability, high strength, and adjustable performance parameters (Jiang, X.H. et al.,

2010; Lu, L.C., et al., 2005; Yan, Z.P. et al., 2006). Elimination of high water material setting liquid for gas outburst has been demonstrated by experiments and filed experiments by Zhang C.Y. and Xiao P.C. et al., and after handling of setting liquid, f of coal seam was highly increased and ΔP was decreased from 35.5 to 2 (Zhang, Y.H. et al., 2003; Feng, G.M. et al., 2011). Whatever, elimination effects of gas outburst is still not ideal, and high water material has the characteristics of adjustable performance, therefore, a new type of high water material can be researched by compounding with admixtures, which can improve the efficiency of elimination of gas outbursts.

2. MECHANISM OF REINFORCING COAL AND ELIMINATING OUTBURST

When grouting setting liquid into coal, on the one hand setting liquid infiltrate into the space of the coal, and free gas, partially adsorbed gas is driven out of the grouting coal seam, on the other hand setting liquid and coal is cemented together, which close the passage of gas desorption. At the same times, the

*Corresponding author – email : huang_za@qq.com

water prolapsed by solidification enter small pores, closing gas desorption passage with capillary force, which made the free gas cannot be formed by the adsorption gas, reducing the amount of gas involved and decreasing gas desorption rate (Xiao, P.C., 1994; Wu, Q. et al., 2010; Zhang, C., 2014).

3. NEW HIGH-WATER SOLIDIFIED MATERIALS TO ELIMINATE OUTBURST

The key of the method of reinforcing coal and eliminating gas outburst is the development of setting liquid. To conform to the special environment of coal mine and the requirements of grouting, the setting liquid must be low viscosity, good fluidity and can enter tiny pores. High water material is a new type of special cement mixed material, which is constituted of A component and B component, A component is sulphate-aluminate cement clinker and B component consists of gesso and lime. Powder material of A component and B component mixed with water respectively, then rapid setting and solidify through physical and chemical reactions (Cha, J. et al., 2010).

3.1 Experimental materials

Sulphate-aluminate cement clinker, deflocculant; retarder (calcium lignosulfonate and tartaric acid), rapid setting and early strength cement (sodium silicate, triethanolamine, sodium chloride and sodium aluminate), coal powder et al..

3.2 Methods and Instruments

Refer to the cement testing procedures and standards, make experiments on mobility, viscosity, syneresis rate, stability, setting time, compressive strength, tensile strength. Main instruments: NJ-160B cement paste mixer, NDJ-5S digital rotary viscosimeter, setting time standards detector, 40mm×40mm×160mm testing module, digital hydraulic pressure testing machine, HBY-40B standard curing box, et al..

3.3 Results and discussion

1) Effects of water cement ratio (W/C) on the properties of high water material

The W/C of high water material can be as high as 3:1, which has effects on mobility and early strength. High water materials when W/C=1.0, 1.5, 2, 2.5, 3 were prepared respectively, among them the ratio of A component and B component was 1:1, researching on the viscosity and setting time of the setting liquid, the results were shown as Table 1.

It can be seen from Table 1 that: As the increase of W/C of A component and B component, viscosity was decreased, and setting time was increased, final setting time when W/C=3.0 was 4 times of W/C=2.5, the increase of final setting time was larger than the

initial setting time. Hence, as the increase of W/C, the mobility was increased, but the increasing of setting time too much was not conducive to grouting. The following study focused on the strength of different W/C.

Table 1: Effects of W/C on viscosity and setting time

W/C	Viscosity		Setting time	
	A component / mPa · s	B component / mPa · s	Initial setting time / min	Final setting time / min
1.0	817	502	17	24
1.5	60	464	25	50
2	15	316	30	56
2.5	12	86	43	70
3.0	15	50	100	240

Weighed a certain amount of A component and B component, and the ratio was 1:1, mixed with bentonite whose dosage was 10% to improve stability, poured into the blender, then, make testing module for the experiments.

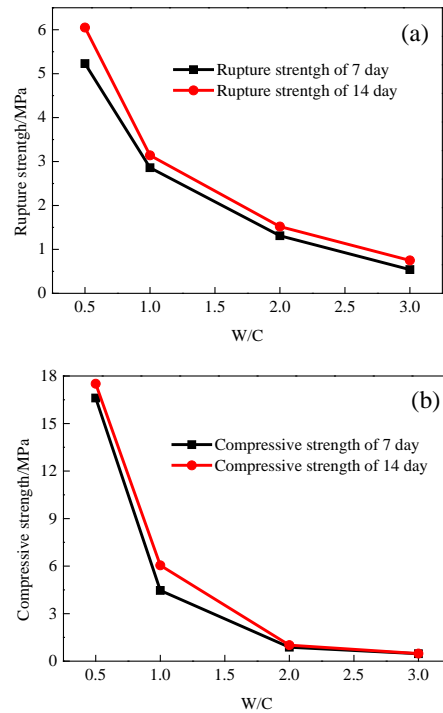


Figure 1: Strength of 7 day and 14 day under different W/C

(a) Rupture strength; (b) Compressive strength

As shown in Figure 1, compressive strength and rupture strength declined as W/C increased, 14 day compressive strength was 17.51MPa and 14 day rupture strength was 6.05Mpa when W/C=0.5, but 14 day compressive strength and 14 day rupture strength

was less than 1MPa. 14 day compressive strength and rupture strength were almost close to 7 day compressive strength and rupture strength, indicating that high water material had the character of early strength, the strength of 7 day had reach 80% of 14 day, this performance is very good for dealing with urgent situations.

2) Influence of rapid setting and early strength cement on the high water material

High water material with adjustable performance, therefore, the better performance setting liquid can be obtained by compounding with admixture. When W/C=2.5, bentonite dosage is 12%, adding rapid setting and early strength cement to the high water material, then, studied on the properties of setting liquid. The species and dosage of rapid setting and early strength cement was shown in Figure 2.

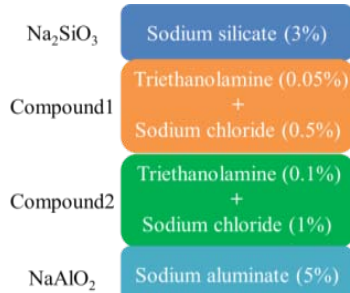


Figure 2: Species and dosage of rapid setting and early strength cement

It can be seen from Figure 3 that setting time was decreased obviously when there was rapid setting and early strength cement. Among the rapid setting and early strength cements, Na_2SiO_3 that dosage was 3% had the biggest influence on initial setting time, initial setting time of the setting liquid with Na_2SiO_3 was 17min, which was 13min shorter than the blank sample. The greatest impact on the final setting time was that liquid with NaAlO_2 , which was 24min shorter than the blank sample. As the increase dosage of compound, setting time was declined but changed a little. Not only the setting time changed but also the solidification strength, when adding rapid setting and early strength cement. Compressive strength and rupture strength were used to represent the mechanical strength of grout stone, as shown in Figure 4, the strength were all increased when added rapid setting and early strength cement.

(1) From the aspect of rupture strength, the strength of setting liquid with Na_2SiO_3 was biggest each period, rupture strength of 14 day was 0.68MPa higher than blank sample. For the same sample, 7 day rupture strength was the biggest, because of the evaporation of water, 14 day rupture strength was decreased, among them, liquid with compound

reduced the maximum and liquid with Na_2SiO_3 reduced minimum. Therefore, the setting liquid with Na_2SiO_3 has big early strength and changed little over time.

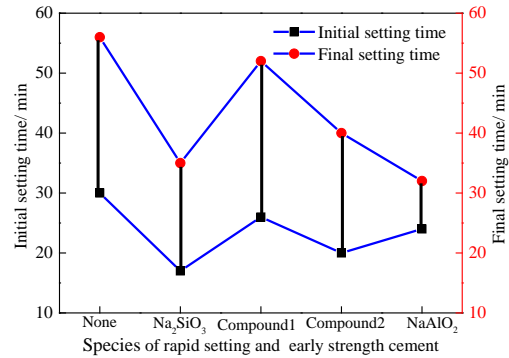


Figure 3: The effects of rapid setting and early strength cement on setting time

(2) From the aspect of compressive strength, it was increased as time increased. Compressive strength was increased after adding rapid setting and early strength cement, the most obviously was Na_2SiO_3 , whose 1 day strength was 1.58MPa and was 2.4 times of blank sample (0.65MPa), 7 day and 14 day strength was the biggest too. The 14 day compressive strength of setting liquid with NaAlO_2 was 1.64MPa, which was small than that with Na_2SiO_3 .

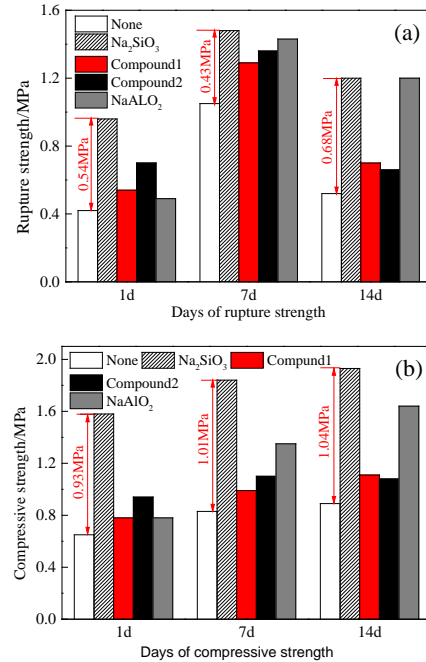


Figure 4: The effects of rapid setting and early strength cement on compressive strength and rupture strength
(a) Rupture strength; (b) Compressive strength

3) Influence of retarder on the high water material

The early strength of high water material increased after compounding with rapid setting and early strength cement, nevertheless, the mobility of the liquid was declined, and setting time decreased too much, which was not conducive to the penetration in coal. On the other hand, mobility and setting time can be adjusted through mixing with retarder.

In this work, calcium lignosulfonate and tartaric acid was used as retarder, Table 2 depicted that setting time increased as the increase of dosage of retarder. The effects of tartaric acid on the setting time was relatively large, the initial setting time of calcium lignosulfonate when dosage was 0.2% was close to that tartaric acid that dosage was 0.2%. When the dosage of tartaric acid was 0.2%, the initial setting time was 118min and final setting time was 167min, which were 83min and 108min longer than that of blank sample respectively.

Table 2: Influence of retarder on the high water material

Retarder		Initial setting time/ min	Final setting time/min
Name	Dosage (%)		
Calcium lignosulfonate	0.25	35	59
Calcium lignosulfonate	0.35	41	62
Calcium lignosulfonate	0.45	58	135
Tartaric acid	0.2	43	78
Tartaric acid	0.3	67	105
Tartaric acid	0.4	119	167

In addition, compounding with retarder influenced the mobility of the liquid. As shown in Figure 5, mobility was increased obviously, the increasing effects of tartaric acid was bigger than calcium lignosulfonate. As the increase of the dosage of retarder the mobility increased. The mobility can be 410mm when the dosage of tartaric acid was 0.4%, which was 1.4 times of blank sample, when the dosage of calcium lignosulfonate was 0.45%, the mobility of the liquid was 1.2 times of blank sample.

Because of high water material is in the range of easy setting, thus, if mobility is the reference standard, then, tartaric acid will be the best retarder.

Above all, W/C, rapid setting and early strength cement and retarder were the factor influence the

performance of setting liquid. Ultimately, the best composition was determined by multi factor orthogonal experiment, which was W/C=2:1, retarder was tartaric acid whose dosage was 0.2%, rapid setting and early strength cement was Na_2SiO_3 whose dosage was 3%, bentonite dosage was 12%.

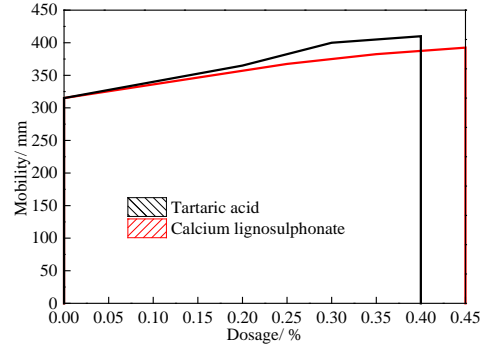


Figure 5: Effects of retarder on mobility of high water material

4. COAL REINFORCEMENT EXPERIMENT

In order to study the effects of grouting setting liquid, grouting process was simulated in the lab, the experiment model as Figure 6. Firstly, particle size of coal particles was selected, which were more than 2mm and less than 5mm, secondly, grouting new setting liquid on the coal. The grouting effect were showed in Figure 7.

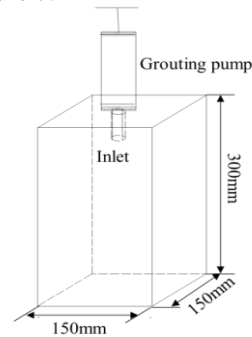


Figure 6: Grouting simulation experiment model

From the simulation experiment can be drawn that, dispersed particles were bonded together effectively by new setting liquid, and the strength was great. The grouting radius was 250mm when grouting pressure was 60KPa, which indicated that the new setting liquid had good adhesion and permeability.

Testing the strength of solidified body, rupture strength and compressive strength were showed as Figure 8. From Figure 8 we can see that the 1d, 7d, 14d strength of new setting liquid all have increased, 7d rupture strength and compressive strength were

5.2MPa and 6.4MPa respectively, and were respectively 37% and 88% higher than ordinary high water material.



Figure 7: Grouting effect picture

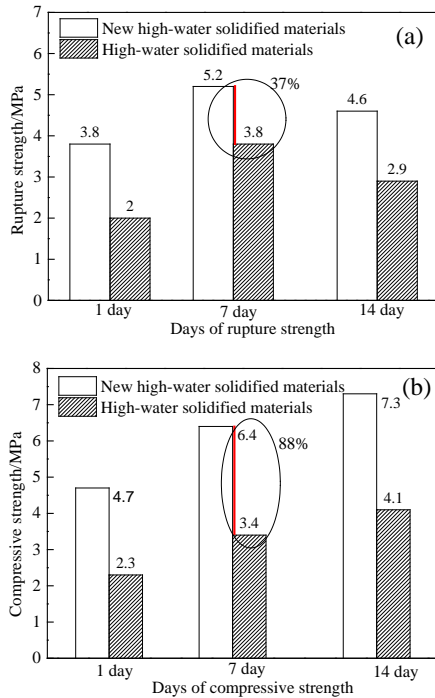


Figure8: Strength of coal dealing with new setting liquid
(a) Rupture strength; (b) Compressive strength

5. CONCLUSIONS

(1) As W/C of high water materials increased, setting time increased, viscosity declined and strength declined too. When W/C=0.5, 14d compressive strength was 17.51MPa, rupture strength was 6.06MPa, nevertheless, 14d compressive strength and rupture strength were less than 1MPa when W/C=3.0.

(2) While high water material mixed with different rapid setting and early strength cement, which has the most obviously changing effects was Na_2SiO_3 . When setting liquid compound with

Na_2SiO_3 of dosage of 3%, initial setting time can be shortened by 13min, 14d rupture strength and compressive strength were increased by 0.68MPa and 1.04MPa.

(3) Setting time and mobility can be adjusted by retarder, as a retarder tartaric acid had significant influence on the setting liquid. The initial setting time of tartaric acid that dosage was 0.2% was equal to that calcium lignosulfonate that dosage was 0.35%, the initial setting time and final setting time were extended 83min and 108min. When the dosage of tartaric acid was 4%, the mobility of setting liquid was 410mm, which was increased by 31%.

(4) Finally, the best ratio was: W/C=2, tartaric acid with dosage of 0.2%, Na_2SiO_3 with dosage of 3%, bentonite with dosage of 12%.

(5) Reinforcement simulation experiment of the new setting liquid showed that, grouting radius was 250mm when grouting pressure was 60KPa, 7d rupture strength and compressive strength were 5.2MPa and 6.4MPa respectively. The new high-water solidified materials with high strength and high fluidity was effective for the reinforce coal and eliminate gas outburst.

6. ACKNOWLEDGEMENT

It is with great pleasure that we acknowledge the generous financial support of National Natural Science Foundation of China (project number: 51474017) and Natural Science Foundation of Xinjiang Uygur Autonomous Region of China (2014211B013).

7. REFERENCES

- Anon. (2006). Self-consolidation grout. *Masonry Construction the World of Masonry*. Volume 19, No. 1, pp. 30-34
- Cha, J., Li, S.K., Li, J.H. (2010). Study on the durability of super early strength concrete. *Journal of Wuhan University of Technology*. Volume 32, No. 7, pp. 48-50
- Fu, J.H., Chen, Y.P. (2007). The status and control countermeasures of coal and gas outburst in coal mine in China. *Journal of Mining and Safety Engineering*. Volume 24, No. 3, pp. 1253-259
- Feng, G.M., Jia, K.J., Li, F.K. (2011). Research on the control of open backfill mining with ultra high water materials. *Journal of China University of Mining and Technology*. Volume 40, No. 6, pp. 841-845
- Gao, G.F. (2006). Status and related problems of coal gas outburst mechanism. *Industrial Safety and Environmental Protection*. Volume 32, No. 12, pp. 36-38

Huang, Z.A., Li, Y.F., Zhang, Y.H., Gao, Y.K., Chen, S.G. (2010). New grouting material to reinforce coal and eliminate outburst. *Journal of University of Science and Technology Beijing*. Volume 32, No. 7, pp. 833-837

Jiang, X.H., Guo, Z.X., Liu Q.Z. (2010). Effect of the amount of admixture of sulphoaluminate cement concrete chloride ion permeability. *Twenty-first Century building materials*. Volume 2, No. 2, pp. 23-25

Lu, L.C., Chang, J., Ye, Z.M. (2005). Aluminate silicate minerals and synthesis of high performance cement. *Journal of silicate*. Volume 33, No. 1, pp. 57-62

Qin, B.T., Lu, Y., Yin, S.J., Cao, K. and Wang, M.G. (2013). Prevention and control technique of complex disaster caused by gas and spontaneous combustion for fully-mechanized sublevel caving face in close-distance seams. *Journal of Mining & Safety Engineering*. Volume 30, No. 2, pp. 311-316

Wu, Q., Zhang, B.Y., Wang, H.Q. (2010). New hydrate-based technique for coal and gas outburst prevention and low-concentration coal mine gas separation. *Journal of Heilongjiang Institute of Science and Technology*. Volume 20, No. 1, pp. 23-27

Xiao, P.C. (1994). New technology of coal outburst prevention in Shimen. *Coal Mine Modernization*. Volume 10, No. 4, pp. 24-26

Yan, Z.P. (2006). Study on the microstructure of a soft soil in high water setting material. *Rock and soil mechanics*. Volume 25, No. 2, pp. 275-278

Yong, Q.L., Liu, Z.D., Sun, X. J. (2005). Theoretical calculation for equilibrium solubilities and compositional coefficient of titanium carbonitrides in Ti-bearing micro alloyed steel. *Steel Iron Vanadium Titanium*. Volume 26, No. 3, pp. 12-18

Zhu, J.K. (2011). Application of Shimen coal curing technology to prevent coal and gas outburst. *Coal Engineering*. No. 1, pp. 39-40

Zhang, Y.H., Liang, T.Z., Cui, J.K. (2003). Application Research of high water material in water injection, dust prevention and sealing technology in "Three Soft" coal seam. *Journal of China Coal Society*. Volume 28, No. 1, pp. 46-49

Zhang, C. (2014). Research on instability mechanism for sealing segment of boreholes and reinforcing dynamic sealing techniques. *China University of Mining and Technology*. 23p

Key technologies for extinguishing large-area goaf fires in closely spaced shallow coal seams

Botao Qin^{a,*}, Quanlin Shi^a, Junzhe Yang^a, Hetang Wang^a, Lihui Zhang^b

^a Faculty of Safety Engineering, Key Laboratory of Gas and Fire Control for Coal Mines of Ministry of Education, China University of Mining & Technology, Xuzhou, Jiangsu 221116, China

^b Bulianta Coal Mine, Shenhua Shendong Coal Group Corporation Limited, Erdos, Inner Mongolia 017209, China

ABSTRACT

The present study examines the spontaneous combustion fire in large-area goaf of the 22305 fully caving face at the Bulianta coal mine in north-western China. The cause of the spontaneous combustion in the goaf of closely spaced shallow coal seams is analysed. To deal with the problem of serious air leakage combined with a large fire area and a hidden fire source that could easily re-ignite, a proposed set of key techniques for extinguishing goaf fires is put into practice. This mainly comprises sealing the air leakage cracks, high-flow injection of liquid nitrogen, and infusion of a large quantity of foam inhibitor. The results show that these measures rapidly extinguished the goaf fire, lowered the CO concentration from 43,051 ppm to less than 25 ppm, and reduced the temperature in the goaf to about 20°C. The 22305 face was subsequently safely reopened and quickly put back into production within three months.

KEYWORDS: coal seam; spontaneous combustion of coal; goaf fire; liquid nitrogen; foam inhibitor

1. INTRODUCTION

Coal is the main energy source in China, accounting for about 70% of the production and consumption of primary energy (Tang and Li, 2013). The Chinese coal mining industry is mainly concentrated in the north-west (Fan, 2016). The Shendong mining area, located in north-western China, is China's largest coal production base, with a 250 million tonne output in 2012. However, the coal seams in the Shendong area are prone to spontaneous combustion. Contributing to this problem is the shallow burial depth (30-200 m) and the close spacing between the two coal seams (30-50 m), both of which are factors that lead to severe air leakage during the mining process. Thus, spontaneous combustion occurs very frequently in this mining area, threatening mineworkers' safety and producing large amounts of toxic gases, as well as sulfur, mercury, selenium and other harmful substances that cause significant local atmospheric pollution (Luo and Liang, 2003; Gu and Zhang, 2012; Kuenzer et al., 2007; Wang, 2009). Therefore, it is of great importance to take effective measures to prevent and extinguish spontaneous combustion fires in closely spaced shallow coal seams.

At present, coal mines in Shendong usually use conventional technologies, such as water injection, clay grouting, nitrogen injection and so on, to control spontaneous combustion fires. However, the effectiveness of these conventional technologies is unsatisfactory, since water injection and clay

grouting commonly encounter the problems of small diffusion range, easily drained water and slurry, and a weak cooling capacity of nitrogen (Wang et al., 2012; Wang, 2008). For example, in June 2012, a serious spontaneous combustion fire occurred in the goaf of the 22305 fully caving face in the Bulianta coal mine, which is the largest mine in the Shendong area. The peak concentration of CO was detected to be in the tens of thousands of parts per million. Initially the mine used water injection and clay grouting in an attempt to extinguish the fire, but the CO concentration showed no obvious decrease and the fire zone continued to spread. This caused the closure of the 22305 face, cutting off abundant coal resources and trapping expensive mining machinery. Clearly, a more positive and effective fire control technology was urgently needed.

This paper takes the Bulianta fire as a typical case. By analyzing the characteristics and causes of spontaneous combustion in this shallow coal mine where the coal seams are closely spaced. A set of efficient fire prevention and extinguishing techniques is proposed and practiced.

2. METHODS AND SCHEME

2.1 Analysis of causes of coal spontaneous combustion

The 22305 face was put into operation on 16 June 2012. At 2:00 p.m. on 23 June, blue charcoal smoke was detected coming from the goaf alongside

*Corresponding author – email : qbt2003@163.com

the return airway. The CO concentration was up to 1600 ppm in the upper corner and reached 300 ppm in the return airway. The coal face stopped production during the morning shift of 24 June when the face had advanced only 47 m. As mentioned above, water injection and clay grouting did not control the fire in time, and on 24 July the coal face was sealed off. The reasons for the goaf fire were as follows:

(1) About 2.0 m of top coal was not mined out, so abundant broken coal remained in the goaf. The 12 goafs of the Bulianta mine, together with the adjacent Shangwan mine, formed a total goaf area of 19.7 million square metres. The coal seams are prone to spontaneous combustion, and the shortest spontaneous combustion period, between the date of coal seam exposed to air and the date of occurring spontaneous combustion, was only 30 days. Adding to the problem, the porosity of the coal increased dramatically when soaked in water (Figure 1), rapidly raising its oxygen absorption rate and further increasing the risk of spontaneous combustion.

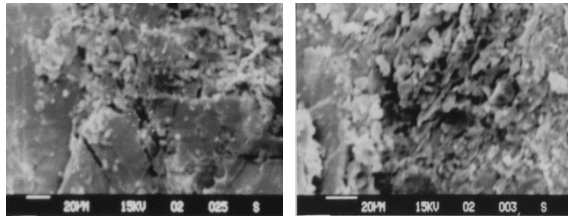


Figure 1: SEM image of pore structure of coal (a) before water soaking; (b) after water soaking.

(2) The coal seams in the Shendong mining area are very shallow, with a thick layer of loose overburden material that has very low strength in tension and compression, and low resistance to deformation, all of which make it vulnerable to the formation of mining-induced fissures and fractures. The roof rock of the goaf is very thin; consequently, surface subsidence and deformation is very difficult to control. As a result, pathways for air leakage between the goaf and the ground surface formed readily during mining, causing serious air leakage into the goaf (Figure 2). In addition, the Bulianta Mine has more than 90 connecting roadways between the goaf and the lower coal seam currently being mined, potentially providing a very large number of underground air leakage pathways.



Figure 2: Typical air leakage fractures in the Shendong mining area.

(3) When mining the upper coal seam, a great many mining-induced fractures form in the roof rock of the goaf and propagate to the ground surface (Figure 3), allowing surface water and underground water seepage to enter the goaf, with the result being that a large volume of water accumulates there. Then, when the underlying coal seam is mined, the accumulated water is discharged into the mine, causing large volumes of air to leak from the mine below the goaf to replace the lost water. For example, in the goaf above the 22305 face—originally the result of mining the upper seam (the 22304 face)—1.1 million m³ of water was discharged. This amount, together with the 475,000 m³ of water drained from the goaf of the 22305 face itself, greatly increased the air leakage.

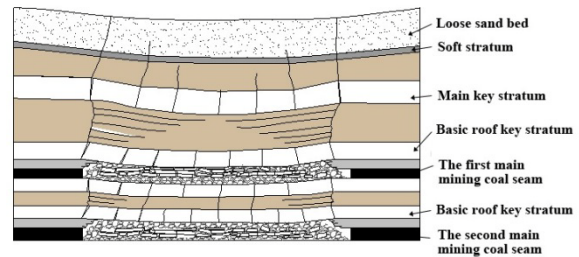


Figure 3: Schematic diagram of mining-induced fractures connected to the ground surface.

2.2 Plugging air leakage channels

At the surface, a combination of artificial and mechanical backfill was used to plug the leakage fractures and cut off the air leakage channels. To block the underground air leakage channels, shotcrete was used to reinforce the sealing walls in the connecting roadways.

As shown in Figure 4, sulfur hexafluoride (SF₆) tracer gas was used to investigate the distribution of the air leakage pathways and analyse the air leakage effect of fracture propagation over different periods.



Figure 4: Detection of air leakage pathways using SF₆.

2.3 Injecting liquid nitrogen

The temperature of liquid nitrogen is $-195.8\text{ }^{\circ}\text{C}$, and its latent heat of vaporisation is 199 kJ/kg . Liquid nitrogen quickly evaporates into gaseous nitrogen at a temperature of $-193\text{ }^{\circ}\text{C}$; one tonne of liquid nitrogen forms 780 m^3 of nitrogen gas. Thus liquid nitrogen absorbs more heat-in other words, has a greater cooling effect-than nitrogen gas (Yuan and Wan, 2013).

The liquid nitrogen system consisted mainly of a moveable storage tank containing liquid nitrogen produced by Shenhua Coal Liquefaction Plant (as shown in Figure 5), a cryogenic centrifugal pump and stainless steel piping. Figure 6 illustrates the process of injecting the liquid nitrogen: first, the liquid nitrogen was transferred by the cryopump to the delivery pipeline; then, the liquid nitrogen was directly injected into the high temperature points of the fire zone through a series of 20 holes drilled from the ground surface. The liquid nitrogen extinguished the fire and suppressed the possibility of explosion, and also absorbed a great deal of heat as it vaporized.



Figure 5: Lorry carrying storage tank of liquid nitrogen.

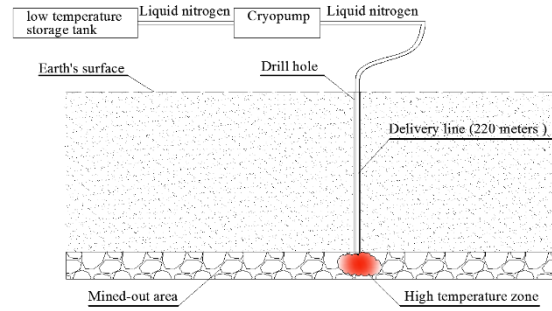


Figure 6: Liquid nitrogen injection process.

To rapidly reduce the temperature of the fire zone and displace the harmful gases accumulated in the goaf, the liquid nitrogen was poured into the goaf through 20 drill holes (MH26–MH45) from the ground surface, as show in Figure 7. Between 24 July and 7:00 a.m. on 20 August 2012, approximately 13,250 tonnes of liquid nitrogen were poured into the high-temperature zone.

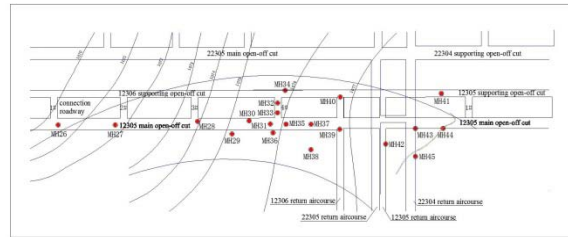


Figure 7: Location map of drill holes MH26–MH45 for liquid nitrogen injection.

2.4 Diffusion of foam inhibitor

The foam inhibitor was generated from slurry of yellow mud or fly ash, compressed air and a solution of foaming agent and retardant. The foam was generated at a rate of $600\text{--}1000\text{ m}^3/\text{h}$, with a stability time of 12 h, and an effective diffusion radius more than 60 m. Using this volume of foam as the carrier, together with its wide diffusion characteristics, the retardant was carried to greater lateral distances and higher points in the fire area than could be reached by conventional liquid or solid fire-fighting mediums. The foam generating equipment mainly consisted of a metering pump, foam generator and foam delivery hose.

Figure 8 shows the fire extinguishing process of the foam. First, a metering pump adds the solution of foaming agent and retardant at a given ratio into the slurry of yellow mud or fly ash; then, compressed air is mixed with the slurry, producing a large volume of

foam; finally, the foam is injected into the fire zone via a delivery hose and drill holes.

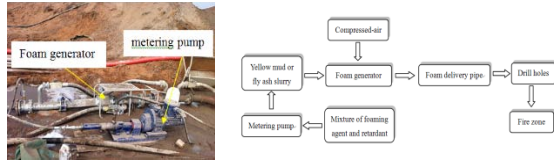


Figure 8: Preparation equipment of foam inhibitor.

Between 10 and 20 August 2012, a total of 770 tonnes of foam inhibitor was injected into the fire zone through 10 holes (ZJ5–ZJ14) drilled from the ground surface. The locations are shown in Figure 9.

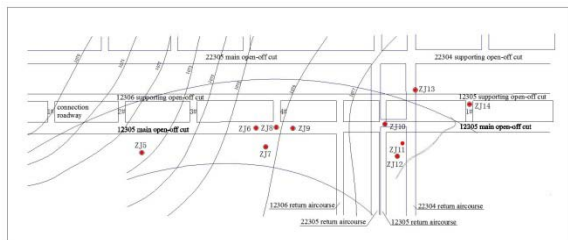


Figure 9: Location map of drill holes ZJ5–ZJ14 for foam injection.

3. RESULTS AND DISCUSSION

Following the injection of liquid nitrogen and foam into the goaf fire zone, sampling analysis of the fire index gases was conducted at eight measuring points (Figure 10) at ground level and underground. The continuous sampling test results showed that the concentration of fire index gases, O₂, CO, C₂H₂ and C₂H₄, declined continuously (Figure 11).

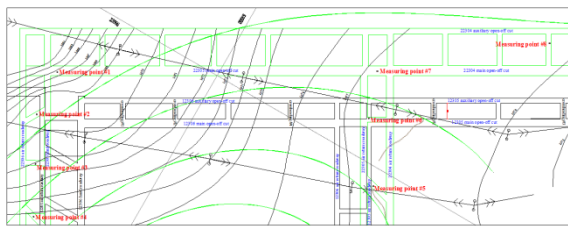


Figure 10: Location map of measuring points for fire zone.

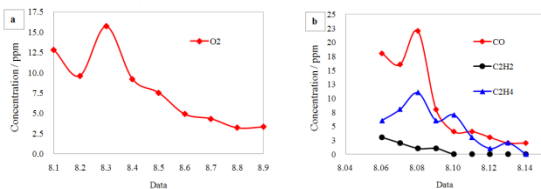


Figure 11: Change trend of different index gases.

Seen from Figure 11a and 11b, the oxygen concentration in the fire zone was below 5.0% from 6 August 2012, the acetylene (C₂H₂) concentration remained steady at 0 ppm from 9 August and the concentration of ethylene (C₂H₄) remained steady at 0–5 ppm from 11 August. In addition, the concentration of carbon monoxide (CO) gradually decreased during the period that the coal face was closed from a peak value of 43,051 ppm to a stable value of 5 ppm. The air temperature of the closed fire zone stabilized at around 20°C. According to Chinese Coal Mine Safety Regulations, these values indicated that the goaf fire at the 22305 coal face had been extinguished, and conformed to the conditions under which the face could be unsealed. The face was safely unsealed on 21 August and production smoothly resumed on 23 August.

After production was resumed at the Bulianta coal mine, the concentrations of index gases remained normal, with CO concentration steady at 6–7 ppm, the minimum concentration of O₂ was 19.8%, and the concentration of the other gases was 0.02–0.08%. This indicated that the foam inhibitor had effectively prevented the further fragmentation of coal in the goaf. From 8 October 2012, the 22305 coal face had safely advanced 558 m.

4. CONCLUSIONS

Spontaneous combustion fires in the goaf of fully mechanized caving faces mining two closely spaced shallow coal seams are characterized by a large volume of air leakage, a large fire zone and a hidden fire source. These conditions are highly prone to spontaneous combustion ignition and re-ignition, and conventional fire prevention and extinguishing methods such as water injection, grouting and nitrogen gas injection are largely ineffective in controlling such fires.

In these conditions, air leakage cracks are readily caused by the mining process, causing a high rate of air leakage into the goaf and providing a sustainable oxygen supply that is ideal for initiating spontaneous combustion of coal. Therefore, taking positive measures to block the air leakage channels is very important.

When low-temperature liquid nitrogen fills a sealed goaf, it quickly vaporises at normal pressures and temperatures. The cold nitrogen gas then quickly spreads to fill the entire fire area, displacing the other gases generated by the fire. The oxygen concentration drops rapidly, smothering the fire. The cold nitrogen gas also lowers the temperature of the fire zone by absorbing heat as it converts from the liquid to the gaseous phase, due to its latent heat of evaporation.

Foam inhibitor pumped into the goaf spreads widely throughout the fire-prone zone, transporting the fire retardant to areas that would otherwise be inaccessible to single liquid or solid fire-extinguishing materials. This makes it highly suitable for controlling fires occupying large spaces in the goaf, and/or hidden fires, and for preventing spontaneous combustion re-ignition.

5. ACKNOWLEDGEMENT

This work was supported by the National Natural Science Foundation of China (No. U1361213, 51476184) and A Project Funded by the Priority Academic Program Development of Jiangsu Higher Education Institutions (PAPD).

6. REFERENCES

- Fan W., Liu B.F., Ouyang X., An D. and Hu Z.H. (2016). Analysis on market sales status and measures of coal enterprises, *Coal Economic Research*, Volume 36, No. 1, pp. 68–70
- Gu, D. and Zhang, J. (2012). Modern Coal Mining Affected to Underground Water Deposit Environment in West China Mining Area, *Coal Science and Technology*, Volume 40, No. 12, pp. 12–15
- Kuenzer, C., Wesslin, W., Zhang J. et al. (2007) Concepts for Green House Gas Emission Estimation of Underground Coal Seam Fires, *Geophysical Research Abstracts of the EGU General Assembly*, pp. 164-170.
- Luo, H. and Liang, Y. (2003). Current Status and Perspective of Forecast and Prediction Techniques for Spontaneous Combustion of Coal, *China Safety Science Journal*, Volume 3, No. 13, pp. 76–78
- Tang, X. and Li, S. (2013). Research on the measures of energy problem of industrialization in our country, *Economic Issue*, No. 1, pp. 124-126
- Wang, H. (2009). The research of coal mine fire safety and the phenomenon of spontaneous combustion in China, *Science & Technology for Development*, No. 12, pp. 12-15
- Wang, B., An, S. and Guan W. (2012). Detection and Governance of the Spontaneous Combustion High-temperature Region in Shallow Burial and Thick Coal Seam. *Safety in Coal Mines*, Volume 43, No. 45, pp. 45-49
- Wang, D. (2008). *Mine fires*, Xuzhou: China University of Mining and Technology Press, 245 p.
- Yuan, Z. and Wan, L. (2013). Application of liquid nitrogen system to control fire in coal mine. *Coal Engineering*, No. 3, pp. 45-49.

The assessment of emergency capability of coal mines based on AHP-fuzzy comprehensive method

Shu Jiao Tong^{a,*}, Zong Zhi Wu^b, Ru Jun Wang^a, Ying Quan Duo^a

^aKey Laboratory of Major Hazard control and Accident Emergency Technology, State Administration of Work Safety, China Academy of Safety Science and Technology, Beijing, China, 100012

^bChina's State Administration of Work Safety, Beijing, China, 100713

ABSTRACT

In order to improve emergency management capabilities and the prevention and control of major accidents, it is important to study various methods for the assessment of the emergency capabilities of coal mines. This paper aims to bring about an analytic hierarchy process (AHP) and fuzzy comprehensive method to assess the emergency capabilities of coal mines. Firstly, the key elements of the emergency management for coal mines are analyzed based on the theories of the emergency management. From the precaution, response, and recovery aspects, the assessment index system of the emergency management capabilities for coal mines is built and the basic indexes of each element are confirmed and discussed. Furthermore, a multi-level fuzzy comprehensive evaluation model for mine emergency management capability is built based on the AHP (Analytic Hierarchy Process) and fuzzy mathematics. The assessment index system and mathematical model are applied to a selected mining enterprise whose assessing result was "high". Some shortcomings of the emergency system of the coal mine were analyzed and some suggestions were proposed to improve the emergency capabilities for the coal mine. The study is helpful for emergency management and the prevention of major accidents in coal mines.

KEYWORDS: coal mine; emergency capability; AHP; fuzzy comprehensive assessment

1. INTRODUCTION

It is well known that coal resources are an important foundation for energy and raw materials. China's coal industry has made remarkable achievements after nearly a decade of rapid development and production safety in mining has greatly improved. However, safety management in coal mines is still not good enough and lots of accidents have happened in the last decades. According to the statistics, the mortality rate of coal mines in China is 2.81 in 2005, 2.04 in 2006, 1.49 in 2007, 1.18 in 2008, 0.89 in 2009, 0.75 in 2010, and 0.56 in 2011. Meanwhile, the mortality rate of coal mines is about 0.05 to 0.03 in the United States, Australia, and other developed countries in recent years. The mortality rate for one million tons of coal mines in China is almost 30 to 50 times that of the United States and other advanced countries. The most important reasons for the coal mine accidents in China are the imperfect emergency system and poor emergency management.

Effective emergency and rescue can lessen the casualties and wealth losses of mining accidents. Emergency management capability assessment is an important part of safety management in coal mines. At present, the relevant research on the safety of coal mines mainly concentrates on risk assessment and safety management methods, and it is limited in the

study of emergency management, especially in the quantitative calculations. Most studies focus on theoretical discussion and qualitative analysis. Therefore, in order to improve the emergency management capabilities to prevent or control major accidents, it is important for the safety of coal mines to study the methods of assessment of emergency management capabilities.

In this paper, the key elements of the emergency management for coal mine were analyzed based on the theories of emergency management. The assessment index system of the emergency management capability for coal mines was built and a multi-level fuzzy comprehensive evaluation model for mine emergency management capability was built based on AHP and fuzzy mathematics. The assessment index system and mathematical model were applied to a selected mining enterprise to find out the shortcomings of the existing emergency system. Finally, some conclusions and suggestions were proposed to improve the emergency capabilities of coal mines. The study results will be helpful in advancing safety and emergency management scientifically to prevent and control major accidents in coal mines. At the same time, the results provide a theoretical basis and management guidance for government departments to manage coal mines.

*Corresponding author – email: tongshujiao@mail.neu.edu.cn

2. KEY ELEMENTS OF EMERGENCY MANAGEMENT FOR COAL MINES

Emergency refers to how to answer the emergent conditions. Usually it means the treatment measures adopted when the emergent conditions happen, and it includes a series of safety techniques and measures adopted to avoid accidents or lessen casualties and wealth loss in production. Therefore, it is often called accident emergency. Emergency management includes rapid and early warning, effective control, and active treatment to minimize losses during the concurrent and feedback of the unexpected accidents. Emergency management capability is the capability to deal with and avoid risk, and it involves the former preparation, disaster response, and support and rebuilding after the natural or manmade disaster.

The objects of emergency management are the unexpected incidents that could induce large casualties, wealth loss, and environment pollution. The capability of emergency management is the capability to control the unexpected incidents. The capability of emergency management for coal mines means the capability to control major unexpected accidents. The assessment of emergency management can be useful in realizing the precaution and control of major accidents.

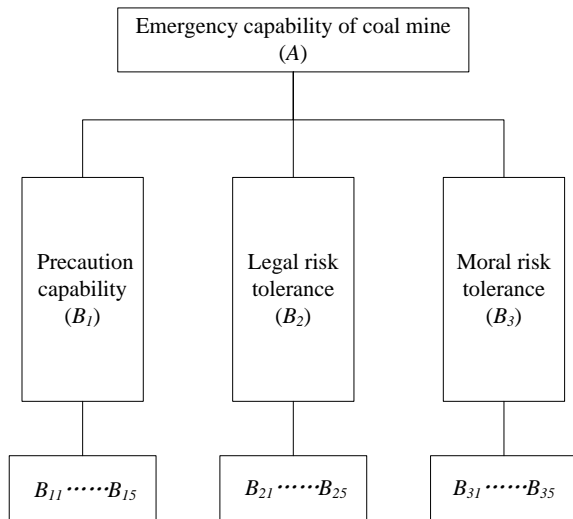


Figure 1: Structure of emergency capability of coal mine.

Emergency management is a lasting and persistent process. The key elements of emergency management include four phases: precaution, preparation, responds and recovery (Fan, 2011). The precaution and preparation phases share many common elements, so they are always combined in practice. The structure of emergency capabilities of coal mines is shown in Figure 1.

From the Figure 1, it can be seen that the precaution capability, response capability, and recovery capability constitute the emergency capability of coal mines. The precaution capability B_1 includes six indexes such as regulations and standards B_{11} , safety management B_{12} , emergency organization and plans B_{13} , emergency resources B_{14} , and training and education B_{15} . The response capability B_2 includes six indexes such as emergency communication B_{21} , rescue actions B_{22} , medical aid B_{23} , resources allocation B_{24} , and refuge and evacuation B_{25} . The recovery capability B_3 includes five indexes such as scene cleaning B_{31} , damage evaluation and insurance B_{32} , emergency plan update and improvement B_{33} , rebuilding B_{34} , plan improvement, and perfection B_{35} .

In order to assess the emergency capability of coal mine, it is necessary to build the scientific and reasonable index system and apply the operable assessment methods to the emergency management system, and make comprehensive assessment to get a conclusion periodically. All the jobs will find out the merit and shortcoming of the emergency management, and the actual capability of emergency management of coal mine will be enhanced step by step.

3. ASSESSMENT INDEX SYSTEM OF EMERGENCY CAPABILITS FOR COAL MINES BASED ON AHP

3.1 Analytic Hierarchy Process

AHP (Analytic Hierarchy Process) (Chen et al., 2009; Zheng et al., 2010) is a kind of decision-making method that is applied widely to solve relatively obscure or complicated decision problems by qualitative and quantitative analysis methods. Because the emergency capability of coal mines is a complex decision problem, the assessment model of the emergency capability of coal mines can be established based on the AHP (Analytic Hierarchy Process) method.

AHP quantifies the judgement made by the experience of the decision maker. Furthermore, it can layer our thought process and compare related items and check the rationality of the compared result step wisely to supply the convictive criterion. Many decisions can be solved by the analytic hierarchy process.

The steps of AHP include:

- (1) Building hierarchy structure model;
- (2) Establishing judgment matrix;
- (3) Consistency checking for judgment matrix;
- (4) Calculating weight vector;
- (5) Calculating combinatorial weight vector;
- (6) Overall consistency checking;

(7) Fuzzy comprehensive judgment.

3.2 Assessment indexes

According to research on the emergency capability evaluation of coal mines and the AHP method, combined with the advices of emergency, safety, management, and fire experts, a comprehensive index system of emergency capability for coal mines is built from the perspective of the whole process of the emergency management of coal mines. The assessment indexes system of the emergency capability of coal mines is built in Table 1.

Table 1: Assessment indexes system for coal mines.

Top layer	Second layer	Third layer (index layer)
Emergency capability of coal mine A	Precaution capability B ₁	Regulations and standards B ₁₁
		Safety management B ₁₂
		Emergency organization and plan B ₁₃
		Emergency resources B ₁₄
		Training and education B ₁₅
	Response capability B ₂	Emergency communication B ₂₁
		Rescue actions B ₂₂
		Medical aid B ₂₃
		Resources allocation B ₂₄
		Refuge and evacuation B ₂₅
	Recovery capability B ₃	Scene cleaning B ₃₁
		Damage evaluation and insurance B ₃₂
		Emergency plan update and improvement B ₃₃
		Rebuilding B ₃₄
		Plan improvement and perfection B ₃₅

It is obvious that the assessment index system includes multilevel indices. There are three emergency elements in the second-level and seventeen elements in the third-level. Each second-level index includes many third-level indices. There are six items in the precaution capability, six items in the response capability, and five items in the recovery phase. All the seventeen items reflect the capability of the emergency management for major accidents of coal mines.

3.3 Calculating index weight

Based on the AHP, the assessment model of the emergency capability of coal mines has been built to analyze the actual emergency management capability of the enterprise in this paper. Firstly, the weight that each index affects the object was assured by analyzing all the scores confirmed by experts, then the qualitative indexes were quantified, and the emergency capability of coal mines was confirmed at

last. Thus, we can estimate the actual emergency management capability of coal mine enterprises.

The judgment matrix can be established by inviting the experts to mark all of the indices. The indices judgment of A is illustrated in Table 2.

Table 2: Judgment Matrix for A

A	A ₁	A ₂	A ₃
A ₁	1	1/3	4
A ₂	3	1	6
A ₃	1/4	1/6	1

According to the above judgment matrix, the weight of each index can be calculated by mathematical tools such as MATLAB, and also the weight vector and the consistency test. All the results are shown in Table 3.

Table 3: Consistency checking of the judgment matrix.

Judgment matrix	n	λ_{max}	CI	RI	CR	consistency
A	3	3.03	0.01	0.58	0.03	Pass
B ₁	5	5.23	0.05	1.12	0.05	Pass
B ₂	5	5.33	0.08	1.12	0.07	Pass
B ₃	5	5.08	0.04	0.90	0.03	Pass

Where, n is the number of indexes; λ_{max} is the maximum eigenvalue of judgment matrix; CI is the consistency index, When CI is more than 0 slightly, the matrix A will be in relatively good agreement, otherwise, the consistency of A is poor.

Based on the above table, the consistency ratio CR of each judgment matrix is less than 0.1, which indicates the consistency checking is ok. The weight of each index is shown in Table 4.

Table 4: Weight vector of each layer of index system.

Judgment matrix	Weight vector(w)
A	0.2706 0.6442 0.0852
B ₁	0.2615 0.0634 0.5128 0.1290 0.0333
B ₂	0.4047 0.1769 0.0590 0.2551 0.1043
B ₃	0.4620 0.1739 0.1778 0.0862 0.1002

4. FUZZY COMPREHENSIVE ASSESSMENT MODEL

The fuzzy comprehensive evaluation is performed by using the single factor evaluation results and evaluation object related. The corresponding evaluation matrix is constructed and the decision

weighting factor importance degree of each factor is used for the fuzzy transformation. Finally the evaluation results are found. Through the fuzzy comprehensive evaluation, risk management decisions can be quantitatively calculated for each oil and gas pipeline construction project. In order for the final evaluation results to have practical reference significance, the vector and the fraction vector are used to calculate a total score, and then the control method of rating scores to determine the result of the evaluation belongs to the grade.

4.1 Building indices

According to the indices system built in Table 1, establish collection U:

$$U = \{B_1, B_2, B_3\}$$

$$U_1 = \{B_{11}, B_{12}, B_{13}, B_{14}, B_{15}\}$$

$$U_2 = \{B_{21}, B_{22}, B_{23}, B_{24}, B_{25}\}$$

$$U_3 = \{B_{31}, B_{32}, B_{33}, B_{34}, B_{35}\}$$

4.2 Establishing judgement collection

The capability of emergency management for coal mines can be divided into five levels from high to low.

$$\text{Judgement collection} = \{V_1, V_2, V_3, V_4, V_5\}$$

V_1 =higher, V_2 =high, V_3 =middle, V_4 =lower, V_5 =low.

In the calculation of the total system scores, risk management and decision-making can refer to Table 5 to determine the pipeline risk tolerance decision value. Then, the level of risk factor can be confirmed according to the decision value and also risk decision can be determined.

Table 5: Value and level of emergency management capability.

Risk level	Assessment Values	Level of	measurement
1	>90	Higher	maintain
2	90 ~ 76	High	Advanced
3	75 ~ 60	Middle	need Advanced
4	59 ~ 50	Lower	Must Advanced
5	< 49	Low	rectify

4.3 Fuzzy comprehensive assessment

There is a fuzzy mapping from U to V, where $u_i \rightarrow f(u_i) = (r_{i1}, r_{i2}, \dots, r_{im}) \in F(V)$. The fuzzy mapping f can identify a fuzzy relationship between U and V $R_f(u_i, v_j) = f(u_i)(v_j) = r_{ij}$; therefore, R_f can be expressed as a fuzzy matrix.

$$R = \begin{pmatrix} r_{11} & r_{12} & \dots & r_{1m} \\ r_{21} & r_{22} & \dots & r_{2m} \\ \dots & \dots & \dots & \dots \\ r_{n1} & r_{n2} & \dots & r_{nm} \end{pmatrix}$$

Thus, a comprehensive evaluation can be performed.

5. A CASE STUDY

In this paper, a coal mine was taken as a case to study risk tolerance and decision making. Using the established emergency capability model of fuzzy comprehensive assessment, the emergency capability value of the coal mine is carried out to determine the level of the emergency of the coal mine.

Before evaluation, relevant experts to judge ,ust be recruited and the importance of each index of emergency capability on the effect of each index of the coal mine must be compared. By inviting 10 relevant experts including coal mine, safety, technology, emergency, and fire experts, the importance of each index of the coal mine can be confirmed. The arbitrarily corresponding matrix of risk factors can be determined to find the score of the fuzzy comprehensive evaluation. Finally, the level of emergency capability of the coal mine can be determined.

In order to explain the calculation, we can take the precaution capability B_1 as an example. The experts' judgments on the precaution capability are listed in Table 6.

Table 6: Judgments of experts to the precaution capability B_1 .

	Higher	High	Middle	Lower	Low
B_{11}	0.3	0.5	0.2	0	0
B_{12}	0.8	0.2	0	0	0
B_{13}	0.7	0.3	0	0	0
B_{14}	0.2	0.3	0.5	0	0
B_{15}	0	0	0	0	1

So the R_f can be expressed as a fuzzy matrix as follows.

$$R(B_1) = \begin{pmatrix} 0.3 & 0.5 & 0.2 & 0 & 0 \\ 0.8 & 0.2 & 0 & 0 & 0 \\ 0.7 & 0.3 & 0 & 0 & 0 \\ 0.2 & 0.3 & 0.5 & 0 & 0 \\ 0 & 0 & 0 & 0 & 1 \end{pmatrix}$$

Then,

$$R_{B1} = w_{B1} \bullet R(B_1)$$

$$= \begin{pmatrix} 0.2615 \\ 0.0634 \\ 0.5128 \\ 0.1290 \\ 0.0333 \end{pmatrix}^T \bullet \begin{pmatrix} 0.3 & 0.5 & 0.2 & 0 & 0 \\ 0.8 & 0.2 & 0 & 0 & 0 \\ 0.7 & 0.3 & 0 & 0 & 0 \\ 0.2 & 0.3 & 0.5 & 0 & 0 \\ 0 & 0 & 0 & 0 & 1 \end{pmatrix}$$

$$= (0.5139 \quad 0.3360 \quad 0.1168 \quad 0 \quad 0.0333)$$

Also,

$$R_{B2} = (0.3490 \quad 0.2326 \quad 0 \quad 0 \quad 0.4184)$$

$$R_{B3} = (0.7393 \quad 0.1472 \quad 0.0274 \quad 0 \quad 0.0862)$$

So,

$$R(A) = \begin{pmatrix} 0.5139 & 0.3360 & 0.1168 & 0 & 0.0333 \\ 0.3490 & 0.2326 & 0 & 0 & 0.4184 \\ 0.7393 & 0.1472 & 0.0274 & 0 & 0.0862 \end{pmatrix}$$

$$R_A = w_A \bullet R(A)$$

$$= \begin{pmatrix} 0.2706 \\ 0.6442 \\ 0.2856 \end{pmatrix}^T \bullet \begin{pmatrix} 0.5139 & 0.3360 & 0.1168 & 0 & 0.0333 \\ 0.3490 & 0.2326 & 0 & 0 & 0.4184 \\ 0.7393 & 0.1472 & 0.0274 & 0 & 0.0862 \end{pmatrix}$$

$$= (0.4949 \quad 0.2895 \quad 0.0773 \quad 0 \quad 0.1383)$$

Then, the emergency capability of the coal mine can be got by $R_A \cdot (93,80,70,55,45)^T$, and the result is 82.16. Therefore, according to the decision standard values listed in Table 5, the level of the coal mine is high but the emergency regulations and standards, emergency training, and education still need to be strengthened.

6. CONCLUSIONS

(1) The capability of emergency management for coal mine means the capability to control major unexpected accidents. Emergency management is a lasting and persistent process which includes precaution, response, and recovery.

(2) The assessment index system includes multilevel indices. The three phases of emergency management constitute the second-level indices. Each second-level index includes many third-level indices, which sum to fifteen items. There are five items in the precaution phase, five items in the preparedness phase, five items in the response phase, and four items in the recovery phase. All the fifteen items directly reflect the capability of the emergency management for major accidents.

(3) The capability of the emergency management for coal mines can be assessed by establishing the analytic hierarchy process model, and the assessment result can reflect the actual emergency management degree. All the studies are helpful in improving the

emergency management level and preventing major accidents.

(4) The practical application shows that the emergency capability of the coal mine is "high". However, the emergency regulations and standards, emergency training, and education still need to be strengthened.

7. ACKNOWLEDGEMENT

The research work was supported by National Science and Technology Foundation of China under Grant No. 2015BAK16B03 and Basic Science and Technology Foundation of CASST under Grant No. 2016JBKY12.

8. REFERENCES

- Chen G.H, Zhang X.M. (2009). Fuzzy-based methodology for performance assessment of emergency planning and its application, *Journal of Loss Prevention in the Process Industries*, Volume 22, No. 2, pp. 125-132.
- Deng Y.F., Zheng S.Z., Liu G.Z. (2005). Urban emergency capability assessment system, *Journal of Safety Science and Technology*, Volume 1, No. 6, pp. 33-36.
- Fan J.P. (2011). Problem and countermeasure of emergency management system construction in China, *Journal of Law and Society*, 2011, Volume 29, No. 2, pp. 209-210.
- Hapue C.E., Burton I. (2005). Adaptation Options Strategies for Hazards and vulnerability Mitigation: An International Perspective, *Journal of Mitigation and Adaptation Strategies for Global Change*, Volume 10, No. 3, pp. 335 ~ 353.
- Hong L, Wang H.P. (2009). Evaluation of emergency management level mutation theory of coal mine emergency, *Journal of Coal Mine Safety*, Volume 6, No. 1, pp. 111-113.
- Liu T.M. (2004). Emergency system construction of major accident, *Journal of Labor Protection*, Volume 2, No. 4, pp. 7-10
- Liu J.X, Chen X.J. (2009). A comprehensive review of the theories and practices of emergency management capability assessment, *Journal of Yanshan University*, Volume 5, No. 33, pp. 272-275.
- Ma M.D, Han Y, Zhang Q. (2009). Study on evaluation method of emergency response capabilities based on Fuzzy Analytic Hierarchy Process (AHP), *Journal of safety science and technology*, Volume 5, No. 2, pp. 98-102.
- Montoya L.M. (2005). Management of natural hazard risk in Cartago, *Journal of Costa Rica*, Volume 29, No. 3, pp. 493~509.

Paeka H.J., Hilyard K. (2010). Theory-Based Approach and Understanding Public Emergency Preparedness: Implications for Effective Health and Risk communication, *Journal of Health Communication: International Perspectives*, Volume 15, No. 4, pp. 428-444.

Wu Z.Z., Liu M. (2015). A major accident emergency rescue system and preparedness introduction, *Metallurgical Industry Press*, 2003: pp. 38~69.

Zheng S.Z., Deng Y.F. (2006). City public emergencies emergency capability assessment system and application, *Journal of Liaoning Engineering Technology University*, Volume 25, No. 6, pp. 9-13.

Zheng W , Hui N. (2010). Analysis of the risk and emergency management of enterprise, *Journal of Management world*, Volume 2, No. 2, pp. 124-125.

Study on local temperature controlling technology and equipment in heat disaster coal well

Haijun Wu^{a,b}, Haifei Yao^{a,b}, Changfu Xu^{a,b}, Haiyan Wang^{a,b}, Laizai Tan^c

^a Mine Safety Technology, China Coal Research Institute, Beijing, China, 100013

^b National Key Lab of High Efficient Mining and Clean Utilization of Coal Resources, Beijing, China, 100013

^c Nanjing Wuzhou Refrigeration Limited Liability Company, Nanjing, China, 211100

ABSTRACT

Along with the continuous increase of coal resource mining depth, high temperature and heat disaster is becoming more and more serious. The health of workers under coal wells can be threatened at any time and the safe mining of coal resources is seriously impacted. In order to eliminate coal well heat disasters, scholars at home and abroad have inputted a lot of time and energy. They have researched the controlling theory of coal well heat disasters. They developed cooling equipment for high temperatures and have achieved some results. However, the equipment is too large and as a result it is hard to move. The power of the equipment is high so it costs a large amount of electric power. Maintenance costs are huge, and therefore the application of this technology is not ideal.

Based on this, the present study firstly analyzed the influence factors of coal well heat disaster. Then, the calculation method of cooling load in coal wells was researched. The authors put forward the technology for controlling local high temperatures. The ZLS-90 movable cooling equipment was developed successfully which includes a refrigeration compressor, evaporator, water cooling condenser, and expansion valve. The property of the compressor plays an important part in the cooling effect of the whole system. After comparing, the GEA bock compressor was chosen. The enthalpy difference comprehensive testing system was used to test the performance of the equipment. Test results showed that all performance indexes comply with the design requirements. The property is also stable.

This paper also proposes discharging heat with a heat-rod to deal with the heat of condensation as well as using the heat synthetically. Effective cooling can be carried out by means of local temperature controlling technology and equipment. In that case, the working environment under coal wells would be guaranteed and the safe production of coal wells would be guaranteed. It would realize efficiency, conservation, and the environmental protection of resources.

KEYWORDS: heat disaster; temperature controlling technology; enthalpy difference; heat-rod

1. INTRODUCTION

Coal is the main energy source for our country and world. It occupies an irreplaceable position in the primary energy consumption structure (Yang D D, 2013). With the increasing mineral resources exploitation level and gradual enhancing of degree of mechanization, shallow buried coal resources are draining off and deep mining is gradually dominating (Cao X L, 2010). In recent years, countries around the world have entered deep mining areas (Singh et al., 2003). The mining depth of some coal in Germany and Russia has amounted to 1400-1500 m (Nimaje and Tripathy, 2010). The depth of Kariton Vere gold mine in South Africa is 3800 m underground and its upright shaft is about 4500 m deep (Gangopadhyay and Dutt-Lahiri, 2005). Some metal mines in India and Brazil are more than 2000 m (Li H J, 2009). There are more than 30 mines that exceed 1000 m deep in Canada and more than 10 mines in America (Abdelaziz et al., 2003). At present in our country's proven reserves, 1000-2000 m deep

coal reserves accounted for 53.2% of total reserves (Wu J T et al., 2010). Dozens of mines are more than 1000 m deep (Feng D Q et al., 2013). Currently, the mining depth is rising at a rate of 8 to 16 m/a in China (Feng X L and Chen R H, 2005). Deep mining of coal will be the main problem we face in the future.

With the increase of mining depth, temperature of the surrounding rock is rising constantly (Vosloo et al., 2012). Electromechanical devices, people, hot water, coal, and gangue all emit heat. All of these cause severe environments of high temperature and high humidity which lower the working efficiency and affect equipment operation (Hughes et al., 2006). It seriously hinders the normal construction and efficient production of mines. Even worse, it gives rise to worker's sunstroke and dehydration, or even death. Besides water, fire, gas and roof, deep well heat disaster has been one of the major disasters that restricts the development of the coal industry (Xin S et al., 2012). In order to control deep well heat

disasters, scholars at home and abroad have done a lot of research from the aspects of theory, technique, and equipment. The scholars have developed a series of cooling equipment. However, there are still many problems such as a lack of theoretical research, large and hard to move cooling equipment, expensive to maintain, and difficult to let out the heat of condensation (Cao Q K et al., 2010). It is necessary to carry out research on cooling technology and equipment of deep coal well heat disasters.

2. DISTRIBUTION CHARACTERISTICS AND INFLUENCING FACTORS ANALYSIS OF HEAT DISASTER COAL WELL

By 2014, there are more than 150 heat disaster coal wells which mainly distribute in the east of China (Figure 1). Among these heat coal wells, 20 wells represented by Pingdingshan, Fengcheng and Xuchang are distributed in Central China. More than 40 wells represented by Yanzhou, Xinwen, Xuzhou (including Datun), Juye, Huainan and Huaibei are distributed in East China. In Northeast and North China, there are more than 30 heat disaster coal wells represented by Fengfeng (Handan), Xingtai, Datong, Kailuan, Tiefsa, Beipiao, Fushun, Liaoyuan and Jixi (Zhang L et al., 2009). The rest are scattered in Hunan, Gansu, Guangxi, etc.

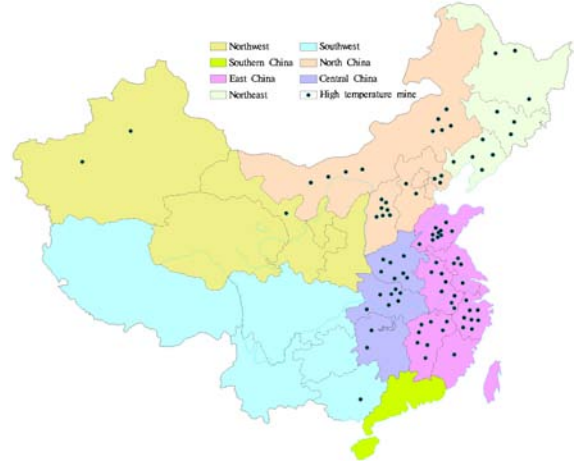


Figure 1: Distribution of heat disaster coal wells.

According to the survey, heat sources that cause deep coal heat disasters are the changes of surface atmospheric state, temperature rise of air self-compression, heat emitting from surrounding rock, heat emitting from electromechanical device, heat releasing from transport of coal and gangue, heat of hot water, and other heat sources. Take typical heat disaster coal wells, Panxi mine, Jining 3# mine, Pingdingshan 5# mine, Tangkou mine, Dongtan mine etc. for example. We analyzed the proportion of all these influence factors in heat disaster. The research shows that heat emitting from surrounding rock, electromechanical devices, and hot water are the main factors of heat disaster, as shown in Table 1 and Figure 2.

Table 1: factors incidence of part heat disaster coal wells.

heat sources	surrounding rock	electromechanical device	terrestrial heat	hot water	oxidation	air compression	transportation process	human body	lack of air	surface climate
Dongguashan copper mine	√	√√	√√	√	√	√				
Panxi coal well	√√	√		√√	√	√	√	√		
Jining 3# coal well	√√	√√			√√	√	√			
Pingdingshan 5# coal well	√√	√√		√√	√	√	√		√	
Qishan coal well	√	√	√√		√	√				
Chengjiao coal well	√√	√		√√	√	√	√		√	
Sanhejian coal well	√√	√√			√	√				√
Baiji coal well	√√	√			√	√			√	
Pingdingshan 8# coal well	√√	√		√√	√	√		√		
Dongtan coal well	√√	√	√√	√√	√	√				

Annotation: “√√” represents main reasons. “√” represents general reasons.

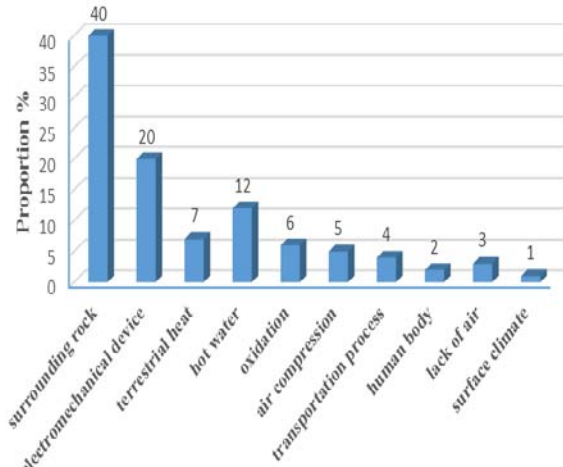


Figure 2: Affecting factors ratio of heat disaster coal wells.

3. COOLING LOAD COMPUTING METHOD OF COAL WELL TEMPERATURE DECREASING

There are multiple methods for the cooling load calculation of heat disaster coal well temperature decreasing. Some are based on the heat sources of the coal well, some are based on the air enthalpy of the air intake and air outlet, while others are based on the refrigeration station (Xin S et al., 2011). Computed results belied with the actual cooling load needed. Therefore, it is not scientific to confirm the refrigerating capacity of cooling equipment. Resource utilization is low and the cooling effect is not ideal. Based on this, the current study puts forward the correction cooling load calculation method of coal well temperature decrease. The computational formula is:

$$Q_{cold} = k (Q_{emit} - \Delta Q) = k (Q_w + Q_j + Q_r + Q_m + Q_k + Q_c + Q_y + Q_s - \Delta Q)$$

In the formula: Q_{cold} -refrigerating capacity needed, kW; k -correction factor, 1.05; Q_{emit} -emiting heat of heat sources, kW; ΔQ -absorption heat of roadway air, kW; Q_w -emiting heat of surrounding rock, kW; Q_j -emiting heat of electromechanical device, kW; Q_r -emiting heat of people, kW; Q_m -emiting heat of coal and gangue, kW; Q_k -emiting heat of air self compression, kW; Q_c -emiting heat of air leak from goaf, kW; Q_y -emiting heat of oxidization, kW; Q_s -emiting heat of hot water, kW.

4. LOCAL TEMPERATURE CONTROLLING TECHNOLOGY AND EQUIPMENT IN HEAT DISASTER COAL WELLS

Aiming at numerous problems in preventing and treating coal well heat disaster, such as temperature

decreasing equipment being bulky in volume, high in energy consumption, expensive to maintain, difficult to move and so on, we present local temperature controlling technology and movable equipment. By means of the technology and equipment, we can cool the local thermal environment of working-face in exploiting and mining. It not only reduces the energy consumption of the equipment, but also meets the requirements for local temperature controlling.

4.1 Develop movable cooling equipment

Aiming for local thermal environment cooling only, the refrigerating capacity of the equipment can lower suitably. According to the air supply situation of the exploiting and mining working-face in most coal wells, we chose 90kW as the effective refrigeration capacity of the equipment (nominal working conditions: dry-bulb temperature of inlet air 30°C, relative humidity 85%, temperature of air-out 25°C, air capacity 300 m³/min). It can guarantee that the temperature of air transmitted to the working-face is lower than 26°C. The relationship between air capacity disposed and inlet air temperature is shown in Figure 3.

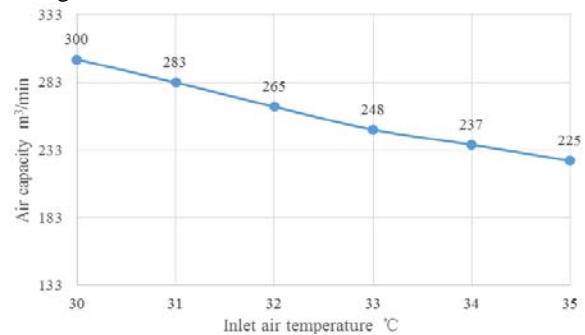


Figure 3: Relationship between air capacity disposed and inlet air temperature (air-out temperature 25°C).

The movable cooling equipment is comprised of a compressor, condenser, evaporator, electronic control system, and so on. In order to accord with explosion-proof requirements, we chose a BOCK (FX14/1366) piston open-type compressor equipped with an explosion-proof electric machine. The power source of the electric machine is a three-phase four-wire system, quaternary. A thermostatic expansion valve was used in the throttle mechanism. Performance parameters of the compressor are shown in Table 2.

Either an evaporative condenser or shell-and-tube condenser can be chosen. These two types of condenser each have their own merits and demerits. The ultimate length of the refrigerating fluid connecting hose should firstly be considered (Figure 4). The W type represents the single biggest length of connecting hose 1 and connecting hose 2. The

evaporator is lower than the compressor in the right side while higher in the left side. N type represents the single biggest length of connecting hose 3 and connecting hose 4. The condenser is higher than the compressor in the right side while lower in the left side. L_v/L is the ratio of the connecting hose height difference value and single tube length. $L_v/L \approx 0$ in coal wells. Analysis conclusion: the biggest

connecting hose length of the condenser is about 60 m and the biggest connecting hose length of the evaporator is about 22 m. Based on the above analysis, the shell-and-tube condenser was selected. R407C was chosen as the refrigerating fluid and water as the cooling medium.

Table 2: Performance parameters of the compressor.

Condensation temperature $T_c/^\circ\text{C}$		Evaporation temperature $T_e/^\circ\text{C}$								
		15	10	5	0	-5	-10	-15	-20	-25
30	Cold capacity/W	168000	140000	116000	95000	77300	62200	49400	38600	29600
	Power /kW	15.7	17.3	18.1	18.1	17.6	16.6	15.3	13.9	12.4
35	Cold capacity/W	159000	133000	110000	89700	72800	58400	46200	35900	27200
	Power /kW	19.6	20.6	20.8	20.3	19.3	18.0	16.4	14.8	13.2
40	Cold capacity/W	150000	125000	103000	84200	68200	54500	43000	33200	24800
	Power /kW	23.3	23.6	23.2	22.3	20.9	19.2	17.4	15.6	13.9
45	Cold capacity/W	141000	117000	96300	78600	63500	50600	39700	30400	22500
	Power /kW	26.7	26.4	25.5	24.1	22.4	20.4	18.4	16.5	14.7
50	Cold capacity/W	132000	110000	89700	73000	58700	46600	36400	27600	20100
	Power /kW	29.9	29.0	27.7	25.9	23.8	21.6	19.4	17.3	15.6

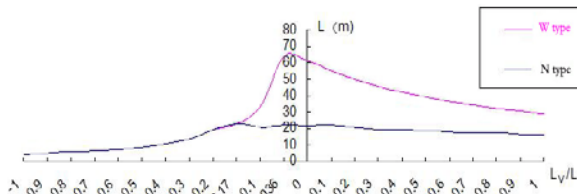


Figure 4: Ultimate length analysis of refrigerating fluid connecting hose.

The evaporator is an important component of the refrigeration system. It is a sort of dividing wall type heat exchanger. Direct evaporative cooling was designed. Floating air temperature outside the coiled tube is reduced by the evaporation of refrigerating fluid in the coiled tube. In order to decrease the influence of dust under the well on heat transfer of the heat exchanger, slick coil pipes were used for the evaporator. This type of pipe is convenient to rinse. Calculating parameters of the evaporator are as follows: air supply volume 300 m³/min, dry-bulb temperature/wet bulb temperature of inlet air 30/28 °C, the temperature of air-out 25 °C. Slick copper pipes (φ16×1.2) were bent to an 800 mm single length. There are 36 pathways with 342 pipes. The air resistance is about 900 Pa.

As a kind of movable cooling equipment used in coal wells, its electronic control system should automatically monitor the main technical parameters and running status of the equipment. It should also adjust automatically according to actual situation. The electronic control system should show air-out temperature, air-out humidity, air suck, and exhaust pressure of the compressor. The electronic control

system is the key of equipment operation and automatic control. So, it should have the function of being explosion-proof as well as have air exhaust pressure protection, over temperature protection, overload protection and so on. After systematic design and manufacturing, the movable cooling equipment was named ZLS-90 mine explosion-proof refrigeration unit.

4.2 Performance testing of the cooling equipment

The comprehensive enthalpy difference method was used to test the performance of the cooling equipment. The enthalpy difference test system adopts the testing philosophy of air enthalpy-difference method or means of liquid secondary refrigerant in the primary side and water heat meter method in the subordinate side. The system can test air blast capacity, refrigerating capacity, consumed power, electric current, EER (energy efficiency ratio) and other technical parameters of cooling equipment accurately. Using the programmable controller as the core, running equipment can adjust test conditions automatically during the testing process. Data collecting, processing, and saving are carried out by a computer. It can also generate testing reports and analyze the results by itself. Testing principles of the system are shown in Figure 5.

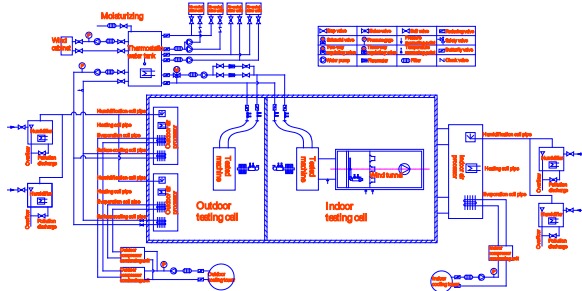


Figure 5: Testing principle of the enthalpy difference test system.

In accordance with the relevant procedures, performance testing of the refrigerating equipment

Table 3: Calculating data and results of ZLS-90 mine explosion-proof refrigeration unit.

items	unit	NO1	NO2	NO3	NO4	NO5	NO6	NO7	result
air quantity	m ³ /h	18065.330	18063.747	18071.212	18076.135	18074.847	18072.565	18081.917	18072.251
heat exchange of air side	kW	112.884	111.136	112.282	112.801	112.185	112.539	113.016	112.406
heat exchange of water side	kW	121.733	121.712	121.850	121.592	122.080	122.169	122.121	121.894
input power	kW	30.106	30.094	30.097	30.093	30.098	30.080	30.094	30.095
COP	kW/kW	8.771	8.683	8.744	8.775	8.739	8.768	8.787	8.752
deviation	%	7.904	9.561	8.578	7.850	8.855	8.710	8.087	8.506
water resistance	kPa	26.047	26.070	26.103	26.074	26.054	26.057	26.127	26.076
sensible heat	kW	37.906	37.120	37.580	37.218	36.674	37.150	36.355	37.143
latent heat	kW	74.979	74.015	74.702	75.583	75.511	75.388	76.661	75.263
inlet air enthalpy	kJ/kg	91.039	90.832	91.116	91.224	91.535	91.618	91.847	91.316
outlet air enthalpy	kJ/kg	70.919	71.019	71.107	71.128	71.537	71.555	71.707	71.282

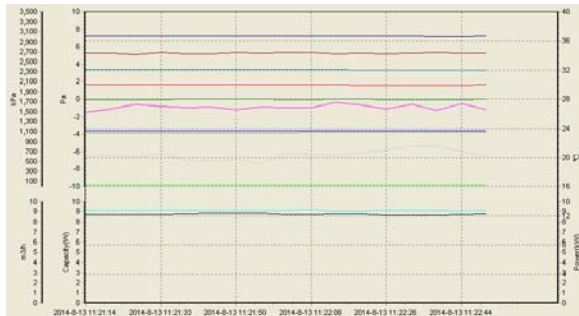


Figure 6: Performance test curves of ZLS-90 mine explosion-proof refrigeration unit.

5. MINE CONDENSING HEAT EMISSIONS TECHNOLOGY

There are currently three primary types of mine condensing heat emissions to local cooling under wells: heat discharging by water, heat discharging by water and fresh air, and heat discharging by water and ventilation air methane (Zhou T et al., 2012). There are some problems, such as being difficult to discharge or having a high failure rate of the discharging device. In view of this, we proposed to discharge condensation heat by heat-rod technology.

was carried out. Calculating data and results are shown in Table 3 and Figure 6.

As shown in Table 3 and Figure 6, refrigerating capacity and other performance indexes of the cooling equipment all satisfy the design values. The performance is good and stable. The cooling equipment is portable, so it can be moved easily and quickly with the help of a mine platform lorry. This can save a lot of time because it is not necessary to add refrigerating fluid repeatedly after each move. With this equipment, we can implement effective cooling to mining and driving work face and other local thermal environments.

The heat collector is connected to the discharging port of the movable refrigeration unit. The evaporation zone of the heat-rod is inserted into the heat collector. In that case, the condensation heat in the heat collector can be discharged to the upper space or surface by the heat-rod. Finally, the heat can be used synthetically.

6. CONCLUSION

Through the above research, we can come to the following conclusions:

(1) Heat disaster coal wells are mainly distributed in Central China, East China, Northeast and North China. The rest are scattered in West and South China.

(2) For most of the mines, heat emitting from surrounding rock, electromechanical devices, and hot water are the main factors that cause heat disaster.

(3) The ZLS-90 mine explosion-proof refrigeration unit was designed to cool local high temperature environments. It is the ideal equipment to improve local thermal environments and has the advantage of being lightweight to move, having low energy consumption, stable properties, good cooling

effects and it is not necessary to add refrigerating fluid repeatedly after each move.

(4) Using heat-rod technology to discharge mine condensing heat, it is simple in craft, convenient, swift, long in service life, and good in its discharging effect.

7. ACKNOWLEDGEMENT

The authors gratefully acknowledge foundation by International Cooperation in Science and Technology Special Project (2015DFR70900), Technology Innovation Fund of China Coal Research Institute (2010CX09).

8. REFERENCES

- Abdelaziz EA, Saidur R, Mekhilef S. (2011) A review on energy saving strategies in industrial sector. *Renew Sust Energy Rev.* Volume 15, pp. 150-168.
- Cao Q K, Zhang S H, Yang W. (2010) Deep mine cooling and geothermal resource utilization. *Journal of Liaoning Technical University(Natural Science)*. Volume 29, Supp 1, pp. 40-42.
- Cao X L. (2010). Deep mine high temperature heat hazard resourceful utilization technology in Sanhejian coal well. BeiJing, China University of Mining and Technology.
- Feng D Q, Zhao X D, Chen Z. (2013) Application of local cooling technology in deep mining of Xuzhuang Coal well. *Industry and Mine Automation*. Volume 39, No. 3, pp. 92-97.
- Feng X L, Chen R H. (2005) Research and Development on Air-cooling in Deep High-temperature Mines at Home and Abroad. *Yunnan Metallurgy*. Volume 34, No. 1, pp. 7-10.
- Gangopadhyay, P. K., Dutt-Lahiri, K. (2005) Detecting Coal Fires with Remote Sensing: A Comparative Study of Selected Countries , *Resource Management in Asia-Pacific Region (RMAP) Working Paper No. 58, RMAP Program, Research School of Pacific and Asian Studies. The Australian National University, Canberra, ISSN- 1444.*
- Hughes A, Howells MI, Trikam A, Kenny AR, van Es D. (2006) A study of demand-side management potential in South African industries. In: *Proceedings: Industrial and commercial use of energy (ICUE) conference, August, Cape Town.*
- Li H J. (2009) Technology for Air Control in Coal well Cooling. *Warm Circulating and Air Control*. No. 6, pp. 43-45.
- Nimaje D. S., Tripathy D. P. (2010) Thermal Studies on Spontaneous Heating of Coal. *The Indian Mining & Engineering Journal*. p. 10.
- Singh, R. V. K., Singh, V. K. (2009) Status of Mine Fire of Jharia Coalfield and Suggestions for Prevention and Control. *National Seminar on*

Reinventing Jharia Coalfield, MGMI, Dhanbad Chapter.

Vosloo J, Liebenberg L, Velleman D. (2012) Case study: energy savings for a deep-mine water reticulation system. *Apply Energy*. Volume 92, pp.328-35.

Wu J T, Chen X M, Xia J. (2010) Research and Application of Mobile Refrigerator to Deep Mine Temperature Reduction. *Coal Science and Technology*. Volume 38, No. 10, pp. 86-88.

Xin S etc. (2011) Prevention and Cure of Heat Disaster in Coal Wells. Beijing, Coal Industry Publishing House, 216 p.

Xin S, Fu H L, Yan X Y. (2012) New Designing Idea of Centralized Cooling System for Coal Well. *Safety in Coal Wells*. Volume 43, No. 3, pp. 60-63.

Yang D D. (2013) Research on feature of thermal disaster and the control effect in zhuji coal well. *An Hui, AnHui University of Science and Technology*.

Zhang L, Chen S, Yu F. (2009) Several mine cooling technologies. *Shandong Coal Science and Technology*. No. 3, pp. 152-153.

Zhou T, Xiang D, Chen Y H, etc. (2012) Engineering practice and discussion on condensing heat emission during local cooling engineering. *China Coal*. Volume 38, No. 12, pp. 90-94.

Effect of forming technology on oxygen supply performance of oxygen candles in refuge spaces

Liu Jian-guo, Jin Long-zhe, Gao Na*, Wang Wei-xiang, Shen Jie

Civil and Environment Engineering School, University of Science and Technology Beijing, Beijing, China, 100083

ABSTRACT

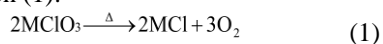
The present study investigated the forming technology of oxygen candles in a refuge space, for a more stable and reliable oxygen supply. Chlorine was found in the wet pressing process, revealing that dry pressing has a better forming effect on oxygen candles. Three types of oxygen candle blocks (OCBs) were pressed through dry pressing at pressure-application speeds of 0.1, 0.3, and 0.5 kN/s, respectively, for a pressing time of 10 min. From compression strength and combustion experiments, the ultimate compressive strengths (UCS) obtained for the three OCBs were 3.83, 5.48, and 5.83 kN. The stability coefficients of oxygen production (SCOP) were $U_1 = 0.966$, $U_2 = 0.724$, and $U_3 = 0.770$. From the results of these experiments and observation of combustion residue of OCBs, it was found that the stability of oxygen production decreases when the pressure-application speed within an appropriate pressure range is increased.

KEYWORDS: Oxygen candle; forming technology; dry pressing; pressure-applying speed; Stability of oxygen production

1. INTRODUCTION

In China, the current mode of oxygen supply to refuge spaces is through conventional forced air systems or compressed oxygen cylinders (Gao et al., 2012). However, in forced air systems oxygen is supplied through underground pipe networks, which usually have poor independence, as they might be destroyed in big mine accidents. Furthermore, compressed oxygen cylinders require regular maintenance, and are prone to quick discharge or explosions when exposed to high temperatures or fire (Jin et al., 2015). With technological developments regarding refuge spaces in China, the use of oxygen candles as an emergency oxygen source has attracted the attention of many scholars.

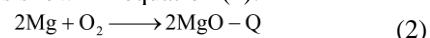
Oxygen candles are a type of oxygen supply equipment that releases oxygen through chemical reactions using chlorate or perchlorates as the source material. They have several advantages such as ease of use, large oxygen storage capacity (OSC), and fast oxygen production (Wang et al., 2010). The working principle of oxygen candles is the release of oxygen through thermal decomposition of chlorates (Fan et al., 2006). The decomposition reaction of chlorate is shown in equation (1):



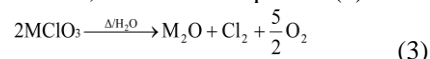
where M is a type of alkali metal.

The heat required for the decomposition of chlorate is provided by the combustion of metal powders, such as iron powder and magnesium

powder. The reaction for the combustion of magnesium is shown in equation (2):



At high temperatures or in the presence of impurities, a small amount of chlorate decomposes and releases chlorine, as shown in equation (3):



After passing through a filter material, the oxygen is directly released into the refuge space. Wang et al (2010) studied chlorine suppressants and chlorine gas filtering materials for oxygen candles. Zhang et al. (2013) studied the adsorption properties of carbon monoxide in emergency refuge facilities. Furthermore, Gao et al. (2015) studied an oxygen supply system and purification in a mine refuge space.

However, considering their use in refuge spaces, oxygen candles also present some shortcomings, such as heterogeneous, fast and uncontrollable oxygen release rate, and concentrated and high heat output from the reaction. In foreign countries, oxygen candles were extensively studied during the 1990s, followed by a systematic study of the catalysts, metal fuels, combustion fluctuations in oxygen candles, and the effect of particle size on combustion performance. In China, (Jin et al., 2014; Jin et al., 2015; Wang et al., 2014) the characteristics of oxygen supply in refuge spaces and the effect of M (M = catalysts, formula, candle structure) on oxygen

supply performance (OSP) of oxygen candles were studied through thermogravimetric analyses and orthogonal experiments (Zhang et al., 2013). However, effective research is still lacking regarding the effect of forming technology on the OSP of oxygen candles.

In this study, the influence of different forming technologies on the OSP of oxygen candles was investigated by changing the forming technology, pressure-application speed, and holding time. The results have important significance in improving the stability and reliability of oxygen candles regarding OSP.

2. EXPERIMENT

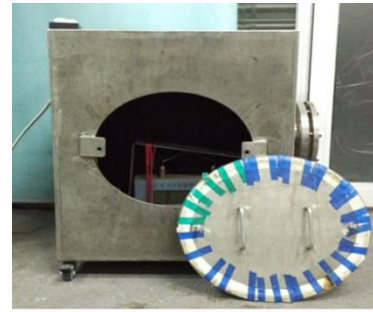
2.1 Experimental Apparatus

A ball mill (KE-2L Planetary ball mill, Qidong HONGHONG Instrument Equipment Factory, China) was used to crush the components. Three oxygen candle blocks (OCBs) were prepared using a stainless steel die, which was designed and fabricated in-house (dimensions: 160 mm long, 60 mm ID, 80 mm OD), and an oil press (YES-300, Jinan Huaxing Testing Machine Co., Ltd., China).

After wet pressing, the OCBs were dried in an incubator (WM-BD temperature incubator, Shanghai Weiming Electronic Mechanical Equipment Co., Ltd., China).

The OCBs were subjected to reactions in a sealed chamber, which was also developed in-house (600 × 600 × 600 mm), as shown in Figure 1a. Oxygen concentration in the sealed chamber was monitored in real time using a mining multi-parameter measuring device (CD7, Beijing

Zhong ShengZhou Mine Technology Center), which is shown in Figure 1b, and the dates were recorded using the KJ70N system in a computer.



a



b

Figure 1: Sealed chamber and CD7 mining multi-parameter measuring device.

Details of the chemicals used in the experiments are provided in Table 1.

Table 1: Chemicals used in the experiments.

Chemicals	Mol.wt.	Grades of purity (China)	Manufacturer
Sodium chlorate (NaClO ₃)	106.44	EP	Sinopharm Chemical Reagent Co., Ltd.
Manganese (Mn)	54.94	2N	Johnson Malthey Chemicals Ltd.
Cobalt(III) oxide (Co ₂ O ₃)	165.86	2N	Shanghai Fengshun Fine Chemicals Co., Ltd.
Kaolin	258.16	CP	Sinopharm Chemical Reagent Co., Ltd

2.2 Methods

Dry pressing and wet pressing experiments:

The components (86.22% NaClO₃, 5.88% Mn, 4.90% Co₂O₃, 3% kaolin) (Jin et al., 2015) were processed in the ball mill for 5 min (particle size ≤ 100 μm), and a powder was obtained. In the dry pressing experiment, 145 g of the powder was placed on the stainless steel die, and subjected to a pressure of 35 kN at a pressure-application speed of 0.1 kN/s, and then the pressure was held for 5 min. They were then unloaded, and dried at 60°C for 12 h. Finally, the blocks were observed and their physical parameters

were measured. In the wet pressing experiment, 5 ml and 10 ml of water were added to two groups of the powder weighing 145 g each and stirred homogeneously. The following processes were the same as in dry pressing.

Pressure-application speed and holding time experiments: in this study, three pressure speeds were defined, including slow pressing (0.1 kN/s), medium pressing (0.3 kN/s) and rapid pressing (0.5 kN/s). Three groups of the powder each weighing 145 g were subjected to slow pressing, medium pressing, and rapid pressing, and after reaching the

target pressure (35 kN), it was maintained for 10 min (Table 3). They were unloaded and their physical properties were measured. Later, the combustion experiment was conducted in the sealed chamber, in which oxygen concentration was monitored in real time using the CD7. The experiment was stopped until the oxygen concentration no longer increased, and then the combustion residue of OCBs were observed. Finally, the OSP of all OCBs was determined.

2.3 Data processing

Processing of data from the pressure-application speed and holding time experiment: Complete pressing time of the oxygen candles is equal to the sum of the holding time and pressing time, as shown in equation (4):

$$t_c = t_p + t_h \quad (4)$$

where t_c is complete pressing time of oxygen candle, t_p is pressing time, and t_h is holding time.

Oxygen concentration can be determined using CD7, and the growth rate of oxygen concentration per second can be calculated by equation (5):

$$V_{X1-X2} = (C_{X2} - C_{X1}) / C_{X1} \quad (5)$$

where V_{X1-X2} is the growth rate of oxygen concentration from time $X1$ to time $X2$ ($X2 - X1 = 1$), and C_{X1} and C_{X2} are the oxygen concentrations at time $X1$, and $X2$, respectively.

In this study, U is defined as the stability coefficient of oxygen production (SCOP), and is expressed in equation (6):

$$U = \frac{2}{\pi} \arctan \frac{1}{|V_{X1-X2} - V_{X2-X3}|} \quad (6)$$

A larger value of U indicates more stable performance of oxygen production. The value of U lies between 0 and 1.

Table 2: Parameters of dry-pressed and wet-pressed OCBs.

Number	Pressure /kN	Pressurized speed /kN/s	Quantity /g	Highly /mm	Density $\times 10^{-3}$ /g. mm^{-3}	MCS /kN
D1	35	0.1	144.06	28	1.821	2.87
W1	35	0.1	145.04	22	2.333	24.81
W2	35	0.1	139.34	21	2.348	32.46

Note: D1 is the dry-pressed OCB; W1 is the OCB with 5 ml of added water; W2 is the OCB with 10 ml of added water.

The UCS of the wet-pressed OCBs was higher than that of dry-pressed OCBs. However, as constant heat is required for drying, the wet pressing process requires a longer time. In addition, the distribution of internal pores are heterogeneous after drying since it is difficult to mix the powder and water homogeneously, leading to differences in the amount of water inside the OCB. Homogeneous pores were produced after the water evaporated during the drying process. In addition, the powder appeared to react with water because the surface temperature of the aqueous powder was clearly

3. RESULTS AND DISCUSSION

3.1 Dry pressing and wet pressing experiments

In the dry pressing and wet pressing experiments, pressure-application speed was 0.1 kN/s, the target pressure was 35 kN, holding time was 5 min, and the OCBs were dried at 60°C for 12 h. As shown in Figure 2, after drying, a number of irregular cracks appeared in the surface of wet-pressed OCBs with slight expansions in upper and lower bottom parts. The color of the wet-pressed OCBs was darker than that of dry-pressed OCBs. During wet pressing, surface temperature of the OCBs was increased, and trace amounts of chlorine was detected. Through compression strength experiments, the density and ultimate compressive strength (UCS) of W1 and W2 were found to be significantly higher than that of D1, as shown in Table 2. In addition, although the density was similar between W1 with W2, the UCS of W2 was higher than that of W1.



COG by DPF COG by WPF
Figure 2: Dry-pressed and wet-pressed OCBs.

increased and trace amounts of chlorine were detected. This is not only harmful but also reduces the effective oxygen occlusion amount and the performance of OCBs. Consequently, dry pressing is considered to have a better forming effect.

3.2 Pressure-application speed and holding time experiments

As shown in Table 3, the density of OCBs, pressed at different pressure-application speeds for a constant complete pressing time, showed a slight increasing trend with increases in

pressure-application speed. The pressure-application speed had little effect on the density of the oxygen candle. As shown in Figure 3, the UCS of the three

OCBs were 3.83 kN, 5.48 kN, 5.83 kN, and there was a positive correlation between the UCS of OCBs, pressure-application speed, and holding time.

Table 3: Parameters of OCBs in the pressure-application speed and holding time experiments.

Number	Pressurized speed/ KN/S	Pressure time /min	Holding time /min	Quality /g	Highly /mm	Density/ $\times 10^{-3}$ g·mm ⁻³
1	0.1	5.8	4.2	144.50	29.0	1.762
2	0.3	1.9	8.1	144.65	29.0	1.764
3	0.5	1.1	8.9	144.71	28.9	1.771

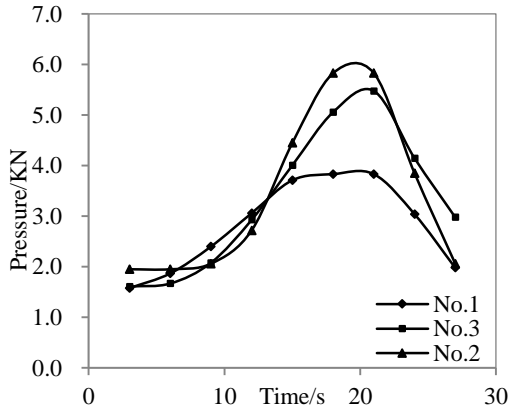


Figure 1: Experimental curves of compressive strength.

The results of the combustion experiment are shown in Figure 4. Oxygen concentration began to rise from 2 s and reached the highest at 4 s, and then it remained fluctuating at around 31%. Note that the main reaction occurred between 2–4 s. The growth rate of oxygen concentration was calculated, and the results are shown in Figure 5. According to the results, $U_1 = 0.966$, $U_2 = 0.724$, and $U_3 = 0.770$.

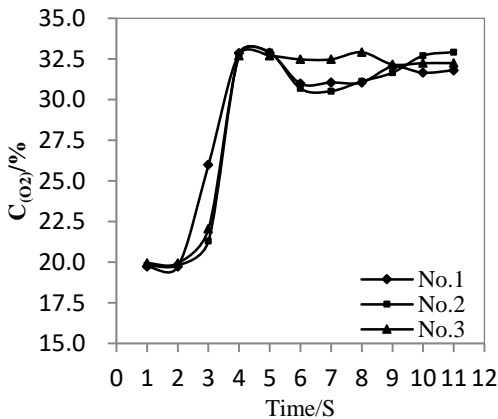


Figure 2: Oxygen concentration curve in a sealed chamber.

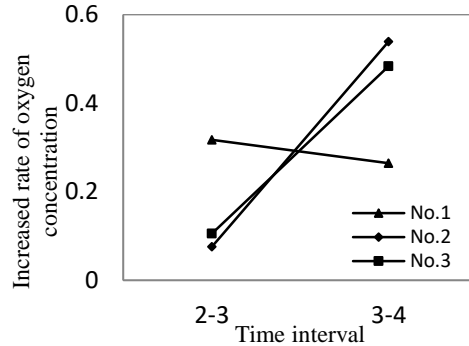


Figure 5: Velocity diagram of oxygen concentrations in a sealed chamber.

After the reaction was complete and the OCBs cooled to room temperature, the asbestos cloth wrapped around the OCBs were removed, and the OCBs were cut along the diameter, as shown in Figure 6. According to the observation of the sections, OCB No. 1 was completely burnt, and homogeneous holes were distributed across the burnt area in the shape of an upright cone. The burnt area of OCB No. 2 was small and distributed with heterogeneous holes. The combustion area of No. 3 was even smaller than that of No. 2 and was concentrated around the center of upper part; heterogeneous holes were also observed. In addition, caking was also observed in the right part of OCB No. 3.

During the entire process, not only did the shape of powder particles change, but the volume and density also changed constantly (Yu et al., 2000). In pressing processes, friction exists between the mold wall and powder particles, as well as between individual powder particles. The friction between powder particles increased when the pressure-application speed was increased, and consequently, powder flow ability was decreased. This resulted in increased pressure loss and heterogeneous distribution of density in the OCBs. This is the main reason for the larger and heterogeneous holes that occurred in the combustion area of OCBs No. 2 and No. 3 and also for the caking in the unburned area in OCB No. 3. In addition,



Figure 6: Photographs of OCBs after combustion

although a long holding time can enhance the physical properties of the OCBs, the air between powder particles is reduced, and the average distance between powder particles is decreased. As such, the effective area of combustion decreases, weakening the heat absorption capacity of unburned areas. The decomposition reaction of sodium chlorate powder stops without adequate heat, resulting in the large unburned areas in OCBs No. 2 and No. 3. According to the value of SCOP and observation of combustion residue of OCBs, the collating sequence of combustion stability is No. 1 > No. 2 > No. 3.

From the experiments, the following conclusion can be drawn: in dry pressing, the physical properties of oxygen candles can be improved by increasing the pressure-application speed and holding time. However, the rate of oxygen production is inconsistent. Furthermore, long holding times will increase the density of oxygen candles, reduce heat transfer capability, and eventually lead to a stop in the middle of the reaction.

4. CONCLUSIONS

Through dry pressing and wet pressing experiments, this study revealed that the dry pressing of oxygen candles has a better forming effect. The UCS and SCOP of the OCBs, pressed at pressure-application speeds of 0.1 kN/s, 0.3 kN/s, and 0.5 kN/s, were 3.83 kN, 5.48 kN, and 5.83 kN and $U_1 = 0.966$, $U_2 = 0.724$, and $U_3 = 0.770$, respectively. From the observation of combustion residue, it can be concluded that increases in the pressure-application speed, within an appropriate pressure range, decreases the stability of oxygen production.

Further research will focus on optimizing the pressing process of oxygen candles through quantitative studies on target pressure, pressure-application speed, and holding time.

5. ACKNOWLEDGEMENT

This study was supported by the National Natural Science Foundation of China (5150417), the

Fundamental Research Funds for the Central Universities (FRF-TP-15-043A3), and the China Postdoctoral Science foundation (2014T70039, 2013M540666).

6. NOMENCLATURE

OCB	oxygen candle block
UCS	ultimate compressive strengths
SCOP	stability coefficients of oxygen production
OSC	oxygen storage capacity
OSP	oxygen supply performance
t_c	complete pressing time
t_p	pressing time
t_h	holding time
V_{X1-X2}	growth rate of oxygen concentration from time X1 to time X2 ($X2 - X1 = 1$)
C_X	oxygen concentrations at time X

7. REFERENCES

- Fan, M., Bu, J.J., and Zhen, H.Y. (2006). The research on actuality and development of oxygen candle. *Ship Science and Technology*, Volume 28, No. 2, pp. 16–20
- Gao, N., Jin, L.Z., Wang, L., and You, F. (2012). Research and application of oxygen supply system in Changcun coal mine refuge haven. *Journal of China Coal Society*, Volume 37, No. 6, pp. 1021–1025
- Gao, N., Liu, J.G., Jin, L.Z., Li, L., Huang, X., Zhou, L., and Fan L.L. (2015). Study and experiment of the system of oxygen supply and purification in the mine refuge space. *Journal of China Coal Society*, Volume 3, pp. 616–622
- Jin, L.Z., Wang, Y., Wang, S., and Zhan, Z.N. (2014). Distribution regularity study of air pressure supply to mine refuge chambers. *Journal of University of Science and Technology Beijing*, Volume 08, pp. 1007–1012

- Jin, L.Z., Wang, S., Liu, S.C., and Zhang, Z. (2015). Development of a low oxygen generation rate chemical oxygen generator for emergency refuge spaces in underground mines. *Combustion Science and Technology*, Volume 187, No. 8, pp. 1229–1239
- Shafirovich, E., Garcia, A., Swamy, A.N., Mast, D.J., and Hornung, S.D. (2012). On feasibility of decreasing metal fuel content in chemical oxygen generators. *Combustion and Flame*, Volume 159, No. 1, pp. 420–426
- Shafirovich, E., Mukasyan, A.S., Varma, A., Kshirsagar, G., Zhang, Y., and Cannon, J.C. (2002). Mechanism of combustion in low-exothermic mixtures of sodium chlorate and metal fuel. *Combustion and Flame*, Volume 128, No. 1, pp. 133–144
- Shafirovich, E., Zhou, C., Ekambaram, S., Varma, A., Kshirsagar, G., and Ellison, J.E. (2007). Catalytic effects of metals on thermal decomposition of sodium chlorate for emergency oxygen generators. *Industrial & Engineering Chemistry Research*, Volume 46, No. 10, pp. 3073–3077
- Shafirovich, E., Zhou, C., Mukasyan, A.S., Varma, A., Kshirsagar, G., Zhang, Y., and Cannon, J.C. (2003). Combustion fluctuations in low-exothermic condensed systems for emergency oxygen generation. *Combustion and Flame*, Volume 135, No. 4, pp. 557–561
- Wang, B., Wang, Y.J., and Ma, L.E. (2010). Two oxygen-generating techniques by chemical method in closed environment. *Chemical Defence on Ships*, Volume 04, pp. 10–14
- Wang, S., Jin, L.Z., Liu, S.C., and Zhang, Z. (2010). Research on application of chlorate oxygen candle to emergency refuge facility in non-coal mine. *China Safety Science Journal*, Volume 04, pp. 10–14.
- Wang, Y.J., Ma, L.E., and Ning, J.F. (2010). Chlorine suppressants and chlorine Gas filtering materials for the oxygen-generating candles. *Chemical Defence on Ships*, Volume 1, pp. 21–24
- Yu, Z.Y., Kang, Y.L., and Li, Y.J. (2000). Metal powder compaction methods and its quality control. *Forging & Stamping Technology*, Volume 01, pp. 33–37
- Zhang, N., Jin, L.Z., Huang, Z.L., and Li, F.W. (2013). Research on carbon monoxide adsorption properties in emergency refuge facilities. *Journal of Safety Science and Technology*, Volume 8, pp. 135–139
- Zhang, Z., Jin, L.Z., Liu, S.C., Wang, S., Gao, N., and Li, J. (2013). Study on optimization of oxygen candle formula for refuge chamber. *Journal of Safety Science and Technology*, Volume 9, pp. 129–135

Experimentation on a new type of mining emergency rescue relay cabin

Shen Jie*, Gao Na, Jin Long-zhe, Fan Lin-yu, Wang Wei-xiang, Liu Jian-guo

Civil and Environmental Engineering, University of Science and Technology Beijing, Beijing, China, 100083

ABSTRACT

This study designed an innovative mining emergency rescue relay cabin by comparison with existing hedging facilities with respect to function, service object, structure, size, and system components. The structures and systems of the emergency rescue relay cabin were designed and implemented. An air-tightness test indicated a test chamber relief rate of 26 Pa/min, which meets the requirements. Furthermore, an airsleeve air supply test indicated an air supply rate of 220 L/min, which is sufficient for the staff replacing the equipment in the emergency rescue relay cabin. The total air supply volume was 9680 L, which can be supplied via two bottles of 40 L, 15 MPa compressed air.

KEYWORDS: Emergency rescue relay cabin; relay cabin site selection; system and structure; tightness test; airsleeve air supply test

1. INTRODUCTION

The main hedging facilities of existing underground emergency systems include fixed refuge chambers and movable rescue capsules, both of which possess advantages such as being able to accommodate a considerable number of personnel, complete internal protection systems, and broad security protection ranges. However, several problems are currently hindering the application of refuge chambers and rescue capsules. Among these are long construction time, high usage, operation, and maintenance costs, and concentrated protection on the work surface in the mining area. To resolve these issues, this study investigated and designed a new type of mining emergency rescue relay cabin. Compared with existing underground hedging facilities, the new mining emergency rescue relay cabin has various advantages, such as small size, flexible usage, easy installation and transportation, diversity in protection objects, and low production cost (Li, 1989; Ni et al., 2013; Wang et al., 2010; Sun, 2011a). Combined with existing underground hedging facilities, this new type of emergency rescue relay cabin can achieve comprehensive coverage of the underground hedging space, not only lowering the cost of building underground emergency rescue systems, but also providing timely resources and equipment to underground hedging and rescue personnel, and both improving mine rescue efficiency and reducing casualties.

2. CHARACTERISTICS

2.1 Application feature comparison

The key feature of existing major hedging facilities, fixed refuge chambers, and movable rescue capsules is the internal life-support system—the main function of which is to provide a safe space for the hedging personnel waiting for rescue underground (Moncef et al., 1996). In contrast, the main function of the emergency rescue relay cabin is to provide materials and energy supply for the mine rescue personnel and hedging personnel so as to ensure the continuity of the rescue and hedging actions. Overall, the proposed relay cabin provides temporary protection for the rescue workers and hedging personnel.

2.2 Comparison of application objects

The application object of existing major hedging facilities, fixed refuge chambers, and movable rescue capsules is primarily the underground personnel (Gao et al., 2011; Jin et al., 2012; Sun, 2011b; Gao, 2011). In contrast, the emergency rescue relay cabin can not only serve for hedge personnel, but also provide mine rescue personnel with oxygen bottles, self-help equipment, food, water, communication devices, batteries, and other essential hedging and rescue energy supplies.

2.3 Structure and dimensions comparison

The average dimensions of a movable rescue capsule in existing hedging facilities are 23 m × 2.4 m × 2 m, which can accommodate 30 people. The internal structure is divided into transition area, living area and equipment area. The average dimensions of a refuge chamber for 30 people are 25 m × 4.5 m × 3.5 m. The internal structure is divided into refuge chambers on both sides and the hedging area in the middle. For the emergency rescue relay cabin to provide energy and

*Corresponding author – email : Mrshenjie@126.com

supplies for 40 people, the overall cabin dimensions are only 1.52 m × 1.30 m × 1.77 m, as shown in Figure 1. The internal structure is divided into battery and power source area, supply storage area, equipment replacement area, and communication area, as shown in Figure 2.

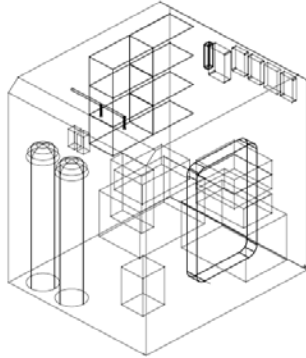


Figure 1: Internal structure of the emergency rescue relay cabin.

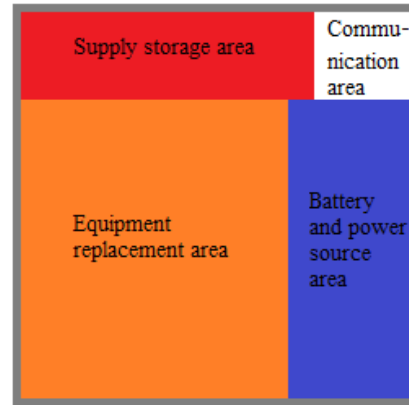


Figure 2: Functional compartments of the relay cabin.

The comparison shows that, for the same number of people, the emergency rescue relay cabin has a smaller size. Further, compared to the movable refuge chambers, it can move flexibly along pre-laid tracks by the roadway, allowing for rescue missions near and above the work surface, and others near and outside of the mining area along the roadway.

Table 1: Costs associated with hedging facilities.

Items	Relay cabin	Movable rescue capsule	Fixed refuge chamber
Material cost	263,000	2,000,000	3,000,000
Site Transfor - mation cost	300,000	1,500,000	4,000,000
Daily Maintenance fee /year	55,000	97,000	150,000
Total	618,000	3,597,000	7,150,000
Number of people	Ventilation and rest space for more than 40 people	Hedging for 30 people	Hedging for more than 30 people

2.4 Comparison of system components

The life-support system of existing major hedging facilities, fixed refuge chambers, and movable rescue capsules primarily includes the following: fire and explosion protection system, closed buffer system, air curtain isolation system, oxygen supply system, cooling and dehumidifying system, monitoring and control system, and communications systems (Sun, 2010). The main function of the emergency rescue relay cabin is to provide a temporary hedging place and supplies and energy for the rescuers and endangered workers. Therefore, its internal systems consist of a basic protection system, pressure air supply system, communication and lighting system, supply and distribution system, and power supply system.

2.5 Construction cost comparison

The cost of the emergency rescue relay cabin, which includes material cost, site transformation cost, and daily maintenance fee, as listed in Table 1, is far less than that of current hedging facilities.

3. SYSTEM COMPONENTS

3.1 Exterior structure of the relay cabin

According to the features of the emergency rescue relay cabin and the condition of the domestic underground transportation equipment and roadway sizes, the final shape of the emergency rescue relay cabin is designed to be rectangular, with specific dimensions of 152 cm × 130 cm × 177 cm. The interior dimensions of the cabin are 150 cm × 128 cm × 175 cm. The entire relay cabin is steel welded to ensure a certain degree of strength and weight, thereby preventing cabin body inclination as a result of shock

waves from the side (Han et al., 2011). In addition, the compressive and tensile properties are good. The front of the relay cabin has an explosion-proof door and an emergency switch. Furthermore, necessary interfaces are set up to enable connection with the outside, such as the ventilation port connecting to external air supply devices, water supply port, power supply interface, communication interface, and air vent.

3.2 System components of the relay cabin

The interior of the relay cabin consists of five sub-systems: enclosed system, air supply system, resource system, power supply system, and lighting and communications system.

Enclosed system. The emergency rescue relay cabin has relatively low design requirements in terms of guaranteeing the survival of personnel, but it must provide protection. The entire cabin body comprises an enclosed system consisting of the steel shell structure and the explosion-proof door. The steel shell of the system body is built with steel welding technology. The front panel located in the tunnel and the explosion-proof door can withstand an impact of 0.3 MPa, and ordinary shock waves. In addition, the relay cabin has a certain degree of air-tightness to prevent infiltration of toxic gases. After the personnel enter the cabin, a positive pressure of $+200 \pm 100$ Pa with a relief rate less than 30 ± 20 Pa/min is maintained, which is slightly less than that of refuge chambers and movable rescue capsules.

Airsleeve air supply system. This system is mainly used for personnel to replace supplies. The airsleeve can be used to cover the upper body to form positive pressure and prevent poisonous gases from entering. In addition, the personnel can temporarily hedge in the airsleeve. There are two oxygen supply systems for the airsleeve air supply system: compressed oxygen bottles and external oxygen supply. The overall air supply system comprises compressed air bottles, compressed air bottle connectors, external pressure air ports, pressure regulators, airway, pressure gauge, muffler, ventilation isolation bag, and oil-water separator (Zhao et al., 2003; Zhang et al., 2009). The cabin also has two airsleeves, although only one is used when the equipment is being replaced. In emergency situations, both can open to ensure the hedging of two people.

Resource system. The emergency rescue relay cabin can be filled with self-rescuer, water, food, and first aid supplies based on actual need. In this study, the number of emergency rescue personnel and the safety factor were set to 40 and 1.2, respectively.

Self-rescuer. The emergency rescue relay cabin has 50 chemical oxygen 45 self-rescuers (with a safety factor of 1.2) meeting the equipment replacement requirement of 40 people. The rescuers are placed on

the window. A consistent model specification for each rescuer and field worker is maintained. The emergency rescue relay cabin can also be used as a complementary mine warehouse to assure routine replacement (Gao et al., 2012; Jin et al., 2012).

Water and food. The emergency rescue relay cabin should have enough water and food for two people to use for four days (with a safety factor of 1.5). The cabin should contain 30 L of pure water. Further, the port is connected to the external water supply, which provides a significant amount of potable water. Referring to the relevant standards, the emergency energy intake should be above 2000 KJ/day-per person; the shelf life should be no more than three years. Further, 3 kg of emergency food should be stored in the compartment to provide food for emergency hedging personnel.

First aid supplies. Essential rescue supplies should be stored in the relay cabin, such as explosion-proof flashlights and explosion-proof batteries, for rescue workers to replace the rescue equipment and, thereby, increase the scope and time of rescue. According to the actual situations, the cabin can also store toolboxes, first aid kits, medicines, and the equipment required in emergency situations.

Power supply system. In the emergency rescue relay cabin, equipment such as lighting and communication devices require electricity supply. The power storage has two explosion-proof power supplies (one is the backup power supply); battery life is monitored regularly to ensure its electrical storage capacity. At the same time, an external electrical connection port is setup to ensure external power supply.

The provided power supply needs to guarantee four consecutive days of electricity supply.

4. EXPERIMENT AND ANALYSIS

A relay cabin air-tightness test and airsleeve air supply test were conducted in accordance with the design requirements for a closed air supply system.

4.1 Relay cabin air-tightness test

This test determined the cabin air-tightness performance by varying the gas pressure in the cabin.

Method. A compressed air bottle was connected to the air ventilation port of the cabin, and pressure sensor testing devices connected in the cabin; the pre-drilled holes in the cabin body were sealed with leak-proof mud. The monitoring and control system were then turned on, the data parameters adjusted, and the door closed. This was followed by the opening of the air bottle valve and injection of air into the cabin at a uniform rate of 1.5 L/min. Throughout the process, the cabin pressure was monitored using pressure sensors. When the cabin pressure rose to 500 Pa, the CO₂

cylinders were switched off and the pressure recorded every 20 s until the pressure dropped by 100 Pa, that is, 400 Pa higher than the initial value. The test was repeated five times and the pressure relief rate calculated.

Conclusion. As shown in Figure 3, the pressure relief rate can be obtained using the equations

$$y = -0.4334x + 500, R^2 = 0.9307 \quad (1)$$

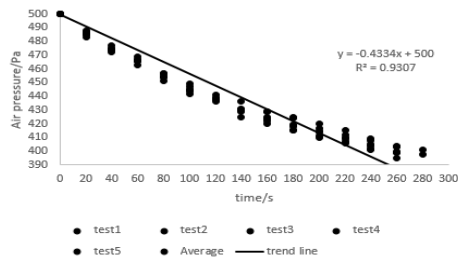


Figure 3: Pressure variation over time.

The pressure relief rate per minute calculated from the formula is 26 Pa, which meets the design requirements. The design models are therefore qualified and can be used as the carrier of the airsleeve air supply test.

4.2 Airsleeve air supply test

The airsleeve air supply test replaces poisonous gases with carbon dioxide, thereby determining the amount of compressed air needed to replace the equipment.

Method. The CO₂ cylinders, carbon dioxide detectors, sensors, cameras, and corresponding pipes were connected. The carbon dioxide detectors were placed in isolation airsleeves, simulating human head position, and the flowmeter inserted into the airsleeve. One camera was then focused on the meter reading, and another on the carbon dioxide detector readings. Finally, the cabin door was shut, the carbon dioxide cylinder valve opened, and carbon dioxide injected at a uniform rate through the backup port into the cabin. When the concentration of carbon dioxide in the airsleeve reached 2%, the carbon dioxide cylinder valves were adjusted to maintain the carbon dioxide concentration at 2%. The compressed air bottle was then connected to an external air vent, the gas-regulating flowmeter opened to a flow rate of 190 L/min, and the time, T₁, recorded. Subsequently, the carbon dioxide concentration was recorded once every five seconds and, when the carbon dioxide concentration had fallen to 1%, the isolation airsleeve valve was closed and the test terminated. The above steps and test were again repeated with a flow rate of 220 L/min. Finally, the test data were exported to facilitate calculation of the wind pressure and enable the correct wind pressure rate to be chosen.

Conclusion. It can be concluded from Figures 4 and 5 that when the rate is 190 L/min, the time needed to reduce the carbon dioxide concentration to 1% is approximately 54 s. From the formula:

$$V = kStx \quad (2)$$

where: V is the amount of air required, k is the safety factor, S is the aeration rate, t is time, x is the number of people.

The required amount of air is 10260 L.

According to Figures 4 and 5, at an aeration rate of 220 L/min, the time needed to reduce the carbon dioxide concentration to 1% is approximately 44 s. According to the Formula 2, the required amount of air is 9680 L.

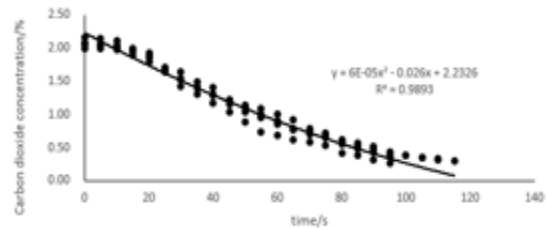


Figure 4 Carbon dioxide concentration-time curve for a rate of 190L/min.

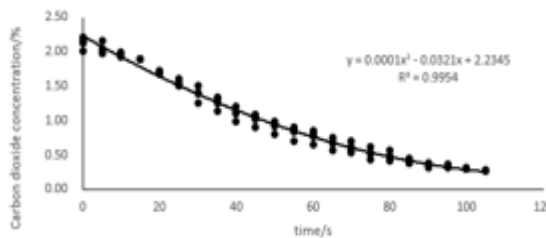


Figure 5 Carbon dioxide concentration-time curve for a rate of 220 L/min.

Because of the small amount of air required at the supply rate of 220 L/min, 220 L/min was selected as the final aeration rate, with two bottles of 40L compressed air used to meet the requirements.

5. CONCLUSIONS

The main difference between the mining emergency rescue relay cabin and existing hedging facilities are as follows: From the perspective of function the former focuses more on providing a safe environment for the rescuer and hedging personnel to replace equipment and supplement supplies, it can serve both rescue workers and hedging personnel, and the structure and dimensions are simpler and more flexible. In addition, it is more streamlined in terms of system components.

The exterior dimensions of the emergency rescue relay cabin are 152 cm × 130 cm × 177 cm. The cabin consists of five sub-systems: enclosed system, air

supply system, resource system, power supply system, and lighting and communication system.

The pressure relief rate of the relay cabin was determined to be 26 Pa/min via a relay cabin air-tightness test. The result obtained meets the stipulated air-tightness requirements.

The air supply rate for the personnel to replace equipment in the emergency rescue relay cabin was determined to be 220 L/min via the airsleeve air supply test. The total air supply volume was 9680 L. This air supply volume requirement can be satisfied using two bottles of 40 L compressed air, which is in line with the relay cabin space-saving size requirements.

6. ACKNOWLEDGEMENT

This work is financially supported by the National Natural Science Foundation of China (No. 51504017), the Fundamental Research Funds for the Central Universities (No.FRF-TP-15-043A3), the China Postdoctoral Science Foundation (No.2014T70039), the Doctor Science Research Foundation of the Education Ministry of China (No.20130006120020), the China Postdoctoral Science Foundation (No.2013M540666), which is gratefully acknowledged.

7. REFERENCES

Gao, N., Jin, L.Z., Wang, L., You, F. (2012). Research and application of oxygen supply system in Changcun Coal Mine refuge haven. *Journal of China coal society*, Volume 37, pp. 1021-1025

Gao, N., Jin, L.Z., You, F., Wang L. (2011). Research and experiment on fireproof anti-explosion air tightness system of refuge haven in underground mine. *Journal of China Coal Society*, Volume 37, pp. 132-136

Gao, N. (2011). *Research and Application of the Key Technology of the Permanent Refuge Haven of Changcun Coal Mine*. Beijing: School of Civil and Environmental Engineering University of Science and Technology Beijing.

Han, H.R., Jin, L.Z., Gao, N., Wang Y. (2011). Study on confined positive pressure system in mine refuge station. *Journal of Safety Science and Technology*. Volume 7, pp. 89-93

Jin, L.Z., Zhao, Y., Gao, N., You F., Wang L. (2012). Study on oxygen supply system of mine refuge haven. *Journal of Safety Science and Technology*, Volume 8, pp. 21-26

Li, R.S. (1989). Mine refuge chamber. *Yunnan Metal*, Volume 1, pp. 47-50

Krarti, M., Kreider, J. F. (1996). Analytical Model for Heat Transfer in an Underground Air Tunnel. *Energy Conversion and Management*, Volume 37, pp. 1561-1574

Ni, H., Wang, P., Huang, Y.Y. (2013). Study on Refuge Chamber Construction of Coal Mine. *Coal Science and Technology*, Volume 41, pp. 209-212

Sun, J.P. (2010). Personnel Position Monitoring Technology and System in Underground Mine. *Coal Science and Technology*, Volume 38, pp. 1-4

Sun, J.P. (2011a). The key technologies of the refuge chamber and rescue capsule in the underground coal mine. *Journal of China Coal Society*, Volume 36, pp. 713-717

Sun, J.P. (2011b). Research on emergency refuge system in underground mine. *Coal Science and Technology*, Volume 39, pp. 69-71

Wang, S., Jin, L.Z., Li, J. (2010). The present states of overseas mine emergency refuge chamber technology. *Journal of Safety Science and Technology*, Volume 6, pp. 119-123

Zhang, D.M., Ma, Y.D., Ding, Y.D. (2009). Research and design of mine refuge chamber. *Journal of Safety Science and Technology*, Volume 5, pp. 94-98

Zhao P.S., Hu, J.F. (2003). Status Analysis on Rescue Technology and Equipment for Personnel in Difficult in Underground Mine. *Coal Science and Technology*, Volume 34, pp. 33-36

Chemical equipment failure probability correction model based on the Multi-layer Grey Evaluation Method

Yue Zhang^a, Wentao Yang^a, Yuanyue Zhu^a, Kai Zhang^b

^a Safety Evaluation Center, China Academy of safety Science and Technology, Beijing, China, 100012

^b Special Grease Chemical Plant, Henan Jiaozuo Coal Energy Co.,Ltd, Jiaozuo, China, 454000

ABSTRACT

At present, the role of basic leak probability of chemical equipment cannot be distinguished from the influence of many other factors on failure probability in the petrochemical field. Due to the defects in other methods, in this study, by applying Analytic Hierarchy Process (AHP) and introducing grey theories, the chemical equipment failure probability correction model based on the multi-layer grey evaluation method was proposed. By applying AHP, six first level indicators including safety management, production equipment, process, production environment, natural environment, and personal quality were analyzed, as well as twenty-seven second level indicators. The influence of various factors in the chemical equipment failure system was obtained. Then, the correction factor value was calculated according to grey system theories, and the correction coefficient was applied to correct the failure probability. By taking a vinyl chloride tank of a chlor-alkali company as an example, the results indicated that the corrected factor value of failure probability for the tank was 3.335, the correction coefficient was 1.25, and the actual failure probability of the tank was larger than the basic leak probability. This method provides a new way to measure the failure probability correction, and has a theoretical significance and practical value on accurate calculation of the quantitative risk evaluation.

KEYWORDS: chemical equipment; failure probability; multi-layer grey evaluation method; whitening weight function; index system

1. INTRODUCTION

With the development of China's industrial economy, the safety situation of the petroleum chemical industry is becoming more and more serious (Wu, 2008). Therefore, quantitative risk assessment in the petroleum chemical industry is very important. The core of quantitative risk assessment is the fitting together of the accident occurrence probability and the accident consequence. The accuracy of chemical equipment failure probabilities can greatly affect the rationality and applicability of quantitative risk assessment results. At present, the statistical data of basic leak probabilities in the petroleum chemical industry are mainly from abroad, which generally represent the industry, but do not reflect actual failure probabilities of particular plants. The equalization of statistical figures makes effects of many factors on failure probabilities indistinguishable; therefore, these defects must be corrected.

Although the calculation of failure probabilities has been realized to a certain degree in the literature (Shi et al., 2011; American Petroleum Institute, 2000; Qingdao Safety Engineering Institute of SINOPEC, 2007; Zhu, 2005; Liu and Li, 2007; Koutsourelakis et al., 2004; Au and Beck, 2001; Yuan et al., 2007), the

current methods are subject to many problems, such as: some methods completely depend on experiences, calculation processes are too simple, the index systems are not comprehensive, indicators are not primary or secondary, and calculation processes are long and complicated in order to improve calculation accuracy. For these reasons, they could untruthfully reflect actual failure probabilities of chemical equipment, especially where there are greater differences in the aspects of personal quality, production equipment, process, production environment, and safety management.

Because the main chemical equipment of petroleum chemical industries are large scale, high speed, and complex, internal factors and risks are only partially known. Therefore, it is very difficult to realize objectivity by applying traditional methods. The method proposed in this study calculates failure probability correction by the multi-layer grey evaluation method, which combines the advantages of AHP and the grey evaluation method, and has better adaptability for complex systems with distinct layers. This method not only makes full use of existing information and focuses on internal connections among behavioural data in the internal system, but also effectively corrects the lack of a single evaluation method. This makes evaluation

results more accurate (Liu et al., 2004; Huang et al., 2015). Basing on the multi-layer grey evaluation method, the multi-layer grey evaluation model of the chemical equipment failure probability correction factor was established, and the model application was illustrated with examples.

2. THE MULTI-LAYER GREY EVALUATION MODEL OF THE CHEMICAL EQUIPMENT FAILURE PROBABILITY CORRECTION FACTOR

2.1 Establishing evaluation index systems

According to accident analysis theories (He et al., 2000; Tian and Jing, 2009; Xu et al., 2012), and by combining properties and environment conditions of chemical equipment, the evaluation index system of the chemical equipment failure probability correction factor was established.

Through the investigation of some petroleum chemical production plants, and by combining with the analysis situations of investigated relevant safety accident statistics, as well as expert investigation, practical experiences of safety, and environmental protection staff and technicians, the comprehensive evaluation index system of the chemical equipment failure probability correction factor was established, as shown in Figure 1.

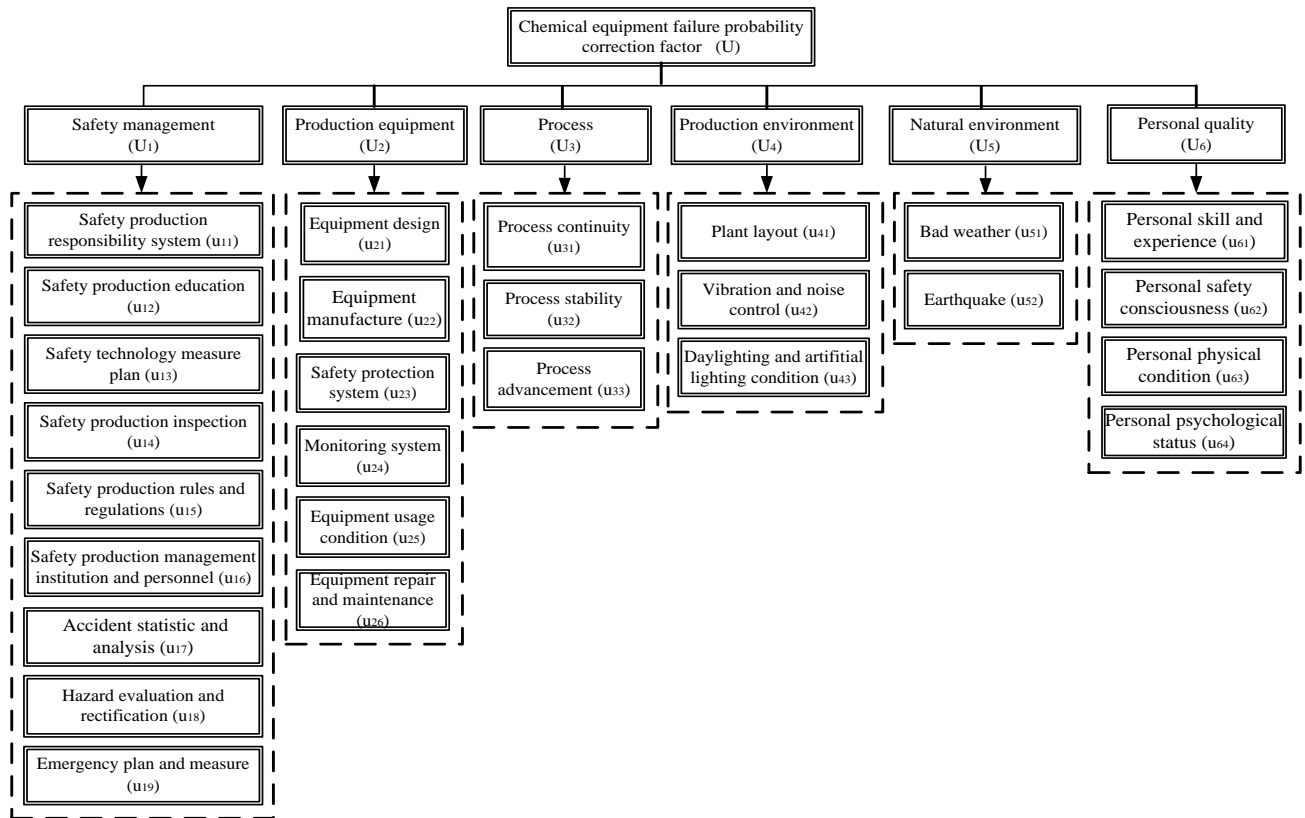


Figure 1: The chemical equipment failure probability correction factor model.

2.2 Determining weights of evaluation indictors

The influence of factors on evaluation objects (chemical equipment failure probability correction factors) was reflected by the weight set of evaluation indicators. In this paper, by using AHP, the judgment matrix was constructed by applying the scaling value method, and weight values of factors were calculated by the asymptotic normalization coefficient.

2.3 Set scoring criteria of evaluation indicators

Evaluation index grades were divided into “low”, “general”, “higher”, “high” and “very high”. Corresponding values were 1, 2, 3, 4 and 5, respectively. When the index grade was between adjacent grades, the corresponding score values were 1.5, 2.5, 3.5 and 4.5, respectively.

2.4 Organizing evaluation experts to score and establish evaluation sample matrixes

The evaluation expert number was supposed k , $k=1,2,3,\dots,p$, that was to say, there were p evaluation experts. According to the scoring criteria, the p evaluation experts were organized to score the evaluation index u_{ij} and filled the score table. Basing on the score value d_{ijk} of the k th evaluator, the evaluation sample matrix D was obtained as follows:

$$D = \begin{bmatrix} d_{111} & d_{112} & \cdots & d_{11p} \\ d_{121} & d_{122} & \cdots & d_{12p} \\ \vdots & \vdots & & \vdots \\ d_{211} & d_{212} & \cdots & d_{21p} \\ \vdots & \vdots & & \vdots \\ d_{ij1} & d_{ij2} & \cdots & d_{ijp} \end{bmatrix} \begin{matrix} u_{11} \\ u_{12} \\ \vdots \\ u_{21} \\ \vdots \\ u_{ij} \end{matrix} \quad (1)$$

$$i=1,2,\dots,m; j=1,2,\dots,n; k=1,2,\dots,p.$$

2.5 Determining evaluation grey-grades

This study used 5 evaluation grey-grades. The evaluation grey-grade number was supposed e , so that $e=1,2,3,4,5$. The corresponding grey number and definite weighted function were as follows (Wen, 2010; Ren and Zhu et al., 2008).

(1) “low” ($e=1$), the grey number \otimes_1 was supposed $\otimes_1 \in [0,1,2]$, and the definite weighted function $f_1(d_{ijk})$ was supposed as follows:

$$f_1(d_{ijk}) = \begin{cases} 1 & d_{ijk} \in [0,1] \\ (2-d_{ijk})/1 & d_{ijk} \in [1,2] \\ 0 & d_{ijk} \notin [0,2] \end{cases} \quad (2)$$

(2) “general” ($e=2$), the grey number \otimes_2 was supposed $\otimes_2 \in [0,2,4]$, and the definite weighted function $f_2(d_{ijk})$ was supposed as follows:

$$f_2(d_{ijk}) = \begin{cases} d_{ijk}/2 & d_{ijk} \in [0,2] \\ (4-d_{ijk})/2 & d_{ijk} \in [2,4] \\ 0 & d_{ijk} \notin [0,4] \end{cases} \quad (3)$$

(3) “higher” ($e=3$), the grey number \otimes_3 was supposed $\otimes_3 \in [0,3,6]$, and the definite weighted function $f_3(d_{ijk})$ was supposed as follows:

$$f_3(d_{ijk}) = \begin{cases} d_{ijk}/3 & d_{ijk} \in [0,3] \\ (6-d_{ijk})/3 & d_{ijk} \in [3,6] \\ 0 & d_{ijk} \notin [0,6] \end{cases} \quad (4)$$

(4) “high” ($e=4$), the grey number \otimes_4 was supposed $\otimes_4 \in [0,4,8]$, and the definite weighted function $f_4(d_{ijk})$ was supposed as follows:

$$f_4(d_{ijk}) = \begin{cases} d_{ijk}/4 & d_{ijk} \in [0,4] \\ (8-d_{ijk})/4 & d_{ijk} \in [4,8] \\ 0 & d_{ijk} \notin [0,8] \end{cases} \quad (5)$$

(5) “very high” ($e=5$), the grey number \otimes_5 was supposed $\otimes_5 \in [0,5,10]$, and the definite weighted function $f_5(d_{ijk})$ was supposed as follows:

$$f_5(d_{ijk}) = \begin{cases} d_{ijk}/5 & d_{ijk} \in [0,5] \\ 1 & d_{ijk} \in [5,10] \\ 0 & d_{ijk} \notin [0,10] \end{cases} \quad (6)$$

2.6 Calculating grey evaluation coefficients

The grey evaluation coefficient was recorded as X_{ije} , then there was:

$$X_{ije} = \sum_{k=1}^p f_e(d_{ijk}) \quad (7)$$

For the evaluation index u_{ij} , the total grey evaluation coefficient of each evaluation grey-grade was recorded as X_{ij} , then there was:

$$X_{ij} = \sum_{k=1}^p X_{ije} \quad (8)$$

2.7 Calculate grey evaluation weight vectors and weight matrixes

All evaluators advocated that the grey evaluation weight r_{ije} of the e th evaluation grey-grade was $r_{ije}=X_{ije}/X_{ij}$, the grey evaluation weight vector r_{ij} of the evaluation index u_{ij} was:

$$r_{ij}=(r_{ij1},r_{ij2},r_{ij3},r_{ij4},r_{ij5}) \quad (9)$$

So the grey evaluation weight matrix R_i of each evaluation grey-grade was obtained, for the index u_{ij} affiliated to U_i . Then there was:

$$R_i = \begin{bmatrix} r_{i1} \\ r_{i2} \\ \vdots \\ r_{ij} \end{bmatrix} = \begin{bmatrix} r_{i11} & r_{i12} & r_{i13} & r_{i14} & r_{i15} \\ r_{i21} & r_{i22} & r_{i23} & r_{i24} & r_{i25} \\ \vdots & \vdots & \vdots & \vdots & \vdots \\ r_{ij1} & r_{ij2} & r_{ij3} & r_{ij4} & r_{ij5} \end{bmatrix} \quad (10)$$

2.8 Comprehensive evaluation

The comprehensive evaluation results were:

$$B_i=A_i \cdot R_i=(b_{i1},b_{i2},b_{i3},b_{i4},b_{i5}) \quad (11)$$

The grey evaluation weight coefficient matrix was:

$$R = \begin{bmatrix} B_1 \\ B_2 \\ \vdots \\ B_5 \end{bmatrix} = \begin{bmatrix} b_{11} & b_{12} & b_{13} & b_{14} & b_{15} \\ b_{21} & b_{22} & b_{23} & b_{24} & b_{25} \\ \vdots & \vdots & \vdots & \vdots & \vdots \\ b_{51} & b_{52} & b_{53} & b_{54} & b_{55} \end{bmatrix} \quad (12)$$

Therefore, U_i was made comprehensive evaluation, and its results were recorded as B , then there was:

$$B = A \cdot R = (b_1, b_2, b_3, b_4, b_5) \quad (13)$$

The comprehensive evaluation value W of U_i was calculated. When each evaluation grey-grade was assigned through "grey level", then each evaluation grey-grade value vector C was $C=(1,2,3,4,5)$. Therefore, the comprehensive evaluation value W of the evaluation index U could be calculated according to the following formula:

$$W = B \cdot C^T B \quad (14)$$

Where, C^T was transposition of each evaluation grey-grade value vector.

2.9 Determining correction coefficients

Values of correction coefficients were as shown in Table 1. After the comprehensive evaluation value W was obtained, according to Table 1 and W the correction coefficient of the failure probability was determined. The product of the correction coefficient and the basic leak probability was the corrected chemical equipment failure probability.

Table 1: Values of correction coefficients.

Comprehensive evaluation value	Value of the correction coefficient r
[4.5, 5.0]	>2.00
[4.0, 4.5)	1.50~2.00
[3.5, 4.0)	1.50
[3.0, 3.5)	1.25
[2.5, 3.0)	1.05
[2.0, 2.5)	1.00
[1.5, 2.0)	0.95
[1.0, 1.5)	0.90

3. CASE ANALYSIS

In order to illustrate the validity of this model, a vinyl chloride tank of polyvinyl chloride (PVC) plant of a chlor-alkali company in China was taken as an example. The tank was horizontal type, and its volume was 112m³. There were 8 flanges with different sizes on tank body connections. It was e, and its volume was 112m 112mThe failure probability was corrected based on the multi-layer grey evaluation model.

3.1 Weight coefficient matrixes

The index weight of each layer was calculated through AHP. According to the 1-9 scale method,

judgment matrixes of six first level indicators in the criterion layer were constructed by experts, which were shown as Table 2. The weight vector of each factor was calculated by the "scaling value method", and the consistency test was made.

Table 2: Values of correction coefficients

Criterion layer	U ₁	U ₂	U ₃	U ₄	U ₅	U ₆
U ₁	1	3	4	7	7	3
U ₂	1/3	1	3	5	5	1
U ₃	1/4	1/3	1	3	3	1/3
U ₄	1/7	1/5	1/3	1	1	1/5
U ₅	1/7	1/5	1/3	1	1	1/5
U ₆	1/3	1	3	5	5	1

The weight of U was $A=(0.413,0.202,0.098,0.042,0.042,0.202)$, $\lambda_{max}=6.159$, $CR=0.026 < 0.1$, and the consistency test passed.

In the same way, weights of the second level indicators for the criterion layer were obtained as follows:

$$A_1=(0.019,0.052,0.288,0.090,0.037,0.026,0.128, 0.128,0.232);$$

$$A_2=(0.068,0.111,0.289,0.035,0.192,0.306);$$

$$A_3=(0.106,0.633,0.260);$$

$$A_4=(0.143,0.571,0.286);$$

$$A_5=(0.500,0.500);$$

$$A_6=(0.584,0.286,0.080,0.050).$$

3.2 Organizing evaluation experts to score and establish evaluation sample matrixes

According to score sheets filled by 10 experts, the evaluation sample matrix D was obtained.

$$D = \begin{bmatrix} 1 & 1 & 1 & 1 & 1 & 1 & 2 & 1 & 1.5 & 1.5 \\ 2 & 2 & 2 & 1.5 & 1.5 & 2 & 2 & 1 & 1 & 1.5 \\ 2.5 & 3 & 3 & 1.5 & 1.5 & 2 & 2 & 1 & 1.5 & 1 \\ 1.5 & 2 & 2 & 1.5 & 1.5 & 1.5 & 1.5 & 1 & 1.5 & 1 \\ 1 & 1 & 2 & 1.5 & 1.5 & 1.5 & 2 & 1 & 1.5 & 1.5 \\ 1.5 & 2 & 1 & 1 & 2 & 1.5 & 2 & 1 & 2 & 1.5 \\ 1.5 & 1 & 2 & 1.5 & 2 & 2 & 2 & 1 & 1.5 & 1 \\ 1 & 1.5 & 2 & 1 & 2 & 1.5 & 1.5 & 1 & 2 & 1.5 \\ 2 & 2 & 2 & 1.5 & 2.5 & 1.5 & 2 & 1 & 1 & 1 \\ 1 & 1.5 & 3 & 2 & 1.5 & 2 & 2 & 1.5 & 1 & 1.5 \\ 1.5 & 2 & 3 & 1.5 & 2 & 2 & 2.5 & 1 & 1.5 & 1 \\ 2 & 1.5 & 2 & 1.5 & 1.5 & 1.5 & 1.5 & 1 & 1.5 & 1.5 \\ 2 & 2.5 & 2 & 1.5 & 1.5 & 1.5 & 2.5 & 1.5 & 1.5 & 1 \\ 1.5 & 2 & 3 & 1.5 & 2.5 & 1.5 & 3 & 1.5 & 2 & 2 \\ 2.5 & 3 & 3 & 1.5 & 2.5 & 1.5 & 2.5 & 2.5 & 1 & 2 \\ 1.5 & 1.5 & 2 & 1.5 & 1.5 & 1.5 & 2 & 1 & 1 & 1.5 \\ 1.5 & 1.5 & 2 & 2 & 1.5 & 1.5 & 1.5 & 1.5 & 1 & 2 \\ 1.5 & 2 & 2 & 2 & 1.5 & 2 & 1 & 2 & 1 & 1 \\ 1 & 1 & 3 & 1 & 3 & 2 & 1 & 1.5 & 1 & 1 \\ 1 & 1 & 1 & 1.5 & 1.5 & 2 & 2.5 & 1.5 & 2 & 2 \\ 1 & 1 & 1 & 1.5 & 1.5 & 1.5 & 1 & 1 & 1 & 1.5 \\ 1.5 & 2 & 2 & 1.5 & 2 & 2 & 2 & 1 & 2 & 1 \\ 1.5 & 2 & 2 & 1.5 & 2 & 2 & 1 & 1.5 & 2 & 1 \\ 2.5 & 2.5 & 3 & 1.5 & 1.5 & 2 & 2 & 2 & 2.5 & 1.5 \\ 1.5 & 2 & 2 & 1 & 2 & 2 & 2.5 & 1.5 & 1.5 & 2 \\ 1 & 1 & 2 & 1 & 1.5 & 1.5 & 1.5 & 1.5 & 2 & 1.5 \\ 2 & 2 & 2 & 1.5 & 2 & 1.5 & 3 & 3.5 & 2 & 1 \end{bmatrix}$$

$$R_3 = \begin{bmatrix} 0.235 & 0.353 & 0.235 & 0.176 & 0.235 \\ 0.188 & 0.375 & 0.250 & 0.188 & 0.188 \\ 0.188 & 0.375 & 0.250 & 0.188 & 0.188 \end{bmatrix};$$

$$R_4 = \begin{bmatrix} 0.305 & 0.270 & 0.243 & 0.182 & 0.305 \\ 0.211 & 0.352 & 0.250 & 0.188 & 0.211 \\ 0.381 & 0.286 & 0.190 & 0.143 & 0.381 \end{bmatrix};$$

$$R_5 = \begin{bmatrix} 0.140 & 0.397 & 0.265 & 0.198 & 0.140 \\ 0.164 & 0.386 & 0.257 & 0.193 & 0.164 \end{bmatrix};$$

$$R_6 = \begin{bmatrix} 0.069 & 0.368 & 0.322 & 0.241 & 0.069 \\ 0.116 & 0.395 & 0.279 & 0.209 & 0.116 \\ 0.259 & 0.342 & 0.228 & 0.171 & 0.259 \\ 0.094 & 0.363 & 0.304 & 0.240 & 0.094 \end{bmatrix}.$$

3.4 Comprehensive evaluation

Evaluation indicators affiliated to U_i were evaluated. The results were recorded as B_i , where:

$$B_1=A_1 \cdot R_1=(0.198,0.348,0.258,0.193,0.194)$$

$$B_2=A_2 \cdot R_2=(0.143,0.347,0.292,0.219,0.143)$$

$$B_3=A_3 \cdot R_3=(0.193,0.372,0.248,0.187,0.193)$$

$$B_4=A_4 \cdot R_4=(0.273,0.321,0.232,0.174,0.273)$$

$$B_5=A_5 \cdot R_5=(0.152,0.392,0.261,0.196,0.152)$$

$$B_6=A_6 \cdot R_6=(0.099,0.373,0.301,0.226,0.099)$$

The grey evaluation weight coefficient matrix of U_i for each evaluation grey-grade was obtained by B_i .

$$R = \begin{bmatrix} 0.198 & 0.348 & 0.258 & 0.193 & 0.194 \\ 0.143 & 0.347 & 0.292 & 0.219 & 0.143 \\ 0.193 & 0.372 & 0.248 & 0.187 & 0.193 \\ 0.273 & 0.321 & 0.232 & 0.174 & 0.273 \\ 0.152 & 0.392 & 0.261 & 0.196 & 0.152 \\ 0.099 & 0.373 & 0.301 & 0.226 & 0.099 \end{bmatrix}$$

The evaluation weight vector of the failure probability correction factor grey-grade for the vinyl chloride tank was obtained, that was:

$$B=A \cdot R=(0.167,0.356,0.271,0.203,0.166)$$

The comprehensive evaluation value of the tank failure probability correction factor was:

$$W=B \cdot C^T=3.335$$

3.5 Determine the correction coefficient

The correction coefficient was obtained according to W and Table 1., The failure probability correction coefficient of the vinyl chloride tank was determined to be 1.25, which when multiplied with the basic leak probability gave the corrected failure probability.

4. CONCLUSIONS

By combining with actual situations of chemical equipment and by objectively and reasonably choosing evaluation indicators, the chemical equipment failure probability correction model based

3.3 Calculating grey evaluation weight matrixes

According to formulas 2-6, 9, and 10, calculated results were as follows:

$$R_1 = \begin{bmatrix} 0.342 & 0.256 & 0.171 & 0.128 & 0.103 \\ 0.164 & 0.386 & 0.257 & 0.193 & 0.164 \\ 0.162 & 0.324 & 0.293 & 0.220 & 0.162 \\ 0.235 & 0.353 & 0.235 & 0.176 & 0.235 \\ 0.259 & 0.342 & 0.228 & 0.171 & 0.259 \\ 0.211 & 0.364 & 0.243 & 0.182 & 0.211 \\ 0.211 & 0.364 & 0.243 & 0.182 & 0.211 \\ 0.235 & 0.353 & 0.235 & 0.176 & 0.235 \\ 0.187 & 0.363 & 0.257 & 0.193 & 0.187 \end{bmatrix};$$

$$R_2 = \begin{bmatrix} 0.187 & 0.350 & 0.265 & 0.198 & 0.187 \\ 0.163 & 0.349 & 0.279 & 0.209 & 0.163 \\ 0.211 & 0.364 & 0.243 & 0.182 & 0.211 \\ 0.163 & 0.361 & 0.272 & 0.204 & 0.163 \\ 0.092 & 0.357 & 0.315 & 0.236 & 0.092 \\ 0.092 & 0.321 & 0.336 & 0.252 & 0.092 \end{bmatrix};$$

on the multi-layer grey evaluation method was established, and then was applied to the case study.

By using AHP to determine index weights, and applying the multi-layer grey evaluation method, the failure probability of the vinyl chloride tank in a chlor-alkali company was corrected. Comprehensive evaluation results showed that the failure probability correction factor value of the vinyl chloride tank in the chlor-alkali company was 3.335, and the determined correction coefficient was 1.25. So the failure probability correction factor value of the tank was between “higher” and “high”, and its actual failure probability value was larger than that of the basic leak probability. This model not only provides a new approach to the correction of the chemical equipment failure probability, but also has important practical significance with the accurate calculation of the quantitative risk assessment.

The comprehensive evaluation of the chemical equipment failure probability correction factor was a very complicated research topic. However, the determination of scientific and reasonable comprehensive evaluation index systems and evaluation methods was necessary to correct failure probabilities. Established models should constantly be optimized.

5. REFERENCES

- American Petroleum Institute. (2008) Risk-based inspection technology. API 581, Second Edition. 654p.
- Au S K and Beck J L. (2001) Estimation of small failure probability in high dimensions by subset simulation. Probabilistic Engineering Mechanics. Volume 16, pp. 263-277.
- He X., etc. (2000) Safety engineering. China Mining University Press. Xuzhou, 443p.
- Huang C., He S. and He L. (2015) Urban Passenger Hub Transfer Evaluation Based on Multilevel Grey Evaluation Method. Journal of Chongqing Jiaotong University(Natural Science), Volume 16, No. 4, pp. 89-92.
- Koutsourelakis P S, Pradlwarter H J and Schueller G I. (2004) Reliability of structures in high dimensions, Part I: Algorithms and applications. Probabilistic Engineering Mechanics. Volume 19, pp. 409-417.
- Liu S., Dang Y., Fang Z., and Xie N. (2004) Grey system theory and application(the third edition). Science Press, 415p.
- Liu X. and Li Z. (2007) Using Monte-Carlo method to calculate failure probability of oil pipeline. Oil & Gas Storage and Transportation. Volume 26, pp. 16-20.
- Qingdao Safety Engineering Institute of SINOPEC (China Petroleum & Chemical Corporation). (2007) Quantitative risk assessment guide for petrochemical plant. China Petrochemical Press. Beijing, 210p.
- Ren H. and Zhu L. (2008) Multi-hierarchical grey evaluation on the construction enterprises' information level based on combinational weight. Systems Engineering-Theory & Practice. No. 2, pp. 82-88.
- Shi C., Luo A., Chen W., Duo Y. and Wu Z. (2011) Chemical equipment failure probability model based on JC method. Science & Technology Review. Volume 29, No. 8, pp. 35-38.
- Tian S. and Jing G. (2009) Safety management. China Machine Press. Beijing, 322p.
- Wen J. (2010) Airline flight safety risk assessment based on grey hierarchy method. China Safety Science Journal. Volume 20, pp. 29-34.
- Wu, Z. (2008(s)) Several cognition and countermeasure discussion to promote safety development. Journal of Safety Science and Technology. pp. 1-3.
- Xu X., Zhang L., Duan L. and Zhang Y. (2012) Research on reciprocating compressors safety assessment system based on AHP. Industrial Safety and Environmental Protection. Volume 38, pp. 27-30.
- Yuan X. and Lv Z. (2007) Markov chain simulation for fast evaluation of failure probability. China Mechanical Engineering, Volume 10, pp. 2355-2359.
- Zhu J. (2005) The use of multi-hierarchical grey evaluation methods into the risk based inspection for modern petrochemical equipment. Zhejiang University of Technology. Hangzhou, 72p.

Mechanisms and applications of formatting unsafe behaviour motivation

Yuebing Zhang* Zhiliang Wang

North China Institute of Science and Technology, East Yanjiao 101601, China
Foundation item: the fundamental research funds for the Central Universities Fund (3142014014)

ABSTRACT

This paper aims to reveal the mechanism of work safety behaviours in order to effectively curb various unsafe behaviours. For this, various motivations for unsafe behaviour are analyzed based on the work safety behaviour features, application need, motivation, behaviour theory of psychology, the logic analysis method, and accident cases analysis, as well as the source of need producing the motivations. The results show that the need comes from the source of human behaviour. To improve the level of people's safety needs and to appropriately weaken the level of other needs is the basic measure of preventing unsafe behaviours. The main means to adjust the level of needs is to regulate the imbalance of corresponding conditions. For instance, "on-the-spot meeting for accident investigation" can change the lack and imbalance senses of people's safety conditions and improve the level of safety need.

KEYWORDS: unsafe behaviour; need; motivation; accident prevention; safety psychology

1. FOREWORD

Productive labor can be considered a process of understanding and changing nature. In this process, each human has experiences countless painful lessons due to error behaviour or "incompetence", such as natural disasters, wars, accidents, and disease. Some of these disasters can be avoided, such as in the field of work safety. Statistics show that more than 90% of accidents are caused by improper human behaviour, and can be considered a "responsibility accident". Each of the 30 major work safety accidents announced during 2007-12-23 to 2012-08-28 in the website of China's State Administration of Work Safety is a responsibility accident (Fu et al., 2013). Theoretical derivation also shows that the vast majority of accidents are people-related (Zhang et al., 2013), either directly due to improper human behaviour, or due to a wrong decision and management. For example, in 2013 the devastating Shandong "11 • 22" Sinopec Dong Huang oil pipeline leakage and explosion accident was attributable to the impact spark produced by the site disposal using hydraulic breaking hammer punching in a culvert cover plate. Similarly, the fatal Babao coal mine gas explosion was triggered by the improper control of coal spontaneous combustion in a mined out area. Therefore, it is of significance for work safety to study the behaviour of humans, analysis, forecast and control human behaviour, both theoretically and practically.

2. THE HUMAN BEHAVIOUR MECHANISM

Human psychology is a very complex phenomena. Human psychological activity is expressed through external behaviour, or people's explicit behaviour is controlled by implicit psychological activity. All human behaviours (including unconscious behaviours) are dominated by psychological activities, and in turn, psychological activities are developed and expressed through behaviour (Shao and Wang, 2004).

Psychology thinks that human behaviour is decided by needs and motivation; behind people's behaviour there must be motivation, and motivation comes from the people's need, therefore, the need is the original power of human behaviour (Chen, 2010). However needs do not lead to behaviour directly, but instead act through motivation as the direct cause of human behaviour (Chen, 2010). Motivation is being studied more and more extensively in the education and law fields, such as in studies of learning motivation (Gao et al. 2003) and crime motivation (Chen, 2010). The safety behaviour field has been paid little attention, because no people subjectively expect accidents to occur, and the motivation of unsafe behaviour is indirect (Zhang et al., 2013). Chen suggests in their research on criminal motivation that the occurrence of criminal behaviour should have experienced a process of one passive need and two active direction selections. That is, needs exist in everyone's objectively, with no good or bad. Instead, people can choose by themselves whether or not or by what manner to meet a need according to the objective conditions, thus resulting in the corresponding motivation. People also choose

whether or not to move according to a code of conduct and ethical standards. This theory is also applicable to other behaviours such as safety behaviour.

Psychology says that needs produce the psychological tension state, which is transformed into motivation in a situation where the needs can be met. People are stimulated to engage in certain activities to achieve their objectives. When the objectives are achieved, the needs are met and the psychological tension state is removed.

3. THE UNSAFE BEHAVIOUR MOTIVATION ANALYSIS

The transformation of needs into motivation is a very complex process. In general, the actor will weigh the advantages and disadvantages in the decision-making process.

Based on the behaviour control model of Chen Hong (2006), the behaviour control model can be proposed as shown in Figure 1. It can be seen that the physiological and psychological aspects of a lack and imbalance always stimulate the person's needs at a certain level (Chen, 2010). This need makes actor selectively sense the environmental information, judge and process the information based on their own experience and knowledge, determine whether conditions exist that can satisfy some need, and then take some kind of behaviour to meet the needs. Hence, the motivation occurs.



Figure 1: the human behaviour model.

The author argues that whether need is transformed into motivation depends on two aspects: one is the need intensity; the other is the behaviour cost to meet the needs. Human behaviour at first perceives the information of the environment, and then based on the human's knowledge, sends out a response. According to Maslow's theory of hierarchy of need, the needs of people can be divided into five hierarchies, from low to high: Physiological needs, Safety needs, Love and belonging, Esteem, and Self-actualization (Maslow, 1954). However Maslow insists that only the needs at lower levels can be met. Maslow argues that this hierarchy can only be established in the general case. Numerous cases show that society, organizations, and people can adjust the needs level by themselves, such as various

behaviours of laying down one's life for justice. Chen Hehua thinks that need is a kind of lack and imbalance. Therefore, the author considers that the level of need is adjusted artificially or by eliminating this lack and imbalance. For example, in the face of a war or death threat, the lack of living conditions places the survival need at a higher level. Then, morale sets up the ideal to improve Self-actualization.

The actor can perceive the information around situations using the sensory organs. The amount of the information that can be perceived is limited, so perception is selective. Needs at higher levels will prompt the actor to input more attentional resources to the information that can help to meet the related need. At the same time, the strength of the information and whether there are significant differences between the information and others around will also affect the information perception selection. Then, the actor processes the information according to his own experience and knowledge. If he is assured that in this situation, he is able to complete a behaviour, and behaviour results can meet the needs, the actor will feel the motivation to implement the behaviour. Motivation has a clear directivity, and is linked to means of behaviour to meet the need.

Finally, the actor will further think if this kind of behaviour may cause other results, make a trade-off between costs and profit, and determine whether or not to implement this behaviour. If he chooses to implement, but the behaviour fails, the actor may choose to give up or continue to work hard according to the judgment of the task difficulty, and eventually satisfy the need or leave it unsatisfied and cause mental stress. This judgment process, of course, is not always very prudent, due to the complexity of causality or due to time limits. Thus the actor will also show impulse.

4. UNSAFE BEHAVIOUR MOTIVATION ANALYSIS AND PREVENTION COUNTERMEASURES

4.1 Unsafe behaviour motivation analysis

There are many kinds of unsafe human behaviours. Appendix 7 of "The enterprise worker casualty accident classification standards" (GB6441-1986) classifies the unsafe human behaviours into four kinds: first, the ones because of inattention, the individual physiological function defects which cause behaviour mistake; second, the ones because of actors' lack of scientific understanding or the consequences of the behaviour, not knowing the seriousness of the consequences, not knowing the

uncontrollable consequences, or not knowing what behaviour is beyond their ability. This kind of situation sometimes is due to inadequate mastery of environmental information, sometimes due to a lack of experience and knowledge. It can also be due to a lack of serious judgment, namely the paralysis of thought; third, when one knows the possible consequences, but between the positive benefits and possible loss a preference exists to save energy, time or bravado; fourth, because one does not agree with the system. There is no equal information between system makers and system conformance.

From the theory of need-motivation-behaviour, the occurrence of the above unsafe behaviours are all due to the safety needs of the actor. And their organization causes a low-level relative to the other needs.

Generally speaking, in the enterprise's work safety, the physiological need of the actor is usually in a relatively high level, because the enterprise should make profits and the workers should earn salaries, which causes the enterprises to generate the motivation and the behaviour of production, and the workers to generate the motivation and behaviour of finishing tasks. In addition, since fierce market competition leads to the growing shortage of living conditions, the physiological need is in a higher level.

As for safety needs, although they are in an inferior level, considering the conditions for work safety, the actor rarely has an accident or is in distress. Therefore, the lack and imbalance sense of the safety conditions is low, and thus the safety need is in the lower level.

Social needs, esteem needs, and self-actualization needs are in the higher hierarchy. These need levels can be increased because of the corresponding lack and imbalance.

4.2 Preventive measures of unsafe behaviours

In order to prevent the unsafe behaviour of the people, the fundamental method is to improve the lack and imbalance senses of the safety conditions, and to reduce the lack and imbalance senses of other needs, thus to put the actor's safety needs in a higher level. Only in this way can the actor pay more attention to the work safety, reduce the formation of the motivation and the implementation of the unsafe behaviours. Meanwhile, it can also help employees learn safety knowledge and skills.

(1) Improve the level of safety needs

To improve the level of the safety needs mainly relies on improving the lack and imbalance senses of the safety conditions. The improvement of this kind of lack and imbalance senses is not to literally reduce the conditions for work safety but to make people feel the seriousness and importance of safety

problems. On-the-spot accident meeting is a good way by which employees feel the seriousness of the safety problems and the accident consequences, thus their lack and imbalance senses of the safety conditions are enhanced. Of course, for the company alone, the accident probability is low, so it is helpful that the company should hold some meetings about the near-miss accident, or play some videos of the accident scene.

(2) Reduce the level of other needs

Risk-taking is a typical unsafe behaviour. Although it can bring injuries, it give psychological satisfaction and easy profit. It can meet the Physiological needs and Esteem needs. According to this situation, enterprises can cultivate safety culture to form a belief that risk-taking is shameful and that observing discipline is glorious within the enterprise. They can implement activities to satisfy the employees' esteem needs by observing discipline. Meanwhile, to exercise workers' stamina and endurance, they should reduce the labor intensity and time, thus to lessen the lack and imbalance senses of fatigue and the level of physiological need.

The performance of violation conformity sometimes is to meet the Love and belonging needs. For example, under circumstances where others are not wearing a seat belt, the actors tend not to wear one either. Enterprises can solve the above problems by strengthening the communication among the employees and enhancing the independence of safety behaviour through publicity of public opinion.

Organizational citizenship behaviour exists to satisfy the Self-actualization needs. These "extra tasks" sometimes are beneficial for safety, and sometimes not. For example, three women in Jilin Province managed to stop a train and prevented a major traffic accident, but conversely, the collieries removal of a miner's lamp may lead to a gas explosion.

The actor here means decision-maker, management, or executive. For the decision-maker, making decisions is their behaviour, like decisions concerning work safety investments and safety measures. The nuclear field offers many examples of how "external" errors or omissions have been significant contributing factors to accidents (Mosey, D. 2014). As for the management, their behaviours are planning, implementing, checking and improving the system, crystallizing, detailing, programming the final policy, and implementing it. They must arrange for someone to do some tasks, prepare materials and equipment, coordinate among different departments, and set up effective control systems like checking and supervising behaviours and correcting them. As for the executives, they need to execute the tasks given by the management according to the relevant

regulations. Obviously, these behaviours are influenced by the need level of the actors. Enterprises should strengthen publicity, establish the values of being people-oriented, and improve the level of safety needs to reduce the acceptable level of risks. Meanwhile, to make the management realize the expectations from the grassroots, the grassroots should know the management's policy. Effective communication is a prerequisite that is necessary for the improvement of the safety needs level, and the value everyone places on safety.

5. CONCLUSIONS

No behaviours can exist without motivations, and needs are the source of behaviours. It is of theoretical and practical significance for the prevention of work safety accident to study the mechanism of the theory of need-motivation-behaviour.

To prevent the unsafe behaviours of the people, the fundamental method is to put the actors' safety needs in a higher level. Only in this way can the actors pay more attention to the work safety, actively learn the safety knowledge and skills, reduce the formation of the motivation and the implementation of the unsafe behaviours.

In order to improve the level of the safety needs, one must mainly improve the lack and imbalance sense of the safety conditions, and reduce the lack and imbalance sense of life conditions, social conditions, esteem condition and self-actualization conditions. Methods include having meetings at the scene of accidents, increasing the employees' income, exercising workers' stamina and endurance, reducing the labor intensity and time, enhancing communication between the staff, and establishing the right values. All these measures can change the neediness and the sense of imbalance.

6. REFERENCE

CHEN He-hua. (2010). Origin, Character and Formation of Criminal Motivation. *Journal of Political Science and Law*, Volume 2, pp. 21-27.

CHEN Hong. (2006) Research on unsafe behaviors of coalmine fatal accidents in China. Beijing : Science Press, pp. 122-141.

FU Gui, YAN Wen-tao, DONG Ji-ye, et al. (2013) Behavior-based accident causation: the "2 - 4" model and its safety implications in coal mines. *Journal of China Coal Society*, Volume 7, pp.1123-1129

GAO Yi-hong, ZHAO Yuan, CHENG Ying, et al. (2003) Motivation Types of Chinese College Undergraduates. *Modern Foreign Languages*, Volume 1, pp. 28-38.

GB6441-1986, Standard for classification of casualty accidents of enterprise employees, National standard of the people's Republic of China.

Maslow, A (1954). *Motivation and personality*. New York, NY: Harper. p. 236. ISBN 0-06-041987-3.

Mosey, D. (2014), Looking beyond operator, NEI Magazine, <http://www.neimagazine.com/features/featurelooking-beyond-the-operator-4447549/>

SHAO Hui, WANG Kaiquan. *Safety psychology* (2004). Chemical Industry Press, 65p.

ZHANG Yue-bing, WANG Kai, WANG Zhi-liang (2011). Theoretical research on hazards and its application in accident prevention. *China Safety Science Journal*, Volume 21, pp. 10-16

ZHANG Yue-bing, ZHANG Chao, WANG Zhi-liang. (2013). Research on Safety Behavior Features and Its Application. *China Safety Science Journal*, Volume 7, pp. 3-7.

Examining safety and sustainability in longwall coal mining through case studies of disasters and reviewing global trends in environmental stewardship

Ben de Wit ^a, Xinglong Zhao ^b, Malcolm Scoble ^a

^aNBK Department of Mining Engineering, University of British Columbia, 6350 Stores Road, Main Office Room 517, Vancouver, BC, Canada V6T 1Z4

^bSchool of Mines, China University of Mining and Technology, No1, Daxue Road, Xuzhou, Jiangsu, 221116, China

ABSTRACT

The coal mining industry has struggled recently with numerous operations being closed due to poor market conditions and profitability. In spite of these low prices however the industry is seeing longwall projects develop and continue operations, which seems to present an opportunity that can be economical and sustainable.

This paper examines longwall coal projects and what makes them successful. The topic of safety is a primary focus, with coal mining disasters highlighted and operational challenges addressed. It includes summary root-cause analyses that may serve as a risk register to highlight significant issues and challenges facing the industry.

The paper discusses sustainability and the influence longwall operations could have on the future of the coal industry, while also highlighting global trends in environmental stewardship and fossil fuel reduction. **KEYWORDS:** Coal; Safety; Mine Disasters; Root Cause Safety Analysis; Fossil Fuels; Sustainability

1. CURRENT COAL DOWNTURN AND SLUMP RESILIENT LONGWALL MINES

The coal mining industry has been facing challenging operating conditions the past few years and in combination with a global shift towards renewable energy and a focus on sustainability, the viability of coal mining has been impacted. The effects of these conditions have been seen through the closure of numerous coal operations, the shelving of projects, and companies restructuring and selling assets to adjust to new market conditions.

The effects of low coal prices can be seen by looking at the traditionally active coal mining region of North East BC where 5 mines have closed and more than 1,300 employees are out of work. Communities such as Tumbler Ridge have been impacted, where the town's mayor estimates its population has decreased from over 3000 to just 2000 (Cryderman 2015).

The severity of market conditions was highlighted in 2015 when Anglo American announced it would cut its workforce of 135,000 by 85,000 in response to continued low prices (Saunders 2015). Anglo also announced its intentions to sell numerous assets and focus on priority assets. "Negative cash flow assets will either be closed, placed on care and maintenance or sold," Mark Cutifani, CEO Anglo American (Saunders 2015).

Despite low coal prices Anglo American announced that its longwall coal mines, Moranbah and Grosvenor, were not for sale and would continue

operations (Saunders 2015). "Together with the additional material capital, cost saving and productivity measures announced, we are setting out an accelerated and aggressive strategic restructuring of the portfolio to focus it around our 'Priority One' assets, being those assets that are best placed to deliver free cash flow through the cycle and that constitute the core long-term value proposition of Anglo American," Mark Cutifani (Saunders 2015).

The statements from Anglo's CEO highlight the advantages of longwall coal mines, primarily low operating costs, and the ability to stay cash positive during periods of low prices. Unfortunately, longwall mines are restricted by geological conditions and they require large up-front capital expenditures, however, once established a longwall mine can be very valuable.

2. SAFETY PERFORMANCE IN THE USA

The risks associated with underground mines are much greater than surface mines, which is evidenced by the higher accident and fatality rates in underground mines. In 2015 for example, the US coal industry had 11 fatalities, 7 of which were in underground mines, with 4 of the 7 attributed to roof or wall failures (CBC 2015). By reviewing the statistics from the Mine Safety and Health Association's (MSHA) 2015 report, it is evident that in the USA citations and orders are generally being reduced. By reviewing Table 1 from MSHA 2015 it can be seen that with the exception of 2010, when the

Upper Big Branch disaster occurred, the fatality rate has remained relatively constant around 0.016 fatalities per 200,000 hours worked, which is roughly 50% higher than in metal and non-metal mines. (If the Upper Big Branch disaster is excluded from 2010 figures, the fatality rate is approximately 0.152).

It is also interesting that the number of citations ordered is higher in coal mines, even though there are 6 times more metal and non-metal mines. Also, there are roughly 3 times as many workers at coal mines, which could be a contributing factor through issues with congestion and communication.

Table 1: Safety Performance at Coal Mines in the USA (MSHA 2015).

<i>Coal Mine Safety and Health</i>	<u>2008</u>	<u>2009</u>	<u>2010</u>	<u>2011</u>	<u>2012</u>	<u>2013</u>	<u>2014*</u>
Number of Coal Mines	2,129	2,076	1,944	1,973	1,871	1,701	1,632
Number of Miners	133,828	133,089	135,500	143,437	137,650	123,259	116,010
Fatalities	30	18	48	20	20	20	16
Fatal Injury Rate (per 200,000 hours worked)	0.0237	0.0148	0.0384	0.0148	0.0159	0.0176	0.015
All Injury Rate (per 200,000 hours worked)	3.89	3.69	3.43	3.43	3.16	3.11	3.11
Coal Production (Millions of Tons)	1,172	1,075	1,086	1,095	1,018	984	1,000
Citations and Orders Issued ³	106,793	101,904	96,352	93,077	78,857	63,217	62,684
S&S Citations and Orders (%)	32%	30%	32%	31%	27%	26%	26%
Dollar Amount Assessed (Millions)	111.5	96.5	110.7	120.2	89.5	64.9	61.2

3. SAFETY PERFORMANCE IN CHINA

Coal mines are common in China because of how widely used coal is for energy production. From 2000 – 2015, approximately 70% of China’s total energy consumption was from coal, and prior to 2000 it was even greater (Bloomberg 2015). However, mines in China have experienced many issues with safety and the future of coal mining in China is uncertain.

Information compiled by Askci (2013) indicates that China’s coal production accounted for roughly half of global production from 2012 to 2014. This high production rate contributes to higher accident rates in that because of scarcity, marginally profitable deposits are exploited and small margins can cause operators to take greater risk. These risks could include failing to implement certain safety measures to reduce costs.

An article by Xi (2015) highlights China’s poor safety record and cites that in 2009 China had the highest number of fatalities globally, with 2,631. The figures indicate that total fatalities in China have been decreasing, but fatalities per unit produced are still 15 times greater compared to figures from US mines.

However, though there are a significant number of safety incidents and fatalities in Chinese mines, research by Chen and Zhao (2012) indicates that the majority of accidents can be attributed to ownership. The research divides China’s coal mines into 3 types including state-owned, local, and private enterprises.

State-owned refers to mines controlled by China’s federal government. These mines are large, have high yields and production rates, are highly mechanized, and have generally strong safety

records. Local refers to mines controlled by the local government without influence from the state, and are generally smaller than state-owned mines. Private refers to mines that are individually owned and operated without influence from the government. These mines are relatively small, with low yields and production rates, low level of mechanization, and have very poor safety records (Zhang et al., 2007).

Table 2: Safety Incidents in Chinese Coal Mines from 2001 – 2010 (Chen and Zhao, 2012).

Coal Mine Ownership	Number of Accidents	%total accidents	%total casualties
Private Enterprise	6911	87.7	90.2
Local government	938	11.9	9.2
State government	35	0.4	0.6

These statistics indicate that state-owned mines account for less than 1% of incidents, with the majority occurring in mines that are privately owned. However, relative values can be misleading and investigating total fatalities shows a significant number occurring at state-owned coal mines. A contributing factor to this is the sheer number of mines, where in 2008 for example, there were 16,000 active Chinese coal mines. However, a telling statistic of how bad times were previously is that in 2001 to 2005 China had on average 6,000+ fatalities annually (MAC 2006).

Recent reports indicate that annual fatalities, which peaked in 2002 at over 7000, have been decreasing with less than 1000 reported in 2014 (Lelyveld, 2015). However, figures show that

China's coal industry is still experiencing severe risks and there is discussion about the validity of reporting by the Chinese government.

China Cuts Coal Mine Deaths, But Count in Doubt.

In a 2006 article for the Jamestown Foundation research organization, energy expert Jianjun Tu argued that official reports understate the real totals, "as mine owners routinely falsify death counts in order to avoid mine closures or fines."

The highest accident category of 30 or more deaths automatically triggers an investigation led by the State Council, or government cabinet, the Hong Kong-based China Labour Bulletin said.

In what may be the worst recent case involving the accident definitions in 2013, a State Council probe found that operators in northeastern Jilin province understated the death toll from a gas explosion to avoid falling into the 30-or-more category.

The Babao Coal Mine Co. reported 28 deaths and 13 injuries from the accident, although the real death toll reached 36 (Lelyveld 2015).

A good example of strong safety at a Chinese coal mine is the Daliuta mine owned by ShenHua Group. The Daliuta mine was the world's largest underground coal mine in 2011 and at the time of reporting the mine had an ongoing record of 7 years of safe production with no fatalities (Daliuta 2011).

The Chinese coal industry faces many challenges with safety, and the high number of accidents and fatalities highlights the need for improvement and transformation. Overall, it seems state-owned mines can have safety performance comparable or superior to mines in the USA, but it is difficult to separate these from the local and private mines.

4. LONGWALL DISASTERS: CASE STUDIES

Sadly, there are numerous cases of underground coal disasters throughout history. It seems to be a repeating cycle. Below are three summaries of root cause investigations.

4.1 Soma Mine Disaster (Turkey)

On May 13, 2014 an electrical malfunction created an explosion and fire in the Soma coal mine in Enez, Turkey. An analysis of the disaster is outlined in the report by Kilic (2014). A fire started in the mine shaft which rapidly depleted oxygen and also created smoke. Smoke was blown into the mine and resulted in 301 miners dying of carbon monoxide poisoning, and 162 others being injured.

Investigations revealed the mine was a "Death Trap" with numerous cases of gross negligence. A

root cause analysis by Kilic (2014) and Ultas (2014) found:

1. There was no refuge chamber in the mine and workers were not provided functioning gas masks.
2. There were faults in the electrical system and many issues found in the weeks prior to the accident.
3. Plans for the electrical layout were not sent to regulators for inspection and approval.
4. The mine's gas sensors had not been inspected
5. The ventilation system did not meet requirements and there wasn't an adequate supply of fresh air or removal of polluted air.
6. Workers were unable to exit the mine because exit routes were being used for production, and because no escape plan had been created.
7. The communication system used in the mine was not suitable for an underground mine.
8. Production was 2.5 times greater than originally planned with more workers were present. However, the ventilation system was not adjusted to provide the increased volumes of clean air required.
9. Employees were not trained adequately before beginning their work.

The Kilic report concluded with "Our group is of the opinion that there were many negligent practices, and that this accident was avoidable."

4.2 Upper Big Branch Disaster (USA)

On April 5th, 2010, the Upper Big Branch Mine in West Virginia exploded and killed 29 miners, making it the worst mining disaster in the US since 1970. As outlined by McAteer et al. (2011) the methane and coal dust explosion is believed to have been ignited by a spark created as a shearer cut into the sandstone roof at the mining face. The shearer was equipped with water sprays designed to douse flames like these at the point of ignition, however, the investigation found that the water sprays were ineffective because they had either been removed or were clogged with dust.

McAteer et al. (2011) determined the root causes to be:

1. Water sprinklers and methane detectors were not properly maintained and failed to extinguish the small ignition that led to the massive explosion.
2. Massey failed to remove accumulated coal dust which allowed the explosion to propagate.
3. The ventilation system did not function adequately, allowing explosive gases to build up well beyond safe levels. Stoppings and seals had been removed that could have controlled the spread of fire, but instead blocked the mines escape route.
4. Many pieces of faulty equipment indicated that maintenance of safety equipment was not a priority. A misaligned conveyor belt allowed coal dust to accumulate at the face and created a huge

hazard.

Massey Energy had a history of incidents prior to this disaster with 25 other workers being killed in Massey mines from 2000 to 2010 (Stickeler, 2012). The unsafe conditions were well known and in 2009 26 citations were issued for coal dust accumulation and for failure to adequately apply rock dust. In the 15 months prior to the incident, the mine received 40 citations with the majority classified as substantial.

Massey received federal indictments and as outlined by Biggers and Nelson 2010, the company entered into guilty pleas for 10 criminal violations of mine safety and agreed to pay \$2.5 million in fines. Also, over 1,300 citations were issued which resulted in another \$1.7 million in civil penalties. In 2015, former Massey Energy CEO Don Blankenship was found criminally guilty for a conspiracy to willfully violate the Mine Safety and Health Act.

4.3 Jiangjiawan Coal Mine Disaster (China)

On April 19, 2015, 24 miners were killed at the Jiangjiawan mine when a shaft flooded (Mkaq, 2015). 247 workers were inside the mine when the accident occurred, of which 223 made it out safely while 3 trapped workers were rescued (Mkaq, 2015).

According to Mkaq, on April 14, water flow increased very suddenly at the mining face but the mine didn't stop production to investigate the hazard. Instead, the mine continued production by installing pumps to drain the water, rather than evacuating workers. On April 19, the flooding accident occurred at the mining face, and 24 miners were killed.

The Mkaq 2015 report determined root causes as:

1. The Mine failed to take effective measures when water flow increased suddenly at the mining face and did not respond to the new risks adequately.
2. Failed to evacuate workers effectively when water flow increased at the mining face.
3. Controlled caving in the gob area created fractures in the rock above the coal seam. The fractures allowed surrounding groundwater to flood into the working area very rapidly.
4. Detailed exploration was not conducted prior to mining, which caused the accumulated water above the active mining face to go undetected until its inflow.

5. IS COAL MINING WORTH THE RISKS?

It is clear that there are risks associated with longwall coal mining and past disasters can be heeded as warnings to its dangers. However, there are many cases of successful longwall operations and with proper planning these mines can be successful.

In the case studies outlined in this paper all of the disasters were preceded by cases of negligence. In

hindsight it is easy to identify the root causes, but tragically the problems did not receive the necessary attention, and focuses of production and profitability surpassed safety and sustainability.

Current and future coal mines are greatly affected by each disaster and it raises the question "are coal mines, particularly underground coal mines, worth the risk?" The global shift towards renewable and clean energy, along with increasing focuses on environmental and social stewardship has impacted all fossil fuel projects and it is challenging to generate positive attitudes and excitement about projects.

Coal's decline is perhaps best illustrated by the Dow Jones U.S. Coal Index, which has decreased more than 95% from 2011 to 2016 (Finance, 2016). Clearly times are tough, and a fundamental shift seems to be occurring with alternative energy looking to replace fossil fuels.

6. GLOBAL SHIFT FROM FOSSIL FUELS

In November 2015 the government of Alberta announced that by 2030 they plan to close all 18 of the coal-fired power plants that generate around 55% of the province's electricity, with two-thirds of that power replaced by renewable sources (Wilt, 2015).

Alberta's decision follows a trend of moving away from coal, which is highlighted by comments made by the Environmental Protection Agency (EPA) administrator Gina McCarthy. "We know in the U.S. that we are transitioning away from coal because coal is no longer marketable. We have cleaner natural gas, and we have opportunities for low-carbon sources like renewables and using energy efficiency to lower energy demand." (Henry 2015)

The UK has also pledged to close all 12 of its coal power plants by 2025, and research by Levey (2015) found that "to achieve the international goal of limiting global warming to less than 2°C above pre-industrial revolution averages, the least expensive way of doing so is to close a significant number of coal power stations by 2030". Also, the Levey research shows that some of the lowest cost scenarios involve eliminating coal power by 2030, even if that means shutting down generators earlier than planned.

However, demand in Asia still makes coal mining feasible and using safe and sustainable methods is paramount for coal to be an option. The New York Times reported in 2015 that China has underreported its use of coal. "China Burns Much More Coal than Reported, Complicating Climate Talks" said Lin Boqiang, a Research Director at Xiamen University (Smith, 2015). While in India a senior government official explained "Paris climate deal won't affect plans to double coal output," and

that India still plans to double coal output by 2020 because no alternatives are available (Wilkes and Das, 2015).

Coal reserves in Asia are slowly depleting and more remote deposits are being mined with advanced technology. With North American mines shipping coal to Asia, a global connection is already in place. This promotes coal's development in North America even if there is no local market. Demand in Asia can be expected to continue because of the high costs of alternatives, and the infrastructure already established in North America facilitates opportunities for Asian companies to extract coal from overseas.

Ontario phased out coal fired power plants in 2014. The transition's costs and challenges are explained in the report by Cundiff (2015). The cost for Ontario to transition to alternative energy was estimated at \$9.2 Billion. These prices were relatively high, as much as 3.5 times for solar and 2.0 times for wind compared to the US average, because infrastructure was not already established and private power generators with higher prices were relied upon. These high costs were rebuked by presenting cost savings through less pollution, including savings of over \$1 Billion in Health Care and improved productivity. Savings of \$10 Billion were estimated when accounting for loss of life, pain, and suffering.

However, it seems Asia will be coal dependent until prices for alternatives become more competitive. The transition away could be initiated by prices increasing through depleted reserves, higher extraction costs, or relying on imports, however, because many places are phasing out coal, and sustained low prices indicate an oversupply, it seems that Asia's transition away could be driven by environmental stewardship.

Pollution has been a major problem in China and though costs are accounted differently in each country, if Ontario was able to show that up to \$10 Billion could potentially be saved annually by eliminating coal power plants, China could be able to show exponentially higher savings because its population is roughly 100 times greater than Ontario's and its pollution levels are much more severe.

7. LOOKING AHEAD: FOCUSING ON SAFETY AND SUSTAINABILITY

Longwall coal mining is common in China and applying the method to deposits in more places seems like a natural progression. However, the current coal mining industry faces risks with regards to safety, sustainability, and economics, and aligning a coal project within a larger framework of long-term growth and development can be challenging.

An operating coal mine can stimulate an economy locally and regionally by providing many high paying jobs and numerous opportunities for indirect employment. Once a longwall coal mine is established its operating costs are relatively low and it is more capable of staying cash positive during a downturn compared to other methods, and this is very advantageous for long term stability and overall sustainability. Advances in clean coal technology also provide the opportunity to increase efficiency and reduce pollution, particularly in regions that do not have access to viable alternative energy sources.

Alternatively, there are many risks associated with longwall coal mines and it is critical to identify the contributions and impacts a project may have. The risk of a mining disaster is always present, and even though safety practices have advanced the industry has a long and sad history of disasters. Statistically, coal mines have injury and fatality rates approximately 50% higher than metal and non-metal mines, and the increased risks need to be considered (MSHA, 2015). The increased risk could potentially be offset with comprehensive safety programs, and the costs funded through the lower operating costs and increased margins. There are also environmental risks, such as pollution, waste, subsidence, and impacting water resources, which can greatly affect the local region, while extracting fossil fuels impacts pollution levels and global warming. Understanding these risks is critical before developing a project, along with identifying and reviewing project specific risks.

There are many opportunities and benefits of having a mine operating, particularly when the coal mining industry has been struggling, but concerns over safety, local and regional participation in the project, and long-term viability remain. Finding a balance is key and keeping safety at the forefront is critical if coal mines are going to be successful in future.

8. REFERENCES:

Askci (2013). Askci.com. "Top 10 Coal Producing Countries Of 2012" askci.com/news/201307/13/131061494532.shtml

Biggers and Nelson (2010). "Massey Energy Mine Cited For 1,300+ Safety Violations". http://www.democracynow.org/2010/4/7/massey_energy_mine_cited_for_1

Bloomberg (2015). "China To Halt New Coal Mine Approvals Amid Pollution Fight" <http://www.bloomberg.com/news/articles/2015-12-30/china-to-suspend-new-coal-mine-approvals-amid-pollution-fight>

CBC (2015). "As Coal Jobs Disappear, U.S. Mine Fatalities At Record Low" cbc.ca/news/business/coal-mine-deaths-1.3382981

Chen and Zhao (2012). Statistical analysis and inspiration of coal mine accidents over the past decade [J]. *Coal Engineering*, 2012, 44(3): 137-139.

Cryderman (2015). "How The Collapse Of Coal Is Hitting Home In Western Canada" *The Globe and Mail*. <http://www.theglobeandmail.com/report-on-business/industry-news/energy-and-resources/how-the-collapse-of-coal-is-hitting-home-in-westerncanada/article27731329/>

Cundiff (2015) "Ontario's Coal Phase Out: Lessons learned from a massive climate achievement," Ontario Clean Air Alliance Research <http://www.cleanairalliance.org/support-a-clean-energy-future/ontarios-coal-phase-out/>

Daliuta (2011) Daliuta Mine-Baidu Encyclopedia http://baike.baidu.com/link?url=yIfUyva_wENoQytWOvpH1IDiHfCZYogcNPZyHfZ5ueB_cxMtHuP3jYiTD0JHNpZ70ATIDz9WHwjYDf7yfvJAK

Finance (2016). Google Finance: http://www.google.com/finance?q=INDEXDIX%3ADJUSCL&ei=bx41V_C_JI2amAGC3rOAAQ

Henry (2015). "EPA Chief: Coal 'No Longer Marketable'". *The Hill*. <http://thehill.com/policy/energy-environment/262776-epa-chief-coal-not-in-uss-future>

Kilic (2014), Expert report: Gross negligence led to Soma mine disaster. todayszaman.com/anasayfa_expert-report-gross-negligence-led-to-soma-mine-disaster_359378.html

Lelyveld (2015) "China Cuts Coal Mine Deaths, But Count In Doubt". *Radio Free Asia*. http://www.rfa.org/english/commentaries/energy_wat/ch/china-coal-deaths-03162015103452.html

Levey (2015). "Phasing Out Coal Power Makes Economic Sense, Says Analysis of Global Future" www3.imperial.ac.uk/newsandeventspggrp/imperialcollege/newssummary/news_7-12-2015-16-25-54

MAC (2006), Minesandcommunities.org "China and US Coal Disasters" www.minesandcommunities.org/article.php?a=1155

McAteer et al. (2011). Upper big branch: The April 5, 2010, explosion: A failure of basic coal mine safety practices. <http://www.nttc.edu/ubb/>

Mkaq (2015). "Analysis with The Coal Mine Flooding Accident Cases - Jiangjialiang". N.p., 2016. <http://www.mkaq.org/html/2015/08/27/322542.shtml>

MSHA (2015). [Arlweb.msha.gov](http://arlweb.msha.gov). "Mine Safety and Health at A Glance. MSHA". <http://arlweb.msha.gov/MSHAINFO/FactSheets/MSHAFCT10.asp>

Saunders (2015) "Anglo American Fire Sale To Reshape Global Coal Industry". *Financial Review*. [http://www.afr.com/business/mining/coal/anglo-](http://www.afr.com/business/mining/coal/anglo-american-restructure-to-reshape-global-coal-industry-20151209-glj8f7)

[american-restructure-to-reshape-global-coal-industry-20151209-glj8f7](http://www.afr.com/business/mining/coal/anglo-american-restructure-to-reshape-global-coal-industry-20151209-glj8f7)

Smith (2015). *The National Law Review*. "Perspectives on COP21 and Future Coal Production" www.natlawreview.com/article/perspectives-cop21-and-future-coal-production#sthash.jyu0eHMF.dpuf

Stickeler (2012). *USF Scholarcommons*. <http://scholarcommons.usf.edu/cgi/viewcontent.cgi?article=5427&context=etd>

Ultas (2014), *Soma Mine Disaster and the Reality of Privatization*. (EMO) <http://researchturkey.org/soma-mine-disaster-and-the-reality-of-privatization/>

Wilkes and Das (2015). India says Paris climate deal won't affect plans to double coal output <http://www.reuters.com/article/us-climatechange-summit-india-coal-idUSKBN0TX15F20151214>

Wilt (2015). *The Nitty Gritty on Alberta's Coal Phase-Out*. *Desmog Canada*. November 26, 2015 <http://www.desmog.ca/2015/11/26/nitty-gritty-alberta-s-coal-phase-out>

Xi (2015) *Sustainalytics.com* "Coal In China: A Sunset Business" www.sustainalytics.com/coal-china-suset-business

Zhang et al. (2007), Comparison of the geological conditions of the major coal-producing country in the world [J]. *Coal geology and exploration*, 2007, 35(6):1-9.

Research on Safety Incentive Model of Coal Miners and Strategy Analysis

Cao Qinggui^a, Xie Changzhen^{a,*}, Zhang Shouming^{a,b}, Zhang Sai^a, Liu Weihua^a

a Department of Mining and Safety Engineering, Shandong University of Science and Technology, Qingdao, China, 266590

b Zibo Mining Group Co., Ltd., Zibo, China, 255120

ABSTRACT

Based on the safety incentive theory and safety incentive mode, the system dynamics model of safety incentive for coal miners is established, and the simulation of the model is provided. The research shows that the effect of improving reward measure and environmental conditions are the most significant. According to the influence to the safety incentives, other measures are in the following order: technical equipment, safety culture, enterprise goals and punishments. The safety incentive strategy of coal miners is put forward with the simulation results.

Keywords: Safety, Behavior, Incentive, Miners, System dynamics, Simulation, Strategy.

1. INTRODUCTION

A large number of statistics shows that more than 80% of coal mine accidents are related to workers' unsafe behaviors (Chen Hong, Song Xuefeng, 2006). Workers' unsafe behaviors are caused by many factors, such as psychology, physiology, environmental, etc. According to the related theories of organizational behavior, people's behavior is dominated by the motivation. Moreover, people's inner desire and motivation is inspired by incentive. So the research of incentive can help us find the effective way to guide the safety behavior of workers.

Since 1920s, many experts and scholars in the world have made researches on the incentive, and put forward different theories of incentive. Generally, these theories are divided into three categories (Shi Jutao et al., 2003; Li Jizu, 2009): Content-based Motivation Theory (e.g. Hierarchy of Needs Theory, ERG Theory, Two-factor Theory), Behavior Transforming Incentive Theory. (e.g., Frustration Theory, Attribution Theory) and Process Incentive Theory (e.g. Equity Theory, Expectation Theory, Goal-Setting Theory).

Many Chinese experts and scholars have also studied the safety incentive. Li Hongxia (2001) studied the safety incentive system, and put forward three types of safety incentive methods: Educational effect, Economic effect and Power effect. On the basis of motivation theory, Huang Mingxia (2006) described the incentive methods in safety management, such as work incentive, achievement incentive, criticism and encouragement incentive, training and education incentive. Mao Xiaoxin (2013) put forward the positive incentive scheme of safety

behavior, and it was discussed from material incentive and spiritual incentive. Liu Haibin et al. (2015) established the incentive mechanism of coal mine safety production based on the research of unsafe behavior. Combining with three types of incentive theory (Content-based Motivation Theory, Behavior Transforming Incentive Theory and Process Incentive Theory), Zhang Lili (2008) put forward the incentive mechanism of safety production management. Liu Ying and Shi Shiliang (2009) constructed the coal mine safety behavior incentive system.

The studies of the safety incentive is on theoretical level, and some are still in the period of experience. There are few studies on specific employee safety incentive mode. Moreover, there are few quantitative analysis of employees' behavior and psychology. In view of this, based on the theory and method of system dynamics, the incentive model of coal miners safety behavior is researched, and to seek the strategies and effective ways to control the unsafe behaviors of coal miners.

2. SAFETY INCENTIVES AND SAFETY BEHAVIOR IMPROVEMENT

Safety incentive refers to inspiring people in the system reasonably, and guiding and controlling the behavior of people to make sure that their behavior meets the safety standard (rules), with the integrated use of management, economics and other modern scientific principles and methods. The aim of safety incentive is to prevent system from accidents and disasters, and to ensure that system is at an acceptable safety level. It ensures not only the individual safety but also the safety of the

*Corresponding author – email: changzhenxie@hotmail.com

organization (enterprises), environment and society (Liu Ying and Shi Shiliang, 2009).

In the process of development enterprise should guide the employees' behavior by incentive method. According to the source of need, the incentive method can be divided into material incentive and spiritual incentive (Liu Haibin et al., 2015). The former refers to the bonus, salary, welfare and other material incentives while the latter refers to the corporate goals, leadership, interpersonal relationships, group cohesion, job satisfaction, etc.

At present, coal miners' safety awareness is improved by material incentive factors such as rewards, compensation and punishment. These incentives may have a good effect in a short time, but the enthusiasm of the workers will be changed alongside the disappearance of the reward or punishment. So the enthusiasm of the workers cannot be sustained. In addition, it is difficult for coal mining enterprises to make appropriate safety incentive measures to reduce the unsafe behavior of employees, so as to achieve the proleptic incentive effect. Therefore, in this paper, the safety incentive mode of coal miners is studied by the system dynamics simulation.

3. SD SIMULATION OF SAFETY INCENTIVE MODE

System dynamics (SD) is a science that scientific theory of system science and computer simulation are integrated to study system feedback structure and behavior. It is used to study and deal with complex system problems by qualitative analysis and quantitative analysis (Zhong Yongguang et al., 2012). The commonly used system dynamics software are STELLA/iThink, Vensim, Powersim, Anylogic, etc. Vensim is the most widely used among them. In this paper, Vensim will be used for the research.

3.1 Establishment of the stock flow chart of safety incentive mode

According to the actual situation of coal mine safety management, the safety incentive model of coal miners is analyzed and established. The stock and flow chart of safety incentive model of coal miners is established with "Safety performance level" as the measure of safety incentive effect (As is shown in Figure 1).

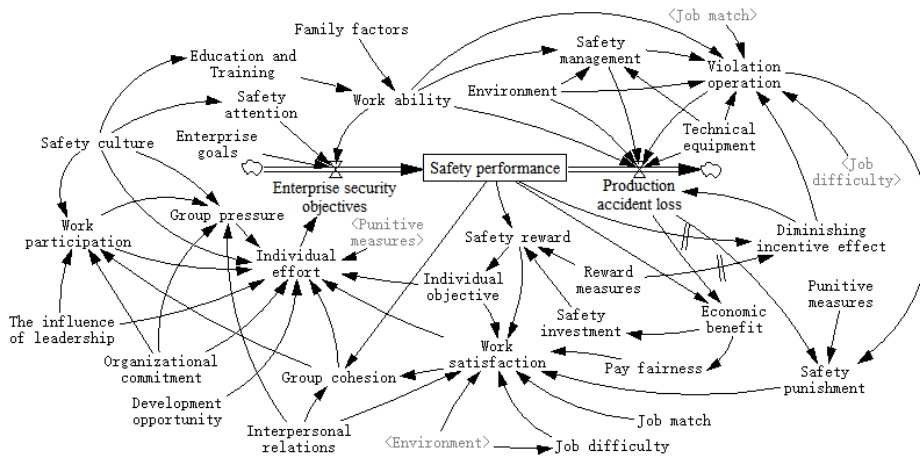


Fig.1: Stock and flow diagram of coal miners' safety incentive model

Table 1 Set of SD simulation variable

Variable type	Number	Variable name
Level Variables	1	Safety performance
Rate Variables	2	Enterprise security objectives, Production accident loss
Auxiliary Variables	18	Work participation, Job difficulty, Individual effort, Group cohesion, Group pressure, Individual objective, Safety work satisfaction, Safety reward, Safety investment, Pay fairness, Safety punishment, Economic benefit, Violation operation, Safety management, Work ability, Education and Training, Diminishing incentive effect(Zheng Guoduo. 2005), Safety attention
Constant	12	Family factors, environment, Technical equipment, Safety culture, The influence of leadership, Organizational commitment, Development opportunity, Job match, Interpersonal relations, Reward measures, Punitive measures, Enterprise goals

The mode includes level variables, rate variables, auxiliary variables and constants (Zhong Yongguang et al., 2012) (As is shown in Table 1). The constant in Table 1 is the standard or the desired goal which is set by the system, and the initial value is determined by the author and the coal mine enterprise experts.

3.2 Determination of parameters of SD model

The determination of the parameters in the SD mode is mainly about the weight coefficient of the independent variable to the dependent variable. In this paper, the parameters are determined by AHP and expert estimation (Tian Shuicheng et al., 2014; Wu Liping, 2006; Wang Lianfen, Xu Shubai, 1990).

Due to space reasons, take safe working satisfaction and its related variable, for example, to introduce the determination of weight coefficient. The variables related to safety job satisfaction(L) are: individual objective (a_1), interpersonal relations (a_2), safety punishment (a_3), safety reward (a_4), job match (a_5), job difficulty (a_6), environmental (a_7) and pay fairness (a_8), so the set of variables is: $U=\{a_1, a_2, a_3, a_4, a_5, a_6, a_7, a_8\}$. Three engineers who engaged in safety supervision in coal mine enterprises were invited to discuss with the author. So the judgment matrix is established by expert evaluation and the scaling method of 1-9 Grade(Wu Liping, 2006). It is:

$$A = \begin{bmatrix} 1 & 4 & \frac{1}{3} & \frac{1}{5} & 5 & 3 & \frac{1}{7} & \frac{1}{7} \\ \frac{1}{4} & 1 & \frac{1}{5} & \frac{1}{7} & \frac{1}{2} & \frac{1}{3} & \frac{1}{7} & \frac{1}{8} \\ 3 & 5 & 1 & \frac{1}{3} & 5 & 3 & \frac{1}{2} & \frac{1}{4} \\ 5 & 7 & 3 & 1 & 5 & 4 & \frac{1}{2} & \frac{1}{3} \\ \frac{1}{5} & 2 & \frac{1}{5} & \frac{1}{5} & 1 & \frac{1}{2} & \frac{1}{6} & \frac{1}{7} \\ \frac{1}{3} & 3 & \frac{1}{3} & \frac{1}{4} & 2 & 1 & \frac{1}{5} & \frac{1}{6} \\ 7 & 7 & 2 & 2 & 6 & 5 & 1 & \frac{1}{2} \\ 7 & 8 & 4 & 3 & 7 & 6 & 2 & 1 \end{bmatrix};$$

In the study, the consistency test and sensitivity analysis of the judgment matrix A are made. Result shows that the maximum eigenvalue of the matrix is: $\lambda_{\max}(A) = 8.6486$, and the eigenvectors is: $W_A = [0.145, 0.047, 0.238, 0.385, 0.063, 0.093, 0.500, 0.717]^T$. The consistency index is: $CI = 0.09266$, $CR = 0.06571$; Both CI and CR are less than 0.1, so the consistency passed test.

The weights are calculated by the AHP: $W = \{0.073, 0.023, 0.111, 0.172, 0.032, 0.047, 0.22, 0.323\}$.

Given judgment matrix A with a small perturbations, the perturbation matrix is B.

$$B = \begin{bmatrix} 1 & 1 & \frac{2}{3} & 1 & 1 & 1 & 1 & 1 \\ 1 & 1 & 1 & 1 & \frac{4}{5} & \frac{2}{3} & 1 & 1 \\ \frac{3}{2} & 1 & 1 & 1 & 1 & 1 & 1 & 1 \\ 1 & 1 & 1 & 1 & 1 & 1 & \frac{2}{3} & 1 \\ 1 & \frac{5}{4} & 1 & 1 & 1 & \frac{3}{4} & 1 & 1 \\ 1 & \frac{3}{2} & 1 & 1 & \frac{3}{4} & 1 & 1 & 1 \\ 1 & 1 & 1 & \frac{3}{2} & 1 & 1 & 1 & 1 \\ 1 & 1 & 1 & 1 & 1 & 1 & 1 & 1 \end{bmatrix}$$

The matrix C is a Hadamard product of A and B. (Wang Lianfen, Xu Shubai, 1990)

$$C = \begin{bmatrix} 1 & 2 & \frac{2}{9} & \frac{1}{5} & 5 & 3 & \frac{1}{7} & \frac{1}{7} \\ \frac{1}{4} & 1 & \frac{1}{5} & \frac{1}{7} & \frac{2}{5} & \frac{2}{9} & \frac{1}{7} & \frac{1}{8} \\ \frac{9}{2} & 5 & 1 & \frac{1}{3} & 5 & 3 & \frac{1}{2} & \frac{1}{4} \\ 5 & 7 & 3 & 1 & 5 & 4 & \frac{1}{3} & \frac{1}{3} \\ \frac{1}{5} & \frac{5}{2} & \frac{1}{5} & \frac{1}{5} & 1 & \frac{3}{8} & \frac{1}{6} & \frac{1}{7} \\ \frac{1}{3} & \frac{9}{2} & \frac{1}{3} & \frac{1}{4} & \frac{3}{2} & 1 & 2 & \frac{1}{6} \\ 7 & 7 & 2 & 3 & 6 & 5 & 1 & \frac{1}{2} \\ 7 & 8 & 4 & 3 & 7 & 6 & 2 & 1 \end{bmatrix}$$

Result shows that the maximum eigenvalue of matrix C is: $\lambda_{\max}(C) = 8.810$. and the eigenvectors is: $W_C = [0.138, 0.044, 0.255, 0.366, 0.062, 0.094, 0.523, 0.703]^T$. Compared with the maximum eigenvalue and eigenvector of matrix A, the change is small. The weight set of matrix C is: $W' = \{0.063, 0.020, 0.117, 0.168, 0.028, 0.043, 0.239, 0.322\}$. Compared with the weight set of A, the ranking of each factor does not change, and the numerical difference is very small. According to the above algorithm, given A with different small perturbations, and the results are stable. So, it is considered that the sensitivity of the judgment matrix A is within the acceptable range.

Therefore, the weight set obtained from the judgment matrix A is reasonable. So the relation on safe working satisfaction is:

$$L = 0.073a_1 + 0.023a_2 + 0.111a_3 + 0.172a_4 + 0.032a_5 + 0.047a_6 + 0.22a_7 + 0.323a_8$$

3.3 SD simulation and result analysis

After the parameters of the SD model are determined, Vensim is used to simulate the model on the basis of the stock and flow chart. The simulation period is set to 72 months, the simulation step is set to 1 month, and the initial value of safety performance is set to 10, so as to analyze the long-term trend of safety incentive effect in 6 years.

The main positive feedback loop in the model is: Safety performance→Safety reward→ Individual objective→ Safety work satisfaction → Individual effort → Enterprise security objectives → Safety performance. The main exogenous variables that affect the positive feedback loop are: Enterprise goals, Safety culture, Environment, Reward measures, and Punitive measures. The main negative feedback loop is: Safety performance→ Diminishing incentive effect→ Production accident loss→ Safety performance. The main exogenous variables that affect the negative feedback loop are: Environment Reward measures and Technical equipment. In addition to the simulation of the original model, the effect of exogenous variables on safety performance is studied by changing the initial value of 6

exogenous variables in turn, and the 6 exogenous include these: Enterprise goals, Safety culture, Environmental conditions, Reward measures, Punitive measures and Technical equipment. The simulation is divided into 3 groups

In the first group of simulation, the research obtained the level of safety performance through the SD simulation by increasing the initial value of one of the exogenous variables 1 units, and the initial value of the other exogenous variable remain unchanged. The second group and third group were increased separately by 2 units and 3 units. Comparing the simulation results of the three groups, it is found that the trends of the safety performance are the same. Table 2 shows the average value of safety performance of 72 months.

Table 2: Average value of the safety performance

	Original model	Reward measures	Technical equipment	Environment	Safety culture	Enterprise goals	Punitive measures
First group	49.708	55.365	53.510	55.339	52.764	51.784	49.957
Second group	49.708	62.764	57.311	60.709	55.819	53.860	50.205
Third group	49.708	72.732	61.112	66.601	58.875	55.936	50.454

Second group of simulation was selected for further analysis. The simulation results of the second groups are shown in Table 3, and the change trend of safety performance can be see from Figure 2.

The simulation results of the original model can be seen from Figure 2 and Table 3. The safety performance increased gradually from start to 30th month, it shows that the positive feedback loop plays a leading role in the model, that is, the safety incentive factors in the model play an incentive role

and lead to the growth of enterprise security objectives, which promote the level of safety performance. It reaches the minimum value at 54th month, and then it shows an upward trend to 72th month, but it does not reach the maximum value in 30th months. It shows that the negative feedback loop plays a leading role, that is, the incentive effect of safety incentive is weakened in the model and the loss of production accidents increases, which leads to the decrease of safety performance level.

Table 3: SD results of simulation

Time (month)	0	6	12	18	24	30	36	42	48	54	60	66	72
Original model	10.000	25.321	37.700	49.281	57.518	72.888	55.466	60.588	54.567	35.770	45.541	64.555	71.866
Reward measures	10.000	25.742	40.331	56.215	69.295	94.040	73.439	81.781	74.742	44.477	57.134	85.282	100.014
Technical equipment	10.000	28.324	43.044	56.445	66.068	83.595	64.156	70.102	63.357	42.068	53.208	74.866	83.199
Environment	10.000	29.762	45.612	59.937	70.250	88.910	68.341	74.702	67.557	44.935	56.794	79.845	88.717
Safety culture	10.000	27.706	41.979	55.186	64.615	82.040	62.457	68.305	61.527	40.274	51.350	72.898	81.185
Enterprise goals	10.000	26.918	40.593	53.412	62.523	79.552	60.221	65.889	59.210	38.374	49.199	70.268	78.369
Punitive measures	10.000	25.512	38.046	49.776	58.117	73.686	56.036	61.223	55.123	36.082	45.979	65.239	72.645

It can be known from Figure 2, Table 2 and Table 3 that, with the initial value of the reward measures increases, the safety performance level increased significantly. It shows that the reward

measures are most sensitivities. The safety performance level increases the smallest after increasing the initial value of the punishment measure, and it shows that the punishment measure is

the least sensitive. The safety performance also increases after increasing initial value of the enterprise goals, safety culture, environment and technical equipment. It shows that these incentives can effectively improved safety behavior of coal miners. So the safety incentive effect of variables can be obtained by SD simulation. The sequence according to the effect of the incentive factors is as follows : reward measures, environment , technical equipment, safety culture, enterprise goals and punishment measure.

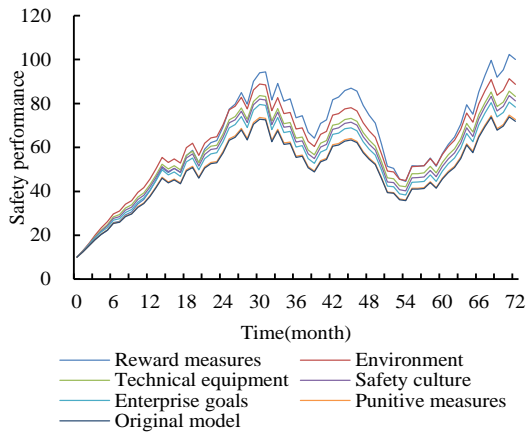


Fig. 2: Trend of simulation result

As it mentioned above, the judgment matrix A passed the sensitivity analysis, and the result is relatively stable after a small perturbation. Accordingly, simulation is made by reducing the weight of compensation rationality, and remaining the ranking of the weight coefficient, the simulation result is shown in Figure 3.

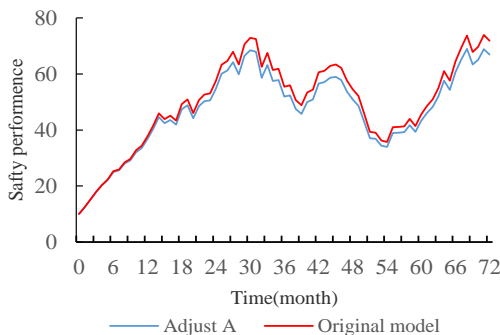


Fig. 3: The simulation results after adjusting weights

It can be seen that the trend of simulation result does not change too much. According to the same method, the simulations are provided after adjusting

other variables, and the trend of simulation result also does not change too much. It shows that the model is stable and the parameters are quite reasonable, and the conclusion is reasonable and credible.

4. SAFETY INCENTIVE STRATEGY OF COAL MINE WORKERS

According to the SD simulation results, the following strategies are put forward to inspire coal miners and to promote their safety behavior

1) To combine material incentive with spiritual incentive. SD simulation results show that reward and other material incentive measures, safety culture, development opportunities, enterprise goals and other spirit incentives can improve the safety performance of enterprises. Therefore, it should be taken to create a good development opportunities for the miners and other measures should be taken to enhance the level of spiritual motivation, and to promote miners safety behavior effectively with the help of the material incentives.

2) To establish a fair and reasonable system of rewards and punishments. Simulation results show that the reward measures to improve the safety performance is the most sensitive, and its incentive effect is more significant than that of punishment measures. Therefore, coal mining enterprises should implement positive reinforcement in the safety management, be cautious to use negative reinforcement, and establish a fair system of rewards and punishments. To give reasonable rewards and punishments to miners

3) To improve coal mine's environment and technical equipment. The simulation result shows that, in the early stage, improving environment can lead to the fastest growing safety performance, technical equipmen also works out. Therefore, coal mining enterprises should improve the environmental and technical equipment of coal mines, so that miners have a safe and comfortable working environment, and miners' enthusiasm for production safety can be improved.

4) To establish a harmonious and effective enterprise safety culture. Enterprise safety culture can make all employees operate voluntarily, avoiding unsafe behaviors. It is initiative technical measure in the enterprise security management, and it should be vigorously promoted in the coal mine enterprise.

5) To establish a reasonable enterprise security objectives. Coal mining enterprises should consider the employee's individual needs, completing ability and enterprise's actual situation , etc, develop a clear and reasonable security goals, and guide the miners complete the security objectives voluntarily and actively

6) Strengthening the pertinence of safety incentive. Because of different characteristics of coal coal enterprises and each employee, safety incentive should be targeted, and different incentive measures should be taken according to different production systems or post, so as to guide the safety behavior of miners.

5. CONCLUSIONS

1) The system dynamics model of safety incentive system for coal miners is established, which can be used to simulate and analyze the safety incentive effectively.

2) SD simulation results of safety incentive model for coal miners show that the effect of reward measures and environment is the most significant. According to the influence to the safety incentives, other measures are in the following order: technical equipment, safety culture, enterprise goals and punishments.

3) The safety incentive strategy for coal miners is put forward, which can provide reference for the establishment of safety incentive system and safety management of coal mining enterprises.

6. ACKNOWLEDGEMENT

The authors acknowledge the National Natural Science Foundation for supporting reach. Thanks the doctoral students Zhou Lujie and Wang Linlin for providing advice and help in modeling.

7. REFERENCES

- Chen Hong, Song Xuefeng. (2006) Study on unsafe behavior of major accidents in China Coal Mine. Science Press, Beijing, pp. 27-29.
- Huang Mingxia. (2006) Motivation in safety management. Journal of Safety and Environment. Volume 06, pp. 57-59.
- Li Jizu. (2009) Safety behavior. Machinery Industry Press, Beijing, pp. 117-133.
- Liu Haibin, Wang Qingqing, Huang Hui. (2015) Based on the incentive mechanism for safety production of coal mine employees unsafe ACTS//.Proceedings of the second International Conference on safety and security management. Beijing, China: 4p.
- Li Hongxia. (2001) Analysis of safety incentive mechanism .Mining Safety and Environmental protection. Volume 03, pp.8-9.
- Liu Ying, Shi Shiliang. (2009) Study on behavior incentive mechanism of coal mine accident prevention. China Safety Science Journal. Volume 02, pp. 85-91.
- Mao Xiaoxin. (2013) The study and scheme design Safety behavior positive incentive scheme design. Capital University of Economics and Business, pp. 38-39.
- Shi Jutao et al..(2015) Organizational behavior. Petroleum Industry Press, Beijing, pp 74-75.
- Tian Shuicheng, Li Guangli, Li Tingjun,et al.(2014) Simulation on Miners' Unsafe Behavior Intervention Model Based on SD. Safety in Coal Mines, Volume 08, pp. 245-248.
- Wu Liping. (2006) The Study on Fuzzy Comprehensive Evaluation and its application. Taiyuan University of Technology, pp.33-39.
- Wang Lianfen, Xu Shubai (1990) Introduction of Analytical Hierarchy Process, China Renmin University Press, Beijing, pp 114-148
- Zhang Lili. (2008) Study on incentive mechanism of safety production management. Jiangxi University of Science and Technology, pp. 42-43.
- Zheng Guoduo. (2005) Theory of enterprise incentive. Economic and Management Press, Beijing, pp. 59-87.
- Zhong Yongguang, Jia Xiaojing, Li Xu. (2012) System dynamics. Science Press, Beijing, pp. 3-9.

A new Virtual Reality training system for underground coal mines

Hui Zhang^{a,c,*}, Xueqiu He^{a,b}, Baisheng Nie^a, Hani Mitri^{c,d}

^a Faculty of Resource and Safety Engineering, China University of Mining and Technology (Beijing), Beijing, China, 100083

^b Faculty of Civil and Environmental Engineering, University of Science and Technology Beijing, Beijing, China, 100083

^c Department of Mining and Material Engineering, McGill University, Montreal, Canada, H3A 0E8

^d Faculty of Civil Engineering, Henan Polytechnic University, Jiaozuo, China, 454000

ABSTRACT

Virtual Reality (VR) technology in mining is a new field of research. The successful application of VR to mining is critical to mine safety and production. Based on different input/output devices that are used in the VR system, the current VR mining system can be divided into three types: screen-based general system, projector-based customized system, and Head Mount Display (HMD)-based intuitive system. Based on a VR headset, a smartphone and a Leap Motion, an HMD-based intuitive VR training system was built and tested by 10 students who tried both the HMD-based system and a normal screen-based system to experience the difference between the two systems. The results showed that the HMD-based system can give a better user experience, and is easier to use. In the future, with the employment of more intuitive input devices and improved system software, the VR training system for mines could play a much more important role in mine training.

KEYWORDS: Virtual Reality; training; Head Mounted Display; tracker; immersion; intuitive

1. INTRODUCTION

Virtual Reality (VR) technology is based on computer graphics, and can build a virtual scene, which could be interacted by users through input devices, and seen, heard, touched, even smelt through output devices (Mazuryk and Gervautz, 1996; Burdea and Coiffet, 2003; Zhao, 2009). With a well-designed virtual reality system, people can feel almost like they are in the real world. Burdea and Coiffet (Burdea and Coiffet, 2003) raised the three I's conception – imagination, immersion, and interaction – of VR.

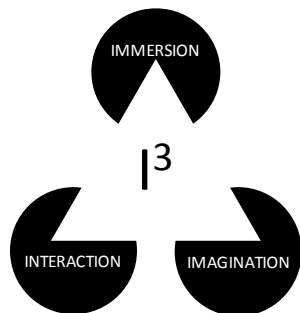


Figure 1: The three I's of virtual reality (Burdea and Coiffet, 2003).

VR is used in many fields, such as military, aerospace, medical, entertainments, etc. After decades of developments, a lot of theoretical and practical experiences have been suggested. Stone (2012) raised some basic rules and principles for developing serious games of military; Burdea and

Coiffet (2003) and Stone (2012) discussed the importance of considering the factors of users. Others (Bertram and Moskaliuk et al., 2015) have studied the effectiveness evaluation of VR training systems. Though VR has been studied for several decades, there are still many things need to be studied in the future, especially with the rapid development of the input and output devices in recent years. Nowadays, there are many kinds of Head Mounted Display (HMD) devices on the market, such as the separated devices – Oculus Rift, HTC Vive, etc., or the VR headset plus smartphone solutions.

In many mining countries such as Australia, the U.S., Canada, South Africa, the U.K., and China, many researchers in the past two decades have been studying the possibility of using virtual reality (VR) as a tool for operator's training (Bukowski and Sequin, 1997; Squelch, 2001; Kizil, 2003; Foster and Burton, 2004; Tichon and Burgess-Limerick, 2011). Dozens of prototypes have been developed and some of them have become popular products (ThoroughTec, 2010; CAE-Mining, 2012; QinetiQ, 2012). The current popular mature VR mine training systems are mainly composed of a multi/curved screen projector, which could provide some immersion to the trainees, and customized operation platform.

Just like other VR systems, the VR mine training system also contains 5 components: input/output (I/O) Devices, VR Engine, User, Task, and Software & Databases (Figure 2).

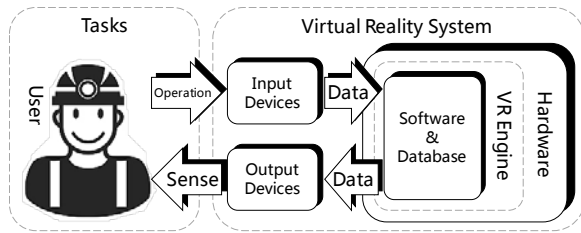


Figure 2: Components of VR system, adapted from (Burdea and Coiffet, 2003).

2. INPUT AND OUTPUT DEVICES

Among the 5 components in the VR mine training system, the I/O devices are critical as they are the exclusive way through which users can interact with and sense the virtual. As a result, all the available I/O devices for the VR systems are summarized in this paper.

2.1 Input devices

Based on previous studies (Mazuryk and Gervautz, 1996; Burdea and Coiffet, 2003; Mihelj and Novak et al., 2014), the common input devices can be classified into two types: physical input devices and automatic track devices, as shown in Table 1. It can be seen that all the automatic track devices are more intuitive and easy to use, while the general type of physical devices such as keyboard and joystick are less intuitive and more difficult to use.

Table 1: Summary of VR input devices.

Category	Type	Devices	Intuitive Level	Difficulty level
Physical	General	Keyboard, joysticks, etc.	Low	Medium/High
	Customized	Customized operational platform	Medium/High	Low/Medium
Automatic	Body tracing	Camera, IR sensor, depth camera, etc.	High	Low
	Movement capturing	Data gloves, gyroscope, etc.	High	Low
	Voice control	Microphone	High	Low

2.2 Output devices

A VR mine training system must have output devices so that the users can “sense” the virtual world. According to Mazuryk et al. (1996) and Kizil et al. (2001), visual sense and auditory sense only take charge of 70% and 20% respectively of the total sensing for human beings, and other three kind senses – tactility, olfaction, and taste sense – only take the remaining 10%. As a result, visual sense is the most important one for users of the VR system.

Based on previous studies (Milgram and Kishino, 1994; Stothard and Squelch et al., 2015), the common visual output devices can be classified as screens, projectors, Head Mounted Displays (HMD), and holographic devices (immature technology) (see

Table 2). It can be found that HMD devices are the only available devices that provide the full immersion and at a low/medium cost.

Table 2: Summary of VR display devices.

Category	Type	Immersion	Number of user	Cost
Screen	Normal screen	None	Single	Low
	3D screen	None	Single	Low
Projector	Flat screen fabric	Partial	Single/multiple	Medium
	Curved/multi-screen fabric	Partial	Single/multiple	High
HMD	Small high-res screen	Full	Single	Low/medium
	Small optical projector	Full	Single	Medium
Holograms	Holographic emitter	Full	Single/multiple	Invalid

2.3 Different VR mine training systems

Based on the classification of the input and output devices, a new taxonomy of VR mine training systems, which contains three kinds, is raised as follows:

(1) Screen-based general VR mine training system

The screen-based general system uses a desktop monitor as the output device, and general physical devices, such as keyboard, joystick, etc. as the input devices. The whole system has little/no immersion, and is mainly used to develop the basic VR mine training systems.

(2) Projector-based customized VR mine training system

This is currently the most popular VR mine training system, and there are many commercial products in the market (CAE-Mining, 2012; QinetiQ, 2012; ImmersiveTechnologies, 2015). The output devices for visual sense are projectors with different kinds of screen fabrics – flat, multiple, curved, domed, etc. At the same time, a lot of customized operational platforms based on the real equipment are used in this kind of system. With the help of projectors and large screen fabrics, this system could provide some immersion to the users.

(3) HMD-based intuitive VR mine training system

The HMD-based intuitive system means that the high immersive visual output devices (Head Mounted Display) and intuitive input devices (auto tracing & capturing devices) are employed in the system. In this kind of system, trainees can feel full immersion, and interact with the virtual environment and equipment naturally and intuitively. For now, the immersive natural system is not wildly developed and used, but

it is the most advanced system and the future of mine VR training system.

3. AN INTUITIVE VR MINE TRAINING SYSTEM

In this paper, a new VR mine training system, which is a HMD-based intuitive system, was built for drilling scenario training in coal mines. In this system, the movement track device was used to capture the trainee's hands' movements and gestures, and the HMD was used as the visual output device through which the trainee can feel full immersion. At the same time, a screen-based general system was also built as a control system. The HMD used in this system, was composed of a VR headset and a NEXUS 6P smartphone. When the smartphone is inserted into the headset and turned on, the HMD is

ready to use, and the user could see the virtual environment through the lenses of the headset. With the help of the sensors built-in the smartphone, such as the gyroscope and the accelerometer, the smartphone could track the user's head turning, and the pictures in the HMD could update along with the head's movement.

The intuitive input device used in this system was a Leap Motion movement tracker with IR camera built-in. The Leap Motion was glued in the front cover of the HMD as shown in Figure 3(b), and it had a valid tracking angle of 135°, which is sufficient to track the user's hands (Figure 3(c)).

At the same time, a screen-based general system was also built as a control system.

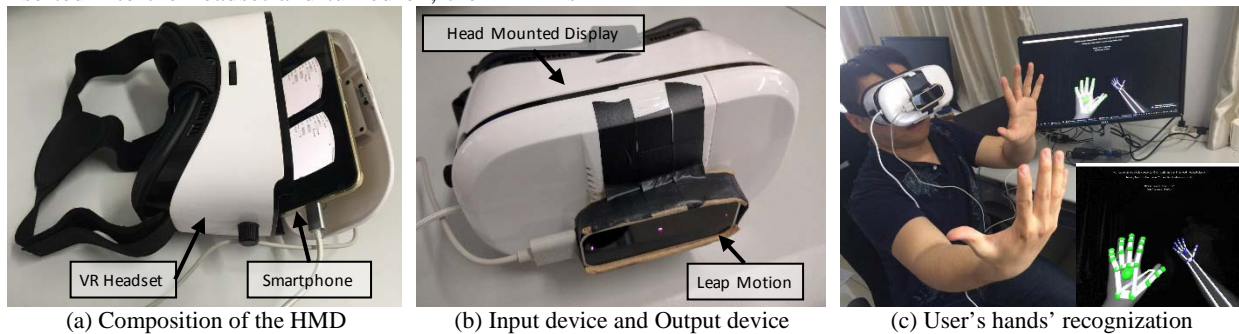


Figure 3: HMD and Leap Motion as I/O devices.

As for the software & database and VR engine parts, the Blender and Unity 3D software were employed: the virtual miner model was built in Blender, and the underground coal mine scene, the trigger and interaction rules between the user and the virtual environment, etc., were developed and coded in Unity 3D.



(b) HMD-based intuitive VR training system
Figure 4: Two different training systems.



(a) Screen-based general VR training system



In Figure4, the pictures on the left show the real utilization situation of each system, and the pictures on the right show the graphics that the user could see from the screen or the HMD. It can be seen that in the screen-based general system (figure 4 (a)), the user is controlling the character to drill by using a joystick, and the screen shows the third person view of the drilling scenario, which means that the immersion of the system could not be high. In the HMD-based intuitive system (figure 4 (b)), the user can experience the first person view through the HMD, and at the same time, thanks to the gyroscope built in the smartphone, the turning of the head could be monitored, and the sight in the HMD could change in real time. What's more, the user could manipulate the virtual miner's hands directly, instead of the whole

virtual character, and through the previous mentioned Leap Motion device, the user could control the fingers respectively, which means the user could do some more complicated movements and gestures to interact with the virtual drill in the virtual environment.

4. RESULTS AND DISCUSSION

In order to evaluate the effects of each mining training system, ten students tested both training systems. After that, they filled out questionnaires about the two systems to evaluate the levels of immersive, intuitive, interactive, easy to use, and easy to learn. Each aspect was evaluated in five grades. The results are shown in

Through the results, it can be seen that the HMD-based intuitive VR training system has a dramatically higher immersive grade (4.8) than the screen-based general system (1.3), and 1.5 to 2 times higher grade of intuitive, interactive and easy to use, this means that the HMD-based system has a better user experience than the screen-based system. As to the easy to learn – the training results of each system – the screen-based system is only a little lower than the HMD-based system, which means that both systems have quite good training results, and the HMD-based one is a little higher. After experiencing both systems, 9 of 10 students prefer the training experience of the HMD-based system, and would like to use it in the future.

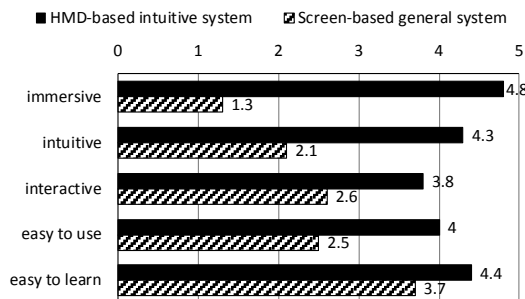


Figure 5: Evaluation of both training systems.

The students also suggested some limitations of the current HMD-based intuitive VR training system, and the main ones are as follows:

(1) In the HMD-based system, a user could not move the character through moving his own body, instead he must use other devices such as keyboard or joystick to move the character in the virtual environment, which will lower the immersion of the system.

(2) With long-term utilization, the user could feel tired or suffer from motion-sickness.

(3) For the current system, the Leap Motion device is used to track the user's hands, while the user could not feel any tactile sense, which will also

reduce the immersion of the system, because when people see they are touching something in the virtual environment, they could not feel the tactile sense in the real world.

(4) The users found that they could only interact with the drill, but could not interact with other things in the virtual environment, which is due to the limitations of the current software.

The points mentioned above are the main limitations of the current HMD-based VR system, and most of them are due to the limitations of the hardware and software used in the system. With the development of the VR input/output devices, and the updates of the HMD-based VR training system, the limitations of the current system might be solved in the future.

5. CONCLUSION

This paper classifies the input and output devices of mine training VR system into screen-based general systems, projector-based customized systems, and HMD-based intuitive systems. Using the Head Mounted Display as the output device which is composed of a VR headset and a smartphone, and a Leap Motion as the input device, an HMD-based intuitive VR training system was built. Users can feel full immersion through the HMD and control the virtual character's hands to manipulate the drill just by moving their own hands. After 10 students had tested both the HMD-based system and a controlled screen-based system, they found that the HMD-based system is more immersive, intuitive, interactive, and easy to use, and most of them believe the HMD-based system is better and would like to use the immersive system in the future.

6. ACKNOWLEDGEMENTS

The authors would like to thank China Scholarship Council for financially supporting the first author of this paper to study at McGill University – Mine Design Laboratory.

7. REFERENCES

Bertram, J. and J. Moskaliuk, et al. (2015). "Virtual training: Making reality work?" *Computers in Human Behavior* 43: 284-292.

Bukowski, R. and C. Sequin (1997). *Interactive simulation of fire in virtual building environments*.

Burdea, G. and P. Coiffet (2003). *Virtual reality technology*. New York, Wiley-IEEE Press.

CAE-Mining (2012). *CAE TERRA™ MINING SIMULATOR*.

Foster, P. and A. Burton (2004). "Virtual reality in improving mining ergonomics." *The Journal of The South African Institute of Mining and*

Metallurgy 104 (2): 129-134.

ImmersiveTechnologies (2015). Mining Training Simulators.

Kizil, M. S. and J. Joy (2001). "What can virtual reality do for safety." University of Queensland, St. Lucia QLD.

Kizil, M. (2003). Virtual reality applications in the Australian minerals industry. Application of Computers and Operations Research in the Minerals Industries.

Mazuryk, T. and M. Gervautz (1996). "Virtual reality-history, applications, technology and future."

Mihelj, M. V. Z. and D. Novak, et al. (2014). Virtual Reality Technology and Applications, Springer.

Milgram, P. and F. Kishino (1994). "A taxonomy of mixed reality visual displays." IEICE TRANSACTIONS on Information and Systems 77 (12): 1321-1329.

QinetiQ (2012). Global Mining Industry Virtual Reality Training.

Squelch, A. P. (2001). "Virtual reality for mine safety training in South Africa." Journal-South African Institute of Mining and Metallurgy 101 (4): 209--216.

Stone, R. J. (2012). Human factors guidelines for designers of interactive 3D and games-based training systems.

Stothard, P. and A. Squelch, et al. (2015). "Taxonomy of interactive computer-based visualisation systems and content for the mining industry - part 2." Mining Technology 124 (2): 83-96.

ThoroughTec (2010). CYBERMINE Mining Simulators.

Tichon, J. and R. Burgess-Limerick (2011). "A review of virtual reality as a medium for safety related training in mining." Journal of Health & Safety Research & Practice 3 (1): 33--40.

Zhao, Q. (2009). "A survey on virtual reality." Science in China Series F: Information Sciences 52 (3): 348-400.

Study of roadside packing to go with gob-side entry retaining technology on crisp surrounding and blasting face in the Xinzhuang mine

Ya-ge LI^{a,b}, Wei-xiang WANG^{a,b}, Long-zhe JIN^{a,b}, Shu WANG^{a,b}, Jiang LU^c

^a School of Civil and Environmental Engineering, University of Science and Technology Beijing, Beijing, China, 100083

^b Mine Emergency Technology Research Center, Beijing, China, 100083

^c Henan Shenhuo Group Co.,Ltd., Yongcheng, China, 476600

ABSTRACT

In order to improve the recycle rate of coal resources, extend the service-life of the mine, and alleviate the tensions of excavation-replacement in the Xinzhuang mine, this paper presents a high-water material for roadside packing to go with gob-side entry-retaining technology on crisp surrounding rock and blasting working face. Based on the conditions in the field, the authors analyzed the utility of the filling structures of the 12011 machine roadway. On the basis of the engineering analogy method and laboratory experiments, the authors determined the ZKD new high-water material ratio of each component and the filling process parameters. The results show that when four conditions are met—rectangular packing is used; water cement ratio of the new high-water material is 1.8:1; the Φ 18 mm \times L 3400 mm anchor bolt is imbedded in the filling body; and supplementary support, which consists of anchor bolt, wire rope, and steel beam, is applied—the average contraction rate of the roadway section is 13.38%, achieving a satisfactory effect. Compared with gob-side entry driving, it can improve the indirect profit by 9.86 million yuan; compared with digging a new roadway, it can increase the profit by 5688.5 yuan per metre.

KEYWORDS: gob-side entry retaining; high-water materials; observation of mine pressure; contraction rate of section

With the increase of mining service-life, the Xinzhuang coal mine now faces the problem of running out of coal mine resources, and the pressure of excavation-replacement is becoming increasingly great. In order to reasonably exploit existing coal resources, improve the mining rate of coal resources, extend the service-life of the mine, and alleviate tensions of excavation-replacement in the Xinzhuang coal mine, this paper presents a high-water material for roadside packing to go with gob-side entry retaining technology on crisp surrounding rock and blasting working face. This is based on the features of blast mining technology, a crisp and dry coal seam, and the fact that blasting vibration may cause the roadway wall to cave into the Xinzhuang coal mine at the three (3) 12011 working face.

To date, the new high-water rapid-hardening material for roadside packing to go with gob-side entry-retaining technology has been applied in different coal mines with satisfactory results. Tao Yi coal mine, Heng Jian coal mine, and Guo Er Zhuang coal mine of Handan Mine Group and Qiu Ji coal mine and Wang Lou coal mine of Lin Yi Mine Group are examples of this. It is worth mentioning that although the technology implemented in the aforementioned coal mines has unique characteristics,

there are still significant differences between these mines and Xinzhuang coal mine. The working face implements a blasting excavation process, and coal seam is crisp and dry; the blasting vibration may cause the roadway wall to cave into Xinzhuang coal mine. These features bring great difficulties to the implementation of gob-side entry retaining technology in Xinzhuang coal mine.

1. SURVEY OF GEOLOGICAL AND PRODUCTION CONDITIONS ON 12011 MACHINE ROADWAY

Xinzhuang coal mine three (3) coal 12011 machine roadway is located in the west wing of three (3) 12th mining area. The elevation of this roadway is between 246.5 m and 162.6 m below base level, and the strike length is approximately 525 m. Three (3) coal seam is revealed in this region, and the thickness is 1.2 m to 1.8 m, with the average thickness being 1.3 m. The average dip angle is 9°, and hardness ratio f is 1.5. The stratification and joint is developmental and the immediate roof is mudstone, which has a thickness of 3 m to 3.5 m. The fissures are developed and hardness ratio f is 2. The floor is mudstone with a thickness of 3.15 m. It is gray and black, containing plant fossils. The fissures are developed, and hardness

ratio f is 2. There exists about 0.5 m carbonaceous mudstone, soft and broken, under the coal floor. The section of 12011 roadway is rectangular; it has a net width of 4000 mm and clear height of 2600 mm.

2. FILLING MATERIAL

As necessitated by roof activities, at the beginning, the activity of the roof is mainly based on rotation and subsidence where the load is small, and the utility of the filling structure is primarily to balance the weight of the immediate roof. When the working face continues to move forward, the immediate roof and a range of old roof collapses and breaks up. In order to reduce the time of the presence of the old roof and the deformation of the surrounding rock, it is required that the filling structure has enough support resistance. When the support structure of old roof rock mass breaks up, the roof activity comes to an end, and the filling structure is there to maintain the stability of the structure.

Therefore, it is required that the filling structure is to be of high strength in the early stages, and increasing resistance as time passes. It is to be stable and reliable with high load bearing capability. ZKD new high-water filling material is better at meeting these requirements. This material consists of two components, A and B. Component A, based on special cement clinker, is made from suspension concentrate and a compound super-retarding agent. Component B is mixed with lime, gypsum, and compound accelerator. Both component A and B can be used at mass ratio of 1:1. According to the standard tests in the laboratory, the basic properties of the new high-water material are shown in Table 1.

Table 1: Basic properties of the new high-water material.

initial setting time (min)	uniaxial compressive strength (MPa)			
	2 h	24 h	7 d	28 d
3–20	≥2.0	4.2	8–9	10–11

The experimental results show that the compressive strength of the filling body, which consists of new high-water filling material, is generally more than 20% when the anchor bolt is placed in the filling body. The longitudinal and lateral deformation of the filling body can reach up to 7% and 10% respectively when there is no anchor bolt in the filling body. The whole anti-deformation capacity of the filling body can be increased by 6% to 28%. The placement of the anchor bolts can significantly improve the overall strength and stability of the filling body.

3. FIELD APPLICATION

3.1 Field filling technology

Combined with geological conditions in the Xinzhuang mine and based on engineering analogy methodology, this paper adopts the American MTS 815 rock mechanics test system to measure rock samples derived from different rock strata. These samples were compared to standard test specimens of new high-water material that have different proportions, taking the cost, equipment selection, operation flexibility, and requirements of the roadway support resistance into consideration. The water cement ratio was determined as 1.8:1, and under this condition, the average compressive strengths of the new high-water filling material are 1.7 MPa, 3.8 MPa, 4.9 MPa, and 5.9 MPa at the time of 6 h, 1 day, 3 days, and 7 days.

According to the production status of blasting mining face in three (3) coal 12011 roadway, the pumping station is planted at the corner of the roadway in three (3) coal 12 mining area. The schematic diagram of equipment layout in the filling chamber is shown in Figure 1. As is shown, materials are transported by a hydraulic injection pump that is specified for coal mine operations. The filling pipe is composed of a high-pressure hose with a diameter of 40 mm and seamless tube with an inner diameter of 40 mm. There are two feeding pipes: one for material A and one for material B that separately convey the materials from the pumping station to the filling point. To make the filling technology more convenient and reliable, a high-pressure hose is used between the filling pump and the tube, and between the filling pipe and the external tee mixer. The mixing pipe utilizes the high-pressure hose, with the inner diameter being 55 mm. A quick coupling was used between the rubber hose and steel pipe.

Considering the characteristics of the surrounding rock and the requirements for retaining roadway section in the Xinzhuang mine, it is determined that the filling body should be entirely arranged in the goaf, and the rectangular filling bag should be used with a size of 2400 mm × 3000 mm × 2600 mm. Its height and width can be adjusted according to the actual conditions. The diameter of the feed hole is 100 mm, and the length of the feed tube is less than 550 mm. There are six anchor holes in the filling bag, with the diameter being 25 mm, and the length of anchor bolt that is exposed on both ends being 150 mm.

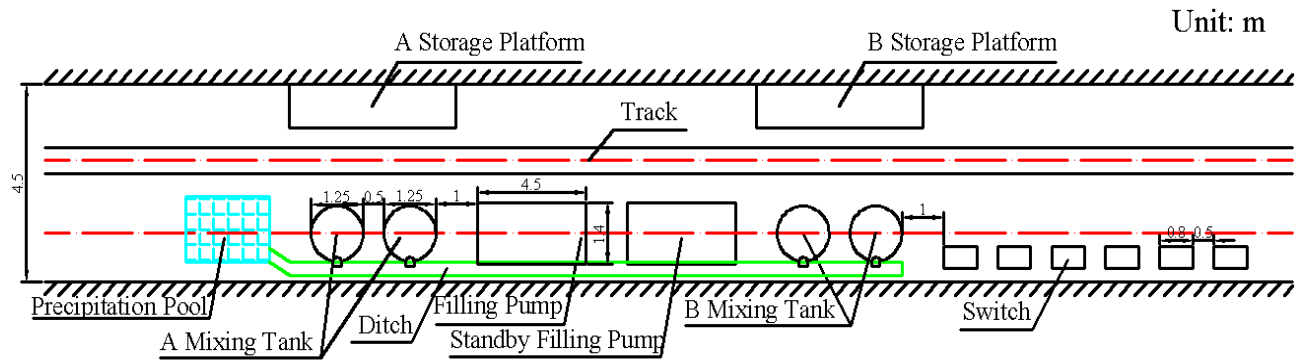


Figure 1: Schematic diagram of equipment layout in filling chamber.

3.2 Control of the stability of the filling body

According to field observation, the average dip angle of three (3) coal 12011 working face is 9° ; however, parts of the area have a larger angle. There is a step between the roof and the floor with a height of 1.3 m. The filling body was placed along the angular surface with a large angle. In order to prevent the lateral deformation of the filling body, which leads to instability affected by the load from the goaf side or affected by the force from the side of the working face and the roof, an anchor bolt was placed in the filling body. The anchor bolt has two thread ends of sizes $\Phi 18 \text{ mm} \times L 3400 \text{ mm}$. After the shaping of the filling body and dismantling the basic template with dimensions of $2400 \text{ mm} \times 200 \text{ mm} \times 30 \text{ mm}$ and dismantling the front template with dimensions of $3200 \text{ mm} \times 200 \text{ mm} \times 30 \text{ mm}$, the anchor bolt was fixed with light steel tape, which is suitable for roadway support at both ends. The nut and tray has dimensions of $300 \text{ mm} \times 250 \text{ mm} \times 50 \text{ mm}$. This too, enhances the strength and stability of the filling body. Results from the field application showed that the resistance of the anchor bolt improved the overall strength and stability of the filling body significantly, and the effect of reinforcement became obvious. Figure 2 is a schematic diagram of the roadway beside the filling support.

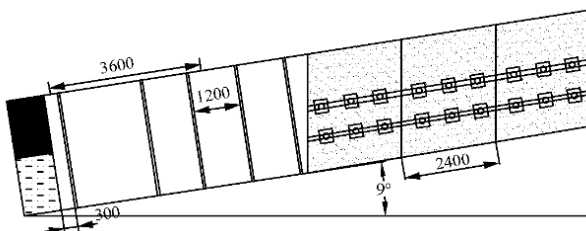


Figure 2: Schematic diagram of roadway beside the filling support.

3.3 Reinforce support of gob-side entry retaining

The crisp surrounding rock in three (3) coal 12011 machine roadway and the significant roof

caving resulted from the tunneling process resulted in an ultrahigh roadway segment of 30 m length by 3.4 m to 6.0 m height. Because the roadway was subjected to a blasting vibration influence before implementation of the gob-side entry retaining, the degree of surrounding rock fracture in this part was further increased, and the ultrahigh segment became the most difficult area in gob-side entry retaining. In view of this situation, the reinforced support of the roof of roadway and the east side of the coal wall was decided to be implemented before the working face, 50 m in front of the retained roadway. In the original position between the two rows of anchor bolts, 2 anchor cables were added in the middle of the east side of the roadway, and the anchor cable used the steel strand with dimensions $\Phi 18 \text{ mm} \times L 5000 \text{ mm}$. The row spacing was 1.4 m and the column spacing was 1.5 m. At the same time, the flange beam was used to connect the anchor cable along the vertical direction, to form the structure that consisted of cables and beams to limit wall caving. At the bottom, from the 3.0 m baseboard, at an oblique upward angle of 5° to 10° , one steel strand cable was set, the size of which was $\Phi 18 \text{ mm} \times L 5000 \text{ mm}$. Two parts of it were fixed with the tray, the dimensions of which were $350 \text{ mm} \times 350 \text{ mm} \times 10 \text{ mm}$. Then, depending on the distance between the anchor cable hole and roadway floor, two or three anchors were set under the anchor cable. To ensure enough supporting force and the integrity of the coal wall, the spacing of anchors was not more than 800 mm. The spacing between the anchor bolt and the anchor cable was not more than 1000 mm, and the spacing between adjacent two rows of reinforce support was not more than 1.6 m.

4. ANALYSIS ON THE EFFECT OF MINE PRESSURE OBSERVATION AND GOB-SIDE ENTRY RETAINING

For this study, many measured control points were set. On these points, single cross wiring method was used to measure the surface displacement of the

roadway. Beside the roof and bottom of filling body there were set control points forming a baseline along the vertical direction. On the middle of the filling body, a transverse steel pole was installed in advance. Its exposed end was fixed, then a tape measure was used to measure the distance between the two base points and the variable length of the exposed end. The change of displacement over time of the roadway at various locations is shown in Table 2.

From Table 2, it was concluded that the

maximum and the average displacement of roof and floor were 239 mm and 222 mm. The maximum and the average displacement of the roadway's sides were 255 mm and 212 mm. The maximum and the average displacement of the filling body were 136 mm and 100.5 mm. The maximum contraction percentage of roadway section was 14.49%, and the average contraction percentage of roadway section was 13.38%. The effect is better and can meet the requirements of secondary use.

Table 2: Summary of roadway section contraction percentage.

survey section	roof and floor		roadway's sides		filling body		contraction rate of section
	the displacement (mm)	the average displacement rate (mm/d)	the displacement (mm)	the average displacement rate (mm/d)	the displacement (mm)	the average displacement rate (mm/d)	
16 [#]	222	6.94	229	7.16	100	3.12	13.77%
17 [#]	207	6.27	243	7.36	109	3.30	13.55%
18 [#]	214	6.48	255	7.5	136	4	14.08%
39 [#]	230	6.97	227	7.09	112	3.5	14.02%
40 [#]	214	6.11	241	7.09	103	3.12	13.76%
41 [#]	228	6.33	251	7.17	101	2.97	14.49%
58 [#]	202	6.73	174	5.8	92	3.07	11.78%
59 [#]	224	7.22	188	6.06	96	3.10	12.91%
60 [#]	239	7.47	208	6.5	96	3	13.91%
83 [#]	217	7	167	5.06	96	2.91	12.17%
84 [#]	235	7.34	178	5.23	85	2.5	13.09%
85 [#]	228	6.91	185	5.29	83	2.37	12.99%
average	222	6.81	212	6.44	100.5	3.08	13.38%

Compared with digging a new roadway, gob-side entry retaining can increase the profits by 5688.5 yuan per meter; as opposed to gob-side entry driving, gob-side entry retaining reduces the excavation work significantly, cuts down the work time, alleviates tensions of excavation-replacement, prevents fire disaster, extends the service-life of mines, and improves indirect profits by 9.86 million yuan. To summarize, it results in substantial economic as well as social benefits.

5. CONCLUSION

This study adopted the new mine-fill whose water cement ratio is 1.8:1. The size (length × width × height) of rectangular filling bag was 2400 mm × 3000 mm × 2600 mm, and the size of anchor bolts which were imbedded in the filling body were Φ 18 mm × L3400 mm. Moreover, the supplementary support, which consisted of anchor bolts, wire rope, and steel beams, was used to ensure the stability of the lateral supporting force in the roadway, which had a crisp and dry coal seam. It was impacted by blasting work, and had ultrahigh height, with the size of wire rope being Φ 18 mm × L 5000 mm. These measures restricted the displacement of the coal wall, and

improved overall strength and stability of the filling body.

The result of the mine pressure observation survey showed that the maximum of roadway section contraction percentage was 14.49%, and the average roadway section contraction percentage was 13.38%. The effect of gob-side entry retaining netted marked improvement and demonstrably met the requirements of secondary use.

6. ACKNOWLEDGMENTS

First, I would like to extend my deepest gratitude to my supervisor, Dr. Long-zhe JIN, who provided valuable guidance in every stage of writing for this thesis. I also extend thanks to barmaster Jiang LU for his support. Furthermore, I would like to thank my friends Shu WANG and Wei-xiang WANG for their help and encouragement. Finally, I gratefully acknowledge the experts who reviewed this thesis and others who strive to make this international symposium a success.

7. REFERENCES

Bai J. (2006). Surrounding Rock Control of Entry Driven along Goaf. Xuzhou, 171p

Bai J., Zhou H., Hou C., Tu X., and Yue D. (2004).Development of support technology beside roadway in goaf-side entry retaining for next sublevel. *Journal of China University of Mining and Technology*. Volume 33, pp.183-186

Bu T., Feng G., and Jia K.(2010).Gateway Side Backfilling Support Technology of Goaf Side Gateway in Fully Mechanized High Cutting Longwall Mining Face. *Coal Science and Technology*. Volume 38, pp.41-44

Chen Y., Bai J., and WANG X. (2012). Support technology research and application inside roadway of gob-side entry retaining. *Journal of China Coal Society*. Volume 37, pp.903-910

He T. (2012).The breaking place prediction of face end main roof flap top in the gob-side entry retaining. *Journal of China Coal Society*. Volume 25, pp.28-31

Hua X., Ma J., and Xu T. (2005).Study on controlling mechanism of surrounding rock of gob-side entry with combination of roadside reinforced cable supporting and roadway bolt supporting and its application. *Chinese Journal of Rock Mechanics and Engineering*. Volume 24, pp.2107-2112

Hua X., Zhao S., and Zhu H. (2006) .Research on combined support technique of gob-side entry retaining. *Rock and Soil Mechanics*. Volume 27, pp.2225-2228

Ju F., Sun Q., and Huang P. (2014).Study on technology of gob-side entry retaining in thin seam surrounded by soft roof and floor. *Journal of Mining and Safety Engineering*. Volume 31, pp.914-919

Li J., Feng G., and Ning S. (2009).The technology and application of roadside supporting for gob-side entry retaining in full-mechanized mining. *China Mining Magazine*. Volume 18, pp.77-79

Qian M., Shi W., and Xu J. (2010).Mining pressure and strata control. *Xuzhou*, 374p

Tang J., Hu H., and Tu X. (2010) .Experimental on roadside packing gob-side entry retaining for ordinary concrete. *Journal of China Coal Society*. Volume 35, pp.1426-1429

Xie W., Da J., and Feng G. (2004).Mechanism of controlling surrounding rock around gob-side entry retaining in top-coal caving mining face. *Journal of Central South University (Science and Technology)*, Volume 35, pp. 657-661

Xu J., Zhu W., and Li X. (2006).Study of the Technology of Partial-Filling to Control Coal Mining Subsidence. *Journal of Mining and Safety Engineering*, Volume 2, pp.6-11

Zhang D., Miao X., and Mao X. (2001).Simulation on Roof Activities of Gob-Side Entry Retaining in Fully-Mechanized Top-Coal

Caving Faces. *Journal of China University of Mining and Technology*. Volume 30, pp.261-264

Optimization of bit nozzle parameters of reverse circulation sampling used in coal mines

Kang Jianning^{a, b}, Hu Qianting^c, Zhang Rui^{b, *}

^a Shandong University of Science and Technology, Qingdao, China, 266590

^b Chongqing Research Institute of China Coal Technology & Engineering Group Corporation, Chongqing, China, 400037

^c Chongqing University, Chongqing, China, 400044

ABSTRACT

The coal mine air reverse circulation sampling technique is important for improving the accuracy of direct determination of gas content. The sampling drill is an important structural element to realize this technique. The embedded annular ejector and external nozzle of the drill are the main structures that can achieve reverse circulation. The external bit nozzle divides the mine compressed air into two parts. One part is used to wash the drill hole in order to prevent hole collapse, and the other part can press cuttings at the hole bottom into the drill pipe center tube and provide the transmission power. Bit nozzle dip angle and position are studied by numerical simulation, and the results are proved by the filed test. The results show that when the dip angle of the nozzle is 15° and the position is appropriate away from the drill cutter, the reverse circulation is better and the sampling depth increases. This improves the quality of sampling and prevents damage to the drill bit and buried drill accidents.

KEYWORDS: Coal mines; reverse circulation sampling; bit nozzle; numerical simulation

1. INSTRUCTIONS

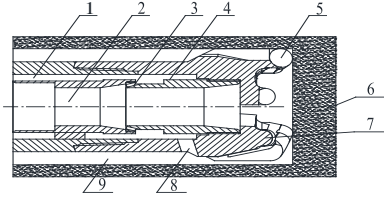
The air reverse circulation sampling technique is widely used in the geological prospecting industry in China and other countries, as it is a kind of sampling technique with large sampling depth, high sampling rate, spot sampling, low sample contamination rate, and strong representation. In this technological field, Jilin University has formed a series of specifications for reverse circulation drilling equipment (Zhang et al., 2007). Due to the advantages of the technique, from the year 2005 to 2010, the CCTEG Xi'an Research Institute in China and the Commonwealth Science and Industries Research Organization (CSIRO) in Australia used it for coal sampling in mines, in order to improve the accuracy of direct determination of gas content of coal seams. Because the drilling cuttings stress state and the mine air pressure in the coal seam borehole is different from the geological prospecting borehole, the sampling depth of the underground coal mine air reverse circulation equipment has not been able to effectively break through 60 m (Yuan et al., 2011; Yuan et al., 2014; Hu, 2011). From the year 2011 to 2015, the China Coal Technology Engineering Group Chongqing Research Institute (Referred to as Chongqing Research Institute) developed the SDQ type deep hole fixed-point sampling device (Li, et al, 2014 and Zhang, 2014), increased the depth of coal mine air reverse circulation sampling to 120 m, which has provided the technical and equipment

support for the accurate determination of gas content in large inclined long coal mining working faces. The sampling drill designed by Chongqing Research Institute leads the drilling cuttings from the bottom of the hole into the double-wall drill pipe inner tube by the effect of center tube extraction under external pressure (Zhang et al., 2014). The external bit nozzle is an important structure for providing the external pressure. Based on computational fluid dynamics (CFD) and field tests, this study will probe into the optimum design of the dip angle and position of the external nozzle, in order to enhance the effectiveness of reverse circulation sampling.

2. THE MECHANISM OF THE UNDERGROUND REVERSE CIRCULATION SAMPLING BIT

A sampling bit with internal and external jet flow control (air flow) functions is developed with reference to the air reverse circulation sampling bit in the geological exploring industry and previous research results and according to the characteristics of drilling sampling in current underground coal seams, as shown in Figure 1. The sampling bit adopts a composite design, that is, the annular ejector with an internal injection function is embedded in the inside of the drill bit, a positive pressure injection orifice with external injection function is installed outside the side wall, and the end head designed to be

a cutting structure of cuttings granularity control with an anti-blocking type. This structure can make the fresh cuttings automatically adjust to be the gas-solid two phase flow with appropriate solid-gas ratio and flow rate, according to the change of drilling resistance, under the triple control of external collection, internal extraction, and hole wall shunting. The fresh cuttings then enter the center pipe of double-wall drill pipe to form the reverse circulation. The principles of underground reverse circulation sampling are shown in Figure 2.



1-annular space, 2- center pipe, 3- jet nozzle, 4-annular ejector, 5- drilling cutter, 6-coal wall, 7- bit body, 8- external bit nozzle, 9- gap between the drill bit and hole wall

Figure 1: The structure of sampling bit with internal and external jet flow control.

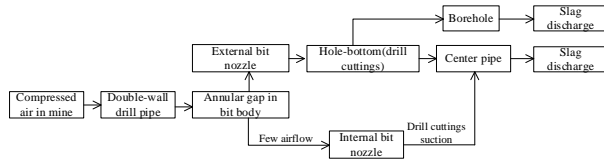


Figure 2: The mechanism of the underground reverse circulation sampling.

As can be seen from Figure 2, the borehole wall shunts compressed air after it flows through the external bit nozzle. A portion of the gas stream continues to flow to the hole bottom, providing positive pressure power for making the drill cuttings get into the center pipe and cooling the drilling cutter at the same time. Another portion of the gas flows to the nozzle, carrying the residual cuttings to avoid the occurrence of buried drilling accidents. With the gradual increase of the drilling depth, the slag discharge resistance of the drill hole and center pipe increases gradually. It is easy to cause problems such as drilling difficulties, low service life of drill bits and poor effects of reverse circulation sampling, if the air distribution of the two air-return slag discharging space is unreasonable. Therefore, this paper takes the dip angle of the external bit nozzle and hole position as the research object, through a combination of the Fluent numerical simulation and field test method to optimize the two parameters, in order to further improve the effect of reverse circulation sampling under the premise of normal drilling.

3. PARAMETERS OPTIMIZATION RESEARCH OF SAMPLING BIT NOZZLE BASED ON THE NUMERICAL SIMULATION

3.1 Modeling

Because the longitudinal section of the sampling bit is symmetrical, it can be used to study half of the sample structure when researching the parameters of the external bit nozzle. A two-dimensional model was established in order to study the influence of the external nozzle parameters on the reverse circulation effect, as shown in Figure 3. The grid was divided by using gambit. The air inlet is the inlet of compressed air, where the pressure is 0.2 MPa. The outlet1 and outlet2 are for export, and the pressure is the atmospheric pressure.

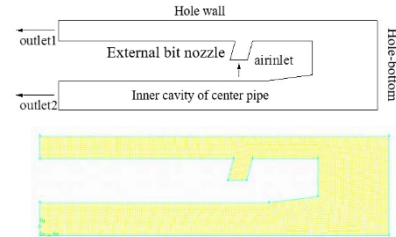


Figure 3: The simplified model and mesh of sampling bit.

3.2 Dip angle optimization of the external bit nozzle

3.2.1 The internal flow field of the model with different dip angle

As shown in Figure 4, α refers to the dip angle of the external bit nozzle, which is defined as the angle between the central axis of the external bit nozzle and the normal which is vertical to the hole wall.

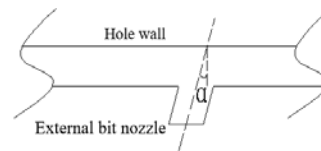


Figure 4: The dig angle of external bit nozzle.

With reference to the design experience of the common drill in the drilling tool industry, the model of different dip angles of the external bit nozzle was set up, with the dip angle α set as 0° , 15° , 25° , 35° , 45° , and 55° . Numerical simulation was carried out using Fluent software, and the distribution of compressed air velocity in the internal flow space of the model was obtained, as shown in Figures 5-10.

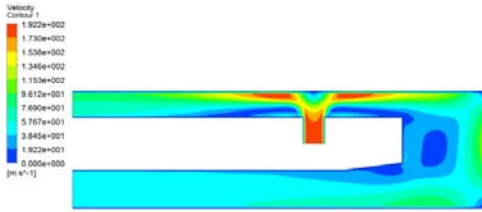


Figure 5: The flow field when dip angle is 0°.

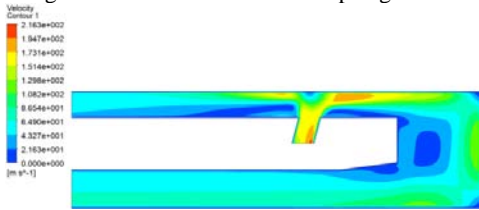


Figure 6: The flow field when dip angle is 15°.

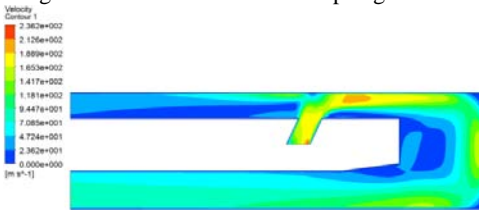


Figure 7: The flow field when dip angle is 25°.

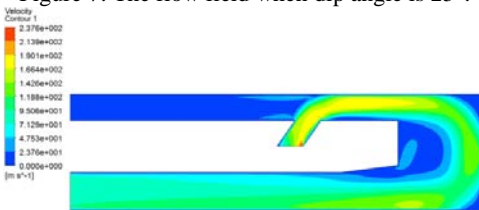


Figure 8: The flow field when dip angle is 35°.

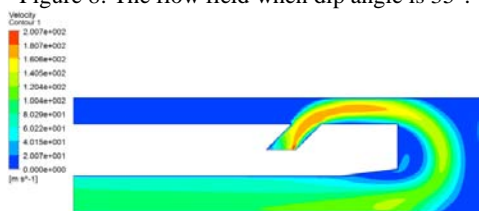


Figure 9: The flow field when dip angle is 45°.

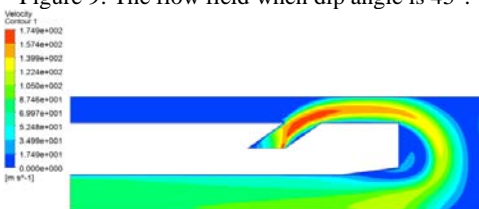


Figure 10: The flow field when dip angle is 55°.

The following observations are made from Figures 5 to 10:

(1) Compressed air jets out from the external bit nozzle flow to the orifices and bottom of drill hole by

a rebound off of the borehole wall. With the increase of dip angle of the bit nozzle, the airflow into the bottom increases gradually.

(2) With the increase of the dip angle of the external bit nozzle, the pressure on the hole bottom increases gradually, but the air flow velocity decreases.

3.2.2 The analysis of airflow velocity on the hole bottom

As shown in Figure 11, the center cross section of the drilling cutter near the bottom of hole is taken as the analysis object. The cross section is the most concentrated area of drilling cuttings when cutting coal.

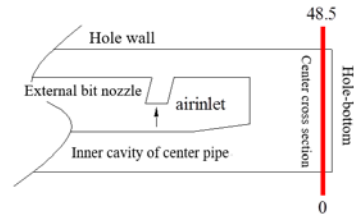


Figure 11: The location of center cross section of the drilling cutter.

The velocity distribution of different locations (range of 0-48.5 mm at hole-bottom line) in the center cross section of the drilling cutter under different dip angles of the external bit nozzle is shown in Figure 12.

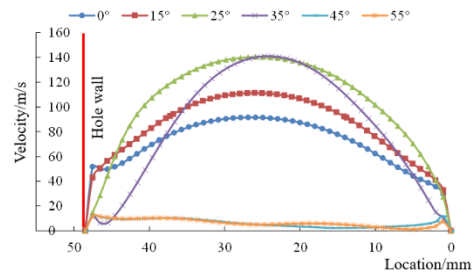


Figure 12: The velocity distribution of different location in the center cross section of the drilling cutter.

It can be concluded from Figure 12 that:

(1) When the dip angle of the external bit nozzle is in the range of 0°-15°, the velocity distribution on the center cross section of the drilling cutter is more uniform, and the air flow is wider through the cross section, which can carry most of the drilling cuttings.

(2) When the dip angle of the external bit nozzle is in the range of 25°-35°, the velocity of air in the center section of the drill cutter reaches a maximum but the distribution is not uniform, and the airflow velocity decreases near the wall of the hole.

(3) When the dip angle of the external bit nozzle is 45° and 55°, the center cross section of the drill

cutter becomes smaller and the velocity becomes less than 15 m/s in most locations. The drilling cuttings at the hole bottom are not easily disturbed at this velocity.

In conclusion, when the external nozzle angle is in the range of 0°-35°, it is conducive to form the reverse circulation which can carry cuttings from the bottom of the hole. However, when in the range of 0°-15°, the air flow in the cross section of the drill cutter is uniform. On the one hand, this is conducive to cooling the drilling cutter, but on the other hand, high-speed airflow can completely cover the area of the hole bottom, giving the drill cuttings easier access to the center pipe to form the reverse circulation.

3.2.3 The analysis of outlet flow rate

As shown in Figure 13, the rate of air flow which flows to the bottom is defined as positive, while flow to the nozzle is negative. According to the simulation results, the air flow rate of outlet1 and outlet2 under different dip angles of the bit nozzle are found, as shown in Figure 14.

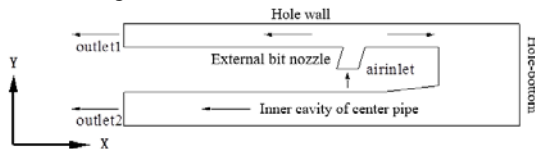


Figure 13: The flow direction in the model inner.

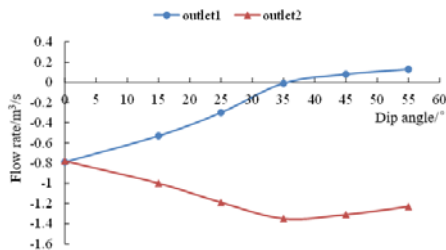


Figure 14: The flow rate of outlet1 and outlet2 changed with the dip angle of the external nozzle.

The following conclusions can be drawn from Figure 14:

(1) When the outlet pressure is the same, the air flow through the external bit nozzle is the outflow from outlet1 and outlet2. When the dip angle of the bit nozzle is 0°, the flow rate of the two exits is the same. With increases of the dip angle, the amount of air flowing through outlet1 decreases gradually, and the air quantity flow through outlet2 increases gradually.

(2) When the dip angle of the external bit nozzle is 35°, the air quantity flow through outlet1 is 0. When the dip angle is greater than 35°, outlet1 not only does not discharge the wind, but sniffs the wind.

When the dip angle is greater than or equal to 35°, the air quantity flow through outlet2 increases, but in practical application, it is not conducive to the discharge of the hole wall residual cuttings and the phenomenon of buried drill or clamp drill are likely to occur.

3.2.4 The analysis of outlet flow velocity

Figure 15 is the variation diagram of average velocity of the outlet with the change of the dip angle of the external bit nozzle, obtained from the simulation results.

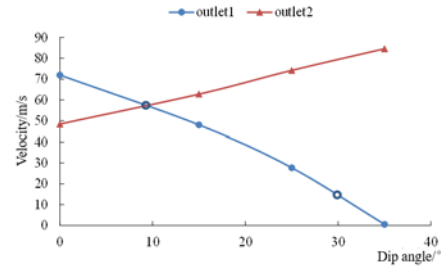


Figure 15: The flow velocity of outlet1 and outlet2 changed with the dip angle of the bit nozzle.

It can be concluded from Figure 15 that:

(1) When the dip angle of the external bit nozzle is more than 30°, the average velocity of flows through outlet1 is less than 15 m/s. In practical applications, the speed is less than pneumatic conveying speed which is the minimum suspension speed of cuttings, therefore, this dip angle is not conducive to the discharge of residual cuttings, and may cause the phenomenon of buried drill or clamp drill.

(2) When the dip angle of the external bit nozzle is about 10°, flows through outlet1 and outlet2 have the same average velocity. The energy of wind in this angle has reasonable allocation and utilization for carrying drilling cuttings.

Based on the above numerical simulation results, it is concluded that when the dip angle of the external bit nozzle is in the range of 0°-15°, it can form the reverse circulation which is favourable to carry the drilling cuttings. When dip angle is about 10°, the energy of the air flow is reasonably allocated and utilized. Taking into account the actual application process, the smaller the dip angle, the greater the gas etching by the air flow. Dip angles close to 0° are not conducive to the maintenance of the molding and stability of drilling, and should therefore be avoided. At the same time, based on the purpose of sampling which expects to discharge more cuttings through outlet2, practical applications should make the air quantity through the outlet2 slightly greater than outlet1, so the dip angle should be greater than 10°.

By comprehensive analysis, the range of the dip angle of the external bit nozzle should be 10° - 15° .

3.3 The determination of location of external jet orifice

On the basis of the optimization of the dip angle of the external bit nozzle, a physical model of the bit nozzle in different locations is established, as shown in Figure 16. The internal flow field of three kinds of situations model was simulated in order to determine the position of the bit nozzle which is the most beneficial in promoting the formation of reverse circulation at the bottom of the hole.

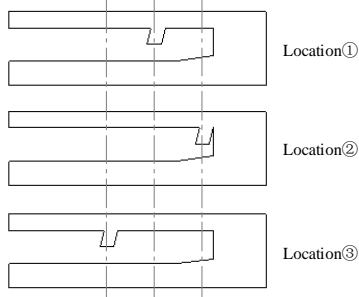


Figure 16: The bit nozzle models of different location.

The velocity images of compressed air in the model are obtained by numerical simulation, as shown in Figures 17 to 19.

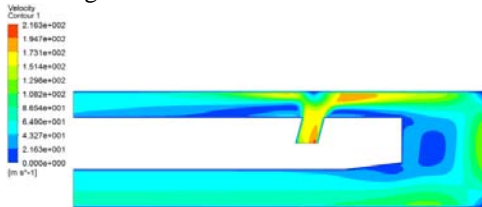


Figure 17: The velocity images when bit nozzle is in location ①.

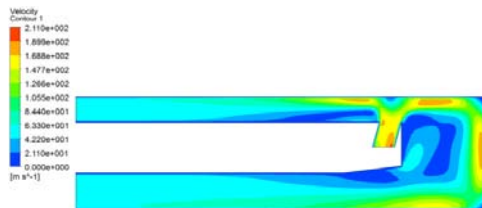


Figure 18: The velocity images when bit nozzle is in location ②.

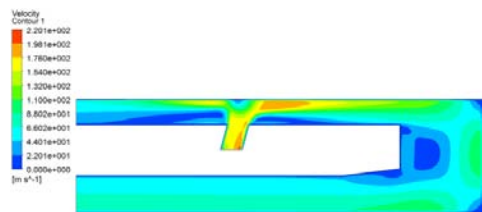


Figure 19: The velocity images when bit nozzle is in location ③.

Data from the analysis of the air flow rate and the average velocity of outlet1 and outlet2 are shown in Table 1. The flow rate through outlet2 is about 65% of the total flow at location ①, about 60% at location ②, and about 66% at location ③. Regardless of the location of the jet orifice, the flow of outlet2 is dominant, while the average velocity of outlet1 and outlet2 is greater than 15 m/s, which can satisfy the transportation conditions of drilling cuttings. Therefore, on the basis of the optimization of the dip angle of the external bit nozzle, the position of the external bit nozzle has little influence on the effect of the reverse circulation.

Table 1: The air flow rate and the average velocity of outlet in different location of the bit nozzle.

Location	Flow rate/m ³ /s		Velocity/m/s	
	outlet1	outlet2	outlet1	outlet2
①	0.53	1	48.1	62.8
②	0.61	0.9	55.4	56.2
③	0.51	1	46.1	65.1

The flow lines of space velocity and effective air flow rate are analyzed as shown in Figure 20. When the external bit nozzle is in the three positions, the flow field in the hole bottom are not the same. When the external bit nozzle is at location ①, the vortex area of the hole bottom space is small, and the direction of the air flow velocity is very smooth. When the external bit nozzle is at location ②, the vortex area of the hole bottom space becomes larger, the effective air flow line is mainly concentrated in the vicinity of the coal wall in the hole bottom, and the flow line compression phenomenon is generated. When the external bit nozzle is at location ③, the vortex area of the bottom space is small, but the direction of the airflow velocity is not more smooth than with the bit nozzle at location ①.

In summary, models can be obtained through the simulation of the internal flow field under three kinds of external bit nozzle locations. At the same dip angle of the external bit nozzle, the influence of bit nozzle location on the distribution of the air outflow rate of the model is small, and the outlet velocity can meet the transmission speed of the cuttings. The vortex area of the bottom space has an increasing trend, which is not conducive to make the drilling cuttings from bottom-hole get into the center pipe space to form an effective reverse circulation, when the bit

nozzle location is moved forward. Compared with the simulation results, it is concluded that the reverse circulation of the hole-bottom drilling cuttings can be better realized when the bit nozzle location is far away from the drilling cutter.

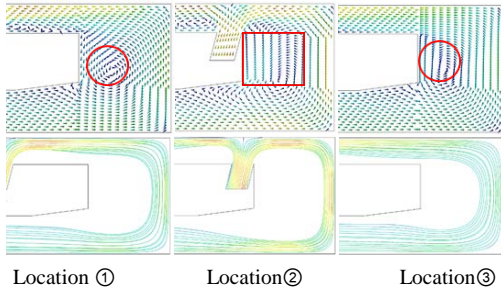


Figure 20: Velocity vector diagram and flow chart of bit nozzle in different position.

4. FIELD TEST

In order to verify the correctness of the numerical simulation results, the diameter of a 95 mm drill was processed according to the above conditions for a real coal mine reverse circulation sampling test. The range of sampling depth, the average sampling quality of single drill pipe, and the drilling situation in the sampling process was investigated, as shown in Tables 2 and 3.

Table 2: The sampling effect of drill bit with different dip angle of the bit nozzle.

Investigation targets Dip angle (°)	Sample depth/m	Average sampling quality of single drill pipe /Kg	Drilling situation in sampling process
0	80~110	4.2	good slag discharge
15	90~120	5.7	good slag discharge
25	80~90	4.5	good slag discharge
35	50~70	2.1	buried drill
45	20~45	2.2	buried drill
55	20~30	1.7	buried drill

Note: the largest quality cuttings of single drill pipe drill were about 9.3Kg.

According to the field test, it is known that when the dip angle of the external bit nozzle is 15° the inspection parameters are all optimal. At the same time, with the dig angle of the external bit nozzle become larger, the phenomenon of buried drill often happens because the normal drilling in the sampling process cannot be guaranteed. Therefore, the sampling depth is shallow and the sampling quality is low. When the external bit nozzle position is in the three kinds of situations, the sampling depth of the field test is better, but the quality of the sample is less

in location ②. The field test is consistent with the numerical simulation results.

Table 3: The sampling effect of drill bit with different locations of the bit nozzle.

Investigation targets Location	Sample depth/m	Average sampling quality of single drill pipe /Kg	Drilling situation in sampling process
①	90~120	5.7	good slag discharge
②	80~110	2.4	good slag discharge
③	90~120	4.9	good slag discharge

5. CONCLUSIONS

The external bit nozzle of the sampling bit can split the compressed air in the mine into the hole-bottom space, which is the key configuration for promoting the anti-cyclical effect in the process of sampling, guaranteeing normal drilling slag discharge, and cooling the drill cutter.

The dig angle and the position of the external bit nozzle of the sampling bit was studied through the use of numerical simulation and a field test. The results show that when the dig angle of the external bit nozzle is 15°, the drill cutter can make the sampling bit produce a better anti cyclical effect, increase sampling depth, improve the quality of sampling, prevent bit damage, and prevent the occurrence of buried drill accidents.

6. ACKNOWLEDGEMENT

This study was financially supported by Special Foundation of Liang Jiang Scholars Program.

7. REFERENCES

- Hu Z.Y. (2011). Research and application of air reverse circulated drilling tools in mining seam. Coal Engineering, No.4, pp. 116-118.
- Li J.G., Lv G.C, Long Q.M, and Hu J. (2014). Application effects research on deep hole fixed-point fast sampling technology in gas content measurement. Industrial Safety and Environmental Protection, Volume 40, No. 11, pp. 5-7, 51.
- Yuan L., Xue S., and Xie J. (2011). Study and application of gas content to prediction of coal and gas outburst. Coal science and technology, Volume 39, No. 3, pp. 47-51.
- Yuan L. and Xue S. (2014). Theory and technology of coal and gas outburst prediction by gas content in coal seam. Science Press, Beijing, 174 p.
- Zhang Y.G., Yin K., and Wang R.S. (2007). Design and experimental study of the air jet bit of

reverse circulation continuous sampling. West-china Exploration Engineering, No.3, pp. 77-79.

Zhang S.T. (2014). Key technology for gas content direct determination method in underground mine. Journal of Mining & Safety Engineering, Volume 31, No. 2, pp. 328-332.

Zhang R., Long Q.M, Li J.G, and Li Q.L. (2014). Research on nozzle parameters of annular ejector embedded in sampling drill. Zhong zhou Coal, No. 5, pp. 77-80.

Electrical equipment certification in Canadian underground coal mines – problem solved?

Ronald (Ron) F. King, P.Eng.^a, Peter Cain, Ph.D., P.Eng.^{b*}

^a R.F King and Associates, Brentwood Bay, BC, Canada, V8M 1A8

^b Director of Engineering, DMT Geosciences Ltd., Calgary, Alberta, Canada, T2R 0E4

ABSTRACT

Certification of electrical equipment for underground coal mines in Canada is problematic. EX protected electrical distribution equipment to Group 1 standards is not manufactured in Canada, and even if it were, there is no facility in Canada that is accredited to certify it. The Canadian Federal laboratories previously tasked with the job are now closed. Provincial regulations require certification by either a now-defunct facility or by the US authorities (MSHA). Unfortunately the underground coal legislation in the US is significantly at odds with Canadian Provincial legislation and equipment approval requirements, which presents problems with equipment certified there.

Although the underground coal mining industry in Canada is small, the western Provinces are blessed with substantial resources of high quality steel-making coal, much of which can only be accessed by underground mines. There are perhaps half a dozen large underground projects awaiting a price revival in Alberta and British Columbia, and it was the authors' experience at one of these projects that led to this paper.

The project in question was owned by a Chinese company that wanted to use Chinese electrical distribution equipment certified in China to IEC equivalent standards. The process of convincing the Provincial regulators that the Chinese equipment was safer than the equipment that would be allowed under Canadian standards was arduous, but ultimately successful. The next step was to seek changes in the Canadian electrical standard applicable to mines so that the benefits could be felt across the country. This has recently also been accomplished.

This paper examines the problem through an important aspect of electrical safety in underground coal mines - protection against electric shock and arcing. It compares the requirements of the Canadian legislation, US, and UK legislation and IEC standards used by other countries.

It concludes that the levels of safety against shock and arcing afforded by IEC-certified multi-point systems can be orders of magnitude better than the single point systems mandated or traditionally used in Canada. Additionally, multi-point systems may be better suited to protect high voltage equipment beginning to be deployed in large open pits than the current Canadian protection standards. The recommendations arising for changes to Canadian standards await ratification, and the authors are hopeful that they will be adopted by Provincial regulators as soon as practicable.

KEYWORDS: ground fault protection, equipment certification, hazardous locations, electrical standards.

1. INTRODUCTION

The Canadian underground coal mining industry has a long history, although currently it is almost extinct. However, Nova Scotia and the western Provinces of Alberta and British Columbia still hold valuable resources of steel-making coal, much of which can only be accessed from underground. There are perhaps half a dozen large underground projects awaiting a price revival in Alberta and British Columbia, and it was the authors' experience at one of these projects that led to this paper.

The major underground mining Provinces, Nova Scotia, Alberta and British Columbia have developed their own safety legislation in response to their history of mining tragedies and the idiosyncrasies of their underground mines. These safety codes rely on

underlying safety standards developed and updated as required by stakeholder committees struck by the Canadian Standards Association. The safety of electrical installations in mines, including underground coal mines, in Canada is governed by CAN/CSA M421-11 "Use of Electricity in Mines" (CSA, 2011).

M421 sets out the standards which electrical equipment must achieve and requires that equipment used in underground coal mines either be certified by a certification organization accredited by the Standards Council of Canada in accordance with the requirements of a CSA Standard (or another recognized document when an applicable CSA Standard does not exist) or it must meet the requirements of the authority having jurisdiction.

Provincial regulators require that the certification be issued by the long extinct UK Ministry of Fuel and Power, the Canadian Explosive Atmospheres Research Laboratory, which no longer provides certification services, or MSHA in the USA.

Thus, certification of electrical equipment for underground coal mines in Canada is problematic. EX protected electrical distribution equipment to Group 1 standards is not manufactured in Canada, and even if it were, there is no facility in Canada that is accredited to certify it. The Canadian Federal laboratories previously tasked with the job are closed. Unfortunately the underground coal legislation in the US is significantly at odds with Canadian Provincial legislation and equipment approval requirements, which presents problems with equipment certified there.

2. BACKGROUND

An underground coal project in NE BC provided the initial impetus for a re-assessment of the Canadian standards and certification requirements. The Chinese owners wanted to import Chinese equipment to use in the mine. The equipment was certified in China to Explosion Protected IEC Group 1 Standards (gassy mines) by laboratories in China accredited under ISO/IEC Standard 17025.

Certification to IEC Group 1 (gassy mines) Standards can be achieved using most internationally recognized explosion protection technologies, for example: explosion-proof or flame-proof “d”; intrinsically Safe “i”, or increased Safety “e”, among others.

The electrical classification of underground coal mines internationally is varied. In some jurisdictions a zoning system is required and is defined, in general, to similar requirements of Section 18 of the CEC, although there can be differences dictated by the authority having jurisdiction; other provinces in Canada and other countries allow only equipment certified to Group 1 standards to be installed in underground coal mines. In 2004, Alberta allowed the application of the CEC zoning system to be applied in underground coal mines.

The Canadian Standards Association has adopted these technologies and applies them to their surface hazardous location (Group 2) certification requirements. The technical requirements of these categories are detailed in the CSA and IEC 60079 series of Standards.

There are significant differences between MSHA and other international “Explosion Protection” standards for Group 1 applications, although in general they achieve the same levels of safety; MSHA only recognize “explosion proof” and “intrinsically safe” technologies in underground coal

mines, although they do legislate a form of “increased safety” and apply it to battery installations on “permissible” machines. The underground coal mine is divided into two areas or zones, namely “permissible” and “non-permissible”. Equipment inbye of the last fresh air cross-cut is required to be certified to their EXP and I.S. standards while equipment outbye in the fresh air is generally to industrial standards.

The British Columbia Health, Safety and Reclamation Code for Mines (HSRC, 2008) only accept equipment certified for use in gassy mines by the Canadian Explosive Atmospheres Laboratories (NRCAN) and the Mines Safety and Health Administration in the United States (MSHA). Since NRCAN no longer certify electrical equipment for use in gassy mines, and EX protected electrical distribution equipment to Group 1 standards is not manufactured in Canada, and the underground coal legislation in the US is significantly different to Canadian provincial legislation and equipment approvals, it has proved necessary to review other international standards for equipment produced and imported from countries other than the US.

Notwithstanding the fact that the Chinese equipment had not been certified by authorities recognized by the Provincial regulators, there were also questions raised about the ground fault protection methods used on the equipment which were very different from those which have become commonplace in Canadian underground coal mines. This prompted a detailed review of the ground fault (earth leakage) protection systems incorporated into the switchgear and transformer assemblies to determine if it could be used under a variance to safety codes on the grounds of “equal or greater safety”.

3. GROUND FAULT PROTECTION

Ground fault protection systems in underground coal mines have been developed to a far greater degree of safety than the rest of the mining industry due to the many hazards associated with mining in gassy atmospheres; the sophistication, sensitivity and speed of operation of the two systems discussed below are designed to eliminate the electric shock hazard produced by ground fault voltages completely and to limit ground fault energy levels to reduce the possibility of gas ignitions due to damage or malfunction of electrical equipment.

The two systems are:

1. Single point (SEL)
2. Multi-point (SEL)

Both systems have been used extensively in underground coal mines since the early 1960’s and have proven to be reliable and effective in reducing

electrical incidents; the systems are unique and cannot be interconnected or mixed in any way without affecting their safety levels and/or rendering the protection systems inoperative.

The review of IEC certified equipment from China recently installed in a BC underground coal mine shows significant differences of electrical protection technology when compared to Canadian requirements set out in the Canadian mining electrical standard (CSA M421-2011). While the Canadian requirements generally apply themselves to single point high resistance neutral grounding systems, specifically referenced to achieving limits to ground potential rise due to ground faults, the Chinese earth leakage protection systems are based on the principals of a multi-point grounding system, developed in the 1960's by the National Coal Board in the U.K. These systems achieve greater sensitivity and speed of operation than the requirements of M421, and thus have a greater degree of safety in gassy atmospheres where incendive sparking from damage to electrical equipment is a distinct hazard.

The single point and multi-point grounding protection systems are described below and compared to the requirements of the Canadian standard.

3.1 Single Point Systems

The single point system of protection has, over the past 40 years or so, been adopted in Canada in the coal mines in Nova Scotia, Alberta, and British Columbia, and uses UK manufactured FLP transformers and switchgear. Some of this equipment, with protection systems based on the earlier relay technology, is still in use at the Quinsam Mine in Campbell River, BC.

Figure 1 shows a protection unit for high-impedance single point earthing systems and incorporates an earthing or grounding impedance directly coupled to the transformer secondary star point. The original value of this impedance was set to limit fault current to 0.25 ampere with a "solid" earth fault. The systems imported into Canada were designed to operate with a 5 to 10 amp current limiting reactor connected to the star point of the FLP transformer. When an earth or ground fault occurs on the system, the flow of current to ground unbalances the three-phase system and the resulting unbalanced currents are detected by a core balance transformer, or zero sequence current transformer, causing the protection unit to trip.

Of note is the search circuit or look ahead circuit, which prevents closure onto an existing fault after the unit has tripped.

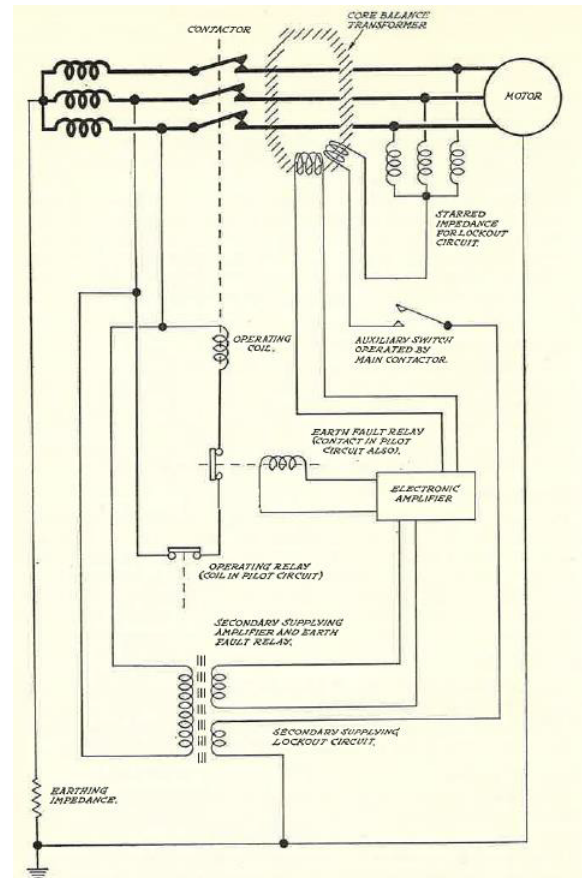


Figure 1: Typical Single Point Earthing System (after NCB, 1976).

3.2 Multi-Point Systems

In multi-point systems the transformer neutral is left "free" and is not directly grounded (Figure 2); each transformer secondary and each section switch and motor control switch protection unit is fitted with a starred impedance connected across the power conductors and the star point or artificial neutral is connected to ground through a further high impedance.

When a ground fault occurs on the system, return paths for the fault current are provided by the ground conductors on the system and the derived neutral impedance of each protection unit, and there are as many ground return paths as there are units on each system. The fault currents are limited to a level that cannot produce heating and any incendive sparking is confined to the area of the fault, and reduces the possibility of a shower of sparks. The ground fault current will pass through every detection circuit in each unit in operation on the system at the time the fault occurs; it can therefore be expected that every unit will trip, although this does not always occur in

practice. The unit feeding the ground fault is prevented from being re-energized onto the fault by a lock-out or look ahead circuit which cannot be reset if the fault still exists; other units operating on the system which may also have tripped can be restarted without any reset.

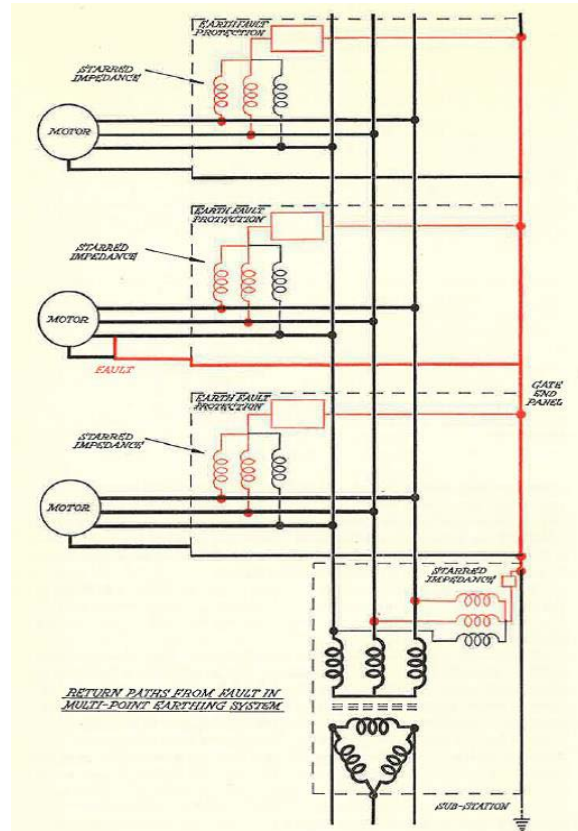


Figure 2: Typical Multi-Point Earthing System (after NCB, 1976).

The Chinese IEC certified units proposed for use in Canada utilize a starred impedance and signal amplifying system that is used to trip the primary switch feeding the transformer. They also include an earth leakage test facility built into the system which, when operated, connects a phase to ground through a 1K ohm resistor and facilitates regular testing of the protection system.

Both systems meet the standard. Given the superiority of the multi-point system and the lack of facilities to certify any overseas systems in Canada, a strong case is made to expand the scope of the Canadian standards so that Canada is not left behind.

4. SYSTEM COMPARISON

The CAN/CSA M421-11 standard requires that ground fault protection, where required, is provided through a neutral grounding device that limits ground fault voltage to 100 V or less and is de-energised in

less than 1 s if the ground fault current exceeds 20% of the prospective ground fault current. It should be noted that the standard refers to a “device” not a resistor, although another section of the Standard requires a “neutral resistance”.

An interpretation of certification requirements was that “neutral resistance” had to be a resistor lead to the initial rejection of the Chinese equipment proposed for use underground.

5. NEXT STEPS

Presented with two problems, namely an unfamiliar earth fault protection system and equipment that had not been certified by a listed agency, a program was developed to provide a means of allowing the BC Chief Inspector to allow the equipment to be used on the grounds of “equal or greater safety” under a process known as a “variance” to the written code.

This process involved visits to China by company consultants and inspectors working for the Chief Inspector. Meetings were held with equipment manufacturers, testing facilities, underground mines and regulators. The certification and testing standards were thoroughly reviewed and compared to the appropriate IEC standards.

During the analysis of the information, the CANMET Report “Equipment Approval Guide for Underground Coal Mining Equipment” (CERL Report 2009-19 (TR) was used to develop an approval process for the Chinese equipment that would ensure that it met the high levels of safety enshrined in the Canadian standards.

This guide specifically states that making a direct point-by-point comparison of the two certification schemes (IEC & MSHA) for explosion-proof protection is not easily accomplished. Each is considered an effective system, despite being developed independently. Although the approaches are dissimilar, both are technically valid and have a history of successful application, although the differences in approach to explosion-proof and flameproof standards, as well as the single and multi-point protection systems dictate that the two systems cannot be mixed.

Establishing that the approaches were technically valid was a major step in obtaining the variance. Perhaps more compelling was the argument that although M421 limits ground fault voltages in underground coal mines to 50 V with a maximum tripping time of 1 second when fault current exceeds 20% of the prospective ground fault current, the Chinese system, which is performance tested to the specifications of Chinese Standard MT/T 661 – 1997 limits ground fault voltage to less than 1 volt on

systems up to 1140 V, effectively eliminating the shock hazard, and tripping times of less than 100 ms.

The 10.5 KV systems are limited to less than 25 V ground fault voltage, currents are limited to a maximum of 6 amps, with tripping times of less than 100 ms.

The insulation (look ahead) monitoring system, which is designed to prevent closure onto an existing ground fault is set to trip at 20 k-ohms, and not allow reset and restoration of power until the insulation resistance has been raised to 40 k-ohms.

After a period of two years and much discussion, a variance to use the equipment in British Columbia was obtained.

6. CONCLUSIONS

A comparison of the single and multi-point systems discussed above does not favor one over the other; they are both proven technologies and have, for many years, operated throughout the international mining industries.

The single point system has one fault limiting device inserted directly into the supply transformer star point, the failure of which would render the protection system inoperable which is why neutral grounding resistors are required to be continuously monitored. However, the multi-point system has a number of derived neutral grounding devices and ground paths in the system and thus has a degree of protection against failure of one protection unit.

The objectives of the ground fault protection requirements in CSA Standard M421-11 are to limit touch potentials (ground fault voltages) to tolerable levels (see Table 52 CEC) and to trip the supply in less than 1 second. Section 7.9.6 of M421 requires that ground fault voltage be limited to 50 V in underground coal mines. There is no consideration given to limiting the energy in ground faults to levels that reduce the likelihood of incendive sparking.

As the use of electricity in surface and underground mines expands and the size of distribution transformers is increased, it is becoming more difficult to achieve the GPR limits on single point high resistance grounded systems because of the increased magnetizing currents on the system which dictate the limits of prospective ground fault current. On some 72K V distribution systems to mining moveable equipment in Canada, due to the size of the supply transformers, up to 150A is the minimum that ground fault current can be limited to in order to achieve the 20% ratio between prospective current and trip settings.

Other difficulties are being experienced on installations where the resistance of the return ground path, due to the distances involved, cannot be maintained to achieve the required GPR limits. The

Potash mines in Saskatchewan are experiencing this kind of challenge and the “Petersen Coil” based system is being investigated for possible use in mines. The theory behind this resonant system is based on a tuned circuit and is widely used in Europe for HV transmission systems, where the source star point is grounded through a reactor sized to three times the system per phase capacitance. When there is a ground fault, the reactor tunes with the capacitance and the fault current is very small, therefore the GPR is small. For mining, ground conductor monitoring can still be done, as the cables are the same. Apparently these systems are used in mines in Europe and a few in the USA and are certainly worthy of further investigation.

The Chinese equipment installed in BC is not subject to the limits imposed by supply transformer size and maintains resulting touch potentials from a ground fault to less than 1 volt on the systems up to 1140 V thereby eliminating this electric shock hazard completely, and significantly reducing the potential for gas ignitions from electric arcs or sparks in the area of the fault. Tests conducted at the manufacturers in China on the 1140 V systems demonstrated tripping levels at less than 30 milli-amps in less than 100 ms. Ground fault limiting devices, which can include resistors, reactors, transformers, capacitors, and other components sometimes used in combination, are tuned to the cable range they operate on and can be adjusted to suit changes in the distribution system to achieve the most sensitive tripping levels.

7. RECOMMENDATIONS

The requirements for grounding systems in underground coal mines should be directed at limiting fault current rather than ground potential rise, where even at the present 50 V limit, current levels of 25 amps and higher can meet the requirements of the Canadian standard.

The Canadian standard would benefit from wording similar to the UK Approved Code of Practice, which stipulates that for power systems where there is a high risk of fire, shock, or ignition of flammable gas, limitation of the maximum prospective leakage fault current should be practiced. The fault current and its duration should be limited to as low a value as is reasonably practicable to minimize the risk of shock or damage leading to incendive sparking or arcing.

In addition to this change, reference to “resistances” for ground fault protection should be replaced by references to “current limiting devices”

All alternating current systems in underground coal mines should be subject to a maximum allowable ground fault current depending on their

location in the mine and subject to any Zoning or electrical classification requirements.

8. ACKNOWLEDGEMENT

The authors acknowledge the support of H.D. Mining International Ltd. of Vancouver BC who sponsored much of the review work described above.

The views expressed are those of the authors, and may not represent the views of their employers.

9. REFERENCES

CSA (Canadian Standards Association) (2011) M421-11 Use of electricity in Mines, CSA, Mississauga, 79p.

NCB, (1976) Colliery Electrician, National Coal Board, London. 338p.

Lobay, G. (2009) Equipment Approval Guide for Underground Coal Mining Equipment CERL report 2009-19 (TR) CANMET, Natural Resources Canada.

Improving shovel safety using SAFEmine's situational awareness technology

Marco de Werk^a, Todd Ruff^b

^a Engineering, Aecon Mining, Fort McMurray, Canada

^b Product Development, Hexagon Mining, Tucson, United States

ABSTRACT

Mining operations involve risks that can be controlled through engineering and process control. The human factor however, is extremely difficult to quantify and control. Best practices, proper rest, and a good work/life balance contribute to safer operating conditions, but there is no way of predicting when an employee has had a bad day. Impacts of external stressors that are beyond the control of the employer can be minimized by implementing safety technology such as Hexagon Mining's SAFEmine collision avoidance system. Technology is another layer of protection, but it does not give the desired outcome without proper implementation, business processes, and continuous effort to improve. Aecon has successfully completed a pilot project with the SAFEmine system and has committed to operating a 5500 shovel and supporting dozer with the system. This paper aims to outline the process and results obtained during the pilot project.

KEYWORDS: Collision avoidance; shovel pit safety; equipment safety; safety equipment

1. OBJECTIVE FOR INSTALLING SAFEMINE

Safety first is Aecon's #1 core value and a recent metal-to-metal contact incident has been driving changes to mine pit safety. In a mining operation the pit involves the largest number of variables in generally the smallest physical space. A shovel, dozer, trucks, and light duty vehicles all interact in a congested, but organized fashion. The cleanup dozer is exposed to the highest risk factors in the pit, as it works in close proximity to a large shovel that has numerous blind spots. Operator situational awareness plays a crucial role in pit safety, yet situational awareness is greatly impacted by the operator's state of mind. External stressors that cannot always be controlled or monitored by the employer are impacting pit safety directly. Using technology to enhance the operator's awareness and provide an additional layer of protection can help mitigate many of these risks. There are three main areas of risk that were looked at to be reduced by using a collision avoidance system:

1. Shovel and dozer interaction
2. Shovel and pit feature interaction
3. Light vehicle and shovel interaction

Proper business process controls can help define safe movement of the dozer in relationship to the shovel; however, the human factor can sometimes interfere with the business process. Reduced focus or constant repetition of the same scenario can put the shovel

operator at risk of moving the shovel towards the dozer when business process prohibits this movement. At the same time, the dozer operator can enter the swing radius of the shovel without following the established business process. If both the shovel operator and dozer operator could be made aware when such an event occurs it could prevent a metal-to-metal contact.

The second risk is impact between the mining face and the shovel body. Generally, every precaution is taken to allow for sufficient room, but some situations are challenging due to design constraints or the sinking of a new bench. An experienced operator will be aware of the swing radius, but the mining face might contain ground water or frost that can cause small collapses during regular operating of the shovel. If such collapse occurs during the swing motion of the shovel, it is nearly impossible for the operator to recognize this. A system that can detect objects and alert the operator about the changes in his/her surroundings increases situational awareness, reduces possible contact between equipment and surroundings, and thereby increases pit safety and production.

Light vehicles enter the pit throughout the day for surveying operations, shovel inspections and servicing. Light vehicles can easily be overlooked compared to the size of the equipment around them in a mining operation. The shovel operator controls the pit and the access to the pit, however the shovel operator cannot always see all the traffic that is moving in the pit. If the shovel operator were to

know, at all times, where all light vehicles are that enter the pit, this would help ensure that no light vehicles are in the operating area of the shovel when it starts moving after service, inspection, or a break. The situational awareness gives the shovel operator an additional layer or “last line” of defense.

The SAFEmine configuration selected by Aecon does not require the complete fleet to be outfitted with a SAFEmine system. While the focus was mainly on the three scenarios described above, other vehicles, such as haul trucks, were also detected by the system on the shovel. The radar portion of the system provides information on proximity at which the trucks spot relative to the shovel. Once the shovel swings towards the face, the radar on the near side of the shovel will pick up if the truck is spotted too close. This was a benefit of the system, but it was not part of the scope of the evaluation.

2. SAFEMINE CAS SYSTEM

Hexagon Mining’s SAFEmine Collision Avoidance and Traffic Awareness System (CAS) provides vehicle and equipment operators with information concerning the location of nearby vehicles and provides an audible alarm if an approaching vehicle is on a collision course.

Using GPS, the system determines the location, speed, and heading of the vehicle in which it is installed, and transmits this information to other nearby vehicles, along with vehicle ID, using a vehicle-to-vehicle radio network. Sophisticated algorithms constantly monitor vehicle traffic to determine if a collision is likely. An audible alarm is generated only if two or more vehicles are at high risk of collision, which greatly reduces nuisance alarms.

The system monitors the full 360° around the vehicle and vehicle locations are indicated on an LED display (Figure 1) or on a graphical display called ScopeScreen (Figure 2).



Figure 1: SAFEmine LED display showing vehicle locations and distances (e.g. green LED indicates a vehicle to the left at 100 m, red LEDs indicate vehicles behind and to the right at 50 m).



Figure 2: SAFEmine ScopeScreen showing TopView for nearby traffic information.

The standard SAFEmine system consists of: 1) an antenna unit that houses the GPS, vehicle-to-vehicle radio, and WiFi antennas (Figure 4, top); 2) the main processing unit and receiver (Fig. 4, left); and 3) the remote LED display (Figure 4, right). These are the typical components installed on light vehicles, haul trucks, and other secondary heavy equipment. For the Aecon application, light vehicles and dozers were outfitted with this system.



Figure 4: Hexagon Mining SAFEmine system components.

The system provides two main functions: traffic awareness and collision avoidance. Traffic awareness gives the operator an indication of nearby equipment, but no audible alarms are generated. This information is displayed using the LED display or ScopeScreen and is meant to improve situational awareness (Figure 5). The collision avoidance function provides audible and visual alarms when two or more vehicles are on a collision course. This is determined using Dynamic Safety Zones which extend in the vehicle’s direction of travel and are adjusted according to vehicle size, type, speed, heading, and braking distance. If two vehicles are approaching each other and their Dynamic Zones intersect, then a collision alarm is generated (Figure 6).



Figure 5: Traffic awareness function provides the operator with location and distance to nearby vehicles.



Figure 6: Collision avoidance function provides audible alarms and visual indicators when two vehicles are on a collision course as determined by their Dynamic Safety Zones.

3. CAS FOR SHOVELS

The SAFEmine ShovelCAS system installed on a shovel at Aecon differs from the standard CAS system in a few respects: a second CAS unit, called a Beacon, is installed on the rear of the shovel to provide improved heading information for machines that can rotate around a center point; radar sensors, called TrackingRadar, are installed around the perimeter of the shovel to provide precise location information of nearby equipment in the shovel's body swing radius; and the ScopeScreen is installed to show vehicle location and ID, along with radar alarms for body swing protection.

Other vehicles outfitted with the SAFEmine CAS system components, such as Aecon dozers, are shown on the shovel's ScopeScreen as an icon

representing that vehicle type, along with their ID number. Typically all vehicles in the mine are outfitted with the CAS system so collision avoidance is functional everywhere in the pit. However, Aecon's situation as a contractor is unique in that only Aecon-owned vehicles are outfitted. Other contractor or mine-owned vehicles that do not have SAFEmine installed are still detected by the TrackingRadar system if they enter the body swing radius of the shovel. An audible radar alarm warns the shovel operator of this critical encroachment (Fig. 7). This way all vehicles are protected in the loading area.

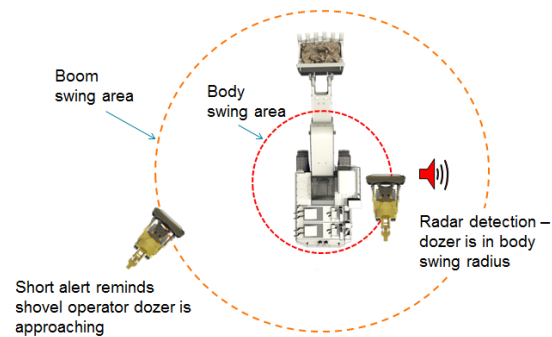


Figure 7: Example of the ShovelCAS functions for detecting a nearby dozer. Shovel operator receives short alert when dozer enters the boom swing area. A full collision alarm is generated in the shovel if the dozer is detected in the body swing radius.

4. EFFECTIVE SYSTEM IMPLEMENTATION

A safety system is a risk mitigation system that will reduce the likelihood of an event occurring. It is important to establish, prior to the project, what is considered "successful mitigation". Without putting a standard in place there is no measure of success. One of the key elements that has to be recognized with a safety system is that it is only "a system". The operational processes associated with the system are critical to a lasting change in operating safety.

Frequently, technology is seen as an answer to the complete problem, but this is rarely the case. With the SAFEmine system it is important to involve all levels of the organization with the solution and ensure that adequate checks and validations are carried out on a frequent basis. Aecon had to change its operational process by ensuring that all light vehicles that enter the pit on a regular basis were using the mobile SAFEmine units. The radars are inspected daily for damage and any damage is reported immediately to ensure the system can be repaired at the next available opportunity.

A system will only work if the operators are receptive to the solution that is being installed. Operators were made aware of the SAFEmine system prior to installation and its functionality was explained in detail. Providing a transparent and open dialogue about SAFEmine ensured that once the system was installed operators would be willing to give it a fair test. It is human nature to be opposed to change, but Aecon succeeded with open dialogue to have minimal hesitation by the operators to adopt the additional system.

The SAFEmine system installation was planned well in advance, minimizing delays during installation. During a major outage all wiring was pre-routed on the machine reducing the final installation time down to nine hours. Performing the installation in phases effectively eliminated interruption to production. The most important part of the installation is keeping in mind what repairs could be required once the system is activated and how to plan for simple replacements. Installing the radars on poles rather than welded plates for easy access has proven to be a major time saving solution (Figure 8).



Figure 8: Rear mounting locations for TrackingRadar (just below counterweight).

When running the required communication cabling, including connector locations, thought must be given to where the shovel will be disassembled for transportation - this facilitates future moves. Running wiring in locations where it will not need to be touched for regular maintenance, including component replacements, also decreases maintenance delays

The SAFEmine system was commissioned in a phased process to ensure that operators were adequately trained and alarms were verified. The initial deployment had all alarms silenced and daily downloads were completed to check the frequency of alarms. When radar alarms were excessive, radar parameters were adjusted to bring the alarm frequency down. After two weeks of adjusting and monitoring, all alarms were activated in the shovel

and dozer. At the same time an engineer was on the shovel to coach the operator on the alarms and make any required adjustments. It is critical to ensure that the alarms are meaningful for the operator so that alarms are acknowledged. If the alarms are configured incorrectly, the operator may ignore them and lose interest in the system, resulting in no additional layer of protection.

5. RESULTS AND KEY FINDINGS

The key objective of this project was to create a safer pit operation by providing the shovel and dozer operator with improved situational awareness. The system has been very well received by the operators from the start. The inclusive implementation strategy resulted in minimal negative feedback. Minor adjustments had to be made to the alarm settings to ensure that alarms in both the shovel and the dozer were meaningful and correctly indicated risk.

Since the implementation of the SAFEmine system in January 2015, there have been no metal-to-metal contacts involving the shovel and dozer. No near misses have been reported either and no maintenance has been required on the system. Only semi-annual verification has been done on the system.

The largest impact that has been observed is the change in shovel operator behavior. When truck drivers spot the truck very close to the shovel, they say that it increases production by reducing the amount of boom travel that is required per bucket dumped. But this also increases the risk of contact. In the months post-deployment, the radar system detection range was slowly extended to allow for a safer separation distance (just beyond the counter weight swing radius); however, the observed alarm frequency was reduced. This shows that shovel operators are loading the trucks farther away from the car body to avoid alarms and thereby reducing the risk of accidental contact between the truck and shovel. This change in behavior has had no negative impact on production.

Using the GPS-based portion of the system, the shovel operators can see at all times where the cleanup dozer is located. The additional situational awareness has been described by all shovel operators as “a great tool” and “a must for all pits”.

The SAFEmine system has created a safer work environment for Aecon, however it is absolutely paramount that proper procedures are in place and adhered to. Any safety system adds a layer of protection, but it will not guarantee no metal-to-metal contact.

An evaluation of Soma underground coal mine disaster with respect to risk acceptance and risk perception

H. Şebnem Düzgün^a *, Evren D. Yaylacı

Department of Mining Engineering, Middle East Technical University, Ankara, Turkey, 06800

ABSTRACT

The underground coal mine disaster that occurred in Soma-Eynez Mine (SEM), Turkey, is one of the largest coal mine disasters of this Millennium. A fire suddenly started in the mine and could not be controlled, resulting in 301 fatalities and approximately 100 injuries. Although the cause of the fire has not yet been determined and there are various hypotheses related to the ignition of the fire, most of the casualties were mainly due to decision-making related problems in various hierarchical levels. Moreover, the decision making related problems in the emergency management have cascading effects and impacts on the casualties, and are related to risk acceptance and perception of the mine management. In this paper, the casualties of Soma Mine Disaster (SMD) are analyzed in terms of risk acceptance and risk perception in order to establish related guidelines for better decision-making practice in case of emergencies in underground mines in Turkey. It is found that quite a high degree of risk was accepted for mine fires by the high-level decision makers, which led mine employees to have a false safety perception. This also resulted in almost full ignorance of self-escape, inappropriate use of personal safety equipment, and unstructured emergency management which yielded large number of mine staff to wait in the mine during the fire instead of a quick implementation of the mine evacuation plan.

KEYWORDS: risk perception, risk acceptance, underground coal mining, Soma Mine Disaster

1. INTRODUCTION

Coal mining, especially underground operations, is still one of the leading sectors in terms of occupational incidents and illnesses, injuries, and fatalities. The US statistics show that fatality rate per 100 000 full-time equivalent workers in coal mining is almost 1.5 times more than in metal and nonmetal mining and 6 times more than other industrial activities. Additionally, coal mining has the highest rate of non-fatal injuries among all types of mining operations. More specifically Margolis (2010) states based on Bureau of Labor Statistics in the USA in 2007 that underground coal mining has considerably more injuries than surface coal mining operations.

As compared to mine fires, explosions, use of explosives, dust and colliery explosions result in a higher number of fatalities in coal mines in the USA, as they are sudden onset incidents. For example, 10,390 fatalities were recorded as a result of 420 explosion related incidents. On the other hand, 727 fatalities were recorded in 35 mine fires in coal mines in the USA between 1900 and 2006 (CDC, 2009). Between 1983 and 2013, 647 fatalities were recorded in Turkey as a result of 18 major mining incidents (i.e. incidents causing more than three fatalities) and only one of these incidents was a mine fire, caused 19 fatalities and occurred in a metallic mine in Turkey (Düzgün, 2015).

While the number of fatalities due to fires has always been lower than the casualties of explosions among mining accidents since the 20th century both in Turkey and around the world, the Soma Mine Disaster (SMD), which occurred due to a fire in the underground coal mine and caused 301 fatalities, is unique in this respect and requires further investigation. Considering the complex nature of the SMD, where the fire resulted in cascading hazards, various factors were involved in the high number of casualties. Among them, socio-technical factors like unstructured organizational and human performance as well as inadequate safety culture play critical roles (Leveson, 2011).

Risk perception is one of the key parameters in safety culture development as well as effective human and organizational performance. In this paper the role of risk perception and acceptance in cascading hazards after occurrence of the fire in Soma-Eynez Mine (SEM) and the amplified number of fatalities in the SMD's case are analyzed.

2. RISK PERCEPTION AND ACCEPTANCE

Although there are various definitions of hazard and risk (e.g. ISO Guide 73:2009, UNESCO), in this paper the definitions used in natural disaster risk are adopted due to the nature of the SMD.

*Corresponding author – email: duzgun@metu.edu.tr

In quantitative risk assessment (QRA) risk is the multiplication of hazard and its consequences. Hazard is the probability of danger for a given place in a specified period of time. In the SEM case, hazard can be simply defined as the frequency of annual mine fires. The consequences of the mine fires can be listed as production and equipment losses, injuries, and fatalities. Hence the level of risk is controlled by the hazard and its consequences, which should be considered in determining effective risk assessment and management strategies for a safe mine operation. Risk assessment refers to the computation of risk and evaluation of it based on certain acceptability/tolerability criteria (Düzgün and Laccase, 2005). Therefore, understanding the nature of mine fire risks and their systematic management as well as associated uncertainties are key factors for risk acceptance.

Risk perception plays a vital role in the establishment of risk acceptance criteria for mine safety management, because an individual's behavior highly interacts with the degree on his/her perception of danger, professional and personal objectives, and his/her contacts within the organization (Badri et al., 2013). Moreover, risk perception is highly related with behavioral factors of mine executives and employees in the framework of organizational safety behavior (Zhao et al., 2016). Consequently, understanding the behavioural factors is significant for reduction of risks, as behavior based safety is one of the major contributors to accident prevention and risk reduction (Paul and Maiti, 2007).

Various hazard assessment methodologies based on several parameters, such as machinery, housekeeping, geotechnical data, age, experience, frequency, physical and environmental conditions, etc. are proposed in the literature (e.g. Düzgün and Einstein, 2004; Sarı et al., 2004; Coleman and Kerkerin, 2007; Margolis, 2010), as well as risk assessment methods (e.g. Düzgün and Einstein, 2004; Khanzode et al., 2014). Recent works on the determination of optimal evacuation routes in case of mine fire for underground coal mines (e.g. Klote, 2002; Adjiski et al., 2015) have potential for development of effective risk mitigation strategies for mine fires. However, despite the well-developed methodologies for hazard and risk assessment, the risk acceptance and perception is rarely taken into account in underground coal mining, which also plays critical role in risk mitigation.

Rohrmann (2008) defines risk perception as the individuals' judgments and evaluations of hazards. The occupational risks and mitigation methods differ for the sectors and sectorial stakeholders, including the individuals, operational, and regulative institutions/decision-making bodies.

Therefore, it should be expected that understandings of each stakeholder are variable and subjective (Rohrmann, 2008). Hence, different socio-psychological factors such as fear, culture, education, norms, value systems, society, experiences, and type of hazard and knowledge affect the risk perception of individuals and organizations (Zhao et al., 2016; Rohrmann, 2008). Furthermore, these factors are highly related with the risk acceptance and risk behavior of diverse stakeholders (Rohrmann, 2008).

Osei et al. (1997) and Renn (1998) lists factors influencing risk perception and acceptance:

- being voluntary vs. involuntary
- controllability vs. uncontrollability
- familiarity vs. unfamiliarity
- short vs. long-term consequences
- presence of existing alternatives
- type and nature of consequences
- derived benefits
- presentation in the media
- information availability
- personal involvement
- memory of consequences
- degree of trust in regulatory bodies

Voluntary risks (e.g. cigarette smoking) tend to be higher than involuntary risks (building a new chemical plant). Once the risk is under personal control (e.g. driving a car), it is more acceptable than the risk controlled by other parties (e.g. traveling as a passenger). In case of mine fires, for coal mines having frequent fires due to spontaneous combustion propensity of the coal, management may be more willing to accept it. Hence mine management experiencing frequent fires may have different risk acceptance than those experiencing rare fire situations.

Moreover, having frequent mine fires and mitigating them successfully may lead to accepting higher fire risks due to personal involvement and controllability. The risk acceptance also depends on for example level of available information. Informed mine workers can have better preparedness for mine fires when they have fresh memories of the consequences. In this paper, these factors are taken into account in order to analyze perceived and accepted risk for the SMD case.

3. BRIEF DESCRIPTION OF SOMA-EYNEZ MINE (SEM) AND THE INCIDENT

Soma coalfield, located in the Aegean Region in the western Turkey, is one of the first reserves with Seyitömer coalfield, explored in Turkey after the establishment of MTA in 1935 (Ediger et al., 2014). The coalfield is one of the most economically

valuable lignite resources with around 600 million tonnes reserve in 11 different locations (Bilgin et al., 2015). Soma coalfield has higher calorific values with Tunçbilek coalfield compared to other lignite reserves in Turkey; the calorific values vary from 2080 to 3340 kcal/kg (Ediger et al., 2014; Bilgin et al., 2015).

Soma-Eynez Mine (SEM) is one of the underground mining operations in the Soma coalfield and the mining activities have three operational periods. The first one is the period of Turkish Coal Enterprises (TKİ), the state-owned mining company, which covers between 1990 and 2006. In this period the mining operations were conducted in seven underground mines, including the Eynez operation. The state-own period in the SEM ended in 2006 after the privatization of the mine for a period of 10 years with a planned production of 15 million tonnes (Union of Turkish Bar Associations, 2014). The private company, Park Teknik A.Ş., operated the SEM between 2006 and 2009 (the second period). After production of 0.852 million tonnes of lignite in three years, the company applied for the termination of the contract due to the technical problems and operational difficulties in the SEM. As a result, the third period in the SEM started in 2009 after signing the transfer agreement among the parties with TKİ as the license owner, Park Teknik A.Ş. as the company willing to end its operations in the SEM, and Soma Coal Enterprises A.Ş. as the private company willing to take over the SEM to produce the 14.1 million tonnes of lignite for seven years (Union of Turkish Bar Associations, 2014).

In this third period, the production is performed by conventional, semi-mechanized, and fully-mechanized systems. Conventional and semi-mechanized systems have mostly short face lengths of 40-70 m, and coal is extracted with pneumatic hand drills and explosives and moved with the face conveyors. The main difference between the conventional and semi-mechanized systems is the type of support, where hydraulic and timber supports are used in semi-mechanized and conventional systems, respectively. Coal is extracted by a drum shearer and loaded into armed face conveyor with longer face lengths in the mechanized system (Sari et al., 2004).

The coalfield has three seams, namely, upper-KP1, lower-KM2, and middle-KM3 (Hokerek and Ozcelik, 2015) with thickness ranges of 7-8 m, 15-35 m, and 6-10 m, respectively. Because of the thickness of the coal seams, longwall top coal caving (LTCC) is adopted. The simplified mine layout is given in Figure 1.

In 2014 the production in the SEM, were based on five panels with 10 production faces. The mining

method, adopted in each face in the SEM, is given in Table 1.

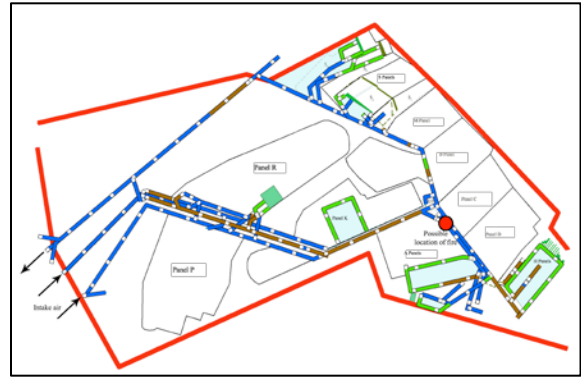


Figure 1: Mine layout for the SEM.

Table 1: List of the mining method in each face in SEM.

Panel	Face	Type
A	A1	Semi-mechanized
A	A2	Fully-Mechanized
H	H1	Semi-mechanized
H	H2	Semi-mechanized
S	S2 upper	Semi-mechanized
S	S2 lower	Conventional
S	S3 upper	Semi-mechanized
S	S3 lower	Conventional
R	R7 (East)	Fully-mechanized
K	140	Conventional

Due to the spontaneous combustion propensity of the coal, ventilation rate was kept around 2300 m³/min. Moreover, coal seams in Panel A contained a considerable amount of methane (Erdoğan, 2015). The SEM worked in three shifts with approximately 800 workers per shift.

On May the 13th, 2014, a fire started between 14:40-14:45 in the roof of the main road (Figure 1) and ignited the wooden pieces used for fixing steel sets. Due to the existence of methane, the upper part of the belt conveyor also ignited. The possible location of the mine fire (Figure 1) is the point where the conveyor number 4 conveys materials to the belt number 3. The airflow was quite slow to the point of almost being stagnant and there were no methane detectors in this area. Therefore, it is not possible to find out whether there was an accumulation of methane here that would trigger or contribute to the fire before it broke out.

The outbursting smoke and the smoke from the open flaming fire that broke out in the gallery combined and spread in a short time moving with high pressure through all the main roads to the A and H panels and in the main road to the S panel in the main ventilation direction of the mine. By the time the fire started (14:40-14:45) there was an electricity blackout in U3 area (Figure 1), belts stopped, and

intense smoke appeared on the main road of the belt conveyor number 4 and evacuation team was requested to the accident scene. At around 15:00 smoke appeared in the A panel and at approximately 15:10 smoke first appeared in the main road of the H panel going to the S panel. At 15:20 smoke arrived at the first floor of the faces in the S panel. At this point fainting and deaths began. At around 17:00 the mine management decided to change the direction of ventilation, which was changed at around 17:30. Due to this change, 142 workers, who accumulated at the A panel area, where smoke was not effective, started fainting and some died. At around 20:20-20:30 the mine rescue teams reached the A panel area. The search and rescue operation took almost three days and the mine management was unable to announce the number of fatalities until the research and rescue operations were finalized.

4. ANALYSIS OF THE SMD BASED ON RISK PERCEPTION AND ACCEPTANCE

In order to understand the accepted risk levels and risk perception by the SEM management, the decisions made during the onset of the fire as well as the emergency management activities should be considered. Moreover, the mine layout and mine operational conditions indicate risk perception of the mine management and organizations that approve and audit the mine operations.

4.1. Risk Perception and Acceptance Related to Decision Making and Emergency Management

Based on the testaments of the survivors in the case files, it can be clearly stated that the mine management did not make a decision of evacuation for the whole mine; rather, the decision of evacuation was made only for some parts of the mine. Almost all of the survivors of the SMD, were those who received an order to evacuate the mine based on the news of the fire and who left the mine immediately. Those who did not leave the mine and stayed behind lost their lives.

The principle of self-escape in coal mining, especially in mine fires, proves its validity. Although there were no records of the exact location of fatalities who were found by the rescue staff, based on the distribution of locations where the rescue teams accumulated the bodies for taking them to surface, the distribution of the fatalities in the mine layout can be predicted (Table 2).

Table 2: The distribution of bodies according to where they were collected before they were taken to the surface.

Panel	Number of Victims
S Panel and around	209
R Panel and around	10
140 Face	4
A and H Panels and Fire Zone	78
Total	301

Since the S Panel is located remotely in the mine layout (Figure 1) and clearly separated from other panels, it is obvious that most of the bodies kept here belonged to those who worked in this panel and its surroundings. Accordingly, 209 people lost their lives in this panel and its surroundings (Table 2). On the other hand, 78 people lost their lives around A and H panels. The low numbers of casualties in the R panel and around the 140 Face was because fewer people worked in these panels and those who worked there could evacuate the mine immediately after the fire broke out.

It can also be decisively said that the decision for evacuation of the S Panel, where the biggest number of deaths occurred (209), were not made. As it can be seen in the statements of the surviving victims in the case file, the safety engineers responsible for the S Panel did not allow workers in this panels to leave the panel. The main reason for not evacuating the S panel is related to the factors of familiarity and controllability. As the mine experiences frequent fires due to spontaneous combustion propensity of the coal, the mine management considered this case to be similar to previous cases and assumed they would be able to control it in a short period of time.

However, mine management ignored the location of the fire in the SMD, where it started in one of the main roads handling ventilation air intake with probable methane in the environment. The majority of the fires experienced in the past took place in the production faces, which were easier to mitigate. As these fires are always controlled, the fire of the SMD was also considered to be the one that could be controlled easily.

For this reason the engineers responsible for the safety of the S panel were not given inadequate information about the severity of the accident by the control center and the top management. Moreover, the ventilation of the S panel was serial ventilation, which does not allow the workers to take an alternative safe escape route. Under such a mine environment with the assumption of the controllability of the fire, the decision for keeping workers in this area rather than evacuating the mine was considered to be the best option.

This decision is in fact related to the risk acceptance parameter of the presence of existing alternatives (unavailability of alternative escape

route), and derived benefits (assumption of safer faces than the main road full of smoke). It was most probably thought that the fire would soon be taken under control, so the workers should wait. It was assumed that the workers might be exposed to smoke while evacuating the mine before the fire was controlled, and their masks would not function sufficiently during evacuation.

For this reason, the engineers fought against the smoke by blowing clean air to the faces in the S panel using the compressed air pipes so that the workers in the S panel faces would not get affected by the smoke. However, they all died during this action.

The information availability and personal involvement aspects of risk acceptance emerge when the actions of executive mine management are examined. All the top management bodies that had heard about the fire entered the mine and were trying to reach the scene of the fire, in order to increase the level of information availability. This prohibited the effective application of an organized emergency management and evacuation plan.

In other words, instead of focusing on evacuating the mine safely and implementing emergency management, they tried to respond to the fire, which is directly related to personal involvement of the risk acceptance. In fact, some of the workers of the following shift, who did not know about the fire, entered the mine and lost their lives due to inefficient emergency management.

4.2. Risk Perception of the Mine Management and Organizations for Approval of the Mining System

The S and H panels are ventilated by means of serial ventilation. The workers, who were working at the H panel, learned about the fire since they were very close to the fire were informed about the decision to evacuate the mine. This decision was probably conveyed to the H panel by the safety engineer, who was in that area and took the first precautions to ensure the safety of workers after the outbreak of the fire. Some of those workers working in the H panel could not leave because of the smoke, but they waited safely first in the A panel area and then in this area, which were nearby and ventilated through parallel ventilation.

Construction of a second ventilation gallery for the S panel was planned in 2012, but this was not realized. Without doubt, if this gallery had existed at the time of the incident, workers could have been saved. As A panel was ventilated by parallel ventilation system, it allowed safety engineers to make a short circuit with the use of ventilation doors in the A panel area to protect workers in this zone from the smoke. Since the H panel was close to A panel, the workers of the H panel were able to reach

this safe zone. It was not questioned by supervising institutions why this gallery, which had been planned in the mine since 2012 but had not been constructed.

Although risk assessment and emergency drills were conducted in the SEM, a fire that might occur in the main roadway was not among the anticipated risks. An effective drill in which all of the mine was evacuated was never performed. Therefore, the liability of all the institutions that checked and approved the risk assessment cannot be overlooked.

In the SEM, the production increase (from 1.5 million ton/year to 3 million ton/year) was realized before the ventilation system was improved. Hence, all the institutions who approved such a production increase, before the ventilation conditions were improved in the mine, accepted a high level of risk, which is mainly associated with the short/long-term consequences. The long-term consequences of such a decision were ignored and trust for the regulatory bodies led all the organizations to take a high level of risk.

The production increase also brought about increases in the labor force in the mine since the production was mainly dependent on semi-mechanized and conventional systems. Among the 10 production faces, only two operated in a fully mechanized system. Risk is the combination of probable losses when a hazard occurs. In other words, even if the danger is slight, the risk is still high if the losses that will occur are significant. Therefore, the high number of workers in the S panel had already increased the risk level of the SEM.

5. RESULTS AND DISCUSSION

The production with high risks in the SEM was in fact supported by the legislation prior to the accident. The legislation was renewed shortly before the SMD and details about the actions to be taken for safety were removed. The new legislation had some general statements that stipulated that the mine enterprise should take any precautions necessary. With this legislation, internal and external bodies making audits in the mine were also unable to report problems related to mine systems threatening safety. Though there are such legislations available around the world, standards or protocols have been developed for their implementation. Hence audits are performed based on whether these protocols are followed or not.

In Turkey, specific sections in the old legislation were taken out without developing such protocols for both coal mining and other types of mining, and the legislation containing the general statements valid before the accident resulted in risks being taken more easily. Unfortunately, the amendments made in the legislation following the disaster are not sufficient to

improve the safety conditions in current coal mines. Besides, any type of legislation enacted to improve safety cannot achieve the expected outcome without developing the standards or protocols, which has never been taken into account during legislation changes.

6. CONCLUSION

The reason why there was an extraordinary number of fatalities in the SMD was not the fact that a fire started in the mine, rather the decisions taken in the mine after the fire broke out. These decisions were made under the perceived risks, which were accepted despite their high level and caused a cascading impact of the fire due to the adopted mining system and management in the SEM. This also resulted in almost full ignorance of self-escape, inappropriate use of personal safety equipment, and unstructured emergency management that led a large number of mine workers to wait in the mine during the fire instead of implementing the mine evacuation plan. Therefore, regulations based on research on risk acceptance and perception of the mine management and organizational bodies is required for effective risk management in underground coal mines.

7. ACKNOWLEDGEMENT

The authors thank to Research Commission of the Grand National Assembly of Turkey, Turkish Bar Association and Chamber of Mining Engineers of Turkey for providing access to the data related to the incident, İlke Arıcan and Mahmut Çavur for their help in organizing the data and Bilge Çelik for editing the paper

8. REFERENCES

Adjiski V., Mirakovski, D., Despodov, Z., and Mijalkovski, S. (2015) Simulation and optimization of evacuation routes in case of fire in underground mines (in press), *Journal of Sustainable Mining*. pp. 1-11, <http://dx.oj.org/10.1016/j.jsm.2015.10.001>

Badri, A., Nadeau, S., Gbodossou, A. (2013) A practical approach to risk management for underground mining project in Quebec. *Journal of Loss Prevention in the Process Industries*, Volume 26, pp.1145-1158

Bilgin, N., Balci, C., Cpour, H., Tumaç, D. and Avunduk, A. (2015) Cuttability of coal from the Soma coalfield in Turkey. *International Journal of Rock Mechanics & Mining Sciences*, Volume 73, pp.123-129

Centers for Disease Control and Prevention (CDC) (2009) *Underground Coal Mining Disasters and Fatalities - United States, 1900-2006*. <http://www.cdc.gov/mmwr/preview/mmwrhtml/mm5751a3.htm>, date of access: 09.12.2015

Coleman, P. and Kerkering, J. (2007) Measuring mining safety with injury statistics: lost workdays as indicators of risk. *Journal of Safety Research*, Volume 38, pp. 523-533

Düzgün, H.S. and Einstein, H. (2004) Assessment and management of roof fall risks in underground coal mines. *Safety Science*, Volume 42, pp.23-41

Düzgün, H.S.B. and Lacasse, S. (2005) Vulnerability and Acceptable Risk in Integrated Risk Assessment Framework. *Proc. of International Conference on Landslide Risk Management and 18th Vancouver Geotechnical Society Symposium*, May 31 - June 4 2005, Vancouver, Canada

Düzgün S. (2015) Willful blindness: Soma Disaster. *Indecent Analyze Report*, not published, in Turkish

Ediger, V.Ş., Berk, İ. and Kösebalaban A. (2014) Lignite resources of Turkey: Geology, reserves, and exploration history. *International Journal of Coal Geology*, Volume 132, pp.13-22

Erdoğan, H. (2015) Coal and coal bed methane studies in Turkey. The United Nations Economic Commission for Europe (UNECE) Meeting, Geneva, web page: https://www.unece.org/fileadmin/DAM/energy/se/pp/coal/cmm/9cmm_gmi_ws/7_TURKEY.pdf, date of access: 15.12.2015

Hokerek, S. and Ozcelik, O. (2015). Organic facies characteristics of the Miocene Soma Formation (Lower Lignite Succession-KM2), Soma Coal Basin, western Turkey. *Energy Procedia*, Volume 76, pp.27 – 32

ISO Guide 73 (2009)<https://www.iso.org/obp/ui/#iso:std:iso:31000:ed-1:v1:en>, date of access: 20.02.2016

Khanzode, V.V, Maiti, J. and Ray, P.K. (2014) A methodology for evaluation and monitoring of recurring hazards in underground coal mining. *Safety Science*, Volume 49, pp.1172-1179

Klote, J. (2002) Principles of smoke management in Klote, J. and Milke, J.A. eds. *Principles of Smoke Management*, American Society of Heating, Refrigerating and Air-Conditioning Engineers Inc., USA, pp.87-111

Leveson, N.G. (2011), *Engineering a Safer World, Systems Thinking Applied to Safety*, The MIT Press, Cambridge MA; <http://mitpress.mit.edu/books/engineering-safer-world>, date of access: 20.02.2016

Margolis, K.A. (2010) Underground coal mining injury: A look at how age and experience relate to days lost from working following an injury. *Safety Science*, Volume 48, pp.417-421

Osei, E.K., Amoh, G.E.A. and Schandorf, C. (1997) Risk ranking by perception. *Health Physics*, Volume 72, pp. 195-203

Paul, P.S. and Maiti, J. (2007) The role of behavior factors on safety management in underground mines. *Safety Science*, Volume 45, pp.449-471

Renn, O. (1998) The role of risk perception for risk management. *Reliability Engineering and System Safety*, Volume 59, pp.49-62

Rohrmann, B. (2008) Risk perception, risk attitude, risk communication, risk management: A conceptual appraisal. The International Emergency Management Society Annual Conference, 17-19 June 2008, Prague, Czech Republic, web page: http://tiems.info/dmdocuments/events/TIEMS_2008_Bernd_Rohrmann_Keynote.pdf, date of access: 09.12.2015

Sari, M., Duzgun, H.S.B., Karpuz, C., and Selçuk, A.S. (2004) Accident analysis of two Turkish underground coal mines. *Safety Science*, Volume 42, pp. 675-690

Union of Turkish Bar Associations (2014) Soma Mine Disaster Report. Publication No:269, in Turkish UNESCO, Glossary of Basic Terminology on Disaster Risk Reduction, <http://unesdoc.unesco.org/images/0022/002257/225784e.pdf>, date of access: 20.02.2016

Zhao, D., McCoy, A.P., Kleiner, B.M., Mills, T.H., Lingard, H. (2016) Stakeholder perceptions of risk in construction. *Safety Science*, Volume 82, p.111-119

From operational hazards to organizational weaknesses: changing the focus for improvement

Georges Loiselle^a, Dragan Komljenovic^{b*}, Mustafa Kumral^c

^a Engineer; Hydro-Quebec Production, Canada

^b Researcher; Hydro-Quebec Research Institute (IREQ), Canada

^c Professor; McGill University, Mining Engineering, Canada

ABSTRACT

The daily operations in the mining industry are still a significant source of risk with regard to occupational safety and health (OS&H). Various research studies and statistical data world-wide show that the number of serious injuries and fatalities still remains high despite substantial efforts to decrease those numbers put in place by the industry in recent years. This paper argues that the next level of safety performance will have to consider a transition from coping solely with workplace dangers, to a more systemic model taking organizational risks into consideration. In this particular aspect, lessons learned from the nuclear industry may be useful, as organizational learning processes are more universal than the technology in which they are used. With the notable exception of major accidents, organizational performance has not received all the attention it deserves. A key element for reaching the next level of performance is to include organizational factors in low level events analyses, and approach management as a risk control system. These factors will then appear not only in event analysis, but also in supervision activities, audits, change management and the like. Many recent event analyses across various industries have shown that organizational factors play a key role in creating conditions for triggering major accidents (aviation, railway transportation, nuclear industry, oil exploitation, mining etc.). In the following paper, we will present a perspective that may be used in supervisory activities, self-assessments and minor events investigations. When ingrained in an organizational culture, this perspective has the highest potential for continuous safety improvement.

KEYWORDS: Occupational safety and health, safety culture, organizational performance, risk analysis and management

1. INTRODUCTION

The business and operational environment has changed considerably for the majority of organizations. One of the peculiarities of this change comes from the integration of various industrial, technical, political, economic, environmental, and financial pressures with regulatory adjustments ensuing from it (OECD, 2009, Homer-Dixon, 2011, Rzevski 2011, Komljenovic et al, 2015). The operation of these sectors, which were previously relatively autonomous and independent, becomes more complex as the number of stakeholders increases, including the advent of new technologies and interrelations between entities that are not anymore isolated and independent. A direct consequence of these changes is the nature of the events which continue to occur. While the accidents which arose previously generally found their cause in known and assumed factors,

modern events find their origin in unforeseen interactions between elements without visible links. The linear story-telling of events is thus less suited for improvement in conventional and public safety (Carrillo, 2011; Dekker et al, 2011; Homer-Dixon, 2011; Leveson, 2011). This diagnosis is not limited to major accidents but also applies to other types of events (such as process disruptions or bankruptcy). In this paper, we discuss the evolution of the nature of the causal factors, and talk about approaches and tools developed and used in the nuclear industry to take into account the complexity of its operational environment. This experience can be transposed to other industries, including mining.

2. THE CLASSIC VIEW OF AN EVENT: FAILURE OF A WEAK LINK

We are accustomed to simplistic story-telling of significant events and accidents. It is natural

to identify a barrier, which if it had worked adequately, would have prevented the undesired occurrence. The barrier analysis allows us to identify the less than adequate performance of defences and to propose specific corrective actions. Even more elaborate methodologies, such as MORT (Johnson, 1975), stands on the identification of independent administrative barriers in complicated organizational systems, but not necessarily complex interactions. This view of an event supposes some linearity (a time line) which could be representative of reality to a certain extent. Even if some aspects were not reflected by the analysis, the identification of some weak barriers remained good enough for effective actions. Today, for most situations, such a linear approach is insufficient to allow a complete and useful understanding of the stakes and challenges regarding safety (Carrillo, 2011; Dekker et al, 2011; Leveson, 2011).

3. A NEW SOURCE OF RISK IN THE 21ST CENTURY: THE ORGANIZATION

Our understanding of events has changed for one main reason: the nature of its contributory factors. The main source of risk today is the organization itself (DoE, 2009; Leveson, 2011; Kahneman, 2012; IAEA, 2013). Indeed, we can notice that many industrial accidents have essentially organizational components, such as the company's culture, safety culture, communication between groups, decision-making by people in authority, centralization and decentralization, organizational clarity, and several other attributes which are more a matter of collective than individual work (Perrow, 1999; DoE, 2009; Carrillo, 2011; Dekker et al, 2011; IAEA, 2013; Mosey, 2014). These new characteristics are consequences of the evolution of two things: the type of barriers which ensure a safe environment, and the new interrelations between entities that were previously isolated and practically independent. Barriers enabling safety of the operational activities evolved with both the complexity of the tasks and the multiplication of involved persons. The main consequence is to change redundant barriers into dependant and interrelated ones, and to make it difficult to anticipate weaknesses in these barriers, leading to failures. This trajectory is well pictured by the metaphor of the slices of cheese, where degradation propagates through holes in lines of defence. This picture is still adequate, but a sequential display of such an event is not so representative of the underlying reality anymore; lines of defence have no more

the same redundancy. A more appropriate model would rather present the situation as a degradation of margins, which locally would be individually acceptable but which, collectively, have important consequences that could not be anticipated by a local analysis.

This peculiarity brings us to certain characteristics of complexity. Complexity of the operational environment asks for an organizational answer adapted to face new stakes and challenges.

4. NEW STAKES AND CHALLENGES: COMPLEX INTERFACES

The technological evolution brings an important source of complexity. The automation of several processes conveys more opacity, with many control rules and new information technologies involved. One of the consequences of this situation is the necessity of increasing the technical training for the operator. This training is taken for granted during commissioning but invariably undergoes dilution in time, the in-service training being reduced to certain aspects more critical to health and safety.

Maintenance is another domain where training is often neglected. We usually believe that the procedures of maintenance prove the quality of the tasks output. This hypothesis is not unreasonable at the beginning of the operation of new equipment or system. However, experience shows us that we observe a degradation of conformity with time, with staff developing local adjustments and the management taking certain liberties with regards to the maintenance schedule. We slowly deviate from manufacturer's requirements without providing a new technical basis for changes. Indeed, because a decrease of maintenance does not necessarily cause immediate declining in performance, these deviations are tolerated and even sometimes reinforced because of their short term advantage.

The last element of the impact of these changes is the difficulty for the workers to anticipate the global behavior of all the systems components in interaction. The complexity is thus a matter of interactions between simple and relatively autonomous systems, which brings unexpected reactions of the whole, often amplified by the operator's actions erroneously adapted to those situations (Perrow, 1999; DoE, 2009; Carrillo, 2011; Dekker et al, 2011; Mosey, 2014).

5. COUPLING, COMPLEXITY AND NORMAL ACCIDENTS

This reality brings us to the concept of coupling and complexity introduced by Perrow (1999). In this model, the various types of industries have their characteristics mapped on two axes: complexity and coupling (Figure 1).

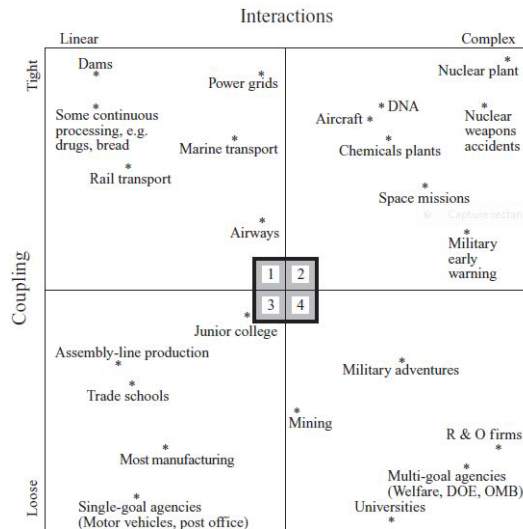


Figure 1: Interactions/coupling (Perrow, 1999).

Key attributes of complexity are related to the nature of interactions (interdependent components, common mode vulnerabilities, numerous feedback loops, multiple interacting controls, nonlinear reactions, phase transitions, indirect information, adaptability, phase transitions, etc.), and couplings (short delays, intolerance to variation, uniqueness of the sequence of actions, etc.). Thus, the complexity is associated with the strength of linkages between several autonomous constituent elements of a system that yield interactions that are difficult to grasp and anticipate. It creates an emergent system behaviour which is influenced by uncertain cause-and-effect relationships and unscheduled discontinuities (OECD, 2009; Dekker, 2011; Homer-Dixon, 2011; Rzevski, 2011; Komljenovic et al, 2015). Those interactions and characteristics create both significant uncertainties and overall opaqueness, which consequently make the operator dependent on indirect information reducing his capacity for immediate analysis and ulterior action.

These peculiarities highlight the importance of an organized situational awakening, which can be described as the capacity to estimate the anticipated effects in the short term following actions, and to at least ensure that obvious anomalies are quickly detected and corrected.

6. IMPACT OF THE NATURE OF RISK ON THE FUNCTIONS OF THE ORGANIZATION

Figure 1 shows that mining is an activity having complex interactions but loose coupling. This statement does not always apply to the management of tailing dams or underground coal mining, which may have tight coupling as an attribute. The characterization of an industry on Perrow's diagram also gives an indication of its organizational structure and work process requirements. An organization operating in a complex and strongly coupled operational environment has to pay attention to centralization and decentralization of the decision-making process (Rzevski, 2011). Considering the unique and irreversible character of particular event initiators, some decision-making in the field cannot allow delays. The chain of authority has to then be modified to allow a timely reaction, reflecting a global direction already known by the organization members (system behavior is too complex to enable a centralized real-time control). Thus, organization should have enough flexibility to be applicable in a large number of different and unanticipated situations. Such "on-the-spot" decision-making has to be supported by transverse (cross-functional) functions. The latter involves a participation of several ad hoc specialized units which can act in unison to realize an analysis by taking into account all the relevant aspects while facing an unforeseen situation.

7. HUMAN AND ORGANIZATIONAL PERFORMANCE MODEL

An organizational and human performance model has to be coherent, adapted and universal. The advantage of such a higher level model consists in enabling to share a taxonomy, which is common to event analyses, supervision, and planning an even safety and organizational culture. Indeed, operating experience can benefit a lot from a model that can be used in all activities, a must in pre-job briefings for the infrequent evolutions.

Strength of the model resides also in its capability to present events as complex interactions with several potential influences and not limiting itself to a unique sequence. It goes beyond the "simple" approach of redundant barriers, which gives a very linear reading of the events.

To err is human: The basic premise of human performance is that everyone is willing to

perform adequately and tries to fulfill his tasks to meet expectations. However, we all make mistakes and this cannot be avoided. These errors are basically predictable and controllable in many ways. Thus, their frequency may be reduced. An improvement in human performance means reducing the factors favourable to error occurrences. Given that they cannot be completely eliminated, one should limit their consequences (DoE, 2009; IAEA, 2013). Figure 2 provides an illustration of the elements that exist before a typical event occurs. Breaking the linkages may prevent events.

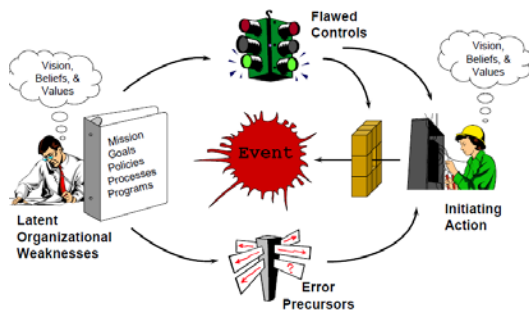


Figure 2: Anatomy of an event (DoE, 2009).

For events involving human performance, the most interesting aspect is the error itself. Not as a cause of an event, but as the event itself. In fact, both success and failure share the same mental processes and only the outcome differs. An error is considered as such because of the unwanted result it brings. The human error which generates an event is only a symptom for which we have to find the cause. In this context, an analysis will have to determine why the event happened (direct cause) and why it was not prevented (fundamental cause). That fundamental cause should question and target the organization (expanded fundamental causes). The direct cause is associated to preventive barriers, mitigating barriers, and error precursors.

The function of a preventive barrier is to preclude errors or lapses. Procedures, training, qualification, work practices are all preventive barriers and aim at reducing the number of errors. Mitigating barriers, on the other hand, aim to limit the consequences that may follow an inadequate action. Steel cap boots or inflating bags in cars are mitigating barriers to limit consequences of mistakes.

Precursors are sneakier. They include more or less subtle elements in the working environment, or invisible constraints within the task. Abnormal configurations or pressure to execute a task with tight deadlines are all

conditions which have a direct or indirect negative influence on the cognitive processes required for the safe execution of a task (DoE, 2009; Kahneman, 2012; IAEA, 2013).

Both supervision and the organizational oversight are processes designed for validating that barriers are adequate and efficient. Such as mentioned above, people in positions of authority ensure the adequacy of the measures in place to allow the orderly, secure and effective completion of the tasks assigned to the staff. This adequacy must be verified by an ongoing process to make sure that the required measures are well organized, that expectations are communicated and met, and that nothing invalidates the organizational hypotheses. Supervision is the real time twin of audit and oversight. If gaps are detected between expectations and observations, additional error prevention tools should be considered.

We call “organizational” the various factors that imply a collective behaviour. Communications, organizational clarity, and centralization of decision-making are examples of such factors. The weakness of one or several of these factors can compromise the quality of the activities and their products.

8. IMPORTANCE OF A MODEL FOR EVALUATING DEVIATIONS

As noted earlier, the notion of deviation or anomaly can vary significantly from an organization to another. However, this concept implies inevitably a model of conformity (to define non-compliances). For example, a lost time accident will initiate a formal causal analysis. The expectation then may be to identify failures and improvement opportunities under the influence range of supervisors. We shall thus ask the analysts to evaluate conformity in terms of procedure adherence, use of protective equipment, fitness for duty, and employees motivation. This first evaluation can then be completed by the evaluation of the qualification and the staff training, the profile of the actors (individual capacity to realize the tasks which are assigned to them) or the workload.

Such an approach thus considers implicitly an occupational incident as a possible although unwanted situation. Indeed, it does not question the organization and represents an implicit model which does not exclude such events because we already are expecting to handle such situations. We call that first loop learning, because the event does not indicate a loss of control (as it was

considered possible) and does not challenge the organization.

On the other hand, second learning loop involves investigating why an event was not prevented and what the organizational (fundamental) cause of the mishap is (Argyris and Schön, 1996). This part is a real challenge for management as it requires introspection and is often perceived as a self-blaming exercise. Nevertheless, it is an inescapable for root cause identification.

9. CASE STUDY

We will use the official MSHA report on Upper Big Branch Mine Accident to illustrate the model discussed above. On April 5, 2010, at approximately 3:02 p.m., a massive coal dust explosion occurred at the mine, killing 29 miners and injuring two (MSHA, 2011; NRC, 2012). The physical conditions that led to the explosion were the result of a series of basic safety violations and were entirely preventable. When violations of particular safety standards led to the conditions that resulted in the explosion, the unlawful policies and practices implemented by the owner were the root cause of this tragedy.

First, the preventive and mitigating barriers were not adequately implemented or maintained. Corrective action program (CAP) weaknesses led to understating assessed hazards. The basic training in non-compliance, hazard recognition, and prevention of accidents, roof control, ventilation, and new tasks was less than adequate. Tests for dust and methane were not consistently carried out. Those barriers, required for worker's health and safety protection, were not effective.

Precursors, on-the-spot factors that facilitates committing errors, were also numerous. For instance, conditions like not performing adequate pre-shift, on-shift, or weekly examinations were observed frequently. Numerous existing hazardous conditions were not identified, hence not corrected. Multi-gas detectors were often not energized, leading to less than adequate air measurements. Log wall shearers were not kept in safe operating conditions (worn bits on the face ring). Cleaning and rock dusting (90% of samples were non-compliant) were not satisfactory. Clogged water sprays were impacting particle detection. Finally, there was a significant accumulation of loose coal, coal dust, and float coal dust.

Validation processes (audits and CAP) did not report safety problems. Employees were discouraged from listing hazards, hence not

correcting them. For instance, there were numerous non-compliances to the approved ventilation plan.

As for supervisory activities, it was noted that advance notice was given to personnel of MSHA presence on site. Correcting and fixing hazards was a priority only prior to MSHA visits. False measurements were recorded on numerous times. Hazardous conditions were not corrected or even posted as hazards.

As for decision making, even if for safety concerns it should be a decentralised, the right of workers to participate in their own safety was not recognized.

The accident of Upper Big Branch also brought a comment from the NRC about weaknesses in safety cultural attributes expected in an organization with a solid safety culture. They mention among other missing attributes leadership in valuing safety, identification, processing and issue resolution of safety problems, work processes, continuous learning, and questioning attitude (NRC, 2012).

10. CONCLUSION

Initiatives in human performance are percolating from nuclear power industry and high risk organizations, where they were used successfully in the last decades, to other types of industries. For instance, the NERC initiated the implementation of a methodology of event analyses directly borrowed from INPO (Institute of Nuclear Power Operators). This initiative doubtlessly reflects the thinking on the lessons learned from the loss of North-East Grid in 2003 (NERC, 2011).

The nuclear industry developed multiple tools to integrate human performance into the daily activities of operation. Human factors, initially a technical speciality centred on ergonomics and man-machine interfaces, became a set of fundamentals of the everyday life used by all the actors and agents of the organization. This implementation succeeded because the basic statement was that the working environment was essentially complex and that attributes of complexity must be taken into account.

Considering the evolution of the industrial environment characteristics, we believe that these approaches and tools can and should be used as a more global methodology for analyses of accidents and low level events (LLE), and for their inclusion in a general frame of organizational culture. Recent events illustrate the presence of these factors and the advantages

to recognize their harm and the potential consequences of organizational failures, which can be detected in a preventive way with a LLE analysis process.

11. REFERENCES

Argyris, C. and Schön, D. (1996), *Organizational learning II: Theory, method and practice*, Reading, Mass: Addison Wesley.

Carrillo, R.A. (2011), Complexity and safety, *Journal of Safety Research* 42 (2011) 293–300

Dekker, S., Cilliers, P., Hofmeyr, J-H, (2011), The complexity of failure: Implications of complexity theory for safety investigations, *Safety Science* 49 (2011) 939–945

Department of Energy, DoE, (2009), *Human Performance Improvement Handbook*, vol. 1, DOE Standard, Washington D.C., http://energy.gov/sites/prod/files/2013/06/f1/doe-hdbk-1028-2009_volume1.pdf (accessed on 26 November 2015)

Homer-Dixon, T., (2011), Complexity Science, Shifting the Trajectory of Civilisation, *Oxford Leadership Journal*, Volume 2, Issue 1, 2-15

IAEA, (2013), *Managing human performance to improve nuclear facility operation*, Vienna, http://www-pub.iaea.org/MTCD/Publications/PDF/Pub1623_web.pdf (accessed on 25 November 2015)

Johnson, W.G., (1975), *Accident/Incident Investigation Manual*, U.S. Energy Research and Development Administration, Division of Safety, Standards, and Compliance

Kahneman, D. (2012), *Thinking, Fast and Slow*, Farrar, Straus and Giroux, New York, 533p.

Komljenovic, D., Abdul-Nour, G. and Popovic, N. (2015), An approach for strategic planning and asset management in the mining industry in the context of business and operational complexity, *Int. J. Mining and Mineral Engineering*, Vol. 6, No. 4, pp.338–360.

Leveson, N.G. (2011), *Engineering a Safer World, Systems Thinking Applied to Safety*, The MIT Press, Cambridge MA; <http://mitpress.mit.edu/books/engineering-safer-world> (accessed on 20 November, 2015)

Mosey, D. (2014), Looking beyond operator, NEI Magazine, <http://www.neimagazine.com/features/featurelooking-beyond-the-operator-4447549/>, (accessed on 26 November, 2015)

MSHA Investigation, (2011), *Fatal Underground Mine Explosion, April 5, 2010:*

Upper Big Branch Mine-South, Performance Coal Company, Montcoal, Raleigh County, West Virginia, ID No. 46-08436, <http://www.msha.gov/Fatals/2010/UBB/PerformanceCoalUBB.asp>; <http://www.npr.org/documents/2011/may/giip-masse-report.pdf> (accessed on 24 November 2015)

NERC, (2011), *Cause Analysis Methods for NERC, Regional Entities, and Registered Entities*; <http://www.nerc.com/files/Cause-Analysis-Methods-Version1-2-Oct10.pdf> (accessed on 26 November 2015)

OECD Global Science Forum, (2009), *Application of Complexity Science for Public Policy; New Tools for Finding Unanticipated Consequences and Unrealized Opportunities*, Erice, Italy, <http://www.oecd.org/science/sci-tech/43891980.pdf> (accessed on 26 November 2015)

Perrow C. (1999), *Normal Accidents: Living with High Risk Technology*, Basic Books, New York.

Rzevski, G. (2011) A practical methodology for managing complexity, *E:CO Issue Vol. 13 No. 1-2*. 38-55

US NRC, (2012), *Safety Culture Communicator, Case Study 4: April 2010 Upper Big Branch Mine Explosion – 29 Lives Lost*, Washington D.C. <http://pbadupws.nrc.gov/docs/ML1206/ML12069A003.pdf> (accessed on 26 November 2015)

Risk management in the mining sector through complex systems

Maria S. Q. Domingues^a, Adelina L. F. Baptista^b, Miguel T. Diogo^{a,*}

^a CERENA – Centre for Natural Resources and the Environment, Faculty of Engineering of the University of Porto, Rua Dr. Roberto Frias, s/n, 4200-465 Porto, Portugal

^b Universidade Lusíada do Norte, Edifício da Lapa, Largo Tinoco de Sousa, 4760-108 Vila Nova de Famalicão, Portugal

ABSTRACT

There is a wide diversity of concepts related to complexity. What the Santa Fe Institute (USA) calls “systemic” corresponds to what Morin (Morin, 2006) calls “complex”. Mariotti (2000) outlines the need for a unified terminology. When understanding complexity, it can be perceived as a fabric (what is woven together) of heterogeneous inseparably associated constituents (...) (Morin, 2006). According to different authors, the main drivers of complexity can be found in human behaviour and in uncertainty. This structural of dynamic complexity can be organizational, technological, or nested in human relationships. The complex interrelationship that exists between individuals within an organization or project and its influence on competitiveness can be studied by individual emotional intelligence and organizational behaviour (Love, Edwards, and Wood, 2011).

According to ISO 31000:2009, risk management “*refers to a coordinate set of activities and methods that is used to direct an organization and to control the many risks that can affect its ability to achieve objectives*”. When concerning any sector, industry, services, project, or activity, the use of models or theories are required as guidelines. Therefore when its basic elements comprehend human behaviour and/or uncertainty, in order for risk management to be effective and adapted as much as possible to reality, it must be operational within complex systems, as already demonstrated in different R&D environments. Risk management faces particular challenges when approaching more specific needs, such as in the mining sector. The ILO convention (C175, 1995) concerning Safety and Health in Mines, establishes “*that workers have a need for, and a right to, information, training and genuine consultation on and participation in the preparation and implementation of safety and health measures concerning the hazards and risks they face in the mining industry*”, and furthermore recognizes “*that it is desirable to prevent any fatalities, injuries or ill health affecting workers or members of the public, or damage to the environment arising from mining operations*”. In this context, risk assessment of integrated operations can be improved by complex risk models and dynamic environments (Grøtan, Størseth and Albrechtsen, 2011).

Hence, complex systems can provide decision makers with a supporting tool comprising a three axis analysis model. Each of the three axes (X, Y and Z) comprehends a multi-variable linear function f_i : X: f_1 (management variables related to mining); Y: f_2 (variables related to risk management systems) and Z: f_3 (variables related to complex systems. Designing, developing, and testing a risk management decision-making model within complex systems, transversal to other hazard sectors of all economic activities, may provide organizations with sustainable and integrated risk management indicators.

KEYWORDS: complex systems; risk management, uncertainty, human behaviour, high hazards

1. INTRODUCTION

Risk management is an important tool for any business sector. In an economy of global scale and high volatility due to the uncertainty of markets, this tool is even more important because through it high productivity gains can be obtained.

In some industries risk management has to be taken particularly seriously because of the effect of project failure on public safety or on the environment, e.g. in the mining sector due to risk perception, feasibility decision-making, and uncertainty. Technical and socioeconomic complexity and organizational culture are among the

main characteristics of complex systems. In the same sense the mining sector is by nature complex, and major hazards, socioeconomic impacts and resource nationalism must all be considered.

The present study intends to present the aforementioned variables in a multi-variable linear function analysis methodology approach through complex system modelling, and effectively correspond to a risk management tool in the mining sector.

2. COMPLEX SYSTEMS

In physical sciences when joining or connecting a large number of systems, the macroscopic or collective properties of the outcome system are not generally related with the properties of their individual constituents. In this case, the resulting system is a complex system. Complexity, as in collaborative design, comprehends the interaction of many participants working on different elements of the design (Klein et al., 2003), such as in diverse economic activity sectors, i.e. the mining sector.

2.1 Complex thought

The complex thought is an instrument of change and resilience, and is a method in the sense of Descartes. Its main objectives are laid out in Table 1 (Mariotti, 2010).

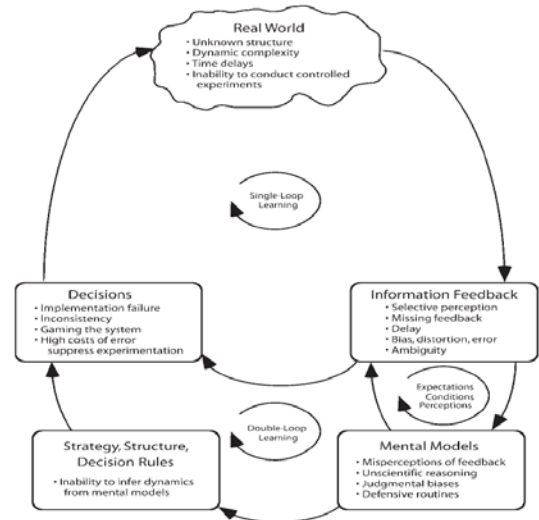
Table 1: Objectives of complex thought.

ID	Description
1	Understand the uncertainty and learn to live with it
2	Learn to deal with paradoxes and situations that cannot be resolved by the binary logic
3	Provide more thinking flexibility
4	Better understanding life, the nature systems and the systems created by man
5	Provide better relationships in the natural world
6	Better understand the ego and learn to deal with it in a less self and hetero destructive mode

Contrasting a dynamic and ever-changing world, human mental models support decision-making processes, which are normally conservative and narrow-minded. “Like organisms, social systems contain intricate networks of feedback processes, both self-reinforcing (positive) and self-correcting (negative) loops” (Sterman, 2006).

2.2 Complexity as a diversity of concepts

Complexity is far from being a simple concept or a single point of view: from the Santa Fe Institute (USA) “systemic” designation, through to the Morin (2006) “complex” classification, to the need for a unified terminology claimed by Mariotti (2000), complexity overlaps multiple labels and approaches. According to Morin (2006) complexity must be perceived as a “fabric” (what is woven together) of heterogeneous inseparable associated constituents (...). In general, complexity is defined in terms of potential states in a system or a number of components (Sterman, 2006), and what is particularly important to identify is the origin of complexity, its level, and its implications (Ameen and Jacob, 2009). Human behaviour and uncertainty are the keystone of basic research in complexity, as established by many authors.



Note: The diagram shows the main impediments to learning. Arrows indicate causation.

Figure 1: Feedback process of learning (Sterman, 2006).

2.3 Complex systems and complex projects

A complex system implies software, cultural and political issues, and people and organisations that can affect the whole or a part of a system (Marashi and Davis, 2006). With more complex systems, more control must be exerted on the local environment (Sayama, 2003). Knowing the nature and ways of expression of complex systems in organizations can be an important tool for managers (Amaral and Uzzi, 2007).

Each different context (simple, complicated, complex, or chaotic) requires different managerial responses (Snowden and Boone, 2007). In this sense, the ‘soft’ world of systemic thinkers is complex, chaotic and ever changing, but it is also true that a process of questioning can be a suitable learning system (Checkland, 2011).

Organizational behaviour and individual emotional intelligence may support studies concerning the complex interconnection between individuals in an organization or a project team and competitiveness (Love, Edwards, and Wood, 2011). Cognitive systems engineering maintains that an individual’s cognitive system is capable of controlling their behaviour using information about the self and the situation, where prior information (competence, knowledge) can be applied to a specific situation (feed-back, indicators) and constructs (hypotheses, assumptions) (Hollnagel, 1998).

The discussion about complex behaviours of a system at different scales does not explain why the systems are simple or complex, however, a profile that quantifies the relationship between independence, interdependence, and scale of collective behaviour may accomplish this (Bar-Yam, 1997). When a complex system adapts to disruptions and changing conditions, this is called resilience.

Resilience is also understood as an emergent property of complex systems (Dahlberg, 2015).

Resilience engineering (for safety management) exists to help people to deal with complexity under pressure in order to achieve success (Hollnagel, Woods, and Leveson, 2006). To understand the complex systems approach in the design and implementation phases, one must recognize the many differences between the traditional practices of engineering and the natural evolutionary process (Bar-Yam and Kuras, 2003). The response of hierarchical control structures, control and central planning are limited and inadequate as a solution to complex social problems in the functioning of complex organizations (Bar-Yam, 2003).

Marashi and Davis (2006) propose a systemic methodology based on negotiation and argumentation to help in the resolution of complex issues and to facilitate evaluation options during design of systems. The decision-making processes supported by the quantification of complex areas are reinforced because they help set priorities and direct management efforts (Sivadasan, et al, 2010).

To deal with ambiguity and interdependency, people seek a plausible sense of resolve that makes sense (Weick, Sutcliffe and Obstfeld, 2005). The multiple perspectives related to complex situations are supported by the combination of two methods: “multiple criteria decision making” and “techniques from soft systems” (Petkov, et al, 2007).

Research has shown that the complexity of projects is imperative to establish exceptional preventive measures (Domingues, 2012). In order to obtain a measure of project complexity, Fitsilis and Damasiotis (2015) study the effect of time, cost, and quality, as well as the three in combination. This analysis shows that project complexity can have a logical and valid representation.

Other researchers present a framework for project complexity that identifies both technical and organizational complexity. For Bosch-Rekvelde et al. (2011), the majority of the elements in the technical category of the proposed framework have a structural character, like the number of goals, largeness of scope, number of tasks, and dependencies between tasks, and uncertainties in goals and methods are covered in the elements of the technical category. Further, the stakeholder’s multiplicity and multi-objectivity are covered in elements like goal alignment (technical category) and the number of stakeholders and the variety of stakeholder’s perspectives (environmental category) (Bosch-Rekvelde et al., 2011).

3. COMPLEX RISK MANAGEMENT

Complexity offers an interesting theoretical framework for the interdisciplinary studies of integrated safety management and risk management methods (Le Coze, 2005). A risk management strategy must be developed in order to identify as many potential risks as possible and then to decide how to deal with them. Risk analysis is an important process of risk management that can identify and evaluate risk that has to be controlled, minimized or accepted. This is essential information for the identification of threats, and is a vital element for decision-making (Bosch-Rekvelde et al., 2011).

The focus of engineering is on the risk factors, development, and implementation of the measures of control; from design, construction, operation processes, systems maintenance, and operation limit states such as emergencies, and start/stop processes (Domingues et al., 2013).

Traditional risk analysis is not sufficient to recognize the heterogeneity of the input criteria (*wildness in wait*) because it does not recognize the difference between the assumptions aimed at emerging order nor the possibility of heterogeneity of criteria to be incorporated in such apparent order. “Hence, (...) Risk Assessment (as part of Governance) should be recognized as a (social) knowledge practice (...)”, (Grøtan, Størseth and Albrechtsen, 2011).

Perminova et al. (2008) explained the link between uncertainties and risk management and introduced a new perspective on how to manage uncertainties in projects. Traditional risk management assumes risk as uncertainty, while the author understands risk as one of the implications of uncertainty. They define uncertainty as “a context for risks as events having a negative impact on the project’s outcomes, or opportunities as events that have beneficial impact on project performance” (Perminova et al., 2008).

Risk management needs to be thoroughly defined; such is the case in ISO 31000:2009, where risk management “refers to a coordinate set of activities and methods that is used to direct an organization and to control the many risks that can affect its ability to achieve objectives”. In a similar context, an important change related to risk perception can be found in ISO 9001:2015. The risk management integration approach is now a major component of the organisational culture.

According to Afgan, and Veziroglu (2012) the change of social elements (health hazards) is a property of complex systems. Some of these social changes are an inherent characteristic of a system, therefore, mutual interaction between the system and its surrounding are imminent and changes in their interaction rate will affect its safety. If these processes

are in steady state, the system is considered safe. It is of interest to investigate the essential characteristics of construction site systems (or other hazardous sectors like the mining sector), which may lead to resilience changes.

In the prevention domain, the most effective elements of a safety program are the support of top management commitment, the selection of human resources (own or outsourced) and strategic management. In turn, the least effective factors are the records, accident analysis, and planning of emergencies (Hallowell and Gambatese, 2009). The role of safety technicians and the need for training concerning the impact of maintenance activities in the industrial process have been specified for the oil refining industry (Cardoso et al., 2014).

In order to demonstrate how risk can be managed in high-risk workplaces, one may utilize an analysis of communication gaps (Rasmussen and Lundell, 2012). Jaafari (2001) states that risk management should have a strategy-based project management approach, using life cycle objective functions as the main drivers for risk reduction and value addition. Systematic management of complex projects requires important information skills and decision support systems which can combine the management of “hard” and “soft” aspects, and facilitate decision evaluation on a real time basis (Jaafari, 2001).

4. DISCUSSION

Guidelines for risk management need the support of models and/or theories in every sector, industry, service, organization, or project. Thus, in order to achieve effectiveness and adaption to reality, risk management as a consequence of its basic elements, human behaviour and uncertainty, must be operational within complex systems, as already applied in various R&D environments.

Risk management faces particular challenges when approaching specific needs. In the mining sector, “workers have a need for, and a right to, information, training and genuine consultation on and participation in the preparation and implementation of safety and health measures concerning the hazards and risks they face in the mining industry”, as established by ILO convention C175 (1995) concerning Safety and Health in Mines. The same ILO regulation furthermore recognizes “that it is desirable to prevent any fatalities, injuries or ill health affecting workers or members of the public, or damage to the environment arising from mining operations”. Risk assessment of integrated operations is enhanced by dynamic environments and complex risk models (Grøtan, Størseth and Albrechtsen, 2011).

The mining sector faces unprecedented challenges due to unexpected internal factors (lack of trained people and frequent equipment failures) and external factors (mineral commodity prices, market volatility, increasing regulations, dwindling profits, and changing global demand) and inadequate risk management can lead to failures in production or even serious injuries to people and the environment. These events can interrupt projects and even cause the complete loss of the business (Kumar, 2015). Badri (2015) “puts into perspective the complexity of the challenge of integrating OHS into industrial project risk management” and emphasizes that the interdisciplinary nature of this problem must be the starting point of any research (Badri, 2015).

The mining industry is complex due to the numerous operations; however, its principal concern is safety. Haas and Yorio (2016) consider the performance of a health and safety management system (HSMS) “a critical and pressing issue for organizations”. Their study analyses the state of current HSMS methods, recommending reports based on three metric categories: organizational performance, worker performance, and interventions. Nelitz, et al. (2015) consider the principal environmental stressors in this field to be: human intrusion in ecosystems, gas emissions, noise and dust in the air, soil disturbance and contamination, linear infrastructure, traffic and solid waste in land, and water pollution. These vectors must be considered for any risk management analysis in the mining industry.

5. CONCLUSIONS

Complex systems can be a supportive tool for decision-makers. An algorithm proposal is designed based upon a three axis (X, Y, Z) analysis model. Each of the three axes represents a multi-variable linear function f_i :

$X : f_1$ (mining management variables);

$Y : f_2$ (risk management systems variables);

$Z : f_3$ (complex systems variables).

A risk management decision-making model, designed, developed and tested within complex systems, aimed at being transversal to other hazard sectors in any economic activity, may provide sustainable and integrated risk management indicators for organizations.

Table 2: Variables proposal.

VECTOR ANALYSIS					
X		Y		Z	
M	Mining	RMS	Risk Management Systems	CS	Complex Systems
f	related to mining	f_2	related to risk management systems	f_3	related to complex systems
x	major hazard industry	y_1	Risk perception	z_1	technical complexity
x	Resource nationalism	y_2	feasibility decision making	z_2	Organizational culture
x	socio economic impacts	y_3	uncertainty	z_3	socio economic complexity
x_n		y_n		z_n	
PLAN ANALYSIS					
$XY : (f_1, f_2)$		M vs RMS		e.g.: (Haas and Yorio, 2016)	
$XZ : (f_1, f_3)$		M vs CS		e.g.: (Nelitz, et al., 2015)	
$YZ : (f_1, f_3)$		RMS vs CS		e.g.: (Badri, 2015)	
VOLUME ANALYSIS					
$XYZ : (f_1, f_2, f_3)$		M vs RMS vs CS		Risk Management Within Complex Systems in Mining	

The analysis methodology proposed above is supported by a three-dimensional scope, $F = (f_1, f_2, f_3)$ (complex systems, risk management, mining sector), with F being a comprehensive model of analysis that can be used to determine scenarios among different options, where several objectives can be set, such as “zero accidents”. The mining sector can thus be thought of as a complex system and the risk involved in the sector understood as a management variable and integrated through the risk management function.

6. REFERENCES

Afgan, N. and Veziroglu, A. (2012). Sustainable resilience of hydrogen energy system. *International Journal of Hydrogen Energy*, 37, 5461-5467.

Amaral, L. A. N. and Uzzi B. (2007). *Complex Systems - A New Paradigm for the Integrative Study*

of Management, Physical, and Technological Systems. *Management Science*, 53(7), 1033-1035.

Ameen, M. and Jacob M. (2009). Complexity in Projects: A Study of Practitioners Understanding of Complexity in Relation to Existing Theoretical Models. In *School of Business 2009*, Umeå University: Umeå, Sweden.

Badri, A. (2015). The Challenge of Integrating OHS into Industrial Project Risk Management: Proposal of a Methodological Approach to Guide Future Research (Case of Mining Proj. in Quebec) *Minerals* 5, 314-334. doi:10.3390/min5020314.

Bar-Yam, Y. (1997). *Complexity Rising: From Human Beings to Human Civilization, a Complexity Profile*, N.E.C.S. Editor, New England Complex Systems Institute: Cambridge, MA, USA.

Bar-Yam, Y. and Kuras M. L. (2003). *Complex Systems and Evolutionary Engineering*, in An AOC WS LSI Concept Paper, Complex Systems Institute and The MITRE Corporation.

Bar-Yam, Y. (2003). When Systems Engineering Fails - Toward Complex Systems Engineering, in *International Conference on Systems, Man & Cybernetics*, I. Press, Editor New England Complex Systems Institute: Piscataway - NJ, USA.

Bosch-Rekveltda, M., Jongkindb, Y., Mooia, H., Bakkerc, H., Verbraeckb, A. (2011). Grasping project complexity in large engineering projects: The TOE (Technical, Organizational and Environmental) framework. *International J. of Project Management*, 29(6), 728-739. doi:10.1016/j.ijproman.2010.07.008.

Cardoso, A., Queiroz, S., Fernandes, A., Roçadas, A. S. and Diogo, M. T. (2014). Técnico de Segurança numa refinaria: responder às especificações de uma indústria. *Proceedings Book of SHO 2014 – Intern. Symposium on Occupational Safety and Hygiene*, Guimarães, Portugal.

Checkland, P. (2011). *Autobiographical retrospectives: Learning your way to ‘action to improve’ – the development of soft systems thinking and soft systems methodology*. *International Journal of General Systems*, 40(05), 487-512.

Dahlberg, R. (2015). *Resilience and Complexity: Conjoining the Discourses of Two Contested Concepts*. *Culture Unbound, Volume 7*, 541-557. Published by Linköping University Electronic Press

Domingues, M. S. Q. (2012). *Uma abordagem aos projetos complexos na perspetiva da prevenção*. Dissertation of Master Degree in Engineering of Occupational Safety and Hygiene, University of Porto, Portugal, 92 p.

Domingues, M. S. Q., Roçadas, A. S. A., Fernandes, A. F., Silva, C. O., Martins, J. M. M., Cabral, A. M. and Diogo, M. T. (2013). *Complex Systems Application at Risk Prevention in Processing and Use of Hydrogen Technologies*. In *IV Iberian*

Symposium on Hydrogen, Fuel Cells and Advanced Batteries, Estoril, Portugal.

Fitsilis, P. and Damasiotis V. (2015). Software Project's Complexity Measurement: A Case Study. *Journal of Software Engineering and Applications*, 8, 549-556.

Grøtan, T. O., Størseth, F., and Albrechtsen, E. (2011). Scientific foundations of addressing risk in complex and dynamic environments. *Reliability Engineering and System Safety*, 96(6), 706-712. doi: 10.1016/j.ress.2010.12.009.

Haas, E. J. and Yorio, P. (2016). Exploring the state of health and safety management system performance measurement in mining organizations. *Safety Science* 83 (2016) 48–58.

Hallowell, M. R. and Gambatese, J. A. (2009). Construction Safety Risk Mitigation. *Journal of Construction Eng. and Management*, 135(12), 1316-1323. doi: 10.1061//asce/co.1943-7862.0000107.

Hollnagel, E. (1998). Commentary Comments on "Conception of the cognitive engineering design problem" by John Dowell and John Long. *Ergonomics*, 41(2), 160-162.

Hollnagel, E., Woods D. D., and Leveson N. G. (2006). *Resilience Engineering Concepts and Precepts*. Aldershot, Hampshire, England: Ashgate Publishing Limited. 410.

International Labour Organization (1995). Convention N. 176 - Safety and Health in Mines Convention.

Jaafari, A. (2001). Management of risks, uncertainties and opportunities on projects: time for a fundamental shift. *International Journal of Project Management*, 19(2), 89-101. doi:10.1016/S0263-7863(99)00047-2.

Klein, M., Faratin, P., Sayama, H., and Bar-Yam, Y. (2003). The Dynamics of Collaborative Design: Insights from Complex Systems and Negotiation Research. *Concurrent Engineering*, 11(3), 201-209. doi: 10.1177/106329303038029.

Kumar, P., Rathore, I. (2015). The Need of Mining Industry – A SWOT analysis. *International Research Journal of Earth Sciences*, 3(8), 32-36.

Le Coze, J. (2005). Are organisations too complex to be integrated in technical risk assessment and current safety auditing? *Safety Sc.*, 43, 613–638.

Love, P., Edwards, D., and Wood, E. (2011). Loosening the Gordian knot: the role of emotional intelligence in construction. *Engineering, Construction and Architectural Management*, 18(1), 50-65. doi: 10.1108/09699981111098685.

Marashi, E. and Davis, J. P. (2006). An argumentation-based method for managing complex issues in design of infrastructural systems. *Reliability Engineering & System Safety*, 91(12), 1535-1545.

Mariotti, H. (2000). Reduccionismo, "Holismo" e Pensamentos Sistêmico e Complexo (Suas consequências na vida cotidiana). In P. Athena (Ed.), *As paixões do ego: complexidade, política e solidariedade*. São Paulo, Brasil.

Morin, E. (2006). *Introdução ao Pensamento Complexo*. Edit. Sulina, ISBN: 978-85-205-0598-4.

Nelitz, M. A., Beardmore, B., Machtans, C. S., Hall, W. A., and Wedeles, C. (2015). Addressing complexity and uncertainty: conceptual models and expert judgments applied to migratory birds in the oil sands of Canada. *Ecology and Society* 20(4):4. doi:10.5751/ES-07906-200404

Perminova, O., Gustafsson, M., Wikstro, K. (2008). Defining uncertainty in projects – a new perspective. *International J. of Project Management*, 26(1), 73-79. doi:10.1016/j.ijproman.2007.08.005

Petkov, D., Petkova, O., Andrew T., Nepal T. (2007). Mixing Multiple Criteria Decision Making with soft systems thinking techniques for decision support in complex situations. *Decision Support Systems*, 43, 1615–1629.

Rasmussen, J. and Lundell, Å. K. (2012). Understanding "communication gaps" among personnel in high-risk workplaces from a dialogical perspective. *Safety Science*, 50(1), 39-47. doi: 10.1016/j.ssci.2011.06.009

Sayama, H. (2003). *Workplace Construction: A Theoretical Model of Robust Self-Replication in Kinematic Universe*. In Eighth International Symposium on Artificial Life and Robotics.

Sivadasan, S., Smart, J., Huatucó, L. H., et al., (2010). Operational complexity and supplier–customer integration: case study insights and complexity rebound. *Journal of the Operational Research Society*, 61(12), 1709-1718.

Snowden, D. J. and Boone M. E. (2007). *A Leader's Framework for Decision Making*. Harvard Business Review.

Sterman, J. D. (2006). Learning from Evidence in a Complex World. *American Journal of Public Health*, 96(3), 505-514.

Weick, K. E., Sutcliffe K.M. and Obstfeld D. (2005). Organizing and the Process of Sensemaking. *Organization Science*, 2005. 16(4), 409-421.

Application of Cognitive Task Analysis in mining operations

Serenay Demir*, Elie Abou-Jaoude and Mustafa Kumral

Department of Mining and Materials Engineering, McGill University, Montreal, Canada, H3A 0E8

ABSTRACT

Through the advancement of human-machine interactions in various fields, understanding beyond the technical components has become prominent. Traditional methods for analyzing human behavior in a work setting, which mostly centralize in identifying material and observable traits, don't seem to fit modern technology and systems used in various industries today. The concept of Cognitive Work Analysis (CWA), in this regard, has gained interest in academic and business settings in the last few decades. A cognitive analysis expands the observation of worker's interactions to a more cognitive and behavioural level and sets a safety standard for a well-designed project. This research essentially aims to fully comprehend the five steps of CWA through the examination of cases and finally, seeks possible applications in the mining industry, where accidents due to human error are impactful. In this paper, an initial proposal of a CWA model for the mining industry is developed based on an existing model of quantifying human error in maintenance in various industries.

KEYWORDS: cognitive work analysis, work domain, human behavior, safety.

1. INTRODUCTION

Many industries operate in hazardous fields, including but not limited to nuclear power, manufacturing, aircraft operation, and mining. While the successful human-computer interaction is generally ensured, there are still a number of concerns and room for improvement when uncertainties are taken into consideration. While there are many possible reasons for industry accidents, human error is considered to be one of the main causes. Furthermore, the mining industry, being acknowledged as a particularly hazardous industry, experiences numerous accidents caused by neglect, lack of knowledge, or simply by a combination of human error factors. In order to better comprehend the design process of such hazardous and complex systems, a number of cognitive analysis tools have been introduced, such as Cognitive Work Analysis (CWA).

This analysis is defined as a “conceptual framework that makes it possible to analyze the forces that shape human-information interaction” by Fidel and Pejtersen (2004). Therefore, the psychological and cognitive thought of a worker are important factors. Interview processes and analysis tools are used to uncover the operator's approach to a human-machine system, beyond the formal training. Qualified workers can sometimes be unaware of their actions, despite their motivation to fully complete the tasks. This might occur due to a number of conditions such as mental and physical state, work environment, and the equipment's design. Later on, the steps of the analysis will reveal that through document

analysis, interviews, and observations, besides cognitive processes, the cognitive work system includes five different aspects. The focus of the present study is to discuss the application of an improved cognitive work analysis to a mine environment. The paper firstly elaborates on the background of the research and its reflections in the related literature; this is followed by the steps for cognitive analysis data collection; and finally based on those data, an initial cognitive analysis model is formed in order to quantify the cognitive work quality of a mine.

2. RELATED WORK

Behavioral researchers in different fields address issues such as analyzing the process of decision-making under uncertainty (Kahneman & Tversky, 1979) and the effect of cognitive and motivational biases on the output of risk analysis (Montibeller & Winterfeldt, 2015). More specifically, engineering systems have also tried to comprehend the factors affecting human performance and potential ways to improve it (DoE, 2009). Among many others, some of the techniques and concepts mentioned in these papers, such as Skills-Rules-Knowledge Taxonomy and Strategic Analysis, are related to the specific concept of Cognitive Work Analysis, which is the basis of this paper.

The domain of human factors engineering started in the 19th century during the industrial revolution, where physical tasks were repetitive and required none of the cognitive ability necessary in today's

*Corresponding Author – email: serenay.demir@mail.mcgill.ca

work domains. As such, the first forms of task analysis simply question the best possible and only way to perform a task (Vicente, 1995). However, in the case of unanticipated events taking place, this type of analysis would not be prepared since it only involves the completion of a specific task.

Through the late 20th century, when the need for a more adaptive tool arose in order to meet the demands of a more complex system, the concept of cognitive task analysis was introduced. CWA was then developed by Rasmussen in 1986, in order to provide a more general approach that examines the task, the work domain, the strategies, and the cognitive processes all at the same time. Also, it was identified that nuclear power plants are extremely vulnerable domains in the sense that they are fairly complex systems, and accidents mostly occur when the incident is unfamiliar to operators (Vicente, 1995).

Starting from 1989, the cognitive work analysis (CWA) changed its scope towards a different framework called Ecological Interface Design, whose focus is to design the interfaces in complex socio-technical systems (Naikar, 2011). The concept found applications in process control systems of various domains, such as petrochemical and nuclear power, addressing both small and medium-scale problems. In the following decade, this concept was applied to questions regarding training needs of systems in many different domains (Pawlak & Vicente, 1996; Jamieson, 2007; Lau et al., 2008).

Therefore, the development of CWA started with the consideration of nuclear power plants but can surely be adapted to many other hazardous industries where conditions are similar. Hazardous industries with high levels of human-machine interaction and uncertainty, such as mining, would surely benefit from further applications of Cognitive Work Analysis.

3. COGNITIVE ANALYSIS DATA

This section aims to elaborate the five steps of the Cognitive Work Analysis (CWA) to be used in the mining industry, and also, introduce general data structure for the model in the next section. Each step of this analysis serves a different purpose of elaborating on more detailed aspects of data collection.

3.1. Work Domain Analysis

Having defined the scope and purpose of the CWA, the first step is to apply Work Domain Analysis, which illustrates the domain where the task is performed. All, the purposes are determined and the functional units are illustrated. The mining domain can be described as complex, combining

together different operations such as drilling and blasting, materials handling, loading-hauling or concentration, mineral processing, equipment reliability, and so on.

It is essential to fully comprehend the aspects of the work domain and define the external constraints to be faced. The Work Domain Analysis helps to realize what the system is supposed to do rather than what it is actually doing. In this step, the recommended tool is Abstraction Hierarchy, along with Abstraction Decomposition Space (Jenkins et al., 2008). Through the examination of documents, operation manuals, and interviews with subject matter, the functional purpose, the elements and the constraints in the system are revealed.

3.2. Control Task Analysis

This second phase takes the analysis a step further and evaluates the required task in the working system. The necessary task/operation to be performed to meet the functional purposes are examined in detail. For example in drilling-blasting operations cognitive experts should understand, from a human interaction perspective, the following information: drilling geometry, drilling equipment maintenance, drill bit replacement, bit-rock interaction, explosive storage, type and placement, operator performance, and inventory management.

The acquisition methods are Cognitive Walk-Through and study of work practices (Lintern et al., 2004), and the tools recommended for this step by Vicente (1999) are either Decision Ladder or Contextual Activity Template. These steps reveal the relevant detailed information regarding the comprehension of the task, the steps to make a decision, and which levels of knowledge the operator uses.

3.3. Strategies Analysis

Strategies Analysis constructs the third phase of the CWA. After outlining the work domain and the required task in previous stages, the strategies analysis moves towards the specific factors that may prevent the task from completion and what are the most efficient ways to complete it. All human factors affecting a mining operation are documented.

The acquisition methods are Critical Decision Methods, Interaction Analysis and Verbal Protocol Analysis (Lintern et.al, 2004). After gathering the necessary information, the recommended tool for demonstration is Information Flow Map (Vicente, 1999).

3.4. Social Organization and Cooperation Analysis

The fourth step of the CWA is Social Organization and Cooperation Analysis. As the name

suggests, this step investigates how the team members interact with each other within the constraints that are posed on the team as a whole. This stage moves from individual to team, with the analysis being conducted in terms of team performance.

The acquisition method is Communication and Interaction Analyses (Lintern et al., 2004), which mainly discovers the relationship of actors through verbal processes.

3.5. Worker Competencies Analysis

The final phase of the analysis is Worker Competencies Analysis. It aims to discover the factors affecting the behaviors of actors within a specific workplace, when different situations are in question. Through the review of previous steps such as the Decision Ladder and Repertory Grid Analysis (Lintern et al., 2004), a specific tool called Skills Rules Knowledge Taxonomy is formed (Vicente, 1999).

When a specific strategy for a specific task is considered, The Skills, Rules, Knowledge (SRK) Taxonomy demonstrates both the SRK information and the information about the activity and how different they are in each knowledge state (Jenkins et al., 2008). The SRK Taxonomy classifies human behavior in relation to various restrictions in a workplace. As a result of this analysis, Vicente (1999) suggests that the most important parts of cognitive processes can be awakened and used for the betterment of the design. Furthermore, according to Kilgore and Cyr (2008), the SKR inventory can also refer to the worker competencies that are essential for task completion.

It is important to mention that this paper attempts to provide a different approach by including the analysis of physical and mental fitness of the workers as well. These elements are specifically found important in the sense that the cognitive factors for the workers strictly depend on these conditions. This will be introduced in the following sections where the model is presented.

4. COGNITIVE ANALYSIS MODELLING

4.1. Cognitive Work Quality Factors

In an attempt to form an applicable and similar tool in mining to quantify the CWA explained in the previous section, some related research is summarized here. One of the most significant papers develops a method to quantify human error using graph theory and matrix approach (Kumar and Ghandi, 2011). The current study adopted this method and combined it with the extensive

framework of CWA as an effective tool in assessing mining reliability.

In an attempt to understand the complex structure of the mining domain, Cognitive Work Quality (CWQ) is computed as a percentage describing the qualities of the mine domain, such as its management, safety, and feasibility. The information derived from the cognitive analysis data in Section 3 forms the CWQ factors. Each factor has different characteristics, each of which was assigned a quality rating ranging from “Excellent” to “Poor”.

4.2. Quantifying the Cognitive Work Quality Index

In order to calculate the cognitive work quality index for a task, it is crucial to determine the severity value of each factor, as well as the influence between these factors. First of all, each of the eleven CWQ factors mentioned in Table 1 (See Appendix 1) has a weight (ranging from 0 to 1) attributed to it, which represents the role and importance of a factor for the studied task. The total sum of the weight should be equal to one, such as:

$$W_{CWD} + W_{MD\&E} + W_{TD} + W_{TI} + W_{SA} + W_S + W_{MC} + W_{T\&C} + W_{PR} + W_{P\&MF} + W_{CDT} = 1$$

The higher the weightage of a factor, the more significant it is in the assessment of cognitive work quality.

Secondly, as seen in the table in the appendix, each factor has different attributes, “Cognitive work characteristic”, associated with it. Each of those characteristics is rated from a scale from 5-excellent to 0-poor. For each factor, the sum of its characteristics ratings corresponds to the level value, L_i . As an example, to know the level value of the “Tools Design” factor, we would need to sum the rating assessed for its characteristics such as: “Design Compatibility”, “Efficiency for Task Completion” and “Availability of Equipment”.

Based on the weightage (W_i) and the level value (L_i) of each factor, Quality value, Q_i is formed as following:

$$Quality\ value, Q_i = W_i \cdot L_i$$

Finally, the influence between two factors, F_{ij} , with a scale from 5 to 0 such as 5- Strong Influence, 3- Medium Influence, 1- Weak Influence, and 0- No Influence, are assessed. These weightages and influences between factors are assessed by experts using human reliability analysis techniques. These techniques, such as THERP, CREAM and NARA set an error probability to the execution of necessary actions taken by the workers at every cognitive work quality factor. Many aerospace industries, such as

NASA, use these techniques to considerably reduce operational and procedural errors (NASA, 2010).

The quality values Q_i and the influence values F_{ij} are placed in a matrix as followed, with the permanent of this matrix being the cognitive work domain quality index.

$$CWQ_{index} = \text{Permanent of } \begin{bmatrix} Q1 & F12 & F1M \\ F21 & Q2 & F2M \\ FM1 & FM2 & QM \end{bmatrix}$$

With M being the number of factors involved for the work domain of the mine.

4.3. Cognitive Work Quality Results

The cognitive work domain quality index is turned into a percentage by computing the index for the ideal case work quality and for the worst work quality, such as:

$$CWQ(\%) = \frac{CWQ_{index} - CWQ_{Ideal}}{CWQ_{Ideal} - CWQ_{worst}}$$

Table 1 shows the range and signification of the Cognitive Work Quality percentage obtained.

Table 1: Cognitive Work Quality Ratings and Recommendations.

Rating range	Cognitive Work Quality	Recommendations
85-100	Excellent	Mine domain does not require any major adjustment.
70-85	Good	Minor adjustments are needed to attain excellency in the mine domain.
60-70	Average	The mine domain is efficient but major changes are needed to improve its quality.
45-50	Poor	Enhance the management system by seeking advice from suitable experts.
0-45	Insufficient	The mine requires major update in its system. Should close until a safe and feasible environment is attained.

As can be observed, this tool can be used to evaluate the standing point of a mine site through a thorough examination of all its subsystems and finally, forming a set of recommendations in which the weakest parts would be improved. Furthermore, this tool can also be used to determine which of the factors contribute to the final rating more, with a simple regression type analysis.

While there are a number of other design solutions that can be provided within this framework, specific recommendations to improve working

performance may need further attention. According to the rating range in which the mining system is in, some adjustment can be made to the work quality of operators regarding the task performance. Therefore, today, many mining companies track the workers' general performance such as the production targets achievements, computer tracking, safety performance, reported injuries, safety procedure flaws, daily physical/mental state observation by the supervisors, meeting the task deadlines, and drug testing when required, all with the purpose of reducing human error.

Finally, the prospect theory by Daniel Kahneman explains that decision-making appears subjective for every human worker, and so, assessing probabilities to errors (weightage and influences) could lead to biases in the cognitive work quality results (Kahneman & Tversky, 1979). Also, the experts' judgments may lead to biases on choosing the characteristics rating. The field of neurotechnology could be used in the future to directly connect the consciousness of an individual with equipment and improve human-machine interaction in the mine site.

5. CONCLUSION

The Cognitive Work Analysis (CWA) is a relatively new and powerful tool in assessing the workplace in every aspect. Taking its roots from 19th century ergonomics research, this type of analysis evolved from traditional terms and finally, has room for cognitive research as well. The method allows the design to be prepared for unanticipated events by detecting the constraints on task completion. As it analyzes aspects independent from the task and the actor, CWA provides a more flexible and comprehensive point of view. Furthermore, analyzing all the different aspects simultaneously leads to understanding and forming strong interactions between these aspects, which is beneficial for the design.

As a highly risky industry with constant human-machine interaction, the mining industry is a good candidate for the application of the CWA in order to improve its system. After data gathering and modeling, the Cognitive Work Quality was assessed using probability factors. The quantified quality found is associated the mining system state and possibly, can present some specific recommendations. Furthermore, factors affecting the workers are better addressed than in Cognitive Work Analysis, simply because mining is found to be difficult to manage in terms of human factors and reliability, moreso than any other industry. Mining systems and many other hazardous industry domains can benefit from the introduction of this framework

in quantifying and improving the quality of design in the work environment. Since this is only the initial stage of this research, a case study should be conducted on an actual North American mine to test its efficacy.

6. REFERENCES

Department of Energy, DoE, (2009), Human Performance Improvement Handbook, vol. 1, DOE Standard, Washington D.C

Fidel, R. & Pejtersen, A.M. (2004) From information behaviour research to the design of information systems: the Cognitive Work Analysis framework. *Information Research*, 10(1) paper 210 [Available at <http://InformationR.net/ir/10-1/paper210.html>]

Jamieson, G. A. (2007). Ecological interface design for petrochemical process control: An empirical assessment. *IEEE Transactions on Systems, Man, and Cybernetics - Part A: Systems and Humans*, 37(6), 906-920.

Jenkins, Daniel P., Stanton, Neville A., and Salmon, Paul M. (2008). *Cognitive Work Analysis : Coping with Complexity*. Abingdon, Oxon, GBR: Ashgate Publishing Group, ProQuest ebrary. Web. 3 August 2015.

Kahneman, D. & Tversky, A. (1979). Prospect Theory: An Analysis of Decision Under Risk. *Econometrica*, 47(2), pp. 263-291.

Kilgore, R., St-Cyr, O., & Jamieson, G. A. (2008). From Work Domains to Worker Competencies: A Five-Phase CWA for Air Traffic Control.

Kumar, V. N. A. & Gandhi, O. P. (2011). Quantification of human error in maintenance using graph theory and matrix approach.. *Quality and Reliability Eng. Int.*, 27, 1145-1172.

Lau, N., Jamieson, G. A., Skraaning, G., Jr., & Burns, C. M. (2008). Ecological interface design in the nuclear domain: An empirical evaluation of ecological displays for the secondary subsystems of a boiling water reactor plant simulator. *IEEE Transactions on Nuclear Science*, 55(6), 3597-3610.

Lintern, G., Cone, S., Schenaker, M., Ehlert, J., and Hughes, T. (2004) *Asymmetric Adversary Analysis for Intelligent Preparation of the Battlespace (A3-IBP)*, United States Air Force Research Department Report.

Montibeller, G. and Winterfeldt, D. (2015), Cognitive and Motivational Biases in Decision and Risk Analysis, *Risk Analysis*, 35 (7): 1230-1251

Naikar, N. (2011). *Cognitive work analysis: foundations, extensions, and challenges* (No. DSTO-GD-0680). Defence Science and Technology Organisation Edinburgh (Australia) Air Operations Div.

NASA (2010, September), *NASA Human Error Analysis*. National Aeronautics and Space Administration, Washington D.C.

Pawlak, W. S., & Vicente, K. J. (1996). Inducing effective operator control through ecological interface design. *International Journal of Human-Computer Studies*, 44, 653-688.

Vicente, K. J. (1995, October). Task Analysis, Cognitive Task Analysis, Cognitive Work Analysis: What's the Difference?. In *Proceedings of the Human Factors and Ergonomics Society Annual Meeting* (Vol. 39, No. 9, pp. 534-537). SAGE Publications.

Vicente, K.J. (1999). *Cognitive Work Analysis*. Mahwah, NJ: Lawrence Erlbaum Associate

Appendix 1: Cognitive analysis modeling table for the quantification of the Cognitive Work Domain Quality (CWQ).		
Cognitive Work Quality Factors (CWQ_i)	Cognitive Work Characteristics	Characteristic Rating 5-Excellent; 3-Good; 1-Average ;0-Poor
<u>MINING DOMAIN</u>		
Characteristics Of Mine Domain (CWD)	System Functionality	Defining the function and the purpose of the system and creating a work environment accordingly.
	Constraint Management	Effectively managing the environmental, legal and technical constraints posed on the working domain.
	Target Attainability.	Achieving the defined common goals and targets of the domain.
Mine Design And Environment (MD&E)	Mine Planning And Scheduling	Meeting long range planning goals by creating an efficient mining production plan.
	Safety Precautions (Mine And Assets)	Ensuring a safe environment for employees and equipment (i.e. Ground support, geotechnical design).
	Operation System	Attaining optimal operation system. Creating the most time-efficient schedule to meet production deadlines and targets.
<u>CONTROL TASK ANALYSIS</u>		
Tools Design (TD)	Design Compatibility	The equipment suitability for the required task.
	Efficiency for Task Completion	How efficient is the current set of tools for the task completion (quality, safety, productivity and so on).
Task Implementation (TI)	Availability of Equipment	Having an easily accessible and available equipment for the task completion.
	Guidelines and Procedures of Task	Ensuring the accessibility of information sources and data.
	Performance Criteria Well-Defined	How well-defined is the criteria for assuring outstanding performance.
<u>STRATEGIES ANALYSIS</u>		
Strategy Analysis (SA)	Management of Uncalculated Event	Handling unanticipated events and being prepared for novel situations.
	Availability of Methods of Task Completion	Ensuring the accessibility of available methods and different strategies pathways.
<u>SOCIAL ORGANIZATION AND COOPERATION ANALYSIS</u>		
Supervision (S)	Clarity of Instructions and Procedures	Excellent communication is necessary between the employees and supervisor in order to assure optimal and safe performance.
	Mine and Asset Sustainability	Maintain mine and assets quality to be fit for continuous activity.
	Time Management	Activities must maintain their time deadlines and ensure that tasks are completed on time.
Mining Culture (MC)	Incentives	Encourage good working habits by evaluation financial business and safety performance and rewarding with salary and bonus.
	Mining Community Involvement	Workers participate in volunteering and community activities in the mine domain
	Safety and Emergency Plan	The mine site is well-structured for any possible emergency situation, with specific plans and guidelines.
Teamwork and communication (T&C)	Roles and Responsibilities	Roles and responsibilities for each actor is different and should be well-defined to comprehend abilities and specializations.
	Communication	Information flows freely according to the organizational structure of the mine domain, and the different workers have access to that information by efficient communication system.
	Involvement and Coordination	The activities of the workers require a certain level of coordination and feedback mechanism.
<u>WORKER COMPETENCIES ANALYSIS</u>		
Performance Requirements (PR)	Formal/Continuous Training	Level of formal and professional training completed by the workers.
	Skill-Based Behavior	Automated responses to alerting events. Does not require much cognitive process. Mostly used in physical processes, i.e. operating a machine.
	Rule-Based Behavior	The workers are able to verbalize their thoughts and generate behaviors through their experiences, i.e. following safety instruction for truck haulage.
Physical And Mental Fitness (P&MF)	Knowledge-Based Behavior	More complex and demanding process where the workers take the individual and system goals into consideration with analytical reasoning and problem solving skills
	Arm, Leg, Back Strength And Endurance Level.	Physical condition to conduct any required task using mining equipment.
	Emotional Stability	Stress management and handling unexpected situations. Mental health issues.
Cognitive Demand Of Task (CDT)	Concentration Alertness And Memory	The workers are able to stay focused during task completion and memories important details and facts.
	Self-Satisfaction	The workers are confident in the abilities and satisfied with the way of task completion.
	Acute Sight	The workers have a great vision and a rapid reflex to any situation.
Cognitive Demand Of Task (CDT)	Logical Reasoning	Dealing with novel situation by improving knowledge-based behavior and high level of logical reasoning.
	Perception Skills And Knowledge	Perceiving a thorough outline of the task and applying knowledge to a problem with an extensive perspective
	Stress Handling Capacity	Managing the stress facing a situation or a problem.
	Learning Skills and Experience.	The ability to learn and adapt new and professional knowledge; level of experience of workers.

Avoiding workplace accidents: the importance of pre-job safety analyses

Colin Morrish

Safety Engineer, Westgate-on-Sea, UK, CT8 8PZ

ABSTRACT

Careful, thorough, individual and group pre-job safety analyses completed by knowledgeable and competent individuals can significantly reduce workplace incidents. Benefits include: decreased costs, improved productivity and morale of employees, and an increased perception by those outside of positive safety consciousness.

Pre-job safety analyses can be done either by a team of workers or by a solitary worker. In both cases these workers need to be trained in the completion of pre-job safety analyses. Supervisors must check to see that these analyses are completed competently.

The current study presents pre-job safety analyses, namely the Neil George Five Point Safety system and a construction field level risk assessment. Workers may be guided by one of these systems to complete a pre-job safety analysis but must also have access to safe work procedures, and equipment and area inspection reports.

Examples of accidents that were investigated during the author's 18 years as a Saskatchewan mine inspector will be discussed within the context of the above. The causes of the accidents will be explored with close reference to how pre-job safety analyses could have prevented their occurrence.

KEYWORDS: safety; incident; worker; management; supervision; pyramid; domino; tool; analysis; morale; five; field; mining; answering; construction

1. INTRODUCTION

Incidents occur at mine sites, with some resulting in serious injury. In order to reduce the number of incidents that occur, the entire workforce of the company should work together in various ways to provide a strong, integrated and constructive force. One way to involve the entire workforce is for the worker to conduct a pre-job safety analysis. Two means of pre-job safety analysis are the Neil George Five Point Safety System and Field Level Risk Assessment.

2. WORKPLACE INCIDENTS

Models developed using available data show that historically, serious injuries occur less often than incidents where nobody has suffered an injury. This is displayed in the pyramid model in Figure 1. The accident data put into this model was based on 1 753 498 accidents reported by 297 companies to a US insurance company; it was analysed by Frank Bird. The actual ratio varies between industries, circumstances, and the reporting of incidents. However, a large discrepancy between "close-calls" and "serious or disabling incidents" remains.

The incidents that occur with greater frequency have less damaging outcomes. There is a potential for the causes of incidents to produce outcomes of different severity. It is vitally important that incident investigations should be carried out in instances

where there is an injury potential, not just those causing damage or injury. These investigations would find the causes of the incident occurring. This information could be used to help prevent similar incidences from being repeated.

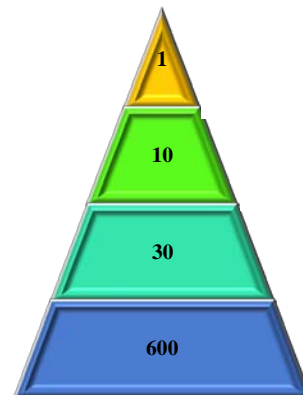


Figure 1: Bird's Pyramid Model. (Sundstrom, 2000).

2.1 Preventing workplace incidents

Incidents occurring at mine sites range from harmless to one where workers are seriously injured. The more severe accidents occur less frequently. To work towards a safe work place, the mining company

in which work is conducted must have a positive health and safety culture. This is one where the aim of all employees is to have no incidents occurring. In virtually all countries today, the workers of mining companies have the legislative right to refuse work that they believe poses a risk of injury to others or themselves.

An accident causation paradigm is referred to as the *Edward Adam's Domino Sequence for Accident Causation* which is shown in Figure 2. The term "Management Structure: defines the mining company's objectives, organization, and the operations. The terms "Management Behaviour" and "Supervisor Behaviour" capture operational factors. The term "Tactical Errors" describes unsafe acts and conditions. Accident/Incident represents all reported incidents including those where nobody was injured. Finally, Injury or Damage describes the outcome to persons or property.

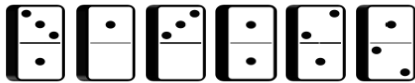


Figure 2: Edward Adam's Domino Sequence for Accident Causation (Strahlendorf, 2008).

Management and supervisors are responsible for ensuring that the tools are in place to minimise unsafe acts and conditions. A major responsibility of the employer is to ensure that the minesite and the work process are both safe. The workers are directly exposed to the unsafe acts and conditions; they should conduct a pre-job safety analysis at the workplace and work processes. As evident in the term, pre-job safety analyses should be conducted before beginning work.

Pre-job safety analyses may be conducted individually or as a group. Unsafe conditions of the work environment or work process should be noted and rectified to negate the risk to workers. The major benefit from this should be decreased accident frequency and their related costs. Production can be halted in order to investigate incidents that have occurred. Mining company employee morale would improve this tool was used, and incident frequency would decline. Finally, public perception of a mining

company which is sincerely concerned about employee health and safety will be enhanced.

3. PRE-JOB SAFETY ANALYSIS

The primary aim of an accident investigation is to learn from the incident that is being investigated to find not only the causes but also how to eliminate the cause in the future. Management, Supervision, and Workers all have roles within their category of employment to identify aspects such as the safety of the workplace and equipment, safety controls initiated, and critical procedures necessary. An accountable pre-job safety analysis can identify potential accident causes and prevent them from surfacing before an incident occurs.

An adjustment of *Edward Adam's Domino Sequence For Accident Causation* depicts the partnership of employee groups that must work together to avoid Tactical Errors. This *Pre-Job Safety Analysis Domino Model* is shown in Figure 3.

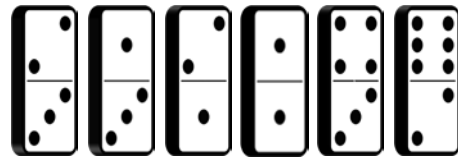


Figure 3: Pre-Job Safety Analysis Domino Model.

1. Management: Management must be involved to maximise the effectiveness of a pre-job safety analysis system. They decide which system to use and must ensure it is implemented and documented. They monitor it by checking regular summaries of the analyses. They can compare incidents that have occurred with reference to the points noted in pre-job safety analyses. Pre-job safety analyses are repetitive and workers can become complacent in their accurate and appropriate completion; frequent management monitoring should ensure proper attention is paid to them. In addition, the pre-job safety analyses completed by workers should be explored to see if there are any trends in unsafe conditions. It would be advisable to have a section on the pre-job safety analysis where workers can communicate safety improvement suggestions.

2. Supervision: Supervision must ensure workers are trained in how to complete pre-job safety analyses effectively. All pre-job safety analyses should be checked while the work shift is ongoing to

see whether they have been completed adequately and if not, further coaching must be given to those completing them. Positive feedback provided by supervisors for well-conducted pre-job safety analyses can be a powerful incentive to reinforce the importance of pre-job safety analyses. Management must then respond to these observations. This would help keep workers positively engaged in the health and safety process.

3. Worker: Workers are required to focus on pre-job safety analyses before beginning work. Management has given them a tool and requires them to use it to make their workplace safe. Effective supervision teaches workers how to use the tool to help them identify unsafe characteristics. The pre-job safety analysis is completed by checking the worksite, equipment and applicable work procedures. Any observations concerning the workplace, equipment, and work process is noted down. Any safety improvement suggestions should also be noted. To use this tool effectively, workers must be thoughtful and not simply “tick-boxes”. Management and supervisor may disseminate the data accrued from past pre-job safety analyses if it is applicable to other workplaces; this data may be used effectively to support subsequent pre-job safety analyses.

If Management, Supervision, and Workers all follow their responsibilities for the pre-job safety analysis, the possibility of accidents/incidents occurring will be significantly reduced. If an incident should occur, the existence of a pre-job safety analysis may also decrease the severity of the incident. All levels of the workforce must be committed to pre-job safety analysis, communication must be maintained, and personal accountability to how accurately it is completed be kept.

3.1 Neil George Five Point Safety System

This first pre-job safety analysis system was developed by Neil George in 1942 for the Ontario mining industry. At the beginning of each shift the worker, in this case a miner, must inspect his worksite by using the Five Point Safety System, noting what was observed. This system is completed by the miner at the area where the work is being conducted. As the name suggests, miners must consider five points before beginning work. These points are:

1. Check the entrance to the place of work: The miner must check his surroundings as entry to the workplace is made. This includes travelling from the dry to the work place, and going between workplaces.

2. Are working place and equipment in good order: The miner checks the working place and equipment to ensure it is safe. Checking the working

place and equipment may require checking specific checklists. If there are records detailing when the working place or equipment were inspected by a qualified professional, check to ensure the records are current.

3. Are people working safely: The miner must check that the required *Personal Protective Equipment* (PPE) is being worn. Is everyone following safe work procedure? Ensure that the correct procedures are being followed by the crew or a risk assessment is being completed if warranted.

4. Do an act of safety: The miner should note an act of safety accomplished by himself/herself. During the course of completing work, an instance will present itself where a safe act is required to do the job safely or prevent a hazard from presenting itself. It is a constant reminder for miners to think about safety.

5. Can, and will, miners continue to work properly: The miner must keep safe work in mind. Before beginning the task, consider what is necessary to complete the job safely in terms of personal protective equipment, materials, equipment, and procedures or risk assessment as the job progresses. The miner must check to see if all that is required to do the job safely can be accessed. If something new comes to light during the course of work and the means to do the job safely is not immediately available, consider what must be done to ensure that all workers remain safe.

The Neil George Five Point Safety System is a straightforward and structured means for miners to assess their workplace, equipment and work procedures. It is used at the workplace immediately before work tasks begin. It can be used at the beginning of shift and stand as a pertinent reminder of health and safety issues throughout the shift. A card is often carried by the miners with the five points noted down for them to consider. Columns for successive tasks to which the miners are assigned during their shift are sometimes present. It is a general card that does not have specifics and can therefore be used at different workplaces. Mine workplaces are dynamic and continually change. In order to complete the Five Point Safety System, it is often necessary to complete checklists and refer to maintenance log books to ensure they are current. They encourage independent thinking and real time engagement because the miners must check their workplace, equipment, and required workplace procedures and continue to do so throughout the shift.

3.2 Field Level Risk Assessments (FLRA)

This second system is used on many construction sites and involves teams of workers who work together to assess risks at the workplace. Instances

when this would be necessary include before beginning work, when a new worker joins the crew, when work procedures change due to site conditions or when new equipment is introduced, and when the activities of others in the area may pose a risk. The FLRA is completed by:

1. Noting hazards to which workers are exposed: As work is being conducted it is necessary to question what hazards are present to them and the surrounding workers.

2. Assess the risk: Note and assess the probability of the hazard causing an adverse outcome and the possible severity.

3. Control those risks: Note the means to control the risk by noting the hazards, the means to control the hazards, who will control them, and who will check if the controls are adequate.

4. Follow up: At this point, what follow-up is required after the job is completed. This would include reactivating controls that were suspended to conduct work and notifying any personnel with interest of the work being completed.

Some forms or checklists may be used in conjunction with the FLRA such as hot work permits, confined space entry, ground disturbance checklists, working at heights checklists, critical lift checklists, and mobile lift equipment checklists. These lists combine assessing and effectively controlling risks.

4. REAL LIFE EXAMPLES

Field Level Risk Assessments (FLRA) or the Neil George Five Point Safety System as applied to real life accidents:

4.1 Worker falling 20 metres

A worker fell 20 metres through a lifting well to the ground. He, along with the rest of his scaffold construction crew, were part of a team building a mill transfer tower which was 20 metres above ground level. He was a junior member of the crew. He had completed a field level risk assessment for the crew by himself from ground level and the entire crew signed it off even though they were not present at its completion. Although it had been noted that fall arrest was required, the locations and job tasks when the fall arrest should have been worn were not. The worker was passing construction material from 20 metres above ground level to the more senior members of the crew constructing the scaffold above. He was not wearing fall arrest. He had to collect some tubing from a collection area beside the lifting well. He went around the collection area to fetch tubing when he stepped into the open hole of the lifting well and fell 20 metres to the ground.

If the pre-job safety analysis had been completed properly, the questions that need answering in this example are:

1. What would have been revealed if the entire crew including more experienced members had done the risk assessment at the elevation where the work was carried out?
2. Would the open hole have been noticed if they were at the workplace 20 metres above ground?
3. If noticed, would the open hole have been covered or would they have been wearing fall arrest while working around it to prevent them from falling through the hole?

4.2 Load-haul-dump vehicle driving into open stope

A miner drove a *Load-Haul-Dump vehicle (LHD)* into an open stope. He started his shift working on the construction crew. During the shift, a supervisor assigned him to work on the production crew for the rest of the shift. The job to which he was assigned was to remove ore from a stope in the lower levels of the mine with an LHD. He was performing this task but it was hot and dusty deep in the mine. He drove the LHD to higher levels in the mine to look for dust masks. For some reason, he drove into the upper level of the stope from which he was removing ore. There was a sign that prohibited passage past the point beyond which the ore was being withdrawn from the stope from the level from where he was working. This sign was on a rope that was meant to stretch across the cross-cut; the rope was not connected across the cross-cut. He drove past this point. It is thought there was a crust of rock over the stope for which the ore was being withdrawn that he successfully drove over. When he drove over this crust while returning, the LHD went through this crust.

If the pre-job safety analysis had been completed properly, the questions that need answering in this example are:

1. Would the sign preventing entry on top of the stopes had been noticed even though it was not connected?
2. Would the miner have been aware of the reason the sign was present?
3. Should contact have been made with someone before driving anywhere near this stope?

4.3 Miner detonating drill hole

A surface driller drilled into a hole loaded with explosives, causing the explosives to detonate. The surface driller was assigned to clear drill holes of material that had sloughed into them by drilling from surface to an underground stope. These holes were loaded. The resulting explosion expelled the drill

string from the drill hole. Workers underground in the cross-cut that was driven into the open stope where this incident took place were flattened by percussion of the explosion.

If the pre-job safety analysis had been completed properly, the questions that need answering in this example are:

1. Would the driller have checked for evidence of the holes having been loaded?
2. Would the underground miners have checked what work was being conducted near the stope including any surface work?

4.4 Drill rig fire

Two workers inside a surface diamond drill rig were burned. While the drill was operating, a hose carrying hydraulic oil was transported detached from a nipple and sprayed the driller and helper with the hydraulic oil. It was an extremely cold day and the inside of the drill rig was being heated with an open flamed propane heater. This open flame set the workers alight.

If the pre-job safety analysis had been completed properly, the questions that need answering in this example are:

1. Would the competence of the connections have been tested?
2. Would the preventative maintenance records of the drill rig been checked and noted as not up-to-date?
3. Would open-flamed propane heaters inside a drill rig have been identified as unsafe?

5. CONCLUSION

Pre-job safety analyses are essential in helping to prevent incidents, which often have the potential to cause serious injuries. Incidents which have already occurred must be investigated to find their causes and thereby preventing a repetition.

For pre-job safety analyses systems to be effective, Management, Supervision, and Workers must all work together to make them operate effectively. Management must implement and document a system as well as monitor it to ensure it is working. Supervision must teach Workers how to complete pre-job analyses effectively and check to see that they are being done competently. The pivotal employees to make pre-job safety analyses effective are workers: they must complete them competently.

There is no doubt that competent pre-job safety analyses would have helped prevent the four serious mining incidents discussed here.

6. ACKNOWLEDGEMENT

I am thankful to Professor M. Scoble (UBC) for giving me encouragement to submit this paper to this symposium. I am also thankful to my father, Alan Morrish (retired Mine Manager) & my wife (Jennifer Morrish) for giving me support and editing the manuscript.

7. REFERENCES

- Carlson G.K. (2014): It's not mine safety but mind safety: a Henderson approach. 3rd international symposium on block and sublevel caving. pp. 53-60
- Cann N., Casey S., Mills R., Ross J. (2011): Reducing mining and mineral processing plant fatality rates. MetPlant 2011: plant design and operating strategies: world's best practice. pp.27-38
- Davies F, Spencer R, Dooley K (2001). Summary guide to safety climate tools. Offshore Technology Report.
- Pillay M. (2013): Disasters, accidents and safety: a review of theory and applications for advancing mine safety management. Proceedings of the 35th international conference of safety in mines research institutes. pp.367-376
- Strahlendorf, P.(2008): Accident Theory Study Guide. Board of Canadian Registered Safety Professionals Study Guide.
- Towsey C.A.J. (2001): Managing occupational health and safety risk in mining: implementing behavioural change. Bull. Australasian Institute of Mining and Metallurgy. no. 3. pp. 26-30.
- www.safeopedia.com/definition/684/field-level-risk-assessment, (2016)

Notification systems and risk management

Maria M. Antunes, Miguel T. Diogo*, Joaquim Góis

CERENA-Centre for Natural Resources and the Environment, Faculty of Engineering of the University of Porto, Rua Dr. Roberto Frias, s/n, 4200-465 Porto, Portugal

ABSTRACT

In an occupational context, “Notification” understood as “the act of telling someone officially about something, or a document that does this”, (in Cambridge Advanced Learner’s Dictionary & Thesaurus), may reveal a management approach. The ILO Code of Practice on Recording and Notification of Occupational Accidents and Diseases provides practical guidelines for establishing and use a national system for recording and notification of occupational diseases.

In the European Union, there is a legal obligation to report occupational accidents and diseases. Such is the case, e.g. with RIDDOR making reporting certain incidents a legal requirement. The report informs the enforcing authorities about deaths, injuries, occupational diseases, and dangerous occurrences. Mandatory notification procedures may also arise from certain types of specific hazards, such as exposure to biological agents.

Also relevant are reporting procedures in non-compulsory management systems, namely the ILO Guidelines on OH&S management systems, when considering performance monitoring and measurement, clearly states that “Reactive monitoring should include the identification, reporting and investigation of: (a) work-related injuries, ill health (including monitoring of aggregate sickness absence records), diseases and incidents (...)”.

Findings from a case study over a 5-year period, based upon a notification system from one organization alone with 736 records and 915 workers directly involved, supports a main conclusion. A notification system is not by itself enough in prevention terms. The validity of the required information and the way it is demanded is also fundamental to obtain the best adequate records. The statistical data treatment is a critical stage, for changes regarding preventive actions and measures are based upon such findings and conclusions.

Statistical treatment of data is fundamental to achieve adequate use of the data collected. Multiple correspondences analysis privileges tables of relevant size simultaneously comprising variables of distinct nature: quantifiable and qualitative. It helps in describing the complex relationships that may exist among variables, both independent and dependent (Dohoo, 1996).

The mentioned study comprises a total of 47 management variables and a set of multiple sub-variables, resulting from the notification system analysed. The results obtained identify management variables that may be considered transversal to other economical sectors, from the workers’ point of view (gender, professional classification and others) and specific to the sector if the employers’ point of view is considered (day of the week, type of accident, communication procedures, contributing factors, etc.).

The present study aims to design, implement and validate a notification system as both a transversal and sectorial information system in OH&S risk management. A notification system should provide effective and adequate flow of information within a proactive prevention context.

KEYWORDS: notification systems; risk management

1. INTRODUCTION

In an occupational context, “Notification” understood as “*the act of telling someone officially about something, or a document that does this*”, (in Cambridge Advanced Learner’s Dictionary & Thesaurus), may reveal a management approach.

The International Labour Organization (ILO) Code of Practice on Recording and Notification of Occupational Accidents and Diseases provides practical guidelines for establishing and use a national system for recording and notification of

occupational diseases. Not only at national level, but also at the level of the enterprise, it establishes that “6.2.1. *The employer, (...), should set up arrangements within the enterprise, in accordance with national laws or regulations, to notify occupational accidents, occupational diseases, dangerous occurrences and commuting accidents, as appropriate.*”

In the European Union, there is a legal obligation to report occupational accidents and diseases. Such is the case with Reporting of Injuries, Diseases and

*Corresponding author – email: tatodiogo@fe.up.pt

Dangerous Occurrences Regulations (RIDDOR) making reporting certain incidents a legal requirement. The report informs the enforcing authorities about deaths, injuries, occupational diseases and dangerous occurrences. Mandatory notification procedures may also arise from certain types of specific hazards, such as exposure to biological agents. The Directive 2000/54/EC of the European Parliament on the protection of workers from risks related to exposure to biological agents at work establishes that “Art. 13 - Notification to the competent authority, Art. 14 - 4. The notification referred shall include (...) the name and capabilities of the person responsible for safety and health at work and (...) the protection and preventive measures that are envisaged”.

Also relevant are reporting procedures in non-compulsory management systems, namely the ILO Guidelines on OH&S management systems, when considering performance monitoring and measurement, clearly states that “Reactive monitoring should include the identification, reporting and investigation of: (a) work-related injuries, ill health (including monitoring of aggregate sickness absence records), diseases and incidents (...)”.

2. ORGANIZATION PRESENTATION

The organizational set for the present assessment of an institutional Notification System, in the Health Care sector, and for a five years period of the analysis, has a human resources framework as shown in Table 1.

Table 1: Workers.

Year	Number of workers
N	411
N+1	415
N+2	433
N+3	400
N+4	391
Mean (5 years)	410

Over the five-year period, there is no significant variation concerning the job categories amid the workers. The most relevant job categories are Operational assistants, representing in average 39% of the total number of workers; nurses are the second job category, with 32%; the third professional group are the Doctors (aprox. 18%) and the technical assistants are the smallest group with 11%.

The workers’ age profile, as viewed in Figure 1, identifies the higher percentage (19.22%) in the “50-54 year” age group, followed by the “45-49 years” age group, for the first three years, and a slight reduction for the last two years.

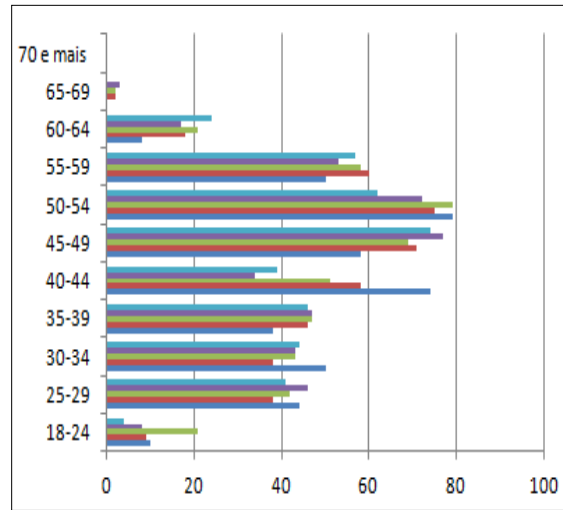


Figure 1: Age groups.

Education is diverse and the largest percentage of workers holds a university diploma within the first five years: (year N (41.12%); year N+1 (41.2%); year N+2 (48.96%); year N+3 (51.25%) and year N+4 (52.17%). The educational qualification has been increasing in a general manner over the years.

Another variable, in a management point of view is the working schedule.

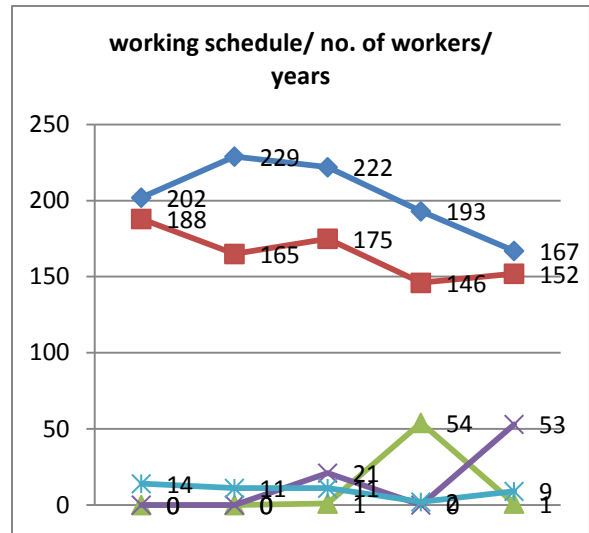


Figure 1: Working schedule.

(Note: blue (non-flexible); red (shifts); green (flexible); purple (lapse timetable) and blue (open schedule))

The non-flexible working schedule was undertaken for the five years from year N to year N+4, 49.15%, 55.18%, 51.27%, 48.25% and 42.71% respectively. Working in shifts (three shifts)

represented in the same five years 45.74%, 39.76%, 40.41%, 36.50% and 38.87%.

3. CASE STUDY

A preliminary analysis was undertaken to assess the potential of information flow and variables correlation. A sample register procedure was designed, including only ten (10) fields (variables) considered crucial for a first rough analysis.

Table 2: Sample register procedure.

Field	Content	Remarks	Management
0	Notification	Counter	S
1	Register	Monthly counter for the event & counter of number of persons involved in the event (Year)	S
2	Date	Day of the week	M
3	Time	In a 24 hour	M
4	Shift	Morning	M
		Afternoon	
		Night	
5	Location	Drop down menu of a inside map of the establishing	M
6	Gender	Female	W
		Male	
7	Professional Category	Drop down menu of the legal professional category	W/M
8	Type of Accident	Drop down menu of different accident's description	R
9	Accident classific	Accident	M
		Incident	

	ation	Near-miss	
		Incident event	
		Unknown/Not assess	

Note: S – system; M – management; W – worker and R – Risk

The sample register procedure comprehends ten (10) fields (a subset from the total of forty-one (41) fields of the main notification system. These ten fields are grouped into four (4) management criteria: S – system; M – management; W – worker and R – Risk. For the five (5) years period of the study, Table 3 shows the figures related to total number of records (events); number of workers involved in those events.

Table 3: Case Study characterization.

Year	Number of Records (Workers)	Number of Workers Involved	Total Workers
N	93	101	411
N+1	126	166	415
N+2	165	199	433
N+3	183	235	400
N+4	169	214	391
Total	736	915	

Out the 915 workers exposed to events subjected to register, over the five years period: 208 are nurses (22.73%); 17 operational assistants (1.86%); 18 doctors (1.97%) and 19 nursing students (2.085). The remaining registers comprise different job categories accounting for 15.74% of the total workers.

For analysis purposes, out of the five (5) years period, one particular year was selected (year n+3).

Table 4: Year N+3.

Year	Number of Records (Workers)	Number of Workers Involved	Total Workers
N+3	183	235	400

Findings from a case study over a 5 year period, based upon a notification system from one organization alone comprehending 736 records and 915 workers directly involved, supports a main conclusion. A notification system is not by itself enough in prevention terms. The validity of the required information and the way it is demanded is also fundamental to obtain adequate records.

The statistical data treatment is a critical stage, for changes regarding preventive actions and measures are based upon such findings and conclusions

4. RESULTS

Statistical treatment of data is fundamental to achieve adequate use of the data collected:

- Combinatory analysis,
- Multiple correspondences analysis (MCA), privileges tables of relevant size comprising simultaneously variables of distinct nature: quantifiable and qualitative. MCA helps in describing the complex relationships that may exist among variables, both independent and dependent (Dohoo, 1996).

For the five years, Table 5 presents the number of possible combinations ($n C p$) according to ten (10) variables of the sample register procedure.

Table 5: Case Study characterization.

n = 10			No. of combinations	Total of combinations
p =	2	n C p =	45	45
p =	3	n C p =	120	165
p =	4	n C p =	210	375
p =	5	n C p =	252	627
p =	6	n C p =	210	837
p =	7	n C p =	120	957
p =	8	n C p =	45	1002
p =	9	n C p =	10	1012
p =	10	n C p =	1	1013

However the present study only analyses combinations resulting from 2, 3 and 4 variables.

Table 6: Year “N+3” combinations.

n = 10			No. of combinations	Total of combinations
p =	2	n C p =	45	45

=		=		
p =	3	n C p =	120	165
p =	4	n C p =	210	375

In this set of a total of 375 combinations (45 (2 vars) + 120(3 vars) + 210(4 vars)), there is an essential aspect of always including field 00 (variable “Notification”) and field 01 (variable “Register”). Thus the total number of 224 combinations (17(2 vars) + 67(3 vars) + 140(4 vars)) as presented in Table 7.

Table 7: Year “N+3” combinations (Field 0 & 1).

n = 10			No. of combinations	Total of combinations
p =	2	n C p =	17	17
p =	3	n C p =	67	84
p =	4	n C p =	140	224

The register system under study, supporting the notification system can be viewed as a global set in the management cycle. It comprises a total of 47 management variables and a set of multiple sub-variables, resulting from the notification system analysed. The results obtained identify a set management variables such as: working schedules; job categories and the accident’s description as management variables essential in a risk assessment procedure. Also crucial, is the legal framework of accident work-related classification of all the records.

The codification system adopted, pretends to highlight the importance of a set of management variables which may be considered transversal to other economical sectors, from the workers’ point of view (gender, professional classification and others) and another set which is specific to the sector if the employers’ point of view is considered (day of the week, type of accident, communication procedures, contributing factors, (...)).

This study aims to design, implement and validate a notification system as both a transversal and sectorial information system in OH&S risk management.

A notification system should provide effective and adequate flow of information within a proactive prevention context.

Thus, the present study analyzed 736 records, involving 915 workers. This set of records is however part of a global notification system, not only work-related accidents, but also comprising all type of adverse events occurring, (total of 3763 records for the 5 year period, involving 4636 persons for the studied establishing)

5. FINAL REMARKS

Risk management has been described as “the adoption of financial, technological and organizational measures designed to modify the relationship between the turbulence of an environment and the variability of the results obtained therein”. Risk management is based essentially on analysis and evaluation of all of the relevant information available (Badi, 2015).

The mining sector, despite considerable efforts in many countries, remains the most hazardous occupation when the number of people exposed to risk is taken into account. Decision makers need a sustainable and consolidated reporting and notification system in order to implement effective improvements in the occupational and health safety (OH&S) management systems.

Table 8: Notification System: variables.

Health Care Variables	Notification variables	Mining variables
Legal framework	Notification	Mandatory
Date/time	Date/time	Date/time
Shifts (...)	Working schedule	24 hours production
Psychological risks	Type of accident (risk exposure)	Work-related diseases

In order for an action to be truly preventive or corrective, hazards must be identified first on the basis of rigorous analysis of information or data. Such an approach and further procedure can create conflict areas with a certain organizational operational day-to-day basis. Several management issues, such as financial, economic, social and operational, may be constrained concerning data sources (Badi, 2015).

Besides the mandatory legal framework procedure 1 “If workplace injuries or illnesses occur, the employer constructor, or mine or mining plant owner, have the following duties to notify certain people (...)”, notification systems, regarded as a full component of an OH&S management system, provide employers as decision-makers with a prevention design management tool, in all economic sectors in general, and in major risk sectors in particular.

6. REFERENCES

- Dohoo, I., R., Ducrot, C., Fourichon, C., Donald, A., Humik, D. (1996). An overview of techniques for dealing with large numbers of independent variables in epidemiologic studies. *Preventive Veterinary Medicine*, No. 29, pp.22 1-239.
- ILO-International Labour Office. 1996. *Recording and Notification of Occupational Accidents and Diseases*. ILO Code of Practice, Geneva.
- RIDDOR-Reporting of Injuries, Diseases and Dangerous Occurrences Regulations, 2013.
- Directive 2000/54/EC of the European Parliament and of the Council, of 18 September 2000, on the protection of workers from risks related to exposure to biological agents at work.
- ILO-International Labour Office, 2000. *Guidelines on occupational safety and health management systems*, (ILO-OSH 2001). Geneva, ISBN 92-2-111634-4.
- Badri, A. (2015) *The Challenge of Integrating OHS into Industrial Project Risk Management: Proposal of a Methodological Approach to Guide Future Research (Case of Mining Projects in Quebec, Canada)*. *Minerals* 2015, No. 5, pp. 314-334.

Full-scale fire experiments in an underground mine

Rickard Hansen

Malmfältens Brandkonsult, Nyköping, Sweden, 611 67

ABSTRACT

Few full-scale fire experiments have been performed in underground mines, therefore the information needed to validate calculations and estimations in preventive work, risk mitigation as well as incident planning is not readily available. This paper presents two full-scale fire experiments involving a loader and a drilling rig in a mine drift in Sweden. The heat release rate in the fire experiments was determined through oxygen calorimetry, i.e. by measuring the mass flow rate, gas concentrations and temperatures at certain heights at the far end of the mine drift, downstream of the fire source. The resulting heat release rate curve of the loader fire displays a fire that is initially dominated by a sudden increase in heat release rate when the first tire is engulfed by flames and then by the slowly declining heat release rates of the large tires of the vehicle. The calculated peak heat release rate of the loader was 15.9 MW and occurred approximately 11 minutes after ignition. The resulting heat release rate curve of the drilling rig displays a fire with high heat release rates and is relatively short lived – compared with the fire in the loader. Practically all the combustible items were ignited in the early phases of the fire. The calculated peak heat release rate of the drilling rig was 29.4 MW and occurred approximately 21 minutes after ignition. The fuel load of the loader consisted mainly of the tires, the hydraulic oil and the diesel fuel. The fuel load of the drilling rig consisted mainly of the hydraulic oil and the hydraulic hoses. The heat release rate curves were validated by comparing the summed up energy contents of the participating components with the integrated heat release rate curves.

KEYWORDS: Heat release rate, mining vehicle, full-scale fire experiment, underground mine

1. INTRODUCTION

Collecting information about relevant risks, fire spread in mining vehicles and mobile equipment, and heat release rates for different types of fires is fundamental in preventive work, risk mitigation as well as in incident planning. Few full-scale tests have been performed in underground mines and the information needed to validate calculations and estimations is not readily available. Studies have shown that vehicles and mobile equipment are the dominating source of fire in underground hard rock mines (Hansen, 2009; De Rosa, 2004). The studies have shown that better knowledge about fire behaviour and fire spread is needed for service vehicles, drilling rigs and loaders. Two full-scale fire experiments on mining vehicles were conducted in an underground mine in Sala, Sweden. The full-scale fire experiments involved a loader and a drilling rig and were conducted in order to provide much needed data for future fire safety designs in underground mines.

2. INVOLVED VEHICLES

The loader in question was a Toro 501 DL, a diesel driven loader used for hauling iron ore. Table 1 presents an inventory of the combustible components on the loader. The effective heat of combustion of the hydraulic hoses, low voltage cable and driver seat

was taken as the average value using results from cone calorimeter tests. The effective heat of combustion of the tires and rubber covers was set to 27 MJ/kg (Ingason, 2008). The effective heat of combustion of the diesel fuel was set to 42.6 MJ/kg (Totten et al., 2003) and 42.85 MJ/kg for the hydraulic oil (Simonson et al., 1998). When summing the energy contents of the individual components a total energy content of 76,245 MJ was calculated. The loader used in the experiments can be seen in Figure 1.

Table 1: Combustible component inventory – loader.

Component	Estimated amount	Energy content (MJ)
Tyres (rubber material)	~1560 kg	42120
Hydraulic oil	500 liters	16283
Hydraulic oil in hoses	70 liters	2280
Hydraulic hoses (rubber material)	~170 kg	4905
Diesel	280 liters	10138
Driver seat	~10 kg	228
Electrical cables	~1.5 kg	21
Rubber covers	~10 kg	270



Figure 1: Loader used in the experiments.

The drilling rig in question was an Atlas Copco Rocket Boomer 322, an electrically driven drilling rig that is also equipped with a diesel powered engine which is used when moving from one site to another. Table 2 presents an inventory of the combustible components. The effective heat of combustion of the hydraulic hose was also applied for the water hose. The effective heat of combustion of the plastic covers (ABS plastic) was set to 30 MJ/kg (Tewarson, 2002). When summing up the energy contents of the individual components a total energy content of 45,758 MJ was calculated.

Table 2: Combustible component inventory - drilling rig.

Component	Estimated amount	Energy content (MJ)
Tyres (rubber material)	~155 kg	4185
Hydraulic oil	350 liters in tank and 150 liters in hoses	16283
Hydraulic hoses (rubber material)	~390 kg	11252
Water hose (rubber material)	~40 kg	1154
Diesel	100 liters	3621
Driver seat	~10 kg	228
Electrical cables	~450 kg	8735
Plastic covers	~10 kg	300

3. DETERMINATION OF THE HEAT RELEASE RATE

The heat release rate in the fire experiments was determined through oxygen calorimetry, i.e. by measuring the mass flow rate, gas concentrations and temperatures at certain heights at the far end of the mine drift – downstream of the fire source - where the fire experiments were conducted. The method relies heavily on installed thermocouples at every measuring point – which are inexpensive, robust and

relatively easy to install – in order to reduce the dependence upon expensive and sensitive gas analysis instruments.

Assuming that the local gas temperature and the local gas concentration correlate through the average values over the cross-section (Ingason, 2006), the heat release rate can be calculated using the following expression:

$$\dot{Q} = \frac{13100 \cdot \rho_0 \cdot u_0 \cdot A \cdot \left(\frac{M_{O_2}}{M_a} \right) \cdot (1 - X_{H_2O,0})}{\frac{0.1}{X_{O_2,0}} + \frac{1 - X_{O_2,avg} \cdot \left(\frac{X_{O_2,avg}}{1 - X_{CO_2,avg}} \right)}{X_{O_2,0} - \left(X_{O_2,avg} \cdot \left(\frac{1 - X_{CO_2,0}}{1 - X_{CO_2,avg}} \right) \right)}} \quad [\text{kW}] \quad (1)$$

Where:

ρ_0 is the ambient air density [kg/m³]

u_0 is the cold gas velocity in a mine drift [m/s]

A is the cross-sectional area [m²]

M_{O_2} is the molecular weight of oxygen [g/mol]

M_a is the molecular weight of air [g/mol]

$X_{H_2O,0}$ is the mole fraction of water in the ambient air

$X_{O_2,avg}$ is the average concentration of oxygen

$X_{CO_2,avg}$ is the average concentration of carbon dioxide

$X_{O_2,0}$ is the mole fraction of oxygen in the ambient air

$X_{CO_2,0}$ is the mole fraction of carbon dioxide in the ambient air

The average concentration of oxygen, carbon dioxide and carbon monoxide are calculated using the above mentioned correlation. In equation (1) it is assumed that 13100 kJ/kg is released per kg of oxygen consumed and that the air mass flow rate of combustion gases equals the ambient air mass flow rate. Equation (1) has been used when determining the heat release rate for a number of large scale tunnel fire tests (Ingason and Lönnemark, 2005).

4. THE EXPERIMENTAL SITE

The full-scale fire experiments were conducted in a dolomite mine in Sweden. The fire experiments were conducted at level 55, an inactive part of the mine. Nonetheless, the infrastructure was still in place with power outlets, etc. The preconditions of the potential test site were the following: an active mine with an intact infrastructure, the possibility to

steer the smoke in one direction and through one single exhaust, and accessibility for vehicles. Figure 2 presents a plan of the level.

As there was only one exhaust on one side of the test site, all the smoke was ventilated out through the single exhaust, thus allowing for heat release rate measurements on this side of the test site. The intake of air was from the entrance and the lower regions of the mine.

Approximate dimensions of the mine drifts in the test area were 6 meter in height and 8 meter in width.

The mine drift where the experiments took place was approximately 100 meters long, approximately 150 meters from the entrance to the mine and 40 meters from the exhaust. There were practically no differences in height between the entrance of the mine and the exhaust.

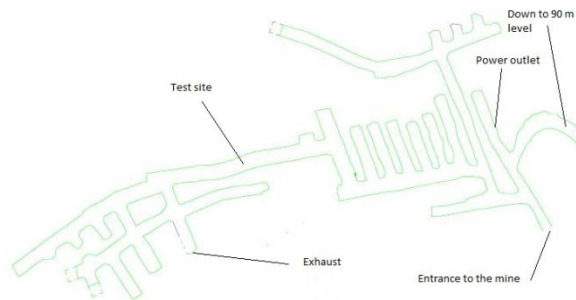


Figure 2: Experimental area.

5. EXPERIMENTAL SET UP

At the end of the mine drift – where all the fire gases would pass - the data needed for calculating the heat release rate was collected at a measuring station (see Figure 3 for the experimental set up in the mine drift). The data was measured using six thermocouples, four velocity probes and one gas monitor (measuring O₂, CO and CO₂) positioned at different heights. The temperature above each vehicle was measured with a thermocouple attached to the ceiling. A video camera was placed in the mine drift aimed at the side of each vehicle in order to record the fire behavior and the time of ignition of the combustible items.

On each vehicle a number of thermocouples were placed on the combustible components, i.e. the tires, hoses, cables and the interior of the cab. Four plate thermometers were placed at the ground at each tire during the tests in order to measure the heat flux at the locations.

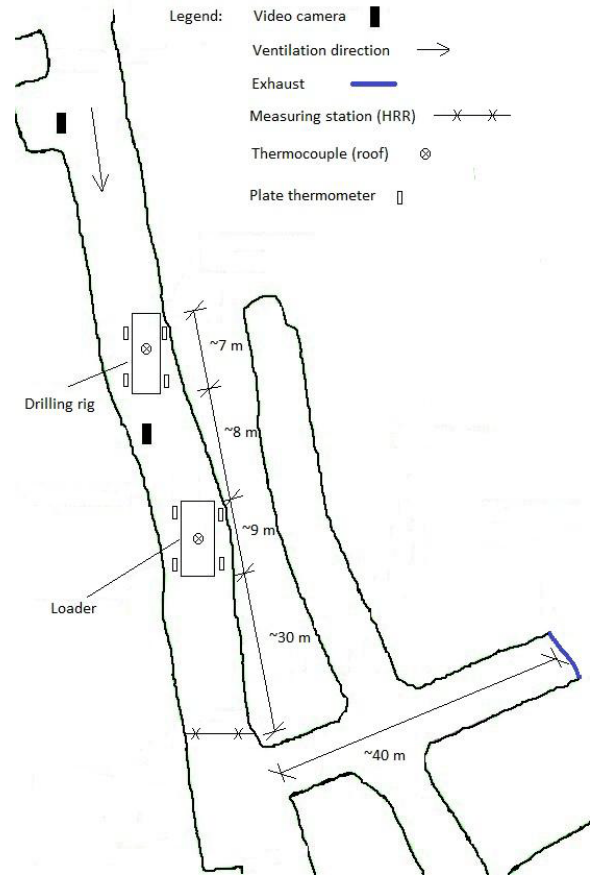


Figure 3: Experimental set up.

The existing ventilation flow in the area was found to be insufficient to ventilate all the smoke in one predetermined direction - in order to obtain adequate heat release rate measurements. Additional ventilation resources were therefore needed and a mobile fan with a capacity of 217,000 m³/h was used during the experiments.

Regarding fire initiation, a circular tray was placed underneath the fuel tank of each vehicle and it was located close to at least one tire. The trays were filled with diesel fuel in order to simulate a pool fire caused by leaking diesel from the tank.

6. EXPERIMENTAL RESULTS

6.1 Loader Experiment

After the completion of the loader experiment it was found that the front tires had not been consumed in the fire and were therefore intact. Also, the hydraulic hoses from the vertical hinge (the vehicle is split into a front and a rear half which are connected by a vertical hinge approximately at the middle of the vehicle) and forward and in some parts of the rear section behind the rear tires also remained intact.

Other parts had participated fully in the fire. The resulting heat release rate curve can be seen in Figure 4. The maximum heat release rate from the experiment was 15.9 MW. The maximum heat release rate was reached approximately 11 minutes after ignition. The resulting heat release rate curve displayed a fire that was dominated by a sudden increase of the pool fire and when the first tyre was engulfed by flames and then by the slowly declining heat release rates of the large tyres of the vehicle. Still, the stop of fire spread from the vertical hinge and forward clearly shortened the duration of the fire considerably.

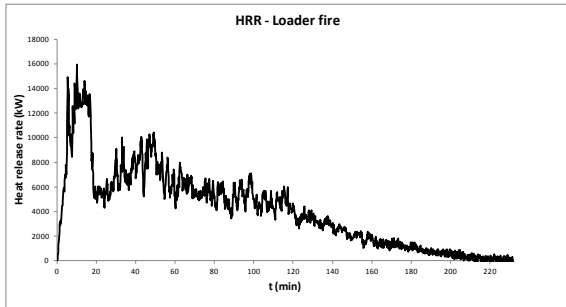


Figure 4: The resulting heat release rate of the loader.

The maximum average gas temperature at the measuring station (74°C) occurred after approximately 11 minutes, which is the same time as the occurrence of the maximum heat release rate. This latter observation is expected, as the average oxygen and carbon dioxide concentration correlates with the average gas temperature at the measuring station. The average gas temperature measurements can be seen in Figure 5.

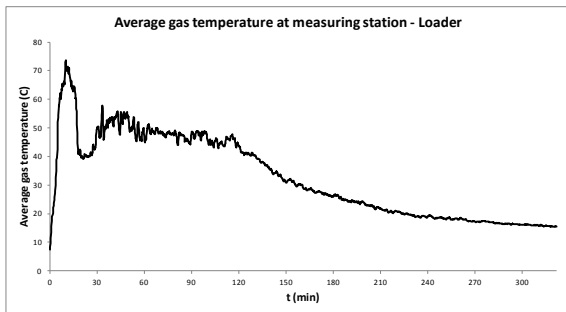


Figure 5: The average gas temperature at the measuring station - loader experiment.

Using the heat release rate curve the energy content of the combustible materials consumed in the fire was calculated at 57 GJ. When summing the energy contents of the materials participating in the fire the summation results in an energy content of

50.5 GJ. The difference is most likely due to the uncertainties when estimating the amount of combustibles available and the amount of combustibles consumed in the fire.

6.2. Drill Experiment

After the completion of the drilling rig experiment it was found that a small portion of the hydraulic oil did not participate in the fire. Except for the hydraulic hoses approximately two meters in front of the cab and forward, some amount of hydraulic oil as mentioned above, and a major part of the low voltage cable on the cable reel, the entire vehicle had participated in the fire and the combustible material had been consumed. The heat release rate curve from the experiment can be seen in Figure 6. The maximum heat release rate from the experiment was 29.4 MW and was attained after 21 minutes. The resulting heat release rate curve of the drilling rig displays a fire with high heat release rates and relatively short lived – compared with the fire in the loader. Practically all the combustible items were ignited in the early phases of the fire.

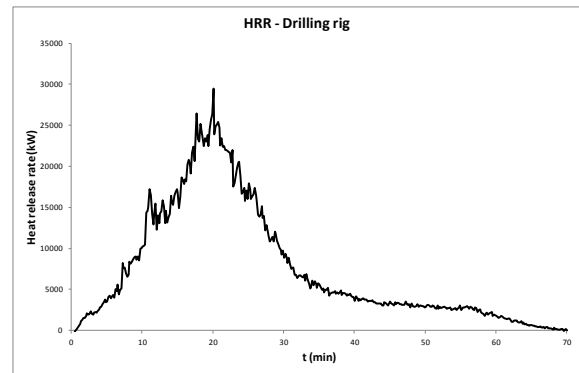


Figure 6: The resulting heat release rate of the drilling rig.

The maximum average gas temperature at the measuring station - 93°C - occurs after approximately 21 minutes, which is the same time as the occurrence of the maximum heat release rate (see Figure 7 for the average gas temperature at the measuring station). When comparing the average gas temperature in Figure 7 and the heat release rate curve in Figure 6 it can be seen that the average gas temperature at the measuring station correlates well with the measured heat release rate.

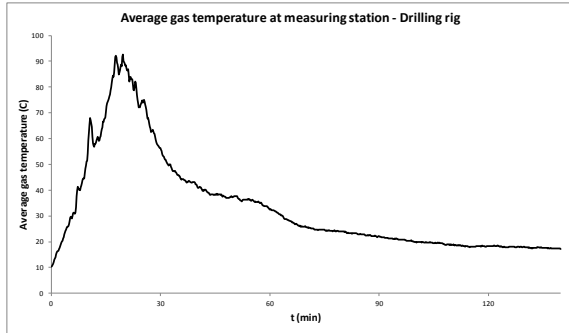


Figure 7: The average gas temperature at the measuring station - drilling rig experiment.

The energy content of the combustible materials consumed in the fire was calculated at 30.9 GJ. When summing up the energy contents of the materials participating in the fire the summation results in an energy content of 32.5 GJ. The difference is most likely due to the same uncertainties as in the case of the loader.

7. DISCUSSION

The initial sharp rise and high heat release rate for the first 20 minutes of the loader fire can be explained mainly due to the pool fire and the fire in the rear, right tire. The sharp drop after about 20 minutes was due to the pool fire burning off. The burn off time of the diesel pool fire at the loader experiment was calculated to be about 43 minutes (assuming a regression rate of $0.066 \text{ kg/s}\cdot\text{m}^2$ (deep pool)). Assuming a maximum heat release rate per unit area of 1.33 MW/m^2 (Lönnermark et al., 2008) for a thick fuel bed, the maximum heat release rate of the diesel pool fire was calculated to be 1.26 MW. When studying the heat release rate curve in Figure 4, the decrease in heat release rate was about 8 MW which was much larger than the calculated 1.26 MW of the pool fire. The difference can be explained by the fact that the diesel tank of the wheel loader was not equipped with a magnetic valve – as in the case of the drilling rig – which suggest that the fuel hoses in the proximity of the fuel tank could have been burned off during the early stages, draining the tank and thereby increasing the size of the pool fire and consequently the heat release rate of the diesel pool fire. Also, the pool fire was underneath the loader and thus the re-radiation back to the pool surface would be much larger than for a free standing pool fire and thus the heat release rate would be larger. This observation is further enforced by the fact that the calculated burn off time of the diesel pool fire was more than twice as long as the observed burn off time. The differences will have to be investigated further in order to be fully explained.

The slow increase in heat release from about 20 minutes to about 50 minutes was due to the slow flame spread along the surface of the rear, left tire. The sudden – and temporary - decrease in the ventilation velocities and heat release rate approximately 10 minutes after ignition can be related to the change of position of the mobile fan, where the fan was geared down temporarily during the transport. The change of position was due to extensive backlayering reaching and passing the initial position of the fan.

The plate thermometers positioned at the forward tires did not record incident heat fluxes exceeding 14 kW/m^2 (unfortunately the plate thermometer at the right, forward tire stopped functioning approximately 40 minutes after ignition) and were therefore in line with the fact that ignition of the forward tires did not take place - if assuming and applying a critical heat flux of 17.1 kW/m^2 (Babrauskas, 2003) for natural rubber.

Approximately two minutes after ignition both rear tires of the drilling rig were ignited and the fire spread further to hydraulic hoses in the rear, upper part. About 12 minutes after ignition the right, forward tire was ignited. At about the same time a sudden increase in intensity occurred, most likely due to the bursting of the right, rear tire. After 26 minutes there was a second sudden increase in intensity, due to the bursting of the right, front tire.

The temperature at the forward part of the drilling rig boom – where the hydraulic hose did not ignite and burn – exceeded 930°C approximately 25 minutes after ignition, when studying the temperature recordings of the thermocouple at the boom. It is unclear why the hydraulic hoses did not ignite and burn. It could possibly and partially be explained by the hydraulic hoses already being drained of all hydraulic oil and thus decreasing the heat release rate and the fire spread when initially ignited. The incident radiation level was simply too low to propagate the fire in the direction of the ventilation flow.

8. CONCLUSIONS

Two full scale fire experiments involving a loader and a drilling rig were carried out in an operative underground mine in Sweden, in order to produce total heat release rate curves for representative mining vehicles.

It was found in the loader experiment that the front part of the vehicle with front tires never ignited. The maximum measured heat fluxes at the front tires were found to never exceed the critical heat flux of natural rubber and was thus in line with the fact that ignition did not occur.

The maximum heat release rate from the experiment was 15.9 MW and it was reached approximately 11 minutes after ignition.

The resulting heat release rate curve of the loader fire displayed a fire that is dominated initially by the sudden increase in heat release rate when the first tire is engulfed by flames and then by the slowly declining heat release rates of the large tires of the vehicle. Still, the stop of fire spread from the vertical hinge and forward clearly shortened the duration of the fire considerably.

Regarding the drilling rig fire experiment it was found that except for the hydraulic hoses approximately two meters in front of the cab and forward, some amount of hydraulic oil, and a major part of the low voltage cable on the cable reel, the entire vehicle had participated in the fire.

The maximum heat release rate from the drilling rig experiment was 29.4 MW and it was attained after 21 minutes.

The resulting heat release rate curve of the drilling rig displayed a fire with high heat release rates and was relatively short lived, compared with the fire in the loader. Practically all the combustible items were ignited in the early phases of the fire.

9. REFERENCES

Babrauskas V. (2003), Ignition handbook. Fire Science Publishers, Issaquah, USA.

De Rosa M.I., 2004. Analysis of mine fires for all US metal/non-metal mining categories, 1990-2001. NIOSH.

Hansen R., 2009. Literature survey – fire and smoke spread in underground mines. Mälardalens Högskola, MdH SiST 2009:2, Västerås.

Ingason H., and Lönnemark A. (2005). Heat release rates from heavy goods vehicle trailers in tunnels. Fire Safety Journal, Volume 40, pp. 646-668

Ingason, H. (2006). Correlation between temperatures and oxygen measurements in a tunnel flow. Fire Safety Journal, Volume 42, pp. 75-80

Ingason H., 2008. Fire test with a front loader. SP report P801596, SP, Borås.

Lönnemark, A., Kristensen, P., Helltegen, M., and Bobert, M. (2008). Fire suppression and structure protection for cargo train tunnels: macadam and hotfoam. ISTSS.

Simonson M., Milovancevic M. and Persson H., 1998. Hydraulic fluids in hot industry: fire characteristics and fluid choice. SP Report 1998:37, SP, Borås

Tewarson A. (2002), Generation of Heat and Chemical Compounds in Fires. In: The SFPE Handbook of Fire Protection Engineering (P J DiNenno, D Drysdale, C L Beyler, W D Walton, R L

P Custer, J R Hall and J M Watts, Eds.). NFPA, Quincy, USA.

Totten G.E., Westbrook S.R. and Shah R.J. (2003) Fuels and lubricants handbook: technology, properties, performance, and testing, volume 1. ASTM International.

Diesel exhaust exposures in an underground mine

Hugo Coulombe ^a, Guillaume Lachapelle ^b, Eve Neesham-Grenon ^c, Stéphane Hallé ^d,
Maximilien Debia ^{c,*}

^a Health and Safety, Westwood Mine (IAMGOLD), Preissac, Canada, JOY 2E0

^b Health and Safety, Agnico Eagle Mines, Toronto, Canada, M5C 2Y7

^c Department of Environmental and Occupational Health, School of Public Health, Université de Montréal, Montreal, Canada, H3T 1A8

^d Department of Mechanical Engineering, École de Technologie Supérieure, Montreal, Canada, H3C 1K3

ABSTRACT

The mining industry is a major contributor to the Quebec and Canadian economy. In Canada, more than 400,000 workers are involved directly or indirectly in the mining industry. Health and safety challenges in underground mines are unique due to the complexity of the environment. Exposure to diesel engine exhaust is a major concern in underground mines due to the presence of off-road diesel-powered machinery. Diesel engine exhaust has been linked to cardiopulmonary diseases and was classified as a human carcinogen by the International Agency for Research on Cancer in 2012. Here we present the results of a preliminary study conducted in an underground gold mine in the province of Quebec in 2014-15 to assess diesel engine exhaust exposures among mine workers. The goal of this study was 1) to compare three surrogates of diesel engine exhaust exposure (total carbon, elemental carbon and respirable combustible dust) and 2) to assess diesel exhaust concentrations among the similar exposure groups and the variability of the exposures. Results were also compared to the Ontario and Quebec occupational exposure limits for compliance purposes. Environmental and breathing zone measures were taken. Average environmental results of 0.31 mg/m³ in total carbon, 0.24 mg/m³ in elemental carbon, and 0.17 mg/m³ in respirable combustible dust were obtained. Average breathing zone results of 0.32 mg/m³ in total carbon, 0.19 mg/m³ in elemental carbon and 0.36 mg/m³ in respirable combustible dust were obtained. The highest exposures were obtained in the conventional, scooptram and jumbo workers. The average total carbon/elemental carbon ratio was 1.3 for environmental measures, and 1.9 for breathing zone measures. The variability observed in the total carbon/elemental carbon ratio shows that interferences from non-diesel related organic carbon can skew the interpretation of results when relying only on total carbon data. However, more data is needed to support this.

KEYWORDS: diesel; exposure; underground mine; respirable combustible dust; elemental carbon; total carbon; similar exposure groups

1. INTRODUCTION

Exposure to diesel engine exhaust (DE) has been linked to increased cancer risk and cardiopulmonary diseases. DE has recently been classified as a human carcinogen (group 1) by the International Agency for Research on Cancer (IARC, 2012) and has become a contaminant of primary interest at the international level. Vermeulen et al. (2014) reported that 6% of deaths from lung cancers could be linked to occupational exposures to DE. Acute exposures to DE have been associated with respiratory irritation and inflammation, and cardiovascular effects (Hussain et al., 2012; Kipen et al., 2011; Lucking et al., 2008; Mills et al., 2005; Nordenhall et al., 2000; Salvi et al., 1999).

DE refers to the complex mixture of chemical substances found in solid, liquid or gaseous states resulting from the incomplete combustion of fuel. The type of engine, fuel, oil, and operation are all factors

that can affect the composition of DE. Carbon (mono- and di-) oxides (CO and CO₂), nitric oxide (NO), nitrogen dioxide (NO₂), sulfur dioxide (SO₂), water vapour, sulfur compounds, low molecular weight hydrocarbons (e.g. benzene, 1,3-butadiene), and oxygenated compounds (e.g. aldehydes) can all be found in the mixture. Diesel particulate matter is composed of elemental carbon (EC) onto which organic carbon (OC) compounds and other particles (unburnt fuel, lubricant droplets, metallic additives, etc.) are adsorbed. The majority of the particles in diesel particulate matter are within the respirable fraction (4 µm in diameter or less) and most are ultrafine particles (100 nm in diameter or less) (Carex Canada, 2015).

Occupational exposure limits (OEL) for DE vary greatly between and within countries. In the province of Quebec, Canada, a limit value of 0.6 mg/m³ of respirable combustible dust (RCD) applies to the

*Corresponding author – email: maximilien.debia@umontreal.ca

mining industry (Government of Quebec, 2016). The Canadian province of Ontario has recently adopted a regulatory time-weighted value of 0.4 mg/m³ of total carbon (TC) transposable to EC via a conversion factor of 1.3 (i.e. about 0.31 mg/m³ for EC) for the mining industry (Government of Ontario, 2016). The U.S. Mine Safety and Health Administration (MSHA) has prescribed an 8-hour OEL of 0.16 mg/m³ of TC based on recommendations and methods of the National Institute for Occupational Safety and Health (NIOSH) (MSHA, 2008). There is currently no regulation for TC or EC in the province of Quebec. However, a proposition for the modification of the Quebec regulation of 0.6 mg/m³ of RCD to 0.4 mg/m³ of TC has recently been published in the Official Gazette of Quebec (*Éditeur Officiel du Québec*, 2015). There is currently no time-weighted average Threshold Limit Value proposed by the American Conference of Governmental Industrial Hygienists.

Underground mines pose great occupational health and safety challenges due to their very unique work environments. The presence of off-road, diesel-powered mobile machinery is one of these challenges, which is briefly addressed in this paper.

2. METHODS

The DE assessment methods compared were the NIOSH 5040 method (NIOSH, 2003) used for sampling the carbon fraction (EC and OC), and the RCD method (IRSST, 2016). For the NIOSH 5040 method, 37-mm aluminum cyclones (SKC) were used with 37-mm quartz filter cassettes, SKC model 225-1 cassette holders, and SKC pumps (PCXR4 model). Interferences from cigarette smoke, non-metal mining (e.g. coal) and oil mist are to be considered with this method. For the RCD method, 25-mm aluminum cyclones (SKC) were used with 25-mm silver membrane cassettes, SKC model 225-1 cassette holders, and SKC pumps (PCXR4 model). Interferences from oil mist and mineral dust (e.g. sulfides in rock) are to be considered with this method. Personal RCD and NIOSH 5040 samples were taken during two separate periods of two to three weeks; the RCD samples were taken in November and December 2014 while the NIOSH 5040 samples were taken in March 2015. Personal samples were taken 30 centimeters from the workers' breathing zone during their full 10-hour shift. Environmental RCD and NIOSH 5040 samples were taken simultaneously in main circulation routes (i.e. bypasses and ramps) over periods of about 8 hours. The pumps were hooked to the ground support at about 8 feet high to avoid damage to the equipment.

Most samples were taken during the day shift. Field observations were noted throughout the sampling periods. The RCD samples were sent to SGS

Laboratories (Lakefield, Ontario, Canada) and the carbon samples were sent to Galson laboratories (New York, USA).

Statistical analyses were done with IHSTAT (American Industrial Hygiene Association - Exposure Assessment Strategies Committee). The geometric mean (GM) and geometric standard deviation (GSD) were used for describing the exposure profiles. The estimated arithmetic mean (AM) and the corresponding 95% confidence limits were used for comparing personal exposure levels to exposure limits and for evaluating the cumulative damage from exposure to diesel exhaust. Non-detected values were replaced by the corresponding limit of quantification (LOQ) for the sample. Similar exposure groups (SEG) were based on job titles and were pre-defined by the company.

3. RESULTS

3.1 Environmental measures

Environmental TC, EC, and RCD concentrations are presented in Table 1. The average TC/EC ratio for environmental measures was 1.3.

Table 1: Summary of environmental TC, EC and RCD measures.

	TC (mg/m ³)	EC (mg/m ³)	RCD (mg/m ³)
GM	0.31	0.24	0.17
GSD	2.00	2.22	1.90
N	5	5	5

TC: total carbon; EC: elemental carbon; RCD: respirable combustible dust; GM: geometric mean; GSD: geometric standard deviation; N: sample number

3.2 Personal measures

Descriptive and inferential statistics for personal TC, EC, and RCD concentrations are summarized in Table 2. Personal TC measures were close to the Ontario OEL of 0.4 mg/m³ (AM = 0.32 mg/m³ [LCL = 0.28; UCL = 0.38]). Personal EC measures were at about half the Ontario OEL of 0.31 mg/m³ (AM = 0.19 mg/m³ [LCL = 0.15; UCL = 0.24]). The personal RCD concentrations were at about half the Quebec OEL of 0.6 mg/m³ (AM = 0.36 mg/m³ [LCL = 0.29; UCL = 0.52]). The average TC/EC ratio for personal measures was 1.9.

Table 3 presents the TC, EC and RCD concentrations according to the different SEG. Conventional, scooptram and jumbo operators were

the most exposed. At the opposite, mechanics, foremen and rock bolter operators were the least exposed groups. As presented in Table 3, most of the geometric standard deviations were around 2 or below. The TC/EC ratio for the conventional and chisel operators were higher than for other SEG (4.1 and 5.8, respectively).

Table 2: Summary of personal TC, EC and RCD measures.

	TC (mg/m ³)	EC (mg/m ³)	RCD (mg/m ³)
AM	0.32	0.19	0.36

95% CL	LCL=0.28 UCL=0.38	LCL=0.15 UCL=0.24	LCL=0.29 UCL=0.52
GM	0.30	0.15	0.25
GSD	1.53	1.87	2.41
N	30	30	36

TC: total carbon; EC: elemental carbon; RCD: respirable combustible dust; AM: estimated arithmetic mean; 95% CL: 95% confidence limits; LCL: lower confidence limit; UCL: upper confidence limit; GM: geometric mean; GSD: geometric standard deviation; N: sample number

Table 3: TC, EC and RCD results by SEG.

SEG*	TC (mg/m ³)			EC (mg/m ³)			RCD (mg/m ³)			TC/EC ratio
	GM	GSD	N	GM	GSD	N	GM	GSD	N	
Shotcrete operators	na	na	na	na	na	na	0.51	1.59	2	na
Truck operators	0.28	1.37	6	0.19	1.47	6	0.19	1.80	3	1.5
Scooptram operators	0.36	1.52	8	0.21	1.54	8	0.30	2.20	8	1.7
Foremen	0.20	1.28	2	0.13	1.17	2	0.14 ^a	5.80	2	1.5
Conventional	0.74	1.28	2	0.18	1.42	2	0.72	1.96	4	4.1
Electricians	na	na	na	na	na	na	0.21	1.63	2	na
Diamond driller operators	na	na	na	na	na	na	0.13	1.91	2	na
Jumbo operators	0.33	1.26	2	0.17	1.09	2	0.35	1.39	3	1.9
Mechanics	0.19	1.29	2	0.14	1.36	2	0.11 ^a	2.35	3	1.4
Chisel operators	0.29	1.37	2	0.05	10.01	2	na	na	na	5.8
Rock bolter operators	0.21	1.00	2	0.12	1.19	2	na	na	na	1.8

TC: total carbon; EC: elemental carbon; RCD: respirable combustible dust; GM: geometric mean; GSD: geometric standard deviation; SEG: similar exposure group; N: sample number; na: not available

*Only SEG for which there were two samples or more are reported

^aOne value was <LOQ

4. CONCLUSION

In conclusion, as long-term risk indices, arithmetic mean estimates and the corresponding upper confidence limits did not exceed the Ontario and Quebec OELs for personal TC, EC and RCD measures. More data is needed for each SEG to better understand the exposure profiles and to make a comprehensive long-term risk assessment.

The variability observed in the TC/EC ratio shows that interferences from non-diesel related organic carbon can skew the interpretation of results when relying only on TC data. This was most obvious when comparing the ratios between the different SEG. The conventional and chisel operators had a higher ratio, indicating greater interferences from non-diesel related organic carbon, most likely from oil mist. Our

results question the use of TC as a measure of occupational exposure to DE. However, more data is needed to validate this.

In future studies, direct reading instruments will be used in addition to the integrated sampling methods described in this paper, in order to better understand the determinants of exposures.

Overall, this preliminary study gives an overview of diesel exhaust exposures in an underground mine.

5. ACKNOWLEDGEMENT

The authors would like to thank all workers who have participated in the study. This project was financially supported by the Fonds de recherche du Québec - Nature et technologies (FRQNT).

6. REFERENCES

Carex Canada. (2015). Diesel Engine Exhaust. http://www.carexcanada.ca/en/diesel_engine_exhaust/.

Éditeur Officiel du Québec. Regulation Respecting Occupational Health and Safety in Mines, Chapter S-2.1, r. 14, SECTION IV 1.102(1)(a) Quebec City, Québec, Canada.

Éditeur Officiel du Québec. (2015). Part 2: Regulation modifying the Regulation Respecting Occupational Health and Safety in Mines Official Gazette of Quebec, 28 october 2015, 147th year, no 43, 4085-4086.

Government of Ontario. Mines and Mining Plants, Occupational Health and Safety Act, R.R.O. 1990, Regulation 854, PART VIII 183.1(5) (a). Ottawa, Ontario, Canada.

Hussain, Sabiha, Laumbach, Robert, Coleman, Jakemia, Youseff, Hatim, Kelly-McNeil, Kathie, Ohman-Strickland, Pamela, Kipen, Howard. (2012). Controlled exposure to diesel exhaust causes increased nitrite in exhaled breath condensate among subjects with asthma. *Journal of occupational and environmental medicine/American College of Occupational and Environmental Medicine*, 54(10), 1186.

IARC. (2012). Diesel and gasoline engine exhaust and some nitroarenes IARC monographs on the evaluation of carcinogenic risks to humans (Vol. 105). International Agency for Research on Cancer, Lyon, France.

IRSST. (2016). Respirable combustible dust (RCD) analysis. Method 384. <http://www.irsst.qc.ca/en/laboratories/references-tools/guidetools/workplace-air-contaminant/substance/i/307>.

Kipen, Howard M, Gandhi, Sampada, Rich, David Q, Ohman-Strickland, Pamela, Laumbach, Robert, Fan, Zhi-Hua, Madura, Kiran. (2011). Acute decreases in proteasome pathway activity after inhalation of fresh diesel exhaust or secondary organic aerosol. *Environmental health perspectives*, 119(5), 658.

Lucking, Andrew J, Lundback, Magnus, Mills, Nicholas L, Faratian, Dana, Barath, Stefan L, Pourazar, Jamshid, . . . Badimon, Juan J. (2008). Diesel exhaust inhalation increases thrombus formation in man†. *European heart journal*.

Mills, Nicholas L, Törnqvist, Håkan, Robinson, Simon D, Gonzalez, Manuel, Darnley, Kareen, MacNee, William, Sandstrom, Thomas. (2005). Diesel exhaust inhalation causes vascular dysfunction and impaired endogenous fibrinolysis. *Circulation*, 112(25), 3930-3936.

MSHA. (2008). Limit on Exposure to Diesel Particulate Matter, Code of Federal Regulations Title

30, Part 57.5060(b),(3) (pp. 370-371). Washington, DC.

NIOSH. (2003). Method 5040: Diesel Particulate Matter (as Elemental Carbon) NIOSH Manual of Analytical Methods, 4th Ed. (4th ed.). National Institute for Occupational Safety and Health, Atlanta, GA, USA

Nordenhall, C, Pourazar, Jamshid, Blomberg, Anders, Levin, Jan-Olof, Sandstrom, T, & Adelroth, E. (2000). Airway inflammation following exposure to diesel exhaust: a study of time kinetics using induced sputum. *European Respiratory Journal*, 15(6), 1046-1051.

Salvi, Sundeep, Blomberg, Anders, Rudell, Bertil, Kelly, Frank, Sandstrom, Thomas, Holgate, Stephen T, & Frew, Anthony. (1999). Acute inflammatory responses in the airways and peripheral blood after short-term exposure to diesel exhaust in healthy human volunteers. *American journal of respiratory and critical care medicine*, 159(3), 702-709.

Vermeulen, Roel, Silverman, Debra T, Garshick, Eric, Vlaanderen, Jelle, Portengen, Lützen, & Steenland, Kyle. (2014). Exposure-response estimates for diesel engine exhaust and lung cancer mortality based on data from three occupational cohorts. *Environmental health perspectives*, 122(2), 172.

Liquid-solid coupling analysis of tailings dam under complex engineering conditions

Shuren Wang^{a,*}, Haiqing Zhang^b, Zhengsheng Zou^a, Xiliang Liu^a

^a Opening Project of Key Laboratory of Deep Mine Construction, Henan Polytechnic University, Jiaozuo, China, 454003

^b School of Engineering and Technology, China University of Geosciences, Beijing, China, 100083

ABSTRACT

The tailings pond, a place for stockpiling tailings, is a necessary facility for maintaining normal production of a mine. On the other hand, the tailings dam is a major danger for metal and non-metal mines, because dam failure may occur. The present study takes the flat land tailings pond of the Sanshan Island gold mine, Shangdong Province, China, as an example. The tailings dam 3D numerical model was built using MIDAS/GTS and FLAC^{3D} techniques. The safety factor and the potential slide face of the tailings dam were calculated under different conditions using the strength reduction method. It is concluded from the liquid-solid coupling analysis that there are three potential failure modes of the tailings dam under preloading. Under the present conditions, the tailings dam meets the safety requirements, however, it does not in the event of additional heaping. The height of the present heap must be cut to satisfy the stability requirements under the condition of rain infiltration.

1. INTRODUCTION

The tailings pond is a necessary facility for maintaining the normal production of a mine, and as a place for stockpiling tailings. On the other hand, the tailings dam is a major danger for metal and non-metal mines, as dam failure may occur. In the case of a possible tailings accident, it will cause not only great losses and harm the safety of life and property to the residents downstream of the mine, but also serious environmental pollution.

Many scholars have studied the stability of the tailings pond and dam failure disasters. Shakesby and Richard (1991) studied the tailings dam accident in Arcturus gold mine in Zimbabwe. They hypothesized that the dam failure resulted from the poor seepage conditions of the dam foundation, as the dam slope was too steep and the tailings were saturated under heavy rain. Through investigating the tailings dam failure in America, Strachan (2001) held that the dam failure was a result of flood overtopping, static or dynamic instability, seepage, internal corrosion and poor foundation conditions. Chakraborty and Choudhury (2009) investigated the behavior of tailings earthen dam under static and seismic conditions, and found that the dam deformation was affected seriously by seismic action. Additionally, the underlying input acceleration of tailings dam had an amplification effect along the height of dam. Bussière et al. (2003) modeled the flow field characteristic for exposed and covered tailings dams using the finite element method (FEM). Valenzuela and Barrera (2003) analyzed the seismic stability of the dam up to

a height of 195 m by the limit equilibrium method in Los Quillayes copper mine in Chile, indicating that a dam height of 195 m was feasible.

Li et al. (2012) summarized two instability models based on the combination of the liquid-solid coupling method with the strength reduction method. One method concerned global instability and the other local instability, which is mostly caused by the too shallow saturation line in the tailing dams. Chen et al. (2008) provided a comprehensive method to evaluate the tailings dam stability with numerical calculation of the seepage stability, static stability and dynamic stability of a specific project. Yin et al. (2010) studied the change regularity of the saturation lines during normal and flood conditions, when the dam had been heaped to about two thirds of the total height of 120 m. Hu et al. (2004) analyzed the anti-slide stability of the upstream tailing by changing the dam height, saturation line conditions and the drainage system operating conditions. Li et al. (2005) analyzed the stability of a tailings dam using the Sweden method and Bishop method, giving the interrelated parameter of the stability and the credibility of the dam structure when its level was raised to 510-520 m. Lou et al. (2005) calculated the stress-strain isoline of the higher dam in the future by using FEM, and evaluated the dam's stability with the residual thrust method.

The main causes of tailings dam failure include flood overtopping, slope stability, seepage failure, structural damage and seismic liquefaction. The influence of the seepage field on the stability of the tailings dam cannot be ignored. The current study is

*Corresponding author – email: w_sr88@163.com

mainly based on a two-dimensional plane strain assumption. In order to correct the lack of analysis of three-dimensional (3D) stability of the tailings seepage and deformation, a 3D numerical model was built based on a flatland tailings pond project, to conduct the liquid-solid coupling analysis of the potential risk due to successive preloading in front of the dam. Afterwards, engineering countermeasures were put forward according to the evaluated results.

2. ENGINEERING OVERVIEW

As shown in Figure 1, taking the flatland tailings pond in China as an example, the pond covered an area of about 0.22 km², and had a catchment area of about 0.21 km². The ground level was about 3.1 m - 4.2 m, and the reservoir elevation was about 3.5 m - 20.7 m. The starter dam consisted of roller compacted sand, with a height of 11.0 m, top width of 3.0 m, and outer slope ratio of 1:1.8 - 1:2.5. Figure 1 shows the plan of the tailings pond and the mullock heap.

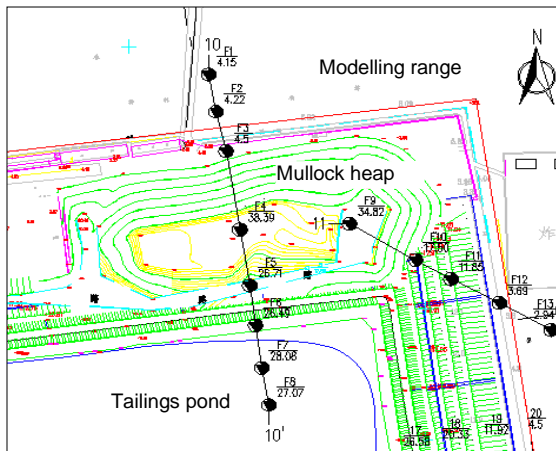


Figure 1: Schematic of borehole layout and the calculation range.

The waste rock heaped up from 2010 in the northwest corner of the tailings dam, with an accumulation level up to 38.5 m, a height 11 meters higher than that of the tailings stacking dam (status elevation 27.5 m). The plane shape of the waste rock heap was approximately rectangular with an east-west length of 260 m, and a 110 m length from north to south, covering an area of about 1.89×10^4 m² and occupying a volume of 36.67×10^4 m³. The mullock heap was about 50 m wide in the south, and it weighed on the north slope of the dam. The mullock heap slide was unaffected until a natural repose slope ratio of 1.0:1.1 - 1.0:3.0, and no obvious collapse or crack was found during the site investigation.

According to the survey results of drilling, the stratum was divided into three layers from top to bottom: mullock material, tailings material and the natural formation. The mullock heap was mainly gravel with silt. Tailings fill dam were mainly tailings silt and silty clay. The original ground was composed of medium coarse sand of alluvial-diluvial and marine deposit genesis and alluvial-diluvial silty clay.

3. 3D MODEL AND SIMULATION ANALYSIS SCHEME

3.1 Building the computational model

In view of the technical difficulties of FLAC^{3D} for complex 3D engineering modelling, the finite element software MIDAS/GTS of South Korea was adopted for geometric modeling of complex geologic body and mesh generation, followed by model data transformation from MIDAS/GTS to FLAC^{3D}, to make up for the pre-processing shortcomings of FLAC^{3D} and give full play to its powerful calculating function.

Although the element shape of MIDAS/GTS is basically the same as that of FLAC^{3D}, the node numbering rules and node order are different, therefore, the element and node data exported from MIDAS/GTS should be rearranged according to the FLAC^{3D} recognizable format and then be imported, thus realizing data transformation between the two programs. This can be achieved by programming. The entire modeling process is shown in Figure 2.

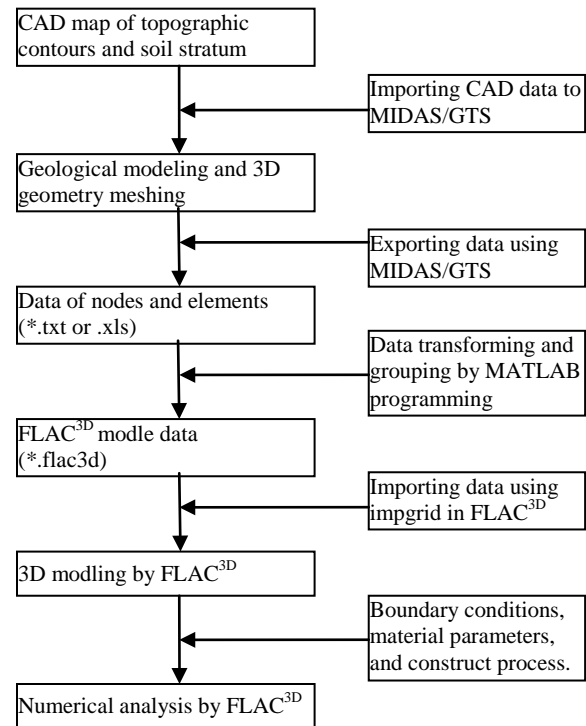


Figure 2: Flow chart of three-dimension modeling process.

The tailings dam 3D numerical model (Figure 3) was built following the aforementioned procedure, corresponding to the scope of the blue dashed line in Figure 1. A system of coordinate axes was defined with the origin at the silty clay layer beneath the natural ground of 34 m, with the z-axis pointing upward. The model was approximately 280 m long, 250 m wide, and 38.5 m high in the x-, y-, and z-axis, respectively. The present height of the waste rock was 38.5 m, with a future height of up to 42.0 m.

The horizontal displacement of four lateral boundaries of the model were restricted, the bottom was fixed and the top was free. To obtain the initial stress field, only the geomaterial dead weight was taken into account. The material of the model was made to meet the Mohr-Coulomb strength criterion, and the physics and mechanics parameters were selected as listed in Table 1.

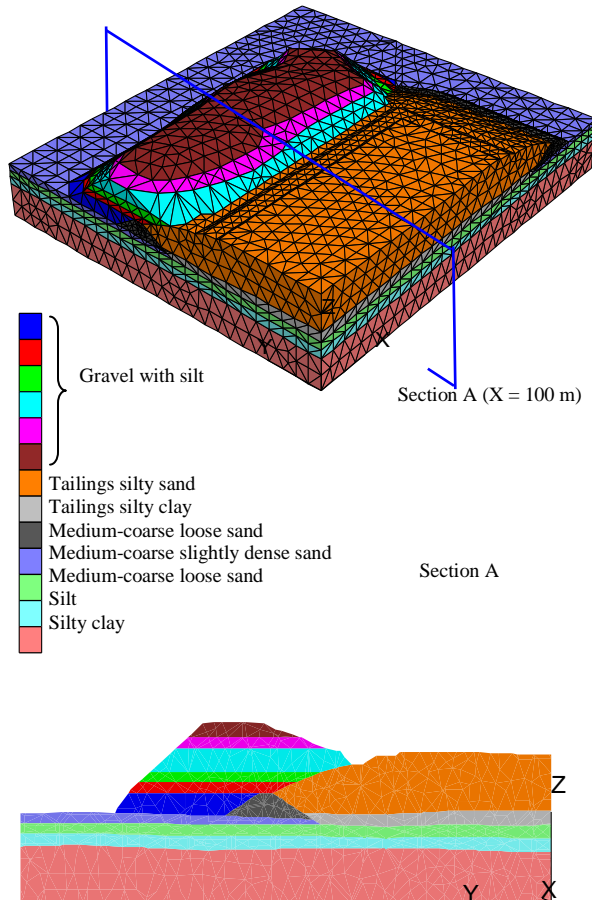


Figure 3: 3D model mesh and its material sets.

3.2 Liquid-Solid Coupling in FLAC^{3D}

The fluid-solid coupling behaviour involves two mechanical effects in FLAC^{3D}. First, changes in pore pressure cause changes in effective stress of the solid. Second, the fluid in a zone reacts to mechanical volume changes by a change in pore pressure.

The variables of fluid flow through porous media such as pore pressure, saturation and the specific discharge are related through the fluid mass-balance equation, Darcy's law for fluid transport, a constitutive equation specifying the fluid response to changes in pore pressure, saturation, volumetric strains, and an equation of state relating pore pressure to saturation in the unsaturated range. Assuming the volumetric strains are known, substitution of the mass balance equation into the fluid constitutive relation, using Darcy's law, yields a differential equation in terms of pore pressure and saturation that may be solved for particular geometries, properties, boundary and initial conditions.

In summary, possible causes of tailings dam failure include flood overtopping, slope instability, seepage failure, structural damage, and seismic liquefaction. In general, the stability of a tailings dam being influenced by the seepage field cannot be ignored. The current study is mainly based on the assumption of two-dimensional plane strain. There is currently little literature on three-dimensional (3D) stability of the tailings seepage and deformation, so a 3D numerical model was built based on a flatland tailings pond project, to conduct a liquid-solid coupling analysis of the potential risk due to successive preloading at the front of the dam. Some engineering countermeasures are put forward corresponding to the evaluation results.

3.3 Simulation Analysis Schemes

The numerical simulation consisted of four steps, as follows:

Step 1: The initial seepage field and initial stress field were calculated under the current operating water level of 27.0 m and then the displacements were reset to zero.

Step 2: The heap process was divided into six steps up to the present level of 38.5 m to analyze the deformation characteristics of the tailings dam under the current conditions.

Step 3: The heap height was increased with an additional accumulation to 42.0 m high, and the deformation characteristics analysis of the tailings dam was repeated.

Step 4: The stability evaluation and potential risk analysis of the tailings dam were carried out by using liquid-solid coupling method considering different preloading conditions, and the corresponding safety factors were proposed.

Table 1: Physics and mechanics parameter of the model.

No.	Name	Density /kg/m ³	Elasticity modulus /GPa	Poisson ratio	Cohesion /kPa	Friction angle / °	Permeability coefficient /cm·s ⁻¹
1	Gravel with silt	2250	50	0.32	1	35	0.134
2	Tailings silty sand	1710	15	0.40	3	25	2.93×10 ⁻³
3	Tailings silty clay	1910	8	0.35	19	8	2.3×10 ⁻⁶
4	Medium-coarse loose sand	1950	70	0.30	3	30	1.7×10 ⁻²
5	Medium-coarse slightly dense sand	1960	75	0.30	3	32	3.2×10 ⁻²
6	Medium-coarse loose sand	1870	63	0.30	3	29	2.8×10 ⁻³
7	Silt	2190	47	0.32	30	20	1.2×10 ⁻⁴
8	Silty clay	2030	80	0.30	35	15	1.5×10 ⁻⁶

4. LIQUID-SOLID COUPLING ANALYSIS OF TAILINGS DAM

4.1 Pore pressure distribution of the flow field under current operating level

In order to facilitate the analysis, a vertical cross section at $x = 100$ m (section A) was defined, as shown in Figure 2. All of the results below are shown in section A under the current operating water level of 27.0 m.

It can be seen from the pore pressure distribution (Figure 4) under the condition of the current operating water level that the stable seepage line in tailings dam extended from the embankment to the outer toe of the slope of the mullock heap, where failure occurred more easily due to the seepage of groundwater.

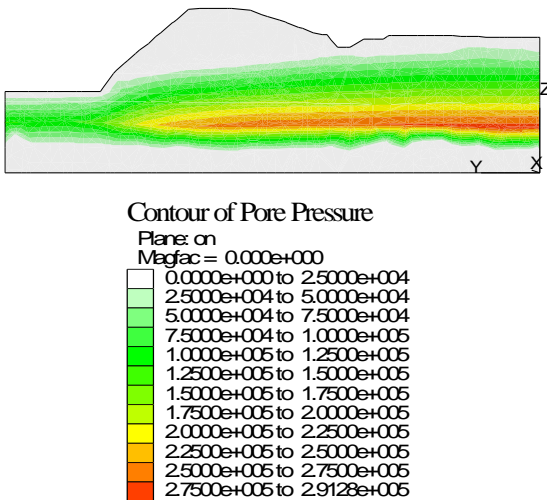


Figure 4: Pore pressure distribution under the current water level.

4.2 Deformation characteristics of the tailings dam under gradual accumulation

The calculation results of displacement fields are displayed below, with Figures 5 and 6 corresponding to the current elevation of the mullock heap (38.5 m) and Figures 7 and 8 corresponding to the additional heaped elevation (42.0 m). By comparative analysis it can be seen that:

Apart from its consolidation deformation owing to self-gravity under gradual accumulations of the mullock heap, the outside ground surface, starter dam and outer slope of tailings fill dam are loaded and crushed with different deformation characteristics as a result of their different stiffnesses. The outer slope toe of mullock heap is mainly surface settlement and lateral uplift. The tailings dam deforms inward under pressure with a certain lateral deformation that results in a little uplift of tailings silty sand. From the view of magnitude, the horizontal displacements toward inner tailings dam are close to that in the opposite direction. The aforementioned deformations developed significantly with the increasing height of the mullock heap.

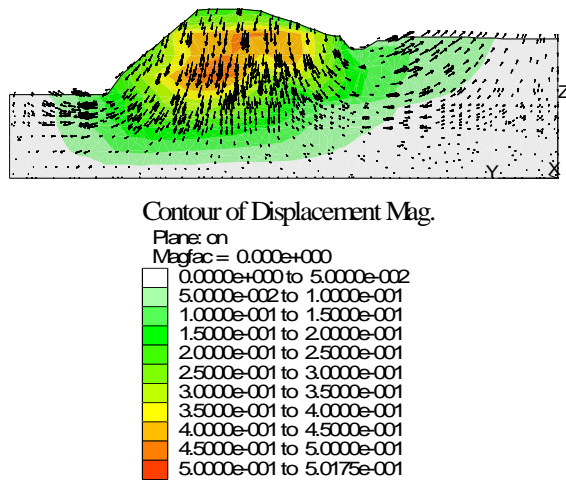


Figure 5: Displacement field and arrow under the current height.

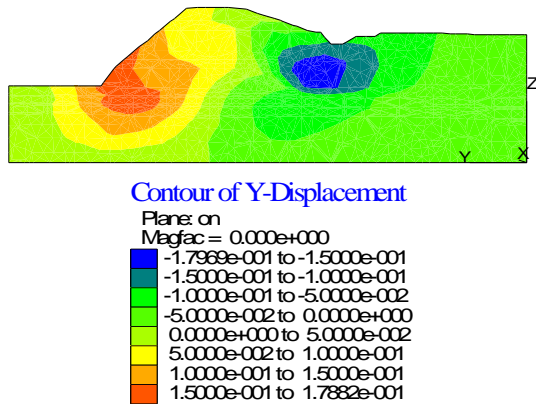


Figure 6: Horizontal displacement field under the current height.

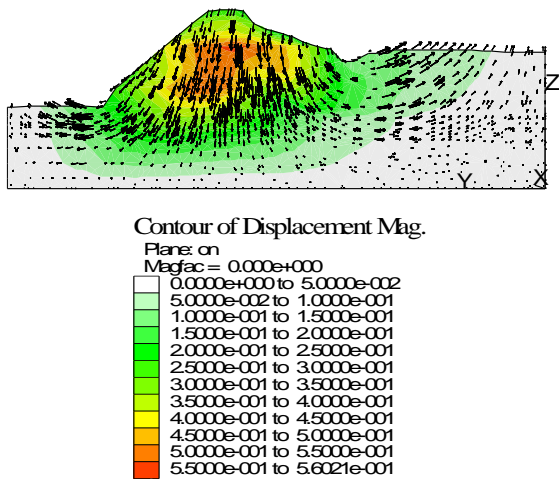


Figure 7: Displacement field and arrow under the future height.

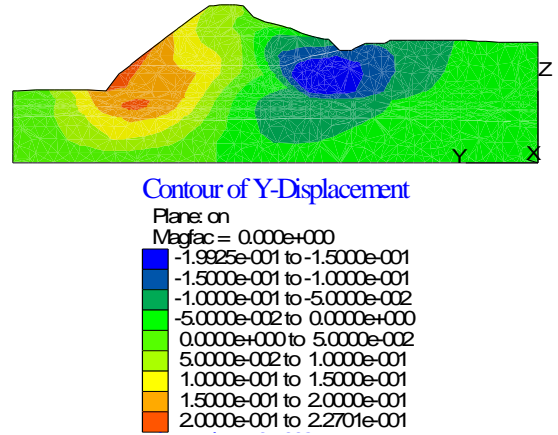


Figure 8: Horizontal displacement field under the future height.

The results suggest three potential failure modes of tailings dam under preloading: (1) Compressive shear zone in the outside ground is likely to induce sliding failure through the outer slope toe of tailings dam in cases where additional loadings are continued; (2) Local compression and shear failure could appear during the deformation process of tailings dam under gradual preloading; (3) Uplift failure might occur in tailings embankment as load increases with the increasing height of the mullock heap.

4.3 Safety risk analysis of tailings dam under gradual accumulation

According to Chinese technical codes, the safety factor of the tailings dam in this example project should not be less than 1.25 under normal operating conditions. The internal shear strength reduction method of FLAC^{3D} was adopted to calculate the safety factors of tailings dam with different heap heights and to determine the potential slip surface position. The safety factor of tailings dam was 1.28 under the present heap height of 38.5 m (Figure 9), which would reduce to 1.23 when the mullock heap height increased to 42.0 m (Figure 10). This would constitute a lack of safety reserve, and therefore the heap height should not be increased.

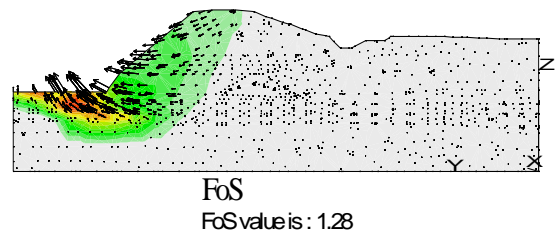


Figure 9: Potential slip surface and safety factor under the current height.

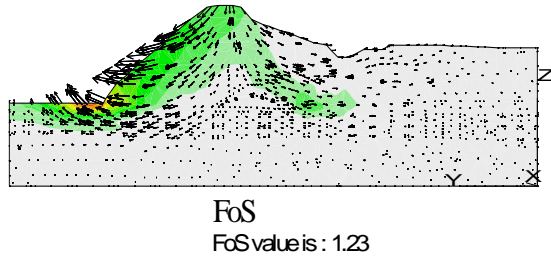


Figure10: Potential slip surface and safety factor under future height.

5. CONCLUSION

It is concluded from liquid-solid coupling analysis that there are three potential failure modes of tailings dam under preloading. Under present conditions, the tailings dam meets safety requirements whereas in the event of additional heightened heap, safety requirements would not be met.

According to the above results, these engineering countermeasures were put forward: The height of the present heap must be cut to satisfy the stability requirement under the condition of rain infiltration. Sound monitoring and regular inspections should be established to ensure the safety of the tailings pond operation. The engineering practice showed that these safety measures achieved good results.

6. ACKNOWLEDGMENTS

This work was financially supported by the National Natural Science Foundation of China (51474188; 51074140; 51310105020) and the Natural Science Foundation of Hebei Province of China (E2014203012), 2015 Endeavor Research Fellowship and the Program for Taihang Scholars, all these are gratefully acknowledged.

7. REFERENCES

- Bussi re B., Chapuis R.P. and Aubertin M. (2003) Unsaturated flow modeling for exposed and covered tailings dams. In: The Montreal ICOLD Conference, Montreal, pp. 1-20.
- Chakraborty D. and Choudhury D. (2009) Investigation of the behavior of tailings earthen dam under seismic conditions, *American Journal of Engineering and Applied Sciences*, Volume 2, pp. 559-564.
- Chen D.Q., Wang L.G. and Li G. (2008) Analysis of tailing dam's stability, *Journal of Liaoning Technical University (Natural Science)*, Volume 27, pp. 349-361.
- Hu M.J., Guo A.G. and Chen S.Y. (2004) Reflections on anti-slide stability analysis of a gangue dam, *Rock and Soil Mechanics*, Volume 25, pp. 769-773.

Li G.Z., Li P.L. and Xu H.D. (2005) Tailing dam stability analysis based on structural confidence level, *Gold*, Volume 26, pp. 48-50.

Li Q., Zhang L.T., Qi Q.L., Zhou Z.L. (2012) Instability characteristics and stability analysis of a tailings dam based on fluid-solid coupling theory, *Rock and Soil Mechanics*, Volume 33, pp. 243-250.

Lou J.D., Li Q.Y. and Chen B. (2005) Tailing-dam math simulation and stability analysis, *Journal of Hunan University of Science & Technology (Natural Science Edition)*, Volume 20, pp. 58-61.

Shakesby R.A. and Richard W.J. (1991) Failure of a mine waste dump in Zimbabwe: Causes and consequences, *Environmental Geology and Water Sciences*, Volume 8, pp. 143-153.

Strachan C. (2001) Tailings dam performance from USCOD incident-survey data, *Mining Engineering*, Volume 53, pp. 49-53.

Valenzuela L. and Barrera S. (2003) Seismic design of Los Quillayes tailings dams in Chile, In: The 12th soil mechanics and geotechnical engineering Panamerican conference, Massachusetts, pp. 2235-2240.

Yin G.Z., Li Y., Wei Z.A., Jing X.F. and Zhang Q.G. (2010) Regularity of the saturation lines' change and stability analysis of tailings dam in the condition of flood, *Journal of Chongqing University (Natural Science Edition)*, Volume 33, pp. 72-86.

Numerical analysis of Westwood Mine tailings embankment stability during the restoration phase

Yaya Coulibaly*, Tikou Belem, Li Zhen Cheng

Research Institute on Mines and Environment (RIME)
 Université du Québec en Abitibi-Témiscamingue (UQAT)
 Tel: +1 819-874-8728 ext. 6233

ABSTRACT

Stability analysis of Westwood Mine tailings embankment performed using SLOPE/W and SIGMA/W codes showed that the minimum factor of safety obtained is higher than the recommended value of 1.5 set by some authors and the Quebec Ministry of Natural Resources and Wildlife for static loading and steady flow conditions. Pore pressures that must be controlled are higher in bottom layers of the embankment, and these pressures move toward the downstream side. In addition, low electrical resistivity values (by geophysical method) associated with the high water content tailings layer, suggest its susceptibility to internal erosion.

1. INTRODUCTION

The mining industry is the lung of the economy of any country possessing active mines, but it also generates large quantities of solid wastes such as tailings and waste rock that must be properly confined either in a tailings storage facility (TSF) or waste rock pile, respectively. The exposure of these solid wastes to atmospheric conditions could result in environmental pollution by acid mine drainage (AMD) or contaminated neutral drainage (CND). When underground mining methods require that the stopes are artificially supported to allow full ore recovery, backfilling is an effective way of solid wastes management. Mine tailings are surrounded in the TSF by embankments that must be monitored to prevent spillage of slurry tailings due to their potential failure. Failure is a physical process (mechanical or hydraulic) by which the embankment can be broken by tearing off and dumps potentially contaminated slurry tailings and, consequently, floods the downstream side of the dam. In general, breakdown of embankment dams is *via* four classical mechanisms (Mériaux et al., 2001): external erosion, internal erosion, external instability and liquefaction. Runoff of rainwater can also be the cause of external erosion. The settlement on the ridge causing cracking and water infiltration into the dam can cause internal erosion or slippage in an area of weakness.

Numerical analysis methods have been widely used to solve complex problems of slope stability, which otherwise would not be possible using conventional techniques (Eberhardt, 2003; Barbour and Krahn, 2004; Ormann et al., 2010; GEO-SLOPE International Ltd., 2007). Also, the geophysical method using electrical resistivity has excellent

potential, as the measured parameters (resistivity or conductivity) are sensitive to the presence of water or cavities (Denahan and Smith, 1984; Ernstson and Kirsch, 2006). Among other things, electrical resistivity method makes it possible to detect the internal structure and cracks in the embankment.



Figure 1: Aerial view of the tailings embankment studied.

The Westwood Mine (owned by IAMGold Corp.) aims at reusing their TSF #1 for solid wastes storage, but on the other side of the Northwest separation embankment is located a small polishing pond (Figure 1). Some sporadic and localized slumps and slippage on the embankment have been reported. The slippage occurs on the downstream side slope (external instability) and the upstream slope side for some reason (e.g. liquefaction of the tailings or

*Corresponding author – email : yaya.coulibaly@uqat.ca

foundation soil as a result of a probable low magnitude seismic event).

The aim of this study is to assess the embankment stability by the means of numerical analysis using SLOPE/W and SIGMA/W codes (from GEO-SLOPE International Ltd.) and of geophysical methods that use electrical resistivity and ground-penetrating radar (GPR). The SLOPE/W code is based on limit-equilibrium analysis, while the SIGMA/W code is based on finite element method (FEM). The SLOPE/W code was used for assessing the embankment slope stability analysis through the calculation of the factor of safety (FS) based on the strength reduction factor (SRF) method. The SIGMA/W code was used for obtaining the stress and strain distribution across the embankment. The geophysical methods (electrical resistivity and GPR) show excellent potential of correlating all the data since the tailings dam properties (resistivity or conductivity) measured are sensitive to the presence of water or cavities. This paper presents the main results obtained.

2. METHODS OF SLOPE STABILITY ANALYSIS USING NUMERICAL CODES

2.1 Factor of safety (SLOPE/W)

In conventional methods of limit equilibrium analysis, the factor of safety (FS) is defined as the ratio between the resisting forces and the forces leading to tilting movements (Krahn, 2007, in GEO-SLOPE International Ltd., 2007).

$$FS = \frac{\sum S_r}{\sum S_m} \quad (1)$$

where S_r = resisting force due to friction and cohesion; S_m = driving force tending to drag the block.

Alternatively, the factor of safety can also be expressed as follows:

$$FS = \frac{\text{Moments resisting sliding}}{\text{Moments causing sliding}} \quad (2)$$

Amongst the most popular analytical methods of limit equilibrium analysis (see Figure 2), the Morgenstern-Price method was chosen as the analysis method (which is close to the Spencer's method), because it expresses two basic concepts for determining the factor of safety. The factor of safety versus lambda (Lamé coefficient) indicates the minimum factor of safety at the point of intersection of equilibrium moment and equilibrium force. From Figure 2 the point of intersection of the moment and

the force corresponds to a factor of safety of 2.15, according to Morgenstern-Price or Spencer methods. In practice, the use of FS greater than 1.5 for static analysis of embankment stability and steady flow conditions is recommended (Eberhardt, 2003; Ormann et al., 2010; Quebec Ministry of Natural Resources and Wildlife).

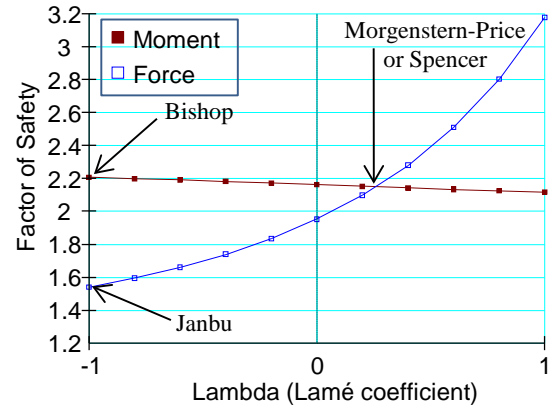


Figure 2: Graphical plot of the factor of safety as a function of Lamé coefficient for the moment and equilibrium force.

2.2 Stress-strain analysis (SIGMA/W)

The stress-strain analysis was performed by the finite element method using the SIGMA/W numerical code. The embankment slope stability was assessed by the effective stress analysis and the Mohr-Coulomb failure criterion was chosen:

$$\tau = c' + \sigma' \tan \phi' \quad (3)$$

where τ is the shear strength (kPa), c' is the effective cohesion (kPa), ϕ' is the effective internal friction angle ($^\circ$) and σ' is the effective normal stress (kPa) which is given as follows:

$$\sigma' = \sigma - u \quad (4)$$

where u is the pore water pressure (kPa) and σ is the normal or vertical total stress (kPa).

The reduction of the effective stress σ' will reduce the shear resistance and this could promote some instabilities. For each simulation, the convergence of the calculations were be analyzed by the unbalanced forces. An unstable model is usually characterized by a non-zero value, often fluctuating; the maximum unbalanced force and increased displacements (Eberhardt, 2003). Also, areas of low stresses are favorable to the internal erosion (Ormann et al., 2010).

2.3 Geophysical analysis by computed tomography

The computed images of the electrical tomography using a freeware (RES2DINV software) can be interpreted as an electrical conductivity map

showing that the conductive areas through the embankment are correlated with water saturated areas where electrical resistivity values are low in favor of a high conductivity.

3. RESULTS

3.1 Embankment stability analysis using SLOPE/W

The input parameters for each type of material are: unit weight (γ), effective cohesion (c') and effective internal angle of friction ϕ' (cf. Table 1).

Figure 3 shows the result of the analysis that indicates a factor of safety (FS) value of 1.833 which is higher than the recommended value of FS = 1.5. This value corresponds to the start of the tailings impoundment filling which is the current state of the embankment. This result shows that the embankment is currently stable (Figure 3). When 10 tons static dead-weight is applied on the crest of the embankment, simulating a stationary truck during waste rock dumping, the factor of safety remains

above 1.5 but decreases to 1.754. When the tailings impoundment is entirely filled the factor of safety decreases slightly from 1.833 to 1.814.

To determine the effects of the change in cohesion and the angle of friction of fill layers (rockfill and tailings), several simulations were performed and the values the factors of safety are shown in Table 2. One can observe that there would be embankment failure when the tailings effective cohesion c' is zero and the effective internal angle of friction is 12° (FS = 0.755). Also, when the tailings effective cohesion is zero with an angle of friction of 35° and a unit weight of 12 kN/m^3 , the factor of safety FS = 1.28 (which is lower than the recommended value of 1.5).

It should however be noted that these two scenarios are unlikely because the tailings effective angle of friction would be close to 30° while it is very unlikely that the tailings can have a unit weight lower than 14 kN/m^3 (specific gravity of 2.67 and slurry solid mass content of 50%).

Table 1: Values of parameters used in SLOPE/W simulations (from the report of the closure plan and restoration, 1999).

Type of material	Unit weight (kN/m ³)	Angle of friction (°)	Cohesion (kPa)	Undrained shear strength (kPa)
Tailings	19.0	35	0	0
Upper silt	19.2	28	0	0
Lower silt	19.2	28	0	0
Silty clay	16.5	30	0	40
Rockfill	20	42	0	46
Filling material	19	35	0	0

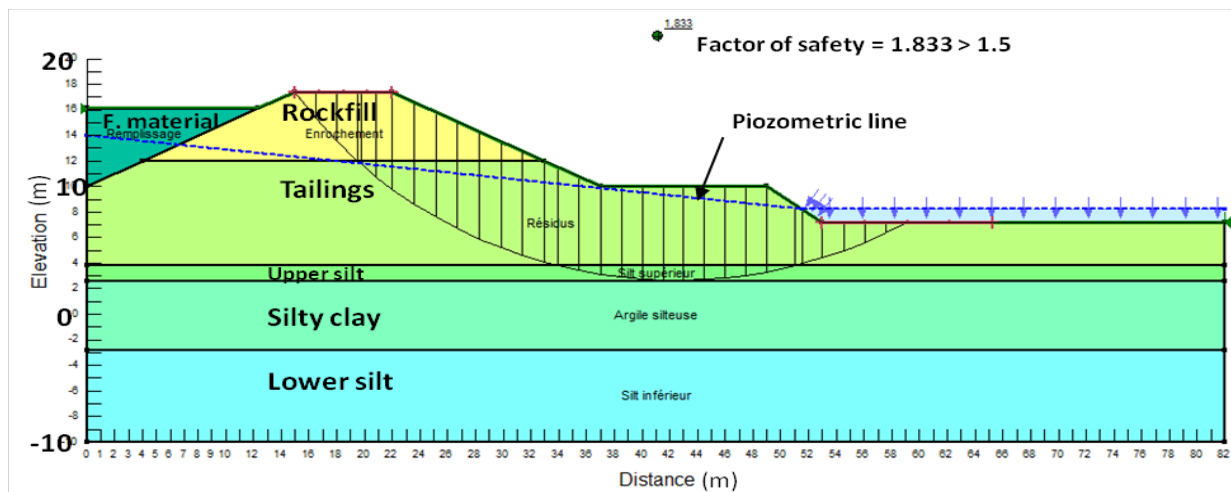


Figure 3: Stability analysis of the embankment slope showing a FS of 1.833 at the start of the tailings impoundment filling.

Data in Table 2 are used to construct different graphs that are presented in Figures 4, 5, and 6 and illustrate the influence of the effective cohesion and internal angle of friction on the factor of safety. These figures show that the effective cohesion and angle of friction (which are the shear strength parameters shown in Eq. 3) have a direct influence on

the factor of safety. In fact, FS increases with the increase of the cohesion and the angle of friction. For a similar range of variation of c' and ϕ' the trend of the factor of safety is more pronounced for the tailings than for the rockfill (Figure 6).

Table 2: Factor of safety when we vary the cohesion and the angle of friction of rockfill and tailings layers independently.

Type of material	Cohesion (kPa)	Angle of friction (°)	Unit weight (kN/m ³)	Factor of safety
Rockfill	0	20	18.1	1.856
	0	42	18.1	1.964
	0	60	18.1	2.072
	0	42	18.1	1.964
	10	42	18.1	2.013
	20	42	18.1	2.064
	0	42	18.1	1.964
	0	42	23.1	1.848
	0	42	24.3	1.824
	0	42	30	1.729
Tailings	0	12	19	0.755
	0	35	19	1.964
	0	53	19	2.582
	0	35	19	1.964
	10	35	19	2.222
	20	35	19	2.391
	0	35	12	1.28
	0	35	19	1.964
	0	35	25	2.349

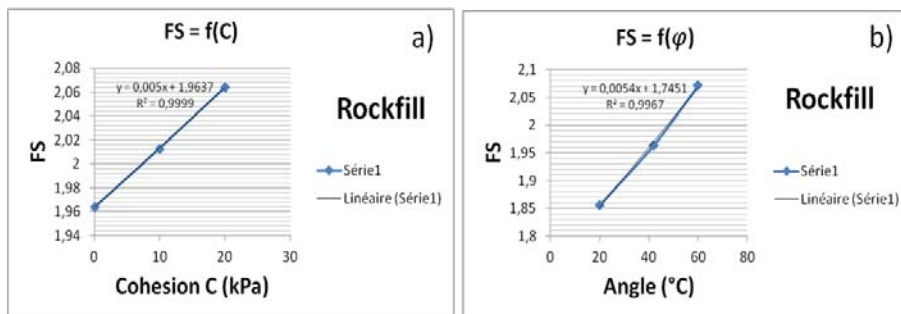


Figure 4: Variation in the factor of safety as a function of a) the cohesion and b) the angle of friction of the rockfill layer.

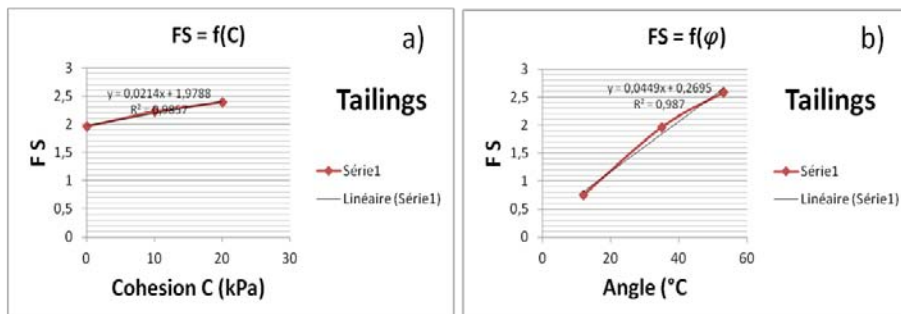


Figure 5: Variation in the factor of safety as a function of a) the cohesion and b) the angle of friction of the tailings layer.

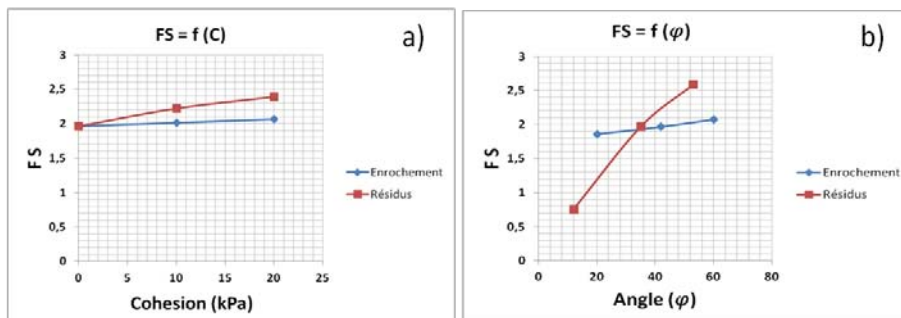


Figure 6: Variation in the FS as a function of a) effective cohesion and b) internal angle of friction for rockfill and tailings.

3.2 Stress-strain analysis using SIGMA/W

The input parameters to perform the stress-strain analysis of the embankment using the SIGMA/W code are listed in Table 3. The values are representative of each material in the embankment. The stress analysis shows that if the pore water

pressure does not dissipate easily in short term, the total stress could increase progressively and put the embankment stability in question. The pore water pressure was relatively high in the deeper layers, particularly in the regions directly below the embankment (i.e. below the rockfill and tailings) and moving toward the downstream side (Figure 7).

Table 3: Values of parameters used in SIGMA/W.

Parameters	Rockfill	Tailings	Upper silt	Silty clay	Lower silt	Filling material
Young's Modulus E (kPa)	40000	7200	3895	9312	9800	3048
Unit Weight (kN/m ³)	24.3	19	19.2	16.5	19.2	19
Poisson's ratio	0.334	0.334	0.334	0.334	0.334	0.334
In situ pressure coefficient K ₀	0.5001	0.5001	0.5001	0.5001	0.5001	0.5001

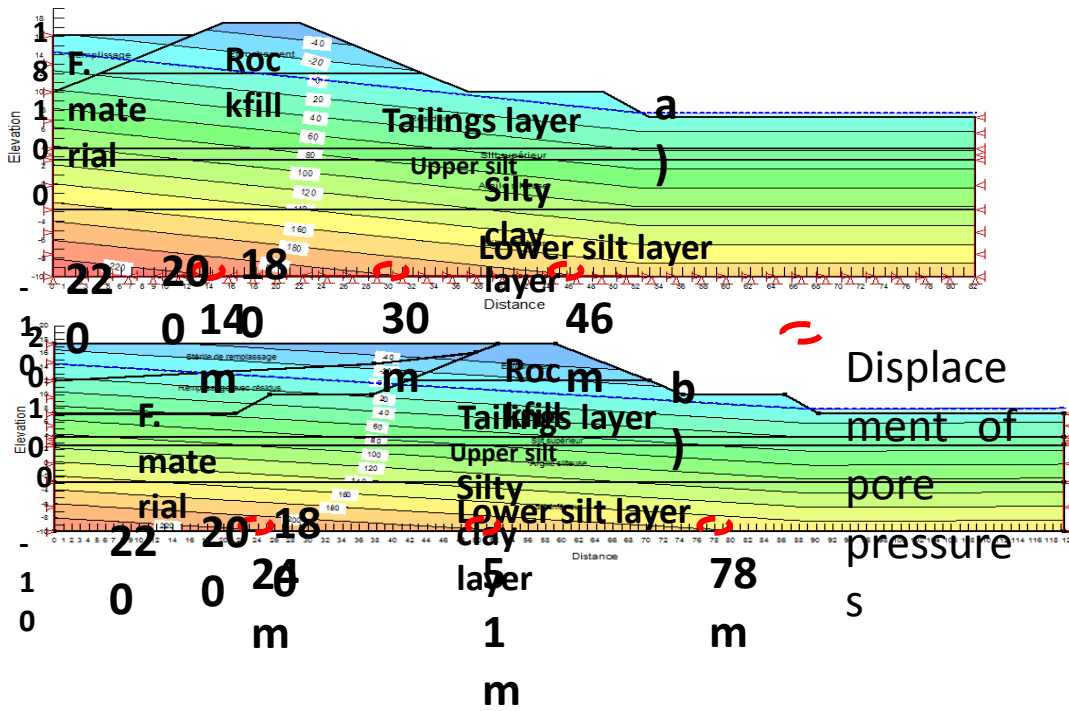


Figure 7: Illustration of the iso-value curves of pore pressure for a) current in-situ condition, b) filled state.

3.3 Geophysical tomography using RES2DINV software

The geophysical method used was the electrical resistivity method in which an electric current is injected into the embankment using different electrodes placed at different locations, and then the potential difference between a pair of potential electrodes is measured. The apparatus used was the ground penetrating radar (GPR). According to the system set up, a section of the apparent resistivity was calculated from the potential measurements. Two measurement configurations were used: Wenner and Wenner-Shlumberger (Syscal R1 Plus Switch 72)

in order to look at the variation of the resistivity within the embankment related to its internal structure. Figure 8 shows an inversion result from data collected with Wenner-Schlumberger configuration using the RES2DINV software. In this figure the blue color represents the low resistivity (i.e. high conductivity) and the red color represents the high resistivity. The distribution of the apparent resistivity outlines a layered structure of the embankment. An outcrop (observed in the field) at the end of the profile on the right (at around 320 m) corresponds to the highest resistivity area (dark brown to purple). The resistivity variation with the

depth correlates very well with the internal structure observed from the geotechnical drilling F-95-1 observations performed by Golder and Associates in 1996; especially at the depth of the interface between the moraine and the bedrock. Based on the drilling data, the following lithological limits from top to bottom on the sections in Figure 8 were identified:

The rockfill layer (0 – 5 m approximately), with electrical resistivity of between 65 and 117 Ωm ;

Tailings layer (5 – 26 m approximately), electrical resistivity between 20 and 65 Ωm ;

Upper silt, silty clay, lower silt, dense moraine and bedrock (> 26 m of depth), electrical resistivity between 117 and 1222 Ωm ;

The bedrock is located in sub-surface to the right end of the section and it might have the same composition as that on the bottom of the embankment. Lateral variations in resistivity may imply that there are resistivity heterogeneities within the embankment in particular between the moraine and the sub-surface rock (lowest resistivity area). These heterogeneities may be due to cracks filled with water (dark blue);

In the pond (downstream of the dam), it seems that there is a penetration of tailings drainage water through the dam. It could be caused by small cracks where there is a discontinuity of resistivity (red dashed cycle on Figure 8) of the embankment layers materialized by resistivity variations.

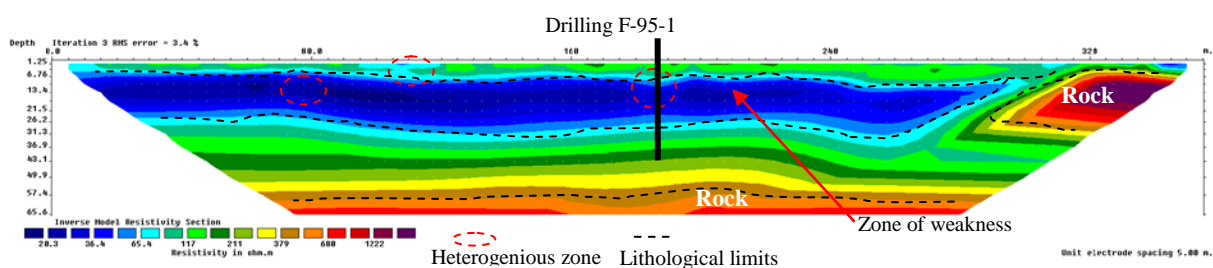


Figure 8: Tomographic inversion image, Wenner-Schlumberger with 5m distance between electrodes.

4. CONCLUSION

Stability analysis performed was particularly interesting as a monitoring tool for the Westwood Mine embankment. The calculated values of the factor of safety were higher than 1.5, which meets the standard recommendations set by some authors and by the Quebec Ministry of Natural Resources and Wildlife for static loading and steady flow conditions. In all cases of realistic geometric representation of the embankment, the minimum factor of safety was greater than 1.5, thus confirming the stability of the embankment studied. The stress analysis suggests that the pore water pressure is higher in the layers directly below the embankment (i.e. higher in the upper silt, silty clay and lower silt). The performed electrical tomography shows that it is possible to distinguish the different structures of the Northwest embankment of Westwood Mine tailings storage facility without employing a destructive method. The electrical tomography image shows that the conductive areas across the embankment correlate well with water saturated areas such as tailings layer where electrical resistivity values are low in favor of a high conductivity. These water-saturated areas are susceptible to the risk of internal erosion. The change in electrical resistivity scale in the rockfill layer (5 m depth) shows that it is unsaturated layer having a lower electrical resistivity (approximately 65 – 117 Ωm). These zones could reflect heterogeneity of the

particle size of these materials, which could cause differential settlement in the long term.

5. ACKNOWLEDGEMENT

This research was financially supported by the RIME (Research Institute of Mining and Environment) of UQAT. The authors would like to acknowledge them for this support. The authors also wish to thank our mining partner, IAMGOLD Corporation (Westwood Mine), including the Superintendent of Environment Department, Mr. Sylvain Lortie for their collaboration in this project.

6. REFERENCES

- Barbour, S. L., and Krahn, J. (2004). Numerical modelling – prediction or process? Geotechnical news, December 2004.
- Denahan B. J., Smith D. L., (1984). Electrical resistivity investigation of potential cavities underlying a proposed ash disposal area. *Environmental geology and water sciences*. Volume 6, Issue 1, pp 45-49.
- Eberhardt, E. (2003). Rock slope stability analysis - Utilization of advanced numerical techniques.
- Ernstson, K., Kirsch, R., (2006). Geoelectrical methods. In: Kirsch, Reinhard (Ed.), groundwater geophysics. Springer. ISBN: 3-540-29383-3, pp. 85–117.

GEO-SLOPE International Ltd. (2007). Geo-Slope Office (Slope/W, Seep/W, Sigma/W, CTran/W, Temp/W, Quake/W, Air/W). Geo-Slope International Ltd., Calgary, Canada.

Mériaux P., Royet P., Folton C. (2001). Surveillance, entretien et diagnostic des digues de protection contre les inondations. Cemagref Editions, 191 p.

Ormann, L., Zardari, M.A., Mattsson, H., Bjelkevik, A., and Knutsson, S., (2010). Numerical analysis of strengthening by rockfill embankments on an upstream tailings dam.

Application of an economy comparison model for mine cooling system technology

Miao Dejun^{a,b,*}, Chang Dehua^{a,b}, Tan Dongwei^{a,b}

^a College of Mining and Safety Engineering, Shandong University of Science and Technology, Qingdao, China 266590

^b State Key Laboratory Breeding Base for Mining Disaster Prevention and Control, Shandong University of Science and Technology, Qingdao, China 266590

ABSTRACT

The existing selection methods for mine cooling schemes are complex and have incomprehensive index values. In order to rectify this problem in the specific circumstance of high temperature mines, this paper puts forward 13 index values, including the machine power, project investment, operation cost, etc. A comparative model of technical and economic benefit of mine cooling systems is established by using the objective entropy weight and TOPSIS method. Using objective entropy weight, the entropy weight of evaluation index and the weight decision matrix are determined. Using the TOPSIS method, the ideal solution and the negative ideal solution are determined. The optimal scheme can be determined by using the closeness degree calculation for the scheme sort. Optimization calculation and comparisons are carried out for four cooling schemes in a mine. Scheme 4 is found to be the optimal scheme for cooling systems.

KEYWORDS: Mine cooling; Technical and economy model; Scheme optimization

1. INTRODUCTION

With the increase of mining depth and the improvement of comprehensive mechanical mining capacity, high temperature heat damage has become one of the problems that seriously restricts the safe production of mines, and affects the economic benefit of the mine (Qi Yudong et al., 2014). Since the causes of high temperature mine heat damage are different, reasonable solutions should be chosen for each individual mine. Miao Sujun (2010) puts forward a mine cooling system scheme optimization method to aid in choosing a mine cooling scheme. Feng Xiaokai (2009) and Chen Xiaoyou (2013) have researched the economy of cooling projects, the economic benefit of coal mines, and constructed a mine cooling system cost economic evaluation method that focuses on mathematical analysis and scheme comparison. Zhang Hui (2009), Chen Jianmei (2009), Jian Congguang (2008), and Li Hongyang (2010) have optimized the economic and technological indexes of cooling systems and improved the mechanical cooling system evaluation method by comparing the economic costs in multiple dimensions. Of the above schemes, some are very complex, and need more experts to determine the weights. Therefore, it is necessary to build a mine cooling system technology and economic benefit model to improve the effectiveness and practicality of scheme selection.

2. ESTABLISHMENT OF MINE TECHNICAL AND ECONOMIC BENEFIT COMPARATIVE MODEL

In this paper, the mine cooling technical and economic benefit comparison model is based on the objective entropy weight and TOPSIS method. Firstly, target decision matrix are constructed, and normalized processing is carried out. Secondly, the entropy weight of the evaluation index is determined according to the objective entropy weight. The weighted decision matrix is constructed and the ideal solution and the negative ideal solution are determined. Finally, the feasible scheme is determined. The feasible scheme makes the distance between the scheme solution and the ideal solution the smallest, and the distance from the negative ideal solution the largest (Ma Zhipeng et al., 2009).

The decision rule of the scheme is found by comparing the actual feasible solution with the positive ideal solution and the negative ideal solution. The close degree between the scheme and the best scheme can be used as a basis for evaluation of the merits of each program (Yue Chaoyuan, 2003). This can be found by calculating the weighted Euclidean distance between a scheme, the best scheme, and the worst scheme. The calculation steps of the model are as follows:

1) Formation of decision matrix

The decision matrix is formed according to the actual situation of the high temperature mine and the machine-operating power and investment costs. In

the cooling schemes, the corresponding target decision matrix is established. Set multiple target decision scheme set as $M = (M_1, M_2, \dots, M_m)$, the index set as $C = (C_1, C_2, \dots, C_n)$, set the project M_j to the index C_i value as x_{ij} ($i=1,2,\dots,m; j=1, 2,\dots,n$), multi-objective decision matrix (A) is:

$$A = \begin{bmatrix} x_{11} & x_{12} & \cdots & x_{1n} \\ x_{21} & x_{22} & \cdots & x_{2n} \\ x_{31} & x_{32} & \cdots & x_{3n} \\ \vdots & \vdots & & \vdots \\ x_{m1} & x_{m2} & \cdots & x_{mn} \end{bmatrix} \quad (1)$$

Target decision matrix A is normalized and the normalized judgment matrix B is obtained:

$$b_{ij} = \frac{x_{ij} - x_{\min}}{x_{\max} - x_{\min}} \quad (2)$$

The value b_{ij} is determined by the superior degree of running power and investment cost index. Specific performance is in the following two aspects:

$$b_{ij} = \frac{x(i, j) - x_{\min}(j)}{x_{\max}(j) - x_{\min}(i, j)} \quad (3)$$

Choice criterion: the bigger the better index

$$b_{ij} = \frac{x_{\max}(j) - x(i, j)}{x_{\max}(j) - x_{\min}(i, j)} \quad (4)$$

Choice criterion: the smaller the better index

Where b_{ij} is normalized value of characteristic value, $x_{\min}(j)$, $x_{\max}(j)$, the j evaluation indexes are the minimum and the maximum.

2) H_j determined by objective entropy weight

According to the definition of entropy, there are m schemes and n evaluation indexes. They can determine the evaluation index of entropy.

$$H_j = \frac{1}{-\ln m} \left(\sum_{i=1}^m f_{ij} \ln f_{ij} \right) \begin{matrix} (i=1,2,\dots,m; \\ j=1,2,\dots,n) \end{matrix} \quad (5)$$

In order to make $\ln f_{ij}$ meaningful, it is necessary to modify the f_{ij} . It is defined as:

$$f_{ij} \neq 0, \quad f_{ij} = \frac{b_{ij}}{\sum_{i=1}^m b_{ij}} \quad (6)$$

$$f_{ij} = 0, \quad f_{ij} = \frac{1 + b_{ij}}{\sum_{i=1}^m (1 + b_{ij})} \quad (7)$$

3) Establish entropy weight of evaluation index w

(8)

$$\omega_j = \frac{1 - H_j}{n - \sum_{j=1}^n H_j}, W = (\omega_j)_{1 \times n}, \sum_{j=1}^n \omega_j = 1$$

4) Constructing the weighted decision matrix

Multiplying the normalized judgment matrix and the weight of each index can obtain the weighted decision matrix:

$$R = (r_{ij})_{m \times n}, r_{ij} = w_j \cdot b_{ij} \quad (i=1, 2, \dots, m; j=1, 2, \dots, n) \quad (9)$$

5) Determining the ideal solution and negative ideal solution

The ideal solution S^+ and the negative ideal solution S^- of each scheme can be determined from the weighted decision matrix. The selection of ideal solution and the negative ideal solution can be found via the selection condition of each index in the design scheme.

$$S_j^+ = \begin{cases} \max\{r_{ij}\}, (j=1,2,\dots,n) \\ 1 \leq i \leq m \end{cases} \quad (10)$$

$$S_j^- = \begin{cases} \min\{r_{ij}\}, (j=1,2,\dots,n) \\ 1 \leq i \leq m \end{cases} \quad (11)$$

6) Distance between the ideal solution and negative ideal solution

The ideal solution S^+ and the negative ideal solution S^- of each scheme can be determined from the weighted decision matrix. The selection of ideal solution and the negative ideal solution can be found via the selection condition of each index in the design scheme

$$S_{d_i}^+ = \sqrt{\sum_{j=1}^n (s_j^+ - r_{ij})^2} \quad (12)$$

$$S_{d_i}^- = \sqrt{\sum_{j=1}^n (s_j^- - r_{ij})^2} \quad (13)$$

In equations (12) and (13), $i=1,2,\dots,m; j=1,2,\dots,n$

7) Calculation of cooling system close degree and decision

According to the mathematical model, the relative closeness degree ξ_i can be calculated. Its value is between 0 and 1. The values close to 1 show that the evaluation objects will be closer to the optimal level.

$$U_i = \frac{S_{d_i}^-}{S_{d_i}^- + S_{d_i}^+} \quad (14)$$

In equation (14), $i=1,2,\dots,m$

According to the size of value U_i , they can be sorted. The project will be better if the U_i is closer to the ideal solution.

3. APPLICATION OF TECHNICAL AND ECONOMIC BENEFIT COMPARISON MODEL IN MINE COOLING SYSTEMS

3.1 General Situation of Mine

The average geothermal gradient of a mine is $2.0^\circ /100$ m, namely, each 50 m increases by 1° . It belongs to the normal temperature gradient zone. Due to the complexity of the coal bearing strata lithology combination, the general geothermal gradient is higher than that of the non coal measure strata, with an average of $2.2^\circ /100$ m. The ground temperature of the recoverable coal seam belongs to the normal gradient (first and second grade high temperature zone), the upper coal seam mostly in the first high temperature zone, and the lower coal seam mostly in second grade high temperature zone. Initial mining was in 3 coal seams. In the north the ground temperature is low, and near the southeast of F2 and F3 is a high temperature zone, belonging to the second grade high temperature zone and the rest belonging to the first grade high-temperature zone.

The level of the mine is about -1000 meters. The inlet air volume is $1200 \text{ m}^3/\text{min}$. The original rock temperature is 37° . Mechanical equipment in the working face installed capacity is larger. Underground heat damage is very serious in the summer and mechanical cooling should be used at that time.

3.2 Four cooling schemes for high temperature coal mines

According to the specific conditions of the mine, the four cooling schemes are ice cooling, centralization on the ground, centralization underground, dispersion underground and condensation heat centralization.

1) Ice cooling

Cold Source: low temperature water is made from a ground water chiller, transported to the ice making machine, and made into ice.

Cold transportation: ice through the wind is sent to the wellhead while cold water is sent to the underground ice melting pool through the insulation

pipe. Melted ice is transported to the required cold place through a pipeline.

Scatter cold: in order to reduce the inlet air temperature of the working face, an air cooler is arranged on the intake airflow roadway. The method of spraying cool. water is used in the working face.

Condensation heat emission: heat is discharged via the cooling tower.

2) Centralization on the ground

Cold source: low temperature cold water is made on the ground by a refrigerator.

Cold transportation: low temperature cold water is sent to the underground high and low pressure heat exchanger through the insulation pipe along the shaft. It is exchanged into low pressure chilled water to the various required cold locations.

Scatter-cold: in order to reduce the inlet air temperature of the working face, the air cooler is arranged on the intake airflow roadway. Small air coolers are arranged on the working face.

Condensation heat emission: it is discharged on the ground through the cooling tower.

3) Centralization underground

Cold source: the cooling chamber can be built in the well and equipped with a refrigeration unit. Cold water is made from a refrigeration machine.

Cold transportation: chilled water is delivered to each required cold locations through insulation pipes.

Scatter cold: in order to reduce inlet air temperature of the working face, an air cooler is arranged on the intake airflow roadway. Small air coolers are arranged on the working face.

Condensation heat emission: it is discharged to the ground through the two pipes of the shaft.

4) Dispersion underground and condensation heat centralization

Cold source: a local refrigeration machine is used to produce the chilled water.

Cold transportation: chilled water is delivered to each required cold location through insulation pipe.

Scatter cold: a large air cooler is arranged on the intake airflow roadway. Mobile cooling is used on the working face.

Condensation heat emission: the cooling water of the refrigerating machine is transported to the bottom of the well through pipelines by a high and low pressure heat exchanger, Heat is discharged to the ground of the cooling tower through the shaft pipeline.

3.3 Comparison of mine cooling schemes

Using the above technical and economic benefit comparison model, the four schemes of mine cooling

and heat energy utilization are compared with 13 indexes, including the choice of power machine, engineering investment, annual operating cost, the length of transmission line, the cold loss ratio,

comprehensive utilization of heat energy, the reliability of the system, pressure-bearing, heat emission, expansion capacity, load regulation performance and shaft bottom occupancy space, and the mining influence, as is shown in Table 1.

Table 1: Indexes of four design schemes.

Order number	Index	Index value				Remarks
		Scheme 1 : ice cooling	Scheme 2 : centralization on the ground	Scheme 3 : centralized underground	Scheme 4 : dispersion underground and condensation thermal centralization	
1	Installed power (KW)	2374	2250	2180	2140	S
2	Engineering investment (equipment cost, engineering investment) (Thousand yuan)	34700	32800	33500	31200	S
3	Annual operating cost (Thousand yuan)	3500	2800	3000	2600	S
4	Transmission line length (m)	20020	22300	22300	22300	S
5	Cold loss ratio	28%	24%	20%	10%	S
6	Comprehensive utilization of heat energy	3	3	3	7	H
7	System reliability	7	7	7	5	H
8	Pressure bearing property	3	7	7	5	S
9	Heat emission effect	7	7	7	7	H
10	Expansion capacity	5	3	3	7	H
11	Load regulation performance	3	5	5	7	H
12	Bottom space	7	3	5	3	S
13	Mining influence	1	1	1	3	S

In Table 1, S represents the smaller the better; H represents the higher the better.

From the technical and economic benefit model, it is easy to calculate the following values:

$$A = \begin{pmatrix} 2374 & 3470 & 350 & 20020 & 28\% & 3 & 7 & 3 & 7 & 5 & 3 & 7 & 1 \\ 2250 & 3280 & 280 & 22300 & 24\% & 3 & 7 & 7 & 7 & 3 & 5 & 3 & 1 \\ 2180 & 3350 & 300 & 22300 & 20\% & 3 & 7 & 7 & 7 & 3 & 5 & 5 & 1 \\ 2140 & 3120 & 260 & 22300 & 10\% & 7 & 5 & 5 & 7 & 7 & 7 & 3 & 3 \end{pmatrix}$$

$$b_{ij} = \frac{x_{ij} - x_{\min}}{x_{\max} - x_{\min}} = \begin{pmatrix} 0 & 0 & 0 & 1 & 0 & 0 & 1 & 1 & 0 & 0.5 & 0 & 0 & 1 \\ 124/234 & 19/35 & 7/9 & 0 & 2/9 & 0 & 1 & 0 & 0 & 0 & 0.5 & 1 & 1 \\ 194/234 & 12/35 & 5/9 & 0 & 4/9 & 0 & 1 & 0 & 0 & 0 & 0.5 & 0.5 & 1 \\ 1 & 1 & 1 & 0 & 1 & 1 & 0 & 0.5 & 0 & 1 & 1 & 1 & 0 \end{pmatrix}$$

$$H_j = \frac{1}{-\ln m} \left(\sum_{i=1}^m f_{ij} \ln f_{ij} \right) = (0.9793 \quad 0.9421 \quad 0.9828 \quad 0.6966 \quad 0.8900 \quad 0.6966 \quad 0.9930 \\ 0.9064 \quad 1 \quad 0.9064 \quad 0.9654 \quad 0.9687 \quad 0.9930) \\ 0 \quad 0.0867 \quad 0.0320 \quad 0.0290 \quad 0.0065)$$

$$w_j = \frac{1 - H_j}{n - \sum_{j=1}^n H_j} = (0.0192 \quad 0.0536 \quad 0.0159 \quad 0.2810 \quad 0.1019 \quad 0.2810 \quad 0.0065 \quad 0.0867$$

$$r_{ij} = \begin{pmatrix} 0 & 0 & 0 & 0.2810 & 0 & 0 & 0.0065 \\ 0.0102 & 0.0291 & 0.0124 & 0 & 0.0226 & 0 & 0.0065 \\ 0.0159 & 0.0184 & 0.0088 & 0 & 0.0453 & 0 & 0.0065 \\ 0.0192 & 0.0536 & 0.0159 & 0 & 0.1019 & 0.2810 & 0 \\ 0.0867 & 0 & 0.04335 & 0 & 0 & 0.0065 \\ 0 & 0 & 0 & 0.0160 & 0.0290 & 0.0065 \\ 0 & 0 & 0 & 0.0160 & 0.0145 & 0.0065 \\ 0.04335 & 0 & 0.0867 & 0.0320 & 0.0290 & 0 \end{pmatrix}$$

$$S_j^+ = (0 \quad 0 \quad 0 \quad 0 \quad 0 \quad 0.2810 \quad 0.0065 \quad 0 \quad 0 \quad 0.0867 \quad 0.032 \quad 0 \quad 0)$$

$$S_j^- = (0.0192 \quad 0.0536 \quad 0.0159 \quad 0.281 \quad 0.1019 \quad 0 \quad 0 \quad 0.0867 \quad 0 \quad 0 \quad 0 \quad 0.0290 \quad 0.0065)$$

Table 2: Analytic solutions of 4 schemes

Index value	Scheme 1	Scheme 2	Scheme 3	Scheme 4
Ideal solution	0.41034	0.29871	0.29952	0.12896
Negative ideal solution	0.12896	0.30620	0.30247	0.41034
Closeness degree	0.23912	0.50619	0.50245	0.760875

The analytical solutions of the 4 schemes can be obtained from equations (8) to (12), as shown in Table 2.

As can be seen from Table 2 : $U_1 < U_3 < U_2 < U_4$

The closeness degree of scheme 4 is the largest, so scheme 4 is optimal. Scheme 4 is chosen by the mine as the mine cooling project.

4. CONCLUSIONS

According to the specific conditions in heat damaged coal mines, 13 index values are determined. A simple and reliable comparison model of mine technical and economic benefits is put forward based on objective entropy weight and the TOPSIS method. The model can be used to optimize the mine cooling scheme.

The mine technical and economic benefit comparison model not only inherits the characteristics of multi-objective decision making,

but also can easily and quickly select the best of the designed cooling schemes. The model is preferred to

avoid the serious problem of decision making mistakes.

Calculations and analyses are conducted on four cooling schemes for a high temperature mine and the optimal scheme is determined. The selection of the optimal scheme not only meets the requirements of coal mine safety regulations, but also reduces total investment and saves cooling costs for the mine, which verifies the feasibility and practicality of the model.

5. ACKNOWLEDGEMENT

We are very thankful to The Natural Science Foundation of Shandong Province (Grant No. ZR2012EEM004) for sponsoring to publish this paper.

6. REFERENCES

Chen Xiaoyou. (2013). Research on Cooling Technology And Economics in High Temperature Deep Well. Anhui University Of Science & Technology. pp. 63-70

Chen Jianmei, Zhang Hui, Jian Congguang. (2009). Research on economical operation of the cold-water mine cooling system. Mining & Processing Equipment. Volume 37, No. 24, pp.54-56

Feng Kai. (2009). The Research of the Cooling Technology in High-temperature Mine and Its Economic Analysis. Xi'an University of Science and Technology. pp.42-53

Jian Congguang, Wei Xiujun, Yue Jun. (2008). Ansys on economical operation of the ice refrigeration and air conditioning system. Mining Safety & Environmental Protection. Volume 35, No. 4, pp. 33-37

Li Hongyang. (2010). Technical and economic analysis of mine cooling system. Safety in Coal Mines. No. 3, pp. 93-96

Miao Sujun, Xin Song, Peng Peng. (2010). Research and application optimization and decision theory of mine cooling system. Journal of China Coal Society. Volume 35, No. 4, pp. 614-618

Ma Zhipeng, Yuan Jianguo, Shi Yunyun. (2009). Grey Decision Model for Flood Control of Cascade Reservoirs Based on Stochastic Weight Assignment method. Water Resources and Power, Volume 27, No. 1, pp. 77-80

Qi Yudong, Cheng Weimin, Yu Yanbin. (2014). Status Summarization and Progress of Heat Hazard Control Technology in Coal Mine of China. Safety in Coal Mines. Volume 45, No. 3, pp. 167-174

Yue Chaoyuan. (2003). Decision theory and method. Science Press, 2003

Zhang Hui, Jian Congguang, Zhang Bo. (2009). Economical performance of ice refrigeration and air conditioning system in high temperature mine. Journal of Xi'an University of Science and Technology. Volume 29, No. 2, pp. 150-152

Behaviour of cable bolts in shear: experiment and mathematical modelling

Naj Aziz, Ali Mirza, Haleh Rasekh, Jan Nemcik, Xuwei Li

Rock Bolting Research, School of Civil, Mining and Environmental Engineering, Faculty of Engineering and Information Sciences, University of Wollongong, Wollongong, Australia 2500

ABSTRACT

The application of cable bolts for ground support is increasing in underground coal mines worldwide. Currently, two methods of evaluating the performance of the cable bolt are favoured: the short encapsulation pull test, and the shear test. The former method can be used both in the laboratory and in the field while the latter can be undertaken mainly in the laboratory. There are two methods of shear strength testing: single and double shear tests. This paper examines the double shear testing of several cable bolts currently marketed in Australia under various pre-tension stresses. Both plain and indented wire cable bolts were tested. It was found that the shear strength of the cable bolt was a function of the wire geometry and initial pre-tension. Indented wire cable bolts were lower in shear strength than the plain wire cable bolts. A mathematical model was proposed to evaluate the shear strength of cable bolts using Fourier series and a linear relationship between shear and normal loads. The model coefficients were determined based on the experimental results. The findings from the mathematical modelling tallied well with the experimental results.

KEYWORDS: cable bolt; short encapsulation pull test; shear strength; double shear testing; mathematical model; Fourier series

1. INTRODUCTION

Cable bolts have been used for ground support in mines worldwide since the 1960s. Cable bolts have been mostly used as a secondary support in addition to conventional rebar type primary support. Longer cable bolts act to reinforce strata above the primarily bolted beam, and also to suspend the primary bolted beam to the higher competent stratification layers. Shorter cable bolts have also been used as flexible primary roof support, known as FLEXIBOLT, replacing the ordinary rigid rebar (Fuller and O'Grady, 1993).

Traditionally the mechanical integrity of cable bolts and rebar is evaluated for tensile strength and axial load transfer assessed by the pull testing method. Various publications have reported on the subject, covering studies undertaken both in the laboratory and field (Hyett et al., 1992; Hyett et al., 1996; Clifford et al., 2001; Thomas, 2012). Pull tests are generally carried out to evaluate the axial reinforcement behaviour of cable bolts as the necessary requirement for cable bolt application to strata support in underground coal mines. Cable bolts are typically installed vertically above a coal mine opening, perpendicular to the sedimentary rock bedding planes. Rock movement resulting from *in situ* and mining intensified horizontal stresses often occurs along these horizontal bedding

planes, resulting in shearing loads across the cable bolts.

Recently in Australia's coal mining industry, there has been increasing interest on the evaluation of cable bolt shear behaviour. Generally, there are two main methods of testing cable bolts in shear, single, and double shear methods. Goris and Martin (1996) reported on single shear tests conducted in pairs of 0.025 m³ concrete blocks having joint surfaces ranging from smooth to rough. The failure of cable bolt strands in the field may not occur in shear alone, but could be a combination of tensile and shear due to the movement of bedded strata formations in various directions.

The understanding of cable bolt behaviour in shear is still in its infancy as there are various practical issues to be examined. Many theories and mechanisms involved are yet to be fully explored, which could provide a better understanding of any particular cable bolt's behaviour in shear. The double shear testing study reported by Aziz et al. (2004) used a three piece concrete block double shear apparatus to simulate the shear behaviour of rock bolts in rock at the University of Wollongong. Aziz (2010) and Craig and Aziz *et al.* (2010a and b) used a similar but larger apparatus and examined the failure behaviour of 28 mm hollow strand "TG" cable bolts taken to complete failure. Their findings demonstrated the symmetric characteristics of the double shear equipment with the cable bolt being sheared to failure on each side of the sheared joints. Analysis of the failure mode and loads achieved indicated that the cable strand undergoes bending

and crush the concrete surrounding the borehole at the shear plane. This kind of behaviour of the cable will not occur when the cable bolt is grouted in steel pipes instead of rock, as the case of the single shear method as recommended by the British Standard BS 7861-part 2 (British Standards 2009). The equipment used in BS 7861 is a guillotine style tool, where the cable bolt is sheared fully in the steel frame (see Figure 1). Crushing of the rock will enable a cable bolt to bend and subsequently load in both shear and tension; hence, the British Standard methodology using steel pipe is inappropriate and may be misleading.

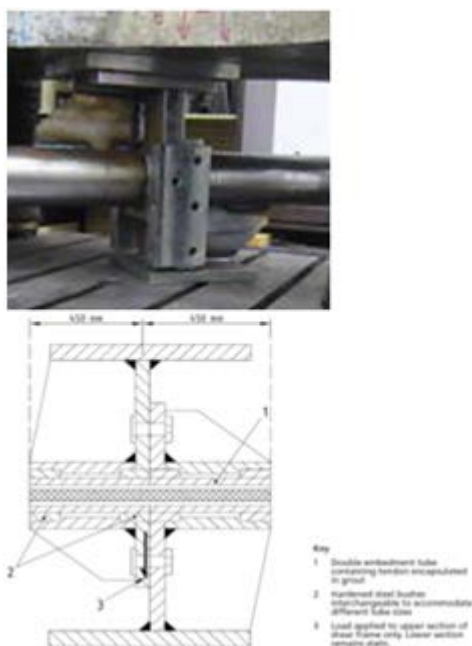


Figure 1: Sectional diagram of double embedment shear frame with the unit being tested (BS 7661-2: 2009).

With Australia having the largest variation of high capacity, pre-tensioned and post-grouted cable bolts in the world, there exist a minimum of literature on shear testing of these products using a recognised shear testing methodology. While pull testing of cable bolts can be practiced both in the field and in the laboratory, testing of cable bolts in shear is normally carried out in the laboratory. The difficulty of monitoring shearing process in holes drilled in the ground formation in remote locations renders testing in the field an inconvenient approach.

Further, Aziz et al. (2014) carried out a comparative study on 22 mm diameter plain and indented wire cable bolts, as the cable bolt surface indentation remains an issue of concern, particularly in shear. The study indicated that shear properties of indented wire cables were inferior to plain wire cables of the same type. The indentation appeared to

cause a reduction in the cable strand cross section, leading to the loss of strength (see Figure 2), including the failure in shear initiated at the indent. The three types of cable tested to date included hollow plain wire, PC plain wire, and PC indented wire. Thomas (2012) reported on laboratory axial pull tests of all the Australian cable bolts on the market including the design variables of bulbs, nutcages (birdcages), hollow, PC, multi-strand, indented, and plain wires. It was requested of manufacturers to provide the shear performance of cable bolts with these multiple variables, and Jenmar proceeded to test their cable bolts at the University of Wollongong. The University has since expanded upon the laboratory tests to include mathematical modelling of the cable bolt behaviour in shear.

2. EXPERIMENTAL STUDY

A total of six different cables were subjected to double shear testing in 40 MPa concrete. Figure 3 shows the schematic view of various cables as assembled in concrete blocks. Each double shear testing process requires three concrete blocks with two outer 300 mm side cubes and a central rectangular block 450 mm long. The casting of the concrete blocks can be carried out either in a specially prepared plywood mould or directly in the confining steel frame of the double shear apparatus. A plastic conduit 20 mm in diameter, set through the centre of the mould lengthways, will create a centralised hole for cable installation in the concrete blocks. Once the concrete blocks were allowed to set, and the plastic conduit was taken out, the hole in each block hole was reamed to the desired diameter. The concrete blocks were left immersed in a concrete curing solution to cure for a minimum period of 28 days.

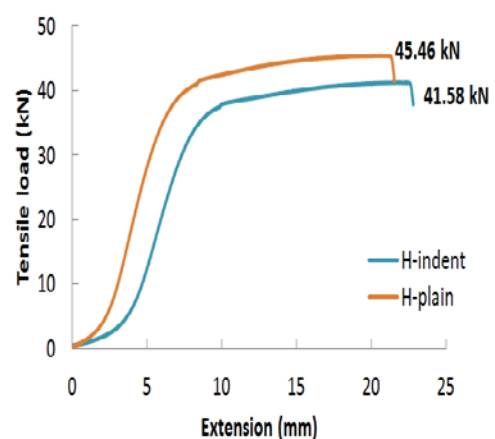


Figure 2: Tensile load / elongation profiles of both plain and indented 5.5 mm wire from cable bolts.

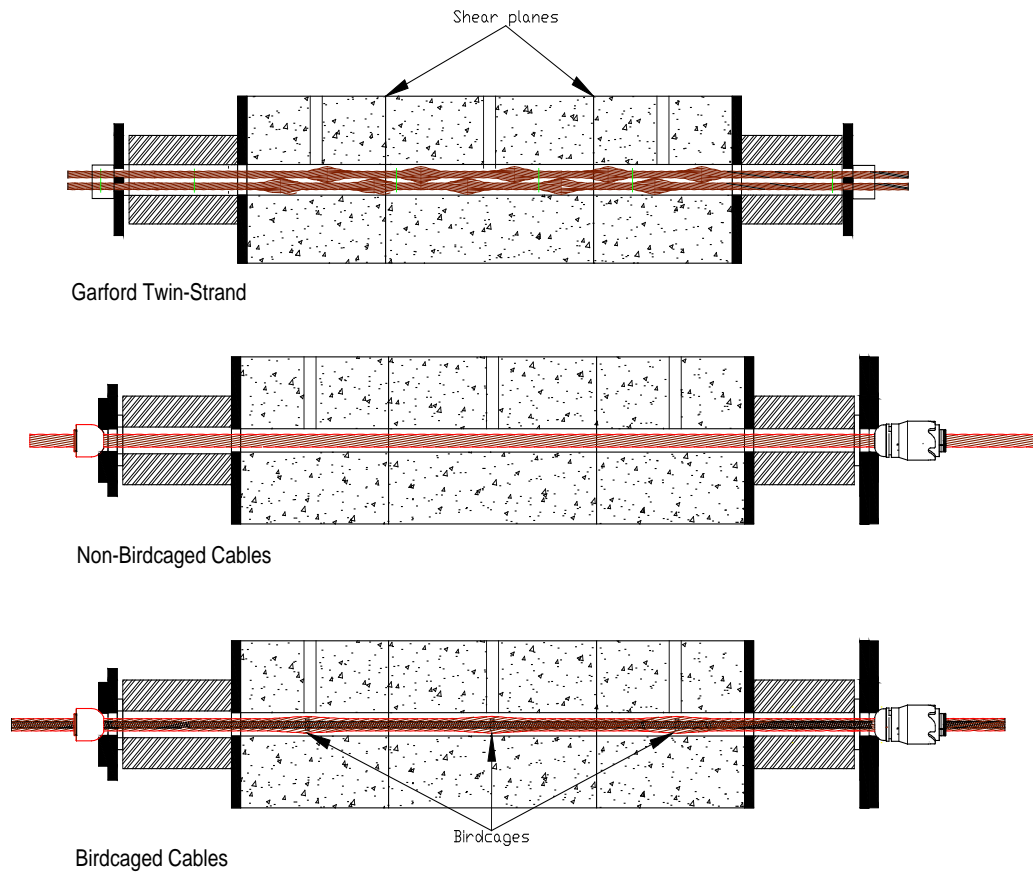


Figure 3: Cross section of double shear blocks and cables.

The cured blocks are then mounted in the double shear confining steel frames and the cable bolt specimen placed into the borehole. Two 60 t load cells were inserted onto each end of the cable followed by the typical cable bolt end fitting. The load cells were connected to the data logger during tensioning. Once the cable is pre-tensioned, the grout was injected to the annulus between the cable and borehole through the intersecting small holes on top of the block. Cables with hollow central tubes were also filled with grout, and the grout or polyester resin left to cure for at least 7 days. The top of the concrete blocks were covered by the bolted steel plates and the whole assembly was then mounted on the carried base platform. The whole double shear assembly and the base frame was then mounted on to the 500 t compression testing machine for the shearing process, as shown in Figure 4.



Figure 4: Arrangement of shearing apparatus on compression machine.

The properties of the eight different cable bolts are described in Table 1. The study focused on the main cables in the market as supplied by Jenmar, with indented wire hollow cable included for additional research. Cables were subjected to three different values of initial axial load ranging from 0 to 25 t. Three types of bonding agent were used in this particular study; Jenmar bottom-up grout (BU100), Jenmar top-down grout (TD80) and J-Lok standard oil based resin. The values of shear and axial loads

versus shear displacement were monitored and recorded. It is noted that the double shear test delineates two times of the cable bolt shear strength. Therefore, half of the shear load obtained from the data tacker was considered in this study.

The process of double shear testing consists of loading the central block vertically in the 500 t

compression testing machine (Figure 4). The 450 mm long middle section of the double shear apparatus is then vertically shear loaded at the rate of 1 mm/min for the maximum 100 mm vertical displacement. The rate of loading and displacement are monitored and simultaneously displayed visually on a PC monitor.

Table 1: list of tested cables and the test environment.

Test No.	Cable Bolt Properties					Drill bit (mm)	Bonding agent	Pre-tension load (kN)/Peak axial load	Peak shear load (kN) [½ double shear]
	Product name	Cable Ø (mm)	Wire geometry	Cable cross-section	Cable geometry				
1	Superstrand	21.8	Spiral	19 wire, PC strand	Non-birdcaged	28	Oil based resin	250	558
2	Superstrand	21.8	Plain	19 wire, PC strand	Non-birdcaged	28	Oil based resin	250	628
3	TG	28	Spiral	9 wires, hollow centre	Non-birdcaged	42	TD80 Grout	250	604
4	SUMO	28	Spiral	9 wires, hollow centre	35mm birdcage	42	TD80 Grout	250	414
5	SUMO	28	Spiral	9 wires, hollow centre	35mm birdcage	42	TD80 Grout	100	488
6	Plain SUMO	28	Plain	9 wires, hollow centre	35mm birdcage	42	TD80 Grout	250	711
7	Plain SUMO	28	Plain	9 wires, hollow centre	35mm birdcage	42	TD80 Grout	100	659
8	Gardford twin-strand	15.2	Plain	2 x 7 wire, PC strand	25mm Bulbs	55	BU100 Grout	0	501

3. MATHEMATICAL MODELLING

The mathematical model was developed by assuming a linear relationship between the shear and normal stresses:

$$S - N \tan(\varphi) - c = 0 \quad (1)$$

where, S is the shear load, N is the normal load, φ is the friction angle, and c is the cohesion.

The Fourier series concept as described below is applied to replicate the variation of the normal load against shear displacement. Fourier series is a mathematical technique incorporated to solve a large variety of engineering problems mainly adopting the principle of superposition:

$$N = \frac{a_0}{2} + \sum_{n=1}^{\infty} \left[a_n \cos\left(\frac{2n\pi u}{T}\right) + b_n \sin\left(\frac{2n\pi u}{T}\right) \right] \quad (2a)$$

$$a_n = \frac{2}{T} \int_0^T \sigma_n \cos\left(\frac{2n\pi u}{T}\right) du \quad (2b)$$

$$b_n = \frac{2}{T} \int_0^T \sigma_n \sin\left(\frac{2n\pi u}{T}\right) du \quad (2c)$$

where, a_n and b_n are Fourier coefficients, n is the number of Fourier coefficient, u is the shear displacement, and T is the shearing length.

Introducing Equations (2a, b, and c) in equation (1) by considering a_0 to a_3 , the shear strength is obtained as:

$$S = \left(\frac{a_0}{2} + \sum_{n=1}^3 \left[a_n \cos\left(\frac{2n\pi u}{T}\right) \right] \right) \tan(\varphi) + c \quad (3)$$

The shear displacement at peak shear strength is determined by taking derivation of the above

relationship respect to the shear displacement and equating to zero as:

$$\frac{d \left\langle \frac{a_0}{2} + \sum_{n=1}^3 \left[a_n \cos\left(\frac{2n\pi u}{T}\right) \right] \tan(\varphi) + c \right\rangle}{du} = 0 \quad (4)$$

Thus, the peak shear displacement at peak shear strength (u_p) is obtained as:

$$u_p = \frac{T}{2\pi} \cos^{-1} \left[\frac{-4a_2 + \sqrt{16a_2^2 - 48a_1a_3 + 144a_3^2}}{24a_3} \right] \quad (5)$$

Introducing equation (5) in equation (3), the peak shear strength (S_p) is proposed as:

$$S_p = \left(\frac{a_0}{2} + \sum_{n=1}^3 a_n \cos\left(\frac{2n\pi \frac{T}{2\pi} \cos^{-1} \left[\frac{-4a_2 + \sqrt{16a_2^2 - 48a_1a_3 + 144a_3^2}}{24a_3} \right]}{T} \right) \right) \tan(\varphi) + c \quad (6)$$

The model coefficients including Fourier coefficients (a_n), cohesion (C), and angle of friction (φ) were determined according to the measured data for various conditions of cable type and pre-tension as listed in Table 2. Generally, the values of Fourier coefficients showed a decreasing trend with the increasing the number of Fourier coefficients.

Above equation determines the total shear strength of reinforced concrete blocks. This consists of the cable bolt shear strength and the additional shear force generated by the concrete surface friction. In order to obtain the pure shear strength of the cable bolt, the frictional term should be quantified and subsequently deducted from the total shear strength as indicated by equation 6.

The frictional force generated in the process of shearing follows the Coulomb tribological equation as:

$$S = N \tan(\varphi_b) \quad (7)$$

where, φ_b is the concrete surface basic friction angle determined by tilt testing.

Deducting equation 7 from equation 6, the pure shear strength of cable bolt (S_p^b) is obtained as:

$$S_p^b = \left(\frac{a_0}{2} + \sum_{n=1}^3 a_n \cos\left(\frac{2n\pi \frac{T}{2\pi} \cos^{-1} \left[\frac{-4a_2 + \sqrt{16a_2^2 - 48a_1a_3 + 144a_3^2}}{24a_3} \right]}{T} \right) \right) [\tan(\varphi) - \tan(\varphi_b)] + c \quad (8)$$

Concrete surface basic friction angle

A double shearing test without cable bolt as the reinforcing element was carried out to determine the

concrete surface basic friction angle. The normal load subjected to concrete blocks started with 50 kN and increased incrementally every 20 mm, reaching to 250 kN at the end of the test. The value of shear load against shear displacement was measured and subsequently incorporated to calculate the concrete surface basic friction angle as shown in Figure 5. The basic friction angle was indicated as 26.94°.

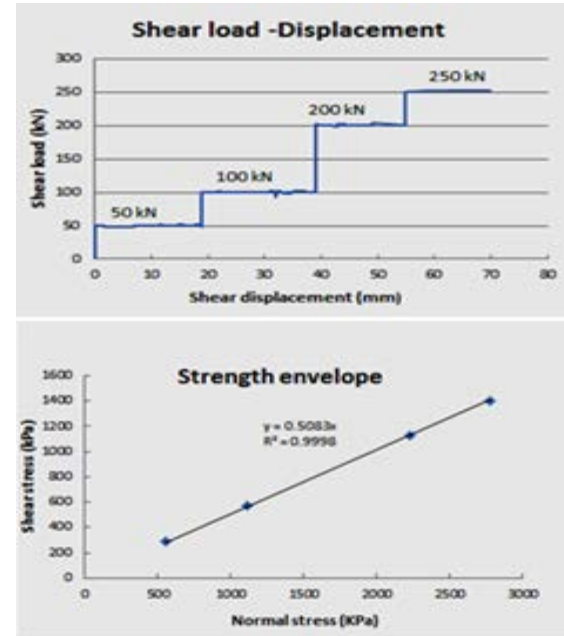


Figure 5: test results of the concrete blocks sliding test.

Introducing the value of basic friction angel in Equation 8, the pure shear strength of cable bolt is obtained as:

$$S_p^b = \left(\frac{a_0}{2} + \sum_{n=1}^3 a_n \cos\left(\frac{2n\pi \frac{T}{2\pi} \cos^{-1} \left[\frac{-4a_2 + \sqrt{16a_2^2 - 48a_1a_3 + 144a_3^2}}{24a_3} \right]}{T} \right) \right) [\tan(\varphi) - \tan(26.94^\circ)] + c \quad (9)$$

4. RESULTS AND ANALYSIS

Figures 6 to 13 show the shear load and axial load profiles against shear displacement for the tests conducted in this study. The solid lines show the shear loads and dash line show the axial loads. The initial changes in some of the shear load graphs after the elastic state may be related to the barrel/wedge settlement as the cable ends begins to take axial load due to cable bending at the shear planes. Various shear drops beyond the peak value are attributed to individual cable strand failures. The larger shear drop corresponds to the higher diameter strand failure while the smaller ones are due to the small strand failures. It is of interest to note that the number of visible sudden drops in load upon shear displacement is equal or slightly less than the number of failed strand, which might be due to two strands snapping near the same time. The strand failure in the cable at the shear plane was also

observed as load drop at the load cells measuring axial load near the end fittings. Figure 14 shows snapped strands of the tested cables. It is obvious that the failures of strands in the cable are a mix of tensile and shear, depending on the location of the strand in the cable cross-section, the direction of the

shearing and cable construction. For multiple mixed wire diameter cables of the superstrand cable, it was observed that smaller diameter strands of the inner layer appear to fail in tension with con and cup pattern (Aziz et al., 2014 a, b).

Table 2: Model coefficients for different types.

Test No.	a_0	a_1	a_2	a_3	ϕ	c
1	624.59	-53.97	-28.72	25.73	52.13	8.82
2	619.70	-7.87	-77.06	65.73	51.41	0.27
3	636.82	-67.87	-14.88	18.57	37.53	0.16
4	387.59	83.53	-36.68	-5.05	51.23	67.8
5	335.31	-27.32	-62.84	40.02	61.7	0
6	534.76	3.47	-75.64	55.49	59.56	12.66
7	449.78	-136.34	16.39	-3.91	61.33	0.44
8	235.38	-157.50	42.83	-4.21	47.61	137.89

Table 3 summarises the peak shear strength of the different cable bolt and testing configurations. It is obvious from the results that the plain wire birdcaged cables had higher shear strength when compared to the indented wire birdcaged cables. The shear performance of non-birdcaged superstrand and hollow TG cable was lower when wires were indented, but the shear strength was still close to the UTS (Uniaxial Tensile Strength) of the cable bolts.

The lower shear behaviour of the indented wire of the same cable type was likely attributed to the fact that the indented wires have a small cross section and the indent geometry forms a stress raiser to initiate failure. The indented wire cable bolts display lower deflection (stiffer) than the plain wire equivalent type. No cable rotation was observed in either the plain or indented strand cable bolts during the double shearing tests.

As can be seen from Figure 15, the shear strength values of cable bolted concrete blocks subjected to shearing are in reasonable agreement with proposed model results for different initial pretension load, bonding agents and cable bolt types. To verify the proposed equation for the pure shear strength of cable bolts, two new double shear tests were performed. In these tests, one test was with concrete surfaces of the concrete faces being in contact with each other and the others without, that is no frictional resistance. Other parameters such as pretension value, grout type, and concrete strength were kept constant in both tests. To have cable bolt shearing without contact between concrete blocks, the double shear instrument was modified by installing two lateral braces on each side of the apparatus (Figure 16a). The lateral braces were intended to impede subjection of normal load on concrete blocks during shearing. To further assure

no friction between concrete blocks, a pair of Teflon sheets with negligible friction coefficient was introduced between concrete joints, as illustrated in Figure 16b. Table 4 compares the values of the pure shear strength of cable bolts obtained from the proposed equation and experiments. It is inferred that the results of proposed equation fits reasonably close with the experimental data.

In order to compare the method of double shearing used in this study with single the shear test of British Standard, Superstrand cables both indented and plane ones were also sheared as suggested by British Standards (2009). Figure 17 shows the comparison between the shear load against shear displacement using double shear and single shear test methods. It is inferred that the single shear testing method significantly underestimates the shear strength of Super strand cable bolts. The conspicuous difference between the value of shear load in single shear and double shear tests can be related to the fact that the single shear test is only a metal to metal shearing and does not carry any pretension or axial load during shearing. Thus, all the strands only experience shear failure without having any tension failure as observed in double shearing and shown in Figure 14. Nevertheless, in the process of double shearing, the initial pretension value is subjected to the cable before shearing and increases upon shearing due to the cable deformation. This profoundly increases the strength at which cables can resist against shearing and simulate properly the field conditions.

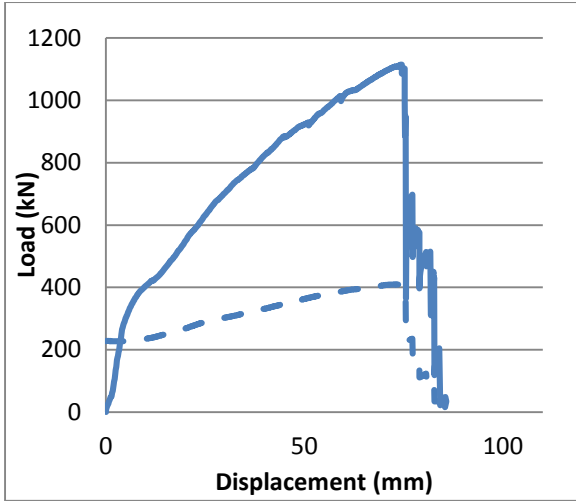


Figure 6: Shear behaviour of cabled concrete [test 1].

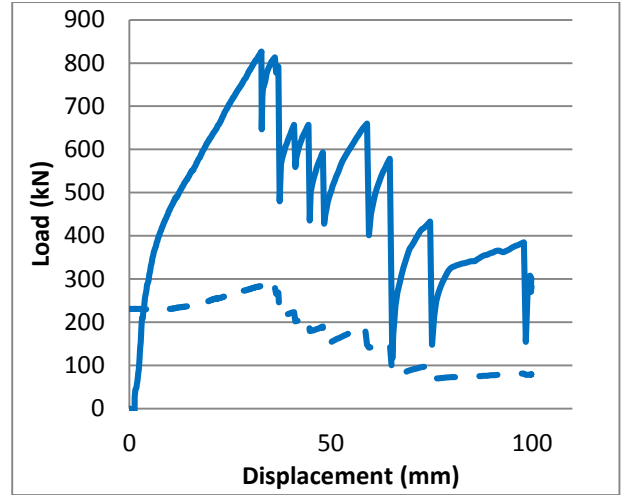


Figure 9: Shear behaviour of cabled concrete [test 4].

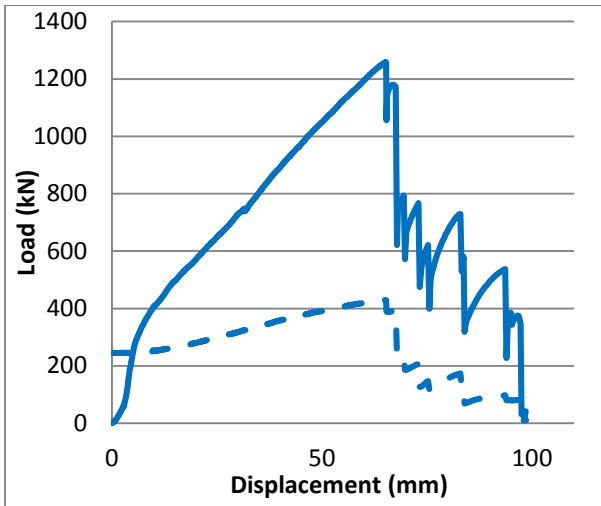


Figure 7: Shear behaviour of cabled concrete [test 2].

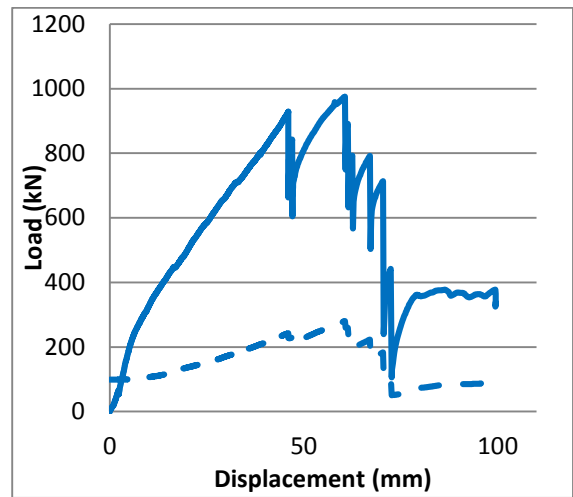


Figure 10: Shear behaviour of cabled concrete [test 5].

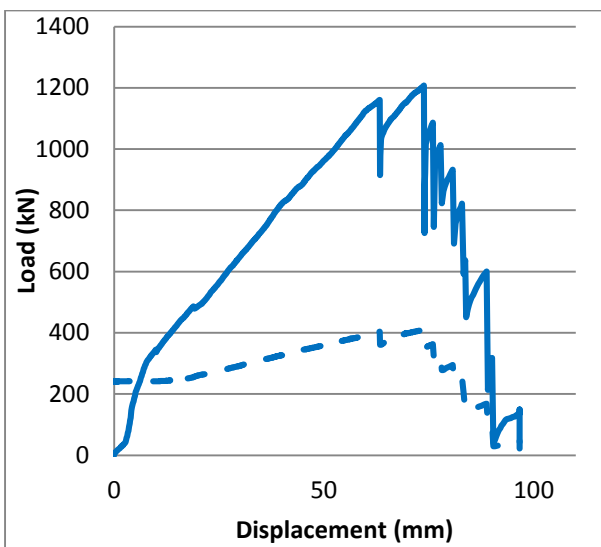


Figure 8: Shear behaviour of cabled concrete [test 3].

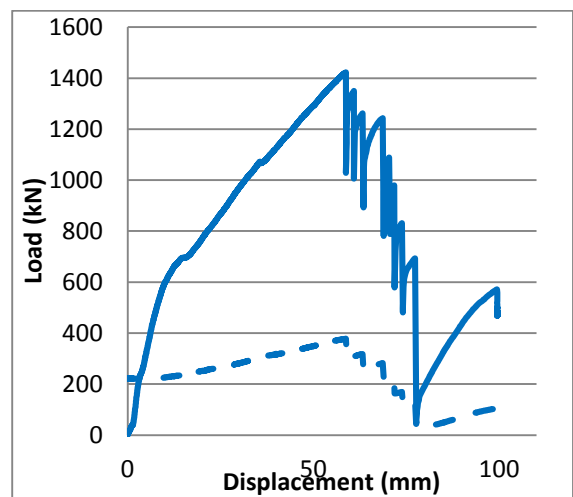


Figure 11: Shear behaviour of cabled concrete [test 6].

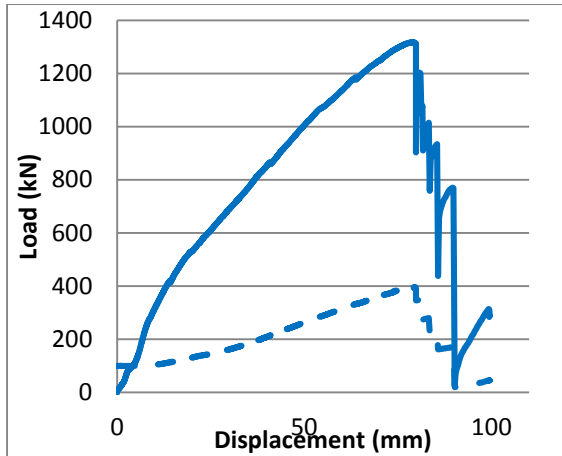


Figure 12: Shear behaviour of cabled concrete [test 7].

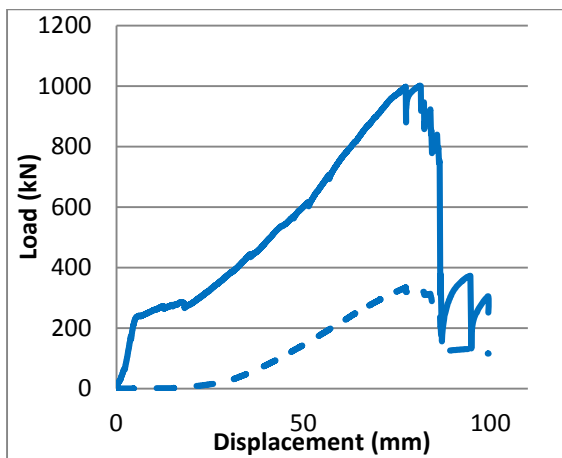


Figure 13: Shear behaviour of cabled concrete [test 8].

Table 3: Peak shear load for different cabled concrete blocks.

Test Number	Peak shear load per surface (kN)
1	558
2	628
3	604

4	414
5	488
6	711
7	659
8	501

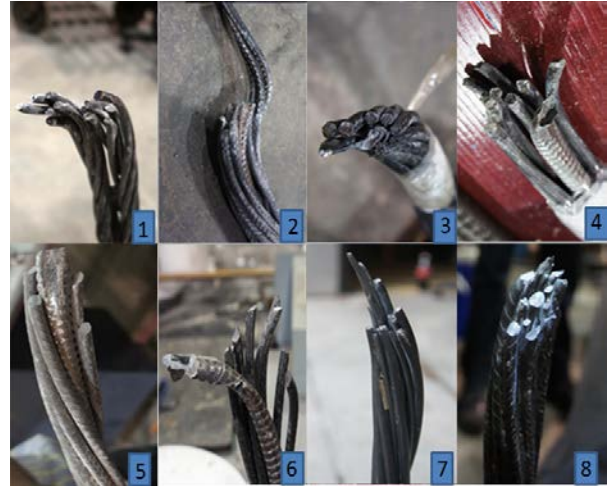


Figure 14: Strands snapped of the tested cables.

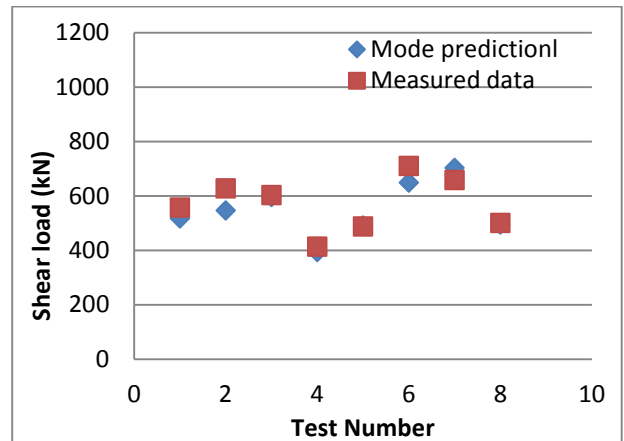


Figure 15: Comparison between the model results and measured data.



Figure 16: Up to date double shear instrument (a) the whole assembly inside compression machine (b) Teflon sheet layers between concrete blocks.

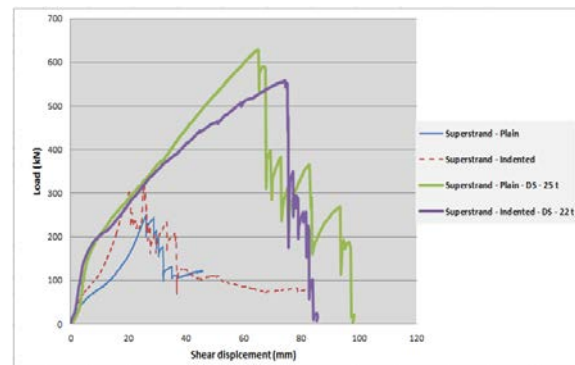


Figure 17: Comparison between the double and single shear method.

Table 4a: Comparison between the proposed model for the pure shear strength of cable bolts and experimental data.

Test No.	Product type	Bonding agent	Pre-tension load (kN)	Peak shear load per face (kN)	Friction between surfaces
9	Plain	Strata binder HS	5	645.64	with
10	Plain	Strata binder HS	5	442.16	without

Table 4b: Determination of shear load by the model.

Test	a_0	a_1	a_2	a_3	Model normal load (kN)	Tan ϕ	Tan 26.94°	c (kN)	Measured peak shear load per face (kN)
Plain superstrand with 5 kN pre-tension load (with friction)	324.77	182.37	18.65	3.04	366.316	1.47	0.508	88.61	441.006

5. CONCLUSIONS & RECOMMENDATIONS

The following conclusions are drawn from this investigation:

- Spiral profiled strand wires combined with birdcaging of cable bolts is detrimental to the cable shear performance.
- Shear strength of non-birdcaged cables bolts are less affected by spiral profiling of the wire.
- It is likely that the reduced cross-section reduces tensile strength and the geometry forms a stress raiser to initiate failure.
- A mathematical model was proposed incorporating a linear relationship between shear and normal loads and Fourier series concept to simulate the shear strength of cabled concrete blocks. The model values are in close agreement with the experimental results.

- The values of Fourier coefficients decreased as the number of Fourier coefficients increased.

Recommendations include:

- Due attention must be given to the study of the cable shear across closed and interlocking sheared beds as well as across separated beds with no contacts between sheared faces.
- More experiments are suggested to calibrate the model for practical purposes.
- The double shear method in simulated rock has proven to provide valuable insight into in-situ performance. The British Standard BS 7861 (part 2)* cannot be applied to the study of the shear behaviour of the cable bolt in rock. The equipment used in the BS 7861 (part 2) is a guillotine style tool, where the cable bolt is sheared fully in the steel frame.

Shearing of the cable bolt in rock normally undergoes both shear and tension; hence, the British standard methodology is inappropriate and may be misleading.

5. REFERENCES

Aziz, N. (2014a). Double shear testing cable-bolts for Jenmar Australia, a report of study prepared for Jenmar Australia, School of Civil, Mining and Environmental Engineering, University of Wollongong, May 27, 9p

Aziz, N. (2014b). Double shear testing of Secura Hollow Groutable Cable-bolt (SHGC) for Orica Australia Pty Ltd, a report of study, School of Civil, Mining and Environmental Engineering, University of Wollongong, July, 9p

Aziz, N., Heemann, K., Nemcik, J. and Mayer, S. (2014). Shear strength properties of Hilti plain and indented strand cable bolts, in proceedings Coal Operators Conference (Coal 2014), Wollongong, February 12-14, ISBN 978 1 925100 02 0, pp156-162 (Eds. N Aziz, B Kinninmonth), <http://ro.uow.edu.au/coal/509/>

Aziz, N., Nemcik, J., Jalalifar, H. (2011). Double shearing of rebar and cable bolts for effective strata reinforcement, in proceedings 12th ISRM International Congress on Rock Mechanics, Beijing, China, 18-21, October. Pp 1457-1460. Published in Harmonising Rock Engineering and the Environment –Qian and Zhou (Eds), 2012 Taylor and Francis Group, London, ISBN, 978-0-415-80444-8

British Standard BS 7861- Parts 1 and 2. (1996). Strata Reinforcement support system components used in Coal Mines-Part 1, Specification for rock bolting and Part 2: Specification for Flexible systems for roof reinforcement

Clifford, B., Kent, L., Altounyan, P. and Bigby, D. (2001). Systems used in Coal Mine Developments in Long Tendon Reinforcement, 20th International Conference on Ground Control in Mining. ICGCM, <http://icgcm.conferenceacademy.com/papers/detail.aspx?subdomain=icgcm&iid=735>

Craig, P. and Aziz, N. (2010a). Shear testing of 28 mm Hollow Strand "TG" Cable Bolt, in proceedings 10th Underground Coal operators Conference, Wollongong, February 11/12, pp171-179 (Ed.N Aziz and Jan Nemcik. 375 p), <http://ro.uow.edu.au/coal/303/>

Craig, P. and Aziz, N. (2010b). Shear testing of 28 mm hollow strand "TG" cable bolt, In proceedings 29th International Conference on Ground Control in Mining, ICGCM (pp. 169-174), (Publication ID=35591), <http://icgcm.conferenceacademy.com/papers/detail.aspx?subdomain=icgcm&iid=273>

Goris, J.M., Martin, L.A.(1996). Shear behaviour of cable bolt supports in Horizontal bedded deposit. Laboratory pull tests of resin –grouted cable bolts, 15th International Conference on Ground Control in Mining, Golden, Colorado, August 13-15, pp. 511-521,

<http://icgcm.conferenceacademy.com/papers/paperlist.aspx?iid=407>

Fuller PG, O'Grady P. (1993). FLEXIBOLT flexible roof bolts: A new concept for strata control, 12th International Conference on Ground Control in Mining, Morgantown, West Virginia, USA, pp. 24-34,

<http://icgcm.conferenceacademy.com/ebook/view.aspx?PaperID=1235>

Hyett, A.J., Bawden, W.F. and Reichert, R.D. (1992). The effect of rock mass confinement on the bond strength of fully grouted cable bolts, Int. J. Rock mechanics and Min. Sci. & Geomech. Abstr, 29(5), pp. 503-524

Hyett, A.J., Mossavi, M. and Bawden, W.F. (1996). Load distribution along fully grouted bolts, with emphasis on cable bolt reinforcement, Int. J. for Numerical and Analytical Methods in Geomechanics, 20, pp 517-544

Thomas, R. (2012). The load transfer properties of post-groutable cable bolts used in the Australian coal industry, 31st International Conference on Ground Control in Mining, Morgantown, 10p, <http://icgcm.conferenceacademy.com/papers/detail.aspx?subdomain=icgcm&iid=1011>

Operating conditions of a mine fan under conditions of variable resistance

Zhang Yinghua^a, Chen Li^{a, b}, Huang Zhian^{a, *}, Gao Yukun^a

^a State Key Laboratory of High-Efficient Mining and Safety of Metal Mines (University of Science and Technology Beijing), Ministry of Education, Beijing, 100083, China

^b College of resources, Hebei University of Engineering, Handan, 056038, China

ABSTRACT

According to the basic fluid principles and ventilation laws combined with the ventilation network computing method, this study proposes the concepts of relative sensitivity and absolute sensitivity, and studies these two sensitivities' variation law under conditions of variable airway resistance. The result showed that when the airway resistance increased, the fan air volume, relative sensitivity, absolute sensitivity and fan pressure's relative and absolute sensitivity tend to decrease. At the same time, fan pressure shows an increasing trend. Conversely, when the airway resistance goes down, the above parameters follow the opposite trend. These results provide a basis and guidance for adjusting the fan operation condition in the mine production process.

KEYWORDS: variable resistance, operating conditions, change rule, sensitivity

1. INTRODUCTION

Mine Ventilation System is one of the basic production systems that ensures the safety of underground work personnel life (Zhou et al., 2005). In recent years, the mining strength, depth, and the production level have all been increasing, which leads to increasingly complex ventilation systems and existing diagonal structures in the mine ventilation system, which make the ventilation management increasingly difficult. The actual production process needs timely adjustment of volume, because the working face to replace, wind resistance of roadways, the network structure and the need to air volume are constantly changing (Mi, 2009). Air conditioning is a dynamic process, and the nonlinear changes not only increase the difficulty of air volume adjustment for complex ventilation networks, but also have a significant impact on production safety. Therefore, mastering the complex network air regulation change rules requires more and more attention. Zhou (1995) put forward and illustrated the simple calculation method of the adjustable resistance value, based on the influence of the network. Zhao et al. (2003) developed measures of increasing and decreasing the resistance to adjust the air volume on the individual ventilation networks. Zhou et al. (2005) analyzed the sensitivity of the branch airflow to the wind resistance and the natural wind pressure, in order to judge the stability of ventilation networks. Jiao et al. (2009) analyzed the partial ventilator regulating ability and introduced the concept of air volume adjustable tunnelling faces. Wu, (2011) used the sensitivity to quantify the selection criteria of the air regulation point. Yan et al. (2011) studied the

ventilation system air volume and wind resistance changes between the superpositions. Hu et al. (2014) explored the complexity of mine ventilation network and fan control. There are few reports on air regulation change law for complex ventilation network. The present study examines the fan air volume and air pressure change rules and regulation of sensitivity for the main branches of the complex ventilation network system, in order to provide a basis and guidance for mine air regulation.

2. MODEL OF THE VENTILATION NETWORK SYSTEM

The set of the ventilation network nodes is

$$J = (j_1, j_2, \dots, j_m)$$

where m is the number of nodes.

The set of the ventilation network branches is

$$E = (e_1, e_2, \dots, e_n),$$

where n is the number of branches.

The ventilation network can be expressed as

$$G = (V, E)$$

A typical complex ventilation network that included series, parallel, and angle type and containing eight nodes and twelve branches was built, as shown in Figure 1.

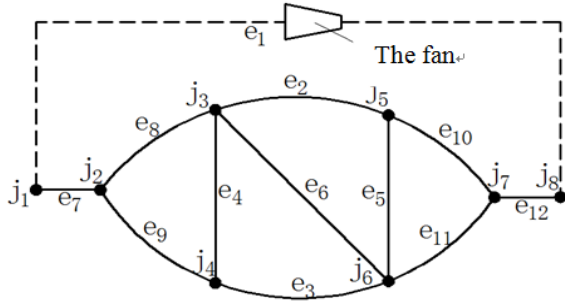


Figure 1: The ventilation network.

The wind resistance change of branch is defined as the variable resistance branch. When the variable resistance branch of wind resistance changes the air flow and pressure of the fan, this magnitude of the air volume change is defined as the sensitivity of air volume for variable resistance, called γ . The ratio of the air flow (pressure) variation and the wind resistance of variable resistance branch is defined as the absolute sensitivity, called ψ . The formulas are as follows:

$$\gamma_q = \frac{d(\Delta Q)}{d(\Delta R)} = \frac{d(Q_{ij} - Q_{i0})}{d(R_j - R_0)} \quad (1)$$

$$\gamma_q = \frac{d(\Delta Q)}{R_j} = \frac{d(Q_{ij} - Q_{i0})}{R_j} \quad (2)$$

$$\gamma_f = \frac{d(\Delta H)}{d(\Delta R)} = \frac{d(H_{ij} - H_{i0})}{d(R_j - R_0)} \quad (3)$$

$$\gamma_f = \frac{d(\Delta H)}{R_j} = \frac{d(H_{ij} - H_{i0})}{R_j} \quad (4)$$

Where: Q_i is the fan branch air volume after variable resistance of the j time measured in m^3/s ; H_i is the fan branch of wind pressure after variable resistance of the j time; Pa ; Q_{i0} is the fan branch air volume air volume after variable resistance of the $j-1$ time measured in m^3/s ; H_{i0} is the fan branch of wind pressure after variable resistance of the $j-1$ time; Pa ; R_j is the resistance value of the variable resistance branch after the j time variable resistance; R_0 is the resistance value of the variable resistance branch after the $j-1$ time variable resistance measured in $N.s^2/m^8$.

The wind resistance information of each branch was as shown in Table 1. The basic information of the fan was as shown in Table 2.

Table 1: The value of the each branch wind resistance.

Branch number	Value of the wind resistance ($N.s^2/m^8$)
e ₁	0.001
e ₂	0.026
e ₃	0.005
e ₄	0.065
e ₅	0.082
e ₆	0.099
e ₇	0.126
e ₈	0.048
e ₉	0.087
e ₁₀	0.032
e ₁₁	0.029
e ₁₂	0.134

Table 2: The basic information of the fan.

Fan model	FBCDZ-6-№20
Wind pressure(Pa)	661-1917
Air volume (m^3/s)	25.9-65.5
Motor model	YBF ₂ -315S-8
Rated speed (r/min)	900
Rated power (kW)	2×55

3. VENTILATION NETWORK SOLUTION

Network solution is one of the important ways to adjust and analyze the ventilation network. This is theoretically based on the three laws of ventilation, which are the air volume balance law, the mesh air pressure balance law, and the law of resistance (Zhang, 2000).

(1) The balance law of air volume:

The mass flow of each branch that inflows and outflows of a node algebraic addition is zero. The formula is as follows:

$$\sum M_i = 0 \quad (5)$$

(2) The balance law of the mesh air pressure:

In a closed loop without a power source, the ventilation resistance of the branches algebraic addition is zero, while with a power source, the ventilation resistance of the branches algebraic addition is equal to fan air pressure of the loop. The formula is as follows:

$$\sum h_i = 0 \text{ or } \sum h_i = h_f \quad (6)$$

(3) The law of the resistance:

The resistance of the roadway is equal to the product of the wind resistance and air flow square. The formula is as follows:

$$h = RQ^2 \quad (7)$$

By combining (5) to (7), the air volume was calculated using the Scot-Hinsley algorithm. The network solver is written using the VB. net platform.

4. THE DISCUSSION AND ANALYSIS

e_8 and e_9 were selected as a branch of variable resistance, which are parallel branches. e_8 is the increased resistance branch, while e_9 is the reduced resistance branch, resistance changed 20 times in succession, and the network was calculated once the resistance changed. The computed results are as shown in Table 3.

Table 3: The computed results

Adjustment times	Value of the increased resistance ($N.s^2/m^8$)	Pressure of the fan (Pa)	The air volume of the fan (m^3/s)	Adjustment times	Value of the reduced resistance ($N.s^2/m^8$)	Pressure of the fan (Pa)	Air volume of fan (m^3/s)
1	0.088	1183.079	64.242	1	0.077	1180.815	64.274
2	0.128	1199.206	64.011	2	0.067	1178.297	64.310
3	0.168	1210.512	63.849	3	0.057	1175.465	64.350
4	0.208	1219.151	63.725	4	0.047	1172.222	64.396
5	0.248	1226.125	63.624	5	0.037	1168.427	64.450
6	0.288	1231.953	63.540	6	0.035	1167.583	64.462
7	0.328	1236.946	63.468	7	0.033	1166.704	64.475
8	0.368	1241.300	63.405	8	0.031	1165.787	64.488
9	0.408	1245.152	63.349	9	0.028	1164.335	64.509
10	0.448	1248.597	63.299	10	0.026	1163.310	64.523
11	0.488	1251.708	63.254	11	0.024	1162.235	64.538
12	0.528	1254.539	63.213	12	0.022	1161.106	64.554
13	0.568	1257.133	63.175	13	0.020	1159.915	64.571
14	0.668	1259.522	63.140	14	0.018	1158.657	64.589
15	0.868	1264.768	63.064	15	0.016	1157.324	64.608
16	1.068	1273.026	62.943	16	0.014	1155.904	64.628
17	1.668	1279.335	62.851	17	0.012	1154.387	64.650
18	2.668	1292.079	62.664	18	0.008	1150.991	64.698
19	4.668	1304.128	62.487	19	0.004	1146.940	64.755
20	6.668	1316.509	62.304	20	0.001	1143.241	64.807

4.1 The change rule of the fan air volume and air pressure

When the airway resistance changed, the fan air volume and air pressure changed, as shown in Figures 2 and 3. The figure shows that, when the airway resistance increases, the fan pressure will increase and the fan air volume will decrease; On the contrary, when the airway resistance decreases, those parameters' change follows the opposite trend. This is due to the changes of total wind resistance in the ventilation network system caused by the airway resistance.

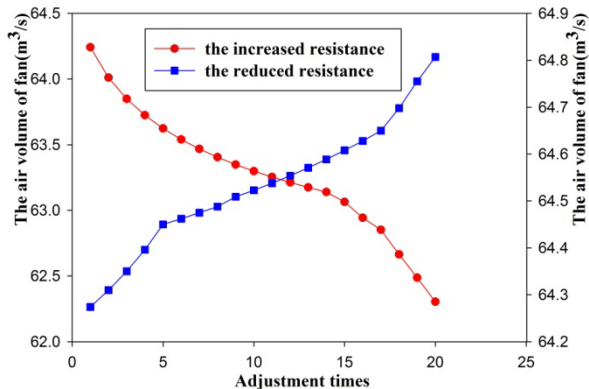


Figure 2: The changed curve of the fan air volume when variable resistance.

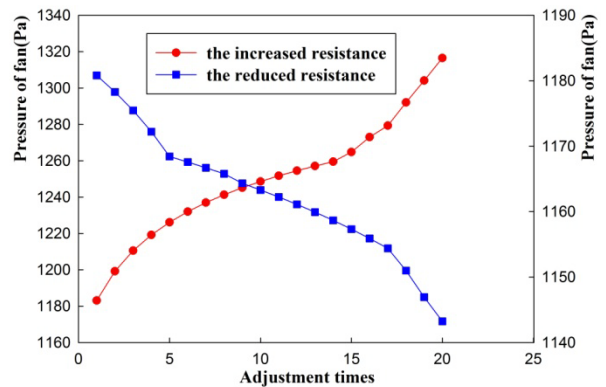


Figure 3: The changed curve of the fan pressure when variable resistance.

4.2 The sensitivity of the fan air volume and air pressure

The computed results were substituted into formulas (1) to (4). The relative and absolute

sensitivity of the fan air volume and air pressure were computed when varying the resistance, as shown in Figures 4 to 7. The figures show that, when the airway resistance increases, the relative and absolute sensitivity of the fan air volume and air pressure showed a decreasing trend. The curve is initially steep before gradually slowing. When the airway resistance goes down, the relative and absolute sensitivity of the fan air volume and air pressure showed an increasing trend, with the relative sensitivity stability increased gradually. The early stage of the absolute sensitivity changes smoothly, while the late stage increases suddenly. This suggests that the influence of the fan air volume and air pressure is obvious when the airway resistance increases in the early stage and the airway resistance goes down in the later stage.

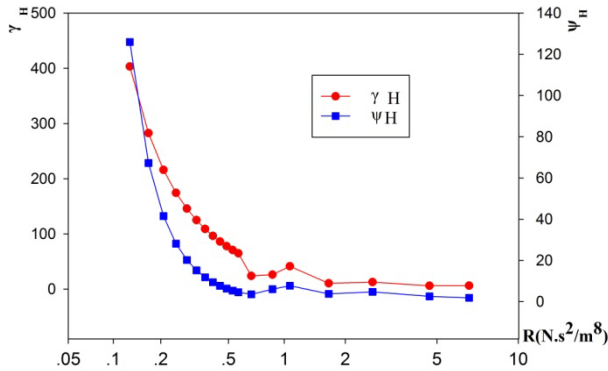


Figure 4: The sensitivity curve of the fan pressure when increased resistance.

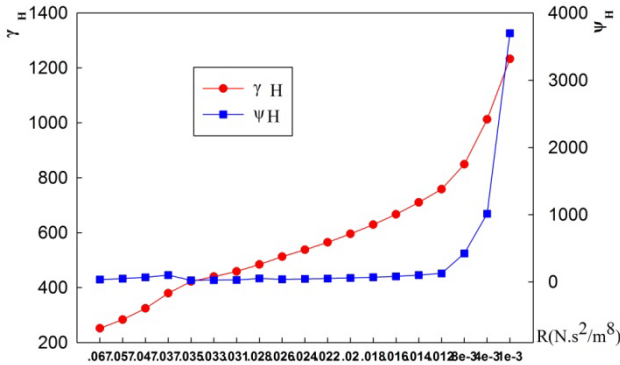


Figure 5: The sensitivity curve of the fan pressure when reduced resistance.

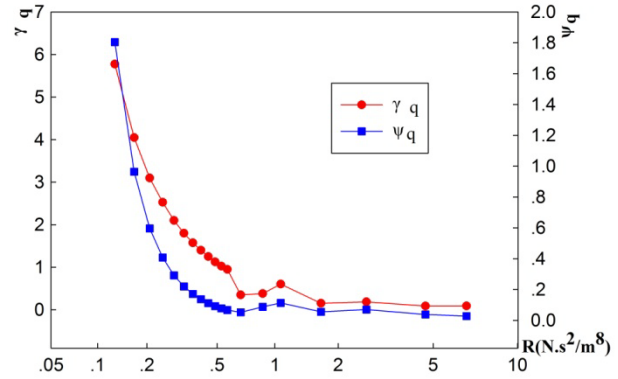


Figure 6: The sensitivity curve of the fan air volume when increased resistance.

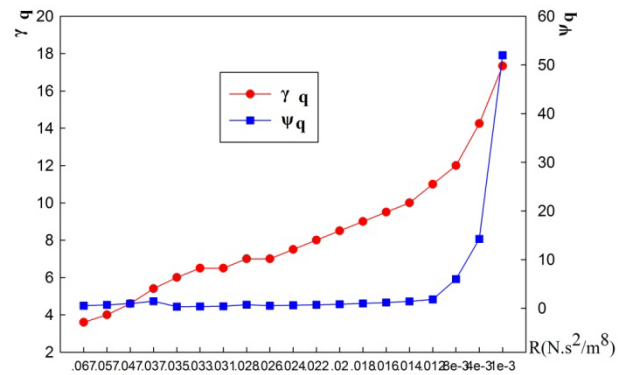


Figure 7: The sensitivity curve of the fan air volume when reduced resistance.

5. CONCLUSIONS

The following conclusions can be drawn:

First, when the airway resistance increases, the fan air volume, its relative and absolute sensitivity, and fan pressure's relative and absolute sensitivity, tend to decrease. At the same time, fan pressure showed an increasing trend. Conversely, when the airway resistance goes down, the above parameters change in the opposite direction.

Second, the influences of the fan air volume and air pressure is obvious when the airway resistance increases early on, and then gradually weakens. Conversely, when the airway resistance goes down, the influence of the fan air volume and air pressure follow the opposite trend. These results provide a basis and guidance for adjusting the fan air volume in mines.

Finally, when increasing the resistance, even the appearance of the fan air pressure being too high should be avoided, as it could cause unstable running of the fan, and ultimately impact safe production.

6. ACKNOWLEDGEMENT

It is with great pleasure that we acknowledge the generous financial support of National Natural Science Foundation of China (project number: 51474017) and Natural Science Foundation of Xinjiang Uygur Autonomous Region of China (2014211B013).

7. REFERENCES

- Hu, H. H., Yang, G. Z. (2014). Quantified calculation on complexity of mine ventilation network and control force from main ventilator. *Journal of Safety Science and Technology*, Volume10, No. 7, pp. 152-157
- Jiao, Y., Zhou, X. Q., Gong, W. (2009). Network analysis of air volume adjustment in mine tunnelling faces during the period of the normal production. *Mining Safety & Environmental Protection*, Volume 36, No. 6, pp. 76-78
- Mi, X. K. (2009). Mine local air volume and total air volume adjustment. *Coal Technology*, Volume 28, No. 5, pp. 107-108
- Wu, F. L. (2011). Using sensitivity to optimize mine air regulation point and parameter. *Mining Safety & Environmental Protection*, Volume38, No. 5, pp. 1-3
- Yan, Z. G., Fan, J. D. , Wang, H. (2011). Superposition features of air flow ' s changes in a mine ventilation system. *Science & Technology Review* , Volume29, No. 34, pp. 37-40
- Zhang, G. S. (2000). *Ventilation Safety*. China University of Mining and Technology Press, 85-92p
- Zhao, D., Liu, W. H., Yao, L. Z. (2003). Calculation and Regulation of the Local Air Volume in Mine. *COAL*, Volume 12, No. 3, pp. 35-36
- Zhou, J., Liu, J. and Jia, J. Z. (2005). Analysis sensitivity of mine ventilation system. *Journal of Liaoning Technical University*, Volume 24, No. 4, pp. 1-3
- Zhou, L. H. (1995). Calculation and analysis of the air condition in mine ventilation network. *J. XIANGTAN MIN. INST*, Volume10, No. 4, pp. 14-18

Analysis of slag debris flow initiation based on laboratory tests of slag

Hongbiao Zeng, Hongming Yu

Department of Engineering, China University of Geosciences, Wuhan, China, 476400

ABSTRACT

Accumulated slags and waste in mines are major physical resources for slag debris flow, which are potentially major disasters that threaten mine safety. Initiated by heavy rain, slag debris flow has happened in Ganjiang gully around Luanchuan county, China. Studies have been carried out to further understand the formation and initiation mechanism of slag debris flows. Slag samples with different fines content were collected from the gully and the slag strength and permeability were investigated by direct shear tests and by falling head permeability tests, respectively. The results indicate that the fines content has a significant impact on both the strength and permeability characteristics of slags. With the fines content increasing, both the strength and the hydraulic conductivity of the slag decrease. The strength of saturated slag samples is extremely weak, meaning that water will easily soften the slag. In addition, as the fines content increases, the hydraulic conductivity would decrease at an accelerated rate, down to a very small constant. Based on the current investigation, it can be concluded that two different types of slag debris flow would form in the specific conditions: shallow debris flows are mainly dominated by surface erosion, while deep debris flows are dominated by bottom tearing and suffusion erosion.

KEYWORDS: slag, debris flow, initiation, strength, hydraulic conductivity

1. INTRODUCTION

Mine debris flow is different from the natural debris flow, also referred to as slag debris flow, which mainly occurs in the fragile ecological environment of mountainous and hilly areas. With the development of the mining industry, mine debris flow is quickly becoming one of the major reasons restricting mining and production safety. According to Xu (2007), as of the end of 2005, mine debris flows have occurred 247 times in the northwest region of China, killing 426 people and causing direct economic losses of \$384 million. There is much research on general debris flow; however, research related to slag debris flow is currently lacking due to the particularity of the material resource and dynamic conditions.

Debris flow occurs in all regions with steep relief and at least occasional rainfall, and tends to occur on slopes that are geologically young, steep, and naturally only marginally stable, (Jakob, 2005; Anderson, 1995). The initiation of the debris flow is related to three issues of resources, water (rainfall), and underlying conditions. Cannon et al. (2008) specify the significant role of rainfall in the initiation of debris flow by using a rain gauge and response data. Stoffel et al. (2011) studied the formation mechanism of debris flow in the Alps of Switzerland. Chen and Cui (2006) have carried out research on the formation process of debris flow through artificial rainfall experiments. Jakob et al. (2012) studied the formation mechanism of debris flow induced by

rainstorms. Mergili (2012) developed a GIS model to simulate the initiation and movement of debris flows.

The related research on mine debris flow is mainly on the qualitative analysis of provenance characteristics, formation conditions, classification, and initiation mechanisms. Fang (2007) summarized the material sources of mine debris flow, and considered hydrodynamic conditions to be the external factor that triggers the initiation. Waste and dump induced debris flows were classified into 5 types according to their formation mechanism: dump outburst, bottom tearing, side eclipse, surface erosion, and other complex types (Ni, 2011). Deng (2009) analyzed the development characteristics and the initiation conditions of slag debris flow for one gully in a gold mining area. Cao (2008) classified slag debris flow into two types, slope flow and trench flow, and studied their initiation mechanisms.

Other studies have focused on the penetration characteristics of slag, and tried to analyze and predict the mechanisms of mine debris flow through the use of quantitative methods. However, the impact of slag strength and permeability characteristics on the initiation of slag debris flow is still poorly understood. This paper consists of two main parts. First, the shearing strength and permeability of the slag with different fines content taken from Ganjiang Gully, in Luanchuan county, are studied using laboratory tests. Second, based on the test results of the shearing strength and permeability characteristics of the slag as well as some previous initiation models

of general debris flow, the initiation of slag debris flow is analyzed.

2. LABORATORY TESTS

Test samples were taken from the slag heaps in Ganjiang Gully, Luanchuan County, with the sample's dry density (ρ_d) being $1.90 \text{ g}\cdot\text{cm}^{-3}$, specific gravity (C_s) being 2.86, and field moisture (W) being 3.2%. Three remoulded samples were prepared for direct shear tests and variable head permeability tests. The grading curves of the slag samples were as shown in Figure 1.

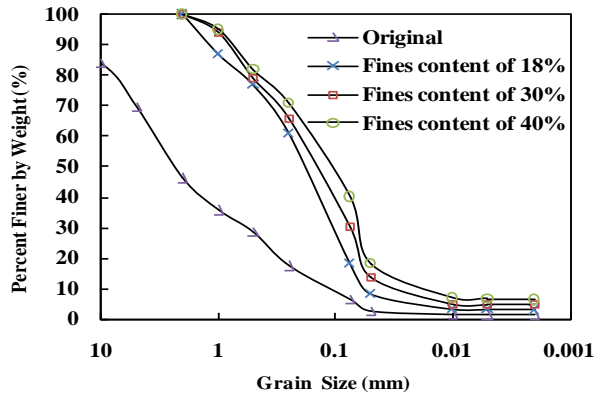


Figure 1: Grading curves of original and remoulded samples.

2.1 Direct shear test



Figure 2: The direct shear apparatus.

Direct shear tests were carried out to obtain the strength parameters of the slag samples. The three remoulded samples have different fines content of 18%, 30%, and 40%, with two different saturation of natural water contents: 50% and full saturation. The test was conducted in the strain controlled direct shear apparatus (Figure 2). The quick shearing test was applied at a rate of 0.8 mm/min , with the samples destructed in 3-5 minutes.

2.1.1 Shear Stress vs. displacement

The remoulded samples with fines content of 18% were chosen for explaining the variation of shear displacement as the shear stress increased under different saturations of 21%, 75%, and 100%.

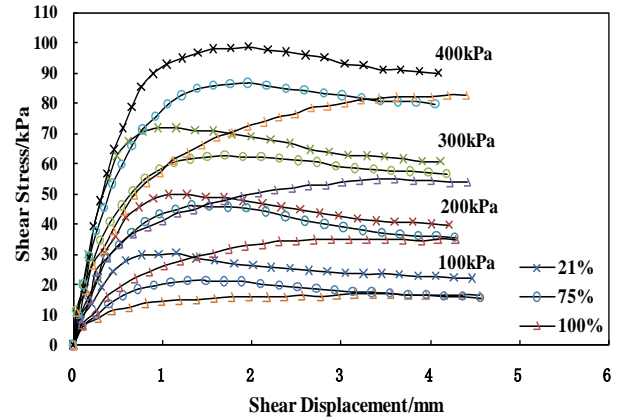


Figure 3: Shear stress vs. horizontal displacement under different saturation (21%/75%/100%).

As Figure 3 shows, the slag samples of 21% and 75% saturation were mostly destructed with the peak horizontal displacement between 3-5 mm, which proved to be strain softening. When the shear stress reached a peak, shear failure occurred, and the shearing strength continued to decrease, with the shear displacement going down to a certain value of residual strength. While under full saturation (100%), there were no significant peaks at different vertical pressure, which shows the characteristics of creep deformation and strain hardening.

In the shearing process, the particles rearrange on the shear plane with the effort of vertical stress, and the shear dilatancy occurs when the pore pressure builds up in the undrained condition. Fully saturated slag samples with high water content may have a certain plasticity flow, with fluctuating curves of stress-displacement. In addition, it can be seen that the corresponding peaks of the curve declined with increases in slag saturation level, and the shear stress of the saturated slag declined more sharply than the slag of 21% and 75% saturation, demonstrating that the slag strength is weaker in saturated states. Rainfall results in slags reaching a saturated state, which may accelerate the initiation of slag debris flow due to the deterioration of stability.

2.1.2 Slag Strength vs. Fines Content

Shear tests for three samples with different fines content of 18%, 30%, and 40% were conducted to investigate the relationship between slag fines content and the shear strength, as shown in Figure 4.

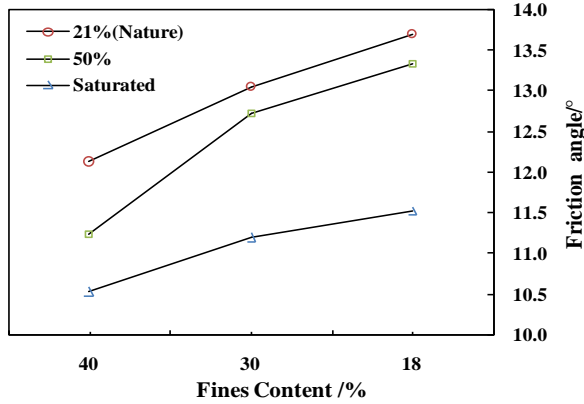


Figure 4: Relationship between fines content and ϕ .

Since the clay content of slag is very low, and the cohesion measured from the test by Xie (2013) is close to zero, in this study the tested slag was considered sandy soil, without considering the cohesion. The Mohr-Coulomb theory was employed to determine the shear strength of slag, using the following equation (1):

$$\tau = \tan \phi \quad (1)$$

Where

ϕ is the internal friction angle;
 τ is the shear strength.

In this study, friction angle (ϕ) is used to express the strength of slag samples. As Figure 6 shows, it can be seen that slag strength decreases with increases in fines content, with the three different slag samples all showing the same phenomenon. Strength of the slag samples with 40% fines content was 8.6%-15.6% lower than that of slag samples with 18% fines content. The fines content has a significant influence on the microstructure of the slag, and the increased fines content leads to weakening of the interactions between the coarse particles, causing a reduction of its shearing strength. In addition, it shows an obvious decrease when the saturation of slag with the certain fines content increases, and the inflection points of the curve are more apparent for the 50% and natural saturation levels. While the slag sample is in a saturated state, the friction angle declines to a minimum, since the water in the slag samples destroys the cementation of the particles of slag.

The results indicate that the particle gradation characteristics of slag have a limited effect on slag strength, while the saturation level shows a more important influence on shearing strength of slag.

2.2 Variable head permeability test

The South 55-type variable head permeameter was carried out to obtain the slag permeability characteristics, using three different fines content

(18%, 30%, 40%) slag samples. In order to measure the saturated hydraulic conductivity, the cutting ring samples for testing are prepared and controlled at natural saturation levels.

In order to determine the saturated hydraulic conductivity, the slag in natural states are prepared to for testing using the vacuum saturation method. The following equation (Darcy Law) was used (2):

$$K = Q_L / Aht \quad (2)$$

Where

$A=0.23758 \text{ cm}^2$;

$L=4\text{cm}$, represents Penetration Path;

Q , h and t are obtained from the test records.

The test results are listed in Table 1, and graphed in Figure 5.

Table 1: Results of variable head permeability test.

Fines Content	18%	30%	40%
Hydraulic Conductivity/ $\text{cm}\cdot\text{s}^{-1}$	1.68E-04	7.22E-05	4.67E-05

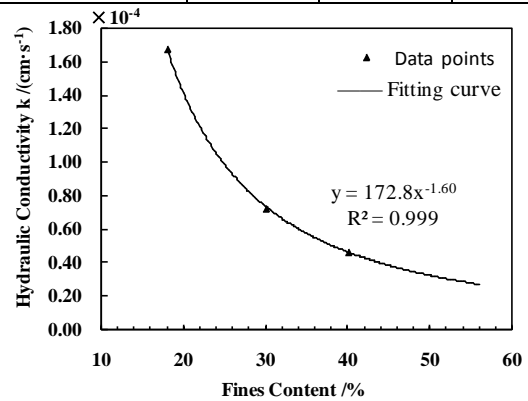


Figure 5: Fitting curve between fines content and hydraulic conductivity.

As shown in Table 1 and Figure 5, there is an apparent gap between the hydraulic conductivity of slag samples with different fines contents of 18%, 30%, and 40%. The gap between the slag samples of 18% and 30% fines content is much larger than that between the slag samples of 30% and 40% fines content. The fitting curve between fines content and hydraulic conductivity, according to the distribution of data points, is expressed as the following equation (3) with a correlation coefficient (R) of 0.999:

$$y = 172.8x^{-1.60} \quad (3)$$

In which, $y=K \times 10^4$, $x=C \times 10^2$, where K and C represent the hydraulic conductivity and fines content, respectively. Equation (3) can then be changed to the following equation (4):

$$K = 1.0903E-05C^{-1.60} \quad (4)$$

With increases in the fines content of slag samples, the hydraulic conductivity decreases, and

the trend of decline is such that the difference gap of the hydraulic conductivity between the slag of 40% fines content and one of 30% fines content is larger than the gap between the slag of 18% fines content and the one of 30%.

Meanwhile, from the trend of the fitting curve, when the fines content of slag reaches a certain value, the decline of hydraulic conductivity gradually becomes weaker, and reaches an almost stable state with values of more than 40%. Kong (2011) and Wang (2012) have found similar sequences by studying the variation of hydraulic conductivity of sand. It can then be noted that the greater the hydraulic conductivity, the stronger the infiltration ability, therefore, the slag will more easily reach a saturated state under certain rainfall conditions.

3. ANALYSIS OF SLAG DEBRIS FLOW INITIATION

3.1 Initiation Models of General Debris Flow

As Liu (2002) summarized in his overview of foreign debris flow mechanism models, the primary classical debris flow initiation mechanism models that have been widely accepted include: Coulomb's particle flow model containing pore water pressure, the Johnson model (1970), the Takahashi model (1978), the general viscous plastic flow model put forward by Chen (1986), O'Brien's dilated plastic flow model (1993), and the mixed flow theory of momentum conservation equation applied for complicated debris flows as proposed by Verson (1997).

In addition, many researchers have developed diverse initiation mechanisms for debris flow with different types of solid content and formation, including:

1. Takahashi model

Takahashi (1991) proposed that the wash and erosion of the sediments in gully beds by water flow, resulting from rainfall or underground water, is the key factor causing the initiation of hydraulic debris flow. After rainfall, runoff with a depth of h develops and forms on the underground surface or on a brook with an inclination angle θ . The shearing force produced from water flow acting on deposits is τ , and the shearing resistance of deposits is τ_L . According to the relationship between τ and τ_L , the initiation of debris flow can be discussed. If the effect of flow velocity on the deposits with a certain depth is ignored, the total shearing force acting on the deposits can be calculated using the following equation (5):

$$\tau = g \sin \theta [C_* (\rho_m - \rho) a + \rho (a + h_0)] \quad (5)$$

Where

C_* is the volume concentration of deposits.

a is the layer thickness of deposits which is possibly sheared and move, m.

ρ_m is the soil density of debris, g/cm³.

ρ is for the density of water (containing a small suspended solids, $\rho = 1$), g/cm³.

g is the acceleration due to gravity, m/s².

h_0 is for the depth of surface flow, m.

The totally shearing force is made up of two parts, the solid material in the flow and the water, as shown in the equation.

The shear resistance τ_L of the deposits can be calculated using the following equation (6):

$$\tau_L = g \cos \theta \left[C_* (\rho_m - \rho) a + \frac{\rho_m d}{\cos \theta} \right] \tan \varphi \quad (6)$$

When $\tau > \tau_L$, it is believed that debris flow is likely to form and develop.

2. Sediment movement model

Xie et al. (1993) established the mechanical model for the initiation of deposits loosely piled up in gully beds, based on sediment movement theory. It is believed that loose deposits in gully beds is critical in debris flow initiation, and deposits containing a lot of water show the characteristics of saturated slurry. This is especially true for the deposits contracted with the bottom of the gully bed. For hydraulically driven debris flow, the flow initiation theory can be regarded as the sediment movement theory for bed material flow initiation.

3. Hydrodynamic model

Tang et al. (2001) proposed a mechanical model for the initiation of deposits piled up in gully beds based on hydrodynamic theory. This type of debris flow initiation model mainly considers that the debris flow is initiated by the fluid's drag force on the deposits. Therefore, it is called the drag-imitation model. The drag force is determined according to hydrodynamic theory, and it is a key factor influencing the initiation of deposits.

3.2 Analysis of slag debris flow initiation

Based on the findings above, the strength of slag samples is greatly influenced by slag saturation state, and is quite weak in a saturated state. Slag strength has shown little sensitivity to grain-size distribution characteristics. However, the hydraulic conductivity makes a significant difference because of the different fines content of slag. Therefore, slag debris flow initiation can be analyzed according to the strength and permeability characteristics of slag.

As Cui et al. (2003) studied, there is a direct relationship between soil saturation and rainfall, and with some initial rainfall, a slag pile reaches a certain saturation state. In addition, antecedent moisture content directly governs the hydraulic conductivity of

partially saturated soils and also influences the strength characteristics of the slag. Generally, with ongoing rainfall, slag strength declines constantly. In contrast, its weight would be increasing, causing the stability of the slag pile to become worse, and eventually causing damage.

Secondly, judging from the experimental data, slag strength is lowest when its hydraulic conductivity has the minimum fines content of 40%, for conditions where the stability of the slag pile is worst. It should be noted that a value of 40% for fines content is already great, according to the analysis of the particle composition of slag material collected from different location.

Hereafter, if the fines content of slag, which is considered a quantitative evaluation factor, is high, the slag strength would be weak, while permeability and infiltration capacity would be also weak with a lower saturated velocity, that is, with a decreased velocity of slag strength. Generally in this case, such slag pile induced debris flow is initiated slowly, and with conditions of continuous rainfall, both surface flow and pore water pressure of the slag pile also increase constantly, and shallow debris flows mainly dominated by surface erosion may form easily. On the other hand, the lower the fines content of slag, the stronger the slag strength, and the slag pile would be more susceptible to damage in the same topographic and rainfall conditions. While, there is a large hydraulic conductivity among the slag pile and rainfall can quickly penetrate into the bottom of slag pile through the void in particles, due to the higher saturated velocity and the higher decreased velocity of slag strength, such slag piles induced debris flow generally initiates quickly. With ongoing rainfall, deep debris flows mainly dominated by bottom tearing and suffusion erosion may easily form, which would carry a larger amount of provenance and be more dangerous than shallow debris flows.

3.3 A Field Case of Slag Debris Flow

On July 22 to 24, 2010, impacted by the typhoon "chan had", heavy rain occurred around Luanchuan county in China, inducing a centralized outbreak of debris flow because of the torrential rains. The affected slag pile had been accumulating in Ganjiang gully, and had a lack of protection. The debris flow initiation induced by the slag pile was analyzed according to the strength and permeability characteristics controlled by the particle composition of the slag.

First, the fines content of slag pile in Ganjiang gully was between 20% and 30%, and the slag strength was relatively high. Correspondingly, due to the large hydraulic conductivity, the slag pile was in a saturated state within a short time during the heavy

rainfall that occurred, and the slag strength decreased quickly. Therefore, as the heavy rain continued, runoff occurred and the hydrodynamic conditions were prepared for the initiation of debris flow. Finally, on July 24, 2010, the slag pile in the source area of Ganjiang gully experienced outburst, forming deep debris flows mainly dominated by bottom tearing and suffusion erosion. This was accompanied by shallow debris flows in the other partial area. The following picture is the slag left behind after the debris flow burst in Ganjiang gully, as shown in Figure 6.



Figure 6: Slag left behind after the debris flow burst.

In conclusion, when the slag debris flow in Ganjiang gully was evaluated, the main factors affecting the initiation of slag-induced debris flow were the fines content and permeability characteristic of slag, because particle size distribution is more sensitive to permeability characteristics than to slag strength.

4. CONCLUSIONS

Based on the current study's analysis of the slag debris flow in Ganjiang gully in Luanchuan county, the following main conclusions are obtained:

1) The fines content of slag is a significant factor not only for the slag's strength but also its permeability characteristics. With fines content increasing, both the strength and the hydraulic conductivity of the slag decrease. If the value of the fines content of the slag exceeds 40%, the hydraulic conductivity decreases constantly, with the acceleration of decline becoming more gradual, down to an almost stable state.

2) Considering the change in slag strength and permeability characteristics in conditions of continuous rainfall, two different types of debris flow can be induced: shallow debris flows, which are mainly dominated by surface erosion, and deep debris flows, which are mainly dominated by bottom

tearing and suffusion erosion. Fines content and the permeability coefficient are the main factors that affected slag debris flow in Ganjiang gully.

5. ACKNOWLEDGMENTS

The work is supported by the research grant from National Natural Science Foundation of China (Project Number: 41272377), Henan Scientific and Technological Research Projects (Project Number: 122102310477).

6. REFERENCES

Cannon, SH, Gartner, JE and Wilson, RC (2008). Storm rainfall conditions for floods and debris flows from recently burned areas in south western Colorado and southern California. *Geomorphology*. DOI: 10.1016/j.geomorph.2007.03.019.

Cao Y.B (2008). Experiment of Initiation Mechanism of Mine Debris Flow [D]. Chang'an University.

Chen X Q, Cui P, Feng Z L, et al. (2006). Artificial Rainfall Experimental Study on Landslide Translation to Debris Flow. *Chinese Journal of Rock Mechanics and Engineering*. Volume 25, No. 1, pp. 106-117

Cui P, Yang K, Chen J (2003). Relationship between occurrence of debris flow and antecedent precipitation: taking the Jiangjia gully as an example. *Science of Soil and Water Conservation*. Volume 1, No 01, pp. 11 -15

Deng L.S, Fan W, Xiong W, et al. (2009). Development features and risk of inducing slag debris flow at daxicha gully. *Journal of Engineering Geology*, Volume 17, No. 3, pp.415-420

Fang Q.J, Ren J.Q, Guo S.K (2007). Summary of formation conditions of mine debris flow. *Geotechnical Engineering World*. Volume 11, No. 5, pp. 66-67

Jakob M. and Hungr O. (2005). *Debris-flow Hazards and Related Phenomena*. CA: Berlin Heidelberg

Jakob M, Owen T and Simpson T (2012). A regional real-time debris-flow warning system for the District of North Vancouver, Canada. *Landslides*. DOI: 10.1007/s10346-011-0282-8

Kong L.W, Li X.M and Tian H.N (2011). Effect of fine particles content on permeability coefficient of sand and its correlation with state parameters. *Rock and Soil Mechanics*, Volume 32, No. S2, pp. 21-27

Liu X.L (2001). An Overview of Foreign Debris Flow Mechanism Models. *Journal of Catastrophology*. Volume 17, No. 4, pp. 1-7

Mergili M, Fellin W, Moreiras S, et al. (2012). Simulation of debris flows in the Central

Andes based on Open Source GIS: possibilities, limitations, and parameter sensitivity. *Natural Hazards*. DOI: 10.1007/s11069-011-9965-7

Ni H.Y, Tie Y.B, Cui, P (2011). Classification and disaster prevention system of debris flows induced by waste dumps. *Resources Industries*. Volume 13, No. 3, pp. 107-113

Anderson, Scott A and Nicholas, Sitar(1995). Analysis of Rainfall-induced Debris flows. *Journal of Geotechnical Engineering*. DOI:10.1061/(ASCE)0733-9410(1995)121:7(544)

Stoffel M, Bollschweiler M and Beniston M. (2011). Rainfall characteristics for periglacial debris flows in the Swiss Alps: past incidences-potential future evolutions. *Climatic Change*. DOI: 10.1007/s10584-011-0036-6

Takahashi T (1991). *Debris flow*. Balkema, Rotterdam, International Association for Hydraulic Research.

Tang H.M, Weng Q.N, Wang K, et al. (2001). Research on substances start up types and mechanisms of debris flows in impact-deposit debris flow valleys. *Journal of Chongqing Jiaotong University*. Volume 20, No. 2, pp. 65-69

Wang Z.K, Zhang M, Zheng Q.L (2012). Impact on permeability coefficient for fines content of coarse sand. *Heilongjiang Science and Technology of Water Conservancy*. Volume 40, No. 10, pp. 63-64

Xie K, Yu H.M, Peng Z.W, et al. (2013). Large scale direct shear test of debris flow source soil in Luanchuan of Henan. *Journal of Mountain Science*. Volume 31, No. 6, pp.738-744

Xie M.S, Wang Y.J, Zhang H.J, et al. (1993). The Deposit Analysis of Water Dynamic Conditions to Form Debris Flow and to Set up Mathematical Model in Debris Flow Valley. *Journal of Beijing Forestry University*. Volume 15, No. 4, pp. 1-11

Xu Y N, He F and Chen H Q. (2007). Mine Debris Flow and Its Distribution in Northwestern China. *Journal of Mountain Science*. Volume 25, No. 6, pp. 729-736

Hydrogeological challenges and strategies at McArthur River Operation

Xiaoyou Yun^{a,*}, Baoyao Tang^a, Greg Murdock^b, Brian McGill^a, Brian Mattie^a

^a McArthur River Operation, Cameco Corporation, Saskatoon, Canada, S7M 1J3

^b Rabbit Lake Operation, Cameco Corporation, Saskatoon, Canada, S7M 1J3

ABSTRACT

High pressure, radon-bearing water has been identified as one of the most critical challenges in mining the high grade uranium deposit at the McArthur River Operation, Cameco Corporation. The ore deposits are located between 490 m and 640 m below the surface and surrounded by water bearing Athabasca sandstone, a graphitic fault zone, and highly altered ground. This paper introduces the inflow risk management program at McArthur River Operation which includes various hydrogeological challenges and the corresponding strategies applied, such as risk based probe and grout programs (geological, hydrogeological, and geotechnical), ground freezing programs, and comprehensive ground control programs. These programs have been developed, tested, and proven successful over years of mining practices. Working with this world-class deposit of high risk and low tolerance, the authors believe that these experiences might be beneficial to other mining operations with similar hydrogeological characteristics.

KEYWORDS: Inflow risk management; Geotechnical and development probe and grout programs; Ground freezing; Ground control

1. INTRODUCTION

The McArthur River Operation is an underground mine located in the eastern part of the Athabasca Basin of northern Saskatchewan, approximately 620 km north of Saskatoon, Canada.

As the world's largest high-grade uranium mine, it has proven and probable reserves of 336.5 million pounds U_3O_8 (Cameco's share – 234.9 million pounds) with an average ore grade of 10.94 % U_3O_8 at December 31, 2015. Cameco is the operator of the mine with 69.805% ownership in partnership with AREVA Resources Canada Inc. who owns the remaining 30.195%. Multiple mining methods have been developed and approved and are being employed at McArthur River: the first one is a unique non-entry Raisebore mining method; the second one is Boxhole mining; and the third is drill and blast stope mining, which has the potential to be one of the major mining methods in the future at McArthur River. The ore is grinded into slurry at underground, and then pumped to surface where it is loaded into special containers and shipped to Key Lake for milling. In 2015, the total ore production at McArthur River was 19,782,596 lbs (8,973,235 kg) of U_3O_8 .

As an underground high-grade uranium mining operation, the protection of workers and the environment during the mining activities have been the top priorities in all phases of the design, development, and operation of the mine. The mining activity at this operation faces three major challenges:

- Hydrogeological: the ore is located in proximity to water enriched sandstone with high hydrostatic water pressures.
- Geotechnical: mine openings have to be developed in highly variable ground conditions ranging from excellent rock to wholly unconsolidated clays and gravels.
- Radiation protection: workers have to be protected from radon bearing water and mineralization with high-grade uranium.

This paper intends to introduce the hydrogeological challenges at this Operation, and present the corresponding strategies that have been successfully employed by the site to permit safe mine operations.

2. MINE GEOLOGY AND INFLOW MECHANISMS

The McArthur River uranium deposit is located in the southeastern portion of the Athabasca Basin, within the southwest part of the Churchill structural province of the Canadian Shield. The crystalline basement rocks underlying the deposit are members of the Aphebian Wollaston Domain meta-sedimentary sequence. These rocks are overlain by flat lying sandstones and conglomerates of the Helikian Athabasca Group. These sediments are over 500 m thick in the deposit area.

High-grade uranium mineralization has been delineated from surface drilling over a strike length of 1,700 m, occurring at or close to the unconformity,

*Corresponding author – email: Xiaoyou_Yun@Cameco.com

which separates the overlying, horizontally bedded sandstones of the Athabasca Group from the metamorphosed basement rocks, located between 500 m and 640 m below the surface. Underground exploration drilling programs have covered approximately 750 m of the 1,900 m strike length delineated from surface. Ore body widths are variable along strike but the most consistent, high grade mineralization occurs proximal to the main graphitic thrust fault around the “nose” of the up thrust basement rock. Less consistent and generally lower grade mineralization occurs down dip along this fault contact between basement rock and sandstone. Locally the basement rocks include pelitic gneisses and significant quartzite units. Alteration is characterized by intense silicification of the sandstone with less intense clay alteration compared with other Athabasca deposits. The mineralization at McArthur River is associated with a northeast trending, southeast dipping zone of reverse faulting, along which the unconformity is displaced vertically 60 m to 80 m, as shown in Figure 1.

Hydrogeologically, the brittle, flat lying sandstone has been highly fractured by the tectonic forces of the thrust fault and these fractures are water bearing. Drawdown testing has demonstrated that the fracture patterns, along with water bearing joints and bedding planes are directly connected to the surface groundwater table. This indicates an unlimited volume of high-pressure water is sourced within the sandstone, and significant flows could be produced if the water is intersected by the mine development.

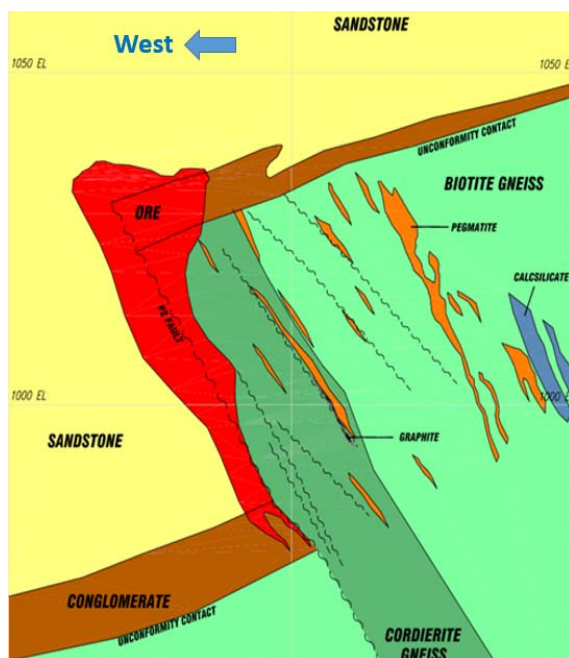


Figure 1: Typical Zone 4 geological section.

There are two major channels by which the water could enter the underground openings:

- Boreholes - grouted or ungrouted,
- Geological formation - directly or indirectly

Underground probe/exploration holes are drilled into all planned mining areas to collect hydrogeological and structural information prior to mining through it. These drill holes could intersect intervals, generally structural related, which contain a substantial amount of high-pressure water. Any loss of control might result in these holes being conduits for a significant inflow of water into the mine. To minimize this risk, rigorous collar security standards have been developed for all underground drilling.

There is a potential risk for encountering ungrouted or poorly grouted surface holes during underground excavation. Therefore additional precautions need to be taken in the vicinity of a surface hole during design and development phases. Any underground development within 8 m of a surface borehole is treated as high risk as per ENG-01-09.

Water inflows into the mine could also occur if a water bearing geological structure was encountered during development or if the mine development inadvertently breached the unconformity. In 2003, a breach of the unconformity in Bay 12 during development resulted in a peak inflow of 1,069 m³/hr, and then stabilized at 700 m³/hr.

In order to prevent high pressure and radon-bearing water from entering the mine, several different tactics have been developed and applied at the McArthur River Operation:

- Artificial ground freezing to form a frozen curtain between the water bearing sandstone and the ore body.
- Probe and grout drilling to evaluate hydrogeological and structural conditions prior to drift development and to reduce the water conductivity of the surrounding rocks with pressure grouting, if no freeze wall protection exists.
- Strategically locate the underground excavations away from known water sources whenever possible.

3. GROUND FREEZING

Artificial ground freezing is an excavation support method that involves the use of refrigeration to convert in-situ pore water into ice. Over the last several decades, many mining operations have successfully utilized artificial ground freezing for deep excavation support while shaft sinking. McArthur River successfully maintains a very large-scale ground freezing infrastructure. The resulting

freeze walls act as barriers between the underground mine workings and the water bearing formations.

Freeze methods used consist of the following three categories:

3.1 Freeze Wall Isolation

Freeze wall isolation consists of creating one or more freeze walls to isolate an area from water bearing ground. In order to be effective, the freeze walls must be tied together and completely enclosed or anchored into non-water bearing and non-permeable ground. The lower portions of Zones 2 and 4 were isolated from the ground water by creating three freeze walls (north, west and south) and by using the geometry of the thrust fault to take advantage of the non-water bearing basement rock to seal the top, east and bottom of the zone (Refer to Figure 2). More recently, freeze wall protection for the upper portions of Zone 2 and Zone 4 have included a frozen cap, as shown in Figure 3. The freeze hole drilling for Zone 1 is currently in progress and is based on this design.

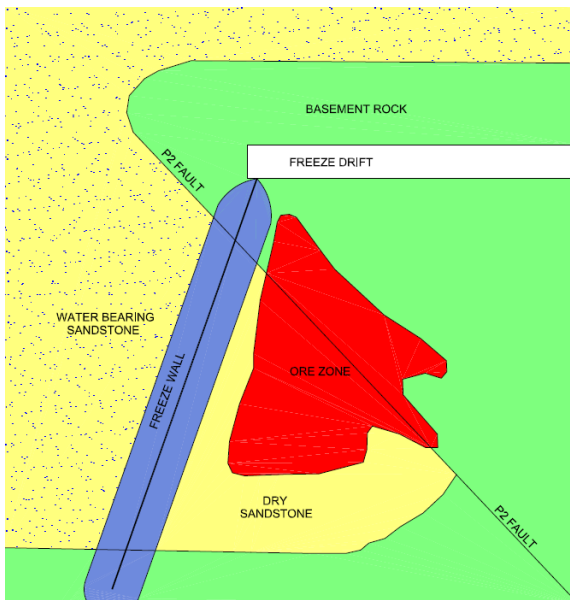


Figure 2: Typical freeze wall insulation situation with three freeze walls.

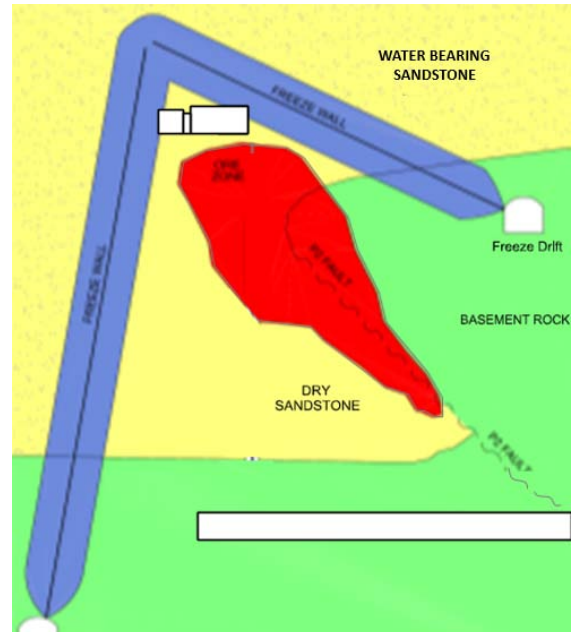


Figure 3: Typical freeze wall insulation situation with top freeze cap as well.

3.2 Mass Freezing

Mass freezing consists of freezing an entire area to isolate it from water bearing ground. To date, mass freezing has been used at McArthur River only for the Boxhole mining test at Zone 4 North. This might be considered as an option for the upper portions of Zone 2 and 4 mining area due to the presence of a massive clay zone right above the high grade ore (Refer to Figure 4).

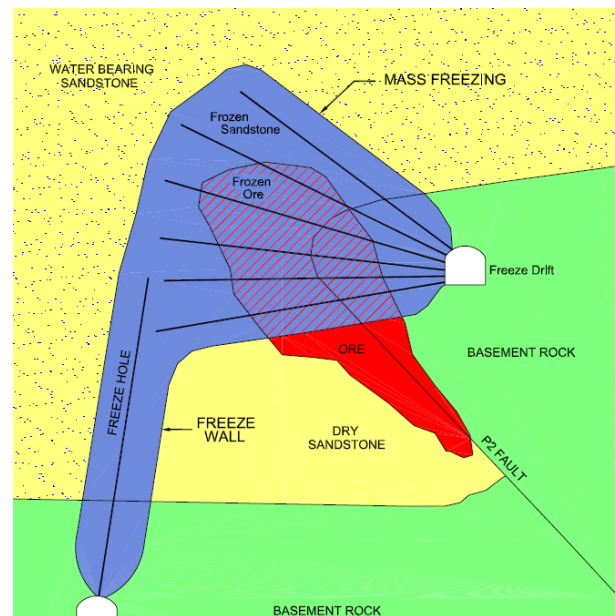


Figure 4: Massive freeze insulation.

3.3 Freeze Shield Protection

Freeze shield protection consists of creating freeze walls that are not completely enclosed in certain situations where potential water sources are strongly dominated from one direction. They do not provide full protection from water, but do help mitigate the risks associated with developing near water bearing ground. Freeze shields have been used for some 530 level development in the Zone 4 Central Lower mining area. (Refer to Figure 5).

Freeze holes spacing is determined by various factors such as geothermal properties, drilling accuracy, schedule requirements, and cost. Hole spacing has varied slightly, but is typically in the range of 2.5 to 4 m.

3.4 Freeze Drilling

A freeze hole drilling program is carried out according to an approved engineering design. Each hole typically begins with a 9 m long grouted standpipe, which is pressure tested to ensure that it is secure and that there is no leakage to the mine workings. The hole is drilled to depth and the outer freeze rods are grouted to the rock. A second set of freeze steel is grouted inside of the outer steel. A deviation survey is performed on the hole and the data is entered into the drill hole database. The location of the hole is compared to the adjacent freeze holes to ensure that the final spacing is within the design criteria. Infill holes are occasionally required to fill gaps. At regularly spaced intervals adjacent to a freeze wall, temperature monitoring holes are drilled. Thermocouplers are inserted and grouted at 5 to 10 m spaced intervals within each of these holes and the resulting temperature data is recorded into a central database. This information is used to monitor the temperatures and to provide data for 3D modelling of the freeze wall as it forms.

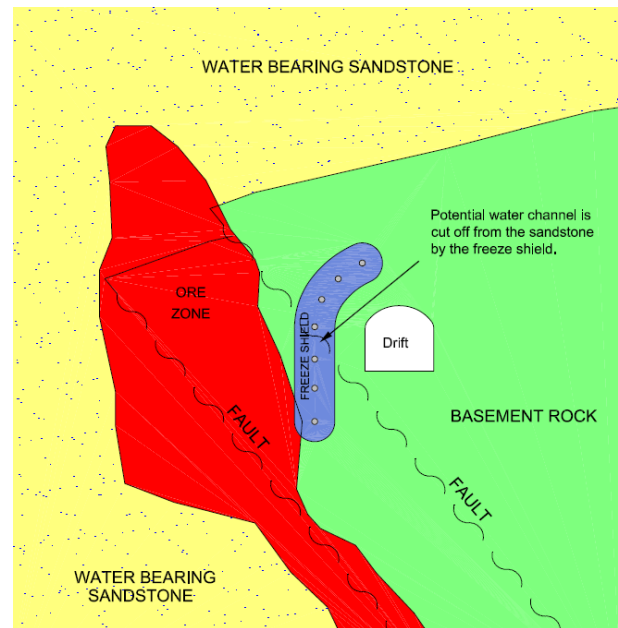


Figure 5: Freeze shield insulation situation.

3.5 Ground Freeze Commissioning

After the freeze holes are drilled off, the brine distribution system is installed and the brine is circulating, the freeze wall is left to develop for approximately six months. The freeze wall is considered to be in place when temperatures from the monitoring holes and results from the block modelling indicate that ground conditions meet the minimum criteria of -3°C or lower and a freeze structure thickness of at least 4 m. Within the confines of the freeze wall, the ground will contain unfrozen water that remains at full hydrostatic pressure. A series of strategically placed diamond drill holes, with full collar security, will target the unfrozen rock within the freeze wall. These holes will dewater and depressurize the area before any mine development or other production activities are carried out within the freeze structure. Water flows and pressures will be regularly measured to confirm that the isolated ground is not recharging from outside the freeze wall. The results will be subjected to a review and approval process before the freeze wall is officially commissioned.

3.6 Ground Freezing Maintenance

After a freeze structure is established sufficiently for mining operations to proceed, the wall will continue to grow. Ground temperatures are monitored throughout the life of the freeze structure. This helps the operation to monitor the freeze wall status, make decisions on brine circulation rates, verify or refine future freeze design criteria and assists in establishing the baseline for the overall freeze loading capacity requirements. If temperature readings indicate

unusual or unknown changes, an investigation will be conducted to diagnose and resolve the problem in a timely manner.

4. PROBE AND GROUT PROGRAMS

All mine development will be assessed and assigned a risk level: low risk, medium risk, or high risk based on the available hydrogeological, geotechnical, and radiological information. Once the risk level for the proposed development area is assigned, a probe and grout design will be created based on the standards that have been established for each risk level. The probe and grout coverage will extend 10 m beyond the designed development end and at least 5 m on either side of the proposed development. An extra probe hole might be required to confirm the location of the unconformity. In the case of water concerns encountered during normal probe drilling for the upcoming development, extensive probe and grout might be needed to seal off the paths of water. A probe and grout program done with a jumbo might be considered for covering short distances within low risk development.

Figure 6 is a typical example of probe and grout patterns for high risk development.

Once a probe and grout program is completed, a formal review will be conducted to identify any risk (geological, hydrogeological, and geotechnical) and provide recommendations for the future development. Geological structures and hydrogeological information will be documented. Geotechnical information will be assessed through a Ground Hazard Model and Rock Mass Rating system. The heading will be formally released for development with proper controls in place for excavation and ground support.

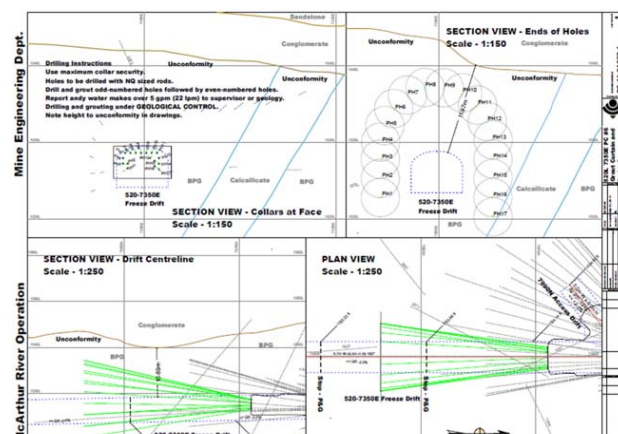


Figure 6: Typical probe and grout pattern for high risk development.

5. CONTINGENCY DEWATERING OF HIGH RISK DEVELOPMENT WITHOUT FREEZE PROTECTION

Any high risk development less than 15 m to the unconformity without ground freeze protection may have risk of unknown water interception. In order to mitigate this risk, contingency plans have to be in place to manage the risk, such as contingency dewatering infrastructure including water hitch, drainage holes, and sufficient dewatering pumping capacity.

6. CONCLUSIONS

The practices used for dealing with hydrogeological challenges at McArthur River Operation are:

- Probe and grout drilling programs prior to any development without freeze protection to collect detailed geological, hydrogeological, geotechnical, and radiological information. Results collected are formally reviewed and then the heading can be released for development with proper controls applied if required.
- Freeze walls have been used effectively to isolate production areas from water enriched formations, such as Zone 2, Zone 4 Lower, Zone 4 North upper, and Zone 4 Central upper.
- Freeze shield protection was used for the 530-7300E Raisebore drift to allow for the mining of Zone 4 Central Low portion.
- Dewatering and pressure relief drilling were used in Zone 2 Panel 5 and Zone 4 North Upper as part of the freeze wall commissioning process.
- Additional precautions are taken with underground development in the vicinity of known surface drill holes. If a new development without freeze wall protection from the water source is located within 8 m of any ungrouted surface hole, it will be considered as high risk development.
- Before any hydrological high risk development without freeze wall protection is allowed to take place, an emergency water handling plan must be in place, such as water hitches or drainage holes, etc. The corresponding mine dewatering capacity must also be sufficient.

7. ACKNOWLEDGEMENT

The authors would like to thank Cameco Corporation for permission to publish this paper. The authors would also like to thank all of those who have contributed and have been involved in ground control and related programs at McArthur River over the years of operation.

8. REFERENCES

Baoyao Tang, June, 2014, Interoffice Memo. MCA Zone 4NU Freeze Wall Commissioning.

McArthur River Operation, 2014. ENG-08 Underground Dewatering and Groundwater Control Systems Design Procedure.

McArthur River Operation, 2014. ENG-10 Ground Control Procedure.

McArthur River Operation, 2014. ENG-12 Ground Freezing Procedure.

McArthur River Operation, 2014, MOP-09-04 Freeze Hole Pressure and Leak Testing.

McArthur River Operation, 2015. GEO-03-07 Drilling Instructions for Freeze Hole.

McArthur River Operation, 2016, ENG-01-09 Underground Development Risk Classification.

McArthur River Operation Groundwater Control, 2016.

Experimental Study on Bolt Pull-Out Property Coupled by Plate and Shotcrete

Xiliang LIU^{a,*}, Jiaqi GUO^a, Long Wan^b, Jianhua Wang^a

^a School of civil engineering, Henan polytechnic university, Jiaozuo Henan, 454003, PR China

^b Yellow River Construction Engineering Group Co., Ltd, Zhengzhou Henan430071, PR China

ABSTRACT

Based on a self-developed multi-function bolt mechanical test system, axial pull-out loads were applied on same bolts under the different conditions, combining with a flat plate, a butterfly plate, a new-type plate and three kinds of shotcrete(C15, C20 and C25 plain concrete). Experimental results showed that the relationship between bolt elongation and drawing force has three stages, including elastic, yielding and strengthening. The strength of shotcrete lining has an obvious influence on the bolt stiffness during the elastic stage i.e. the strengthening of the concrete leads to the increase of bolt stiffness. The strength and width of the yield platform of the bolt reach the maximum for the butterfly plate and the yield plate with C20 plain concrete lining. The butterfly plate and the new-type plate both have yield functions, and the latter one can effectively prevent the damage of shotcrete. The damage of shotcrete lining usually begins around the drill holes, when the interfacial stress between the initial shotcrete lining and surround rock is higher than that in the initial lining and secondary lining. With the new-type plate used, the cracks in the secondary lining cut through along the same direction.

KEY WORDS: Pull-Out Test; Coupling Effect; Strain; Fracture Morphology

1. INTRODUCTION

Anchor bolt-spray has become one of the most economic and effective support methods applied in underground projects (WANG Jin-hua, 2007; Anders Ansell, 2005). The main function of bolts in the bolting and shotcreting technology is to improve deformation resistance of surrounding rock and control the rock deformation, making the surrounding rock as a part of the support system. In recent years, many scholars around the world have carried out massive and in-depth theoretical researches about the bolts (HE Manchao et al, 2014; ZHAO Tong-bin et al, 2011; M.Cai and D.Champaigne, 2012). Shotcrete lining plays an important structural roles in the combined support system. Shi Ling analyzed the functions of shotcrete lining under the stress-control and the structure-control mode (SHI Ling, 2011). Wen Jingzhou developed the bearing model of the surrounding rock-shotcrete lining structure (WEN Jingzhou et al, 2011). Fang Shulin et al monitored the stress state of the post-shot concrete in a roadway (FANG Shu-lin et al, 2012). Xiang Wei et al. investigated the deformation law and interaction mechanism of surrounding rock and shotcrete lining under freeze-thaw cycles (XIANG Wei et al, 2011). Plates play significant roles during the load transmission between different parts of the support

system. Jiang Tieming analyzed the influence of the plate on the stress distribution in the surrounding rock after the pre-stressing of bolts based on the FLAC (JIANG Tieming, 2008). Wang Jianzhi et al. studied the influence of plates on the internal stress distribution of bolts (WANG Jianzhi et al, 1989). Kang Hongpu et al. studied the influence of a plate on the bolt pre-stress field and its support effect on the surrounding rock. Above-mentioned researches have vastly perfected the anchor bolt-spray support theory and effectively promoted the massive application of this technology in engineering.

All the aforementioned studies focused on only a certain bearing part or two in the whole bolt-spray support system. Studies on the interaction between plate and shotcrete, as well as the bolt stress behavior under the coupled action of them, are still very limited. Therefore, a self-developed multi-function bolt mechanical test system was adopted to conduct pull-out tests of the same type of bolts under different combination conditions between plate types and plain shotcrete linings with various strength values. Based on the experimental results, the bolt stress state under the coupled action of plates and shotcrete linings, and the deformation and fracture behaviors of shotcrete linings were discussed.

2. TEST SYSTEM AND METHOD

*Corresponding author – email: xlliu@hpu.edu.cn

2.1 Test system

Due to the limitation of maximum drawing force and test range, commercially available bolt testing machines cannot meet the requirements of the mechanical performance testing of new types of bolts such as high-strength bolts and large-deformation bolts developed based on pressure principle. Meanwhile, they also cannot precisely simulate the in-site interaction between bolts and surrounding rock as well as the coupled action between plates and shotcrete linings. Hence, they are unable to meet the requirement of this study. The authors designed a multi-function bolt mechanical test system, as shown in Fig.1. The test system consists of counter force frame, anchorage, loading device, measurement device, control system and data acquisition and processing system. It can provide drawing force as great as 600 kN, and the maximum pull-out stroke is 300 mm. It can simulate the in-site interfacial interaction between the bolt and adhesive material, and that between the anchoring body and surrounding rock. Moreover, it can also simulate axial/eccentric pull-out property of bolt under the coupled action of plates and shotcrete linings, and the deformation behavior of surrounding rock and shotcrete lining. In addition, it can realize the real-time acquisition, dynamic displaying and paragraph preparation of test data.



Fig.1. The self-developed multi-function bolt mechanical test system

2.2 Test materials

Cast-in-situ shotcrete linings were used in this study. The principal raw materials of the shotcrete linings were cement, aggregate and water. The cement used was 32.5# ordinary Portland cement produced by Henan Jiaozuo Jiangu Cement Co., LTD. Coarse aggregates were gravels with diameters ranging from 20 to 35 mm. The gravels were well graded, clean, dry and had crush indexes between 7.9% and 8.1%. Fine aggregates were river sand with high quality. The fineness modulus of sand was 2.63, with the maximum particle size lower than 5 mm. The sand was well graded, clean and dry. Plain concretes with strength values of C15, C20 and C25, were prepared according to calculation. The prepared concretes were poured into shotcrete linings in detachable special mould made of Q235 steel plates.

9 pieces of C30 concrete substrate blocks with dimension of 500 mm × 500 mm × 300 mm were poured in mould to simulate surrounding rock.

Left-handed ribbed high-strength bolts produced by Jiaozuo coal company of HNCC were selected in this study. The bolts were made of MG400 bolt steel, with 3 m in length and 22 in diameter. Their yield strength is 400 MPa and ultimate tensile strength is 540 MPa. During testing, three types of plates, flat plate, butterfly plate and new-type plate, were used, as shown in Fig. 2.



(a) flat plate (b) butterfly plate and (c) new-type plate.

Figure 2. Plates used in tests

2.3 Test method and scheme

(1) Preparation method of the plate and shotcrete lining system: The shotcrete lining used in the pull-out test had a dimension of 500 mm × 500 mm × 150 mm (JIANG Tieming, 2008), with a hole of 50 mm in diameter reserved at the center as the anchoring reserved hole for bolts. During pouring the shotcrete lining, an initial lining with a thickness of 60 mm was firstly poured and then a secondary shotcrete lining with a thickness of 90 mm was poured. When pouring the secondary shotcrete lining, a square hole with a dimension of 160 mm × 160 mm was reserved at the center adjacent to the initial lining, in order to install the plate. After the installation of the plate, concrete was poured to both inside and outside the square hole to a certain thickness at the same time. After that, the wood die for the square hole was removed and the square hole was poured to the designed thickness and vibrated. The pouring process of the shotcrete lining is illustrated in Fig. 3.



Figure 3. Pouring process of the secondary shotcrete lining, (a) before pouring, (b) after pouring.

(2) Test method of bolt pull-out under the coupled action of plates and shotcrete linings: The prepared detachable die was firstly fixed at one end of the test system. Then, substrate blocks and shotcrete linings were placed inside the die and fixed.

The substrate blocks and shotcrete linings were constrained by the die. Bolts were then anchored to the drawing end and the shotcrete lining end through the reserved hole. The drawing end was the anchored end and the spherical anchorage with 21 mm in diameter produced by Henan Yujian Mining Technology Co., LTD was used. After the installation of the shotcrete-bolt support system, tests were conducted under specific conditions, with the pull-out load and bolt elongation recorded. When the loading system reached its maximum stroke, the shotcrete lining was seriously damaged or the bolt tail was fractured, tests were ended. In this study, 9 sets of pull-out tests with 3 kinds of plates and 3 strength grades of shotcrete linings were carried out. To analyze the strain features of different locations at the contact interface between the initial lining and surrounding rock, the contact interface between the initial lining and the secondary lining, the external surface of the secondary lining during testing, SZ120-50AA resistance strain gages were pasted on these locations.

3. RELATIONSHIP CURVES OF DRAWING FORCE AND ELONGATIONS

Relationship curves between the bolt drawing force and elongation under the different combination conditions of plates and shotcrete linings are shown in Fig. 4.

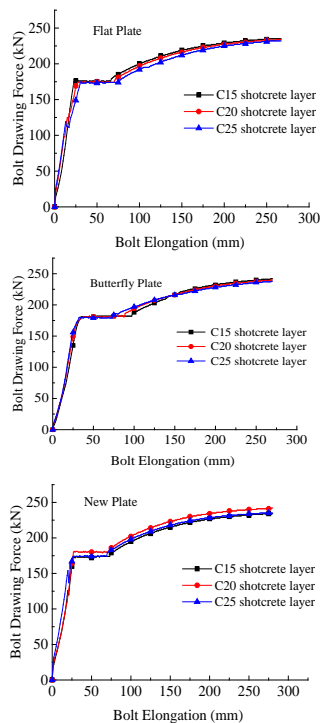


Figure 4. Bolt drawing force-elongation relation curves under different combination conditions of plates and shotcrete linings

According to Fig. 4 and related test data, we can find that: (1) Under different plate/lining combination conditions, the relation curves between the bolt drawing force and elongation present similar variation trends. By taking the combined influence of plates and shotcrete linings, the bolt drawing process can be divided into three stages with obvious features, which are elastic, yield and hardening. (2) With the same plate type, the intrinsic strength of shotcrete lining has limited influence on the bolt yield strength. The shotcrete lining strength has significant influence on the bolt stiffness at the elastic stage, at which the bolt stiffness increases with the improvement of shotcrete lining strength. When butterfly plates are used, the bolt stiffness increases from 4.45 MN/m to 4.86 MN/m when the shotcrete strength increasing from C15 to C25. When flat plates are used, the bolt stiffness increases from 6.42 MN/m to 9.22 MN/m, and the bolt stiffness increases from 5.89 MN/m to 7.89 MN/m when new-type plates are utilized. This is mainly attributed to that the influence of the shotcrete in the early bearing stage of the shotcrete-bolt support system is more dominant. In addition, above test results can also explain the reason why exorbitant shotcrete lining strength is not beneficial to the release of surrounding rock pressure and the play of the intrinsic bearing capacity of surrounding rock in shotcrete-bolt support systems. (3) With the same shotcrete strength, the curve slope of the flat plate is greater than those of the butterfly plate and new-type plate at the elastic stage, due to the lack of pressure relief function of the flat plate. Thus, it is indicated that the flat plate is not beneficial to the full development of the elastic deformation stage of the shotcrete-bolt support system, thereby affects the controllable release of surrounding rock during the early excavation of tunnels or roadways. (4) When flat plates are used, the bolt yield strength under the coupled influence of plates and shotcrete linings is not obviously affected by the shotcrete lining strength, and the widths of the yield platforms are all 42 mm. However, after the bolt is yielded, the elongation slightly increases with the improvement of shotcrete lining strength. (6) When butterfly plates are used, the elongation and yield strength of bolts during yielding are almost the same. But the yield platform width gradually increases with the reduction of shotcrete lining strength. Based on calculation, the yield platform width of the C15 shotcrete strength is 1.24 times of that of C20 and 1.219 times of that of C25. Hence, it is implied that the increase of shotcrete lining strength when butterfly plates are used, is not beneficial to bolt yielding. (7) When new-type plates are utilized, under the coupled action of plates and shotcrete linings, the bolt yield strength firstly

increases and then decreases with the increase of shotcrete lining strength. The bolt yield platform widths and elongations during yielding are almost similar.

4. SHOTCRETE LINING STRAIN UNDER THE COUPLED ACTION OF PLATE AND SHOTCRETE

The relation curves between the shotcrete lining strain and bolt drawing force under different combination conditions between C20 plain shotcrete and three types of plates are displayed in Fig.5. Since the variation tendencies of shotcrete lining strain corresponding to different combination conditions between C15 and C25 plain shotcrete with different types of plates, are similar to that of C20 plain shotcrete, only the C20 plain shotcrete lining is discussed here.

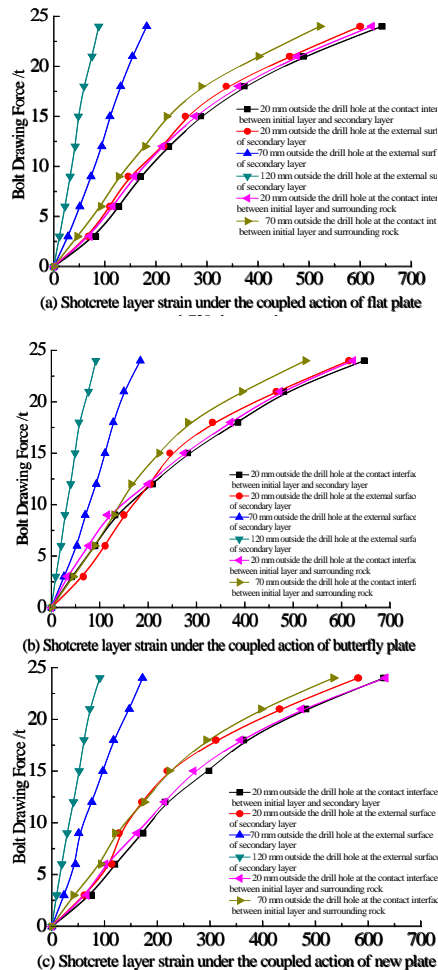


Figure 5. Relation curves between the shotcrete lining strain and bolt drawing force

Some results drawn from Fig.5 are as follows: (1) The shotcrete lining strain increases with the increase

of the bolt drawing force. Around the drill hole, the shotcrete lining is obviously yielded at the late loading stage. (2) For strain gages on the same lining, the further they are away from the drill hole, the lower their strain will be. This phenomenon also explains why the shotcrete lining often starts to break around the drill hole during pull-out tests under the coupled action of plates and shotcrete linings. (3) The contact interface between the initial lining and surrounding rock has strain slightly greater than that of the interface between the initial lining and secondary lining, even their distances to the drill hole are the same. The strain at the contact interface between the initial lining and surrounding rock is greater than that of the external surface of the secondary lining, though they are equal far away from the drill hole. Thus, it is indicated that the stress at the contact interface between the initial lining and the surrounding rock is greater than those at the contact interface between the initial lining and the secondary lining, and at the external surface of the secondary lining. (4) When butterfly plates are used, the initial strain around the drill holes at the contact interface between the initial lining and the secondary lining, and the contact interface between the initial lining and the surrounding rock is lower than those at the same positions when flat plates or new-type plates are used. But the strain will gradually increase to the same value. This is attributed to that at the early stage of loading, the center of the butterfly plate cannot contact with the initial lining, and with the loading increasing, the butterfly plate deforms and contacts the initial lining until the test ends. Thus, it is demonstrated that the butterfly plate has the function of pressure relief. (5) When new-type plates are adopted, the slope of the strain-drawing force curve around the drill hole at the external surface of the secondary lining experiences a sharp increase. This is caused by that with the increasing load, the new plate deforms and introduces pressure on the shotcrete lining, which hinders the further increase of strain. The new plate presents the property of limiting the exorbitant deformation of shotcrete lining.

5. SHOTCRETE FRACTURE PROPERTY

Plain concrete possesses remarkable brittleness, which becomes more obvious with the increase of strength. The brittleness of plain concrete in bolting and shotcreting support system mainly reflects in this mode, that is, the micro cracks on the plain shotcrete lining surface rapidly develops wider, deeper and longer until cutting through the shotcrete lining surface and fully fracturing the shotcrete lining. By taking the C20 plain shotcrete lining as an examples, the fracture morphologies under the coupled action of

plates and shotcrete linings after bolt axial pull-out tests are shown in Fig. 7.



Figure 7. Fracture morphologies of C20 plain shotcrete linings

As demonstrated in Fig.7, the fracture modes of the flat plate and butterfly plate are similar. The cracks extend from the vicinity of drill hole in the initial lining to the border as well as the secondary lining, until the shotcrete lining gets fractured. The crack pattern is outward radial with the drill hole as the center point. Under the coupled action of new plates and plain shotcrete linings, the fracture morphology is cracks radiating outward in the initial lining with the drill hole as the center point. The cracks in the secondary lining run through along the same direction, which is attributed to that the plate deforms with the increasing drawing force and introduces pressure on the shotcrete linings to hinder the generation of cracks. Thus, it is indicated that the new plate has the function to prevent shotcrete lining fracturing.

6. CONCLUSIONS

Based on axial pull-out of bolt tests conducted on the self-developed multi-function bolt mechanical

test system with three types of plates combining with C15, C20 and C25 plain shotcrete linings, a couple of conclusions can be drawn:

(1) The relation curves between bolt drawing force and elongation under different combination conditions of plates and shotcrete linings can be divided into three stages with obvious features, which are elastic, yield and strengthening. The influence of shotcrete strength on the bolt yield strength is very limited, but has a significant effect on the bolt stiffness at the elastic stage, during which the bolt stiffness increases with the increase of shotcrete strength.

(2) Under the condition that flat plates are used, the bolt yield strength is not obviously affected by the shotcrete lining strength, but bolt elongation expands slightly with the shotcrete strength increasing after yielding. When butterfly plates are used, the bolt yield platform width increases with the reduction of shotcrete strength. As for the new-type plate condition, the bolt yield platform width and the elongation to yield are similar. The butterfly plate and new-type plate are revealed to have the function of pressure relief

(3) The shotcrete lining strain increases with the increasing drawing force, and the shotcrete linings present obviously yielding features at the late loading stage. The shotcrete lining often starts to break around the drill hole. The stress at the contact interface between the initial lining and surrounding rock is greater than those at the contact interface between the initial and secondary linings, and at the external surface of the secondary lining.

(4) When flat plates or butterfly plates are used, the cracks are radically distributed outward with drill holes at the center points. As for the new-type plate, the fracture morphology is cracks radiating outward in the initial lining with the drill hole at the center point, while cracks cut through along the same direction in the secondary lining. Thus, a certain degree of layer-fracture resistance of the new-type plate is revealed.

7. ACKNOWLEDGEMENTS

This work is financially supported by National Natural Science Foundation of China(Grant No. 51474097) and Provincial Key Technologies and Development Program of Henan(Grant No. 152102210318).

8. REFERENCES

- Anders Ansell. (2005). Laboratory testing of a new type of energy absorbing rock bolt[J]. Tunneling and Underground Space Technology, 20 (4):291-330.

FANG Shu-lin et al. (2012). Mechanical monitoring and analysis on shotcrete layer of soft rock main roadway supported by bolt-shotcrete[J]. *Journal of Mining & Safety Engineering*, 29(6): 776-782.(in Chinese)

HE Manchao et al. (2014). Development of a Novel energy-absorbing bolt with extraordinarily large elongation and constant resistance[J]. *International Journal of Rock Mechanics & Mining Sciences*, 67: 29-42.

JIANG Tieming. (2008). Mechanism of support unit of anchor bolt in coal roadway and application research in Jincheng mining area[D].Beijing: China university of mining and technology (Beijing).

M.Cai, D.Champagne. (2012). Influence of bolt-grout Bonding on MCB cone bolt performance[J].*International Journal of Rock Mechanics & Mining Sciences*, 64: 165-175.

SHI Ling. (2011). Development of study on support mechanism of sprayed concrete liners in tunneling and Caving engineering[J]. *Chinese journal of underground space and engineering*, 7(4): 759-763.(in Chinese)

WANG Jianzhi, He Tangyong, Yang Gengshe. (1989). The influences of bearing plate on the internal force of overall reinforced bolts[J]. *Journal of Xi an Mining Institute*, (3): 7-12,18.(in Chinese)

WANG Jin-hua. (2007). New development of rock bolting technology for coal roadway in China[J]. *Journal of China coal society*, 32(2): 113-118.(in Chinese)

WEN Jingzhou, ZHANG Yongxing, WANG chen. (2011). Analysis on interfacial stress between surrounding rock and shotcrete lining[J]. *Journal of railway engineering society*, 01: 39-46.(in Chinese)

XIANG Wei et al. (2011). Model test study of rock-shotcrete layer structure under freezing-thawing cycles[J]. *Chinese Journal of Rock Mechanics and Engineering*, 30(1): 1819-1825.(in Chinese)

ZHAO Tong-bin et al. (2011). Mechanical test of Bolt Interface and Microscopic Simulation of transfer Law for Shear Stress[J]. *Journal of Mining & Safety Engineering*, 8(2): 220-224.(in Chinese)

Part 3

Coal

Mathematical model for gas diffusion from non-homogeneous coal particles

Yanwei Liu^{a,b,c,*}, Mingju Liu^{a,b}, Hani S. Mitri^{c,d}

^a School of Safety Science and Engineering, Henan Polytechnic University, Jiaozuo 454000, China

^b The Collaborative Innovation Center of coal safety production of Henan Province, Jiaozuo 454000, China

^c Department of Mining and Materials Engineering, McGill University, Montreal, H3A0E8 Canada

^d School of Civil Engineering, Henan Polytechnic University, Jiaozuo, China, 454000

ABSTRACT

By establishing model and experimental verification, this paper aims to improve the accuracy and applicability of gas diffusion mathematical models from coal particles in engineering applications. Firstly, based on Fick's second law and the continuity theory of gas diffusion in porous media, a new constitutive model for gas diffusion from non-homogeneous coal particles with three-layer pore structure is constructed by considering the difference of characteristics in pore structure between soft coal and hard coal. Then, the analytical solution is derived from the new model, that is, the quantitative relationship between gas diffusion rate (Q_t/Q_∞) and diffusion time (t). The pore structure parameters of soft coal and hard coal from Juji coal mine are determined by using the mercury injection method. Gas desorption and diffusion rules of coal samples are numerically calculated and investigated by using physical simulation methods. Lastly, the applicability of the constitutive model is verified. The results show that the homogeneous model that is currently widely used only applies to the description of the gas diffusion process of the hard coal within the initial 10 minutes, while the new model can describe the gas diffusion law of different pore structure characteristics. The calculated results from the new model and the physical experimental results are nearly identical within the initial 30 minutes. The difference in the gas diffusion process between soft coal and hard coal can be effectively reflected by the parameters of pore structure in the new model.

KEYWORDS: soft coal and hard coal; gas desorption and diffusion rules; pore structure; mathematical models

1. INTRODUCTION

Gas diffusion laws and models from coal particles are the key theoretical bases for the determination of gas content in coal seams. At present, there are a couple of theoretical models to describe the law of gas diffusion from coal particles based on different perspectives. These models can be classified into two types, including homogeneous diffusion models (Qiluan and Youan, 1986; Nie, et al, 2001) and Bidisperse diffusion models (Clarkson and Bustin, 1999; Ruckenstein, et al, 1971). However, when these models are applied to describe the gas diffusion laws of outburst prone soft coal, there are usually noticeable deviations that lead to not meeting the requirements of engineering (Liu, et al, 2015).

The conventional model commonly used is a transient mathematical model of gas diffusion based on uniform porous coal particles and the solution to Fick's second law for spherically symmetric flow (J. Crank, 1975). Its analytical solution is an infinite series

function of diffusion rate vs. time, as shown in equation (1). Based on the numerical model calculations, Yang (Qiluan and Youan, 1986) found that the relationship between $\ln [1-(Q_t/Q_\infty)^2]$ and t is linear.

$$\frac{Q_t}{Q_\infty} = 1 - \frac{6}{\pi^2} \sum_{n=1}^{\infty} \frac{1}{n^2} e^{-n^2 B t} \quad (1)$$

Where, Q_t is the total volume of the diffusing gas at time t , cm³/g; and Q_∞ is the total diffusion volume cm³/g; t is the time of gas diffusion, s. $B = \pi^2 D / a^2$, The value of B ranges from 6.5797×10^{-6} to 6.5797×10^{-3} . D is the diffusion coefficient of gas in coal particle, m²/s,

To verify the homogeneous model, the experiment concerning gas diffusion from soft coal and hard coal of Juji coal mine was performed. The experimental results showed that the relationship between $\ln [1-(Q_t/Q_\infty)^2]$ and t is not linear, as illustrated in Figure 1.

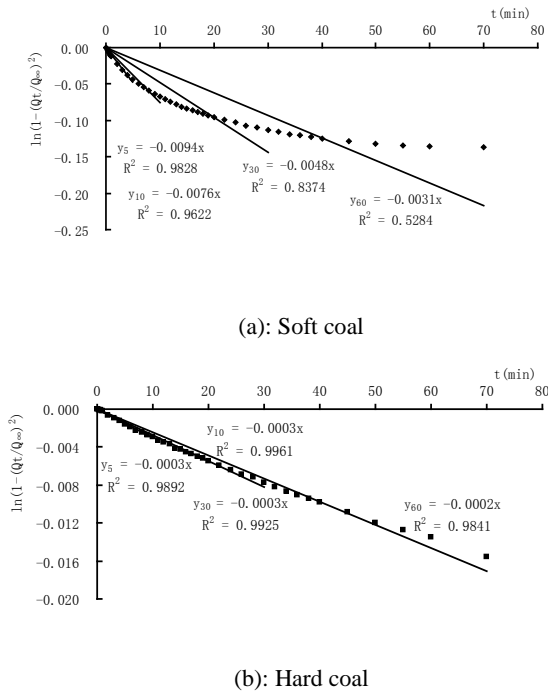


Figure 1: Fitting curves of Juji coal samples according to the unipore model.

Considering the mass transfer resistance of the surface of coal particles, Nie et al. (2001) adapted the unipore diffusion model based on the third kind boundary condition. Its analytical solution was obtained using the mathematical and physical methods. The simplification of the solution to the equation is similar to the empirical formula developed by Bolt and Innes (1959).

Bi-disperse diffusion models are based on the assumption that pore structure of coal merely consists of macro-porous and micro-porous.

Ruckenstein et al. (1971) developed the continuous bi-disperse diffusion model by considering the adsorbent to be a spherical particle (macrosphere) containing an assemblage of microspheres of uniform size. The Henry linear adsorption model and a step change in concentration of the adsorptive external to the particle are assumed in Ruckenstein's model. Smith and Williams (1984) adapted Ruckenstein's model and found that the bidisperse diffusion model better described the entire desorption rate curve than the unipore model for some coals. Crosdale et al. (1998) has verified successfully the bidisperse model by investigating Australian coal gravimetric transient adsorption data. In particular, it is believed that dull coal adsorption rate data are better a fit with the bidisperse model than with the unipore model when the whole process of diffusion from coal particles is

described. Clarkson and Bustin (1999) developed an isothermal adsorption rate model based on Ruckenstein's model, considering variable pressure adsorption rate experiments as described by Mavor et al. (1990) and the adsorption isotherm that can be described by the Langmuir equation. They indicate that dull or banded coals have a more complicated pore structure, and are adequately modeled with diffusion models that incorporate a bidisperse pore volume distribution. However, it is inadequate to describe the gas diffusion process from soft coal.

2. THE DEVELOPMENT OF MODEL AND DISCUSSION

The current desorption model assumes a tridisperse pore structure for coal, as schematically shown in Figure 2, considering a macroporous particle which consists of uniform size mesoporous particles containing uniform microporous particles. The radius of the larger sphere is much more than that of the smaller sphere. Unlike the previous models, the current model takes into account the tridisperse pore structure based on the difference between soft coal and hard coal. It also assumes that there is no pressure gradients during intra-particle diffusion. The only driving force is the concentration of gas. In addition, the adsorption is occurring in both micropores and mesopores. The assumptions for the current model may be summarized as follows.

- (1) Isothermal system.
- (2) Applicable transport equation is Fick's second law.

$$\frac{\partial C}{\partial t} = \frac{D}{r^2} \cdot \frac{\partial}{\partial r} \left(r^2 \frac{\partial C}{\partial r} \right) = D \left(\frac{\partial^2 C}{\partial r^2} + \frac{2}{r} \frac{\partial C}{\partial r} \right)$$

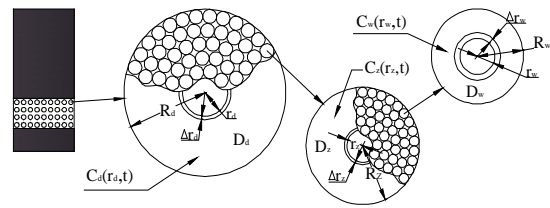


Figure 2: Conceptual model for tridisperse pore structure.

- (3) Transport is the diffusion in both macro, meso and micropores.
- (4) Significant adsorption occurs in both micro-, meso- and macroporosity and the adsorption isotherm can be described by Langmuir equation as follows.

$$C_s = a \cdot b \cdot C / (1 + b \cdot C)$$

Where, C_s is adsorption of gas concentration on the surface, mol/m³, C Free gas concentration in pore

after desorption, mol/m³, stands for a gas concentration which is complete monolayer coverage of micropore of gas-solid surface, mol/m³, b langmuir constant, b=bRT/MPa-1, R gas constant, R=8.314(cm³.MPa)/(K.mol), T stands for the temperature, K;

(5) Pores are incompressible.

(6) Void volume is constant with time. No correction is made for void volume shrinkage during adsorption of gas.

(7) Coal particle is spherical in shape and uniform in size.

(8) The gas transport through pores complies with mass conservation and fluid continuity theorem.

The concentration field inside macropore satisfies the following equation (2).

$$D_d \phi_d \left(\frac{\partial^2 C_d}{\partial r_d^2} + \frac{2}{r_d} \frac{\partial C_d}{\partial r_d} \right) = a b' S_d \frac{\partial}{\partial t} \left(\frac{C_d}{1+b C_d} \right) + D_z \frac{3(1-\phi_d)}{R_z \phi_d} \frac{\partial C_z}{\partial r_z} \Big|_{r_d=R_d} \quad (2)$$

Where the first term is due to variation of diffusional flux in the macropore, the second to accumulation in the macropore, and the third to the diffusional flux at the surface of mesospheres.

The mesopore (3) and micropore (4) transport equation used in the current study are thus.

$$D_z \phi_z \left(\frac{\partial^2 C_z}{\partial r_z^2} + \frac{2}{r_z} \frac{\partial C_z}{\partial r_z} \right) = a b' S_z \frac{\partial}{\partial t} \left(\frac{C_z}{1+b C_z} \right) + D_w \frac{3(1-\phi_{z,p})}{R_w \phi_{z,p}} \frac{\partial C_w}{\partial r_w} \Big|_{r_z=R_z} \quad (3)$$

$$D_w \phi_w \left(\frac{\partial^2 C_w}{\partial r_w^2} + \frac{2}{r_w} \frac{\partial C_w}{\partial r_w} \right) = a b' S_w \frac{\partial}{\partial t} \left(\frac{C_w}{1+b C_w} \right) \quad (4)$$

With initial conditions:

$$C_d(0, r_d) = C_z(0, r_z) = C_w(0, r_w) = C_0 \quad (5)$$

And boundary conditions:

$$\frac{\partial C_d}{\partial r_d} = 0, \quad i \geq 0, \quad r_d = 0, \quad \frac{\partial C_z}{\partial r_z} = 0, \quad t \geq 0, \quad r_z = 0, \quad \frac{\partial C_w}{\partial r_w} = 0, \quad t \geq 0, \quad r_w = 0 \quad (6)$$

$$C_d(t, R_d) = C_1$$

$$C_z(t, R_z) = C_d(t, r_d) \quad C_w(t, R_w) = C_z(t, r_z) \quad (7)$$

$$Q_t = \int_0^t -4\pi R_d^2 D_d \phi_d \frac{\partial C_d}{\partial r_d} \Big|_{r_d=R_d} dt, \quad t \geq 0, \quad r_d = R_d \quad (8)$$

Where, Dw is micropore diffusion coefficient, m²/s; Dz mesopore diffusion coefficient, m²/s; Dd macropore diffusion coefficient, m²/s; Cw micropore sorbate concentration, moles/m³; Cz mesopore sorbate concentration, moles/m³; Cd macropores sorbate concentration, moles/m³; C0 sorbate concentration at

t=0, moles/m³; C1 sorbate concentration at r=Rd, moles/m³; rw the radius of small coal particle in spherical coordinate, m; rz the radius of medium coal particle in spherical coordinate, m; rd the radius of coal particle in spherical coordinate, m; Rw the radius of small coal particle, m; Rz the radius of medium coal particle, m; Rd the radius of coal particle, m. t is the time of diffusion, s; φw the average porosity of micropores; φzp the average porosity of mesopores and transition pores in a single coal particle, φz.p=φz/n m³/m³; n the number of the lower grade coal particle in unit volume, n=(1-φ)/(4πR³/3); φd the porosity of macropores, m³/m³(%); Sw the specific surface area of micropores, m²/m³; Sz the specific surface area of mesopores and transition pores, m²/m³; Sd the specific surface area of macropores, m²/m³; Qt total diffusion volume at time t, cm³/g.

At t=0, gas concentration is assumed to be equal in the macro, meso and micro-spheres (Eq. (5)). A no gas diffusion flow internal boundary condition is used for the macro, meso and micro-spheres (Eq. (6)). Eq.(7) states that the gas concentrations at micro and meso-spheres boundary are equal to the gas concentration in the meso and macro-porosity at rz and rd respectively, and the gas concentration at macro-spheres boundary is eternally equal to the constant C1. Eq. (8) is a balance statement which express that the change in mass of gas stored interparticle void space is equal to the mass flux of gas across all particle boundaries for t>0.

The initial and boundary conditions are substituted into Equations (2) - (4). After a series of derivations, the relationship between Qt and t is obtained. As shown in equation (9), the function is an exponential relation, and also a solution of infinite series. The infinite diffusion amount (Q∞) is shown in Eq. (10). The relationship between Gas diffusion rate (Qt/Q∞) and time t is shown in Eq. (11).

$$Q_t = -16\pi^2 \phi_d R_d^3 D_d (C_1 - C_0) \varepsilon \sum_{k=1}^{\infty} \sum_{q=1}^{\infty} \frac{k^2 \pi R_z^2 \left(1 - e^{-\alpha \varepsilon \frac{z^2}{\omega} t} \right) \delta}{\omega} \quad (9)$$

$$Q_{\infty} = -16\pi^2 \phi_d R_d^3 D_d (C_1 - C_0) \varepsilon \sum_{k=1}^{\infty} \sum_{q=1}^{\infty} \frac{k^2 \pi R_z^2 \delta}{\omega} \quad (10)$$

$$\frac{Q_t}{Q_{\infty}} = \frac{\sum_{k=1}^{\infty} \sum_{q=1}^{\infty} \frac{k^2 \left(1 - e^{-\alpha \varepsilon \frac{z^2}{\omega} t} \right) \delta}{\omega}}{\sum_{k=1}^{\infty} \sum_{q=1}^{\infty} \frac{k^2 \delta}{\omega}} \quad (11)$$

Where

$$\alpha = \frac{D_w R_z^2 \frac{abS_z}{\phi_z}}{D_z R_w^2 \frac{abS_w}{\phi_w}} = \frac{D_w R_z^2 S_z \phi_w}{D_z R_w^2 S_w \phi_z}$$

$$\varepsilon = \frac{D_d R_z^2 \frac{abS_z}{\phi_z}}{D_z R_d^2 \frac{abS_d}{\phi_d}} = \frac{D_d R_z^2 S_z \phi_d}{D_z R_d^2 S_d \phi_z}$$

$$\eta = \frac{3D_d R_z^2 (1-\phi_d)}{D_z R_d^2 \phi_d} \quad \delta = \sqrt{\alpha \xi_{qk}^2 - \xi_{qk} \cot(\xi_{qk}) \beta + \beta}$$

$$\beta = \frac{3D_w R_z^2 (1-\phi_d - \phi_z)}{D_z R_w^2 \phi_z}$$

ξ_{qk} is the root of transcendental Eq. (12)

$$\alpha \xi_{qk}^2 - \eta \sqrt{\alpha \xi_{qk}^2 - \xi_{qk} \cot(\xi_{qk}) \beta + \beta} \cdot \cot \sqrt{\xi_{qk} \cot(\xi_{qk}) \beta + \beta} + \eta = \varepsilon k^2 \pi^2$$

(12)

3. EXPERIMENTAL VERIFICATION

The soft coal and hard coal samples were collected from Juji coal mine in China, and the physical parameters that reflect their characteristics were determined. As shown in Table 1, these parameters show the differences between soft coal and hard coal in hardness, industry analysis, adsorption constants, and porosity. Then, these samples were dried, sieved, and classified. The porous structure parameters needed to be provided when calculating according to the new

model, and were determined by mercury porosimetry method, as shown in Table 2.

The above data and the intermediate parameters shown in Table 3 were substituted into equation (12). The theoretical curves of (Qt/Q_∞) vs. t are plotted, as shown in Figure 4. Meanwhile, the effective diffusivity (D/R²) was determined by fitting experimental data according to unipore analytical solution (equation (2)).

Dynamic process tests of gas diffusion from coal particles were carried out on specially prepared coal samples 1-3mm in diameter by the experimental system shown in Figure 3. The experimental process can be classified as having 4 stages: firstly, vacuums pumping of the air-proof system bearing samples is performed until the gas pressure becomes stable at 10±0.1 Pa. Then, methane is gradually charged into the samples until the adsorption achieves equilibrium at 0.74 ±0.01 MPa. The third step is to release the free gas in void space until the pressure becomes 0. This step takes about 10 seconds. Lastly, the data of desorption volume and corresponding time are measured. The experimental temperature is kept at 298 K by constant temperature bath across the process.

As shown in Figure 4, the dots are experimental data, and the curves are the theoretical values from the analytical solution. A comparison of experimental rate curves for hard and soft coal samples with theoretical curves gives some indications of the process of gas diffusion from coal particles. Experimental results show that the numerical calculation results by the new model are almost identical to the experimental data within the first 30 minutes, although there are increasing deviations between the two types of results after 30 minutes. The main reasons for this finding may be the truncation error of infinite series solution and that the values of k and q in the series general solution are taken as 100, as well as the determination error of porous parameters.

Table 1: Physical properties of soft coal and hard coal from Juji coal mine.

Samples	Firmness coefficient <i>f</i>	Industry analysis/%			Adsorption constants		Porosity /%	Apparent density /(t·m ³)
		Mad	Aad	Vdaf	a/m ³ ·t-1	b/MPa-1		
Hard coal	0.85	0.89	10.08	10.00	36.117	0.668	4.0793	1.41
Soft coal	0.15	0.92	9.92	8.64	32.654	0.930	6.1406	1.43

Table 2: porous structure parameters by mercury intrusion porosimetry method.

Samples	Vdaf /%	Pore specific surface area/(m ² ·g ⁻¹)				Ratio of pore volume /%			Connectivity /%
		S _w	S _z	S _d	S _t	φ _w	φ _z	φ _d	
Hard coal	10.00	10.00	3.922	1.428	0.002	22.32	26.91	50.76	26
Soft coal	8.64	8.64	4.167	1.807	0.014	15.31	37.78	46.92	39

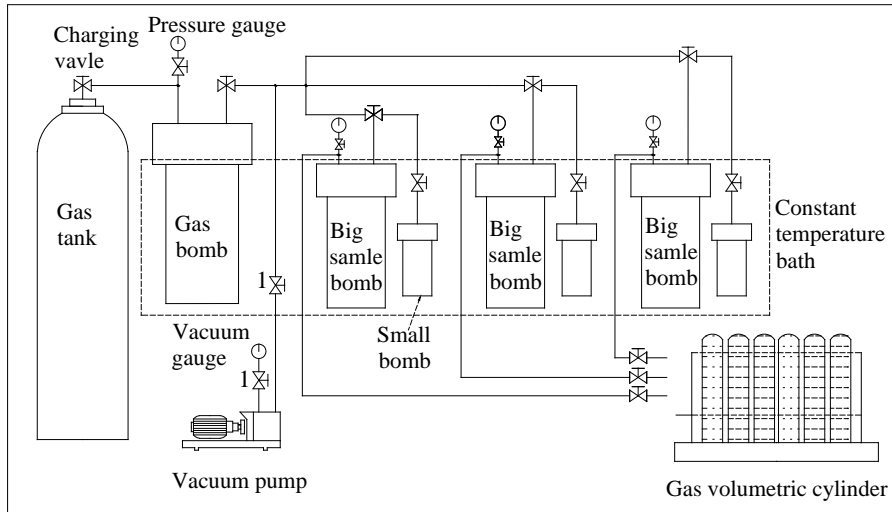
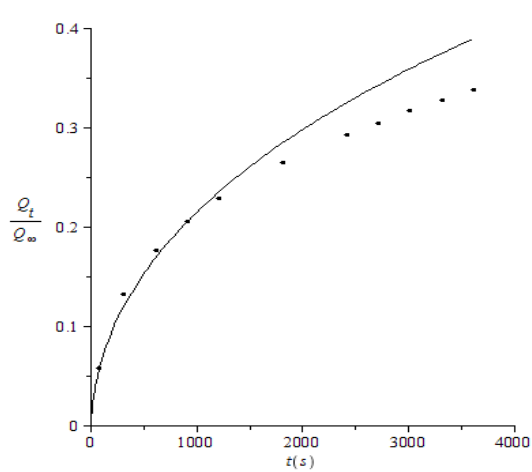


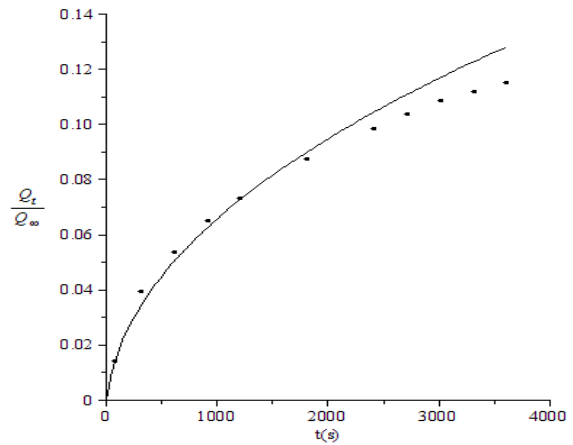
Figure 3: Experimental set up.

Table 3: Results of gas diffusion parameters according to the new model

Samples	α	ϵ	β	η	β/α	η/ϵ	Dd/R2d	Dz/R2z	Dw/R2w
Hard coal	0.256	315.0	220.0	302.6	860.0	0.96	1.57E-04	8.00E-05	5.50E-05
Soft coal	9.62E-03	4.23E+04	3.52707	10526.85	9.62E-03	0.25			



(a) Verification of soft coal



(b) Verification of hard coal

Figure 4: Experimental verification of the new model.

4. CONCLUSIONS

(1) Due to the different porous structure between soft coal and hard coal, there is a noticeable distinction of transient gas desorption rules. The previous models are inadequate to describe the transient process from soft coal.

(2) A model for transient desorption from coal particles, which shows the influence of competing effects of macropore, mesopore and micropore diffusion has been developed. Compared to previous models, the new model considers the effect of the mesopore based on the difference between soft coal

and hard coal, and the gas adsorption equation of coal as Langmuir equation.

(3) The general solution of infinite series of the new model is theoretically derived. The relationship of the rate of diffusion with time is an exponential function. The results of experimental verification show that the new model precisely describes the gas diffusion process from coal particles within the first 30 minutes.

(4) The new model should be optimized and simplified in the future to be satisfactory for field application.

5. ACKNOWLEDGEMENTS

This article is supported by the National Natural Science Foundation of China (51374095) and Doctoral Fund of Henan polytechnic University (B2013-005) and the China Scholarship Council.

6. REFERENCES

Bolt, B.A. and Innes, J.A. (1959). Diffusion of carbon dioxide from coal. *Fuel*, volume 38, No.3, pp.333-337.

Clarkson, C.R. and Bustin, R.M. (1999). The effect of pore structure and gas pressure upon the transport properties of coal: a laboratory and modeling study.2.

Adsorption rate modeling. *Fuel*, volume 78, No.11, pp.1345-1362.

Crank, J., 1975. *The Mathematics of Diffusion*: 2d Ed. Clarendon Press.

Crosdale, P.J., Beamish, B.B. and Valix, M. (1998). Coalbed methane sorption related to coal composition. *Int Jour of Coal Geology*, volume 35, No.1, pp.147-158.

Liu Y., Liu M. (2015). Effect of particle size on difference of gas desorption and diffusion between soft coal and hard coal. *Journal of China Coal Society*, 40 (3):579-587.

Mavor, M.J., Owen, L.B. and Pratt, T.J., (1990). Measurement and evaluation of coal sorption isotherm data. January. In *SPE Annual Technical Conference and Exhibition*. Society of Petroleum Engineers.

Nie B, Guo Y, Wu S. (2001). Theoretical model of gas diffusion through coal particles and its analytical solution. *Journal of China University of Mining & Technology*, volume 30, No.1, pp.19-22.

Qiluan, Y. and Youan, W. (1986). Theory of methane diffusion from coal cuttings and its application. *Journl of China Coal Society*, No. 3, pp. 88-94.

Ruckenstein, E., A. S. Vaidyanathan, and G. R. Youngquist (1971). Sorption by solids with bidisperse

pore structures. *Chemical Engineering Science*, volume26, No.9, pp. 1305-1318.

Smith, D.M. and Williams, F.L. (1984). Diffusion models for gas production from coals: Application to methane content determination. *Fuel*, volume 63, No.2, pp.251-255.

Permeability prediction for coal reservoirs and reconstruction of a different scales pore-fractures network

Ni Xiaoming^{a,b}, Chen Wenxue^{c,d,*}, Li Zheyuan^a and Gao Xiang^a

^a School of Energy Science and Engineering, Henan Polytechnic University, Jiaozuo, CHINA, 454000

^b Collaborative Innovation Center of Coalbed Methane and Shale Gas for Central Plains Economic Region, Henan Province, Jiaozuo CHINA, 454000

^c Opening Project of Key Laboratory of Deep Mine Construction, Henan Polytechnic University, Jiaozuo, China, 454000

^d School of Civil Engineering, Henan Polytechnic University, Jiaozuo, CHINA, 454000

ABSTRACT

Describing the connectivity of different scaled pore-fractures and quantitatively expressing permeability can provide an important basis for the output degree of the gas. A network for different scales pore-fracture was reconstructed by observing a large number of coal samples, and using software simulation of the Monte Carlo method. A seepage model about the different scales pore-fractures network was established by assigning zero method and using MatLab software. The effect permeability about different scales pore-fractures network was obtained using a two-dimensional seepage equation. Predicted permeability results are compared with the measured permeability results, and the results show that: the dominant order of different scales pore-fractures connected from highest to lowest is millimeters fractures, seepage pores and micron-sized fractures. The contribution of coal reservoir permeability from biggest to smallest is millimeters fractures, micron-sized fractures and seepage pores. Different parameters in different scales pore-fractures have differing influence on permeability. The reconstruction of a different scales pore-fractures network can clearly display the connectivity of pore-fractures, which can provide a basis for selecting migration paths and studying flowing patterns for gases.

1. INTRODUCTION

Coal reservoir permeability is one of the quantitative parameters that characterizes the fractures development degree in coal. Researchers have previously conducted fruitful research examining the relationship between the coal reservoir fractures and permeability, at home and abroad. Through experimental tests about pore size, permeability and porosity, it has been found that the relationship between fracture width and permeability is a factor of 3 (He and Liu, 2011; Feng Zengchao et al., 2007). The relationship between fracture porosity and permeability is proportional (Zhang et al., 2008; Cui et al., 2005). According to the fractal theory, the coal reservoir permeability increases exponentially with an increase of the fractal dimension of the fracture (Barton C C., 1988; Babagagli Tayfun, 2001). The differences between coal reservoir fracture width, length, density, and connectivity result in differences of gas migration speed and mode. Establishing the relationship between fracture porosity and permeability could lead to certain deviations in the process of studying gases. Reconstructing the different scales of the pore-fractures network can more help to more clearly understand and master the flow state of gas in coal

(Sisavath et al., 2004; Chen and Feng, 2006). Microscopic fracture information can be extracted by using the image processing method (Chen et al., 2016), and different scales of pore-fractures networks can be reconstructed by using the Monte Carlo method. In order to obtain the different scales of pore-fractures networks and the impact of coal reservoir permeability, the microscopic observation and Monte Carlo pore fissure network reconfiguration method are used. Connectivity and contribution of permeability to different scales of pore-fractures are studied. This can provide the basis for studying gas migration in coal.

2. THE BASIC IDEAS AND METHODS FOR THE RECONSTRUCTION OF DIFFERENT SCALES PORE-FRACTURES NETWORK

Coal reservoir permeability is one of the quantitative parameters that characterizes the fractures development degree in coal.

2.1 Different fracture scales diversion

In order to describe fine distribution characteristics of the pore-fracture, it is necessary to classify the coal reservoir fracture. Based on

*Corresponding author – email: wen1xue2@126.com

divisions of different scales of pore-fractures in the past, the millimeter scale is called a millimeter scale in millimeter, and the scale between the micron and the millimeter is called micron. Based on B.B decimal division, combined with studying results about Fu Xue-hai et al, seepage pores are greater than 75nm pores.

1.2 The basic ideas concerning the reconstruction of different scales pore-fractures network

In order to reconstruct the different scales pore-fractures network, it is necessary to find the geometrical parameters of different scales pore-fractures in coal samples. Different scales pore-fractures in coal samples were observed and counted using scanning electron microscopy, optical microscopy, and a series of testing instruments. According to the statistical results, the probability distribution model of pore-fractures network was established. Finally, a random pore-fractures network graph was produced based on the principle of the Monte Carlo simulation and using Matlab software.

1.3 Realization method of the reconstruction of the different scales pore-fractures network

- Sample Preparation

Coal samples in Sihe Mine in Shanxi Province were collected and crushed into small pieces. These small pieces were polished and made into briquettes. The sizes of these briquettes are approximately 3cm

× 3cm × 2cm. these briquettes were observing. Parts of the briquettes were shown in figure 1.



(a) (b) (c)
Figure 1: Parts of the briquettes.

- The statistics about geometrical parameters of different scales pore-fractures

The geometrical parameters of pore-fractures simulation mainly include density, direction, trace length, and opening degree. First, the uniformly distributed random numbers of the geometrical parameters were generated using statistical data. Second, the other distributed random numbers were generated using a direct sampling method (LU B. et al., 2005; ODA M A. 1988).

$$\begin{cases} b_n = (ab_{n-1} + c) \pmod{M} \\ r_n = \frac{b_n}{M}, n \in N \\ \text{initial value is } b_0 \end{cases} \quad (1)$$

Where: M is the modulus; mod M is the residual value of the modulus; a is a multiplier; c is increments; b0 is the initial value; and rn is uniformly distributed random numbers in the range from 0 to 1.

Table 1: Geometric parameters of pore-fractures.

	packet	density (strip/mm ²)	Trend (°)		Fracture length (mm)		Fracture width (mm)	
			means	Standard deviation	means	Standard deviation	means	Standard deviation
Millimeter fracture	1	0.1	77.8	4.2	2.89	0.16	0.00065	0.0002
	2	0.1	156.7	7.8	3.74	0.19	0.00065	0.0002
Micron fracture	packet	density (strip/um ²)	angle (°)		fissure length (um)		fissure width (um)	
			means	Standard deviation	means	Standard deviation	means	Standard deviation
	1	0.0004	40.8	1.6	46.1	4.9	0.75	0.02
	2	0.0004	127.4	5.8	92.3	8.6	0.75	0.02
Seepage pore	packet	density (strip/nm ²)	angle (°)		fissure length (nm)		fissure width (nm)	
			means	Standard deviation	means	Standard deviation	means	Standard deviation
	1	0.000005	60.3	2.8	531.4	9.3	12.32	2.35
	2	0.000005	136.4	6.2	453.7	12.4	12.32	2.35

When uniformly distributed random numbers were generated, then other distributed random numbers could also be generated. Such as:

$$x = \mu_x + \sigma_x \times \sqrt{-2\ln(rand)} \times \cos(2 \times \pi \times rand)$$

Where: x is the normally distributed random numbers; rand is the uniformly distributed random

numbers in the range from 0 to 1, and so on. Other distributed random numbers were obtained.

The briquettes were observing by the best magnification of the microscope. The direction, length and width of different scales pore-fractures

were counted. Statistical geometrical parameters are shown in Table 1.

The center of pore-fractures were uniformly distributed, the tracing length of pore-fractures were normally distributed, the trend of pore-fractures were lognormal distributed, and the opening degree of pore-fractures were normally distributed.

- The reconstruction about different scales of pore-fractures network

1) Generating domain and characterization of pore-fractures

The pore-fractures network was generated via the Monte Carlo method. In order to generate the pore-fractures network, the generating domain and characterization of pore-fractures were needed. The following steps were performed:

(1) The generating domain of pore-fracture network was determined by the pore-fracture length.

For example, the average length of fractures was l , so the size of the generating domain about the fracture was $6l \times 6l$.

(2) If pore-fractures were always straight, the center coordinate of pore-fractures was (x, y) , the length of pore-fractures was s , trend angle of the pore-fractures was α (defined as the angle from x-axis rotated counter clockwise to the pore-fractures), and the endpoint coordinates of pore-fractures were as follows:

starting point coordinates :

$$\begin{cases} x_0 = x - (s/2)\cos\alpha \\ y_0 = y - (s/2)\sin\alpha \end{cases}$$

end coordinates :

$$\begin{cases} x_1 = x + (s/2)\cos\alpha \\ y_1 = y + (s/2)\sin\alpha \end{cases} \quad (2)$$

(3) The number of fractures in each group was calculated using the following formula:

$$N = S \cdot \rho \quad \text{or} \quad N = \frac{S}{s \cdot d} \quad (3)$$

Where: N is the number of fractures; ρ is surface density of fractures; S is the generating domain area; s is the length of fractures; and d is average value of fractures spacing.

2) The realization of reconstruction of the different scales of pore-fissure network

According to Table 1, the average length value of millimeter fractures is 3.315mm. Thus the size of generating domain about the millimeter fractures network can be determined to be 20 mm \times 20 mm, with the size of analysis domain being 10 mm \times 10 mm. The sizes of the generating domain about micron fractures and seepage pores were obtained by the same method, with the sizes being 400 $\mu\text{m} \times$ 400 μm , 3000 nm \times 3000 nm, respectively. Sizes of the

analysis domain about micron fractures and seepage pores were 200 $\mu\text{m} \times$ 200 μm , 1500 nm \times 1500 nm, respectively. According to equation (3), the numbers of each group about millimeter fractures, micron fractures and seepage pores were 40, 64 and 45, respectively.

The Millimeter fracture network models were shown in Figure 2.

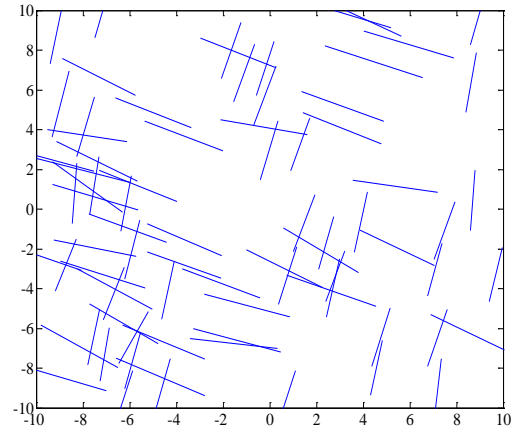


Figure 2: Millimeter fracture network.

3. PERMEABILITY PREDICTION AND VERIFICATION ABOUT DIFFERENT SCALES OF PORE-FISSURE NETWORK

3.1 The establishment of penetration model diagram

The fluid could not flow in generating disconnected pore-fractures, therefore, disconnected pore-fractures should be eliminated. The method of elimination was assigned zero (Min et al., 2004; Xu ZhongJi., 1985; Liu et al., 2007). The intersection of each pore-fissure was calculated using Matlab software, which exists in a lower triangular matrix. While the matrix corresponding position was assigned zero among not intersect fractures, a symmetric matrix was given by the sum of the original matrix. The point of intersection was then found between the boundary and the pore-fractures, and the same place was assigned in another intersection matrix. When an intersection was disjointed or located in boundary extension cord, the corresponding position at the intersection matrix was assigned zero. The boundary node matrix was placed under the inner point of intersection, which was combined into the new total intersection matrix. Those not meeting the requirements of pore-fractures were eliminated by judging the number of intersection points of the pore-fractures. The pore-fractures network model diagram can be obtained by using the pore-fractures intersection connection. The network models are shown in Figure 3.

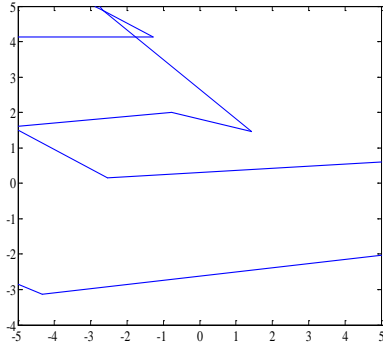


Figure 3: Millimeter seepage model.

3.2 The calculation method for permeability

If the direction of water flowing in fractures was one-way, fracture width in the coal reservoir was not changed. Coupling effects between seepage field and stress field were ignored. According to the second type of boundary conditions combined with the water balance principle, water seepage in fractures was analyzed by establishing a computing matrix. A two-dimensional computing equation of steady flowing was used: (Baghbanan et al., 2008; Chen et al., 2012; He et al., 2013)

$$\begin{aligned} A_1TA_1^T H_1 + A_1TA_2^T H_2 + A_1TA_3^T H_3 + Q_1 &= 0 \\ A_2TA_1^T H_1 + A_2TA_2^T H_2 + A_2TA_3^T H_3 + Q_2 &= 0 \\ A_3TA_1^T H_1 + A_3TA_2^T H_2 + A_3TA_3^T H_3 + Q_3 &= 0 \end{aligned} \quad (4)$$

Where: A1, A2, A3 are the convergence matrix; T the is diagonal matrix; H1 is head vector within a node (m); H2 and H3 are respectively intersection head vector in upper / lower and around bounds of the model (m); Q1 is water sink sources within node (m3); Q2 is flow value about intersection of the upper and lower boundary of the model (m3); and Q3 is flow value around the intersection of the boundary of the model, inflow is positive and outflow is negative (m3).

It can be found from the above equation that:

$$\{H\} = -[D]^{-1}\{Q\} \quad (5)$$

Where: $[D] = (A_iTA_i^T)$, $[D]^{-1}$ is inverse matrix of $[D]$; $\{Q\} = \{Q_1 + A_1TA_3^T H_3\}$

When H1 was calculated, equation (6) could be obtained combined with equation (4), namely:

$$\begin{cases} Q_2 = -A_2TA_1^T H_1 - A_2TA_2^T H_2 - A_2TA_3^T H_3 \\ Q_3 = -A_3TA_1^T H_1 - A_3TA_2^T H_2 - A_3TA_3^T H_3 \end{cases} \quad (6)$$

The size of the analysis domain was a square of 10mm × 10mm. According to Darcy's Law, permeability coefficient can be obtained as follows:

$$K = \frac{v}{\nabla H/L} = \frac{Q/L}{\nabla H/L} = \frac{Q}{\nabla H} \quad (7)$$

According to the relationships between permeability coefficient and permeability, equation (8) can be obtained:

$$k = \frac{K\eta}{\rho g} \quad (8)$$

Where: η is the dynamic viscosity coefficient of water; ρ is the density of water; g is gravitational acceleration, and k is permeability.

3.3 The prediction and verification of permeability

The matrix equation could be calculated using Matlab software. The permeability coefficient about different scales of pore-fractures can be calculated using the matrix equation. Combined with equation (8), the permeability about different scales of pore-fractures can be calculated. At the same time, in order to verify the accuracy of the predicted results, permeability tests were carried out by collecting coal samples in Sihe mine. The testing results and matrix calculations result were shown in Table 2.

The average permeability was 0.56 mD. The matrix weighted permeability was from 0.172 to 0.531 mD.

Table 2: Comparisons with experimental results and calculated results about permeability in Sihe coal samples.

Sample	Rock samples description	density g/cm ³	Effective porosity %	Permeability(mD)				Actual test
				millimeter fractures	micron fracture s	seepage pore	Weight calculation n	
SH-1	coal	1.45	3.2	0.19	0.0098	2.85×10 ⁻⁶	0.17198	0.28
SH-2	coal	1.46	3.4	0.31	0.00047	3.69×10 ⁻⁵	0.279047	0.39
SH-3	coal	1.45	3.5	0.46	0.00082	3.3×10 ⁻⁶	0.414082	0.42
SH-4	coal	1.45	2.0	0.59	0.00218	3.6×10 ⁻⁵	0.531218	0.75
SH-5	coal	1.44	2.4	0.23	0.0133	6.1×10 ⁻⁶	0.20833	0.47
SH-6	coal	1.45	3.9	0.55	0.00632	4.5×10 ⁻⁵	0.495632	0.83

Average permeability was 0.352 mD, the calculated results were on the same order of

magnitude with the experimental results. Millimeter fractures were major contributors to the permeability,

followed by micron fractures, and finally seepage pores were minimal contributors. The simulation results were corroborated with testing results. This paper discusses the influencing law of permeability by different scales fractures parameters.

4. INFLUENCE ON THE VALUES OF THE PERMEABILITY IN DIFFERENT SCALES FRACTURE PARAMETERS

3.1 The influence on the permeability by the density of the fractures

The relationship between the permeability and the density of millimeter fractures is as shown in Figure 4.

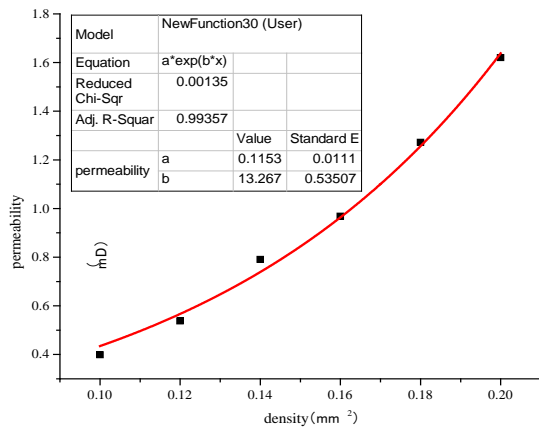


Figure 4: Relationships between the density of millimeter fractures and permeability.

The diversion ability of the fractures increased exponentially with increases of the fracture density. Therefore, increasing density can raise connectivity and permeability.

3.2 The influence on the permeability by the length of the fractures

The relationship between the permeability and the length of fractures is as shown in Table 3.

Table 3: Calculated results for permeability in different lengths about millimeter fractures.

Fissure length (mm)	Permeability coefficient (mm/s)	Permeability (md)
2.87/3.74	4.3157×10^{-6}	0.399
3.09/ 3.94	4.3749×10^{-6}	0.400
3.29/4.14	4.5473×10^{-6}	0.420
3.49/4.34	4.7433×10^{-6}	0.441
3.69/4.54	4.7616×10^{-6}	0.443
3.89/4.74	4.7649×10^{-6}	0.443

The number of nodes and connectivity increased with increases of the length. When the length of the fractures achieves a certain value, the value of the permeability was almost increased.

3.3 The influence on the permeability by the width of fractures

The relationship between the permeability and the width of fractures was found by fitting. It is as shown in Figure 5.

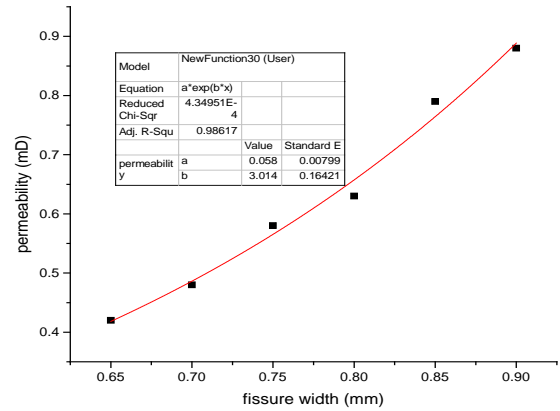


Figure 5: Relationships between the width of millimeter fractures and permeability.

The diversion ability of the fractures was increased with increases in the fracture width and increases in the permeability of the coal reservoir. The relationship between the permeability and the width of the fractures was exponential.

The influence laws of the main parameters of the fractures were such that: density and width in the millimeter fractures and seepage pores have a larger influence on permeability, and the length has little influence on permeability. The density and length of micro fractures have a larger influence on permeability, and the width has little influence on permeability.

5. CONCLUSIONS

According to the simulation about different scales pore-fractures and predicting permeability, the following conclusions can be made:

(1) The networks for different scales pore-fractures were reconstructed using observation and the Monte Carlo method. The networks can clearly show the connectivity between pore-fractures.

(2) The contribution order of different scales pore-fractures on the coal reservoir permeability from largest to smallest are the millimeter fractures, micro fractures, and seepage pores. The advantages of connected paths for different scales pore-fractures from highest to lowest are millimeter fractures, seepage pores, and micro fractures.

6. ACKNOWLEDGEMENT

The authors thank for financial assistance in major projects of Henan province university science and technology innovation talent support program (15HASTIT050), Henan Province the high school youth backbone teacher assistance program (2013GGJS-049), Science and Technology Department of Henan province (142102210050), Henan Polytechnic University Funds for Distinguished Young Scientists (No.J2013-01) and International Cooperation Project of Henan Province (144300510041).

7. REFERENCES

Barton C C. (1988). Fractal geometry of two-dimensional fracture networks at Yucca Mountain, Spathwestern Nevada. In:proc.Int.Symp.on Fundamentals of Rock Joints. Rotterdam:A.A.Balkema, pp. 77-84.

BABADAGLI TAYFUN. (2001). Fractal analysis of 2D fracture networks of geothermal reservoirs in south-western Turkey. Journal of Volcanology and Geothermal Research, Volume 11, No. 2, pp. 83-103.

Baghbanan A and Jing L. (2008). Stree Effects on Permeability in a Fractured Rock Mass with Correlated Fracture Length and Aperture. International Journal of Rock Mechanics and Mining Sciences, Volume 45, No. 3, pp. 1320-1334.

CHEN S H and FENG X M.(2006). Composite element model for rock mass seepage flow. Journal of Hydrodynamics: Series B, Volume 18, No. 2, pp. 219-224.

CHEN S H, HE J and SHAHROUR I. (2012). Estimation of elastic compliance matrix for fractured rock masses by composite element method. International Journal of Rock Mechanics and Mining Sciences, Volume 49, No. 1, pp. 156-164.

CUI X and BUSTIN R M. (2005). Volumetric strain associated with methane desorption and its impact on coalbed gas production from deep coal seams.AAPG Bulletin, Volume 89, No. 9, pp. 1181-1202.

Feng Zengchao,Zhao Yangsheng and Lu Zhaoxing. (2007). Study on percolation law of 2D porous and fractured double-medium. Acta Physica Sinica (in Chinese), Volume 56, No. 5, pp. 2796-2801.

HE J, CHEN S H and SHAHROUR I. (2013). Numerical estimation andprediction of stress-dependent permeability tensor for fractured rock masses. International Journal of Rock Mechanics and Mining Sciences, Volume 59, No. 1, pp. 70-79.

He Yaoyao and Liu Jianjun. (2011). Numerical experimental research of equivalent seepage characteristic for fractured porous media. Advances in Porous Flow (in Chinese), Volume 1, No. 2, pp. 17-20.

LIU Y R, ZHOU W Y and YANG Q.(2007). A distributed memory parallel element-by-element scheme based on Jacobi-conditioned conjugate gradient for 3D finite element analysis. Finite Elements in Analysis and Design, Volume 43, No. 6/7, pp. 494-503.

LU Bo, CHEN Jian-ping and GE Xiu-run. (2005). Fractal study on the representative element volume of jointed rock masses. Chinese Journal of Rock Mechanics and Engineering, Volume 24, No. 8, pp. 1355-1361.

Min K B, Rutqvist J and Tsang C F.(2004) Stress dependent Permeability of Fractured Rock Masses: A Numerical Study. International Journal of Rock Mechanics and Mining Sciences, Volume 41, No. 5, pp. 1191-1210.

ODA M A. (1988). Method for evaluating the representative elementary volume based on joint survey of rockmass. Canadian Geotechnical Journal, Volume 25, No. 3, pp. 281-287.

SISAVATH S, MOURZENKO V and GENTHON P. (2004). Percolation and transport properties of fracture networks derived from line data. Geophysical Journal International, Volume 157, No. 2, pp. 917-934.

Wenxue Chen, Xueqiu He, Mingju Liu, Hani Mitri & Qian Wang (2016). Meso- and macro-behaviour of coal rock: observations and constitutive model development, International Journal of Mining, Reclamation and Environment, 30:1, 13-24, DOI: 10.1080/17480930.2013.878561

Xu Zhongji.(1985). Monte carlo method. Shanghai: Shanghai Science and Technology Publishing House (in chinese), 324p.

ZHANG H B, LIU J S and ELSWORTH D. (2008). How sorption-induced matrix deformation affects gas flow in coal seams: A New FE Model. International Journal of Rock Mechanics and Mining Sciences, Volume 45, No. 8, pp. 1226-1236.

Quantitative risk assessment on large-scale oil depots of opencast coal mine

Ru Jun Wang, Shu Jiao Tong*

Key Laboratory of Major Hazard control and Accident Emergency Technology, State Administration of Work Safety, China Academy of Safety Science and Technology, Beijing, China, 100012

ABSTRACT

In recent years, many large-scale oil depots have been built in the opencast coal mine in China. In order to prevent and control major accidents of the opencast mine, it is important to assess the risk of large-scale oil depots. This paper aims to bring about a quantitative risk assessment (QRA) method to assess the fire risk of opencast coal mines. Firstly, risk analysis of large-scale oil depots for coal mine are made, the hazardous characters of gasoline and diesel are described, and the risk consequences are discussed. It is found that pool fire is the most typical and serious consequence, therefore, a mathematical model of pool fire is introduced. Furthermore, the quantitative risk assessment (QRA) method is developed to assess the fire risk of the large-scale oil depots. The QRA method is applied to assess the risk of a selected large-scale oil depot in a large opencast coal mine in China based on the QRA software CASSTQRA. For the gasoline tank of $1 \times 104 \text{ m}^3$, the death, serious injury, and light injury affected radius of a pool fire are 64.75 m, 75.66 m, and 106.86 m and the individual risk was acceptable. Finally, some suggestions are proposed to improve the safety of the large-scale oil depots. The study is useful for the safety management and prevention of major accidents in opencast coal mines.

KEYWORDS: opencast mine; oil depot; risk assessment; QRA

1. INTRODUCTION

With the development of the economy and society, China's coal industry has made remarkable achievements in recent years. The production safety of coal mines has greatly improved. However, many major accidents have happened in the last decades. Many large-scale oil depot have been built in the opencast mine in China in order to meet the demands of the production of opencast coal mines. The emergence of those large-scale oil depots have brought new challenges to the safety of the opencast coal mine. In order to prevent or control major accidents of the opencast mine, it is important to assess the risk of the large-scale oil depots.

Risk is the sum of accident consequence and its probability caused by the risk. It has been shown that the main accidents associated with large-scale oil depots are fires and explosion of the oil tanks. Further, as a flammable liquid, pool fire is the most frequent and has more serious consequences than explosion once the gasoline and diesel oil leak in the fire dike. Based on the quantitative risk assessment, the mathematic model of pool fire consequences is introduced in this paper. A large-scale oil depot in an opencast coal mine in China is assessed based on the QRA method. Pool fire consequences such as death radius, serious injury, and light injury radius of the large-scale oil depot are also calculated by the QRA software CASSTQRA developed by the China academy of safety science and technology. The

acceptable individual risk of the large-scale oil depot can be drawn. Finally, some conclusions and suggestions are proposed to improve the safety of the large-scale oil depots for opencast coal mines. The results can provide a theoretical basis and management guidance for government departments to manage opencast coal mines.

2. PROCEDURE OF QUANTITATIVE RISK ASSESSMENT

Quantitative risk assessment (QRA) is a complex and technical risk assessment method, which not only analyzing the causes of accidents qualitatively, but also calculates the frequency and consequence of accidents quantitatively. The risk result is compared with the existing acceptable risk standard to put forward measures to reduce or mitigate risk. The general procedure of QRA is shown in Figure 1.

*Corresponding author – email : tongshujiao@mail.neu.edu.cn

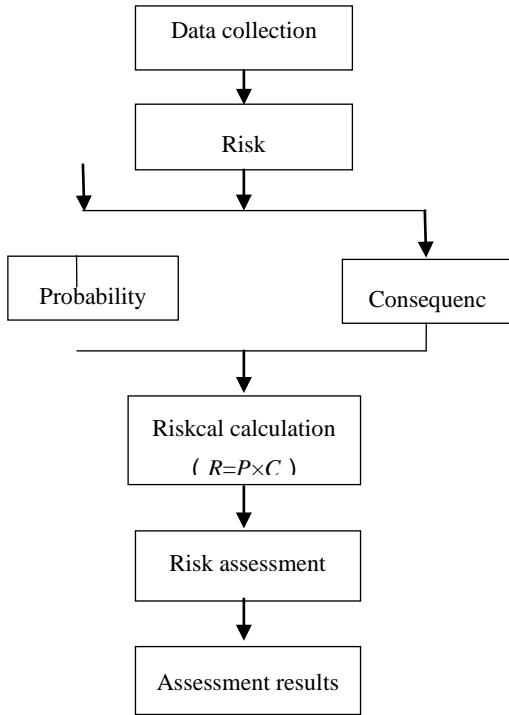


Figure 1: Procedure of quantitative risk assessment.

Individual risk is the key quantitative index of the quantitative risk assessment. The so-called individual risk refers to the risk of a variety of potential fire, explosion, and toxic gas leakage accidents caused by a fixed position in the region of a fixed position of the individual probability of death, which is the individual mortality. It is usually shown as a risk contour line (as shown in Figure 2), which can measure the size of an individual risk via a comparison with an acceptable risk criteria.

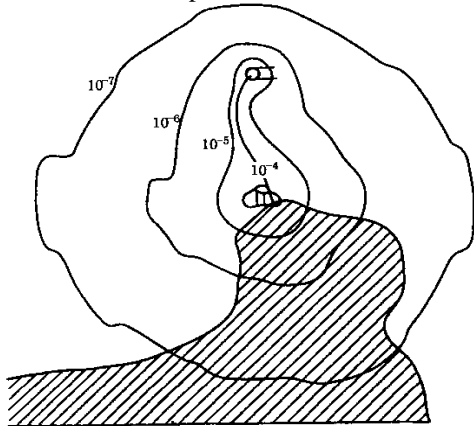


Figure 2: Sketch map of individual risk contour line.

In viewing of the risk to the surrounding people, facilities and environment, the acceptable individual risk criterion of the newly-built and existing facilities with hazardous chemical materials are defined in 2014 in China (as shown in Table 1).

Table 1: Acceptable individual risk criteria of China.

Protection target	Individual acceptable risk criteria (probability)	
	Newly-built facilities (per year) ≤	In-service facilities (per year) ≤
Low density areas (person number <30) : Single or a small amount of exposure persons.	1×10^{-5}	3×10^{-5}
High density residential places ($30 \leq$ person number < 100): residential areas, hotels, resorts etc. Public gathering places with high density ($30 \leq$ person number < 100): office, shopping malls, restaurants, entertainment etc.	3×10^{-6}	1×10^{-5}
High sensitive places: schools, hospitals, kindergartens, nursing homes, prisons, etc. Important goals: military forbidden zone, military management area, cultural relics protection unit, etc. Special high density sites (person number ≥ 100): large stadiums, transportation hub, open-air market, living district, hotels, resorts, offices, shopping malls, hotels, entertainment venues.	3×10^{-7}	3×10^{-6}

Seen from the Table 1, for the existing facilities, the acceptable individual risk cannot exceed 3×10^{-5} /year in the low density areas, 1×10^{-5} /year in high density residential places and public gathering places with high density, and 3×10^{-6} /year in high sensitive places, important goals and special high density sites. For the newly-built facilities, the acceptable individual risk cannot exceed 1×10^{-5} /year in the low density areas, 3×10^{-6} /year in high density residential places and public gathering places with high density, and 3×10^{-7} /year in high sensitive places, important goals and special high density sites.

3. MATHEMATICAL MODEL OF POOL FIRE FOR OIL DEPOTS

3.1 Mathematical Model of pool fire

When the boiling point of the combustible liquid in the liquid pool is higher than the temperature of the surrounding environment, the velocity of combustion of the unit area on the surface of the liquid pool can be expressed by equation (1).

$$\frac{dm}{dt} = \frac{0.001H_c}{C_p(T_b - T_0) + H} \quad (1)$$

When the boiling point of the flammable liquid in the liquid pool is lower than that of the ambient temperature, the velocity of combustion of the unit area on the surface of the liquid pool can be expressed by equation (2).

$$\frac{dm}{dt} = \frac{0.001H_c}{H} \quad (2)$$

Where,

H_c — Combustion heat of combustible liquid,

j/kg ;

C_p — Constant pressure specific heat of liquid,

j/kg·°K;

T_b — Boiling point of liquid, °K;

T — Ambient temperature, °K;

H — Liquid steam heating, j/kg.

For analysis, it is assumed that the liquid pool is round. If the liquid has reached the artificial boundary, the liquid pool area is the area of the artificial boundary, and the radius of the liquid pool can be expressed by equation (3).

$$r = \sqrt{\frac{S}{\pi}} \quad (3)$$

Because of the dangerous goods transportation accidents occurring in the road and the leakage of liquid usually without an artificial boundary, it is assumed that liquid to leaks as a cylindrical flat smooth surface toward the outer edge of the diffusion. At this time, the area of the liquid pool is changed with time, and the radius of the liquid pool can be calculated according to the following method.

For instant leaks, the pool radius can be expressed by equation (4).

$$r = \sqrt{\frac{t}{\left(\frac{\pi\rho}{8gQ}\right)^{\frac{1}{2}}}} \quad (4)$$

For continuous leakage, the liquid pool radius can be expressed by equation (5).

$$r = \left(\frac{t}{\sqrt[3]{\frac{9\pi\rho}{32gQ_0}}}\right)^{\frac{3}{4}} \quad (5)$$

Where,

r — radius of liquid pool, m;

S — Area of fire dike, m²;

ρ — Density, kg/m³;

g — Acceleration of gravity, 9.8m/s²;

Q — leakage amount, kg;

Q_0 — leakage velocity, kg/s.

And then, the total heat flux from the liquid pool can be expressed as Eq(6).

$$E = (\pi r^2 + 2\pi r h) \frac{dm}{dt} \eta H_c \left[\left(\frac{dm}{dt}\right)^{0.61} + 1 \right] \quad (6)$$

Where,

η — efficiency factor, 0.13 ~ 0.35 ;

h — flame height, m;

Assuming that all the radiation heat is emitted from a small spherical surface of the center of the liquid pool, the heat radiation intensity at a distance from the center of the liquid pool can be expressed by equation (7).

$$I = \frac{Et_c}{4\pi x^2} \quad (7)$$

Where,

E — total heat radiation flux, w;

t_c — air coefficient of thermal conductivity;

x — object point to the center distance of the liquid pool, m.

Therefore, for the pool fire situation, personnel and equipment under the influence of different damage effects can be expressed by equation (8).

$$x = \sqrt{\frac{Et_c}{4\pi I}} \quad (8)$$

Where,

x — Pool fire damage distance, m;

I —the criteria for judging the damage, w/m^2 .

3.2 Influence Area Analysis

Generally, the affected area can be divided into the death radius, serious injury, and light injury radius. The influence radius is the threshold distance of the oil fire accident, which experiences the consequences of death, environmental pollution, property loss, etc. Therefore, the influence area of large-scale oil depots is a certain threshold distance from the surrounding. The closer to the oil tank or depot, the higher the risk of the impact of an accident.

4. CASE STUDY

In this paper, a large-scale oil depot of a large opencast coal mine is taken as a case to study the risk assessment. There are 9 oil tanks in the large-scale oil depot, two gasoline tanks (each $1 \times 10^4 m^3$) and seven diesel oil tanks (each $2 \times 10^4 m^3$). Aiding with the QRA software CASSTQRA, the affected area and individual risk are shown as the following figures.



Figure 3: Influence area of pool fire of gasoline tank (each $1 \times 10^4 m^3$).

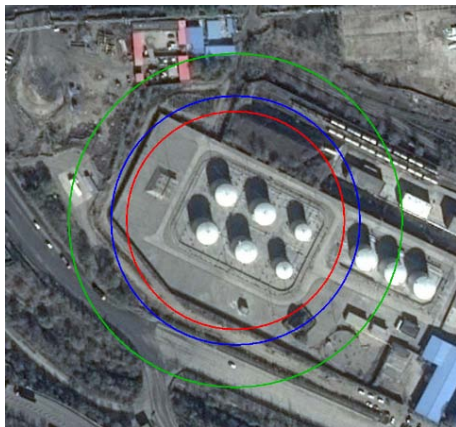


Figure 4.1: Influence area of pool fire of diesel oil tank (each $2 \times 10^4 m^3$).

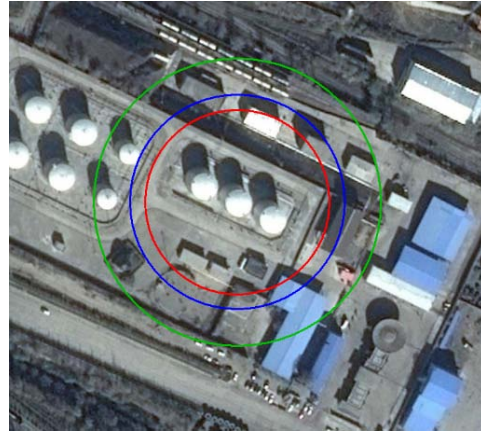


Figure 4.2: Influence area of pool fire of diesel oil tank (each $2 \times 10^4 m^3$).

The individual risk contour line of the large-scale oil depot can be drawn as Figure 5.

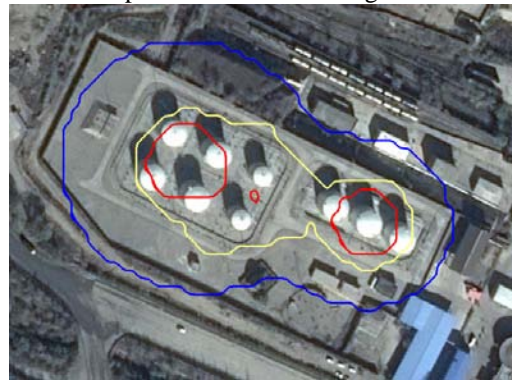


Figure 5: Individual risk contour line of the large-scale oil depot.

For the influence area (Figures 3-5), the red line is the death area, the blue line is the serious injury area and the green line is the light injury area. For the individual risk (Figure 5), the red line is 3×10^{-5} , the yellow line is 1×10^{-5} , and the blue line is 3×10^{-6} .

5. CONCLUSIONS

Quantitative risk assessment (QRA) is a complex and technical risk assessment method to assess the risk of large-scale oil depots for opencast coal mines. The pool fire is the most frequent and serious consequence, followed by explosion once the oil has leaked in the fire dike.

For the gasoline tank of $1 \times 10^4 m^3$, the death, serious injury and light injury affected radius of a pool fire were 64.75 m, 75.66 m, and 106.86 m, respectively. For the diesel oil tank of $2 \times 10^4 m^3$

gasoline, the death, serious injury, and light injury affected radius of a pool fire were 78.61 m, 88.72 m, and 120.13 m, respectively. For the diesel oil tank of $1 \times 10^4 \text{ m}^3$, the death, serious injury, and light injury affected radius of a pool fire were 53.43 m, 63.75 m, and 85.59 m, respectively.

All the individual risks were acceptable. However, some of the facilities may be affected by the pool fire of the large-scale oil depots, therefore, the opencast coal mine should take effective measures to avoid the risk of pool fire.

6. ACKNOWLEDGEMENT

The research work was supported by National Science and Technology Foundation of China under Grant No. 2015BAK16B03 and Basic Science and Technology Foundation of CASST under Grant No. 2016JBKY12.

7. REFERENCES

Baozhi Chen. (2011). System safety assessment and forecast (the second edition), Metallurgical Industry Press, Beijing.

Boling Zhu, Xiaochun Yu. (2009).. Research for PHAST in the process of liquefied natural gas discharge and dispersion, Computers and Applied Chemistry 26, p.1418.

Cumber, PS. (2009). Efficient calculation of the radiation heat flux surrounding a jet fire, Fire Safety Journal 44, p. 580

Deming Yu. (2000). Quantitative risk assessment to the storage and transportation process of the inflammable, explosive and toxic dangerous goods, China Railway Press, Beijing.

Gomez-Mares, M., Munoz, M., Casal, J. (2009). Axial temperature distribution in vertical jet fires, Journal of Hazardous Materials 172, p. 54.

Han, Z.Y, Weng, W. G. (2011). Comparison study on qualitative and quantitative risk assessment methods for urban natural gas pipeline network, Journal of Hazardous Materials 18, p. 509.

Hapue C.E., Burton I. (2005). Adaptation Options Strategies for Hazards and vulnerability Mitigation: An International Perspective, Journal of Mitigation and Adaptation Strategies for Global Change , Volume 10, No. 3, pp. 335 ~ 353.

Hong L, Wang H.P. (2009). Evaluation of emergency management level mutation theory of coal mine emergency, Journal of Coal Mine Safety, Volume 6, No. 1, pp. 111-113.

Jianguo Ren, Shunqing Lu. (2006).. Application of Gas Diffusion Mathematical Model to Safety Assessment, China Safety Science Journal 16, p. 12.

Ma, Lei, Li, Yongshu. (2010). Research and Realization of Urban Natural Gas Pipeline Network

Pre-warning System, Journal of China Safety Science 20, p.171.

Majid, ZA., Mohsin, R. (2012). Failure Investigation of Natural Gas Pipeline, Arabian journal for Science and Engineering 37, p.1083.

Paeka H.J., Hilyard K. (2010). Theory-Based Approach and Understanding Public Emergency Preparedness: Implications for Effective Health and Risk communication, Journal of Health Communication: International Perspectives, Volume 15, No. 4, pp. 428-444.

Palacios, A., Munoz, M., Casal, J. (2009). Jet Fires: An Experimental Study of the Main Geometrical Features of the Flame in Subsonic and Sonic Regimes, AIChE Journal 55, p.256.

Wu Z.Z, Liu M. (2000). Risk assessment method, Chemical Industry Press, pp. 38~69.

Young, Do Jo, Bum, Jong Ahn. (2005). A method of quantitative risk assessment for transmission pipeline carrying natural gas, Journal of Hazardous Materials 123, p. 1.

Development and realization of a coal and gas outburst simulation device

NIE Baisheng^{a,b}, HU Shoutao^{a,b,*}, LI Xiangchun^{a,b}, MENG Junqing^{a,b}, FAN Penghong^{a,b}

^a State Key Lab of Coal Resources and Safe Mining, China University of Mining and Technology(Beijing), Beijing, China 100083

^b School of Resource & Safety Engineering, China University of Mining and Technology(Beijing), Beijing, China, 100083

ABSTRACT

Similar coal and gas outburst simulation devices both at home and abroad are analyzed and their advantages and disadvantages are examined. A large size experimental device of coal and gas outburst simulation is developed based on the congeneric testing device. This device consists of coal and a gas outburst model system, gas injection system, loading system, stress measurement system, gas pressure measurement system, temperature measurement system, electromagnetic radiation testing system, and high-speed photography system. The functions of the device are as follows: (1) to study the laws of roof break development and stress evolution during outburst process by simulating coal seam, roof and floor with similar material, (2) to simulate stress distribution of a roof at high strength springs of different sizes, (3) to realize the uniform adsorption in coal by 3 gas injection pipes that are pre-buried, (4) to induce coal and gas outburst at predetermined gas pressure by blasting bursting disc instantly that set on the outburst hole, (5) to observe and record fracture and migration process of coal in the cavity during outburst that is achieved by a visual glass window on the side of cavity.

KEYWORDS : coal and gas outburst; testing device; similar simulation; gas pressure; ground pressure

1. INTRODUCTION

Coal and gas outburst is a kind of complicated dynamic instability that occurs in underground coal mines (Hu Qianting et al., 2007). Most researchers study the mechanism of coal and gas outburst through laboratory simulation because of the danger involved in tracking studies of real coal and gas outburst occurring in coal mines. The one dimensional outburst simulation tests were conducted firstly in Soviet Union in the 1950s (Аируни, 1955). The results showed that the coal can be broken and thrown only under conditions of great gas pressure gradient. In the beginning of the 1960s, Japanese scholars conducted a simulation test of the ejection of coal through a shock tube (SHI Ping, 1985). In the test, ice crystals of carbon dioxide, rosin, cement, and coal particles were used to make a model. Driving was also simulated. Adsorption performance of the model varied wildly from the coal. Researchers believe that the degree of metamorphism, the diffusion coefficient, permeability, and porosity are closely related with coal and gas outburst, as shown through experiments and theoretical analysis (Beamish BB, Crosdale PJ., 1998, Sobczyk J., 2011). Norbert Skoczylas conducted an externally induced outburst test and the results showed that the intensity of outburst is affected by unloading time (Norbert Skoczylas, 2012).

In China, many universities and research institutes such as Shenyang Branch of China Coal Research Institute, Institute of mechanics of China Academy of Sciences, China University of Mining and Technology,

Henan Polytechnic University, and Chongqing University furthered the research of coal and gas outburst by developing different simulation test devices. Deng Quanfeng et al. (1989) simulated the coal and gas outburst of IV, V coal induced by rock cross-cut coal uncovering, and the coal model was conducted without any additive agent. Jiang Chenglin (1994; 2003) simulated the coal and gas outburst of IV, V coal induced by rock cross-cut coal uncovering with a one dimensional outburst simulation test. Meng Xiangyue et al. (1996) conducted many tests using a two-dimensional simulation test device, and the results showed that the destruction of coal exists with “dehiscence” and “outburst”. Cai Chenggong (2004) designed a three dimensional simulation test device based on the similarity theory and mechanical model. A mathematical model of the relationship between the intensity of outburst and gas pressure, coal forming strength, three dimensional stress, and gas pressure was established. The simulation condition between briquette outburst and real coal seam outburst was put forward and dimensionless parameter criterion of outburst was established based on the comprehensive function hypothesis of outburst and similarity theory by Zhang Jianguo (Zhang Jianguo and Wei Fengqing, 2002). The change trend of temperature in the process of outburst was analyzed by Guo Liwen (Guo Liwen et al., 2000). The research team of Yin Guangzhi and Xu Jiang developed a comprehensive simulation device. In this device, different forming stress, different loading stress, different loading form and different diameter of outburst

*Corresponding author – email: hst510@163.com

can be simulated for coal and gas outburst simulation tests. The cusp catastrophe instability model of creep fracture of coal containing gas based on testing machine and specimen system was established (Xu Jiang et al., 2008; Wang Dengke, 2009; Tao Yunqi, 2009; Ying Guangzhi et al., 2009). Wei Chunfu et al. (2014) studied the gas pressure effect in coal and gas outburst through a self-designed coal-rock gas dynamic disaster simulation test system. Wang Zhirong et al. (2014) discussed the mechanism of delayed outburst in “three soft” mining area through establishing nonlinear viscoelastic to plastic rheological model of soft coal containing gas. Wang Gang et al. (2015) established a model of energy conditions for outburst and a prediction model for outburst intensity.

2. THE DEVELOPMENT IDEA AND PURPOSE

2.1 The development idea

In the light of deficiency of current coal and gas outburst devices, the development ideas of the simulation test device are as follows:

(1) The simulation test device is a large size device. The roof and floor of coal seam can be simulated by sand, quartz sand, gypsum and other aggregate, from which development of cracks in the roof and evolution of stress after and during the process of coal and gas outburst can be analyzed.

(2) The change of various physical parameters is very important for the research of outburst. Physical parameters such as coal temperature, gas pressure, stress, strain, and acoustic signal need to be collected in the test. This function will be realized by a variety of sensors and enameled wire.

(3) The simulation of real roof stress distribution of coal in front of mining face is always a difficult point in simulation tests. In this device, a series of springs are installed between the loading piston and the top of the roof. And the size and specifications of springs need to be calculated by real roof stress distribution of coal in front of mining face.

(4) This device should simulate coal and gas outburst under different condition such as different stress, different gas pressure, different loading form, and different diameter of outburst. In addition, the process of outburst can be record by high-speed camera. So the observation windows need to be installed at the device for the recording of the high-speed camera.

(5) The gas can be aerated and adsorbed evenly in the coal sample. To insure the gas can be aerated and adsorbed evenly in the coal sample, three inflatable tubes will be carried evenly in the coal sample in the process of coal forming. Some small holes will be drilled at the inflatable tubes for the inflow of gas into the coal sample.

(6) Blasting sheet and clamping device need to be

installed at the outburst hole. Coal and gas outburst can be induced through fast blasting of blasting sheet at a prescribed gas pressure.

The design idea of a coal and gas outburst simulation device is shown in Figure 1.

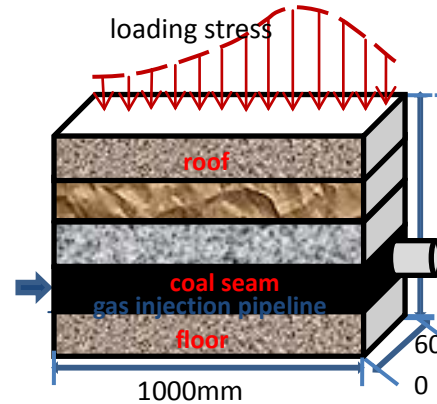


Figure 1: The design idea of a simulation device.

2.2 The development purpose

This test device is designed to simulate coal and gas outburst. Outburst process under conditions such as different forming stress, loading stress, gas pressure, loading form, thickness of coal seam, roof and floor conditions, and diameter of outburst is researched using this device. The stress, temperature, roof strain, gas pressure, acoustic parameters in the process and migration law, size classification, and distribution characteristics of the coal sample after outburst are studied in order to study the mutual coupling effect of stress, gas pressure, and the physical and mechanical properties of coal and its comprehensive mechanism for outburst. The coal and gas outburst mechanism can be revealed based on a comprehensive mechanism (Wang Jiren et al., 2008, Zhang Yugui et al., 2007).

3. THE DESIGN OF THE SIMULATION DEVICE

The outburst simulation device consists of the outburst model system, vacuum pumping and gas injection system, stress loading system, stress testing system, gas pressure testing system, temperature testing system, the electromagnetic and radiation measurement system, high speed photography system, and the data acquisition, control and processing system. A system diagram of the coal and gas outburst simulation device is shown in Figure 2.

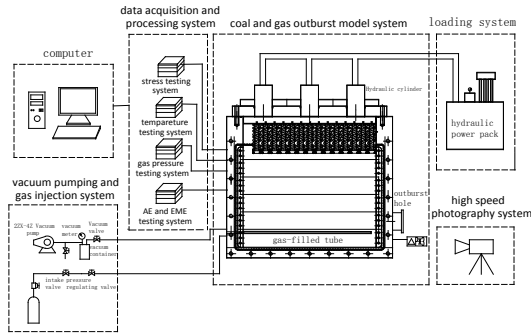
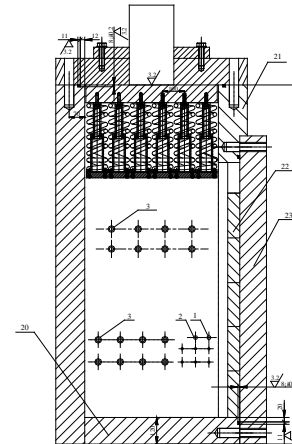
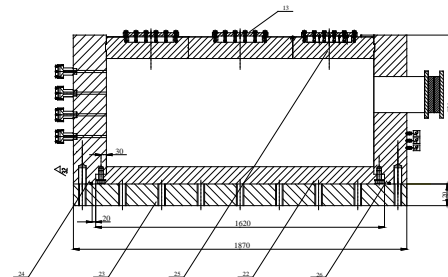


Figure 2: System diagram of simulation device.

The cavity size of outburst model system is 1500 mm x 600 mm x 1000 mm. The various physical parameters are tested through sensors such as temperature, gas pressure, stress cell, electromagnetic radiation, and acoustic emission and so on. The roof and floor of the coal seam can be simulated using similarity material. A series of springs are installed between the loading piston and the top of the roof to simulate the real roof stress distribution of coal in front of mining face. The front cover plates consist of two layer cover plates. The outboard plate is used for sealing. The inboard plates consist of five small plates, which are used for compression molding of coal, roof, and floor. The height of the small plate is 20 cm. Blasting sheet and clamping devices need to be installed at the outburst hole. Coal and gas outburst can be induced through fast blasting of the blasting sheet at a prescribed gas pressure. Three observation windows are installed on the device for the recording of the high-speed camera. Three inflatable tubes are carried evenly in the coal sample in the process of coal forming. A structure diagram and physical diagram of the coal and gas outburst simulation device are shown in Figure 3 and 4.



(b) Side view of simulation test device



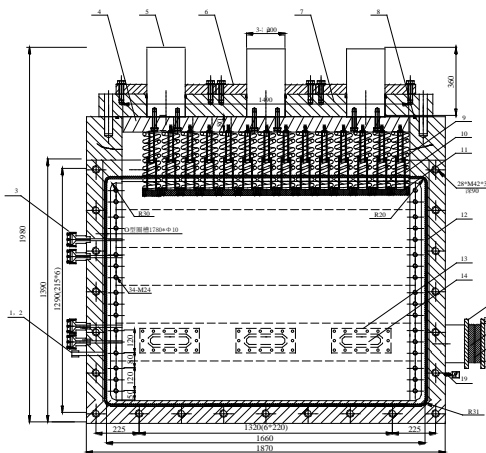
(c) Top view of simulation test device

1-vacuum interface 2-charging port 3-patch board 4-big press plate 5-hydraulic piston 6-piston base 7-upper cover plate 8-sealing ring of upper cover plate 9-spring group 10-guiding mechanism of spring 11-small press plate 12-sealing ring of front cover plate 13-fixing mechanism of observing window 14-glass observing window 15-inner flange of outburst hole 16-outer flange of outburst hole 17-clamping device of blasting sheet 18-blasting sheet 19-differential pressure sensor 20-floor 21-front supporting plate 22-inner front cover plate 23-outer front cover plate 24-the left side plate 25-the rear side plate 26-the right side plate

Figure 3: Structure diagram of coal and gas outburst simulation device.

4. THE TEST CASE

Two successful tests were conducted through coal and gas outburst simulation test device. The coal samples were from 2# coal seam in Zhenxing Er coal mine and 2# coal seam Dashucun coal mine. The coal samples were crushed into a 1mm particle size, in the laboratory. The floor was laid by similarity material. The molding stress was 20 MPa, and the loading stress was sustained for 30 min. The crushed coal sample was placed into the cavity layer by layer. The molding stress is 20 MPa, and the loading stress was sustained for 30



Front view of simulation test device

(a)

min. The roof was laid by similarity material. The molding stress was 20 MPa, and the loading stress was sustained for 30 min. In the two tests, the weights of the coal sample and similarity material are 1109 Kg and 1186 Kg, respectively. After the model was completed, it was dried for fifteen days. After leakage detection was successful, the cavity was vacuumed. Carbon dioxide with 99.99% concentration was aerated into the cavity, and adsorption equilibrium was ensured. Adsorption equilibrium pressure was 0.4 MPa and 0.6 MPa, respectively. The time for adsorption equilibrium was 7 days and 13 days. The blasting pressure of the blasting sheet was 0.5 MPa and 0.74 MPa. After adsorption equilibrium, gas was aerated to the blasting pressure continuously and blasting sheet bursts and the outburst occurred. The state diagram during the coal and gas outburst experiment and the distribution of the coal sample after coal and gas outburst are as shown in Figures 5 and 6.



Figure 5: The state diagram during coal and gas outburst experiment.



Figure 6: the distribution map of coal sample after outburst.

The results were as follows:

(1) The weight of coal sample and rock sample that was ejected outside the cavity was 369.9 Kg and 373.6 Kg respectively in the two tests.

(2) The shape of the outburst hole was pear-shaped with a small opening and big cavity.

(3) The coal sample and rock sample that were ejected outside the cavity present obvious sorting features. The sample with big particles was near the outburst hole and the sample with small particle was far from the outburst hole.

(4) The sample which was ejected outside showed axisymmetric fan-shaped distribution and the center line

of the outburst hole was the symmetry axis. The farthest ejection distance of sample from the outburst hole was 41.4 m and 49.5 m, respectively.

5. CONCLUSIONS

Development, purpose, ideas, and scheme design of a coal and gas outburst similar simulation device were introduced in detail based on similar devices at home and abroad. The functions are as follows:

(1) To study the laws of roof break development and stress evolution during outburst process by simulating coal seam, roof and floor with similar material. (2) To simulate stress distribution of a roof at high strength springs of different sizes. (3) To realize the uniform adsorption in coal by three gas injection pipes that were pre-buried. (4) To induce coal and gas outburst at a predetermined gas pressure. (5) To observe and record the fracture and migration process of coal in the cavity during outburst, achieved using a visual glass window on the side of the cavity.

6. REFERENCES

Аируни.(1955). А Тидр Отдел рудничной аэолгии лабораия взапных выбросов утляигаза. Москва Институт Горного Дела Академии НаукСССР, pp. 128-132.

Beamish BB, Crosdale PJ. (1998). Instantaneous outbursts in underground coal mines:an overview and association with coal type. *International Journal Coal Geology*, volume 35, pp. 27–55.

DOI: 10.1016/S0166-5162(97)00036-0

CAI Chenggong. (2004). Study on three dimensional simulation experiment of coal and gas outburst. *Journal of China Coal Society*, 29(1), pp. 66–69.

DOI: 10.13225/j.cnki.jccs.2004.01.015

DENG Quanfeng, LUAN Yongan, WANG Youan. (1989). Experimental study of simulation of coal and gas outburst. *Safety in Coal Mines*, volume 11, pp. 5–10.

GUO Liwen, YU Qixiang, JIANG Cheng-lin, et al. (2000). Experimental study of temperature change in the process of coal and gas outburst. *Journal of Rock Mechanics and Engineering*, 19(3), pp. 366–368.

HU Qianting, ZOU Yinhui, WEN Guangcai. (2007) New technology of outburst danger prediction by gas content. *Journal of China Coal Society*, 32(3), pp. 276–280.

DOI: 10.13225/j.cnki.jccs.2007.03.012

JIANG Chenglin. (1994). The research of shell instability mechanism of dynamic phenomenon in the process of rock cross-cut coal containing gas uncovering. Xuzhou: China University of Mining and Technology, pp. 62-63.

JIANG Chenglin. (2003). Study of forming mechanism of outburst hole. *Chinese Journal of Rock Mechanics and Engineering*, 19(2), pp. 225–228.

MENG Xiangyue, DING Yansheng, CHEN Li, et al. (1996). Study on two dimensional simulation experiment of coal and gas outburst. *Journal of China Coal Society*, 21(1), pp. 57–62.

DOI: 10.13225/j.cnki.jccs.1996.01.011

Norbert Skoczylas. (2012). Laboratory study of the phenomenon of methane and coal outburst. *International journal of rock mechanics & mining sciences*, volume 55, pp. 102-107.

DOI: 10.1016/j.fuel.2010.11.004

SHI Ping. (1985). Study on model and theory of coal and gas outburst mechanism. The 21st international conference on coal mine safety research, pp. 83-87.

Sobczyk J. (2011). The influence of sorption processes on gas stresses leading to the coal and gas outburst in the laboratory conditions. *Fuel*, volume 90, pp. 1018–1023.

DOI: 10.1016/j.fuel.2010.11.004

TAO Yunqi. (2009). Study on the gassy coal thin coupling model and coal and gas outburst simulation. Chongqing: Chongqing University, pp.73-72.

WANG Dengke. (2009). Research on constitutive models and instability rules of gas-saturated coal. Chongqing: Chongqing University, pp.56-57.

WANG Gang, WU Mengmeng, WANG Haiyang, et al. (2015). Sensitivity analysis of factors affecting coal and gas outburst based on a energy equilibrium model. *Journal of Rock Mechanics and Engineering*, 34(2), pp. 238-247.

DOI: 10.13722/j.cnki.jrme.2015.02.003

WANG Jiren, DENG Cunbao, DENG Hanzhong. (2008). Study on microscopic mechanism of coal and gas outburst. *Journal of China Coal Society*, 33(2), pp. 131–135.

DOI: 10.13225/j.cnki.jccs.2008.02.016

WANG Zhirong, SUN Lingxia, SUN Long. (2014). Mechanism of delayed coal and gas outburst on working face in “three soft” mining area. *Journal of China University of Mining & Technology*, 43(1), pp. 56-63.

DOI: 10.13247/j.cnki.jcumt.000027

WEI Chunfu, LI Huamin, YUAN Ruifu. (2014). Gas pressure effect in the process of coal and gas outburst. *Coal Geology & Exploration*, 42(6), pp.24-28.

XU Jiang, TAO Yunqi, YIN Guangzhi. (2008). Development and application of coal and gas outburst simulation test device. *Journal of Rock Mechanics and Engineering*, 27(11), pp. 2354-2362.

YING Guangzhi, ZHAO Hongbao, XU Jiang, et al. (2009). Experimental study of simulation of coal and gas outburst. *Journal of Rock Mechanics and Engineering*, 28(8), pp. 1674-1680.

ZHANG Jianguo, WEI Fengqing. (2002). The experiment of coal and gas outburst of coal seam containing gas. *Mining Safety & Environmental Protection*, 29(1), pp.7–10

ZHANG Yugui, ZHANG Zimin, CAO Yunxing.

(2007). Deformed coal structure and control to coal-gas outburst. *Journal of China Coal Society*, 32(3), pp. 281–284.

DOI: 10.13225/j.cnki.jccs.2007.03.013

The distribution and origin of hydrogen sulfide abnormal enrichment coal mines in China

Deng Qigen^{a,b*}, Liu Mingju^{a,b}, Zhang Sai^a, Cui Xuefeng^a, Wen Jiejie^a

^aSchool of Safety Science and Engineering, Henan Polytechnic University, Jiaozuo, China, 454003

^bState Key Laboratory Cultivation Base for Gas Geology and Gas Control (Henan Polytechnic University), Jiaozuo, China, 454003

ABSTRACT

Coal mines that contain hydrogen sulfide (H₂S) are widely distributed in China. At present they are mainly located in Zaozhuang in east China, Xin'an, Anyang, and Shuangfeng in central China, Qinshui basin, Taiyuan - Liulin and Wuhai in north China, and Tongchuan-Xianyang area in northwestern China, as well as places such as Shizuishan, Houdon, Changji, Liuhuanggou, and Sikeshu which belong to Xinjiang, mainly in northwest China. These coal mines are showing a rapid increase. The contents of H₂S in coal mines has changed greatly, from 10 ppm to 5000 ppm. The abnormal coal seams are mainly distributed in the Permian Longtan Formation of southwest China, Permian Shanxi Formation and Carboniferous Taiyuan Formation of east, north and central China, and Jurassic Xishanyao and Yan'an Formation of northwest China. The abnormal areas have a favourable overlying strata, and the hydraulic connections between the underground water and other aquifers are weak, therefore, they are good thick reservoir-seal combinations, which are beneficial to the origin of Bacterial Sulfate Reduction (*BSR*) or Thermochemical Sulfate Reduction (*TSR*). The main origin of H₂S in coal mines are *BSR* or *TSR*, and the origin model can be identified synthetically via the tectonic evolution, coal thermal evolution history, isotopic characteristics of carbon and sulfur, methane gas component testing, sulfate sources, and sulfate-reducing bacteria activity features.

KEYWORDS: coal mine; hydrogen sulfide; distribution; origin; *BSR*; *TSR*

1. INTRODUCTION

Disasters and the potential hazards caused by the abnormal enrichment of hydrogen sulfide (H₂S) frequently occur in coal mines in China as well as abroad. In recent years, more than 30 sudden releases of H₂S has been recorded in 10 provinces in China, such as in Guizhou, Sichuan, Shandong, Henan, Shanxi, Shaanxi, Inner Mongolia and Xinjiang, etc. These incidents have caused more than 20 casualties. In addition, a considerable number of coal mines experiencing the abnormal enrichment of the low content of H₂S do not cause serious casualties, and thus do not call up widespread concern. H₂S acts as a kind of potent nerve poison upon contact. The main target organs, on which its toxicity has an effect, are the central nervous system and the respiratory system. The tissues that are the most sensitive to the toxicity are the brain and the contact sites of mucous membranes, thus, H₂S can cause systemic poisoning, or even respiratory arrest (Ma et al., 2008; Liu et al., 2011). In the long term, it poses a serious threat to the miners' occupational health and safety. Therefore, conducting research like geological surveys, distribution characteristics, and causes of coal mines

that are rich in H₂S is an urgent issue and has important significance.

2. DISTRIBUTION OF COAL MINES OF HYDROGEN SULFIDE ABNORMAL GATHERING IN CHINA

In China, coal mines that are rich in H₂S are widely distributed. The statistics concerning partial coal mines containing H₂S are as shown in Table 1.

Table 1: Distribution characteristics of hydrogen sulfide abnormally accumulated in China's coal mines.

Coal mines	Coal forming environment	Reservoir layer	H ₂ S (ppm)	S (%)	R ₀ (%)	Abnormal zone
Xintian of Guizhou	Sealand	Longtan	20	0.98~7.91	3.50~3.80	Drilling process
Longtan of Sichuan	Marine facies	Longtan	1300	2.14~4.52	1.44~1.88	Working surface
Guang'an of Sichuan	Marine facies	Longtan	2500	2.01~5.26	1.21~1.79	Aquifer of roof
Anyang of Henan	Littoral zone	Shanxi	--	0.51~0.98	1.94~3.22	Working surface
Xin'an of	Littoral	Shanxi	--	1.80~2.30	1.02~	Drilling

*Corresponding author – email : dengqigen@hpu.edu.cn

Henan	zone				2.32	process
Cuizhuang of Shandong	Sealand	Shanxi	5000	0.65~0.83	0.65~1.25	III mining area
Shandong Bayi	Sealand	Shanxi	1500	2.68	0.59~1.24	Well area
Xiqu of Shanxi	Sealand	Taiyuan	350	Low-medium	0.98~1.60	Working surface
Wuda of Inner Mongolia	Sealand	Taiyuan	400	1.56~6.69	0.81~1.22	Mining area
Xishan of Urumqi	Continental facies	Xishanyao	1500	Low-medium	0.64~0.79	Mining area
Tingnan of Shaanxi	Sealand	Yan'an	56	0.13~2.90	0.51~0.72	Working surface

Currently, the known coal seams that contain high levels of H₂S mainly are Permian Longtan Formation in southwest China, Permian Taiyuan and Carboniferous Shanxi Formations which are in east, north, and central-south China, and Jurassic Xishanyao and Yan'an Formations in northwest China. Xinjiang is not only the region with the most coal mines that contain H₂S in China, but also the region which has the largest number of mines with an abnormal gathering of H₂S in China. In China, most coal mines are hydrogen sulfide-bearing gas reservoirs or micro hydrogen sulfide-bearing gas reservoirs (Dai, 1985).

3. CHARACTERISTICS OF TYPICAL HYDROGEN SULFIDE ABNORMAL GATHERING COAL MINES IN CHINA

The three necessary conditions for the production of BSR are plenty of organic matter, abundant sulfates, and conditions that suit sulfate reducing bacteria to grow and reproduce (Machel, 2001; Cai et al. 2003; Oayer, 1999). The $\delta^{34}\text{S}$ value of H₂S in the coal mines mainly depends on the characteristics of sulfur isotopic composition of the sulfur source itself, the abundance of sulfur in the sulfur source, and the genesis model of H₂S in the gas generation medium. The $\delta^{34}\text{S}$ value of H₂S and pyrite is generated by BSR, as the alienation effect of sulfate-reducing bacteria can result in the large-scale sulfur isotope fractionation, so the isotopic composition of this sulfur is usually negative. The fractionation of the H₂S $\delta^{34}\text{S}$ value usually can reach the range of -30% - -15%, which is generally around 20% lower than the sulfur isotope of sulfate. Accompanying H₂S, the CO₂ gas component is generally lower, usually less than 5%. The carbon isotope of CO₂ has a lighter characteristic and the $\delta^{13}\text{C}_{\text{CO}_2}$ value is generally less than -5‰. The shape of the byproduct (pyrite) generated by BSR is generally spherical berry. The main hydrocarbon component in

methane gas is CH₄. The CH₄ usually has biogenic features and its accompanying hydrocarbon may have many heavy hydrocarbon components (C₂₊). The generation and preservation reservoirs of H₂S may have traces of biological effects.

The three basic conditions for the origin of TSR are the higher temperature that coal and rock strata experience, plenty of hydrocarbon organic matter, and the abundant supply of sulfates (Liu et al. 2011; Machel, 2001; Cai et al., 2003; Oayer, 1999; Zui et al. 2006). The $\delta^{34}\text{S}$ value of H₂S generated by TSR is usually larger. The sulfur isotopic compositions of H₂S are slightly less than or equal to the $\delta^{34}\text{S}$ value of the homologous sulfate, and the $\delta^{34}\text{S}$ value of H₂S is generally between 10‰ and 20‰. The coal and rock strata generally experience environments of high temperatures above 120°. Accompanying H₂S, the carbon isotope composition of CO₂ is heavier and usually around 0‰. It is often similar to the carbon isotopic composition of carbonates in strata. The shape of pyrite generated by TSR is usually cubic or columnar. Since TSR is a process which gives priority to the consumption of heavy hydrocarbons, the dry coefficient of the methane gas is usually higher. The content of heavy hydrocarbons in the gas is less, but the content of non-hydrocarbon generally increases.

3.1 Characteristics of H₂S in Xiqu coal mine of Shanxi Province

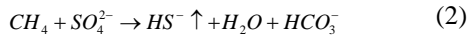
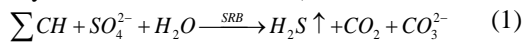
The location map of Xiqu coal mine of Shanxi Province is shown in Figure 6. The No. 9 coal seam is located at middle and lower part of the Taiyuan formation and is high grey, medium-low sulfur. The average sulfur content in raw coal is 1.37%. The main type of coal is coking coal, and the average value of the maximum vitrinite reflectance of coal ($R_{o,max}$) is 1.60% (Liu et al. 2012). The roof and floor is mostly sandy shale or mud sandstone. The abnormal area of H₂S in the No. 9 coal seam is located in a wide and gentle folding wing of the 19101 and 19102 working face in the south panel. It presents the zonal distribution and its width is about 400 m. In the leeward side of the mining machine, the maximum concentration of H₂S measured is up to 350 ppm^[10]. In the gas produced by spontaneous combustion of the ground coal gangue piles, the content of H₂S reaches 89 ppm (Zeng et al. 2012). Within the area of the above two working faces, the geological structure is simple and it has no faults collapse column, but in the northwest side of the faces, it develops a large number of faults and collapsed pillars. The biggest slip of fault is 5.0 m and the slip of the small secondary fault is in the range of 1.0 m - 2.0 m. The inside of the collapsed pillars which formed in Yanshan movement period are often found to be filled by the later generated

epigenetic calcite and pyrite crystals. The subsided columns are finely cemented, and less permeable to water in the deep.

The overlying seam of the abnormal area of H₂S in the No. 9 coal seam is the gob area of No. 8 coal seam whose thickness is 8 m – 12 m. The average sulfur content in No. 8 coal seam is 2.57% (pyrite accounts for 1.58%, organic sulfur accounts for 0.98%) (Song et al., 2000). The distribution of Pyrite is in an irregular grain shape (tetrahedral) and mouldiness. The roof of No. 8 coal seam is composed of limestone, mudstone, carbonaceous mudstone or sandy mudstone. Its floor is composed of sandy mudstone or shale, and some is carbonaceous mudstone or sandstone.

The groundwater of coal mine is acidic, where sulfate ions are abundant and the content is up to 1928.9 mg/L, much higher than that in other water bodies, such as the deep groundwater and the Fen River Reservoir (Yang et al., 2013). The content of Na⁺ increases significantly, and the content of HCO₃³⁻ declines dramatically. The total hardness of water is high and the type of water is Na-Ca-SO₄.

Sulfate-reducing bacteria reduction is a process which consumes sulfate ions constantly. The process that generates H₂S is as shown by formulas (1) and (2) (Cai et al., 2003; Oayer et al., 1999; Pan et al. 1992; Rye, 2005; Dai et al., 2000).



Formulas (1) and (2) shows that if the H₂S is caused by BSR, during the reduction process, the sulfate ions in the water body will usually reduce and the content of CO₃²⁻ and HCO₃³⁻ will increase. This is in contradiction to the fact that in this area, sulfate ions obviously increase, and the content of HCO₃³⁻ decreases. Therefore, the BSR cause can be initially ruled out. In the groundwater of the original Gujiao No. 2 and No. 3 mines, the values of δ³⁴S are in the range of 8.2‰ - 11.6‰ (Pan, 1989), with all of the values being positive. They do not have the characteristics of BSR. In the process of coal and rock formation, this area does not exhibit magma intrusion, so the magmatic origin can be excluded.

The metamorphic degree of regional coal is high metamorphic focal smoke, and the average value of the maximum vitrinite reflectance of coal (R_{o,max}) is over 1.5%. According to the corresponding relation between vitrinite reflectance and temperature, the coal and rock should has experienced a thermal evolution environment with temperatures of over 120°, in order to have the temperature conditions of TSR. Regional water and coal petrography are rich in sulfate ions. The roof of No. 8 coal seam is limestone (good reservoir stratum), and it has plenty of

hydrocarbon compounds. Every condition that is necessary for the occurrence of TSR is met. The δ³⁴S value in groundwater is about 10‰, has the characteristics of TSR genesis. Therefore, according to the changes of temperature, sulfur isotope characteristics, and sulfate ions in water bodies, it is possible that the generation of H₂S in this area is caused by TSR. However, it should not be ruled out that, due to the effect of microbe assimilation reduction in the gob area of No. 8 coal seam which is the overlying adjacent layer, the H₂S generated under the role of corrupt migrated to the abnormal enrichment zone of No. 9 coal seam by the mining fissure.

3.2 Characteristics of H₂S in Xishan coal mine of Xinjiang Uygur Autonomous Region

Xishan coal mine of Xinjiang is located in the binding sites which combine the middle of the Southern Junggar Basin with the northern Tianshan. Its location map is shown in Figure 6. The main coal bearing strata of mines are the lower segments of Xishanyao formation of Jurassic system middle Triassic, and belong to coal formations in terrestrial facies. Most of the coals belong to the range of middle - ultra low sulfur. The reflectance of coal vitrinite (R_o) is in the range of 0.64% - 0.79%, so coals belong to the low rank bituminous coal. Each coal seam in this region exhibits the abnormal enrichment of H₂S. The concentration of H₂S is not distributed evenly, having distinct subdivision and zoning phenomenon. The underground water of mines is rich in H₂S. The methane gas in coal seams is mainly composed of N₂ and CH₄, accompanied with CO₂ and heavy hydrocarbon components, like C₂H₆, C₃H₈, and H₂S. In the gas component, CH₄ accounts for 2.42% - 86.5%, N₂ accounts for 15.91% - 73.68%, CO₂ accounts for 0.81% - 12.31%, H₂S accounts 0 ppm - 1500 ppm. One hour after blasting, the concentration of H₂S in the air flow reached 100ppm. At 0:00 on November 5, 2011, after blasting in the working face of the track uphill, due to the impact of the vibration, a lot of water and harmful gases suddenly rushed out from the roof of No. B₁₉ coal seam. The H₂S concentration in the air flow was up to 400ppm, and the gas concentration was up to 19.5%. Since in the process of H₂S generation, heavy hydrocarbons are preferentially generated, TSR thereby leads to the increase of the gas dry coefficient. Methane gas of Xishan coal mine is primarily wet gas, indicating that the genetic features of H₂S by TSR in the coal seams are not distinct.

The changes of H₂S concentration which are monitored daily in each point of mine are shown in Figure 1.

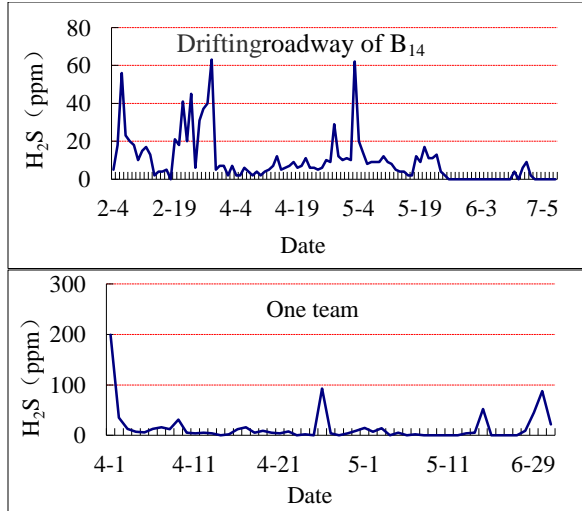


Figure 1: The monitored concentration of H₂S in the each point.

The testing of gas composition in No. B₇ coal seam by exploration holes was conducted in 2011 for Xishan coal mine. The results are shown in Figure 2.

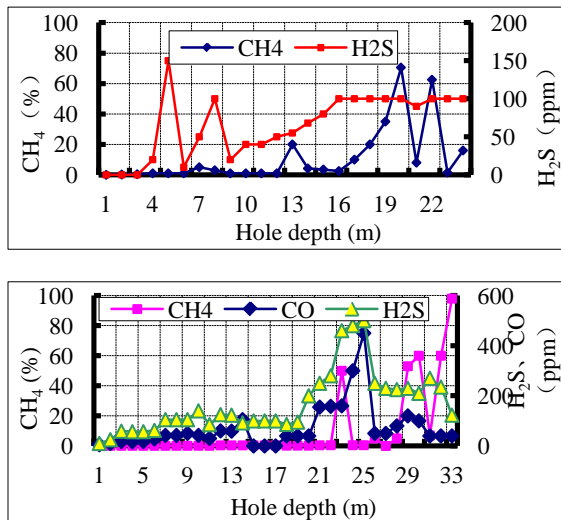


Figure 2: Gas composition of 1# and 3# exploration holes.

Figure 2 shows that, the maximum volume component of CH₄ measured by exploration holes is 98.0%. The maximum concentration of H₂S is 500ppm, and the maximum concentration of CO is 450ppm. The number of sulfate-reducing bacteria in the inspected samples of mines and adjacent mines is shown in Table 2 (Cheng et al., 2009). It is known that the SRB breed acts fiercely, so a large amount of H₂S will be generated by BSR.

Table 2: Distribution of SRB in the each mine of region.

Stage positions	Depth (m)	T (°C)	SRB (A/g sample)
Beishan coal mine-1	272.8	30	100
Xiaolongkou coal mine-1	312.0	55	3500
Beishan coal mine-2	209.5	55	650
Qitai coal mine-1	463.5	30	234
Xishan coal mine	563.0	25	235
Xishan coal mine	750.0	28	528

The values of carbon isotope $\delta^{13}C_{CO_2}$ of regional CO₂ change within the range of -18‰ - -11‰ (Dai, 1985), indicating that CO₂ in the region is a product of the carbonate decomposition leaching effect as well as the organic decomposition oxidizing effect. The CO₂ represents characteristics of organic origin, and also represents the genesis features of BSR. The $\delta^{34}S$ of pyrite in the each coal seam of region has a distribution range of -15.3‰ - +3.7‰, further confirming that the H₂S in the each coal seam of the study area is generated by BSR.

4. GENESIS CHARACTERISTICS OF HYDROGEN SULFIDE IN CHINA'S COAL MINE

Due to the geological movement and various chemical reductions in China, H₂S that is generated by biodegradation under the early accumulation of peat in the oxygen-rich conditions of the early coal-forming period is impossible to preserve in the coal rock strata.

The content of H₂S in the coal rock strata is concerned with the sulfur content in coal, and has a positive correlation with the content of sulfur in pyrite. Coals of the Permian Longtan group in the Province of Guizhou, Sichuan and Chongqing are mostly high-sulfur coal, and pyrite is widely developed. The sulfur content in Guiding coal of Guizhou Province is up to a range of 9.49% - 10.46%, and more than 70% of coals in Sichuan Province are high-sulfur coal. According to the Ministry of Environmental Protection of the People's Republic of China (<http://www.zhb.gov.cn>), acid rain mainly focuses on the south of the Yangtze River, Sichuan, and eastern Yunnan, including the Zhejiang, Fujian, Jiangxi, Hunan, etc., and cities of the Yangtze River, the Pearl River Delta region. Figures 3 and 4 show that high-sulfur coal producing areas have characteristics consistent with the distribution of acid rain in China (Deng et al., 2013).

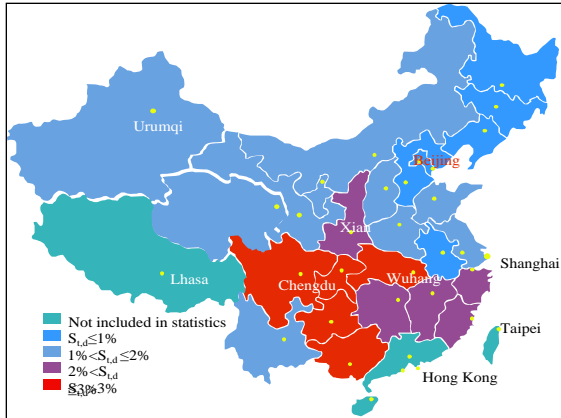


Figure 3: The distribution of sulfur in coal in China.

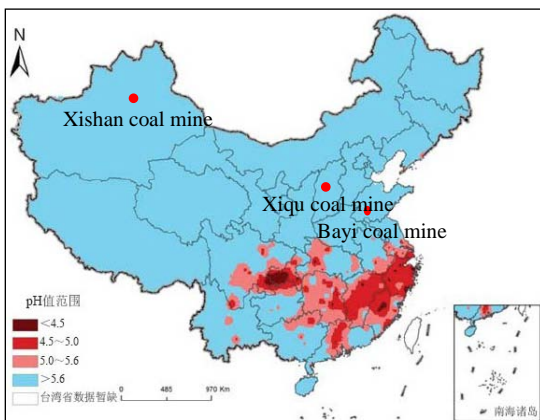


Figure 4: The contours of the annual average pH value in China in 2014.

In the high sulfur coal of the late Permian Longtan Formation in Guizhou Province, the $\delta^{34}S$ values of pyritic sulfur and organic sulfur are in the range of -30.30% - 62.69% and -13.43% ~ -10.87% respectively. The peak values of $\delta^{34}S$ in pyrite are in the range of -30.30% - -9.18% and 9.45% - 38.40% (Ni et al., 1999; Luo et al., 2005). These data suggest that the formation of the regional H_2S may experience the double genesis of *BSR* and *TSR*.

The sulfur content in coal has an increasing trend from the east to the west in China. In the three northeast provinces, coals have the lowest sulfur content and currently, coal mines in the region have not reported that H_2S is abnormal. The sulfur content in coal of the Carboniferous Taiyuan formation in the southwest of Shandong Province is mostly over 1%, and some are up to 5%. The maximum sulfur content in coal of the Permian Shanxi formation in the southwest of Shandong Province and in the Yongxia coal field which belongs to Henan Province is up to 3%. In the methane gas of the above regional coal

seams, sulfur isotopes have the characteristics of positive end, whose value is closer to the $\delta^{34}S$ of sulfate. It may be that under the action of thermal properties of the magmatic rock intrusion, the coal, sulfur-bearing organic matter, and sulphate rocks in the surrounding rock conduct the thermal chemical decomposition and the thermal chemical reduction to generate H_2S . For carboniferous coal seams in north China, the high sulfur coal is widespread. Types of coal are mostly coking coal and above. The average maximum vitrinite reflectance $R_{o,max}$ of coal from part of coal seams is over 1.2%, having the genesis conditions of *TSR*. For example, the coal rock strata of Qinshui basin in Shanxi Province may have experienced high temperatures of more than 268° , with the temperature generally being above 150° (Cheng et al., 2009). Through measurement of gas samples from the exhaust gas of the block surface well head in Fanzhuang and Panzhuang, the content of H_2S in the coal seam gas component is 0.0001% - 0.001%. The H_2S content in the desorbed gas of two coal samples from Sihe coal mine is 0.0001% and 0.0002%, respectively (Ma et al., 2008). Since H_2S can easily react with metal, the actual content of H_2S is much larger than the above data. The distribution of coal mines in which H_2S is caused by *BSR* is broader, such as Wuda of Inner Mongolia, Tingnan of Shaanxi Province and the vast region of Xinjiang Autonomous Region.

5. DISCUSSION AND PROSPECTS

The H_2S content in the coal rock strata is concerned with the sulfur content in coal, and has a positive correlation with the content of sulfur in pyrite. In the coal-forming environment of marine facies, the sulfur content in the coal rock strata is generally higher and H_2S is easy to generate and preserve. Due to the insufficient sulfur ion abundances and sufficient heavy metals, H_2S of coal formation in terrestrial facies is relatively difficult to generate, reserve and accumulate. The coal seams of Xishanyao Formation in Xinjiang Autonomous Region belong to terrestrial facies of coal. The H_2S in this region is abnormally accumulated and widely distributed. Therefore, conducting research on the causes and distribution of H_2S in coal, which belongs to terrestrial facies of coal, is particularly important.

The polarity characteristics of H_2S determine that the distribution (enrichment) of H_2S is controlled by many factors. The control action of factors in the abnormal gathering of H_2S in coal mines, such as, the regional structure, the nature of the reservoir cap, groundwater activity, temperature, and the burial depth of the coal seam should be considered synthetically.

At present, research on the mechanisms causing H₂S is still low. The genesis category of H₂S in the coal mine can be judged comprehensively by geologic and tectonic evolution, thermal evolution history of coal and rock series, characteristics of carbon and sulfur isotope, groundwater chemistry, methane component characteristics, source of sulfate, enrichment state of pyrite in coal and activity characteristics of sulfate-reducing bacteria.

Coal mines that contain H₂S are widely distributed in China. With the increasing depth of coal mining, the threat that H₂S poses to miners' occupational health as well as the safe and efficient exploitation of the mine is increasingly serious. Therefore, it is important to identify the genesis and distribution characteristics of hydrogen sulfide in coal mines as soon as possible, to ensure effective prediction and safety and efficient mining.

6. ACKNOWLEDGEMENTS

This work was supported by "National Natural Science Foundation (U1504403)", "the research of basic and cutting-edge technology of Henan Province (142300413210)" and "the Fundamental Research Funds for the Universities of Henan Province". In the study process, Deng, Q. is grateful to Professor Liu, M. of Henan Polytechnic University for his ardent guidance and help.

7. REFERENCES

Cai, C., Worden, R.H. and Bottrell, S.H., (2003). Thermochemical sulphate reduction and the generation of hydrogen sulphide and thiols (mercaptans) in Triassic carbonate reservoirs from the Sichuan Basin, China. *Chemical Geology*, Volume 202, pp. 39-57.

Cheng, J., Wang, X., Wang, X., (2009). The thermal history of the Qinshui basin in Shanxi province. *Geo Science*, 23 (6): pp. 1093-1099.

Dai, J. (1985). Distribution, classification and origin of natural gas with hydrogen sulphide in China. *Acta Sedimentologica Sinica*, Volume 3, No. 4, pp. 109-120

Dai, S., Ai, T. and Jiao, F. (2000). Components of sulfur isotopes and characteristics of sulfur evolution in Wuda coalfield Inner Mongolia. *Acta Petrologica Sinica*, Volume 16, No. 2, pp. 270-274.

Deng, Q., Liu, M. and Wang, Q. (2013). *Geochemistry Characteristics of Sulfur in Coals*. Disaster Advances, Volume 6, pp. 234-240.

Fu, X., Wang, W. and Yue, J. (2006). Genesis analyses of H₂S gas abnormality in gas of Bayi coal mine in Zaozhuang. *Journal of China Coal Society*, Volume 31, No. 2, pp. 206-210.

Liu, H., Liu, C., Wang, H., et al. (2006). Simulation experiment of biogenic gas in northwest

China. *Xinjiang Geology*, Volume 24, No. 2, pp. 149-152.

Liu, M., Li, G. and Hani M. (2011). Genesis modes discussion of H₂S gas in coal mines. *Journal Of China Coal Society*, Volume 36, No. 6, pp. 978-983.

Liu, G., Zhang, Z. and Song, Z. (2012). Adsorption experiments on CH₄ under the conditions of high temperature and pressure and equilibrium water. *Journal of China Coal Society*, Volume 37, No. 5, pp. 794-797.

Luo, Y., Li, W., Jiang, Y. (2005). Distribution of sulfur in coals of China. *Coal Conversion*, 28(3): pp. 14-18.

Ma, Yu., Tao, M. and Zhang, X. (2008). Hazard of H₂S and SO₂ contents in coalbed gas and natural gas. *Acta Geologica Sinica*, Volume 82, No. 10, pp. 1408-1411.

Machel H G. (2001). Bacterial and thermochemical sulfate reduction in diagenetic settings-old and new insights. *Sedimentary Geology*, Volume 140, pp. 143-175.

Ni, J., Hong, Y. (1999). Sulfur isotopic composition of late permian coal from Guizhou province[J]. *Geology Geochemistry*, 27 (2): pp. 63-69.

Oayer R A, Rose M, and Dehmer J. (1999). Impact of sulfur and trace element geochemistry on the utilization of a marine influenced coal: Case study from the South Wales Variscan foreland basin. *Inter.J Coal Geol*, pp. 151-157.

Pan, S. (1989). Application of stable isotope to the research on karst water in Taiyuan area, *Carsologica Sinica*, Volume 8, No. 2, pp. 151-155.

Pan, G., Dai, J. and Qi, H. (1992). Research on sour gas in China. *Natural Gas Geoscience*, Volume 3, No. 3, pp.1-10.

Rye R. O. (2005). A review of the stable-isotope geochemistry of sulfate minerals in selected igneous environments and related hydrothermal systems isotope properties of sulfur compounds in hydrothermal processes. *Chemical Geology*, Volume 215, No. 1-4, pp. 5-36.

Song, S., He, J. and Lu, M. (2000). The study of the Characteristic of sulfur in Xiqu coal and the probability of desulfur by preparation. *Coal Conversion*, Volume 23, No. 1, pp. 76-78.

Yang, Y., Meng, Z., Qin, Z., et al. (2013). Water resource destruction processes of mining in Shanxi province combining isotopic and hydrochemical tracer. *China Environmental Science*, Volume 33, No. 8, pp. 1447-1453.

Zeng, F., Tian Y., Lu, G., et al. (2012). Detection and control technology of spontaneous combustion area in coal rejects dump of Xiqu mine.

Coal Science and Technology, Volume 40, No. 6, pp. 41-43, 85.

Zhao, Y. and Zhang, C. (2011). H₂S gas control of Xiqu mine N0.9 coal seam. Coal Science and Technology, Volume 39, No. S, pp. 26-29.

Zhu, G., Zhang, Y. and Lian Y., (2006). Genesis and evidence of hydrogen sulfide in Weiyuan gas field of Sichuan basin. Chinese Science Bulletin, Volume 51, No. 23, pp. 2780-278.

Accumulation pattern of groundwater containing Hydrogen Sulfide in the southern Junggar basin in China

Deng Qigen^{a,b*}, Liu Mingju^{a,b}, Cui Xuefeng^a, Wen Jiejie^a

^a School of Safety Science and Engineering, Henan Polytechnic University, Jiaozuo, China, 454003

^b State Key Laboratory Cultivation Base for Gas Geology and Gas Control (Henan Polytechnic University), Jiaozuo, China, 454003

ABSTRACT

The surface water and groundwater flows from south to north to the interior basin in the midst of southern Junggar basin in China. The thick and loose gravel sand layer accumulates in the region, Tectonic depressions of echelon are arranged. Tectonic depression or basement uplift, under the control of hydrodynamic block gas, provides a large space for the occurrence and migration of groundwater (Hydrogen Sulfide). The water is rich in sulfate and chloride. Runoff, dissolution, and leaching may occur in the infiltration and runoff process, and under intense evaporation. The water with high salinity may form $HCO_3-Ca-Na$, $HCO_3-SO_4-Na-Ca$, $Cl\cdot SO_4-Na$, and $HCO_3-SO_4-Cl-Na-K$. The water rich in SO_4^{2-} , Cl^- , Ca^{2+} , Mg^{2+} and Na^+ through the hydrocarbon-rich zone ($\Sigma CH, C$), plays a role in geothermal warming. Under suitable geological conditions BSR or TSR may occur, and H_2S can be generated, resulting in a significantly lower concentration of calcium and higher concentration of hydrogen sulfide in the water.

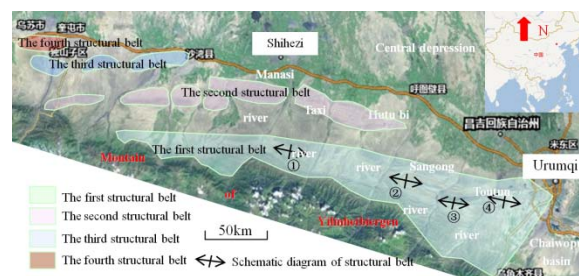
KEYWORDS : Southern margin of Junggar basin; Groundwater, Hydrogen Sulfide; Accumulation pattern

1. INTRODUCTION

The midst of southern Junggar basin lies in the combining site of southern Junggar and north Tianshan. The surface water and groundwater flows from south to north to the interior basin. Salinity and hardness is both in increase, while the concentration of Ca^{2+} reduces greatly. Hydrogen sulfide (H_2S) is rich in underground water. Although regional water containing hydrogen sulfide are widely distributed, the current understanding of the patterns of water containing hydrogen sulfide is still limited. Developing the accumulation pattern of hydrogen sulfide-bearing groundwater has theoretical significance and practical value.

2. REGIONAL STRUCTURE

Two or three belts of arching and syncline depression formed in the regional piedmont zone., These alternate with each other in the piedmont depression, and are divided into four secondary units, including, Shihezi sag, West of Urumqi piedmont fold belt, and Sikeshu sag (Jia et al., 2003; Fang et al., 2005; Wang et al., 2013). The lineament distribution and Tianshan fold belt direction structure consists of a series of syncline and anticline and thrust faults which lie east west-north east, as shown in Figure 1.



- ①Structural belt of Qingshuihe, ②Structural belt of Qigu,
③Structural belt of Changji, ④Structural belt of Kalazha

Figure 1: Regional structure in the midst of southern Junggar basin of China.

3. THE CHEMICAL CHARACTERISTICS OF WATER

The chemical composition, ion concentration, and salinity of groundwater have an important influence on the genesis and enrichment of H_2S . Sulfate ion is a sufficient condition in order for bacterial sulfate reduction (BSR) and thermochemical sulfate reduction (TSR) to occur. The chemical characteristics of groundwater in each coal mine of the study area from south to north are as shown in Table 1.

Table 1: Coal mine groundwater chemical properties from south to north basin areas.

Coal mines	Hydrochemistry type	Salinity (g/L)	H ₂ S (mg/L)	pH
Daxigou	SO ₄ -Cl-HCO ₃ -Ca	1.1	7.89-25.32	8.3
Qianshuihe	SO ₄ -Cl-Na	2.6	9.26-51.29	8.5
Liuhuanggou	SO ₄ -Cl-K+Na	3.5	23.89-69.45	8.5
Xishan	Cl-SO ₄ -K+Na	6.2	41.89-259.63	9.0

(1) The depth of groundwater in Toutun river becomes gradually more shallow from south to north. There is a large amount of water surface overflow and flow into big and small Quangou in the first belt of the structure, leading to the development of hot river in the first row structure. The H₂S is rich in the water. Along the flow direction, the chemical types of groundwater by HCO₃-Ca-Na, HCO₃-SO₄-Na-Ca water evolve into HCO₃-SO₄-Cl-Na-K.

(2) The water salinity and hardness of surface water and shallow groundwater goes from low to high from the mountains of Yilinheibiergen to the research area. The salinity starts at less than 1.0 g/L, and increases to more than 6.0 g/L. The pH value also gradually becomes larger, from 7.1 to 9.6. The water is weak alkaline saline water.

(3) The ion constants (except HCO₃³⁻) mass concentration components increase along the direction of deep confined water runoff. The cationic content of Na⁺ and K⁺ show a strong increasing trend, from 27.4% to 72.9%. The dominant evolution of Ca²⁺ dominant is given priority over Na⁺. Ca²⁺ is reduced to 21.2%, from 57.8%. Anionic concentrations (mainly HCO₃³⁻) are reduced, except for SO₄²⁻ and Cl⁻. HCO₃³⁻ is reduced from 73.5% to 48.1%. SO₄²⁻ increases from 19.3% to 30.2% and Cl⁻ increases from 6.7% to 13.3%. The evolution of the regional deep confined water chemical composition reflects the leached and the roles of cationic alternating adsorption effect on the evolution of deep confined water (Duan et al., 2007; Hou, 2001).

4. REGIONAL HOT SPRING (WELL) WATER FEATURES

New tectonic movement leads to the exposure of hot springs (well), most of which are fault springs. The water chemical characteristics of hot springs (well) in the study area are as shown in Table 2 (Wang, 1998; Gao et al., 2000; Xu 1994)..

Table 2: Water chemical characteristics of hot springs (well) in the study area.

Areas	Water chemical characteristics	H ₂ S (mg/L)	pH	Salinity (g/L)	T (°C)
Ergong	SO ₄ -HCO ₃ -Cl-Na	--	7.7	0.88	10.8
North gate	SO ₄ -HCO ₃ -Cl-Na+K	--	7.1	2.86	11.5

Maliaodi	SO ₄ -Cl-Na	--	7.2	2.86	10.4
Jianquangou	SO ₄ -HCO ₃ -Na+K	--	8.6	0.78	11.3
Shuimogou	Cl-HCO ₃ -SO ₄ -Na	135~204	9.6	1.66	19.5
Shuimogou	CO ₃ -HCO ₃ -Cl-Na	160~210	9.3	7.98	21.0
Hongyanchi	SO ₄ -HCO ₃ -Na	2.1~3.3	8.0	0.85	11.6
Hongyanchi	HCO ₃ -SO ₄ -Cl-Na	2.8~3.5	8.6	1.04	12.0
Gongyuan	SO ₄ -HCO ₃ -Cl-Ca+Na	--	7.6	0.86	10.4
Yongfengqu	Cl-Na+K	--		14.4	11.4
Daquangou	Cl-SO ₄ -HCO ₃ -Na	56.0~89.0	8.2	1.78	8.0
Baiyanghe	Cl-Na	6.4	7.3	0.44	35.8

As shown in Table 2, regional hot springs (well) are more exposed in the complex faults, anticline structure belt. Water is weakly alkaline and rich in H₂S, with the water chemical characteristics being HCO₃³⁻, SO₄²⁻, Cl⁻, and Na⁺.

5. ACCUMULATION MODEL OF WATER CONTAINING HYDROGEN SULFIDE

5.1 Hydrological control function in the region

The mountain of Yilinheibiergen is rich in ice and snow, which is the main source of groundwater. Surface water and groundwater flow from south to the north basin. Constituting a centripetal water system, the water system follows developed track extensional faults, where the end point is the northern edge of the desert, as shown in Figure 1.

The thickness of the regional quaternary sediments is about 400-1300 m. In the first and second structural belt between tectonic uplift, and the third and fourth structural belt format the echelon arrangement structure depressions there is a piled up thick and loose sand gravel layer. Sag tectonic or basement uplift provides a huge space for groundwater (H₂S) occurrence and migration. The groundwater circulation characteristics are as shown in Figure 2.

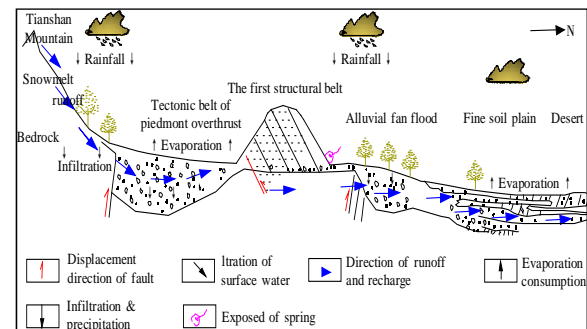


Figure 2: Characteristics of the water cycle in the region

Regional water types can be divided into loose rock pore water, clastic pore water, and fissure water. Local areas have the loess layer cross water, therefore

local groundwater is under pressure, Hydrogen sulfide has significantly higher solubility under stress conditions, resulting in the abnormal enrichment of water containing H_2S . On 0 o'clock November 5, 2011 in Xishan coal mine, after drilling and shooting on the mountain track working face a large amount of water and harmful gas suddenly poured out from the B₁₉ coal seam roof, due to the effect of the impact and vibration. Instantaneous H_2S concentration was as high as 400 parts per million, and the gas concentration was as high as 19.5%.

Regional hydrogeology controlling gas is the main factor in the effect of hydrodynamic seal controlling gas (Qiao et al., 2005), as shown in Figure 3.

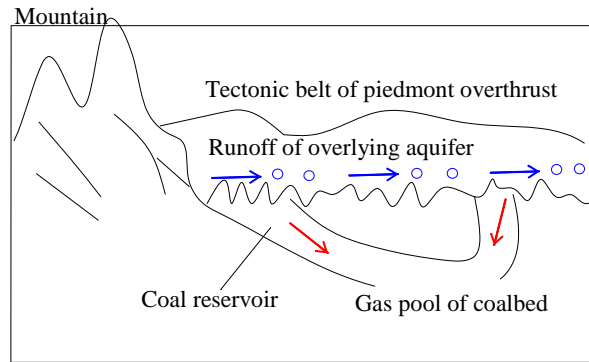


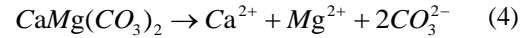
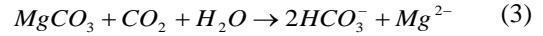
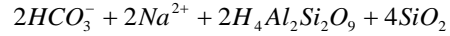
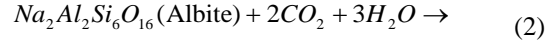
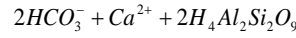
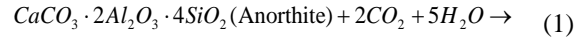
Figure 3: Regional hydrogeology controlling gas & archive mode of coalbed methane.

The groundwater accepts melting (surface water) supplies in sealing black bill root at the northern foot of the mountain strata outcrop, with bedding going from shallow to deep down the steep slope. Mudstone water-resisting layers develop at the top and bottom of the coal. The movement of the internal waters and gases are stopped due to the lithostatic pressure, which makes the coal seam permeability vary in the deep. In addition to the worsening continuity of sand body of surrounding rock, the coal bearing period of the groundwater movement was slow. Upward dissipation of H_2S in coal strata (gas) was blocked, and the groundwater carrying H_2S (gas) makes it move deeper, resulting in the abnormal concentration of H_2S in water and coal rock.

5.2 Regional lithologic control function

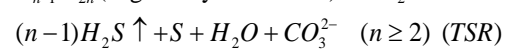
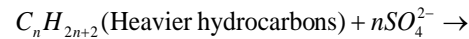
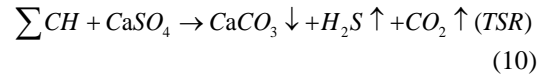
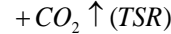
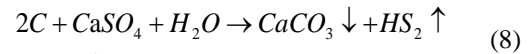
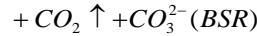
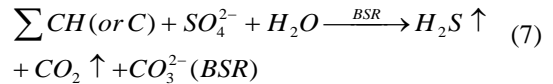
Most mountains towering in the southern region of the black bill mountain have snow and ice melt that is rich in SO_4^{2-} and Cl . Because the hydraulic gradient is large along the radial direction, the water exchange effect is strong. The make-up water with sulfuric acid salt rocks, silicate rock, carbonate rock, glauber's salt, and salt may be dissolved and leached

in the process of rainfall infiltration and runoff. The potential chemical reactions are expressed by reactions 1 to 6:



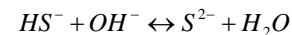
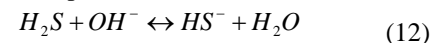
High salinity of HCO_3^- - Ca - Na , HCO_3^- - SO_4 - Na - Ca , Cl - SO_4 - Na and HCO_3^- - SO_4 - Cl - Na - K type water can be formed under the action of the above dissolution, leached and strong drought evaporation.

Deep confined water in a closed environment is relatively good, under the effect of revivification and microorganisms and thermodynamic factors. When sufficient hydrocarbon organic matter is in coal strata ($\sum CH$, C), under appropriate conditions like a suitable temperature range, BSR or TSR can occur (Liu et al., 2011; Deng et al., 2013). The hydrocarbon organic matter can react with sulphate, producing H_2S and other compounds. The possible reactions are as follows:



The result is lower Ca^{2+} concentration in groundwater, and the water becoming rich in H_2S and CO_2 .

The groundwater of the mines (district) area is weakly alkaline, but H_2S is acidic, so there may be a balanced relationship as shown in reaction (12).



Groundwater is blocked near the fault, and water that is rich in H_2S (spring) is exposed on the surface. The accumulation mode of water containing H_2S in the region is as shown in Figure 4.

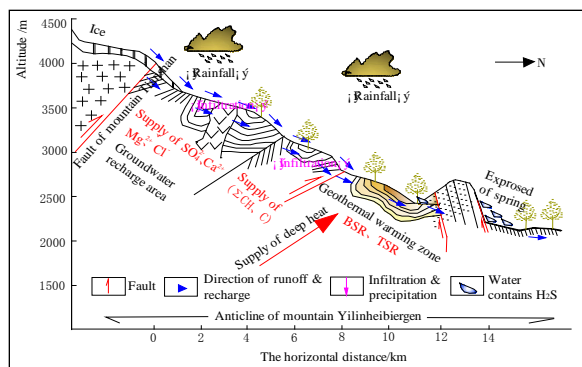


Figure 4: Accumulation mode of water containing hydrogen sulfide in regional

6. CONCLUSIONS

(1) The surface water and groundwater flows from south to north to the interior basin of southern Junggar basin. The thick and loose gravel sand layer accumulates in the region. Tectonic depressions of echelon are arranged. There is tectonic depression or basement uplift, under the control of hydrodynamic block gas, which provides a large space for the occurrence and migration of groundwater (Hydrogen sulfide).

(2) The water rich in SO_4^{2-} and Cl along the radial direction can form high salinity type water of $HCO_3-Ca-Na$, $HCO_3-SO_4-Na-Ca$, $Cl \cdot SO_4-Na$, and $HCO_3-SO_4-Cl-Na-K$ under the action of the dissolution, leached, and strong drought or evaporation reactions.

(3) When water rich in SO_4^{2-} , Cl , Ca^{2+} , Mg^{2+} , and Na^+ flows through the area rich in hydrocarbons (ΣCH , C), BSR or TSR may occur. H_2S may then be produced in proper geological conditions, which lead to a large loss of Ca^{2+} in water, but a large increase of hydrogen sulphide in the water. Therefore, it is possible to draw the accumulation pattern of water containing H_2S .

7. ACKNOWLEDGEMENTS

This work was supported by “National Natural Science Foundation (U1504403)”, “the research of basic and cutting-edge technology of Henan Province (142300413210)” and “the Fundamental Research Funds for the Universities of Henan Province”. In the study process, Deng, Q. is grateful to Professor Liu, M. of Henan Polytechnic University for his ardent guidance and help.

8. REFERENCES

Deng, Q., Wang, Q. and Liu, M. (2013). Geological Factors Controlling H_2S in Coal Seams. Germany, October 14-19, C. Drebenstedt and R. Singhal (eds.), Springer International Publishing Switzerland, pp. 12: 619-625.

Duan, L., Wang, W. and Cao, Y. (2007). Hydrochemical Characteristics and Formation Mechanics of Groundwater in the Middle of Northern Slope of Tianshan Mountains. Journal of Arid Land Resources and Environment. Volume 21, No. 9, pp. 29-34.

Fang, S., Jia, C. and Guo, Z. (2005). The southern margin of Junggar basin thrust belt structure form the initial set time. Earth Science Frontiers. Volume 12, No. 3, pp. 66.

Gao, X., Xu, Q. and Zhang, X. (2000). Urumqi fluid observation of 10 spring and reflected shock sensitivity preliminary analysis. Inland Earthquake. Volume 14, No. 3, pp. 43-251.

Hou, S. (2001). Chemical Characteristics of Precipitation at the Headwaters of the Urumqi River in the Tianshan Mountains. Journal of Glaciology and Geocryology. Volume 23, No. 1, pp. 80-84.

Jia, C., Wei, G. and Li, B. (2003). Tectonic evolution of two phases foreland basins and its control for natural gas accumulation in China midwestern areas. Acta petrolei Sinica. Volume 24, No. 2, pp. 13-17.

Liu, M., Deng, Q. and Zhao, F. (2011). Origin of hydrogen sulfide in coal seams in China. Safety Science, pp. 1031-1038.

Qiao, X., Wang, W. and Chen, Y. (2005). Storage water structure modes and water cycle characteristic on Tianshan Mountain foot. Journal of Earth Sciences and Environment. Volume 27, No. 3, pp. 33-37.

Wang, D. (1998). Tianshan region ground water level dynamic anomalies of sensitive preliminary analysis (new 04 well for example). Inland Earthquake. Volume 2, No. 3, pp. 235-239.

Wang, T., Jia, C. and Guo, Z. (2013). Mesozoic inverted structure analysis of the southern margin of the Junggar Basin. Chinese Journal of Geology. Volume 48, No. 1, pp. 176-190.

Xu, Q. (1994). Research of Urumqi spring 4 transgression. Inland Earthquake. Volume 10, No. 1, pp. 57-60.

Application research on gas drainage technology at low permeability coal seam

Shengchu Huang, Li Zhang*

China Coal Strategies Research Center & China Center for Occupational Safety and Health, Beijing, China, 100713

ABSTRACT

Gas drainage at low gas permeability coal seams is a main barrier affecting safety and efficient production in coal mines. The research and application of drainage technology in low gas permeability coal seams is key for coal mine gas control. In order to improve the drainage effect, this paper establishes a three-dimensional solid-gas-liquid coupling numerical model and studies the gas drainage amount of different schemes inside the overburdened rock around the goaf. Yangquan mine area is chosen as the research target, and the gas movement regularity and emission characteristics are comprehensively analyzed, as well as the stress and fissure variation regularity, the scope of released gas movement, enrichment range, and movement regularity during coal extraction. Then the gas drainage technology and parameters for the current coal seam are studied. After measuring the gas drainage amount in-situ, it was found that the technology can achieve notable drainage results, where gas drainage rate increase by 30%~40% for low permeability coal seams.

KEYWORDS: gas drainage; low permeability; ground drilling holes; coupling model; abutment stress

1. INTRODUCTION

Mine gas incidents are the main disaster associated with coal mines. Mine gas extraction in China is difficult due to characteristics such as micro-porosity, low-permeability, and high adsorption of coal seams. However, coal seams in most coal mining areas belong to difficult-to-drain coal seams with low permeability, making it difficult to conduct pre-drainage as the drainage efficiency is quite low. Gas drainage in low permeability coal seams is a main barrier affecting safe and efficient production in coal mines. Therefore, the research and application of drainage technology in low gas permeability coal seams is a key technical problem in coal mine gas control.

Wang et al. (2014) studied the Klinkenberg effect of coal seams and raised an improved model. Alam et al. (2014) studied the change of permeability induced by the change of confining pressure. Wang et al. (2014) studied and utilized the drainage technology for high gas and low permeability. Guo et al. (2013) also studied methods of predicting the permeability of coal seams. Through experiments Chen et al. (2013) discussed the development of damage and permeability in coal. Other scholars have also studied coal seam permeability (Gu and Chalaturnyk, 2010; Liu and Chen et al., 2010; Liu and Rutqvist, 2010; Wang and Wei et al., 2010; Cappa and Rutqvist, 2011; Liu and Chen et al., 2011; Wang and Elsworth et al., 2011; Mitra and Harpalani et al., 2012; Pan and Connell, 2012; Aziz, 2013; Wang and Elsworth et al., 2013)

In this paper, the solid-gas-liquid coupling model will be employed to study the permeability of the coal seam

in Yangquan Coal mine, and the gas drainage procedures will be addressed. At the same time, the measurements in-situ will help to test the coupling model and the drainage technology utilized in the coal mine.

2. THE SOLID-GAS-LIQUID COUPLING MODEL

2.1. The measuring method for properties of low permeability coal seam

The initial speed of methane emission (Δp) is one of the predictions of risk indicators in coal and gas outburst. It can reflect the speed of coal body containing gas radiation gas and uses WT-1 gas diffusion velocity test system to measure. In addition, the competent coefficient of coal shown soundness of coal. The methane adsorption constants on coal were measured by the isothermal adsorption instrument so as to obtain adsorption constants a and b .

2.2. The analysis of gas distribution patterns by using the coupling model

Surface borehole well drawing gas is chiefly used in mining face goaf gas extraction. However, gas reservoirs and flow patterns depend on the motion features and the movement rule of overlying strata. As is well known, the moving crack of overburden can be divided into three vertical zones and cross three areas caused by mining. The three vertical zones were distributed from the bottom to the top of the caving zone, fault zone, and bending zone along the roof

*Corresponding author-email: zhangli@ccsr.cn

of the goaf in the vertical direction, while the cross three areas were divided into the area effected by the solid, separation area, and recompaction zone along the direction of the advancing working face. With the failure of the floor caused by mining, there were “the next three-zone”, the goaf floor from top to bottom respectively including direct damage, effect, and the small changes zone. The cracks of rock strata on the working face goaf provided space and channels for the gas reservoir and transport, and made it possible for the surface borehole well gas extraction. The changes of goaf gas flow field were analyzed by 3D model using COSFLOW simulation of the working face to the vertical stress distribution. The simulation working face was 240 m wide and 3000 m long. The mining 11.2#coal seam had an average thickness of 2.8 m and an inclination of about 13~16° on the working face. Figure 1 shows the plan view of the panel. Figure 2 shows the geologic log of the model. Table 1 shows the different schemes of the model.

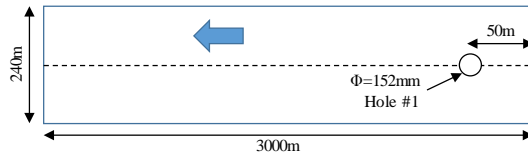


Figure 1: The plan view of the working face.

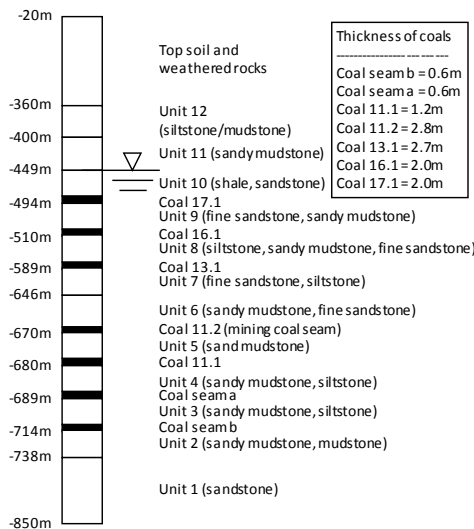


Figure 2: The geologic log of the model.

Table 1: Gas content of coal of different schemes.

Scheme	Coal 11.1	Coal 11.2	Coal 13.1	Coal 16.1	Coal 17.1
1 – 1 borehole in the goaf, low gas content in coal 11.1 and 11.2	3.84	3.84	10.4	9.6	8.0
2 – 1 borehole in the goaf, high gas content in coal 11.1 and 11.2	4.6	4.6	10.4	9.6	8.0
3 – 1 borehole in the goaf, low gas content in coal 13.1 and 16.1	4.6	4.6	9.3	9.3	8.0
4 – without borehole, high gas content in coal 11.1 and 11.2	4.6	4.6	10.4	9.6	8.0

The simulation results of panel methane emission are shown in Figure 3, in which the value of face methane emission is between 9.2-10.5 m³/min, which approximately corresponds to the average value of methane emission of 9.6 m³/min that is measured in the working face.

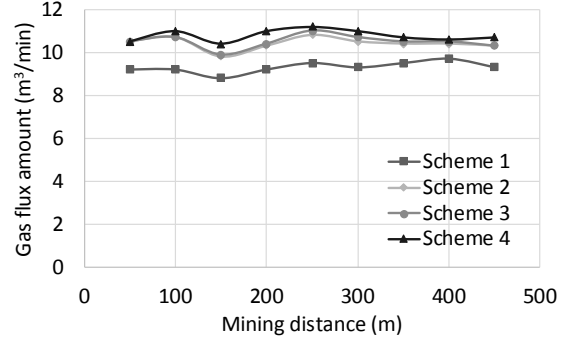


Figure 3: Comparison between the simulated and measured results.

For the specific circumstances of the measured face, the basic distribution pattern of goaf was established from a CFD model. The data which was used in the model was collected from the coal mine field, the result of COSFLOW, and the experience of the previous CFD modelling of methane flow. The basic model to the working face which was advanced 500 m from the open-off cut was used to research its goaf methane flow. The width of the basic model is 240 m, the height of the goaf fracture development zone is 100 m, the height of seam and roadways is 3.0 m, the width of all roadways is 4.0 m, the elevation of return roadways is 60 m higher than the machine roadways, and face elevation is the same with the open-off cut. Those geometric characteristics of the basic model are shown in Figure 4, which correspond with the actual situation.

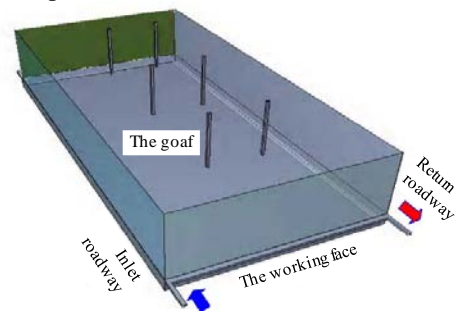


Figure 4: The numerical model.

There are two groups of ground well drilling to the goaf in the model, that is, one of the groups is along the centerline of the working face, and the other is 75 m from the return roadways. Those drillings can be opened and closed individually. The first hole is 50 m away from the working face open-off cut; the interval for the rest of the boreholes is 150 m. Table 2 provides detailed information on the modelling parameters.

Table 2: Parameters of the models.

Model parameter	Value
Working face size	length 500m/1000m, wide 240m , high 3.0m
Roadway size	wide 4m , high 3.0m (12m ²)
CFD model size - roof and bottom	High 100m –include segment 90m above and 10m below
Seam inclination	14°
Vertical face (advance) direction & Along the face (promote) direction	Return roadways in the upper (haulage roadways above 60 m) & the left panel with the open-off cut of working face at the same level.
The ventilation system, air volume	“U” type ventilation, 35m ³ /s
Goaf gas emission quantity	The goaf 300 l/s – 400 l/s
Gas component	100% CH ₄
Goaf gas drainage	along the center line of the working face and near return road (75m), the first hole is 50m away from the working face open-off cut; the interval in the rest of boreholes is 150m.

Figure 5 shows the methane distribution in the working face. It indicates that the gas concentration in the upper corner ranges between 2% to 6%, which fits the site measurements well. The figure also indicates that due to the low density of the methane, there is a small concentration at the upper part of the inlet roadway. According to the simulation, it is better to arrange the drilling holes around the inlet roadway from the surface.

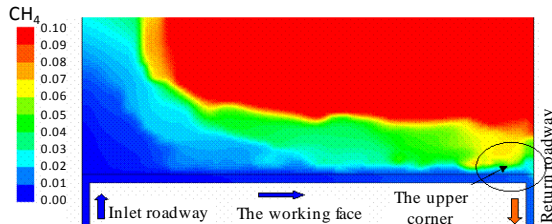


Figure 5: The methane distribution near working face.

2.3. Gas migration and emission regularity in low permeability coal seam

During the extraction, abutment pressure ahead of the working face will give the coal different degree of deformation, and coal permeability changes with this deformation, then affects the coal gas deposit and transport conditions in the coal, thus influencing the drainage effect of the coal seam gas drainage hole.

The relationship between the abutment pressure of the working face and the gas drainage amount of working face 9404 is shown in Figure 6.

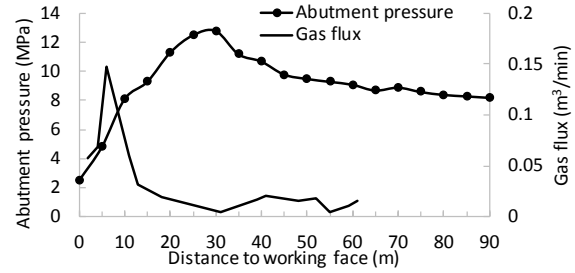


Figure 6: The relationship between the confining pressure and the gas drainage amount.

According to Figure 6, the area in front of the working face could be defined and divided into 5 zones, which are: a) zero abutment pressure and freed gas zone, where there is no abutment pressure and the gas could go through the fractures and cracks freely; b) distressed surrounding rock zone, mainly 0-10 m in front of the working face, the pressure of the surrounding rock lows, and the pressure of the coal seam lows as well, and the coal expanded due to the lower pressure, and gas has more paths to release; c) decreased abutment stress zone, which is usually 10-30 m in front of the working face, in this zone, the closer to the working face, the higher the gas emission speed; d) increased abutment stress zone, which is usually 30-60 m ahead of the working face, and with the increment of the stress, the fractures and cracks in the coal shrink and close, the permeability is lower than the original coal and as a result, the gas flux gets smaller; e) the original coal and gas area, which is more than 60 m ahead of the working face, and is barely influenced by the extraction, and the parameters of the coal and gas remain the same.

3. GAS DRAINAGE IN LOW PERMEABILITY A COAL SEAM

3.1. Gas drainage plan

Based on the numerical modelling results and the in-situ measurements, the gas drainage plan in the current coal seam is determined as follows.

The drilling holes of the current coal seam, which is perpendicular with the middle line of the transportation roadway, are drilled from the wall of the working face side. The drilling holes are separated into two vertical rows with a distance of 1.5 m, and the angles of the drilling holes are determined by the dip angle of the coal seam. Meanwhile, there are drilling holes with a 3 m distance between each other on the opposite side of the working face side. The starting drilling hole is located 18 m away from the working face in the transportation roadway and 21 m from the return roadway. All the drilling holes are 50 m long. The plan view of the drilling holes' arrangement is shown in Figure 7.

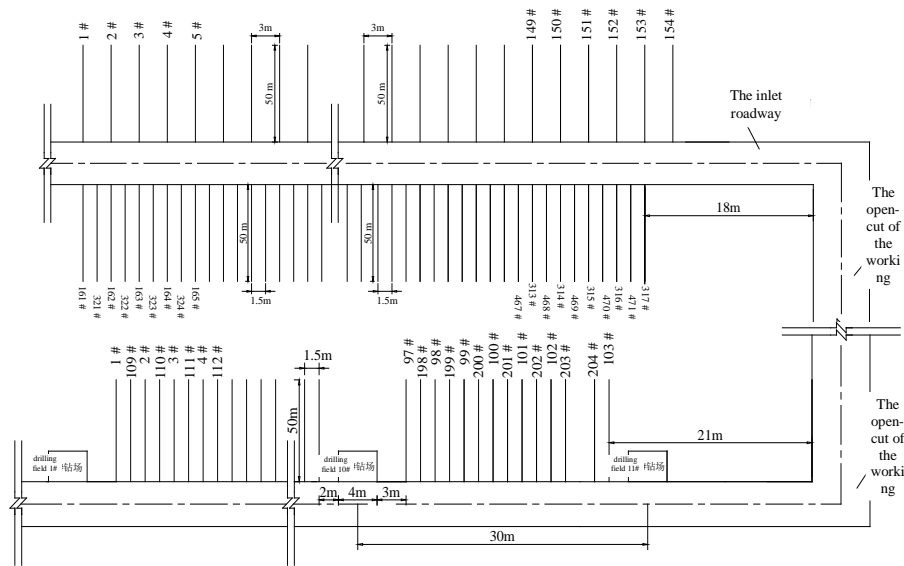


Figure 7: The layout of the drilling holes.

3.2. The drainage effect

The 15# coal seam is difficult to drain, and the increment of the abutment pressure during the coal extraction has a significant influence on increasing the drainage effect of the coal seam drilling holes. As shown in Figure 8, the drainage amount results through measurements could roughly be divided into four stages: I) the original drainage stage which is 40 m away from the working face; II) the weakening drainage stage, which is located between 40 m and 21.3 m away from the working face; III) the increasing drainage stage, which is located between 21.3 m and 10.3 m away from the working face; IV) the attenuate drainage stage, which is located within 10.3 m away from the working face.

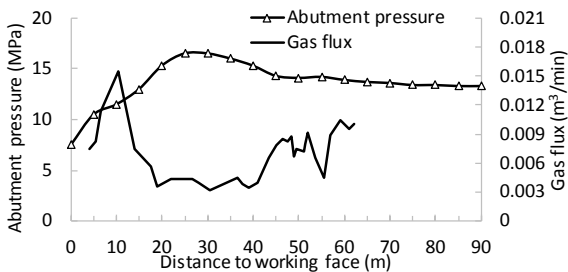


Figure 8: Relationship between confining pressure and gas drainage amount.

We can see from Figure 8 that the four drainage stages correspond to the abutment stress in front of the working face.

In stage I, the drainage amount is at a normal value, and it represents the in-situ stress before extraction. As a result, the coal is not influenced by the working face, the

stress, porosity, and the storage situation of the gas are not changed, and the drainage results remain the same.

In stage II, due to the effect of the working face, there is increased abutment stress in this stage, and the pores in the coal are compressed to shrink and shut, which leads to the decrease of the coal permeability, gas flux, and gas drainage amount.

In stage III, the coal seam is located in the decreased stress zone, and the pores distribution field and the stress field are also changed, which lead to the mining-induced fractures in the coal seam. Meanwhile, the gas pressure is lowering, which causes some adsorbed gas to turn into free gas, and the gas drainage amount from the drilling holes also grows. In this stage, the gas drainage amount keeps growing and reaches a maximum value. The measurement in-situ indicates that the drainage amount of a single drilling hole is 1.88 to 5.84 times more than in stage I, with an average of 4.7, while for the drilling hole group, the drainage amount of a group is around 3.5 to 6.4 times more than a single drilling hole, with an average of 4.3.

In stage IV, though the coal seam is still located in the decreased stress area, there are too many fractures and cracks that connect to the free space of the working face and as a result, there is a lot of air pumped from the free space mixed in the drainage gas, which reduces the gas amount of the drilling holes.

4. CONCLUSIONS

This paper studies the gas drainage technology in low permeability coal seams and the main factors that affect the gas drainage with the help of theoretical analysis, numerical modelling, laboratory experiments,

and in-situ measurements.

Through the measurements, the abutment pressure field, the displacement field, and the gas movement near the working face are studied, and a solid-gas-liquid coupling model is built to simulate the gas emission and the gas drainage from the ground surface.

The Yangquan coal mine gas movement and emission characteristics are studied, and the gas drainage method and key parameters of the drainage technology for the current coal seam are determined.

According to the numerical model, the arrangement of the drilling holes from the ground surface is optimized and refined. After the in-situ application, the drainage effect and the stability of the drilling holes are tested, and it indicates that the technology of gas drainage used in this paper could indeed enhance the drainage effect by 30%-40% and improve the efficiency of drainage in low permeability coal seams.

5. REFERENCES

- Alam, A. K. M. B. and M. Niioka, et al. (2014). "Effects of confining pressure on the permeability of three rock types under compression." *International Journal of Rock Mechanics and Mining Sciences* **65**: 49-61.
- Aziz, N. (2013). "Permeability and volumetric changes in coal under different test environment." *Acta Geodynamica et Geomaterialia*: 163-171.
- Cappa, F. and J. Rutqvist (2011). "Modeling of coupled deformation and permeability evolution during fault reactivation induced by deep underground injection of CO₂." *International Journal of Greenhouse Gas Control* **5** (2): 336-346.
- Chen, H. and C. Yuan-Ping, et al. (2013). "Damage and Permeability Development in Coal During Unloading." *Rock Mechanics and Rock Engineering* **46** (6): 1377-1390.
- Gu, F. and R. Chalaturnyk (2010). "Permeability and porosity models considering anisotropy and discontinuity of coalbeds and application in coupled simulation." *Journal of Petroleum Science and Engineering* **74** (3-4): 113-131.
- Guo, P. and Y. Cheng (2013). "Permeability Prediction in Deep Coal Seam: A Case Study on the No. 3 Coal Seam of the Southern Qinshui Basin in China." *The Scientific World Journal* **2013**: 1-10.
- Liu, H. and J. Rutqvist (2010). "A New Coal-Permeability Model: Internal Swelling Stress and Fracture – Matrix Interaction." *Transport in Porous Media* **82** (1): 157-171.
- Liu, J. and Z. Chen, et al. (2010). "Linking gas-sorption induced changes in coal permeability to directional strains through a modulus reduction ratio." *International Journal of Coal Geology* **83** (1): 21-30.
- Liu, J. and Z. Chen, et al. (2011). "Evolution of coal permeability from stress-controlled to displacement-controlled swelling conditions." *Fuel* **90** (10): 2987-2997.
- Mitra, A. and S. Harpalani, et al. (2012). "Laboratory measurement and modeling of coal permeability with continued methane production: Part I – Laboratory results." *Fuel* **94**: 110-116.
- Pan, Z. and L. D. Connell (2012). "Modelling permeability for coal reservoirs: A review of analytical models and testing data." *International Journal of Coal Geology* **92**: 1-44.
- Wang, G. X. and X. R. Wei, et al. (2010). "Sorption-induced swelling/shrinkage and permeability of coal under stressed adsorption/desorption conditions." *International Journal of Coal Geology* **83** (1): 46-54.
- Wang, G. and T. Ren, et al. (2014). "Improved apparent permeability models of gas flow in coal with Klinkenberg effect." *Fuel* **128**: 53-61.
- Wang, S. and D. Elsworth, et al. (2011). "Permeability evolution in fractured coal: The roles of fracture geometry and water-content." *International Journal of Coal Geology* **87** (1): 13-25.
- Wang, S. and D. Elsworth, et al. (2013). "Permeability evolution during progressive deformation of intact coal and implications for instability in underground coal seams." *International Journal of Rock Mechanics and Mining Sciences* **58**: 34-45.
- Xufeng, W. and Z. Dongsheng, et al. (2014). "Methane Drainage and Utilization Technologies for High Gassy and Low Permeability Coal Seams in Tiefsa Mining Area.".

Influence of temperature on gas desorption-diffusion laws of coal particles

Linchao Dai^{a,b,*}

^a State Key Laboratory of the Gas Disaster Detecting, Preventing and Emergency Controlling, Chongqing, China, 400037

^b Chongqing Research Institute Co.,Ltd. of China Coal Technology and Engineering Group, Chongqing, China, 400037

ABSTRACT

With the continuous increase in coal mining depth in China, temperature has a more and more apparent effect on the coal seam gas adsorption, desorption-diffusion, and seepage. To investigate the effect of temperature on the gas desorption and flow law of coal, the coal gas desorption test system by independent research and development is used. The gas desorption diffusion process of coal particles was studied under the conditions of adsorption equilibrium pressure 1.1 MPa and desorption temperature (20°C, 30°C and 40°C). The variation law of the coal particle gas desorption-diffusion amount and the gas desorption-diffusion rate change with temperature are defined. Subsequently, the mathematical physics equations of coal particle gas desorption diffusion is established based on the third boundary condition, and the desorption-diffusion coefficient is solved by using the piecewise fitting method combined with the dynamic process characteristic of gas desorption-diffusion and the experimental data. The variation law of the gas diffusion coefficient change with temperature is found. The results show that: (1) the cumulative amount of coal particle gas diffusion desorption is a capped monotonically increasing function, and the higher the temperature, the faster the initial rate of gas desorption-diffusion. (2) in the short time ($t < 10$ min), the gas desorption-diffusion coefficient decreases as the temperature increases, and when $t > 10$ min, temperature change has little effect on the desorption-diffusion coefficient. This effect is mainly due to the fact that the rise in temperature accelerates the velocity of the gas molecules, therefore increasing the probability of collisions between the gas molecules. The diffusion length of gas molecules is reduced, followed by a decrease in the effective diffusion cross-sectional area. Finally, the gas desorption-diffusion coefficient is reduced. This provides theoretical guidance for the prevention of coal and gas outburst and the prediction of gas emission quantity and extraction.

KEYWORDS: coal particles; gas; desorption-diffusion; temperature

1. INTRODUCTION

More than 95% of China's coal resources are obtained from underground coal mines. Gas, water, fire, dust, ground pressure, heat damage and other disasters often influence the process of mining due to the complex condition of coal resources, the poor geological conditions, and the large depth of burial (Yu, 2011). Mining depth increases at an annual rate of 10 to 30 m deep (the deepest to 1501 m). Many shallow low gas mines gradually change into high gas mines, resulting in increases in stress, temperature, and pressure (Xie et al., 2015). According to data obtained from the observation of a coal field in China, temperature increased from 1.5 to 4.5 K/100m (Zeng et al., 2011). In China's state-owned mines, the average temperature of the original rock is 35.9°C to 36.8°C in 650 m production levels, and in mines more than 1000 m, the original rock temperatures reaches as high as 40 to 45 degrees. At present, there exist more than 80 mines showing the patterns of differing levels of heat. At the same time, the effect of downhole temperature on coal gas adsorption, desorption, diffusion, and percolation is

becoming increasingly outstanding (Sun et al., 2003; Zeng et al., 2009; Li et al., 2003).

The process of gas desorption-diffusion in the coal seam is extremely complex, and much research has been conducted by domestic and international scientists. Winter et al. (1969) discovered that after adsorption equilibrium is reached, the amount of gas adsorption is determined by the gas content of the coal, time, temperature, adsorption equilibrium pressure, and the particle size of coal samples. Jaroniec et al.'s (1990) study on the process of gas desorption in coal showed that some deformation will occur when the coal body adsorbes gas. Yee et al. (1993) put forward the theory of diffusion, finding that the square root of desorption quantity and time does not show a simple linear relationship. Marecka (1995) found that the pores in coal and coal metamorphic degree play an important role in the process of gas desorption. Pokryszka et al. (2010) study the competitive adsorption of CH₄ and CO₂ diffusion behaviour, considering the influence of temperature on the effective diffusion coefficient. Sun (1983) studied coal seam gas solution

*Corresponding author – email : dailinchao@126.com

desorption, desorption rate, and grain size of coal samples as factors influencing the desorption rate. Nie et al. (2000) studied the micro mechanism of coal bed methane diffusion in coal pores. Cao et al. (2007) studied gas desorption attenuation coefficients and desorption intensities as a function of coal granularity in different samples, and analyzed the influence of particle size on desorption intensity. Fu et al. (2008) analyzed the difference between tectonic coal and non-coal structures on the microstructure carried on by the structure of coal gas radiation, using mathematical models of micro and macro theory research. Liu et al. (2013) studied the quantitative relationship between diffusion flux and the temperature of coal particles with different coal rank, and the influence of temperature on the gas diffusion dynamic process of coal particles.

At present, these theoretical and experimental studies of coal particles gas desorption-diffusion are mostly carried out under isothermal conditions. However, the changes in and mechanism of the coal particle gas desorption-diffusion flux, the gas desorption-diffusion rate and the diffusion coefficient still lack in-depth study. Therefore, based on previous research, and in order to further investigate the effect of temperature on the gas desorption and flow law of coal, the coal gas desorption test system by independent research and development is used to study the variation law of the coal particles gas desorption-diffusion under different temperatures. The present study has practical significance on the prediction of coal and gas outburst, as well as coal seam gas content prediction.

2. EXPERIMENTAL SYSTEM AND METHODS

2.1 Experimental system

To achieve the law of coal particles gas desorption-diffusion under different temperature, the experimental system was independently designed and assembled. The system mainly consisted of the temperature control system, the adsorption-desorption system, the data acquisition and processing system, the desorption-diffusion gas gathering system, the gas supply and control system, and other auxiliary devices. A schematic diagram of the experimental system is as shown in Figure 1.

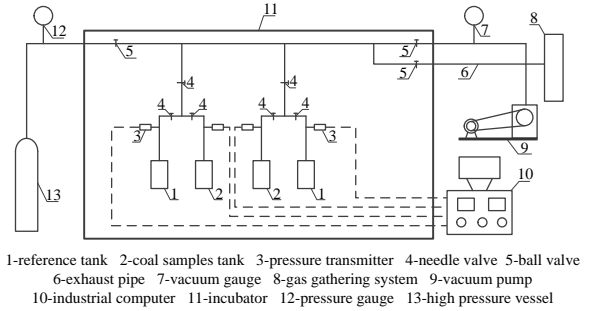


Figure 1: The schematic diagram of the experimental system.

2.2 Experimental coal sample

Samples of Shanxi Jincheng Phoenix Mountain coal seam face 9# were collected. The coal sample industry analysis data is shown in Table 1. A balance was used to weigh the coal sample of 50 g (weighing accuracy 0.001 g), with the bottle containing the coal sample being pre-numbered and weighed. In order to exclude the impact of moisture, the weighed coal sample was placed in a vacuum oven, and heated to 100~105°C for 4~6 hours. The vacuum degree of the oven was at least 700 mmHg. The coal sample was then dried and placed in a desiccator to cool and save.

Table 1: Experimental coal industry analysis.

Sample	Moisture content %	Volatile content %	Ash content %	Fixed carbon %
Jincheng Phoenix Mountain 9#	3.17	7.09	8.32	81.42

2.3 Experimental procedure

The purpose of this experiment is to study the dynamic rule of coal particles gas desorption-diffusion under different temperatures (20, 30 and 40 °C) with pressure held constant (1.1 MPa).

Using coal particles of 40~60 mesh at a temperature of 20°C as an example, the specific experimental procedure is as follows:

(1) Weigh the prepared coal sample of 50 g, and load it into the sample tank. Connect with the experimental system.

(2) Open the temperature control system and keep the temperature at 20°C.

(3) Access the methane gas cylinders to the experimental system, open the vacuum pump, and perform vacuuming tanks and piping systems for about 1 hour.

(4) Fill the reference tank with the methane gas to keep it at a stable pressure, and adjust the valve to

connect the reference tank with the sample tank. Collect the pressure values of the reference tank with the sample tank.

(5) After the adsorption equilibrium is reached, adjust the valve to connect the sample tank with the atmosphere.

(6) Once the sample tank pressure drops below atmospheric pressure (0.1 MPa), access it using the desorption gas gathering system quickly. Meanwhile, open the gas desorption acquisition software to record the gas desorption change varying with time, until the end of the desorption experiments. Lastly save the experimental data.

3. RESULTS

The variation law of the coal particles gas desorption-diffusion amount and the gas desorption-diffusion rates of change with temperature were measured, as shown in Figures 2 and 3.

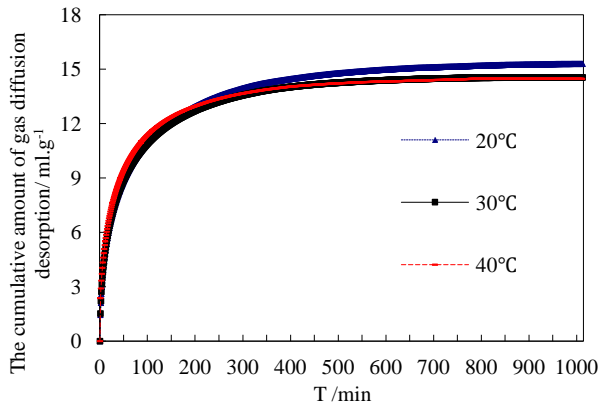


Figure 2: The gas desorption diffusion amount curve.

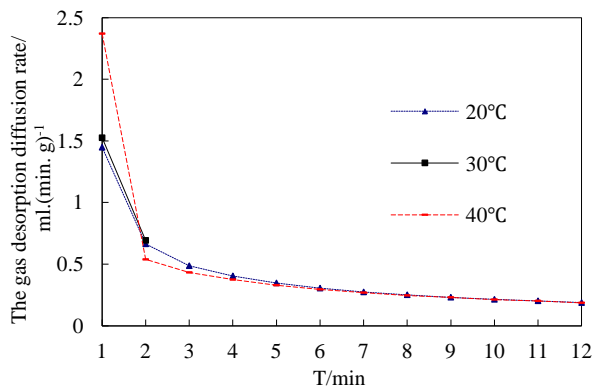


Figure 3: The gas desorption diffusion rate curve.

Figures 2 and 3 show that: (1) the cumulative amount of coal particles gas diffusion desorption is a capped monotonically increasing function. (2) The limit cumulative amount of coal particles gas

diffusion desorption decreases when the temperature increases. (3) The higher the temperature, the faster the initial rate of gas desorption diffusion. Meanwhile, the rate of gas desorption diffusion gradually decreases and finally stabilizes with time.

This is because of two main reasons: (1) The kinetic energy of gas molecules will increase due to the increase in temperature, giving a greater chance of surpassing the higher adsorption barrier energy, shortening the residence time on the coal pore surfaces. This reduction in the adsorption capacity leads to a reduction in the amount of gas adsorption. Finally, the amount of desorption will decrease, so the limit cumulative amount of coal particles gas diffusion desorption also decreases. (2) Under the same size and adsorption equilibrium pressure in the same coal sample, the thermal motion of gas molecules will be increased because of the increase in temperature. Thus the desorption diffusion capacity is enhanced, and the desorption-diffusion rate also accelerates.

4. EFFECT OF TEMPERATURE ON THE GAS DIFFUSION COEFFICIENT

Most scholars (Charriere et al., 2010; Yang et al., 1986; Zhou, 1990; Gives, 1992; Li, 2005) find that the process of coal particle gas irradiation is the desorption-diffusion process, and the methane adsorption (desorption) on the coal surface is physical adsorption (desorption). In principle, it can be completed in an instant ($10^{-10} \sim 10^{-5}$ s) and be negligible, therefore, the process can be described using Fick's second law and the driving force is the concentration gradient. In the complex system of coal, gas adsorption in the pore system follows Fick's diffusion law and free gas in the fractures follows the Darcy law. Most studies research the kinetics of coal particles gas desorption-diffusion.

According to the literature (Dai, 2012; Nie et al., 2001), the mathematical physics equations of coal particle gas desorption-diffusion were established based on the third boundary condition. The meaning of symbols is as shown in the literature.

$$\left\{ \begin{array}{l} \frac{\partial C}{\partial t} = D \left(\frac{\partial^2 C}{\partial r^2} + \frac{2}{r} \frac{\partial C}{\partial r} \right) \\ 0 < r < r_0, C|_{r=0} = C_0 \\ t > 0, \frac{\partial C}{\partial r} \Big|_{r=0} = 0 \\ -D \frac{\partial C}{\partial r} \Big|_{r=r_0} = \alpha(C|_{r=r_0} - C_f) \end{array} \right. \quad (1)$$

The approximate solution is obtained by using the variable separation method.

$$\ln\left(1 - \frac{Q_t}{Q_\infty}\right) = \ln A - \lambda t \quad (2)$$

Where: $A = \frac{6(\sin \beta_1 - \beta_1 \cos \beta_1)^2}{\beta_1^2 (\beta_1^2 - \beta_1 \sin \beta_1 \cos \beta_1)}$, $\lambda = \frac{\beta_1^2 D}{r_0^2}$,

Q_t is the cumulative amount of gas diffusion at any time. Q_∞ is the limit cumulative amount of gas diffusion desorption. D is the desorption-diffusion coefficient in m^2/s .

According to the obtained approximate analytical solution, the desorption-diffusion coefficient was solved by using the piecewise fitting method combined with the dynamic process characteristic of gas desorption-diffusion and the experimental data. The results are shown in Table 2 and Figure 4.

Table 2: The solution results of desorption-diffusion coefficients under different temperature.

Temperature	Time (min)	Fitting formula	R ²	D × 10 ⁻¹¹ (m ² /s)
20°C	t < 10	y = -0.028x - 0.0672	0.9802	0.2765
	10 < t < 100	y = -0.0094x - 0.453	0.9875	0.0460
	t > 100	y = -0.0051x - 1.3544	0.9987	0.0176
30°C	t < 10	y = -0.0308x - 0.1067	0.9794	0.2534
	10 < t < 100	y = -0.0104x - 0.4978	0.9882	0.0493
	t > 100	y = -0.0064x - 1.4028	0.9971	0.0218
40°C	t < 10	y = -0.0301x - 0.1369	0.9889	0.2251
	10 < t < 100	y = -0.0115x - 0.561	0.9888	0.0524
	t > 100	y = -0.0061x - 1.6426	0.9986	0.0198

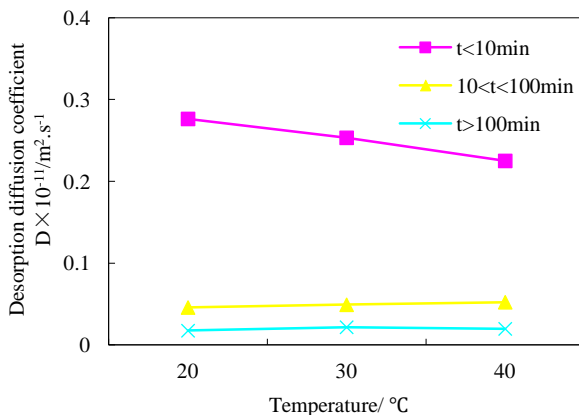


Figure 4: The segment fitting results under different temperature.

Figure 4 shows that temperature has a greater impact on the gas desorption-diffusion coefficient when $t < 10$ min, but is less affected when $10 < t < 100$ min and $t > 100$ min. For short times ($t < 10$ min), the

gas desorption-diffusion coefficient decreases as temperature increases, and when $t > 10$ min, temperature changes have little effect on the desorption-diffusion coefficient. This is mainly because the rise in temperature accelerates the velocity of the gas molecules, and increases the probability of collisions between the gas molecules, decreasing the diffusion length of gas molecules. The effective diffusion cross-sectional area decreases, and finally the gas desorption-diffusion coefficient are reduced.

5. CONCLUSION

The coal gas desorption test system by independent research and development was used and the gas desorption-diffusion process of coal particles was studied under conditions of adsorption equilibrium pressure of 1.1 MPa at desorption temperatures of 20°C, 30°C and 40°C. The variation law of the coal particles gas desorption-diffusion amount and the gas desorption-diffusion rate of change with temperature were defined.

The mathematical physics equations of coal particle gas desorption-diffusion were established based on the third boundary condition, and the desorption-diffusion coefficients were found by using the piecewise fitting method combined with the dynamic process characteristic of gas desorption-diffusion and the experimental data. The variation law of the gas diffusion coefficient change with temperature was found.

Studying the influence of temperature on gas desorption-diffusion laws of coal particles is practically significant for use in coal and gas outburst prediction, as well as coal seam gas content prediction.

6. ACKNOWLEDGEMENTS

This work was financially supported by the National Basic Research Program of China (2012CB724206), the National Natural Science Foundation of China (51574280). The author would like to thank the reviewers of this paper for their constructive comments and suggestions to improve the publication.

7. REFERENCES

Cao, Y.L. and Qiu, H.S. (2007). Gas desorption laws of clastic coal core study. China Mining Magazine, Volume 16, No. 12, pp.119-123

Charriere, D., Pokryszka, Z. and Behra, P. (2010). Effect of pressure and temperature on diffusion of CO₂ and CH₄ into coal from the Lorraine basin (France). International Journal of Coal Geology, Volume 81, No. 4, pp.373-380

- Dai, L.C. (2012). Experimental and theoretic research on gas desorption-diffusion in coal. China University of Mining & Technology (Beijing)
- Fu, X., Wang, K.J. and Yang, T.H. (2008). Gas irradiation feature of tectonic coal. Journal of China Coal Society, Volume 33, No. 7, pp.775-779
- Gives, H.F. (1992). The process of coal gas desorption. Coal Engineer, Volume 2, pp.52-56
- Jaroniec, M., Lu, X. and Madey, R. (1990). Use of argon adsorption isotherms for characterizing microporous activated carbons. Fuel, Volume 69, No. 4, pp.516-518
- Li, G.X. (2005) Adsorption science. Chemical Industry Press
- Li, Q.G., Kang, Y.L. and Luo, P.Y. (2003). Analysis of the factors affecting processes of CBM desorption, diffusion and percolation. Coal Geology & Exploration, Volume 31, No. 4, pp.26-29
- Liu, Y.W., Wei, J.P. and He Z.G. (2013). Influence rules and mechanisms of temperature on dynamic process of gas diffusion from coal particles. Journal of China Coal Society, Volume 38, pp.100-105
- Nie, B.S., Guo, Y.Y. and Wu, S.Y. (2001). Theoretical model of gas diffusion through coal particles and its analytical solution. Journal of China University of Mining & Technology, Volume 30, No. 1, pp. 19-22.
- Nie, B. S., Zhang L. and Ma, W.F. (2000). Diffusion micro-mechanism of coal bed methane in coal pores. Coal Geology & Exploration, Volume 28, No. 6, pp.20-22
- Marecka, A. (1995) .Effect of grain size on diffusion of gases in coal. Coal Science
- Sun, C.X. (1983). Study on coal samples gas desorption and the characteristics of prominent coal seam gas desorption. Chongqing Institute of Coal Science Research Institute
- Sun, Y.L. and Gui, X.Y. (2003). Research on mine heat-harm and its treatment. Journal of Liaoning Technical University, Volume 22, pp.35-37
- Winter, K. and Janas, H. (1969). Gas emission characteristics of coal and methods of determining the desorbable gas content by means of desorbometers. XIV International Conference of Coal Mine Safety Research
- Xie, H.P., Gao F. and Ju Y. (2015). Quantitative definition and investigation of deep mining. Journal of China Coal Society, Volume 40, pp.1-10
- Yang, Q.L. and Wang Y.A. (1986). Cinder gas diffusion theory and its applications. Journal of China Coal Society, Volume 3, pp.87-93
- Yee, D., Seidle, J. P. and Hanson, W.B. (1993). Gas sorption on coal and measurement of gas content. In: Law B E, Rice D D (Eds.), Hydronecarbons from Coal. AAPG Studies in Geology, Volume 38, pp.203-218
- Yu, B.F. (2000). Prevention of coal-mine gas hazards and utilization manual. Coal Industry Press, China
- Zeng S.J., Ma, D.M. and Wang, P.G. (2009). Effect of temperature changing on desorption of coalbed methane. Journal of Xi'an University of Science And Technology, Volume 29, pp.449-453
- Zheng, G.S., Luan, Y.B. and Bai, L.Y. (2011). Discussion on the zonations of shallow geothermal energy resources in China. City geology, Volume 6, pp.12-16
- Zhou S.N. (1990). Mechanism of gas flow in coal seams. Journal of China Coal Society, Volume 15, No. 1, pp. 61-67.

Numerical simulation of gas migration rule in mining-induced fractures field

Cao Jie ^{a,b,*}, Li Minghui ^c, Li Wenpu ^c

^a State Key Laboratory of Gas Disaster Detection, Prevention and Emergency Control, Chongqing, China, 400037

^b Chongqing Research Institute Co.,Ltd. of China Coal Technology and Engineering Group, Chongqing, China, 400037

^c State Key Laboratory of Coal Mine Disaster Dynamics and Control, Chongqing University, Chongqing, China, 400044

ABSTRACT

Gas extraction practice has proven that the vast majority of mining areas in China use unfavourable gas drainage technology, such as ground drilling hole, and should instead use mining-induced fractures for gas extraction. Therefore, research concerning the gas migration rule in mining-induced fractures field above the goaf can provide technical support for optimizing system arrangement of pressure-relieved gas extraction, and increasing the rate of gas extraction.

At present, scholars are utilizing numerical simulation to study the gas migration rule in working face and goaf without considering the influence of the mining-induced fractures. There is currently no simulation software that can simulate not only the space-time evolution of the mining-induced fractures field, but also the rule of gas migration. This study takes the mining face of the 10th mine in Pingdingshan Coalmine Group in Henan China as an example case. First, a numerical calculation model is established, and then UDEC software is used to calculate the evolution formation of the mining-induced fracture field. Afterwards, a spatial diagram is obtained by the image processing method, and then imported into COMSOL MULTIPHYSICS software in order to simulate the process of gas migration.

By combining the UDCE and COMSOL software, the gas migration rule in mining-induced fractures above goaf is numerically simulated. The results are as follows: When the working face advances to a certain distance, goaf overburden gradually forms a mining-induced fractures trapezoid table, and with the working face advancing, the height of the mining-induced fractures trapezoid table increases; Compared to the gas migration in the overburden matrix, the gas flow in abscission layer crack and vertical fracture of mining-induced fractures is directional, and the gas enrichment area is located in the biggest abscission layer crack area in upper end of mining-induced fractures trapezoid table; When drilling for gas extraction in mining-induced fracture field, the gas concentration declines in the whole region during the process of gas drainage, and the rate of gas concentration declines faster in fractured zones. With the gas drainage, the velocity of the gas flow in the mining-induced fracture is faster.

1. INTRODUCTION

The geological conditions of coal seams in China are complex and permeability is generally low. Gas extraction practices has proven that the vast majority of the mining areas in China use unfavourable gas drainage technology, such as ground drilling hole. Mining-induced fractures should instead be used for gas extraction. In the process of coal mining, the surrounding rock stress is redistributed and generates the mining-induced fractures caused by mining stope. The gas desorption of coal mass is promoted, and the permeability of coal is also increased in order to provide a gas flow channel in coal and rock mass near the working face. Therefore, research concerning the gas migration rule in mining-induced fractures field above the goaf can provide technical support for optimizing system arrangement of pressure-relieved gas extraction, and increasing the rate of gas extraction.

At present, scholars have carried plenty of research on the gas migration law in mining-induced fracture field above goaf. Qian and Xu (1998) studied the distribution characteristics of mining-induced fractures in the overlying strata by means of model experiments, image analysis, and discrete element simulation method. Their findings revealed a two stage development law of fracture caused by mining and distribution characteristics of “O-shape” circle in long wall faces, and a guide for hole patterns of relieving gas drainage. Li (1998) classified the mining induced fracture field through research on the formation and characteristics of fracture fields above the goaf and in front of the working face. Tu and Liu (2002) researched the influence of formation, development, closure, and variation of the cracks in the roof of a coal seam on coal mining, and described the range of fracture development. Liu et al. (2012) found that according to the breakage and fracture developing of overlying strata, the layer with a

*Corresponding author – emai: cqcaoj@126.com

fracture diameter of more than 10^{-1} mm is the mining gas channels development area. Other scholars have studied the gas migration law of coal seams using the numerical simulation method. However, no simulation software has been developed that can simulate not only the space-time evolution of the mining-induced fractures field, but also the rule of gas migration.

This study takes the mining face of the 10th mine in Pingdingshan Coalmine Group in Henan China as an example case. Establishing numerical calculation model according to the different laws of gas flow in different zones of the working face, and combining the UDCE and COMSOL software to research the gas migration rule in mining-induced fractures above goaf, which can provide technical support for optimizing the system arrangement of pressure-relieved gas extraction.

2. MATHEMATICAL MODEL OF GAS MIGRATION UNDER THE MINING INFLUENCE

Mining fissure fields belongs to a porous medium and the gas therein can be regarded as the ideal gas mixture consisting of gas and air. The gas flow follows the continuity equation, momentum equation, and mass conservation equation.

2.1 Continuity equation

The gas flow in coal and rock follows the law of mass conservation. If the mass sources (sink) are not considered, the gas continuity equation is:

$$\frac{\partial(\rho_g \phi)}{\partial t} + \nabla \cdot (\rho_g \phi \mathbf{v}_g) = 0 \quad (1)$$

The gas transportation in mining fissures should satisfy the law of conservation of the gas quality. It should consider the mass sources of gas, so the gas continuity equation is:

$$\frac{\partial(\rho_g c_g)}{\partial t} + \frac{\partial}{\partial x_i} (\rho_g c_g u_i) = -\frac{\partial}{\partial x_i} (J_g u_i) + S_g \quad (2)$$

Where u_i is average flow velocity for porous medium in the i direction, S_g is the additional production rate of gas source term, and J_g is gas diffusion flux.

2.2 Momentum conservation equation

In a given fluid system, the time variation of its momentum is equal to the sum of the external forces acting on it. For porous media, the momentum conservation equation of the i direction in the inertial (non accelerating) coordinate system is:

$$\frac{\partial(\rho_g u_i)}{\partial t} + \frac{\partial}{\partial x_j} (\rho_g u_i u_j) = \frac{\partial \tau_{ij}}{\partial x_j} - \frac{\partial p}{\partial x_i} + \rho_g g_i + F_i \quad (3)$$

Where τ_{ij} is stress tensor, $\tau_{ij} = \mu_{eff} \left[\left(\frac{\partial u_i}{\partial x_j} + \frac{\partial u_j}{\partial x_i} \right) - \frac{2}{3} \frac{\partial u_i}{\partial x_i} \delta_{ij} \right]$, δ_{ij} is Kroneker symbol, g_i is the gravity force and the external volume force on the i direction, and F_i is a custom porous media source term.

2.3 Motion equation

Because of the complex gas flow channel in coal and viscous effect, the motion equation of the gas flow in the porous media of coal and rock needs to be described according to different area conditions. According to previous research (Yang et al., 2010), the Navier-Stokes equation is appropriate for describe the fluid flow in the roadway, and the Brinkman equation focuses on the fracture zone while simultaneously considering the characteristics of the fluid pressure and movement, which is appropriate for describing the fluid flow in the caving zone. Using the two equations can build a working face airflow model, as shown in Figure 1. The velocity and pressure on the interface is consistent in the region where the gas flow is in accordance with the Navier-Stokes and Brinkman models. The velocity and pressure distribution of the coal face and goaf can be predicted by solving the model.

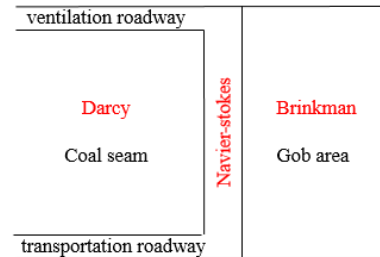


Figure 1: The schematic diagram of description of the fluid motion equation in different areas front and after the working face.

(1) Fluid motion equation in front of working face

To determine the fluid flow with Reynolds number of gas flow in the coal seam, the expression for the Reynolds number, R_e is:

$$R_e = \frac{q \cdot k}{v \cdot d_m} \quad (4)$$

Where q is the gas flow velocity, m/s, k is the permeability, m^2 , v is coefficient of kinematic viscosity, m^2/s , d_m is the average particle size, m. When the $R_e \leq 2320$, the fluid flow state is laminar flow, it is transition flow for $2320 < R_e < 4000$, it is turbulent flow for $R_e \geq 4000$ (Xu xianliang et al., 2011).

When the fluid flow state is laminar flow, the flow in coal bed is in accordance with Darcy's Law:

$$u = -\frac{K}{\mu} \cdot \frac{dp}{dx} \quad (5)$$

Where u is the gas flow velocity in coal bed, m/s, K is the permeability of coal, m^2 , μ is dynamic viscosity of the fluid, Pa/s, and dp/dx is the fluid pressure gradient.

When the fluid flow state is turbulent flow, the gas flow in the coal bed is Non-Darcy flow, and the fluid pressure gradient can be expressed as follows:

$$-\frac{dp}{dx} = \frac{\mu}{K}u + \beta\rho u^n \quad (6)$$

Where n is related to the characteristics of the porous media of coal, and β is the β -factor of Non-Darcy flow.

The coal permeability in front of the working face is related to its effective stress. Considering the effect of gas pressure, mechanical effect and absorption effect, the expression of the relationship between permeability and effective stress of coal in the condition of mining dynamic loading and unloading is:

$$k = ck_0 \exp \left(d \left\{ \Theta - 3p \left[1 - \frac{3K(1-2\nu_s)}{E_s} \left[1 - \frac{\rho RTa \ln(1+bp)}{p(1-\phi)} \right] \right] \right\} \right) \quad (7)$$

(2) Fluid motion equation in working face

Navier-Stokes equation can describe the fluid flow in the pipeline. The fluid flow is faster in the working face, and it can be solved by Navier-Stokes equation:

$$-\nabla \cdot \eta \left[\nabla u_{ns} + (\nabla u_{ns})^T \right] - \rho_g (u_{ns} \cdot \nabla) u_{ns} + \nabla p_{ns} = 0 \quad (8)$$

$$\nabla \cdot u_{ns} = 0$$

Where η is coefficient of viscosity, kg/(m·s), u is velocity vector, m/s, ρ_g is the fluid density, kg/m³, and p is pressure, MPa. The subscript ns means described by the Navier-Stokes equation.

(3) Fluid motion equation in gob area

The Brinkman equation describes a flow between Darcy and Navier-Stokes. The fluid flow in porous media can be described by Darcy's law when the velocity is small, not considering the energy transfer caused by shear stress. When the flow velocity is relatively large, the energy transfer caused by shear stress is considered, and the Brinkman equation is used:

$$-\nabla \cdot \eta \left[\nabla u_{br} + (\nabla u_{br})^T \right] - \left(\frac{\eta}{k} u_{br} + \nabla p_{br} - F \right) = 0 \quad (9)$$

$$\nabla \cdot u_{br} = 0$$

Where the subscript br means described by the Brinkman equation.

3. NUMERICAL SIMULATION OF OVERLYING STRATA MOVEMENT LAW IN MINING-INDUCED FRACTURES FIELD

The fracture field is formed within a certain distance in overlying strata above the gob area after coal mining. There are two main types: bed separated fissures and vertical rupture fissures. Overlying strata will have different degree of deformation, resulting in different gas migration and accumulation rules in different positions of the mining-induced fracture field. Therefore, the moving law of overlying strata in mining-induced fractures field simulated by UDEC software is firstly carried out.

3.1 The establishment of numerical model

The 15# coal seam 24080 coal mining working face in No.10 mine of Pingdingshan Tianan Coal Mining Co., Ltd is used as the example case. The calculation model is established according to the integrated histogram and physical and mechanical parameter of coal seam, as shown in Figure 2. The model is 200 m × 100 m, the working face advance distance is 120 m, left and right sides of the recovery boundary reserve 40 m distance from the model boundary to eliminate the boundary effect, and the coal seam is divided into 12 times for excavation, where each time excavates 10 m. The simulated coal seam mining depth is 890 m, the thickness of the coal seam is 2.4 m, the upper boundary is loaded with 20 MPa, and the left or right side and the bottom of the model are normal to the displacement constraint. The bottom boundary limits the vertical displacement. The physical and mechanical parameters of the coal or rock and the mechanical parameters of the joints of model are shown in Tables 1 and 2, respectively.

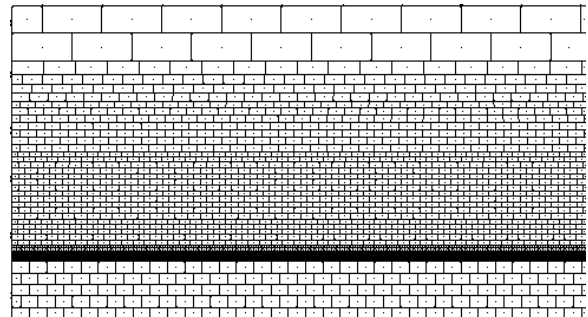


Figure 2: Numerical simulation model.

Table 1: Physical and mechanics parameters of coal or rock.

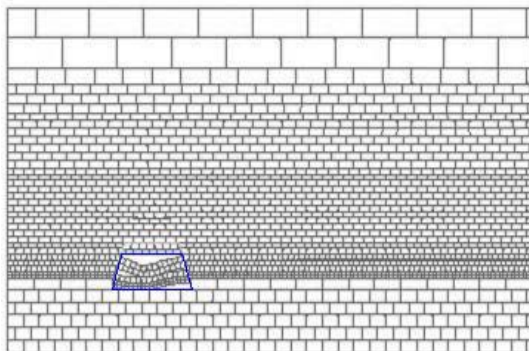
Lithology	Density (kg/cm ³)	Elasticity modulus (GPa)	Compressive strength (MPa)
Mudstone	2.4	17	39
Coal	1.4	13	21
Sandstone	2.8	41	68.5
Sandy mudstone	2.5	20	42.4
Medium-coarse sandstone	3.1	43	70.6
Fine sandstone	2.6	37	58.2

Table 2: Mechanics parameters of joints of the model.

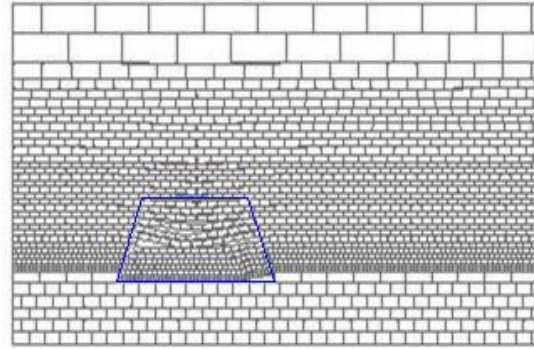
Lithology	Normal stiffness (GPa)	Shear stiffness (GPa)	Frictional angle (°)
Mudstone	7	1	30
Coal	3	0.3	28
Sandstone	21	15	39
Sandy mudstone	14	7	34
Medium-coarse sandstone	25	17	41
Fine sandstone	19	13	37

3.2 The simulated results

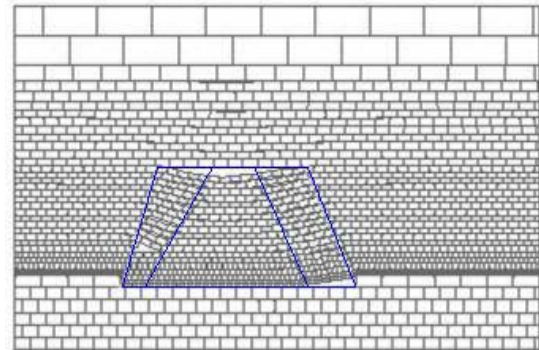
The evolution raw of the fracture field when the excavation distance is 30 m, 60 m, 90 m, and 120 m is shown in Figure 3. It can be seen from Figure 3 that the overlying strata movement follows a dynamic spatiotemporal evolution process. When the working face is advanced different distances, the overlying strata above the gob area form the mining-induced fracture trapezoidal platform. With increases of the excavation distance, the height of the platform is also increased.



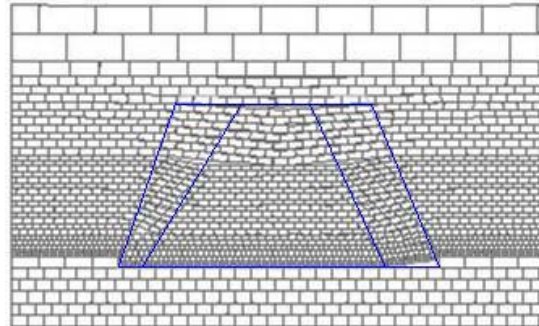
(a) The excavation distance is 30 m



(b) The excavation distance is 60 m



(c) The excavation distance is 90 m



(d) The excavation distance is 120 m

Figure 3: The distribution form of mining fracture field under different excavation distance.

4. NUMERICAL SIMULATION OF GAS MIGRATION IN MINING-INDUCED FRACTURE FIELD

The shape of the mining induced fracture field is obtained using UDEC numerical simulation, and then colour is given to the fracture field, and finally extracted using CORE DRAW software. The fracture distribution of the extracted fracture field is as shown in Figure 4.

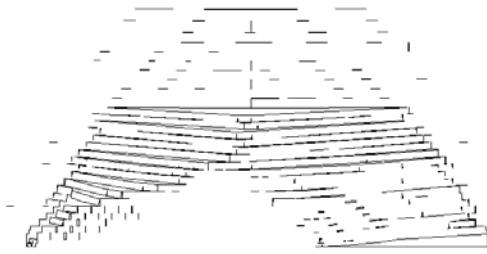
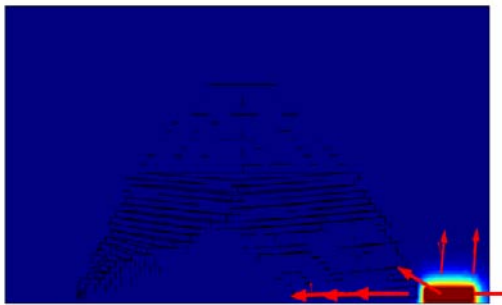
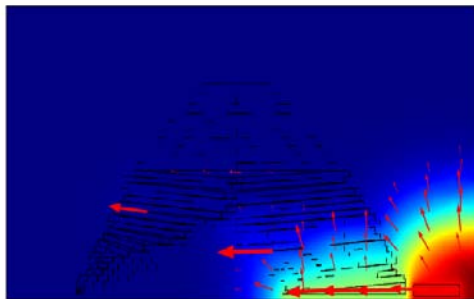


Figure 4: The distribution situation of fracture in the mining fracture field.

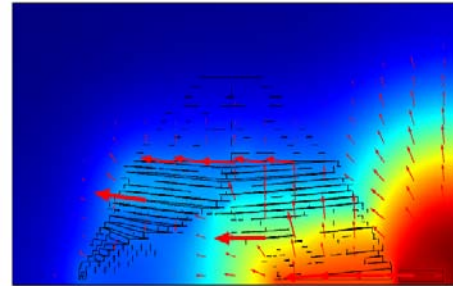
The extracted fracture field is imported into the COMSOL MULTIPHYSICS software for numerical simulation, and the gas migration law at different times in the mining-induced fracture field can be obtained, as shown as Figure 5. The size of the arrow in the figure represents the size of the gas flux. It is clear that the gas flux in mining-induced fracture is far greater than that in the matrix of overlying strata. The bed separated fissures and vertical rupture fissures are the channels of gas flow, compared with the matrix of overlying strata, the gas flow in there has more guiding. With the gas migrate in the mining-induced fracture field, the gas fluxes are larger in the overlying area where the bed separation degree is large. The gas enrichment area is basically located in the largest mining fracture region at the upper end of the trapezoidal table.



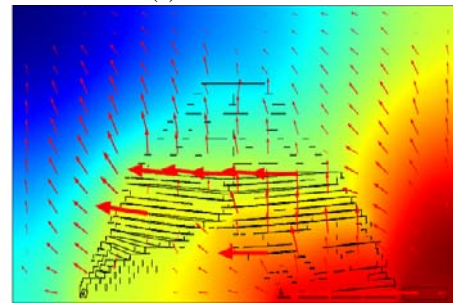
(a) $t = 200$ s



(b) $t = 200\ 000$ s



(c) $t = 800\ 000$ s



(d) $t = 2\ 400\ 000$ s

Figure 5: The schematic diagram of gas migration at different time in the mining fracture field.

The schematic diagram of gas concentration nephogram and streamline diagram of gas flux are shown in Figure 6. Assuming that the gas flow to a certain time, the gas concentration in the whole region reaches equilibrium, and the gas drainage is carried out in the fractured zone. From the distribution of gas concentration in Figure 6, it can be seen that the gas concentration in the whole region is falling, and the decreasing rate is relatively large in the fracture development area.

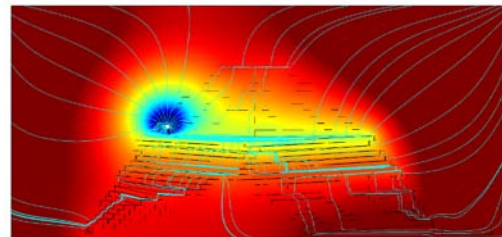


Figure 6: The schematic diagram of gas concentration nephogram and streamline diagram of gas flux.

Figure 7 shows a schematic diagram of gas concentration by height expression. As can be seen from the chart, the height in the surrounding coal matrix descends gently, and it decreases rapidly in the fractured zone of the mining-induced field. The gas concentration rate decrease in overlying strata matrix is smaller, and in the fractured zone of the mining-induced fracture field the decrease rate is

faster, indicating that with the drainage, gas flow orientation in the mining-induced fracture field is stronger.

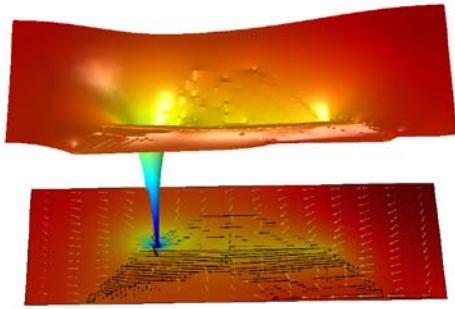


Figure 7: The schematic diagram of gas concentration by height expression.

5. CONCLUSIONS

The mathematical model of gas migration in the coal seam is established according to the flow type in different positions. Using the combination of UDEC software and COMSOL software, the numerical simulation of gas migration in mining-induced fracture above the goaf is carried out. The following conclusions are made:

(1) The movement of overlying strata above goaf is a dynamic spatiotemporal evolution process. With increases of the excavation distance, the areas form the mining-induced fracture trapezoidal platform, and the height of the platform is also gradually increased with excavation.

(2) Compared with the matrix of overlying strata, the gas flows in fractures are more guiding. With the gas migrate in the mining-induced fracture field, the gas enrichment area is located in the largest mining fracture regional at the upper end of the trapezoidal table.

(3) If gas drainage is carried out in the fractured zone, the gas concentration rate decrease in overlying strata matrix is smaller than that in the fractured zone. This means that with the drainage, gas flow orientation in the mining-induced fracture field is stronger.

This paper has carried out a preliminary analysis of gas migration in mining-induced fracture above the goaf using numerical simulation. In the future, the gas content test will be carried out on the scene to validate the simulation results, and to ensure the validity of the model.

6. ACKNOWLEDGEMENT

This study was financially supported by Special Foundation of Par-Eu Scholars Program, National Natural Science Foundation of China (No.51374236,

No.51574280), Chongqing Research Program of Basic Research and Frontier Technology (No. cstc2015jcyjBX0076), The Science and Technology Innovation Fund of China Coal Technology & Engineering Group (No.2014QN007, No.2015ZDXM14).

7. REFERENCES

- Guo, Z.L. (2002). Lattice Boltzmann model for incompressible flows through porous media. *The American Physical Society*, Volume 66, No.3, pp.1-9.
- Gao, J.L. (2010). Simulation study on the influence of permeability on gas migration in gob. *China Safety Science Journal*, Volume 20, No.9, pp.9-14.
- Li, S. G. (1998). Gas delivery feature and it's control influenced by movement of the surrounding rock in fully-mechanized top coal caving. Xi'an University of Science and Technology, Xi'an, China.
- Liang, D. and Zhou, X.H. (1999). Numeric simulation on gas movement law in working face. *Journal of Liaoning Technical University (Natural Science)*, Volume 18, No.4, pp.337-340.
- Liu, H.Y., Cheng, Y.P., Chen, H.D., Kong, S.L. and Xu, C., (2012). Characteristics of mining gas channel and gas flow properties of overlying stratum in high intensity mining. *Journal of China Coal Society*, Volume 37, No.9, pp.1437-1443.
- Qian, M.G. and Xu, J.L. (1998). Study on the 'O-shape' circle distribution characteristics of mining-induced fractures in the overlaying strata. *Journal of China Coal Society*, Volume 23, No.5, pp.466-469.
- Tu, M. and Liu, Z.G. (2002). Research and application of crack development in mining seam roof. *Coal Science and Technology*, Volume 30, No.7, pp.54-56.
- Teng, G., Tan Y.L. and Gao, M. (2007). Simulation of gas seepage in fissured coal based on lattice Boltzmann method. *Chinese Journal of Rock Mechanics and Engineering*, Volume 26, No.supp1, pp.3503-3508.
- Yang, T.H., Chen, S.K., Zhu, W.C., Liu, H.L., Huo, Z.G., Jiang, W.Z. (2010). Coupled model of gas-solid in coal seams based on dynamic process of pressure relief and gas drainage. *Rock and Soil Mechanics*, Volume 31, No.7, pp.2247-2252.
- Xu, X.L., Wang, K.S., Meng, L.M. (2011). *Fluid Mechanics*. National Defence Industry Press, Beijing, 242p.
- Yang, M.D., Li, Y.M. and Zhang, H. (2013). Numerical simulation of gas concentration field in the partial W-type ventilation system. *Journal of Safety and Environment*, Volume 13, No.6, pp.186-190.

Methods of measuring the effective drainage radius of 3# coal seam in Huoerxinhe coal mine

Linchao Dai^{a,b,*}, Kai Wang^{a,b}, Jie Cao^{a,b}, Bo Wang^{a,b}

^a State Key Laboratory of the Gas Disaster Detecting, Preventing and Emergency Controlling, Chongqing, China, 400037

^b Chongqing Research Institute Co.,Ltd. of China Coal Technology and Engineering Group, Chongqing, China, 400037

ABSTRACT

At present, the radius of coal seam gas drainage can be determined using the theoretical calculation method, the in-situ test method, and the numerical simulation method. Determining a reasonable gas drainage radius parameter has important practical significance for improving drainage and for eliminating the danger of quick outburst. In order to determine the gas drainage parameters of Huoerxinhe 3# coal seam and to efficiently eliminate the prominent risks of mining, the current methods of determining the gas drainage radius are analyzed. Based on the gas and geological conditions of Huoerxinhe 3# coal seam, the theoretical calculations, laboratory parameters, and site measurement were used to investigate the effective drainage radius of Huoerxinhe 3# coal seam. The results show that the method of site measurement of gas drainage radius is more difficult to test and has worse precision, as well as other issues. However, the exact value of effective drainage radius can be obtained by combining the theoretical calculation method with the in-situ test method. By using this combined method, the effective drainage radius of Huoerxinhe 3# coal seam is found to be 1.6 m. This combined method provides a basis for gas drainage borehole design, increasing gas drainage efficiency, and ensures safe mining. Simultaneously, the method put forth in the present study can be used as a general method to determine effective drainage radius.

KEYWORDS: Huoerxinhe coal mine; gas drilling; effective drainage radius; theoretical calculation method

1. INTRODUCTION

Coal seam gas is the main measure to control coal and gas outburst, and the distance between holes is an important consideration in the design of mine boreholes. Whether it is reasonable or not is directly related to the effect and cost of controlling outburst. If the distance between holes is too small, the perforation phenomenon will occur, and it will increase the cost of controlling the outburst, reduce the effect of extraction, and exacerbate the mining shortage situation. If the distance between holes is too large, it will form the drainage blind, therefore the drainage effect will not reach the target, and will fail to eliminate the prominent risk on the mining face. However, the distance between holes is determined by the size of drainage radius. Therefore, it has important practical significance to determine reasonable gas drainage radius parameters for improving drainage effect and eliminating the danger of outburst. In order to determine the gas drainage parameters of Huoerxinhe 3# coal seam, and to eliminate the prominent risk of on the mining face, the effective drainage radius of Huoerxinhe 3# coal seam was determined based on the gas and geological conditions of the coal seam.

2. THE CALCULATION METHOD OF DRAINAGE RADIUS

In the pre-seam gas extraction, with the joint action of seam gas pressure and hole negative pressure, gas around the borehole is continuously pumped into the borehole. It then forms a similar circular hole centerline axis as the drainage effect. The influence circle radius is called the pumping influence radius. With the extension of the pumping time, the influence radius will gradually increase until the difference between the gas pressure in the coal seam and the negative pressure in the hole bottom is not enough to overcome the resistance of the deep coal seam gas migration to the borehole. In the borehole pumping influence circle, the coal body gas pressure will be reduced, and the gas emission quantity will be increased.

At present, theoretical calculation, field tests, and numerical simulations are generally used to determine the pumping radius. However, due to the complexity of coal seam occurrence and the rheological properties of coal containing gas, the numerical simulation method has a large error in determining the effective drainage radius. The present study focuses on the theoretical calculation method and the field test method.

2.1 The theoretical calculation method of drainage radius

Research has found that whatever the numerical simulation calculation, the measured data analysis, or approximate analytical solution, the relationship between the gas emission quantity of borehole surrounding rock and time is approximately consistent with the exponential function law with e as the bottom.

$$Q=Q_0e^{-At} \quad (1)$$

In the formula, Q is the drilling gas flow at any time in m³/min. Q₀ is the drilling initial gas flow in m³/min. A is the drilling gas flow attenuation coefficient, d⁻¹. t is the borehole gas drainage time, d.

The relationship between the amount of gas drilling cumulative emission and the time is obtained by the formula (1) integral.

$$\begin{aligned} Q_t &= \int_0^t 24 \times 60 \times Q_0 e^{-At} dt \\ &= \frac{1440Q_0}{A} (1 - e^{-At}) = Q_{\max} (1 - e^{-At}) \end{aligned} \quad (2)$$

In the formula, Q_t is the drilling cumulative gas drainage in m³. Q_{max} is the drilling limit pumping gas quantity in m³.

The effective drainage radius of gas drainage borehole is defined so that in the specified time, the gas pressure or gas content in the radius is reduced to the safe allowable value.

When the impact between the two holes is not considered, according to formula (2) and mass balance principle, then the formula (3) and (4) can be obtained.

$$\int_{r_1}^r 2\pi r L \times M \times \eta dr = Q_{\max} (1 - e^{-At}) \quad (3)$$

$$r(t)^2 - r_1^2 = \frac{Q_{\max} (1 - e^{-At})}{\pi LM \eta} \quad (4)$$

Due to $r \gg r_1$, so

$$r = \sqrt{\frac{Q_{\max}}{\pi LM \eta}} \times \sqrt{1 - e^{-At}} \quad (5)$$

$$\eta = \frac{M_c}{M} \times 100\% \quad (6)$$

$$t = -\frac{\ln(1 - \frac{\pi r^2 LM \eta}{Q_{\max}})}{A} \quad (7)$$

In the formula, η is the coal seam gas extraction rate when coal seam gas content is at the safe concentration in %. M_c is the coal seam residual gas content after drainage in m³/t. M is the coal seam original gas content in m³/t. The remaining symbols are as previously listed.

In order to meet the requirements of coal and gas outburst prevention, "coal and gas outburst prevention rules" and "coal mine safety regulations" stipulate the coal seam gas extraction rate ($\eta=25\%$ or 30%).

2.2 Field test method for pumping radius

The method of site measurement of gas drainage radius leads to greater difficulties in testing, worse precision, and other issues. It cannot determine the gas drainage radius with consideration to the change in gas geological conditions. The pressure reducing method and flow method are most commonly used in the coal mine. The pressure reducing method involves the set up of more pressure measuring boreholes, and the gas pressure measurement is influenced by many factors. It can be difficult to measure the gas pressure, as the pressure is sometimes too large, and the hole leakage pressure often decreases rapidly.

Coal and gas outburst prevention rules determine the method of measurement for the effective discharge radius. Firstly, gas flow measuring parallel drillings (diameter of 42 mm) are placed in the work face layer with variable spacing. Then a parallel discharge hole is placed to one side of the measuring hole, and the variation in gas emission quantity in the holes by time is observed. If within two hours the amount of gas emission in the hole is increased by 10%, the distance between the hole and the discharge hole is called the effective radius.

3. THEORETICAL CALCULATION OF HUOERXINHE PUMPING RADIUS

Shanxi Huoerxinhe Coal Industry Co. Ltd. is located in Zhangzi County, Changzhi City. The mine area is 71.3947 km², and the 3# coal seam is located in the lower part of the Shanxi formation. The coal seam dip angle is about 5 degrees, and the coal thickness is 4.49-7.17 m with an average of 5.65 m. The 3# coal seam gas content is 8-10 m³/t.

According to "the 3# coal seam coal and gas outburst hazard identification", the maximum gas pressure of 3# coal seam is 0.52 MPa, the maximum initial velocity of gas emission is 23.1, the minimum coal firmness coefficient is 1.27, and the damage type of coal is II. The 3# coal seam in the identification range above +430 m level is without outburst danger.

In the Huoerxinhe 3301 return air trough, measurements of the attenuation coefficient of gas flow and borehole flow in one hundred meters were conducted by field test. Four measuring points were arranged, with a pore diameter of 94 mm, a hole depth 100 m, a drilling angle of 0 degrees horizontal,

a vertical angle degree of 1, and a hole distance 10 m. The following four holes are as shown in Figure 1.

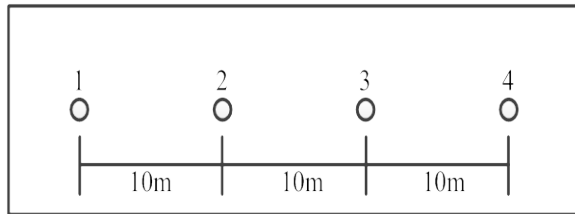


Figure 1: Drilling layout.

After the end of sealing, the gas meter was connected and observed every day for 30 min. Through the data acquisition, it is found that the four holes had zero flow in the three days.

The data were recorded for the first two day's 30 min (as shown in Tables 1 and 2). In order to get the hole attenuation law, the data were fitted and the results were as shown in Figures 2 and 3.

Table 1: Instantaneous flow on the first day.

Time/min	1#	2#	3#	4#
1	2.6	3.2	2.8	2
2	2.4	3.4	3	2
3	2.4	3.4	2.8	2.2
4	2.6	3.6	2.8	1.8
5	2.4	3.4	2.6	1.8
6	2.6	3.4	2.6	1.8
7	2.4	3.4	2.8	2
8	2.6	3.2	2.6	2
9	2.4	3.2	2.4	2
10	2.6	3.2	2.8	2
11	2.4	3.4	2.8	2
12	2.6	3.2	2.6	1.8
13	2.4	3.2	2.8	1.8
14	2.6	3	3	1.8
15	2.4	3	2.6	1.8
16	2.6	3.2	2.8	1.8
17	2.4	3	2.6	1.8
18	2.4	3	2.4	1.6
19	2.2	2.8	2.4	1.6
20	2.2	2.8	2.6	1.6
21	2.2	2.8	2.8	1.6
22	2.4	2.6	2.6	1.6
23	2.2	2.6	2.6	1.8
24	2.2	2.8	2.8	1.6
25	2	2.6	2.6	1.6

26	2	2.4	2.6	1.8
27	2	2.4	2.4	1.8
28	2	2.4	2.4	1.6
29	2	2.4	2.6	1.6
30	2	2.2	2.4	1.6

Table 2: Instantaneous flow on the second day.

Time/min	1#	2#	3#	4#
1	1	1.2	1.2	1
2	1	1.2	1	1
3	0.8	1.2	1	0.8
4	0.8	1	1	0.8
5	0.8	0.8	1	0.8
6	0.8	0.8	1	0.8
7	0.8	1	1.2	0.8
8	0.8	1.2	1.2	0.8
9	0.6	0.8	1	0.8
10	0.6	0.8	1	0.8
11	0.6	1	0.8	0.8
12	0.6	1	1	0.8
13	0.6	1	0.8	0.8
14	0.6	1	0.8	0.6
15	0.6	1	1	0.6
16	0.6	1	1	0.6
17	0.6	1	1	0.6
18	0.6	1	1	0.6
19	0.4	0.8	1	0.6
20	0.6	0.8	1	0.6
21	0.6	0.8	1	0.6
22	0.6	0.8	0.8	0.6
23	0.6	0.8	0.8	0.6
24	0.6	0.8	0.6	0.6
25	0.6	0.8	0.6	0.6
26	0.6	0.8	0.6	0.6
27	0.6	0.6	0.6	0.6
28	0.6	0.6	0.6	0.6
29	0.6	0.6	0.4	0.4
30	0.6	0.6	0.4	0.4

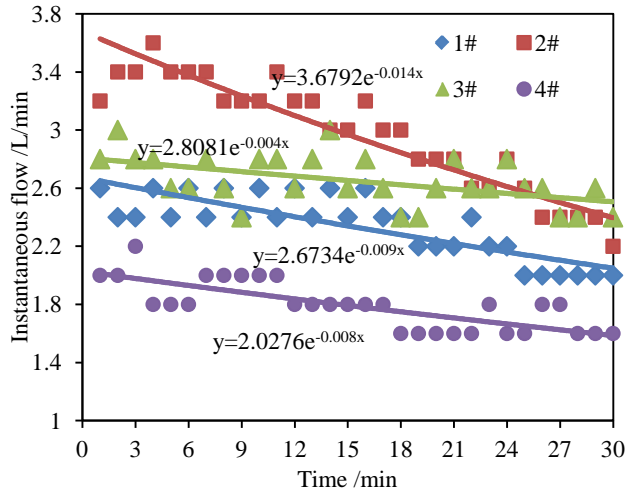


Figure 2: 1, 2, 3, 4 hole flow chart within the first day 30 min.

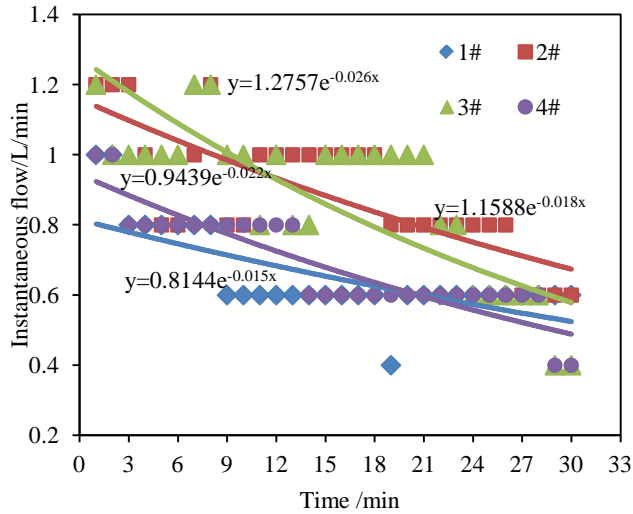


Figure 3: 1, 2, 3, 4 hole flow chart within the second day 30 min.

According to the formula of the hole flow attenuation fitting of four holes, gas flow attenuation coefficient A and the initial speed of 100 m drilling Q_0 can be obtained by the corresponding formula (1).

The theoretical pumping radius r of four holes can be calculated by coal seam gas extraction rate 30% and A , Q_0 into the formula (5). The specific parameters are shown in Table 3.

Table 3: Theoretical pumping radius calculation results.

Time	Hole	$A(\text{min}^{-1})$	$Q_0(\text{m}^3/\text{min})$	$r(\text{m})$
first day	1	0.009	2.6734	2.006479
	2	0.014	3.6792	2.272102
	3	0.004	2.8081	2.132388
	4	0.008	2.0276	1.76
second day	1	0.015	0.8144	1.061569
	2	0.018	1.1588	1.240409
	3	0.026	1.2757	1.233736
	4	0.022	0.9439	1.089657

From the Table 3, the effective pumping radius of Huoerxinhe is 2.043 m on the first day, and the average is 1.156 m on the second day. Therefore, the total average is 1.6 m.

4. FIELD TEST OF HUOERXINHE PUMPING RADIUS

4.1 Measurement point arrangement and method

The field test of gas drainage radius was tested in Huoerxinhe 3203 singh transport trough. Five measuring points were arranged, as shown in Figure 4. Among them, drilling holes 1-4 are the test holes, and drilling hole 5 is the pre drainage hole.

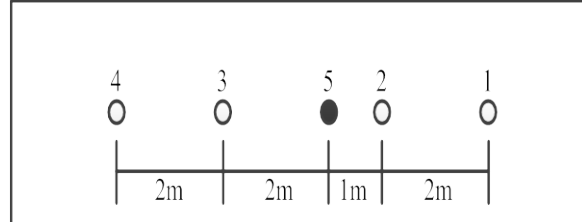


Figure 4: Drilling layout.

The steps of the determination method are as follows:

(1) Four parallel test holes were arranged along the soft stratification seam with a pore diameter of 94 mm, hole depth 100 m, a drilling angle of 0 degrees horizontal angle and a vertical angle of degree 1, with hole distances as shown in Figure 4.

(2) Polyurethane was used to seal holes 1-4. The gas flow of the boreholes was determined immediately after the end of sealing. Meanwhile, each hole was tested every 1 min with each test hole measurement time being at least 30 min.

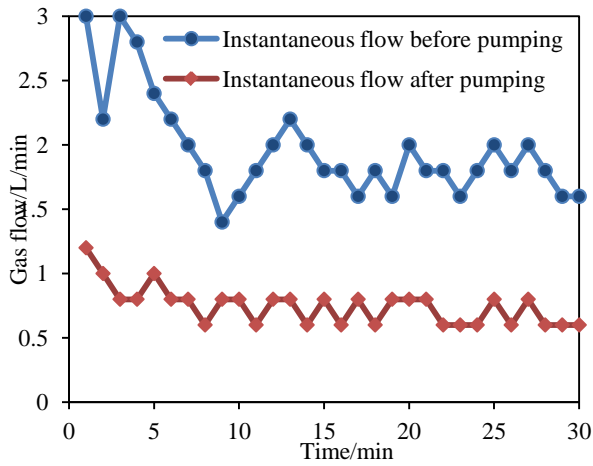
(3) The pre-pumping hole was arranged in parallel between holes 2 and 3. After the construction of the pre pumping hole, polyurethane was used to seal the hole immediately. Sealing length was at least 8m.

(4) After the end of the sealing, networking drainage was implemented immediately. Holes 1-4 were then tested every 1 min with each test hole measurement time being at least 30 min.

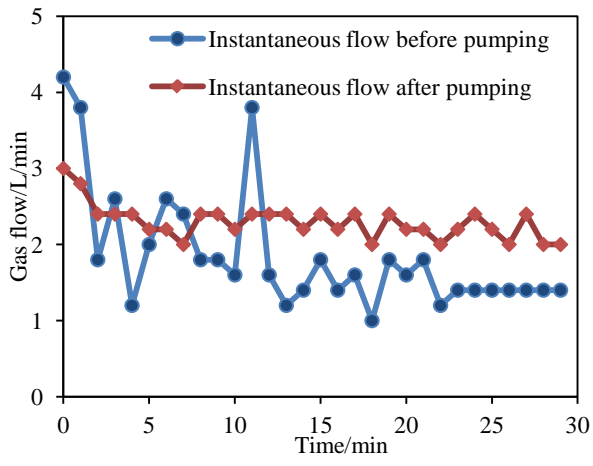
(5) After completing the pre drilling within 2 h, the gas flow rate of each test hole was determined and plotted. If the test hole gas flow rate is increased by 10% compared with that of the pre drilling hole for 3 continuous measurement times, it then follows that the test hole is in the effective radius of the hole drilling. The most distant in accordance with the above test hole distance is the effective radius of the pre-drilling hole.

4.2 Determination of gas drainage radius

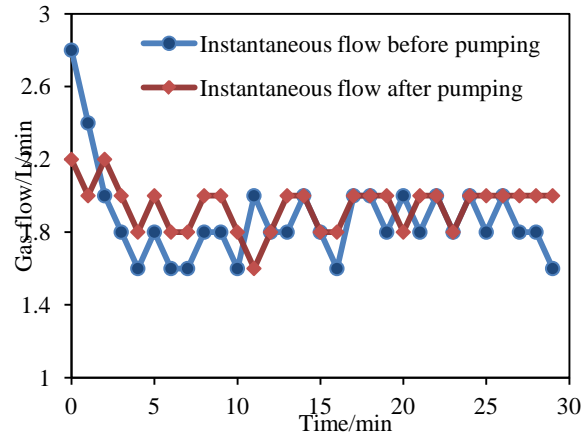
With time as the horizontal coordinates and gas flow as the longitudinal coordinates, the gas flow observation data was used to draw the hole gas flow curve, as shown in Figure 5 and Table 4.



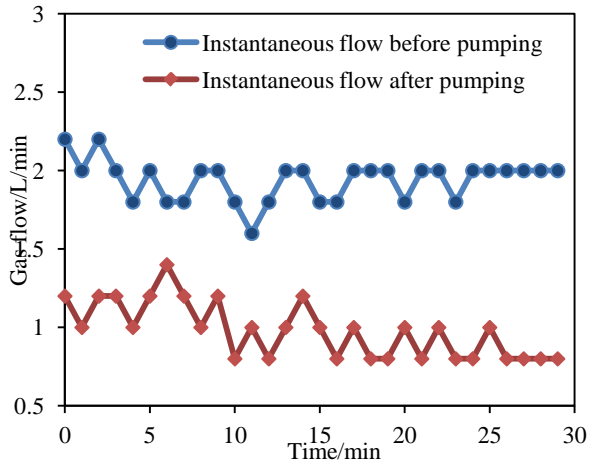
(a) No. 1 test hole



(b) No. 2 test hole



(c) No. 3 test hole



(d) No. 4 test hole

Figure 5: The test hole gas flow before and after the pre pumping.

Table 4: Average flow before and after the pre pumping.

Hole	Average flow (L/min)	
	Before pumping	After pumping
1	1.96	0.75
2	1.86	2.29
3	1.87	1.94
4	1.94	0.98

From Figure 5 and Table 4, it can be seen that the gas flow rate of test hole 2 is increased by more than 10% after the pre pumping. The gas flow rate for hole 2 is increased by 23%, 3% for hole 3, and the gas flow for holes 1 and 4 are decreased.

According to the principle of the gas drainage radius, the Huoerxinhe 3# coal mine gas drainage radius is 1-2 m. It can be seen that the site measurement of gas drainage radius leads to greater

difficulty in testing, worse precision, as well as other issues.

5. CONCLUSION

(1) When taking the pumping rate of 30% above the standard as the condition, the effective pumping radius of Huoerxinhe 3# coal mine is 1.6 m as found through the theoretical analysis and calculation.

(2) Using the field test method to measure the effective extraction radius is feasible, and the effective drainage radius of Huoerxinhe 3# coal mine as measured by the field test method is 1-2 m.

(3) Through a combination of the field measurement and the theoretical calculation, the effective extraction radius of Huoerxinhe 3# coal mine is 1.6 m.

6. ACKNOWLEDGEMENT

This study was financially supported by Special Foundation of Par-Eu Scholars Program, National Natural Science Foundation of China (51374236, 51574280), The Science and Technology Innovation Fund of China Coal Technology & Engineering Group (2014QN007, 2015ZDXM14).

7. REFERENCES

Cai C.G., Zhou G.Z. (2004). Gas drainage in seam with large auto variable diameter bore holes. *Coal Science and Technology*, Volume 32, No. 12, pp.39-41

Cao X.Q., Xin H.H., Xu L.H. (2009). Determination of effective drainage radius of gas drainage borehole, *Coal Engineering*, No. 9, pp.88-90

Hao F.C., Liu M.J., Sun L.J. (2012). Study on comparison of methods to determine gas drainage radius and existed problems. *Coal Science and Technology*, Volume 40, No. 12, pp.55-58

Li Z.W., Lin B.Q., Guo M.G. (2014). Determination on effective influence radius of gas drainage through borehole based on one-dimensional radial flow. *Coal Science and Technology*, Volume 42, No. 12, pp.62-64

Liu S.J., Ma G., Lu J. (2011). Relative pressure determination technology for effective radius found on gas content. *Journal of China Coal Society*, Volume 36, No. 10, pp.1715-1719

Wang Z.F., Zhou S.H., Li Z.Q. (2011). Numerical calculation method of effective drainage radius for gas drainage borehole. *Coal Engineering*, No. 6, pp.82-84

Xu S.M. (1996). Discussion on the method to determine the effective gas drainage radius. *Coal Engineer*, No. 3, pp.43-45

Yu, B.F. (2000). Prevention of coal-mine gas hazards and utilization manual. Coal Industry Press, China

Yu T., Lu P., Sun J.H. (2012). Measurement of effective drainage radius based on gas flow and pressure of boreholes. *Journal of Mining & Safety Engineering*, Volume 29, No. 4, pp.596-600

Temperature Variation of Coal during the Gas Adsorption Process

Tao Yang ^{a,*}, Baisheng Nie ^b, Xuexi Chen ^a, Peng Chen ^b

^a Department of Safety Engineering, North China Institute of Science and Technology, East Yanjiao, Beijing, China, 101601

^b Faculty of Resources & Safety Engineering, China University of Mining and Technology (Beijing), Beijing, China, 100083

ABSTRACT

Using a self-made coal gas adsorption-desorption instrument, laboratory research on temperature variations of the adsorption process under different conditions was completed to study the adsorption law of coal gas and to reveal coal gas adsorption mechanisms. Under the same conditions, the order of unit mass of coal's gas adsorption and the temperature variation is: Zhenxing 2# Coal > Runhong 3# coal > Malan 8# coal. The results show that gas adsorption gets lower as the temperature increases. For the same coal sample under the same conditions, the smaller the particle size, the greater the pressure variations of the methane adsorption process and the larger the gas adsorption in the same period. The results of this paper reveal the mechanism of coal and gas outburst.

KEYWORDS: coal particles; gas adsorption; thermal effect; temperature variation; experimental study

1. INTRODUCTION

China is the largest coal producer in the world and it also has the most serious coal mine disasters. According to the statistics, there are nearly a thousand coal mines in China, including more than 110 key state-owned mines that at a risk for coal and gas outburst. Hundreds of coal and gas outburst events occur each year, often causing serious casualties and economic losses (State Administration of Work Safety, 2007). With the continuing exploitation of coal resources, the depth of Chinese coal mines increases about 100 meters every year, causing serious (Xie et al., 2006). Face coal temperature is closely related to ground stress, gas content, and coal's physical and mechanical properties. The three factors above are related to coal and gas outburst (Zhang, Z Z et al., 2010. Liu, Z et al., 2012. Chen, G et al., 2014). Gas in the coal body is mainly in the adsorption state hosted in coal matrix when undisturbed.

At present, the real mechanism of gas adsorption, desorption, and the diffusion process in coal and the influence factors are not clear. Because of the limits of current prediction methods and technological level, gas accident prevention theory and technology are not valid.

Energy conversion is associated with the process of gas adsorption and desorption (Nie et al., 2013a; Chaback et al., 1996; Nodzeński, 1998; An, ZX., 1983; Rike & Yuan, 1989; Zhao, 1994; Niu, GQ., 2003). Temperature variation exists along with the process of coal and gas outburst (Nie et al., 2013b; Guo et al., 2000a; Guo & Jiang, 2000; Zhang et al., 2011; Wang et al., 1999). Some scholars try to predict gas accidents according to temperature

variation (Wang, 2001; Guo et al., 2000b; и.а. Renke & и.я. Lieming, 1985; Lun and Tang, 1992). The predictive indexes that have been developed are mainly empirical values. There is a gap between the practical application and theory, because there is currently no systematic study of temperature change in the process of gas desorption and diffusion, especially the relationship between the equilibrium pressure, adsorption volume, adsorption rate, and temperature variation.

This paper aims to systematically study the laws of temperature variation in the process of gas adsorption under laboratory conditions to reveal the energy conversion and transmission process.

2. TESTS OF THE BASIC PARAMETERS OF COAL BODY

2.1 Basic information of coal samples

Three kinds of coal samples were taken from high gas coal mines in different areas of China, including coal 8# from Malan coal mine, coal 2# from Zhenxing second coal mine, and coal 3# from Runhong coal mine. The industrial analysis and density test results of three kinds of coal samples are shown in Tables 1 and 2.

Table 1: True density and apparent density of coal.

Coal sample ID	Name of coal sample	True density, g/cm ³	Apparent density, g/cm ³
1	Malan coal 8#	1.28	1.12
2	Zhenxing coal 2#	1.42	1.24
3	Runhong coal 3#	1.303	1.18

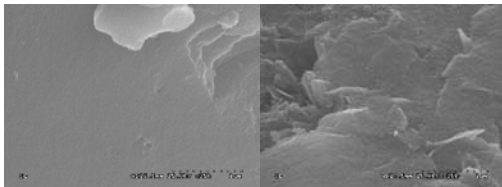
Table 2: Industry analysis of coal.

Coal sample ID	Name of coal sample	M_{ad} (%)	A_d (%)	V_{daf} (%)	F_c (%)
1	Malan coal 8#	0.44	2.66	51.18	45.72
2	Zhenxing coal 2#	2.22	11.96	9.45	76.37
3	Runhong coal 3#	2.02	16.05	12.25	69.68

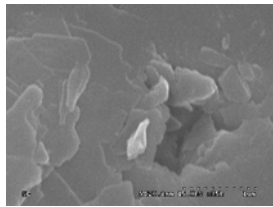
Among them, M_{ad} is the moisture content of coal, V_{daf} is the volatile content of coal, A_d is the ash content of coal, and F_c is the fixed carbon content of coal.

2.2 Test of pore structure in coal samples

After being collected and processed, coal samples were scanned with electron microscopy in different magnification. Scanning results reflect the coal samples' pore structure conditions. The micro-pore's development situation is one of the most important factors affecting the adsorption of methane. Using a Hitachi S-4800 scanning electron microscope, morphology of the coal samples was scanned. The scanning magnification was 35,000 times, as shown in Figure 1.



a) Malan 8#, 35000 times b) Runhong 3# , 35000 times



c) Zhenxing 2# , 35000 times

Figure 1: SEM images of Coal Samples.

Experimental results showed the presence of a large fissure structure and an obvious loose layered structure in the coal sample from Zhenxing coal mine. Degree of pore developments were roughly: Malan 8 # coal < Runhong coal < Zhenxing second mine coal.

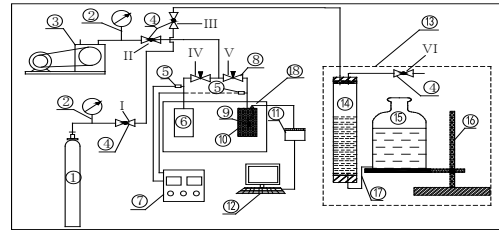
3. TEMPERATURE TEST DURING GAS ADSORPTION PROCESS

According to certain experimental standards, the coal samples were crushed and those particles measuring 60-80 mesh, namely between 0.178 mm-

0.25 mm in diameter, were collected with a sorting sieve.

3.1 Experimental system

To study the temperature response characteristics during gas adsorption process, temperature change tests were carried out. The structure diagram of the adsorption-desorption instrument is shown in Figure 2.



①high pressure gas cylinder ②pressure gauge ③vacuum pump ④ ball valve ⑤ pressure sensor ⑥ reference tank ⑦ industrial computer ⑧needle valve ⑨temperature sensor ⑩sample tank ⑪ temperature signal acquisition card ⑫sample tank ⑬desorption test system ⑭ measuring cylinder ⑮ leading bottle ⑯ lifting platform ⑰rubber hose

Figure 2: The system schematic diagram of gas adsorption and desorption experiment.

3.2 Experimental procedure of adsorption process

The system should first be debugged. The main steps are as follows:

- 1) Connect the high-pressure gas tank to the experimental system.
- 2) Turn on the vacuum pump, open valves II, IV and V and make sure other valves stay closed. After vacating the sample tank for 4 hours, close valves II, IV and V.
- 3) Open the temperature acquisition system and pressure collection system. Adjust the high-pressure gas tank outlet valve to the desired pressure value. Open valve I and then slowly open valve IV until the reference tank pressure reaches the predetermined value. Close valve I, open valve V slowly, and continuously inflate for 12 hours. Record and save the temperature and pressure values.

4. TEMPERATURE VARIATION RESULTS OF THE COAL GAS ADSORPTION EXPERIMENTS

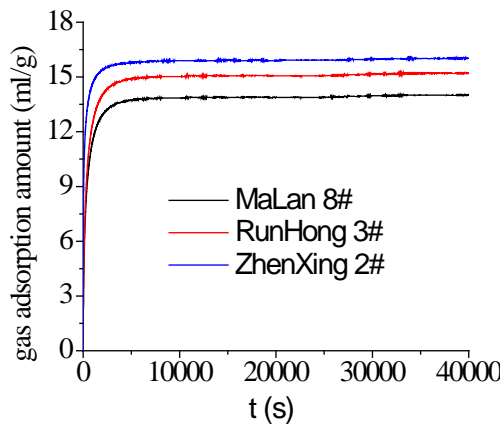
The three coal samples were sealed from different coal mines and were transported to the laboratory. They were processed into four different mesh sizes such as 10 to 20 meshes, 20 to 40 meshes, 40 to 60 meshes and 60 to 80 meshes. The information about coal samples are presented in Table 3.

Table 3: The parameters of coal sample in coal gas adsorption experiment.

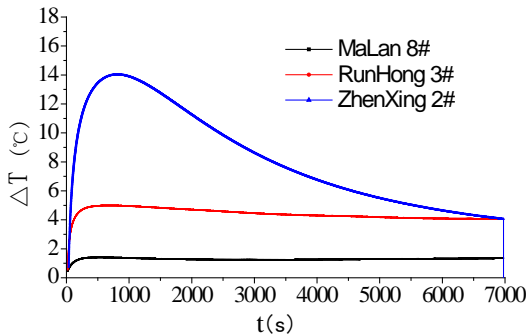
Coal sample name	Coal sample size	Free volume of sample canister	Coal sample quality
		ml	g
Zhenxing second mining	10-20 mesh	551.8266	769
	20-40 mesh	603.1798	701.4
	40-60 mesh	621.5689	657.6
	60-80 mesh	556.6884	695.82
Malan8#	10-20 mesh	489.9777	784.9
	20-40 mesh	541.13	600
	40-60 mesh	530.4417	618.3
	60-80 mesh	431.8605	467.4
Runhong	60-80 mesh	493.9033	562

4.1 Temperature variations during gas adsorption for different coal samples

Figure 3 shows the adsorption process results for the three coal samples in 60 to 80 meshes under a gas pressure of 3.1 MPa.



a) Relationship of adsorption volume and time of the 3 coal samples



b) Temperature variation of the 3 coal samples during the adsorption process

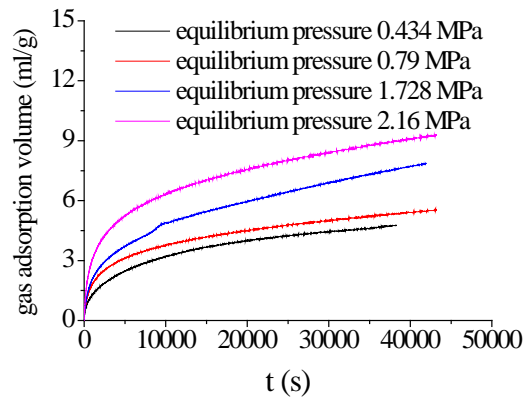
c) Temperature change rate of the 3 coal samples during the adsorption process

Figure 3: the adsorption experimental results of three coal samples in 60 to 80 meshes under gas pressure of 3.1 MPa.

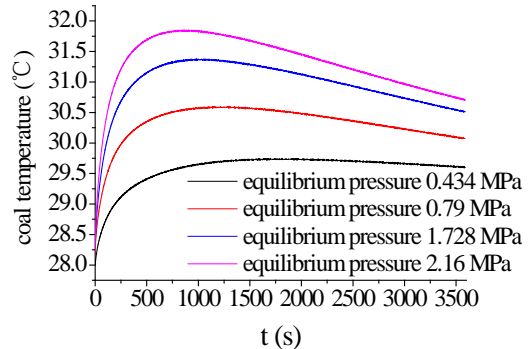
The results showed that under the same conditions, the order of gas adsorption reaching equilibrium was: Zhenxing second mining 2# coal > Runhong 3# coal > Malan 8# coal. Equilibrium adsorption capacity values were 15.06 ml/g, 15.2 ml/g and 16.1 ml/g, respectively. Similarly, temperature variations during the adsorption process were different, and the order of temperature variation for a unit mass of coal sample was: Zhenxing second mining 2# coal > Runhong 3# coal > Malan 8# coal. The variations were 14.056°C, 5.0°C and 2.304°C, respectively. The methane adsorption was an exothermic physical process, where the higher the adsorption the more heat was released.

4.2 Temperature variations of gas adsorption under different adsorption equilibrium pressures

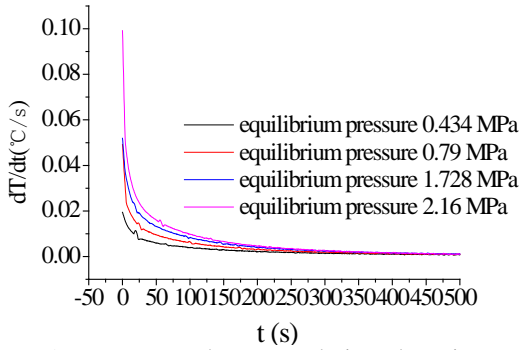
The current study examined the gas adsorption law of coal under different adsorption equilibrium pressures. The adsorption experiment results of 40 to 60 mesh coal samples from Malan 8# mine and Zhenxing 2# mine were analyzed. Figure 4 shows the adsorption experiment result for the Malan 8# coal sample while Figure 5 shows the adsorption experiment result for Zhenxing 2# coal sample.



a) Adsorption volume change

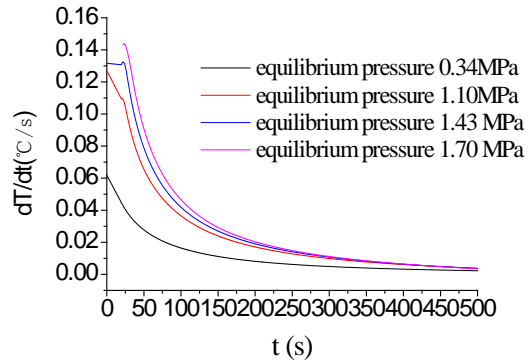


b) Temperature variation during adsorption process



c) Temperature change rate during adsorption
 Figure 4: adsorption experimental results of Manlan 8# coal sample(40-60 mesh) under different equilibrium pressure.

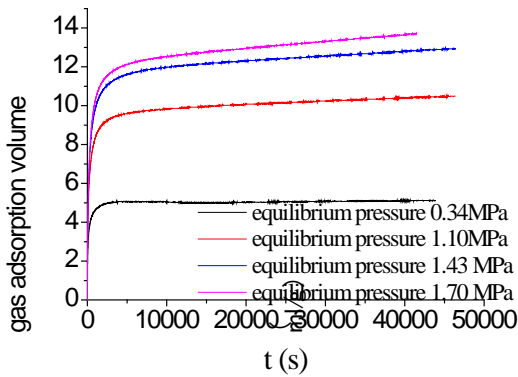
The initial aeration pressures were 1.0 MPa, 2.7 MPa, 3.4 MPa, and 4.1 MPa, respectively in the reference tank. After equilibrium, the pressures were 0.434 MPa, 0.79 MPa, 1.782 MPa, and 2.16 MPa, respectively. The pressure variations ΔP were 0.206 MPa, 0.24 MPa, 0.2712 MPa, and 0.411 MPa, respectively while the adsorptions were 4.756 ml/g, 5.536 ml/g, 6.345 ml/g, and 9.254 ml/g, respectively. The maximum amounts of temperature variations were 1.66 °C, 1.856 °C, 2.845 °C, and 3.108 °C respectively.



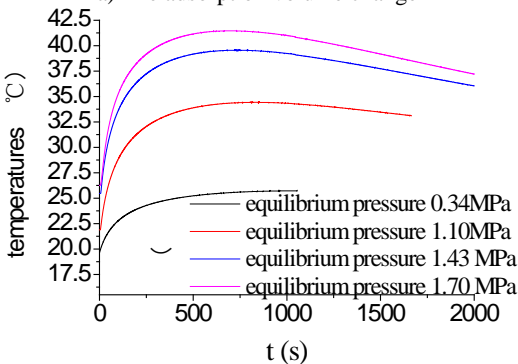
c) The change rate of adsorption temperature
 Figure 5: the adsorption experiment result of Zhenxing mine coal samples in 60 to 80 mesh.

As shown in Figure 5, the initial aeration pressures were 1.0 MPa, 2.7 MPa, 3.4 MPa, and 4.1 MPa, respectively in the reference tank when the sample can was filled with coal samples in 40 to 60 mesh. The coal sample was selected from Zhenxing coal mine. After equilibrium, the pressure values were 0.34 MPa, 1.1 MPa, 1.43 MPa, and 1.7 MPa, respectively. The pressure variations ΔP were 0.218 MPa, 0.44 MPa, 0.557 MPa, and 0.589 MPa, respectively. The adsorptions were 5.118 ml/g, 10.488 ml/g, 12.96 ml/g and 13.702 ml/g, respectively. The maximum amounts of temperature variations were 6.307 °C, 11.81 °C, 13.23 °C, and 14.28 °C, respectively.

The experiment results showed that the coal's adsorption for gas increased with the rising of gas pressure for a specific temperature. In the initial adsorption stage, the smaller the particle size, the larger the gas adsorption volume and the greater the temperature rise gradient. Adsorption is an exothermic process. Theoretically, coal temperature will always rise. However, the experimental system is not an adiabatic system. There is heat exchange with the external environment in the adsorption process, thus the adsorption temperature will reach a maximum at about 700 s in the adsorption temperature change chart. After that, as the adsorption gets weaker, heat exchange will occur between the coal and the external environment because of the temperature gradient. Thereby, the coal temperature decreases until it reaches the same temperature as the external environment.



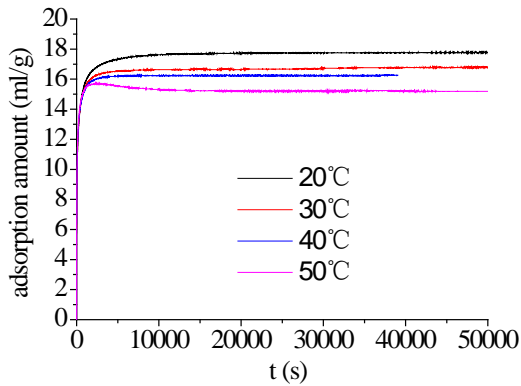
a) The adsorption volume change



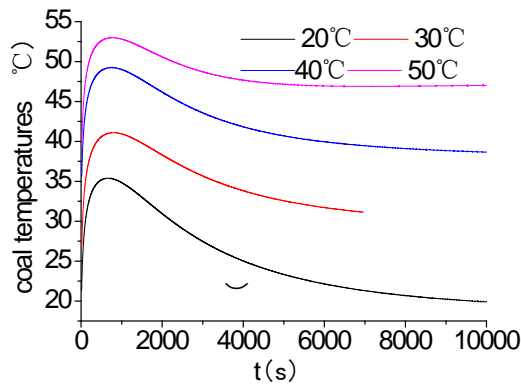
b) The temperature variation during adsorption

4.3 The temperature variation of gas adsorption at different temperatures

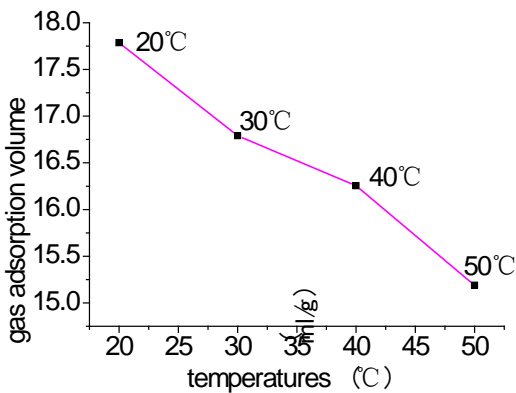
Figure 6 shows the results of the adsorption process for the Zhenxing 2# coal sample in 60 to 80 meshes at 20 °C, 30 °C, 40 °C, and 50 °C when the charging pressures were all 3.1 MPa.



a) The adsorptions at different temperatures



b) The adsorption temperature



c) The equilibrium adsorption volume

Figure 6: The experiment results of adsorption processes of Zhenxing second mining coal samples in 60 to 80 mesh at different temperatures

The gas adsorption capacity for coal was easily influenced by the temperature change. For the coal samples in 60 to 80 meshes from Zhenxing coal mine, the final equilibrium pressure was very different under the same charging pressure. The coal sample's adsorption equilibrium pressures at 20°C, 30°C, 40°C, and 50°C were 1.269 MPa, 1.2455 MPa, 1.303 MPa, and 1.33 MPa, respectively. The pressure drops were 0.214 MPa, 0.188 MPa, 0.1816 MPa, and

0.179 MPa, respectively. The unit mass coal's adsorptions were 17.787 ml/g, 16.79 ml/g, 16.255 ml/g, and 15.19 ml/g, respectively after equilibrium, which showed that the gas adsorption dropped as the temperature was getting higher.

The coal adsorption of methane was an exothermic physical process. The larger the adsorption, the more heat released. This law can also be reflected by the temperature variation in adsorption experiments. The ΔT_{max} at 20°C, 30°C, 40°C, and 50°C were 15.93°C, 14.06°C, 13.57°C, and 13.43°C, respectively. ΔT_{max} represents the absolute difference between the initial temperature and the maximum temperature of the adsorption process. Because the adsorption-desorption experiment system was not an adiabatic system, with the decrease of the adsorption rate, the external environment had more and more impact on the temperature inside the sample tank. When temperature reached the peak, the environmental temperature played a dominant role. Therefore, the temperature variations from beginning to the temperature peak were studied in this experiment.

4.4 Temperature variations during gas adsorption in different particle size

Figure 7 shows the adsorption equilibrium curves of coal samples in 10 to 20 mesh, 20 to 40 mesh, and 40 to 60 mesh from Malan 8# coal mine when the charging pressure were 1 MPa, 2 MPa, 3 MPa, and 4 MPa, respectively. Under the same charging pressure, the smaller particle size was, the larger gas adsorption was after adsorption equilibrium.

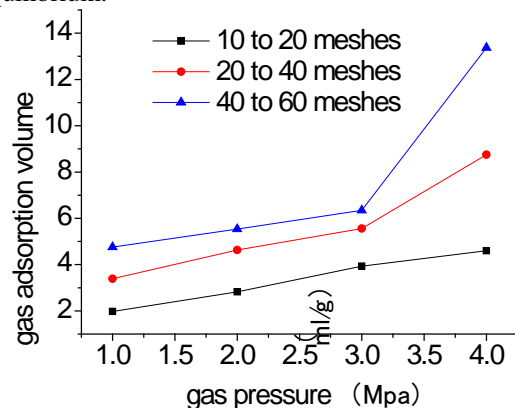


Figure 7: The Malan 8# coal samples adsorption in different particle sizes and pressures.

The charging pressure of the 10-20 mesh, 20-40 mesh, and 40-60 mesh coal samples tank were 1.06 MPa, 1.07 MPa, and 1.0 MPa, respectively. The initial pressures were 0.6835 MPa, 0.65875 MPa, and

0.643 MPa, respectively after opening the valve between the reference and sample tanks. The final equilibrium pressures were 0.60 MPa, 0.539 MPa, and 0.434 MPa, respectively. The pressure variations ΔP were 0.0835 MPa, 0.145 MPa, and 0.206 MPa, respectively from the beginning of the adsorption to the end.

The adsorption of Malan 8# coal samples in 10-20 mesh, 20-40 mesh and 40-60 mesh after adsorption equilibrium were 1.971 ml/g, 3.388 ml/g, and 4.756 ml/g, respectively when the charging pressure of the reference tanks were 1 MPa.

The results showed that for the same coal sample under the same condition, the smaller particle size is, the greater the pressure variations for the methane adsorption process and the larger the gas adsorption volume. In addition, the influence of particle size on adsorption was also reflected on the temperature variations of the coal adsorption process. Namely, the smaller the particle size, the greater the temperature variation of the adsorption process was when other conditions remain unchanged. The reasons were that the smaller the coal particle size is, the greater the specific surface area. The greater the adsorbed area of methane molecules, the larger the methane adsorption volume under the same gas pressure and temperature conditions.

According to adsorption potential theory (Dubinin M M, 1960; Clarkson C R et al., 1997; Mosher K et al., 2013), methane molecule adsorption would release a part of the potential energy in an exothermic physical process. Thus, the higher the gas adsorption volume, the more heat was generated, and the greater the temperature variation.

5. CONCLUSIONS

Adsorption laws of coal gas were tested with different coal samples at different temperatures, in different sizes and under different adsorption equilibrium pressures. Specific conclusions are as follows:

(1) The difference of temperature variations in adsorption process was large. The order of unit mass of coal samples' temperature variation was: Zhenxing 2# coal > Runhong 3# coal > Malan 8# coal. Their variable quantities were 14.056°C, 5.0°C, and 2.304°C, respectively. The rate of temperature variations followed the same order: Zhenxing 2# coal > Runhong 3# coal > Malan 8# coal, indicating that Zhenxing 2# coal has a stronger adsorption capacity.

(2) At a specific temperature, with the increasing gas pressure, coal's gas adsorption capacity increased. At the initial adsorption stage, the smaller

the particle size, the higher the gas adsorption volume, as well as the temperature rise gradient.

(3) For Zhenxing 2# coal samples in 60 to 80 mesh at 20°C, 30°C, 40°C, and 50°C, the adsorption and desorption process were studied when the charging pressure was 3.1 MPa. The results showed that gas adsorption decreased as the temperature increased.

(4) For the same coal sample under the same conditions, the smaller the particle size, the greater the pressure variations of the methane adsorption process and the larger the gas adsorption volume in the same period.

6. ACKNOWLEDGEMENT

This research was supported by the Fundamental Research Funds for the Central Universities (3142015002, 3142015020) and by the Research project of science and technology in Hebei Province (Z2015104).

7. REFERENCES

Bi D, Wu Z. (2010) Research on the regular pattern of temperature distribution when gas gushes out from the semi-infinitely great coal body. *Science Technology and Engineering*. Volume 10, No. 7, pp.1607-1610

Chen G, Li T, Zhang G, et al. (2014) Temperature effect of rock burst for hard rock in deep-buried tunnel. *Natural Hazards*. Volume 72, No. 2, pp. 915-926

Clarkson C R, Bustin R M, Levy J H. (1997) Application of the monomultilayer and adsorption potential theories to coal methane adsorption isotherms at elevated temperature and pressure. *Carbon*. Volume 35, No. 12, pp. 1689-1705

Feng J, Li W, Xie K. (2002) Research on coal structure using FT-IR. *Journal of China University of Mining and Technology*. Volume 31, No. 5, pp. 362-366

Guo L, Jiang C. (2000) The theoretical analysis of the influencing factors on temperature change in the process of coal and gas outburst. *Journal of China Coal Society*. Volume 25, No. 4, pp. 401-403

Ferraro J R, Louis J. (2012) *Fourier Transform Infrared Spectra: Applications to Chemical Systems*. Academic Press.

Mosher K, He J, Liu Y. (2013) Molecular simulation of methane adsorption in micro-and mesoporous carbons with applications to coal and gas shale systems. *Journal of Coal Geology*. Volume 109, pp. 36-44

Liu Z, Feng Z. (2012) Theoretical study on adsorption heat of methane in coal. *Journal of Coal*

Science & Engineering. Volume 37, No. 4, pp. 647-653

Dubin M M. (1960) The potential theory of adsorption of gases and vapors for adsorbents with energetically no uniform surfaces. Chemical Reviews. Volume 60, No. 2, pp. 235-241

Solomon P R, Carangelo R M. (1988) FT-ir analysis of coal: 2. Aliphatic and aromatic hydrogen concentration. Fuel. Volume 68, No. 7, pp. 949-959

Zhang Z Z, Gao F, Liu Z. (2010) Research on rock burst proneness and its microcosmic mechanism of granite considering temperature effect. Chin J Rock Mech Eng. Volume 29, No. 8, pp. 1591-1602

Zhang Y. (2012) Study on the Microcosmic Characteristics and Macro Parameters in the Process of Coal Oxidation and Spontaneous Combustion. Xi'an: Xi'an University of Science and Technology.

Zhang H, Zhou M, Song C, et al. (2010) Research on coal mine gas sensor systems based on near infrared spectrum. In: Hefei, China.

Zhang L, Lu H, Yan H, et al. (2013) Quantitative Analysis and Research on Coal Quality Based on Near Infrared Spectrum. Infrared Technology. Volume 35, No. 8, pp. 522-525

Statistical analysis of coal mine accidents in China from 2005-2013

Xinsheng Hu^a, Zongzhi Wu^{b,*}, Rujun Wang^{c,d}, Yingquan Duo^{c,d}

^a Faculty of Resource and Safety Engineering, China University of Mining and Technology (Beijing), Beijing, China, 100083

^b The Occupational Safety and Health Administration, State Administration of Work Safety, Beijing, China, 100713

^c Institute of safety technology for hazardous chemicals, China Academy of Safety Science and Technology, Beijing, China, 100012

^d Key Laboratory of Major Hazard control and Accident Emergency Technology, State Administration of Work Safety, Beijing, China, 100012

ABSTRACT

The present study files and categorizes coal mine accidents in within China from 2005-2013 using mathematical statistics Aspects such as accident types, occurrence time, geographical distribution, and death rate per million tons are focused on. The characteristics of the coal mine accidents are analyzed, and the coal mine accident potential regularity is summarized. From this analysis, technical prevention means and safety management measures to prevent and reduce coal mine accidents scientifically and effectively are proposed. According to the accident categories, it is found that the number deaths caused by roof accidents are the highest, while the average mortality of fire related accidents are the highest. The curve of accidents is in line with the curve of death toll and both show fluctuation according to month. February has the lowest accident rate and death toll. This effect is closely related to the low temperatures. According to the 27 provincial units, the death toll of Guizhou, Sichuan, Hunan, Shanxi, and Chongqing coal mine accidents is relatively high. To combat this, China should strengthen the supervision of these places.

KEYWORDS: Statistical analysis; Coal mine accidents; Prevention countermeasure; Safety management

1. INTRODUCTION

Safety production level is an important symbol of the progress of a social civilization. Safety production is closely related to economic and social development level, industrial structure, regulatory system, the rule of law, education, science and technology, culture and other factors (Wu, 2007; China Academy of Safety Science and Technology, 2005; Wang, 2008). China's safety production level has increased stably with the rapid development of a national economy, the striking improvement of safety management, and technical measures. However, the coal mining field remains an industry where supervision needs to be strengthened, as there is a high accident rate (State Administration of Work Safety, 2008; Shi et al., 2014; Wei et al., 2014).

On July 22, 2001, a gas explosion tore through a coal mine in Xuzhou city, Jiangsu province, killing 92 people. On February 14, 2005, a gas explosion ripped through a coal mine in Fuxin mining group co., LTD, Liaoning province, leaving 214 people dead. On March 29, 2013, a gas explosion tore through a coal mine in Tonghua

mining group, Jilin province, killing 36 people. These coal mine accidents, which have caused huge property losses and casualties, have drawn wide attention.

This paper completes data analysis based on China's Coal Mine Accident statistics during 2005-2013 provided by State Administration of Work Safety (State Administration of Work Safety, 2015). The characteristics of the accident are analyzed on the basis of objective data. These statistics provide related industry practitioners and regulators with countermeasures and suggestions based on facts, in order to prevent and control coal mine accidents, avoid loss of life, and reduce accident loss.

2. ACCIDENT ANALYSES

2.1 Accident overall condition

Coal mine accidents and the death toll from 2005-2013 were submitted to statistical analysis. The corresponding curve is shown in Figure 1. According to analysis, a total of 16,229 coal mine accidents occurred in China from 2005-2013,

*Corresponding author – email: huxinsheng1989@126.com

causing a total of 27,173 casualties. The equivalent of an average of 1,803 coal mine accidents occurred annually with an average death toll of 1-2 people per accident. Figure 2 shows the raw coal production (one hundred million tons) and death rate per million ton. It can be seen from the figure that China's raw coal production is increasing each year, Conversely, the death rate per million tons is dropping year by year.

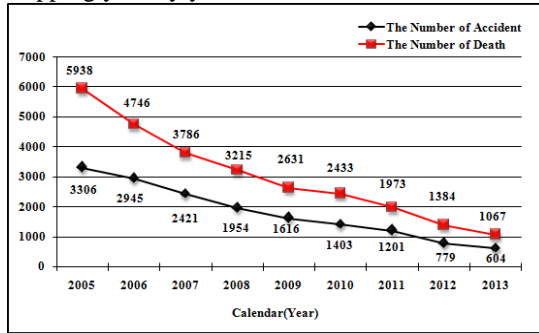


Figure 1: The number of coal mine accidents and deaths from 2005-2013.

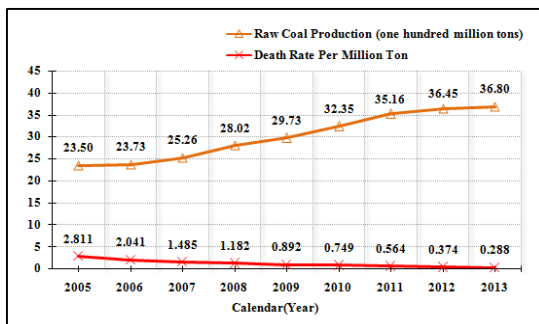


Figure 2: Raw coal production and death rate per million ton from 2005-2013.

It also can be seen from Figure 1 that the trends of the accident curve and the death toll curve are consistent. These two curves trend down, which illustrates that the number of accident and the number of deaths is proportional to the decrease. It also can be seen from Figure 2 that the trends of the raw coal production curve and the death rate per million tons curve are contrary to each other, showing that high production does not mean high accident rate.

Overall, China's raw coal production has increased steadily from 2.35 to 3.68 billion tons from 2005-2013 (National Bureau of Statistics of the People's Republic of China, 2015). The annual average growth rate was 5.45%. On the contrary, the total number of coal mine accidents, total deaths, and death rate per million tons all decreased with the average annual decline rate of 19.14%, 19.31%, and 24.78%. This shows that improvements in

safety management level and technical level play a vital role in reducing coal mine accidents and mortality (Yang and Li, 2014).

2.2 The accident category analysis

Coal mine accidents from 2005-2013 were input to statistical analyses according to 8 kinds of accident categories, including roof, gas, electromechanical, transportation, blasting, flood, fire, and other accidents, as shown in Figure 3.

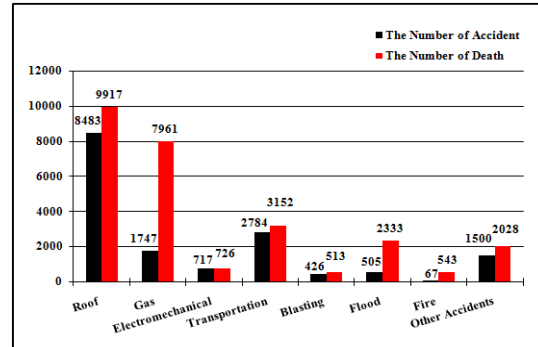


Figure 3: The number of coal mine accidents and deaths according to the accident categories from 2005-2013.

The number of accidents and the death toll in the roof category is the largest. A total of 8,483 roof-related accidents occurred, killing 9,917 people, accounting for 52% of the total number of accidents and 36.5% of all deaths. Fire-related accidents were the least common, with a total of 67 cases. Blasting deaths were the least common, killing 513 people. The average death toll of fire-related accidents was 8 deaths per accident, which is the highest average death toll of each accident type. The second most fatal are flood and gas-related accidents, with 4-5 deaths per accident. Therefore, we should focus on strengthening the management of fire, flood, and gas accidents.

2.3 Accident analysis according to the month

Coal mine accidents during 2005-2013 are input to statistical analyses according to the month, as shown in Figure 4. It can be seen from Figure 4 that in the month with the highest accident rate, April, there were 1,679 accidents; there were 2,770 casualties which is the highest of any month. In February, the number of accidents and the death toll were 664 and 664, respectively, which is the least of any month. In addition, accident rate and the death toll in January were relatively low.

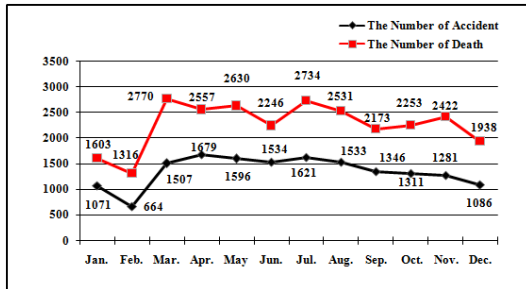


Figure 4: The number of coal mine accidents and deaths according to the months from 2005-2013.

The accident rate is lower in January and February because all the working strength is low at the beginning of the year. Moreover, low temperatures result in a decrease of fire-related accident risk (Wang and He, 2013). Therefore, there are fewer accidents in this period of the year. Conversely, there are more accidents in March and April due to the increasing workload on the employees who have not yet fully adapted to the working environment. As a result, weak safety consciousness and fluky mentality lead to more accidents. Therefore, the government should strengthen supervision in this accident-prone period.

2.4 The accident area analysis

In the 27 provincial coal-producing statistical units (with the exception of Tianjin, Shanghai, and Hainan), 5 regions including Chongqing, Shanxi, Hunan, Sichuan, and Guizhou suffered the largest number of deaths from 2005-2013, as shown in Figure 5. The corresponding death tolls were 2,185, 2,340, 2,681, 2,862, and 3,865 people, respectively, accounting for 51% of the total death toll.

On November 5 and 12, 2006, 7 days apart, 2 coal mine accidents occurred in Shanxi Province, 47 and 34 people were killed, respectively. These two accidents were the "11•5" gas explosion accident in Jiaojia ore coal group and the "11•12" Explosive burning accident in Nanshan coal mine, Jinzhong city. On October 20 and November 11, 2004, 22 days apart, 2 coal mine accidents occurred in Henan Province. 148 and 34 people were killed, respectively. These two accidents were gas explosion accidents in Zhengzhou coal group and Lushan County, Pingdingshan city. It can be seen from Figure 5 that coal mine accidents are relatively concentrated in the northeast, central and southwest regions, mainly in coal production areas. The coal mine production in these areas is relatively dense, leading to a high probability of coal mine accidents

and an increase in the death toll.



Figure 5: Region distribution of death toll in coal mine accidents from 2005-2013.

3. ACCIDENT CAUSE ANALYSES

According to the curve trend of overall accident situation, China's coal mine accidents were decreasing yearly from 2005-2013. The improvements in safety production situation are closely related to the supervision work of all localities and departments. In 2010, the State Council issued a "notice on carrying out the safe production activities further" and a "notice on strengthening safety production work in enterprises further". These two files not only clarified general requirements and major target tasks of safety production work in enterprises, but also created comprehensive requirements for the enterprise's safety production work. At the same time, the State Council issued a "notice on strengthening backward production capacity further" and a "notice on several opinions of accelerating the coal mine enterprise merger and reorganization", to put forward the requirements of eliminating backward production capacity, optimizing the industrial structure, promoting the healthy development of the coal mine industry, and ensuring national energy security. Focusing on coal mines, metal and nonmetal mines, State Administration of Work Safety issued "the decision of modifying part of the terms about coal safety regulations", "take the leadership class to go down and mine safety supervision and inspection requirements", "take the leadership class to go down and metal and nonmetal mines safety supervision and inspection requirements". These rules are emphasized to strengthen the site safety management and discover and eliminate hidden dangers.

In 2010, China is focusing on prevention, strengthening supervision, and increasing responsibility through promulgating a series of regulatory documents, rules and regulations to advance "three actions" stably, intensify "three constructions", and concentrate on illegal special operation, rectification, comprehensive supervision and inspection of key industries (sectors) in safety production. As a result, coal mine gas accidents have dropped, coal mine gas extraction and utilization has increased, villages and towns coal mine accidents have declined dramatically, and coal mine gas control and closed work has had great achievements. At the same time, cracking down on illegal production and business operation construction behaviour has made new progress and significant results were obtained in safety production management action.

From 2011-2013, the State Council issued "the opinions of adhering to the scientific development and safe development to promote safety production situation steadily", and the "notice on deepen the "safe production" activities continually" in order to effectively prevent and curb serious accidents. The main focus was on strengthening and carrying out the safety production "three responsibilities" of enterprise main body, department supervision and territorial administration. At the same time, they continue to crack down on illegal production and business operation construction behaviour. China's series of major policy decisions over safety production work show their strict, which directly led to a decline in coal mine accidents. Thus, perfecting legal system and enhancing superintendence strength are important measures to curb production safety accidents and are strong protections to reduce safety production accidents (Cao, Q. and Li, K., 2012).

4. CONCLUSIONS

China's coal mine accidents curve trend and the death toll curve trend from 2005-2013 are consistent, and both show an overall downward trend. This shows that the development momentum of China's coal mine accidents tends to improve. Perfecting the safety law system and improving safety supervision system are key actions to control accidents.

Roof accidents are the most common, making up about half number of the total accidents. From a safety level, we should strengthen the safety management of coal mine industry, and especially focus on reducing roof accidents.

Few accidents happen at the beginning of the

year. The accident-prone period falls around the month of April. The government should increase safety investment in order to reduce the accident rate during the accident-prone period.

Coal mine accidents in the northeast, central and southwest regions are relatively concentrated, mainly in coal production areas. Regional safety production technical support ability should be balanced and safe investment for high-risk areas and accident-prone areas should be increased in order to reduce the accident rate.

5. REFERENCES

Cao, Q., Li, K. (2012) Risk management and workers' safety behavior control in coal mine. *Safety Science* Volume 50, pp. 909-913

China Academy of Safety Science and Technology. (2005) *Dangerous chemical accident cases*. Chemical Industry Press, Beijing, 225p.

National Bureau of Statistics of the People's Republic of China. <http://www.stats.gov.cn/tjsj/ndsj/>

Shi, L., Wang R., and Duo Y. (2014) Problems and suggestions of safety supervision of dangerous chemicals major hazard in China. *Journal of Safety Science and Technology*. Volume 10, pp. 162-166

State Administration of Work Safety. (2008) *Accident Analysis Report of Hazardous Chemicals in 2007*. *Economic Analysis of China Petroleum and Chemical Industry*. Volume 4, pp.54-59

State Administration of Work Safety. <http://media.chinasafety.gov.cn:8090/iSystem/shigumain.jsp>

Wang, K. (2008) *Chemical production accident analysis and prevention*. China petrochemical Press, Beijing, 209p.

Wang, C., He, M. (2013) Temperature influence on macro-mechanics parameter of intact coal sample containing original gas from Baijiao Coal Mine in China. *International Journal of Mining Science and Technology*. Volume 23, pp. 597-602

Wei G., Yang Z., and Li Y. (2014) Non-explosive Dangerous Chemical Accidents in Major Chinese Cities. *Environmental Pollution & Control*. Volume 28, pp. 711-714

Wu, Z. (2007). Study on some strategy problems of China's work safety by 2020. *Journal of Safety Science and Technology*. Volume 3, pp. 3-7

Yang, C., Li, X. (2014) Statistical Analysis and Countermeasures of Gas Explosion Accident in Coal Mines. *Procedia Engineering*. Volume 84, pp. 166-171

Analysis of coal crack and permeability characteristics slotted by water jet and the effect on gas outburst

Chunming Shen ^{a,b,c,*}, Baiquan Lin ^c, Lang Zhang ^{a,b}, Dong Wang ^{a,b}

^a Mine Safety Technology Branch of China Coal Research Institute, Beijing, China, 100013

^b State Key Laboratory of Coal Mining and Clean Utilization, Beijing, China, 100013

^c Faculty of Safety Engineering, China University of Mining & Technology, Xuzhou, China, 221116

ABSTRACT

Water jet slotting technology is an effective method of increasing coal permeability, improving gas extraction quantity, and preventing mine gas dynamic disasters. The designs of the slot parameter and layout are the key factors. The present study investigated the mechanical properties of slot samples and acoustic emission characteristics in different slotting numbers and angles by uniaxial loading tests. Tests indicated that the coal strength was weakened by slotting and reduced significantly with increasing slotting numbers, and the coal was damaged more easily when the slot plane was perpendicular to the axial stress. Using Guhanshan coal mine 1603 working face as an example, the paper analyzed the evolution of the coal fracture, stress and porosity when the slots were at the same level and at the different levels by numerical simulation of Particle Flow PFC2D. The results showed that, to the sample of slots at the same level, the area around the slot was damaged significantly and the stress concentration was distributed between the adjacent slots, which easily induced coal and gas dynamic risk. However, the stress and crack fields were distributed uniformly when the slots were at the different levels, the stress was decreased significantly, and the porosity of coal was 1.5 times higher than the original value.

KEYWORDS: Mine safety; gas extraction; permeability improve; hydraulic cutting; slot layout

1. INTRODUCTION

Underground coal seam hydraulic technology, such as water jet slotting technology and hydraulic fracturing technology, can effectively increase the coal permeability, (Huang et al., 2011). The influence of hydraulic fracturing technology is large, but the fractures improving permeability are easily closed again when the coal is soft and the geostress is high. However, water jet cutting forms large-sized slots and fractures, which can reduce the geostress level and expand the coal cracks (Shen et al., 2012). It is an effective method to prevent outburst occurrence and improve gas extraction. Research on the improvement of coal permeability by water jet cutting has been done. Based on the rock dynamic damage model, Li and Lu analyzed and numerically simulated coal dynamic damage and fracture impacted by the high-pressure pulse water jet, and considered that the pulse function significantly affected the state of coal fracture field (Li et al., 2000; Lu et al., 2010). Lu (Lu et al., 2009; Lu et al., 2011) considered that water jet cutting technology can release the internal energy and reduce the coal seam stress level, which improves the gas drainage volume and eliminates the outburst risk. However, the permeability influence on the coal damage induced by the slots isn't negligible, especially multi-level slotting. Therefore, the authors have carried out

research on the coal permeability improvement mechanism of the slot crack network by water jet multi-level slotting, in order to improve CMG extraction. The study took Guhanshan Coalmine as the background, and using acoustic emission (AE) technology analyzed the multi-level slotting coal mechanical properties and crack propagation characteristics under the condition of uniaxial loading. Then, using PFC2D the fracture was numerically simulated as well as stress and porosity evolutions of the slotting coal. The study results are of great significance for the improvement of Chinese CMG extraction underground.

2. CRACK PROPAGATION EXPERIMENT

2.1 Experiment system

The experiment system mainly includes the MTS servo machine, AE instrument, and video camera. When slotting the coal under the uniaxial loading, AE was monitoring the crack extension and at the same time the camera was monitoring the deformation and the failure of the sample surface (Figure 1). The type of MTS was C64.106, of which the rated load was 1000 kN and the displacement resolution was 0.2 μm . The AE system with 8 channels was produced by PAC company, of which the center resonance frequency was 120 kHz, the pre-amplifier and main

*Corresponding author – email : scmcmu@163.com

amplifier gain were 40 dB, and the adjusting threshold voltage was 1.0 V.

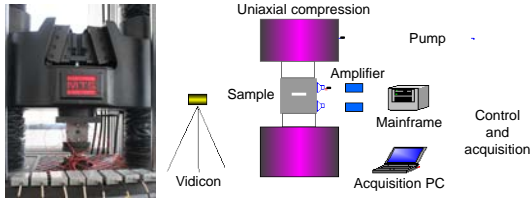


Figure 1: Experiment system schematic of uniaxial compression.

2.2 Sample preparation

Using similar materials the side length of 100 mm cubic coal samples with no slot and with three slots were prepared. The slot width was 20 mm, the thickness was 2.5 mm, and the angle of the slot surface and horizontal plane was 0°. The raw materials of the samples were pulverized coal (grain diameter of 0.2-1.0 mm), cement, gypsum powder and water and mixed into the mold. The samples were maintained 45 days to form and the slots were formed through pre-embed metal bars. In order to compare the sample mechanics performance with the original coal, firstly, large pieces of original coal from Guhanshan Coalmine 1063 working face were collected, then processed into the standard specimens in the laboratory. Lastly, the mechanics parameter of the similar material and the original coal samples were tested. As Table 1 shows, the mechanics parameters were similar.

Table 1: Mechanics parameters of coal and similar material samples.

Sample	Compressive strength σ_c /MPa	Elasticity modulus E/GPa	Tensile strength σ_t /MPa	Shear strength τ /MPa
raw coal	5.60	0.78705	0.72	3.03
similar material	6.24	0.954	0.87	4.28

2.3 Text operation

Each type of sample test was repeated three times, and the test parameters and conditions were as follows: ① select MTS loading mode and set the stress loading rate as 1.0 kN/s, when the sample damaged, stop loading, ② eight sensors of AE are evenly placed on the four free surfaces, and each surface has two pieces. Before testing, set up and debug the instrument, and paste the sensor on the sample surface. Then, contact the MTS pressure plate with the sample by a small load, and then start the MTS loading system, the AE instrument, and the

camera. When the loading up to the sample is damaged, stop the test and collect the features of the broken sample.

3. RESULTS AND ANALYSIS

3.1 Slot coal mechanical strength

The different slot angle and slot number of peak stress block statistics are shown in Figure 2. The peak stress of the single slot sample was the largest, and as slot angle increases, the peak stress increases. When the slot angle was 0° to 45°, peak stress increased obviously. The slot number increased and peak stress was decreased. Compared to the single slot sample, the peak stress of the double slot and three slot samples were decreased by 30-50%. Based on the test results, slotting could change rock mechanics properties, where when slot number increases the coal compressive strength is decreased. When the slot number reaches a certain amount, there is less of an effect on the coal rock mass mechanics performance. For single slot samples, when the slot plane and the maximum principal stress were vertical, the sample failed easily.

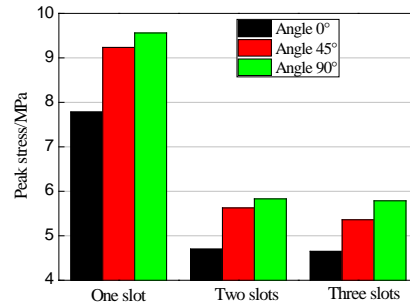


Figure 2: Peak stress distributions of different slotted samples.

3.2 Crack propagation of AE features

The peak stress of three slots sample with two levels distributed was far less than that of the no slot sample (Figure 3). AE parameters were very small in the initial compaction stage and elastic deformation stage, increased in the plastic deformation stage, and increased significantly when approaching the peak stress. In the yield strain stage, the value of AE energy and accumulated events increased markedly, the number of AE hits maintained a high rate and slowly decreased, which shows that the crack propagated easily. The locations of AE events were as shown in Figure 4. The cracks between the slots surfaces grew early on. At 60% of peak stress, the cracks distributed between the slots above and below were concentrated and at the same time, the cracks around the slot expanded to the boundary. At the

peak stress, a lot of cracks around the slots grew quickly.

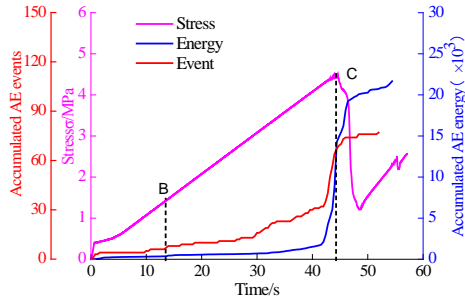
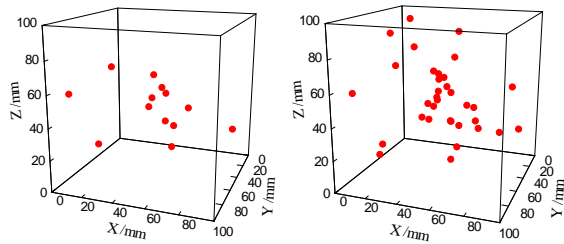
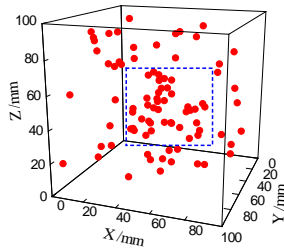


Figure 3: AE parameter variation of three slots sample with two level distributed.



(a) 20% peak stress (b) 60% peak stress



(c) Peak stress

Figure 4: AE events locating process of three slots sample with two level distributed.

4. CRACK EVOLUTION PFC SIMULATION

4.1 Numerical model

Using particle flow PFC2D to build a rectangular model with the incompetent bed (Cundall, 2004), the model length as 1400 mm and the width was 900 mm. The model was divided into three stratum, including the roof rock stratum (200 mm), incompetent bed (500 mm), and bottom rock stratum (200 mm), the original particle model was as shown in Figure 5. The parameters of the roof and floor rocks were the same, the bond strength of which was five times more than the incompetent bed, as shown in Table 2. The parallel bond parameters were as

shown in Table 3. In order to simulate the confining stress limiting conditions, the limit wall was set all around the model, and four walls would load in the calculation. To simulate and analyze the effect of different slot fracture size and distribution, two slot models were established by deleting particles from the incompetent bed. The parameters and distributions of the slot fractures were as shown in Figure 6. The slot distribution was heterogeneous. The particle parameters between the surfaces and on both ends of the slots were recorded in the processing of the simulation, shown as the circles in Figure 6.

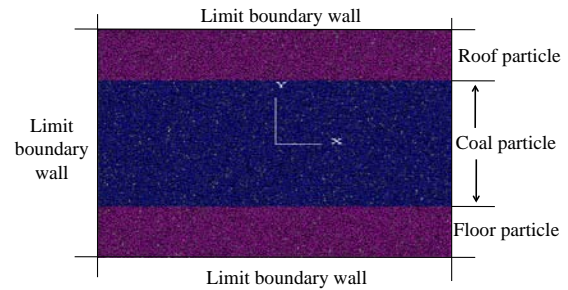


Figure 5: Particle model including boundary and particles stratum.

Table 2: Basic parameters of the model.

Parameter name	value
Minimum grain diameter (mm)	0.3
Particle diameter ratio	1.66
Particle density (kg/m ³)	1450.0
The ball - the ball contact modulus (GPa)	0.8
Particle stiffness ratio	1.0
Friction coefficient between particles	0.5

Table 3: Parallel bond parameters.

Parameter name	value
Parallel bond radius multiplier	1.0
Parallel bond modulus (GPa)	0.8
Normal stress average value of parallel bonding (MPa)	4
Normal stress standard deviation of parallel bonding (MPa)	0.01
Tangential stress average value of parallel bonding (MPa)	4
Tangential stress standard deviation of parallel bonding (MPa)	0.01

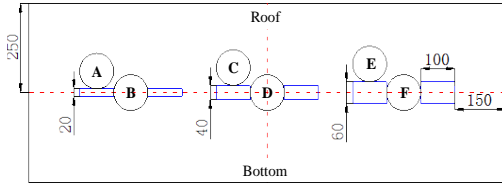


Figure 6: Slot fractures model parameters and distributions.

4.2 Simulation results and discussion

The single-level slots rock model structure, stress and crack distribution are shown in Figure 7. With the load step increasing, the deformation displacement around big slot happened first, and the slots were filled with particles. Stress appeared around the small and medium-sized slots, and the stress concentration appeared between the adjacent slots. As the calculating steps increased, the stress around large slot and medium slot area were reduced. With the stress increasing, crack propagation around the big slot was not significant, and mainly took the form of tension fractures. However, the cracks around the secondary slot increased mainly due to shear failure, and the crack around the small slot grew and expanded to the roof and floor.

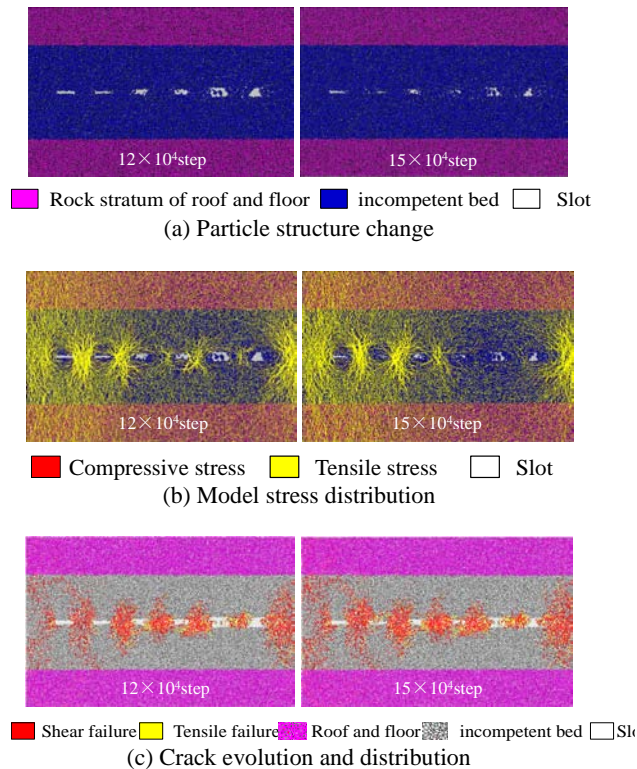


Figure 7: Crack evolution of single-level slots model in loading.

The instantaneous stress, porosity and coordination number and particle migration around the small slots in the unit circle A and B were as shown in Figure 8. The stress of A position showed continuous increase, lower porosity, and coordination number increase. The stress of location fluctuated and increased to about 12 MPa. The porosity increased after the first reduction, but remained lower than the original. The instantaneous stress, porosity and coordination number and particle migration around the medium slot in the unit circle C and D were as shown in Figure 9. The stress of C position increased slowly and the porosity declined. The stress of D location increased to about 10 MPa first, and then reduced to 2 MPa. The porosity significantly increased to far more than the original porosity at the first peak stress. The instantaneous stress, porosity and coordination number and particle migration around the large slot in the unit circle E and F were as shown in Figure 10. The stress of E position slowly increased, the maximum of which was lower than the small and medium slots. The porosity was similar to the original, however, the coordination number and particle instantaneous displacement were not obviously changed. The stress of F position was irregular. In the first peak stress, the porosity increased rapidly and then increased slowly. The porosity increased to about 1.5 times higher than original value.

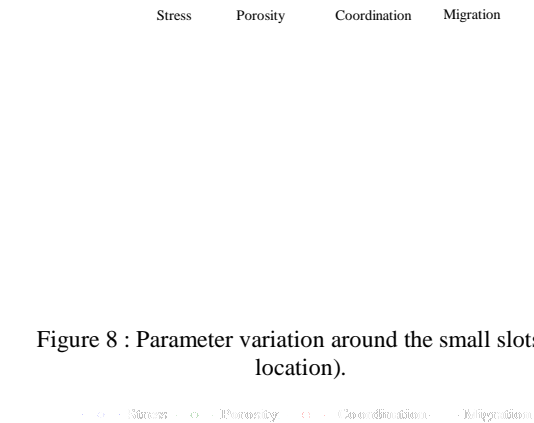


Figure 8 : Parameter variation around the small slots (B location).



Figure 9 : Parameter variation around the medium slots (D location).

Figure 10: Parameter variation around the large slots (F location).

The analysis above found that the greater the slot width, the lower the rock peak stress around the slot, and the rock mass was more easily broken. Due to the low stress, the porosity was increased significantly. The cracks were mainly distributed around the area of the adjacent slots. Compared with the multi-level slots model, the cracks and stress were unevenly distributed, inducing the instability phenomenon.

5. CONCLUSIONS

(1) The experiment found that multi-level slots can significantly weaken the coal strength, cause the occurrence of micro-cracks around the slot, cause crack propagation to form a rock-bridge, and lead to the appearance and extension of numerous micro-cracks around slot surface.

(2) Under the conditions of the same slot arrangement, the peak stress of the big slots model was smaller and the fracture distribution was uneven. As the slot size increased, the rock model became more unstable and the porosity increased significantly after the peak stress. The fractures of the uneven slot distribution model grew and extended more significantly than the even distribution model, and induced the coal and gas to more easily lose stability.

6. ACKNOWLEDGEMENTS

Gratefully acknowledged the financial supports of National Key Basic Research Development Program (973 Program) (2011CB201205) and National Major Projects of Oil and Gas (2011ZX05040-001).

7. REFERENCES

Cundall P.A., PFC2D user's manual (Version 3.1) (2004). Minnesota: Itasca Consulting Group Inc.: 15p.
Huang B.X., Liu C.Y., Fu J.H., Guan H. (2011). Hydraulic fracturing after water pressure control blasting for increased fracturing. International

Journal of Rock Mechanics and Mining Science. Volume 48, No.6, pp. 976-983.

Li X.H., Wang J.S., Lu Y.Y., Yang L., Kang H.M., Sun J.J. (2000). Experimental investigation of hard rock cutting with collimated abrasive water jets. International Journal of Rock Mechanics and Mining Science. Volume 37, No.7, pp. 1143-1148.

Lu T.K., Yu H., Zhou T.Y., Mao J.S., Guo B.H. (2009). Improvement of methane drainage in high gassy coal seam using waterjet technique. International Journal of Coal Geology. Volume 79, No. 1-2, pp. 40-48.

Lu Y.Y., Liu Y., Li X.H., Kang Y. (2010). A new method of drilling long boreholes in low permeability coal by improving its permeability. International Journal of Coal Geology. Volume 84, No. 2, pp. 94-102.

Lu T.K., Zhao Z.J., Hu H.F. (2011). Improving the gate road development rate and reducing outburst occurrences using the waterjet technique in high gas content outburst-prone soft coal seam. International Journal of Rock Mechanics and Mining Science. Volume 48, No.8, pp. 1271-1282.

Shen C.M., Lin B.Q., Meng F.W., Zhang Q.Z., Yang W., Zhang L.J. (2012). Induced drill-spray during hydraulic slotting of a coal seam and its influence on gas extraction. International Journal of Mining Science & Technology. Volume 22, pp. 785-791.

Numerical simulation on Gob gas migration law

He Ning^{a,*}, Xiang Cong^b

^a Department of Safety Engineering College, North China Institute of Science and Technology, Beijing, China, 101601

^b Department of Safety Engineering College, Beijing Institute of Technology, Beijing, China, 100083

ABSTRACT

In the mining process, gas accumulation and overrun often occur in the upper corner of mining face, making it important to create a numerical simulation to study goaf gas migration. In this paper, the numerical simulation of goaf gas was solved based on the ShenDong 1201 working face. The goaf gas concentration distribution was performed, the heaviest accumulation area was given, and the goaf gas migration was developed.

1. INTRODUCTION

High gas mines and coal and gas outburst mines make up about 49.5% of state-run coal mines in China. Gas emissions in one year are more than 15 billion squared. It is more common for gas accumulation and overrun to occur in the upper corner of mining face in the high gas mines and the coal and gas outburst mines. Controlling methane overrun in the working face has definite theoretical value and practical significance. This is accomplished by studying the gas concentration distribution, mastering the rules of gas migration, and determining the heaviest accumulation area. This paper used numerical simulation to research the gas migration law, based on SD1201 in fully mechanized caving faces of the Shendong coalmine, which provides a strong basis for optimizing the layout of the underground ventilation system and mine gas control.

2. GOAF GAS MIGRATION LAWS OF MATHEMATICAL MODELLING

Establish the control in differential equation with a porous medium and control theory of differential equations.

(1) Equation of Continuity:

$$\frac{\partial u_i}{\partial x} + \frac{\partial u_j}{\partial y} + \frac{\partial u_k}{\partial z} = 0 \quad (1)$$

Where, u_i, u_j, u_k is the mean velocity or the surface velocity of the unit, in other words, it is the average velocity of the unit; its relationship with the mean velocity of the pore is:

$$u_i = v_i \cdot n \quad (1-2)$$

where, n is the porosity. In the following mathematical model, the velocity is referred to as the mean velocity of the unit, unless otherwise stated.

(2) Momentum Equation:

$$\frac{\partial(\rho_j u_i)}{\partial t} + \frac{\partial}{\partial x_j}(\rho_j u_i u_j) = -\frac{\partial p}{\partial x_i} + \frac{\partial \tau_{ij}}{\partial x_j} + F_i \quad (2)$$

Where, p – static pressure, τ_{ij} – stress tensor.

(3) Gas Component in differential equation:

$$\frac{\partial(\rho Y_i)}{\partial t} + \nabla \cdot (\rho \bar{v} Y_i) = -\nabla \bar{J} + R_i + S_i \quad (3)$$

Where, R_i is the net production rate of the chemical reactions, S_i is the extra production rate causing by the source terms that consist of discrete phase and user defined.

(4) Energy equation:

$$\frac{\partial}{\partial t}(n\rho_j c_j T + (1-n)\rho_s c_s T) + \nabla \cdot (\bar{v}(\rho_j c_j u T)) = \nabla k_{eff} \nabla T + S_h \quad (4)$$

S_h is the calorific value of residual coal (w/m^3):

$$S_h = \eta \frac{2(b_1 + \beta b_2)}{1 + 2\beta} \cdot r \quad (5)$$

Where, η is the coefficient of flow geometry factor, selected as 0.8 for this paper; b_1, b_2 is the thermal oxidation of coal oxidation that generates CO and CO₂ under a balanceable state, J/mol ; β is the ratio oxidized to form CO and CO₂, taken as $\beta=10$ in this paper; r is the oxygen consumption velocity to crushed coal in unit volume, $kg/(s \cdot m^3)$.

3. NUMERICAL SIMULATION OF GOAF GAS MIGRATION

3.1 SD1201 working face Overview

SD mine is a high-gas coal mine. SD1201 working face main aquifer 3# coal has large gas content in this coal seam, with gas content at 15.87 m³/t and gas emission at 40-50 m³/min. The working face uses the "U+L" ventilation system, and has a face length of 240.3 m and a strike length 1011.9 m. The specific arrangement to be used for drilling through layers of goaf gas drainage has a drilling hole entrance arranged in the gas emissions lane layout, the drilling hole exit in the rock above the mined-out area within the fracture zone, four drill holes uniformly arranged between the two contact lanes (approximately 50 m) drilled directly at 94 mm with a hole length of 120 m, and a vertical coal wall with an elevation of 14°.

3.2 Computational grid and calculation conditions

Roadways are laid out and the computational model is built According to the actual production of the SD mine. The structured non-uniform grid of discrete computational domain is used. The grid number is 429,596. Roadway entrance and exit turbulence parameters are shown in Table 1. Assume goaf gas emission at the backplane and an emission rate of 0.0076 m³/s (according to the actual case of gas emission).

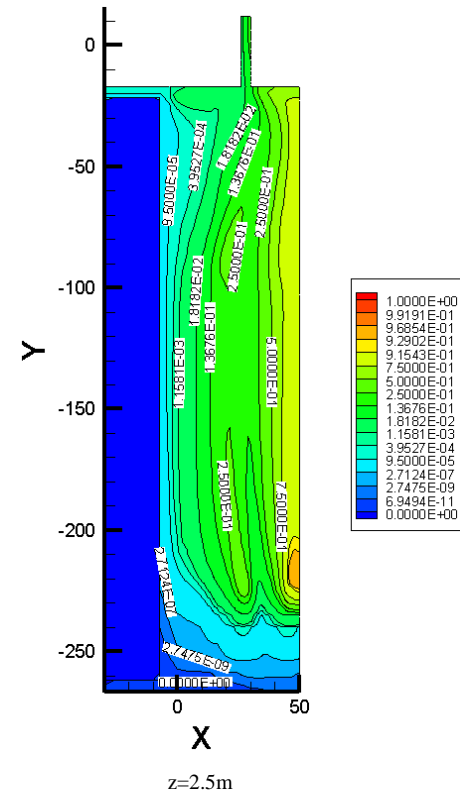
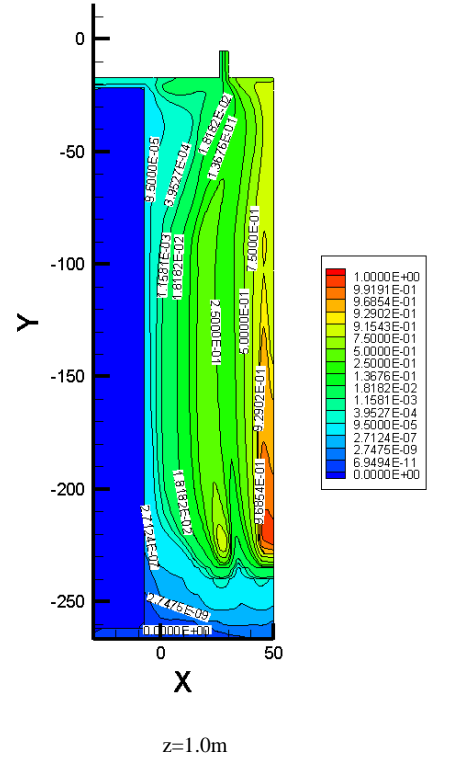
Table 1: The boundary conditions.

boundary conditions	
Into the air inlet air flow trough	$v_{in}=60.8m^3/s$
Auxiliary inlet air flow Cut	$v_{in}=24.8m^3/s$
Entrance into the wind trough the turbulent kinetic energy	$k_{in}=(0.5\sim 5\%)\times 1/2 v_{in}^2$
Entrance into the wind trough turbulent kinetic energy dissipation	$\varepsilon_{in}=c_D k^{3/2}/D$
Gushing outlets gas velocity, gas concentration	0.0076m ³ /s , 100%
return airway export boundary	Pressure conditions of export boundary
Technical roadway export boundary	Pressure conditions of export boundary
Boundary wall	Wall function

4. RESULTS AND ANALYSIS

4.1 Results

Figures 1 and 2 showed the different sections along the z-direction of air flow and the gas concentration distribution. The cross-sections along the z-coordinates of the location (the distance from the bottom) are: 1.0 , 2.5, and 5.0 m. It can be seen from the figure that gas concentration basically follows the same trend at the different sections along the z distribution. Figures 3 and 4 show the velocity contours and the gas concentration distribution at the different sections along the x direction. The location of the profile along the x direction cut-hole from 0, 10.0, 20.0, and 30.0 m



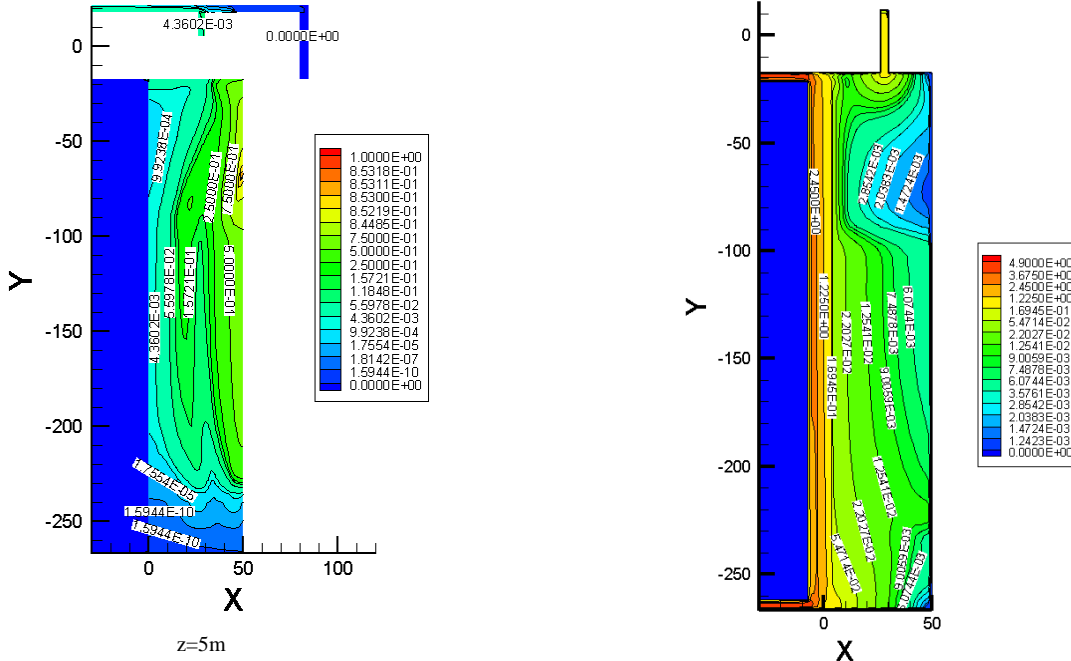


Figure 1: The gas concentration contours perpendicular to Z direction.

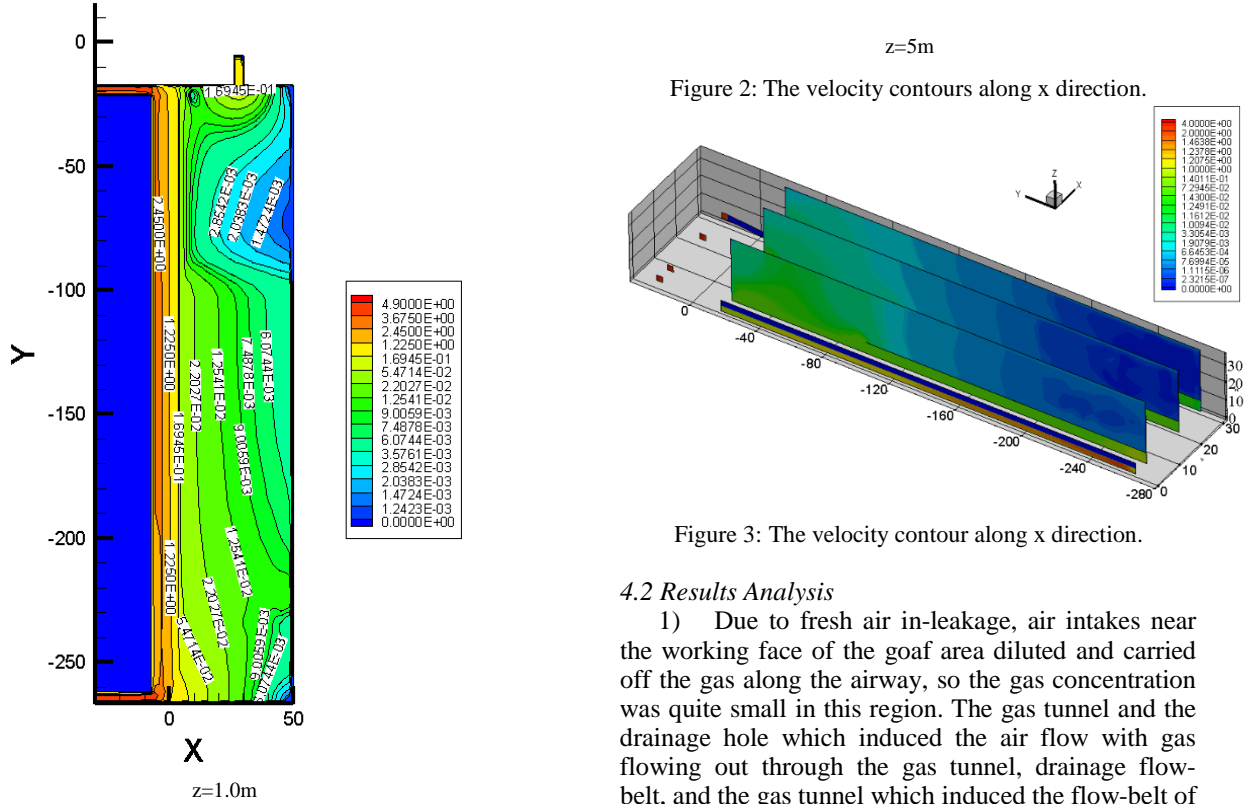


Figure 2: The velocity contours along x direction.

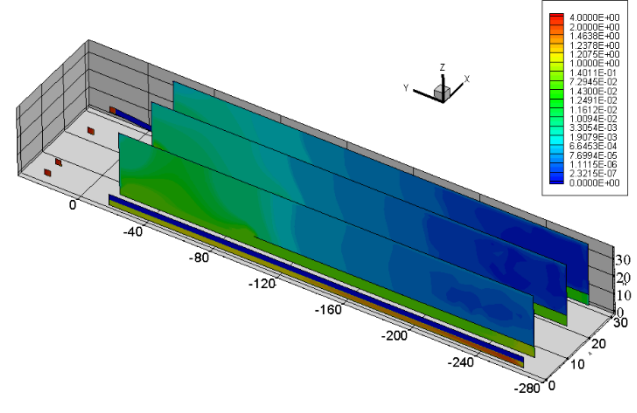


Figure 3: The velocity contour along x direction.

4.2 Results Analysis

1) Due to fresh air in-leakage, air intakes near the working face of the goaf area diluted and carried off the gas along the airway, so the gas concentration was quite small in this region. The gas tunnel and the drainage hole which induced the air flow with gas flowing out through the gas tunnel, drainage flow-belt, and the gas tunnel which induced the flow-belt of the air with gas formed an effective "barrier" preventing gas in deep goaf flow into the upper corner. The gas concentration within the goaf area and the upper corner was largely reduced.

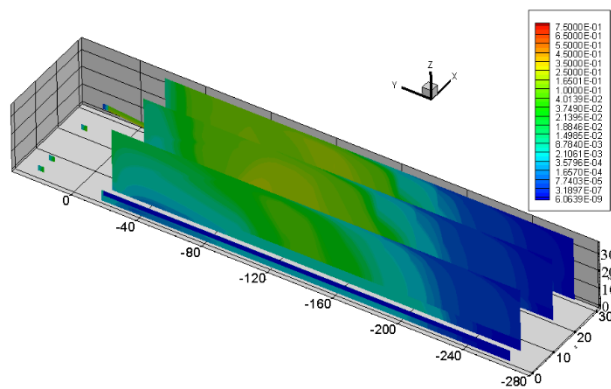


Figure 4: The gas concentration contours along the x direction.

2) With the advance of the working face, the scope of the mined area has increased. In the goaf area beside the interconnection, the compaction degree of coal rock was weak, porosity was large, the air flow velocity faster, and the gas concentration lower. The gas concentration showed a rising tendency as the distance from the interconnection increased. It was more effective for diluting the gas while the air quantity and drainage quantity was large. This will lead to a fresh air flow into the goaf area which will cause spontaneous combustion in the goaf.

5. CONCLUSION

Based on the production conditions in SD coal mine, the numerical simulation of goaf gas was solved. It can be seen that the gas tunnel and the drainage hole, which induced the air flow with gas flowing out through the gas tunnel, drainage flow-belt, and the gas tunnel which induced the flow-belt of the air with gas formed an effective "barrier" preventing gas in deep goaf flow into the upper corner.

The numerical simulation of goaf gas found the gas concentration distribution in SD1201 working face, thus concluding the gas delivery law. The gas roadway and the drainage hole largely reduced the gas concentration within the goaf area and upper corner of the working face by inducing the air flow with gas flowing out through the gas roadway; a larger volume of face air quantity and drainage value will help somewhat ease the problems of gas accumulation in the upper corner.

In the mining process, gas accumulation and overrun often occur in the upper corner of the mining face, making it important to build a numerical simulation to study goaf gas migration. In this paper, the numerical simulation of goaf gas was solved based on the ShenDong 1201 working face. The goaf gas concentration distribution was performed, the heaviest accumulation area was given, and the goaf gas migration was developed.

6. ACKNOWLEDGMENT

This work was supported by Special Fund for Basic Scientific Research of Central Colleges (AQ1202A).

7. REFERENCES

- Fan Weitang, "The status quo and development orientation of long-wall mining technic in thick coal seam in China", *Journal of China Coal Society*, 1993, 18(1): pp.5-6
- Hu Qianting, Liang Yunpei, and Liu Jianzhong, "CFD simulation of goaf gas flow patterns", *Journal of China Coal Society*, vol.32, pp.719-723, July.2007
- Li Shugang, "Gas delivery feature and its control irrfluenced by movement of the surrounding rock in fully-mechanized top coal caving", *Chinese Journal of Rock Mechanics and Engineering*, 2009, 19(6): pp.809-810.
- Meng Xianrui, Chen Haibo, "Top-coal movement theory of top-coal mining and establishment of its mathematical model", *Coal Engineering*, 2003, 4(10): pp. 32-33.
- Meng Xianrui, Zhang Wenchao, and Heyongqiang, "Study of Gas Emission Characteristic in Long-Wall Top Coal Caving Face with a High Gas Content", *Journal of Ming & Safety Engineering*, vol. 23, pp. 419-422, Dec. 2006.
- Qin Yaoping, Liu Peng, "Research on calculation error of simplified mathematical model of gas emission in coal seam", *Journal of Ming & Safety Engineering*, vol.45, pp.19-24, Jan. 2016
- Yuan Liang, "Strategic thinking of simultaneous exploitation of coal and gas in deep mining", *Journal of China Coal Society*, vol.41, pp.1-6, Jan.2016
- Zhang Xuebo, Zhangfan, "Determination on reasonable length of wind curtain for 'U + L' type ventilation in fully mechanized face", *Journal of Safety Science and Technology*, vol.12, pp.163-168, Jan, 2016

Research on the negative pressure distribution law and its application for boreholes in coal seam bedding gas extraction

Linchao Dai ^{a,b,*}, Kai Wang ^{a,b}

^a State Key Laboratory of the Gas Disaster Detecting, Preventing and Emergency Controlling, Chongqing, China, 400037

^b Chongqing Research Institute Co., Ltd. of China Coal Technology and Engineering Group, Chongqing, China, 400037

ABSTRACT

Making boreholes along seams is a part of the distribution process of gas extraction in coal mines, and a fundamental measure for preventing and controlling gas disasters as well as an important means to explore coal-bed methane resources. Recently, the borehole technology along the seam has been widely applied to gas extraction with the development of borehole rigs and kilometer-borehole rig. Presently, research by domestic scholars on the extraction theory mostly focuses on pre-extraction by boreholes through beds and shallow boreholes along the seam, with few considering the influence of viscous mechanics of gas flow in boreholes. Therefore, the research on the variation of negative pressure inside the borehole along the seam is greatly important to guide the design of boreholes along the seam for gas extraction, the determination of key parameters, and the theoretical application of the technology.

This paper focuses on the distribution of negative pressure inside the boreholes along the seam and its application, with two sections: (1) The distribution of negative pressure inside the borehole along the seam in the borehole direction. Based on gas occurrence, flow theory, fluid dynamics theory, and the definite mechanism of negative pressure inside the borehole along the seam on gas extraction, both gas flow models around boreholes and inside boreholes are established. Distribution of the negative pressure inside the borehole along the seam in the borehole direction was found by classifying the pressure loss inside boreholes and coupling the flow conservation equations of two models. The distribution of negative pressure inside the borehole was technically determined via field tests to verify the feasibility of the proposed models. (2) The application of the distribution of negative pressure inside the borehole along the seam in the borehole direction. Considering the shortages of traditional extraction processes, two new ones were put forward applying the distribution of negative pressure inside the borehole along the seam in the borehole direction, and the extraction pipe reaching a certain distance or covering the whole length. Technical processes such as theory analysis, field test, and numerical simulation verified the superiority of the new extraction processes.

This study found the variation of negative pressure inside the borehole along the seam in the borehole direction and the distribution of negative pressure inside the plume borehole along the seam, derived the calculating formula of reasonable borehole length, put forward new extraction processes, and verified the superiority of the new extraction processes in some conditions.

KEYWORDS: coal mine; bedding gas extraction; bedding borehole; inside-borehole negative pressure distribution law

1. INTRODUCTION

Gas extraction is fundamental for the prevention and control of gas disasters in coal mines, and also an important means to develop coalbed methane resources. Particularly, bedding boreholes is one of the important ways to distribute boreholes in gas extraction of the coal mines (Wang, et al., 2005; Wang, et al., 2006). In recent years, with the development of the drill and borehole rig as well as the emergence of 1,000m borehole machine, the bedding long boreholes gas extraction technology has been widely used. Hu (2011) carries out a theoretical analysis, field expedition, and numerical simulation

process concerning seam long boreholes used for preventing coal and gas outburst using Pan-yi mine and Pan-san mine as the experimental cases. The purpose is to reduce construction volume, improve pumping rate, shorten the cycle of outburst, and achieve safe and fast driving. Xie, et al. (2013) selected Xin'an mine as a trial zone of the gas pre-extraction technology and studied the boreholes drilled along the mining seam and the rational parameter values of the gas pre-extraction technology for coal seam.

However, with the increasing length of the borehole, the extraction effect is not necessarily

*Corresponding author – email : dailinchao@126.com

necessarily improved (Lin, et al., 1990; Xu, et al., 2010). With the increase of borehole length, the pressure drop generated from the gas flow along the borehole length direction should not be ignored. Extraction negative pressure will decay in the transfer process. The extraction negative pressure has significant influence on the extraction effect to the extent that the extraction effect is possibly not significant when reaching a certain length. At present, the domestic research on extraction theories applies to cross-layer borehole pre-extraction and bedding borehole shallow borehole extraction, without considering the mechanical impact of viscosity on the gas flow in the borehole (Xin, 1998; Li, 2012; Li, 2013). The changing law of negative pressure along the length of long coal seam boreholes is of great significance for the theoretical guidance of the bedding borehole gas extraction design, the determination of key parameters, and technology applications. Therefore, research on the distribution of negative pressure inside the borehole along the seam in the borehole direction and its applications were studied.

2. THEORETICAL ANALYSIS

Bedding borehole gas extraction can be divided into two processes: the first process is the gas flow in porous media like coal; the second process is gas flow inside the borehole.

The surrounding-borehole coal gas flow model and the inside-borehole gas flow model can be set up to characterize these two flow processes.

2.1 Surrounding-borehole gas flow model

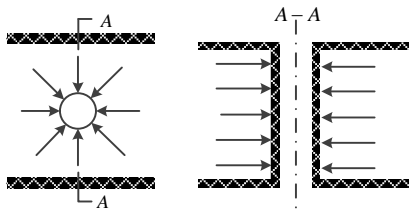


Figure 1: Radial flow in coal around the borehole.

From the Figure 1, the unit length of coal at the borehole length direction is analyzed with the conclusion that field of gas flow in the coal corresponds to a radial unsteady flow field. Gas flow speed, direction, and pressure at any point in the flow field change over time. The following equations can be derived based on porous media theory, coal seam gas adsorption theory, and thermodynamics (Zhou, et al., 1965; 1990; Yu, et al., 1989).

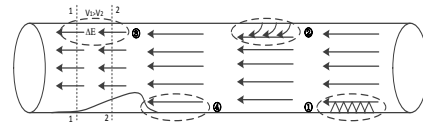
$$\begin{cases} \text{div}(\rho \vec{v}) = -\frac{\partial X}{\partial t} \\ \vec{v} = -\frac{K}{\mu} \cdot \text{grad} p \\ X = \frac{abc p}{(1+bp)} \cdot \rho + np \\ \rho = \frac{\rho_n}{p_n} \cdot p \end{cases} \quad (1)$$

(For concrete parameters refer to Sun, 1991; 1993; Wang, 2014). The solution to the solution-determination problem leads to the approximate analytical solution of the gas seepage model of unit length of coal, as is shown in formula (2).

$$q(t) = (R - r_0) \cdot (p_0^2 - p_1^2) \cdot \sqrt{\frac{\lambda \pi}{2 p_n p_0 t} \left[n + \frac{abc p_0 (2 + bp_0)}{(1 + bp_0)^2} \right]} \quad (2)$$

2.2 Inside-borehole gas flow mode

In the process of gas flowing to the orifice, the inside-borehole gas flow corresponds to variable mass flow due to the constant gas emission off from the borehole wall with the changing quality. The inside-borehole gas flow will result in pressure loss, the four major factors being: on-way frictional resistance loss, acceleration pressure drop, mixing loss, and local resistance loss resulting from gas in-flow of the borehole wall (Ozkan, 1992; Yuan, et al., 1996; Zhou, et al., 1997; Schulkes, et al., 1997), as is shown in the Figure 2.



- ① On-way frictional resistance loss
- ② Mixing loss
- ③ Acceleration pressure drop
- ④ Local pressure loss

Figure 2: Classification of gas flow losses in the borehole.

In reality, due to the uncertainty of the borehole deformation, and to facilitate the theoretical analysis, it is presumed that the borehole wall is not deformed in the process of extraction; therefore, the local pressure loss is zero.

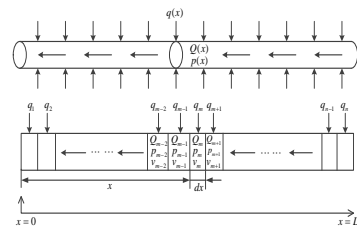


Figure 3: The differential schematic of coal seam borehole along the length direction.

It can be seen from Figure 3 that when the coal body that is around the borehole is dispersed into infinitesimal sections along the borehole length direction, each gas flow in an infinitesimal section

can be represented by the previously built gas flow model around the borehole. Wall inflow mixing loss is not calculated separately. Instead, the on-way frictional resistance coefficient is modified, and the mixing loss is included in the on-way frictional loss. The on-way friction formula, continuity equation, and momentum equation can respectively infer on-way frictional resistance loss Δp_{fri} and the acceleration pressure drop Δp_{acc} . When x is the variable, the total pressure drop of dx infinitesimal section can be drawn (Ihara et al., 1994; Wu, 1999; Liu, et al., 2000).

$$\frac{dp(x)}{dx} = \Delta p_{fri} + \Delta p_{acc} \quad (3)$$

$$= \frac{2f_i \rho [2Q(x) + q(x)]^2}{\pi^2 D^5} + \frac{16\rho [q^2(x) + 2Q(x)q(x)]}{\pi^2 D^4}$$

In formula (3), f_i is the frictional resistance coefficient of wall fluid when it flows into the borehole, and its size can be calculated through the borehole flow state in the infinitesimal section, that is, by calculating the Reynolds number (Re) of each infinitesimal section, determine the flow state of the fluids, and use the calculation formula of the frictional resistance coefficient f_0 when there is no wall fluids inflow to obtain the frictional coefficient. Concrete parameters can be found in Fan, et al. (2000) and Zhang (2009).

2.3 Modal coupling

According to the theory of fluid dynamics, the gas flow of the infinitesimal section x from the orifice is in line with the flow conservation equation (Ben, 1990; Liu, et al., 2006), as is shown in formula (4).

$$\frac{d[Q(x)]}{dx} = -q(x) \quad (4)$$

The gas flow model of surrounding-borehole coal and inside-borehole gas flow model can be coupled through the following inside-borehole flow conservation equation (5).

$$\begin{cases} q(x,t) = (R - r_0) \cdot (p_0^2 - p_1^2) \cdot \sqrt{\frac{\lambda \pi}{2 p_n p_0 t} \left[n + \frac{abc p_0 (2 + bp_0)}{(1 + bp_0)^2} \right]} \\ \frac{dp(x)}{dx} = \frac{2f_i \rho [2Q(x,t) + q(x,t)]^2}{\pi^2 D^5} + \frac{16\rho [q^2(x,t) + 2Q(x,t)q(x,t)]}{\pi^2 D^4} \\ \frac{d[Q(x,t)]}{dx} = -q(x,t) \end{cases}$$

Through boundary condition:

$$\begin{cases} x = 0, & p(0) = p_1 \\ x = 0, & Q(0,t) = Q \end{cases}$$

The inside-borehole negative pressure distribution formula of bedding borehole can be

obtained from the definite-solution problem (5). However, the analytical solution to second order nonlinear partial differential equations is very complex; generally, the parameter substitution process can greatly simplify the solving process.

The Chongqing Songzao Yuyang coal mine was selected for the field test in this study. When using the industrial parameters of Yuyang No. 7 coal seam into the formula (5), it can be found that: when the orifice negative pressure is 7 KPa, the borehole pressure loss in the 100 meters process is 466.7 Pa.

3. FIELD MEASUREMENT

The borehole that is 100m deep in the N3702 transportation lane of Yuyang Coal Mine uses copper pipe as its connecting pipe. Combined with the full-hole-section downing sieve pipe process, hollow copper pipes with different lengths are sent into the borehole to determine different negative pressure values at varying depths. The negative pressure field test process diagram is shown in Figure 4.

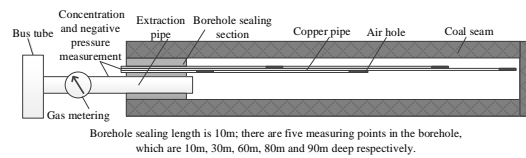


Figure 4: Field test process for measuring the negative pressure within the borehole.

In the 90 day extraction inspection period, three sets of representative data at three time points are selected for analysis. The negative pressure values at different depths inside the borehole with extraction times of 10 days, 40 days, and 80 days are measured and recorded, as is shown in Figure 5.

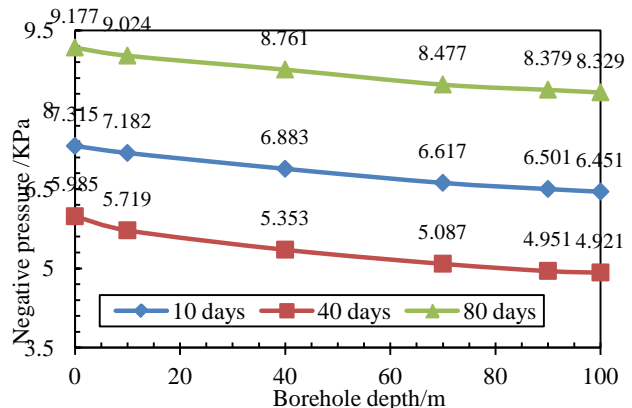


Figure 5: Negative pressure distribution in borehole in different extraction time.

From Figure 5, the curve of negative pressure distribution of different depths inside the borehole at different time shows that the inside-hole negative

pressure of bedding gas extraction decays along the borehole length direction. The 100 m attenuation in the extracted borehole is about 800 Pa in the field measurement. However, the theoretical calculation does not consider factors such as the occupied area of copper pipe, borehole leakage, and borehole deformation, which will increase pressure loss. The built theoretical model is feasible and in accord with the requirements of engineering practice.

4. APPLIED RESEARCH

The traditional extraction process has many shortcomings, as shown in the negative pressure distribution law in the bedding borehole of Figure 6. (1) With longer boreholes, borehole pressure loss is more serious and the extraction effect is more and more poor along the borehole length direction. (2) The maximum negative pressure at the orifice and the formation of the differential pressure on both ends of the borehole sealing section are very big, therefore, it is easy to cause leakage that leads to low extraction concentration and a poor extraction effect. (3) Coal quality in many of China's coal mines is soft and easy to deform after forming the borehole. This increases the frictional resistance coefficient of the coal wall and causes negative pressure attenuation if the borehole collapse blocks the negative pressure in the direction of the borehole's bottom due to borehole scraps.

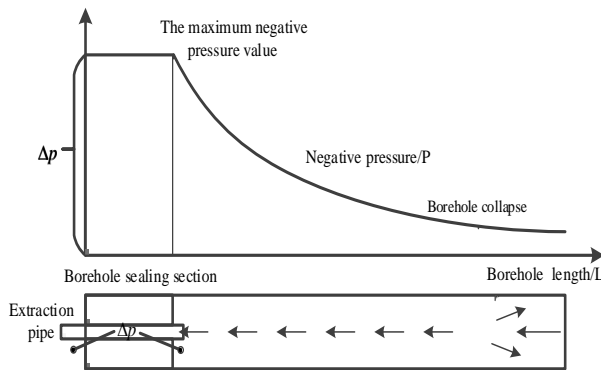


Figure 6: The traditional extraction process.

Two new extraction processes in view of the hard and soft coal quality were put forward to address the deficiency of traditional extraction processes, combined with borehole forming conditions and negative pressure distribution in the borehole.

(1) Hard coal - extending extraction pipe

As shown in Figure 7, compared with the traditional extraction process and under the same borehole length, extending the extraction pipe places the maximum negative pressure in the middle of the borehole. The distance of the maximum negative pressure on both sides in the borehole is shorter,

reducing negative pressure loss and increasing the negative pressure of the whole borehole section. At the same time, because of the frictional resistance loss, the differential pressure on both ends of the borehole sealing section will be reduced and the leak situation will be improved compared to the traditional extraction process.

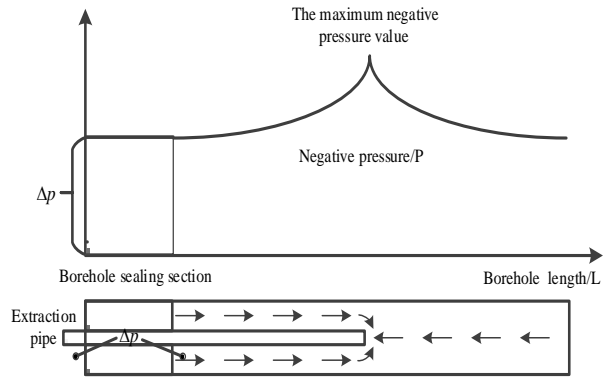


Figure 7: Extending extraction pipe process.

(2) Soft coal - using sieve pipe

As shown in Figure 8, the friction factor of the sieve pipe is much smaller than the coal wall (commonly used industrial piping equivalent roughness). New polyethylene pipe K_s (the stability against sliding coefficient) is 0 - 0.002, concrete pipe K_s is 0.3 - 3.0), reducing the negative pressure losses from orifice to bottom. At the same time, it can keep the gas flow channel clear when borehole collapse occurs, improving the extraction effect and raising the utilization rate of the borehole.

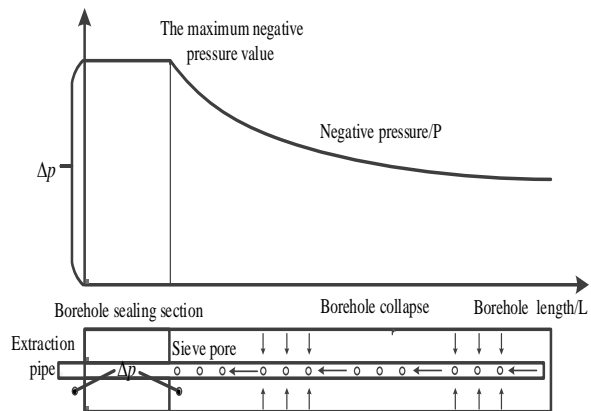


Figure 8: Using sieve pipe to replace extraction pipe.

In order to verify the superiority of the new extraction process, a field test was carried out in N3702 working face. Traditional extraction process were used for the No. 1 borehole, extending extraction pipe process was used for the No. 2 borehole, and the sieve pipe process was used for the No. 3 borehole, as shown in Figure 9.

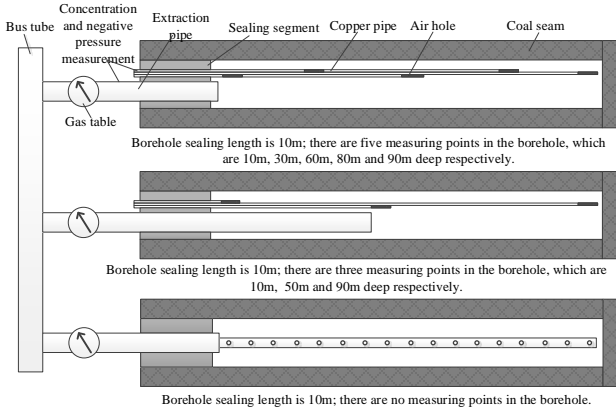
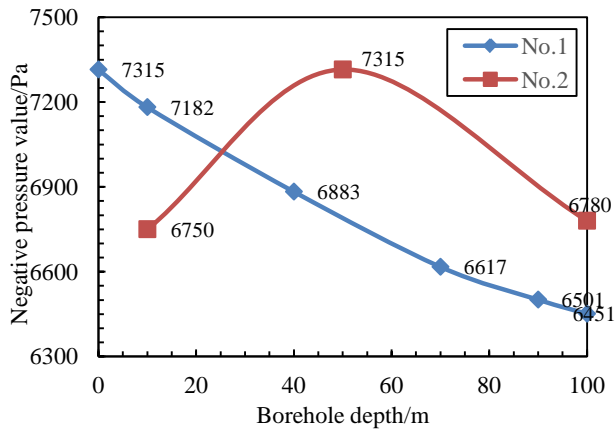
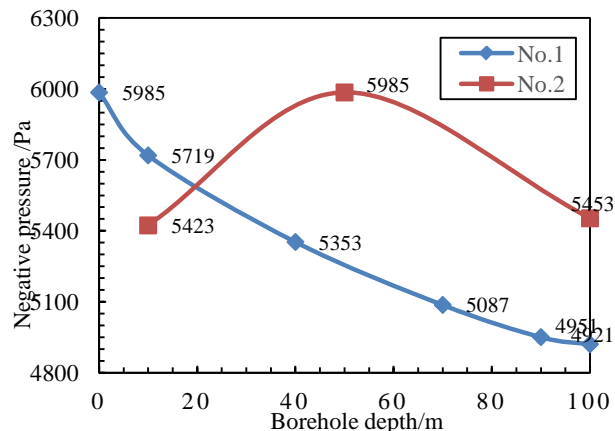


Figure 9: The compared field test of extraction effect under different extraction processes.

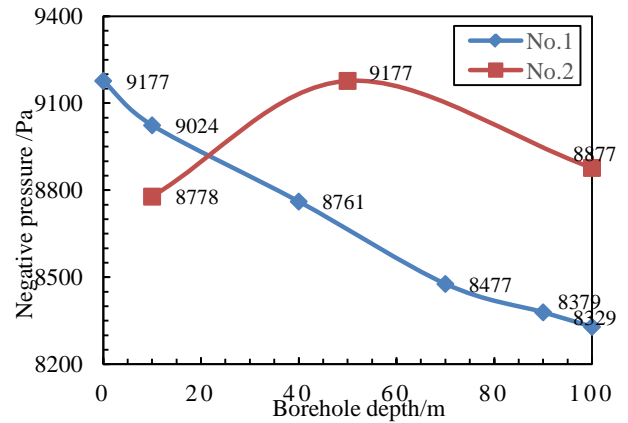
The negative pressure distribution in the borehole of the traditional extraction process and the extending extraction pipe process were compared and studied under conditions of the same borehole sealing quality. The inspection period of extraction time was 90 days. The negative pressure values of different depths in the borehole were determined and analyzed by field measurement under the three representative stages in extraction time for 10 days, 40 days, and 80 days, as shown in Figure 10(a), (b), and (c).



(a) Extraction for 10 days



(b) Extraction for 40 days



(c) Extraction for 80 days

Figure 10: Negative pressure distribution of No. 1 and 2 borehole.

From Figure 10 (a), (b), and (c), negative pressure in the borehole presents an attenuating trend distribution along the borehole under conditions of the traditional extraction process, and negative pressure in the borehole presents a "mountain" trend distribution along the borehole under conditions of the extending extraction pipe process. The area covered by the curve in the figure shows that the average negative pressure value and full negative pressure energy of the extending extraction pipe process are bigger than for the traditional extraction process. Using the sieve pipe process in the full borehole section can not set pressure measuring points, therefore the experiment of negative pressure determination in the borehole was not carried out.

The two extraction effects (extraction concentration and flow) were taken for indexes, and compared under the different extraction processes in order to verify the superiority of the new extraction process.

The extraction concentration investigation for borehole No. 1, 2, and 3 are shown in Table 1.

Table1: Extraction concentration of borehole No.1, 2, 3.

Extraction time(d)	Extraction concentration (%)		
	No.1	No.2	No.3
0	93%	89%	90%
3	66%	95%	95%
11	89%	95%	95%
27	89%	85%	95%
37	30%	50%	90%
50	30%	50%	90%
58	30%	50%	30%
64	30%	93%	30%
78	70%	90%	80%
86	66%	80%	83%
93	65%	85%	85%

Within 90 days of extraction time, extraction effect: No.2 borehole > No.3 borehole > No.1 borehole. Under the same borehole sealing quality, the extending extraction pipe process is superior to the sieve pipe process, and the extraction effect of the traditional extraction process is the worst.

The cumulative mixed flow and the accumulative gas flow trend figures of boreholes No. 1, 2, and 3 found by field measurement are shown in Figures 11 and 12.

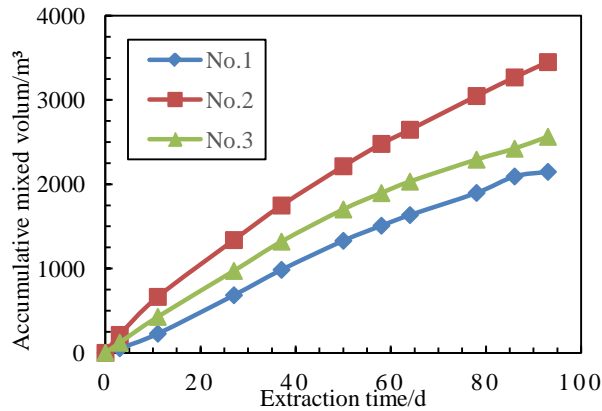


Figure 11: No. 1, 2, 3 borehole accumulative mixed flow trends.

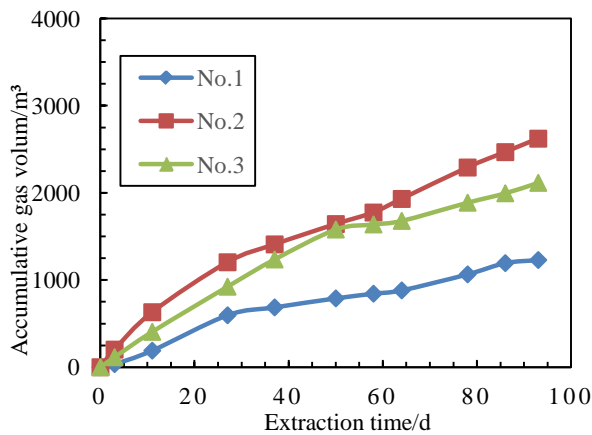


Figure 12: No. 1, 2, 3 borehole accumulative gas flow trends.

From Figures 11 and 12, the accumulative mixed flow and accumulative mixed gas flow of three boreholes show a rising trend with the increase of extraction time. The borehole extraction effect is such that No. 2 > No. 3 > No. 1. Under the same borehole sealing quality, the extending extraction pipe process is superior to the sieve pipe process, and the extraction effect of the traditional extraction process is the worst.

According to the above, it can be obtained that the extraction effect of No. 1 borehole using the traditional extraction process is the worst. Meanwhile

the two indexes are the lowest and the borehole is likely to leak. Negative pressure loss is the most serious, therefore it should be improved. The concentration and flow rate for the No. 2 borehole using the extending extraction pipe process are better than that of No. 1 and 3 borehole. Implementation is simple in the field, and is worth promoting. The extension concentration and flow rate for No. 3 using the sieve pipe process are better than No. 1 borehole and smaller than No. 2 borehole. The reason is that the small sieve pore on the pipe restrains the gas flow into the pipe. When the borehole undeforms, the advantage of using the sieve pipe process is not obvious. However, using the sieve pipe process in soft coal seams has a better effect.

5. CONCLUSION

(1) The gas flow model in the coal body around the borehole and the calculation model of gas flow in the borehole were established. The pressure distribution calculation model in the bedding gas extraction borehole was found, and a field test calculation was carried out to verify the feasibility of the built model.

(2) The field test process was applied to determine the different depth points of negative pressure values in bedding gas extraction boreholes. The negative pressure distribution law along the long boreholes was summarized, Results showed that the negative pressure presents an attenuation trend distribution along the long borehole direction in the bedding gas extraction boreholes.

(3) In order to address the shortcomings of the traditional extraction process, two new extraction processes were put forward, namely the extending extraction pipe process and the sieve pipe process.

(4) Through the extraction effect contrast test under different extraction processes, the extraction effect of the new extraction process was found to be better than the traditional extraction process. In coal seams with good borehole forming conditions, it is optimal to use the extending extraction pipe process. In coal seams with bad borehole forming conditions, using the sieve pipe process is optimal.

6. ACKNOWLEDGEMENT

This study was financially supported by National Natural Science Foundation of China (51574280, 51374236), Chongqing Frontiers and Application-based Research Program (cstc2015jcyjBX0076), The Science and Technology Innovation Fund of China Coal Technology and Engineering Group (2015ZDXM14, 2015ZYJ002).

7. REFERENCES

- Ben, J.D. (1990). Pressure drop in horizontal wells and its effect on production performance. Society of Petroleum Engineers, Volume 42, No.10, pp.1426-1433
- Fan, Z.F., Li, Y.J. and Ji, S.H. (2000). Reasonable water injection pressure of water flooding of multi-layer sand stone oilfields. Petroleum Geology and Oilfield Development in Daqing, Volume 19, No.6, pp. 28-30,33
- Hu, S.T. (2011). Optimization of process parameters and application of along seam long drilling. Henan Polytechnic University, Henan
- Ihara, M. (1994). Flow in horizontal wellbore with influx through porous wells. SPE 28, pp.485
- Li, J. (2012). Research on extraction effect change law along the extraction drilling. Henan Polytechnic University, Henan
- Li, S.W. (2013). Study on the bedding extraction borehole negative pressure distribution in different depth of Xin'an mine. Coal Engineering, No. 5, pp.103-104
- Lin, B.Q. (1990). Coal seam gas extraction factors analysis. Safety in Coal Mines, No.9, pp.30-35
- Liu, X.P. and Zhang, Z.S. (2000). Pressure drop calculation model of coupling with seepage flow in the horizontal wellbore. Journal of Southwest Petroleum Institute, Volume 22, No.2, pp.36-39
- Liu, J.J. and Zhang, B.H. (2006). Fluid mechanics. Peking University press, Beijing
- Zhang, L. (2009). Research on coupling theory of horizontal borehole and coalbed methane reservoir. China University of Petroleum (East China), pp.30-31
- Ozkan, S. (1992). Effect of conductivity on horizontal well pressure behavior. SPE Advanced Technology Series 3, pp.85-94
- Schulkes, R. and Utvik, O.H. (1997). Pressure drop in horizontal wells: multiphase flow with radial inflow. BHR Group Multiphase, pp.45-55
- Sun, P.D. (1991). Distribution of gas pressure in a radial flow field. Mining Science Technology, No.13, pp.409-415
- Sun, P.D. (1993). Study of the gas flow mathematical models. Coal Geology and Exploration, Volume 21, No.1, pp.32-40
- Wang, Z.F. and Liu, J. (2005). Problems and countermeasures of gas extraction in coal mine in China. Safety in Coal Mines, Volume 36, No.3, pp.29-32,44
- Wang, K.J. and Zhang, X.H. (2006). Development status and prospect of gas extraction process in China coal mine. China Coalbed Methane, Volume 3, No. 1, pp.13-16,39
- Wang, K. (2014). The research on negative pressure distribution law and its application of borehole for consequent landslide gas extraction. China Coal Research Institute, Beijing
- Wu, S.H. (1999). A Simplified Model of Flow in Horizontal Wellbore. Petroleum Exploration and Development, Volume 26, No.4, pp.64-65
- Xie, X.G., Li, X.J. and Yu, Z.Y. (2013). Study on pre-extraction seam gas technology with borehole drilled along seam in outburst mine. Coal Science and Technology, Volume 41, No. 1, pp.78-81
- Xin, X.P. (1998). Parameters optimization of Jiaozuo coal seam gas extraction. Safety in Coal Mines, No.9, pp.7-10
- Xu, M.G., Lin, H.F. and Li, S.G. (2010). Study on the influence law of gas extraction in coal seam. Mining Safety and Environmental Protection, Volume 37, No. 5, pp.1-3,10
- Yu, C.X., Xian, X.F. and Tan, X.S. (1989). Study about flow theory and governing equation of gas seepage flow in coalbeds. Journal of Chongqing University, Volume 12, No.5, pp.1-10
- Yuan, H., Sarica, C. and Brill, J.P. (1996). Effect of perforation density on single phase liquid flow behavior in horizontal wells. SPE 37, pp.109
- Zhou, S.N. and Sun, J.Z. (1965). Theory and application of coalbed gas flow. Journal of China Coal Society, Volume 2, No.1, pp.24-37
- Zhou, S.N. (1990). Mechanism of gas flow in coal seams. Journal of China Coal Society, Volume 15, No.1, pp.61-67
- Zhou, S.T. and Zhang, Q. (1997). An analytic model of horizontal section pressure drop. Petroleum Exploration and Development, Volume 24, No.3, pp.49-52

Mathematical simulation and experiment of CBM detection

LIANG Qing-hua*

China Coal Technology Engineering Group Chongqing Research Institute, Chongqing, China, 400039

ABSTRACT

In order to accurately detect the underground Coal Bed Methane (CBM) accumulation in coal mining faces by mine radio wave perspective method, this study simulated the characteristic curve of received values through coal seams and discussed the feasibility of CBM. The experiments were conducted in Chinese mines. The study concluded that the existence of CBM could cause abnormal areas. Compared to the normal reception curve, the abnormal curve of CBM showed a much smaller value, and the attenuation was larger in the middle area and smaller on both sides. The pattern formation was a "saddle" shape. The radio wave penetration method could be a more reliable method for the detection of CBM in underground coal mines.

Coal Bed Methane (CBM) has a great influence on the normal production of coal mines. When coal mines are enriched there is a chance of explosion. Mining methods have changed in order to avoid this. Coal and CBM total mining technology is a main research direction for coal mines in China. The distribution of CBM is irregular and the physical parameters of CBM are not obvious, therefore, research into CBM detection technology and equipment is difficult. At present, there exists no effective method to detect CBM in the working face of coal mines in China. Previous studies have not been concerned with radio wave instrument detection through CBM. There has been no research on the characteristic curve perspective of radio waves for CBM detection. For the present study, the authors conducted curve theory perspective detection on radio waves through CBM using mathematical simulation tools, combined with coal mine experiments to verify the reliability of the theoretical analysis in order to make reference for similar mines.

1. THE BASIC PRINCIPLES

Mine radio wave perspective is used to detect various geological formations through two tunnels. The transmitter and receiver are located in different tunnels. The transmitter is in a relatively fixed position within a predetermined time and the receiver received field strength values are within a certain range (Liu et al., 2014; Wan et al., 2011) point by point, as shown in Figure 1.

Assume that the radiation source midpoint O is the origin, in the approximately uniform and the same nature seam, the distance from the observation point P to the point O is r , electromagnetic field strength at

point P H_p is represented by (Liang et al., 2009; Liu et al., 2012; Li et al., 2011; Wu, 2002):

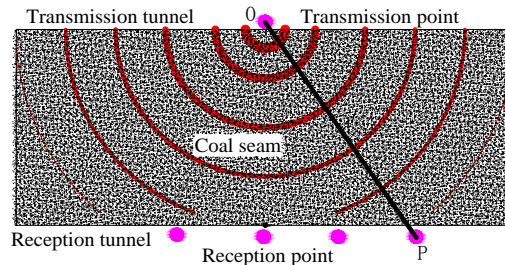


Figure 1: Schematic diagram of radio wave tunnel perspective instrument.

$$H_p = H_0 \frac{e^{-\beta r}}{r} f(\theta) \quad (1)$$

In formula (1), H_0 is the initial field intensity around the antenna seam at a certain transmission power, A/M. β is the coal absorption coefficient of electromagnetic waves. r is the straight-line distance of P point to O point, m. $f(\theta)$ is the directivity factor. θ is the angle between the dipole axis and the direction of the observation point, which is generally used to calculate $f(\theta) = \sin(\theta)$.

According to the literature (Liang et al., 2010), take $\ln(H_p) = H'_p$, $\ln(H_0) = H'_0$:

$$H'_p = H'_0 - \beta r - \ln(r) \quad (2)$$

$\ln(r)$ is little change in the formula (2), it can be approximated that formula (3) is the slope of the straight line $-\beta \cdot H'_p$ and r are considered to have an approximately linear relationship.

2. MATHEMATICAL MODELLING STUDIES OF CBM

According to most of the coal mining face features in China, the length of the tunnel model was 500 m, and width was 200 m. The transmission point was below the midpoint in the tunnel, with the tunnel below the midpoint as origin O (0,0), as shown in Figure 2. According to the experience of underground exploration, H'_0 was generally in the 110-155 dB range, and the β varied between 0.2 and 0.55. Most simulation parameters were selected as coal mine normal physical parameters.

Here $H'_0 = 130\text{dB}$ and normal seam $\beta = 0.3$.

According to formula (3), the change in H'_p with r can be simulated.

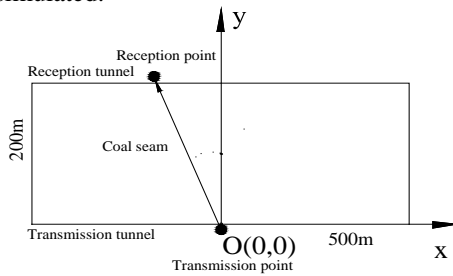


Figure 2: Normal coal seam simulation model.

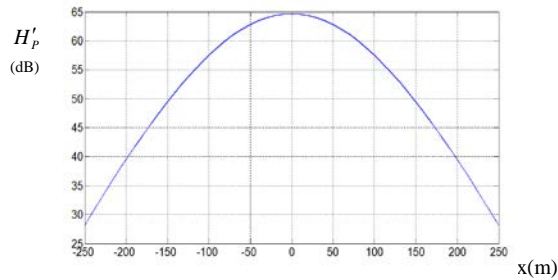
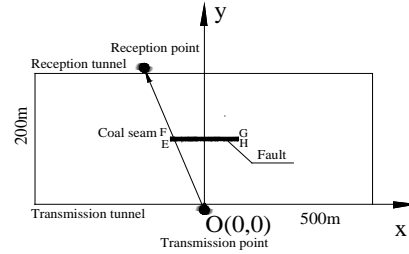


Figure 3: The reception value changes of abnormal cases.

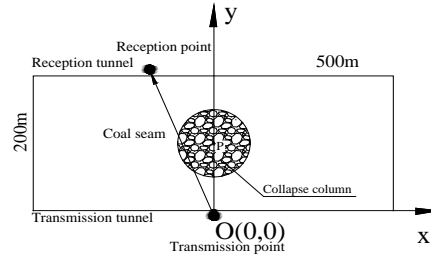
In the normal case, coal seam function was $F(x,y) = \{-250 \leq x \leq 250, 0 \leq y \leq 200\}$. According to formula (2), when the reception points moved in a straight line, we had:

$$H'_p = \begin{cases} 130 - 0.3\sqrt{x^2 + y^2} - \ln\sqrt{x^2 + y^2}, \\ (y = 200, -250 \leq x \leq 250) \end{cases} \quad (3)$$

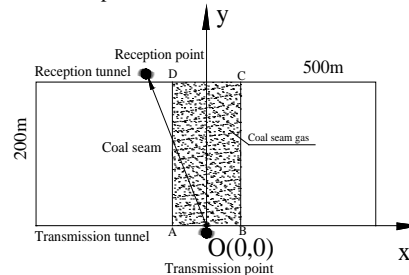
According to formula (3), using the MATLAB simulation, the field-strength curves of the normal coal seam reception values were found, as shown in Figure 3.



4-a Model of a fault



4-b Model of a collapse column



4-c Model of CBM

Figure 4: The simulation model of various abnormal cases.

Impact of fault simulation: To simplify the calculations, the intermediate simulation model was a fault with a fault length of 100 m and distance of 5 m (Figure 4-a). The attenuation coefficient of the fault was $\beta = 0.5$ and changes on the fault model abscissa were $x: -50 \sim 50$, ordinate $y: 100 \sim 105$. Fault function was $F_1(x,y) = \{-50 \leq x \leq 50, 100 \leq y \leq 105\}$. When electromagnetic waves went through the fault:

$$H'_{pf} = \begin{cases} 130 - 0.3\sqrt{x^2 + y^2} - \ln\sqrt{x^2 + y^2} - 1, \\ (y = 200, -100 \leq x \leq 100) \end{cases}$$

Impact simulation of collapse column: A circular collapse column was in the middle of the model (Figure 4-b). The attenuation coefficient was $\beta = 0.5$ and the radius was 50 m. The circular collapse column equation was: $x^2 + (y - 100)^2 = 2500$.

The function of collapse column: $F_2(x,y) = \{x^2 + (y - 100)^2 \leq 2500\}$. When electromagnetic waves went through the collapse column:

$$H'_{pcc} = \begin{cases} 130 - 0.3\sqrt{x^2 + y^2} - \ln\sqrt{x^2 + y^2} - \\ 0.4\sqrt{50^2 - [100\sin(\arctg \frac{x}{y})]^2}, (y = 200, -\frac{200}{\sqrt{3}} \leq x \leq \frac{200}{\sqrt{3}}) \end{cases}$$

Impact simulation of CBM: CBM was located in the middle of the model (Figure 4-c). The attenuation coefficient was $\beta=0.5$. The influence scope of CBM was: $-50 \leq x \leq 50, 0 \leq y \leq 200$. CBM function: $F_3(x,y) = \{-50 \leq x \leq 50, 0 \leq y \leq 200\}$. When the electromagnetic wave through the CBM:

$$H'_{P_{wz}} = \begin{cases} 130 - 0.3\sqrt{x^2 + y^2} - \ln\sqrt{x^2 + y^2} + 10\sqrt{x^2 + y^2} / x, \\ y = 200, -250 \leq x < -50 \\ 130 - 0.5\sqrt{x^2 + y^2} - \ln\sqrt{x^2 + y^2}, \\ y = 200, -50 \leq x \leq 50 \\ 130 - 0.3\sqrt{x^2 + y^2} - \ln\sqrt{x^2 + y^2} - 10\sqrt{x^2 + y^2} / x, \\ y = 200, 50 < x \leq 250 \end{cases}$$

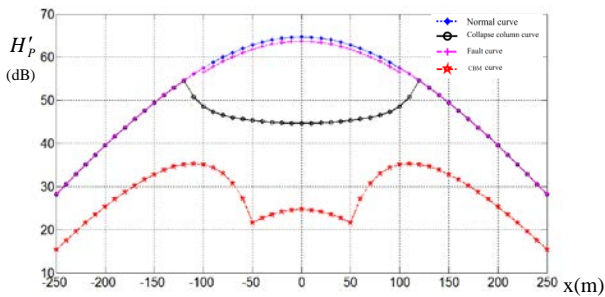


Figure 5: The reception value changes of various abnormal cases.

Based on the above abnormalities, the comparison diagram of various abnormal conditions could be simulated, as shown in Figure 5. With respect to the reception value for normal seam, the fault curve was relatively gentle; however, the received values were significantly decreased at the fault. The values of the collapse column curve were gradually smaller, and then gradually became larger. In contrast, the values of the CBM curve were small, further intermediate region attenuation was larger, and the sides relative attenuation were relatively smaller, forming a "saddle" shape. Therefore, under the conditions of CBM the reception value of radio wave perspective was significantly decreased, and curves showed the overall attenuation characteristics, a typical characteristic of CBM. The conclusion of this curve has been verified in the thesis of Dr. Wu Yanqing (2002), and has also

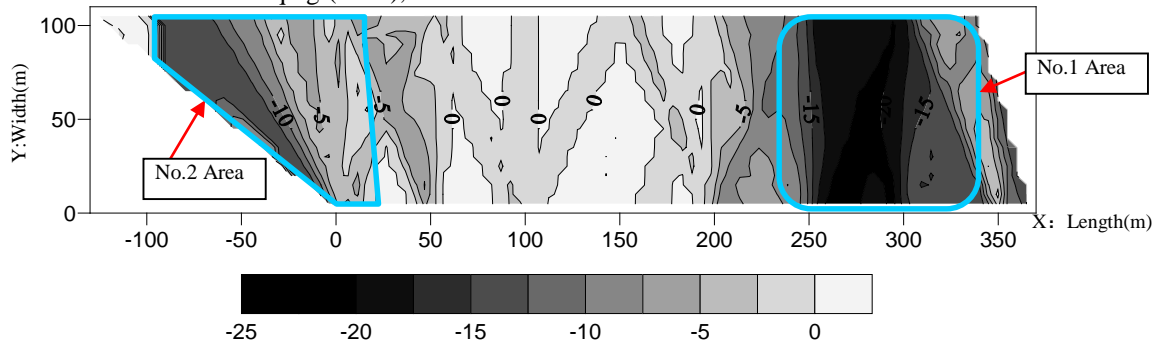


Figure 6: Radio wave penetration result map of 27131 working face in Yanmazhuang mine.

been verified many times in actual detection experiments.

In the actual detection process, due to the influence of other factors, changes in the data might not be in strict accordance with this rule, but the basic trend is substantially the same.

3. EXPERIMENTAL STUDY ON CBM

Yanmazhuang mine had a CBM enrichment phenomenon in Henan Province of China, which brought some difficulties to the production and safety of coal. In order to discover the enrichment of CBM the coal seam was detected.

The coal seam thickness of 27131 working face was 5.9-6.5 m in Yanmazhuang mine, the length was 370 m, the inclination was 110 m, and the average dip angle of the coal seam was 5°. To ensure the penetration distance and detection accuracy, a frequency of 0.5 MHz was chosen and the fixed point scanning method was selected. The reception points space was 5 m and the transmission point space was 50 m. The results of the survey are shown in Figure 6, from left to right of the upper roadway: 800 to 895, from left to right of lower roadway: 200 to 274. Through the computer data processing, two more concentrated anomaly areas were drawn and numbered the no.1 and no.2 areas. The detected anomaly areas colour was mainly gray and black.

No.1 abnormal area: The abnormal area was located in the right of Figure 6 and was the largest area of electromagnetic wave attenuation. Combined with coal mine geological data, there was no large geological structure. Coal gas content was 16-18 m³/t, therefore, the anomaly analysis was mainly caused by the change of gas concentration, and this area was a coal and gas outburst danger area.

No.2 abnormal area: The abnormal area was located in the left of Figure 6. The coal gas content in this area was relatively low, at 3-4 m³/t, but there was a large F147 fault. Therefore, the regional anomaly was mainly caused by large faults, which was not in danger of outburst.

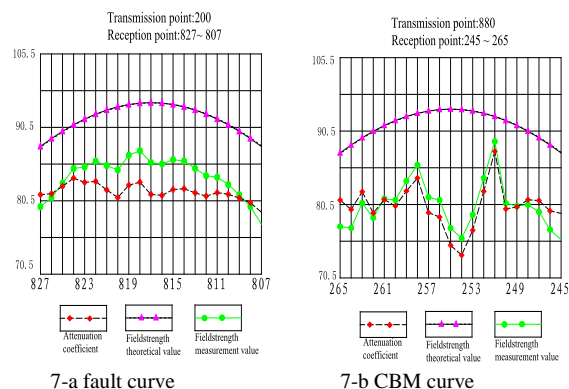


Figure 7: Typical curves of CBM and fault in mine.

The typical curves of Figure 7 were analyzed. Figure 7-a was a variation of the fault curve. The coordinate of transmission point number 200 was (x:0, y:0) in Figure 6, and the coordinate of reception point number 807-827 was (x: -100-0, y: 110) in the vicinity of the No.2 abnormal area. The measurement curve was below the theoretical curve in Figure 7-a, and the basic form was similar to the theoretical curve. It was in line with the change of the abnormal fault curve in Figure 5.

Figure 7-b was a variation of the CBM curve. The coordinate of transmission point number 880 was (x:265, y:110) in Figure 6, and the coordinate of reception point number 245-265 was (x: 225-325, y: 0) in the vicinity of the No.1 abnormal area. From the CBM curve, the measurement curve was below the theoretical curve. The curve changed from relatively flat at the beginning to a more rapid decay, and then quickly climbed to the initial value. The characteristic of the measurement curve was in agreement with the theoretical curve of Figure 5. The existence of a gas enrichment zone in the area was described, and it was also proven that the curve of the simulation was correct.

4. CONCLUSIONS

Because of the differences between CBM and normal coal seam, the exist of CBM made the electromagnetic wave refraction, reflection and absorption vary. The CBM could be seen as a loss of electromagnetic energy, therefore CBM could cause abnormal erosion areas on radio wave perspective. After the scene of the experiment in coal mine, radio waves perspective method could be more reliable to detect CBM. In the actual detection process, changes in the data were affected by other factors, which would not change in strict accordance with this law, but the basic trend was roughly the same. This required a

comprehensive analysis based on the analysis of the data.

From the simulation analysis of the radio wave perspective curve, with respect to the reception value for a normal seam receiver, the values of CBM curve were smaller. The values for attenuation were bigger in the middle region and smaller in the side edge, forming a 'saddle' shape. Therefore, in the conditions of CBM, the reception value of radio wave perspective was significantly decreased and the curves showed a large area of overall attenuation characteristics typical of CBM.

Detection and qualitative analysis of CBM enrichment area by radio wave perspective method broke through the blind zone of the CBM accumulation area, filling a gap in the research. The technology of underground CBM detection has strong practical significance for safe production in coal mines.

5. REFERENCES

- CHENG Jiu-Long, LI Li, YU Shi-Jian. (1999). Research on direct current electric field characteristics of overburden failure and its applications. *Journal of Coal Science & Engineering*, Volume 5, No. 1, pp. 24-29
- Li J H, Zhu Z Q, Feng D S, et al. (2011). Calculation of All-time Apparent Resistivity of Large Loop Transient Electromagnetic Method with very Fast Simulated Annealing. *Journal of Central South University of Technology*, Volume 18, No. 4, pp. 287-291
- LIANG Qing-hua, SONG Jin. (2009). Advanced detection theory and experimental research of multi-wave and multi-component seismic exploration in mine. *Journal of Central South University (Science and Technology)*, Volume 40, No. 5, pp. 1392-1398
- LIANG Qing-hua, WU Yan-qing, SONG Jin. (2010). Study on the qualitative analysis and application of radio wave tunnel perspective. *Journal of Chongqing University(Natural Science Edition)*, Volume 33, No. 11, pp. 113-118
- LIU Jian-xin, DENG Xiao-kang, GUO Rong-wen, et al. (2012). Numerical simulation of advanced detection with DC focus resistivity in tunnel by finite element method. *The Chinese Journal of Nonferrous Metals*, Volume 22, No. 3, pp. 970-975
- LIU Sheng-dong, LIU Jing, YUE Jian-hua. (2014). Development status and key problems of Chinese mining geophysical technology. *Journal of China Coal Society*, Volume 39, No. 1, pp. 19-25
- MEI K K, FANG J Y. Superabsorption—a method to improve absorbing boundary conditions[J]. *IEEE Trans*, Volume 40, No. 9, pp. 1001-1010
- WAN Guoxiang, LI Xibing, WANG Qisheng. (2011). Effect of linear joint on propagation of rock electromagnetic emission. *Journal of Central South*

University (Science and Technology), Volume 42,
No. 4, pp. 1133-1139

WU Yan-qing. (2002). Study on the underground
electromagnetic wave detection and application.
Changsha: Central South University, 75p.

Numerical modelling and rescaled range analysis on spontaneous combustion under surface methane drainage in a Chinese coal mine

Xincheng Hu^{a,b,c}, Shengqiang Yang^{a,b,*}, Wei Victor Liu^c, Jiawen Cai^{a,b}, Xiuhong Zhou^{a,b}

^a School of Safety Engineering, China University of Mining and Technology, Xuzhou, China, 221008

^b Key Laboratory of Gas and Fire Control for Coal Mines, Xuzhou, China, 221008

^c Department of Civil & Environmental Engineering, University of Alberta, Edmonton, Canada, T6G 2W2

ABSTRACT

In China, surface boreholes have frequently been used to drain methane/gas emitting from overlying layers and longwall mining gobs in underground gassy coal mines. In this work, a numerical model was established using COMSOL™ to study the influence of surface drainage boreholes on coal spontaneous combustion and Rescaled Range Analysis (R/S analysis) was employed to investigate the chaos characteristic of Nitrogen (N₂)/Oxygen (O₂) drained from the gob. The simulation results show that there is a circular “dissipation zone” around the drainage borehole all the time and an elliptic “spontaneous combustion zone” when the borehole is located in deep gob. It is also found that the advancement of drainage boreholes has little influence on spontaneous combustion zones on the intake side of the gob but it can tremendously enlarge the width of a “spontaneous combustion zone” in the middle gob and reduce the depth of self-heating zones near the return side. The R/S analysis indicates that the influence of surface boreholes on spontaneous combustion can be divided into two stages: the safety drainage stage (Hurst index > 0.85) and the spontaneous combustion initiating stage (Hurst index ≤ 0.85). It can be concluded that the gas drainage from gob through surface boreholes can tremendously intervene spontaneous combustion “three zones” in gob. In addition, the length-fixed R/S analysis on N₂/O₂ series from surface boreholes can effectively reflect coal spontaneous combustion conditions in gob.

KEYWORDS: Coal spontaneous combustion; surface drainage borehole; Hurst index; R/S analysis

1. INTRODUCTION

Coal spontaneous combustion has long been one of the most serious disasters in underground longwall coal mines, especially in the working face gobs (Ham, 2005). In China, about 32% of underground coal mines are spontaneous combustion prone and highly gassy (high methane content), which may cause severe disasters, especially when mining goes increasingly deeper (Zhou et al., 2013).

In highly gassy coal mines, methane drainage must be carried out before or along with mining. However, improper gas drainage may induce coal spontaneous combustion, leading to disastrous methane combustion and even explosions. In spite of long-time research on coal spontaneous combustion and methane prevention (Song and Kuenzer, 2014), few recent studies have addressed the severe threat of the combined effects of methane and coal spontaneous combustion (Madeja-Struminska and Widzyk-Capehart, 2006).

Although much research has focused on fracture development and gas migration after mining, little attention has been paid to coal spontaneous combustion caused by methane drainage. The 10416 working face in Yangliu Co.ltd., Huaibei, Anhui Province, China, was chosen to investigate the influence of surface methane drainage on coal

spontaneous combustion in gob. COMSOL™ was adopted to simulate the influence of surface drainage boreholes on coal spontaneous combustion in gob. The chaos characteristic of N₂/O₂ indicator series collected from one surface borehole was analyzed using Rescaled Range Analysis (R/S analysis). The risk of coal spontaneous combustion in 10416 working face gob was divided and the corresponding critical values were confirmed in the end.

2. WORKING FACE DESCRIPTION

Coal 10, with an average distance of 74 m, 81 m, and 106 m from overlying coal 8₂, 8₁, and 7₂, is mined in 10416 working face. As the middle coal seams (7₂, 8₁ and 8₂) are coal and gas outburst prone, it serves as the remote protective layer for these three middle coal seams. In order to control the methane in the middle coal seams and the gob, surface drainage boreholes were drained before the advancement of 10416 working face to extract methane relieved from overlying methane-bearing strata and the longwall face gob.

As seen in Figure 1, the surface boreholes were located at the middle of working face, 70 m from the return tunnel in the dip direction. The surface drainage holes were drilled to the gob of the face, with an opening diameter of 311 mm and a final

*Corresponding author – email: ShengqiangYang@hotmail.com

diameter of 91 mm. To guarantee long-term extraction effect, the interval was set as 120 m.

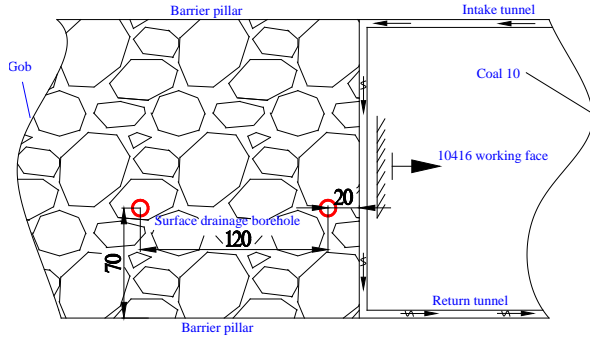


Figure 1: Tunnel arrangement of 10416 working face, Yangliu coal mine (units are in meters)

3. THE INFLUENCE OF SURFACE METHANE DRAINAGE ON COAL SPONTANEOUS COMBUSTION IN GOB

3.1 Modelling of 10416 working face gob

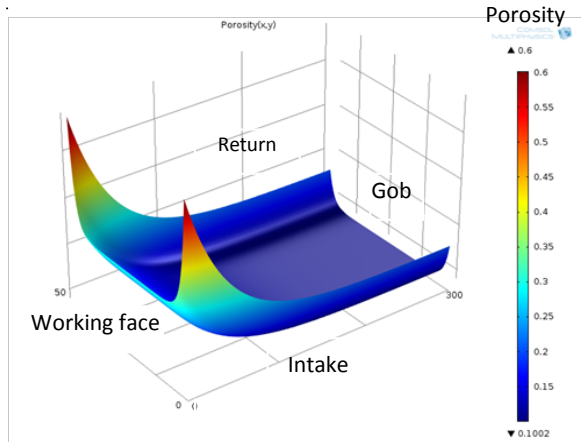


Figure 2: Porosity distribution in 10416 gob area

The height of the fractured zone can be confirmed as 35 m according to the empirical formula used by other researchers (Yang et al., 2011). The 10416 working face gob is slightly affected by the gas that might emit from the middle coal seams because of the long distance to coal 10 (Szlazak, Obracaj et al., 2014). Due to the remoteness of gas-bearing coals, the simulation model of 10416 working face gob can be simplified as a two-dimensional model, as previous researchers have done (Yuan and Smith, 2007).

As the porosity is dustpan-shaped in gobs (Li, Wu et al., 2008), the porosity distribution in 10416 working face gob can be estimated (Figure 2), and is highly permeable along the boundary with low-

permeability in the middle and deep gob. There is a relationship between porosity and permeability in the gob, according to the Carmon equation:

$$k = \frac{D_p^2}{150} \frac{n^3}{(1-n)^2} \quad (1)$$

Where k is the permeability in the gob, m^2 ; n is the porosity in the gob, m ; D_p is the average particle diameter in the gob, m . In order to simulate flow field in the gob, the boundary conditions were confirmed as per the practical parameters of 10416 working face as shown in Table 1.

Table 1: The boundary conditions of 10416 working face

Site	Size	Flow	Boundary
Intake tunnel	4 m×10 m	Free flow	Pressure (0 Pa)
Return tunnel	4 m×10 m	Free flow	Velocity (2.1 m/s)
Working face	180 m×2 m	Free flow	/
Supporter area	180 m×4 m	Free flow	/
Gob	180 m×150 m	Porous flow	/
Surface borehole	91 mm (diameter)	Free flow	Velocity (0.5 m/s)

Although there are three main criteria (O_2 concentration criteria, flow velocity criteria, and temperature rate criteria) in determining “spontaneous combustion zone”, flow velocity criteria was chosen to indicate the self-heating danger in gobs because of the arduousness in simulating O_2 concentration distribution and heat field in gobs. It is recognized that if the flow rate in a gob is between 0.1 m/min and 0.24 m/min, the site is in a spontaneous combustion area. As the gob has been seen as porous media (Karacan et al., 2007), the Free and Porous Media Flow Model was chosen in COMSOL™ to simulate the influence of surface methane drainage on “three-zone” distribution in the gob.

3.2 The influence of surface drainage borehole on “three zones”

Methane can be drained by surface drainage boreholes, thus tremendously disturbing the airflow distribution. Figure 3 describes the distribution of three zones in the gob with different strike depths of surface drainage boreholes. Overall, the influence is more obvious on the return side of the gob than the intake side. There is a circular dissipation zone around the borehole during the whole extraction process and an elliptic ring-sized spontaneous

combustion zone when the borehole reaches the deep gob. With the movement of boreholes to deeper gobs, the spontaneous combustion zone near the return side advances toward the face while the dissipation zone narrows. By contrast, the impact on the intake side is smaller compared with the return side. However, the spontaneous combustion zone near the borehole is reduced at the beginning and then broadened with the increasing depth.

The spontaneous combustion zone is encroached by both the dissipation zone and the suffocation zone, owing to the drainage effect of the surface borehole in shallow gobs (around 30 m). When the location of the borehole approaches the middle gob (around 60 m), there is a round dissipation zone around the drainage hole. The width of the self-heating zone near the intake side of the drill is increased whilst the

depth along the return roadway is reduced. With the further advancement of the face (about 90 m), the influence of the surface borehole enlarges. The spontaneous combustion zone near the drill is drained to deeper gob with greater width, but the width along the return roadway is shortened. When the borehole goes deeper (120 m), an elliptic ring-shaped spontaneous combustion zone emerges. As a result, the gob along the moving route of the drill is more dangerous than other area in gob because of the enlarged spontaneous combustion zone and the long-lasting elliptic self-heating zone around the drill. Due to the complexity of methane drainage through surface boreholes, the prediction of the coal spontaneous combustion condition in gobs is of great importance.

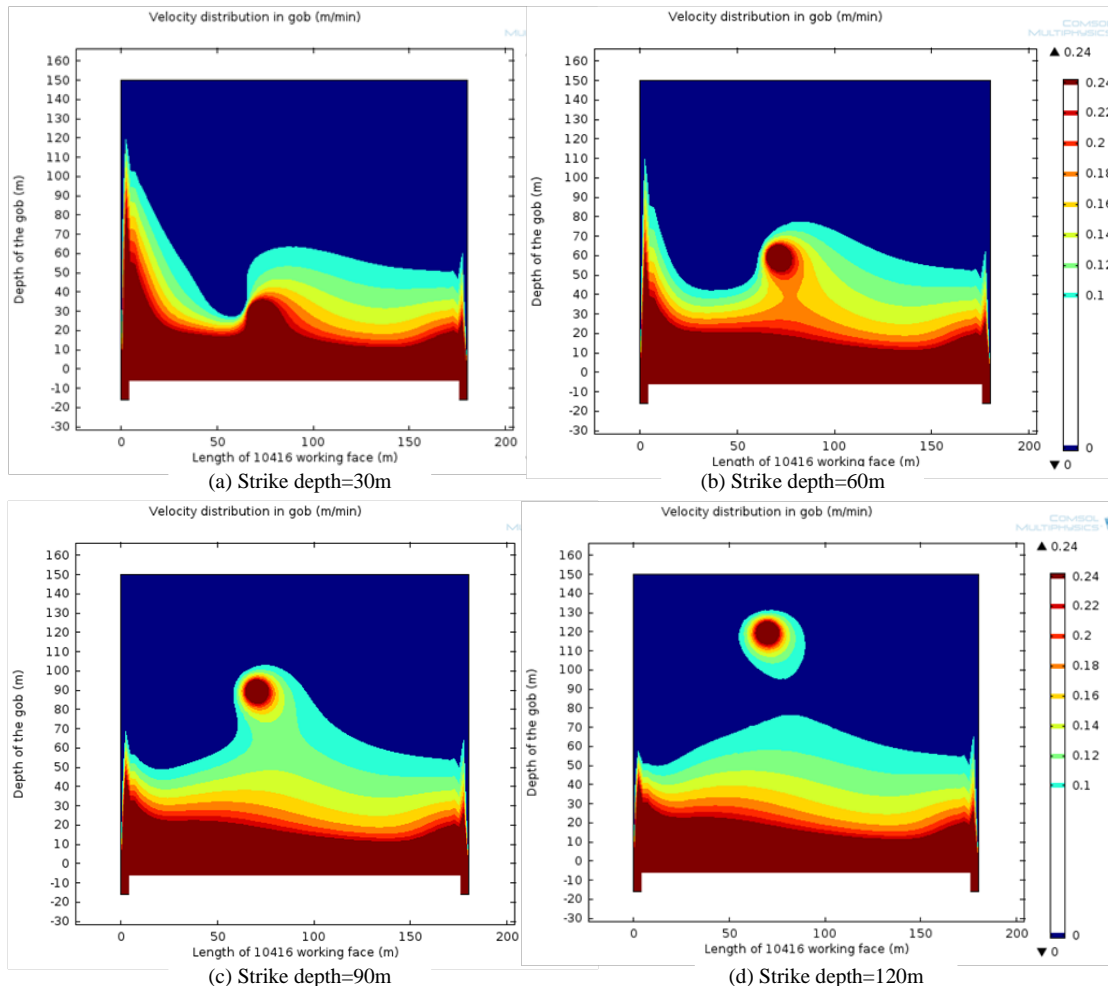


Figure 3: The influence of strike location of surface drainage borehole on spontaneous combustion in gob

4. COAL FIRE PREDICTION DURING METHANE DRAINAGE

4.1 Chaos characterisation

Rescaled range analysis (*R/S* analysis) is widely employed to scale the chaos characteristic of time series. As chaos is pervasive in engineering, gas indexes from surface boreholes are no exception. The relationship between *R* and *S* accords with the formula below (Zhu and Ji, 2011):

$$R/S = (\alpha\tau)^H \quad (2)$$

Where *R* is the extreme range of the time series, *S* is the standard deviation of the time series, *R/S* is the rescaled range, τ is the observational frequency, α is a constant value, *H* is Hurst index. It has been proven that if $0.5 < H \leq 1.0$ the time series is a growing series, implying the future can be reflected by the present (Falconer, 2013).

4.2 Chaos characteristic of the indicator for coal spontaneous combustion

Considering the influence of methane emission and CO₂ injection, most gas indexes including single gas indexes and Graham ratios are not inapplicable in predicting coal spontaneous combustion in gobs, while the N₂/O₂ ratio is an exception (Hu, Yang et al. 2015). Gas samples were gathered from a surface drainage borehole every four hours i.e. two samples every shift. As showed in Figure 4, a total of 218 N₂/O₂ ratios were collected on the ground during methane draining.

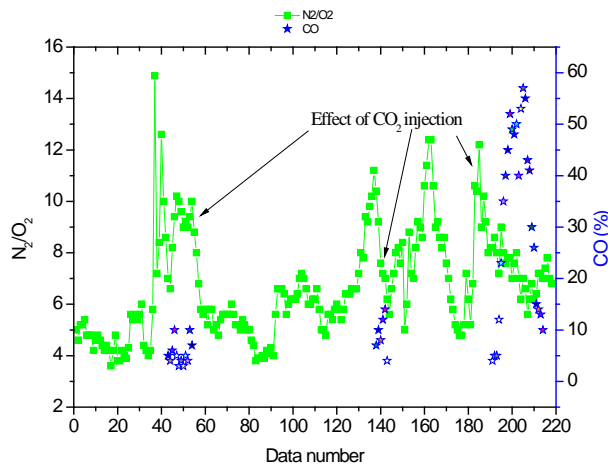


Figure 4: The variation of N₂/O₂ ratio during methane draining from surface boreholes

During the whole draining process, the N₂/O₂ ratio fluctuated up and down. If the N₂/O₂ soared up, CO ensued. Owing to the cooling and stifling effect of CO₂ on self-heated coal, the N₂/O₂ ratio descended and CO faded away.

4.3 Chaos characteristic of N₂/O₂ time series

Figure 5 shows that the Hurst value gradually levels out around 0.9, showing a stable chaos characteristic. Setting the observation frequency as 80, the length-fixed time series can be employed to

weigh the spontaneous combustion condition in gob as shown in Figure 6.

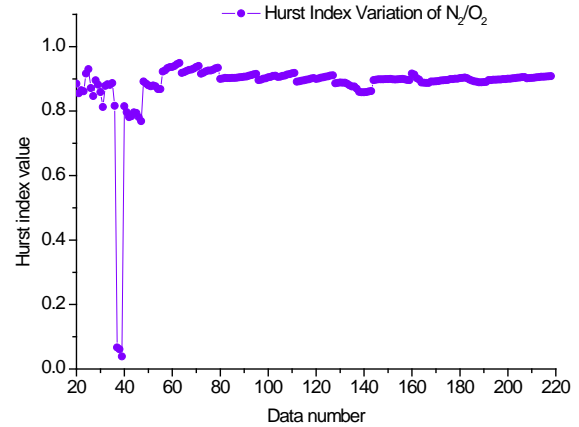


Figure 5: Hurst index variation of N₂/O₂ with data number

It is apparent that whether or not CO was detected, the Hurst value fluctuates between 0.5 and 1. At first, when CO was not detected or in low concentration, the ratio fluctuates regularly. Although CO₂ was injected when CO was detected, the value is still larger than 0.8, showing a stable chaos characteristic. However, a dramatic decline is observed and relatively higher CO concentration follows owing to the deeper oxidation of coal in gobs. Depending on a certain length of statistical data, the influence of seldom abnormal value can be avoided. Therefore, the Hurst value is more stable and misinformation can be eliminated.

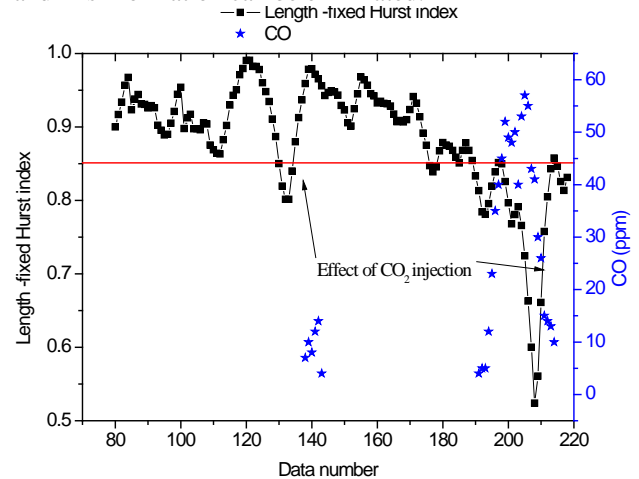


Figure 6: Variation of length-fixed Hurst index and CO

4.4 Critical values

Fixing the length of the N₂/O₂ time series to 80, the risk of surface methane drainage in the working face gob can be divided into two stages based on the aforementioned analysis:

- (1) Safety drainage stage (Hurst index > 0.85)

Pursuant to the analysis above, 0.85 is the lowest value under normal condition when there was no CO, indicating that the oxidation condition of coal in 10416 working face gob was in low-temperature oxidation stage.

(2) Spontaneous combustion initiating stage (Hurst index \leq 0.85)

Similarly, if the Hurst value of N₂/O₂ in surface borehole is lower than 0.85, the oxidation of coal in gob is accelerated. The smaller the Hurst index the deeper the oxidation of coal.

5. CONCLUSIONS

This paper highlights the influence of surface drainage boreholes on coal spontaneous combustion by COMSOLTM simulating and coal spontaneous combustion predicting possibility employing R/S analysis. Several conclusions can be made as follows:

(1) In the vicinity of the working face, the methane drainage can narrow the width of spontaneous combustion zone around the borehole, whilst deeper strike depth leads to a wider spontaneous combustion zone in the middle gob with the advancement of the borehole.

(2) The advancement of the surface drainage borehole has little effect on the spontaneous combustion zone on the intake side but it reduces the depth of the self-heating area dramatically on the return side.

(3) N₂/O₂ time series has a chaos characteristic. The risk of coal spontaneous combustion in 10416 can be divided into two stages: the safety drainage stage (Hurst index $>$ 0.85) and the spontaneous combustion initiating state (Hurst index \leq 0.85).

6. ACKNOWLEDGEMENTS

This work was conducted in the context of coal spontaneous combustion control in Yang Liu Co.ltd and financially sponsored by the National Natural Science Foundation of China (51174198), the State Key Laboratory of Coal Resource and Safety Mining, China University of Mining and Technology (SKLCRSM11X01) and CSC (China Scholarship Council). The authors wish to express their gratitude to the sponsors and especially to the staff of the YangLiu Mining Co. Ltd.

7. REFERENCES

Falconer, K. (2013). Fractal geometry: mathematical foundations and applications, John Wiley & Sons.

Ham, B. (2005). A review of spontaneous combustion incidents. COAL 2005: 6th Australasian Coal Operators' Conference. 2005: 237-242.

Hu, X., S. Yang, X. Zhou, Z. Yu and C. Hu (2015). "Coal spontaneous combustion prediction in

gob using chaos analysis on gas indicators from upper tunnel." Journal of Natural Gas Science and Engineering 26: 461-469.

Karacan, C. "A new method to calculate permeability of gob for air leakage calculations and for improvements in methane control."

Li, Z.-x., Q. Wu and Y.-n. Xiao (2008). "Numerical simulation of coupling mechanism of coal spontaneous combustion and gas effusion in goaf." JOURNAL-CHINA UNIVERSITY OF MINING AND TECHNOLOGY-CHINESE EDITION- 37(1): 38.

Madeja-Struminska, B. and E. Widzyk-Capehart (2006). Correlation between methane and fire hazards in abandoned workings of longwall mining. 11th U.S./ North American Mine Ventilation Symposium 2006: 325-330.

Song, Z. Y. and C. Kuenzer (2014). "Coal fires in China over the last decade: A comprehensive review." International Journal of Coal Geology 133: 72-99.

Szlazak, N., D. Obracaj and J. Swolkien (2014). "Methane drainage from roof strata using an overlying drainage gallery." International Journal of Coal Geology 136: 99-115.

Yang, W., B. Q. Lin, Y. A. Qu, S. A. Zhao, C. Zhai, L. L. Jia and W. Q. Zhao (2011). "Mechanism of strata deformation under protective seam and its application for relieved methane control." International Journal of Coal Geology 85(3-4): 300-306.

Yuan, L. and A. Smith (2007). "Computational fluid dynamics modeling of spontaneous heating in longwall gob areas." transactions-society for mining metallurgy and exploration incorporated 322: 37.

Zhou, F.-B., T.-Q. Xia and B.-B. Shi (2013). "Coexistence of gas and coal spontaneous combustion (II): New prevention and control technologies." Meitan Xuebao/Journal of the China Coal Society 38(3): 353-360.

Zhu, H. and C. Ji (2011). Fractal Theory and Its Applications. Beijing, Science Press.

The strength properties of fibre glass dowels used for ground control in coal mines

Naj Aziz^{a*}, Wenxue Chen^b, Ali Mirzaghobanli^a, Jiao Yuzhao^b

^a Rock Bolting Research Group, School of Civil, Mining and Environmental Engineering
Faculty of Engineering and Information Sciences,
University of Wollongong, Wollongong, Australia 2500

^b Shandong Safety Industries Co Ltd- Tai'an, CHINA

ABSTRACT

Glass-Reinforced Polymer (GRP) bolts, commonly known as Fibre Glass (FG) dowels or plastic dowels are increasingly applied for strata reinforcement in mines as well as in concrete reinforcement in civil engineering. The most popular dowels used in Australian coal mines are the 22 mm diameter fully threaded type. FG bolts are cuttable, easy to handle, lightweight and corrosion resistant. The tested dowels were all black in colour, which is a favoured colour in coal mines. A series of tests were undertaken to evaluate various strength properties of FG dowels. These tests include the tensile failure test by the double-embedment method, single guillotine shear test, double shear test both in steel frame and in concrete blocks, and finally the punch shear test. The study found that the tensile strength by pull testing of the 22 mm diameter fibre glass dowels was in the order of 27 t. The shear strength testing of dowels in both single guillotine and double shear steel frames were in agreement with each other. In general the shear strength values of dowels tested, using single shear guillotine testing, were around 20% of the axial strength in comparison with 70% in the same diameter steel rebar tests. The peak shear load values obtained from double shear tests in concrete blocks was influenced by the encapsulation grout type and the level of fibre glass axial pre-tension. The punch shear tests revealed that there was a more than threefold increase in the punch shear strength value of fibre glass dowels tested perpendicular as against parallel to the dowel axis.

KEYWORDS: Fibre glass dowels; rib support; tensile strength; single and double shear test; punch shear test

1. INTRODUCTION

Glass-Reinforced Polymer (GRP) bolts, commonly known as Fibre Glass (FG) dowels, are increasingly used in Australian coal mines as a means of rib support in heading development and for coal face equipment recovery. The increased mechanisation of coal winning particularly by longwall mining necessitated the use of non-metallic rib dowels for rib support, where extraction includes cutting of bolts. FG dowels are made by pultrusion, a process that combines extrusion and pulling of molten or curable resin and continuous fibres usually arranged in unidirectional layers, through a die of a desired structural shape ("pull" and "extrusion"). FG dowels are made of glass strands pulled through a saturated thermoset resin and heated (Lowenstein, 1973). Presently FG dowels used in coal mines rib support have continuous rope thread profiles providing deformations for high bond strength with resin and rock. Other factors contributing to the increased application of polymeric dowels, as elements of support instead of steel, include:

- Improvement in the strength properties of the non-steel based dowels. The ultimate tensile

strength of presently made 22 mm diameter dowels can range between 57 - 85 % of steel rebar of the same diameter

- Easy and safe handleability of the non-steel dowels particularly FG
- Lightweight, fire resistant and easy to handle,
- FG dowels are relatively cheap,
- Cuttable, longer lasting and can be supplied at a greater length

Presently, there are two types of GRP bolts in the market, they are plastic and FG dowels, however, FG dowel is characterised as having lower yield deformation against shearing, and can twist on torquing. Properties and characteristics of polymeric bolts are variable depending on the chemistry of the product, dowel diameter, solid or hollow core, surface profile shape and composition. FG dowels are used as rib support dowels. Dowels of the same core diameter can vary in length, identified by dowel colour and colour coding. Typical dowel lengths with colour coding include dowel length 1.2 m (blue), 1.5m (orange), 1.8m (red), and 2.1 m (green).

Procedures used for evaluating strength integrity of dowels are based on Australian and various international standards. These include American Standards of Testing Materials (ASTM. C-759, 1991), The British Standard (BS 7861- Parts 1 and 2, 1996), International Standard ISO 10406-1 (2008), South African Standard, SANS1534 (2004), and others. In general, many well-known standards are invariably interrelated; however, the suitability of any particular standard, for testing the given property of the dowel, will depend on the purpose of the dowel used and host medium properties. The current reporting of the shear strength of dowels is normally based on guillotine testing of the FG rod in steel apparatus. Guillotining of the GRP dowels in steel shear apparatus yields lower shear values and is an undesirable test, unless the dowels are contained in very thick grout encapsulation sleeve. It is important that the shear strength of dowels must be determined based on simulated ground conditions, and therefore it is logical to test dowels in rock or cementitious medium of concrete. Accordingly there is a need for establishing a credible testing methodology and procedures for effective marketing strategy. The double shear testing of dowels in concrete blocks represents a novel approach to simulating the shear behaviour of dowel in rock formation *in situ*. This paper discusses tensile and shear strength characteristic of 22 mm core diameter FG dowels, which are used in Australia coal mines.

2. TENSILE STRENGTH PROPERTIES

Six 1.2 m long 22 mm diameter black dowels were tested for tensile strength. Each sample was double embedded in 400 mm length steel tubes and pull-tested to failure. Oil based chemical bolt resin was used to install the dowel in steel tubes. Figure 1 shows a dowel with both embedded ends being encapsulated in the steel tubes. Figure 2 shows the sample being tested in 50 t Instron Universal Testing Machine. Figure 3 shows the load displacement of four failed samples out of six tested samples. Figure 4 shows post-test dowels. Two samples did not fail



Figure1: Black dowel with ends encapsulated in 450 mm long tubes used for tensile strength testing.



Figure 2: Tensile testing of a dowel in 50 t Instron Universal Testing Machine and monitoring system.

because of poor encapsulation. The average peak failure load of four failed dowels is 273.36 kN, as shown in Table 1.

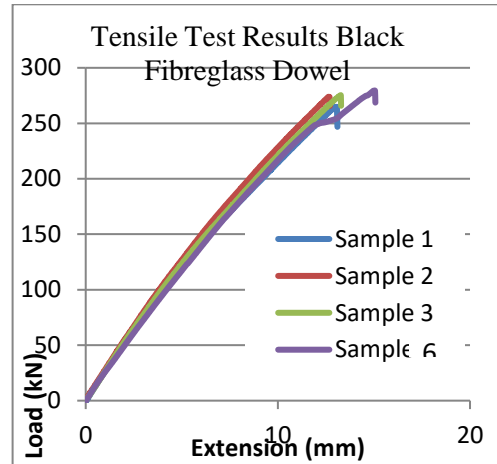


Figure 3: Load displacement profiles of four tested black dowel samples.

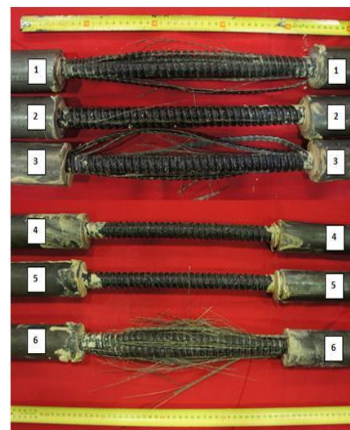


Figure 4: Tensile failure of four out of six tested samples.

Table 1: Average peak load for tested samples.

Sample	Peak Load (kN)
1	264.83
2	273.79
3	275.34
6	279.48
Average	273.36

3. SHEAR TESTING OF DOWELS

3.1 Single shear guillotine test

Figure 5 shows the single shear apparatus used for shear testing of FG dowels. Commonly known as the “guillotine test”, the instrument allows direct shearing of dowels and steel rock bolts to failure. Figure 6 shows typical tested samples. Figure 7 shows typical graphs of single shearing tests of nine, 300 mm long black dowel sections. Details of the test results are also shown in Table 2. The average value of the shear strength was 150.45 MPa. The cut face surface of all ten tested dowels was identically stepped at mid-face as is obvious in Figure 6. This may be attributed to the fact that dowel sections were not grouted in the frame and the guillotining effect may have caused a slight bending and incremental elongation of the uncut half FG elements. Also it should be noted that the slight displacement at the early stage of testing, as indicated in the circled section of the graphs in Figure 7, may be attributed to the early crushing of the dowel rifle profiles.



Figure 5: Single shear testing of black dowel.



Figure 6: Sheared dowel face with stepped cut.

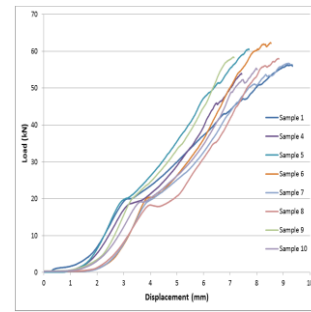


Figure 7: Single shear test results of 22 mm diameter dowels tested for single shear.

Table 2: Single shear test data for nine dowels.

Sample	Peak Load (kN)	Shear Strength (MPa)
1	56.33	148.19
2	52.78	138.86
3	53.98	141.99
4	60.63	159.49
5	62.35	164.01
6	56.75	149.29
7	58.04	152.68
8	58.43	153.71
9	55.42	145.80
Average	57.19	150.45

3.2 Double shear test method - in steel frame

The purpose of this section was to compare the single shear strength capacity of FG dowels using a double shear guillotine testing apparatus. Like the single shear test, this test does not represent the shearing action encountered in underground conditions. The test produces steel on dowel interaction whereas in underground it would be the strata on grout on dowel interaction. However, this test was carried out to compare with the single shear strength result observed using the single shear method. Each dowel was machine cut into 300 mm specimen lengths. Four samples were tested.

Figure 8 shows the double shear test apparatus that was used for the study. It consists of two steel pieces. The bottom piece or ‘U’ shaped piece measured 143 mm x 83 mm x 70 mm. The top piece or ‘T’ shaped piece is inserted into the ‘U’ shaped piece. It measures 131 mm x 92 mm x 70 mm. The dowel was inserted through the middle of the combined apparatus and sheared up to a maximum depth of 30 mm. Figure 9 shows the load-displacement and failure of tested dowel sections. Figure 10 shows sheared samples.

Table 3 shows peak failure load and shear strength of the dowel. The average value of the shear strength is 157.62 MPa. This value is in reasonable agreement with the results of the single tests shown

in Table 2. By taking a biased average of four tests as shown in the right column Table (blue writing), it is clear the results of single shear concur favourably with the results of double shear tests. Also the failure pattern in double shear test is similar to that of single shear test, with step cuts as shown in Figure 10.



Figure 8: Double shear guillotine apparatus set up.

The shear strength of the dowel was determined using:

$$\tau(\text{MPa}) = \frac{F}{A} = \frac{N}{\text{mm}^2} = \frac{\text{Peak Load (kN)} \times 1000}{\pi 22^2 / 4}$$

Where:

- τ = shear strength in mega-Pascals
- F = Peak load at failure in Newtons
- A = dowel cross sectional area in millimetres squared

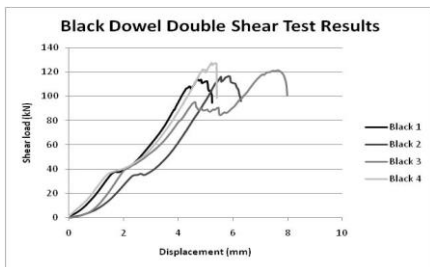


Figure 9: load displacement profiles of four double shear tests in steel frame.



Figure 10: Failure pattern of samples in steel double shared apparatus.

Table 3 shows results of double shear guillotine test, four dowel sections were tested and the average failure load and shear strength of the dowels were 50.48 kN and 123.79 MPa respectively. These results compare favourably with the single shear test results as reported in Table 2. The pattern of the shear failures shown in Figure 10 is similar to the single shear test results, but less pronounced as is shown in Figure 6.

Table 3: Double shear guillotine test results.

Sample	Peak shear Load (kN)	Single face peak load (kN)	Shear Stress (single face) (MPa)
1	107.33	51.88	136.49
2	98.03	49.01	128.94
3	111.04	55.52	146.06
4	90.99	45.50	119.69
Average	-	50.48	132.79

3.3 Double shear tests in concrete

The double shear strength of fibre glass dowels was investigated in three piece concrete blocks consisting of a 300 mm long prism block, sandwiched between two 150 mm side cubes. 40 MPa, Uniaxial Compressive Strength (UCS) mortar blocks were prepared with sand: cement ratio of 3:1. Once mixed the mortar was poured into the internally greased marine plywood mould, measuring 150 mm x 150 mm x 600 mm. The mould was divided into three compartments separated by two metal plates. A plastic conduit, 20 mm in diameter was set through the centre of the mould lengthways to create a hole for FG dowel installation. The cast mortar blocks were left for 24 hours to set and harden. The set blocks were then removed from the mould assembly and kept in a moist environment for a period of 30 days to cure. The central hole of the mortar block was then reamed rifle-shaped to 27 mm diameter, ready for the installation of the dowel with cement grout. Recently the process of mechanical reaming of 20 mm central hole was disbanded in favour of casting of profile holes using double core 3 mm thick electric wire wrapped around the central steel bar. The central steel bar and the wrapped wire were later removed during semi-hardened stage of cast concrete. The strength of the concrete blocks was determined from testing of the representative 100 mm diameter cylindrical concrete specimens, cast at the time of concrete preparation and pouring. Two different cementitious grouts were used when installing and encapsulating FG dowels in concrete blocks:

- (a) Jennchem Top-Down 80 grout (TD80)
- (b) Jennchem Bottom-Up 100 grout (BU100)

The strength of both grouts varied depending on the product composition and water content. In this

study the level of water for each grout was maintained constant at six litres per 20 kg bag. The FG concrete assembly was left to cure for a minimum of seven days before being tested.

A total of 11 tests were conducted in this study. Dowels, for each category of grout used, were pretensioned to various loads up to 22.50 kN and then tested for shear. An attempt to apply pretension load of 25 kN was not possible as extra load torque applied to the dowel nuts caused dowel ends to twist, leading to lower shear loads. The applied axial tension load due to subsequent shearing load, were monitored using two 30 t capacity load cells shown in the assembled setup in Figure 11. A 50 t capacity Instron universal testing machine was used for shearing study. Clearly there were variations to the shear strength properties of the FG dowels based on the level of pretension loads and grout type as shown in Table 4 and Figure 12. It was found that:

- a) The shear values of dowels were higher with increased pretension loads.
- b) Increased pretension loads, greater than 22.5 kN, caused dowel ends to twist thus affecting double shear strength values as is evident from the lower value shear load of the dowel pre-tensioned at 25 kN,
- c) Shear load values of dowels were affected by the grout type, with average shear values obtained for FG dowels tested with grout TD80 being

higher than test results with BU100 grout, despite the fact that BU100 grout has relatively superior strength in comparison with TD80 grout, which is surprising, Further tests will be carried out to verify these findings

- d) The shear value of each tested dowel was determined taking into consideration the shear strength contribution from 150 mm² concrete joint planes.



Figure 11: A double shear assembly mounted in the 500 kN Instron testing machine.

Table 4: Single and double shear test results with different grouts.

a) Encapsulation Grout: BU100

Test	Initial ave axial load (kN)	Final ave axial load (kN)	Peak shear load (kN)	Peak double joint plane shear strength (MPa)	Peak shear per joint plane (MPa)	Contribution from concrete joint surface (%)	shear strength less joint surface shear (MPa)	Direct single shear test (guillotine) ave value from Table 2 (MPa)	Increase (%)
1	2.5	28.7	163.9	431.2	215.6	10	194	133.5	49
2	4.5	43.4	182.9	481.6	240.6	15	205	133.5	58
3	5	62.0	204.7	538.5	269.2	15	229	133.5	76
4	15	31.2	219.7	578.0	289.0	20	231	133.5	78
5	20	40.0	258.1	679.0	339.5	25	255	133.5	96
6*	25	66.2	191.8	504.6	252.3	30	177	133.5	36

* Sample 6 - twisted dowel

b) Encapsulation Grout: TD80

Test	Initial ave axial load (kN)	Final ave axial load (kN)	Peak shear load (kN)	Peak double joint plane shear strength (MPa)	Peak shear per joint plane (MPa)	Contribution from concrete joint surface (%)	shear strength less joint surface shear (MPa)	Direct single shear test (guillotine) ave value from Table 2 (MPa)	Increase (%)
7	2.5	26.9	206.3	542.6	271.3	10	244	133.5	88
8	7.5	49.2	178.5	469.6	234.8	15	200	133.5	54
9	10	20.6	266.6	701.2	350.6	15	298	133.5	229
10	22.5	50.2	296.1	779.0	389.5	15	331	133.5	255
11	25	53.7	172.4	453.5	226.8	25	170	133.5	31

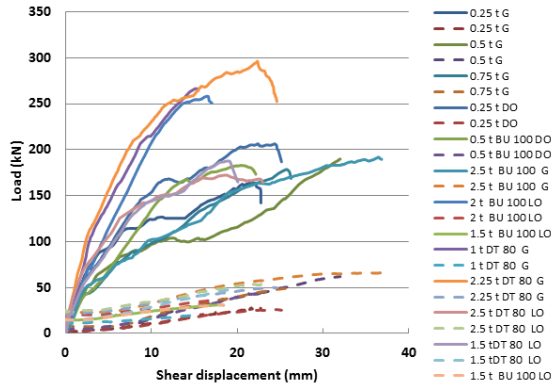


Figure 12- Shear pretention loads versus vertical displacement of double shear testing of 11 dowels.

3.4 Punch Shear Test

Using the punch shear box, shown in Figure 13a, a series of punch shear tests were carried out on FG dowel samples to determine the shear strength of FG dowels. 3 mm thick discs were sliced perpendicular to the dowel axis to examine the shear strength properties of dowels parallel to the strands or FG elements lay, while 3 mm strips were cut parallel to the dowel axis to evaluate the shear strength of the FG elements bonding. These two types of cuts are shown in Figure 13b. Tables 5 and 6 show results of punch shear tests. Values of the shear strength were determined by using the following equation;

$$\tau = \frac{F}{3.142 \times T \times D}$$

where;

F = applied load, τ = shear strength, T = Sample thickness and D = Punch diameter

From Table 5, the average shear strength value of six samples punch tested parallel to the direction of the dowel is shown to be 22.35 MPa, and the average shear strength value of testing three samples perpendicular to the direction of the dowel axis as shown in Table 6 is 104.01 MPa. It is clear that there is an obvious difference in shear strength in the ratio of 4.7:1 in favour of perpendicular to dowel axis or dowel strands compared with parallel to dowel axis. The low shear strength values parallel to the dowel axis may be due to the resin shear strength holding the fibres together, being lower than the strength of the fibre glass. The average shear strength value shown in Table 5 strikingly similar to the average shear strength value of 21 days old standard oil based resin used for bolting encapsulation bolting as reported by Gilbert (2014).



Figure 13a: Punch shear apparatus, Figure 13b: Punch shear apparatus.

Table 5: Punch Test Results of samples cut parallel to dowel axis.

Sample	MN	T (m)	D (m)	τ (MPa)
A	0.0021	0.00249	0.0127	21.12
B	0.0022	0.00253	0.0128	21.70
C	0.0023	0.00279	0.0126	20.64
D	0.0028	0.00336	0.0126	20.98
E	0.0040	0.00363	0.0127	27.97
F	0.0011	0.00178	0.0127	15.38
G	0.0039	0.00342	0.0127	28.67
			Average	22.35

Table 6: Punch test results of samples cut perpendicular to dowel axis.

Sample	Punch load (MN)	T (m)	D (m)	τ (MPa)
A	0.012	0.00297	0.0128	102.22
B	0.012	0.00302	0.0127	102.30
C	0.013	0.00302	0.0129	107.50
			Average	104.01

4. CONCLUSIONS

This study demonstrated that the guillotine method of testing dowels yields lower shear values than results obtained from testing dowels by double shear testing in concrete. Double shear testing in concrete represent a realistic way of simulating the strength property of the composite material in rock and *in situ*. The study also found that:

- Shear values of the FG dowels were higher with higher pretension loads.
- Increased pretension loads greater than 22.5 kN caused dowel ends to twist thus affecting double shear strength values, and this is evident from the lower value dowels double shear load pretensioned to 25 kN.
- The Shear load values of dowels were affected by the grout type, with average shear values obtained from FG dowels tested with grout TD80 being higher than test results with BU100 grout,

despite the fact that BU100 grout has relatively superior strength in comparison with TD80 grout, which is surprising. Further studies is planned to confirm this finding.

- d) Low shear strength results of testing dowel parallel to the dowel axis and thus to FG strands may be due to the resin strength holding the fibres together and resisting the shear force being lower than the shear strength of fibre glass elements. The shear strength values shown in Tables 5 are comparable to the shear strength of a typical oil based standard chemical resin used for bolting installation.

5. ACKNOWLEDGEMENT

The authors wish to thank Colin Devenish, a technical officer of the School of Civil, Mining, and Environmental Engineering, Faculty of Engineering and Information Science, University of Wollongong for his assistance. The project was partially funded by Shandong Safety Industries Co., Shandong Ltd, China.

6. REFERENCES

American Standard for Testing Materials (ASTM. C-759), (1991). Standard test method for compressive strength of chemical –resistant mortar, grouts, monolithic surfacings and polymer concretes.

British Standard BS 7861- Parts 1 and 2 (2009): Strata Reinforcement support system components used in Coal Mines-Part 1. Specification for rock bolting and Part 2: Specification for Flexible systems for roof reinforcement.

Gilbert, D. (2014). Study of fibre glass strength properties, undergraduate thesis, University of Wollongong.

International Standard ISO 10406-1 (2008). Fibre-reinforced polymer (FRP) reinforcement of concrete –test methods, part 1:FRP bars and grits, First edition, 40 p.

Lowenstein, K. L. (1973). The Manufacturing Technology of Continuous Glass Fibers. New York: Elsevier Scientific. pp. 2–94. ISBN 0-444-41109-7.

South African Standard SANS1534 (2004). Resin capsules for use with tendon based support systems, published by Standards South Africa.

Numerical simulation for propagation characteristics of outburst shock wave and gas flow when outburst prevention facilities fail

Zhou Aitao^{a,*}, Wang Kai^b, Kong Yuyu^c, Liu Ang^d

^a School of Resource & Safety Engineering, State Key Laboratory of Coal Resources and Mine Safety, China University of Mining & Technology, Beijing, China 100083

^b School of Resource & Safety Engineering, State Key Laboratory of Coal Resources and Mine Safety, China University of Mining & Technology, Beijing, China 100083

^c Jincheng Zetai Safety Evaluation Center, Jincheng, Shanxi, China 048000

^d School of Resource & Safety Engineering, State Key Laboratory of Coal Resources and Mine Safety, China University of Mining & Technology, Beijing, China 100083

ABSTRACT

In order to numerically simulate the propagation characteristics of outburst shock waves and gas flow when outburst prevention facilities fail, the propagation characteristics model of outburst shock waves and gas flow was established, and the mechanism of gas counter current was analyzed. The propagation characteristics of shock wave and gas flow at two types of geometry models were numerically simulated by using Fluent software. The results show that most of the gas flow produced by outbursts propagates to intake airways when crossheading with an excavation roadway at the same level; however, when crossheading with an excavation roadway not at the same level, gas is mainly discharged from the return airway, and the effect of the gas flow on the intake airway is small. The results have important theoretical and practical significance for mine disaster rescue and preventing secondary accidents.

KEYWORDS: outburst prevention facilities; shock wave and gas flow; gas counter current

1. INTRODUCTION

Shock waves and gas flow are formed during coal and gas outburst, which can induce casualties and property loss. Scholars have performed extensive study in this field. Cheng Wuyi (2004) made a simple theoretical analysis and mathematical deduction based on the forming process and propagation law of outburst shock wave and gas flow. For the dynamic process of the flow, F. Otuonye (1998) proposed a simplified mechanism of outburst and established the corresponding physical model. Wang Kai et al., 2011, Wang Kai et al., 2012, Zhou A.T(2012) systematically studied the formation mechanism and propagation characteristics of the shock wave and flow caused by outburst; based on theoretical analysis, experimental studies, and numerical simulations, they systematically analyzed the attenuation characteristics of the shock wave and gas flow from the outburst in a straight roadway, turning roadway, bifurcation roadway, and variable cross-section roadway. It is well known that when outburst prevention facilities fail, intake airway associate with the excavation airway where outburst occurs and then the shock wave and gas flow pour out from the crossheading into the intake airway (Zhang J, 2007). This paper mainly studies the impact of outburst shock waves and gas flow on the intake airway and proposes appropriate solutions. Firstly, the roadway

model after the outburst prevention facilities was established and process of the shock wave and gas flow was numerically simulated. Secondly, the variation process with time of pressure, velocity, and density in observation points was monitored, and the conditions of pressure, velocity, density, and concentration variation of gas within roadways at different time were obtained. Thirdly, the impact of outburst shock wave and gas flow on the ventilation system after the air door failure was analyzed. The result obtained has important theoretical and practical significance for mine disaster rescue and the prevention of secondary accidents.

2. ANALYSIS OF PROPAGATION CHARACTERISTICS OF OUTBURST SHOCK WAVE AND GAS FLOW

The propagation of outburst shock wave and gas flow can be considered a one-dimensional compressible gas semitropical unsteady continuous flow, which is always accompanied by the movement of disturbance waves. When the disturbance waves propagate through media, physical quantities of shock wave and gas flow at any point change dramatically over time, forming unsteady movements. Therefore, in order to study the unsteady compressible flow of the shock wave and gas flow, one must study the disturbance wave motion.

*Corresponding author – email: cumtbzat@126.com

When gas outburst occurs, the intensity of the shock wave is changed. In other words, the velocity of the outburst shock wave is unchanging, and the gas parameters of the wave-after change over time. To convert the unsteady state to a steady state, it is necessary to coordinate the observation with the shock wave motion, and set up three basic equations for the control-body that surrounds the shock wave. Because the shock wave is extremely thin, its volume can be ignored. The rate of mass, kinetic energy, momentum and internal energy variation over time of the control-body and other items are equal to zero, and the variable intensity on both sides of the shock wave can also be analyzed using the equation of steady flow. This is equivalent to dividing the varying intensity movement process of a shock wave into some limited short moments. Now every small part can be dealt with as a stationary flow process, and this steady flow is known as quasi-steady flow.

Figure 1 is a transient state of a shock wave in the propagation process. The region where shock waves through is called the wave-after, and the region where there is no wave disturbance is known as the wave-front. The rightward direction represents the positive direction of flows. Velocity, pressure, density, enthalpy, and temperature of the wave-front and wave-after were $v_1, p_1, \rho_1, h_1, T_1$ and $v_2, p_2, \rho_2, h_2, T_2$, respectively, and the velocity of shock wave is v . The dotted area is the control plane area for the study of shock wave motion.

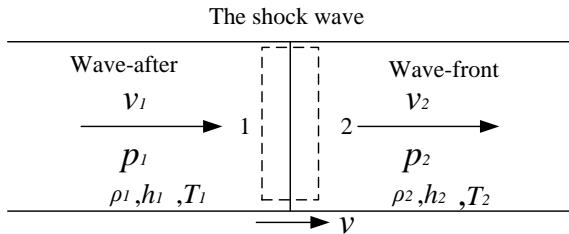


Figure 1: Shock wave communication status model.

Through coordinate conversion, the movement process of the shock wave is transited from unsteady flow into steady flow, namely, the coordinate system that flows with the shock wave is selected for reference, and the velocity of the shock wave becomes zero. At this time a standing vertical impulse wave is formed; the wave-after velocity becomes $v_1 - v$, direction to the left; the wave-front velocity also becomes $v_2 - v$, direction to the left; parameters of wave-after and wave-front are constant, as shown in Figure 2.

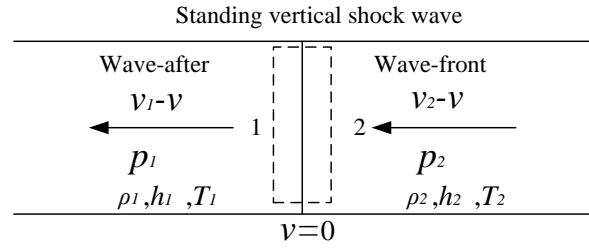


Figure 2: State model of standing vertical shock wave.

According to the state model of a standing vertical shock wave, firstly establish the continuity equation. According to the conservation of mass the continuous equation of a standing vertical shock wave is as follows:

$$\rho_1(v_1 - v) = \rho_2(v_2 - v) \quad (1)$$

Establish the momentum equation. The shock wave within the roadway belongs to the one-dimensional flow, and both sides of it are in the role of air and gas pressures, respectively. Ignoring the body force, the momentum equation of one-dimensional steady flow can be written as:

$$p_1 + \rho_1(v_1 - v)^2 = p_2 + \rho_2(v_2 - v)^2 \quad (2)$$

Establish the energy equation. Because airflow through the shock wave can be considered an adiabatic process, the total temperature T of the wave-front and wave-after can be considered as constant. Friction is negligible, and therefore the shock wave is very thin. For one-dimensional unsteady flow without shaft work and potential role, and $h = u + p / \rho$, the energy equation is as follows:

$$u_1 + \frac{p_1}{\rho_1} + \frac{(v_1 - v)^2}{2} = u_2 + \frac{p_2}{\rho_2} + \frac{(v_2 - v)^2}{2} \quad (3)$$

The three previous equations have seven unknowns : $p_1, \rho_1, v_1, p_2, \rho_2, v_2$ and v (Specific internal energy, u , can be obtained using the state

$$u = \frac{1}{\gamma - 1} RT = \frac{1}{\gamma - 1} \frac{p}{\rho}$$

the p and ρ). Four parameters are independent. Given any of these four parameters the rest can be uniquely identified. For example, p_2, ρ_2, v_2 , and anyone parameter of wave-after is given, then the rest of the parameters and shock wave velocity can be uniquely identified. When putting these parameters into three equations the wave equation is obtained:

$$\left. \begin{aligned} \frac{\rho_1 \rho_2}{\rho_1 - \rho_2} (p_1 - p_2) &= -\rho_1^2 (v - v_1)^2 = -\rho_2^2 (v - v_2)^2 \\ \frac{p_1}{p_2} &= \frac{(\gamma + 1)\rho_1 - (\gamma - 1)\rho_2}{(\gamma + 1)\rho_2 - (\gamma - 1)\rho_1} \\ \frac{\rho_1}{\rho_2} &= \frac{(\gamma + 1)p_1 + (\gamma - 1)p_2}{(\gamma - 1)p_1 + (\gamma + 1)p_2} \\ \frac{T_1}{T_2} &= \frac{\frac{p_1}{p_2} + \frac{\gamma + 1}{\gamma - 1}}{\frac{p_2}{p_1} + \frac{\gamma + 1}{\gamma - 1}} \end{aligned} \right\} \quad (4)$$

Wave front Mach number is : $Ma_2 = \frac{v - v_2}{c_2}$;

Local sonic is: $c_2 = \sqrt{\gamma RT} = \sqrt{\gamma p_2 / \rho_2}$. Then the shock wave equation can be expressed as follows:

$$\left. \begin{aligned} \frac{p_1}{p_2} &= \frac{2\gamma}{\gamma + 1} Ma_2^2 - \frac{\gamma - 1}{\gamma + 1} \\ \frac{\rho_1}{\rho_2} &= \frac{v_2 - v}{v_1 - v} = \frac{\frac{\gamma + 1}{2} Ma_2^2}{1 + \frac{\gamma - 1}{2} Ma_2^2} \\ \frac{T_1}{T_2} &= 1 + \frac{2(\gamma - 1)(\gamma Ma_2^2 + 1)}{(\gamma + 1)^2 Ma_2^2} (Ma_2^2 - 1) \end{aligned} \right\} \quad (5)$$

Wave-after Mach number

$$Ma_1 = \left[\frac{(\gamma - 1)Ma_2^2 + 2}{2\gamma Ma_2^2 - (\gamma - 1)} \right]^{1/2}$$

The above equations also show that the airflow parameter relations before and after the shock wave only decide the wave-front flow Mach number Ma_2 and the specific heat ratio .

Non-ideal properties (such as heat conduction, friction, viscosity) of the medium only affect the thickness of the shock wave, without affecting its strength. It is assumed in the process of gas outburst that spewing gas can maintain the propagation of a shock wave, guaranteeing the continuous flow of the shock wave, therefore the simple shock wave is not attenuated. It is assumed that in the undisturbed roadway area the air is in a stationary state, namely

$v_2=0$ m/s, then $Ma_2 = \frac{v}{c_2}$, and we can know that

parameters in the undisturbed roadway (roadway pressure p_2 , density, specific heat ratio) are constant, $c_2 = \sqrt{\gamma RT} = \sqrt{\gamma P_2 / \rho_2}$. Expressions of

pressure, density ρ_1 , and velocity are shown as follows:

$$p_1 = p_2 + \frac{2\rho_2 v^2}{\gamma + 1} \left(1 - \frac{c_2^2}{v^2}\right) \quad (6)$$

$$\rho_1 = \frac{\rho_0(\gamma + 1)}{\frac{2c_2^2}{v^2} + \gamma - 1} \quad (7)$$

$$v_1 = \frac{2v}{\gamma + 1} \left(1 - \frac{c_2^2}{v^2}\right) \quad (8)$$

3. MECHANISM ANALYSIS OF GAS ADVERSE CURRENT

When the outburst occurs, the coal gas in the body is released in an instant. Due to the large emission and fast transport, relative movement between high concentrations of gas and fresh air flows occurs. Due to the convection-diffusion function, part of the gas is transferred from the high concentration areas to the fresh air, which makes the concentration of gas in the area of fresh air flow rise, causing gas adverse current, as shown in Figure 3.

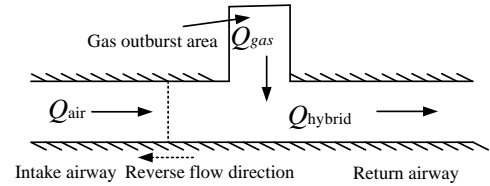


Figure 3: Schematic illustration of gas counter current after outburst.

The theoretical analysis shows that the formation of gas counter current includes two conditions; the volume of gas emission is greater than the air volume after the gas outburst, and the convection diffusion of gas to air. When gas outburst occurs and the volume of gas emission is greater than the volume of the air within the intake airway, the volume within the return airway increases. While in the intake airway, the reverse gas flow pour into the intake airway makes flow volume reduction or flow static, leading to air revering, which is an adverse gas phenomenon. When there is a gas counter-current, there is convection diffusion between fresh air and the high-concentration gas. Convective mass transfer between fresh air and gas occurs, making part of the fresh air gas concentration rise.

After outburst, the gas emission within the intake airway varies. At first, since large coal crushes release a lot of gas instantaneously along with a huge amount of high-pressure gas emission, intake airway

airflow direction is reversed. Gas emission is greatly reduced when outburst ends (Javier T. et al., 2012). In the absence of sustained energy support, gas flow of the intake airway stops moving or returning to normal air flow. While there is convection diffusion between fresh air and high-concentration gas, gas mass transfers with the air, so the concentration of gas in the fresh air flow rises and re-flux still exists. When the volume of fresh air in the intake airway and the gas emission of outburst areas is stable, the impact scope of the gas to the intake airway is determined, and the concentration of gas within the return airway continues to stabilize. Gas adverse current can be divided into three phases, namely the first stage—entering air retrograde phase, the second stage—diffusion stage, and the third stage—stable dilute phase.

The first stage—entering air retrograde phase: the gas emission is enormous (Wang E.Y. et al., 1996), far greater than the volume of the intake airflow, so flow retrogrades. We can assume that the pressure within the gas flow minus the pressure within the roadway is over-pressure, Δp . In the entering air retrograde phase, we can approximate the retrograde process as the overpressure attenuation process, where the relation is:

$$\Delta p = p_1 - p_2 = \delta W / (sx) \quad (9)$$

The relation for Δp is as follows:

$$\Delta p = p_1 - p_2 = \frac{\delta}{\varepsilon} \rho_2^{\frac{1}{3}} \left(\frac{W}{s} \right)^{\frac{2}{3}} t^{\frac{3}{2}} \quad (10)$$

It is important to note that in the place where outburst occurs, the pressure when outburst no longer occurs should be smaller than the pressure at the inlet so as to ensure that under normal circumstances the mine ventilation process, so the pressure difference between the intake airway and the outburst location, is positive. After outburst, the pressure of the outburst shock wave and gas flow that pours into the intake airway is bigger than the pressure of the air which is unaffected by the shock wave and gas flow. The distance of gas retrograde is:

$$x = \delta W / (sp'_1 - sp_0) \quad (11)$$

The second stage—diffusion stage Flores M., 1988: when the counter-current guided by the pressure of gas flow is over, the velocity of the counter-current gas flow is close to zero (Hu W.M. et al., 1998). The phenomenon of gas adverse current is mainly for relative diffusion between gas flow and fresh air. In diffusion, gas flow and air flow can be treated as incompressible fluids. Such gas diffusion

meets the conservation of mass and Fick's first law of diffusion (Jacek S., 2011).

$$J = -D_{AB} \frac{dc_A}{dx} \quad (12)$$

where D_{AB} is diffusion coefficient (m/s); C_A is volume concentration of gas (/m or kg/m); $\frac{dc_A}{dx}$ is concentration; “-” shows diffusion with the concentration gradient in the opposite direction, namely non-component diffuses from the region of high concentration to areas of low concentration. The unit of J is kg/m s.

$$J_t = J_d + J_i + J_c \quad (13)$$

where J_t is variation of gas in micro-body per unit time, $J_i = \frac{\partial c_A}{\partial t} dx$; J_d is the net mass flux through gas in the micro-body per unit time,

$$J_d = - \left[\frac{\partial (uc_A)}{\partial x} + \frac{\partial J}{\partial x} \right] dx; u \text{ is the velocity of}$$

air within roadway, $u=0$ m/s; J_i is the gas amount of increase or decrease, $J_i = \chi c_A dx$; χ is gas flow attenuation coefficient, $\chi < 1$; J_c is due to a chemical reaction the volume of gas increases or decreases in the micro-body in unit time; while the outburst process of this research does not involve chemical reactions, so $J_c = 0$, then equation (13) can be converted to:

$$\frac{\partial c_A}{\partial t} = - \frac{\partial J}{\partial x} + \chi c_A \quad (14)$$

The third stage—stable dilute phase: in this phase, the volume of fresh air is much greater than the volume of gas emission. Gas will flow out of the return airway with the flow in a stable manner, and gas concentration tends to be stable after outburst, as shown in Figure 4.

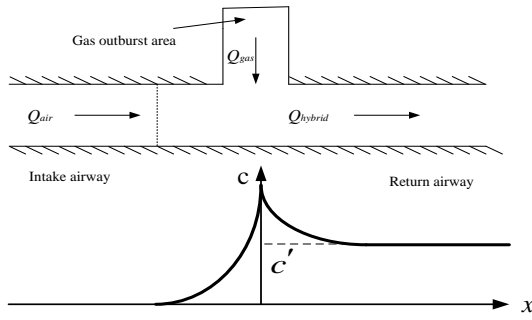


Figure 4: Curves of gas concentration in the laneway at stable dilution stage.

At this time, we focus on the analysis of gas concentration in the return airway, which has certain reference significance to for post-outburst mine rescues. From the above figure, the last stable gas concentration is c' . We can know that:

$$c' = \frac{Q_{\text{gas}}}{Q_{\text{gas}} + Q_{\text{air}}} \quad (15)$$

4. THE PROPAGATION AND NUMERICAL SIMULATION OF THE OUTBURST SHOCK WAVE AND GAS FLOW WHEN THE OUTBURST PREVENTION DAMPERS FAILS

4.1 Numerical simulation of crossheading and excavation roadway associative

(1)The geometric model

The model is shown as Figure 5. The geometry of the model: a outburst cavity length and breadth are 10 m^3 , the excavation roadway is 50 m long, both the total length of intake airway and return airway are 104 m and are relative to the crossheading symmetry. The height of the roadway is 3 m and the width of the roadway is 4 m. Section B – B' is the air inlet side, and section C – C', section D – D' and section E – E' are airflow outlet port. Select a section at a distance crossheading of 25 m as observation points and monitor the change of air pressure, velocity, and gas density.

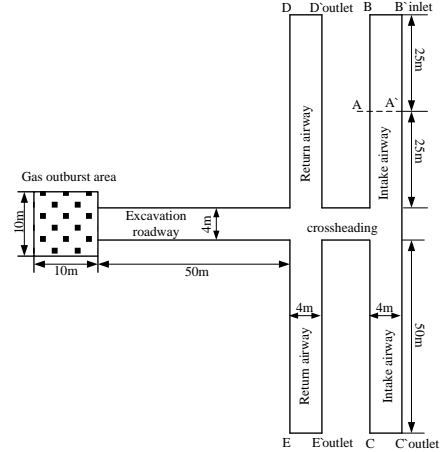


Figure 5: Geometric model numerical simulation of crossheading associated with excavation roadway.

(2) Initial conditions of numerical simulation

In the critical state of outburst, the initial condition of high-pressure gas within outburst region is supposed as:

$$p_1 = 10\text{atm}, u_1 = 0, T_1 = 300\text{K}, C_1 = 1$$

Where P_1 is gas pressure in the outburst region (pressure on the environment set to 1 am), atm; u_1 is velocity, m/s; T is temperature, K; C_1 is relative mass concentration of gas (assumed to be pure methane).

In the critical state of outburst, the initial condition of air within the roadway is supposed as:

$$p_0 = 0\text{atm}, u_0 = 0, T_0 = 300\text{K}, C_0 = 0$$

Where P_0 is gas pressure in the roadway, atm; u_0 is initial velocity within the roadway, m/s. When outburst occurs, due to the great pressure and speed in the roadway, pressure and velocity within the roadway can be approximated as zero; T_0 is temperature within the roadway, K; C_0 is relative mass concentration of gas within the roadway.

The initial condition of the section is supposed as:

$$p_{in} = 300\text{Pa}, C_{in} = 0$$

Where p_{in} is relative pressure of cross-section B – B'; C_{in} is mass concentration of gas in the cross-section B – B'.

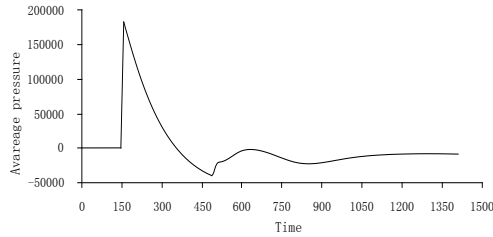
The initial condition of cross-section C – C', cross-section D – D' and cross-section E – E' is supposed as:

$$p_{out} = 0 \text{ Pa}$$

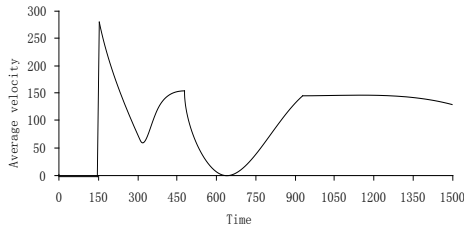
Where p_{out} is relative pressure of cross-section C – C', cross-section D – D' and cross-section E – E'.

(3) Analysis of results of numerical simulation

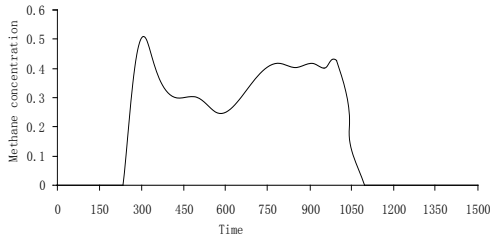
Figure 6 shows pressure, velocity, and gas concentration variation at the cross-section.



(a) Pressure variation at cross-section A-A`



(b) Velocity variation at cross-section A-A`

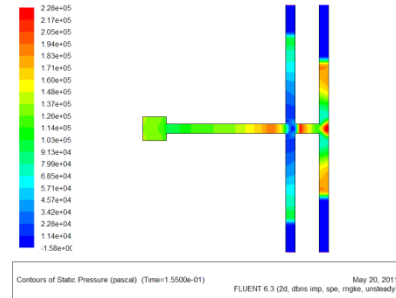


(c) Gas concentration variation at cross-section A-A`
Figure 6: Pressure, velocity, and gas concentration variation at cross-section A-A`.

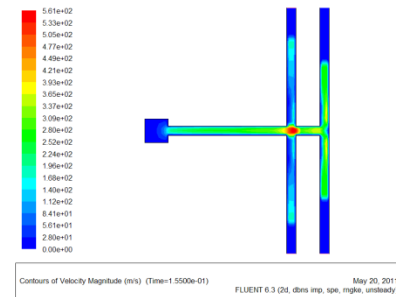
As shown in Figure 6:

- At 0.156 s, the maximum pressure of the cross-section is 185495.6 Pa, and the maximum speed is 282 m/s.
- At 0.23 s, gas flow reaches the observation point and the cross section of the gas concentration reaches a maximum of 0.499.
- According to the analysis in the 900 cross roadway, gas flow in the concave point begins to return.
- According to the vertical cross-roadway simulations conclusion, assuming that the adsorption of methane in coal and coal powder during shock waves and gas flows movement is no longer flooded, then due to the impact of negative pressure, airflow reflow speed will reach 150 m/s.

Pressure and velocity in the roadway are shown in Figure 7 when gas flow arrives at the observation point section, namely 0.156 s..



(a) Contour of pressure



(b) Velocity vector

Figure 7: Contours of pressure and velocity in the roadway at 0.156 s.

As can be seen from Figure 7, the influx of airflow into the intake airway and the pressure and speed of the airflow are greater than the pressure and speed of the return airway. Exporting data can be found from Fluent. The pressure of the return airway is between 0 Pa to 100000 Pa, while the pressure of the intake airway is between 100000 Pa to 200000 Pa. In the return airway flow, the speed of the shock front reaches 200 m/s. In the case of air door damage failure, the impact on the intake airway is greater than on the return airway, but with the throttle prior to the failure, the effects of the shock wave and air flow would obviously be smaller than the return airway in the model of a vertical cross roadway. Because the throttle is damaged, the space of the shock waves and air flows increases and the intake airway and return airway share the influence of shock waves and air flows.

Gas flow reaches the observation point in 0.23 s and leaves in 1.11 s. The concentration of gas within the roadway at 0.23 s, 0.32 s, 0.564 s, and 1.11 s changes as shown in Figure 8.

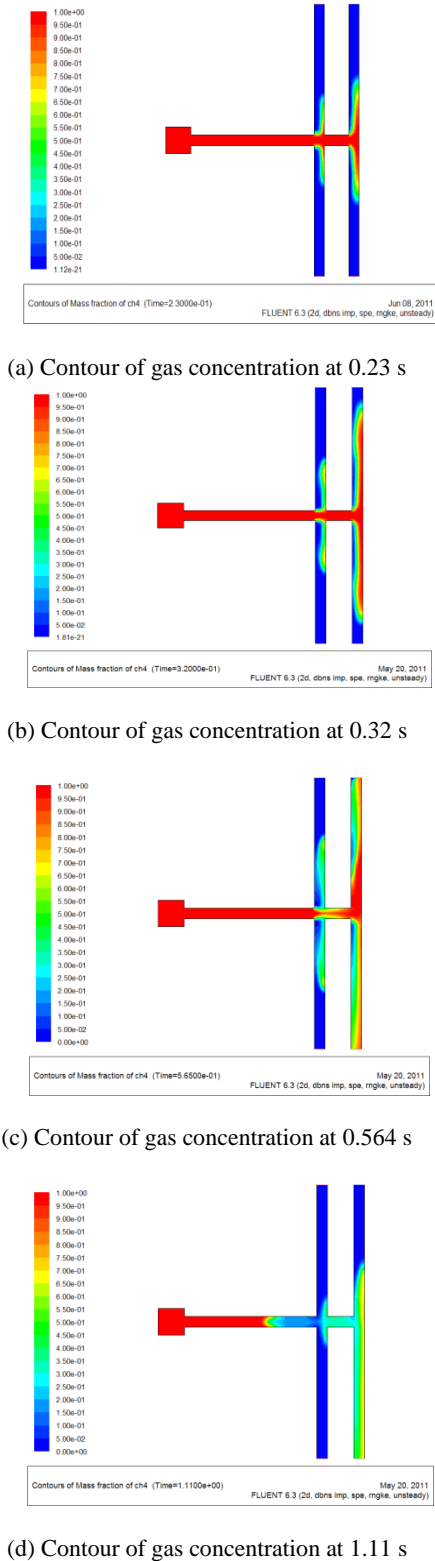


Figure 8: Contours of gas concentration in the roadway at 0.23 s, 0.32 s, 0.564 s and 1.11 s.

As can be seen from Figure 8, the majority of the gas flows into the intake airway. Only a small part of

the gas into the return airway gradually becomes diluted with air and the concentration reduced. Gas flow eventually flows from the high pressure end into the end with the lower pressure, and at this time the concentration in the intake airway is about 0.5. The gas enters the intake airway ultimately along the airflow direction into the mine ventilation system, and the whole mine ventilation systems is subject to the risk of gas explosion.

4.2 Numerical simulation of crossheading and excavation roadway no associative

In order to fix the damage caused by shock wave and gas flow on the intake airway, the most direct approach is to keep the crossheading with the excavation roadway, which may occur not in the same parallel position, and place the air door near the end. It is assumed that the crossheading has an excavation distance of 10 m.

(1) Geometric modelling

The geometric model is shown in Figure 9. The geometric dimensions of the model are described as: the outburst cavity has a side length of 10 m cube; the length of the excavation roadway is 50 m; the length of the intake airway and return airway are 104 m; crossheading is located 10 m above the excavation roadway and the distance to section B – B' and section C – C' are 40 m and 60 m respectively; roadway width is 4 m and height is 3 m; section B – B' is flow inlet side, section C – C', section D – D' and section E – E' for flow outlet. Select the section A – A' as the object of observation, monitoring the change of pressure, velocity and gas concentration.

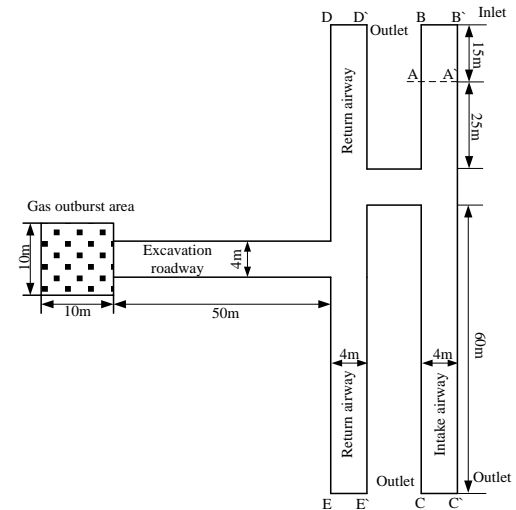


Figure 9: Geometric model numerical simulation of crossheading not associated with excavation roadway.

The initial conditions of the simulation are exactly the same as in the above example. In the critical state of outburst, the initial condition of high-pressure air gas within the outburst cavity is supposed as:

$$p_1 = 10\text{atm}, u_1 = 0, T_1 = 300\text{K}, C_1 = 1$$

Where P_1 is gas pressure in outburst region (pressure on the environment is set to 1 atm), atm; u_1 is velocity, m/s; T_1 is temperature, K; C_1 is relative mass concentration of gas (assuming for pure methane).

In the critical state of outburst, the initial condition of air within the roadway is supposed as:

$$p_0 = 0\text{atm}, u_0 = 0, T_0 = 300\text{K}, C_0 = 0$$

Where P_0 is gas pressure within the roadway, atm; u_0 is initial velocity within the roadway, m/s, when the outburst occurs, due to the great pressure and speed in the roadway, pressure and velocity within the roadway can be approximated as zero; T_0 is temperature within the roadway, K; C_0 is relative mass concentration of gas within the roadway.

The initial condition of section B – B' is supposed as:

$$p_{in} = 300\text{Pa}, C_{in} = 0$$

Where P_{in} is relative pressure of cross-section B – B' ; C_{in} is mass concentration of gas in the cross-section B – B' .

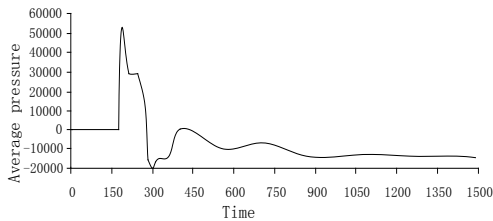
The initial condition of cross-section C – C' , cross-section D – D' and cross-section E – E' is supposed as:

$$p_{out} = 0\text{Pa}$$

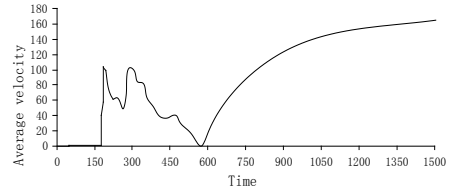
Where P_{out} is relative pressure of cross-section C – C' , cross-section D – D' and cross-section E – E' .

(2) Analysis of results of numerical simulation

Figure 10 shows pressure, velocity and gas concentration variation at cross-section A-A`.



(a) Pressure variation at cross-section A-A`



(b) Velocity variation at cross-section A-A`
Figure 10: Pressure and velocity variation at cross-section A-A`.

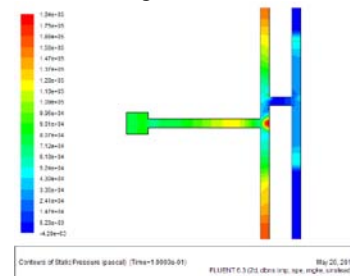
From Figure 10 and Fluent simulation data we can conclude:

- At 0.19 s, the maximum pressure of the cross-section is 53215.86 Pa, and the maximum speed is 106.7 m/s; compared with the conclusion of the previous section, the gas pressure and speed are greatly reduced, and outburst shock wave and gas flow have less effect on the ventilation system and roadway facilities.

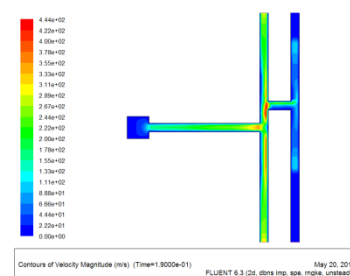
- From the speed change curve in the cross-section it can also be found that when the velocity reverses, namely at 0.57 s, the gas flow direction is reversed.

- After outburst, the counter current speed of the outburst shock wave and gas flow reaches 160 m/s, which is comparable to the previous section, indicating that crossheading change has little impact on the destruction of counter current air caused by shock wave and gas flow due to negative pressure.

Conditions of the pressure and speed within the roadway are shown as Figure 11:



(a) Contours of pressure

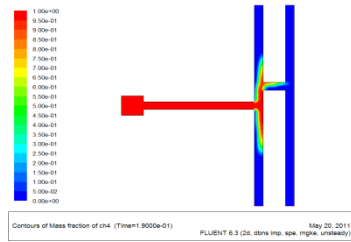


(b) Contours of velocity

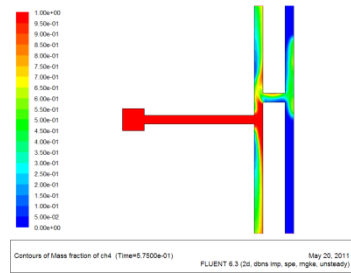
Figure 11: Contours of pressure and velocity at 0.19 s.

As can be seen from Figure 11, if crossheading with the excavation roadway is not on the same level, the pressure and velocity of the outburst shock wave and gas flow in the intake airway are far less than in the return airway, and are less affected by the outburst shock wave and gas flow.

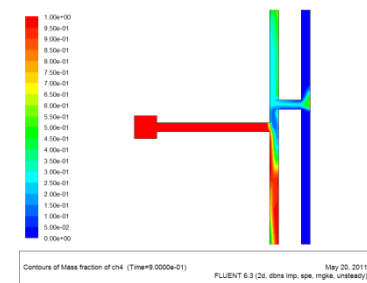
Figure 12 shows the concentration variation curves with time at the roadway.



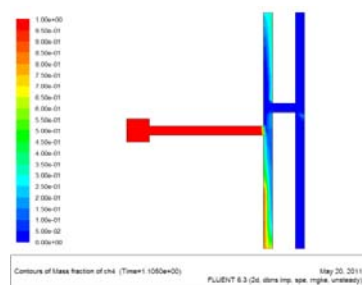
(a) Contours of gas concentration in the roadway at 0.19 s



(b) Contours of gas concentration in the roadway at 0.576 s



(c) Contours of gas concentration in the roadway at 0.9 s



(d) Contours of gas concentration in the roadway at 1.105 s
Figure 12: Contours of gas concentration in the roadway at different times.

Figure 12 shows the migration process of gas flow in the outburst. It can be found that most of the emission gas pours out from the cross-section. Due to reflux, gas within the intake airway also pours into the return airway. This shows that if the crossheading is separated from the roadway where outburst occurs and placed near the inlet of the intake airway, then the intake airway is much less affected by the gas flow.

5. CONCLUSIONS

The methane adverse current was divided into three phases: the entering air retrograde phase, the diffusion stage, and the stability of dilute phase. At the different stages, a qualitative analysis of influence scope of the methane adverse current, driving mode, and countercurrent process was performed.

After outburst prevention air door failure, the role of gas flow in mine air flow constantly spreads and can easily induce intake airway gas explosion. When the crossheading and the roadway where outburst occurs are at the same level, most of the gas flow produced by the outburst shock wave and gas flow spreads to the intake airway. When the crossheading and the roadway where outburst occurs at different levels, the gas flow is mainly exhausted from the return airway, and the influence of the intake airway is very small.

6. ACKNOWLEDGEMENTS

The authors are grateful to the State Key Research Development Program of China (2016YFC0801402, 2016YFC0600708), National Natural Science Foundation of China (51474219, 51304213).

7. REFERENCES

- Cheng W.Y.; Liu X.Y and Wang K.J.(2004). Study on regulation about shock-wave-front propagating for coal and gas outburst. Journal of China Coal Society, vol. 29, no. 5, pp. 57-60.
- Flores M. (1988). Coalbed methane: from hazard to resource. International Journal of Coal Geology, vol. 35, no. 3, pp. 3-26.
- Hu W.M.; Wei J.P and Liu M.J.(1998). Distribution of nonsteady methane in a controlled recirculation system. Journal of China Coal Society, no. 3, pp. 61-66.
- Jacek S.(2011). The influence of sorption processes on gas stresses leading to the coal and gas outburst in the laboratory conditions. Fuel, vol. 90, no. 3, pp. 1018-1023.

Javier T. and Susana T.(2012). Eliseo Alvarez. Application of outburst risk indices in the underground coal mines by sublevel caving. *International Journal of Rock Mechanics and Mining Sciences*, vol. 50, pp. 94-101.

Li S.(2012). Study on dynamic effect of mine ventilation network induced by outburst gas flow[D]. Beijing: China University of Mining & Technology.

María B. and González C.(2007). Control and prevention of gas outbursts in coal mines, Riosa–Olloniego coalfield, Spain. *International Journal of Coal Geology*, vol. 69, no. 4, pp. 253-266.

Otuonye F. and Sheng J.(1994).A numerical simulation of gas flow during coal/gas outbursts. *Geotechnical and Geological Engineering*, no. 1, pp. 15-34.

Wang E.Y.; Liang D. and Bo F.S(1996). Study on the mechanism and process of the methane movement in the tunnel. *Shanxi mining institute learning journal*, vol. 14, no. 2, pp. 24-29.

Wang K.;Li S. and Zhou A.T(2012). Unsteady ventilation network software of mine catastrophic(V1.0): China , 2012SR080591[P].

Wang K.; Zhou A.T. and Zhang J.F.(2012). Real-time numerical simulations and experimental research for the propagation characteristics of shock waves and gas flow during coal and gas outburst. *Safety Science*, vol. 50, pp. 835-841.

Wang K.; Zhou A.T. and Zhang J.F.(2011). Study of the Propagation Characteristics of Shock Wave and Gas Flow during Coal and Gas Outburst at the Roadway with a Right-angled Bend. *Journal of China University of Mining & Technology*, vol. 40, no. 6, pp. 865-869 .

Wang K.; Zhou A.T. and Zhang P. (2011). Study on the propagation law of shock wave resulting from coal and gas outburst. *Journal of Coal Science & Engineering*, vol. 17, no. 2, pp. 142-146.

Zhang J. and Sun Y.R.(2007). Study on propagation law of shock wave induced by coal and gas outburst. *Mining Safety & Environmental Protection*, vol. 34, no. 5, pp. 21-23.

Zhou A.T(2012). Research on propagation characteristics of shock wave and gas flow from gas outburst and induced catastrophic law of mine airflow. Beijing: China University of Mining & Technology.

Influence of Fundamental Internal Parameters to Low-Temperature Critical Temperature in Coal Self-Ignition Process

WANG Hai-yan^{a,b,c,*}, YAO Hai-fei^{a,b}, ZHENG Zhong-ya^{a,b}, XU Chang-fu^{a,b}, ZHANG Qun^{a,b}, ZHU Hong-qing^c

^a Mine Safety and Technology Branch of China Coal Research Institute Corporation Limited, Beijing, China, 100013;

^b National Key Lab of Coal Resource High Efficient Mining and Clean Utilization, Beijing, China, 100013;

^c School of Resource and Safety Engineering, China University of Mining and Technology (Beijing), Beijing, China, 100083;

ABSTRACT

The low-temperature oxidation process of coal self-ignition can be divided into two stages: the slow oxidation stage and the fast oxidation stage. To study the effect of internal factors on low-temperature critical temperature in the coal self-ignition process, eight fundamental internal parameters (volatile, ash, fixed carbon, C, N, S, H, and O) and three characterization parameters of low-temperature critical temperature in the coal self-ignition process (T_{JR} , T_{CO} , and T_{O_2}) were determined through theoretical analysis. Afterwards the self-heating characteristics in pure oxygen atmosphere in the 40 to 180° range and gas releasing atmosphere in the 30 to 180° range for seven coal samples were tested. Based on this, the values of fundamental internal parameters and characterization parameters for seven coal samples were obtained. The relationship between fundamental internal parameters and that of characterization parameters were compared. On grey relational analysis, five important influence parameters are filtered to make the mathematical formula fit with the characterization parameters. The results show that characterization parameters reflect critical temperature from different aspects including temperature rising, CO releasing, and oxygen consumption. These vary for the same coal sample, but are with the same tropism and confirm each other. Critical temperatures are negatively correlated with the contents of volatiles, H and O, have no determined relationship with the content of S, and have small correlation with other parameters.

Keywords: coal self-ignition; critical temperature; fundamental internal parameter; temperature-programmed experiment; heat oxidation experiment; grey correlation; numerical fitting.

1. INSTRUCTIONS

The occurrence of coal self-ignition is the result of the interaction between external and internal factors, and among them, the internal factors are prerequisites (Liu and Zhou, 2012; Adamus et al., 2011). Low-temperature critical temperature is the intermediate link between the slow oxidation stage and fast oxidation stage during the coal self-ignition process. It is of practical significance for doing coal mine fire prevention and control that we grasp the critical temperature of coal self-ignition and make the temperature of coal below the critical temperature. In the past, we primarily focused on monitoring the coal temperature of danger zones through direct temperature measurement or gas collection and testing in terms of coal mine fire prevention (Xie et al., 2011). However, there is little research and application of nonlinear characteristics of spontaneous fires. Currently, some research is being done on the determination of critical temperature of coal self-ignition mainly through fixed stages division, qualitative analysis, and the numerical fitting method (Sahay et al., 2007; Zhong et al., 2010;

TAN et al., 2013; Beamish and Darren et al., 2005; Ren et al., 1999; ZHU et al., 2014). These methods mainly analyze the critical temperature of coal self-ignition in one aspect. Researching the critical temperature from different aspects and contacting the nature and conditions of coal are necessary in order to increase the practical applications and reference significance.

The occurrence and development of the coal self-ignition process can be manifested by different forms, such as changes in temperature, gas concentration, and so on. In this paper, a relationship between coal temperature and gas concentration is established by experiments, the critical temperature of coal self-ignition is determined by different parameters, and the influence of some fundamental parameters of coal, such as industrial components and element composition, on critical temperature are studied.

2. THEORETICAL ANALYSIS

Coal self-ignition is a non-linear evolution process, which is not carried out in accordance with a

certain rate. Research shows that there is critical temperature during this process where the oxidation of coal will accelerate beyond this temperature. However, the critical temperature of coal is limited within a fixed range with no clear distinction between the different kinds of coal. In recent years, scholars have studied in depth the differences of coal self-ignition process for different types of coal, and come to realize the importance of distinguishing the differences in critical temperature. According to the previous studies, the influence of internal and external factors on the occurrence and development of coal self-ignition is very complicated, and the influence of external factors is difficult to be experimentally tested. Therefore, it is of guiding significance to actual work to study the influence of internal factors on critical temperature of coal self-ignition. Therefore, this paper mainly studies the impact of fundamental internal parameters on low-temperature critical temperature of coal self-ignition.

2.1 Fundamental internal factors

The study of coal self-ignition mechanisms shows that the type and quantity of functional groups plays a key role in the coal self-ignition process (Wang et al., 2012; Satoru et al., 2000; Olayinka, 1992). However, it is difficult to explain the difference between functional groups of different types of coal quantitatively, and not operable in engineering practice. Various functional groups in coal are constituted by the respective elements, industrial ingredient is a side reaction of coal structure and composition of functional groups, element composition and industrial components are the basic parameters of coal, and can easily be tested. Therefore, industrial components (volatile, ash, and fixed carbon) and element composition (C, H, O, N, and S) are selected as influence factors, and the influence of these factors on low-temperature critical temperature in the coal self-ignition process is analyzed. It should be noted that the moisture content of coal is not selected as one influence factor in this paper, because coal samples were dried prior to the experiment.

2.2 Characterization parameters of low-temperature critical temperature

The coal self-ignition process shows varying characteristics, especially at the critical temperature. Changes of coal temperature and gas concentration have a large effect on the coal self-ignition process, so this paper uses the following parameters as characterization parameters for low-temperature critical temperature.

1) Mutation temperature of heating rate in the adiabatic oxidation process (T_{JR}), which reflects the

variation characteristics of coal heating rate under adiabatic conditions.

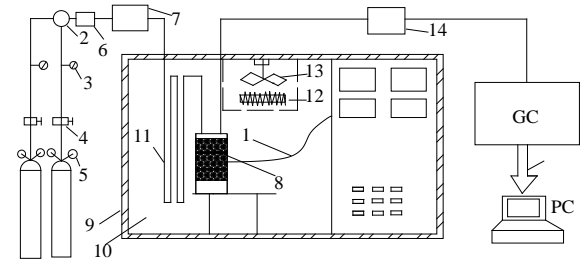
2) Mutation temperature of CO concentration in the programmed temperature rising experiment (T_{CO}). CO is a sort of important indicator gases during coal self-ignition process, the concentration of CO can be used to characterize the reaction rate, so the mutation temperature of CO concentration can be used to characterize the critical temperature.

3) Mutation temperature of oxygen consumption rate in the programmed temperature rising experiment (T_{O_2}). Oxygen consumption rate is a direct exhibit of the reaction rate, so oxygen consumption rate can be used to characterize the critical temperature.

To study the influence of fundamental internal parameters to critical temperature of coal self-ignition, this paper will study the relationship between the characterization parameters and the internal parameters (T_{JR} , T_{CO} and T_{O_2}).

3. EXPERIMENTAL PART

3.1 Experimental device



1-Temperature sensor 2-Three-way valve 3-Pressure gauge 4-Regulator valve 5-Pressure reducing valve 6-Dust collector 7-Mixing chamber for inlet gas 8-Reaction vessel 9-Thermal insulation layer 10- Temperature control oven 11-Preheat copper pipe 12-Heating pipe 13-Fan 14-Mixing chamber for outlet gas

Figure 1: Structure schematic diagram of the device.

This device consists of four parts: the gas distribution part, reaction vessel, temperature control oven, and control part. Figure 1 shows the structures schematic diagram. The design of this device used the adiabatic oven of the University of Queensland as a reference (Beamish et al., 2000). The temperature control oven and its door are double skinned, and there is glasswool in it for insulation. A 2.3 kW heating pipe is used for heating, and there is a fan to force gas flow to ensure temperature uniformity inside the oven. There is a 16 m length of copper pipe in the oven to ensure the temperature of gas is the same as the oven before entering the reaction vessel. Taking the vacuum flask as the adiabatic reaction vessel can effectively reduce conduction and radiation heat transfer. The temperature programmed reaction vessel is made of steel to ensure good thermal conductivity, and type K thermocouples are used for monitoring temperature. The gas used in the

experiment is provided by high-pressure gas cylinders, and the gas is control by mass flow meter after flowing through the pressure valve. The control part is a PC, and the device is controlled by King View software. The flow of gas and temperature of the oven can be regulated and the date can be recorded by operating this software.

3.2 Experimental procedure

1) Preparation of coal samples

The coal samples used in this study were obtained from coal mines of different regions in China. All the coal samples selected for testing were obtained directly from bore holes, and then put into a plastic bag. After this, the coal samples were put into a low-temperature closed container and transported to the laboratory, then placed into a refrigerator until the start of the experiment. Before testing, the coal samples were divided into two parts (nearly the same): one part was returned to the refrigerator after rewrapping. The other part was sieved by jaw crusher and closed grinding machine to select expected particle size for immediate testing.

2) Experimental procedure

(1) Temperature programmed experiment

A 200 g coal sample was crushed into particles with mixed diameters of 1.25-1.6 mm, 1.6-2 mm, 2-3.5 mm, 3.5-5 mm and 5-7 mm, each accounting for 20%. The coal samples were put into the reaction vessel, dried for 9 h in nitrogen environment (120 ml/min) at 105°. After cooling down, nitrogen-oxygen mixed gas (the concentration of oxygen is 21%) was transported into the programmable isothermal oven with a constant flow rate of 60 ml/min. Emission gases were collected once every 15°, and the oxygen concentration was analyzed with a gas chromatograph; the initial temperature and termination temperature were 30° and 180°. In the heating process, temperature rise inside the oven was 15° with a rate of 1°/min, and the temperature kept constant for 10 min, and then increased 15° with a rate of 1°/min again. Similar procedures were carried on until 180°.

(2) Adiabatic oxidation experiment

The granularity of coal samples are <212 μm. All coal samples were dried at 105° for 15 hours under the protection of nitrogen to ensure that the coal samples were dried completely and not oxidized. Then the temperature was cooled down to 40° and allowed to equilibrate. The drying coal sample was moved into the adiabatic reaction vessel quickly and stabilized at 40° under nitrogen atmosphere, then switched to “track temperature mode”. The nitrogen input was cut off and open oxygen valve with a constant flow rate of 60 ml/min. The change in coal temperature was recorded by the control part for later

analysis. When the coal temperature reached 180°, heating and the oxygen flow were automatically stopped. The coal sample was removed from the adiabatic reaction vessel after the sample and oven were cooled down to normal atmospheric temperature. The vessel was cleaned and the adiabatic device was checked.

3.3 Experimental results

Based on the experimental method above, the concentration-temperature curve of O₂ and CO of temperature programmed experiment and temperature-time curve of adiabatic oxidation experiment for seven coal samples can be obtained, which are shown in Figures 2-4.

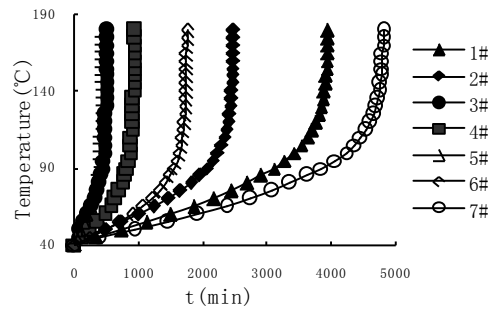


Figure 2: The coal temperature-time curve in isolated heat oxidation experiments.

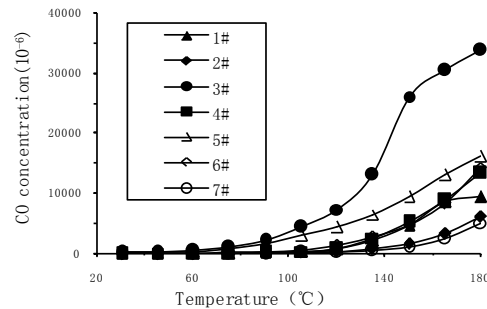


Figure 3: The change of CO concentration with temperature improving in temperature-programmed experiments.

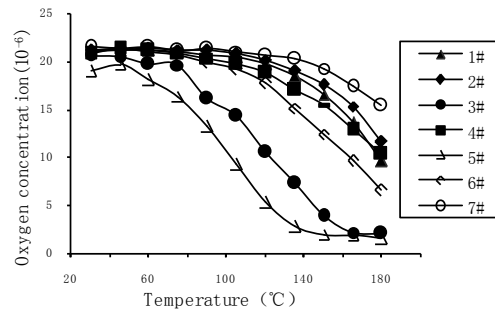


Figure 4: The change of O₂ concentration with temperature improving in temperature-programmed experiments.

3.4 Oxygen consumption rate analysis

The height of the reaction vessel is 0.25 m (coal sample height is 0.221 m, L), Cross-sectional area (S) is 0.007088 m². The temperature of the reaction vessel is considered to be changed evenly for low heating rate and light coal sample weight. It is assumed that the gas used is ideal gas. Depending on the coal oxidation reaction equation (Srinivasan et al., 1996; Copard et al., 2004), oxygen consumption rate equation of physical coal per unit length at a certain position (x) is given by Formula (1):

$$-v_g dC_{O_2}^x = (1-n)R_{O_2}^x(T)Sdx \quad (1)$$

where n is porosity, %; S is cross-sectional area of the reaction vessel, m²; $R_{O_2}^x(T)$ is oxygen consumption rate at position x, mol/(m³·s); v_g is gas flow rate, m³/s; $C_{O_2}^x$ is oxygen concentration at position x, mol/m³; $dC_{O_2}^x$ is variation of the oxygen concentration, mol/m³.

According to chemical kinetics and equilibrium theory (Kudynska and Buckmaster, 1996; Wang et al., 2003; Baris et al., 2012), the average oxygen consumption rate can be expressed as Formula (2).

$$R_{O_2}(T) = R_{O_2}^x T \frac{C_i}{C_{O_2}^x} \quad (2)$$

where $R_{O_2}(T)$ is the average oxygen consumption rate, mol/(m³·s); C_i is oxygen concentration of inlet gas, mol/m³. Substituting equation (2) into equation (1), equation (3) reads:

$$R_{O_2}(T) = \frac{v_g C_i}{(1-n)SL} \ln \left(\frac{C_i}{C_{O_2}^L} \right) \quad (3)$$

Depending on equation (3), the values of RO2 for seven coal samples are given in Figure 5.

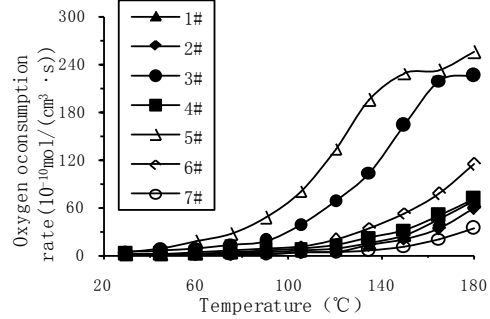


Figure 5: The change of oxygen consumption rate with temperature improving in temperature-programed experiments.

4. PARAMETER CALCULATION AND ANALYSIS

4.1 Internal parameters

Element contents (N, S, H, O, and C) and industrial components (ash, volatile, and fixed carbon) of seven coal samples are tested by vario MACRO CHNS (with Oxygen kit) Elemental analyzer and GF-A6 Automatic Industrial Analyzer. The results are shown in Table 1.

Table 1: The result of industrial analysis experiments and element analysis experiments.

	Volatile property	Ash	Fixed carbon	N	S	H	O	C
	wt% ar	wt% ar	wt% ar	wt% daf	wt% daf	wt% daf	wt% daf	wt% daf
1#	21.42	19.86	57.52	1.185	1.179	3.761	6.332	69.99
2#	25.63	22.72	50.32	1.206	1.01	3.818	8.396	65.29
3#	33.18	8.84	52.57	1.309	2.495	4.814	15.11	69.16
4#	39.15	9.55	46.95	1.239	0.582	4.111	15.92	70.12
5#	30.23	11.34	52.68	1.148	0.929	4.234	14.59	84.98
6#	30.88	3.7	61.45	1.281	0.852	3.834	9.614	75.72
7#	12.95	8.07	77.72	1.332	0.634	3.731	3.321	69.81

3.2 Characterization parameters of critical temperature

According to Arrhenius equation (Bews et al., 2001; Ronald et al., 1989; Anna et al., 2011), reaction rate can be express as:

$$k = A \exp\left(-\frac{E}{RT}\right) \quad (4)$$

where k is Oxidation reaction rate of coal; E is apparent activation energy, KJ mol⁻¹; A is pre-exponential factor, s⁻¹; R is universal gas constant,

0.008314 KJ/(K·mol); T is thermodynamic temperature, K.

Further analysis of the formula (4):

$$\ln k = \ln A - \frac{E}{RT} \quad (5)$$

Replace the Oxidation reaction rate k with adiabatic heating rate, CO concentration and oxygen consumption rate (denoted as k₁, k₂, and k₃), the relationship between lnk and (-1/T) can be obtained. Using linear analysis, the critical temperature can be

obtained by analyzing the changes of slope, which is shown in Figures 6-8.

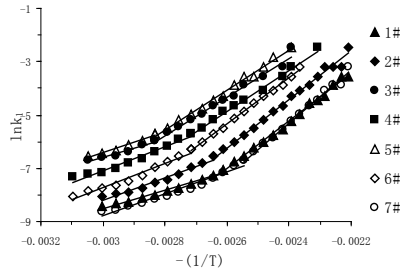


Figure 6: The relationship between $\ln k_1$ and $(-1/T)$.

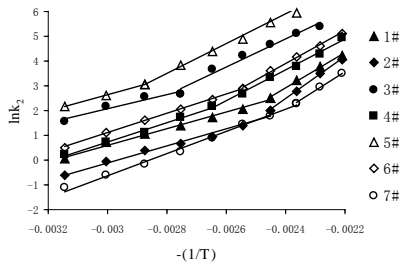


Figure 7: The relationship between $\ln k_2$ and $(-1/T)$.

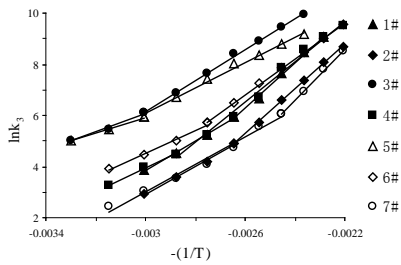


Figure 8: The relationship between $\ln k_3$ and $(-1/T)$.

According to the analysis results above, critical temperatures for seven coal samples are shown in Table 2.

Table 2: Characterization parameters of coal spontaneous combustion critical temperature.

Item	T_{JR} (°C)	T_{CO} (°C)	T_{O2} (°C)
1#	110	105	135
2#	105	105	135
3#	80	60	90
4#	95	75	105
5#	80	60	75
6#	95	90	120
7#	120	135	150

5. INFLUENCE OF INTERNAL PARAMETERS TO CRITICAL TEMPERATURE

5.1 Relationship between internal parameters

The relationship between the eight parameters is shown in Figure 9. Based on this, it can be seen that the relationship between the various parameters is complicated; however, it still can be clearly observed that the trend of O and volatile property is similar, and the trend of fixed carbon is contrary to them.

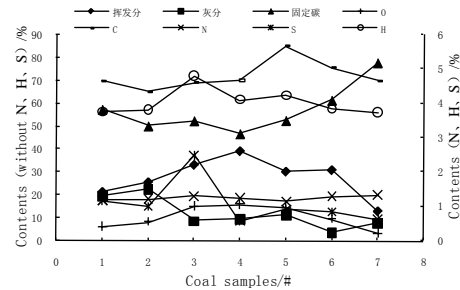


Figure 9: Fundamental internal parameters and the relationship.

5.2 Relationship between characterization parameters

The relationship between the three characterization parameters is shown in Figure 10.

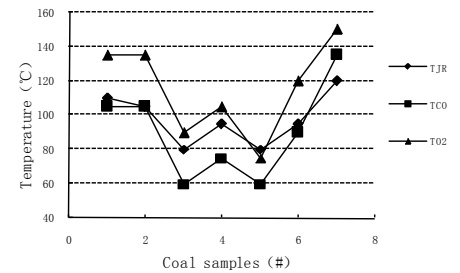


Figure 10: Characterization parameters of coal spontaneous combustion critical temperature.

According to Figure 10, the changing trends of the three parameters for different coal samples are basically the same. In accordance with the ascending parameter values, coal numeral order is 5#, 3#, 4#, 6#, 2#, 1#, and 7#. The 3 parameters for the same coal sample are different, for example, T_{JR} , T_{CO} and T_{O2} for 1# coal sample are respectively 110, 105 and 135, which shows that the changing regulations for the three characteristics are the same, but there is little differences in temperature. Overall, values of the three parameters for a certain coal sample are very close and are valid parameters.

5.3 Gray relational grade analysis

The relationship between internal parameters and characterization parameters of critical temperature is complicated, and the influence is hard to obtain by direct observation. Based on this feature, this paper introduces the gray relational grade analysis method to analysis the relevance of eight internal parameters

and three characterization parameters. The calculation is according to the literature (LIU et al., 2004), and the calculation methods and formulas are not given in this paper. Based on data from Table 1 and Table 2, the calculation result is given in Table 3.

Table 3: Gray relational grade between characterization parameters and fundamental internal parameter.

	T_{JR}	T_{CO}	T_{O_2}	Mean value
Volatile property	0.68	0.69	0.65	0.67
Ash	0.55	0.70	0.64	0.63
Fixed carbon	0.67	0.56	0.54	0.58
N	0.56	0.62	0.56	0.58
S	0.70	0.58	0.54	0.61
H	0.59	0.62	0.59	0.60
O	0.65	0.66	0.62	0.64
C	0.54	0.54	0.52	0.53

According to Table 3, the three highest relevance parameters are contents of volatile property, ash, and O, the lowest ones are contents of fixed carbon, C, and N. In decreasing order: volatile property, O, ash, S, H, fixed carbon, C, and N, which reflects the influence level of parameters.

5.4 Numerical fitting analysis

To further analyze the influence of internal parameters to characterization parameters, this paper makes a mathematical formula fitting to those two sorts of parameters. The fitting expression is labelled formula (10). As in the analysis above, the contents of fixed carbon, C, and N are the lowest relevance parameters. They do not have an obvious influence on the characterization parameters, and therefore we only consider the three characterization parameters and five internal parameters (volatile property, O, ash, S, and H).

$$y = p_0(x_1)^{p_1}(x_2)^{p_2}(x_3)^{p_3}(x_4)^{p_4}(x_5)^{p_5} \quad (10)$$

where y is 3 characterization parameters T_{JR} , T_{CO} and T_{O_2} , x_1-x_5 are 5 internal parameters, volatile property, O, ash, S and H, p_0-p_5 are fit coefficients.

Using the data in Tables 1 and 2, the fitting result is shown in Table 4.

Table 4: Numerical fitting results.

	p_0	p_1	p_2	p_3	p_4	p_5
T_{JR}	430.13	-0.14	-0.004	0.17	-0.50	-0.14
T_{CO}	376.39	-0.23	0.05	-0.07	-0.17	-0.27
T_{O_2}	2317.83	-0.11	-0.04	0.28	-1.54	-0.19

According to Table 4, p_1 , p_4 and p_5 for the numerical fitting of three characterization parameters are negative, which shows that the critical temperature and contents of volatile parameter, O, and H are negatively correlated; the absolute values of p_2 are very small, which shows that critical temperature has very little correlation with the content of ash; p_2 and p_3 are positive or negative, which shows that the influence of contents of ash and S is not certain.

6. CONCLUSIONS

To study the effect of internal factors on low-temperature critical temperature in coal self-ignition process, eight fundamental internal parameters (volatile, ash, fixed carbon, C, N, S, H, and O) and three characterization parameters of low-temperature critical temperature in the coal self-ignition process (T_{JR} , T_{CO} and T_{O_2}) are selected, and the values for each are determined via experiment and calculation. Then, the relationship between fundamental internal parameters and that of characterization parameters are compared. Through grey relational analysis, five important influence parameters are filtered to make a mathematical formula fitting with the characterization parameters. The conclusions are as follows:

(1) Based on the theoretical analysis of the occurrence and development of coal self-ignition, T_{JR} , T_{CO} , and T_{O_2} are selected as characterization parameters of critical temperature, which characterize critical conditions for three aspects: heat rising, CO generation, and O_2 consumption.

(2) Depending on the Arrhenius equation, the values of characterization parameters for seven coal samples were obtained by the segmented fitting method, which shows that the changing regulations for the three characteristics are the same, but there is little difference on temperature; values for the three parameters for a certain coal sample are very close, and are valid parameters.

(3) By analyzing the relevance of characterization parameters and fundamental internal parameters, it is found that the critical temperature and contents of volatile parameter, O, and H are negatively correlated; critical temperature has very little correlation to the content of ash; the influence of contents of ash and S are not certain, and the influence of contents of fixed carbon, C, and N to critical temperature is the least significant.

(4) The accuracy of parameters and the number of coal samples need to be improved to get more accurate results in future research.

7. ACKNOWLEDGEMENT

The authors gratefully acknowledge the financial support provided by National Nature Science Foundation of China (U1261214) and Development Fund Project of China Coal Research Institute (2014JC06).

8. REFERENCES

- Adamus, A., Šancer, J., Guřanov, P., and Zubiřek, V. (2011). An investigation of the factors associated with interpretation of mine atmosphere for spontaneous combustion in coal mines. *Fuel Processing Technology*, Volume 92, No.3, pp. 663-670.
- Baris, K., Kizgut, S., and Didari, V. (2012). Low-temperature oxidation of some Turkish coals. *Fuel*, Volume 93, pp. 423-432.
- Beamish, B. B., Barakat, M. A., and St George, J. D. (2000). Adiabatic testing procedures for determining the self-heating propensity of coal and sample ageing effects. *Thermochimica Acta*, Volume 362, No.1, pp.79-87.
- Beamish, B. B., and Blazak, D. G. (2005). Relationship between ash content and R 70 self-heating rate of Callide Coal. *International Journal of Coal Geology*, Volume 64, No.1, pp. 126-132.
- Bews, I. M., Hayhurst, A. N., Richardson, S. M., and Taylor, S. G. (2001). The order, Arrhenius parameters, and mechanism of the reaction between gaseous oxygen and solid carbon. *Combustion and Flame*, Volume 124, No.1, pp. 231-245.
- Copard, Y., Disnar, J. R., Becq-Giraudon, J. F., and Laggoun-Defarge, F. (2004). Erroneous coal maturity assessment caused by low temperature oxidation. *International journal of coal geology*, Volume 58, No.3, pp. 171-180.
- Krishnaswamy, S., Bhat, S., Gunn, R. D., and Agarwal, P. K. (1996). Low-temperature oxidation of coal. 1. A single-particle reaction-diffusion model. *Fuel*, Volume 75, No.3, pp. 333-343.
- Kudynska, J., and Buckmaster, H. A. (1996). Low-temperature oxidation kinetics of high-volatile bituminous coal studied by dynamic in situ 9 GHz cwpr spectroscopy. *Fuel*, Volume 75, No.7, pp. 872-878.
- Liu Lang and Zhou Fu-bao. (2012). A comprehensive hazard evaluation system for spontaneous combustion of coal in underground mining. *International Journal of Coal Geology*, Volume 82, No. 1-2, pp. 27-36.
- LIU Si-feng. (2004). *Grey System Theory and Its Applications*. Science Press, Beijing, 224p.
- Martin, R. R., MacPhee, J. A., Workinton, M., and Lindsay, E. (1989). Measurement of the activation energy of the low temperature oxidation of coal using secondary ion mass spectrometry. *Fuel*, Volume 68, No.8, pp.1077-1079.
- Murata, S., Hosokawa, M., Kidena, K., and Nomura, M. (2000). Analysis of oxygen-functional groups in brown coals. *Fuel processing technology*, Volume 67, No.3, pp. 231-243.
- Ogunsola, O. I. (1992). Distribution of oxygen-containing functional groups in some Nigerian coals. *Fuel*, Volume 71, No.7, pp. 775-777.
- Raeva, A. A., Pierce, D. T., Seames, W. S., and Kozliak, E. I. (2011). A method for measuring the kinetics of organically associated inorganic contaminant vaporization during coal combustion. *Fuel Processing Technology*, Volume 92 No.7, pp. 1333-1339.
- Ren, T. X., Edwards, J. S., and Clarke, D. (1999). Adiabatic oxidation study on the propensity of pulverised coals to spontaneous combustion. *Fuel*, Volume 78, No.14, pp. 1611-1620.
- Sahay, N., Varma, N. K., and Ahmad, I. (2007). Critical temperature-an approach to define proneness of coal towards spontaneous heating. *Journal of Mines, Metals & Fuels*, Volume 55, No.10-11, pp. 510-516.
- TAN, B., ZHU, G. Q., WANG, H. Y., HAO, Y. Z., and GU, G. W. (2013). Prediction model of coal spontaneous combustion critical point and the characteristics of adiabatic oxidation phase. *Journal of China Coal Society*, Volume 38, No.1, pp. 38-43.
- Wang, H., Dlugogorski, B. Z., and Kennedy, E. M. (2003). Analysis of the mechanism of the low-temperature oxidation of coal. *Combustion and Flame*, Volume 134, No.1, pp. 107-117.
- Wang, L. Y., Xu, Y. L., Jiang, S. G., Yu, M. G., Chu, T. X., Zhang, W. Q., ... and Kou, L. W. (2012). Imidazolium based ionic liquids affecting functional groups and oxidation properties of bituminous coal. *Safety science*, Volume 50, No.7, pp. 1528-1534.
- Xie, J., Xue, S., Cheng, W., and Wang, G. (2011). Early detection of spontaneous combustion of coal in underground coal mines with development of an ethylene enriching system. *International Journal of Coal Geology*, Volume 85, No.1, pp. 123-127.
- Zhong, X. X., Wang, D. M., and Yin, X. D. (2010). Test method of critical temperature of coal spontaneous combustion based on the temperature programmed experiment. *Journal of China Coal Society*, Volume 35, No.8, pp. 128-131.
- ZHU, G. Q., WANG, H. Y., SONG, Z. Y., and HE, C. N. (2014). The relationship between oxidation kinetics characteristic parameters of coal adiabatic progress and metamorphic degree. *Journal of China Coal Society*, Volume 39, No.3, pp. 498-503.

Experimental study of negative pressure gas drainage influences on coal moisture content

Shaojie Chen^{a,b,*}, Longzhe Jin^b, Xianglong Liu^c

^a School of Safety Engineering, North China Institute of Science and Technology, Beijing, China, 101601

^b School of Civil and Environment Engineering, University of Science and Technology, Beijing, China, 100083

^c Safety Supervision Department, Shanxi Lu'an(mining) Group Co.Ltd, Changzhi, China, 046204

ABSTRACT

In light of water loss phenomena of coal by negative pressure gas extraction, the relationship between time and coal moisture content, and the rate of water loss in special conditions of temperature and negative pressure were studied in the laboratory, and the water loss mechanism of coal was analyzed. Results show that the moisture content of three coals decreased as the negative pressure reaction time increased. In the initial phase, the moisture content of coals descends quickly. Afterwards, the decrease trend slows, and finally the moisture content of coals trends to a constant value. The maximum saturated water loss rate reaches 82.19% and the water loss of coal in experimental conditions is larger. The negative pressure by gas extraction reduces the coal pore gas pressure, and the boiling point and the saturated vapour pressure of water decrease; the free water vapourization (no boiling) rate of coals increases. Adsorption water and liquid water can change from a liquid to a gas, and be extracted by negative pressure. This action reduces the coal moisture content. The moisture of coal has great effects on dust quantity by mining. A long and continuous gas extraction will result in water loss of coal, and it is of great disservice to the prevention of coal mine dust, so it is necessary to perform water injection into coal seams or to take enhanced dust prevention measures after gas extraction.

Keywords: dust; gas extraction; negative pressure; coal moisture content; water loss mechanism

1. INTRODUCTION

At present, China's coal mine safety production situation is improving significantly. However, coal mine dust prevention is still a prominent problem, and it leads directly to high pneumoconiosis cases for operators (Fang H. et al., 2011; Tong R. et al., 2013). Occupational safety and occupational health should be equally important for workers. Great importance should be attached to gas disasters as well as dust control. Aimed at low permeability coal seams, closed drilling and long time gas drainage is the main measure to control disasters, especially in high gas mines and coal and gas outburst mines. Gas drainage can lead to the loss of coal moisture content, drying out the coal seam (Bao Q. et al., 2013). The amount of dust produced in mining is directly related to the moisture content of coal. The smaller the coal moisture content, the more dust generation. Some scholars have studied the water vapourization of coal in natural environments (Jin L. et al., 2000; Cong X. et al., 2010). In order to quantitatively study the effects and mechanism of negative pressure drainage on coal moisture content, the relationship between time and coal moisture content, and the rate of water loss in special conditions of temperature and negative pressure, three coal samples were studied in the

laboratory, and the water loss mechanism of coal was analyzed.

2. EXPERIMENTS

2.1 Coal samples

Three representative coal samples were taken as the study and experiment object, and the samples were collected from 6-2# coal seam of Kaida mine, 15# coal seam of Jiarui mine, and 8# coal seam of Xinjing mine. The three coal samples were numbered 1#, 2#, and 3#, respectively. The coal samples were not influenced by gas drainage, and the sealed coal samples were taken to the laboratory. The proximate analysis and rank of coal samples are shown in table 1.

Table 1: Proximate analysis and rank of coal samples.

Sample ID	Moisture content (%)	Volatile component (%)	Ash component (%)	Coal rank
1#	14.16	19.66	22.47	Nonstick coal
2#	1.90	14.05	9.83	Meager coal
3#	0.98	8.81	12.76	Anthracite coal

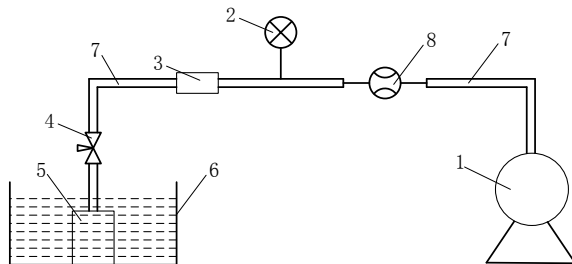
The 300 g coal samples with the particle sizes of 0.1-0.18 mm of three coals (1#, 2#, and 3#) were prepared by crushing and screening by proximate analysis standard. The prepared coal samples were enclosed in Ziploc bags to prevent water vapourization in air. The samples are shown in Figure 1.



Figure 1: Experimental coal samples.

2.2 Experimental device and process

Place the 40 g coal samples into a sealed tank and fix a constant temperature water bath at 30°C. Connect the sealed coal samples tank to a vacuum pump, and then turn on the vacuum pump. The sealed tank was opened after 0.5 h, and the vacuum coal samples were rapidly enclosed in the Ziploc bag and numbered on the outside. According to the above procedure, the coal samples were separately vacuumed at 1 h, 2 h, 3 h, 4 h, and 5 h, and the moisture content of six coal samples of different negative pressure action times (including the original coal sample) were acquired. The different moisture content of coal samples was tested by TGA-2000 automatic industrial analyzer, and the date was analyzed. The three coal samples were tested based on the above experimental method. The experimental apparatus is sketched in Figure 2.



1- vacuum pump; 2-vacuum gauge; 3-desiccator;
4-needle valve; 5- sealed tank; 6-waterbath;
7-sebific duct; 8-flowmeter

Figure 2: Diagram of Experimental apparatus.

The water loss rate of coals at different time under constant temperature and negative pressure were calculated by Eq. (1).

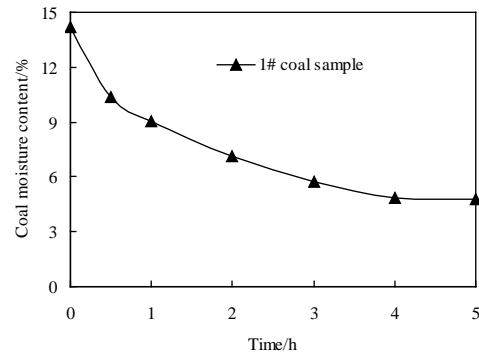
$$\delta = (W_0 - W_t) / W_0 \quad (1)$$

Where δ is the water loss rate of coal sample, %, W_0 is the original moisture content, %, W_t is the moisture content at certain time after negative pressure, %.

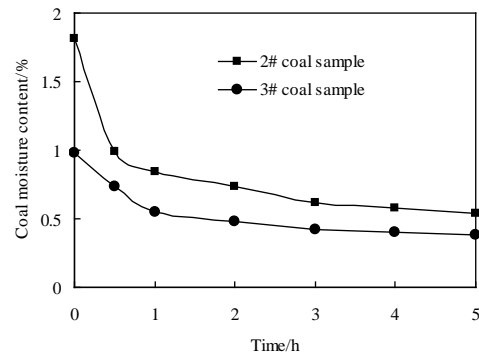
3. RESULTS AND ANALYSIS

3.1 Relationships between moisture content and time

Under particular a experimental temperature and negative pressure, the relationship between moisture content of the three coal samples and time are shown in Figure 3.



(a) 1# coal sample



(a) 2# and 3# coal samples

Figure 3: Relationships between moisture content and time.

From Figure 3, the moisture content of the three coal samples decreases as the negative pressure action time increases. In the initial phase, the moisture content of the coal samples descends quickly. Afterwards, the decrease trend slows and finally the moisture content of coal samples tends to a constant value. For the low metamorphic 3# coal sample, the original moisture content is 14.16%, and the moisture content changes to 4.77% after 5 h negative pressure action time. The water loss

phenomena of coals by negative pressure were serious.

3.2 Relationships between water loss rate and time

The relationships between the water loss rate of the three coal samples and time are shown in Figure 4.

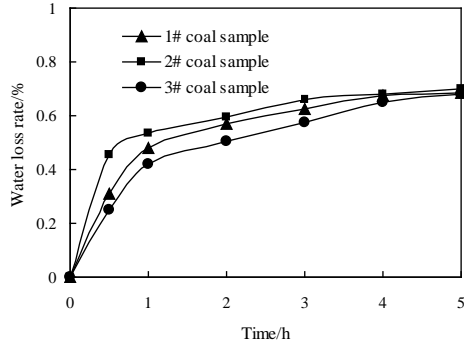


Figure 4: Experimental coal samples.

From Figure 4, the water loss rate of the three coal samples enlarges as the negative pressure action time increases. The water loss rates of the three coal samples are all more than 70%. The relationships between water loss rate and time are analogous to the Langmuir equation, and it has a saturated water loss rate that can be expressed by Eq. (2).

$$\delta = abt / (1 + bt) \tag{2}$$

Where δ is the water loss rate of coal sample, %, a is the saturated water loss rate, %, b is the water loss constant, h^{-1} , t is the negative pressure action time, h.

The water loss rate curve equations of three coal samples are shown in Table 2. Under the specific conditions of the experiment, the maximum saturated water loss rate reached 82.19%. When the water loss rate reached saturation, the coal moisture content no longer reduced under increasing negative pressure action time. This was primarily connected to the existing water form, where the free water in coal was easily lost but the combined water was not.

Table 2: Water loss rate curve equations of coal samples.

Sample ID	Fitting equation	Correlation coefficient	Saturated water loss rate (%)
1#	$\delta = 1.02t / (1 + 1.27t)$	0.9786	80.65
2#	$\delta = 2.36t / (1 + 3.29t)$	0.9701	71.81
3#	$\delta = 0.74t / (1 + 0.90t)$	0.9668	82.19

4. WATER LOSS MECHANISM ANALYSIS

Coal is a porous medium, and water exits in two main forms: free water and combined water. Free water exists in the coal mass pore in the form of

liquid water, and it includes the adsorption water which exists in coal interior particles in the form of physical absorption. Combined water (also called crystal water) binds with the mineral substance of coal in the form of combination. Combined water needs a high temperature to separate out. The micro-mechanism of coal adsorbing water is the result of the attraction between water molecules and coal molecules. These attractions include van der Waals forces and hydrogen bonds (Nie B. et al., 2004).

The water saturation vapour pressure is the pressure when the gas phase water and liquid phase water reaches equilibrium. There is a dynamic balance between liquid water and vapourous water under a particular pressure at the same temperature, and the molecular quantitative mutual transformation of the liquid water and vapourous water are equal in unit time. The water saturation vapour pressure is relative to the escape of water molecules from liquid water trend. The vapour pressure of liquid reflects the evaporation rate. According to the Clausius-Claperon equation, the relationship between the boiling point of water and the vapourization pressure can be represented as follows:

$$\lg p = A + B/T \tag{3}$$

Where p is the vapour pressure, Pa, T is the boiling point, K, A and B is the constant.

The formula shows that decreasing coal pore gas pressure (gas extraction) can lead to a decrease in the boiling point for free water and it can speed up the evaporation of the free water. If the gas drainage negative pressure is 13 Kpa, the temperature of the coal seam is 30°C, and the boiling point of water is 51°C, the vapourization pressure of water is 4.24 Kpa. At this point the boiling point of water is still higher than the temperature of the coal seam, and the vapourization pressure of water is still lower than the gas drainage negative pressure, so the water loss process is vapourization rather than boiling. Compared with the boiling point of water under normal pressure, it has reduced 49% under negative pressure. If we continue to improve the gas drainage negative pressure, the boiling point of water can be lower than the temperature of the coal seam, and the water loss process changes to boiling.

For the actual gas drainage project in mines, the negative pressure affected area around the borehole widens as time goes on. Inside the negative pressure affected area, coal pore gas pressure decreases. The water vapourization is accelerated on account of the water boiling point unloading, and the coal moisture content has a marked loss.

5. CONCLUSIONS

The coal moisture content decreases as the negative pressure action time increases. The saturated water loss rate of three coal samples reaches 82.19% and the water loss phenomena of coal by negative pressure gas extraction are serious. The gas drainage negative pressure reduces the coal pore gas pressure, and the boiling point and the saturated vapourization pressure of water decrease; it increases the water vapourization (no boiling) rate of coal. Free water (including adsorption water and liquid water) can change from a liquid to a gas and be extracted by negative pressure. This action would reduce the coal moisture content. The moisture of coal has a great affect on dust quantity in mining. Long and continuous gas drainage will result in water loss of coal, which is of great disservice to coal mine dust prevention, so it is necessary to perform water injection into coal seams or to take enhanced dust prevention measures after gas drainage.

6. ACKNOWLEDGEMENT

This paper is Supported by the Fundamental Research Funds for the Central Universities (Grant no. 3142015105) and National Natural Science Foundation of China (Grant no. 51074015).

7. REFERENCES

- Bao Q. and Zhou S. (2013). Application research of comprehensive dust control technology in heading face. *Mining Safety & Environmental Protection*. Volume 40, No. 6, pp. 43–46.
- Cong X., Liu X. and Zhan S. (2010). Experimental of water evaporation on the mine surface in natural environment. *Journal of China Coal Society*. Volume 35, No. 1, pp. 93–96.
- Fan H., Cui W., Yuan J., Chen Y., Xu Y. and G W. (2011). Investigation study on current situation of dust management in coal enterprises. *Journal of Safety Science and Technology*. Volume 7, No. 5, pp. 47–51.
- Jin L., Jiang Z., Ren B. and Wu K. (2000). Study on phenomenon of water vaporization during infusing water into coal seam. *China Safety Science Journal*. Volume 10, No. 3, pp. 58–62.
- Nie B., He X., Wang E. and Zhan L. (2004). Micro-mechanism of coal adsorbing water. *Journal of China University of Mining & Technology*. Volume 33, No. 4, pp. 379–383.
- Tong R., Cui Y., Liu X., Li X. and Wang W. (2013). A health damage evaluation method for coal mine dust in its life cycle. *China Safety Science Journal*. Volume 23, No. 10, pp. 126–131.
- Wang H., Wang D., Ren W. and Xi Z. (2009). Research status and development trend for foam dust

control technique in underground coal mines. *Metal Mine*. No. 12, pp. 131–134.

The laws of gas-solid coupling of coal-bed gas in deep high gassy coal seams

Zhou Aitao^a, Wang Kai^{b,*}, Shen shangkun^c

^a School of Resource & Safety Engineering, State Key Laboratory of Coal Resources and Mine Safety, China University of Mining & Technology, Beijing China 100083

^b School of Resource & Safety Engineering, State Key Laboratory of Coal Resources and Mine Safety, China University of Mining & Technology, Beijing China 100083

^c School of Resource & Safety Engineering, State Key Laboratory of Coal Resources and Mine Safety, China University of Mining & Technology, Beijing China 100083

ABSTRACT

In order to analyze the laws of gas-solid coupling of coal-bed gas in deep high gassy coal seams as well as to prevent the gas compound dynamic catastrophes of deep gas-filled coal-rock, a gas-solid coupling theoretical model under the influence of ground stress, gas pressure, and mining depth is established and simulated by using COMSOL Multiphysics software. Research results indicate that under the influence of factors such as high ground stress and gas pressure, the mutual coupling interaction between coal and gas is much more significant, which leads to the emergence of new characteristics of gas compound dynamic disasters. Reducing the ground stress concentration in front of the working face can not only minimize the possibility of rock burst accidents which are mainly caused by ground stress, but also weaken the role of ground stress as a barrier to gas, thereby decrease the number of outburst accidents whose dominant factor is gas; The results have a great theoretical and practical significance on the further optimization of accident prevention technique as well as safety protection of mines, disaster prevention system design, and accident emergency plans.

KEYWORDS : deep mining; high gassy coal seam; gas-solid coupling; dynamic disaster

1. INTRODUCTION

Most of the coal mines in China have reached deep mining, and the interaction among the constantly increasing coal seam ground stress, gas content, and gas pressure is blamed for the increase of gas compound dynamic catastrophes as well as some new emergent disaster characteristics.

On the basis of investigations concerning gas compound dynamic catastrophes in high gassy coal seams that have occurred in recent years, it has been discovered that there are obvious rock burst manifestations such as roof collapse, floor heave, and roadway deformation (often accompanied by high levels of gas gushing) at the scene of this new type of gas compound dynamic disaster. Moreover, there are some gas outburst holes at the scene and coal rock is thrown far away from these holes. Several distinctive features of gas outburst can be found in these accidents. All these illustrate that the coupling interaction between coal and gas in deep high gassy coal seams is more significant, which results in the emergence of new features of gas compound dynamic disasters.

Investigations aimed at coupling laws were made by domestic and foreign scholars. Litwiniszyn et al.

studied the coupling interaction between coal and gas as well as gas migration law from different angles. Liu Jishan et al. built a mathematical model of gas-solid coupling which takes gas-coal's swelling deformation into account. Scholar Zhao Yangsheng took the lead in proposing a new mathematical model of the coupling reaction between coal rock and gas and further analyzed the numerical method. Zhao Guojing, Ding Jihui et al. came up with the instability theory of gas outburst and established a mathematical model based on the coupling relationship of a gas-solid two-phase medium. Liang Bing et al. set up a coal rock constitutive model which takes the gas interaction into account from the intrinsic time angle. Meanwhile, they proposed the destabilization theory of gas outburst/rock burst and established the mathematical model. Considering the fracture evolution process of coal, Yang Tianhong et al. developed a gas-solid coupling model of coal seam containing damage, and then simulated the gas drainage process in a deep coal seam. Tang Chunan, Xu Tao, Yang Tianhong et al. studied the numerical simulation of coal and gas outburst by using the relevant theory of fluid-solid coupling. S.Valliappan established a fluid-solid coupling model for the flow

*Corresponding author – email : safety226@126.com

of coal-seam gas and compiled the corresponding finite element computer program to simulate the process of coal and gas outburst.

Mainly aimed at the characteristics of high gassy coal seams in deep mining, this paper simulated the laws of gas-solid coupling of coal-bed gas under the influence of gas pressure, mining depth, and other factors and then analyzed the influencing factors of gas compound dynamic disasters of coal rock in high gassy seams. The results have great theoretical and practical significance on the further optimization of accident prevention techniques as well as the safety protection of mines, disaster prevention system design, and accident emergency plans.

2. GAS-SOLID COUPLING THEORY OF COAL-BED THEORY

For ideal gas, the content of adsorbed gas satisfies the Langmuir equation and the gas seepage process conforms to Darcy's law, ignoring the effect of gravity and according to the law of conservation of mass at the same time, the following equations can be drawn.

1) The state equation of gas

The state equation of gas can be obtained based on the state equation of ideal gas.

$$\rho_g = \frac{M_g p}{RTZ} \quad (1)$$

With temperature being constant, then

$$\rho_g = \frac{\rho_n p}{p_n} \quad (2)$$

Where p is gas pressure, MPa; ρ_g is gas density when the pressure equal to p , kg/m³; M_g is molar volume of gas, mol/L; R is molar gas constant, kg/(m³*MPa); Z is compressibility factor, the value is approximate to 1 when the temperature variation is not vast; T is absolute temperature, K; p_n is gas pressure in standard state, MPa; ρ_n is gas density in standard state, kg/m³.

This can be simplified as:

$$\rho_g = \beta p \quad (3)$$

2) Gas content model

Gas in coal beds can be divided into two states; absorbed gas (Q_1), that is absorbed between micropore surface and coal particles, free gas (Q_2), which flows freely in pore fissure space.

When adsorbed gas content satisfies the Langmuir equation, then adsorbed gas content formula of unit coal can be written as:

$$Q_1 = c\rho_c\rho_0 \frac{abp}{1+bp} \quad (4)$$

Where ρ_c is the density of coal, kg/m³; ρ_0 is the density of gas under normal atmospheric pressure, kg/m³; a and b are Langmuir adsorption coefficient, the dimension of a is m³/t, the value of a ranges from 10 to 60, the dimension of b is MPa⁻¹, the value

of b ranges from 0.5 to 5; c is correction coefficient when consider factors such as coal moisture and ash temperature, the value of c ranges from 0 to 1.

Free gas content of unite coal can be expressed as:

$$Q_2 = \phi\rho_g \quad (5)$$

Where ϕ is coal porosity, dimensionless.

Above all, total gas content of unite coal is:

$$Q = Q_1 + Q_2 = c\rho_c\rho_0 \frac{abp}{1+bp} + \phi\rho_g \quad (6)$$

The operator form of which is shown as follows:

$$\frac{\partial Q}{\partial t} = -\nabla(\rho_g \mathbf{u}) + Q_m \quad (7)$$

Gas seepage process conforms to Darcy's law and ignores the effect of gravity, then:

$$\mathbf{u} = -\frac{k}{\mu} \nabla p \quad (8)$$

Where k is permeability of coal seam, m²; μ is gas viscosity, Pa*s.

3) Porosity evolution model

Ignore the change of temperature and gas adsorption, evolution equation for coal porosity is:

$$\phi = 1 - \frac{1 - \phi_0}{1 + \varepsilon_v} (1 - K_Y \Delta p)$$

Where ϕ and ϕ_0 are coal porosity and original porosity, dimensionless; K_Y is coefficient of volume compressibility, dimensionless; Δp is pressure changes of gas, MPa; ε_v is volumetric strain of coal, dimensionless.

4) Permeability evolution model

Coal is a dual-porosity reservoir where gas is mostly stored in the coal matrix and Darcy fluid flow occurs in the natural fracture system. The flow capacity of fracture media depends almost entirely on the number and width of fractures and their continuity in the direction of flow. Permeability, a measure of the flow capacity, is directly related to a range of pore characteristics including pore size, continuity, and connectivity. It is generally believed that the change of coal permeability is decided by coal porosity. The Kozeny - Carman equation which is set up on the basis of the capillary model is most widely used. The permeability evolution model is:

$$k = \frac{k_0}{1 + \varepsilon_v} \left[1 + \frac{\varepsilon_v}{\phi_0} + \frac{(1 - \phi_0)K_Y \Delta p}{\phi_0} \right]^3 \quad (9)$$

3. NUMERICAL SIMULATION OF GAS-SOLID COUPLING IN DEEP HIGH GASSY COAL SEAMS

The general finite element analysis software COMSOL Multiphysic was adopted to make a calculation of the established gas-solid coupling model. The geometric model is 80 m long, 30 m high, the roof height of which is 15 m, floor height is 10 m, and coal seam height is 5 m. The excavation block whose length is 5 m is set at the far left of the coal

seam.

3.1 Model parameter

According to the actual situation of high gassy mines in China and taking some relevant literatures as a reference, the model parameters are set up as shown as in Tables 1 and 2.

Table 1: Parametric values of coal and surrounding rock.

N	Value	Description
r1	1250[kg/m ³]	Coal density
E1	2713[MPa]	Coal elastic modulus
po1	0.339	Coal Poisson's ratio
co1	1.25[MPa]	Coal cohesiveness
theta1	37 π /180 [rad]	Coal inner friction angle
r2	2640 [kg/m ³]	Surrounding rock density
E2	33400[MPa]	Surrounding rock modulus
po2	0.235	Surrounding rock Poisson's ratio
co2	3.2[MPa]	Surrounding rock cohesiveness
theta2	π /6[rad]	Surrounding rock inner friction angle

Table 2: Parametric values of gas.

Name	Value	Description
rg	0.714[kg/m ³]	Gas density in standard state
e0	0.01	Initial porosity before excavation
k0	1.0 × 10 ⁻¹⁵ [m ²]	Initial permeability before excavation
mug	1.84 × 10 ⁻⁵ [Pa*s]	Gas viscosity
a	26[m ³ /t]	Adsorption coefficient 1
b	0.714[MPa ⁻¹]	Adsorption coefficient 2
c	0.9957	Adsorption coefficient 3
beta	7.14[kg/(m ³ *MPa)]	Gas state coefficient
alpha	0.99	B-W coefficient

3.2 Simulation scheme and results

Mining depth is set at 800 m and initial gas pressure is 2 MPa. The gas-solid coupling laws of coal-bed gas are studied under the influence of great ground stress and gas pressure.

Firstly, the corresponding body load and edge load are exerted on the model, and the initial state before excavation is obtained. The distribution of vertical stress is shown in Figure 1.

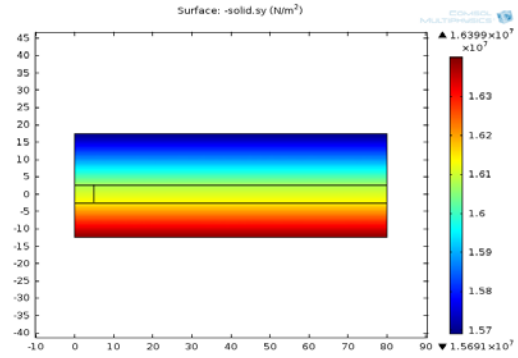
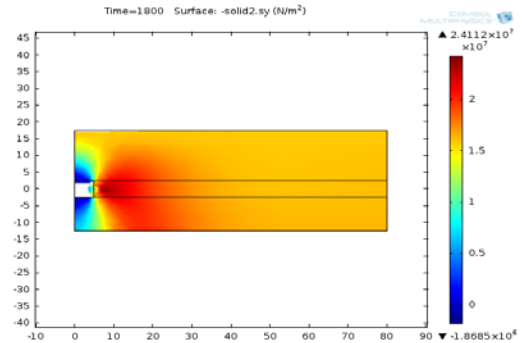
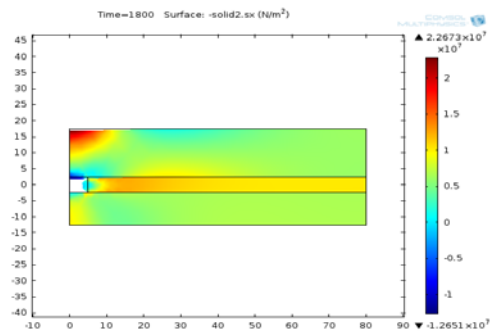


Figure 1: Distribution of vertical stress before excavation.

Excavate the preset block excavation. A transient solver is chosen to solve the gas-solid model of coal-bed gas. The duration is set at 0 to 60 minutes and the step size is 5 minutes. The parameters cloud maps are set at 30 minutes, and the results are as follows:



(a)



(b)

Figure 2: Distribution of vertical stress and horizontal stress after excavation.

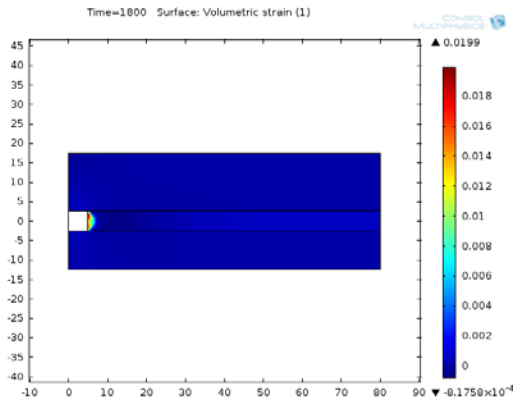
From Figure 2, it can be seen that:

1) Obviously stress unloading area, stress concentration area, and initial stress area exist in the coal beds.

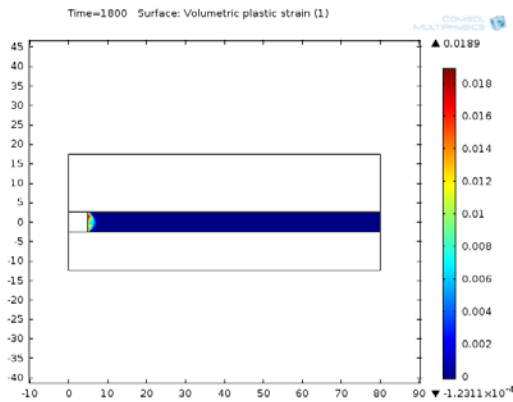
2) The maximum peak of stress lies in the stress

concentration area, close to the coal wall.

3) Obviously pressure-released region exists at upper and down floor of excavation roadway, the height of which is 10 m.



(a)



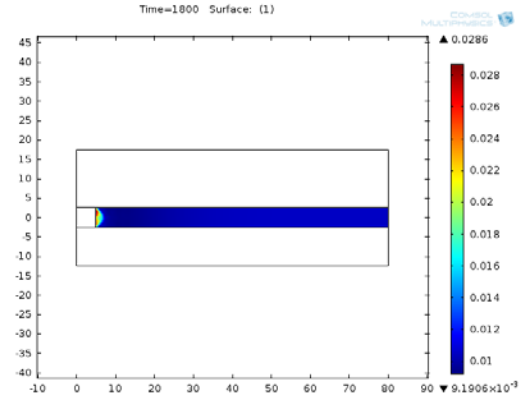
(b)

Figure 3: Distribution of volumetric strain and volumetric plastic strain after excavation.

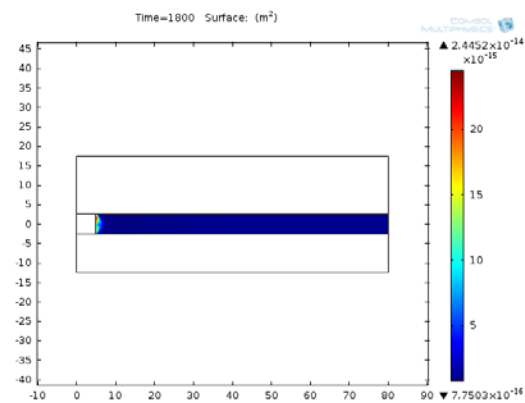
From cloud maps of strain after excavation in Figure 3, we can see:

1) The stress of coal mass near the coal wall passes over the yield strength, plastic strain occurs, and the length of the plastic strain area is about 3 m.

2) Coal mass near the wall is forced and damaged, obvious dilatancy effect and volume expansion occur, then in the elastic region of stress concentration area coal mass is compacted and volumetric strain reaches the minimum.



(a)



(b)

Figure 4: Distribution of porosity and permeability after excavation.

As cloud maps of porosity and permeability shown in Figure 4:

1) Porosity and permeability are all influenced by the strain of coal seams and the gas pressure, they have the same changing trend.

2) Because of the dilatancy effect, the porosity and permeability of coal mass near the coal wall are larger and reach the maximum at the coal wall, then gradually decrease along with the coal seam extends to right. Coal mass is forced and compacted in the elastic region of stress concentration. Porosity and permeability reach the minimum and then gradually recover to the original value.

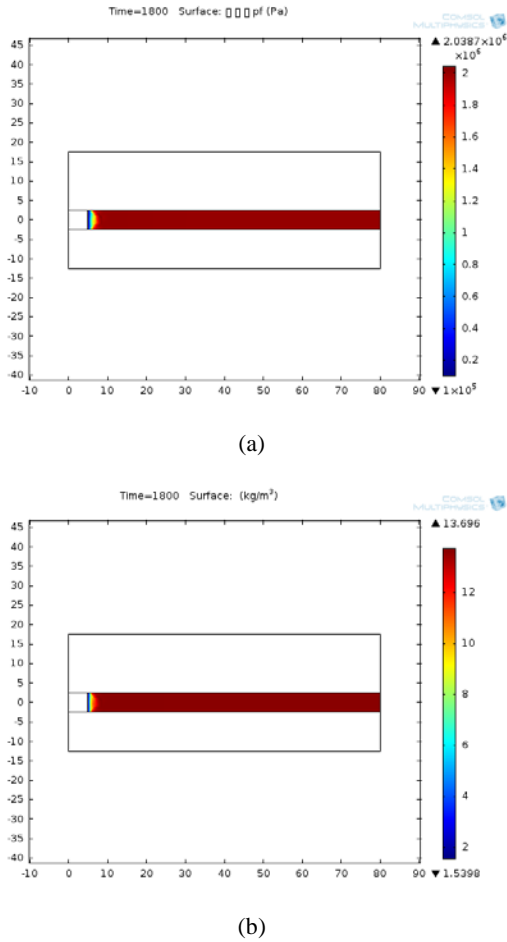


Figure 5: Distribution of gas pressure and gas content after excavation.

What we can see from cloud maps of gas pressure and gas content are as follows:

1) Gas pressure and gas content share the same trend. They sharply reduce near the coal wall and reach the minimum there. They reach the maximum at areas where stress is concentrated, slightly greater than the initial values.

2) Due to the dilatancy damage of coal, gas is easy to outflow from coal seam in the pressure-released region. While at the stress concentration area, the compacted coal mass impedes the process of gas seepage and forms significant gradient differences of gas pressure and content.

4. GAS COMPOUND DYNAMIC CATASTROPHES OF DEEP GAS-FILLED COAL-ROCK

In order to analyze the effect of high ground stress and gas pressure on disasters, several gas compound dynamic catastrophes of deep gas-filled coal-rock are studied in this paper. The rock burst

accident in Laohutai Fushun is taken as an example, and the results are shown in Table 3.

Table 3: Rock burst and gas emission situation in Laohutai Fushun Mines.

Ming depth /m	Total number of rock burst accident	Total number of gas concentration overrun	Percentage of gas concentration overrun /%
<580	165	1	0.61
630	224	13	5.80
680	269	34	12.64
730	135	10	7.41
780	337	83	24.63
830<	87	40	45.98
Sum up	1217	181	100

According to the analysis of the accident, it has been discovered that there are obvious rock burst manifestations such as roof collapse, floor heave, and roadway deformation (often accompanied by high levels of gas gushing) at the scene of gas compound dynamic disasters. Moreover, there are some gas outburst holes at the scene, and coal rock is thrown far away from these holes. Distinctive features of gas outburst can be found in these accidents. The gas gushing quantity per ton of coal is not very large, and the airflow reversal phenomenon is not significant.

Rock burst intensity is in direct proportion to concentration and duration of gas emission. Furthermore, in the coal seam that applied gas drainage measures, the frequency and strength of rock burst significantly increased. For the deep high gassy coal seams under the influence of high ground stress and gas pressure, the coupling interaction between coal and gas is more significant, which results in the emergence of new features of gas compound dynamic disasters.

5. CONCLUSIONS

1) A simulation of the laws concerning the gas-solid coupling of coal-bed gas was made by establishing a theoretical gas-solid coupling model under the influence of gas-pressure, mining depth, and using COMSOL Multiphysics software.

2) For deep high gassy coal seams under the influence of high ground stress and gas pressure, the coupling interaction between coal and gas is more significant, which results in the emergence of new features of gas compound dynamic disasters.

3) Reducing the ground stress concentration in front of the working face can not only work wonders for minimizing the likelihood of rock burst accidents which are mainly caused by ground stress, but also weaken the role of ground stress as a barrier to gas, thereby reducing the number of accidents whose dominant factor is gas. For deep high grassy coal seam, coal seam water infusion is the best method.

6. ACKNOWLEDGEMENTS

This research is financially supported by the State Key Research Development Program of China (2016YFC0801402, 2016YFC0600708), National Natural Science Foundation of China (51474219).

7. REFERENCES

Liang B, Zhang MT and Wang YJ (1995) The endochronic constitutional model of coal containing gas, *Rock & Soil Mech.*, vol. 03, pp. 22-28.

Litwiniszyn J (1985) A model for the initiation of coal-gas outbursts. *Int. J. Rock. Mech. & Min. Sci. & Geomech. Abstracts.*, vol. 22(1), pp. 39-46.

Liu JS(2010) Linking gas-sorption induced changes in coal permeability to directional strains through a modulus reduction ratio. *Int. J. Coal Geol.*, vol. 83(1), pp. 21-30.

Valliappan S and Wohua Z (1996) Numerical modeling of methane gas migration in dry coal seams. *Int. J. Numer. Anal. Meth. Geomech.*, vol.20, pp. 571–593.

Xu T, Tang CA and Yang TH (2005) Numerical simulation of coupled gas flow in failure process of gassy coal-rock. *Chin. J. Rock. Mech. & Eng.*, vol. 10, pp. 1667-1673.

Yang TH (2001) Study on infiltrate character and coupling analysis of seepage and stress in rock failure process, Shenyang, China: Northeastern University.

Zhao GJ and Ding JH (1998) Non-linear numerical simulation of coal and gas outburst as a coupling instability problem of solid-fluid biphasic media. *Journal of China University of Mining & Technology*, vol. 02, pp.103-107.

Zhao YS (1994) Mathematical model of coal mass and gas coupling and its numerical method, *Chin. J. Rock. Mech. & Eng.*, vol. 03, pp. 229-239.

Grey Correlation Model of influence factors analysis of ventilation time in single-way tunnel

Yang Cao*, Hongguang Ji

Department of Safety Science and Engineering, University of Science and Technology Beijing, Beijing, China, 100083

ABSTRACT

Ventilation time is an important parameter in the process of heading face ventilation. Shortening ventilation time has great significance in improving the efficiency of tunneling work. This paper analyzes the influence factors affecting the heading face ventilation time and establishes the grey correlation model based on the ventilation time data of a -118m single-way tunnel in a golden mine. Calculations of the correlation degree between the four influence factors are as follows: blasting fume throwing length (X_0), distance of air duct to tunneling face (X_2), length of tunnel (X_3), initial concentration of CO (X_4), and evaluation of the sensitivity. Results show that tunnel length and blasting fume throwing length are more sensitive to ventilation time of the four influence factors, the distance from the duct to the diving face is less sensitive to ventilation time, and the influence factor of initial concentration is the least sensitive of all. The analysis results can help create practical and instructive effects on ventilation work in single-way tunnels.

KEYWORDS: Single-way tunnel; ventilation time; influence factors analysis; Grey correlation; correlation degree

INTRODUCTION

Driving takes place extensively in mining, tunnels, and underground excavation. As a way of digging tunnels, blasting plays a major role in underground engineering (JI Hong-guang, 2014). Hazardous gases and dust, collectively called blasting fumes, are produced during the explosions. After blasting, it is necessary to ventilate in the one-way tunneling in order to disperse the blasting fumes for preparation of slag removal. Ventilation time is defined as duration time from blasting to when the toxic gas concentration is lower than the state standards to ensure the health and safety of workers. Ventilation time not only marks the efficiency of ventilation, but also provides a reference for the arrangement of the tunneling cycle. Shortening the ventilation time can enhance the work efficiency of tunneling and eliminate toxic gas poisoning accidents (YANG Zan-cheng, 2011).

Theoretically, the nature of ventilation in one-way tunnels is mixture and dilution between fresh air and blasting fumes and drainage with a method of turbulent flow deformation. For a given blasting fume volume and regulated standard concentration of toxic gases, fresh air volume (Q - t)

is needed to satisfy the requirement of ventilation (Q means volume of ventilator, t means ventilation time). Practically, there are a number of influence factors and complicated interactions which cause the extension of ventilation. Several scholars found that volume of air, length of blasting fume throwing, distance of duct to tunnel face, length of tunnel, and original concentration of blasting fume have an influence on ventilation time (WU Li-zhong, 1959; WANG Yin-min, 1993; WU Chao, 2008). In practical engineering, carrying out weight evaluation through introducing proper methods in order to analyze the sensitive degree between the influence factors and ventilation time has a vitally instructive effect on ventilation in one-way tunnels.

In the past, researchers have focused on the mathematical model of removal of blasting fumes in tunnels (SU Li-jun, 2000; YANG Li-xin, 2000). Accurate mathematical models have been established that depict the movement of blasting fumes and the volume of air. The authors have paid less attention to the weight influence factors analysis of ventilation. Although statistical methods show priority on sensitive analysis, these methods need abundant data (WANG Yang, 2004). Applying the grey correlation model to the analysis of

*Corresponding author – email: wwwcaoyang@126.com

sensitive influence factors of ventilation time can obtain better advantages. The grey correlation model not only can fit with less data, but it also avoids the problem of the difference of parameter units and magnitude (WU Ai-you, 2005). Therefore, in this article the grey correlation model is built to carry out weight analysis on the influence factors.

1. INTRODUCTION OF GREY CORRELATION MODEL

The grey correlation model is established via three steps as follows: Firstly, confirm the system feature sequence and influence factors sequence; Secondly, obtain the correlation degree by calculating the influence factors sequence; Thirdly, perform a correlation analysis according to correlation degree (LIU Si-feng, 2013).

2.1 System feature sequence and influence factors sequence matrix

Select system feature sequence as X_0 , influence factors as $X_1, X_2 \dots X_i$ showed in the formulas below.

$$\begin{aligned} X_0 &= (x_0(1), x_0(2), \dots, x_0(n),) \\ X_1 &= (x_1(1), x_1(2), \dots, x_1(n),) \\ &\dots\dots \\ X_i &= (x_i(1), x_i(2), \dots, x_i(n),) \end{aligned}$$

2.2 Calculation Process of Correlation Degree

(1) Sequence original image:

$$X'_i = X_i/x_i(1) = (x'_i(1), x'_i(2), \dots, x'_i(n)) \quad n = 1, 2, \dots, m$$

(2) Difference value of sequence:

$$\Delta_i(k) = |x'_0(k) - x'_i(k)|, \Delta_i = (\Delta_i(1), \Delta_i(2), \dots, \Delta_i(n)) \quad i = 1, 2, \dots, m$$

(3) Maximum and minimum differences:

$$M = \max_i \max_k \Delta_i(k), \quad m = \min_i \min_k \Delta_i(k)$$

(4) For $\xi \in (0, 1)$

$$\gamma(x_0(k), x_i(k)) = \frac{\min_k \min_i |x_0(k) - x_i(k)| \xi + \max_k \max_i |x_0(k) - x_i(k)| (1 - \xi)}{|x_0(k) - x_i(k)| \xi + \max_k \max_i |x_0(k) - x_i(k)| (1 - \xi)}$$

When $\xi=0.5$, the formula can be transformed as follows:

$$\gamma_{oi}(k) = \frac{m + 0.5M}{\Delta_i(k) + 0.5M}, \quad k=1, 2, \dots, n \quad i=1, 2, \dots, m$$

(5) Correlation degree:

$$\gamma_{oi} = \frac{1}{n} \sum_{k=1}^n \gamma_{oi}(k), \quad i = 1, 2, \dots, m$$

Correlation degree is the metric that weights the correlation extent between the influence factor and feature sequence. Its value ranging interval is [0,1]. The closer to 1 the correlation degree is, the higher the influence on the feature sequence the factors have; On the contrary, the closer to 0 the correlation degree is, the lower the influence on the feature sequence the factors have.

2. APPLICATION OF GREY CORRELATION MODEL

3.1 Calculation steps

Take forced auxiliary ventilation in a single-way tunnel at a golden mine as an example. Select X_1, X_2, X_3, X_4 as the influence factors sequence, and X_0 as the feature sequence. Ventilation monitoring tests were conducted to acquire relevant test data in single-way tunnel after blasting according to the practicality.

X_1 stands for length of blasting fume throwing, m; X_2 stands for distance of duct to working face, m; X_3 stands for length of tunnel, here is instead of the distance of test point to working face, m;

X_4 stands for original concentration of blasting fume, ppm;

X_0 stands for ventilation time, min.

Table 1: Original data of feature sequence and influence factors sequence.

Sample ID	X_0 (min)	X_1 (m)	X_2 (m)	X_3 (m)	X_4 (ppm)
1	82	21.4	20	48	3693779.3
2	70	20.6	23	53	859406.7
3	150	15.8	12	42	1648480.3
4	176	19.8	14	36	1443225.6
5	105	21	18	38	1629622.8
6	186	22.2	17	50	6289709.5
7	50	18.2	10	31	508339.4
8	54	20.6	19	35	491464.1
9	81	19.8	24	40	443655.8

(1) Calculation of sequence original image:

$$X_i = X_i / x_i(1) = (x_i(1), x_i(2), \dots, x_i(n)) \quad n = 1, 2, \dots, 9$$

$$X = (X_0, X_1, X_2, X_3, X_4)^T = \begin{pmatrix} 1 & 0.854 & 1.829 & 2.146 & 1.281 & 2.268 & 0.610 & 0.659 & 0.988 \\ 1 & 0.963 & 0.738 & 0.925 & 0.981 & 1.037 & 0.851 & 0.963 & 0.925 \\ 1 & 1.150 & 0.600 & 0.700 & 0.900 & 0.850 & 0.500 & 0.950 & 1.200 \\ 1 & 1.104 & 0.875 & 0.750 & 0.791 & 1.041 & 0.646 & 0.729 & 0.833 \\ 1 & 0.233 & 0.446 & 0.391 & 0.441 & 1.703 & 0.137 & 0.133 & 0.120 \end{pmatrix}$$

(2) Calculation of differences of sequence:

$$\Delta_i = (\Delta_{i1}, \Delta_{i2}, \Delta_{i3}, \Delta_{i4})^T = \begin{pmatrix} 0 & 0.109 & 1.091 & 1.221 & 0.299 & 1.231 & 0.241 & 0.304 & 0.626 \\ 0 & 0.296 & 1.229 & 1.446 & 0.381 & 1.418 & 0.110 & 0.291 & 0.212 \\ 0 & 0.251 & 0.954 & 1.396 & 0.489 & 1.227 & 0.036 & 0.071 & 0.155 \\ 0 & 0.621 & 1.383 & 1.756 & 0.839 & 0.566 & 0.472 & 0.526 & 0.868 \end{pmatrix}$$

(3) Calculation of maximum and minimum differences:

$$M = \max_i \max_k \Delta_i(k) = 1.756$$

$$m = \min_i \min_k \Delta_i(k) = 0$$

(4) Calculation of correlation coefficient:

$$\gamma_{0i}(k) = \frac{m + 0.5M}{\Delta_i(k) + 0.5M} = \frac{0.878}{\Delta_i(k) + 0.878} \quad k = 1, 2, \dots, 9 \quad i = 1, 2, 3, 4$$

Then the corresponding grey correlation matrix is:

$$R_{0i} = \begin{pmatrix} 1 & 0.890 & 0.446 & 0.418 & 0.746 & 0.416 & 0.785 & 0.743 & 0.935 \\ 1 & 0.748 & 0.417 & 0.378 & 0.698 & 0.382 & 0.889 & 0.751 & 0.805 \\ 1 & 0.778 & 0.479 & 0.386 & 0.642 & 0.417 & 0.961 & 0.926 & 0.850 \\ 1 & 0.586 & 0.388 & 0.333 & 0.511 & 0.608 & 0.650 & 0.626 & 0.503 \end{pmatrix}$$

(5) Calculation of grey correlation degrees:

$$\gamma_{0i} = \frac{1}{n} \sum_{k=1}^n \gamma_{0i}(k), \quad i = 1, 2, 3, 4 \quad k = 1, 2, \dots, 9$$

$$\bar{R}_{0i} = (\gamma_{01}, \gamma_{02}, \gamma_{03}, \gamma_{04}) = (0.709, 0.674, 0.715, 0.578)$$

3.2 Results analysis and practical application

Results were acquired through the grey correlation model. The correlation degrees of the four influence factors (X_1, X_2, X_3, X_4) are 0.709, 0.674, 0.715, and 0.578. The length of the tunnel (X_3) shows the maximum influence on ventilation; the second influence factor is the length of blasting fume throwing (X_1); the third influence factor is the distance from the duct to the working face (X_2); the original concentration of blasting fume (X_4) has the minimum influence on ventilation time.

In order to shorten the ventilation time in single-way tunnels, the most effective approach is to improve the influence factor which has the maximum influence on ventilation time. According to the results calculated through the grey correlation

model, shortening the length of tunnel (X_3) should be the most effective. However, this is not practical. Therefore, lessening the length of blasting fume throwing (X_1) is another good way to shorten ventilation time. Limited explosives should be used in every explosion to decrease the original concentration of blasting fumes. Because the correlation degrees of these influence factors show big relativity to ventilation time, enhancing one or several factors can effectively shorten the ventilation time.

3. CONCLUSION

The grey correlation model has better effects on the weight analysis of influence factors to ventilation time. Through making use of the grey correlation model, the qualitative analysis can be expressed in quantitative results, clarifying the major and minor influence factors for ventilation time. This provides rewarding instruction and reference to ventilation management during the process of tunneling.

The grey correlation model was applied to analyze several independent influence factors. Therefore, the selection of influence factors and the use of data sequences has some influence on the accuracy and reasonability of the results of the model evaluation.

The ventilation system in the tunnel can be equal to forcing auxiliary ventilation with a constant air volume. As another influence factor, the extent of air volume to ventilation time has important value in research. For exhausted ventilation and combined ventilation, whether and how much the influence factors above are related to ventilation time remains to be researched and confirmed.

4. ACKNOWLEDGEMENT

First and foremost, I would like to show my deepest gratitude to my supervisor, Dr. Ji Hongguang. He is respectable, responsible and resourceful scholar who provided me with valuable guidance in every stage of writing of this paper. When establishing the index system, calculating the numerous indexes, he put forward the valuable comments for the selection of the index and calculation method. I shall also extend my thanks to my scientific research team for their kindness and help. Finally I wish a great success of ISMS 2016.

5. REFERENCE

Ji Hong-guang, CAO Yang, ZHANG Ge

(2014). Study on prediction of drain-fume time of single-end roadway in tunneling process. *Metal Mining*, Volume 5, No 254, pp. 142-145.

LIU Si-feng, XIE Nai-ming(2013). *Grey System Theory and Its Application*. Science Press,167p.

SU Li-jun, LU Wen-bo(2000). Technique during construction of underground tunnel. *Blasting*. Volume 17, No1, pp.1-6.

WANG Yin-min(1993). *Ventilation and Dust-prevention in Mine*. Metallurgical industry press, 45p.

WANG Yang, YIN Kun-long, An Guan-feng(2004). Landslide sensitive influence factors of grey correlation analysis. *Rock and Soil Mechanics*, Volume25, No1, pp.91-93.

WU Li-zhong(1959). *Ventilation in single-way tunnel after blasting*. Metallurgical Industry Press,46p.

WU Ai-you, XIAO Hong-fei(2005). Establishment and application of weights and grey association model based on coal and gas outburst controlled influence factors assessment. *Journal of Coal China Society*, Volume 30, No1, pp.58-62.

WU Chao(2008). *Mine Ventilation and Air-condition*. ZhongNan University press,26p.

YANG Zan-cheng, YANG Peng, LV Wen-sheng,(2011). Numerical simulation on diffusion law of blasting fume during roadway tunnel across a vein in an alpine mine. *Journal of University of Science and Technology Beijing*. Volume33, No5, pp. 521-525.

YANG Li-xin, LU Mao-cheng, ZHAO Jun-xi(2000). Discussion on ventilation smoke-drain calculation in tunnel construction after blasting. *West-China Exploration Engineering*, Volume23, No1, pp.55-57.

Numerical research on the airflow distribution in mine tunnels

Cui DING^{a,*}, Xueqiu HE^{b,c}, Baisheng NIE^c

^aDepartment of Safety Engineering, China Institute of Industrial Relations, Beijing, China, 100048

^bSchool of Civil and Environment Engineering, University of Science and Technology Beijing, Beijing, China, 100083

^cSchool of Resource & Safety Engineering, China University Mining & Technology (Beijing), Beijing, China, 100083

ABSTRACT

Based on 3D modelling of typical tunnels in mines, the air flow structure in the three hearts arch-section tunnel was investigated and the influence of air velocity and cross section on air flow distribution in tunnels was studied. The average velocity points were analyzed quantitatively. The results showed that the feature of the air flow is similar with the shape of the three hearts arch-section under different ventilation velocities and cross section areas. The shape of the tunnel cross section and wall were the critical factors influencing the air flow structure. The average velocity points were mainly close to the tunnel wall. Characteristic equations were developed to describe the average velocity distribution, and provide the theoretical basis for accurately measuring the average velocity in mine tunnels.

KEYWORDS: mine tunnel; turbulence; air flow structure; three hearts arch; average velocity

1. INTRODUCTION

Mine ventilation is the process of continually inputting fresh air and outputting polluted air. The ventilation system is the basic system in mines. It is estimated that many mine disasters, including fire, coal gas, and dust explosions occur as a result of failures of the mine ventilation system.

Nowadays, the air flow velocity and volume in tunnels are detected by on-line monitoring systems. However, because of the non-uniform distribution of air flow, the velocity measured by sensors is not the average velocity in each section. As such, it is necessary to study the air flow structure, especially the average velocity distribution, so as to calculate the air flow volume accurately. At present, the air flow distribution in cross-sections is macroscopically described with numerical simulation in several studies (Parra et al., 2006; Chen and Yu, 2008; Jia, 2011; Hao et al., 2011). Only a few have quantitatively studied the average velocity distribution in circular and rectangular tunnels, by experimental and theoretical methods (Ma et al., 2007; Yin et al., 2008; Zhou et al., 2012; Wang et al., 2013; Tan et al., 2013; Zhao et al., 2014). However, the relations among the air flow structure, the average velocity, and the cross-section shape and sizes have not been developed and described successfully. The characteristic equations of the average velocity distribution close to the roof have been developed in the three hearts arch-section tunnels and trapezoidal cross section tunnels (Ding et al., 2015; Ding, 2016). The other areas of the average velocity distribution on three hearts arch-sections were not developed

quantitatively. This study aims to present the air flow distribution and develop the characteristic equations of the average velocity distribution in three hearts arch-section tunnels.

2. NUMERICAL SIMULATION

2.1 The physical model of the tunnel

Ding et al. adopted the numerical analysis method to simulate the air flow distribution in three hearts arch-section tunnels and testified on the accuracy of the numerical analysis method. In this paper, the tunnel length is 8 m, the width is 260 mm, and wall height is 113 mm. The small arch radius is 66 mm, and the large arch radius is 183 mm, as shown in Figure 1.

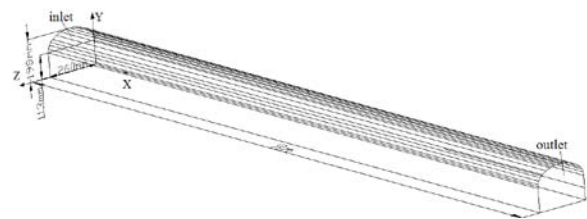


Figure 1: The physical model of the tunnel.

In order to analyze the air flow structure in tunnels quantitatively, the model in Figure 1 was amplified by 2 times, 3 times, 4 times, and 5 times. The sizes of the five three hearts arch-section tunnels are shown in Table 1. The air flow in the tunnels was set to be turbulent, which was similar to the actual ventilation conditions. The air flow distribution was

*Corresponding author--email:cui_ding@163.com

Table 1: The sizes of the five three hearts arch tunnels .

Tunnel number	Tunnel parameters				
	large archradius(mm)	Smaller chradius(mm)	width(mm)	Wall height(mm)	length(m)
1	183	66	260	113	8
2	366	132	520	226	16
3	549	198	780	339	24
4	732	264	1040	452	32
5	915	330	1300	565	40

then studied under different air flow velocities and different tunnel sizes.

2.2 Mathematical model and assumptions

According to the fluid dynamics theory, the air flow in tunnels can be described by using the following equations.

The continuity equation:

$$\frac{\partial \rho}{\partial t} + \frac{\partial(\rho u_j)}{\partial x_j} = 0$$

The momentum equations(i direction):

$$\frac{\partial(\rho u_i)}{\partial t} + \frac{\partial(u_j u_i)}{\partial x_j} = \frac{\partial}{\partial x_j} \left(\mu \frac{\partial u_j}{\partial x_j} \right)$$

The energy equation:

$$\frac{\partial(\rho h)}{\partial t} - \frac{\partial(\rho u_j h)}{\partial x_j} = \frac{\partial}{\partial x_j} \left(\Gamma_h \frac{\partial h}{\partial x_j} \right)$$

The standard k-ε model was used to calculate the turbulence and diffusion of the air flow.

k equation:

$$\begin{aligned} \frac{\partial}{\partial t}(\rho k) + \frac{\partial}{\partial x_i}(\rho k u_i) \\ = \frac{\partial}{\partial x_j} \left[\left(\mu + \frac{\mu_t}{\sigma_k} \right) \frac{\partial k}{\partial x_j} \right] + G_k - \rho \epsilon \\ - Y_M \end{aligned}$$

ε equation:

$$\begin{aligned} \frac{\partial}{\partial t}(\rho \epsilon) + \frac{\partial}{\partial x_i}(\rho \epsilon u_i) \\ = \frac{\partial}{\partial x_j} \left[\left(\mu + \frac{\mu_t}{\sigma_\epsilon} \right) \frac{\partial \epsilon}{\partial x_j} \right] + C_{1\epsilon} \frac{\epsilon}{k} G_k \\ - C_{2\epsilon} \rho \frac{\epsilon^2}{k} \end{aligned}$$

In these equations, G_k represents the generation of turbulence kinetic energy due to the mean velocity gradients, $G_k = -\rho u_i \overline{u_j} \frac{\partial u_j}{\partial x_i}$. Y_M represents the contribution of the fluctuating dilatation in compressible turbulence to the overall dissipation

rate, $Y_M = 2\rho \epsilon M_t^2$. μ_t represents the turbulent viscosity, $\mu_t = \rho C_\mu \frac{k^2}{\epsilon}$.

$C_{1\epsilon}$, $C_{2\epsilon}$ and C_μ are constants. $C_{1\epsilon} = 1.44$, $C_{2\epsilon} = 1.92$, $C_\mu = 0.09$. σ_k and σ_ϵ are the turbulent Prandtl numbers for k and ε, respectively. $\sigma_k = 1.0$, $\sigma_\epsilon = 1.3$.

ρ represents the density, kg/m³. u represents the velocity, m/s. k represents the turbulence kinetic energy, kJ/kg. ϵ represents the turbulence kinetic energy dissipation rate, m²/s³. μ represents the molecular (dynamic) viscosity, Pa.s. t represents the time, s. h represents the static enthalpy, k. Γ_h represents the transport coefficient.

When developing the mathematical model, the following assumptions were made: the air flow was incompressible; the wall was adiabatic; there were no workers and vehicles in the tunnels, and the presence of smoke and dust were ignored.

2.3 Boundary Conditions and Parameters

The tunnel inlet was set to be the velocity-inlet and the air flow velocity was set to 1m/s, 2m/s, 3m/s, 4m/s and 5m/s respectively. The tunnel outlet was set to be the pressure-outlet and the relative pressure was 0 Pa. The air flow distribution in the three hearts arch-section tunnels of five sizes were simulated under the different air flow velocities.

3. ANALYSIS OF THE AIR FLOW STRUCTURE IN TUNNELS

The air flow distribution on fully developed turbulence cross sections were studied. In this paper, the distance between the cross sections analyzed and the tunnel inlet was set according to fluid mechanics theory, and the distance between the analyzed cross sections and the tunnel inlet was 5.6 m (Z_1), 11.2 m (Z_2), 16.8 m (Z_3), 22.4 m (Z_4), 28 m (Z_5),

respectively. The velocity profiles on the above five cross sections (Z_1, Z_2, Z_3, Z_4, Z_5) were analyzed as shown in Figure 2.

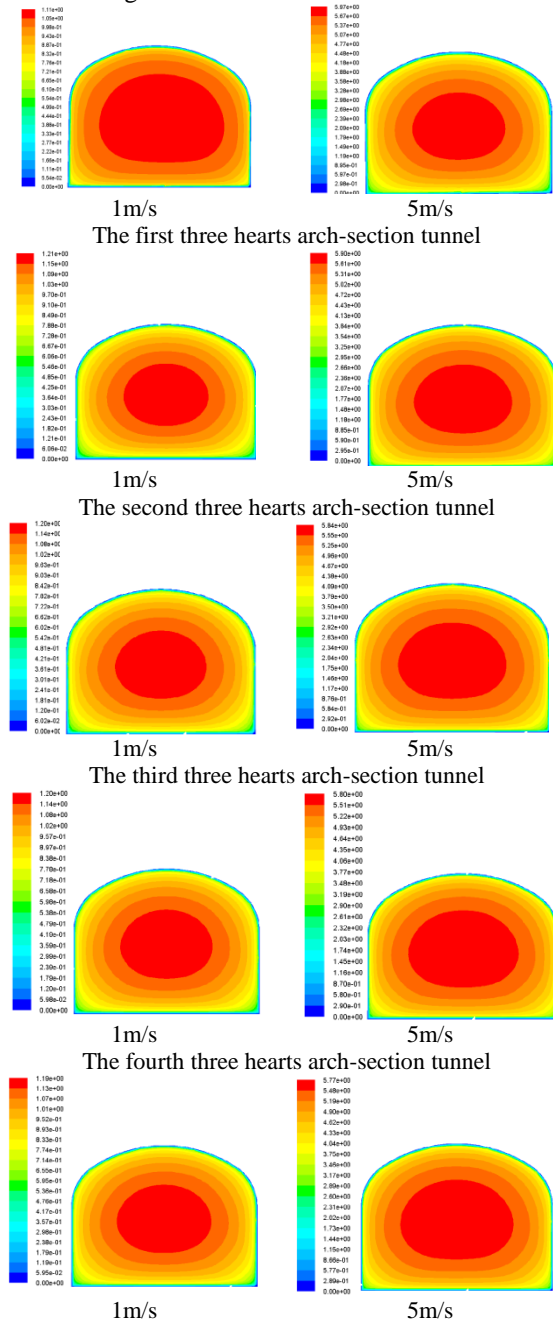


Figure 2: Velocity profiles on fully developed turbulence sections in five tunnels.

It can be concluded from Figure 2 that the air flow structure showed a circular distribution which was similar to the shape of three hearts arch-section under different ventilation velocities and cross section sizes. The shape of the cross section was the critical factor influencing the air flow structure. The

air flow velocity reached its maximum value in the center of the tunnel and decreased from the center to the tunnel wall. The average velocity points were mainly close to the tunnel wall under different air flow velocities and the air flow velocity which was smaller than the average velocity would decrease more quickly when it was closer to the tunnel wall. According to the above analysis, the tunnel wall was also a critical factor influencing the air flow distribution.

4. ANALYSIS OF AVERAGE VELOCITY DISTRIBUTION

The average velocity points are critical to achieving an accurate measurement and monitoring of ventilation volumes in tunnels. According to Ding (Ding et al., 2015), the distribution of the average velocity points in any three hearts arch-section tunnel shows as an annular ring and the ventilation velocity has little influence on the above distribution feature. In order to further analyze the distribution of the average velocity points and develop its characteristic equations, the distribution curve has been separated into six parts as shown in Figure 3.

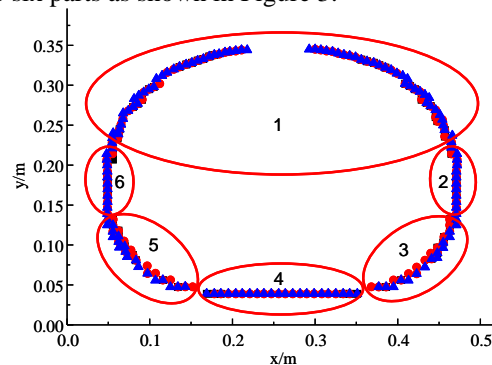


Figure 3: The average distribution curve on three hearts arch-section.

According to Ding (Ding et al., 2015), the characteristic equation of the first part can be described by equation 1-1, and in this paper, the characteristic equations of the other five parts are developed.

$$3.2819r_1^{-2} \left(x - \frac{d}{2} \right)^2 + 8.408r_1^{-1.84} (y - 0.6142r_1 + 0.0138)^2 = 1 \quad (1-1)$$

r_1 — radius of the top circular arc, m ;

d — width of the tunnel, m.

As shown in Figure 3, the curve is symmetrical, so the feature of the fourth, fifth, and sixth parts will be analyzed quantitatively.

(1) The fourth part

Based on an analysis of relationships between the length of the fourth part curve, the tunnel size and the distance between the curve and the tunnel floor, it

has been found that the length of the fourth part curve and the distance between the curve and the tunnel floor had perfect linear relations with the width of the tunnel as shown in Figures 4 and 5, respectively.

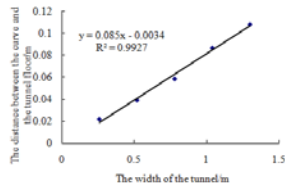


Figure 4: Relationship between the distance from the bottom edge to part 4 and the length of bottom edge.

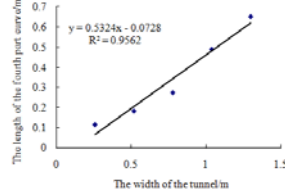


Figure 5: Relationship between the length of part 4 and the length of the bottom edge.

Based on the above analysis, the characteristic equations of the fourth part can be described as equations 1-2 and 1-3.

$$d_1 = 0.085d - 0.0034 \quad (1-2)$$

$$d_2 = 0.5324d - 0.0728 \quad (1-3)$$

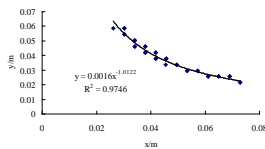
d — width of the tunnel, m ;

d_1 — distance between the fourth part curve and the tunnel floor, m ;

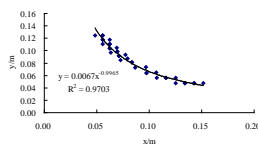
d_2 — length of the fourth part curve, m.

(2) The fifth part

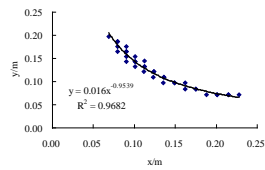
Numerical fitting methods have been used to develop the characteristic equations of the fifth part as shown in Figure 6.



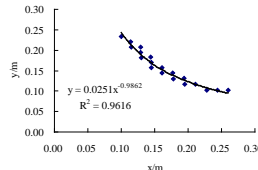
The first three hearts arch-section tunnel



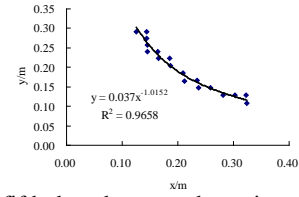
The second three hearts arch-section tunnel



The third three hearts arch-section tunnel



The fourth three hearts arch-section tunnel



The fifth three hearts arch-section tunnel

Figure 6: Part 5 curve fitting diagram of three hearts arch-sections in five tunnels.

By combining the above five equations and the width of different tunnels, the five equations can be normalized into one equation, equation 1-4.

$$y = 0.0236d^{1.965}x^{-1} \quad (1-4)$$

d — width of the tunnel, m ;

x — x-coordinate, $m, x \in [0.2219h - 0.0014, 0.2338d + 0.0364]$

y — y-coordinate, m.

(3) The sixth part

The feature of the sixth part has been studied using the above method. The length of the curve and the distance between the curve and the left wall have a perfect linear relation with the height of the tunnel wall, as shown in Figures 7 and 8.

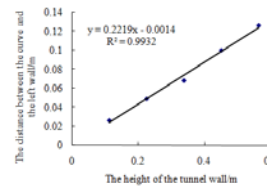


Figure 7: Relationship between the distance from part 6 to the left edge and the height of the wall.

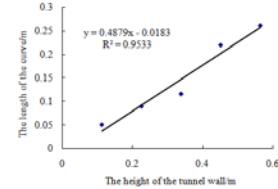


Figure 8: Relationship between the length of part 6 and the height of the wall.

Based on the above analysis, the characteristic equations of the sixth part can be represented by equations 1-5 and 1-6.

$$h_1 = 0.2219h - 0.0014 \quad (1-5)$$

$$h_2 = 0.4879h - 0.0183 \quad (1-6)$$

h — height of the tunnel wall, m;

h_1 — distance between the sixth part curve and the left wall, m;

h_2 — length of the curve, m.

Based on the above analysis, the characteristic equations of all the six parts have been developed as shown in Table 2.

Table 2: Characteristic equations of three hearts arch-section tunnel.

Serial number	Characteristic equations	span of the parameters
1	$3.2819r_1^{-2}\left(x - \frac{d}{2}\right)^2 + 8.408r_1^{-1.84}(y - 0.6142r_1 + 0.0138)^2 = 1$	$y \geq 0.9932h - 0.0087$
2	$x = d - 0.2219h + 0.0014$	$y \in [0.5053h + 0.0096, 0.9932h - 0.0087]$
3	$f(x) = 0.0236d^{1.965}(d - x)^{-1}$	$x \in (0.7662d - 0.0364, d - 0.2219h + 0.0014)$
4	$f(x) = 0.085d - 0.0034$	$x \in [0.2338d + 0.0364, 0.7662d - 0.0364]$
5	$f(x) = 0.0236d^{1.965}x^{-1}$	$x \in (0.2219h - 0.0014, 0.2338d + 0.0364)$
6	$x = 0.2219h - 0.0014$	$y \in [0.5053h + 0.0096, 0.9932h - 0.0087]$

5. CONCLUSIONS

In order to understand the air flow distribution in tunnels and measure the average velocity and ventilation volume accurately, the air flow structure and the average velocity points in different sizes of three hearts arch-section tunnels were investigated. The conclusions were as follows:

1) The air flow structure showed a circular distribution which was similar to the shape of three hearts arch-section under different ventilation velocities and cross section sizes. The shape of the cross section was the critical factor influencing the air flow distribution. The air flow velocity reached its maximum value in the center of the tunnel and decreased from the center to the tunnel wall.

2) The average velocity points were mainly close to the tunnel wall under different air flow velocities and the air flow velocity which was smaller than the average velocity would decrease more quickly when it was closer to the tunnel wall. The tunnel wall was also a critical factor influencing the air flow distribution.

3) Characteristic equations were developed to describe the average velocity distribution, which provide the theoretical basis for accurately measuring the average velocity and ventilation volume in mine tunnels.

6. ACKNOWLEDGEMENT

This research has been funded by the central university basic business expenses(15zy012)

7. REFERENCES

Chen W, Yu X. (2008) Wind flow field simulation on wind pink piping basing on FLUENT. Jiangsu Electrical Engineering, Volume 27, No.6, pp.72-75.

Ding C, He X, Nie B. (2015) Numerical and experimental research on "key ring" distribution of ventilation in mine tunnels. Journal of Liaoning Technical University (Natural Science), Volume34, No. 10, pp.1131-1136

Ding C. (2016) Numerical and experimental research on the average velocity distribution in the trapezoid tunnels. Journal of Safety Science and Technology, Volume12, No. 1.

Hao Y, Chen K, Jiang Z et al. (2011) Study on Amendment of Airflow Velocity in Roadway Based on CFD. Safety in Coal Mines, Volume42, No. 2, pp. 1-4.

Jia J. (2011) Simulation analysis on mine wind monitoring. Coal, Volume 20, No.12, pp. 73-74.

MA Y, Dong B, Zhang X et al. (2007) Study on Vent Mean Wind Velocity Measuring of Solar Collecting Wall in Solar House. Building Energy & Environment, Volume26, No. 4, pp. 60-63.

M.T. Parra, J.M. Villafuella, F. Castro, C. Me'ndez. (2006) Numerical and experimental analysis of different ventilation systems in deep mines. Building and Environment, Volume 41, pp. 87-93.

Tan X, Wang Z, Zhao Y. et al. (2013) Study on Velocity Profile of Turbulent Fluid in Narrow Deep Type Rectangular Channel. Journal of Sichuan University (Engineering Science Edition), Volume45, No. 6, pp.67-73.

Wang B, Luo Y, Zhao Y. (2013) Wind Tunnel Simulation on Wind Speed Distribution Characteristic in Rectangle Roadway Section Laid With Conveyor. Safety in Coal Mines, Volume44, No. 5, pp. 42-45.

Yin J, Lv H, Luan W. et al. (2008) Experimental research on velocity distribution law of trapezoidal channel section. Yangtze River, Volume39, No. 12, pp. 67-69.

Zhao D, Huang F, Chen S. et al. (2014) Relationship between point air velocity and average air velocity in circular roadway. Journal of Liaoning Technical University (Natural Science), Volume33, No. 12, pp.1654-1659.

Zhou X, Meng L, LI C. et al. (2012) Experimental study on determination and correction method of wind speed in circular pipe. Journal of Liaoning Technical University: Natural Science, Volume31, No. 6, pp. 801-804.

Application of a Ventilation Management Program for improved air quality

Euler De Souza *

Department of Mining Engineering, Queen's University, Kingston, Canada, K7L3N6

ABSTRACT

The purpose of Ventilation Management Systems is to ensure the health and safety of underground workers by creating and incorporating structured Plans, Procedures and Processes on the day-to-day operations of the mine ventilation system. Application of Ventilation Management Programs consists of audit, verification and corrective action procedures used to, i) ensure adherence to regulatory standards or to ii) return to compliance and safety standards when an upset condition arises. The present study describes how a Ventilation Management Program can be developed and implemented to ensure regulation compliance, to increase safety, to improve operational efficiency and to reduce the operating costs of an operating mine. A case study is presented in which air quality conditions have been substantially improved with the development and implementation of a Ventilation Management Program for an operating underground hard rock mine.

KEYWORDS: mine ventilation; ventilation management; air quality; ventilation efficiency

1. INTRODUCTION

Mine ventilation systems must not only provide for the health and safety of underground personnel, but also operate in compliance with regulatory bodies. Studious day-to-day management of the mine ventilation system is crucial to meet all the objectives of the ventilation system. A Ventilation Management System is used to provide, measure, and control the quantity and quality of airflow throughout the mine ventilation network.

The Ventilation Management System consists of a series of documents describing means of auditing and controlling the mine ventilation system in order to ensure the system meets all regulatory and safety requirements.

Five main document types form the structure of a Ventilation Management System: Standards and Guidelines, Code of Practice, Procedures, Work Instructions and Directives (Figure 1). These documents provide guidelines for applying audit, verification and correction processes used to ensure the mine ventilation system operates within compliance standards.

The Standards and Guidelines constitute the foundation of the management program. This support documentation is a handbook providing a detailed description of the ventilation system, including all design and operational aspects of the ventilation network. The Code of Practice is documentation that defines the minimum operating standards and action levels based on regulatory bodies, and provides appropriate corrective and emergency action plans when an upset condition

exists. Procedures is documentation that explains inter-departmental activities and each department's or individual's role in specific work procedures. Work Instructions is documentation describing the process of a specific procedure and task; including who is involved, how to do the task, and what materials or supporting documentation is needed. Directives is documentation issued for any changes to the ventilation that will ensure the correct installation or change to any design, equipment or condition.

2. EXECUTION OF A VENTILATION MANAGEMENT PROGRAM

Execution of a Ventilation Management Program follows an iterative process, as illustrated in Figure 2.

Management Plans, which are carried out on a daily basis, are an audit of the state of the entire mine ventilation system. They include detailed inspections of all components and appliances, pressure and flow surveys of the network and air quality surveys. Verification Programs are used to assess the information collected from the management plans in order to verify if the ventilation system is in compliance and if it meets all defined objectives of the program. If the verification process indicates the system not to be in compliance, then action plans and ventilation directives are initiated to restore the system to compliance. Action Plans and corresponding directives can also be directly launched in response to upset ventilation conditions or when problems are encountered during an inspection.

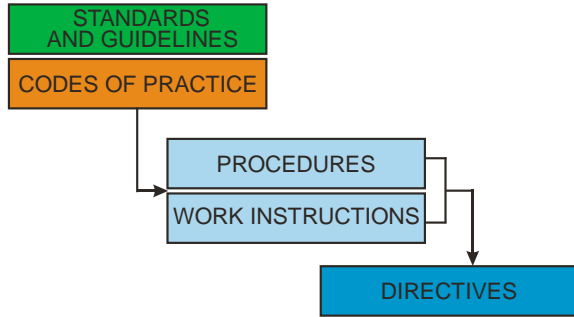


Figure 1: Typical structure of a Ventilation Management System.

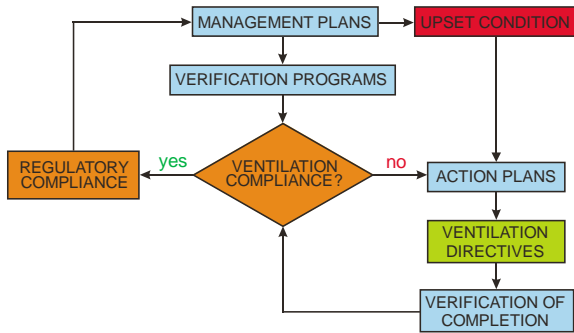


Figure 2: Execution process of a Ventilation Management Program.

3. OPPORTUNITIES AND BENEFITS

The easy to implement iterative framework of a Ventilation Management Program (Figure 2) allows mining operations to efficiently and consistently audit the mine ventilation system.

Significant benefits can be gained from day-to-day management of the mine ventilation system. It ensures: that the ventilation system performs according to design; that all ventilation appliances operate efficiently and economically; an adequate air supply to all active workings; that the mine atmosphere meets quality conditions; compliance with all regulatory requirements; safety; improved system economics.

4. CASE STUDY

A case study is presented in which air quality conditions have been substantially improved with the development and implementation of a Ventilation Management Program for an operating underground hard rock mine.

A two-phase integration approach of the Management Program was successfully completed for the mine. The first phase involved regional leakage control, resulting in an increase in airflow volume in the main production blocks by 28% and

the second phase involved improvements in local ventilation installations in the main production levels, resulting in substantial improvements in underground environment conditions (air quality, dust and heat). This permitted uninterrupted production with much improved safety, reduced re-entry times and lower costs.

The underground mine applies sublevel stoping with backfill to mine gold at a rate of 900 tonnes per day. Mining activities exist at the lower levels of the mine (below 1030 level) with 7 upper levels being mined out. Overall underground flow requirements at the underground production blocks approximate 118 m³/s, determined from the production rate and operating diesel fleet. The mine utilizes a push system with a primary surface air fan installed on a dedicated fresh air raise. Figure 3A presents a distribution of mine flows through the dedicated fresh air raise prior to application of the Management Program.

A detailed ventilation audit was conducted to assess the primary fresh air system prior to implementation of the first phase Ventilation Management Program.

Over the years, prior to application of the Ventilation Management Program, the mine had to limit use of its available diesel fleet and also had to curtail development and production activities due to limitations in fresh air supply to the active levels (available 94 m³/s versus required of 118 m³/s) and also had to limit stope blasting and mucking cycles due to excess concentrations of NO₂ (well above the limit of 3 ppm).

The fresh air system consisted of a surface fresh air fan of 2.13 m casing diameter and 1.27 m hub diameter. It had a 597 kW motor installed, operating at 1200 rpm. The fan was delivering 142 m³/s at a static pressure of 1.84 kPa. The brake power was 539 kW and the annual operating cost was \$377,650. The fan operating point is shown in Figure 4. With the fan delivering 142 m³/s, the flow reaching the active mining area was 94 m³/s; leakage was estimated at 33.6% (Figure 3A). As previously mentioned, leakage occurred at raise connections to 7 mined out levels, above the active mining levels.

As part of the Ventilation Management Program execution, extensive work was conducted to reduce leakage by sealing off and shotcreting all bulkheaded raise connections to the 7 upper inactive levels. Leakage was reduced to 7.2% from 33.6% (Figure 3.B) Where level access was required, appropriate door locks were installed. With the sealing off of the raise connections, the surface fan was now delivering 130 m³/s at a static pressure of 2.38 kPa (Figure 4).

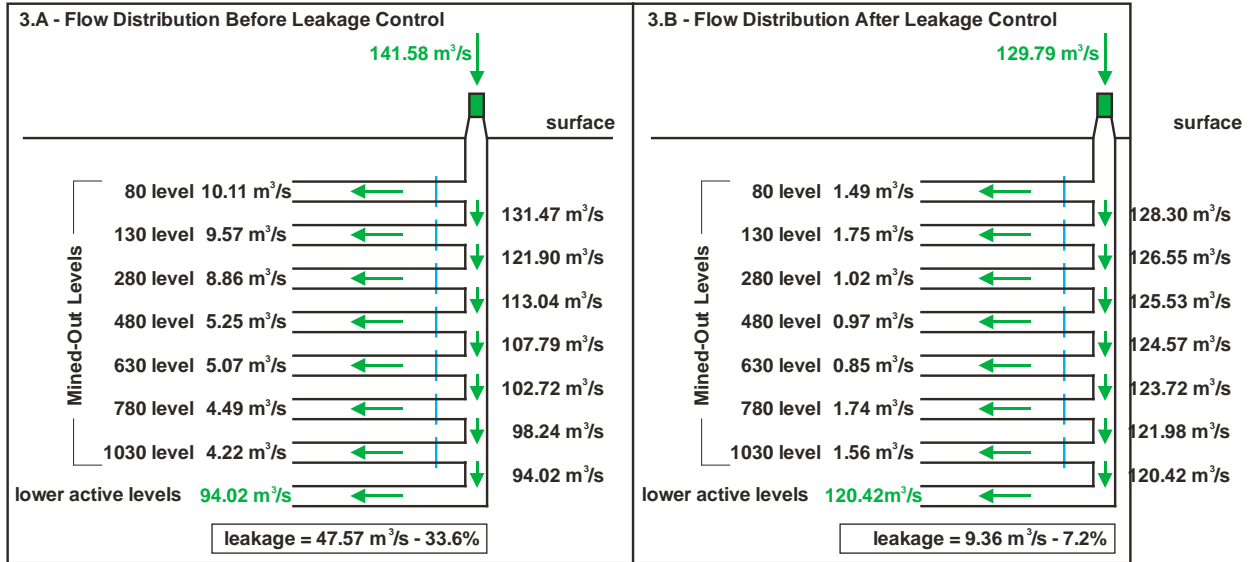


Figure 3: Mine ventilation schematic.

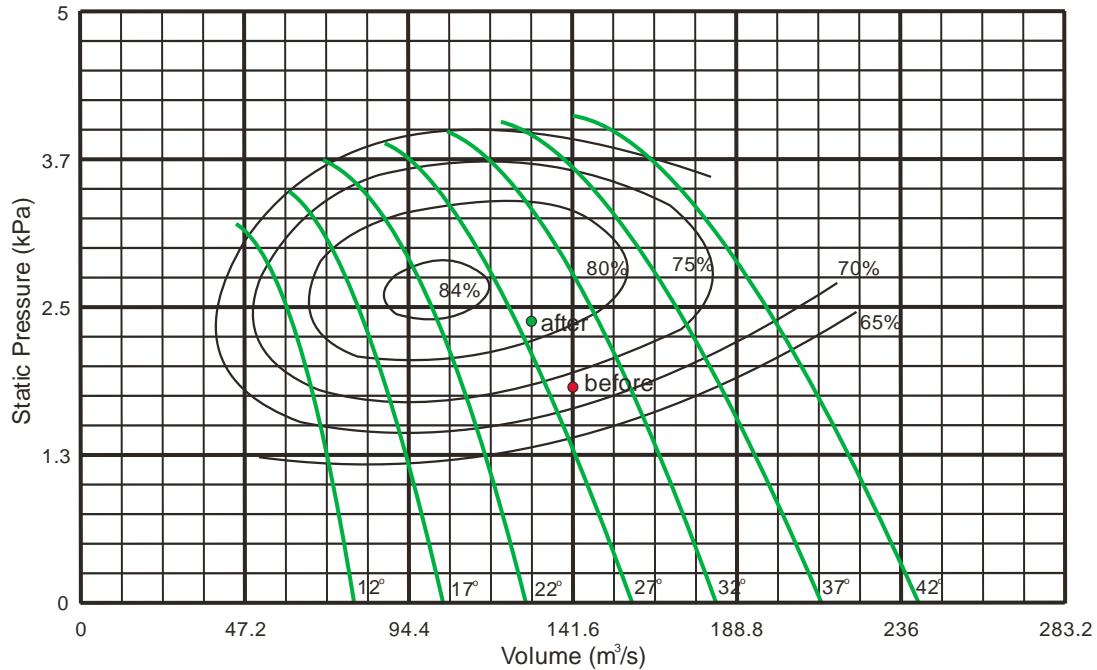


Figure 4: Main fan operation before and after leakage control.

The brake power was 502 kW and the annual operating cost per fan was \$352,018. With the fan now delivering 130 m³/s, the flow reaching the active mining area was maintained at 121 m³/s, above the production based requirements of 118 m³/s. Leakage was estimated at 7.2%.

The reduction in air leakage to 7.2% from 33.6% permitted an overall annual savings in fan operating cost of \$25,630 or a 7% reduction in operating costs. Even though the reduction in fan operating costs is

relatively small, the operation now meets the flow requirements at all active levels, being able to safely achieve and maintain full production activities.

Having successfully improved the mine overall flow conditions, the second phase of system implementation was initiated. This Ventilation Management Program phase aimed at improving safety and air quality conditions in all producing faces.

First, a quality assessment of ventilation installations and airflows in all production stope access drawpoints was performed. To meet production requirements, 10 active faces were ventilated at the mine. All access crosscuts to the sublevel stopes were ventilated with auxiliary ventilation. Face ventilation requires a flow of $9 \text{ m}^3/\text{s}$ per cross-cut, based on the production equipment utilized. Flow surveys at all active faces indicated flows ranging between $5 \text{ m}^3/\text{s}$ and $7.4 \text{ m}^3/\text{s}$, with 3 faces meeting the minimum flow requirements. The auxiliary fans are 1.22 m in diameter with 0.69 m hubs, operating with 22.4 kW motors and running at 880 rpm. Layflat duct of same diameter are utilized.

Detailed inspections and surveys of the 10 duct installations classified the installation practices as

'poor', with much higher than desired static pressure losses along each duct column. Some fans were not correctly hung and duct-to-fan connections were very leaky. Several of the duct columns were not installed straight and had severely damaged sections.

The fan operating point for one of the surveys is presented in Figure 5. The system produced $7.4 \text{ m}^3/\text{s}$ at the face with the fan operating at $17 \text{ m}^3/\text{s}$. Leakage was estimated at 57%. The fan total pressure was 0.72 kPa and the brake power 15.4 kW. The fan annual operating cost was \$11,943. High diesel exhaust gas concentrations were measured at the faces due to insufficient dilution ventilation air volumes.

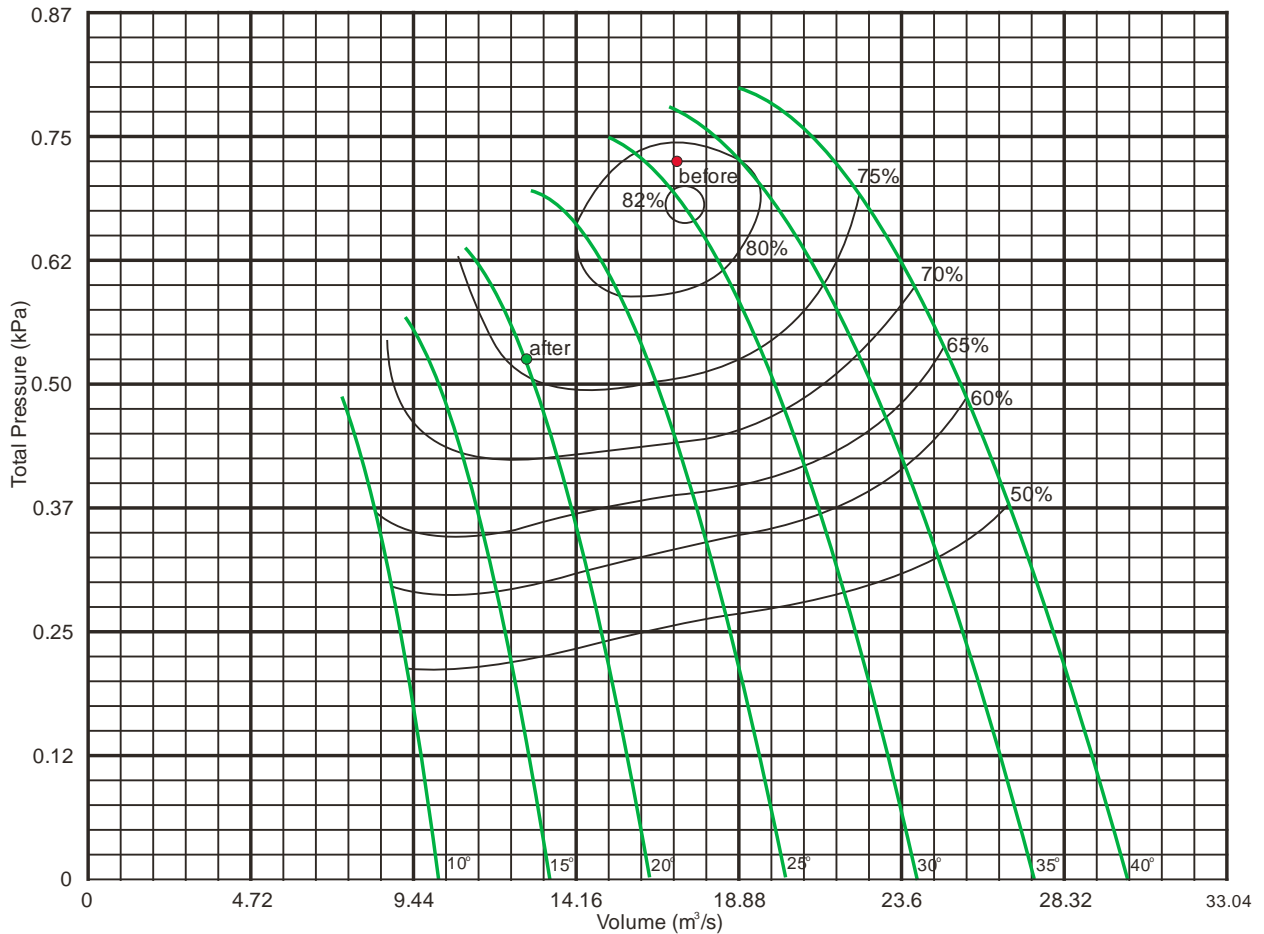


Figure 5: Auxiliary fan operation before and after system installation improvement.

The auxiliary system installation was improved (duct column repaired, column straightened, connections tightened, etc.) to reduce resistance pressures and minimize leakage. The fan blade pitch angle was changed from 30° to 20° . The system produced $9.44 \text{ m}^3/\text{s}$ at the face with the fan operating

at $12.75 \text{ m}^3/\text{s}$ (Figure 5). Leakage was estimated at 26%, a reduction of more than half the original leakage. The fan total pressure was 0.52 kPa and the brake power decreased to 8.77 kW. The annual operating cost for the single fan was reduced to \$6,822, representing a reduction in cost by 43%.

Having now achieved the required flow at the production face the mine could operate safely and in regulatory compliance.

Following this successful application of the Ventilation Management Program, all additional 9 drawpoint auxiliary fan installations were similarly investigated and improved, with annual savings in fan operating costs approximating \$93,000, representing a 58% reduction in operating costs.

The successful application of the 2-phase Ventilation Management Program resulted in overall annual cost savings of \$118,650 for the mine. More importantly, the mine was now operating safely and in compliance with regulations.

The mine continues to incorporate the Management Program in its day-to-day production operations, resulting in increased safety, improved air quality, reduced post blast re-entry times, regulatory compliance and cost savings.

5. CONCLUSIONS

The structure and process implementation of a Ventilation Management Program have been presented in this paper.

Day-to-day application of the Ventilation Management Program ensures the mine operation meets all regulatory requirements and cares for the health and safety of all personnel working underground.

A case study for an operating underground hard rock mine has been presented to demonstrate the functionality of the management program and the safety, efficiency and economic benefits realized by the mine.

6. REFERENCES

De Souza, E. (2015) Mine Ventilation System Management. Section 19. Mine Ventilation Course Notes. Kingston, ON. 16p.

Numerical Study of simultaneous methane and coal dust dispersion in a room and pillar mining face

Yueze Lu ^a, Saad Akhtar ^a, Agus P. Sasmito ^{a,*}, Jundika C. Kurnia ^b

^a Department of Mining and Materials Engineering, McGill University, Montreal, Canada H3A0E8

^b Department of Mechanical Engineering, Universiti Teknologi PETRONAS, 32610 Bandar Seri Iskandar, Perak Darul Ridzuan, Malaysia

ABSTRACT

In underground coal mines, uncontrolled accumulation of methane and fine coal dust often leads to serious accidents such as explosions. Therefore, methane and dust dispersion in underground mines is closely monitored and strictly regulated. Accordingly, significant efforts have been devoted to study methane and dust dispersion in underground mines. In this study, methane emission and dust concentration are numerically investigated using the computational fluid dynamics (CFD) approach. Various possible scenarios of underground mine configurations are evaluated. The results indicate that solitary existence of a continuous miner adversely affects the airflow and leads to increases in both methane and dust concentrations. Nevertheless, it is found that the negative effects of a continuous miner presence on concentrations can be minimized or even neutralized by operating the scrubber fan on suction mode. In addition, it was found that the combination of scrubber fan on suction mode and brattice results in the best performance of methane and dust removal from the mining face.

KEYWORDS: dust; methane; mine ventilation; mining machine

1. INTRODUCTION

Coal mining is considered one of the world's most dangerous operations. There are many hazards associated with coal mining: explosion, structure collapse, hazardous gasses and particulates, moving vehicles, and lack of respirable air. Among these hazards, the most severe is explosion. Firedamp explosions, majorly caused by methane, can trigger more dangerous coal dust explosions, which lead to collapsed areas, trapped personnel, and worker death. Even in developed countries, coal related fatalities are considerably high. For example, more than one hundred thousand coal mine explosion fatalities have been recorded in the U.S. (U.S. Department of Labour, 2015). The situation is more alarming in developing countries, as indicated by the increase of the occurrences and casualties in China (Zheng, et al., 2009). This situation has encouraged the worldwide mining community to explore and evaluate solutions to reduce/eliminate the hazards causing the explosions. A vast number of studies have been conducted and reported. The majority of research has been focused on mine ventilation, as it directly affects the hazardous methane and dust accumulations in the mining face.

Pioneer studies on mine ventilation were directed at the fundamental aspect of mine ventilation. Kaliev and Akimbekov (1990) developed an air motion model based on Bernoulli equation and Runge-Kutta method. The results revealed that

theoretical and experimental airflow rates differ by less than 10%. Riley and Edwards (1991) experimented on the methane drainage system in mining. It was found that the methane drainage system is more efficient at advanced mining as compared to that at retreat mining. Subsequently, computational fluid dynamics (CFD) are widely utilized in mine ventilation studies due to its capability to predict methane dispersion. Some examples are studies conducted by Srinivasa et al. (1993), Uchino and Inoue (1997), and Tomate et al. (1999).

Recently, research has been directed at exploring ventilation methods and designs. This is mainly attributed to the fact that fundamentals have been established and significant advancement in computational power allows CFDs simulations to be run at significantly reduced cost. Parra et al. (2006) examined ventilation near mining faces and found that blowing ventilation, in terms of dust control, offers better dust dispersion than exhaust ventilation if the setback distance is 6m or more. Wu et al. (2007) studied three-dimensional gas transfer in coal mining and discovered that gas concentration along the intake side is lower compared to the return airway side. Later, Torano et al. (2009) justified that simulations are consistent with experimental data, and also demonstrated that CFDs are necessary to analyze ventilation systems. Rodriguez and Lombardia (2010) found that different stone types

*Corresponding author – email: agus.sasmito@mcgill.ca

result in different methane emissions. Sasmito et al. (2012) examined four different turbulence models: Spallart-Almaras, k-epsilon, k-omega and Reynolds Stress Model (RSM). It was found that the Spallart-Almaras model, which consumes the least computational power, would be sufficient to predict flow behavior. Another finding is that in typical room and pillar mining, flow stopping design can largely affect methane concentration. It is also found that the brattice-exhausting system leads to the lowest methane concentration. Kurnia et al. (2014) numerically examined the relation between methane sources and methane dispersion as well as methane distribution within the mining tunnel. Later, Kurnia et al. (2014) investigated intermittent ventilation systems and discovered a possible electricity saving plan. Zhou et al. (2015) simulated scenarios with the existence of a continuous miner. The important findings from their study are 1) only very limited airflow could reach the mining face compared to total airflow, 2) methane release efficiency is not considerably affected by different source locations, however, it is strongly influenced by the amount of methane released.

Dust concentration is another attractive research topic. Inhaling respirable dust can adversely affect workers' health. Moreover, high dust concentration can trigger dust explosions that be a disaster to the mine. The water spray system has been widely used due to its simplicity and effectiveness. As early as 1988, Aziz et al. discovered the system and thus, water is used to reduce dust content. Recent results show that water can reduce dust concentration up to 60% (Colinet et al., 2010). Tornado et al. (2010) extended their own research from methane to dust and developed a CFD model to match with field data. Wei et al. (2011) simulated different scenarios of different exhausting pipe locations and diameters to reduce dust concentrations. Dong et al. (2012) tested a methane-air explosion mechanism with the existence of coal dust and obstacles in a pipe, but lacked theory to explain the results. Zhou et al. (2013) investigated dust diffusion in a specific forced-exhaust hybrid tunnel with a continuous miner. Wang et al. (2015) also did similar dust investigation in a forced-exhausted hybrid tunnel for a rectangular-shaped laneway. Kurnia et al. (2014) investigated different ventilation tools on dust removal and energy saving perspectives and found that brattice generally have the best dust removing efficiency, at the cost of more energy consumption. Kurnia et al. (2015) investigated brattice setup and dust control in a typical mine tunnel. Hu et al. (2015) simulated respirable dust characteristics in another typical mine tunnel.

Many studies have investigated methane and dust concentrations separately. However, none of them have focused on the existence of both methane and dust despite them both being critical pollutants in coal mines. This study investigates the flow behavior and methane and dust dispersion characteristics in the mining face of an underground coal mine. Moreover, a continuous miner and also ventilation tools are included in the study since the mining machine takes up a very large area inside the active mining end, which is likely to cause flow changes (compared to scenarios without a continuous miner) and possibly dead zones for both methane and dust.

2. MODEL FORMULATION

A three-dimensional model is developed to imitate the mining region, as shown in Figure 1. Ventilation air is supplied from inlet at a speed of 2 m/s. At the active mining face, methane is leaking into the tunnel at a speed of 0.002874 m/s and dust is generated by continuous miner at speed of 1 m/s with flow rate of 0.0062 kg/s. Detailed properties are summarized in Table 1.

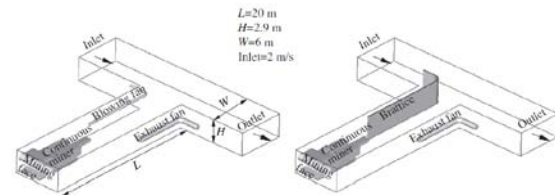


Figure 1: Schematics of mining face with mining machine and auxiliary ventilation: blowing-exhausting (left) and brattice-exhausting (right) (Kurnia, et al., 2014b).

Table 1: Geometric and operating parameters used.

Property	Value
Injection type	Surface (Mining surface)
Density (kg/m ³)	1400 (Coal high value)
Diameter distribution	Rosin-rammler
Diameter range (m)	1×10 ⁻⁶ to 1×10 ⁻⁴
Mean diameter (m)	1×10 ⁻⁵
Spread parameter	2.78
Dust velocity (m/s)	1
Total flow rate (kg/s)	0.0062
Air curtain width (m)	0.2
Jet velocity (m/s)	12
Air velocity (m/s)	2
Tunnel height (m)	2.9
Tunnel length (m)	20
Tunnel width (m)	4
Brattice space (m)	0.5

For the sake of brevity, the mathematical formulation is not repeated here. The interested

reader may refer to earlier publications (Kurnia et al., 2014a; Kurnia et al., 2014b) for details.

2.3 Boundary Conditions

The boundary conditions are prescribed as follows:

- (i) Inlet: air flows into the tunnel is set to have velocity of 2 m/s
- (ii) At the mining face: methane is released at total flow rate of 0.05 m³/s and dust is generated at total flow rate of 0.0062 kg/s
- (iii) At the outlet: stream-wise gradient of the temperature is set to zero and the pressure is set to standard atmospheric pressure (1 bar).
- (iv) At walls: the standard wall function is used in all simulations.

3. RESULTS AND DISCUSSION

In this study, a total of nine possible scenarios are explored under both constant methane emission and dust emission from discrete sources. Table 2 illustrates the detailed case configurations and features with respect to their specific case numbers. For abbreviation purposes, only case numbers are presented in the figures afterward. The standard k-ε turbulence model is used in this study since it provides the required balance between computational time and accuracy. Flow validation for a similar geometry has been performed in another study (Kurnia, et al., 2014a).

Table 2 Cases with their features.

Case 1	No continuous miner, no ventilation tools
Case 2	Continuous miner with scrubber fan off, no ventilation tools
Case 3	Continuous miner with scrubber fan on injection mode, no ventilation tools
Case 4	Continuous miner with scrubber fan on suction mode, no ventilation tools
Case 5	Continuous miner with scrubber fan on suction mode, with ventilation fan blowing air into mining face
Case 6	Continuous miner with scrubber fan on suction mode, with ventilation fan sucking air out of mining face
Case 7	Continuous miner with scrubber fan on suction mode, with brattice installed
Case 8	Continuous miner with scrubber fan on suction mode, with brattice and suction fan
Case 9	Continuous miner with scrubber fan on suction mode, with blowing fan and suction fan

Figure 2 shows the velocity distribution at the mining face for cases 1 to 4. Previous work by Sasmito et al. (2013) shows that for cases with no auxiliary ventilation, the ventilation air is unable to reach the mining face. The same trend is observed in

the present study, as reflected in Figure 2a. As mining machinery is added, the flow behavior at the face changes. Figure 2b demonstrates that the presence of machinery presents flow obstruction thus inducing flow separation resulting in increased recirculation. Case 3 depicts the flow field with the scrubber fan turned on, which creates high air velocity flows to the face. Closer inspection reveals that the blowing air from the scrubber is not sufficient to push air leaving the working area and thus creates a recirculation zone (Figure 2c). In Case 4, on the other hand, the scrubber fan is in exhausting mode and is found to be able to provide sufficient flow from mining face to the laneway tunnel, and thus no recirculation is observed.

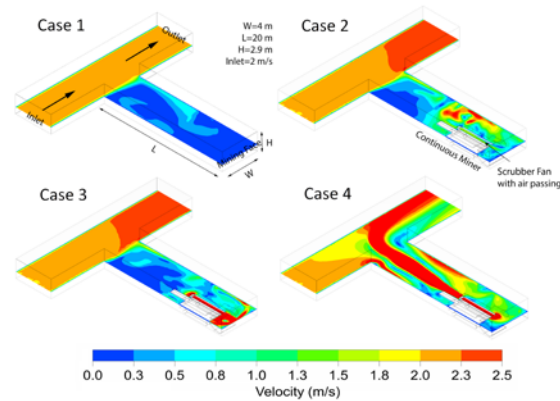


Figure 2: Velocity contour at height of 1 m from the tunnel floor.

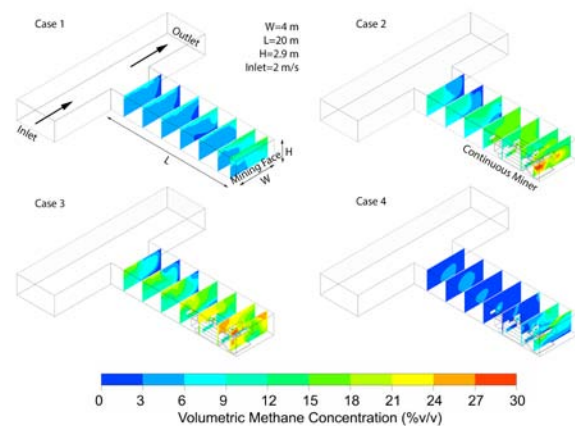


Figure 3: Contour of methane concentrations at 1 m, 3 m, 6 m, 9 m, 12 m, 15 m, 18 m away from mining face.

The presence of recirculation flow, mining machinery and a scrubber fan is expected to have a direct impact on methane and dust distributions. Figure 3 shows the distribution of methane concentration along the active mining tunnel. For instance, the presence of mining machinery and

recirculation flow increases methane distribution at the face as can be inferred from Figure 3a, 3b, and 3c. Case 2 is found to have highest methane concentration, whereas the lowest methane concentration is found in Case 4 where the scrubber fan is in exhausting mode. Note that as compared to earlier work by Sasmito et al (2013), the methane concentration in this case is up to 30% higher. This discrepancy can be attributed to the fact that the mining tunnel used in this study is longer (20 m) as compared to 12 m used in Sasmito et al. (2013). Hence, it can be concluded that extra length in active room and pillar mining significantly reduces ventilation efficiency.

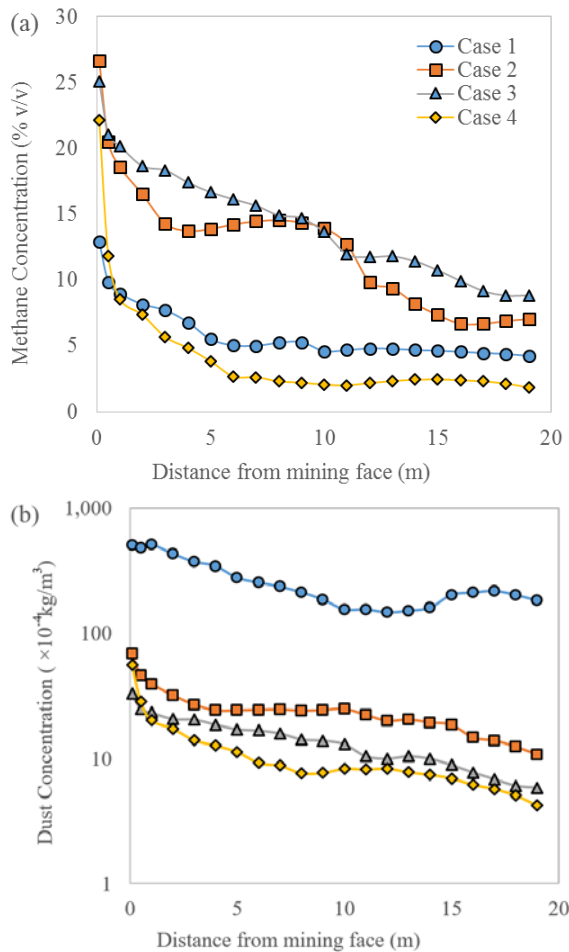


Figure 4: (a) Average methane concentration, (b) Average dust concentration, along the tunnel.

Figure 4a presents the average methane concentration at various distances along the tunnel. The result clearly demonstrate that Case 4, where the fan is in suction mode, provides the best effectiveness in terms of low methane concentration. The percent increase in methane concentration for Cases 2 and 3 is quite significant as compared to Case 1. It is

because a continuous miner takes up a large space in the tunnel and obstructs ventilation air which results in smaller volume in the active mining tunnel resulting in increased methane concentrations. Trends in Figure 4a also reveal that Case 3, in which the scrubber fan is turned on in blowing mode, increases the concentrations in the mining tunnel as compared to Case 2 where the scrubber fan is turned off. This can be explained by the fact that a blowing fan creates stronger recirculation flow while it is unable to push the methane out towards the main tunnel. Therefore, Case 3 is non-effective or can even be concluded as counter-productive to reduce methane concentration in the tunnel. Conversely, Case 4 is found to be beneficial in reducing methane concentration.

The average dust concentration along the tunnel is presented in Figure 4b. Case 1 shows the highest dust concentration among others, as there is insufficient airflow to remove dust from the mining face. The cases with a continuous miner in general yield lower dust concentration due to higher flow recirculation, which somehow is effective in dispersing the dust. Case 2, in contrast to methane control, gives rise to the dust concentration, as there is no auxiliary ventilation turned on. Case 3 with a blowing scrubber fan has a positive effect on dust control, however the exhaust scrubber fan performs best in mitigating dust concentration.

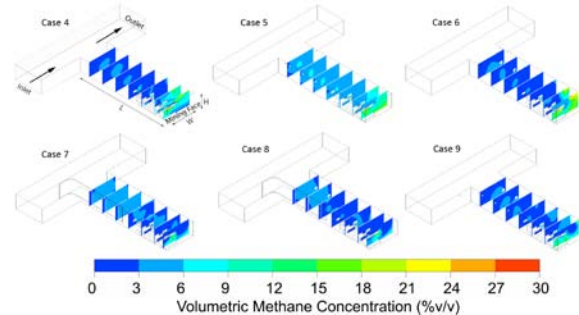


Figure 5: Contour of methane concentrations at 1 m, 3 m, 6 m, 9 m, 12 m, 15 m, 18 m away from mining face.

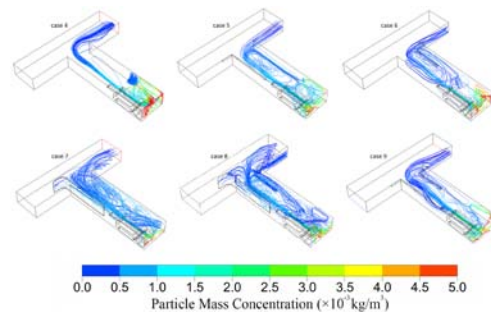


Figure 6: Air outflow from mining face, colored by dust concentration.

Figure 5 shows the performance with regard to methane concentration for Cases 4 to 9. Note that all the cases in Figure have the continuous miner on suction mode and Case 4 serves as the base case to the rest of Cases 5 to 9. Compared to Case 4, Case 5 is found to be counter-productive as it yields higher methane concentration due to recirculation flow created by an additional blowing auxiliary fan. This observation is mirrored in Figure 6b. Case 6 is effective in reducing methane at 6-20 m range from mining face but it is found less effective in reducing the most critical area at the mining face due to recirculation flow (Figure 6c). Cases 7, 8 and 9 are relatively effective in reducing methane concentration close to the mining face, which can be attributed to there being no recirculation flow in the working area for these cases.

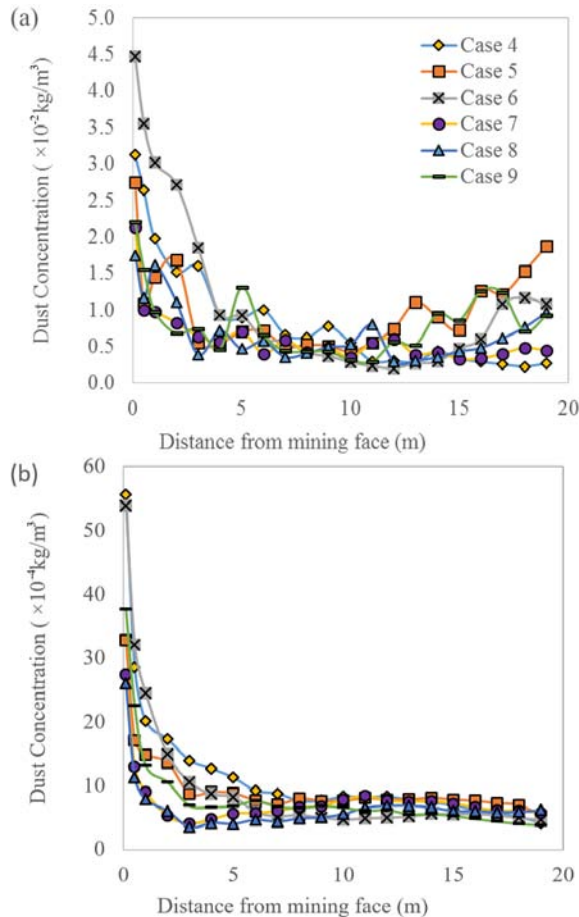


Figure 7: (a) Maximum dust concentration and (b) Average dust concentration along the tunnel.

Looking at the maximum and average dust concentrations, **Error! Reference source not found.** reveals that the maximum dust concentration is about one order-of-magnitude higher than that of average concentration. From the maximum dust

concentrations (Figure 7a), Case 7 gives the best dust removal ability followed by the blowing-exhaust configuration (Case 9) and brattice-exhaust (Case 8). From the average dust concentration perspective, Figure 7b shows that brattice exhaust configuration (Case 8) performs best in removing dust from the mining face, followed by brattice, which has a slightly inferior performance.

4. CONCLUSIONS

A three-dimensional CFD model for a mining face with mining machinery and auxiliary ventilation have been developed and presented. To take into account the turbulence effect, the standard k-epsilon model is used and selective computational results for nine different cases are presented. The effect of a continuous miner presence as well as additional ventilation are evaluated and discussed with the focus being methane and dust dispersion and accumulation.

Several important findings of the study are that (i) higher air flow rate generally yields lower methane and dust concentrations (ii) the presence of a continuous miner negatively impacts the airflow in active mining tunnel and increases concentrations by taking up a large volume in the tunnel and blocking almost half of the tunnel section area, and (iii) a scrubber fan turned to suction mode could counter the continuous miner impact by reducing a significant amount of methane and dust.

Moreover, it is found that brattice cases (Cases 7 and 8) along with the blowing exhaust case (Case 9) are more effective in reducing methane and dust concentrations whereas the solo use of blowing or exhausting fan is not effective. Future studies will be focused on reducing methane concentration to even lower levels as current cases contain quite high levels of methane at places near the mining face. In addition more tunnel geometries will be evaluated and filters for fans will be added into the simulation model to investigate their effectiveness in reducing dust concentrations.

5. ACKNOWLEDGEMENT

The high performance computing (HPC) facility and financial support from McGill University and NSERC-Discovery Grant RGPIN-2015-03945 is gratefully acknowledged.

6. REFERENCES

Aziz, N. I., Johnston, A. J. and Craft, T., (1988). Dust suppression in coal mines using sprayed screens. *Mining Science and Technology*, pp. 177-188.

Colinet, J. F. et al., (2010). Best practice for dust control in coal mining. Pittsburgh, National

Institute for Occupational Safety and Health, Office of Mine Safety and Health Research.

Dong, C., Bi, M. and Zhou, Y., (2012). Effects of obstacles and deposited coal dust on characteristics of premixed methane-air explosions in a long closed pipe. *Safety Science*, pp. 1786-1791.

Hu, S., Wang, Z. and Feng, G., (2015). Temporal and Spatial Distribution of Respirable After Blastking of Coal Roadway Driving Faces: A Case Study. *Minerals*, pp. 679-692.

Kaliev, S. G. and Akimbekov, A. K., (1990). Modeling air motion in a ventilated mine working with a flow-through ventilation scheme for the excavated section. *Soviet Mining*, pp. 553-556.

Kurnia, J. C., Sasmito, A. P., Hassani, F. P. and Mujumdar, A. S., (2015a). Introduction and evaluation of a novel hybrid brattice for improved dust control in underground mining faces: A computational study. *International Journal of Mining Science and Technology*, pp. 537-543.

Kurnia, J. C., Sasmito, A. P. and Mujumdar, A. S., (2014a). CFD Simulation of methane dispersion and innovative methane management in underground mining faces. *Applied Mathematical Modelling*, pp. 3467-3484.

Kurnia, J. C., Sasmito, A. P. and Mujumdar, A. S., (2014b). Dust dispersion and management in underground mining faces. *International Journal of Mining Science and Technology*, pp. 39-45.

Kurnia, J. C., Sasmito, A. P. and Mujumdar, A. S., (2015b). Simulation of a novel intermittent ventilation system for underground mines. *Tunnelling and Underground Space Technology*, pp. 206-215.

Parra, M. T., Villafruela, J. M., Castro, F. and Mendez, C., (2006). Numerical and experimental analysis of different ventilation systems in deep mines. *Science and Direct*, pp. 87-93.

Riley, P. A. and Edwards, J. S., (1991). The measurements and comparison of methane drainage efficiencies in longwall advance and retreat workings. *Mining Science and Technology*, pp. 1-15.

Rodriguez, R. and Lombardia, C., (2010). Analysis of methane emissions in a tunnel excavated through Carboniferous strata based on underground coal mining experience. *Tunnelling and Underground Space Technology*, pp. 456-468.

S., T., Uchino, K. and Inoue, M., (1999). Methane concentration at heading faces with auxiliary ventilation. In: *Proceeding of the 8th US Mine Ventilation Symposium*. SME, Littleton, pp. 187-192.

Sasmito, A. P., Birgersson, E., Ly, H. C. and Mujumdar, A. S., (2012). Some approaches to improve ventilation system in underground coal mines environment - a computational fluid dynamic

study. *Tunnelling and Underground Space Technology*, pp. 82-95.

Srinivasa, R. B., Baafi, E. Y., Aziz, N. I. and Singh, R. N., (1993). Three dimensional modeling of the 6th US mine ventilation symposium. SME, Littleton, pp. 287-292.

Torano, J., Torno, S., Menendez, M., Gent, M., Velasco, J., (2009). Models of methane behaviour in auxiliary ventilation of underground coal mine. *International Journal of Coal Geology*, pp. 35-43.

Torano, J., Torno, S., Menendez, M. and Gent, M., (2010). Auxiliary ventilation in mining roadways driven with roadheaders: Validated CFD modelling of dust behaviour. *Tunnelling and Underground Space Technology*, pp. 201-210.

U.S. Department of Labour, (2015). Mine Safety and Health Administration –MSHA – Protecting Miners’ Safety and Health since 1978. Table: Coal Fatalities for 1900 Through 2014. [Online].

Uchino, K. and Inoue, M., (1997). Auxiliary ventilation at a heading of a face by a fan. In: *proceeding of the 6th US Mine Ventilation Symposium*. SME, Littleton, pp. 493-496.

Wang, Y., Luo, G., Geng, F., Li, Y. and Li, Y., (2015). Numerical study on dust movement and dust distribution for ventilation system in a laneway of coal mine. *Journal of Loss Prevention in the Process Industries*, pp. 146-157.

Wei, N., Zhongan, J. and Dongmei, T., (2011). Numerical simulation of the factors influencing dust in drilling tunnels: its application. *Mining Science and Technology (China)*, pp. 11-15.

Wu, Z., Jiang, S., He, X., Wang L. and Lin, B., (2007). Study of 3-D Numerical Simulation for Gas Transfer in the Goaf of the Coal Mining. *Journal of China University of Mining and Technology*, pp. 152-157.

Zheng, Y., Feng, C., Jing, G., Qian, X., Li, X., Liu, Z. and Huang, P., (2009). A statistical analysis of coal mine accidents caused by coal dust explosions in China. *Journal of Loss Prevention in the Process Industries*, pp. 528-532.

Zhou, G., Wang, D., Cheng, W. and Cao, S., (2013). Numerical Simulation Research on Gas-dust Flow Field of Forced-exhausted Hybrid Ventilation in Whole Rock Mechanized Heading Face. *Applied Mechanics and Materials Vols*, pp. 873-879.

Zhou, L., Prithcharb, C. and Zheng, Y., (2015). Computational fluid dynamic modeling of methane distribution at a continuous miner face under various methane release conditions. *Blacksburg, U.S. North American Mine Ventilation Symposium*.

Reducing Heat Stress Exposure in Mines

Ryan Anderson^{a,*}, Euler De Souza^b

^a K2 Mine Production, Mosaic Potash, Esterhazy, Canada, S0A2A0
Department of Mining Engineering, Queen's University, Kingston, Canada, K7L3N6

^b

ABSTRACT

Heat management must be maintained within the mine working environment to minimize stress on equipment and personnel. Proper application of engineering protocols and work practice controls will have a direct impact on the health and safety of workers and on productivity. Using monitoring stations placed in strategic locations throughout the mine to capture the environmental conditions, various strategies can be used in the planning and prevention of potential hazard exposure. Economic analysis is used to select the most feasible strategy for heat stress control.

1. INTRODUCTION

Heat management is an important factor as mines expand to meet the demand of their growing workforce and extraction rates. The introduction of new equipment and manpower puts additional demands on the ventilation system that is often the primary means of heat control. When mines plan to place additional significant heat sources into the ventilation system a proper methodology used to monitor, establish, and control heat stress with economically viable solutions must be established.

This paper presents a step by step methodology for 1) identifying heat sources, 2) establishing a heat monitoring program, 3) calculating heat loads underground, 4) applying heat management strategies, and 5) selecting engineering solutions to heat control.

A detailed case study, based on a heat stress management study conducted for an underground potash mine is presented to illustrate the application of the proposed strategy.

2. HEAT MANAGEMENT METHODOLOGY

A proposed methodology for establishing a heat management program is presented. In the methodology, heat sources are identified, data is collected from environmental monitoring stations and calculated heat loads are assessed using ventilation modelling software. Application of specific management control strategies allows one to eliminate heat stress and improve safety.

2.1 Identification of heat sources

All heat sources must be identified in the area of interest and quantified in terms of heat load. Such sources include strata heat, auto-compression, ground water, machinery (loaders, trucks, drills, conveyors, scrapers, pumps, fans, transformers), blasting, rock

movement, oxidation, cables, pipelines, lights, human metabolism, etc.

2.2 Establishment of a heat monitoring program

There is a wide range of environmental monitoring programs that are commonplace throughout the mining industry. Mining regulations typically set minimum standards regarding the monitoring and recording of the environment factors relating to heat found within the underground environment. The basic method frequently employed is the use of handheld monitoring equipment, which is checked and recorded at predetermined locations and on a set schedule. Additional monitoring often only occurs as the result of a change to the ventilation conditions. This type of monitoring often presents a level of accuracy that is sufficient to meet regulatory requirements, but may not provide enough detailed information to account for fluctuating conditions that can range from acute cases to seasonal in nature. When an area within the mine is identified as a potential hazard from heat accumulation, additional monitoring is required to ensure the conditions the workforce is entering into are managed to minimize heat stress exposure. Additionally if there is heat sensitive equipment, reducing the environmental heat conditions will often promote equipment function as well as extend equipment life. In order to capture enough information to accurately describe the conditions found within the subject area of concern a minimum monitor recording frequency must be met based on potential daily and in some cases hourly fluctuations. Currently there are a number of stand-alone environmental monitors that can be set to monitor conditions at intervals set by the user and placed in the field for real time observation and data collection.

*Corresponding author – email : ryan.anderson@mosaicco.com

2.3 Calculating heat loads underground

In order to assess the heat load within the underground environment, there are different methodologies that may be employed in order to use the appropriate heat management technique. Heat stress is often considered as a factor of the wet bulb globe temperature when considering the effects of heat on the workers in the mine.

Wet bulb globe temperature (C°) WBGT, can be calculated within the mine environment with the following equation;

$$\text{wet bulb globe temperature} = 0.3t_{gt} \times 0.7t_{wb}$$

Where, t_{gt} (C°) is the globe temperature and t_{wb} (C°) is the wet bulb temperature.

In order to assess the energy that is contained within the air in the underground environment, the enthalpy of the system can be calculated, which takes into account the moisture content of the air. Additionally the sigma heat can also be calculated, which takes into account the energy content less the moisture content. Both of these methods to describe the energy contained within the air are considered on the dry basis (kJ/kg dry air).

In order to calculate the enthalpy of the system the enthalpy of the air (kJ/kg) (h_a) and the enthalpy of the vapour (kJ/kg) (h_v) must be combined.

$$h = h_a + h_v \\ = 1.005 t_{db} + W(2501.6 + 1.884 * t_{db})$$

In order to calculate the apparent specific humidity W (kg/kg dry air) the following equation must be used;

$$W = 0.622 \frac{P_s}{P_b - P_v} \\ P_s = 0.6105 \exp\left(\frac{17.27 * t_{db}}{237.15 + t_{db}}\right)$$

$$P_v = P_s - 0.000644 * P_b(t_{db} - t_{wb})$$

In the above equations, t_{db} (C°) is the dry bulb temperature, P_s (kPa) is the saturation vapour pressure, P_b (kPa) is the barometric pressure, and P_v (kPa) is the vapour pressure.

The enthalpy can then be applied to the mass flow (kg/s) (M_f) in order to find the heat flow (Watt) (q_f) in the system. The following calculation assumes no change in moisture to the system.

$$q_f = M_f(\Delta h)$$

$$M_f = Q * w$$

Where M_f is the mass flow (kg/s), Δh is the sigma heat change (kJ/kg), Q is the flow rate (m³/s), and w is the air density (kg/m³).

In a ventilation system where there is a change in moisture the heat flow can be found using the sigma heat on a dry basis (S).

$$q_f = M_f(\Delta S + B)$$

$$S = h - 4.187 * W * t_{wb}$$

Where, B (C°⁻¹) is a term which depends on the process involved and on the change in moisture content.

Another method of calculating heat loads within the mine environment is by calculating the heat load losses, based on equipment found within the excavation of concern. This method is useful for both reactive heat management planning and predictive heat management. In order to assess the heat losses from equipment, a detailed equipment survey must be conducted on the equipment found within the area of concern. This included the stationary and mobile equipment, the infrastructure used to power the system, and the utilization of the components within the area. It is advisable to break down the area of concern into smaller segments based on changes in features contained within the excavations, or physical changes in the excavation itself. The strata, the excavation, and the changes in moisture content can also have significant impacts on the heat load prediction based on equipment heat losses, so it is important to understand the behaviour of the rock type as well as any significant changes in moisture content within the excavations. This process is described in section 3.

2.4 Applying heat management strategies

The application of a heat management strategy will serve to limit the level of health risk associated with the total heat load imposed on a worker underground. Heat management strategies include refrigeration (bulk air cooling), localized refrigeration (spot coolers), ventilation, administrative controls (air conditioned cabins, cooling vests, acclimatization, rest areas), and engineering controls (controlling/reducing heat at source, shielding, insulation).

2.5 Comparing and selecting engineering solutions on heat control

Selection of the ideal solution for heat control requires an engineering and economic analysis of alternatives. The solution is more likely a combination of strategies and available technologies. The combined application of engineering and administrative controls, together with selected work practices are effective means of reducing excessive heat exposure.

3. CASE STUDY

3.1 Area of study

A management program of heat generated from pumping infrastructure in a Saskatchewan potash mine has been established. The study area is 5.6 kilometers of underground excavations within series

ventilation and recirculation circuits. There are over 20,515 kW of electric motors resulting in 305,000 Watts of lost energy to atmospheric heat. In addition to these motors there are 49.6 kilometers of electrical power cables and the associated electrical controls and transformers, which also lose energy to heat throughout the area.

3.2 Identification of heat sources

In order to identify the locations and sources of heat, the study area was broken down in 14 zones. Each zone was further broken down into 20 meter sections to be used for future computational modeling. Within each section the heat source components were identified. The Heat Management Study Area and zone locations are identified in Figure 1. The primary sources of heat include strata, electrical cable, transformers, motors and settling tanks.

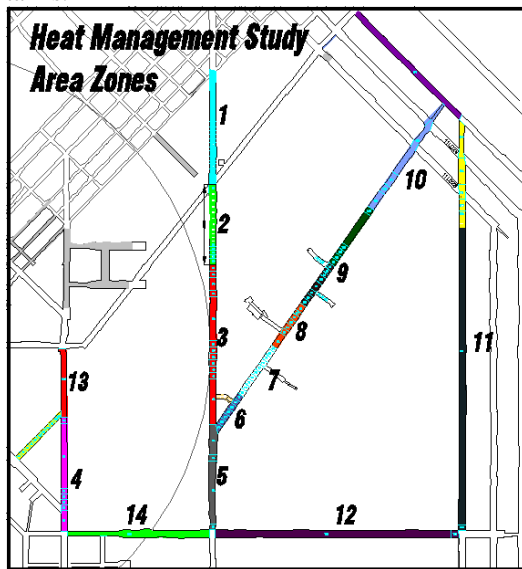


Figure 1: Heat Management Study Area.

3.3 Monitoring program

In the case example used within the potash mine, due to the relatively close proximity to the incoming shaft air there are hourly fluctuations as a result of changes to the surface temperature supply air. As a result of the required high frequency of recordings, a network of environmental monitoring stations were essential in order to capture the characteristics of the air as it moved throughout the study area. The installation of 14 Accutron Climatrax stations in conjunction with data loggers allowed for the monitoring of the following environmental factors: dry bulb temperature, wet bulb temperature, relative humidity, and barometric pressure. These parameters are then applied to determine all important psychrometric properties. In order to find regional changes within the study area,

selecting the appropriate locations to monitor was critical. The study area was broken down into zones that were considered heat source areas and heat sump areas. Observing the areas that had the greatest impact on the area allows for targeting of heat control applications. In addition to the supply air, the surrounding stratum also has an impact on the environmental conditions. To better observe the rock behavior on the air, it was necessary to capture the transfer of heat both into and out of the rock as it behaves as both a source of supply and removal of heat. In order to do this, heat fluctuation plates were installed against the strata to monitor the transfer of heat in and out of the rock. To further improve upon the observation of the rock characteristics, the virgin rock temperature can aid in the identification of the limits to which the rock can act as a source or sump of heat. In the study of the potash mine, 15.25 m long vertical and horizontal bore holes were established to capture this information. Temperature probes were located at 1.5 m, 3 m, 6 m, and 15 m to monitor heat fluctuation with depth.

3.4 Heat load calculations

To calculate the energy lost to the atmosphere as heat, the efficiency of the equipment was calculated at full load and continuous use. This was applied to all sources of heat with the exception of the electrical cables, which are based on 60% of full load. The primary sources of heat energy result from losses with transformers and pumping equipment. The estimated flow of heat is summarized in Table 1.

Table 1: Summary of heat load study.

Summary of Heat Load Study		
Area Number	Total Loss (W)	Total Loss (BTU/hr)
1	187,435.5	639,556.6
2	202,534.2	691,075.5
3	35,620.1	121,541.0
4	82,022.8	279,873.4
5	6,710.6	22,897.6
6	129,160.3	440,713.1
7	224,794.4	767,030.4
8	17,166.5	58,574.5
9	150,918.0	514,953.6
10	485,040.0	2,227,047.1
11	20,239.0	69,058.4
12	10,212.1	34,845.2
13	10,815.3	36,903.3
14	19,789.0	67,522.7
Total Heat Loss	1,582,457.88	5,971,592.33

Survey data was collected at the beginning and end of each zone in order to calculate the change in enthalpy and sigma heat for each zone. The data that was required in order to do the calculations included: dry bulb, wet bulb, relative humidity, pressure, and density. The environmental monitors that were set up

with the areas were programed to record this data on a 10 minute interval that could then be averaged at intervals that best suited the needs of the mine. This data could then be used to calculate the heat loads within the system (Table 2)

Table 2: Survey Data.

Survey Data											
Location	Dry Bulb (C°)	Wet Bulb (C°)	RH (%)	Pressure (kPa)	Density (kg/m³)	Ps (kPa)	Pv (kPa)	W (kg/kg dry air)	Cp (kJ/kg mix)	h (kJ/kg dry air)	S (kJ/kg dry air)
1 in	32.9	20.7	33	107.8	1.21	5.0053877	4.158425	0.025162215	1.052405613	97.57	94.10
1 out 2 in	33.5	21.1	33.3	107.8	1.23	5.1765363	4.315689	0.026157355	1.054280456	100.75	97.08
2 out 3 in	37.4	22.7	28.6	107.7	1.23	6.417911	5.398337	0.033152608	1.067459513	122.86	117.67
3 out	31.7	21	38.4	107.8	1.23	4.6777726	3.934944	0.023734315	1.049715449	92.65	89.50
4 in	28.1	19.7	45.6	107.9	1.23	3.8040593	3.220363	0.019242499	1.041252868	77.40	75.13
4 out	29.6	19.8	41.3	107.8	1.23	4.1491112	3.468764	0.020815751	1.044216875	82.98	80.40
5 in	29.5	19.3	38.7	107.8	1.23	4.1252894	3.417173	0.020501446	1.043624724	82.07	79.54
5 out	29.8	19.5	38.4	107.8	1.23	4.197114	3.482055	0.020905192	1.044385382	83.42	80.81
6 in	30	19.6	38.4	107.8	1.23	4.245599	3.523598	0.021164507	1.04487393	84.29	81.63
6 out 7 in	32.3	20.1	32.6	107.8	1.23	4.839173	3.99221	0.024117469	1.050437312	94.26	91.00
7 out 8 in	32	20.4	35	107.7	1.22	4.7578784	3.953316	0.023886847	1.050002821	93.36	90.15
8 out 9 in	31.7	20.3	35.3	107.8	1.22	4.6777726	3.886348	0.023441198	1.049163217	91.90	88.79
9 out 10 in	32.9	20.9	33.8	107.7	1.21	5.0053877	4.173082	0.025275494	1.052619031	97.86	94.38
10 out	34.1	21.3	31.9	107.7	1.21	5.3527408	4.464948	0.027135048	1.05612243	103.89	100.02
11 in	30.9	19.9	36.2	107.7	1.23	4.4698588	3.706912	0.022335524	1.047080126	88.23	85.34
11 out	30.1	19.5	37.2	107.8	1.23	4.2700237	3.534138	0.021232823	1.045002639	84.57	81.89
12 in	30.1	19.5	37.1	107.8	1.23	4.2700237	3.534138	0.021232823	1.045002639	84.57	81.89
12 out	29.5	19.4	38.4	107.8	1.23	4.1252894	3.424115	0.020543097	1.043703194	82.18	79.64
13 in	31	20.5	36.9	107.8	1.23	4.4954007	3.766457	0.022677948	1.047725254	89.21	86.27
13 out	31.8	20.6	36.9	107.8	1.23	4.7043434	3.926804	0.023691316	1.04963444	92.64	89.49
14 in	29.2	19	38.2	107.8	1.23	4.0545363	3.34642	0.020063268	1.042799196	80.64	78.19
14 out	28.1	19.7	45.6	107.9	1.23	3.8040593	3.220363	0.019242499	1.041252868	77.40	75.13

3.5 Heat management strategy application

In order to manage the heat produced within the workings, there are two goals that should be met. Firstly, minimizing heat stress conditions to personnel, and secondly reducing heat exposure to equipment.

In order to minimize heat stress conditions to personnel, a work plan that decreases work in high wet bulb globe temperatures according to heat stress

guides may be a viable option. The heat stress guide listed in Table 3, outlines working time lengths and job type that can safely be performed based on the environmental conditions. There are limitations to this type of heat management plan, as it does not lower heat exposure to heat sensitive equipment and may not be economically or practically feasible based on the length or type of work being performed.

Table 3: Wet bulb Globe Temperature Index (Section 70, Occupational Health and Safety Regulations, 1996, Saskatchewan).

Wet Bulb Globe Temperature (WBGT) Index				
Work Load	Work Rate			
	Continuous	15 minutes rest per hour	30 minutes rest per hour	45 minutes rest per hour
Heavy	up to 25C°	25C° up to 26C°	26C° up to 28C°	28C° up to 30C°
Moderate	up to 27C°	27C° up to 28C°	28C° up to 29C°	29C° up to 31C°
Light	up to 30C°	30C° up to 30.6C°	30.6C° up to 31.4C°	31.4C° up to 32.2C°

A second option may be setting up spot cooling within the workings to remove the additional heat produced by the equipment. In the case study the location that would see the largest local benefit and to air traveling downstream is zone 2.

In order to set up a cooling plant in zone 2 the following parametric design is conducted.

The mass flow (M_f) entering into zone 2 is 29.6 kg/s
 The specific humidity entering into zone 2 (W_1) is 0.025 kg/kg
 The enthalpy entering into zone 2 (h_1) is 95.04 kJ/kg
 Air to be cooled to 27.8°C

Using a psychometric chart and 27.8°C as the chosen output, the following outgoing enthalpy and specific humidity were found.

The specific humidity leaving zone 2 (W_2) will be 0.20 kg/kg

The enthalpy leaving zone 2 (h_2) will be 78kJ/kg

The specific enthalpy of water (h_{w2}) at 27.8°C is 123.5 kJ/kg

By installing the temperature probes into the rock, the ambient virgin rock temperature of both the salt and potash members were found to be 27.1°C, this is the lower limit of the attainable cooling before the rock becomes an additional heat source for the excavation, limiting the effectiveness of the cooling.

The cooling load requirement (Q) can be found using;

$$Q = M_f * [(h_1 - h_2) - (W_1 - W_2) * h_{w2}]$$

The resultant cooling load is 489kW or 139.2 tons of cooling by an installed cooling plant.

With the installation of a chiller plant within the underground environment, the cost of the plant must be taken into consideration. The initial capital expenditure is the upfront cost, but the cost of operation should be assessed. The cooling plant efficiency can be assessed based on the coefficient of performance (COP). This allows a basic assessment of the cost of running the plant.

A typical cooling plant that could be used within this location is a water cooled electrically operated positive displacement cooling plant. According to Energy Design Resources the COP for this type of plant, would be approximately 4.20. The energy requirements to run the plant would be;

$$\begin{aligned} & \text{energy requirement}_{\text{cooling plant}} \\ &= \frac{\text{cooling capacity requirements}}{COP} \end{aligned}$$

This results in 116.4 kW of energy required to run the plant. The annual cost of operation can then be calculated based on continuous operation at the cost of delivery and kWh usage. The cost of continuous usage at this mine for the case study is 0.065 \$/kWh.

$$\begin{aligned} & \text{cost}_{\text{cooling plant}} \\ &= \text{energy requirement}_{\text{cooling plant}} \\ & * \text{energy cost}_{\text{continuous usage}} * \text{run time} \end{aligned}$$

As a result the annual cost of running a cooling plant in this location will be \$66,278.

It is also possible to estimate the cost of cooling any future additional equipment to the area. Based on the equipment survey, a common motor that is used within zones 2, 7, and 10 has a heat loss of 15 kW based on motor efficiency. Using the same principle the cost of cooling additional motor installs would approximate \$8,541 per motor. This would allow for

the estimate of the additional cost of cooling the zones as additional equipment is added.

4. CONCLUSIONS

Heat management plans are growing in importance when it comes to the health and safety of the workforces within the mines. There are strategies that can be used to minimize the effects on both people and equipment, but the costs of the plans must be realized. There are costs associated with both the efficiency of the work being done as a result of the heat conditions through avoidance. There are also costs that occur as the result of actively attempting to cool the working areas. These costs must be understood and assessed to achieve the greatest impact on the environmental conditions within the mine environment.

5. REFERENCES

De Souza, E. (2011), Mine Ventilation Practitioners Guide. https://energydesignresources.com/media/1681/edr_designbriefs_chillerplant.pdf?tracked=true Section 70, Occupational Health and Safety Regulations, 1996:Working Under Hot Conditions, Saskatchewan

Effect of hydrogen on explosion of methane-air mixture

YANG Chunli ^{a,*}, LI Xiangchun ^{b,c}, Xu Teng ^{b,c}, Qu Wenzhong ^{b,c}, Liu Yanli ^{b,c}

^a School of Mechanics and Civil Engineering, China University of Mining and Technology, Beijing, China, 100083

^b School of Resource and Safety Engineering, China University of Mining & Technology(Beijing), Beijing, China, 100083

^c State Key Lab of Coal Resources and Safe Mining, Beijing, China, 100083

ABSTRACT

Gas explosion is one type of coal mine accidents in China. The main composition of the gas in coal seam is methane, but hydrogen is contained in some coal seams and increases the risk of gas explosion. The main reaction path of methane-air mixture explosion process and elementary reactions characteristics at high temperature are analyzed using detailed mechanism of methane combustion. Different fraction of H₂/CH₄/Air mixture explosion is simulated, and temperature, pressure, mole fraction of different species and elementary reactions rate are analyzed. The simulation results show that hydrogen will reduce the priming induction period of gas explosion and has influence on the temperature and pressure of gas explosion.

KEYWORDS: hydrogen; methane-air explosion; hydrogen; elementary reaction; induction time; reaction rate

1. INTRODUCTION

Gas is produced in the process of coal-forming. The main component of gas all over the world is methane, and there are also C₂H₆, C₃H₈ and other combustible gases of heavy hydrocarbon in some coal seams (Zhou,1999). In addition, there is a small amount of hydrogen in some coal seam because thermal decomposition of coal at a high temperature (Yu and Wang, 2005). Meanwhile, combustible gases of CO, C₂H₄, C₂H₆, C₃H₈, etc. are produced in the process of coal spontaneous combustion (Xiao et al., 2007; Zhang, 2000). So in addition to main specie methane, there may be a small amount of H₂, CO, C₂H₄, C₂H₆ and C₃H₈ and other combustible gases in coal seam. Explosion limits and severity of gas mixture explosion depends on species and fraction of the gas mixture. Combustible gas mixture in methane will influence explosive limits and increase risk of explosion (Pan et al., 2008; Guo, 2002).

Although there is a little hydrogen in methane, risk of explosion can increased greatly because lower explosive limit (LEL) of hydrogen is very low compared to methane. H₂/CH₄/Air mixtures have lower LEL compared to CH₄/Air methane when mole fraction of CH₄ is same, and it is easy to explode. Explosion power and explosion hazard will increase even if there is little hydrogen in CH₄/Air mixture (Ma, 2015).

Many research had been carried out on explosion characteristic of H₂/CH₄/Air mixture(Li et al.2008; Shrestha,1999).Ma(2015) showed in their publication that temperature and pressure of H₂/CH₄/Air mixture explosion is very different when using different

mixing ratios. Pan et al. (2008) demonstrated that hydrogen influences LEL of H₂/CH₄/Air mixture and can increase explosion risk. Luo et al. (2015) showed in their publication that combustion gas CO, H₂, C₂H₄ and C₂H₆ affect explosion limit of CH₄/Air mixture. Ren et al. (2013) conducted methane explosion experiment and found that explosion limit range was extended with fraction of H₂S, CO and H₂ increasing. Jia et al. (2016) analyzed effects of different concentration CO and H₂ mixture on the gas explosion by numerical analysis. Hu et al. (2010) analyzed pressure waves of H₂/CO/CH₄/air mixture explosion and found that hydrogen is key element affecting the explosion. Mahdi et al. (2016) obtained maximum pressure rise rate and deflagration index of methane, hydrogen and their mixtures and examined influence of equivalence ratio, initial temperature and initial pressure on the maximum pressure rise rate and deflagration index. Li et al. (2012) found that the presence of molecular hydrogen yield from coal spontaneous heated process would significantly increase the maximum explosion pressure and pressure rise rate of H₂/CH₄/air mixtures. Li et al. (2015) carried out the explosion experiments of hydrogen/air and methane/air for different gas volumes and found that the flame propagation speed of hydrogen/air explosion is higher than that of methane/air, while the flame duration of methane/air is longer than that of hydrogen/air.

In this paper, the influence of combustible gas hydrogen in coal mine on the explosion mixture of methane air was studied using the chemical kinetic software CHEMKIN. Pressure, temperature and free radicals of mixture gas explosion are analyzed, and

*Corresponding author–email: yangcl_1980@163.com

the influence of the mixed combustible gas on methane-air mixture explosion is obtained. CHEMKIN developed by Sandia laboratory and Kee R.J et al. can solve the problem of gas-phase chemical reaction in the combustion process. Subroutine of Senkin is used in this simulation. Senkin is a Fortran computer program block, which can simulate the tendency of premixed homogeneous gas reaction with time change in a closed container (Li, 2011). Detailed chemical reaction mechanism of H₂/air mixture is relatively simple, which is included in GRI-Mech 3.0, so the simulation of H₂/CH₄/air mixture explosion reaction is calculated by data files GRI-Mech3.0.

2. CHARACTERISTICS OF CH₄/AIR MIXTURE EXPLOSION

2.1 The Main Elementary Reaction of CH₄/air Mixture Explosion

Methane has a tetrahedron molecular structure and bond energy of C-H, which make methane oxidation process complex (Stephen, 2015). In the early 20th century, people have confirmed that all gas phase reaction are conducted by a series of elementary reaction, the complex chain reaction of gas explosion reaction is composed of the elementary reaction (Lin et al., 2013). At present, there are more than a dozen of detailed chemical mechanisms, but methane combustion reaction mechanism by the Lawrence Livermore National Laboratory is generally accepted, which includes 53 species and 325 elementary reactions. Methane combustion process is very complex, but there is only one key oxidation path, and some key elementary reactions.

According to detailed mechanism, in the process of gas explosion, elementary reactions $H+CH_3(+M)=CH_4(+M)$ and $HO_2+CH_3=O_2+CH_4$ produce free radicals and initiate reaction. When initial temperature is low, $HO_2+CH_3=O_2+CH_4$ initiate reaction mainly, and $H+CH_3(+M)=CH_4(+M)$ initiate reaction mainly when the initial temperature is high. Lin et al. (2012) shows that when temperature is more than 2000T, explosion is initiated by $H+CH_3(+M)=CH_4(+M)$ only.

CH₄ is mainly consumed by following three reactions: $H+CH_4=CH_3+H_2$, $OH+CH_4=CH_3+H_2O$ and $O+CH_4=OH+CH_3$. Compared with H and OH, amount of CH₄ consumed by O is much smaller (Peter, 1985). So $O+CH_4=OH+CH_3$ is less important compared with other two reactions. CH₃ is mainly oxidized by the following reactions: $O+CH_3=H+CH_2O$, $OH+CH_3=CH_2(S)+H_2O$, $OH+CH_3=CH_2+H_2O$ and $HO_2+CH_3=OH+CH_3O$. Compared with OH and HO₂, CH₃ is mainly consumed by reaction with O. Combination reaction of $CH_3+CH_3=C_2H_6$ generates

hydrocarbon of C₂ series, which is important when CH₄ is rich. CH₂O is mainly oxidized by the two reactions $H+CH_2O=HCO+H_2$ and $OH+CH_2O=HCO+H_2O$. HCO is mainly oxidized by the two reactions $HCO+M=H+CO+M$ and $HCO+O_2=HO_2+CO$. CO is oxidized essentially by the reaction $OH+CO=H+CO_2$, and the reaction of CO with O and O₂ can be in general neglected. The consumption of oxygen and the formation of radical by the reactions $H+O_2=OH+O$, $OH+H_2=H+H_2O$, $2OH=O+H_2O$ and $O+H_2=H+OH$. The last three of these are linearly dependent. Reaction $H+O_2=OH+O$ is very important as a chain branching reaction since it produces more radicals than it consumes. Finally, chain breaking occurs mainly through three body reactions $H+O_2+M=HO_2+M$ and $H+OH+M=H_2O+M$. While other recombination reaction can be neglected.

2.2 Heat Production of Elementary Reaction

In a reaction, energy produced by old chemical bond breaking and new chemical bond forming can cause heat release. In the process of gas explosion, lots of elementary reaction release heat for a second, which cause temperature and pressure rise immediately and lead to disaster.

Detailed mechanism includes 325 elementary reactions. Some absorb heat and some release heat. Because all the reaction is reversible, a reaction may release heat and absorb heat in different time. But release heat or absorb heat can be identified by positive and negative of a reaction total heat release. Except for 106 elementary reactions which nitrogen oxides participate in, there are 175 heat release reactions and 44 heat absorption reaction during the process of gas explosion. In the process of gas explosion, chain initiation elementary reactions absorb heat when meeting heat source, and produce free radical. So at first, gas explosion system absorbs heat. And then lots of elementary reactions release heat, and there is a peak point of heat release.

CHEMKIN software and closed homogeneous model are used to simulate heat release of mixture CH₄/Air explosion. Initial temperature is 1300K, and initial pressure is 1atm. Reactor volume is 1cm³, and mole fraction of CH₄ is 0.095.

Fig.1 shows system heat releases at different time during explosion process. The total heat release is 0.5124J. Fig.2 shows top ten total heat release of different elementary reactions. In the process of gas explosion, reaction $HCO+O_2=HO_2+CO$, $O+CH_3=H+CH_2O$ and $CH_3(+M)=C_2H_6(+M)$ are top three heat release reactions. The total heat releases of the three release is 0.0489J, 0.0435J and 0.0358J respectively. Total heat release of the three releases

account for more than twenty percent of system total heat release. Key absorption heat release reaction is $H+O_2=O+OH$, total heat release is 0.072J.

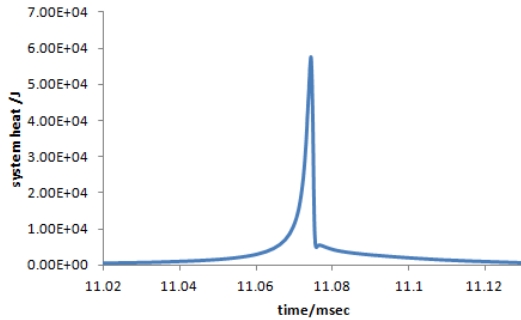


Figure 1: System heat releases at different time

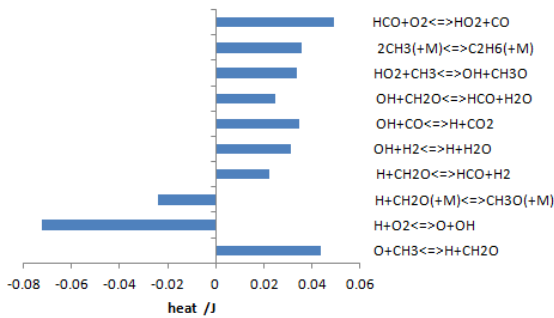


Figure 2: Total heat release of different elementary reactions

3. CHARACTERISTICS OF $H_2/CH_4/AIR$ MIXTURE EXPLOSION

3.1 Characteristics of $H_2/CH_4/air$ Mixture explosion

Considering actual situation, when designing simulation schemes, mole fraction of hydrogen in every scheme should be small because there is little hydrogen in coal seams. Five schemes are designed in the simulation, as is shown in Tab.1. In the five schemes, mole fraction of methane is 8%, mole fraction of hydrogen are 0, 0.5%, 1%, 2% and 4% respectively. Air is assumed consisting of 79% nitrogen and 21% oxygen by volume.

Table 1: Mole fraction of each species of five schemes

species	1	2	3	4	5
CH_4	0.08	0.08	0.08	0.08	0.08
O_2	0.1932	0.19215	0.1911	0.189	0.1848
N_2	0.7268	0.72285	0.7189	0.711	0.6952
H_2	0	0.005	0.01	0.02	0.04

CHEMKIN software and closed homogeneous model are used to do the simulation. Initial temperature is 1300K, and initial pressure is 1atm.

Tab.2 shows max temperature, pressure and percentage increase of temperature and pressure of the five schemes. Max temperature and pressure increase with increase of mole fraction hydrogen, but percentage increase is low. When mole fraction of hydrogen is 4%, percentage increase of temperature and pressure are 2.79% and 2.24% respectively.

Table 2: Max temperature, pressure and percentage increase of temperature and pressure

schemes	1	2	3	4	5
Temperature(K)	2776	2787	2798	2819	2853
Temperature Percentage increase(%)	-	0.41	0.8	1.53	2.79
Pressure(atm)	2.20	2.21	2.21	2.23	2.25
Pressure Percentage increase(%)	-	0.33	0.65	1.24	2.24

Fig.3 shows explosion induction of the five schemes. As can be seen from Fig.3, induction time decreases with the increase of initial hydrogen concentration. Percentage decreases are 45%, 64%, 81% and 92% respectively when the mole fractions of hydrogen are 0.5%, 1%, 2% and 4%. Hydrogen influence induction time of explosion greatly. When there is little hydrogen in CH_4/Air , induction time will change greatly.

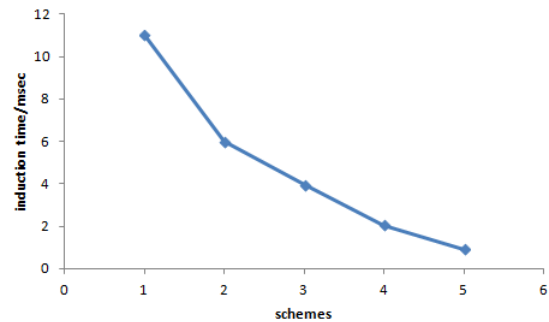


Figure 3: Explosion induction time of the five schemes

Fig.4-Fig.6 is the main free radical change curve with time of different schemes. As is showed in Fig.4-Fig.6, when explosion occurs, the mole fraction of each free radical increases for a section and reaches the peak point, and then decreases rapidly to a stable condition. The mole fraction of O reduces slightly with H_2 increasing. Because with hydrogen increasing, the reactions rate of $O+H_2=H+OH$ and $OH+H_2=H+H_2O$ increase, and H increase, which cause chain reaction rate of $H+O_2=O+OH$ increase.

Because OH is mainly produced by the reaction $H+O_2=O+OH$, free radical OH increase. But with the increase of hydrogen content, the total content of oxygen in the mixture decreased slightly, so the O produced by the explosion is slightly reduced, which cause the rate of OH increase less than H.

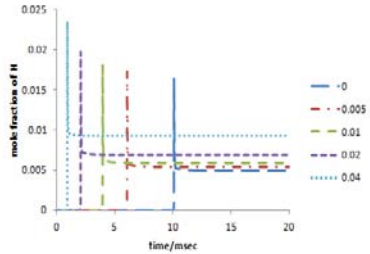


Figure 4: Time-H curve of different hydrogen mole fraction

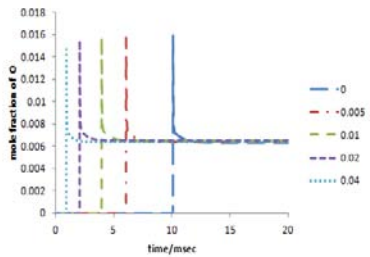


Figure 5: Time-O curve of different hydrogen mole fraction

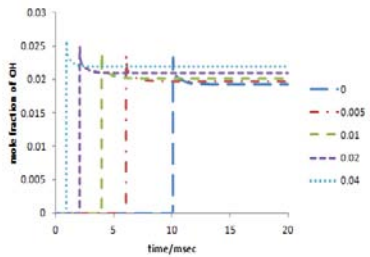


Figure 6: Time-OH curve of different hydrogen mole fraction

The free radicals of CH_3 , CH_2O , and HCO reach the maximum value at the moment of explosion, and then reduced instantly to zero after the explosion, the process is very fast. Fig.7 is the maximum mole fraction CH_3 , CH_2O , and HCO of different scheme during explosion. Fig.7 shows that mole fraction of CH_3 and HCO increase with the increase of hydrogen concentration, but mole fraction of CH_2O reduce reduces with the increase of hydrogen concentration. Because CH_4 is mainly oxidized by the reaction $H+CH_4=CH_3+H_2$. And in the reaction, CH_3 will be produced. Because mole fraction of H increases with the increase of hydrogen concentration, mole fraction

of CH_3 will increase too. CH_3 is mainly oxidized by the reaction $O+CH_3=H+CH_2O$. With the increase of H_2 content, the content of O decreases, so the CH_2O generated by the explosion is reduced. Oxidation reaction of CH_2O is mainly reacted by the elementary reaction $H+CH_2O=HCO+H_2$. Mole fraction of H increase lead to the reaction rate of $H+CH_2O=HCO+H_2$ increasing, so mole fraction of HCO increase.

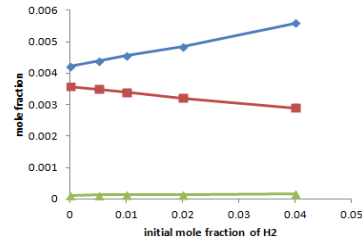


Figure 7: Max mole fraction CH_3 , CH_2O , HCO of different hydrogen mole fraction

Final products of explosion are mainly CO , CO_2 , H_2O , and the mole fractions of each product are not the same. In the explosion, the mole fraction of H_2O and CO_2 reaches the maximum value at the moment of the explosion and then remains the same; but the mole fraction of CO reaches the maximum value at the moment of the explosion and then reduces to a certain value. Therefore max mole fraction of H_2O and CO_2 of each scheme are analyzed, as is shown in Fig.8, but mole fraction of CO varying with time is analyzed, as in showed in Fig.9.

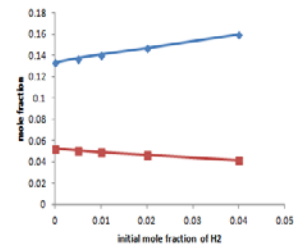


Figure 8: Max mole fraction of H_2O , CO_2 of different hydrogen mole fraction

Fig.8 shows that mole fraction of H_2O increases with the increase of hydrogen, but CO_2 decreases. As showed in Fig.9, the maximum value of CO is almost same at the moment of explosion, but final value of CO decreases with the increase of hydrogen. Because H_2O is mainly produced by the elementary reaction $OH+H_2=H+H_2O$ and CO is mainly oxidized by the elementary reaction $OH+CO=H+CO_2$, and they compete for OH . Therefore, reaction rate of $OH+H_2=H+H_2O$ increases and $OH+CO=H+CO_2$

decreases with hydrogen increasing, so mole fraction CO_2 will decrease

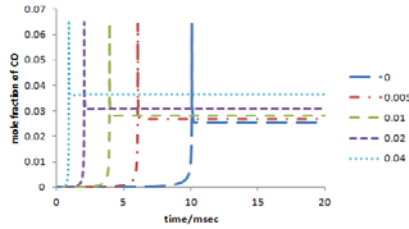


Figure 9: Time-CO curve of different hydrogen mole fraction

Fig.10 is the maximum values of main elementary reactions rate. As shown in Fig.10, the reaction rate of each elementary reactions increase with the increase of hydrogen concentration, so hydrogen can improve main elementary reaction rate in if there are some hydrogen in methane-air mixture.

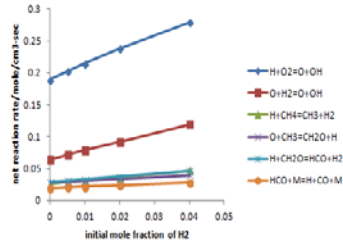


Figure 10: Maximum rate of main elementary reaction of different hydrogen mole fraction

3.2 Effect of hydrogen to gas explosion

Gas explosion which is a kind of special reaction is the chain reaction, and is also called the linked reactions. These reactions include free atoms or radicals. Free radicals are unpaired electron atoms or groups. Besides, it has a highly reactive chemical speciation, which can react with other molecules and form new free radicals, and the new free radicals quickly take part in the reaction to produce other new free radicals. These processes link together closely, until reactions come to end. Chain reactions include the straight chain reaction and the branched chain reaction. Gas explosion is branched chain reaction.

In the process of explosion, breakup reaction are $\text{H}+\text{CH}_3(+\text{M})=\text{CH}_4+\text{CH}_3(+\text{M})$ and $\text{HO}_2=\text{O}_2+\text{CH}_4$, this reaction forms actively free radicals which can causes and accelerates explosion reaction, but rate of the two chain initial reaction are slow, so the gas explosion needs a certain induction period. The oxidation rate of methane to form hydrogen is slow, because CH_4 need dehydrogenation at first, then through a series of elementary reaction to form hydrogen. The gas explosion branched chain reaction will be accelerated

if there are hydrogen in it. For example $\text{H}_2+\text{M}=\text{H}+\text{H}+\text{M}$, $\text{O}+\text{H}_2=\text{H}+\text{OH}$ and $\text{H}+\text{O}_2=\text{O}+\text{OH}$ et al.. These branched chain reactions make the mole fraction of free radicals O, OH and H increase in geometry level, and will accelerated the explosion. Therefore, induction period of explosion will be shorter if there is some hydrogen in methane-air mixture

The main oxidation path of methane-air explosion are through the elementary reactions $\text{H}+\text{CH}_4=\text{CH}_3+\text{H}_2$, $\text{O}+\text{CH}_3=\text{CH}_2\text{O}+\text{H}$, $\text{H}+\text{CH}_2\text{O}=\text{HCO}+\text{H}_2$ and $\text{OH}+\text{H}_2=\text{H}+\text{H}_2\text{O}$, the rate of which are influenced by hydrogen and rate of these reaction will increase with the increase of hydrogen concentration. Max temperature and pressure are not influenced very much by hydrogen because low heat release of hydrogen explosion. Besides, some oxygen is used in the process of hydrogen oxidation, which causes lower oxidation degree of CH_4 .

4. CONCLUSIONS

(1) Main oxidation path of methane-air explosion is $\text{CH}_4-\text{CH}_3-\text{CH}_2\text{O}-\text{HCO}-\text{CO}-\text{CO}_2$. Except for 106 elementary reactions which nitrogen oxides participate in, there are 175 heat release reactions and 44 heat absorption reaction during the process of gas explosion. $\text{HCO}+\text{O}_2=\text{HO}_2+\text{CO}$, $\text{O}+\text{CH}_3=\text{H}+\text{CH}_2\text{O}$ and $\text{CH}_3(+\text{M})=\text{C}_2\text{H}_6(+\text{M})$ are top three heat release reactions.

(2) If there are some hydrogen in methane-air mixture, branch chain reactions $\text{O}+\text{H}_2=\text{H}+\text{OH}$ and $\text{H}+\text{O}_2=\text{O}+\text{OH}$ will be accelerated in the process of explosion, and will produce more active free radicals, which will accelerate other main elementary reactions. Rate of main reaction of explosion will be increased

(3) Hydrogen influences induction period of H_2/CH_4 /Air explosion greatly. And with the mole fraction of hydrogen increase, the induction period will be shorter. But hydrogen has little influence on max temperature and pressure.

5. ACKNOWLEDGEMENTS

This research is supported by National Natural Science Funds of China (51304212). The authors would like to express their gratitude to the foundation.

6. REFERENCES

- Guo Y L. (2002) Abnormal effect on safety production of coal seam gas component, Journal of Longyan Teachers College, Volume 20, NO. 3, pp. 9
- Hu R, Wu X H, Hu Y Y, (2010) Compartmentalization of Explosive Morphology and Waveforms of Multicomponent Gas Mixture

Consisting of H₂, CO, CH₄ and Air, *Acta Chimica Sinica*, Volume 68, No. 7, pp. 623-632

Jia B S; Li C M; Hu R X. (2016) Study on Synergistic Effect Mechanism of CO, H₂ mixed gas on Methane Explosion, *World Sci-Tech R & D*, Volume 38, No. 1, pp. 35-39

LI B Q. (2012) Gas Explosion Mechanism and Control Technology in Coal Mines, China University of Mining and Technology Press, Xuzhou, 468 p.

Li D, Zhang Q, Ma Q J, Shilei Shen. (2015) Comparison of explosion characteristics between hydrogen/air and methane/air at the stoichiometric concentrations, *international journal of hydrogen energy*, Volume 40, pp. 8761-8768

Li Q Z, Lin B Q, Dai H M. (2012) Explosion characteristics of H₂/CH₄/air and CH₄/coal dust/air mixtures, *Powder Technology*, Volume 229, pp. 222-228

LI Y H. (2011) Reaction Kinetics Characteristic Research on chain Reaction Mechanism of Gas Explosion in Enclosed Space, Liaoning Technical University, Anshan, 77 p.

Li Z H, Lin B Q, Zhang L J, Pan S K, He Y H. (2008) Effects of Hydrogen Production on Gas Explosion, *Journal of China University of Mining & Technology*, Volume 37, No. 2, pp. 147-151

Luo Z M; Lin J J; Guo Z C. (2015) Influence of Various other Flammable Gases in Coal Mine on Explosion Limits of Methane, *China Safety Science Journal*, Volume 25, No. 1, pp. 91-97

Mahdi F, Guo X L, Chen Z. (2016) The explosion characteristics of methane, hydrogen and their mixtures: A computational study, *Journal of Loss Prevention in the Process Industries*, Volume 40, pp. 131-138

Ma Q J. (2015) Multicomponent Gas Explosion in Confined Space and the Mechanism of Explosion to Combustion Transition. Beijing Institute of Technology, Beijing, 113 p.

Pan S K, Li Z H, Lin B Q. (2008) Experimental Studies on the Effect of Hydrogen and Heavy Hydrocarbon on Lower Explosion Limits of Gas, *Journal of Hunan University of Science & Technology (Natural Science Edition)*, Volume 23, No 3, pp. 23-27

Peters N. (1985) Numerical and asymptotic analysis of systematically reduced reaction schemes for hydrocarbon flames, *Proceedings of the Symposium*, Volume 241, pp. 90-109

Ren S R; Li H K; Li L B. (2013) An Experimental Study of Effects of Inert and Special Flammable Gases on Methane's Explosion characteristics, *Natural Gas Industry*, Volume 33, No. 10, pp. 110-115

Shrestha S.O., Karim G.A. (1999) Hydrogen as an Additive to Methane for Spark Ignition Engine

Applications, *International Journal of Hydrogen Energy*, Volume 24, No. 6, pp. 577-586

Stephen R T. (2011) *An Introduction to Combustion Concepts and Applications*(Third Edition), McGraw Hill Higher Education, New York, 752 p.

Xiao Y, Ma L, Wang Z P. (2007) Law of Index Gases Adsorption and Condensability of Coal Spontaneous Combustion, *Journal of China Coal Society*, Volume 32, No. 10, pp. 1014-1018

Yu B, Wang Y A. (2005) *Manual of Coal Mine Gas Disaster Prevention and Control and Utilization*(Revised Edition). China Coal Industry Publishing Home, Beijing, 789 p.

Zhang G J. (2010) *Ventilation and safety*. China University of Mining and Technology Press, Xuzhou, 456 p.

Zhang L J, Li Z H, Lin B Q. (2009) The Influence of Oil Gas on Gas Explosion, *Journal of Hunan University of Science & Technology(Natural Science Edition)*, Volume 24, No. 1, pp. 18-21

Zhou S. (1999) *The Theory of Gas Flow and Storage in Coal Seams*. China Coal Industry Publishing Home, Beijing, 195 p.

Drilling escape and rescue system in Wangjialing coal mine

Zhiling Huang*, Longzhe Jin, Yuntong Ma, Hongmin Zhu

Civil & Environment Engineering School, University of Science and Technology Beijing, Beijing, China

ABSTRACT

Many problems are faced in the construction of emergency refuge systems, including the poor reliability of hedging facilities, the contradiction between hedge and escape, the high time consumption, high cost, and the big risk of drilling rescue technology. Shaft drilling escape and rescue systems are a combination of emergency refuge technology and drilling rescue technology. The key parameters of drilling escape and rescue systems are tested through man-loading and live sheep lifting experiments. Key parameters include no-supply guarantee time, response time, and human survival environment. This paper also examines the comfort and physiological parameters of experimenters and the influence drilling has over refuge chamber air supply systems.

KEYWORDS: mine shaft; emergency rescue; escape drill hole; emergency refuge; lifting experiment

1. INTRODUCTION

Ever since 33 miners were rescued from a 700m-deep shaft 69 days after a coal mine accident in Chile, countries with mining industries have paid great attention to the construction of underground hedging facilities. Continuous improvements in facilities and technology have been made. Although existing hedging facilities can provide trapped miners with hedge for some time after an accident happens, they cannot guarantee a successful rescue. There are limitations to the protective capabilities, and the contradiction between hedge and escape still exists.

Drilling rescue technology has recently become an emergency rescue method for coal mine accidents. It was adopted and resulted in success for the 2002 US Quebec Creek mine water penetration accident and the 2010 Chile coal mine accident. Ground and underground drilling, drainage, delivery of fresh air, and a liquid diet were adopted in the 2010 Shenhua Camel Mountain and Wangjialing mine water penetration accidents, with good effect. However, many of the current drilling rescue technologies can only be done after an accident occurs, and are time-consuming, high in cost, and risky. Most of the existing studies aim at problems like the accuracy of after-accident quick-hole and drilling.

This paper examines the combination of emergency refuge and drilling technologies to construct a shaft drilling escape and rescue system and realize miners' safe refuge and quick and efficient rescue. What's more, key parameters like no-supply guarantee time, response time, and human survival environment are studied through man-loading and live sheep lifting experiments.

2. CONSTRUCTION OF WANGJIALING DRILLING ESCAPE AND RESCUE SYSTEM

2.1 System Constitution

The drilling escape and rescue system is composed of the self rescuer, refuge chamber, supply drill hole, escape drill hole, vehicle mobile supply station, emergency rescue vehicle and emergency rescue capsule. It is closely connected to six systems and is not dependent on any existing systems. The refuge chamber is connected to five systems, and is therefore is facilitated with exclusive monitoring, compressed-air, and a water-supply system by the vehicle mobile supply station, as seen in Figure 1.

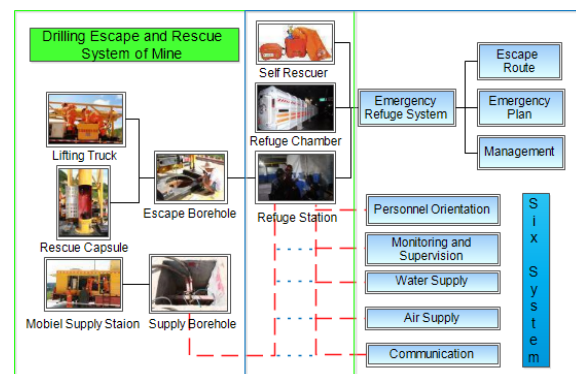


Figure 1: Composition of system.

The system is based on the refuge chamber. A $\phi 244.5$ mm supply drill hole is set up in chamber transition zone. Air-supply, water-supply, electricity-supply, and communication pipes are installed in the supply drill hole. A $\phi 790$ mm escape drill hole is set up in the survival zone. A vehicle mobile supply

*Corresponding author – email : bkdhzl@163.com

station, emergency rescue vehicle, and rescue capsule are deployed on the ground.

The vehicle mobile supply station has many functions, including air-supply, electricity-supply, communication, and lighting. Its output interface is connected to the supply drill hole inner pipe. The emergency rescue vehicle is a unification of a winch, longmen frame, Jack, monitoring system, and operating board. It boasts a hoisting height of 500 m at maximum and a lifting speed of 1.5 m/s. The rescue capsule is a cylinder structure of 540 mm in diameter whose main material is Q345 steel. It boasts multiple functions like monitoring, communication, emergency oxygen supply, and emergency treatment.

2.2 System Operating Principle

In the case of a sudden accident underground, the staff should be evacuated from the wellhead using an established route to avoid the disaster area. The priority in case of a difficult situations should be evacuation to the refuge chamber, and entry into the rescue capsule should the need arise.

It is the ground command center's responsibility to organize rescue personnel from the wellhead to carry out rescue operations, as well as arranging personnel and rescue equipment to quickly drill the ground, in order to get the indoor refuge personnel from the chamber to the ground in time.

Under the premise of determining the environmental safety and the surrounding environment of the underground and the tunnel, rescue workers can be arranged from the borehole into the refuge chamber, improving the efficiency of the rescue.

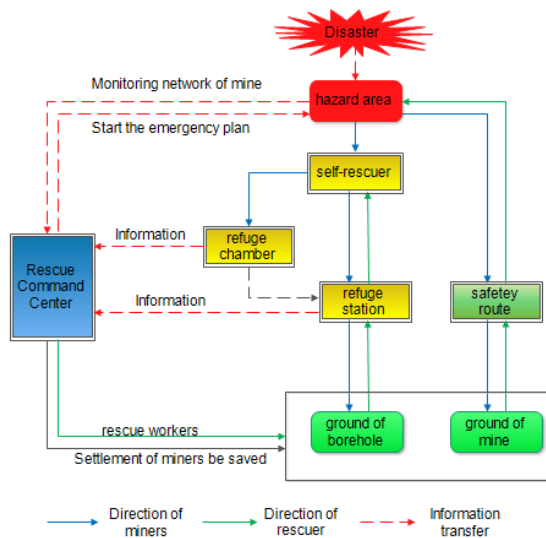


Figure 2: Emergency rescue process based on borehole rescue system.

3. HOLE RESCUE SYSTEM EXPERIMENT

3.1 General Situation of Refuge Chamber in Wangjialing Coal Mine

The Wangjialing refuge chamber is located in the 20106 working face of the outer auxiliary transport roadway between the machine and the big Lane. It has a rated service number of 100 people. The tunnel section has a 4 x 2.8m rectangular cross section. Both ends of the transition region are 9 m, and the living area is 36.5 m and space size is 410 m³.

3.2 Test Instrument

The chamber internal oxygen concentration, carbon dioxide concentration, temperature, and humidity are tested with CD7 type, which is seven in one multifunctional environment parameter sensor. The wind speed was measured by JFY-4 ventilation and multi parameter detectors. Noise was tested via a AWA6270 type noise analyzer. The blood pressure and the pulse produced from a laboratory test are used in the ABP-A091V type multifunctional electronic blood pressure meter.

3.3 Experiment Process

There were 100 experimental personnel in the laboratory. The escape drill used live sheep to enhance the simulation. The tests were carried out for 8 hours and divided into three stages:

1) 4 h no supply experiment - at this stage, there is no oxygen supply and carbon dioxide removal in the chamber. The escape hole and refuge chamber back to the outlet are closed.

2) 1 h oxygen supply experiment by drilling - in this stage, the ground supplies the wind by drilling, and air supply is set to 300 m³/h;

3) 3 h lift up living creatures test - in this stage, the experiments are carried out by using the escape drilling and ground lifting equipment.

4. ANALYSIS OF EXPERIMENTAL RESULTS

4.1 Analysis of Environmental Parameters in Refuge Station

The changes of oxygen concentration, carbon dioxide concentration and temperature-humidity in the refuge chamber during the experiment are shown in Figures 3 and 4.

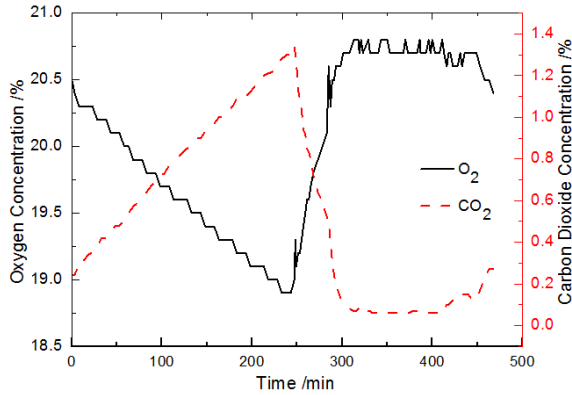


Figure 3: Change of oxygen and carbon dioxide concentration in refuge station during experiment.

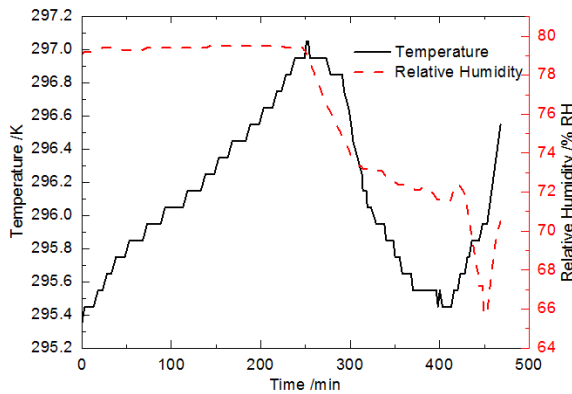


Figure 4: Change of temperature and humidity in refuge station containing experimenters.

By analyzing the changes of environmental parameters inside the refuge station, we can conclude that:

1) System support time without any supply is longer than 4h. In the first 4 hours of the experiment, 100 individuals exercised in an isolated refuge station with no supply. During this time, oxygen concentration in refuge station reduced from 20.6% to 18.7%, carbon dioxide concentration increased from 0.07% to 1.34%, and temperature rose from 295.45 K to 297.05 K. These parameters are within the safety range for human bodies.

2) An air supply volume of 0.05m³/min per person can satisfy survival needs. During the drilling and air supply process, which is the second stage of the experiment, when the volume of air supply is 300 m³/h (0.05 m³/min per person), oxygen concentration increases from 18.7% to 20.8%, carbon dioxide concentration reduces from 1.34% to 0.04%, and temperature decreases to 295.65 K in 60 min.

The results of noise measurement in the refuge station are shown in Figure 5. The height of the measure point from the floor of the refuge station is

1.3 m, which is also the ear height when experimenters are seated. From Figure 6 we can see that when air supply volume is 600 m³/h, the maximum noise intensity is 102.3 dB, and noise intensity is mainly in the range of 50-70 dB.

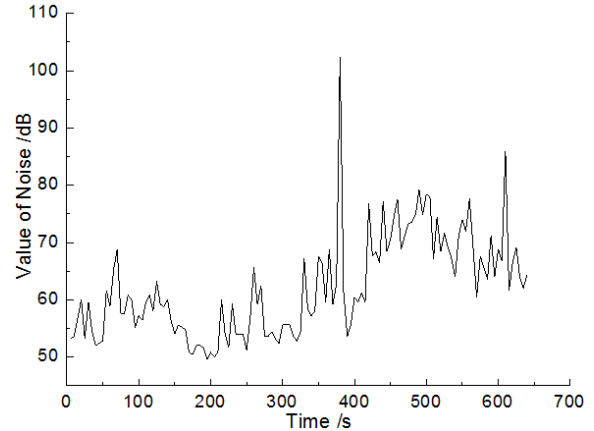


Figure 5: Environmental noise inside refuge station when air supply volume was 600 m³/h.

4.2 Analysis of Environmental Parameters Inside Rescue Capsule

The changes to the environmental parameters inside the rescue capsule during the lifting and falling process are shown in Figures 6 and 7, respectively. From Figure 6 we can conclude that during the lifting process, the concentration of oxygen and carbon dioxide inside the rescue capsule is similar to that of fresh air with less fluctuation, while the change of temperature is influenced by the temperature of the refuge station and ground of drilling.

Tests of noise in the rescue capsule (which is unloaded and loaded with sheep many times during the lifting and descending process) indicate that noise intensity is mainly in the range of 45-70 dB, and the maximum value is no more than 115 dB, which is shown in Figure 8. The noise intensity in the rescue capsule with sheep is slightly less than that without sheep.

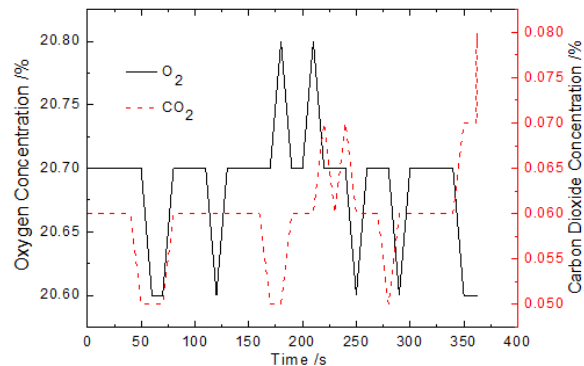


Figure 6: The change of temperature inside rescue capsule during lifting process.

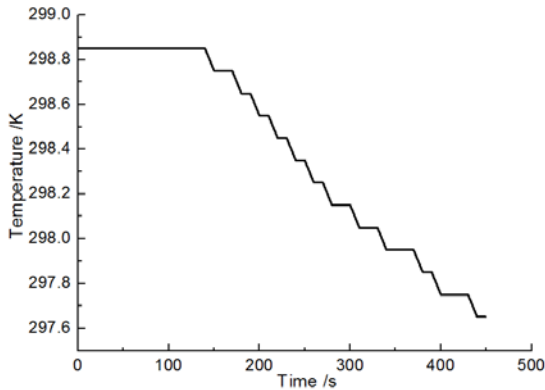


Figure 7: The change of temperature inside rescue capsule during falling process.

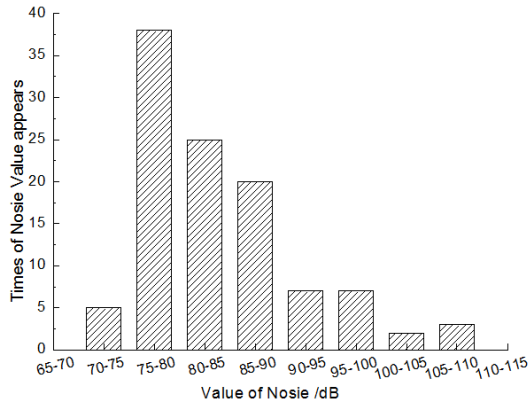


Figure 8: Noise intensity in rescue capsule when lifted.

4.3 Analysis of Experimenters' Comfort Levels and State of Sheep

Several questionnaires were conducted among 50 randomly selected experimenters 0.5 h, 3.5 h and 6.5 h after the beginning of the experiment. The questionnaires included questions probing the satisfaction with environmental comfort levels and status of individual physical conditions. Comfort

levels were then calculated according to questionnaires and the results are shown in Figure 10. In Figure 10, -2, -1, 0, 1, and 2 represent very uncomfortable, uncomfortable, average, comfortable, and very comfortable, respectively. From Figure 9 we can know that most individuals felt comfortable and satisfied with the survival environment of the refuge station. Even after the 4 h experiment without any supply, an uncomfortable reaction does not occur among individuals and few of them feel very uncomfortable.

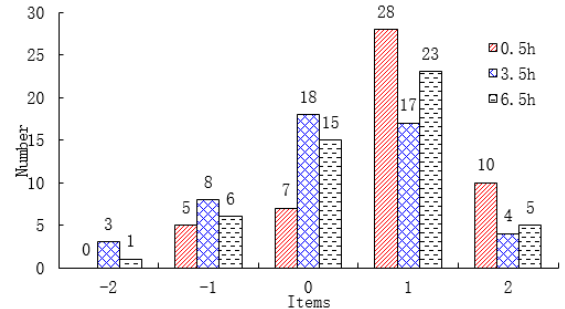


Figure 9: Comfort levels in experiment.

10 other individuals were randomly selected to have their blood pressure and pulse measured 0.5 h, 3.5 h and 6.5 h after the beginning of the experiment. The results are shown in Table 1. From Table 1 we can see that the blood pressure and pulse of experimenters showed no abnormal phenomena. During three measurements, the average value of blood pressure was 130.1/88.5 mmHg, and that of pulse was 71.3.

There were no abnormal phenomena for the sheep, except for two sheep crying and panicking due to fear after each sheep went through the lifting and falling process 4 times. Video monitoring systems showed that sheep behaved quietly with no obvious agitated activity.

Table 1. Results of blood pressure and pulse measurement.

Time	Blood Pressure/mmHg						Pulse/times per minute		
	Systolic Blood Pressure , SBP			Diastolic Blood Pressure , DBP			Min	Max	Avg±Std
	Min	Max	Avg±Std	Min	Max	Avg±Std			
0.5h	123	138	129.9±4.86	82	96	88.6±4.48	65	80	71.2±5.25
3.5h	125	135	130±2.98	84	94	88.1±3.03	67	81	71.9±4.61
6.5h	124	135	130.4±3.63	84	97	88.8±3.65	65	78	70.8±4.69
Average	130.1			88.5			71.3		

4.4 Tests of System Response Time

Response and preparing time of the emergency lifting truck were tested and the results are shown in Table 2. From the time workers inside the refuge station sent distress signals until the time that emergency lifting trucks and the mobile supply station arrived at the ground of drilling holes,

debugged the system, and prepared for rescue, the 121 min had elapsed. This is much less than survival time without any supply. Additionally, test results of hoisting speed indicate that it takes approximately 14min to lift one person, in which fall time makes up 7min and hoisting time makes up 6.3 min.

Table 2. Measurement of system response time.

NO.	Project	Time/min
1	Time consumed for mobile supply station to arrive	74
2	Time consumed to prepare for system	23
3	Time consumed to preheat diesel generating set and screw air compressor	13
4	Time consumed to set up gantry	11
5	Average one-way fall time of capsule	7
6	Average one-way lift time of capsule	6.3

4.5 Influence Borehole Has on Air Supply System

In order to study the borehole's influence on the air supply system, wind speed of the return air outlet and borehole were tested. The results are shown in Table 3. Negative wind speed indicates that wind flows from the refuge station to the ground of drilling.

As it is illustrated in Table 3, when return air outlet is open, escape drilling holes can work as air supply holes, with wind speed at 1.61 m/s. When return air outlets are closed and the compressed air supply is open, escape drilling holes can work as return air outlets, with wind speed at 0.25 m/s under the volume of 300 m³/h and at 0.56 m/s under the volume of 600 m³/h.

Table 3. Wind speed of borehole and return air outlet under different working conditions.

equipment condition			wind speed (m/s)		
Compressed air supply	air outlet	Bore-hole	Bore-hole	outlet1	outlet 2
None	Closed	Open	0.05	—	—
None	Open	Open	1.61	7.24	7.33
Volume of 300 m ³ /h	Open	Open	1.43	6.8	8.28
	Closed	Open	-0.25	—	—
Volume of 600 m ³ /h	Closed	Open	-0.56	—	—

5. CONCLUSIONS

From previous experiments and from summarizing the authors' analyses, the following conclusions are drawn.

(1) The proposed drilling escape and rescue systems consist of emergency refuge facilities, which includes a self-rescuer, refuge chamber, and refuge station, and drilling rescue facilities, which include a rescue capsule, emergency lifting truck, mobile supply station, and escape borehole. The process of emergency rescue based on the system was studied. The system can actualize safety and the high efficiency of escape and rescue in catastrophic conditions.

(2) According to experiments with individuals, the system support time with no supply was 4 h and time to debug and prepare the system was about 2 h. Individuals in the refuge station could get rescued with no supply outside.

(3) An air supply volume of 0.05 m³/h per person could satisfy survival needs for individuals in the refuge station. When air supply volume was 0.05 m³/min per person, oxygen concentration rose from 18.7% to 20.8%, and carbon dioxide concentration reduced from 1.34% to 0.04% in 60 min.

(4) Through the lifting experiment with sheep, environmental parameters inside the rescue capsule when it was lifted in the rescue borehole were measured. The reliability of animal lifting by a drilling escape and rescue system was verified.

6. ACKNOWLEDGEMENT

I would like to express my gratitude to all those who helped me during the writing of this thesis.

My deepest gratitude goes first and foremost to Professor Jin Longzhe, my supervisor, for his constant encouragement and guidance. He has walked me through all the stages of the writing of

this thesis. Without his consistent and illuminating instruction, this thesis could not have reached its present form.

Last my thanks would go to my beloved family for their loving considerations and great confidence in me all through these years. I also owe my sincere gratitude to my friends and my fellow classmates who gave me their help and time in listening to me and helping me work out my problems during the difficult course of the thesis.

7. REFERENCES

Brake, D. J., G. P. Bates. (1999).Criteria for the design of emergency refuge stations for an underground metal mine. Carlton, Australia, December, Australasian Inst of Mining & Metallurgy, pp.1-4.

Brake,D. J.(1999). "An integrated strategy for emergency egress from an underground metal mine." Proc 8th US Mine Ventilation Congress. Reno.

Gao N., Han H., Jin L., Li B., Wang P. and Li Ling.(2011).Life Support System of Ground Boreholes in Refuge Station of Changcun Mine [J]. Metal Mine, Volume 5, pp.49-53.

Gerhard H. (2014).Coal mine rescue system: cover story. Inside Mining, Volume 7, pp. 6-7.

Han H., Jin L. and Gao N.(2011). Study on confined positive pressure system in mine refuge station. Journal of Safety Science and Technology Volume 1, pp. 89-93.

Huang M. and Xie Z.(2012).Design and research on mine refuge chamber with oxygen supply by ground drilling hole in the underground in Wulan coal mine. China Mining Magazine, Volume 12, pp.31-35.

Jin L., Zhao Y., Gao N., You F. and Wang L. (2012).Study on oxygen supply system of mine refuge haven. Journal of Safety Science and Technology, Volume 11, pp.5-9.

Jin L. (2013) Technology of emergency refuge in mine [M].Beijing: China coal industry publishing house, 138p.

Li F., Jin L., Huang Z. and Zhang X. (2012).Establishment of understand emergency system in Xu Zhuang Coalmine of Da Tun [J]. Journal of Liaoning Technical University (Natural Science),Volume 2,pp.53-57.

Sun, J. (2011). Research on key technologies of emergency refuge system in underground coal mine. Meitan Xuebao, Volume 36, pp.1890-1894.

Sun J. (2011). The key technologies of the refuge chamber and rescue capsule in the underground coal

mine. Journal of China Coal Society , Volume 36 , pp.713-717.

Vinokur M. (1974). Conservation Equations of Gas Dynamics in Curvilinear Coordinate Systems. Journal of Computational Physics. Volume 14, pp. 103-118.

Wang Z. (2011).Considering and researching of drilling technology in mine rescue. Journal of safety science and technology, Volume 7, pp.5-9.

Wang H., An W. and Li Y. (2013).The Research and Design for the Controlling System of Coal Mine Rescue Capsule. Sensors & Transducers, Volume 160, pp.1726-5479.

Yang D. (2010).Construction and Development of Emergency Refuge System in Underground Mine. Coal Science and Technology, Volume 11, pp.3-7.

Yang X., Jin L., Li J. and Sun D. (2012). Design and Analysis on the Structure of Coal Mine Rescue Capsule. Journal of Convergence Information Technology, Volume 7, pp.1231-1235.

Zhang D., Ma Y. and Ding Y. (2009). Research and design of mine refuge chamber. Journal of Safety Science and Technology, Volume 3, pp.15-19.

Effects of immediate roof thickness on lower sub key strata movement in ends of large mining height panel

Chuang LIU^a, Huamin LI^{a,*}, Dongjie JIANG^{a, b}, Huigui LI^a, Junfa FENG^a

^a School of Energy Science and Engineering, Henan Polytechnic University, Jiaozuo 454003, Henan, Peoples R China

^b Department of Safety Science & Engineering, Henan Institute of Engineering, Zhengzhou 451191, Henan, Peoples R China

ABSTRACT

Based on the 58 geological drill holes around panel 42105 in the Ordos coal field, a 3D geological model and 2D numerical model with real strata conditions were established. With the models, the effect of the immediate roof thickness on the ground pressure as well as the roof movement patterns under the varying immediate roof thicknesses were explored. Mechanical models of the lower sub key strata under differing immediate roof thickness were achieved through the use of field measurement, theoretical analyses, and numerical simulation methods. Meanwhile the effect of immediate roof thickness on lower sub key strata movement in ends of large mining height coal faces was studied. The discrimination formula of the movement patterns was deduced. The results show that when the immediate roof is relatively thick, the fractured lower sub key strata can be hinged to form a stable “Voussoir Beam” structure, which makes the ground pressure not severe and the shield pressure small in the ends of the panel. When the immediate roof is thin, the arc triangular of the lower sub key strata in the ends of the panel loses mechanical contact to the caved immediate roof and assumes a “Cantilever Beam” structure, which makes the ground pressure severe and shield pressure large in the ends of the panel.

KEYWORDS: immediate roof thickness; large mining height; lower sub key strata movement; ground pressure

1. INTRODUCTION

The mining object is an opaque and changeable geological body. Due to the large spacing among geological exploration drill holes, the changes in rock strata thickness are difficult to find before mining begins. There are many scholars who research the movement patterns of roof strata, mostly based on simplified geological conditions with equal thickness (Yuan et al. 2015; Yang et al. 1999; Fu et al. 2009; Wang et al. 2015; Wang et al. 2014). However, in actual geological bodies, the rock strata are often not of equal thickness. Along with changes in the geological conditions, the movement patterns of the roof strata also change. Thus, it is not accurate to predict the roof strata movement patterns of the whole working face according to data from a single borehole, especially when the thickness of the rock strata varies greatly.

To address this issue, a new method of GMS - ANSYS - CDEM modelling and calculation is put forward, in which a relatively accurate geological model is established based on the geological drill holes data. In order to master the change of the thickness of rock strata, study the determination and prediction of the movement patterns of the roof strata and the modelling of the numerical simulation, the following steps were followed. Firstly, the 3D geological model was established by using the GMS 3D geological modelling software according to the geological drill hole data. Then, the geological model was imported

into the ANSYS software to complete the mesh generation. Finally, the node data information of the meshed model was imported into the CDEM simulation software for calculations. As a result, this method makes up for the shortage of CDEM simulation software in modelling and realizes a quick and accurate method for modeling complex geological bodies. The ANSYS - CDEM - GMS modelling and simulation method can reflect the change trend of the rock strata thickness in complex geological bodies, which greatly improves the accuracy and reliability of numerical simulations.

The existing typical patterns of rock strata structure are the “Transferring Beam” structure (Song et al. 2002), “Voussoir Beam” structure (Qian et al. 1995, 1998) and “Key-Layer” theory (Feng et al. 2008; Ju et al. 2011; Shen et al. 2011; Yang 2008). These theoretical analyses demonstrated the several possible movement patterns of rock strata under certain geological conditions. The roof structure is greatly influenced by the change of the overlying rock conditions and mining technical parameters. For the large mining height panel the mining space is relatively large, leading to a great increasing of the caving and fractured zones of the roof strata. When the thickness of the immediate roof is not the same, the filling degree of the caved immediate roof for the gob will be different. Eventually, the overlying strata movement patterns and the ground pressure distribution are changed (Huang

*Corresponding author-email: lihuamin2007@163.com

2005; Huang et al. 2004; Wu 2014; Zhang et al. 2013). Based on the geological conditions of panel 42105 and the recorded data of shield pressure and the 3D geological model, the current study researched the formation mechanism of the mechanical structure of the lower sub key strata under the large mining height, and deduced the calculation formula of the movement patterns.

2. BACKGROUND

2.1 Panel overview

The width of panel 42105 is 230 m, with an average depth of 440 m. Using the caving coal mining method, it has 3.7 m cutting height and 3.0 m top coal caving height. Panel 42105 is covered with the upper gob of 2-2 coal seam.

2.2 3D geological model

In order to grasp the thickness of the overlying strata in the 42105 working face, the GMS geological modelling software was used to establish the 3D geological model of panel 42105 on the base of the 58 geological drill hole data around this panel, and made the tailgate profile along the advancing direction.

According to the 3D geological model, the thickness of the immediate roof varies greatly. The immediate roof sandy mudstone along the working face advancing direction first follows a thinning and then thickening trend. The profiles were exported to CAD format and then the strata thickness was measured. The immediate roof thickness gradually reduced from 6.2 m to 4.3 m in the first 280 m. The immediate roof thickness gradually thickened to 5.6 m during the advancing distance between 280 m and 350 m. The thickness of the lower sub key strata changed little, with an average of 10.2 m.

3. IMMEDIATE ROOF THICKNESS AND STRUCTURE

In the process of coal mining, the shape and stability of mechanical structure formed by the lower sub key strata directly affects the distribution of the ground pressure in the working face. The typical research findings are the “Voussoir Beam” and “Kichhoff Plate” mechanics models (Qian et al. 1995; Zhu et al. 1987). According to the breaking rules of overlying rock, the periodic fracture rocks of the lower sub key strata can form the “Voussoir Beam” structure in the middle part and arc triangular structure in the end region of the panel (Figure 1) (Qian et al. 1998). The thickness of the immediate roof and lower sub key strata determine the structure movement patterns of the broken rocks. The ground pressure in the panel ends region is mainly affected by the deformation motion of

the rock C and arc triangular A, of which the arc triangular A is the main part (Yang et al. 2012).

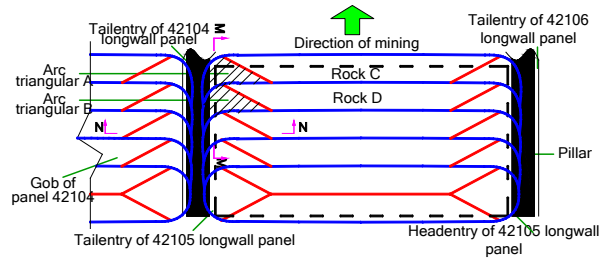


Figure 1: Schematic diagram of the broken form of the lower sub key strata.

3.1 Steady rock structure

When the immediate roof is thick, the caved immediate roof can basically fill the gob. Rock B, C, D, and arc triangular A form the “Voussoir Beam” structure, in which the rock C is the key block in the middle part of the panel. As shown in Figure 2, due to the hinge relationship among rock A and B, C, D, the sliding and rotational deformation instability will not happen for arc triangular A.

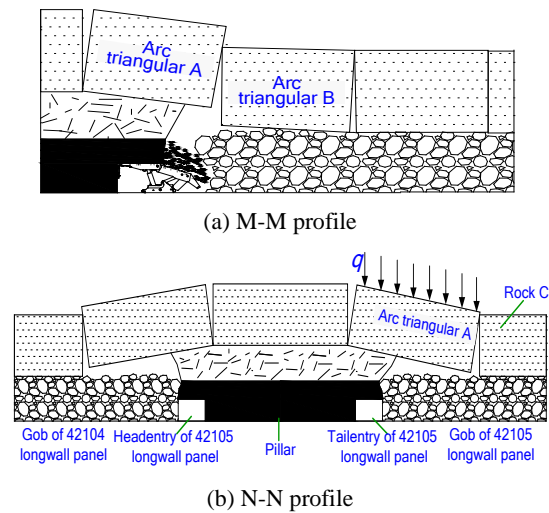


Figure 2: “Voussoir Beam” structure (thick immediate roof).

3.2 Instable rock structure

When the immediate roof is thin, the caved immediate roof cannot fill the gob. Arc triangular A loses the mechanical contact among rock B, C, D, and the “Voussoir Beam” structure cannot be formed, but instead turns into a hanging plate between the coal walls (Figures 1 and 3). Since a structure with carrying capacity cannot be formed from arc triangular A, the pressure of the rock strata in the ends region is mostly transferred to the shield and the roof of gateroads.

When the arc triangular A experiences sliding instability, the ground pressure in the ends of panel is severe.

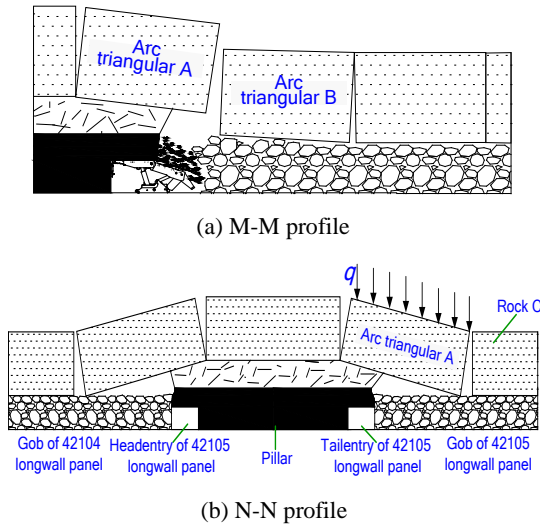


Figure 3: "Cantilever Beam" structure (thin immediate roof).

3.3 Calculation of roof structure movement

An arch structure is formed after the caving of lower sub key strata. When the hinge at the arch center is higher than those of the two ends, the rock block can maintain equilibrium. When the center hinge and those at the two ends are in the same plane, the rock block reaches the state of limit equilibrium, as shown in Figures 4 and 5. In view of the plastic state of the hinge point, the contact length of the unit width of the rock mass is a , the failure condition for any rock strata above the coal seam can be solved and the limit of subsidence Δ_{max} determined (Jiang, 2015).

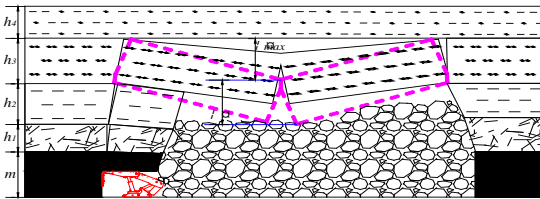


Figure 4: Schematic failure of lower sub key strata.

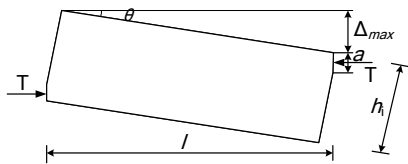


Figure 5: Limit equilibrium condition when the hinge contacts of rock blocks are in plastic state.

$$a = \frac{1}{2}(h_i - l \sin \theta) \quad (1)$$

$$T = \frac{ql^2}{h_i - l \sin \theta} \quad (2)$$

Extrusion stress at the hinged points can be determined by:

$$\sigma_p = \frac{T}{a} = \frac{2ql^2}{(h_i - l \sin \theta)^2} = \frac{2qi^2}{(1 - i \sin \theta)^2} \quad (3)$$

Where, $i = l/h_i$.

Let the ratio of bearing strength σ_p to compressive strength σ_c be K_1 , the maximum allowable load q can be determined by:

$$q = \frac{K_1(1 - i \sin \theta)^2 \sigma_c}{2i^2} \quad (4)$$

When the beam is at ultimate fracture span, the relationship between its load q and tensile strength σ_t can be determined by:

$$\sigma_t = K_2 q \frac{6l^2}{h_i^2} = 6K_2 qi^2 \quad (5)$$

Where:

a = Contact length of broken rock block, m;

θ = Rotation angle of broken rock block, °;

T = Horizontal force required to keep the limiting state, Pa·m;

h_i = Thickness of i^{th} rock layer above the coal seam, m;

l = Broken interval of i^{th} rock layer above the coal seam, m;

q = Weight and load of i^{th} rock layer above the coal seam, Pa;

K_2 = General value 1/3 ~ 1/2;

n = Ratio of compressive strength σ_c to tensile strength σ_t .

Limit of subsidence Δ_{max} can be determined by:

$$\Delta_{max} = h_i \left(1 - \sqrt{\frac{1}{3nK_1K_2}} \right) \quad (6)$$

Where, $\Delta_{max} = l \sin \theta$.

After the failure of the immediate roof, the subsidence of lower sub key strata Δ_{hi} can be determined by:

$$\Delta_{hi} = m - (K_p - 1) \sum h \quad (7)$$

Where:

m = Mining height, m;

K_p = Bulking factor;

σ_{ci} = Compressive strength of i^{th} rock layer above the coal seam, Pa;

$\sum h$ = Thickness of the first to $(i-1)^{\text{th}}$ rock layer above the coal seam, m.

Using the overburden strata mechanics parameters of Panel 42105 ($K_p = 1.25$, $\sum h = 4.1 \sim 6.2$ m), the Δ_{hi} of lower sub key strata can be determined between 5.15 m and 5.68 m.

According to Kong et al. (2010), there is a relationship between the extrusion stress σ_p and compressive strength σ_c of the rock block at the hinge

point: $\sigma_p=0.36\sim 0.45\sigma_c$. Generally $\sigma_p=0.4\sigma_c$ is used. According to the simply supported beam model, $K_2=1/3$, the ratio of compressive strength σ_c to tensile strength σ_t of siltstone is 12 in panel 42105. Therefore, the limit of subsidence $\Delta_{max}=5.54$ m.

Compared to the subsidence of lower key strata Δ_{hi} and the limit of subsidence Δ_{max} , when the immediate roof is more than 4.64 m, the fractured lower sub key strata can form a stable “Voussoir Beam” structure; when the immediate roof is less than 4.64 m, the fractured lower sub key strata will assume a “Cantilever Beam” directly baggy falling form.

3.4 Numerical simulation

Based on the 3D geological model established by the GMS software, a numerical model was built to simulate the geological cross-section along the panel advancing direction. The model was 400 m long by 464 m high. The model contained the full overburden thickness from the coal seam to the surface. The vertical loading was the full overburden gravity load and the boundaries of the bottom, left and right sides of the model were fixed. CDEM (Continuum-based Distinct Element Method) software was used to calculate, in which the Mohr-Coulomb strength criterion was chosen as the material yield criterion of coal and rock mass. By the numerical calculation results, the change of the lower sub key strata structure during the mining process was analyzed with the thickness change of the immediate roof.

(1) Thin immediate roof

When the face has advanced 270 m, the immediate roof is 4.34 m. Simulation results show that the caved immediate roof cannot basically fill the gob. The arc triangular of the lower sub key strata in the ends of the panel lost mechanical contact to the caved immediate roof. The original lower sub key strata can be formed with a load-bearing structure due to the increasing of rotation angle, forming a “Cantilever Beam” structure (Figure 6).

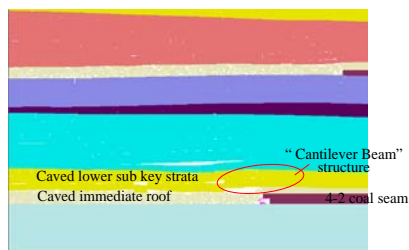


Figure 6: “Cantilever Beam” structure (270 m advancing).

(2) Thick immediate roof

When the face has advanced 230 m, the immediate roof is 4.81 m. Simulation results show that after the

lower sub key strata caving, the broken rock can hinge to each other and form the “Voussoir Beam” structure (Figure 7). Compared to the results of “Cantilever Beam” structure, the vertical displacement range of the upper strata and coal seam is relatively small at this time.

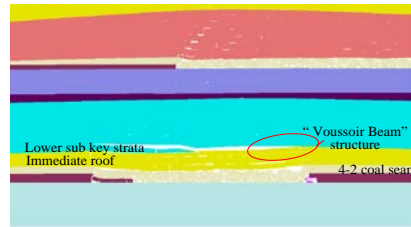


Figure 7: “Voussoir Beam” structure (230 m advancing).

4. SHIELD DATA ANALYSIS

Panel 42105 was equipped with an electric hydraulic control monitoring system that can automatically and quickly upload the shield pressure to the ground control room. Surfer 8.0 was used to draw the 3D map of the relationship among working face, shield pressure, and advancing distance from June 16th - 23th (Figure 8).

Since roof pressure usually varies continuously with time, time-weighted average pressure (TWAP) is more appropriate to illustrate the overall conditions of the shield in a whole cycle and is defined by the following equation (Syd S. Peng, 2013; 2011):

$$P_i = \frac{\sum P_i t_i}{t_i} = \frac{\frac{1}{2}(P_a + P_s)t_a + \frac{1}{2}(P_b + P_a)t_b + \frac{1}{2}(P_c + P_b)t_c + \frac{1}{2}(P_d + P_c)t_d}{t_a + t_b + t_c + t_d} \quad (8)$$

Where, P_i is the average shield pressure during the period of t_i . In other words, P_i is the ratio of the area under the pressure variation curve to the total time in a mining cycle.

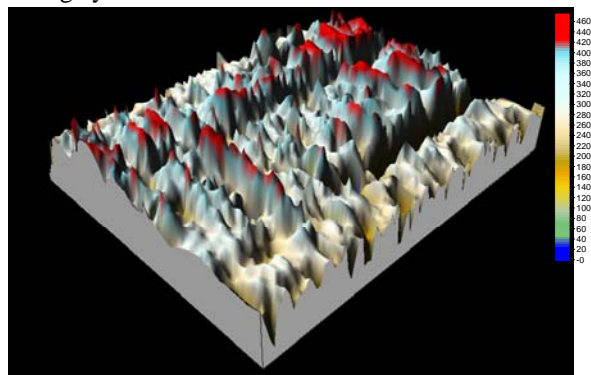


Figure 8: 3D map of the relationship among working face, shield pressure, and advancing distance.

The TWAP and standard deviation of 100# shield

near the tailgate was analyzed in the panel 42105 from June 16th - 28th (Table 1). The results show that: (1) The TWAP and standard deviation of 100# shield were floating large on June 17, 19, 21, 22, (due to the working face being off production on June 18th, the shields weren't moved, resulting in great pressure on the roof), indicating great intensity of the roof strata activity. In these days, 70% of the all shields opened the yield valve, meanwhile the rib spalling was serious,

with an average depth of 0.3 m. (2) When the immediate roof thickness decreases, the TWAP and standard deviation increase. On June 22th, the immediate roof thickness was the smallest and the standard deviation reached the maximum of 10.90 MPa. When the immediate roof thickness increases, the TWAP and standard deviation decrease.

Table 1: TWAP and standard deviation of 100# shield at different advancing distance.

Date	Pt/ MPa	σ /MPa	(Pt+ σ)/ MPa	Advancing distance/m	Immediate roof thickness /m
6.16	29.39	5.38	34.77	218.6	4.84~4.98
6.17	29.41	6.30	35.71	236.5	4.64~4.84
6.18	37.04	7.91	44.94	239.2(Off production)	4.61~4.64
6.19	36.02	9.87	45.89	250.9	4.47~4.61
6.20	29.29	3.46	32.76	251.7(Off production)	4.46~4.47
6.21	29.29	6.14	35.43	266.0	4.32~4.46
6.22	26.58	10.90	37.48	278.5	4.16~4.32
6.23	28.78	3.65	32.43	289.0	4.16~4.76
6.24	28.96	5.27	34.23	301.6	4.76~4.92

When the immediate roof is thick, the lower sub key strata actual subsidence is less than its limit subsidence, the fractured lower sub key strata can be hinged to form a stable "Voussoir Beam" structure. This structure bears part of its own weight, so that the weight of the rock on the shields is reduced. When the immediate roof is thin, the lower sub key strata actual subsidence is more than its limit subsidence. The arc triangular of the lower sub key strata in the ends of the panel loses mechanical contact to the caved immediate roof and assumes a "Cantilever Beam" structure. Therefore, the most weight of the lower sub key strata through the immediate roof directly acts on the shield, which makes the shield pressure large in the ends of the working face.

The influence factors of the shield pressure are related not only to the thickness of the immediate roof and the movement patterns of the lower sub key strata, but also to the shield frame, the advancing speed, and the mining height. However, the above data analysis shows that there is a correlation between the change of shield pressure and the immediate roof thickness. That is, when the immediate roof becomes thin, the TWAP and standard deviation show an increasing trend, and vice versa.

5. CONCLUSIONS

This paper concentrates on the effect of immediate roof thickness on the lower sub key strata movement in the ends of panels. A 3D geological model was established and used to deduce the formula of the movement patterns of roof structure under different immediate roof conditions, and analyzed the numerical simulation results and the monitoring data of the shield

pressure. The following conclusions were obtained:

(1) When the thickness of the lower sub key strata changes little, the immediate roof thickness is an important factor that affects the structure and the ground pressure distribution.

(2) Compared to the actual subsidence of lower key strata Δ_{hi} and its limit subsidence Δ_{max} , when $\Delta_{hi} < \Delta_{max}$, a stable "Voussoir Beam" structure can be formed in the fractured lower sub key strata; when $\Delta_{hi} > \Delta_{max}$, the lower sub key strata assumes a "Cantilever Beam" structure.

(3) The stable "Voussoir Beam" structure bears part of its own weight, so that the weight of the rock on the shields is reduced and ground pressure is not severe, and the TWAP and standard deviation is small. Under the "Cantilever Beam" structure conditions, the most weight of the lower sub key strata through the immediate roof directly acts on the shield, which makes the ground pressure severe and TWAP and standard deviation large.

6. ACKNOWLEDGMENT

This research was funded by the Chinese Natural Science Committee under grant No. U1261207.

7. REFERENCES

- Feng, G., Wang, X. and Kang, L. (2008). Analysis on the mechanism of the face contacted blocks structure in overlying strata above the longwall face. Journal of China Coal Society, 01:33-37.
- Fu, Y., Song, X., Xing, P., Yan, G. and Li, Z. (2009). Stability analysis on main roof key block in

large mining height workface. *Journal of the China Coal Society*, v 34, n 8, 1027-1031.

Huang, Q. (2005). Study on loading distribution law on key roof and its structure upon mining face under thick sandy layer. *Journal of China University of Mining and Technology*, v 34, n 3, 289-293.

Huang, Q. and Zhang, P. (2004). Study on dynamic load distribution on key roof blocks of under thick sandy soil stratum. *Chinese Journal of Rock Mechanics and Engineering*, v 23, n 24, 4179-4182.

Jiang, D. (2015). Research on Overburden Structure and Shields Stability of Fully Mechanized Top Coal Caving Mining Face with Large Mining Height. Henan Polytechnic University, 19-21.

Ju, J., Xu, J. and Wang, Q. (2011). Cantilever structure moving type of key strata and its influence on ground pressure in large mining height workface. *Journal of China Coal Society*, 12:2115-2120.

Kong, L., Jiang, F., Liu, J. and Wang, C. (2010). Relationship between Support and Strata in Extra-thick Coal Seam Fully-mechanized Sublevel Caving Mining based on High Precision Microseismic Monitoring Technology. *Chinese Journal of Geotechnical Engineering*, 32(3): 401-407.

Qian, M. and Miao, X. (1995). Theoretical analysis on the structural form and stability of overlying strata in longwall mining. *Chinese Journal of Rock Mechanics and Engineering*, 02:97-106.

Qian, M. and Xu, J. (1998). Study on the "O shape" circle distribution characteristics of mining-induced fractures in the overlying strata. *Journal of China Coal Society*, 05:20-23.

Shen, J., Meng, D. and Wei L. (2011). Study on the structural system of roof in fully mechanized top coal caving. *Applied Mechanics and Materials*. v 90-93, 2041-2044.

Song, Z., Jiang, J., Sun, X. and Zhao, J. (2002). The structure model and its application to roof rock pressure control in gateways of a deep mine. *Mining Science and Technology '99*, 9-14.

Syd S. Peng. (2013). *Coal Mine Ground Control*. China University of Mining and Technology Press, Xuzhou, pp. 310-312.

Syd S. Peng. (2011). *Longwall Mining*. Science Press, Beijing, pp. 131-138.

Wang, J. and Wang, Z. (2015). Stability of main roof structure during the first weighting in shallow high-intensity mining face with thin bedrock. *Journal of Mining and Safety Engineering*, v 32, n 2, 175-181.

Wang, J., Yuan, Y., Tu, S. and Li B. (2014). Roof structure characteristics in fully mechanized coalface with large mining height and reasonable loading of support. *Journal of Mining and Safety Engineering*, v 31, n 4, 512-518.

Wu, F. (2014). Study on the Law of Roof Broken and Instability and the Control of Mining Height Fully

Mechanized Mining in Thick Coal Seam. China University of Mining and Technology, 9-12.

Yang, P. and Liu, C. (2012). Structure forms of basic roof and reasonable supporting parameters in ends of fully-mechanized top caving face. *Journal of Mining & Safety Engineering*, 01:26-32.

Yang, S. and Jiang, F. (1999). Research on the relationship between sublevel caving support load and roof structure. *Chinese Journal of Rock Mechanics and Engineering*, 18(3): 287-290.

Yang, Z. (2008). Instability behavior for roof strata in shallow seam longwall mining. *Journal of the China Coal Society*, v 33, n 12, 1341-1345.

Yuan, Y., Tu, S., Zhang, X. and Li B. (2015). Dynamic effect and control of key strata break of immediate roof in fully mechanized mining with large mining height. *Shock and Vibration*, v 2015.

Zhang, Q., Jia, H., Fan, L., Zhao, X., Wang, Z. and Xing, J. (2013). The detection research of roadway roof strata structure in coal seam. *Advanced Materials Research*, v 734-737, 677-681.

Zhu, D. and Qian, M. (1987). Numerical simulation of destruction and instability of basic roof in long wall face. *Journal of China University of Mining & Technology*, 16(3): 1-9.

Study on the performances of a protective door in coal permanent refuge havens

Gao Na*, Jin Long-zhe, Fan Lin-yu, Shen Jie, Wang Wei-xiang, Liu Jian-guo

Civil and Environmental Engineering, University of Science and Technology Beijing, Beijing, China, 100083

ABSTRACT

An effective protective door for an underground refuge haven must have anti-explosion properties, anti-pressure properties, and sealing capabilities. In this study, Wulan Coal Mine's situation and the technical requirements for the protective door in the permanent coal refuge haven were analyzed and a numerical simulation analysis for the anti-explosion performance was performed. The materials, structure, and the sizes of the protective door were confirmed. Further, two experiments on the protection and waterproof abilities of the door were conducted. The results showed that a 15 mm thick 16 manganese steel plate door meets anti-blast and economical requirements. In addition, a manual wedge-shaped lock structure, a single-cast door wall, and a welding steel supporting structure can satisfy the airtight sealing and anti-pressure requirements. In the numerical simulation of the blast effect, it was observed that the maximum displacement was at the centre of the door, and the region of the highest stresses was around the door. The protective door could bear a 1 MPa explosion impact, and it could withstand a 1.86 MPa static pressure load with a deformation of 5.8 mm. Further, the door maintained good sealing performance until the hydraulic pressure exceeded 1.6 MPa with a deformation of 14 mm.

KEYWORDS: Refuge haven; protective door; anti-blast; finite element analysis; performance test

1. INTRODUCTION

Coal is an important basic energy source, and coal reserves account for more than 85% of China's energy resources (Wang and Ji, 2012). At present, Coal mining in China is mainly manual and mechanical. The underground mining environment is complex, therefore, mining safety has become a significant concern. Moreover, owing to the lack of mechanization, mining efficiency is low. In order to ensure the safety of coal miners, the research on refuge havens is of great significance both domestically and globally. The research on refuge havens in developed countries such as the United States, Canada, Australia, South Africa, and others started early, and has achieved fruitful results on underground haven refuge sites, basic protection parameters, and internal oxygen supply for the miners. Further, they have successfully rescued several miners via refuge havens. In August 2010, the State Administration of Coal Mine Safety in China issued on the construction and improvement of coal mine safety hedging "six systems". This document provides a complete set of requirements for the construction of the underground safety hedging systems. Based on the most common types of underground accidents, a refuge haven should include features such as anti-fire, anti-blast, sealing isolation, and oxygen supply (Rick and Graham, 1999). In

China, research on refuge havens is in its infancy. At present, China has formed a research system that comprises research institutes, universities, and enterprises. This system has progressed on the basis of the international research achievements, and has gradually developed equipment needed for refuge havens and the related technical requirements (Sun, 2011; Li, 1989; Zhao and Wang, 2007; Michael, 2007; Yang, 2010).

However, studies on protective doors for fire protection, explosion protection, and door sealing are not comprehensive. In this study, the protective door in the Wulan Coal Mine refuge haven is analysed. The stress conditions on the protective door surface are calculated, and the door sealing and blast protection requirements are analyzed to determine the requirements for the door plank material, overall structure, lock structure, supporting structure, and the door size. Further, the capabilities of the anti-blast, anti-stress and waterproofing for the refuge haven-protective door are determined through simulations of the anti-blast, and experiments of anti-pressure, and waterproofing on the door. This study provides evidence and verification for the protective features of the protective door under different conditions. The conclusions made provide important reference to build a complete life protection system and support related technical research.

*Corresponding author – email :aggie198308@163.com

2. MATERIALS, STRUCTURES, AND DIMENSIONS

2.1 Protective door materials

Blast-proof materials commonly used for protective doors include Q235 steel, Grade 45 steel, Grade 70 steel, and 16 manganese (16Mn) steel. The mechanical strengths of these materials are listed in Table 1. Among them, Grade 70 steel has the strongest yield strength and can withstand great pressure; however, the product is easy to break, which leads to door deformation. The anti-pressure ability of Grade 45 steel is superior to that of Grade 70 steel, but its corrosion resistance is lower than other materials. The anti-pressure and corrosion resistance abilities of 16Mn steel outperform Q235; however, it is more expensive than other materials. After a comprehensive analysis, for the Wulan Coal Mine refuge haven, it was decided that the 16Mn steel would be used as the material for the protective door plank of the refuge haven, Q235 for the rest materials of the door structure, and the door surface would be sprayed with fireproof and corrosion-resistant paint.

Table 1: Door materials to anti-blast strength comparison.

Material	Yield Strength (MPa)	Modules of Elasticity (GPa)
Q235	235	210
45 steel	355	204
70 steel	420	210
16Mn	350	206

2.2 Protective door shape

The Wulan Coal Mine refuge haven was built in the wall of a tunnel, therefore, the pressure that the door withstood came from the blast wave with a side impact. The door plank could be flat or curved according to the blast shock. The stress analysis is carried out as follows.

Flat door force analysis: the stress process of a flat door is shown in Figure 1. The impact of the explosion is calculated by the following formulas (Yang, 1996; Jian, 2003).

$$R = \sqrt{X^2 + Y^2} = 0.5PS\sqrt{2 - 2\cos 2\alpha} \quad (1)$$

$$D = \frac{0.5PS\sqrt{2 - 2\cos 2\alpha}}{0.5S/\sin \alpha} = P \sin \alpha \sqrt{2 - 2\cos 2\alpha} \quad (2)$$

where, α is the angle between the incident direction and the flat door plank, °; β is the incident angle and reflection angle of the shock wave, °; P is the average stress of the shock wave on the flat door, Pa; S is the surface area of the door, m^2 ; X , Y are the reaction and the perpendicular reaction to the shock wave, N; R is the total reflection, N; D is the equivalent stress

that the door can bear, Pa. According to formulas (1) and (2), when α has an optimal value of $\pi/2$, R is $P \cdot S$. When D is $2P$, the reflection and equivalent stress decrease as α increases.

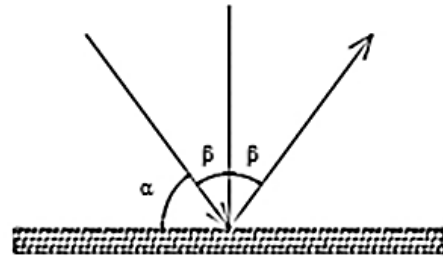


Figure 1: Flat protective door pressure handling

Curved door force analysis: the stress process of a curved door is shown in Figure 2. The impact of the explosion is calculated by the following formulas (Luo et al, 2007; Lin et al, 2008).

$$R = \sqrt{X^2 + Y^2} = \frac{\sqrt{5}}{3} PS \quad (3)$$

$$D = \frac{R}{\pi S} = \frac{\sqrt{5}}{3\pi} P \quad (4)$$

where, α is the angle between the incident direction and the tangential direction of the curved door plank, °; β is the incident angle and reflection angle on the tangential direction of the curved door plank, °; P is the average stress of the shock wave on the tangential direction of the curved door plank, Pa.

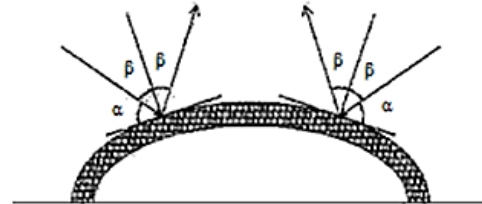


Figure 2: Curved protective door pressure handling.

By comparing the flat door with the curved door in terms of the explosion impact and equivalent stress, it can be seen that both the curved doors and flat panels meet the blast-proof requirements. In particular, the curved door received 25% less impact than the flat door, and the equivalent strength increased to approximately 50%. However, the production of a curved door requires a specialized mold, the processing is more complex, and the cost is relatively high. Therefore, the Wulan Coal Mine eventually selected the flat door for its permanent refuge haven.

2.3 Sealed locking structure

The sealed locking structure of a protective door determines its sealing capability. Common sealing methods include pressure, hydraulic, electric, and mechanical locks. After considering the underground power, air environment, and required door reliability of the Wulan Coal Mine, the mechanical manual lock structure shown in Figure 3 was selected for the refuge haven. The structure adopted the door and four wedge locking devices on the frames. Sealing is carried out by manually rotating the lock against the door frames, with the fire retardant material applied between the flashboards.

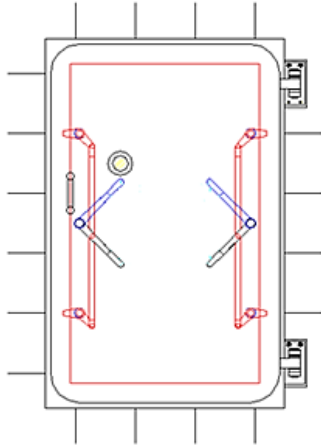


Figure 3: Sealing structure of the protective door.

2.4 Supporting structure

In order to increase the anti-blast ability of the protective door, the overall connection of the door to the wall must be strengthened. To do this, the Wulan Coal Mine permanent refuge haven adopted a welded steel support structure, as shown in Figure 4, for its protective door. The protective door used ferroconcrete, and the wall used concrete casting to create an overall anti-blast airtight seal. When an explosive blast strikes the protective door, the impact would pass through the door supporting structure and be dispersed throughout the wall, which diminishes the effect of the impact (Tian, 1997).

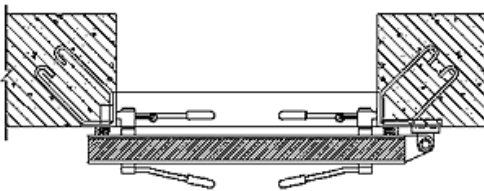


Figure 4: Protective door supporting structure.

2.5 Protective door dimensions

The protective door dimension of the Wulan Coal Mine refuge haven included the door's height, width, and thickness.

(1) Protective door height

The height of the protective door should be decided based on the worker's height and the size of the equipment. It should enhance the door's anti-blast function, yet reduce its exposed area. Through data collection, analysis, and calculations, the average height of the Wulan Coal Mine underground digging, mining, installation, withdrawal, and other operating personnel was determined to be 1730 mm. The largest equipment was the oxygen control device, whose dimensions were 550 × 280 × 1250 mm. Therefore, the protective door height of the Wulan Coal Mine permanent refuge haven was set to 1600 mm.

(2) Protective door width

Through data collection, analysis and calculations, the average shoulder width of the underground workers was determined to be 700 mm. The oxygen purifiers have a maximum width of 600 mm. The width required for equipment transport was also considered, and the width of the protective door was finalized to 950 mm. The overall dimensions of the protective door are as shown in Figure 5.

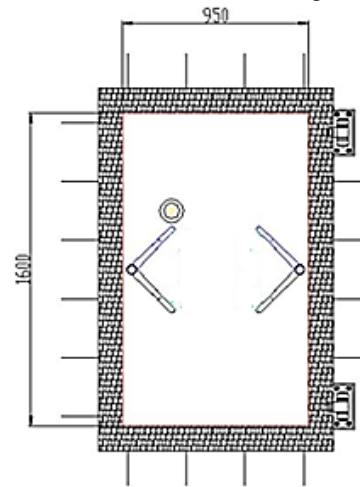


Figure 5: Protective door dimensions.

(3) Protective door thickness

The thickness of the protective door in the Wulan Coal Mine refuge haven was determined based on the incident pressure, reflecting pressure, and static load pressure of the blast (Zhu et al., 2013). The reflecting pressure of the protective door and the static load pressure were determined by the incident pressure. The door thickness (Silvestrini et al, 2008) was calculated using the following formulas.

$$\Delta P_{\lambda} = K \frac{0.196r}{r+1} (M^2 - 1) \quad (5)$$

$$D = \frac{KK_d B}{2\sigma_D} \left(2\Delta P_{\lambda} + \frac{6\Delta P_{\lambda}^2}{0.7 + P_{\lambda}} \right) \quad (6)$$

Where, K is the safety factor; r is the air specific heat ratio; m is the ratio of the blast wave speed to the mean speed of sound; K_d is the dynamic coefficient; B is the width of the protective door, σ_D is the pulling stress on the door, and ΔP_λ is the incident pressure. The calculation result showed that the door thickness was 13.2 mm; therefore, the door thickness was set as 15 mm.

3. ANTI-EXPLOSION NUMERICAL SIMULATION ANALYSIS

Based on the door size and material study, 15 mm thick 16Mn steel was selected for the protective door. For the 16Mn steel, the modulus of elasticity is 206 GPa, Poisson's ratio is 0.31, and the yield strength is 350 MPa. A physical model was of a protective door was developed and meshed through finite element numerical simulation analysis. The door load was set to be 1 MPa. The force and displacement on the door were simulated by software ANSYS. Then, the material, thickness, and structure of the protective door in the Wulan Coal Mine refuge haven were assessed to ensure they met the protection requirement (Liao and Ding, 2009; Tan et al., 1997; Lu and Jian, 2003).

4. EXPERIMENT

4.1 Static pressure test

The test door was installed in a doorframe made with ferroconcrete, and it was placed at the ground level with the door suspended in the air. A 10 cm layer of fine sand was placed on the door surface, and it was loaded with high-pressure gasbags to distribute the weight pressure. Next, the airbags were inflated and a static pressure load was placed on the door. At the same time, a CYG712-5 MPa type soil pressure sensor and a BWG2-100 mm displacement transducer were used to measure the door pressure and deformation.

4.2 Airtight and waterproofing test

Two test doors were welded to both ends of a water container, and it was ensured that the welding was sealed and leak proof (as shown in Figure 6). Next, at the bottom of the container, a water valve, pressure gauge, piping, and pressure pump were placed, and a pressure gauge and an air vent were placed on the top to measure internal pressure changes, i.e., the pressure handling capacity of the door. Then, water was added to the sealed container, thus adding pressure into the container. The door deformation and the pressure at the top were measured until the door experienced plastic deformation. Finally, the level of hydraulic pressure

the door could take and its deformation conditions were recorded.



Figure 6: Protective door and sealed container for water proofing test.

5. RESULTS AND DISCUSSION

5.1 Numerical simulation analysis

(1) Protective door structure displacement

Figure 7 shows the displacement transformations of the protective door after it was loaded. An analysis of the displacement of the protective door after it bore a 1 MPa load showed that the greatest displacement was elliptical and occurred at the door's centre. The displacement became smaller as it moved from the inside toward the door's borders; the door's centre had larger displacements than the parts around the sealed borders.

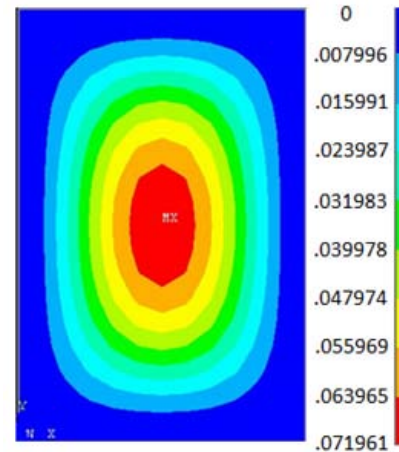


Figure 7: Protect door displacement transformations.

(2) Protective door force

Figure 8 shows the pressure distribution of the protective door model after it was loaded. Based on the door pressure distribution results of numerical

simulation, the pressure at the edge was larger than that in other areas after it bore a 1 MPa load. Although the door was depressed after bearing the pressure, it did not become plastically deformed. This shows that if the load added is less than the yield strength that 16Mn steel can handle, then the door does not undergo plastically deformation.

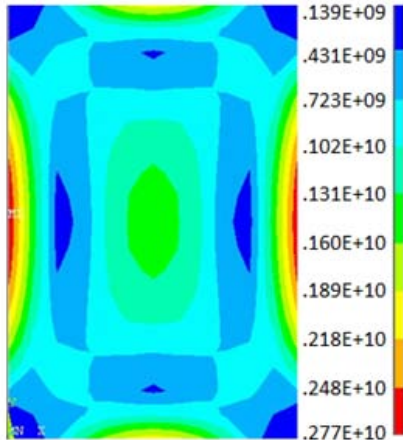


Figure 8: Protective door pressure distributions.

Finite element analysis of the protective door proved that the Wulan Coal Mine’s 15 mm thick 16Mn steel flat door could resist a 1 MPa explosion without damage, and it met the 0.3 MPa requirement for anti-fire and anti-blast abilities specified in the current regulations. In order to protect the sealing function from door displacement, a ferroconcrete structure was added and the doors anti-pressure ability was reinforced in order to reduce door deformation.

5.2 Anti-pressure performance of the protective door

Figure 9 shows the hydrostatic load change in the gasbags on the top of the protective door. The pressure and deformation conditions are shown in Table 2. This test proved that the protective door was capable of withstanding a maximum static pressure load of 1.86 MPa, and the corresponding deformation was 5.8 mm.

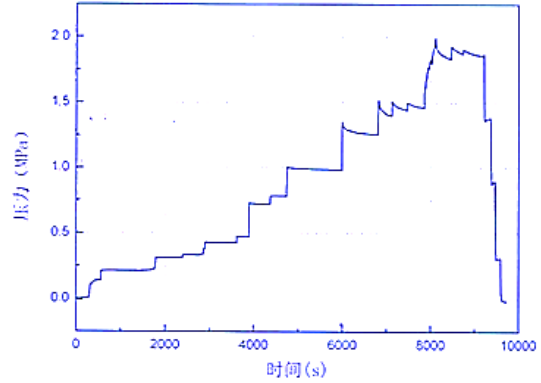


Figure 9: Protective door static pressure load test time - pressure curve.

Table 2: Protective door static pressure load pressure - deformation relationship.

Time(s)	Static Pressure Load (MPa)	Deformation (mm)	Deformation Speed
0-1800	0 -0.35	0-3.0	Steadily increased
1800-6900	0.35-1.50	3.0-4.4	Obvious increase
6900-8100	1.50-1.86	4.4-5.8	Slowly increased
8100-10000	1.86-0	5.8-2.2	Slowly decreased

5.3 Water proof performance of the protective door

Figure 10 shows the relationship between the waterproof feature under pressure and deformation. The hydraulic pressure change for a sealed container filled with water was 0–1.6 MPa. As the hydraulic pressure increased, the door began to deform as follows: “obvious deformation-fundamentally unchanged-slowly increased-maximum deformation”. When the pressure reached 1.6 MPa, the door had a maximum deformation of 14 mm. In the test, there were no leaks or unusual sounds. This test proved that the protective door of the Wulan Coal Mine permanent refuge haven could withstand 1.6 MPa hydraulic pressure and maintain a good seal.

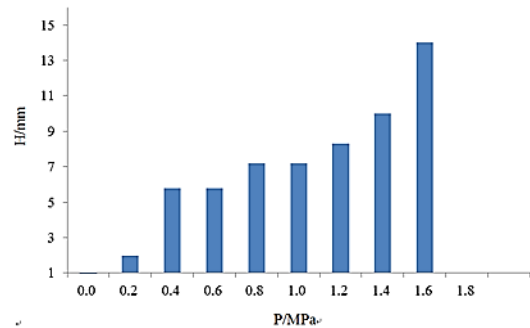


Figure 10: Protective door pressure – deformation.

6. CONCLUSIONS

This study confirmed that the protective door in the permanent refuge haven of Wulan Coal Mine was made with 16Mn steel, with a flat door structure, and used a manual wedge-shaped locking system. The doorframes and walls were supported with ferroconcrete and cast concrete to ensure the ability for anti-blast and airtight sealing. The dimensions of the door were 1600 mm (height), 950 mm (width), and 15 mm (thickness).

Finite element analysis proved that in the permanent refuge haven of Wulan Coal Mine, the door centre had the greatest displacement with the largest pressure at the edges, when it born the blast shock in the tunnel, and it could withstand a 1 MPa explosive impact without plastic deformation. In order to increase the anti-blast protection, the door was reinforced with a ferroconcrete structure.

A static pressure load test confirmed that the door withstood a maximum static pressure load of 1.86 MPa, which corresponded to a deformation of 5.8 mm. The sealed waterproof test confirmed that the largest anti-pressure of the protective door was 1.6 MPa, which corresponded to the deformation of 14 mm with a good seal.

7. ACKNOWLEDGEMENT

This work is financially supported by the National Natural Science Foundation of China (No. 51504017), the Fundamental Research Funds for the Central Universities (No. FRF-TP-15-043A3), the China Postdoctoral Science Foundation (No. 2014T70039), the Doctor Science Research Foundation of the Education Ministry of China (No.20130006120020), the China Postdoctoral Science Foundation (No.2013M540666), which is gratefully acknowledged.

8. REFERENCES

Jian, C.G. (2003). Research on methane explosion propagation character in duct and factors. China University of Mining and Technology.

Li, R.S. (1989). Mine refuge chamber. Yunnan Metal, Volume 1, pp. 47-50

Liao, L.Y., Ding G.Q. (2009). Blast - resistant simulation analysis of protective metal crust under impact load. Computer Simulation, Volume 8, No. 1, pp. 20-26

Lin, B.Q., Ye, Q., Zhai, C., Jian, C.G. (2008). The propagation rule of methane explosion in bifurcation duct. Journal of China Coal Society, Volume 33, No. 2, pp. 136-139

Lu X.Z., Jian, J.J. (2003). Safety assessment of blast - resistant doors using dynamic finite element method and contact analysis. Mechanics Engineering, Volume 2, pp. 24-26

Luo, Z.M., Deng, J.W., Wen, H., Zhang, H. (2007). Experimental study on flame propagation characteristics of gas explosion in small-scale duct. China Safety Science Journal, Volume 17, No. 5, pp. 106 -109

Michael, A. (2007). Parametric design of a coal mine refuge chamber. West Virginia University.

Rick, B., Graham, B. (1999). Criteria for the design of emergency refuge stations for an underground metal mine. Journal of the Aus IMM, Volume 12, pp. 2-5

Silvestrini, M., Genova, B., Parisi, G, Trujillo, F.J.L. (2008). Flame acceleration and DDT run-up distance for smooth and obstacles filled tubes. Journal of Loss Prevention in the Process Industries, Volume 21, No. 5, pp. 555-562

Sun, J.P. (2011). Research on emergency refuge system in underground mine. Coal Science and Technology, Volume 39, No. 1, pp. 69 -71

Tan, D.W., Chen, S.H., Liu, W.H. (1997). Application of finite element analysis in dynamics of explosion. Explosion and Shock Waves, Volume 4, PP. 40-46

Tian, R. (1997). The development and application of the gasproof concrete and JCL interface adhesive in gas tunnel construction. Journal of Shijiazhuang Railway Institute, Volume 9, pp. 64-68

Wang, B.J., Ji, F. (2012). Coal industry chain the endogenous of the inside nodes' collaboration and inter-chain evolution. Journal of China University of Mining and Technology, Volume 11, No. 6, pp. 978-983

Yang, D.M. (2010). Construction and development of emergency refuge system in underground mine. Coal Science and Technology, Volume 11, pp. 6-9

Yang, Y.L. (1996). The overpressure calculation and prevention of gas and coal dust explosion. Coal Engineer, Volume 2, pp. 32-37

Zhao, L.A., Wang T.L.(2007). The application and revelation of overseas mine safe haven. Coal mine security, Volume 8, pp. 88-91

Zhu, C.j., Lin, B.Q., Jiang B.Y., Liu, Q., Hong, Y.D., Sun, Y.M. (2013). Multiphase destructive effects of shock wave resulting from coal mine gas explosion. Journal of China University of Mining and Technology, Volume 9, No. 5, pp. 718-725

Numerical modelling of the goaf: methodology and application

Samar S. Ahmed^{a*}, Marwan ALHeib^b, Yann Gunzburger^a, Vincent Renaud^b, Jack-Pierre Piguet^a

^a GeoRessources, Université de Lorraine, CNRS, Ecole des Mines de Nancy, Nancy, 54042, France

^b INERIS, Ecole des Mines de Nancy, Nancy, 54042, France

ABSTRACT

The mechanical behavior of the goaf is a critical issue that may affect the efficiency of longwall mining. Goaf numerical modelling as a continuous material is a challenge, especially because its large-scale mechanical properties are not precisely known. Many different values of the elastic modulus may be found in the literature to be used for representing the mechanical behavior of the goaf area. In the present study, the elastic numerical modelling is shown to be a useful tool for simulating the stress redistribution and displacement due to longwall mining, while taking into account the goaf geometry and its equivalent mechanical properties. The analysis is applied on the Provence coalmine, in the south of France, which had been in operation for more than 50 years, using the longwall mining method was used. A finite difference numerical model of the mine is constructed and two approaches are carried out in order to simulate the goaf area above the excavated panels where the panels have various length to width ratios. In the first approach, the caved zone and the fractured zone have different but homogeneous elastic modulus, both zones have elastic modulus lower than the unaffected host rock. In the second one, their elastic modulus varies linearly with the vertical distance above the panel, up to the elastic modulus of the host rock. In both cases with and without goaf, the subsidence at the ground surface is calculated and compared with in-situ measured values. Results show that attributing to the goaf area a low elastic modulus increases the vertical stress within the rib pillars as well as the subsidence at the surface. The elastic modulus for the direct roof above the panel after excavation has found to be $225 \leq E_{\text{immediate-roof}} \text{ (MPa)} \leq 180$ in order to satisfy the total convergence between the roof and the floor. Representing the goaf area as a material with linearly varying elastic modulus gives rational results in terms of convergence and ground surface subsidence.

KEYWORDS: Numerical modeling; goaf simulation; longwall mining; stress redistribution

1. INTRODUCTION

The longwall caving mining method is widely used in underground mines and fundamentally in coalmines that involve the exploitation of large rectangular panels. When the coal seam is extracted, three zones of disturbance due to longwall mining can be defined as shown in Figure 1 (Peng and Chaing, 1984). The caved zone corresponds to the immediate roof that totally collapses onto the floor. The fractured zone lies above the caved zone, where the rock strata are broken into blocks by essentially vertical and horizontal cracks associated with bed separation. The continuous deformation zone is only slightly influenced by the excavation. In the three zones, even if major cracks will appear, the rock mass behaves essentially as a continuous medium at large scale. In order to numerically simulate the whole mining process, their geometry and mechanical properties must first be determined. For example, Peng and Chaing (1984) proposed the thickness of the fractured zone to be 28 – 42 times the thickness (t) of the mined seam. Recently Shabanimashcool et al. (2012) found that the height of the caved zone is equal to $4t$.

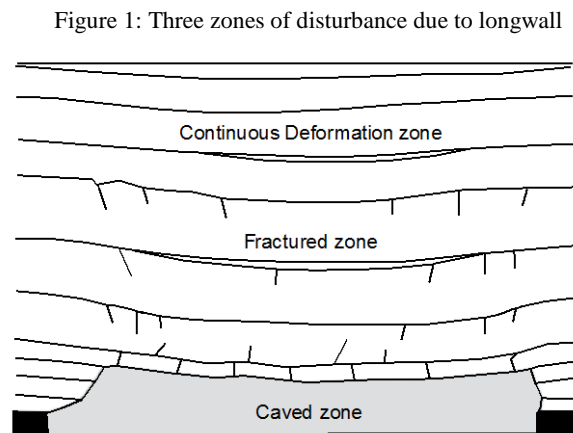


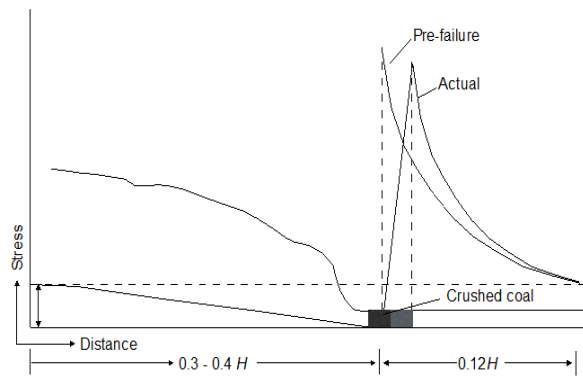
Figure 1: Three zones of disturbance due to longwall caving mining method (Peng and Chaing, 1984).

Assessment of the mechanical behavior of the goaf is very difficult due to the inaccessibility to the damaged area in the mine, as well as the heterogeneity of the goaf material. Much research has been undertaken on this topic, which is essential to determine the stress redistribution within the goaf area itself or onto the ribsides.

*Corresponding author – email: samar.ahmed@univ-lorraine.fr

Wilson (1980a) suggested that, after consolidation of the goaf, the vertical stress within the goaf increases linearly from zero at the ribsides to the pre-mining vertical stress at a distance from the ribsides equal to 0.3 – 0.4 times H where H is the mining depth. Wilson (1982b) also suggested that the peak vertical stress on the ribsides (the “abutment pressure”) might be as high as six times the initial one. The generally accepted stress re-distribution developed by Wilson (1982b) is as shown in Figure 2. However, Wilson proposed a 2D estimation and he did not consider the effect of the third direction that may play an important role. Also, he did not refer to the material properties and its effect in stress redistribution.

Figure 2: Vertical stress distribution within the goaf and



the ribsides (Wilson, 1982b).

Sheory (1993) developed equations (1) and (2) to evaluate the elastic and bulk modulus (E and K) over the goaf span from his experience at Singareni coalfield in India:

$$E(x) = 600\left(\frac{x}{L}\right)^p \quad (1)$$

$$K_{goaf} = 0.0256 K_{hostrock} \quad (2)$$

where x is the distance from the ribsides, L is the half-span of the goaf measured perpendicularly to the work face and $p = 13\left(1 - \frac{x}{L}\right)^{0.29}$. Sheory’s model is very effective to estimate the elastic modulus along the panel span after excavation, but we could not estimate the modulus within the caved volume itself.

Salamon (1990) defined the stress strain relationship of the goaf material as:

$$\sigma = \frac{E_0 \varepsilon}{1 - (\varepsilon/\varepsilon_m)} \quad (3)$$

where, ε and σ are the vertical strain and stress respectively and E_0 is the initial elastic modulus of the

goaf material. ε_m is given by equation (4) using the buckling factor BF:

$$\varepsilon_m = \frac{BF - 1}{BF} \quad (4)$$

E_0 (MPa) can be calculated as a function of the compressive strength of the intact rock, σ_c , and the buckling factor (Pappas and Mark, 1993; Yavuz, 2004):

$$E_0 = \frac{10.39 \sigma_c^{1.042}}{BF^{7.7}} \quad (5)$$

Salamon’s model is valid for cave-in materials under hardening condition, and (non-elastic) behaviour. E_0 and ε_m must be detected firstly then the hardening table will be estimated by using equation (3).

In this research, the elastic mechanical model will be used in order to simulate numerically the goaf area above the excavation as well as to assess the mechanical consequences of longwall mining. Immediately after excavation, the goaf area will be substituted by less stiff material whose properties will be calibrated by the total convergence between the roof and floor of the panel and the ground surface subsidence.

2. CASE STUDY

The case study for this paper is the Provence coalmine, located in the south of France. It had been exploited between 1984 and 2004 using the longwall mining method, with a panel width of 200 m with various lengths, as shown in Figure 3.

Figure 3 represents the exploited panels between 1984 and 1994. The average thickness of the exploited coal seam is $t=2.5$ m, at a depth of 700 to 1100 m. The overburden is mainly composed of Fuvelian limestone and Begudo-Rognacian limestone and marl, as shown in Figure 4. The stiffness of the Rognacian layer is low compared with the adjacent Fuvelian layer because it contains a high percentage of marl and clayey limestone (Gaviglio, 1985). The initial mechanical properties of the different layer within the rockmass are given in Table 1 (Gaviglio et al., 1996).

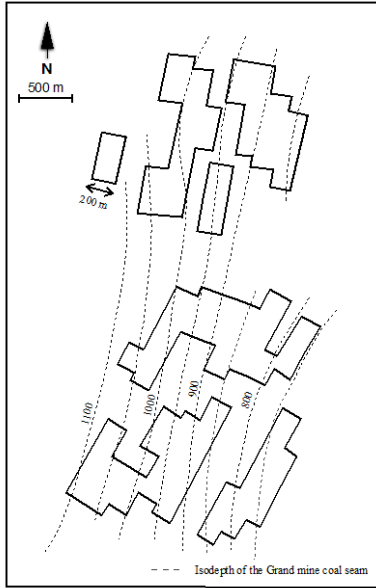


Figure 3: Excavated Panels in Provence coal mine (1984-1994).

Table 1: Rock mass mechanical properties (Gaviglio et al., 1996).

Rock type	E (GPa)	ν	ρ (kg/m ³)
Rognacian	1	0.25	2400
Fuvelian	8.4	0.24	2400
Lignite coal	3	0.32	1500
Jurassic	17	0.25	2400

3. GOAF SIMULATION METHODOLOGY

In the current study, the goaf simulation is composed of two different steps. The first step is to estimate the geometry of the goaf (caved zone and fractured zone), the height of the goaf is taken as $32t$ where t (coal seam thickness) = 2.5m (i.e. $h_{\text{caved-zone}}=4t$, Shabanimashcool et al. and $h_{\text{fractured-zone}}=28t$ Peng and Chaing, 1984). The second step is to estimate numerically the mechanical properties within the goaf area. The elastic modulus within the goaf will be calibrated with the convergence between the roof and the floor for only one panel with minimum width (W) 200 m and length (L) varies between 400 m to 1400 m. Then, once the convergence is fulfilled, the model will be calibrated with the in-situ ground surface subsidence for multi-panel with maximum width (W) 1000 m and maximum length (L) 1400 m.

Two different approaches were developed to present the mechanical properties of the goaf (Model 1 and Model 2).

A 3D numerical model of the mine was constructed using the finite difference code FLAC^{3D} (Figure 4). The model contains approximately 2.5 million mesh elements. The mesh density is adjusted to be fine near

to the excavated area and is increased by ratio 1.2 until the model borders. Four different rock types are specified: the coal seam, the Fuvelian, Rognacian with height 400 m and 600 m above the coal seam, and Jurassic limestone beds. The overall dimensions of the model are 4600 m in the x- direction, 6020 m in the y- direction and 2270 m in the vertical direction (z). The top of the model coincides with the ground surface at level $z=0.0$ while the excavated panels lies at depth of 1000 m below the surface. The model boundaries are fixed except the top.

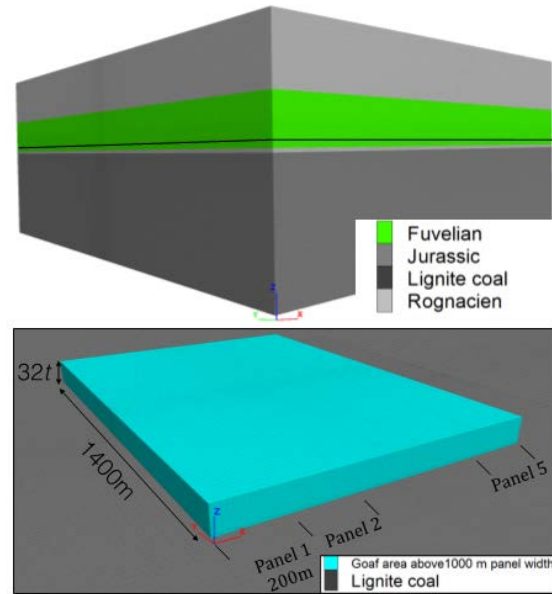


Figure 4: 3D view of the model showing the mining panel and the goaf area.

3.1 Model 1

In this model, we consider that the goaf area is presented by the caved zone and the fractured zone as shown in Fig. 5. The elastic modulus (E) of the fractured zone is assumed to be half of the host rock which is mainly composed of Fuvelian limestone because it is overlying layer above the coal (i.e. $E_{\text{fractured-zone}}= E_{\text{fuvelian}} / 2 = 4.2$ GPa). Nevertheless, iterations were carried out to estimate the caved zone modulus for various length to width ratios ($L/W = 2 - 7$) that satisfy the total convergence between the roof and floor. At first, the elastic modulus of the caved zone is as same as the host rock (i.e. $E_{\text{caved-zone}} = E_{\text{fuvelian}}$) which is called “without goaf”. The last iteration is carried out with $E_{\text{caved-zone}} = 225$ MPa. For all of the performed iteration the Poisson ration has not been changed (i.e. $\nu_{\text{fractured-zone}}= \nu_{\text{caved-zone}}= \nu_{\text{hostrock}}$).

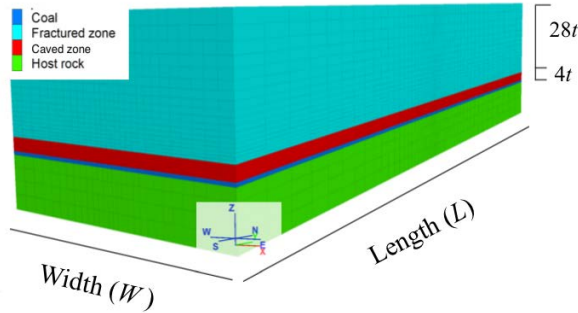


Figure 5: Isometric 3D view of the caved zone and the fractured zone above one panel ($W = 200$ m and $L=1400$ m) (Model 1).

3.2 Model 2

In this model, elastic modulus (E) of the goaf is assumed to vary linearly with the goaf height ($32t$), as shown in Figure 6. The elastic modulus begins from a certain value $E_{immediate-roof}$, which is the value of the elastic modulus of the first few meters in the roof directly above the opening, and increases linearly within the goaf until $E_{hostrock}$ at $32t$ where is the end of the goaf geometry as defined before. $E_{immediate-roof}$ is different than $E_{caved-zone}$ in Model 1, while it is for few meters (not more than 3 m (zone height)), however, $E_{caved-zone}$ has $4t$ height.

Equation (6) was fitted to estimate E_{goaf} at any point within the goaf, by assuming that the Poisson ratio is $\nu_{goaf} = \nu_{hostrock}$ and the direct roof above the excavation has $E_{immediate-roof}$. The only value that could be changed in this model is the $E_{immediate-roof}$, for that, we tried to operate the model with different values of $E_{immediate-roof}$. Four different values have been tried, 600, 450, 225 and 180 MPa respectively. Then, the elastic modulus E_{goaf} could be estimated at any point ($h_g.t$) within the goaf by using equation (6):

$$E_{goaf(h_g.t)} = \left(\frac{E_{hostrock} - E_{immediate-roof}}{x.t} \cdot h_g \cdot t \right) + E_{immediate-roof} \quad (6)$$

where 80, ($32t = 32 \cdot 2.5 = 80$ m), is the maximum height of the goaf that corresponds $E_{goaf(32.t)}$, ($h_g.t$) is the height corresponds to $E_{goaf(h_g.t)}$, h_g ranges between (1 – 32) and t is the coal seam thickness.

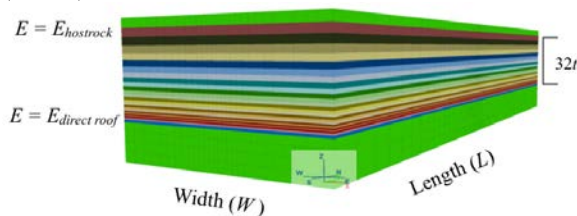


Figure 6: Linear variation of elastic modulus within the goaf area (Model 2).

4. RESULTS AND DISCUSSION

In order to compare the applicability of each of the proposed models each of them were initially calibrated with the total convergence between the roof and floor of the excavated panel that has $W=200$ m and $L=1400$ m. After that, further panels will be exploited with maximum width of 1000 m in order to calibrate the model with the ground surface subsidence. Then, the stress changes due to longwall caving mining will be observed.

4.1 Convergence between roof and floor

In the mine, when a panel is totally mined out, the roof and floor get totally in contact (full closure). However, in the numerical model, due to the hypothesis of elastic behaviour, the convergence between roof and floor might be less than the coal seam thickness. This happens in particular when the stiffness of the roof is equal to that of the host rock (case called “without goaf”).

Figure 7 shows the convergence between roof and floor by using different elastic modulus' within the caved zone. We can see that the convergence is affected by length to width ratio ($L/W = 2 - 4$), however, for ratio more than 4, the convergence stays nearly constant. Decreasing the elastic modulus (E) of the caved zone in (Model 1) to 225 MPa (i.e. $E_{caved-zone} = 225$ MPa) is sufficient to produce total closure of the coal seam. The convergence remains constant when the modulus is further reducing.

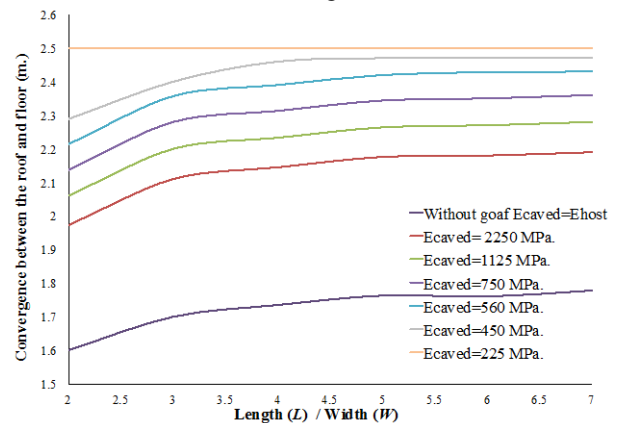


Figure 7: Convergence between roof and floor for different panel lengths with 200 m width (Model 1).

By using Model 2, Figure 8 shows that decreasing the $E_{immediate-roof}$ until 180 MPa is sufficient to produce total convergence between the roof and floor of the panel. For that, in order to get the total touch between the roof and floor (i.e. $convergence = mining\ seam\ thickness (t)$), equation (6) must be written as:

$$E_{goaf(hg,t)} = \left(\frac{E_{hostrack} - 180}{80} \cdot h_g \cdot t \right) + 180 \quad (7)$$

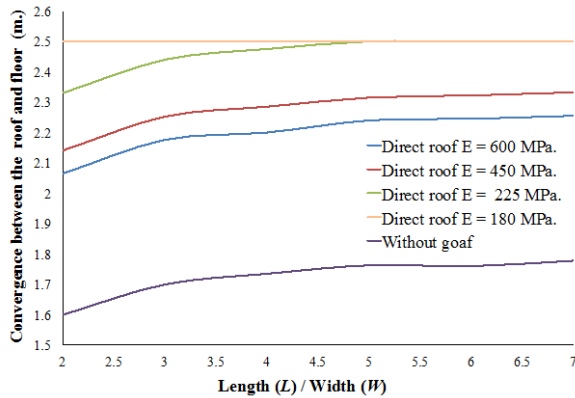


Figure 8: Total convergence between the roof and floor for different panel lengths (Model 2).

Based on the two proposed models, we can find that in case of total convergence after exploitation by using longwall caving, the first damaged few meters in the roof (immediate roof) will have an elastic modulus (E) as:

$$225 \leq E_{immediate-roof} \text{ (MPa)} \leq 180 \quad (8)$$

Although, the two models give approximately a very close range of $E_{immediate-roof}$ and $E_{caved-zone}$ in order to satisfy the total closure of the opining, Model 2 is preferable than Model 1 for simulating the goaf area. Because, the stiffness difference between two adjacent zones should not exceed 10 times, while in Model 1 the difference between the fractured zone and the caved zone is reached to 18 (i.e. $E_{fractured-zone} / E_{caved-zone} = 4200/225 = 18$).

4.2 Ground surface subsidence

One of the very clear observations due to longwall mining is the increasing of the surface subsidence. The panel width has been extended until 1000 m by keeping the maximum length at 1400 m. The proposed model (Model 2) was calibrated with in-situ measurement of the surface subsidence. Figure 9 illustrates the maximum and minimum measured surface subsidence for panel width (W) from 200 m to 1000 m. Model 2 has been applied within various panel widths and the surface subsidence has been measured at the center of the panel. The ground surface subsidence produced by numerical modelling by applying Model 2 is as shown in Figure 9.

The surface subsidence may vary greatly from country to country and from location to location. In case of Provence coalmine, the surface subsidence has been monitored at each excavation step. Figure 9 shows the minimum and the maximum subsidence

values for each panel width to mining depth ratio. For example, for 400 m panel width at 1000 m depth, the (max. subsidence/ t) = 25, so the max. subsidence is $25 \cdot t = 25 \cdot 2.5 = 62.5$ cm.

It is clearly shown that simulating the goaf by using less stiff material has its effect on the surface even with exploitation at very high depth. the influence of the goaf appears on the surface for the panel width (W) / mining depth (H) ratio greater than 0.4. Representing the goaf elastic modulus (E) by using equation (7) gives a rational surface subsidence between the maximum and the minimum in-situ measured subsidence curves. The model without goaf is not able to reproduce even the minimum subsidence curve. The adopted goaf behaviour gives an acceptable subsidence prediction. An improvement can be suggested for large mining areas ($W/H > 1$). In addition, Model 2 will be applied in another future studies to verify its ability to predict the surface subsidence.

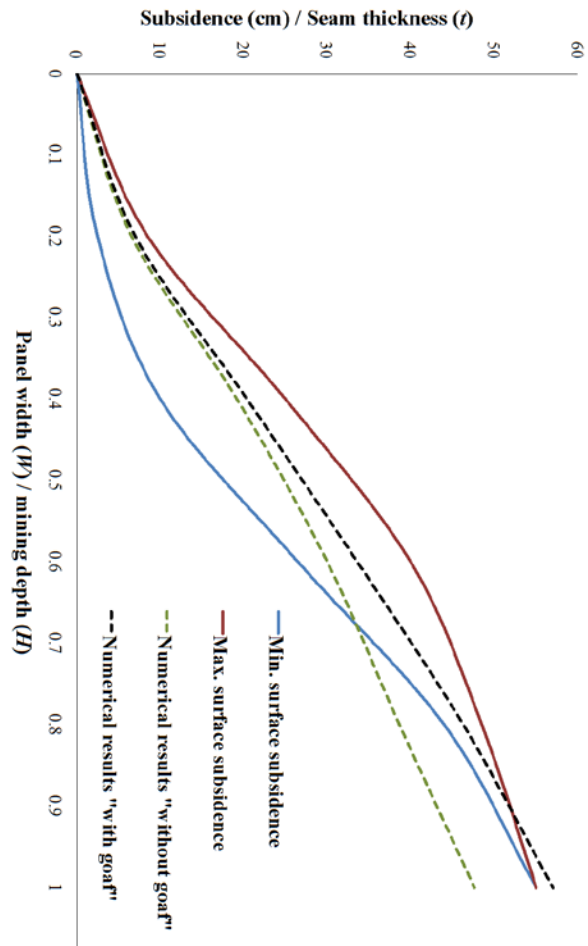


Figure 9: Surface subsidence in case of with and without goaf.

4.3 Stress redistribution

When replacing the goaf area with less stiff material than the host rock, the vertical stress will transfer to the surrounding high stiff materials. The stress distribution due to panel excavation with and without goaf is shown in Figures 10 (a) and (b), respectively. The induced vertical stress within the ribside is 2.5 times the initial one, which is much less than the values given by Wilson (1982b). The induced vertical stress due to goaf has a higher influenced zone horizontally than the case without goaf. Also, the destressing zone is higher in case of the goaf.

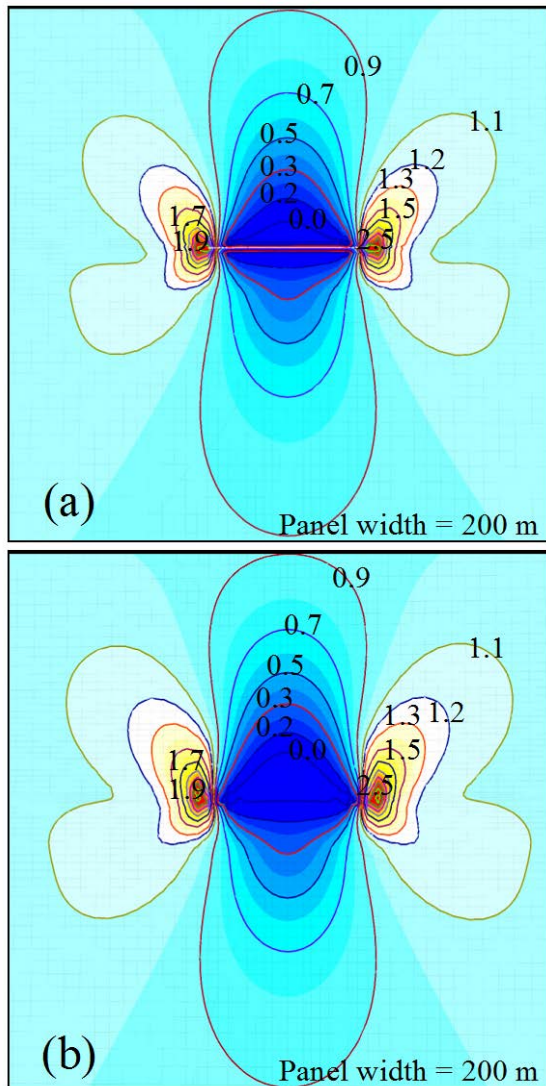


Figure 10: Ratio between induced vertical stress and initial vertical stress (a) without goaf (b) with goaf (Model 2).

As shown in Figure 3, there are rib pillars between two parallel panels. Figure 11 shows the ratio between the induced vertical stress and the initial one in case of excavating two parallel panels with 200 m width and

200 m rib pillar between them. In case of the goaf the influenced zone (horizontally and vertically) within the rib pillar is larger than the case without goaf. By increasing the panel width, the vertical stress will increase at the center of the panel. The induced vertical stress to initial stress ratio is assigned to different panel widths in Figure 12. The results show that when the panel width increases the induced to initial vertical stress ratio increases at the center of the panel. For panel 1000 m width with fully filled mining area, the induced to initial vertical stress ratio is 0.2 at the panel corners until 0.9 at the center without consolidation.

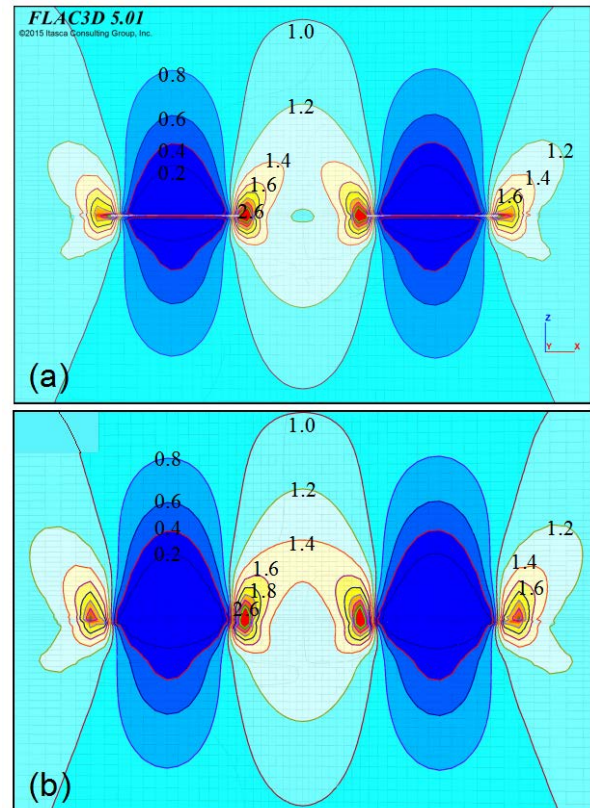


Figure 11: Ratio between induced vertical stress and initial vertical stress within the ribpillar (a) without goaf (b) with goaf (Model 2).

5. CONCLUSION

This research examines the simulation of the goaf area associated with the longwall caving panels of Provence coalmine by using FLAC^{3D}. Two distinct models, Model 1 and Model 2, have been represented to simulate the goaf area after exploitation. Within Model 1 the goaf area is treated as two separated parts (the caved zone and the fractured zone), which have different elastic modulus values.

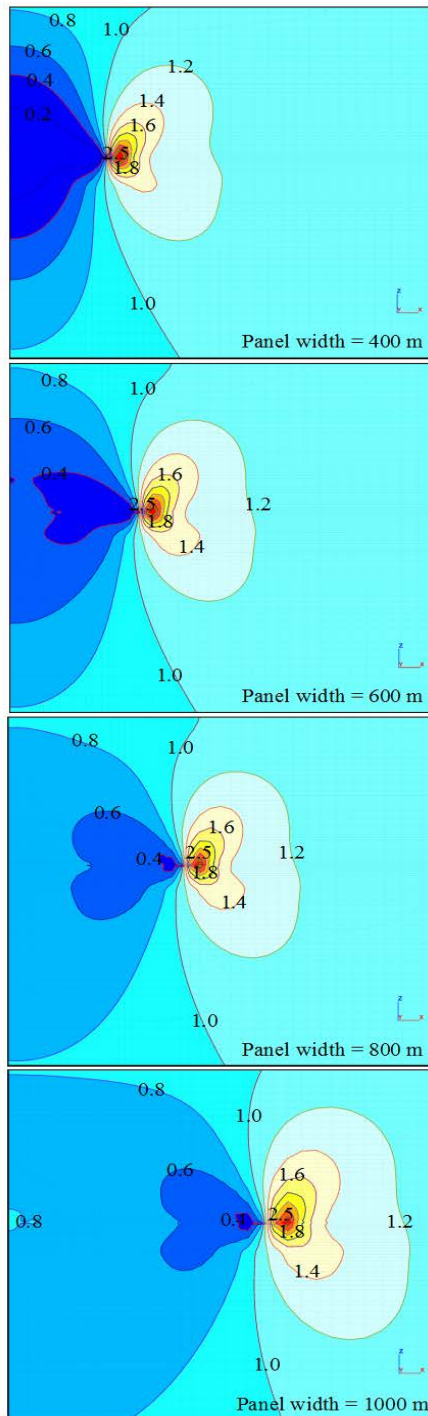


Figure 12: Induced Vertical stress to initial vertical stress distribution within the goaf area for different panel widths.

In Model 2, the goaf area is treated as a one zone with linearly increasing elastic modulus from the direct roof up to the host rock. From the two model, we found that the elastic modulus of the few meters above the panel is ranged between $225 \leq E_{\text{immediate-roof}}$

≤ 180 MPa in order to satisfy the total convergence between roof and floor.

Substituting the goaf area with less stiff material has an effect on the ground surface subsidence for panels whose has width to depth ratio greater than 0.4. Model 2 expresses sufficiently the variation of the elastic modulus within the goaf area. It gave a rational surface subsidence compared with the ‘without goaf’ model. By exploiting a longwall caving panel, the vertical stress within the ribside will increase by 2.5 than the initial value. The vertical stress at the center of a panel whose width to depth ratio is 1 approaches the initial vertical stress value.

6. REFERENCES

- Gaviglio P., 1985. La deformation cassante dans les calcaires Fuvéliens du bassin de l’arc (Provence). PhD thesis. University of Provence, Marseille, France.
- Gaviglio P, Bigarre P, Baroudi H, Piguet J.P and Monteau R. (1996). Measurements of natural stresses in a Provence mine (Southern France). *Journal Engineering Geology*. Volume 44, pp. 77-92.
- Pappas DM and Mark C., 1993. Behaviour of simulated longwall gob material. Report of investigation no. 9458, US Department of the Interior, Bureau of Mines, 39 p.
- Peng S.S. and Chaing H.S. (1984) Longwall Mining. John Wiley & Sons Inc., New York; pp. 17-73
- Salamon MDG. (1990). Mechanism of caving in longwall mining. In: Hustrulid W, Johnson G, editors. *Proceedings of the 31st US rock mechanical symposium*, Golden, Colorado. Rotterdam: Balkema, pp. 161–68.
- Shabanimashcool, M. and Charlie, C.L. (2012) Numerical modelling of longwall mining and stability analysis of the gates in a coal mine. *International Journal of Rock Mechanics and Mining Science*. Volume 51, pp. 24–34.
- Sheorey P. R. (1993) Design of coal pillar arrays and chain pillars. *Comprehension Rock Engineering*, Vol. 2. Pergamon Press, Oxford.
- Wilson A. H. (1982). Pillar stability in longwall mining. *State of the Art of Ground Control in Longwall Mining and Mining Science*, Y. P. Chugh and M. Karmis (eds.), SME, New York; pp. 85-95.
- Wilson A.H., 1980. The stability of underground workings in the soft rocks of coal measures. Unpublished Ph.D Thesis, Univ. Nottingham.
- Yavuz H. (2004) An estimation method for cover pressure re-establishment distance and pressure distribution in the goaf of longwall coal mines. *International Journal of Rock Mechanics and Mining Science*. Volume 41, pp. 193–205.

A coal enterprise scientific-technical progress evaluation system based on the Internet

Shanyang Wei*, Longlong Yang, Zhongbei Li, Shiwei Ding

Safety Engineering College, North China institute of science and technology, Sanhe, China, 065201

ABSTRACT

The evaluation of coal enterprises of scientific-technical progress is a big problem in technology management. Until now in China or abroad there has been no mature and recognized coal scientific-technical progress evaluation system that can make a wide range of evaluations about the coal scientific-technical progress of the whole country or region in the quantitative measurement aspects of scientific and technological progress to economic growth, although there were quite a few successful applications. Under the present conditions of a lot of coal enterprise output decline, laid-off personnel, and asset reorganization, using the traditional production function method is difficult for measuring the effect of technological advances. On the basis of investigation and study, according to the actual situation and balance of payment structures of coal enterprises and with reference to relevant policies and regulations of the national science and technology evaluation, and with the application of universality and agility of the Internet, we constructed a system for the scientific-technical progress evaluation of coal enterprises. According to the computing applications of part of the state-owned key coal mines and local state-owned coal mines, good results have been achieved.

KEYWORDS: Coal enterprise; scientific-technical progress; system of information; comprehensive assessment

From the point of view of the development of the theory of the scientific process, the basic theory of science and technology progress has experienced three stages; ① The theoretical stage of traditional scientific-technical progress (Li, 2002; Wang, 1993); ② The theoretical stage of classic scientific-technical progress in the 1950-1960's (Poter, 1980; Miler, 1999); ③ The theoretical stage of modern scientific-technical progress since the 1960's. China also formed two waves in the aspect of scientific-technical progress evaluation. The first wave lasted from the late 70's of last century to the 10 years before the 80's. Because of the high and rising economic growth targets, the measurement and evaluation method of scientific and technological progress that conforms to the target were in urgent need. The research results meet the needs of decision-making at all levels. After 1986 research and applied work made no progress until after the 90's. At this point the role of science and technology in social and economic development received extensive concern and attention. The research and application team continued to expand and then formed another wave, providing a good environment for the evaluation of scientific-technical progress. However, research in the field of evaluation of scientific and technological progress in China is still very shallow, and methods that can transform theories of scientific and

technological progress of western developed countries into what are suitable for China's national conditions and industry characteristics are few (Li, 2009).

At present, literature and data that specializes in the evaluation of progress of science and technology of coal enterprises are few. The main methods are AHP (Analytic Hierarchy Process), DEA (Data Envelopment Analysis) bonding, the connotation and structure method of the system of coal enterprise scientific-technical progress (Chen, 2011; Zhang, 2002) and the method of interval valued intuitionistic fuzzy set (Jing, 2014). However, a system that can evaluate coal scientific-technical progress objectively, accurately, and comprehensively has not yet been seen. As a result, it is important to keep up with the development of science and technology, make full use of modern Internet technology to build the whole of China, even the world evaluation system of coal enterprise scientific and technological progress, and advance coal scientific and technological progress universally in order to realize the safe, healthy, green, and advanced system of coal production.

1. THE TECHNICAL ARCHITECTURE AND FUNCTION OF THE SYSTEM.

*Corresponding author – email: weishanyang@126.com

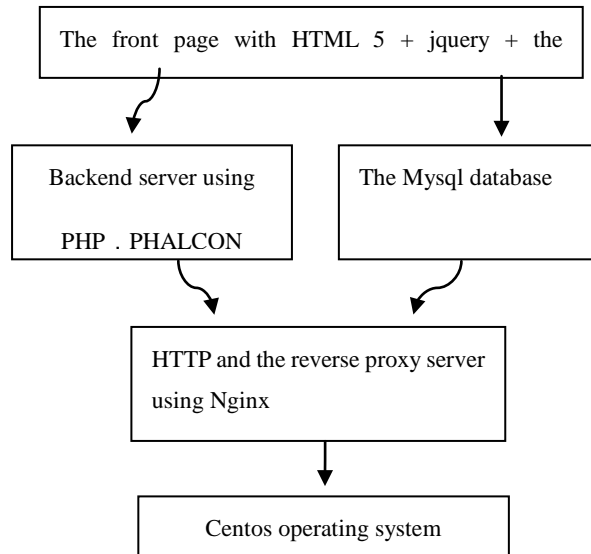


Figure 1: Information system architecture diagram.

The front page uses the popular HTML5 that can support more of the browsers new features and provide a rich expressive ability for display. JQuery and bootstrap is a scripting language framework and the page layout framework, respectively, which provide a strong compatibility with most of the major browsers, and a strong code maintainability.

The backend http server using nginx, which has strong stability, rich feature set, and low system resources.

The server-side language uses PHP and phalcon framework. PHP provides good operational characteristics for the system. There is no need to restart the system to change, ensuring high availability of the system. Phalcon is a plug-in framework using compile PHP zend engine by C language editor. Using the framework, the calculation of the PHP language and the corresponding performance can achieve around 2000 requests per second, which is 120000 requests per minute under the conditions of the hardware resources.

The database using the MySQL server. The system has the characteristics of open source and high performance. A single data reading and writing is in the microsecond, and support the cluster, which greatly improves the system reliability and availability and performance.

Operating system uses the cento Linux system. The system is the open source community edition maintained by Redhat company, and basically has functions like the Redhat system. The system has running stability and it does not need to restart the running perennially.

The use of the technical architecture can save many costs for thw operating system and database system, and the cost savings can be used for the construction of an information system to produce more

value, without spending the budget of the operating system and database system on licensing fees.

The role of the system function modules is mainly to: (1) Fully calculate and display the coal enterprise comprehensive evaluation results, ranking among participant coal enterprises in the mine technology state, choosing "top fifty scientific and technological progresses in coal enterprises" and "top ten hi-tech coal enterprises". (2) "Business analysis" to fully reflect the structural character of the health of the enterprise, and puts forward corresponding measures and management scheme. (3) Enterprise contribution rate of science and technology, the contribution rate of labour, statistically calculated capital contribution, and conclude industry scientific-technical development state. (4) The enterprise environment system can be checked, to conclude whether to belong to the green mining enterprises. (5) To achieve wide interaction, all participants of "the forum" can communicate in all problems of the coal production and management. It is a convenient platform for a thorough understanding of coal mines.

2. DATA COLLECTION METHOD

The data collection method uses the cloud system of science and technology, the function of the database cluster and disaster preparedness, the characteristics of the computing speed, large storage space, and the emergency ability. This method is convenient for the application of coal industry management and supervision department. The data acquisition method of design was as shown in Figure 2.

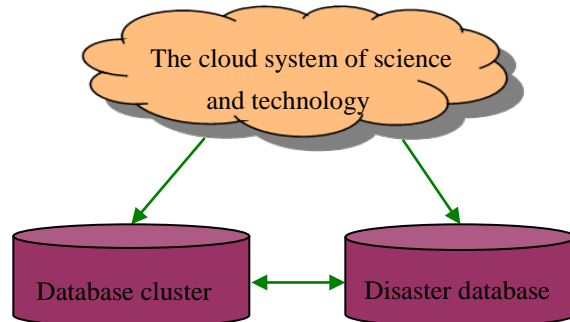


Figure 2: Data acquisition method of design.

Data collection methods use a cloud platform that can expand the system performance in real-time according to the need. The advantage is that it can adequately cope with a large increase of users of the system. It does not need to make changes, and instead applies for an increase in the performance of the system. In the aspect of saving data, the database uses the cluster and disaster mode. When used by a large number of users at the same time it can minimize the impact of database performance bottlenecks. If master database collapse occurs, it can quickly switch to the disaster database to ensure high availability.

3. COMPREHENSIVE EVALUATION INSTANCES OF MINE SCIENTIFIC AND TECHNOLOGICAL PROGRESS

3.1 Mine evaluation index statistics table

According to the comprehensive evaluation system standard of coals scientific-technical progress, we calculated part of the state-owned key coal mines and local state-owned coal mines.

3.2 The comparison of the mine comprehensive evaluation

The indicators and index weights calculated through the application of the computer evaluation system were compared to arrive at four mine scores and rankings that are shown in Table 1.

Since all indicators calculation results were calculated according to the actual situation, the scores were not controlled. The final calculation and ranking was performed, getting enough space for the expansion of the evaluation system.

Comparing the calculation results can provide the image of the evaluation results and knowing the coal mining conditions provides strong support for coal mine supervision departments and coal enterprises.

The establishment of a comprehensive network evaluation system was carried out for Ping Coal LTD Ten Mine, Ping Coal LTD Six Mine, Bai Yuan Coal Mine, and LiZi Ping Coal Mine. The results of the evaluation and comparison are shown in Table 1:

Table 1: Part of the mine comprehensive evaluation and ranking

Rank	Report name	Company Name	Year	Score
1		Ping Coal LTD Ten Mine	2014	12.64
2	Statistical table of indicators of Coal enterprise	Bai Yuan Coal Mine	2014	10.97
3	scientific-technical progress evaluation	Ping Coal LTD Six Mine	2014	10.72
4		LiZi Ping Coal Mine	2014	9.33

Comparison of the calculation results and software analysis finds that the two have the same results. Therefore, the application and popularization of the network evaluation system must provide a good platform for the evaluation of coal enterprise scientific-technical progress, and can provide good

support for the country and regulators to accurately grasp the dynamic coal enterprise technology. This makes great contributions to regulating the coal market economy.

4. CONCLUSIONS AND OUTLOOK

This text was based on coal scientific and technological progress as the research object, in reference to the research results of scholars both at home and abroad, and in combination with the present situation in the coal industry and the progress of science and technology leve. An evaluation and in-depth study of the progress of science and technology systems of coal enterprises was carried out using data acquisition methods based on the Web and the comprehensive index evaluation system method to calculate science and technology progress in four coal enterprises, given a ranking order.

The establishment of this system provides a good basis for further studies of coal industry scientific and technological progress evaluation systems. There is still a lot of room for development, and further study should focus on the following:

(1) Continue to study the synthetic evaluation system of scientific-technical progress, which should be scientific, reasonable, and comprehensive, and make the system more complete and feasible.

(2) Research the relationship between the comprehensive evaluation system of coal scientific-technical progress and the evaluation system of other industries' scientific-technical progress. Explore a kind of formula or conversion rule that can be used generally. Make greater breakthroughs in the evaluation system of scientific and technological progress for China and all over the world, and can reflect the actual situation of the evaluation of scientific and technological progress in all walks of life objectively, authentically, and accurately.

(3) Combine the data collection methods based that was applied in this paper with the evaluation system of scientific-technical progress, and make a set of coal management information systems of science and technology, then apply it to the coal industry, different regions and coal mining enterprises, coal supervision departments, the department manager of supervision and inspection, and the China coal industry associations' strength of control on the scientific-technical progress of coal industry, and to strengthen the promotion of coal science and technology.

5. REFERENCES

- Jing. (2014) Research on Green Mine Evaluation Index System of Underground Mining.[D]. Beijing : Beijing China University of Mining and Technology.
- Li. (2002) Researching the Valuation System of

Science and Technology Progress of Coal Enterprise.
[D]. Hebei : Hebei University of Technology.

Li and Huang. (2009) Empirical Analysis of the Contribution of Scientific and Technological Progress to China's Economic Growth [J].*Science & Technology and Economy*,6. 22(129):65-68. Chen.(2011)Measure the Level of Modernization of Coal Industry [D].

Miler ,D .& Whitney , J .Beyond Strategy. (1999) Configuration as a Pillar of Competitive Advantage . *Business Horizons* . (42) : 8-11.

Poter, M . E . (1980) Competitive Strategy . New York : Free Press , (23) : 8-11.

Wang.(1993) Data Envelopment Analysis Approach on the Industrial Efficiency and scales and Its Application in Shandong[J] . *Journal of Systems Science & Systems Engineering*. (7) : 5-7.

Zhang.(2002) System and Evaluation Research of the Progress in Science and Technology of Coal Enterprise .[D].Liaoning : Journal of Liaoning Technical University.

Simulation of strata behaviour laws of a coal mine in Jungar Coalfield

Zhu Bin^{a,b,*}, Li Ge^a, Kou Weifeng^c, Li Haibin^a

^a School of Architecture and Civil Engineering, Xi'an University of Science and Technology, Yan Ta Street, Xi'an, China

^b School of Highway, Chang'an University, South 2nd Ring Road, Xi'an, China

^c Beijing Urban Construction Design & Development Group Co. Limited, No.5, Fuchengmen Beidajie, Xicheng District, Beijing, China

ABSTRACT

The present study uses a similar material experiment to systematically examine the performance of the law of overlying strata caving, mine ground pressure, and crack development when the first coal mining face in Jungar coalfield was exploited. The overburden movement, roof collapse, severe wall caving, and a range of other issues related to mine ground pressure caused by the exploitation process in Jungar coalfield are considered. The results prove that the pace of the immediate roof caving of the first coalface was about 15.0 m. The pace of the first weighting of the rock stratum of main roof was 45 m, with an average pace of periodic weighting of 17 m. The maximum loading-increasing factor of first weighting was 1.40, and the value of loading-increasing factor for the whole weighting period was 1.32. For the distribution of the three zones of the overlying strata on the first coalface, the height of the caving zone was about 4.5 times the average mining height, the height of the fissure zone was about 14.5 times the mining height. The bending zone is the stratum over 43 m from the coal roof, which takes on the features of overall down movement. Therefore, a reasonable choice of mining method to reduce the thickness of the mining working face should be taken to reduce the disturbance from exploitation to overlying strata of the upper goaf and the earth's surface.

KEYWORDS: Mine pressure; Similar material simulation; Bending zone; Fissure zone; Caving zone; Overlying strata failure

1. INTRODUCTION

Jungar coalfield is located in the southwest of the Inner Mongolia Autonomous Region, and is an important part of the Ordos coal-accumulating basin, which is a Neopaleozoic permo-carboniferous oversized coalfield. Due to the coal properties in the Jungar coalfield featuring natural conditions of especially low-sulfur, low-phosphorous, high ash-melting, high calorific power and high volatile, it is the most appropriate power coal and fossil fuels. Therefore, Jungar coalfield is the largest comprehensive energy base in western China (Cui et al., 2002). In recent years, with the intensity of coal mining increasing, damage to coal mining is increasingly serious and the incurred engineering problems such as goaf overlying strata movement, surface deformation, and the acute weighting and pouring of water and sand of working faces are continuously compounded (Jin et al., 2010).

Chuancao Gedan coal mine is located in the midwest of Jungar coalfield. The recoverable reserve of the whole mine is 1205.57 Mt, with a designed production capacity of 10.00 Mt/a, and a length of service of 86.1 a. However, since there are many minable seams within the mine field, and the hydrogeological conditions are complicated under the mine, coal mining causes a series of negative environmental geology effects, such as overlying strata movement, roof collapse, water resources oversight, and ecological environment deterioration.

At present, there are many major research methods concerning the mine ground pressure and rock stratum

displacement law (Liu, 2015; Tu et al., 2011; Wei et al.). However, it is difficult to accurately predict and analyze its settlement law. Therefore, this paper adopts the method of similar simulation test (Wu, 2013; You, 2000; Zou, 2004) to perform a preliminary study on the law of overlying strata caving, fracture development and mine ground pressure of 4101 first coalface mining of Chuancao Gedan coal mine, which not only has theoretical and practical significance to working face safety mining design and controlling strata movement, but also provides a reference for the safe construction of similar projects in the future.

2. GEOLOGICAL BACKGROUND OF THE MINE PROJECT

Chuancao Gedan coal mine is affiliated with Changtan Township and Xuejiawan Town of Jungar Banner. The mine field is a polygon, with an east-west length of about 8.9 km, north-south width of about 5.5 km, and an area of 42.64 km². The first-mining coal seam is determined as No. 4 coal seam in the first level of the first panel, and the first-mining working face is determined as 4101 working face. The results of a rock mechanical properties test show that the overall intensity of the rock within the mine field is such that fine grained rock has greater crush resistance and shearing resistance than coarse grained rock. The rocks whose crush resistance ≤ 30 MPa account for 68%, and those between 30-60 MPa account for 32%. It indicates that for all kinds of rocks in coal measure strata of this mine field, they are mostly weak

*Corresponding author – email: diskzhu@sina.com

rock, or secondarily are half-hard rock.

3. SIMULATION EXPERIMENT

According to the data on coal mine drill, one must select representative regional strata as the geological model for the similar simulation test, conduct merging homogenization to the stratum stratification character, and establish an engineering geological model reflecting the roof and floor conditions of the coal seam.

The experiment adopts a self-developed plane stress frame model. The model frame is designed with a length of 3 m, height of 2 m, and width of 20 cm. The geometric similarity ratio is 1:100. Based on the histogram of No.Y14 drill hole of this mine, geometric similarity constant of the model is $\alpha_L=100$, density similarity constant is $\alpha_Y=1.56$, and the stress similarity constant is $\alpha=\alpha_L\alpha_Y=100\times 1.56$.

Material used for the model includes quartz sand as aggregate, gypsum and calcium carbonate as the cementing material. This is then mixed with water in accordance with a certain proportion, laid in the model frame in layers, and mica powder is scattered between levels (Figure 1).

A self-developed multiple pressure computer data acquisition system conducts real-time monitoring on the coal column variation of stresses. 57 pressure sensors are arranged at the bottom of No.4 coal seam of the first mining simulation 4101 working face, and the simulation stands to confirm the rational supporting intensity of the force piece. Displacement monitoring is conducted for roof strata. Five measuring lines are arranged at 10 m, 30 m, 50 m, 70 m, and 90 m away from the coal seam roof. The displacement changes of roof strata and the advance of the working face are monitored.

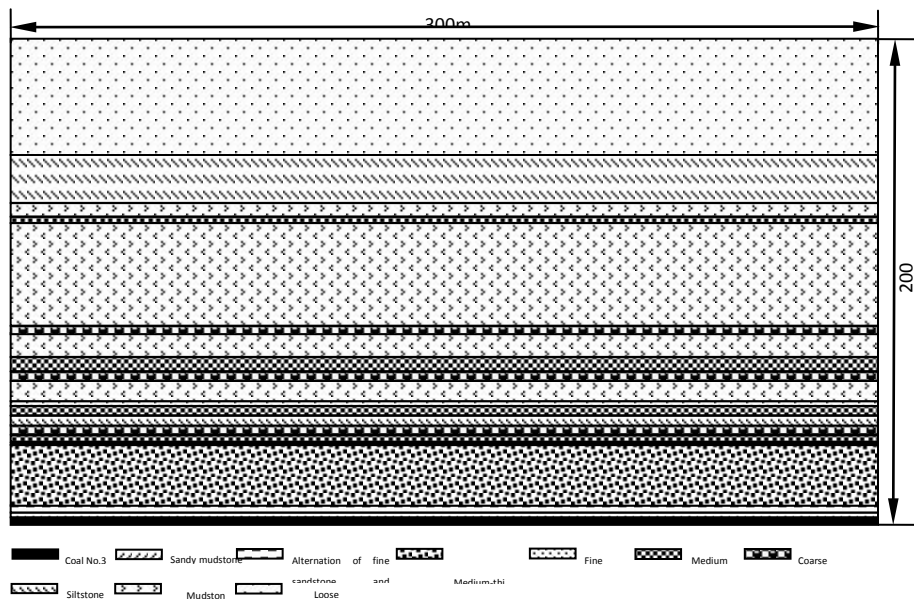


Figure 1: Profile map of simulation working face.

4. ANALYSIS OF EXPERIMENTAL RESULTS

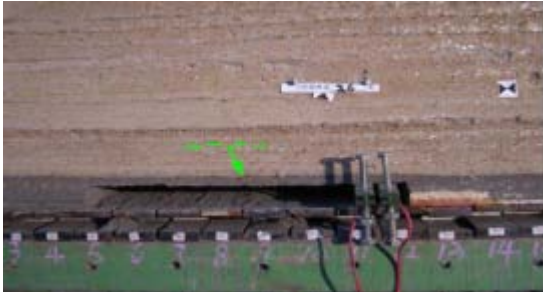
4.1 First mining stage

4101 working face ranges from 2.55 - 3.95 m in thickness, with an average of 3.09 m. The coal property is hard, and the immediate roof is sandy mudstone of 1.5 - 2.1 m. In order to reduce the influence of refuse content during recovery and study the effect of the setting of roof-coal in working face advanced stages on the stability of roadway maintenance, coal seam thickness when filling the model ranges from 3.09 - 3.95 m, the full-seam mining of the working face in the first mining stage is 3.2 m with reserve, and roof supporting coal is set to 0.5 - 0.75 m, and support resistance is set according to 5 times the mining height.

Leave 30 m a boundary pillar when exploiting simulating mining the working surface, with an open-off

cut width of 6 m. When advancing the working face to 12 m, microcracks appear in the coal roof of the roof supporting coal; when advancing the working face to 14 m, the microcracks extend further. When advancing the working face to 16 m, microcracks appear in immediate roof stratum 1.5 m away from the coal roof along with the stratum direction. When advancing the working face to 22 m, microcracks in immediate roof stratum 1.5 m away from coal roof extend continuously. When advancing the working face to 26 m, the coal roof of the roof supporting coal generates an obvious separation layer, as shown in Figure 2 (a). When advancing the working face to 32 m, the roof supporting coal with has a suspended length of 7 m after support collapses (Figure 2 (b)). Advancing the working face to 40 m leaves no roof supporting coal in the working face advance, full-seam mining is 3.85 m, the lower stratum of the immediate roof and main roof in the

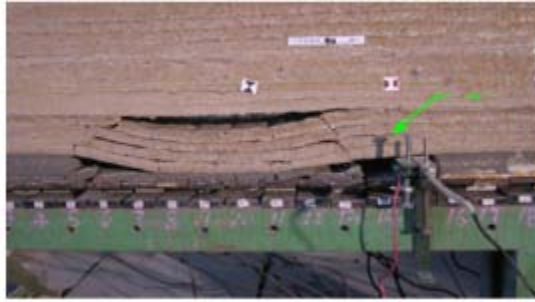
back of the stand fractures, and the upper end of the fracture line is 6 m away from coal roof. The lower end of the fracture line extends to the upward side in front of the stand, and the collapsed rock of fracture rock and goaf takes on a splicing structure with the advancing front of the working surface, and the support load shows no obvious lifting (Figure 2(c)).



(a) Separation layer of coal roof (the working face is to 26 m)



(b) Separation layer of coal roof (the working face is to 32 m)



(c) Separation layer of coal roof (the working face is to 40 m)

Figure 2: Deformation and failure process of roof strata in first mining stage.

Simulation test results show that when advancing the working face to 12.0 m, the reserved roof supporting coal starts to generate damage, until the advance reaches 36.0 m, when immediate roof stratum completely collapses. On this basis, it is deduced that under the circumstance of leaving the roof supporting coal, the first caving pace of the immediate roof is about 20.0 - 25.0 m. Since this experiment belongs to the “plane stress model” and there is no constraint in the front and back of the model, when fitting the model, the immediate roof is inclined to be hard.

It is held that the first caving pace of the immediate roof for first coalface is about 15.0 m. The experiment also shows that when the immediate roof first collapses, the support load has no obvious rise; under the condition of using the comprehensive mechanized coal mining, as long as the stand is in normal operating condition, there is no danger for first caving of the immediate roof, and it is unnecessary to take special protective measures.

4.2 Main roof (upper roof) first weighting

Synthesis analysis shows that the range of first weighting of the basic rock strata is between 44 - 48 m, confirming that the pace of the first weighting is 45 m - 50 m. During first weighting the dynamic load factor is 1.40, showing acute weighting. The caving zone height of the stratum is 14 m, which is about 4.5 times the average mining height. The fracture line of coal wall side is located at the upside of the support front, showing that the setting load of the simulation support designed according to 5 times of mining height is insufficient.

4.3 Periodic weighting of main roof

4.3.1 Weighting pace

The simulated working face is totally advanced at 192 m, showing 1 first weighting and 8 periodic weighting. When excluding the 6 m starting cut width, from the position of starting advancing for the working surface, the pace of the first weighting of basic rock strata is 45 m - 50 m. During 8 periodic weightings, the maximum weighting pace is 20 m, the minimum weighting pace is 14 m, and the average weighting pace is 17 m.

4.3.2 Loading-increasing factor

Based on the working resistance of the whole support, the loading-increasing factor during the weighting of working face is as shown in Table 1. Before periodic weighting, setting load of the support is calculated according to 5 times the mining height, and rises to 8 times the mining height after the first weighting. The maximum loading-increasing factor of the first weighting is 1.40, and the mean value of loading-increasing factor during the whole weighting is 1.32, according to mining pressure theory, the weighting approaching is “relatively strong”.

4.3.3 Roof cutting phenomenon

During the advance of the working face, though there is no roof strata cut falling along with the coal wall in front of the support, during the first, sixth and eighth weightings, the fracture line of roof strata of the coal wall side extends to the upside of the support, causing support load to rapidly increase; it is suggested to further raise the setting load on the basis of the calculation for 8 times the mining height, and adopt hydraulic supports with high resistance.

Table 1: Weighting loading-increasing factor of the first mining face

Indicator weighting	Loading -increasing factor	Mean value
First weighting	1.40	1.32
1 st periodic weighting	1.32	
2 nd periodic weighting	1.32	
3 rd periodic weighting	1.33	
4 th periodic weighting	1.22	
5 th periodic weighting	1.28	
6 th periodic weighting	1.37	
7 th periodic weighting	1.30	
8 th periodic weighting	1.35	

4.3.4 Distribution of three zones

The height of the stratum caving zone is 14 m, which is about 4.5 times the average mining height. The range of the fissure zone is 14 - 43 m, the height of the whole fractured zone is 43 m, which is about 14.5 times the average mining height; the area that is over 43 m from the coal roof is the bending zone, and the stratum takes on the characteristic of overall downward movement (Figure 3).

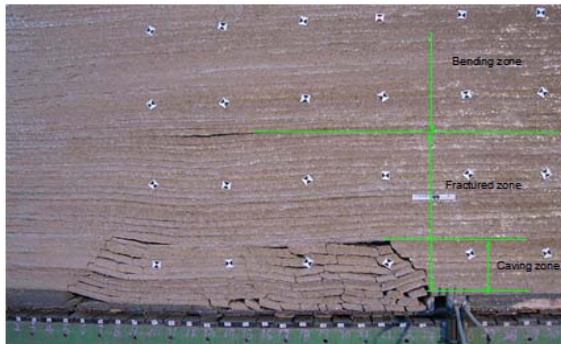


Figure 3: Distribution of vertical three zones of the overlying strata.

5. CONCLUSION

Simulation results show that the first caving pace of the immediate roof of first coalface is about 15.0 m. When the immediate roof first collapses, support load has no obvious rise. As long as the stand is in normal operating condition, there is no danger for caving of the immediate roof, and it is unnecessary to take special protective

measures. Meanwhile, it is important to ensure the setting load of the support to effectively maintain the roof of the head face.

For the main roof (upper roof) stratum, the first weighting pace is 45 m - 50 m, and average pace of periodic weighting is 17 m. The maximum loading-increasing factor of first weighting is 1.40, and the mean value of loading-increasing factor of the whole weighting period is 1.32. According to mining pressure theory, the weighting approaching is "obvious".

In the distribution of the three zones of the overlying strata on the first coalface, the height of the caving zone is 14 m, which is about 4.5 times the average mining height. The range of the fissure zone is 14 - 43 m, the height of the whole fractured zone is 43 m, which is about 14.5 times the mining height. The bending zone is the stratum over 43 m away from the coal roof, which takes on the feature of overall downward movement.

6. ACKNOWLEDGEMENTS

This paper was supported by Shaanxi Provincial Department of Education Science Research Project (11JK0779) and the National Natural Science Foundation of China (41402265, 51508462).

7. REFERENCES

- Cui ,X., Miao, X. and Su, D.(2002). Error analysis in similar material simulation test of the movement of rock strata and surface. *Chinese Journal of Rock Mechanics and Engineering*, Volume 21, No. 12,pp. 1827—1830.
- Jin, L., Jin, W. and Wang, H.(2010). Multi-environmental time similarity theory and its application. *Journal of Zhejiang University (Engineering Science)*,No. 4 , pp. 789—797
- Liu, Y.(2015). Research on Surrounding Rock Migration Law of Working Face with Similar Material Simulation. *Coal Technology*, Volume 34, pp. 93-95
- Tu, S., Dou,F. and Wan, Z. (2011). Strata control technology of the fully mechanized face in shallow coal seam close to the above room-and-pillar gob. *Journal of China Coal Society*, Volume 36, No. 3 ,pp. 366-370
- Wei, J., Li, Z. and Guo ,J. *Mining Safety & Environmental Protection*,Volume 37,No. 4, pp. 11—14.
- Wu, Z. (2013). Discussion on features of high alumina coal resources in zhungeer coalfield. *Journal of Coal Mine Engineering*, Volume 10, pp. 115-118
- You ,C.(2000). Analysis of bond-type bolt stress with overall length. *Chinese Journal of Rock Mechanics and Engineering*, Volume 19, No. 3,pp. 339–341.
- Zou, J., Li,L. and Ruan,B. (2004). Analysis of displacement and deformation of anchor bolt under elastic state. *China Railway Science*, Volume 25, No. 5,pp. 94–96.

Goaf area exploration in Anjialing surface mine based on the C-ALS

WANG Jun*, ZHOU You, ZHAO Ruhui

Mine Safety Technology Branch, China coal research institute, Beijing 100013, China ;
State Key Laboratory of Coal Mining and Clean Utilization (China Coal Research Institute), Beijing 100013, China ;
Beijing Mine Safety Engineering Technology Research Center, Beijing 100013.

ABSTRACT

In order to ensure safety in production, a 3D model is established in the mining boundary of the Anjialing surface mine by using C-ALS to explore goaf. The roof height of the mined out area is consistent with the results of a 3D laser scanner that verified the model by drilling exploration. The coal seam is shallow in the Anjialing district. Small-scale coal mining has a long history. A small kiln mining area in the centre of the first mining area damaged the 4th and 9th coal seam severely. Goaf 3D laser scanning technology has been widely used at home and abroad as an advanced goaf measuring instrument. C-ALS is used for the 1302 and 1316 levels in Anjialing district to carry out goaf exploration; the results show that the volume of the goaf is 21138m³. Through carrying out data processing and 3D modelling for the goaf, a basic idea for subsequent safety evaluation of goafs, disaster warning, and governance programs for the goaf are provided.

KEYWORDS: Goaf area; C-ALS; surface mine; 3D model

1. INTRODUCTION

The mined out area is a cavity produced by artificial digging or natural geological movement under the earth's surface. The goaf of the small kiln is an underground man-made activity site formed by previous mining behaviour. It not only includes the underground space of the well lane and resource exploitation, but also includes secondary space produced by the movement of rock strata caused by mining, as well as the space for the formation of secondary disasters after mining (Liu, 2008; Sun, 2009). The goafs formed by underground mining have a certain influence on the ground environment, and at the same time threaten the life and property safety of residents in the mining area.

Three dimensional laser scanning technology of goaf is a 3D precision detection method based on laser ranging. It can detect the goaf through scanning by stretching a rotating head which can be integrated with a laser distance measuring instrument in the inner goaf. Compared with the traditional geophysical prospecting and drilling methods, C-ALS can accurately grasp information like the three-dimensional shape, space position, the actual boundary, the area of the top floor, and the volume of the goaf (Liu, 2012; Ren et al., 2013; Xia et al., 2009). The information could be used to verify the results of geophysical prospecting and drilling in the goaf, and to guide the further development of geophysical prospecting and drilling in the mined out area of the mine.

2. CAVITY-AUTOSCANNING LASER SYSTEM (C-ALS)

MDL developed a robotic laser exploration system", that can quickly and safely explore the working area in the mine through a hole drilled beforehand. This system is called "Cavity automatic laser scanning system"(C-ALS) (Ma et al., 2013; Ma et al.). THE C-ALS system is a kind of self-navigation, "mechanical" robot probe. It can enter into the dry waste (in use) within the working area of the mine exploration. The diameter of the device is only 50 mm, therefore it can be placed into pre drilled holes whose diameter are at least 65 mm. Using a front micro laser scanner, it measures the three-dimensional shape of the cavity and the surface reflection. C-ALS can be lowered to a depth of 300 m, and the distance between the upper and the horizontal detection is 100 m.

C-ALS has the following advantages:

- (1)Prospecting dangerous underground mine areas in a safe way.
- (2) 3D results available within a few minutes, no need to wait for a few days.
- (3) Automatic scanning operation.
- (4) Flexible use method.
- (5) Small size and convenient transportation.
- (6) 360 degree scanning coverage with no "blind spot".
- (7) High precision and accuracy of goaf and space measurement.

The device structure is shown in Figure 1.



Figure 1: Equipment structure of C-ALS.

Below are the field devices and operating conditions, as shown in Figure 2.



Figure 2: Three-dimensional laser scanning equipment working drawing.

3. EXPLORATION IN ANJIALING

3.1 General Situation of Anjialing Surface Mine

Anjialing surface mine is located in the south central Pingshuo mining area. Construction began in April 1998, and the design and production capacity is 10.0 Mt/a. In 2003, it reached design production capacity when the production of Anjialing Surface Mine reached 32 million tons. The major minable seams are buried from 100 m to 200 m. From top to bottom the recoverable coal seams are No. 4, No. 9 and No. 11. They have an average thickness of 29.5 m. The present mining stope is shown in Figure 3.



Figure 3: Stope situation.

The coal seam is shallow in the Anjialing district, and small-size coal mining has a long history. A small kiln mining area distributed in the centre of the first

mining area damaged the 4th and 9th coal seam severely. The destroyed area of No. 4 and No. 9 seams is 3.5 km² and 0.275 km², respectively. Additionally, the surface subsidence and cracks increase rainwater infiltration. The water in the goaf is in a dynamic process where the no-water area may gradually become a water area. As a long-term collapse area, there is probably a small amount of hydrocele.

3.2 Goaf Scanning

To grasp the characteristics of the goaf in Anjialing accurately, China Coal Research Institute has used a 3D laser scanner to scan the drillings that exposed the goaf. From June 3rd, 2013 to June 6th, 2013 and July 16th to 18th, technicians detected a goaf for the 1302 and 1316 face. In total they scanned 18 drillings and a natural collapse pit (scanned the pit 5 times). 15 of the drillings are successfully scanned while the others are failed. The pit was successfully scanned 5 times. As a result, there were a total of 20 successful scans. The results are satisfactory.



Figure 4: Anjialing three-dimensional laser scanning site.

Table 1: Probe hole information.

Sample ID	location			Result of drilling	Discover goaf or not
	East	North	Height		
1	11703.7	71356.5	1316.8	Appear	Yes
2	11712.0	71345.7	1316.6		
3	11564.1	71292.5	1302.1	Appear	Yes
4	11564.6	71292.0	1302.2		
5	11547.7	71304.0	1302.7		
6	11538.6	71303.6	1302.7		
7	11542.8	71309.3	1302.8	Appear	No
8	11531.4	71304.6	1302.5		
9	11537.6	71250.9	1302.7	Appear	No
10	11529.5	71251.2	1302.7	Appear	Yes
11	11693.2	71356.6	1316.7	Appear	Yes
12	11676.7	71359.2	1315.1	Appear	Yes
13	11648.5	71341.2	1302.4	Appear	Yes
14	11678.4	71348.7	1314.8	Appear	Yes
	11675.6	71344.3	1314.4		
	11676.4	71340.8	1314.9		
15	11687.8	71331.6	1317.8	Appear	Yes

Sample ID	location			Result of drilling	Discover goaf or not
	East	North	Height		
16	11690.0	71334.9	1317.9	Appear	Yes
17	11650.0	71317.4	1302.7	Appear	Yes
18	11648.8	71326.0	1302.6	Appear	Yes

3.3 Description of goaf

According to the recent scans, the goafs exposed by drillings are connected. Descriptions of the goaf are as follows:

(1) The roof and floor are higher in the north and lower in south, which is similar to the coal seams. As a result of the fact that the dip of the floor is increases gradually in the southward direction, the goaf is higher in the south and lower in north.

(2) In the north of the proved area, the lowest height of the roof is 15 m. In the southwest, the highest height of the goaf is 32 m. The longest axis is nearly 60 m. The vertical height is low in the north and high in the southwest. In proved area the lowest vertical height is 5 m and the highest vertical height is 15m. The width of the goaf is about 15 m.

(3) The volume of the proved area in the goaf is 21139 m³.

(4) In the goaf, there is dust and gas of water. The temperature is low. It is judged that there is no water or fire in the goaf.

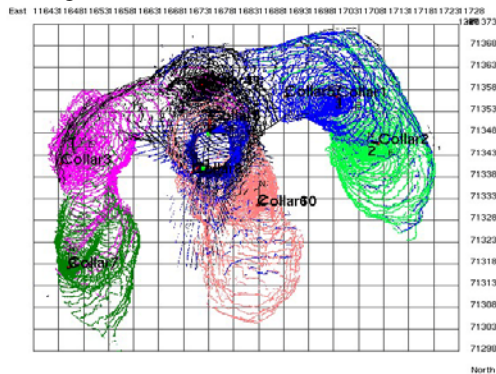


Figure 5: Anjialing goaf three-dimensional laser scanning the overall situation point cloud (Overlook).

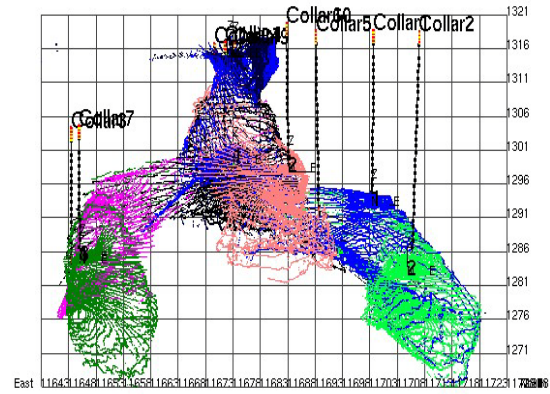


Figure 6: Anjialing goaf three-dimensional laser scanning the overall situation point cloud (Front view).

According to scanning of the caved pit, it was found that there is a goaf around the pit that is connected to the previously discussed goaf. 6 drillings, F(01) , F(02) , G(01) , G(02) , G(03) , and G(04) were drilled by technical personnel. The locations of the drillings are shown in Table 1. The drilling showed that there was a goaf around the drilled area. The height of the roof is similar to the scanned results.

4. GOAF MODELLING AND DISPOSAL

4.1 Goaf modelling

Goaf 3D modeling was performed using the Geomagic Studio software using the data from the 3D laser scans (Liu et al., 2009; Wang et al., 2010; Chen et al., 2012). The volume of the goaf was calculated at the same time. The whole goaf and volume are shown in Figure 7..

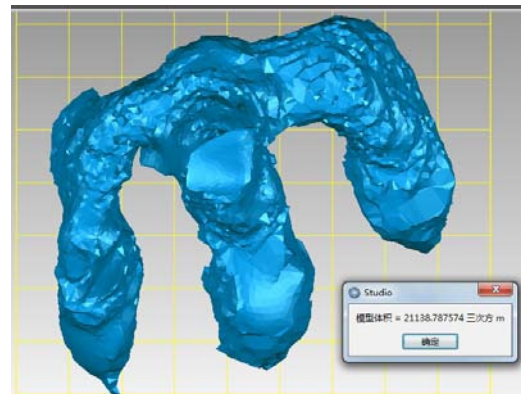


Figure 7: Anjialing goaf 3D modelling view.

Scanning results accurately determined the trend of the goaf. The distribution of goaf is in line with the basic characteristics of small coal mining. The effect is very significant, and therefore provides an accurate basis for the further processing of the goaf.

4.2 Goaf disposal

The blasting method is the most commonly used method in the production process of handling goafs in surface mining. According to the relationship between the mining area and flat bench, the loose blasting method is suggested to treat goafs. The specific practices are as follows:

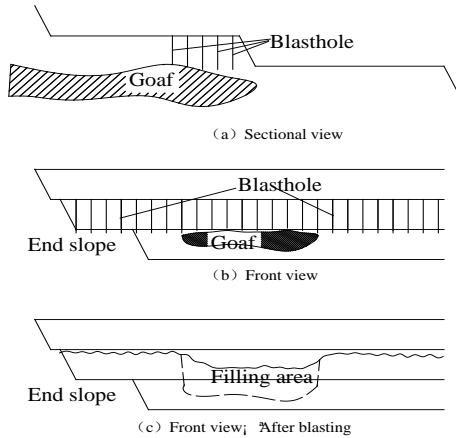


Figure 8: Loose blasting in goaf disposal.

The results of loose blasting in the goaf in Anjialing surface coal mine are as shown in Figure 9.



Figure 9: The goaf after blasting.

5. CONCLUSION

(1) There are many goafs in Anjialing surface mine. Exploring and disposing of the existing goafs has great importance to guarantee safe production in the surface mine.

(2) By using the "cavity automatic laser scanning system", the Anjialing surface mine area goafs were found. A large scale drilling scan discovered that the goafs were connected. By drilling verification, it was found that the gob roof elevation is the same as the 3D laser scanner elevation.

(3) An accurate computation of the goaf's volume was made via goaf 3D modeling. It was prove that the

3D laser scanning results give an accurate judgment of the goaf trends.

(4) Based on the goaf 3D model, the goaf was disposed of with loose blasting to lay a foundation for safe production in the surface mine.

6. REFERENCES

Chen Kai, Yang Xiaocong, Zhang Da(2012). Study on cavity 3D laser scanning deformation monitoring test. *Non-ferrous Metal*, Volume 64, pp. 1-5.

Liu Xiling(2008). Research for stability analysis and safety forewarning of cavity based on laser 3D detection[D]. Central South University.

Liu Jun, Wand Di(2009). Integrated Application of GPS and 3D technology in Detection of Mined-out Area. *Metal Mine*. suppl, pp. 512-515.

Liu Kewei(2012). Study of 3D laser scanning visualization and analysis of the stability of hazardous cavity under open-pit mine[D]. Central South University.

MA Yutao , Peng Wei(2013). Study on Cavity-Autoscanning Laser System (C-ALS) and its application in Anqing Copper Mine(Non-ferrous Metal). *Volume 65*, pp. 9-12.

MA Haitao, LIU Yongfeng, HU Jiaguo. Study on gob detection and visualization of three-dimensional model based on C-ALS. *Journal of Safety Science and Technology*. Volume 6, pp. 38-41.

Ren Hongwen, Liu Zhaofu, Han Zhiyao Wang Jinghai, Deng Guoping.(2013) Application of 3D Laser Scanning Technology in the Surveying and Mapping. *Gold Science and Technology*. Volume 21, pp. 64-68.

Sun Shufang. Analysis and Processing of Goaf dimensional laser scan data[D]. Kunming University of science and technology,2009.

Xia Yonghua, Fang Yuanmin, Sun Hongsheng, Zuo Xiaoqing WA Xuekun Chen Jie(2009). Error Analysis and Calibration of 3D Laser Monitoring System Survey in Finished Stopes. *Bulletin of Surveying and Mapping*. Volume 18, pp.18-21.

Wang Guotao , Luo Zhouquan , Liu Xiaoming, Zhu Qingling(2010). Application of 3D monitoring and mines based on visual modeling cavities in metallic cavity features. *The Chinese Journal of Geological Hazard and Control*. Volume 21, pp. 104-109.

Application of the strength reduction method in coal mine roof support design

Gabriel Esterhuizen^{a,*}, Ihsan Berk Tulu^b

^a Principal Research Engineer, NIOSH Office of Mine Safety and Health Research, Pittsburgh, PA, USA

^b Associate Service Fellow, NIOSH Office of Mine Safety and Health Research, Pittsburgh, PA, USA

ABSTRACT

Ground falls represent a significant proportion of injuries and fatalities in underground coal mines in the US. During 2013, ground falls were responsible for 4 of the 14 fatalities and 16.6% of the 1,577 reportable lost-time injuries. In addition, each year about 400 to 500 large roof falls are reported that can extend up to or above the bolted horizon. Support design for coal mine entries is largely based on past experience and a trial-and-error approach. A numerical model-based approach for support design is presented in which calibrated models are used to determine a stability factor for a supported entry. The stability factor is determined using the strength reduction method (SRM). Applying this technique, the relative merits of various support systems can be evaluated. The numerical models allow the contribution of individual support units to overall stability to be assessed. Two case histories are presented. In the first case the SRM approach is applied to assess the use of passive cable anchors as primary support in a room-and-pillar coal mine. The second demonstrates how the SRM approach was used to evaluate the impact of angled bolts at the rib-roof corner on roof stability. It is concluded that the SRM approach provides useful information to assess the overall degree of stability achieved by a support system, and allows support elements to be optimized for particular geological and stress conditions.

KEYWORDS: FLAC3D; coal mine roof support; strength reduction method; cable bolts

1. INTRODUCTION

Ground falls remain a significant cause of fatalities and injuries in underground coal mines. Over the ten-year period of 2005 through 2014, falls of ground were responsible for 32% of all fatalities in underground coal mines (Mine Safety and Health Administration (MSHA), 2015). While improvements are continuously being made in support technology, design, and application, underground mine workers remain exposed to the hazard of ground falls on a daily basis. Factors contributing to ground falls may include natural planes of weakness within the rock mass, unfavorable loading conditions, low rock strength, unusual depositional features, and dynamic loading events. Furthermore, a specific roof fall may be related to more than one contributing factor. Ground falls can be reduced by supporting the excavation walls and by modifying the excavation layout to improve ground stability.

2. SUPPORT DESIGN APPROACHES

Mine operators in the United States are expected to develop and follow a roof control plan, approved by the MSHA district manager, which is suitable to the prevailing ground conditions and mining methods. The roof control plan specifies the minimum support requirements such as bolt spacing, length, and type that will be used to support the roof

and ribs of coal mine entries. The support design procedure for roof control plans is left open to the mine operator, allowing innovation and development of new technologies.

Current roof support technology makes use of rock reinforcement principles to improve the strength and stability of the rock through the installation of roof bolts. This type of support is called intrinsic support, because it is located within the rock mass, providing internal reinforcement. In some situations where it may be difficult to install intrinsic support or where excessive deformation is expected, external supports in the form of standing supports may be used.

During the early years of the application of intrinsic support systems, in-mine trials and the observational approach were used to determine support requirements (Mark, 2000). Limited support system analysis was conducted, typically using analytic equations based on beam theory (Fairhurst and Singh, 1974). Over the years significant improvements were made in the types of support units and the understanding of the interaction of the rock mass with the support units.

At present there is more than 50 years of experience of the application of intrinsic support systems in coal mines that forms the basis for support design. This experience is captured in many of the support rules found in the mining regulations and

published in MSHA guidelines. The NIOSH-developed Analysis of Roof Bolt Systems (ARBS) (Mark et al., 2001) is an example of a design approach based on a statistical analysis of successful and unsuccessful applications of support systems.

As a result of this wealth of empirical knowledge, the support system for a new mine can simply be based on a support system that was successfully implemented under similar conditions elsewhere. However, the reliance on empirical experience does have limitations. As new support technologies become available, mining techniques change, and as mining depths increase, the historical experience may no longer be applicable. This shortcoming can be solved by following an engineering approach to support design. The engineering approach makes predictions about the stability of a system through the analysis of the strength and expected loads that the system will be subjected to (Hoek et al., 2003). When considering a system that consists of brittle rock materials, bedding planes, rock joints, steel bolts, and resin grout, the stability analysis can become complex. As computational methods have become more efficient and affordable, numerical models are increasingly used to conduct the analysis of excavation stability in rock materials. There are many computational models commercially available that can assist in conducting these types of analysis. However, at present no single engineering-based analysis method has found wide acceptance in U.S. coal mines (Mark, 2000; Tadolini et al., 2006).

3. DEVELOPMENT AND VALIDATION OF THE STRENGTH REDUCTION METHOD FOR ROOF SUPPORT DESIGN

The need for a standardized method to conduct engineering analysis of coal mine roof support systems has been addressed by making use of numerical models that are able to realistically simulate the rock mass response to excavations and the interaction of the support systems with the rock mass. The FLAC3D finite difference code (Itasca, 2014) was selected to conduct the model analyses. The modeling approach allows a “stability factor” (SF) to be determined for a supported entry. The SF is determined by using a modeling technique known as the strength reduction method (SRM) (Zienkiewicz et al., 1975). The SRM has a long history in numerical modeling and has often been applied in rock slope stability engineering to determine the safety factor of rock slopes (Lorig and Varona, 2000), but has not been widely used for underground excavation analyses. The classic SRM approach was adapted and modified to allow the

estimation of coal mine entry stability factors (Esterhuizen, 2012).

3.1 Applying the strength reduction method

The numerical models of coal mine entries simulate a slice perpendicular to the axis of the entry. The thickness of the slice is equal to the support row spacing, typically 1.2 m. The various rock layers are modelled with appropriate strength parameters. The contacts between various units of rock in the roof are modelled as discrete interfaces. The bedded rock within each unit is modelled as a layered material, using the ubiquitous joint material type available in FLAC3D. Support units are also modelled explicitly. The FLAC3D software has the capability to realistically model grouted steel supports, with or without pretension.

The SRM is applied by first conducting a stability analysis using average rock strength properties. Depending on the outcome, the analysis is repeated using either a decreased or increased rock mass strength until the point of collapse is satisfactorily bracketed. Strength adjustments are achieved by simultaneously reducing or increasing the cohesion, tensile strength, and the coefficient of friction of the rock mass. The stability factor is simply calculated as the inverse of the strength adjustment factor at the point of collapse of the modeled excavation. For example, if collapse occurs when the strength is reduced by a factor of 0.8, the stability factor would be 1.25.

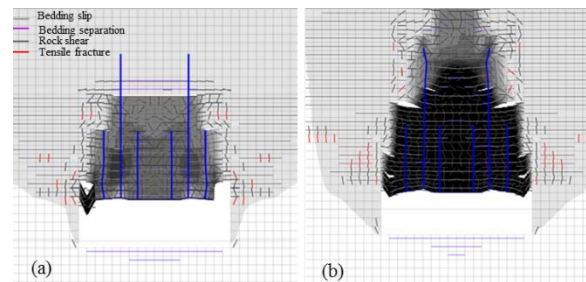


Figure 1: Model results showing a supported entry: a) when the rock strength has been reduced to a point of critical stability, and b) when further reduction of the rock strength causes roof collapse.

The occurrence of collapse is indicated by the inability of the model to reach a state of equilibrium after an extended number of solution cycles. Usually, this means that a section of the roof is accelerating downwards and equilibrium could not be reached. Figure 1(a) shows a plot of a numerical model of an entry in which the rock strength has been reduced to the critical point where collapse is about to occur. Figure 1(b) shows how the roof collapses when the rock strength is reduced by a further 5%.

When applying the SRM to underground coal mine excavations, it was found that floor heave was sometimes the mode of ultimate instability. This would occur if the floor rocks are weaker than the roof rocks. All analyses were therefore conducted by only reducing the rock mass strength above the roof of the excavation while leaving the coal and floor rocks unadjusted. Analyses may be conducted in which the effect of floor instability is assessed.

3.2 Model validation

The outcome of the modeling procedures was validated against empirical design methods that are used in US coal mines (Esterhuizen et al., 2014). The model results were initially assessed to determine if they are able to capture variations in roof stability predicted by the coal mine roof rating (CMRR) (Molinda and Mark, 1996; Mark et al. 2002). Additional verification was conducted by comparing SRM-calculated stability factors to the empirically based ARBS method (Mark, 2000; Mark et al., 2001). The CMRR and ARBS methods are based on extensive observation of entry stability in operating mines, capturing decades of empirical experience of the authors. These empirical methods are used to evaluate potential stability or instability in operating coal mines and are suitable for validating the SRM calculated stability factors.

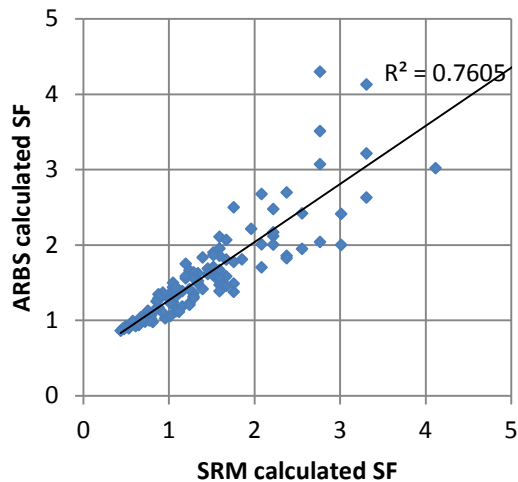


Figure 2: Comparison of stability factors calculated using the ARBS empirical method and the SRM for 120 cases of entries supported by 1.8-m bolts.

The relationship between SRM-calculated and ARBS-calculated SF values for the 120 models of entries supported by 1.8-m fully grouted bolts is shown in figure 2. The results show that the two methods predict similar trends, with a coefficient of determination of 0.76. At lower SF values the scatter of results is small, which is important for design.

The similarity of results achieved by the mechanics-based SRM and the statistically-based ARBS for this wide ranging set of conditions demonstrates that the SRM captures the essential factors affecting entry stability.

4. APPLICATION OF THE SRM TO EVALUATE SUPPORT ALTERNATIVES

The SRM has been applied to evaluate support systems for various operating coal mines. Two case histories are presented here in which support alternatives were evaluated to improve the understanding of the contribution of support elements to overall stability, and to quantify the degree of stability achieved.

4.1 Case history 1: Room-and-pillar mining with cable bolt support

Cable bolting is sometimes used as primary support in coal mines experiencing difficult roof conditions. In low-seam mines, the flexibility of the cable bolts allows greater length supports to be installed near the advancing face without the use of couplers. When used as primary support, the cables are typically installed in the same row as fully grouted bolts, replacing two or more of the bolts in each support row. A heavy steel channel may be used as a strap to spread the support load over a greater portion of the roof. Historically, MSHA has not allowed widespread use of partially grouted untensioned cable bolts for primary support.

At the case study mine, fully grouted rebar bolts with pre-tensioned cable bolts were used as primary support. It was found that when a large roof fall occurred, the cable bolts may be contained within the dome of fallen rock. As problematic roof conditions continued to exist, the mine management decided to modify the system using passive cable bolts as part of the primary support system. The cable bolts were located near the ribs of the entry, to increase the likelihood that they would be anchored outside the dome of potentially unstable roof. The modified system resulted in considerably improved stability conditions in the mine. However, the mine engineer was uncertain whether the modified system was indeed better than the original system for controlling the roof, or whether the improved conditions were related to changes in the geology or other factors. An analysis using the SRM was conducted to identify the differences between the two systems.

4.1.1 Geotechnical Conditions

The case study mine extracts the Lower Kittanning coalbed. The mine uses the room-and-pillar method in a mining height of about 1.2 m. The depth of cover is approximately 120 to 150 m. In

certain locations the roof consists of 10-m-thick laminated dark gray silty shale that is associated with difficult ground conditions. It is overlain by a stronger interbedded sandstone and shale unit. Observations of the rock exposed in roof falls show that it tends to delaminate in thin slabs that are about 2 to 6 cm thick, as shown in Figure 3. The uniaxial compressive strength of the intact shale is 55 to 60 MPa. The available rock strength and bedding information were used to classify the rock mass using the coal mine roof rating (CMRR) (Molinda and Mark, 1996). The CMRR classification of the silty shale roof is estimated at 45.



Figure 3: Typical roof fall showing laminated nature of the silty shale roof rocks and steep-sided collapse cavity.

Stress measured in the vicinity of the mine shows results typical of Northern Appalachia with a relatively high pre-mining horizontal stress associated with regional tectonic loading (Mark and Gadde, 2008; Dolinar, 2003). The major horizontal stress is estimated to be oriented at N80E. Where possible, the mining direction is oriented so that the development is directed favorably relative to the stress field.

4.1.2 Support systems analyzed

The original and modified support systems used at the mine were evaluated using the SRM approach. The support layouts are shown in figure 4.

The original support system consisted of fully grouted conventional bolts and tensioned cable bolts as part of the primary support, installed on-cycle.

Cable bolts are partially grouted, with 1.2 m of resin grout forming the anchorage zone. Each support row was installed through a heavy T3 channel. The first row of the pattern consisted of two, 1.8-m-long, No. 5 tensioned rebar bolts through the center section of the entry and two, 3.6-m-long, 15-mm-diameter cable bolts on the outside. The second row reverses the order. Bolt tension is nominally 5 t. The support rows are 1.2 m apart. Entries are 5.5 m wide.

The modified support system consisted of support rows with four 1.8-m-long No. 5 tensioned rebar bolts and two 3.6-m-long un-tensioned cables installed on a 4.3-m-long T3 channel. The cables are located about 50 cm from the ribs, near the extremities of the channel. Additionally, the entry width was reduced to 4.9 m.

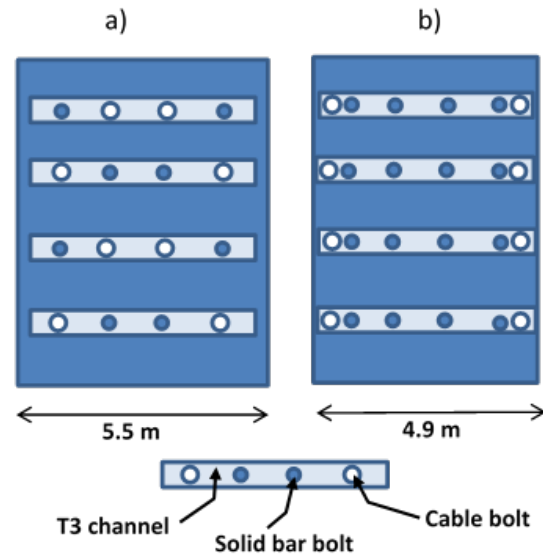


Figure 4: Support systems analyzed at case study 1 mine, showing a) the original system with tensioned cable bolts, and b) the modified system with passive cable bolts.

4.1.3 Results of SRM analysis

The original support system was simulated and the SF was determined to be 2.21. This SF value would be considered to be adequate for most room-and-pillar mining. However, the thinly laminated nature of the roof and relatively high horizontal stress appears to require a higher value of the SF to prevent large-scale roof falls. The modified system, using the greater intensity of fully grouted bolts and passive cable bolts produces a SF value of 2.84. This confirms that a significant increase in support capacity and stability is achieved by the modified system. The increase in stability can be attributed to both the increase in support and the reduction in entry width.

A closer look at the numerical modeling results showed that for the original system, instability occurs

when the roof yielding extends above the top of the cable bolts that are located near the center line of the entry. Under these conditions the cable bolts do not achieve their full load capacity, and collapse while encapsulated inside the failing roof. Under these conditions, the pretension does little to prevent the collapse.

With the alternative system, the location of the cable bolts outside the collapsing dome of rock helps to provide anchorage in the stable rock. In addition, the T3 channel is shown to act as a sling that holds the failing rock in position. The sling-action is able to control the roof over a much greater range of roof sag.

The results also showed that the fully grouted bolts would load up quickly as the roof sagged, but once roof failure developed above the bolts, the passive cable bolts would start to load up, acting almost like a tandem system that controls the roof after the fully grouted bolts started to shed load.

In practice it was found that the mine operational staff could readily identify areas which had sagged when using the modified support system. When this condition was observed, cribs or other types of standing supports were typically installed to arrest further movement. So although roof sag occasionally occurred, the support system was able to control the damaged roof, allowing remedial actions to be taken to prevent collapse.

4.2 Case history 2: Longwall Gateroad Support Changes

Longwall gateroads provide access to the working area of a longwall mine. The gateroads are subject to increased loading as the coal is extracted and loads are transferred to the adjacent unmined coal. Gateroads are expected to remain stable during these changing stress conditions. Gateroads are typically provided with primary support during development consisting of roof bolts. Secondary support in the form of cable bolts and screen may also be installed. Various forms of standing supports may also be required to maintain the integrity of the roof rocks under the severe loading conditions near the longwall face.

At the second case history mine, fully grouted bolts are used as primary support and two additional bolts are installed at 45° in the rib-roof corner, as shown in figure 5. These bolts were originally intended to help support friable roof if stress-related roof damage occurs in the corners. However, as experience was gained it was found that the corner bolts did not appear to be required. In this case the mine management was interested to know if locating the corner bolts 30 cm away from the corner and

installing them vertically would improve the support efficiency.

4.2.1 Geotechnical Conditions

The mine also extracts the Lower Kittanning coalbed using the longwall mining method. The mining height is about 2.1 m and the depth of cover varies between about 150 m and 240 m. The roof rock is a sand shale with an average uniaxial compressive strength of 76 MPa. The CMRR for this roof rock is estimated to range between 47 and 52. The horizontal stress at this mine is expected to be typical of Northern Appalachian mines. Some stress-related roof-cutter formation was observed in the mine roof. The orientation of the longwall panels was optimized to minimize horizontal stress impacts.

4.2.2 Support Systems Analyzed

The support system evaluated consisted of 1.8-m-long fully grouted bolts with 180 kN capacity installed in rows 1.2 m apart. Each row consisted of four vertical bolts and two 45° angled bolts at the rib-roof corner. In addition, two supplementary cable bolts 3 m long were installed in rows 2.4 m apart. The cable bolts were installed on a T3 channel. The entry width is 4.9 m.

This support system was evaluated with corner bolts installed at 45° and with corner bolts installed vertically, located 30 cm from the entry ribs.

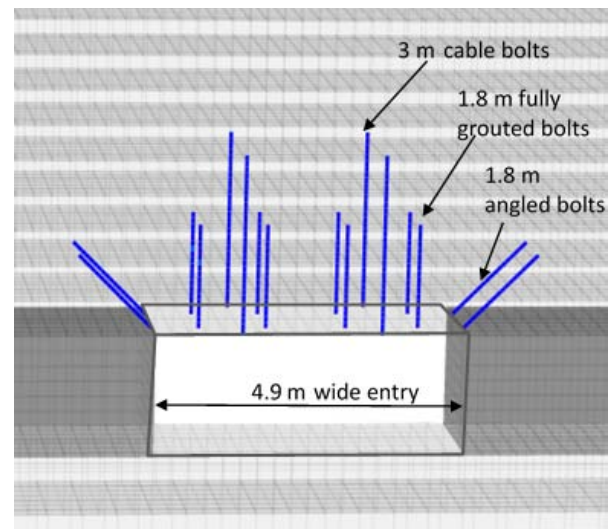


Figure 5: Central portion of a numerical model showing entry and support types evaluated.

4.2.3 Modeling results

The modeled SF against roof collapse for the base case, with the 45° corner bolts, was determined to be 1.85. Inspection of the bolt loading in the model showed that the corner bolts did not attract much load as the roof sagged. The load in the corner bolts only

increased to about 40 kN while the vertical bolts would load up to about 200 kN, which is their ultimate capacity. The cable bolts loading was more gradual, owing to the free length of about 1.8 m. Cable bolts approached their ultimate load after about 150 mm of roof sag.

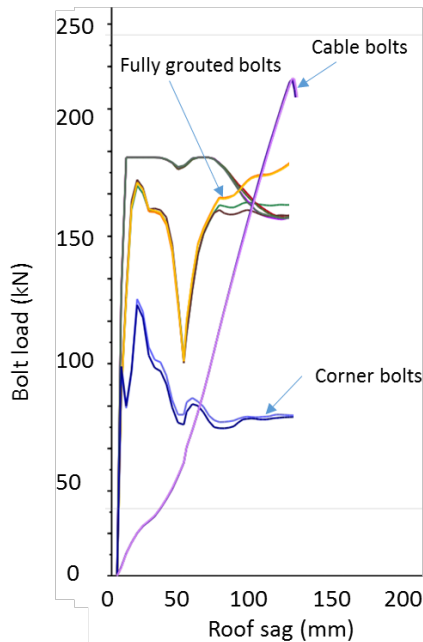


Figure 6: Bolt loads vs. roof sag for the support system in which the corner bolts are installed vertically.

When the corner bolts were located 30 cm from the rib and installed vertically, they attracted loads of up to 130 kN, and maintained a load of about 80 kN as the roof sagged. Figure 6 shows the bolt loads and roof sag for a case in which the rock strength has been reduced to the point of critical stability. The vertical corner bolts clearly contribute more significantly to the overall stability of the roof. The calculated SF was increased to 2.25 by the change in corner bolt location and orientation.

With this configuration, the cable bolts are able to control the roof sag up to about 130 mm when load shedding starts to occur.

These results provided confirmation that the 45° corner bolts were not as effective in contributing to the overall stability of the entry roof, and that the adjusted support system was likely to be more effective.

5. CONCLUSIONS

A numerical modeling approach has been developed that allows the stability factor of supported coal mine entries to be estimated. The numerical models have been calibrated against field-measured rock mass response and support interaction. The

model outputs can be evaluated further to determine the contribution of individual support elements to overall stability.

Two case histories demonstrate the application of the method to assessing support alternatives at operating mines. The calculation of a stability factor allows direct comparison of the overall efficiency of each support alternative.

Insight was also gained into the mechanics of the support-rock interaction, showing how the fully grouted supports are initially loaded-up, followed by loading of the passive cable bolts.

The studies demonstrate that numerical model-based analysis of coal mine entry support systems allows support alternatives to be evaluated and improves understanding of support element contributions. The optimized support systems provide improved safety for mine workers.

6. DISCLAIMER

The findings and conclusions in this paper are those of the authors and do not represent the views of the National Institute for Occupational Safety and Health (NIOSH). Mention of any company name, product, or software does not constitute endorsement by NIOSH.

7. REFERENCES

- Dolar, D. (2003). Variation of Horizontal Stresses and Strains in Mines in Bedded Deposits in the Eastern and Midwestern United States, in Proceedings 22nd International Conference on Ground Control in Mining, 6–7 August 2003, Morgantown, USA, pp. 178–185.
- Esterhuizen, G.S. (2012). A Stability factor for Supported Mine Entries Based on Numerical Model Analysis, in Proceedings 31st International Conference on Ground Control in Mining, Morgantown, USA, 9 p.
- Esterhuizen, G.S., Murphy, M.M., and Bajpayee, T.S. (2014). Analysis of geotechnical and support parameters on coalmine entry stability using the strength reduction method. AusRock 2014: Third Australasian Ground Control in Mining Conference, November 5-6, 2014, Sydney, New South Wales, Australia. Australasian Institute of Mining and Metallurgy, 2014 Nov; pp. 383–391
- Fairhurst, C. and Singh, B. (1974). Roof Bolting in Horizontally Laminated Mine Roof, Engineering and Mining Jour., pp. 80–90.
- Hoek, E., Kaiser, P.K., and Bawden, W.F. (1995). Support of Underground Excavations in Hard Rock, 300 p, (CRC Press).
- Itasca Consulting Group (2014). FLAC3D Fast Lagrangian Analysis of Continua in 3 Dimensions, Itasca Consulting Group, Minneapolis, MN.

Lorig, L. and Varona, P. (2000). Practical Slope Stability Analysis using Finite-Difference Codes, in Proceedings Slope Stability in Surface Mining, W.A. Hustrulid, M.K. McCarter and D.J.A. van Zyl (eds), pp. 115–124 (Society for Mining Metallurgy and Exploration, Littleton, USA).

Mark, C. (2000). Design of Roof Bolt Systems, in New Technology for Coal Mine Roof Support, NIOSH Open Industry Briefing, NIOSH IC 9453, 2000, pp. 111–132.

Mark, C., Molinda, G.M., and Dolinar, D.R. (2001). Analysis of Roof Bolt Systems, in Proceedings 21st International Conference on Ground Control in Mining, WV University, Morgantown, USA, 7–9 August 2001, pp. 218–225.

Mark, C., Molinda, G.M., and Barton, T.M. (2002). New Developments with the Coal Mine Roof Rating, in Proceedings 21st International Conference on Ground Control in Mining, Morgantown, USA, 6–8 August, pp. 294–301.

Mark, C. and Gadde, M. (2008). Global Trends in Coal Mine Horizontal Stress Measurements, in Proceedings 27th International Conference on Ground Control in Mining, WV University, Morgantown, USA, pp. 319–331.

Mine Safety and Health Administration (2015). Web Page: <http://www.msha.gov/stats/statinfo.htm>

Molinda, G.M. and Mark, C. (1996). Rating the Strength of Coal Mine Roof Rocks, U S Department of the Interior, Bureau of Mines IC 9444, Pittsburgh, Pennsylvania 36 p.

Tadolini, S.C. and Mazzoni, R.A. (2006). Twenty-four conferences; more than one-hundred and seventy papers; understanding roof bolt selection and design still remains priceless. Proc. 25th International Conference on Ground Control in Mining, West Virginia University, Morgantown, WV, pp. 382–389.

Zienkiewicz, O.C., Humpheson, C., and Lewis, R. W. (1975). Associated and Non-Associated Visco-Plasticity and Plasticity in Soil Mechanics, Geotechnique, Vol 25, pp. 617–689.

Numerical simulation of the migration laws of supports and surrounding rock for coal seams of large dip angle

Huang Zhian, Feng Caiyun, Wang Hui*, Zhang Yinghua, Gao Yukun

State Key Laboratory of High-Efficient Mining and Safety of Metal Mines (University of Science and Technology Beijing), Ministry of Education, Beijing, China, 100083

ABSTRACT

SDIC Nileke mine district is located in Xinjiang and it contains 6 minable seam layers. The 45° average dip angle of the mine results in the complex processes of the mining working face. Processes such as support moving and mining working face advancing are restricted. The lateral stress of the roof increases, and at the same time the problem of controlling the working face roof becomes serious. Based on practical conditions, the process of excavation and support of the mine working face are simulated using FLAC^{3D}. The results can provide technical support for safety production through the reasonable support mode obtained through the simulation of mine pressure behaviour of the working face.

KEYWORDS: steep seam mining; numerical simulation; support resistance; hydraulic support stability

Deep inclined seam refers to coal seams with an inclination between 35° and 55°. In China, deep inclined seams account for about 15%-20% of all coal resources. Over 50% of the deep inclined seams are high-quality coking coal and anthracite. As we all know, high-quality coking coal and anthracite is a scarce coal in China. (Xie, P. S. et al., 2015a ; Wen, M. M. 2014b; Qu, Q. Y. 2014c). The mine pressure behaviour changes significantly when compared to gently inclined seams while mining. Problems such as the increasing of roof lateral stress and the increasing possibility of dumping and sliding of hydraulic support are highlighted. It is of particular importance to study the relative movement of the support and the surrounding rock of deep inclined coal seams. To solve this problem, much research has been carried out by scholars. For example, the interaction characteristics between surrounding rock movement and support system in large mining height fully-mechanized faces in steeply inclined seams were analyzed by Xie Panshi (2015). The pressure of the surrounding rock of A₆ coal seam was analyzed in this paper using FLAC^{3D}. A₆ coal seam is a part of SDIC Nileke mine

1. MINE INTRODUCTION

SDIC Nileke mine is located east of Nilka county town. The production capacity of the mine is 1.2 Mt/a. The mining district contains 6 coal seams. It is about 2.15-8.06 km from east to west and 1.21-4.38 km from north to south, for a total area of about 28.01 km². This paper mainly discusses the A₆ layer, which is characterized by:

(1) The average thickness is 6.42 m. It is a stable coal seam. The roof of the coal seam consists of carbonaceous mudstone, mudstone, and silty sandstone, and the bottom plate consists of carbonaceous mudstone, silty sandstone, and fine sandstone. It can be concluded that its structure is relatively simple.

(2) The average thickness of A_{6-lower} is 2.94 m. The number of the gangue layer is from 0 to 2, and the gangue layer is mainly composed of carbonaceous mudstone. The roof of the coal seam consists of carbonaceous mudstone, mudstone, and silty sandstone, and the bottom plate is composed of carbonaceous mudstone and mudstone.

2. MODEL ESTABLISHMENT

After the coal resource is exploited, the subsidence of overlying strata occurs. The numerical model is built by using FLAC^{3D}, and Moore-Coulomb criterion were used to judge the destruction of rock.

The depth of N11 working face is 150-350 m. To be safe, the thickness of the overlying rock was set to 350 m in the simulation. The weight of the overlying strata is 2.5 MPa/100 m. A distributed load is set to the top of the model to simulate the overlying strata's weight. The vertical pressure of the overlying strata is 8.75 Mpa. The scale of module is 100×130×180 m. The inclination of the coal seam is 45°. The model is built using the 8-points method, it contains 14400 units and 17702 nodes. The four sides of the model are displacement boundaries and cannot be moved in the horizontal direction. The bottom side

*Corresponding author – email : wanghuiustb@live.cn.

of the model is a fixed boundary. The fixed boundary means it cannot be moved either in a horizontal direction or in a vertical direction. The thickness of the coal seam is 8.7 m, and the mining height and caving height were set to 4 m and 4.7 m, respectively.

The roof thickness of the working face is 25.2 m and the height of the bottom floor is 10.2 m. The model and the mesh are shown in Figure 1. Other parameters were obtained by an experiment, as shown in Table 1.

Table 1: Numerical simulation parameters

Rock properties	Thickness (m)	Density ρ_0 (kg/m ³)	Compressive strength (MPa)	Elastic modulus E (GPa)	Poisson's ratio/ μ	Cohesive strength/C (MPa)	Internal friction angle (°)	Tensile strength (MPa)
Fine sandstone	3.40	2660.00	75.13	18.92	0.23	14.50	47.60	7.67
Powder sandstone	2.00	2540.00	74.17	17.00	0.22	14.70	47.40	9.97
Middle sandstone	2.00	2580.00	68.52	29.20	0.18	15.31	45.25	11.60
Powder sandstone	3.60	2540.00	74.17	17.00	0.22	14.70	47.40	9.97
Coarse sandstone	4.80	2620.00	105.63	33.87	0.16	21.95	48.69	7.89
Powder sandstone	1.60	2540.00	74.17	17.00	0.22	14.70	47.40	9.97
Middle sandstone	4.20	2580.00	68.52	29.20	0.18	15.31	45.25	11.60
Conglomerate	2.40	2500.00	49.78	14.23	0.28	17.80	45.30	7.22
Powder sandstone	1.00	2540.00	74.17	17.00	0.22	14.70	47.40	9.97
A ₆ minelayer	8.70	1400.00	7.26	3.65	0.29	4.05	41.00	4.19
Powder sandstone	10.20	2540.00	74.17	17.00	0.22	14.70	47.40	9.97

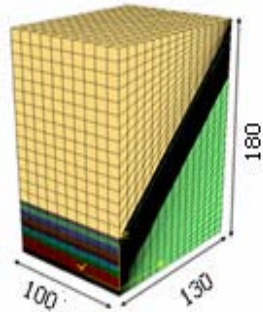


Figure 1: The model and

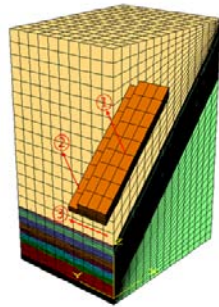


Figure 2: Excavation model: ① goaf ② stent location ③ advanced direction

In the simulation, 25 meters of coal were left in the starting side in the direction of the working face. The excavating speed along the working face advanced direction was 5 meters per time step, and the mining height was 4 meters. Until it came to a balance, the iteration was stopped. During the calculation, the caving coal was 30 to 60 meters the supporting area of the working surface 60 to 65 meters, and the top coal did not collapse. The excavation model is shown in Figure 2.

According to Moore - Coulomb criterion (Wu J. B., 2010), the intensity of rock is calculated as follows:

$$f_s = \sigma_1 - \sigma_3 \frac{1 + \sin \varphi}{1 - \sin \varphi} - 2c \sqrt{\frac{1 + \sin \varphi}{1 - \sin \varphi}} \quad (1)$$

$$f_1 = \sigma_1 - \sigma_3 \quad (2)$$

Where: σ_1 —— the maximum principal stress.
 σ_3 —— minimum principal stress.
 C ——material cohesion.
 φ —— internal friction angle

σ_t is the tensile strength of rock. If $f_s \leq 0$, shear failure of rock will occur; if $f_1 \geq 0$, rock tensile failure will occur (Wang H. W., 2010).

Due to the complicated rock properties of SIDC and the effect of weak surface structure, laboratory calculated parameters are inconsistent with the engineering practice. In order to fit the actual situation, the elastic modulus of coal and rock is set to 50% of the test values from the laboratory.

3. RESULTS ANALYSIS

3.1 Analysis on the trend of surrounding rock before supporting

The vertical direction stress of the surrounding rock after excavation is shown in Figure 3. From

Figure 3 it can be seen that stresses were concentrated in the front of the working face. In the position 6 meters ahead of the coal wall, the maximum stress is 2.24 MPa. However, in the middle of the goaf, the roof undergoes tensile stress because of the damage of rock layer.

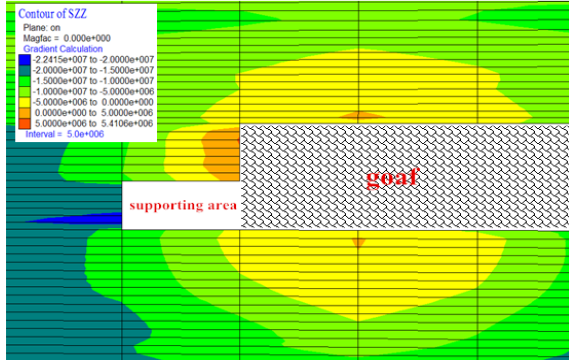


Figure 3: Stress of section along trend.

The change of vertical displacement along the direction of the goaf after excavation without support is shown in Figure 4. Due to the influence of caving coal behind the working face, the maximum displacement of the working face is 4-5 meters from the coal wall, and this is the contact zone of goaf and support. The distribution of maximum displacement boundary looks like a triangular, and the maximum displacement is 36 cm. While the distribution of roof subsidence is arched, the maximum shift is 28.43 cm. In the middle bottom, the maximum displacement is 14.98 m while vertical displacement decreases on both ends at the goaf bottom. The floor may be bulged in the process of excavation. Effective measures should be taken to solve the problems of the roof.

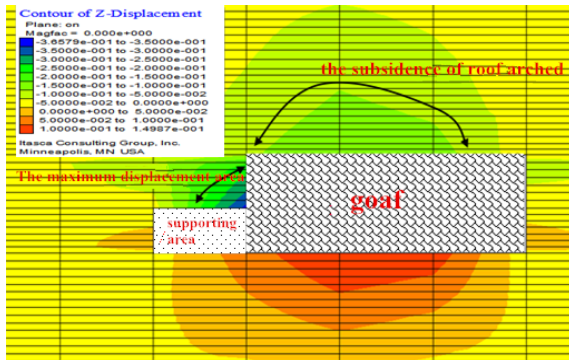


Figure 4: Displacement nephogram of section along trend.

3.2 Analysis on the inclination of surrounding rock before supporting

According to the analysis of Figure 4, four monitor points were set in the model. The first one is 5 meters in front of the coal wall, the second is on the

coal wall, the third is 2.5 meters behind the coal wall, and the last one is 5 meters behind the coal wall. The monitors were set to study the deformation of the inclined plane along the coal seam. The specific displacement is shown in Figures 5 and 6.

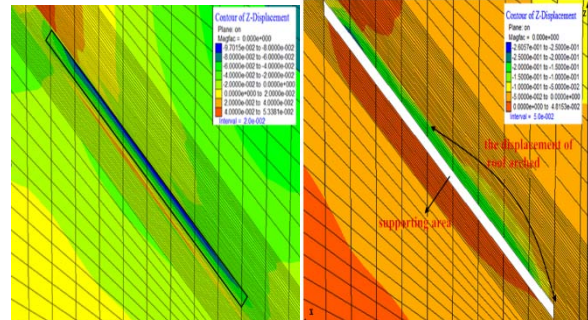


Figure 5: Vertical displacement along coal seam 5 meters ahead coal wall and on the coal wall.

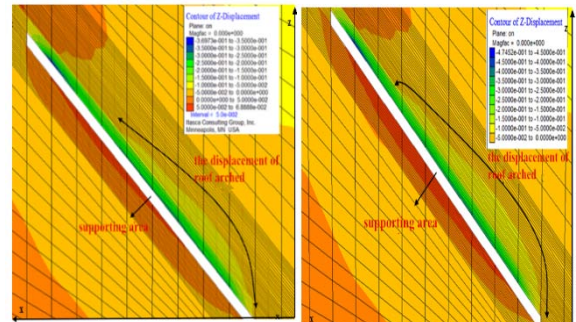


Figure 6: Vertical displacement along coal seam 2.5 meters behind the coal wall and 5 meters behind the coal wall.

As can be seen from Figure 7, the subsidence of top coal is different at different positions of the coal wall. The subsidence is less than 10 cm in front of the coal wall. While the subsidence of top coal in the coal wall is greater than 5 meters ahead of the coal wall, the maximum is 26 cm in the middle of the working face, and the minimum is 5 cm on two sides of the working face. The displacement is about 37 cm in the middle of the working face, while on both sides of the working face the displacement is 8 cm. Five meters behind coal wall, the greatest subsidence of top coal is 47 cm in the middle of the working face, while on both side of the coal wall the subsidence is 10 cm.

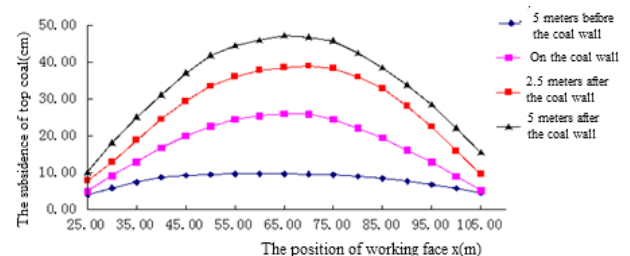


Figure 7: Cures of subsidence of top coal in different positions without supporting.

It can be concluded that the law of subsidence of the top coal along the direction of the working face is that the position of largest subsidence is 5 meters around the coal wall, and the subsidence of 2.5 meters behind the coal wall is the second, and, the subsidence on the coal wall is the smallest. The law of subsidence of the top coal on the inclination of the working face is complicated. In the middle of the working face the displacement is the largest, while on both side of the working face the displacement is the smallest. However, due to the slipping of the falling rock, the bottom of the goaf is filled. This will inevitably lead to less subsidence of the top coal in the bottom of the working face than for the top. Therefore the subsidence of the top coal of the working face is the largest in the central partial, the second largest on the upper, and the smallest on the lower. When the working face is excavated, not only the top coal will have a subsidence, as the coal wall will also produce a displacement. The horizontal displacement of the coal wall is shown in Figure 8.

From Figure 8, it can be seen that the coal wall will have greater levels of horizontal movement without supporting. It is close to 28 cm in the middle upper of the working face, which is the maximum amount. However, the minimum amount is about 10 cm on the both ends. Some measures should be taken to prevent spalling when supporting.

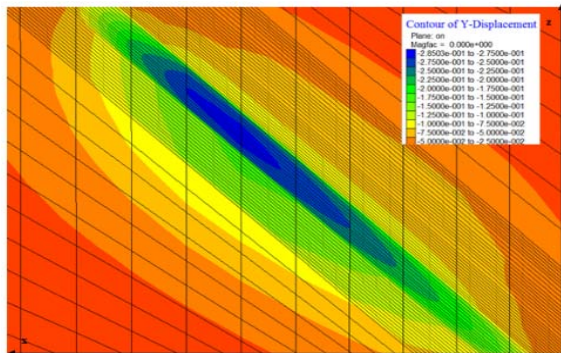


Figure 8: The horizontal displacement of the coal wall ahead supporting.

From Figure 9, it can be seen that the low stress distribution is similar to the law of displacement in the working face 2.5 meters away from the coal wall without supporting. The law is that the roof of the working face is mainly subject to tensile stress, which is arched. In the lower of the working face, the tensile stress is 2.396 Mpa, which is the largest. On both sides of the working face the stress gradually decreases and eventually becomes compressive stress. Due to the weight of rock, the stress of the

baseboard is mainly compressive stress. The compressive stress of the baseboard is about 3.0 MPa in the middle of the working face

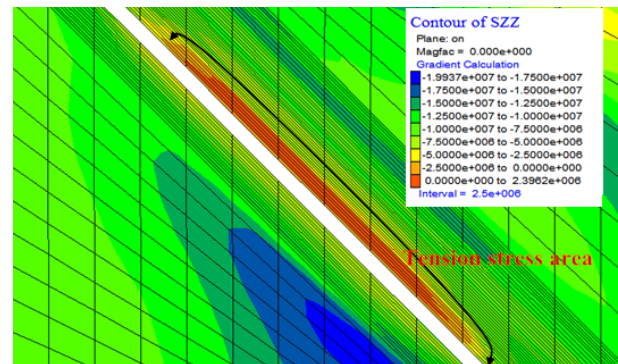


Figure 9: Analysis on the stress distribution along the dip of layer 2.5 m away from coal wall without supporting.

3.3 Analysis on the change of surrounding rock with supporting

From Figure 10 it can be known that the subsidence of the roof is reduced with supporting. The maximum displacement is 37.97 cm without supporting, while the displacement reaches only 28.29 cm with supporting. When comparing these two kinds of situations, the vertical displacement 2.5 meters away from the coal seam is shown in Figure 11.

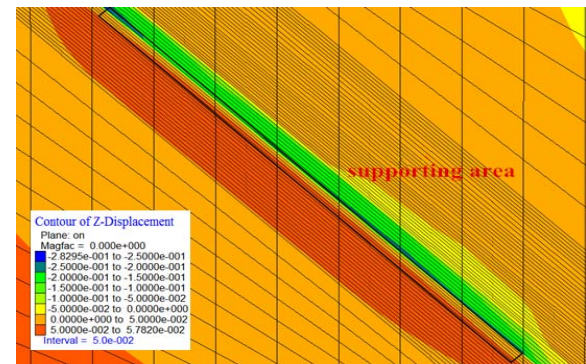


Figure 10: The vertical displacement nephogram along the coal seam 2.5 meters away from coal seam.

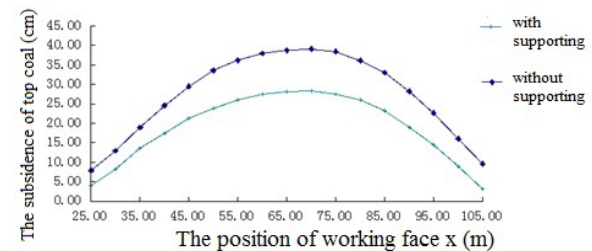


Figure 11: Vertical displacement curve of the support beam along coal seam 2.5 meters away coal wall.

From Figure 11, it can be concluded that the subsidence of the roof noticeably decreased, but the vertical displacement of the top coal is still arched. The maximum displacement is 37.97 cm without supporting in the lower working face, but it becomes 3.2 cm with supporting. At both ends of the working face, the minimum displacement is 3.2 cm. This explains how support can effectively reduce the subsidence of top coal.

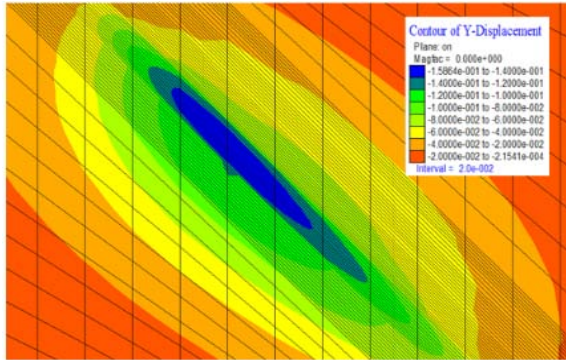


Figure 12: Displacement of coal wall near the working face with supporting.

Just as Figure 12 shows, the horizontal displacement of the coal wall reaches the largest value of 15 cm in the middle of the working face, and the minimum displacement is 4 cm on both sides of the working face with supporting. The maximum displacement of the coal wall is 26 cm without supporting. The supports can effectively reduce the displacement of the coal wall, but effective protective measures for mining should still be taken.

3.4 Analysis of the stress of the supporting bracket

In the simulation, the three-dimensional unit is used to simulate the supporting bracket, and the unit size is consistent with the support size. The length of the unit is 5.0 m, width is 1.5 m, and height is 4.0 m. The elastic modulus of the model is 1/15 of the coal layer, which is 581 MPa. The Poisson's ratio is 0.01. According to formulas (3) and (4), the bulk modulus and shear modulus of the unit can be calculated. The bulk modulus (K) is 197.73 MPa, and the shear modulus (G) is 287.79. The capacity (d) is 7500 kg/m³. The support force is shown in Figure 13.

$$K = \frac{E}{3(1-2\mu)} \quad (3)$$

$$G = \frac{E}{2(1+\mu)} \quad (4)$$

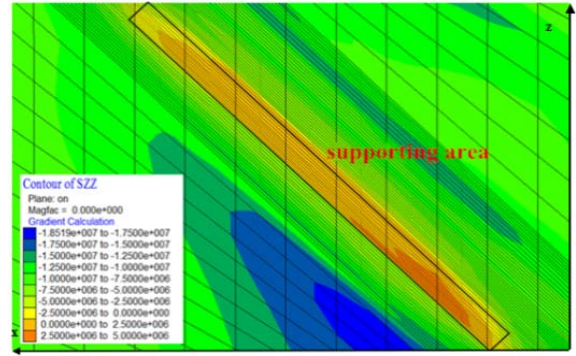


Figure 13: The stress distribution of the support region along the seam 2.5 meters away from coal seam.

As can be seen from Figure 13, the pressure of the support beam is 0.72 MPa in the lower working face. However, the pressure gradually decreases in both ends of the working face, and the smallest vertical stress is 0.28 MPa in the bottom layer. The minimum pressure is 0.21 MPa in the upper layer.

3.5 Determination the supporting resistance

According to the results of the simulation, the intensity of the supporting bracket from top coal is 0.72 MPa, and the supporting resistance was calculated according to the following formula (Wu, J. Y. et al., 2010a; Wu, Y. P. et al., 2007b; Zhao, Y. F. et al., 2007c):

$$P = n \cdot q \cdot \cos \alpha \cdot a \cdot b \quad (5)$$

- Where: n—safety factor, take 1.4.
- q—supporting intensity, take 0.72MPa.
- α—angle of coal seam inclination, take 45°.
- a—maximum control distance, take 5m.
- b—centre distance of supporting, take 1.5m.

The supporting resistance is 5346 KN, so the working resistance of the support should be greater than 5346 KN in practice.

4. CONCLUSIONS

Through the numerical simulation by FLAC^{3D}, the change of the surrounding rock and the bracket forces with and without support was analysed. The following conclusions can be made:

- (1) For deep inclined seams, the roof subsidence could be effectively reduced with stents supporting. The maximum displacement of the roof is 37.97 cm without supporting, while the amount of displacement reduced to 28.29 cm with supporting.
- (2) The deformation of coal walls could also be effectively reduced through the use of stents supporting. The largest deformation of the coal wall is 26 cm without supporting. The largest horizontal displacement of the coal wall reaches 15 cm in the middle of the working face, and the minimum

displacement of the two ends is 4 cm with supporting.

(3) By numerical simulation, it is concluded that the supporting intensity should be 0.72 MPa. The reasonable supporting resistance desired by A₆ coal layer is 3818 KN without considering the safety factor, and if the safety factor is taken to be 1.3, the final support resistance is 5346 KN.

5. ACKNOWLEDGEMENT

It is with great pleasure that we acknowledge the generous financial support of National Natural Science Foundation of China (project number: 51474017) and Natural Science Foundation of Xinjiang Uygur Autonomous Region of China (2014211B013).

6. REFERENCES

Li, Z. (2013). Analysis of surrounding rocks movement on long wall large height mining method along the strike in steeply dipping seam. Xi'an University of Science and Technology, 33p.

Ma, J. K., Liu, J., and Yue, G. W. (2013). Research on mechanical behavior of surrounding rock in steeply dipping seam mining. Mining safety & environmental protection, Volume 40, No. 4, pp. 27-30.

Qu, Q. Y. (2014). Study on mine pressure law of mining coal face with large angle and height in Huashan coal mine. China Coal Research Institute, 19p.

Wen, M. M. (2014). Study on strata moving laws and adaptability of Supports in fully mechanized coal face of high inclined coal seam. China University of mining & technology (Beijing), 11p.

Wang, H. W. (2010). Analysis of overburden structure feature in steeply dipping seam mining. Xi'an University of Science and Technology, 14p.

Wu, J. B. (2010). Numerical simulation on strata behavior regulation in steeply dipping seam mining. Coal Engineering. No. 5, pp. 80-82.

Wu, J. Y., Huang, W. P., and Ma, P. P. (2010). Study on the rule of stope roof movement and strata behavior in large inclined coal seam. Safety in Coal Mines. Volume 6, No. 22, pp. 6-9.

Wu, Y. P., Xie, P. S., and Yang, Y. G. (2007). Numerical simulation and complexity analysis of strata movement in exploiting steep coal seams group. Journal of Mining & Safety Engineering. Volume 24, No. 4, pp. 391-395.

Xie, P. S. (2011). Response of overburden structure and its stability around the long wall mining face area in steeply dipping seam. Xi'an University of Science and Technology, 16p.

Xie, P. S., Wu, Y. P., and Wang, H. W. (2015). Interaction characteristics between strata movement

and support system around large mining height fully-mechanized face in steeply inclined seam. Journal of mining and safety engineering, Volume 32, No. 1, pp. 14-19.

Zhao, Y. F., Zhang, X. Y., and Tu, M. (2007). Roof caving characteristic and strata behavior in exploiting steep coal seams. Journal of Mining & Safety Engineering. Volume 24, No. 2, pp. 231-234.

Theoretical analysis of support stability in large dip angle coal seam mined with fully-mechanized top coal caving

Zhang Yinghua, Ji Yucheng, Huang Zhian*, Gao Yukun, Ji Yuchen

State Key Laboratory of High-Efficient Mining and Safety of Metal Mines (University of Science and Technology Beijing), Ministry of Education, Beijing, China, 100083

ABSTRACT

Support stability is one of the problems in mining at large dip angle coal seams with fully-mechanized top coal caving. Support stability such as anti-dumping, anti-slip, and anti-rotation at support tail assembly were analyzed on the basis of the mechanic model of large dip angle coal seam along face dip and strike. The relations between each factor and stability were researched, which shows that firstly, the support stability was negatively correlated with dip angle along the face dip, secondly, higher top caving means lower anti-rotation at support tail assembly, and thirdly, with initial support force and working resistance of support enhanced, the support anti-slip, and anti-rotation at tail assembly can rise significantly. Along the strike, support strike critical tilting angle is proportional to dip angle, mining height, support weight, support width, and support force. Similarly, support strike critical slip angle is positively correlated with support force, friction coefficient of the roof, and metal support. According to the results of the mechanical analysis, support stability in large dip angle can rise efficiently and support slipping, dumping, and rotation can be avoided by selecting proper technological methods such as enhancing initial support force appropriately and choosing fit-designed support.

KEYWORDS: large dip angle; hydraulic support; stability

anti-dumping, anti-slip and tail anti-rotation along the face dip and strike.

1. INTRODUCTION

Fully-mechanized caving is the current development direction of mining, especially large dip angle mining. Hydraulic support is the key equipment in fully-mechanized caving (Zhizeng et al, 2010). The efficiency and safety will rise if support stability can be ensured. Under the influence of dip angle, the working load of the working face supporting system will decrease while external load resulting in support system instability will increase. Also, the probability of support slipping at the working face and extrusion between supports will be raised. The stability of hydraulic support is one of the problems in mining in large dip angle coal seams with fully-mechanized top coal caving (Zhiyan, 2007). Before this paper, the fracture mode of large inclined seam roof (Changyou et al., 2014), the support stability (Fengfeng et al., 2014), and the working resistance of support (Buzilo et al., 2010) were researched, mainly choosing supports and wall rock as the study objects at large dip coal seam. These studies and mainly focused on support stability along the face dip. The support stability in strike needs to be researched further.

In this paper, the hydraulic support is selected as the study object and its stability is analyzed via judging the

2. STABILITY ANALYSIS OF HYDRAULIC SUPPORT AT LARGE DIG ANGLE ALONG FACE DIP

2.1 *Anti-dumping stability analysis of support along face dip*

The complexity of the stress of the support at the working surface is caused by the complex ore pressure in large dip angle caving. The stability of hydraulic support can be affected by the dig angle, degree of crushing, support moving technology, mining and caving process, and hydraulic support structure and properties (Yuan et al., 2008; Changxi, 2014).

To analyze the stability of hydraulic support, a mechanical model was built in which the hydraulic support was assumed to be under uniform load. The hydraulic support mechanical model of anti-dumping along the face dip is shown in Figure 1.

*Corresponding author-email: huang_za@qq.com

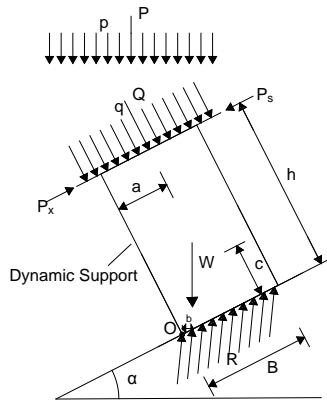


Figure 1: The hydraulic support mechanic model of anti-dumping along face dip.

When the large dip coal seam is mined, the actual movement of the roof is a curve that is close to the direction of gravity, and the force of the roof is also close to the direction of gravity, just as in Figure 1. Considering the simplification of the mechanical model, it is simplified to the gravity direction in this paper. During the mining period, the hydraulic support is inclined to the pressure P , which is also influenced by the support gravity W , the extrusion pressure P_s , P_x , initial support force q , and the supporting force R . The simplified model is shown in Figure 2. When the support is stable, the mentioned force should be in the mechanical equilibrium.

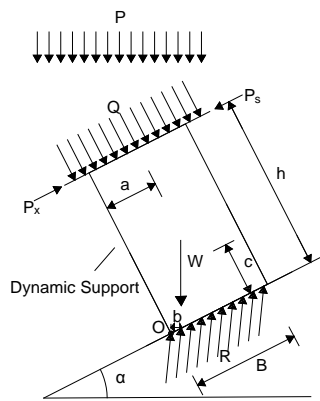


Figure 2: The simplified hydraulic support mechanic model of anti-dumping along face dip.

In the process of mining, the component force on each support changes. When the point of resultant force on the support is beyond the contact surface between the support base and floor, the support will dump. When the support along the face dip is at critical equilibrium state, it means that reaction force, of the floor to the support,

should be on the point O , and each overturning moment and anti-overturning moment caused by every component force of the support to point O should meet the torque limit equilibrium.

Hence, we can write:

$$P_s h + Ph \cdot \sin \alpha = P_x h + p \cdot \frac{B}{2} \cos \alpha + W b \quad (1)$$

$$b = \frac{B}{2} \cos \alpha - c \cdot \sin \alpha \quad (2)$$

h : height of the support

B : width of the support base

b : horizontal distance between gravity direction and edge of support base

c : height of centre of gravity

Due to formulation (2), horizontal distance between gravity direction and edge of support base b has negative correlation with the dip angle α . When the horizontal distance between gravity direction and edge of support base b and anti-dumping torque increases, the height of centre of gravity c , height of the support h and dumping torque of support decreases, and the stability of the support can be enhanced.

2.2 Anti-slip stability analysis of support along face dip

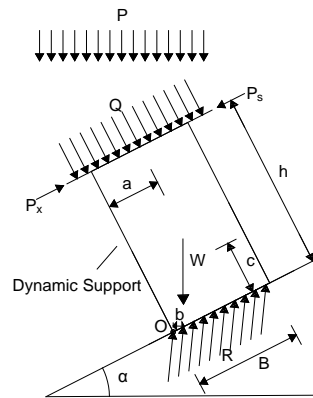


Figure 3: The simplified hydraulic support mechanic model of anti-slip along face dip.

As in Figure 3, the anti-sliding stability of support along the face dip is mainly by the influence of its own gravity W and roof pressure P , whose component force play a main role in causing the support slipping down. To ensure the anti-slip stability of support along the face dip, anti-slip fore F_{kh} must be greater than slip force F_h .

$$F_{kh} \geq F_h$$

Which means

$$[(W+P)\cos\alpha+Q]f \geq (W+P)\sin\alpha+(P_S-P_X) \quad (3)$$

F_{ki} : anti-slip force

f : coefficient of kinetic friction

According to the formulation, the existence of the initial support force increases the anti-slide force, and does not increase the downward force. So, the anti-slide capacity of the support can be significantly improved if the initial support force is improved.

Assuming that the support is only influenced by its own gravity, and the initial support force and the roof pressure are zero. Due to the equation mentioned, we can know:

$$Wf \cos\alpha \leq W \sin\alpha \text{ and } \tan\alpha \geq f \quad (4)$$

The related research shows that the friction coefficient of metal and coal seam is 0.35-0.40 (ZHIYAN, 2007). From the formulation, we can draw the conclusion that the support will slip if the dig angle is more than 15° ($\tan\alpha$ is greater than the friction coefficient of metal and coal seam). As a result, the anti-slip measures should be taken if the dig angle is beyond 15° .

2.3 Anti-rotation stability analysis of support tail along face dip

When using low caving coal process, the possibility of skew angle at the support tail should be considered. In the processing, the component force of caving coal will affect the support tail beam. If the anti-torque is less than the torque, the tail beam will rotate and result in support skewness. The anti-rotation mechanic model of support tail beam is shown in Figure 4.

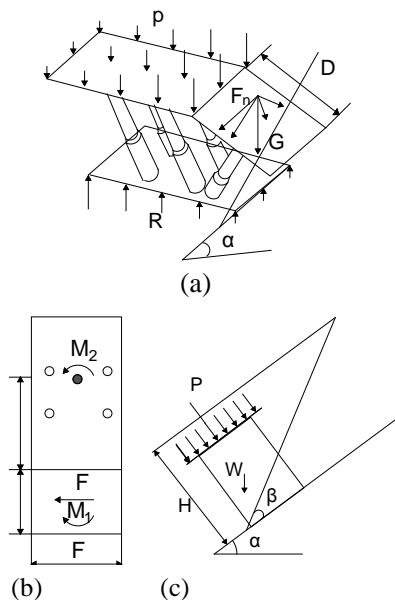


Figure 4: The anti-rotation mechanic model of support tail beam.

The torque and anti-torque, which are generated by the twisting force F_n and the anti-twisting force, should be kept in balance. This ensures that the dynamic support won't rotate.

The gravity of the coal mass G , which is acting on the cover of the support beam, the torsional force of the shield beam F_n , which is the component in the coal seam dip direction of the sliding friction force that the coal mass acts on the cover beam, and the torque of the shield beam M_1 are calculated as follows:

$$G = lBH\rho \quad (5)$$

$$l = D \sin\theta \quad (6)$$

$$F_n = Gf_2 \cos\alpha \sin\theta \cos\beta \quad (7)$$

$$M_1 = F_n(L+l/2) \quad (8)$$

f_1 : coefficient of kinetic friction

$\alpha + \beta$: stopping angle

f_2 : the friction coefficient of coal mass and shield beam

L : the distance from the base of the outer support to the geometric center

l : the projection length of the cover of the support beam

H : coal rock mass height

D : tail beam length

Q : density of bulk coal rock mass

Furthermore, we can know:

$$M_1 = Gf_2(L+l/2)\cos\alpha \sin\theta \cos\beta \quad (9)$$

When the friction force F_{kn} , which is generated by the pressure between the support, the floor and the roof interacts with F_n , the torsional force acting on the shield of the support beam, support to rotate point is influenced by the roof pressure and pillar working resistance, and the distance L (from geometric center of the support to the outer edge of the base) is related with the roof pressure distribution and pillar working resistance. The related research shows that the working resistance of the support is generally greater than that of the rear column (Zhongming et al, 2004). As is shown in Figure 4, due to the measurement of working resistance of the support column, and assuming the roof pressure in the roof has a linear uniform distribution, the model can be simplified to the mechanical equilibrium model of the load on a simply supported beam, and the position of the equivalent action can be determined.

Anti-rotation moment M_2 of the friction force between the base and the top plate is used to obtain the integral of the uniform load friction torque. We can know:

$$M_2 = \left(\frac{2P+W\sin\alpha}{4}\right)L_g f_3 \quad (10)$$

L_g : length of beam

f_3 : coefficient of kinetic friction between the support and the top floor

Conditions to ensure no skew is $M_1 \leq M_2$, torsional stability coefficient is K_3 .

$$K_3 = M_2/M_1 = \frac{(2P+W\sin\alpha)L_g f_3}{8G f_2(2L+l)\cos\alpha \sin\theta \cos\beta} \quad (11)$$

From the analysis of the K_3 , when caving height is increased, the tail bracket torsional stability coefficient is a nonlinear decreasing trend. When the support working resistance increases, K_3 shows a linear increasing tendency. Hence, the working resistance of the support is significantly affected by increasing the anti-rotation stability of the support and the torsion of the support.

3. STABILITY ANALYSIS OF HYDRAULIC SUPPORT AT LARGE DIG ANGLE ALONG STRIKE

3.1 Anti-dumping stability analysis of support along strike

The stability of hydraulic support is a common problem in the mechanical mining of large dip angle coal seam in the inclined direction of the working face. In fact, the hydraulic support is influenced by the angle of the coal seam, and the stability of the hydraulic support is also influenced by the trend of the direction of the slope and the angle of the back (Dongsheng et al., 2013; Panshi et al., 2012).

When the first weighting, periodic weighting, and roof fall occurs in the mining process, the roof becomes more and more fragmentary due to stress increasing, and the roof will trend to be downward. At the same time, under the influence of the inclined angle, the lateral stress of the support will also be increased, which greatly reduces the stability of the large dip angle coal seam. The mechanic model of support along the strike in the processing of downhill-mining was built to analyze the support stability of anti-slip and anti-dumping.

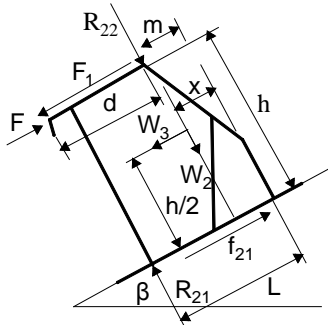


Figure 5: The support mechanic model of anti-dumping along strike when downhill-mining.

Figure 5 shows the support mechanic model of anti-dumping along strike when downhill-mining. According to the mechanical equilibrium conditions, we can know that:

$$f_{21} - F_1 + F = W_3 \quad (12)$$

$$R_{21} = W_2 + R_{22} \quad (13)$$

$$f_{21} = \mu R_{11} \quad (14)$$

$$R_{22}(L-M) + (F-F_1)h + 2W_2L/3 - W_3h/2 = 0 \quad (15)$$

Solving that equation, the critical tilting angle of the support along strike β :

$$\beta = \arccos \frac{3h\sqrt{N-36M^2-24LM}}{N\cos\alpha} \quad (16)$$

In the equation :

$$M = LR_{22} + Fh - F_1h - R_2m; N = W(16L^2 + 9h^2)$$

W_3 : The component force of the support gravity W , which is parallel to the surface along the seam to the bottom of the support direction

F_1 : Lateral force of roof

F : Support force of coal wall to support

μ : Friction coefficient between the support and the rock

d : length of the beam

m : The distance from the base of the outer support to the geometric center

L : length of support base

x : the distance from the center of gravity to the base of the support , $L/3$.

Due to the equation, in the process of mining, if the broken roof trends to slide, the roof lateral force F_1 along strike has a negative correlation with the critical slipping angle. The critical angle is proportional to the dig angle, mining height, support weight, width, and support force.

3.2 Anti-slip stability analysis of support along strike

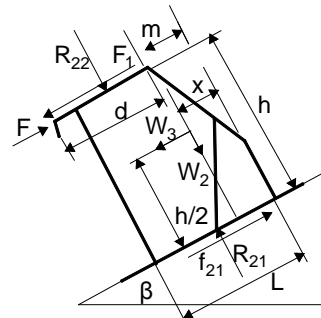


Figure 6: The support mechanic model of anti-slip along strike when downhill-mining.

According to Figure 6, we can know the equations:

$$f_{21} - F_1 + F = W_3 \quad (17)$$

$$R_{21}=W_2+W_{22} \quad (18)$$

$$f_{21}=\mu R_{21} \quad (19)$$

So, the critical slip angle α :

$$\alpha = \arccos \left(\frac{\mu F_1 - \mu F - \mu^2 R_{22} + \sqrt{W^2(\mu^2 + 1) - (F_1 - F - \mu R_{22})^2}}{(\mu^2 + 1) W \cos \beta} \right) \quad (20)$$

As a conclusion, raising the support force, or the friction coefficient between the support and the roof or floor, could lead to the increasing of critical slip angle. The support stability of anti-slip could be enhanced. Also, decreasing the support weight or the angle of the coal seam strike could have the same results.

4. CONCLUSIONS

(1) The mechanical model of anti-dumping, anti-slip and anti-rotation at the support tail along the strike at the large dip angle coal seam is established. When the dip angle of coal and caving height rises, the stability and anti-rotation at the support tail decreases. Also, it is significant to enhance the stability of anti-slip and anti-rotation by raising the initial support force and working resistance.

(2) The anti-dumping and anti-slip mechanic model was built and the equations of dumping angle and slip angle of support along the strike were derived.

5. ACKNOWLEDGEMENT

It is with great pleasure that we acknowledge the generous financial support of National Natural Science Foundation of China (project number: 51474017) and Natural Science Foundation of Xinjiang Uygur Autonomous Region of China (2014211B013).

6. REFERENCE

Buzilo V., Serdyuk, V. and Yavorsky. (2010). A Research of influence of support resistance of the stope in the immediate roof condition In: *New Techniques and Technologies in Mining - Proceedings of the School of Underground Mining*. pp. 127-130

Huang, Z.Z., Ren, Y.F. and Zhang H.J. (2010), Study on key technology of fully mechanized top coal caving in extra-thick soft coal seam with great dip angle. *Journal of China Coal Society*, Volume 35 No. 11, pp. 1878-1882.

Liu, C.Q. (2014), *The Movement Law of the Roof Rock and the Stability of the Support in the Big Dip Thick Coal Seam Large Mining Height Working Face in Quandian Coal Mine*. China University of Mining and Technology, Xuzhou, 67p.

LIU, C.Y., YANG, J.X., Yu, B., and Yang, P.J. (2014). Destabilization regularity of hard thick roof group under the multi-gob. *Journal of China Coal Society*, Volume. 39, No, 3, pp. 395-403.

Liu, Z.M., Chen, Z.H., Xie J.W. et al. (2004) Stability analysis and control measures of powered supports in greater inclined full-mechanized coal seam. *Journal of China Coal Society*, Volume 29, No. 3, pp. 264-268 .

Wu, F.F., Liu, C.Y., Li, J.W.(2014) Combination hydraulic support stability of working face in large inclined and “three-soft” thick seam. *Journal of Mining & Safety Engineering*, Volume 31, No.5 pp. 721-725, 732.

Xie, P.S., Wu, Y.P., Wang, H.W., Gao, X.C., Ren, S.G., and Zeng, Y.F. (2012). Stability analysis of incline masonry structure and support around longwall mining face area in steeply dipping seam. *Journal of China Coal Society*, Volume 37, No. 8, pp. 1275-1280.

Yuan, Y., Tu, S.H., Dou, F.J., et al. (2008). Support instability mechanism of fully mechanized top coal caving face with steep coal seams and its control. *Journal of Mining & Safety Engineering*, Volume 25, No. 4, pp.430-434.

Zhang, D.S., Wu, X., Zhang, W. and Fan, G.W. (2013). Stability analysis on support in large inclined coalface during special mining period. *Journal of Mining & Safety Engineering*. Volume 30, No. 3, pp. 331-336.

Zhang, Z.Y. (2011). Dynamic analysis on stability of hydraulic powered support in deep inclined fully mechanized wall and prevention slips measures. *Journal of China Coal Society*, Volume 30, No.7, pp. 705-709.

Theoretical research on roof damage of the fully mechanized top-caving mining coal seam with deep dip angle

ZHANG Ying-hua, LUO Qiang, HUANG Zhi-an*, GAO Yu-kun

State Key Laboratory of High-Efficient Mining and Safety of Metal Mines (University of Science and Technology Beijing), Ministry of Education, Beijing 100083, China

ABSTRACT

In order to study the roof pressure of steep coal seams, it is necessary to establish a related mechanical model to analyze the roof breaking law. Based on a working face of SDIC Nileke Mine, a mechanical model of roof failure of deep dip angle coal seam for roof pressure and periodic roof pressure was built in the study. The model was analyzed in dip direction and along the advancing direction of the working face. Based on the stress analysis of the model, the formula for the distance of roof breakage was given. The stress, deformation, and failure discipline of complicated full mechanized top-caving coal seam with deep dip angle were studied, which also enriched the theory of roof damage. The research findings provide a theoretical basis for coal mine safety support, and it can be used as a reference for other similar research on the roof failure discipline of full mechanized top-caving coal seams with steep dip angle.

Keywords: steep coal seam; roof failure; model research

1. INTRODUCTION

The mechanical model was established based on the SDIC Nileke Mine N11 first mining face in the study, and the working face diagram is shown in Figure 1. Assume the roof material is homogeneous, continuous, and isotropic. According to production practice and related research (ZHANG, L. L. et al., 2012), the force of the working face's hydraulic support is much less than the weight of overburden, and only a part of the stratum will have a significant impact on the working face pressure which contributes to the roof deformation and fracture. It will form a pressure equalization arch when the face roof is broken, and the height of the arch is usually 4 to 8 times the mining height (GUO, S. et al., 2013). The roof load of mechanical model was 8 times the mining height of rock weight above the hydraulic support (LIU, J. Y. et al., 2010).

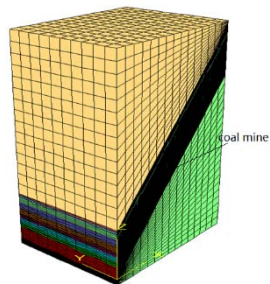


Figure 1: The working face schematic diagram.

2. MECHANICAL MODEL OF THE FIRST ROOF LOADING

Roof before first pressure can be treated as a four-side-fixed inclined plate (WANG, J. A. et al., 2010). The simplified model is shown in Figure 2. In order to calculate the stress distribution under the uniform load of the plate, the calculation was divided into two steps, which were analyzed in dip direction and along the advancing direction of the working face.

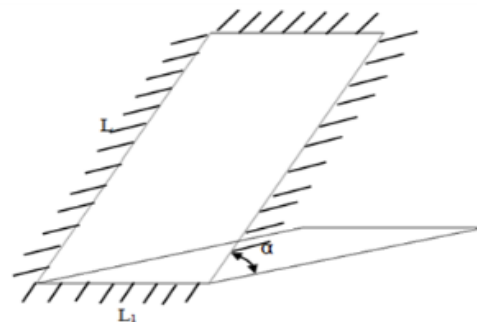


Figure 2: Model of four-side-fixed inclined plate.

2.1 Mechanical model along the direction of face advance

According to structural mechanics, the direction of face advance model was simplified and can be treated as girder with uniform load whose ends are both fixed (ZHANG, W. et al., 2006), as shown in Figure 3(a). Its bending moment is shown in Figure 2(b).

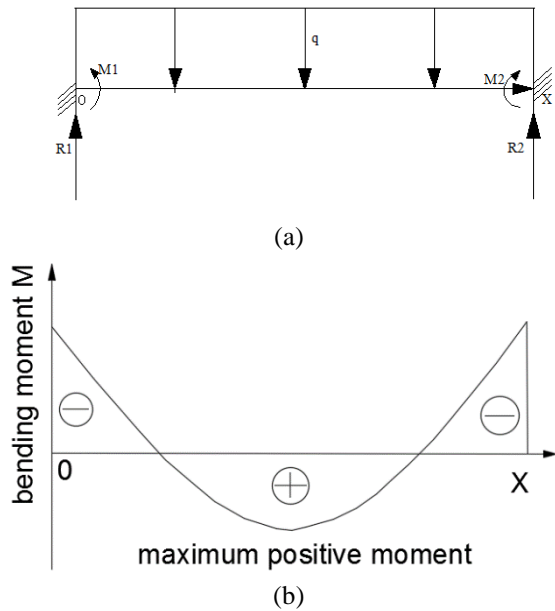


Figure 3: Bending moment distribution of fixed girder under uniform load in the advancing direction.

Fixed end bending moment (Timoshenko and Goodier,1951):

$$M_1 = -M_2 = -\frac{ql^2}{12} \quad (1)$$

End reaction of the girder ends: $R_1 = R_2 = ql/2$
Then:

$$M(x) = -\frac{qx^2}{2} + R_1x + M_1 \quad (2)$$

$$= -\frac{q}{2}\left(x - \frac{l}{2}\right)^2 + \frac{ql^2}{24}$$

In the above formula: q is uniformly distributed load, l is the beam length.

When working face along the advancing direction's mining distance is l , the uniformly distributed load of girder is

$$q = \gamma Hl \quad (3)$$

q is the uniformly distributed load of the girder along the dip direction of the face, γ is the density of overburden, H is the overburden thickness, l is the length of the girder.

When the stress of the rock σ reaches the tensile strength of the rock, roof fracture will occur, then:

$$\sigma = -\frac{M_{max}}{\omega} = -\frac{M_{max}}{\frac{bh^2}{6}} = -\frac{\frac{24}{6}M_{max}}{bh^2} = \sigma_t \quad (4)$$

In the above formula: ω is the beam bending section coefficient, b is the width of the beam, and h is the ply. When combining equation (3), the length of roof breakage formula is:

$$l_1 = \sqrt[3]{\frac{4bh^2\sigma_t}{\gamma H}} \quad (5)$$

According to the SDIC Nileke Mine field data, $\gamma=25 \text{ kN/m}^3$, $H=32 \text{ m}$, $b=1 \text{ m}$, $h=8 \text{ m}$, $\sigma_t=8 \text{ MPa}$, then $l_1=13.7 \text{ m}$.

According to the results, when the face advanced to about 13.7 m, around 6.8 m the top plate in the goaf will fracture.

2.2 Mechanical model along the dip direction of face

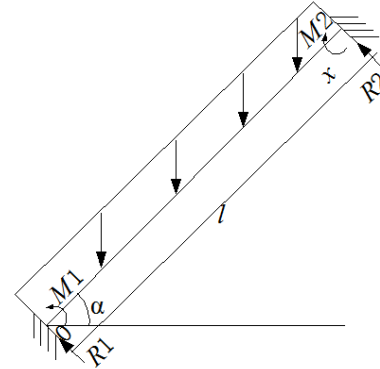


Figure 4: Force distribution of the girder along the dip direction of face.

The uniformly distributed load was decomposed into two mutually perpendicular loads one of which is perpendicular to the axis of the girder and the other along the axis. First, calculate the tensile stress generated by the load which is perpendicular to the axis of the girder; then calculate the tensile stress generated by the axial load; the total tensile stress is the sum of the two.

(1) Perpendicular to the axis of the girder

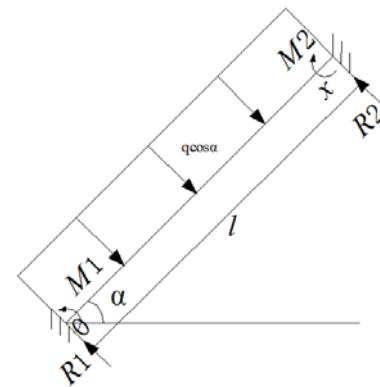


Figure 5: Force diagram of a section perpendicular to the axis of the girder.

Based on the analysis, the bending moment perpendicular to the axis of the girder is (WANG, J. A. et al., 2010):

$$M(x) = -\frac{q}{2} \cos \alpha \left(x^2 - lx + \frac{l^2}{6}\right) \quad (6)$$

M is the girder's axial moment, q is the uniform load, α is the angle of the girder, l is the length of the girder.

(2) Along the girder axis

Stress at both ends along the girder axis:

$$R'_1 = R'_2 = \frac{ql}{2} \sin \alpha \quad (7)$$

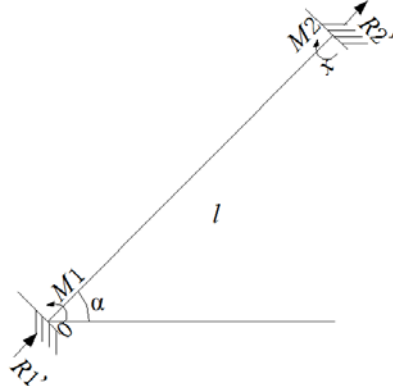


Figure 6: the axial stress of the girder along the dip direction.

$$N(x) = R'_1 - qx \sin \alpha = \frac{q}{2} \sin \alpha (l - 2x) \quad (8)$$

N is the axial tension of the girder, q is the uniform load, α is the angle of the girder, l is the length of the girder.

The stress distribution of the girder along the dip direction:

$$\sigma(x) = -\frac{M(x)}{\omega} + \frac{N(x)}{A} \quad (9)$$

And $\omega = bh^2/6$, $A = bh$.

Then:

$$\sigma(x) = \frac{3q \cos \alpha}{bh^2} \left(x^2 - lx + \frac{l^2}{6}\right) + \frac{q \sin \alpha}{2bh} (l - 2x) \quad (10)$$

σ is the stress of the girder, q is the uniform load, α for the inclination of the girder, l is the length, b is the width, h is the thickness of the girder.

Assuming:

$$\sigma(x) = \frac{3q \cos \alpha}{bh^2} \left(x^2 - lx + \frac{l^2}{6}\right) + \frac{q \sin \alpha}{2bh} (l - 2x) \leq \sigma_t \quad (11)$$

According to the SDIC Nileke Mine field data, $\gamma=25 \text{ kN/m}^3$, $H=32 \text{ m}$, $b=1 \text{ m}$, $h=8 \text{ m}$, $L=15 \text{ m}$, $\sigma_t=8 \text{ MPa}$, $\alpha=45^\circ$, then $x_1=20.5 \text{ m}$, $x_2=87 \text{ m}$.

According to the results of the analysis above, the middle of the roof in the advancing direction will break when the exposure length is 13.7 m along the

advancing of the working face, while the roof, which is about 20.5 m to 87 m apart from the bottom, will break in the dip direction.

3. MECHANICAL MODEL OF THE PERIODIC ROOF PRESSURE

Roof periodic pressure can be treated as a three-side-fixed inclined plate. A simplified model is shown in Figure 7. After first roof pressure, the calculation method of inclined plate's stress distribution under uniform load is the same as first roof pressure's when along the working face advancing distance to L_1 .

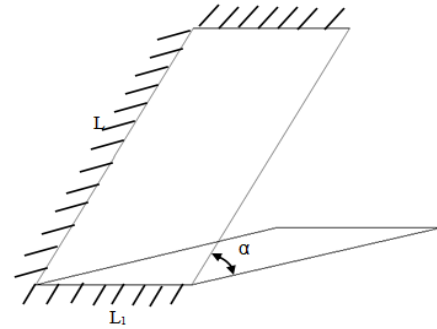


Figure 7: Model of three-side-fixed inclined plate.

3.1 Mechanical model along the face advance direction

A free-body diagram of the hanging stick along the face advance direction when the roof exposure length is l is shown in Figure 8.

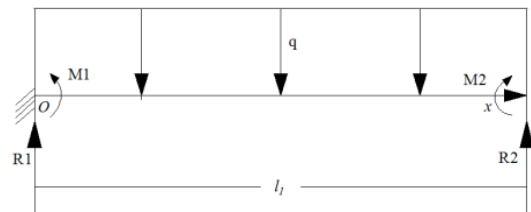


Figure 8: Free-body diagram of the cantilever along the face advance direction.

The formula of uniform load (q) is as shown in equation (3).

The bending moment of the cantilever:

$$M(x) = \frac{qx^2}{2} \quad (12)$$

Then:

$$\sigma_{min} = -\frac{M_{max}}{\omega} = -\frac{M_{max}}{\frac{bh^2}{6}} = -\frac{\frac{ql^2}{2}}{\frac{bh^2}{6}} = \sigma_t \quad (13)$$

In the above formula: σ is the stress of the beam, σ_t is the tensile strength of rock, ω is the beam bending section coefficient, b is the width of the beam, h is the ply, and l is the length of the cantilever. Combined with equation (3), the distance of roof breakage formula is:

$$l = \sqrt[3]{\frac{bh^2\sigma_t}{3\gamma H}} \quad (14)$$

According to the SDIC Nileke Mine field data, $\gamma=25 \text{ kN/m}^3$, $H=32 \text{ m}$, $b=1 \text{ m}$, $h=8 \text{ m}$, $\sigma_t=8 \text{ MPa}$, and $l=5.97 \text{ m}$.

According to the results, around 2.99 m of the top plate in the goaf will fracture when the face advances to about 5.97 m after first roof pressure.

3.2 Mechanical model along the dip direction of face

The mechanical model of the girder along the dip direction of the face is the same as Figure 4, and the way of analysis is also the same as first roof pressure in section 2.2.

We can get an inequality using equation (11).

According to the SDIC Nileke Mine field data, $\gamma=25 \text{ kN/m}^3$, $H=32 \text{ m}$, $b=1 \text{ m}$, $h=8 \text{ m}$, $L=15 \text{ m}$, $\sigma_t=8 \text{ MPa}$, $\alpha=45^\circ$, then $x_1=21.9 \text{ m}$, $x_2=88.9 \text{ m}$.

According to the results of the analysis above, the middle of the roof in the advancing direction will break when the exposure length is 5.97 m along the advancing of the working face, while the roof, which is about 21.9 m to 88.9 m apart from the bottom, will break in the dip direction.

4. CONCLUSIONS

The mechanical model of roof damage when first roof pressure and periodic roof pressure was built in this study based on the beam bending theory of elastic mechanics. The model was analysed in the dip direction and along the advancing direction of the working face. Based on the stress analysis of the model, the formula for the distance of roof breakage was given. Combined with field data, the range of the working face roof fracture was calculated.

The results of the study provide a reasonable hydraulic support scheme for the mine, and provide a theoretical basis for mine safety support.

5. ACKNOWLEDGEMENT

It is with great pleasure that we acknowledge the generous financial support of National Natural Science Foundation of China (project number:

51474017) and Natural Science Foundation of Xinjiang Uygur Autonomous Region of China (2014211B013).

6. REFERENCES

- GUO, S., KONG, X. F, KANG, T. H. and WANG, C. H. (2013). Support Load Analysis of Fully-mechanized Mining Face in Close Distance Coal Seam Under Goaf. *Safety in Coal Mines*, Volume 44, No. 5, pp. 214-217
- LIU, J. Y., LIAN, X. G. and HUANG, X. D. (2010). Experimental study on physical-mechanical properties of rock in Wangjialing Mine. *Mineral Engineering Research*, Volume 25, No. 2, pp. 17-19
- Timoshenko S, Goodier J N. (1951). *The Theory of Elasticity*.
- WANG, J. A., LI, D. Z. and MA, H. T. (2010). Study of rheological mechanical model of pillar-roof system in mined-out area. *Chinese Journal of Rock Mechanics and Engineering*, Volume 29, No. 3, pp. 577-582
- ZHANG, L. L., WU, Q. L. and LI, A. M. (2012). Research on the overlying strata movement rule of hard and super high seam with the propelling progress of working face. *Coal*, Volume 21, No. 2, pp. 6-8
- ZHANG, W., SU, M. L., YU, H. L., JIAO, Z., ZHANG, J. H. and YANG, H. J. (2006). The Elastic Mechanics Solution of Statically Indeterminate Beams Fixed at Two Sides under the Action of Concentrated Load. *Journal of North China Institute of Water Conservancy and Hydroelectric Power*, Volume 27, No. 4, pp. 40-42

Characteristics of acoustic wave velocity variation in the process of deformation and failure of loading coal

LI Xiangchun ^{a,b,*}, NIE Baisheng ^{a,b}, YANG Chunli ^c, CUI Zhe ^{a,b}, MAO Yanjun ^{a,b}

^a School of Resource and Safety Engineering, China University of Mining & Technology(Beijing), Beijing, China, 100083

^b State Key Lab of Coal Resources and Safe Mining, Beijing, China, 100083

^c School of Mechanics and Civil Engineering, China University of Mining and Technology, Beijing, China, 100083

ABSTRACT

For studying characteristics of acoustic wave velocity change during the deformation and fracture of loaded coal, using self-made acoustic parameter test system the characteristics of acoustic wave velocity change in deformation and fracture of loaded coal, the mechanism of stress influencing acoustic wave velocity change, the relation between stress and longitudinal wave velocity and the impossibility of longitudinal wave velocity forecasting coal structure is studied. The research results show that during the deformation and fracture of loaded coal the longitudinal wave and shear wave velocity increases firstly. When the coal is damaged the longitudinal wave velocity decreases and the shear wave disappears. The stress-strain change of coal is similar to the stress-wave velocity change highly. Based on coal structure the formula of stress and longitudinal wave velocity is established and the longitudinal wave velocity can be predicted well under different stress by the formula of stress and longitudinal wave velocity. The mechanism of stress influencing acoustic wave velocity change is coal structure change mainly.

KEYWORDS: coal body; loading; stress; deformation and failure; wave velocity

1. INTRODUCTION

Coal and rock dynamic disaster is a sudden dynamic appearance caused by the dynamic evolutions of coal body deformation and rupture. As a geophysical method, acoustic detection technology (Liu and Cheng., 1999) has been used in the prediction of coal and rock dynamic disasters. Due to the complexity of coal and rock dynamic disasters, if we want to truly achieve accurate prediction and forecast, the further research on the transmission mechanism of acoustic wave in the coal body, the spatial distribution of the acoustic wave and the space-time distribution of the acoustic wave are needed to be done. Therefore, it is necessary to research on the characteristics of acoustic wave propagation in the whole process of deformation and failure.

At home and abroad, a lot of work has been done to study the relationship between stress and wave velocity. In the condition of hydrostatic pressure, the velocity law of metamorphic variation rocks was studied by Christensen (1965). The results show that the rock wave velocity changes with pressure and pore arrangement in rock mass are related to the fracture morphology. Freund (1992) try to research on the variation of the longitudinal and shear velocity of the arenaceous rocks under the multi-parameter condition of the presence of clay content, porosity and confining pressure. Under the pressure of loading conditions, the existence state and closure state of

rock micro fissures and cracks were studied by King et al. (1995). It is concluded that there is a correlation between them and the velocity in the loading process and the shear velocity is related to the micro fracture and the crack closure which is perpendicular to the direction of propagation. Based on the analysis of the compaction effect of the 45 samples by Shi et al. (2004), the acoustic velocity of rock is related to the rock porosity, the pore fluid, the structure of the skeleton and the effective pressure on the rock. Based on case of the colliery No.3 of Huainan coalfield in Anhui Province, Peng et al. (2005) researched on the relations of acoustic velocity and mechanical characteristics of the lithofacies transition rock mass by the physical modeling study and numerical simulation technique. The results show that acoustic velocity increases with the stress increasing. In low stress conditions, the acoustic velocity increases obviously with the stress increasing and becomes steady with the stress increasing. The relationship between coal rock physics parameters and acoustic wave velocity was studied by (Meng and Zhang, 2006; Meng et al., 2008), which shows that the difference between the acoustic wave velocities of different lithology is relatively large, the acoustic wave velocities of rock are the main factors in addition to the composition and structure, mainly rock density and stress and groundwater factor. The granite, gneiss and marble and sandstone loading by Zheng et al. (2009), explore rock wave velocity with

*Corresponding author – email : chinalixc123@163.com

the response characteristics of changes. Experiment results show that the granite and gneiss during the linear elastic loading phase, velocity-stress rises linearly, velocity-stress is quadratic nonlinear change. The damage characteristics of salt rock under uniaxial loading are studied by using acoustic wave technique by Jiang et al. (2009). Along with the increase of the axial stress, the lateral wave velocity is smaller, and the wave velocity decreases rapidly after reaching the ultimate strength. Acoustic test to study the impact trend coal seam by Gong et al. (2012). The experiment was conducted under the condition of uniaxial stress loading path. The results show that with the increase of stress, the changes of longitudinal wave velocity of rock samples faster than the changes of longitudinal wave velocity of coal samples; in the elastic deformation stage of coal sample loading, the impact tendency of the coal rock is greatly increased, with the increase of stress, the deformation enters into the plastic stage, and the speed change area is gentle. It shows that there is a power exponent function relation between the stress change and the change of the wave velocity.

From these studies, it can be seen that the studies on the characteristics of acoustic wave change in the process of loading and failure of coal are less. Some studies are only preliminary studies. The change law and response mechanism of acoustic wave in different stage of coal deformation and failure need to be further analyzed. That the characteristics of acoustic wave variation in the process of coal loading and failure and analyses mechanism of stress influencing on the change of acoustic wave velocity were studied. The relationship between longitudinal wave velocity and stress is also discussed, and the possibility of predicting the structure of pore and fracture in coal body is discussed in order to provide theoretical basis for prediction of coal and rock dynamic disaster.

2. EXPERIMENT

2.1 Experiment System

The system includes coal sample clamping system, stress loading system, acoustic excitation system and wave receiving and acquisition system. The system structure of the system is shown in Fig.1. Coal sample holding system can be put into the standard sample of $\Phi 25\text{mm} \times 50\text{mm}$ standard coal sample, through the interface to connect stress loading system, which is connected to an acoustic wave excitation system and acoustic wave receiving system through an end head with sound wave transducer. Force loading system for manual hydraulic loading system, which can achieve, two different loading and triaxial loading process,

uniaxial loading and triaxial loading, axial pressure and confining pressure of different loading modes were achieved: constant pressure loading, step loading and cyclic loading, wave velocity variation under different loading modes and loading conditions were studied. At the two ends of the coal sample has two detachable ends, the first coal sample is put in the experiment, one end of the end is fixed, and the other end of the end head can be moved under the action of hydraulic pressure to achieve the loading of coal samples. Acoustic wave excitation system was developed by the State Key Laboratory of Southwest Petroleum University. For the sound wave pinger and acoustic probe (sound wave energy converter) its longitudinal wave frequency is 500 kHz and the shear wave frequency is 200 kHz. When system is connected to the digital oscilloscope, sound wave energy converter emitting end of the shear and longitudinal waves are in turn connected to the sound wave pinger of shear and longitudinal waves on the interface connecting lines, the digital oscilloscope external input terminals and EXT connection head of sound wave pinger are respectively connected with a moderate length of double shielded wire, and the two connecting head of the other sound wave energy converter are respectively connected to two CH1 and CH2 terminal on the digital oscilloscope. The acoustic wave receiving and acquisition system use the DSO7012B model of the dual channel oscilloscope, which can be used to measure the time difference between the longitudinal wave and the shear wave passing through the coal sample at the same time.

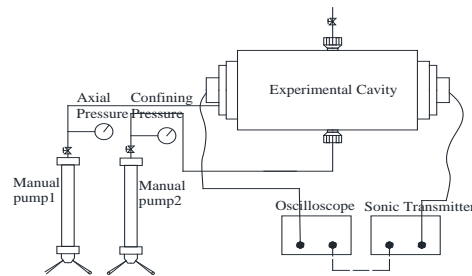


Figure 1: Schematic diagram of acoustic wave parameter test system in coal and rock

2.2 Coal Sample

The coal sampling of this experiment is come from Shanxi Guandi Coal Mine and Malan Mine2#, which is made to the standard of $\Phi 25\text{mm} \times 50\text{mm}$, coal sample section of flatness error is less than 0.02mm, the preparation of coal samples were vacuum drying (12 hours), and placed in dry bottles stored for a long time. Industrial analysis data of coal sample is shown in Table.1.

Table 1: Industrial analysis of the coal samples

coal mine	moisture content (%)	Air dry base volatile (%)	Dry basis ash (%)	Fixed carbon (%)
Malan 2#	0.48	24.55	5.69	69.29
Guandi	0.82	13.28	11.03	75.48

2.3 Experimental Programs

In this experiment, the variation of longitudinal and shear velocity of loading coal in uniaxial loading is studied. During the loading process, the test direction of wave velocity is the same as the direction of axial load of the axial load when the coal sample that the axial load of coal is loaded is destroyed. Limited by the design of the experimental instrument, the deformation of coal sample can only be measured in axial deformation.

2.4 Experimental Procedures

Firstly, coal sample is placed in a coal sample holding system, stress loading system, acoustic excitation system and the sound receiver acquisition system were connected, then the experiment starts, the acoustic velocity of coal samples was measured in the no pressure condition, and in accordance with the pre-set pressure of axial compression loading step by step, sample acoustic velocities of each stage on a loading pressure condition were measured, the experiment ends until the coal is destroyed.

3. EXPERIMENTAL RESULTS

3.1 Measure Principles

The usual method of measuring acoustic velocity is that measuring the ratio that sound wave transmission medium of unit length per unit time. The calculation formula is as follows.

$$V = \frac{L}{T} \quad (1)$$

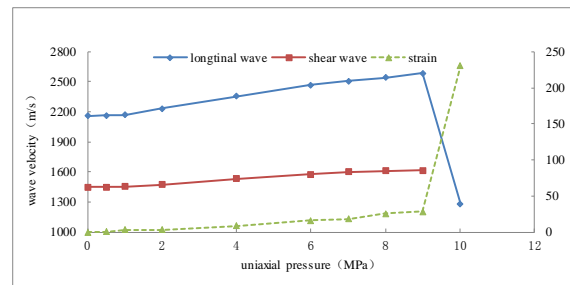
Where L the coal sample length, m; T the propagation time of acoustic wave in the medium, s; V the coal and rock mass acoustic wave velocity, m/s.

3.2 Experimental Results

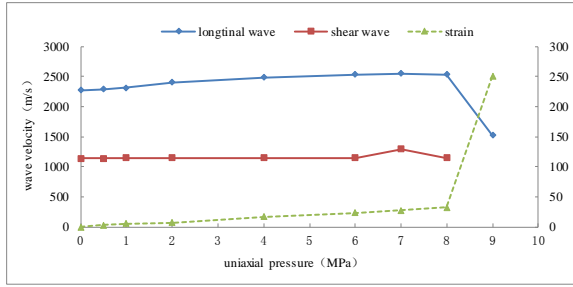
The experiment selected three groups of coal samples, Guandi mine, Malan mine 2#, the change trend of the experimental results is similar, therefore, the typical of a group selected of experimental data is analyzed. Fig.2 shows that the experimental results of the damage process for the Malan mine 2# coal and Guandi coal. The experimental results show that the velocity of longitudinal wave velocity of coal and rock mass increases until the rupture velocity of coal

body decreases, and the shear wave velocity increases firstly, but when the coal body breaks down, the shear wave disappears signally. This is mainly due to the coal and rock mass under loading, the deformation can be divided into two stages: (1) the elastic-plastic deformation stage, namely under stress, voids and fissures inside coal and rock tends to be closed; (2) deformation and failure stages, with the external load stress increasing, beyond the limits of coal and rock mass stress, coal body structure occurred deformation damage, pore fissure structure secondary development. The characteristics of the elastic and plastic deformation stage of the specimen and the change of the wave velocity in the deformation and failure stage. In the elastic plastic deformation stage, with the rapid closing of the pore crack, the acoustic wave velocity increases gradually, and the change of the longitudinal wave velocity is more obvious than that of the shear wave. In deformation and failure stages, after the uniaxial stress loading is beyond the limit of stress, and its internal structure began to damage, micro cracks and micro cracks begin develop to the coal rock broken and fractured (Fig.3). In the coal and rock mass fragmentation fracture moment, its shape variable occurs suddenly Corresponding sample in loading process of stress-strain of the force velocity law also appeared mutation, in specimen loading moment of failure, acoustic velocity decreased suddenly. The shear wave velocity attenuation is much larger than the attenuation of the longitudinal wave velocity, so that the acoustic wave receiving probe is difficult to receive its attenuation signal.

In addition, Fig.2 shows samples stress-strain curves and stress-wave velocity curve have a high degree of consistency. It is also indicated that the acoustic wave velocity can be used as an indicator, which can reflect the stress state and the deformation of the internal structure in coal and rock mass, especially, the change of longitudinal wave velocity can be used as a good indicator that evaluates the stress state and the deformation of the internal structure in coal and rock mass.



Malan 2# coal



Guandi coal

Figure 2: Wave velocity changes with increasing pressure under uniaxial loading



Malan 2# coal

Guandi coal

Figure 3: Fracture map of coal sample under uniaxial loading

4. THE RELATIONSHIP BETWEEN AND LONGITUDINAL WAVE VELOCITY

In a sense, the wave velocity of coal and rock mass mainly depends on the degree of porosity and fracture, namely porosity (Xu et al., 2015). Generally speaking, with the porosity increasing, the wave velocity decreases sharply. The experimental results show that the wave attenuation is very large, so it is difficult to receive the signal when the coal body breaks down. Therefore, it is more significant to study the longitudinal wave in the study of coal and rock deformation and rupture, it is necessary to analyze the relationship between the wave velocity and stress change.

Many scholars have done a lot of work to research on the relationship between wave velocity and stress. These relations include mainly two kinds of fitting formula and theoretical formula. For example, Wang and Xian (1988) for the rock under elastic stress, it is considered that the relationship between stress and elastic wave velocity can be expressed in a linear dependence coefficient. Nur (1997) considered that the stress and the wave velocity are in accordance with the two function relation. Huang (1991) established the relationship between wave velocity and stress by multiple regression analysis. Zhao and Wu (1999) based on linear elastic fracture mechanics and the assumption

that the shape of the crack in the rock is ellipsoid, the relationship between wave velocity and stress is established. Gong et al. (2012) establish a power function relationship between force and velocity by fitting. Chen et al. (2010) believe that there is a transition point in the change of the velocity of rock during the loading and failure process. Below the transition point, the relationship between stress and wave velocity is in the form of power function. And above the transition point, the relationship between stress and wave velocity is in accordance with the two functions. One of the characteristics of these formulas is that the mathematical relation between stress and wave velocity is mainly considered, and the characteristic of wave equation can be known that the elastic wave velocity is related to the structure of the elastic body. They are related to the porosity of the rock, the degree of fracture development, or the degree of closure of the hole under a stress state (Din, 1997). Therefore, it is more scientific and reasonable to establish the relationship between the structure change of the hole and the change of the wave velocity through the stress action. Previous studies have showed that there is a mathematical relationship between the longitudinal wave velocity and the porosity (Luan and Hu, 1985).

$$\phi = be^{aV_p} \quad (2)$$

Where ϕ the porosity, %; a, b the constant; V_p the longitudinal wave velocity, km/s.

Before and after the destruction of coal, porosity changed greatly. It is difficult to use a unified formula to show the porosity change before and after the destruction of coal, so it is difficult to establish a uniform stress effect on the wave velocity change formula. Based on this, the main consideration is to establish the formula of the velocity change of the stress before the failure.

This is the relationship (Tao et al., 2010) between porosity and stress before failure:

$$\phi = 1 - \frac{(1 - \phi_0)}{\exp(-K_y \sigma)} \quad (3)$$

Where ϕ the initial porosity, %; σ the stress, MPa; K_y the volumetric compression coefficient, MPa-1.

The formula (3) taken into the formula (2) can get the relationship between stress and longitudinal wave velocity:

$$V_p = \frac{1}{a} \ln \left(\frac{1 - \frac{(1 - \phi_0)}{\exp(-K_y \sigma)}}{b} \right) \quad (4)$$

According to the parameters measured in the laboratory, as Table.2 shown, a and b can be obtained by using the formula (4) to fit.

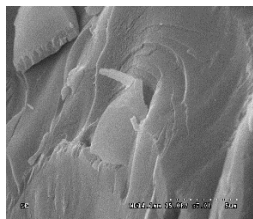
Table 2: a, b constant

coal	$\phi_0 / \%$	$K_y / \text{MP a}^{-1}$	a	b	r
Guandi	10.1	1.7×10^{-4}	4.21×10^{-5}	0.111249	0.9596
Malan 2#	5.4	6.2×10^{-4}	2.3×10^{-4}	0.087522	0.9956

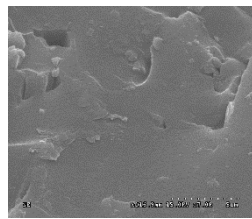
The Table 2 shows that the longitudinal wave velocity fitted by the formula has a high correlation with stress, which can be used to predict the longitudinal wave velocity of coal under different stress.

5. MECHANISM ANALYSIS OF STRESS INFLUENCING ACOUSTIC WAVE VELOCITY CHANGE OF COAL SAMPLES

Coal and rock mass, as a non elastic medium, its wave velocity is highly influenced by the development degree of the internal pore and fissure. When the coal body is subjected to stress, the primary fracture and pore are closed, with the stress increasing, the primary coal, the external cracks and pores are formed, developed and expanded constantly, and finally broke down. Because of the pore in the structure of the coal body, the crack and the new crack have a great influence on the velocity propagation of coal, the characteristics of coal pore and fracture structure are based on analyzing the law of acoustic wave velocity variation under the loading condition of coal body. As shown in Fig.4 The internal structure of coal was studied by scanning electron microscope. From the SEM pictures, it intuitively shows that there is a small amount of micro pores development on Malan 2# coal samples, of which layered structure can be seen obviously; structure of Guandi Coal Samples is relatively entire, and only trace amounts of cement debris existed.



Malan 2# coal



Guandi coal

Figure 4: SEM scanning under the magnifying multiple of 7k

The experimental results show that the longitudinal wave velocity and shear wave velocity of Malan 2# coal and Guandi coal are increasing with the stress increasing. This is mainly because the porosity decreases with the stress increasing, and causing the elastic deformation of the particles, the increase of the contact area between particles and the wave velocity of the particles. But at the same time, due to the coal and rock mass consisted of a number of different structures mutual cementation, and structural surface was formed in the interface of structure, which cause wave velocity decayed in the coal. Under the action of stress, these structural morphology and structural plane will be deformed and damaged, which will change the direction of acoustic wave propagation and increase the acoustic attenuation characteristics. And when the sound waves propagate in the coal and rock mass and encounters a structural morphology or structural plane, for example, the crack and crack development of the place, due to the presence of a certain reflectivity difference between the interface and the air, the sound wave in the transmission occurs at the same time, there will be some reflection and refraction. If the size of the pore is similar to the wavelength of the sound wave, or the difference is very large, the acoustic diffraction phenomenon will occur. And when the fissure is filled with the other phases of matter, the transmitted wave will occur to different degree of attenuation of energy. But before the destruction of coal, the increase of the velocity is larger than the decrease of the wave velocity. Therefore, the increase of the wave velocity is shown on the macroscopic. When the coal body stress reaches the peak value, the fracture in the coal seam is rapidly diffused, with the porosity increasing, the wave velocity decreased greatly.

6. CONCLUSIONS

(1) In the course of full stress and strain of coal loading, the longitudinal wave velocity increases firstly, and then decreases when the coal body broke, and the shear wave velocity also increases firstly, but when the coal body breaks, the shear wave signal disappears.

(2) Stress-strain curves of samples have an high consistency on the stress-wave velocity curve, which suggests that the wave velocity can be as the index of reflecting longitudinal wave velocity variations of coal and rock mass stress and the deformation of the internal structure, specially, velocity variations of longitudinal wave can be as a good evolution index of reflecting stress state of the deformation of internal structure.

(3) The relationship between the stress and the longitudinal wave velocity of coal is based on the change of the pore structure of the coal body, which can predict the longitudinal wave velocity of coal body under different stress states.

(4) With stress changed, the variation of acoustic velocity is increased mainly because that the effect of the wave velocity increasing is larger than the effect of the wave velocity decreasing before the destruction of coal, but the large increase of pore closure caused the wave velocity decreased largely after stress peak of coal body up to its peak.

7. ACKNOWLEDGEMENTS

This research is supported by National Natural Science Funds of China (51304212), Fundamental Research Funds for the Central Universities (2009QZ09). The authors would like to express their gratitude to the foundation.

8. REFERENCES

Chen X., Sun J. Z., Tan C. S. (2010). Relation between P-wave velocity and stress of rock samples and their unloading effect, *Chinese Journal of Geotechnical Engineering*, Volume 32, No. 5, pp. 757-761

Christensen N. I. (1965). Compressional wave velocities in metamorphic rocks at pressures to 10 kilobars, *Journal of Geophysical Research*, Volume 70, No. 24, pp. 6147-6164

Din W. X. (1997). A recent study on the relation between elastic wave velocity and stress of rock (rock mass), *Journal of Geological Hazards and Environment Preservation*, Volume 8, No. 3, pp. 43-47

Freund D. (1992). Ultrasonic compressional and shear velocities in dry clastic rocks as a function of porosity, clay content, and confining pressure, *Geophysical Journal International*, Volume 108, pp. 125-135

Gong S. Y., Dou L. M., Xu X. H. (2012). Experimental Study on the Correlation Between Stress and P-Wave Velocity for Burst Tendency Coal-Rock Samples, *Journal of Mining & Safety Engineering*, Volume 29, No. 1, pp. 68-70

Huang C. X. (1991). Study on elastic wave velocity of rock under confining pressure, *Chinese Journal of geotechnical engineering*, Volume 13, No. 2, pp. 32-41

Jiang D. Y., Chen J., Liu J. P. (2009). Experimental research on acoustic and dissolved properties of stress damaged salt rock, *Rock and Soil Mechanics*, Volume 30, No. 12, pp. 3569-3573

King M. S., Chaudhry N. A., Shakeel A. (1995). Experimental ultrasonic velocities and permeability for sandstones with aligned cracks, *International*

journal of rock mechanics and mining sciences & geomechanics abstracts, Volume 32, No. 2, pp. 155-163

Liu S. D and Cheng X. F. (1999). Acoustic wave detection technology in mining, *The Sixth National Academic Conference on Mining*, Weihai, pp. 107-110

Luan G. T. and Hu Y. L. (1985). Effect of moisture on the longitudinal wave velocity of rock, *Chinese Journal of geotechnical engineering*, Volume 7, No. 5, pp. 80-84

Meng Z. P. and Zhang J. C. (2006). Joachim Tiedemann. Relationship between physical and mechanical parameters and acoustic wave velocity of coalmeasures rocks. *Chinese Journal of Geophysics*, Volume 49, No. 5, pp. 1505-1510

Meng Z. P., Liu C. Q., He X. H. (2008). Experimental research on acoustic wave velocity of coal measures rocks and Its Influencing Factors, *Journal of Mining & Safety Engineering*, Volume 12, No. 4, pp. 389-393

Nur A. (1997) Effects of stress on velocity anisotropy in rock with cracks, *Journal of Geophysical Research*, Volume 76, No. 8, pp. 2022-2034

Peng S. P., Xie H. P., He M. C. (2005). Experimental study on velocity characteristics of lithofacies transition rock mass, *Chinese Journal of Rock Mechanics and Engineering*, Volume 24, No. 16, pp. 2831-2837

Shi G., Shen L. D., Wang J. X. (2004). Study on Compaction Effect of Rock Sonic Wave, *Acta scientiarum naturalium niversitatis pekinensis*, Volume 40, No. 2, pp. 177-183

Tao Y. Q., Xu J., Peng S. J. (2010). Yuan M. Experimental study of influencing factor of porosity and effective stress of gas-filled coal, *Rock and Soil Mechanics*, Volume 31, No. 11, pp. 3417-3422

Wang H. T. and Xian X. F. (1988). The study on characteristics of elastic wave propagation in rocks under complicated stress states, *journal of Chongqing university*, No. 5, pp. 104-112

Xu X. L., Zhang R., Dai F. (2015). Effect of coal and rock characteristics on ultrasonic velocity, *Journal of China Coal Society*, Volume 40, No 4, pp. 793-800

Zhao M. J. and Wu D. L. (1999). Ultrasonic velocity and attenuation of rock under uniaxial loading, *Chinese Journal of Rock Mechanics and Engineering*, Volume 18, No. 1, pp. 50-54

Zheng G. P., Zhao X. D., Liu J. P. (2009). Experimental Study on Change in Acoustic Wave Velocity When Rock Is Loading, *Journal of Northeastern University(Natural Science)*, Volume 30, No. 8, pp. 1197-1200

Numerical Simulation Technique for Gateroad Stability Analysis under Fractured Ground Condition

Lishuai Jiang^{a,b,*}, Atsushi Sainoki^b, Hani S.Mitri^{b,c}, Nianjie Ma^a

^a Faculty of Resources & Safety Engineering, China University of Mining & Technology, Beijing, China 100083

^b Department of Mining and Materials Engineering, McGill University, Montreal, Canada H3A 2A7

^c School of Civil Engineering, Henan Polytechnic University, Jiaozuo, China 454000

ABSTRACT

The ground stability of gateroads is a major concern in underground coal mines, especially where the surrounding strata are weak and fractured. This paper presents a novel numerical modelling technique for gateroad stability analysis based on a case study conducted in Zhaogu No.2 mine, China. Considering the occurrence of fractures and its weakening effect on the stiffness of rock mass, a tension-weakening model is implemented into FLAC3D, whereby the stiffness of rock mass is progressively decreased according to failure state. A relationship between the intensity of fractures and the residual properties is built. A parametric study of the tension-weakening model with respect to weakening parameter is carried out, and the results are compared to perfect elasto-plastic model and strain-softening model. The comparison shows that the tension-weakening model exhibits a noticeable effect on ground deformation and rock support loading, and can simulate more realistic behavior of a gateroad. The proposed model provides a rigorous approach for gateroad stability analysis and can be utilized for rock reinforcement design under similar geotechnical circumstances.

KEYWORDS: numerical simulation; ground stability; coal mine gateroad; tensile failure; fractures

1. INTRODUCTION

The stability of roadways is a long-standing issue in underground coal mines, especially for gateroads that serve and ensure the safety production for longwall panels. Ground stability and failure mechanisms of roadways vary depending on stress, geological and geotechnical conditions. However, as distinct from drifts and other roadways, the difficulties of maintaining gateroad stability are mainly due to weak surrounding rock mass and continuous geotechnical disturbance.

A large number of researchers analyzed gateroad stability with numerical modelling methods for the past few years. Among these studies, the most commonly used constitutive models are perfect elasto-plastic and strain-softening models using Mohr-Coulomb failure criterion (Shen, 2014; Zhang et al., 2015; Li et al., 2015).

Due to the sedimentary effect of coal-forming process, the surrounding rock mass of underground coal mines exhibit a geologically stratified structure. Under this geologic feature, tensile failure plays the dominate role when the surrounding rock is not subjected to high horizontal stress (Vaziri, 2001; Bakun-Mazor, 2009). This rock failure characteristic of underground coal mining activities is also demonstrated with field investigation (Hebblewhite and Lu, 2004) and numerical analysis (Shabanimashcool and Li, 2012). Since joints and

other fractures in rock can offer little or no resistance to tensile stresses, fractures will take place and develop in a brittle manner when rock mass is subjected to tensile stress. Previous studies (Cai et al., 2001; Mitri et al., 1995; Hoek et al., 2002) elaborate on the relation between the modulus of elasticity of rock mass and the occurrence of cracks and fractures, and corresponding formulas are proposed. In light of the previous studies examining the post-peak behavior of surrounding rock, it is therefore reasonable to take the variation of elastic modulus induced by tensile failure into consideration for stability analysis of openings in underground coal mines.

In the present study, tension-weakening model, which allows for the reduction in the stiffness of rock mass due to fracture generation, is developed with FISH (a programming language embedded within FLAC3D) and implemented into FLAC3D - a three dimensional explicit finite-difference program, in order to simulate the gateroad stability based on a case study in Zhaogu No.2 mine. In the numerical model, the failure state of rock mass is continuously monitored during analysis, and the properties are weakened according to different failure states to simulate the post-failure behavior. Numerical simulations with perfect elasto-plastic model, strain-softening model and tension-weakening model are conducted for comparison analysis to the field

measurement. In addition, a model parametrical study of the tension-weakening model is carried out to examine the effect of tension-weakening and provide basis for gateroad stability investigation and rock support design.

2. CASE STUDY

2.1 Geology and geotechnical overview of Zhaogu No.2 mine

Zhaogu No.2 mine is located in Xinxiang City, Henan Province, China. All panels in this mine are using retreat longwall method to extract coal seams. The coal seam is nearly horizontal with a mean thickness of 6.12m.

The target gateroad for this case study is the tailgate of panel 11050 at a depth of 600 m. The panel is approximately 180m wide along the dip and 2000 m long along the strike as illustrated in Fig. 1. The roof strata of this panel are mainly composed of mudstone, sandy mudstone and sandstone. The immediate roof is a layer of less than 2 m thick mudstone, which would cave and fall into the goaf, following the advance of coal extraction and shield support.

The tailgate of panel 11050 is 3.3 m high and 4.8 m wide. The gateroad is driven along the roof line of the thick coal seam, which leaves the ribs and immediate floor consisting of coal. Cable bolt support is employed as primary support, and wire mesh is utilized to prevent rock falling.

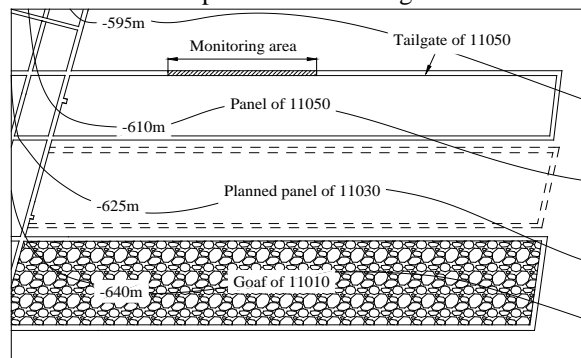


Figure 1: Plan view of local panel layout

2.2 Field monitoring of ground stability

As can be seen from field, as shown in Figure 2, the surrounding rocks are severely fractured into small and loose fragments after the gateroad excavation has advanced, which also is accompanied by significant rib convergence.

3. NUMERICAL SIMULATION WITH TENSION-WEAKENING MODEL

3.1 Local model based on case study

The tailgate of panel 11050 is numerically modelled to investigate its ground stability using finite-difference software FLAC3D.



(a) (b)

Figure 2: Field observations of severely deformed and fractured area (a) Roof (b) Rib

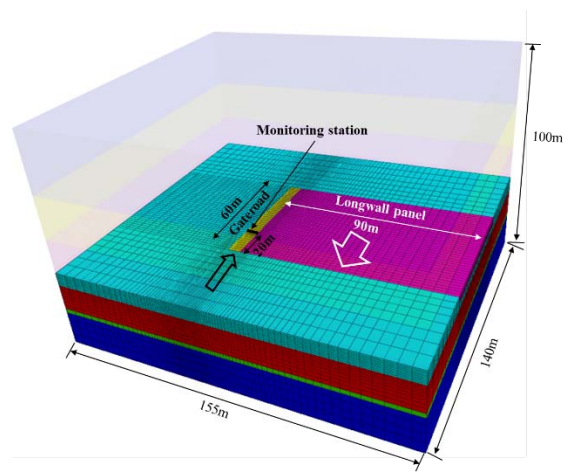


Figure 3: Isometric view of local model

Considering the symmetry of the panel with respect to its centerline, a 3D numerical model encompassing the tailgate of panel 11050 is generated, as shown in Figure 3. The dimensions of the model are 155 m wide, 140 m long and 100 m high, which are determined based on model sensitivity analysis with regard to size and mesh density. A vertical stress of 15 MPa is applied at the top model boundary to simulate overburden pressure. The horizontal-to-vertical stress ratio is set to 0.8 and 1.2 in the x- and y-directions, respectively (Yan et al.,

2013). No horizontal displacement is allowed at side boundaries, and no vertical displacement is allowed at the bottom boundary of the model. Rock mass properties for the numerical simulation, as listed in Table 1, are estimated from the intact rock properties and by using the generalized Hoek-Brown failure

criterion (Hoek et al., 2002). Values of softening parameters, ε_p and c_r are assumed according to the literature on strain-softening behavior in gateroad stability analysis using numerical simulation (Shen, 2014; Zhang et al., 2015; Li et al., 2015; Shabanimashcool and Li, 2012).

Table 1: Rock mass mechanical properties^a

Strata	Lithology	K (GPa)	G (GPa)	c (MPa)	ϕ (deg.)	c_r (MPa)	ε_p (%)
Roof	Sandstone	9.1	5.9	3.9	45	0.39	0.01
	Sandy mudstone	5.2	3.1	3.2	40	0.32	0.01
	Mudstone	2.4	1.1	2.1	35	0.21	0.01
Coal seam	Coal	1.3	0.6	1.4	31	0.14	0.01
Floor	Sandy mudstone	7.2	4.0	3.4	37	0.34	0.01
	Siltstone	9.6	6.5	4.2	47	0.42	0.01

^a K is bulk modulus, G is shear modulus, c is cohesion, ϕ is friction angle, c_r is residual cohesion, ε_p is plastic strain parameter at the residual strength

3.2 Model description of tension-weakening model

As indicated in Section 1, perfect elasto-plastic and strain-softening models are most widely utilized in numerical studies of ground stability of underground coal mines.

When perfect elasto-plastic behavior is assumed, the mechanical properties remain constant after the material yields and fails, which obviously is not in accordance with the true characteristic of most geological material (Cui et al., 2006). While, for the strain-softening model, the strength parameters are decreased with the increase in ε_p until reaching their residual values ultimately. However, for both of the constitutive models, elastic modulus remains constant, irrespective of the occurrence of failure.

The difficulty and feature of gateroad support lie with the ground stability that must be maintained not only during a gateroad driven period, but also when the panel is mined in retreat. According to the case study and numerical simulation, it is evident that the surrounding rocks are heavily fractured after the gateroad is driven. As the modulus of elasticity of rock mass is directly related to the occurrence of cracks and fractures (Cai et al., 2001; Mitri et al., 1995; Hoek et al., 2002), the variation of elastic modulus of the fractured area induced by tensile failure should be taken into consideration in order to simulate and analyze the gateroad stability properly, especially under mining influence. Otherwise, the stability analysis assuming constant elastic modulus may underestimate the ground deformation and fail to predict the stability condition.

For the purpose of simulating the variation of elastic modulus due to the tension-induced fractures, a novel numerical simulation technique, herein

referred to as tension-weakening model, is developed with FISH language and implemented into FLAC3D. The tension-weakening model is developed on the basis of the strain-softening model, whereby it overcomes the limitation of the conventional simulation techniques (Shen, 2014; Zhang et al., 2015; Li et al., 2015; Shabanimashcool and Li, 2012), that is, elastic modulus is kept constant regardless of rock mass failure and fracture propagation. Considering the observed brittle failure manner of the rock sample in laboratory experiments, both tension-weakening and strain-softening model employ an instantaneous decrease in strength parameters to the residual values and express the same post-peak behavior of rock. After the strength reduction, the parameters are kept at the residual values.

In order to take into account the variation of elastic modulus, a brittle tension-weakening parameter A is given as

$$E_r = A \cdot E_m \quad (1)$$

where E_r is the residual elastic modulus of rock mass after tensile failure takes place and E_m is the elastic modulus of rock mass estimated from experiment data. When tensile failure occurs, the elastic modulus decreases to the residual elastic modulus E_r in a brittle manner.

In order to characterize the post-peak behavior of fractured rock mass and estimate the residual elastic modulus, the Geological Strength Index (GSI) system is utilized to study the effect of different E_r on ground stability.

Although the GSI system developed by Hoek et al is generally used to determine the rock mass

deformability and strength on the basis of intact rock properties and geological structures, it is reasonable to assume that this index can be applicable to evaluating the intensity of fractures induced by tensile failure, such as blocky rock mass with tension-induced fractures shown in Fig. 4. In this study, GSI for rock mass with tension-induced fractures is defined as GSI_t . The implication is that GSI varies with the occurrence of tensile failure caused by the gateroad excavation.

For rock with $\sigma_c < 100$ MPa, the elastic modulus of rock mass E_m is estimated with GSI system from the following equation (Hoek et al., 2002):

$$E_r = \sqrt{\frac{\sigma_m}{100}} \cdot 10^{\left(\frac{GSI_t - 10}{40}\right)} \quad (2)$$

where σ_m is the uniaxial compressive strength of rock mass. Assuming $GSI_t = 90$ implies that no tensile failure occurs or no fractures and joints are induced by tensile failure, namely

$$E_m = \sqrt{\frac{\sigma_m}{100}} \cdot 10^{\left(\frac{90 - 10}{40}\right)} \quad (3)$$

By dividing Equation (2) by Equation (3), the weakening parameter A can be expressed as

$$A = \frac{E_r}{E_m} = 10^{\left(\frac{GSI_t - 90}{40}\right)} \quad (4)$$

In order to comprehensively investigate the weakening behavior after tensile failure, a parametrical study of the tension-weakening model is carried out with 4 different values of GSI_t (10, 30, 50, 70), and the obtained results are compared with those simulated with the perfect elasto-plastic and strain-softening models

4. RESULTS OF PAREMETRIC STUDY

Roof sag deformation is a major issue in ground control of gateroads. Failure or instability of the roof may cause not only economic loss, but more importantly also fatalities and injuries.

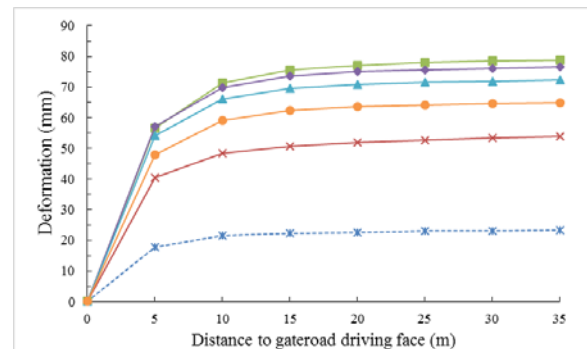
Figure 4 shows the evolution of roof sag for the different models during both the gateroad driven and retreat mining periods. As can be seen, for all the cases, large ground deformation takes place immediately after the gateroad is driven, and the increase rate of ground deformation becomes moderate or quite small after the distance between the monitoring station and the advancing driven face becomes greater than 15m. The surrounding rock begins to deform when the mining operation starts, however this increasing deformation is not noticeable until the mining face reaches a distance of 20 m from the monitoring station, and this effect is generally referred to as mining influence. As a result of the intensive mining influence ahead of mining face, the

gateroad undergoes significant ground destabilization and deformation.

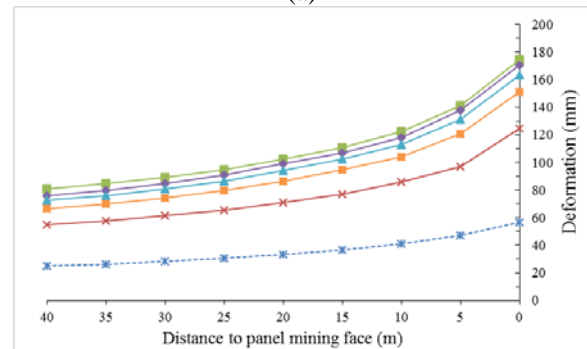
As shown in Figure 4, the ground deformation simulated with the strain-softening and tension-weakening models is remarkably larger than that simulated with the elastic-perfectly plastic model. This large difference is ascribed to the strength reduction and corresponding stress re-distribution during the post-peak behavior.

Also, the magnitude of deformation simulated with the tension-weakening model shows a negative correlation with GSI_t . This is due to the fact that high fracture intensity leads to low modulus of elasticity, ultimately resulting in severe deformation and instability. The maximum difference in deformation between the strain-softening and tension-weakening models during the gateroad driven period and the mining period is 25.1 mm and 49.7 mm for roof sag, 31.0 mm and 74.3 mm for floor heave, 51.9 mm and 99.8 mm for rib convergence. The large deformation induced by tension weakening is reasonable because, although the surrounding rocks almost stop deforming under the effect of ground self-stability and rock support, rocks that undergo tensile failure are weakened as a result of fractures development during the process of mining-induced stress readjustment, causing large deformation and instability.

---*--- Mohr-Coulomb ---x--- Strain-softening ---■--- GSI_t=10
 ---●--- GSI_t=30 ---▲--- GSI_t=50 ---○--- GSI_t=70



(a)



(b)

Figure 4: Evolution of roof sag (a) gateroad driven period;
(b) retreat mining period

5. CONCLUSION

A case study on gateroad stability at the Zhaogu No.2 coal mine in China is carried out. According to field observations and monitoring results, severe fractures and significant deformation severely destabilize the surrounding rock, which leads to potentially high risk to personnel safety.

Based on the geotechnical characteristics of the gateroad, a tension-weakening model allowing for the stiffening of rock mass due to tensile fracture generation is proposed and implemented into FLA3D to analyze the gateroad stability under severely fractured ground conditions. Taking into account the weakening effect of tensile fractures, a brittle tension-weakening parameter A is introduced to establish the relationship between the intensity of fractures induced by tensile failure and the residual property.

A model parametric study with respect to the weakening parameter is conducted, and the obtained results are compared to those simulated with the conventional elastic-perfectly plastic and strain-softening models. It is demonstrated that the effect of tension-weakening on the deformational behavior of the gateroad is significant during not only the gate road driven period but also the retreat mining period.

Considering the intensity of fractures induced by tensile failure and its weakening effect on rock mass, the tension-weakening model provides a rigorous simulation approach to studying the gateroad stability under fractured ground conditions. This model can be utilized for ground stability investigation, pillar design and rock reinforcement design (both primary and secondary support) under similar geotechnical circumstances.

6. REFERENCES

Bakun-Mazor, D., Hatzor, Y. H., & Dershowitz, W. S. (2009). Modeling mechanical layering effects on stability of underground openings in jointed sedimentary rocks. *International Journal of Rock Mechanics and Mining Sciences*, Volume 46, No.2, pp. 262-271.

Cai, M., Kaiser, P. K., & Martin, C. D. (2001). Quantification of rock mass damage in underground excavations from microseismic event monitoring. *International Journal of Rock Mechanics and Mining Sciences*, Volume 38, No.8, pp. 1135-1145.

Cui, X. Z., Jin, Q., Shang, Q. S., & Liu, S. T. (2006). Elastic-perfectly plastic Model Considering Variation of Elastic Modulus and Its Application. *Key Engineering Materials*, 306, pp. 1445-1448.

Hebblewhite, B. K., & Lu, T. (2004). Geomechanical behaviour of laminated, weak coal mine roof strata and the implications for a ground reinforcement strategy. *International Journal of Rock Mechanics and Mining Sciences*, Volume 41, No.1, pp. 147-157.

Hoek, E., Carranza-Torres, C., & Corkum, B. (2002). Hoek-Brown failure criterion-2002 edition. *Proceedings of NARMS-Tac*, pp. 267-273.

Li, W., Bai, J., Peng, S., Wang, X., & Xu, Y. (2015). Numerical modeling for yield pillar design: a case study. *Rock Mechanics and Rock Engineering*, Volume 48, No.1, pp. 305-318.

Mitri, H. S., Edrissi, R., & Henning, J. G. (1995). Finite-element modeling of cable-bolted stopes in hard-rock underground mines. *Transactions-Society For Mining Metallurgy And Exploration Incorporated*, 298, pp. 1897-1902.

Shen, B. (2014). Coal mine roadway stability in soft rock: a case study. *Rock Mechanics and Rock Engineering*, Volume 47, No.6, pp. 2225-2238.

Vaziri, H. H., Jalali, J. S., & Islam, R. (2001). An analytical model for stability analysis of rock layers over a circular opening. *International journal of solids and structures*, Volume 38, No.21, pp. 3735-3757.

Yan, S., Bai, J., Wang, X., & Huo, L. (2013). An innovative approach for gateroad layout in highly gassy longwall top coal caving. *International Journal of Rock Mechanics and Mining Sciences*, Volume 59, pp. 33-41.

Zhang, K., Zhang, G., Hou, R., Wu, Y., & Zhou, H. (2015). Stress evolution in roadway rock bolts during mining in a fully mechanized longwall face, and an evaluation of rock bolt support design. *Rock Mechanics and Rock Engineering*, Volume 48, No.1, pp. 333-344.

AUTHOR INDEX

Last Name	First Name	Pages
Abdellah	Wael	84
Abdelrahman	M.Z.	140
Abou-Jaoude	Elie	387
Abouelkair	M.M.	140
Ahmed	Samar	640
Aitao	Zhou	564, 585
Akhtar	Saad	605
Al Heib	Marwan	78, 640
Anderson	Ryan	611
Andersson	H.	24
Ang	Liu	564
Antunes	Maria M.	398
Aziz	Naj	432, 557
Baptista	Adelina L.F.	381
Barański	Adam	1
Basahel	Hassan	127
Belem	Tikou	102, 419
Benton	Donovan	71
Boltz	Shawn	71
Cai	Jiawen	552
Cai	Ming	12
Cain	Peter	145, 358
Cao	Chen	18
Cao	Jie	508, 514
Cao	Qinggui	335
Cao	Yang	591
Chang	De-qiang	204
Charette	Francois	60
Che	De-fu	199
Chen	Li	442
Chen	Shaojie	581
Chen	Wenxue	208, 471, 557
Chen	Xuexi	199, 520
Chen	Peng	520

Cheng	Li Zhen	419		
Cong	Xiang	536		
Coulibaly	Yaya	419		
Coulombe	Hugo	409		
Cui	Xuefeng	487,	494	
Cui	Zhe	681		
Dai	Linchao	503,	514,	540
De Souza	Euler	600,	611	
De Werk	Marco	364		
De Wit	Ben	329		
Deadman	Allison	176		
Debia	Maximilien	409		
Dehua	Chang	426		
Dejun	Miao	426		
Demir	Serenay	387		
Deng	Qigen	487,	494	
Descamps	Fanny	187		
Ding	Cui	595		
Ding	Shiwei	647		
Diogo	Miguel Tato	381,	398	
Domingues	Maria S.Q.	381		
Dongwei	Tan	426		
Duo	Yingquan	296,	527	
Durkin	Steven	176		
Duzgun	H. Sebnem	368		
Ekman	Jonas	133		
Esterhuizen	Gabriel	659		
Fan	Lin-yu	314,	634	
Fan	Penghong	482		
Feng	Caiyun	666		
Feng	Junfa	628		
Fujii	Yoshiaki	121		
Fukuda	Daisuke	121		
Galera	Jose-Miguel	24,	38	
Gao	Na	308,	314,	634
Gao	Xiang	471		

Gao	Yu-kun	154, 159, 258, 264, 268, 276, 281, 285, 442, 666, 672, 677
Gao	Ge	140
Gardhouse	Gillian	114
Ge	Shuang-you	204
Ghoreychi	Mehdi	108
Góis	Joaquim	398
Gong	Xuejiao	258
Gunzburger	Yann	640
Guo	Jiaqi	459
Hallé	Stéphane	409
Han	Jun	18
Hansen	Rickard	403
He	Xueqiu	341, 595
Henning	John G.	165
Henschel	Michael	133
Hobbs	Stephen	133
Hu	Qianting	351
Hu	Shoutao	482
Hu	Xincheng	552
Hu	Xinsheng	527
Huang	Guozhong	231
Huang	Shengchu	498
Huang	Zhi-an	154, 159, 258, 264, 268, 276, 281, 285, 442, 666, 672, 677
Huang	Zhiling	236, 622
Ji	Hongguang	591
Ji	Yuchen	264, 672
Ji	Yucheng	672
Jiang	Dongjie	628
Jiang	Lishuai	687
Jiao	Yuzhao	208, 557
Jin	Longzhe	231, 236, 308, 314, 346, 581, 622, 634
Johnson	Jeffrey	71
Kai	Wang	564, 585
Kang	Jiandong	248

Kang	Jianning	351		
King	Ronald F.	358		
Kodama	Jun-ichi	121		
Komljenovic	Dragan	375		
Konicek	Petr	45		
Kou	Weifeng	651		
Kumral	Mustafa	375,	387	
Kurnia	Jundika C.	605		
Lachapelle	Guillaume	409		
Lan	Bo	219,	248	
Lan	Tianwei	18		
Laouafa	Farid	108,	170	
Lawrence	Vincent	176		
Li	Ge	651		
Li	Haibin	651		
Li	Huamin	628		
Li	Huigui	628		
Li	Minghui	508		
Li	Song	236		
Li	Wen	243		
Li	Wenpu	508		
Li	Xiangchun	482,	616,	681
Li	Xue	208		
Li	Xuwei	432		
Li	Yage	231,	236,	346
Li	You-Rong	219		
Li	Zheyuan	471		
Li	Zhongbei	647		
Lian	Huiqing	214		
Liang	Qing-hua	254,	547	
Lin	Baiquan	531		
Liu	Chuang	628		
Liu	Fang-zhe	154		
Liu	Jia	268		
Liu	Jian-guo	308,	314,	634
Liu	Jing-xian	204		

Liu	Mingju	465, 487, 494
Liu	Wei Victor	552
Liu	Weihua	335
Liu	Xianglong	581
Liu	Xiliang	413, 459
Liu	Yanli	616
Liu	Yanwei	465
Loiselle	Georges	375
Lu	Jiang	346
Lu	Yueze	605
Luo	Qiang	285, 677
Ma	Hui	214
Ma	Nianjie	687
Ma	Yuntong	622
MacNeil	Bryce	96
Mäkitaavola	Karola	133
Manouchehrian	Amin	12
Mao	Ning	204
Mao	Yanjun	681
Martin	Lewis	71
Masny	Wojciech	54
Mattie	Brian	453
Mazaira	Alejandro	45
Mbonimpa	Mamert	102
McGill	Brian	453
Meguid	M.A.	140
Meng	Junqing	482
Mirzaghurbanli	Ali	432, 557
Mitri	Hani S.	6, 65, 84, 90, 96, 127, 181, 341, 465, 687
Moriya	Ryota	121
Morrish	Colin	393
Murdock	Greg	453
Mutke	Grzegorz	1
Neesham-Grenon	Eve	409
Nemcik	Jan	432

Ni	Xiaoming	471			
Nie	Baisheng	341,	482,	520,	595, 681
Niktabar	Seyed M.M.	193			
Ning	He	536			
Ou	Shengnan	236,			
Pierzyna	Aleksandra	1			
Piguet	Jack-Pierre	640			
Prusek	Stanislaw	54			
Ptacek	Jiri	45			
Pyon	Andrew	181			
Qin	Botao	291			
Qu	Wenzhong	616			
Raffaldi	Michael	71			
Rajwa	Sylwester	54			
Ran	Jerry	114			
Rao	K. Seshagiri	193			
Rasekh	Haleh	432			
Ren	Ting	18			
Renaud	Vincent	78,	640		
Richardson	Jerald	71			
Rietschel	C.	24			
Ruff	Todd	364			
Sainoki	Atsushi	6,	90,	181,	687
Sancho	Marcos	24,	38		
Sasmito	Agus	605			
Scoble	Malcolm	329			
Seymour	Joseph	71			
Shangkun	Shen	585			
Shen	Chunming	531			
Shen	Jie	308,	314,	634	
Shi	Quanlin	291			
Shnorhokian	Shahé	96			
Shrivastava	Amit Kumar	193			
Sjöberg	Jonny	133			
Skogseth	Trond	60			
Song	Shou-yi	276			

Souley	Mountaka	78	
Stöckel	Britt-Mari	133	
Sun	Qian	281	
Sun	Siheng	231	
Tan	Laizai	302	
Tang	Baoyao	453	
Tang	Guoshui	18	
Tasoren	Korhan	114	
Thoese	W.	24	
Tong	Shu Jiao	296,	477
Tshibangu	Jean-Pierre	187	
Tulu	Ihsan Berk	659	
Vennes	Isaac	65	
Veyrat	Santiago	24,	38
Walentek	Andrzej	54	
Wan	Long	459	
Wang	Bo	514	
Wang	Dong	531	
Wang	Haiyan	302,	574
Wang	Hetang	291	
Wang	Hui	154,	159, 666
Wang	Jianhua	459	
Wang	Jun	658	
Wang	Kai	514,	540
Wang	Rujun	296,	477, 527
Wang	Shu	236,	346
Wang	Shuren	413	
Wang	Wei-xiang	308,	314, 346, 634
Wang	Zhiliang	325	
Wei	Shanyang	647	
Wen	Jiejie	487,	494
Wickramanayake	Anura	133	
Wu	Haijun	302	
Wu	Jun	208	
Wu	Zongzhi	296,	527
Xie	Changzhen	335	

Xu	Changfu	302, 574						
Xu	Teng	616						
Yang	Chunli	616, 681						
Yang	Fei	159						
Yang	Junzhe	291						
Yang	Longlong	647						
Yang	Shengqiang	552						
Yang	Tao	520						
Yang	Wentao	319						
Yao	Haifei	225, 302, 574						
Yaylaci	Evren Deniz	368						
Yu	Hongming	447						
Yun	Xiaoyou	453						
Yuyu	Kong	564						
Zeng	Hongbiao	447						
Zhang	Haiqing	413						
Zhang	Hongwei	18						
Zhang	Hui	341						
Zhang	Kai	319						
Zhang	Lang	531						
Zhang	Lihui	291						
Zhang	Qun	225, 574						
Zhang	Rui	351						
Zhang	Sai	335, 487						
Zhang	Shouming	335						
Zhang	Ying-hua	159, 258, 264, 268, 276, 281, 285, 442, 666, 672, 677						
Zhang	Yue	319						
Zhang	Yuebing	325						
Zhang	Li	498						
Zhao	Ruhui	658						
Zhao	Xinglong	329						
Zhao	Xue	231						
Zheng	Jiewen	208						
Zheng	Zhong-ya	574						
Zhou	Peiling	285						

Zhou	Xiuhong	552
Zhou	You	658
Zhu	Bin	651
Zhu	Feng	18
Zhu	Hong-qing	574
Zhu	Hongjie	214
Zhu	Hongmin	622
Zhu	Yuanyue	319
Zimmerman	Karsten	145
Zou	Weifeng	248
Zou	Zhengsheng	413